CHEMICAL
REVIEWS

pubs.acs.org/CR

Review

The Biologically Relevant Coordination Chemistry of Iron and Nitric Oxide: Electronic Structure and Reactivity

Nicolai Lehnert,* Eunsuk Kim,* Hai T. Dong, Jill B. Harland, Andrew P. Hunt, Elizabeth C. Manickas, Kady M. Oakley, John Pham, Garrett C. Reed, and Victor Sosa Alfaro

Cite This: https://doi.org/10.1021/acs.chemrev.1c00253

Read Online

ACCESS | Metrics & More | Article Recommendations

ABSTRACT: Nitric oxide (NO) is an important signaling molecule that is involved in a wide range of physiological and pathological events in biology. Metal coordination chemistry, especially with iron, is at the heart of many biological transformations involving NO. A series of heme proteins, nitric oxide synthases (NOS), soluble guanylate cyclase (sGC), and nitrophorins, are responsible for the biosynthesis, sensing, and transport of NO. Alternatively, NO can be generated from nitrite by heme- and copper-containing nitrite reductases (NIRs). The NO-bearing small molecules such as nitrosothiols and dinitrosyl iron complexes (DNICs) can serve as an alternative vehicle for NO storage and transport. Once NO is formed, the rich reaction chemistry of NO leads to a wide variety of biological activities including reduction of NO by heme or non-heme iron-containing NO reductases and protein post-translational modifications by DNICs. Much of our understanding of the reactivity of metal sites in biology with NO and the mechanisms of these transformations has come from the elucidation of the geometric and electronic structures and chemical reactivity of synthetic model systems, in synergy with biochemical and biophysical studies on the relevant proteins themselves. This review focuses on recent advancements from studies on proteins and model complexes that not only have improved our understanding of the biological roles of NO but also have provided foundations for biomedical research and for bio-inspired catalyst design in energy science.

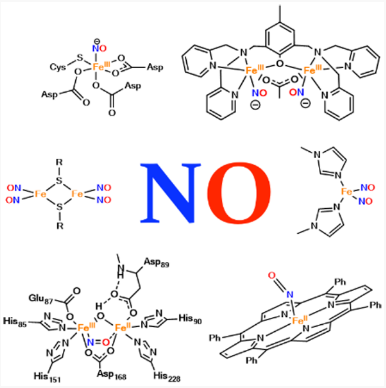

CONTENTS

Received: March 30, 2021

Scheme 1. Latimer Diagram of Nitrogen Species of Various Oxidation States in Acidic (pH = 0) and Basic (pH = 14) Solution[a]

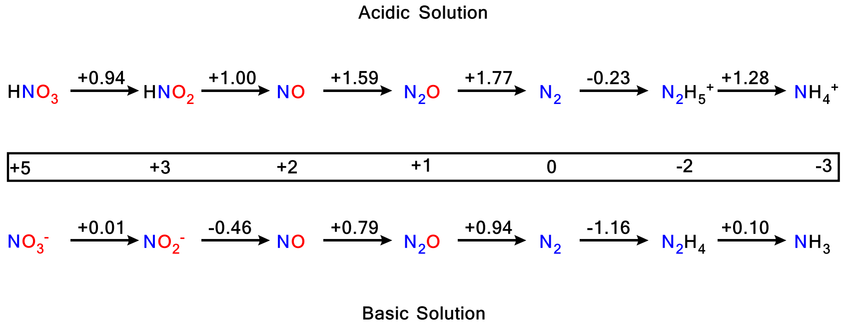

[a] Reduction potentials are referenced against the normal hydrogen electrode (NHE).

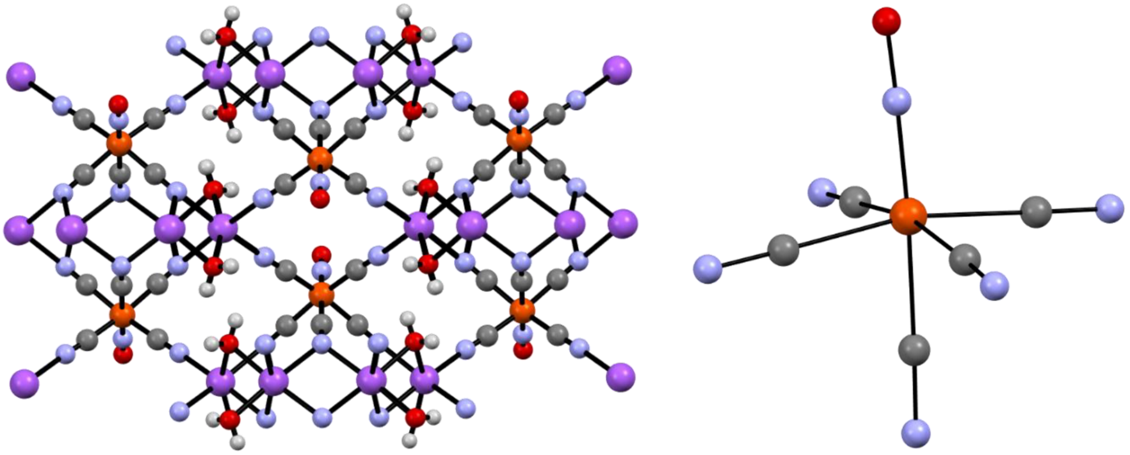

Figure 1. Crystal structure of sodium nitroprusside. Left: lattice. Right: molecular structure.[28] On the right, the sodium counter ions are omitted for clarity.

1. INTRODUCTION

Nitric oxide (nitrogen monoxide, NO) is a colorless gas that owes its uniqueness to the fact that it is a diffusible free radical species that is relatively stable. NO exists in equilibrium with the corresponding ONNO dimer, though with an unfavorable equilibrium constant of 1.12×10^{-5} at 316 K.[1] Correspondingly, the free ONNO dimer is more present at lower temperatures.[1−3] NO has a bond length of 1.15 Å, which is intermediary of the bond lengths for N_2 (1.09 Å) and O_2 (1.21 Å),[4,5] and also in between the N−O distances of the nitrosonium ion (NO^+, ~1.06 Å) and the nitroxyl anion ($^3NO^-$, ~1.20 Å).[4] In the ONNO dimer, the N=O distance is 1.15 Å and the N−N bond distance is 2.26 Å, indicating a weak N−N interaction. Moreover, the ONNO dimer shows the cis conformation and is approximately planar.[6]

Despite being a heteronuclear diatomic, NO is relatively nonpolar, as evident from the relatively low intensity of its N−O stretching mode in IR spectroscopy, observed at 1876 cm^{-1}.[7] Notably, the $^2\Pi$ ground state of NO splits into $^2\Pi_{1/2}$ and $^2\Pi_{3/2}$ components (differing in energy by ~120 cm^{-1}) due to spin-orbit coupling of its single π^*-orbital electron.[7] Consequentially, this gives rise to not only P and R rotational branches in the gas phase vibrational spectrum of NO, but also the Q rotational branch normally forbidden in diatomic species.[7] In organic solvents, this fine structure collapses into a broad, weak IR signal with ε = ~20 M^{-1} cm^{-1}.[5] For the ONNO dimer, strong N−O stretching modes are observed at 1860 and 1788 cm^{-1}, corresponding to the symmetric and antisymmetric combinations, respectively.[3] By comparison, the N−O stretch of NO^+ (in $NOBF_4$) and $^3NO^-$ (in NaNO) is observed at 2387 cm^{-1} and 1358 cm^{-1}, respectively.[7,8] NO owes its importance in biology, in part, to it being a diffusible gas in biological media with diffusion constants of 3300 μm^2 s^{-1} and 390 μm^2 s^{-1} for physiological buffer and biological systems, respectively.[9,10] The solubility of NO in aqueous solution is 1.4 and 1.9 mM atm^{-1} at 310 and 298 K, respectively;[11,12] however, greater solubility is observed in certain organic solvents (i.e., dimethyl sulfoxide and cyclohexane show NO solubilities of 3 and 15 mM atm^{-1}, respectively, at 298 K).[12]

The redox properties of relevant nitrogen-containing species in aqueous media are pH dependent as summarized in Scheme 1; most relevant here are the reductions of nitrite to NO and of NO to HNO.[5,13] With respect to the latter, reduction of NO to $^3NO^-$ is estimated to occur at a potential of -0.68 V (vs. NHE) in aqueous media at pH 7.[14] NO can also be generated from the reduction of NO^+, which is estimated to occur at the highly oxidizing potential of +1.2 V (vs. NHE) in aqueous media at pH 0.[15]

1.1. Historical Perspective and Classification of Nitrosyl Complexes

NO is a molecule with a long history in coordination chemistry research,[16] due to its very interesting properties as a ligand, and its reactivity with transition metals has been studied for more than 150 years.[17,18] A particular fascination of this chemistry originates from the fact that NO is a "non-innocent" (i.e., redox-active) ligand[19,20] that can change oxidation state when binding to a transition-metal center, with common oxidation states being NO^+, $NO^\bullet$, and NO^-. In addition, the bonds between NO and transition metals are often times very covalent, which provides further challenges in arriving at sound descriptions of the electronic structures of these complexes. However, with the rise of powerful spectroscopic and theoretical methods in the last 20 years, we are now in a position to tackle many of these challenges and obtain detailed electronic structure descriptions of transition-metal−NO complexes.[21] The electronic structures of these systems can then further be linked to their observed properties and reactivities, and ultimately to their functions in biology. The main focus of this review is to provide this link between geometric and electronic structure and function in the context of the biologically relevant coordination chemistry of mono- and dinitrosyl complexes of iron. In this way, we complement other recent reviews on the chemistry of NO and its redox congeners (nitrate (NO_3^-), nitrite (NO_2^-), nitroxyl (NO^-/HNO), hyponitrite ($N_2O_2^{2-}$), etc.; generally termed "NO_x" species) in biology.[22−27]

The first NO complex was reported by Playfair in 1849, sodium nitroprusside (SNP), $Na_2[Fe(CN)_5(NO)]$,[29] which was prepared by the reaction of $K_4[Fe(CN)_6]$ with nitric acid and obtained as an orange-red solid.[30] The crystal structure of this compound shows discrete $[Fe(CN)_5(NO)]^{2-}$ octahedra with linear FeNO units (see Figure 1) and unexpectedly short Fe−NO bond lengths of 1.63 Å,[28] which is actually similar to the Fe−O distances typically observed in high-valent Fe(IV)=O intermediates.[31,32] This indicates the presence of a very strong Fe−NO bond in SNP, which is further corroborated by the Fe−NO stretch of this complex of 652 cm^{-1} (Fe−NO force constant: 4.05 mdyn/Å).[33] This metal−NO stretching frequency is one of the highest reported to this date. The N−O stretch of SNP is located at 1939 cm^{-1},[33] indicative of distinct NO oxidation. From these spectroscopic data, the electronic structure (electron distribution in the FeNO unit) of SNP is unclear. On the basis of the fact that the complex shows a strictly diamagnetic ground state, however, the iron center is in the low-spin (ls) state, which means that the nitroprusside dianion likely has one of three possible electronic structures, as shown in Scheme 2. Inspired by these results, inorganic chemists went to work, and many other transition metal cyano/nitrosyl, as well as carbonyl/nitrosyl and halide/nitrosyl complexes were prepared in the 1950s and 1960s. This work is summarized in refs 34−36. Another iconic compound obtained in these studies is Hieber's anion, $[Fe(CO)_3(NO)]^-$,[37] whose electronic structure is still an unsettled area of research.[38−40] This tetrahedral complex is diamagnetic and has Fe−NO and N−O bond lengths of 1.659 and 1.212 Å, respectively. The Fe−N−O angle is observed at 180°. From vibrational spectroscopy, the N−O stretch was identified at 1647 cm^{-1}.[41]

Scheme 2. Possible Electronic Structures of SNP

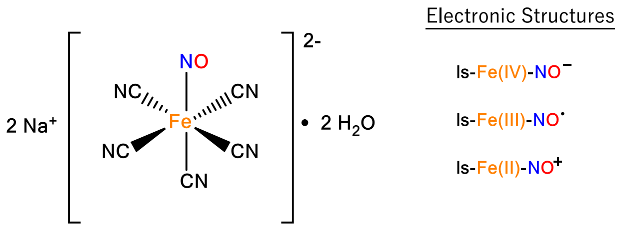

Another interesting observation regarding SNP was the discovery in the 1920s that this compound has beneficial physiological effects and is able to lower the blood pressure in mammals, similar to the effects of sodium nitrite.[42,43] It was later shown that SNP is in fact a drug that safely and efficiently lowers the blood pressure in severely hypertensive patients when administered intravenously.[43] Furthermore, SNP improves general cardiac function following heart failure.[44,45] However, the underlying origins of SNPs beneficial effects (i.e., the release of NO) could not be rationalized before the 1980s, when the important function of NO as a signaling molecule in mammalian physiology was discovered (see below).[46] These findings were finally able to explain why SNP, nitroglycerine, sodium nitrite, and other related molecules act as vasodilators.[47]

Ruthenium nitrosyl complexes were first reported by Joliet, who prepared and isolated $RuCl_3(NO)$ and related compounds, especially $[Ru(NH_3)_4(OH)(NO)]Cl_2$, and reported these findings in 1889.[49,50] The iconic tetra- and pentammine nitrosyl compounds were subsequently investigated in much detail, starting with a report by Werner in 1907,[51] and followed with work by Gleu and Büddecker,[52] Taube,[53] Bottomley,[54] and others.[55] The crystal structure of $[Ru(NH_3)_5(NO)]Cl_3$ was reported first in an original publication in Russian by Khodashova in 1965,[48] and later re-investigated by Bottomley (because of the observed disorder).[56] As shown in Figure 2, $[Ru(NH_3)_5(NO)]^{3+}$ has a linear RuNO unit and a short Ru−NO bond of 1.77 Å, which indicates that the Ru−NO bond is strong and highly covalent. This is reflected by the large Ru−NO stretching frequency of 597 cm^{-1} in this complex,[57] and the corresponding Ru−NO force constant (4.64 mdyn/Å for the tribromide salt, ν(Ru−NO) = 594 cm^{-1}).[58] The N−O stretch is found at high frequency, 1903 cm^{-1} for the complex $[Ru(NH_3)_5(NO)]Cl_3$,[59] indicative of partial NO oxidation.

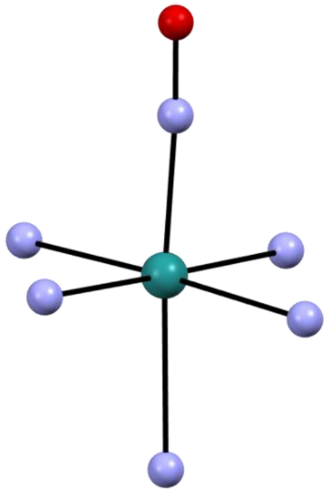

Figure 2. Crystal structure of $[Ru(NH_3)_5(NO)](Cl)_3$.[48] All H atoms and counter ions are omitted for clarity.

Despite the fact that SNP and the above-mentioned ruthenium-pentammine nitrosyls are completely unrelated complexes, it is striking how similar the structural and spectroscopic properties of their M—NO units are (M = transition metal). From early days on, the strong, linear Fe—NO bond in SNP combined with the many analogies of CO and NO complexes were seen as evidence for the NO ligand having distinct nitrosonium (NO^+; isoelectronic with CO; see Figure 3) character in nitroprusside,[60−62] and the same applies to the ruthenium-pentammine nitrosyl complexes.[55,63] In accordance with this electronic structure description, the coordinated NO^+ ligand in these complexes is electrophilic, and reactive towards many different types of nucleophiles.[5,29,64−67] These examples illustrate the many challenges that scientists are facing in pinpointing the correct electronic structures of various transition-metal NO compounds. This is further illustrative of NO's behavior as a non-innocent ligand and highlights the fact that transition-metal—NO bonds are often highly covalent. Because of this, detailed structural, spectroscopic and theoretical studies are necessary to determine the exact electronic structure and electron distribution in a given transition-metal NO complex.

1.1.1. Enemark–Feltham Notation. For the reasons mentioned above, Enemark and Feltham introduced their famous electron counting scheme in 1974,[36] which quickly became popular and is still used in many publications on transition-metal nitrosyl complexes to this date. In the Enemark–Feltham notation, $\{M(NO)_x\}^n$, the $M(NO)_x$ entity (x = number of bound NO ligands) is treated as a covalent unit where the superscript (index) n denotes the number of valence electrons = metal(d) + NO(π^*) electrons of the complex. Accordingly, the nitroprusside trianion and the ruthenium-pentammine NO compounds described above belong to the $\{FeNO\}^6$ and $\{RuNO\}^6$ classes, respectively, where NO (π^{*1}) is formally coordinated to either a Fe^{III} or a Ru^{III} center (both d^5 systems). Scheme 2 shows the possible electron configurations of these $\{MNO\}^6$ complexes with the metal in the ls state. In addition, we propose to add the overall spin state of the metal ion, either low-spin (ls), high-spin (hs) or intermediate spin (is) in rare cases, to the Enemark–Feltham notation as a prefix. As evident from the many examples discussed in this review, the spin state has an important effect on the geometric and electronic structures and reactivity of transition-metal nitrosyl complexes that share the same Enemark–Feltham index, n. Therefore, the spin state is an important property that we also need to consider. By adding the spin state, the nitroprusside trianion and the ruthenium-pentammine NO complexes can now be classified as ls-$\{FeNO\}^6$ and ls-$\{RuNO\}^6$, respectively. Scheme 3 shows different valence tautomers for the $\{FeNO\}^6$ and $\{FeNO\}^7$ cases as another example.

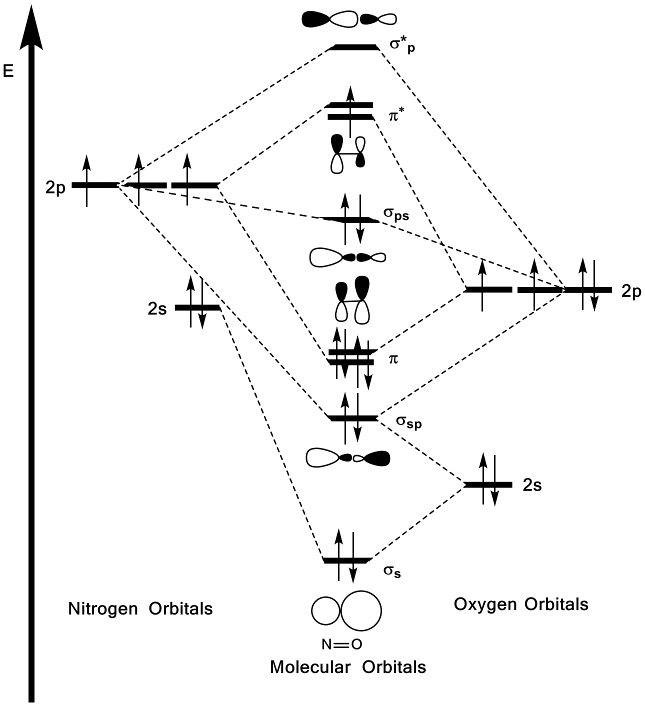

Figure 3. Molecular orbital diagram of free NO. In the case of NO^+ (isoelectronic to CO), the π^* orbitals are unoccupied.

On the basis of all of these considerations, we can now see that the nitroprusside trianion and the ruthenium-pentammine nitrosyl complexes have the exact same number of valence electrons, $n = 6$, and that the metal centers have the same spin state, ls. It is for this reason that these complexes have very similar electronic properties and that their reactivities are similar as well, due to the presence of an electrophilic NO^+ ligand. This example highlights a key strength of the Enemark–Feltham notation, allowing us to categorize transition metal–NO complexes by their number of valence electrons plus the spin state of the metal center, with the general presumption that complexes with the same Enemark–Feltham index n and spin state have similar geometric and electronic structures and reactivities.[17,36]

1.1.2. Transition-Metal Nitrosyl Complexes in Different Redox States. A nice illustration of the power of the Enemark–Feltham notation and a further demonstration of the importance of spin state are the trends observed in redox series of transition-metal nitrosyl complexes. Particularly relevant for this review are the ls-$\{FeNO\}^{6-8}$ and hs-$\{FeNO\}^{6-8}$ redox series $[Fe(cyclam\text{-}ac)(NO)]^{2+/+/0}$ and $[Fe(TMG_3tren)(NO)]^{3+/2+/+}$, respectively (see Figure 4 for structural and spectroscopic properties).[68,69] In the ls case, the electronic structures of the complexes are generally best described as Fe(II)–NO^+ (ls-$\{FeNO\}^6$, total spin of the complex, $S_t = 0$), Fe(II)–$NO^\bullet$ (ls-$\{FeNO\}^7$, $S_t = 1/2$), and Fe(II)–$^1NO^-$ (ls-$\{FeNO\}^8$, $S_t = 0$); that is, the redox chemistry along the ls-$\{FeNO\}^{6-8}$ series is all NO-based.[68] A similar situation is encountered for the ls-$\{FeNO\}^{6-8}$ complexes in hemes, as exemplified by corresponding model complexes and NO adducts in many different proteins,[24,70] and a corresponding tetracarbene analog.[71] Scientists were able to obtain nitroprusside in both the ls-$\{FeNO\}^6$ and the ls-$\{FeNO\}^7$ state, and a further one-electron reduced form was obtained as well, which

Scheme 3. Examples of Different Valence Tautomers for $\{FeNO\}^6$ and $\{FeNO\}^7$ Complexes in Different Spin States

$Fe^{II} + NO \rightarrow \{FeNO\}^7$	$Fe^{III} + NO \rightarrow \{FeNO\}^6$
Fe^{I}—NO^+	Fe^{II}—NO^+
Fe^{II}—$NO^\bullet$	Fe^{III}—$NO^\bullet$
Fe^{III}—NO^-	Fe^{IV}—NO^-

Iron spin states	NO spin states
$Fe^{I} = d^7 \rightarrow S = 1/2, 3/2$	$NO^+ \rightarrow S = 0$
$Fe^{II} = d^6 \rightarrow S = 0, 1, 2$	$NO\cdot \rightarrow S = 1/2$
$Fe^{III} = d^5 \rightarrow S = 1/2, 3/2, 5/2$	$NO^- \rightarrow S = 0, 1$

https://doi.org/10.1021/acs.chemrev.1c00253

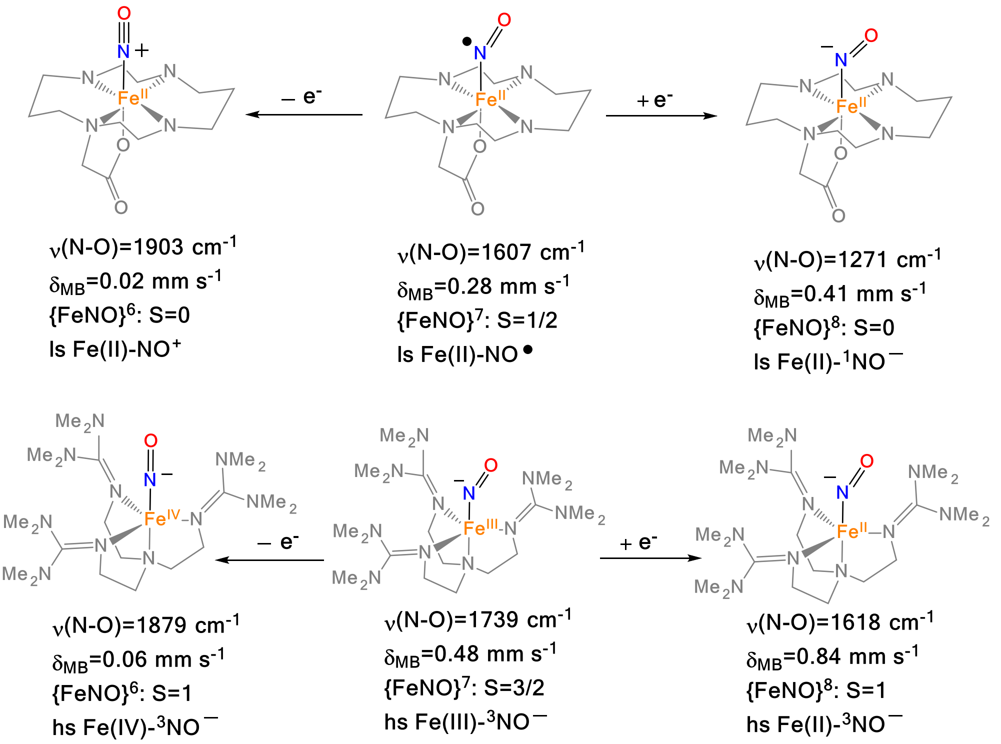

Figure 4. Key spectroscopic properties and spin states of the ls-{FeNO}$^{6-8}$ series with the cyclam-ac$^-$ coligand[68] and the hs-{FeNO}$^{6-8}$ series with the TMG$_3$tren coligand.[69] Adapted with permission from ref 69. Copyright 2018 American Chemical Society.

was initially thought to be the analogous, six-coordinate (6C) ls-{FeNHO}^{8}, or Fe(II)−NHO, species with N-bound HNO.[29,66,72] However, a subsequent computational study pointed out that the putative ls-{FeNO}^{8} complex, $[Fe(CN)_5(NO)]^{4-}$, is susceptible to cyanide release. Loss of cyanide would create a five-coordinate (5C), square-pyramidal HNO complex, $[Fe(CN)_4(NHO)]^{2-}$,[73] and lead to a more complicated speciation in solution than initially envisioned. In contrast, in the hs-{FeNO}$^{6-8}$ series, $[Fe(TMG_3tren)(NO)]^{3+/2+/+}$, the redox chemistry is all iron-based, leading to Fe(IV)−NO$^-$ (hs-{FeNO}^{6}, S_t = 1), Fe(III)−NO$^-$ (hs-{FeNO}^{7}, S_t = 3/2), and Fe(II)−NO$^-$ (hs-{FeNO}^{8}, S_t = 1) electronic structures (see Figure 4),[69,74] in clear contrast to all of the ls-{FeNO}$^{6-8}$ complexes mentioned above.

A ruthenium−nitrosyl compound that was characterized in all three redox states, ls-{RuNO}$^{6-8}$, was reported by Kaim and coworkers. In $[Ru(bpym)(terpy)(NO)](PF_6)_3$, the corresponding redox changes are evident from shifts in the N−O stretching frequencies from 1957 to 1665 and then to 1388 cm^{-1}.[76] In the case of $[Ru(Me_3[9]aneN_3)(bpy)(NO)]^{3+/2/+}$, Slep and coworkers were able to obtain the complete ls-{RuNO}$^{6-8}$ series plus the corresponding HNO complex, ls-{RuNHO}^{8}. In the latter case, the pK_a of the coordinated HNO ligand was reported (9.78 in water) as well.[77,78] The first HNO complex that could be structurally characterized was $[Os(Cl)_2(CO)(PPh_3)_2(NHO)]$ (see Figure 5),[75] obtained by simple protonation of the ls-{OsNO}^{8} precursor $[Os(Cl)(CO)(PPh_3)_2(NO)]$ with HCl. This compound shows an N−O distance of 1.193 Å, an Os−N−O angle of 137°, and an N−O stretch of 1410 cm^{-1}, in line with N-bound HNO with a N=O double bond. Later, $[Ir(H)(Cl)_2(PPh_3)_2)(NHO)]$ was obtained using a similar procedure.[79] On the other hand, the first structurally-characterized ls-{RuNHO}^{8} complex, $[Ru(py^{bu}S_4)(NHO)]^+$,[80] reported by Sellman and coworkers, was obtained by hydride transfer to the ls-{RuNO}^{6} precursor $[Ru(py^{bu}S_4)(NO)]^+$, a reaction that resembles the chemistry of Cytochrome (Cyt.) P450nor (see below). This complex shows again N-bound HNO with an N−O bond length of 1.242 Å, a Ru−N−O angle of 130°, and the N−O stretch was observed at 1358 cm^{-1}.

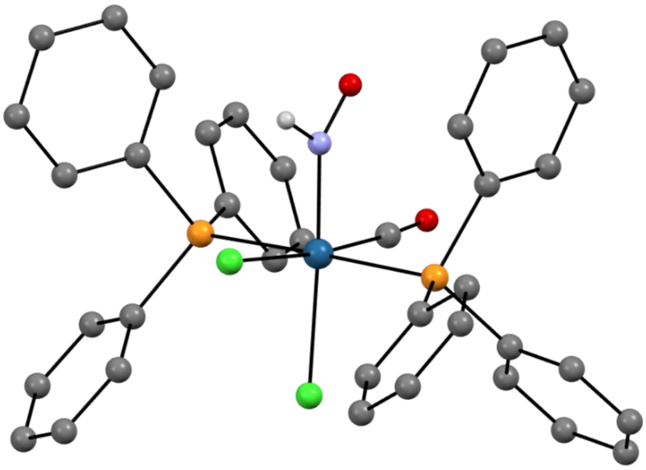

Figure 5. Crystal structure of $[Os(Cl)_2(CO)(PPh_3)_2(NHO)]$.[75] All H atoms are omitted for clarity, with exception of the H atom of the HNO ligand.

Complexes that belong to the {FeNO}$^{9/10}$ class are rare, with examples reported for carbonyl/nitrosyl complexes like $[Fe(CO)_3(NO)]^-$ (see above). More recently, a unique series of highly reduced ls-{FeNO}$^{8-10}$ complexes was reported by Peters and coworkers, making use of their tris(phosphine)-borane coligand (see Figure 6, top).[81] Here, the presence of the boratrane group helps to stabilize the highly reduced nitrosyl complexes.[83] In addition, Meyer and coworkers used a tripodal

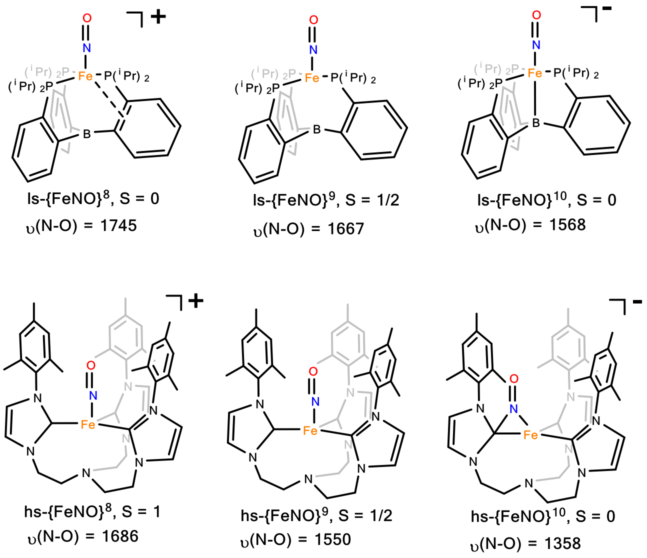

Figure 6. Spin states and N−O stretching frequencies [cm^{-1}] of the ls-$\{FeNO\}^{8-10}$ series with the TPB coligand (top)[81] and the hs-$\{FeNO\}^{8-10}$ series with TIMEN^{MES} (bottom).[82] Adapted with permission from ref 83. Copyright 2020 American Chemical Society.

triscarbene ligand scaffold to create a series of $\{FeNO\}^{6-9}$ complexes (see Figure 6, bottom).[82] Further evidence for a fleeting $\{FeNO\}^{10}$ species was reported as well. Importantly, the $\{FeNO\}^{7-9}$ complexes were shown to be hs, and as a part of this study, the first crystal structure of a hs-$\{FeNO\}^9$ compound was reported as well. Taken together, these recent studies promise many more exciting discoveries in the area of highly-reduced iron−nitrosyl complexes in the future.

These examples, where there are no changes in the coordination environment of the metal center during the redox transformations, are exceptionally useful as they allow for in-depth correlations of spectroscopic properties along the complete redox series of complexes. These data can in turn be used to obtain deep insight into the electronic properties of the corresponding nitrosyl complexes. Other than this variation in metal redox state, Fujisawa and coworkers reported a series of strictly analogous, four-coordinate (4C) hs-$\{MNO\}^{8-11}$ complexes with M = Fe, Co, Ni, Cu (see Figure 7).[84−87] In this series, all complexes utilize an identical hydrotris(pyrazolyl)borate coligand, have the same overall charge, and they only differ in the nature of the metal.[88] Accordingly, this work identifies periodic trends in the structural and electronic properties of transition metal-nitrosyl complexes.

1.1.3. Nitrosyl Complexes of Iron−Sulfur Cores.

Roussin reported the first polynuclear cluster compound of nitric oxide, which was obtained by the reaction of nitrous acid (HNO_2), potassium hydroxide (KOH), potassium sulfide (other alkali metal sulfides can be used as well), and iron(II) sulfate in aqueous solution.[89] He named the resulting, black crystalline material "Binitrosulfure de fer", and the elemental composition of this compound was subsequently characterized as $K[Fe_4S_3(NO)_7]$ (Roussin's Black Salt, RBS) by Pavel in 1882 (as a result of extensive elemental analyses).[90] In this process, a number of alternative synthetic methods were discovered as well.[91] Roussin's Black Salt can be converted to a red compound (Roussin's Red Salt, RRS)[89] in a reversible process by alkalization of the solution (acidification then induces the reverse reaction). Pavel also determined the formula of Roussin's Red Salt, $K_2[Fe_2S_2(NO)_4]$, and he reported the first organic derivative of this compound, $[Fe_2(SEt)_2(NO)_4]$ (Roussin's Red Ester, RRE), obtained from the alkylation of $K_2[Fe_2S_2(NO)_4]$.[90] Subsequent elemental analyses of a range of related compounds obtained from the reaction of thiols, iron(II) salts and NO showed that these complexes had similar, dimeric structures of $[Fe_2(SR)_2(NO)_4]$ type, indicating that Roussin's Red Esters constitute a stability island in iron/thiol/NO chemistry.[92,93] Subsequent work demonstrated that $[Fe_4S_3(NO)_7]^-$, $[Fe_2S_2(NO)_4]^{2-}$ and $[Fe_2(SR)_2(NO)_4]$ are diamagnetic compounds with multimetallic cores.[93,94] Finally, 100 years after the initial report by Roussin of his black and red compounds, the crystal structures of $[Fe_2(SEt)_2(NO)_4]$ and $Cs[Fe_4S_3(NO)_7]$ were reported,[95,96] as shown in Figure 8. The resemblance between these diiron and tetrairon cores and naturally occurring [2Fe2S] and [4Fe4S] clusters in iron−sulfur proteins in biology is remarkable,[97] and these parallels later fueled extensive research in the area of iron/sulfur/NO chemistry.[98] Here, $[Fe_2S_2(NO)_4]^{2-}$ is an exact tetranitrosyl analog of the [2Fe2S] sites in biology, and the corresponding $[Fe_4S_4(NO)_4]^{0/-}$ analogs of [4Fe4S] clusters were later reported by Dahl and coworkers.[99,100] Later studies showed

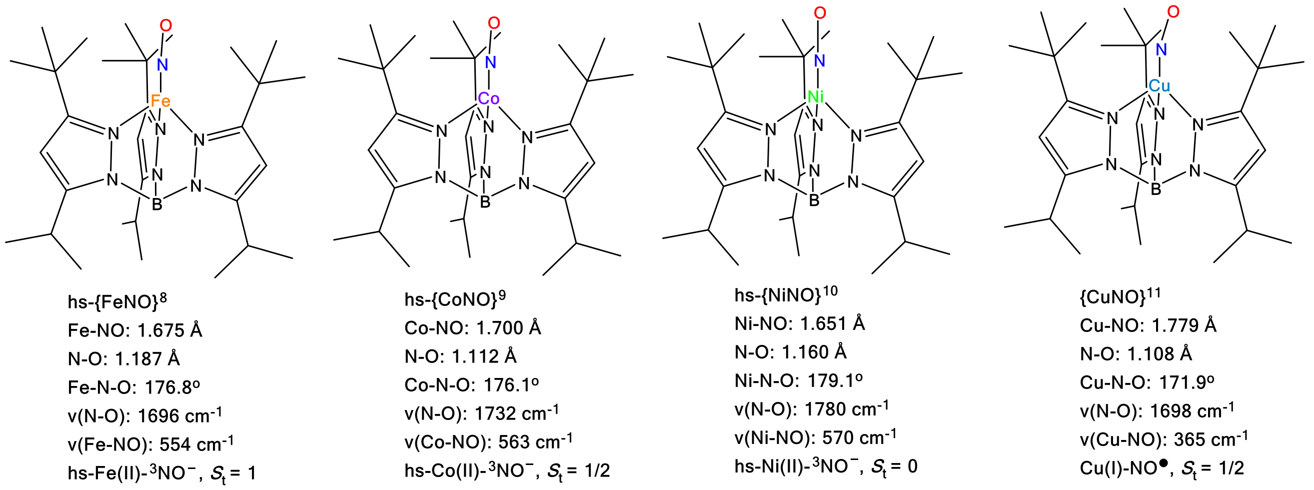

Figure 7. Four-coordinate hs-$\{MNO\}^{8-11}$ complexes that utilize the same hydrotris(pyrazolyl)borate coligand, prepared by Fujisawa and coworkers. Here, M = Fe, Co, Ni, or Cu.[84−87]

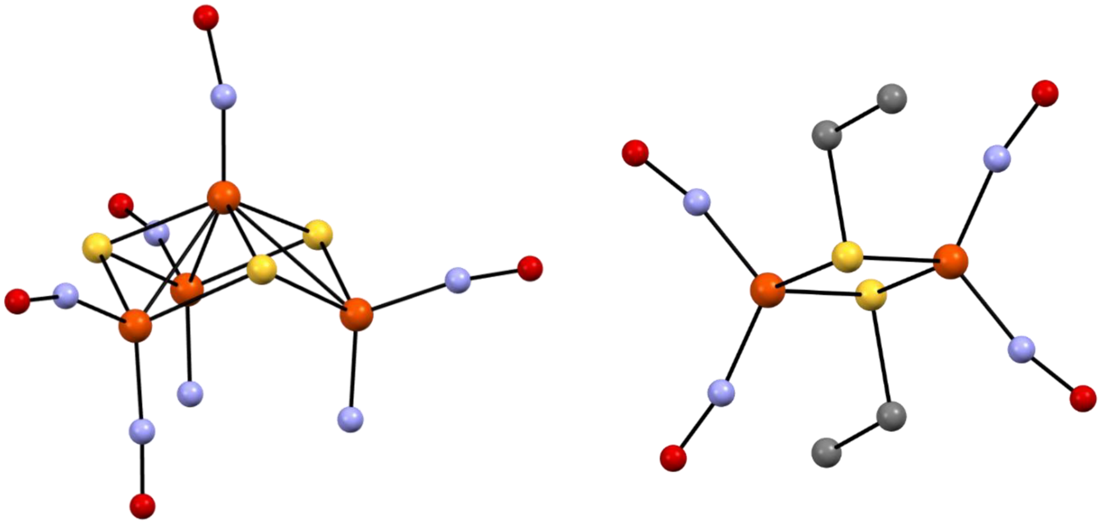

Figure 8. Crystal structures of Cs[$Fe_4S_3(NO)_7$] (RBS, left)[95] and [$Fe_2(SEt)_2(NO)_4$] (RRE, right).[96] Note that in the original crystal structure of RBS, two NO ligands are missing their O atoms. Later crystal structures identified these two additional NO ligands.[108] All H atoms and counter ions (if applicable) are omitted for clarity.

the biological relevance of the interaction of NO with iron−sulfur clusters, as NO can deactivate these clusters by binding to the iron centers and, in some cases, breaking up the clusters into smaller fragments (see below for a detailed discussion). Evidence for corresponding mononuclear "dinitrosyl iron complexes" (DNICs) of [$FeL_2(NO)_2$] type (L = thiolate, halide, phenolate, neutral N-donor ligands, etc.) was first reported in 1965,[101−103] and it was later determined that these species play important roles in mammalian physiology (see Section 3).[104−107]

The crystal structure of the [$Fe_4S_3(NO)_7$]$^-$ anion shows a flattened tetrahedron of four Fe centers, three faces of which are bridged by S^{2-} ions (see Figure 8).[95,108] The unique, apical Fe center binds a single nitrosyl ligand, whereas the three basal irons coordinate two nitrosyl ligands each. Averaged Fe(apical)−Fe(basal) and Fe(basal)−Fe(basal) distances are 2.70 and 3.57 Å, respectively, and the averaged Fe(apical)−S and Fe(basal)−S distances are 2.21 and 2.26 Å, respectively. All of the nitrosyl ligands are bound with approximately linear Fe−N−O angles, with Fe(apical)−N−O = 176°, and the averaged Fe(basal)−N−O = 167°. In the case of [$Fe_2(SEt)_2(NO)_4$], a compound with C_{2h} symmetry (see Figure 8), the Fe−S bond length is 2.27 Å.[96] This compound shows a rather short Fe−Fe distance of only 2.72 Å, allowing for a direct Fe−Fe interaction. The nitrosyl groups are again bound in a close to linear fashion, with an Fe−N−O angle of 167°. The corresponding dianion, [$Fe_2S_2(NO)_4$]$^{2-}$, shows a very similar structure, as first reported in ref 109. Structures with other counter ions are also available.[110]

1.2. Biological Relevance of NO in Medicine

For the longest time, nitric oxide has been viewed as an environmental pollutant, generated from the burning of fossil fuels in power plants, furnaces and engines, due to its highly toxic and corrosive properties. Together with nitrogen dioxide (NO_2), it is one of the main contributors to smog. NO is poisonous to humans at very low concentrations of only a few hundred ppm in air, by formation of highly toxic NO_2, shutting down respiration, disabling iron−sulfur proteins like aconitase, and reacting with oxy-hemoglobin (oxy-Hb, Hb(II)−O_2) to form met-Hb (Hb(III), with iron in the +III state).[111,112] Starting in the late 1960s, biochemists used NO in the laboratory as a "spin-label probe" to study the interactions of ferrous heme centers in proteins like Hb, myoglobin (Mb), Cyt. P450, etc., with dioxygen (O_2). Here, the resulting ferrous heme-nitrosyl complexes, which are ls-{FeNO}^{7} species, are very stable and show characteristic electron paramagnetic resonance (EPR) spectra with S_t = 1/2 ground states and characteristic hyperfine couplings with the N atom of the coordinated NO (see Section 2.2).[113−130] In addition, the obtained EPR spectra are also characteristic of the coordination number of the formed heme−NO adduct (either 5C or 6C), and in this way, provide further insight into the properties of the heme's proximal ligand in the protein.[130] In contrast, the corresponding O_2 adducts of ferrous hemes are diamagnetic and EPR silent. Hence, NO can be used to probe for ferrous hemes in (newly discovered) proteins, even in whole cell assays.[127,131]

Among the different heme proteins investigated, the NO adducts of Hb and Mb are some of the most and longest studied systems in biology. Some of the earliest results in this field relate to the fact that the red color of cured meat is due to formation of the NO adducts of ferrous Hb/Mb, which are ls-{FeNO}^{7} complexes (also formally addressed as "Hb/Mb(II)−NO" for redox state tracking).[132,133] Here, nitrite is believed to first oxidize Mb/Hb(II)−O_2 to met-Mb/Hb, followed by NO binding. In the meat, the NO adducts of ferric (met-) Mb/Hb, which are ls-{FeNO}^{6} complexes (also formally addressed as "Hb/Mb(III)−NO", again just for redox state tracking), are then thought to undergo reduction by endogenous reductants (for example, NADH) or added exogenous reductants (like ascorbate or erythorbate) to yield Mb/Hb(II)−NO, which have a bright red color. In this context, Haldane was the first to prepare the pigment nitrosyl-Hb in 1901 by adding nitrite to Hb, thereby showing that Hb(II)−NO (and Mb(II)−NO) is responsible for the red color of cured meats.[134] Nitrosyl-Hb itself was described first by Herman in 1865, which is therefore the first reported NO adduct of a protein.[135] Shortly after, Gamgee reported the reaction of Hb with nitrite (in blood).[136] However, upon prolonged exposure of the meats to excess nitrite under acidic conditions, the cured meats develop a green tinge ("nitrite burn"),[137] which was later shown to be due to a nitration of the heme *b* cofactor of Hb/Mb at the 2-vinyl position via X-ray crystallography.[138,139] Nitrite also serves as a reservoir for NO in blood, and is reduced by deoxy-Hb (Hb(II), with iron in the +II state) to NO under hypoxic conditions, following the general mechanism of heme cd_1 nitrite reductase (see Section 4.1).[140−142] This reaction was already reported by Brooks in 1937:[143]

$$\mathrm{Hb(II)} + \mathrm{NO_2}^- + 2\mathrm{H}^+ \rightarrow \mathrm{Hb(III)} + \mathrm{NO} + \mathrm{H_2O} \quad (1a)$$

$$\mathrm{Hb(II)} + \mathrm{NO} \rightarrow \mathrm{Hb(II)}{-}\mathrm{NO} \quad (1b)$$

Inspired by the success of using NO as a spin-label to investigate O_2 coordination to ferrous hemes, the same strategy was later applied to non-heme iron enzymes, pioneered by Solomon and coworkers in the 1990s.[144−149] In fact, this strategy was even more successful for non-heme iron enzymes, as the O_2 complexes of heme proteins are often quite stable, whereas the O_2 adducts of non-heme iron enzymes are unstable and reactive intermediates that are hard to observe, even when stopped-flow and rapid freeze-quench (RFQ) methods are used.[150] Binding of O_2 to a ferrous non-heme iron center generally leads to the formation of a ferric superoxo complex, $\mathrm{Fe(III)}{-}\mathrm{O_2}^-$, which, however, is very reactive and unstable. In analogy to this, binding of NO to a ferrous non-heme iron complex generates a stable hs-$\{\mathrm{FeNO}\}^7$ complex with an EPR-active $S_t = 3/2$ ground state.[151] Studies by Solomon and coworkers have further shown that the electronic structures of these types of complexes are best described as a hs-$\mathrm{Fe^{III}}$ ($S = 5/2$) with a bound triplet NO^- ($S = 1$) ligand, where the spins of these fragments are strongly antiferromagnetically (AF) coupled ($S_t = 3/2$).[145,152] Since the geometry and the charge distribution (electrostatic properties) of the $\mathrm{Fe(III)}{-}\mathrm{NO}^-$ and the $\mathrm{Fe(III)}{-}\mathrm{O_2}^-$ complexes are very similar, the nitrosyl adduct is in many cases a faithful model of the O_2 adduct, and there are many examples in the literature where the NO complex has been used to infer the geometric structure, orientation in the active site, and even the electronic structure of the analogous O_2 complex.[146,147,153]

1.2.1. Overview of Physiological Functions of NO. The general view of NO as an environmental pollutant and toxin changed dramatically in the 1980s when it was first realized that NO is biosynthesized in humans for the purpose of signaling and immune defense.[47,154−160] In this way, NO morphed from being a toxic component of smog and a curiosity of coordination chemistry into a target for biomedical research due to its high significance for human health. For this reason, NO was declared the "Molecule of the Year" by the magazine *Science* in 1992,[46] and in 1998 the Nobel Prize in Medicine was awarded to Furchgott, Ignarro, and Murad for the discovery that NO is an endogenously produced vasodilator in mammals, and a key signaling molecule in the human body.[161−163] Much of the biologically-relevant chemistry of NO is linked to iron, including NO biosynthesis, detection (for sensing), and breakdown, which is the reason for the surge in research on the coordination chemistry of NO (and its oxidized and reduced derivatives; in particular nitrite and HNO) with iron complexes in the past four decades.

In mammals, NO is biosynthesized by the nitric oxide synthase (NOS) family of enzymes, which utilize a {heme-thiolate} center in the active site analogous to Cyt. P450s, to oxidize L-arginine to citrulline and NO (see Section 2.1).[164−168] NO is an ideal signal transducer, as it is a stable radical gas with a diffusion length of 10−100 μm and a lifetime of ∼100 ms in tissue.[160] Note that the aqueous oxidation of NO by O_2 is a third-order reaction, the rate of which is dependent on $[\mathrm{NO}]^2[\mathrm{O_2}]$, with a rate constant of $k_{ox} = 2 \times 10^6\ \mathrm{M^{-2}\ s^{-1}}$:[169,170]

$$2\mathrm{NO} + \mathrm{O_2} \rightarrow 2\mathrm{NO_2} \quad (2a)$$

Hence, the rate of NO oxidation strongly depends on its initial concentration: at high concentrations of NO (μM to mM), the reaction takes place in less than a second, whereas the decay is much slower at physiological concentrations ($\leq$ 100 nM), allowing NO to function as a signaling molecule under aerobic conditions.[169] The initially formed NO_2 then reacts further with NO, ultimately forming $\mathrm{NO_2}^-$ in an aqueous environment:

$$\mathrm{NO_2} + \mathrm{NO} \rightarrow \mathrm{N_2O_3} \quad (2b)$$

$$\mathrm{N_2O_3} + \mathrm{H_2O} \rightarrow 2\mathrm{NO_2}^- + 2\mathrm{H}^+ \quad (2c)$$

Note that the N_2O_3 formed intermittently is a strongly nitrosating agent, able to convert thiols (including cysteine in free form and in proteins) to nitrosothiols (RS−NO).

After production of NO in endothelial cells by endothelial NOS (eNOS), it diffuses into the smooth muscle tissue and is subsequently detected by soluble guanylate cyclase (sGC), the universal mammalian NO sensor. The sensor domain of this enzyme contains a heme-based receptor that binds NO, leading to the activation of sGC's catalytic domain that catalyzes the cyclization of GTP to cyclic guanosine-3′,5′-monophosphate (cyclic GMP = cGMP; see Section 2.2).[171−175] The cGMP is subsequently released and acts as a secondary messenger that ultimately induces relaxation of the arterial smooth muscle tissue, which then causes a drop in blood pressure.[176] The 5C, ferrous heme (with axial (proximal) histidine (His) ligation) that is present in the sensor domain of sGC has a very high affinity for NO, allowing for the efficient detection of NO even at subnanomolar concentrations by sGC. Binding of NO induces a breaking of the $\mathrm{Fe{-}N_{His}}$ bond, due to the strong thermodynamic σ-*trans* effect of NO (as illustrated in Figure 9), which is at the heart of the ability of hemes to serve as NO sensors (see Section 2.2). By using such small concentrations of NO, toxicity issues can generally be avoided. In the brain, NO is produced by neuronal NOS (nNOS), and then again detected by sGC. Hence, NO-based signal transduction functions in a

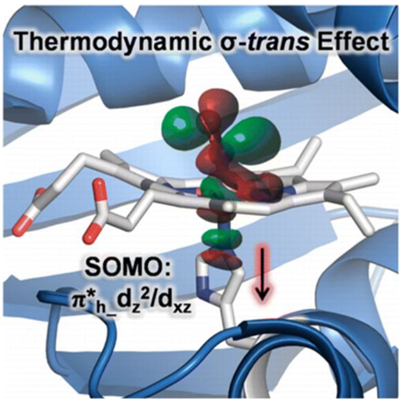

Figure 9. NO binding to the ferrous heme in sGC leads to a breaking of the $\mathrm{Fe{-}N_{His}}$ bond, due to the thermodynamic σ-trans effect of NO, as indicated. This induces conformational changes that activate the catalytic domain of sGC, leading to the production of the secondary messenger cGMP. Reprinted with permission from ref 171. Copyright 2015 American Chemical Society.

similar way in the brain and in the cardiovascular system. Besides its role in arterial vasodilation, the NO produced by eNOS in endothelial cells has additional important functions as well. For example, NO is continuously released from the surface of the endothelium into the blood (NO flux: $(1\text{-}4) \times 10^{-10}$ mol $\text{min}^{-1}\text{cm}^{-2}$)[177] to prevent protein adhesion to the inner arterial surfaces. In addition, the NO released into the blood inhibits platelet aggregation and blood clotting.[178] However, the resulting accumulation of NO in the blood would be detrimental for human health. To prevent this from happening, NO is continuously degraded in blood by reaction with oxy-Hb in the so-called NO dioxygenation (NOD) reaction (see Section 2.5), where NO is oxidized to nitrate via a putative peroxynitrite intermediate:[179−183]

$$\text{Hb}{-}\text{O}_2 + \text{NO} \rightarrow \text{Hb(III)}{-}\text{OONO}^- \rightarrow \text{met-Hb} + \text{NO}_3^- \tag{3}$$

The scavenging of NO according to eq 3 is very efficient, with a second-order rate constant of $(6{-}9) \times 10^7\ \text{M}^{-1}\ \text{s}^{-1}$.[184,185]

Interestingly, very similar sensor domains as the one present in sGC were also identified in bacteria, termed *H-NOX* (heme nitric oxide/oxygen sensor domains). They mostly serve as O_2 and NO sensors (see Section 2.2).[186−190] NosP are another important class of bacterial NO sensors, thought to be involved in the regulation of bacterial biofilms.[191]

Mammals further take advantage of NO's high toxicity in the context of immune defense.[192−194] Using inducible NOS (iNOS), our macrophages, for example, produce up to micromolar concentrations of NO (besides other toxic chemicals, especially superoxide) to kill infectious pathogens.[195,196] In this regard, note that NO inhibits a number of important heme enzymes (i.e, Cyt. P450s, heme−copper oxidases (respiration), etc.) by binding to the heme cofactor. In addition, NO breaks down iron−sulfur clusters and deactivates them. All of these effects are believed to play a part in NO's ability to kill invading microbes. In addition, NO and superoxide combine in a very fast reaction (with an initially reported second order rate constant, $k = (6.7 \pm 0.9) \times 10^9\ \text{M}^{-1}\ \text{s}^{-1}$)[197] to generate peroxynitrite (see Section 2.5):

$$\text{NO} + \text{O}_2^- \rightarrow \text{ONOO}^- \tag{4}$$

Note that later work by Koppenol and coworkers reported a larger rate constant, $k = 1.6 \times 10^{10}\ \text{M}^{-1}\ \text{s}^{-1}$, for this reaction.[198] Peroxynitrite is a highly toxic molecule that oxidatively damages cells, including pathogens, and which is therefore another key component of mammalian immune defense. Unfortunately, NO's important role in immune defense also has a dark side:[199] areas of chronic infection (inflammation) experience a constant NO flux at micromolar concentrations, which can lead to tissue and cartilage degradation, organ failure, etc. via nitrosative stress.[200,201] Similarly, overproduction of NO causes neurodegeneration and neuropathic pain,[202,203] and NO is also being considered now a key contributor to neurodegenerative diseases.[204] Finally, NO is known as a key player in different stages of septic shock.[205−208]

Related to the role of NO in mammalian immune defense, a number of pathogens have been identified that possess defense strategies against NO toxicity. Here, flavodiiron NO reductases (FNORs) are utilized to remove/degrade NO under anaerobic conditions by reduction to less toxic N_2O (see Section 5.2),[209−215] following the 'classic' NO reduction reaction in denitrification:

$$2\text{NO} + 2e^- + 2\text{H}^+ \rightarrow \text{N}_2\text{O} + \text{H}_2\text{O} \tag{5}$$

For this purpose, transcription factors are present in the pathogens that sense NO, and upon NO detection, they induce transcription of genes that lead to the production of defense proteins like FNORs.[211] The active sites of FNORs contain a non-heme diiron center with a Flavin (FMN) cofactor from an adjacent subunit in close proximity,[216,217] only 4−6 Å apart.[218] On the other hand, under aerobic conditions, pathogens use flavohemoglobins for NO detoxification. These heme proteins oxidize NO to nitrate via the NOD reaction, according to eq 3 (see Section 2.5).[219]

NO is mainly stored in three forms in the human body: nitrite, nitrosothiols (RS−NO) and DNICs. Nitrite is generated in blood by the direct oxidation of NO by O_2 (via initial formation of N_2O_3, see above) and it can be converted back to NO by reaction with reduced hemes. In particular, nitrite can bind to deoxy-Hb, followed by reduction to NO accompanied by the formation of met-Hb (following eq 1a; see Section 2.4).[220,221] When NO oxidation takes place in the presence of thiols, nitrosothiols, RS−NO, are generated. Potentially important NO carriers in blood are glutathione (GSH), cysteine, and serum albumin (especially *S*-nitrosoglutathione = GS−NO; see Section 2.4).[222−224] *S*-nitrosothiols react with reduced metal complexes (especially Cu(I)) to liberate NO and are generally quite reactive species.[225−227] Whether nitrite or nitrosothiols (including *S*-nitroso-hemoglobin) could be activated under hypoxic conditions to release NO (and in this way, induce vasodilation in hypoxic tissue) is currently under active investigation.[228,229] DNICs result from the interaction of NO with iron−sulfur proteins, generated both by the reaction of [2Fe2S] and [4Fe4S] iron−sulfur clusters[230] with NO (see Section 3).[104,105,231−233] DNICs are most commonly four- or five-coordinate, depending on the nature and availability of coligands. They exist in two stable redox states, classified as $\{\text{Fe(NO)}_2\}^9$ and $\{\text{Fe(NO)}_2\}^{10}$ in the Enemark−Feltham notation. Besides the formation of DNICs in iron−sulfur proteins, mobile DNICs can form *in vivo* by reaction of labile iron with NO in the presence of cysteine or gluthathione, generating $[\text{Fe(SR)}_2(\text{NO})_2]$-type DNICs.[234] DNICs can serve as an alternative reservoir for NO, for example by transfer of NO to other biological targets like hemes.[235] Finally, DNICs have also been investigated as drugs (see Section 3).[236−239]

The reaction of iron−sulfur clusters with NO is also used by bacteria for NO sensing in transcription factors, to regulate gene expression of different defense proteins (like FNORs) that protect the microbes from NO toxicity (for example, SoxR and potentially FNR, see Section 3).[240,241] In SoxR, [2Fe2S] iron−sulfur clusters are used for NO detection. Here, reaction with NO leads to the reversible formation of DNICs, as shown in Figure 10.[240] Whereas the breakdown of iron−sulfur clusters by reaction with NO has been intensively studied in both biological and synthetic examples,[104,231] the mechanism by which the clusters are repaired is largely elusive and currently an active area of research.[242] Curiously, other bacterial NO sensors use non-heme iron centers as NO receptors (for example, NorR and potentially Fur; see Section 5.6).[243,244]

The role of NO in vasodilation is exploited by certain blood-sucking insects that inject the NO adducts of small heme proteins, called nitrophorins (NPs), into the victim's blood (see Section 2.3).[25,245] The NO subsequently released from the NPs then induces vasodilation in the area of the bite, causing an

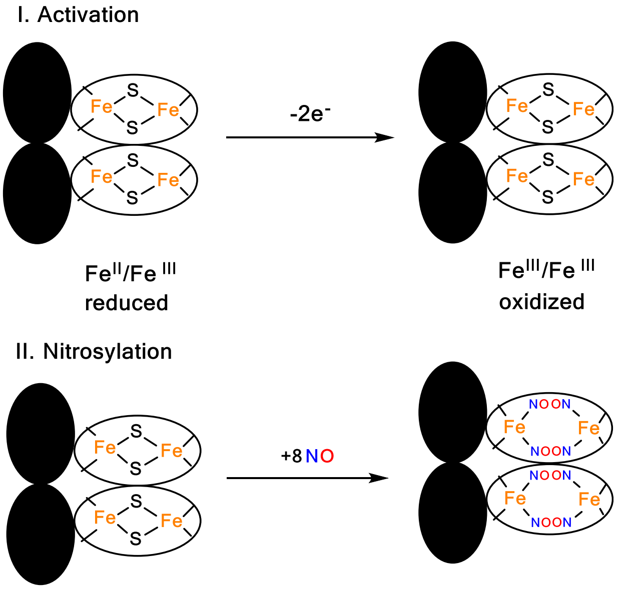

Figure 10. Schematic representation of the SoxR homodimer, where black ovals are DNA binding domains and white ovals are iron-binding domains. Top: Redox regulation of SoxR. In the reduced form, the protein is inactive but when oxidized by at least one electron, the protein becomes a transcription activator. Bottom: Activation of SoxR by nitrosylation. NO binding disrupts the [2Fe−2S] bonds, generating DNICs.[240]

increase in blood flow that allows the predator to finish its meal faster. The nitrophorins from the kissing bug (*Rhodnius prolixus*) were the first class to be identified (labelled rNP; with different isoforms).[246] The rNPs are small (20−32 kDa) heme proteins with a characteristic, lipocalin (barrel-like) fold (built from β-sheets). The barrel contains a heme *b* cofactor with axial histidine coordination as the active site.[247] The NPs are active for NO binding in the ferric oxidation state (in contrast to *H-NOX* type NO sensors, which are active in the ferrous state), and use the corresponding ls-$\{FeNO\}^6$ adduct for NO transport and delivery. The highly ruffled hemes of rNPs are thought to prevent autoreduction of the ls-$\{FeNO\}^6$ complex.[248−251] The autoreduction reaction of ferric heme-nitrosyls is observed for globins, for example, and small-molecule model systems, and proceeds by addition of base to the electrophilic NO^+ ligand in ls-$\{FeNO\}^6$ adducts (due to their Fe(II)−NO^+ electronic structures; see Section 2.3):[252]

$$\begin{aligned} &\mathrm{Hb(III){-}NO} + \mathrm{OH^-} \\ &\quad \rightarrow \mathrm{Hb(II){-}NO_2H} \\ &\quad \rightarrow \mathrm{Hb(II)} + \mathrm{NO_2}^- + \mathrm{H^+} \end{aligned} \tag{6a}$$

$$\mathrm{Hb(II)} + \mathrm{NO} \rightarrow \mathrm{Hb(II){-}NO} \tag{6b}$$

where eq 6a is the inverse of the nitrite reduction reaction in eq 1a.

The nitrophorin from the common bedbug (*Cimex lectularius*), cNP, discovered later is quite simple and has a completely different structure. The β-sheets within the cNP structure do not fold into a barrel configuration as observed for the rNPs,[253] but instead, form a central β-sandwich core that is surrounded by several α-helices. The ferric heme active site of cNP, ligated by Cys60, is located near one of these α-helices. As in the case of rNPs, the protein is active in the ferric state, and is able to bind one equiv of NO to form a ls-$\{FeNO\}^6$ complex, which is then able to transport NO and deliver it to the victim's blood (see Section 2.3).

1.3. Biological Relevance of NO in the Nitrogen Cycle

The nitrogen cycle is one of the most important biogeochemical cycles on earth, as nitrogen is an essential element to all forms of life. An overview of key processes in the nitrogen cycle is presented in Figure 11. Importantly, metalloenzymes, especially with iron, but also molybdenum and copper as the cofactors, catalyze all of the chemical transformations indicated in Figure 11. The nitrogen cycle is rich in unusual and perplexing transition-metal NH_xO_y chemistry, and many of the interconversions indicated in Figure 11 are currently not well understood.[23,254−258]

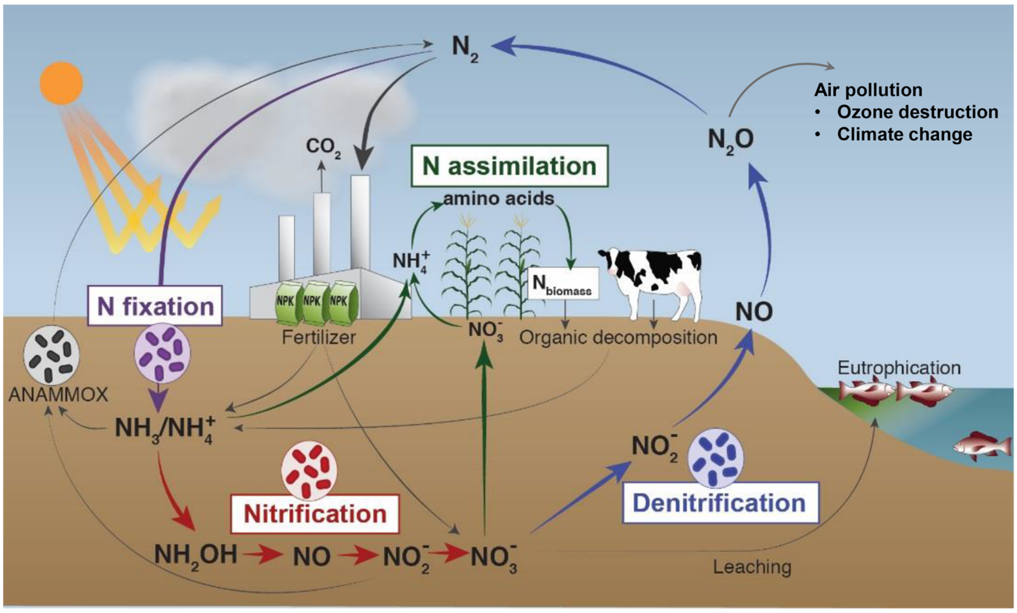

Figure 11. Overview of the nitrogen cycle. Adapted with permission from ref 258. Copyright 2021 Royal Society of Chemistry.

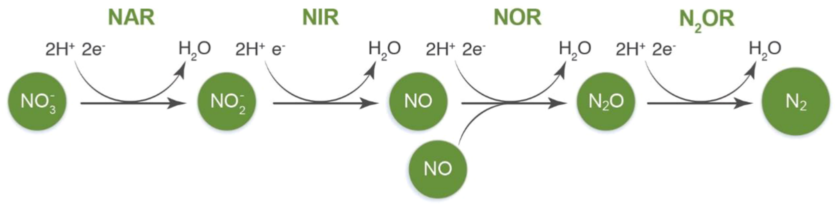

Figure 12. Overview of the denitrification pathway.

Scheme 4. Structures of Naturally Occurring (Top) and Synthetic Hemes (Bottom)

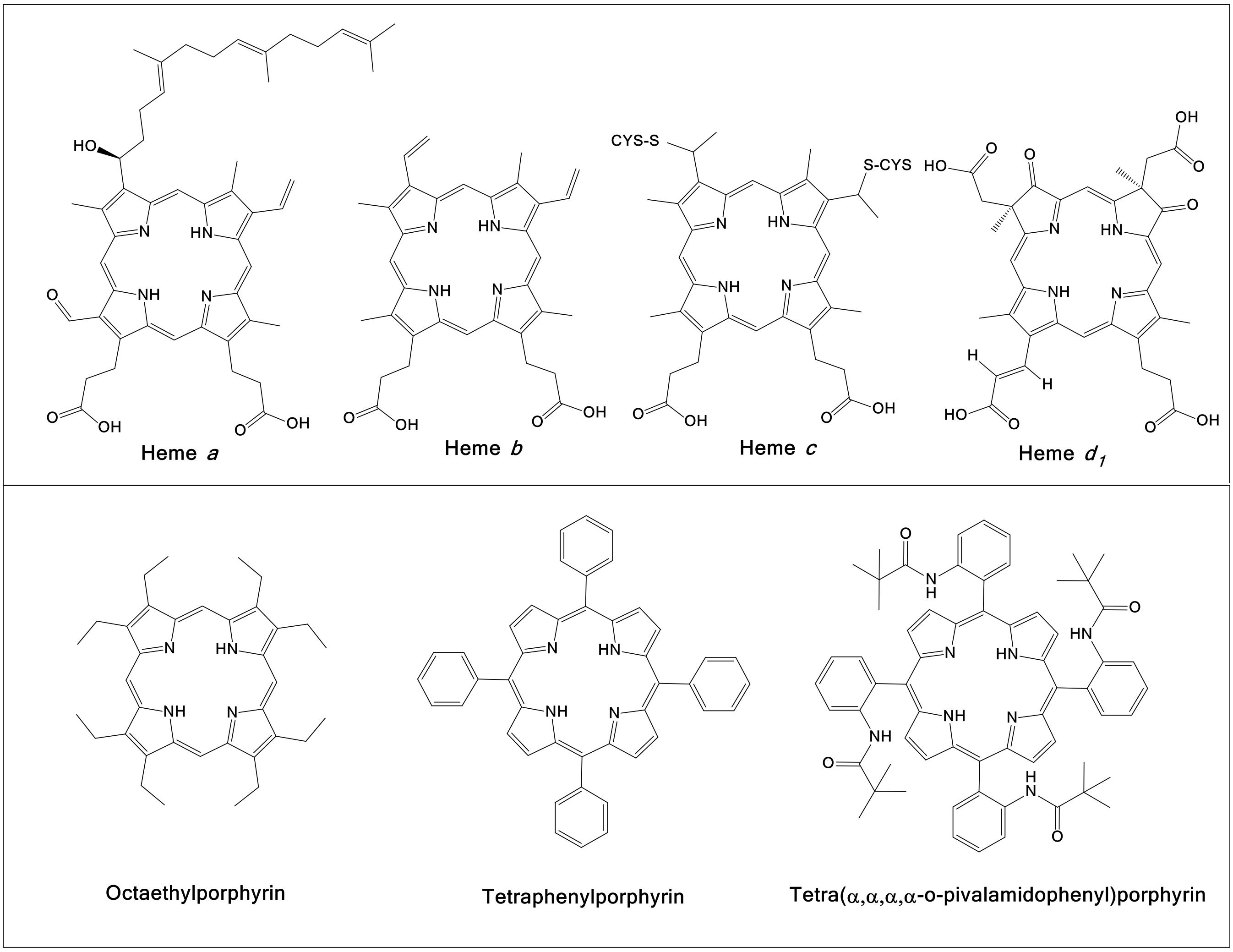

Nitrification, the process responsible for the oxidation of ammonium to nitrite and nitrate, connects biologically reactive nitrogen to the other pathways in the nitrogen cycle. Nitrification is mediated by autotrophic ammonia oxidizing bacteria (AOB)[259−261] and archaea (AOA),[262−264] both of which are capable of oxidizing NH_3 by six electrons to NO_2^- via NH_2OH and NO as obligate intermediates,[22,265,266] thereby generating reducing equivalents for respiration, and nitrite-oxidizing bacteria (NOB)[259,267,268] that mediate the two-electron oxidation of nitrite to nitrate. More recently, "complete ammonia-oxidizing" (COMAMMOX) bacteria, which affect the complete (eight electron) oxidation of ammonia to nitrate, were also identified (using similar enzymes as those found in AOBs and NOBs).[269,270] Nitrification is initiated by the oxidation (hydroxylation) of ammonia to hydroxylamine (NH_2OH), catalyzed by ammonia monooxygenase (AMO). This enzyme is a member of the copper-containing, membrane-bound monooxygenase family that also includes particulate methane monooxygenase (pMMO). Hydroxylamine is the substrate for the multiheme enzyme hydroxylamine oxidoreductase (HAO), which catalyzes its three-electron oxidation to NO.[271−273] The active site heme of HAO, called the P460 center, is a unique cofactor with a heme that is doubly crosslinked to Tyr491 at the 5′ *meso*-carbon and the pyrrole *α*-carbon positions.[272] In the following step of nitrification, NO is then oxidized to NO_2^-, but the enzyme that catalyzes this reaction is currently unknown.[255] The final step of nitrification corresponds to the oxidation of nitrite to nitrate by nitrite oxidoreductases (NXR),[255] which belong to the family of Mo oxotransferases.[274]

Two major pathways are known by which microbes utilize nitrite and nitrate as electron acceptors for anaerobic respiration (see Figure 11). The first one is denitrification, a multi-step process by which nitrate is reduced to N_2O (fungal denitrification) or all the way to N_2 (bacterial denitrification; see Figure 12). In the first chemical step of denitrification, nitrate is reduced by two electrons to nitrite by Mo-dependent nitrate reductases (NARs) via an O-atom transfer step:[274]

$$\mathrm{Mo^{IV}} + \mathrm{NO_3^-} \rightarrow \mathrm{Mo(VI){=}O} + \mathrm{NO_2^-} \tag{7}$$

The one-electron reduction of nitrite to NO:

$$\mathrm{NO_2^-} + \mathrm{e^-} + 2\mathrm{H^+} \rightarrow \mathrm{NO} + \mathrm{H_2O} \tag{8}$$

is catalyzed by both copper-containing nitrite reductases (CuNIRs)[275,276] and heme cd_1 NIRs (see Section 4.1).[25] The former enzymes contain a Type 2 copper center as the active site where nitrite binds and its reduction to NO takes place.[277] Whether the product NO is initially bound to the copper center at the end of the catalytic cycle or directly released is still being investigated.[278] Also, the exact sequence of nitrite binding versus electron/proton transfer to the Type 2 copper site is controversial.[279−283] In 2004, Murphy and coworkers reported the crystal structure of CuNIR with NO bound in an unusual, side-on fashion.[284] This result gathered much attention in the community and inspired more work on CuNIRs,[285−290] and also enticed inorganic chemists to study additional $\{\mathrm{CuNO}\}^{10}$ and $\{\mathrm{CuNO}\}^{11}$ model complexes.[17,275] The discovery of domain extended CuNIRs provided further stimulation for this field.[291−294] Heme cd_1 nitrite reductases are generally homodimers, with an N-terminal heme *c* domain and a C-terminal heme d_1 domain in each monomeric subunit (see Section 4.1). Heme d_1 is unique to denitrifiers and has a unique structure where the porphyrin ring is oxidized and decorated with two carbonyl groups (Scheme 4).[142] In the reduced, ferrous oxidation state, heme d_1 is 5C with proximal histidine coordination. This heme then binds nitrite in the first step of the catalytic cycle.[295] Proton transfer (mediated by two distal His residues) to the coordinated nitrite follows to generate water plus the ferric heme d_1 NO (enzyme-product) complex (analogous to eq 1a). Reduction and loss of NO, which is believed to be facilitated by the unusual properties of heme d_1, then closes the catalytic cycle.[296−299]

The NO produced by the reduction of nitrite is then further metabolized by respiratory NO reductases (rNORs; see Figure 12), following eq 5, to generate N_2O (see Section 4). Two main classes of rNORs have been identified,[25] fungal NO reductase (Cyt. P450nor), which is a Cyt. P450-type enzyme,[300,301] and bacterial *c*NOR, which is closely related to respiratory heme-copper oxidases (Cyt. *c* Oxidases, C*c*Os).[302,303] Cyt. P450nor is an unusual Cyt. P450-type enzyme, as it performs a reduction of its substrate and hence, does not require O_2. The active site of this enzyme is typical for Cyt. P450s and contains a heme *b* with axial Cys coordination. In the first step of the reaction, the ferric heme binds NO to form a ls-$\{\mathrm{FeNO}\}^6$ complex. This step is followed by a direct hydride transfer from NAD(P)H to the ferric NO complex,[304] which generates the so-called "Intermediate I". This species corresponds to a ls-$\{\mathrm{FeNH_nO}\}^8$ type complex, but its protonation state ($n = 1$ or 2) is unknown.[305−308] Intermediate I is catalytically competent to react with a second molecule of NO to generate N_2O, which completes the catalytic cycle.[305,309−311] In bacterial rNORs, *c*NOR (or NorBC) is the main representative, but this enzyme family also includes qNOR and $\mathrm{Cu_A}$NOR, where the "*c*", "q", and "$\mathrm{Cu_A}$" refer to different electron transfer sites.[303,312] In all cases, the active site contains a high-spin heme *b*, termed heme b_3 (due to its analogy to heme a_3 in C*c*Os), and an adjacent non-heme iron center, called $\mathrm{Fe_B}$.[313] The overall active site layout is very similar to C*c*Os, and in fact, *c*NORs are considered evolutionary predecessors of these enzymes.[314,315] The enzyme is catalytically active in the diferrous state of the active site, but mechanistic data for *c*NORs are sparse. For example, whether this enzyme functions via a key mono- or dinitrosyl intermediate, responsible for N−N coupling, is unknown (other than from computational studies[316]) and in fact, even the sequence of NO binding to the active site of this enzyme is still under active investigation.[317] Hence, several mechanisms are being considered for *c*NORs as recently reviewed,[254] but further studies are necessary to fully elucidate the mechanism of these enzymes.[317] Another related question is whether a NorBC analog could catalyze NO dismutation, that is, conversion of 2 NO into N_2 and O_2.[318] Direct evidence for this process, however, is still missing.

In bacterial (but not fungal) denitrification, N_2O is further reduced to N_2 by nitrous oxide reductases (N2OR; see Figure 12), which catalyze the reaction:[319]

$$\mathrm{N_2O} + 2\mathrm{e^-} + 2\mathrm{H^+} \rightarrow \mathrm{N_2} + \mathrm{H_2O} \tag{9}$$

N2ORs are homodimeric metalloenzymes where each subunit contains two copper sites denoted $\mathrm{Cu_A}$ and $\mathrm{Cu_Z}$. The dinuclear $\mathrm{Cu_A}$ center is located in the C-terminal domain and serves as an electron transfer site, whereas the tetranuclear $\mathrm{Cu_Z}$ center corresponds to the active site, which is located in the N-terminal domain. The $\mathrm{Cu_Z}$ cluster then performs the reduction of N_2O.[319] The crystal structure of N2OR from *P. nautica*[320] revealed the unexpected structure of the $\mathrm{Cu_Z}$ center, which is a tetrahedral 4Cu cluster with a bridging sulfide ligand (S^{2-}) in the center ("$\mathrm{Cu_4S}$"). The $\mathrm{Cu_I}$−$\mathrm{Cu_{IV}}$ edge is bridged by a solvent-derived ligand, and it has been proposed that this is the site of substrate binding. The resting state of the $\mathrm{Cu_4S}$ cluster, called $\mathrm{Cu_z}$*, has a mixed valent ($3\mathrm{Cu^I}\mathrm{Cu^{II}}$) (1-hole) electronic structure, which was confirmed spectroscopically.[321] The $1e^-$ reduced form of $\mathrm{Cu_z}$*, where all copper centers are in the +I state ("$\mathrm{Cu^I_4S}$"), has been shown to be catalytically active for N_2O reduction.[322] These ideas were later challenged by Einsle and coworkers, who determined the crystal structure of N2OR from *P. stutzeri* under anaerobic conditions.[323] The resulting structural model features a S^{2-} ligand bridging the $\mathrm{Cu_I}$ and $\mathrm{Cu_{IV}}$ centers of the $\mathrm{Cu_Z}$ cluster, which renders N_2O binding at this edge unlikely. Later reactivity studies by Moura, Solomon, and coworkers showed that the S^{2-}-bridged $\mathrm{Cu_Z}$ cluster is not catalytically active, providing strong evidence that the original N2OR structure, $\mathrm{Cu_z}$*, is a more accurate reflection of the $\mathrm{Cu_Z}$ cluster in the catalytically active state.[322] The mechanistic details of N2ORs are still under active investigation.

The second pathway that allows microbes to use nitrite and nitrate as electron acceptors for anaerobic respiration is the dissimilatory nitrate reduction to ammonia (DNRA) process (see Section 4.4).[23,324,325] Here, nitrate is first reduced by two electrons to nitrite, as observed for denitrification, but nitrite is then reduced directly (by six electrons) to NH_4^+ by the multiheme enzymes Cyt. *c* nitrite reductases (C*c*NIRs), following the reaction:

$$\mathrm{NO_2^-} + 6\mathrm{e^-} + 8\mathrm{H^+} \rightarrow \mathrm{NH_4^+} + 2\mathrm{H_2O} \tag{10}$$

Scheme 5. To Generate Nitric Oxide via Nitric Oxide Synthase, L-Arginine First Converts to NOHA by Hydroxylation[a]

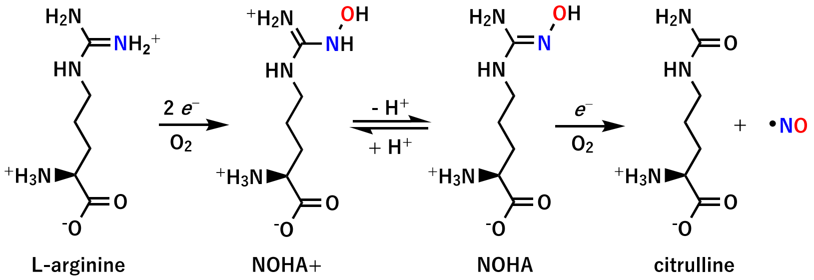

[a]The hypothesis that the intermediate, NOHA, exists in its protonated form when undergoing oxidation has been called into question by DFT studies that suggest a neutral NOHA, as indicated.[339]

The active site heme of *Cc*NIRs is unusual, as it shows axial Lys coordination, although the significance of the proximal Lys for catalysis is unclear. Notably, nitrite reduction to ammonia by *Cc*NIRs is proposed (from computational studies) to involve the complete set of heme-based ls-$\{FeNO\}^{6-8}$ intermediates,[326] but details of the mechanism and experimental characterization of such reaction intermediates are lacking.[327] The DNRA pathway is particularly interesting as a natural mechanism to convert nitrite and nitrate back into ammonium (i.e., fertilizer), instead of converting them into gaseous products and losing nitrogen from the soil.[254]

Anaerobic ammonium-oxidizing (ANAMMOX) bacteria are unique microbes that use hydrazine (N_2H_4) as a primary metabolite. The enzymes involved in the ANAMMOX pathway are highly complex, and therefore, progress in our understanding of the mechanisms of the involved enzymes and the chemistry that they mediate has been slow.[22] In the first step of the ANAMMOX pathway, hydrazine synthase (HZS), a multiheme enzyme with a complex structure (a dimer of heterotrimers), catalyzes the generation of hydrazine from NO (which originates from nitrite reduction) and ammonia via two half reactions.[328] Hence, this is a second pathway, besides nitrification, that competes with plants for ammonia fertilizer. In the proposed mechanism of HZS, one equiv of NO is reduced to hydroxylamine at the first active site of the enzyme. The hydroxylamine product then diffuses through the enzyme complex to the second active site, where it is combined with ammonia to generate hydrazine. In the second step of the ANAMMOX process, hydrazine is then oxidized to N_2 by hydrazine dehydrogenase (HDH).[329−331] Via this process, HDH returns an estimated 50% of the total N_2 to the atmosphere, to close the nitrogen cycle.[331]

1.4. Enzymes and Model Complexes

Model complexes are a key tool utilized in bioinorganic chemistry to investigate the mechanisms of metalloenzymes, help identify putative intermediates, elucidate the roles of the metals' first and second coordination sphere (SCS) in catalysis (including H-bonding and electrostatic interactions), and determine the role of the protein matrix for a given reaction. Studies on model complexes and the corresponding proteins should generally be seen as complimentary. On the one hand, models are not the same as the "real" enzymes, but on the other hand, they allow us to explore a given enzymatic reaction in a broader context, investigate the fundamental reactivity of key intermediates and identify side reactions that may be suppressed in the enzymes, trap intermediates at cryogenic temperatures (typical at −80 °C), define the spectroscopic signatures of such intermediates for future identification in enzymes, and develop small-molecule catalysts that can catalyze similar reactions as the enzymes. Reactions can be conducted in strictly controlled environments, for example water-free conditions, in the hopes of trapping intermediates that may not be accessible in aqueous environments. Finally, the influence of steric and electronic effects on a given reaction are often more straightforward to investigate in model systems, where modifications to the ligand scaffold with predictable outcomes can easily be made, compared to creating corresponding variants in enzymes where we are restricted by the naturally occurring amino acids. By pursuing synergistic studies on enzymes and model complexes in direct comparison, we can best elucidate reaction mechanisms and the factors that contribute to achieving the observed reactivity in a given enzyme. Another approach that has proven of great value is to model the active sites of large, complicated and sometimes unstable proteins by engineering analogs of their active sites into *de novo* designed or other small, stable proteins.[332−334] With respect to the latter, myoglobin, azurin, and rubredoxin are prominent examples for this approach.[332,335,336]

Typical synthetic porphyrins used to model the active sites of heme proteins are H_2[TPP] (tetraphenylporphyrin), H_2[OEP] (octaethylporphyrin), and picket fence porphyrins, which are based on the H_2[TPP] scaffold, and other derivatives of these macrocycles. In addition, the naturally occurring protoporphyrin IX (heme *b*) is often used, H_2[PPIX], and the corresponding dimethylester, H_2[PPIXDME]. A structural comparison of naturally-occurring and synthetic hemes is provided in Scheme 4. Many corresponding metalloporphyrin complexes have been prepared and their reactivity with NO has been studied in great detail, using structural, spectroscopic and theoretical methods (especially density functional theory (DFT) calculations).[5,26,337,338]

1.5. Scope of this Review

This review is focused on the metalloproteins involved in the biosynthesis, signaling, transport, and metabolism of NO in biology, with a focus on those containing iron as the active site metal. This involves both heme and non-heme iron centers involved in NO signaling and metabolism, with corresponding proteins being present in all branches of the tree of life. The available structural, spectroscopic and mechanistic data for the NO adducts and related NH_xO_y-type intermediates of these proteins are further correlated to results for small molecule model complexes, to arrive at unequivocal electronic structure descriptions of these species, which are then related to their functions and reactivity in biology. Here, it is the intimate combination of spectroscopy and quantum-chemistry that allows researchers to determine the often complicated

Scheme 6. Electron Transfer in NOS in the Conversion of L-Arginine and Dioxygen to Citrulline and Nitric Oxide[374a]

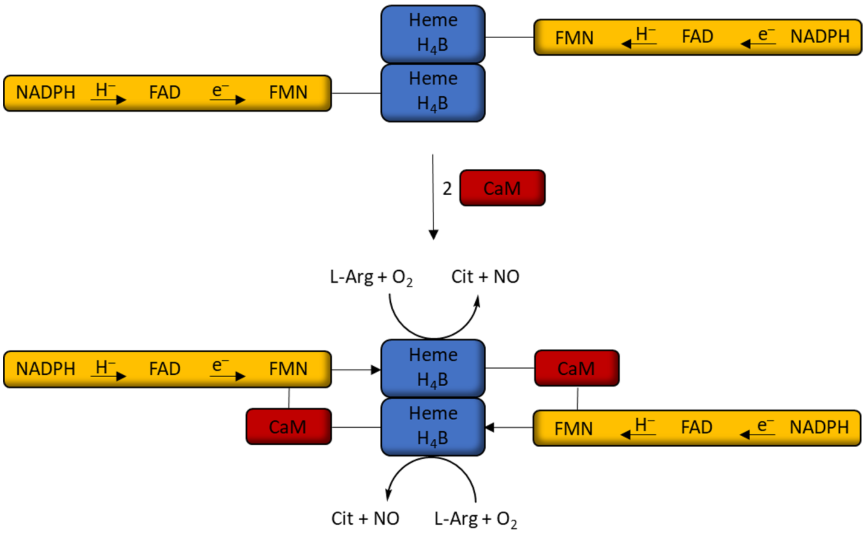

[a]Yellow regions represent the reductase domain, while the blue regions correspond to the oxygenase domain. Electron transfer occurs from the reductase domain of one monomer to the oxygenase domain of the other. Calmodulin (CaM) binding mediates electron transfer necessary to form citrulline and nitric oxide.

electronic structures of these iron−NO and $-NH_xO_y$ complexes. A particularly important transformation that is currently receiving much attention in the field is the N−N coupling reaction in NORs, and correspondingly, we are paying particular attention to this process and literature precedence for N−N coupling in model complexes, leading to the generation of N_2O.

In addition, we also highlight the role of DNICs as products of the reaction of NO with iron−sulfur sites in proteins, as a form of NO storage in mammals (formed from NO and iron from the labile pool), and as NO-delivery platforms and drugs. We also review the interesting spectroscopic properties and electronic structures of these species, and their reactions with other small molecules of biological significance.

2. NITRIC OXIDE IN MAMMALIAN SIGNALING AND IMMUNE DEFENSE

2.1. Nitric Oxide Generation by L-Arginine Oxidation (NOS)

The synthesis of nitric oxide from L-arginine is mediated by nitric oxide synthase (NOS) *in vivo*. The NOS enzymes are known to exist in mammals, bacteria, and archaea. Formation of NO through NOS arises in a two-step process where an N^G-hydroxy-L-arginine (NOHA) intermediate is formed, followed by release of citrulline and NO (Scheme 5). The overall reaction requires consumption of O_2 and the reduced form of nicotinamide adenine dinucleotide phosphate (NADPH):

$$\begin{aligned}&\text{Arg} + 1.5\text{NADPH} + 2\text{O}_2 + 1.5\text{H}^+\\&\rightarrow \text{Citr} + 1.5\text{NADP}^+ + \text{NO} + 2\text{H}_2\text{O}\end{aligned} \quad (11)$$

In mammals, NOS isozymes are divided into three different categories consisting of neuronal (nNOS), endothelial (eNOS), and inducible NOS (iNOS), where each enzyme differs in location and function. Both neuronal and endothelial NOS are also termed constitutive NOS (cNOS), which produce NO at nanomolar concentrations.[340] Endothelial NOS is expressed primarily in endothelial cells as well as other areas such as myocytes and platelets.[341−343] NO generated by eNOS diffuses into smooth-muscle cells to activate sGC (see Section 2.2) and affects blood flow and blood pressure regulation. Diffusion of NO between endothelial and muscle cells is controlled by the oxidation state of hemoglobin α at the cell-cell junction, in which ferrous oxyhemoglobin can block NO diffusion to smooth muscle cells via the dioxygenation reaction (see eq 3 in Section 1.2).[344,345] The presence of another signaling molecule, H_2S, previously thought to be independent of NO, can also affect NO bioavailability by upregulating eNOS.[346] Neuronal NOS is expressed in central and peripheral neurons and some other cells including vascular smooth muscle cells and cardiac neurons.[347,348] The biological functions of nNOS include synaptic plasticity in the central nervous system, central regulation of blood pressure, smooth muscle relaxation, and vasodilatation via peripheral nitrergic nerves.[349,350] Neuronal NOS provides a potential target for new therapeutic opportunities against neuronal and pathological diseases such as skeletal muscle atrophy.[351] Inducible NOS is not expressed in cells under the normal conditions but its expression can be induced in almost any cell type including vascular smooth muscle cells, cardiac myocytes and macrophages, and expressed during proinflammatory conditions.[352,353] Unlike cNOS isozymes, the production of NO by iNOS leads to micromolar concentrations of NO and is not mediated by intracellular calcium concentrations.[354] These elevated levels of NO, in comparison to cNOS nitric oxide generation, can serve as immune or inflammatory responses.[355,356] Notably, overproduction of NO can occur, leading to toxic effects *in vivo* and may lead to the development of several diseases including cancer,[357,358] diabetes,[359−361] Alzheimer's disease,[362] and Parkinson's disease.[362,363]

While NOS has been known to exist in bacteria, the structure and function of several of these enzymes are contrasting to mammalian NOS. In particular, these enzymes lack a reductase domain, requiring external reductants during the synthesis of NO.[364] The function of NO after synthesis is also unclear. Evidence points towards many different purposes such as cellular respiration,[365−367] regrowth,[368,369] and virulence.[370−373] While much effort has been put forth in studying

https://doi.org/10.1021/acs.chemrev.1c00253
Chem. Rev. XXXX, XXX, XXX−XXX

the function of bacterial NOS, there has also been recent interest in targeting these enzymes with inhibitors to fight pathogenic bacteria.[373]

2.1.1. Structure of Nitric Oxide Synthase. In mammals, NOS enzymes consist of a homodimer with each monomer containing both an oxygenase domain and a reductase domain.[375,376] NOS must exist as a dimer due to electron transfer from the reductase domain in one monomer to the oxygenase domain in the other.[377] Two cysteine residues from each monomer are coordinated to a central zinc ion that lies at the interface of the monomers.[378] Several cofactors in NOS isozymes that assist with enzymatic activity are contained in the NOS isozymes, including flavin mononucleotide (FMN), flavin adenine dinucleotide (FAD) and NADPH. FMN and FAD serve as electron shuttles from NADPH to the heme (Scheme 6, Figure 13).[379] In this process, the dimers allow for electrons to move from the reductase domain of one monomer to the oxygenase domain of the other.[380] It is important to note that initiation of NO synthesis and electron transfer to the oxygenase domain are mediated by the binding of calmodulin.[381,382] The binding site of calmodulin is located between the oxygenase and reductase domains. Calmodulin binds much tighter in iNOS than in cNOS. As a result, iNOS is regulated by transcription without the requirement for elevated Ca^{2+} concentrations.[354]

During the synthesis of NO, dioxygen coordinates to the heme-thiolate active site, that is, an iron protoporphyrin IX cysteinate complex, located in the oxygenase domain.[383] A corresponding heme-oxygen intermediate is then able to react with L-arginine bound to the enzyme. Unlike many other heme-based oxygenases like Cyt. P450, the structure of NOS around the distal pocket consists mainly of β-sheets rather than α-helices.[384] Moreover, there exists a hydrogen bond between the thiolate ligand and tryptophan that is not present in Cyt. P450s (Figure 14).[384] Separately, the heme propionate groups have interactions with tetrahydrobiopterin (H_4B) and L-arginine, which therefore have electronic influences and impose conformational changes on the heme.[385] It was reported that the effects of bound H_4B and L-arginine are different for iNOS and nNOS.[386] The difference in heme midpoint potentials (vs SHE) of iNOS and nNOS without H_4B and L-arginine bound, −347 mV versus −239 mV, suggests differences in enzyme activity despite their similar structures.[386] The shift in reduction potential, after binding of H_4B and L-arginine, in iNOS is much greater than that of nNOS, with midpoint potentials (vs SHE) of −263 mV for iNOS and −248 mV for nNOS, which reveals that enzyme activity is much more dependent on H_4B and L-arginine binding in iNOS. Lack of H_4B, L-arginine, and cofactors may cause NOS uncoupling leading to formation of superoxide (O_2^-) instead of NO.[387] Lack of L-arginine has also been shown to also cause formation of peroxynitrite ($ONOO^-$).[388]

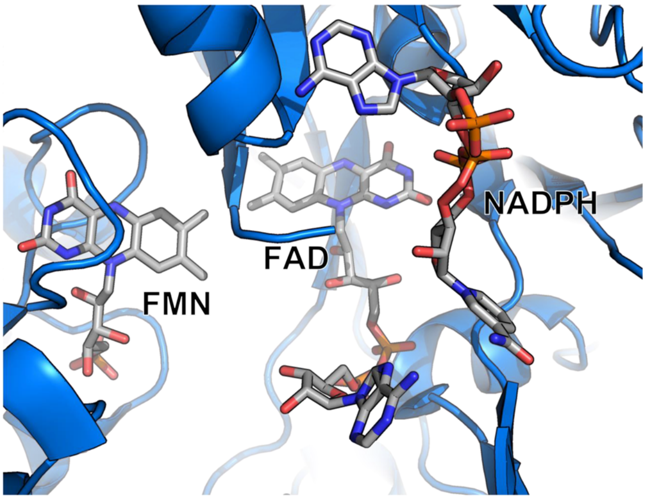

Figure 13. PyMOL generated image of the crystal structure of nNOS (PDB: 1TLL) with cofactors FMN, FAD and NADPH highlighted. These cofactors are responsible for electron transfer during the synthesis of nitric oxide.

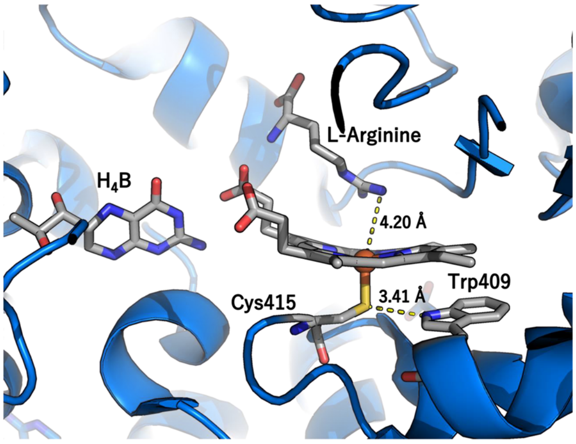

Figure 14. PyMOL generated image of the crystal structure of nNOS (PDB: 2G6H) featuring H_4B, bound L-Arginine and the proximal Cys415 ligand to the heme. Hydrogen-bonding exists between residues Cys415 and Trp409.

Although the location and regulation of neuronal, endothelial, and inducible NOS isoforms are different from one another, there is still 51−57% homology between the different isoforms.[384] A comparison of several known inducible and endothelial NOS crystal structures reveals that the oxygenase domain contains 376 equivalent α-carbons between the two forms.[25] Several high resolution crystal structures of NOS have been studied (Table 1). Although the three isozymes are similar, there are also several differences, including the N-terminal 220 amino acids in nNOS which target synaptic sites in the brain and in skeletal muscle.[384] As stated previously, the NOS isozymes also differ in their reliance on Ca^{2+} concentration for activation. After elevation of Ca^{2+} in constitutive NOS isoforms, binding of calmodulin to NOS occurs. This binding facilitates electron transfer from NADPH to the heme and is a necessary step in the synthesis of NO through cNOS.[382] For example, it has recently been suggested that eNOS exists in erythrocytes and converts L-arginine to L-citrulline with Ca^{2+}-calmodulin binding dependence.[389]

Unlike constitutive NOS, inducible NOS enzyme activity does not depend on increased Ca^{2+} nor is it inhibited by divalent cation chelators or drugs that prevent binding of calmodulin.[354,401,402] This is a result of tightly bound calmodulin where the NOS is always activated, unique to iNOS. However, iNOS is usually not expressed and must be induced by activators such as cytokines or lipopolysaccharide.[403,404] Additionally, slight differences in NOS isozymes can lead to selective inhibition. Although neuronal and endothelial NOS have a single difference in a residue within the active site, this subtle difference leads to greater inhibition of nNOS by

Table 1. Crystal Structures of NOS

protein	organism	PDB code	resolution (Å)	ref
n-NOS(II) + H_4B	*Rattus norvegicus*	2G6H	2.00	390
n-NOS(II)−NO + H_4B + L-Arg	*Rattus norvegicus*	2G6K	2.00	390
n-NOS(II)−NO + H_2B	*Rattus norvegicus*	2G6L	2.05	390
n-NOS(II)−CO + NOHA + H_4B	*Rattus norvegicus*	3HSN	1.91	391
n-NOS(II) + H_4B	*Rattus norvegicus*	3HSP	2.20	391
n-NOS + N(omega)-methoxyl-L-Arg	*Rattus norvegicus*	4FVW	1.81	392
e-NOS(II) + L-Arg	*Bos taurus*	1FOL	2.20	393
e-NOS(II) + L-Arg	*Bos taurus*	1FOO	2.00	393
e-NOS(II)−NO + H_4B + L-Arg	*Bos taurus*	1FOP	2.30	393
e-NOS + L-Arg + WSD	*Bos taurus*	4CUL	2.23	394
e-NOS(II) + L-Arg	*Bos taurus*	4NSE	1.95	395
e-NOS + NOHA	*Homo sapiens*	3NOS	2.40	378
e-NOS + 327	*Homo sapiens*	3EAH	2.44	396
e-NOS + KMM	*Homo sapiens*	6NH7	1.90	397
i-NOS(III)-CN	*Mus musculus*	1N2N	2.40	398
i-NOS(III) + H_4B + H_2O	*Mus musculus*	2NOD	2.60	385
i-NOS + pterin	*Mus musculus*	3E65	2.05	396
bs-NOS(II)−NO + NOHA	*Bacillus subtilis*	2FBZ	2.10	399
bs-NOS(II)−NO + L-Arg + H_2B	*Bacillus subtilis*	2FC1	2.00	399
bs-NOS(III)−NO + L-Arg + H_2B	*Bacillus subtilis*	2FC2	2.20	399
bs-NOS + L-Arg	*Bacillus subtilis*	1M7V	1.95	400
bs-NOS + NOHA	*Bacillus subtilis*	1M7Z	2.14	400

Scheme 7. Proposed Catalytic Cycle for the Hydroxylation and Oxidation Steps of NO Synthesis by NOS[a]

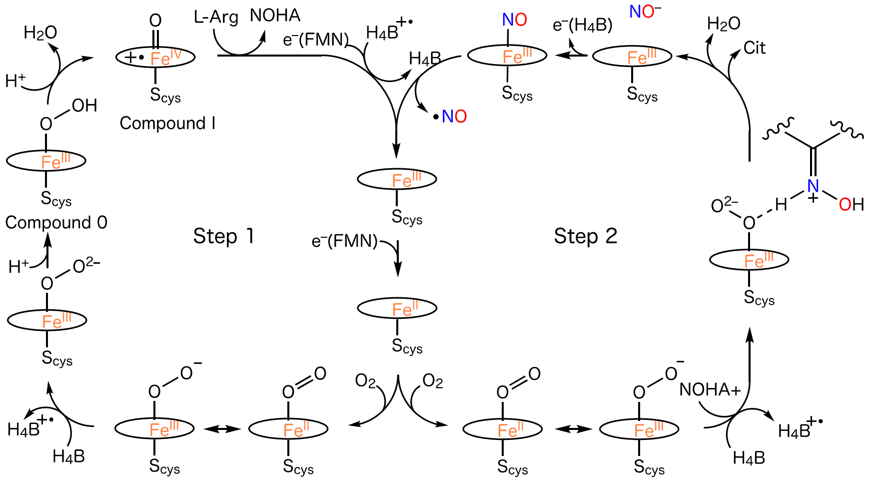

[a] In the primary hydroxylation (left), the ferric heme resting complex requires two electron and proton transfers to form the high-valent intermediate Compound I, while the secondary oxidation (right) requires two electrons and a single proton to form the ferric-peroxo species, which subsequently generates citrulline and NO.

isoform-selective inhibitors developed as therapeutics.[405] Several inhibitors have been studied to prevent overproduction of NO from nNOS, which has been known to cause neurodegenerative diseases.[406]

2.1.2. NO Synthesis Mechanism. Although the structure and function of each of the three NOS isozymes are different, they each follow a similar pathway in the synthesis of NO (Scheme 7). The reaction begins with the binding of L-arginine to the heme where the substrate undergoes an NADPH-dependent hydroxylation to form the intermediate N^G-hydroxy-L-arginine (NOHA).[407,408] This intermediate is oxidized and converted to citrulline and NO.[409] After this cycle, a ferric heme−nitrosyl (enzyme-product) complex releases the relatively weakly bound NO.

The first step in NO synthesis by NOS isozymes involves the hydroxylation of L-arginine where the substrate undergoes a two-electron oxidation to form NOHA (Step 1, Scheme 7). It has been suggested that the initial hydroxylation follows the same mechanism as Cyt. P450s.[410−412] In this initial step, it has been hypothesized that the electrons are shuttled from NADPH to FAD to form $FADH_2$ in the reductase domain.[413] $FMNH^•$ and $FADH^•$ are then formed after the disproportionation of $FADH_2$. The ferric heme can thereby be reduced by electron transfer from $FMNH^•$. Then, the binding of O_2 to the ferrous heme trans to cysteine forms the Fe(II)−O_2 intermediate. However, this species is quickly converted to a ferric-peroxo species by electron transfer from $FMNH^•$ and FAD or H_4B.[411,412] This species further undergoes a proton transfer to form a ferric-hydroperoxo (Compound 0) species and

Scheme 8. Proposed Mechanisms for Synthesis of NO and Citrulline from NOHA through NOS[a]

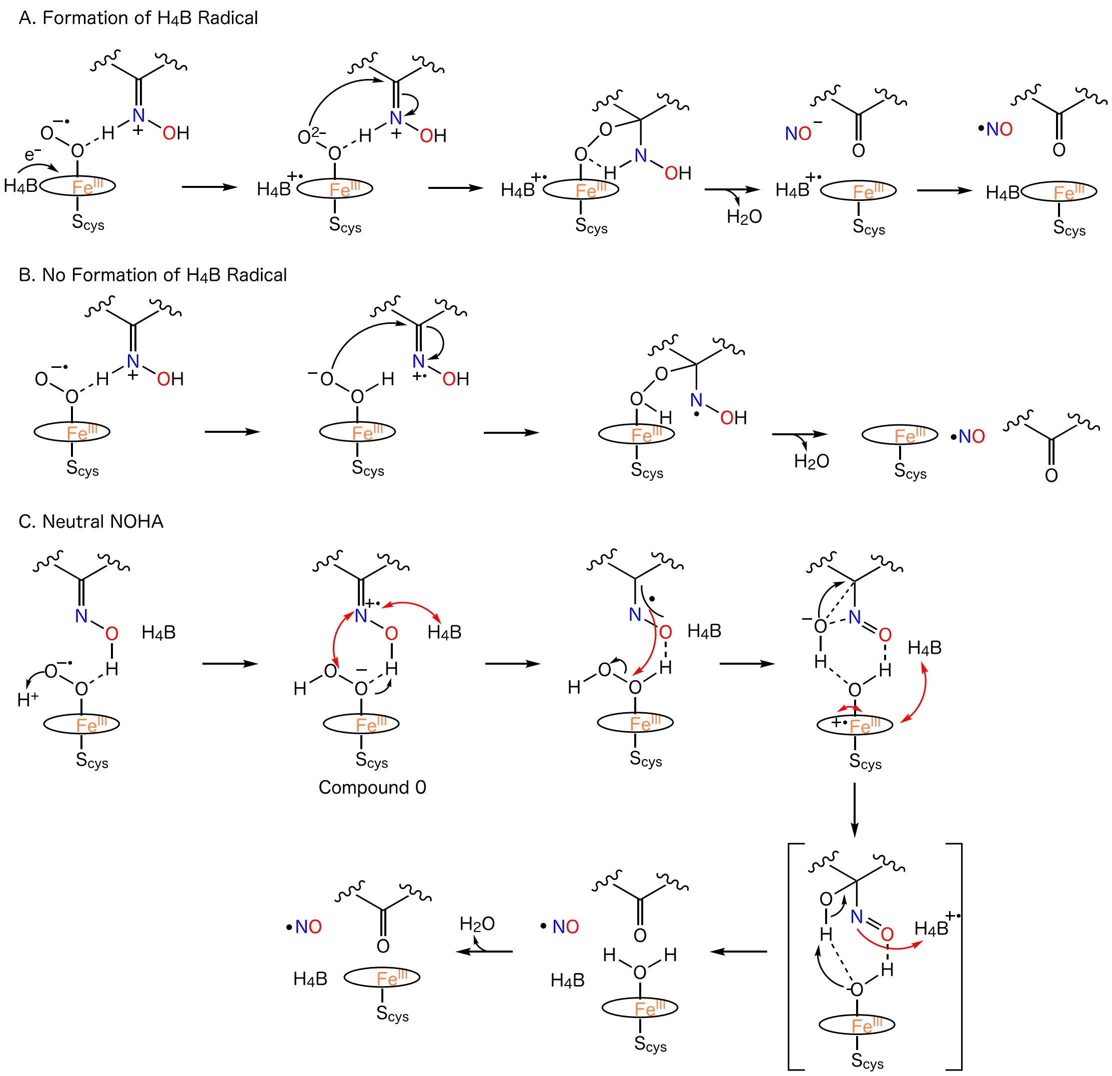
A. Formation of H_4B Radical

B. No Formation of H_4B Radical

C. Neutral NOHA

[a]Mechanisms A and B describe the synthesis with and without the formation of the $H_4B^{\bullet+}$ radical.[421] Mechanism C describes the synthesis using neutral NOHA instead of the protonated form, in which spin delocalization is represented by the red double headed arrows while the electron tunneling is represented by the red single headed arrows.[422]

subsequently a high-valent ferryl species, [Fe(IV)=O($P^{\bullet+}$)] (Compound I), after heterolytic cleavage of the O−O bond.[414] More analysis is necessary to pinpoint the exact proton transfers involved in the first step of NO synthesis. Note that in the mechanism it is hypothesized that two proton transfers take place.[415] Solvent and L-arginine have been suggested to be responsible for proton donation in forming Compound 0 in the first proton transfer and Compound I in the second proton transfer, as supported by previous DFT studies.[416−418] Following the formation of Compound I, L-arginine hydroxylation to generate NOHA is followed by electron transfer from FMN to $H_4B^{\bullet+}$ to restart the cycle. Alternatively, DFT studies have shown a possible path where Compound II is formed from electron transfer to Compound I and is then suggested to be the active species.[416,417]

To generate NO along with citrulline, the intermediate, NOHA, is oxidized in the active site of the enzyme following the hydroxylation step (Step 2, Scheme 7).[419] An altered hydrogen-bonding network and conformational changes with NOHA versus L-arginine bound in the active site are likely the reason for a different pathway for this oxidation.[420] There has been much discussion as to what the exact mechanism is for the second oxidation step. The reaction begins similarly to the first step with reduction of the ferric heme through electron transfer and binding of O_2 to form Fe(II)−O_2. After the formation of Fe(II)−O_2, the exact mechanism remains unclear and several mechanisms have been proposed to understand the oxidation of NOHA.

Two mechanisms have been proposed based on detailed studies of the protonated substrate binding to the ferric-superoxo species (Scheme 8A,B). Mechanism A involves the reduction of the ferric-superoxo species by H_4B to form the ferric-peroxo species (Step 2, Scheme 7 and Scheme 8A). Evidence from crystal structures and ENDOR spectroscopy support the hypothesis that the N−H group of $NOHA^+$ is close enough to interact with the O atom bound to the ferric heme.[391,400,423] The next step requires a cyclic intermediate which ultimately collapses to form NO^- and citrulline. A similar mechanism was observed in certain members of the P450 family, including CYP 17 and CYP 19, whereby the ferric-

Scheme 9. Conversion of GTP to cGMP via sGC

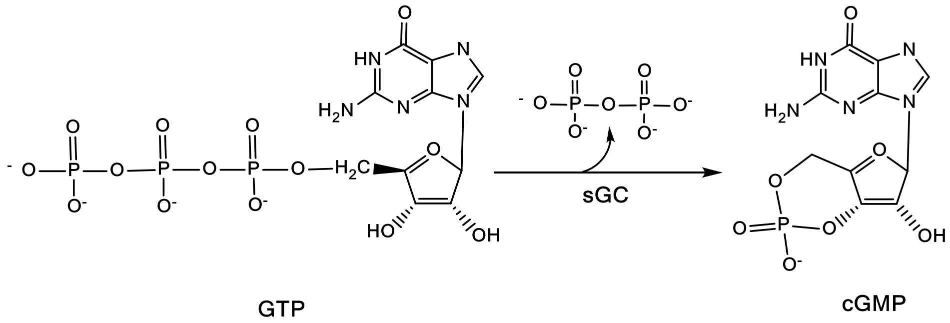

peroxo anion undergoes nucleophilic attack to form a Fe−O−O−C moiety for the hydroxylation and acyl-carbon bond cleavage.[424−426] The oxidized $H_4B^{\bullet+}$ radical and NO^- undergo an electron transfer to form the product, NO, and regenerate H_4B. Although formation of the $H_4B^{\bullet+}$ radical has been observed, reduction to H_4B to form NO has not been demonstrated. The alternative mechanism B avoids the formation of the $H_4B^{\bullet+}$ radical (Scheme 8B). In this mechanism, the ferric superoxo species undergoes an H atom abstraction to form the ferric-hydroperoxo species.[427] This species then undergoes a nucleophilic attack on the substrate for conversion to citrulline and NO. These mechanisms should be studied further as the $H_4B^{\bullet+}$ radical does form in the oxidation step (Scheme 7, Step 2) of NOS, but it remains unclear how $H_4B^{\bullet+}$ is reduced back.[428]

There is also ongoing debate on whether the intermediate, NOHA, is protonated when it enters the cycle. There have been many studies that propose a protonated form as shown in Scheme 8A and B.[429,430] In contrast, a DFT study suggested a potential neutral NOHA pathway that challenges this notion and is supported by experimental observations.[422] Mechanism C (Scheme 8C) occurs through formation of the ferric-hydroperoxo species, Compound 0, after a proton transfer from the heme propionate and electron transfer from two donors, neutral NOHA and H_4B, via long-range spin delocalization. A subsequent proton transfer from the NOHA radical cation to the proximal oxygen allows for formation of the ferriheme−H_2O_2 complex. The following electron transfer from the NOHA-derived radical mediates the O−O bond cleavage of H_2O_2 to form a protonated Compound II intermediate that is stabilized by spin delocalization in H_4B, and the OH^- transfer to the substrate (Scheme 8C, top right). Proton transfer to the Fe^{III}−OH center coupled with eletron transfer to the H_4B radical leads to the final products. The proposed mechanism has been able to support several different experimental observations in the second step of NO synthesis that involve kinetics and intermediates. One observation includes Fe(II)−O_2 being the last observable species due to the high activation barrier in forming Compound 0, followed by low activation barriers for the following steps as calculated by DFT.[431] This barrier in forming Compound 0 also matches the kinetics of decay of Fe(II)−O_2.[428,431,432] These mechanisms should be studied further to better understand the protonation state of NOHA during the second step of catalysis.

2.1.3. Bacterial NOS.

Although NOS isozymes also exist in bacteria, the structures of these enzymes in bacteria and mammals are dissimilar. NOS belonging to gram-positive bacteria, for example, consist of a dimer with two oxygenase domains but no reductase domains.[364] This differs from mammalian NOS that contain both oxygenase and reductase domains. As a result, bacteria rely on external sources to serve as reductants for NOS. Much effort has been placed into studying these external reductants. Inspection of *Bacillus subtilis* shows that bacterial flavodoxin supports nitric oxide synthesis.[433] In the absence of flavodoxin, NOS activity is still present in the bacteria, which suggests that multiple electron sources may act as external reductants. The ability of bacteria to generate NO via other pathways, including nitrate reduction, further complicates ongoing studies. Separately, evidence supports that NOS in *Escherichia coli* generates NO *in vivo* and that the reductase lies within the host.[434] Another bacterium, *Sorangium cellulosum*, does in fact contain a reductase domain with structural differences to mammalian NOS.[435,436] The reductase domain, in particular, is N-terminal to the oxygenase domain instead of C-terminal as with mammalian NOS. Thus, bacterial NOS has been shown to have a wide range of redox partners. More studies into the nature of these reductants are currently being conducted.

The function of bacterial NOS is also unclear since bacteria do not require protection against pathogens or intercellular communication as do mammals. In the *Streptomyces* strain that gives rise to potato scab disease, phytotoxins and thaxtomins are responsible for interference with plant cell-wall synthesis.[437,438] Data indicate that production of NO by NOS has an effect on the nitration of these thaxtomins.[439] More recently, NO synthesis via NOS in *Staphylococcus aureus* has been shown to play a key role in cellular respiration.[365−367] Separately, NO has been shown to mediate growth recovery of *Deinococcus radiodruans* upon exposure to UV light and ionizing radiation.[368,369] In addition to the cellular respiration and growth functions, NO synthesized by NOS within *Bacillus subtilis* has also been shown to function as protection against oxidative stress from hydrogen peroxide by reactivating catalase, normally inhibited by endogenous cysteine.[440] Evidence suggests NO plays a role in protecting pathogens from immune oxidative attack. Studies into the effect of NO synthesis on virulence have also been conducted.[370−373] Lack of NOS in *Staphylococcus aureus*, in particular, leads to increased vulnerability to O_2 and ultimately increased killing of this bacterium by human neutrophils.[373] Future studies of NOS inhibitors as drugs might lead to the development of better therapeutics to fight this bacterium.

2.2. Nitric Oxide Detection by Soluble Guanylate Cyclase (sGC) and *H-NOX*

2.2.1. Structural Features of sGC.

The protein sGC is the universal receptor/sensor for NO in mammals, activating cGMP-based regulatory pathways, which are involved in neurotransmission, control of platelet aggregation, smooth

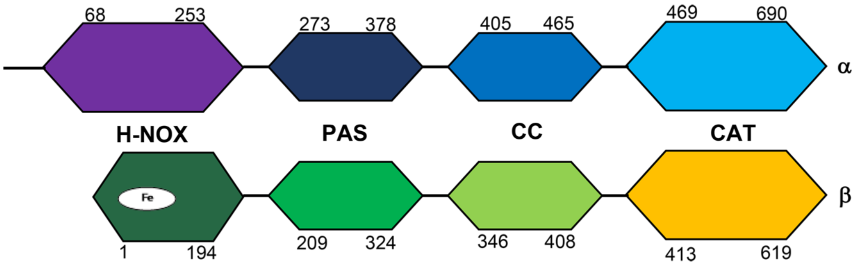

Figure 15. Four domains (*H-NOX*, PAS, CC, and CAT) of sGC in the α and β subunits with approximate numbering of human α1 and β1 domains. The Fe heme active site is found in the β *H-NOX* domain.

muscle relaxation (regulating muscle tone), cellular apoptosis, phototransduction in the eye, etc., many of them ultimately related to cGMP-based regulation of ion channel conductivity.[441−445] For NO-based signaling and cGMP generation, NOS produces pico- to nanomolar concentrations of NO, which avoids toxicity issues. The NO then diffuses into the target cells where it is detected by sGC, causing an intracellular increase of the messenger cGMP (see Scheme 9).[446−448] Problems with this regulatory pathway from hindered NO signaling can cause hypertension and atherosclerosis, leading to heart attack and stroke.[449,450] Correspondingly, sGC has become a primary target for drug discovery, and small molecule stimulators and activators of sGC have been developed, but how they bind to sGC and how they function on a molecular level is often unclear.[451] Insects, worms, algae, and invertebrates all use sGC for NO-based signaling, while bacteria, fungi, and higher plants do not.[452,453] However, the N-terminal heme-based sensor domain of sGC is a member of the larger *H-NOX* family, which is conserved in prokaryotes and higher eukaryotes, and used for the detection of NO and O_2.[454,455] In fact, much of what we know about NO binding to sGC is based on results for analogous *H-NOX* proteins, which are much easier to express and study.[174]

The protein sGC is a ~150 kD heterodimer, containing α and β subunits, and is found in the cytosol.[441−445] The dimerization of the α and β subunits is necessary for activity. On the basis of structural results and sequence analysis, four major domains can be identified in sGC: (a) the *H-NOX*-like N-terminal sensor domain, which is located in the β1 subunit and houses the binding site for the sensory heme, (b) the C-terminal catalytic (CAT) domain, which is responsible for the conversion of GTP to cGMP (see Scheme 9), (c) a Per/Arnt/Sim (PAS)-like domain, and (d) a coiled-coil (CC) domain. The PAS and CC domains are collectively known as the dimerization domain, which is involved in the large conformational changes that activate the catalytic domain upon NO binding in the sensor domain.[456−459] These four domains are indicated in Figure 15.

Because full length sGC is unstable and difficult to heterologously express, a crystal structure of the full length protein is not available (yet). Several methods have been developed for purification, but this continues to be an ongoing issue, with current methods only yielding low amounts of protein.[175] Also, the conformational flexibility in the quaternary structure has likely contributed to the delay in producing a crystal structure.[460] With a resolution of 25−40 Å, negative stain electron microscopy studies first showed the general shape of the full-length sGC from *Rattus norvegicus*.[460] The structural studies along with cross-linking experiments[461] support the idea that sGC is a flexible dumbbell-shaped protein, where the CC connects the *H-NOX* and PAS domains on one end of the dumbbell and on the other side it connects to the CAT domain. These findings were later confirmed using cryo-electron microscopy (cryoEM) images. Figure 16 shows cryoEM images of full-length sGC in different conformations.[462,463] Marletta and coworkers determined the first full length structures of *Manduca sexta* sGC in both inactive and active (NO or YC-1 bound) states with 5.1 and 5.8 Å resolution, respectively.[462] They found that sGC has two dramatically different conformations, answering the question of how the ligand binding in the regulatory domain is communicated to the catalytic domain of sGC on a macroscopic scale. They showed that binding of YC-1 (the first reported small-molecule stimulator specific for sGC[464]) or NO causes a 71° rotation of the heme binding *H-NOX* and PAS domains, which, in turn, moves the CAT domain into the active state. Whereas NO

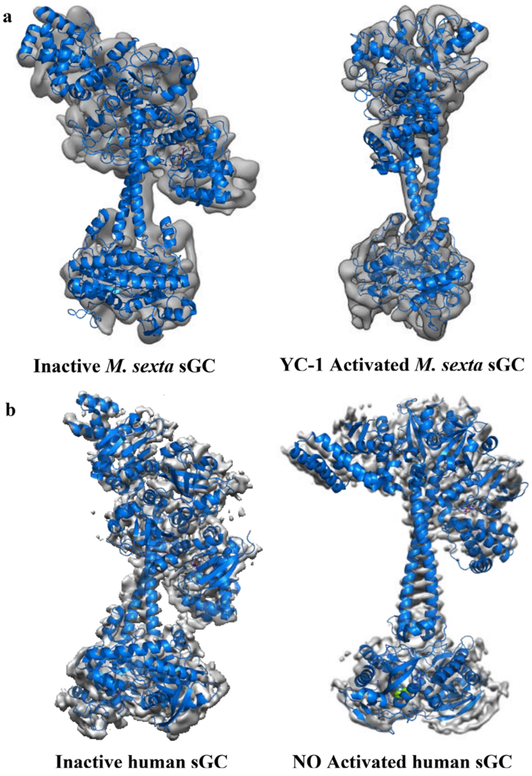

Figure 16. CryoEM images of full-length sGC. (a) PDB: 6PAS overlayed with EMD-2082 from *M. sexta* sGC in the inactive state and PDB: 6PAT overlayed with EMD-2083 in the YC-1 activated form.[462] (b) PDB: 6JT1 overlayed with EMD-9884 from human sGC in the inactive form and PDB: 6JT2 overlayed with EMD-9885 in the NO activated form.[463]

binds to the heme in the *H-NOX* domain (see below), YC-1 was found to bind directly in between the *H-NOX* domain and the CC domain. The CC domain is rigid when in the inactive form, but binding of NO or YC-1 causes a conformational extension or straightening of the enzyme. In this regard, YC-1 is able to lock the protein in the active state, presumably without cleaving the Fe−N_{His} bond of the heme (see below). Complementary studies using EPR spectroscopy support the idea that the sGC stimulators do not bind in the heme domain, but instead to different parts of the protein, as observed for YC-1 by cryoEM.[462,465] The use of activators in the presence of CO has also been investigated. Addition of YC-1, BAY, 41-2272 or Riociguat in concert with CO (using the resulting Fe(II)−CO complex as a probe) to sGC causes activation to almost the level obtained by NO alone.[466,467] Resonance Raman (rRaman) studies revealed that activators allosterically perturb the heme pocket in the presence of CO in full length sGC, inducing two conformations, one of which could correspond to a state of the protein where the Fe−N_{His} bond of the heme is cleaved.[468−471] The role of the CC domain was further explored using a truncated version of *M. sexta* sGC, and it was shown that the conformation of the CC is important for communication between the heme *H-NOX* and CAT domains.[472]

The Chen group used cryoEM to study human sGC ($\alpha1\beta1$) at <4 Å resolution and also noted the straightening of the structure and the movement of the domains upon NO binding, as seen in Figure 16.[463] It was further shown that inhibition of the straightening of the enzyme by incorporation of proline mutations in strategic locations in the CC domain (to destabilize helical structures and favor the inactive form) causes activation by NO to cease, suggesting that this allosteric activation is essential for catalytic activity.[463] The quaternary structure of human sGC was constructed using a hybrid approach that combines protein structure prediction tools with cryoEM experimental data, to give insight into the inter-domain communication upon NO binding.[473] The communication between domains was further explored by molecular dynamics simulations and mutational studies coupled with luciferase reporter assays to identify hot spot linkages in the CC domain of human sGC that could be a part of the propagation of the activating signal through the CC domain when NO binds to the active site heme in the sensor domain.[474] The conformational changes when GTP and cGMP are bound to the CAT domain of human sGC were studied using molecular dynamics simulations, and the results suggest that structural changes in the CAT domain lock and stabilize GTP within a closed pocket for cyclization. On the other hand, binding of cGMP causes a loss of global structure compactness, likely allowing for product release after cGMP is formed during turnover.[475]

While no full-length crystal structure of sGC has been obtained, further structural information has come from isolated domains, which is summarized in Table 2. Structural information for the *H-NOX* domain of sGC has mostly been derived from the crystal structures of analogous bacterial *H-NOX* proteins, which is discussed in more detail below. In general, *H-NOX* domains consist of an N-terminal α-helical subdomain and a C-terminal subdomain that contains both α-helices and four antiparallel β-sheets, with the heme active site situated in the central cavity between the two subdomains. The α-PAS domain was crystallized for the *M. sexta* sGC, showing β-strands and a flexible α-helix which might be important for NO signal transduction (PDB: 4GJ4).[476] The CC was crystallized for the $\beta1$ subunit of human sGC. Here, four CC monomers artificially come together to form an apparent four-helix bundle in an anti-parallel orientation, and in this way, the structure gives insight into the residues involved in dimerization (PDB: 3HLS).[479] The CAT domain was crystallized for the human $\alpha1\beta1$ heterodimer (PDB: 3UVJ, 4NI2).[480,481] For this purpose, the α- and β-subunit components were first expressed separately, and then combined and purified together. The CAT domain forms a heterodimer with one active site and one pseudosymmetric site found at the interface of the α and β subunits. The pseudosymmetric site lacks the key catalytic residues and is thought to be a regulatory site, where ATP potentially binds as an inhibitor.[480] Allosteric effects were investigated by hydrogen/deuterium exchange mass spectrometry on the full length sGC, and the results revealed that PAS and CC domains play a critical role in the activation by NO.[482] The structure of the human isoform of sGC was investigated using far-UV circular dichroism (CD) spectroscopy, intrinsic tryptophan fluorescence, fluorescence of the hydrophobic dye bis-8-anilino-1-naphtalenesulfonic acid (bis-ANS), size exclusion chromatography, and small angle X-ray scattering (SAXS), which allowed for a three-dimensional model of the enzyme to be constructed.[25,483−485]

Table 2. Available Crystal Structures of Isolated sGC Domains

protein	organism	PDB code	resolution (Å)	ref
H-NOX domain	*β_1 subunit of human sGC*	5MNW		
H-NOX domain	*Shewanella oneidensis*	4U99	3.00	189
H-NOX domain with NO	*Shewanella oneidensis*	4U9B	1.65	189
H-NOX domain with O_2	*Caldanaerobacter subterraneus*	1U55/ 1U4H	1.77	187
H-NOX domain	*Caldanaerobacter subterraneus*	5JRU	2.31	477
H-NOX domain with NO	*Nostoc sp*	2O0C	2.60	478
H-NOX domain with CO	*Nostoc sp*	2O0G	2.51	478
α-PAS domain	*Manduca sexta*	4GJ4	1.80	476
CC domain	*β_1 subunit of human sGC*	3HL3	2.76	479
CAT domain	*human $\alpha_1\beta_1$ heterodimer*	3UVJ	2.08	480
CAT domain	*human $\alpha_1\beta_1$ heterodimer*	4NI2	1.90	481

As mentioned above, bacterial *H-NOX* proteins have similar structures as the sensor domain of sGC and were investigated in detail to further elucidate the structure of the heme binding site of sGC and to study small-molecule binding to the heme (see next section).

2.2.2. Structural Features of *H-NOX* Domains. The *H-NOX* proteins, which are homologs of the N-terminal heme-containing sensor domain of sGC, are prokaryotic gas-sensing proteins that sense either O_2 or NO.[455,486] *H-NOX* domains have been found as part of methyl-accepting chemotaxis proteins (MCPs), where they function as O_2 sensors, or as stand-alone proteins in the same operon with signaling partners like histidine kinases, diguanylate cyclases, etc. Here, the *H-NOX* proteins usually function as NO sensors and they control the activity of their partner enzymes via protein-protein complex formation. Stand-alone *H-NOX* are single domain proteins with approximately 180 amino acids and up to 40% sequence identity with the *H-NOX* domain of sGC. In

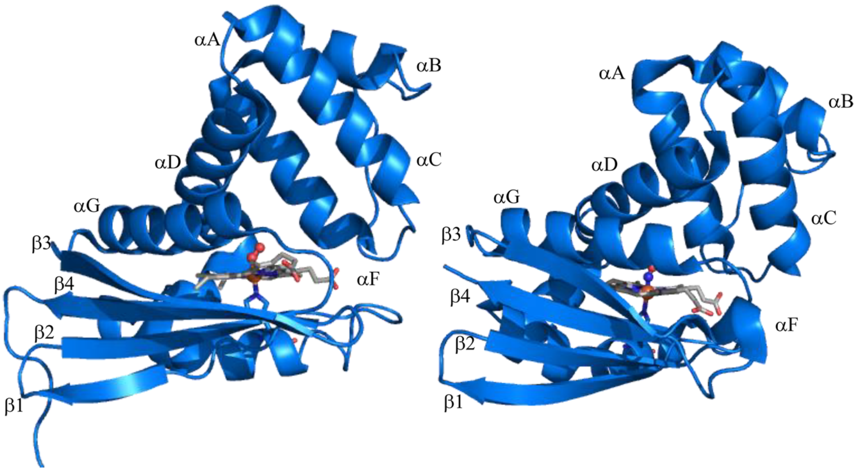

Figure 17. PyMOL generated images of the crystal structures of *Cs H-NOX* with dioxygen bound (left; PDB: 1U55) and *Ns H-NOX* with NO bound (right; PDB: 2O09). αE is not labeled, because it is only a one-turn helix (residues 83-86).

particular, it should be noted that the kinetics of NO binding are similar in *H-NOX* proteins and sGC.[486] Because of their increased stability and easier manipulation (including crystallization), stand-alone *H-NOX* proteins have therefore been instrumental in improving our understanding of the structural changes in *H-NOX* domains that occur upon NO (and O_2) binding to the heme.[187,189,477,478,487,488] Note that CO also serves as a low-affinity ligand for *H-NOX* proteins, but a physiological role of *H-NOX* domains in CO sensing has not been identified yet.[489,490]

The structural characterization of the bacterial *Caldanaerobacter subterraneus* (*Cs*) (also known as *Thermonanerobacter tengcongensis* (*Tt*)) and *Nostoc sp* (*Ns*) *H-NOX* proteins constituted an important breakthrough in our understanding of the mechanism of NO signal transduction and differential NO vs O_2 sensing in *H-NOX* proteins (PDB: 1U55, 2O0C).[187,478] *Ns H-NOX* has a higher sequence identity with sGC (33% sequence identity, and 17 out of 27 amino acids in the heme pocket are conserved) as compared to *Cs H-NOX* (18% identity, and 8 out of 27 amino acids conserved). Crystal structures of *Cs* and *Ns H-NOX* show seven *α*-helices (designated as A-G) and four stranded anti-parallel *β*-sheets (designated as 1−4) as seen in Figure 17.[187,478,487] As mentioned above, *H-NOX* proteins can sense both O_2 and NO and discrimination between these two small molecules originates in the distal pocket. O_2-sensing *H-NOX* proteins usually contain a conserved Tyr residue in the active site, which is held in place by hydrogen-bonding to other residues in close proximity (see below). The presence of a hydrogen-bond donor is absolutely critical to allow for stable O_2 binding to the heme with high affinity, and is therefore a hallmark for O_2-sensing *H-NOX* proteins.[25,491] On the other hand, NO-sensing *H-NOX* proteins lack this hydrogen-bond donor, and show a very low affinity for O_2. Since *in vivo* O_2 levels are generally 1,000 times higher than NO concentrations, discrimination between O_2 and NO is necessary, otherwise O_2 would block NO sensor proteins like sGC.

Interestingly, *Cs H-NOX* resembles small-molecule binding in globins, forming 6C Fe(II)−NO and Fe(II)−O_2 adducts, and correspondingly, this protein serves as an O_2-sensor.[186] The crystal structure of *Cs H-NOX* with O_2 bound (PDB: 1U4H, 1U55 − fit with two different space groups: monoclinic and orthorhombic) shows that the heme is quite distorted with the angles between the planes of the pyrrole groups ranging from ∼15° to 30° and an Fe−N_{His} distance of 2.01−2.14 Å. Recent crystal structures of *Cs H-NOX*, in the unliganded state (PDB: 5JRU) in comparison to the O_2-bound form (PDB: 3TF0), have given greater insight into the heme distortion. In fact, *Cs H-NOX* with O_2 bound had the most non-planar heme of all known heme protein structures at the time when the structure was solved.[249,492−495] Olea et al. discovered through mutational studies that Pro115 is a heme contacting residue, whose steric bulk plays a role in heme distortion.[496,497] In the unliganded state the heme is more planar than in the O_2-bound state, due to decreased interaction with steric residues Pro115 and Ile5. Also, the His102 that is ligated to the heme rotates 90° along the Fe−N_{His} axis in the unbound state, and the H-bonding network that stabilizes O_2 is moved away from the heme. The comparison of the unliganded and O_2-bound structures, highlighting the heme distortion, is shown in Figure 18. The crystal structure of *Cs H-NOX* with O_2 bound also reveals a hydrogen-bonding network that includes Trp9 and Asn74 and a hydrogen bond between Tyr140 and the heme-bound O_2. The importance of the Tyr140 residue was shown by a site-directed mutagenesis study, where Tyr140 was mutated

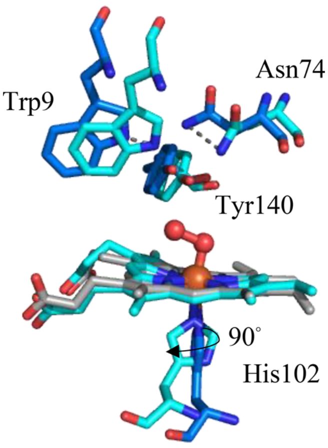

Figure 18. PyMOL overlay of Cs *H-NOX* in the unliganded state (blue; PDB: 5JRU) with the structure of the O_2-bound state (cyan; PDB: 3TF0), showing heme distortion and movement of second coordination sphere residues.[477]

to a hydrophobic residue, resulting in a 20-fold increase in the O_2 dissociation rate constant, indicating the need for the Tyr residue to keep O_2 bound.[498] The enzyme sGC does not contain an analogous Tyr, but instead has Ile145 in that position, in part explaining why sGC has a low affinity for O_2. Correspondingly, when Ile145 is mutated to a Tyr residue in the β1 subunit of rat sGC (β1 *H-NOX* domain), a stable dioxygen complex can form, but O_2 still has a low association rate, so this variant still cannot match the high O_2 binding constant of the *Cs H-NOX* (K_D sGC mutant = $\sim 7 \times 10^{-2}$ M vs *Cs H-NOX* = $\sim 9 \times 10^{-8}$ M).[498] It is therefore proposed that the absence of the Tyr residue in sGC is not the sole determining factor for its high selectivity of NO over O_2. Correspondingly, when the Tyr residue is introduced into full-length sGC, NO still activates the enzyme *in vivo* just like in the wild-type (wt) case.[499]

Interestingly, *Ns H-NOX* does not seem to form the typical 5C Fe(II)−NO complex as observed for almost all NO sensing *H-NOX* proteins, but in this case, the product is predominantly 6C, with only a small amount of 5C Fe(II)−NO adduct present in the crystal structure. For *Ns H-NOX*, crystal structures of the Fe(II)−CO and Fe(II)−NO forms were determined, which show that the heme is significantly less bent compared to the *Cs H-NOX* O_2 bound complex with some ruffling (~ -0.35 Å) and doming distortions (~ 0.5 Å).[478] Unlike the *Cs H-NOX*, the *Ns* protein does not have a residue similar to Tyr140 and does not bind O_2. The sensory heme in *Ns H-NOX* is bound to a proximal His residue (His105). The predominant species formed upon reaction with NO is a 6C Fe(II)−NO complex, with a small amount of 5C Fe(II)−NO formed as well.[478] Reaction with CO similarly generates a 6C species. By analyzing the crystal structures of the CO vs NO adducts (PDB: 2O0G, 2O0C), important structural trends were derived that provide insight into the activation of the protein upon NO binding (Figure 19). In the NO complex, the heme slightly pivots with a shift of the iron center by 0.2−0.3 Å, whereas in the CO adduct, this effect is way more pronounced with a shift of the iron by 0.8−0.9 Å.[478] The propionate groups of the heme act as an anchor point and the heme pivots upon ligand binding away from the distal Trp74 side chain. Here, a greater shift is seen in the CO complex due to the linear geometry of the Fe(II)−CO unit, compared to the bent Fe(II)−NO complex, as shown in Figure 19. The Trp74 residue acts a molecular "ruler", allowing *Ns H-NOX* to selectivity bind NO over CO. In addition to the pivot motion of the heme, a heme bending motion is also thought to be involved in activation, where the heme bends at the pyrrole rings on the side of the propionates and acts as a "flexing wedge", initiating the shift of the N-terminal region. These results point towards a potential mechanism for signal transduction in sGC, where the wedging of the heme could initiate the N-terminal region to shift in parallel with the transition of the Fe(II)−NO complex from 6C to 5C, leading to the activation of sGC.[478]

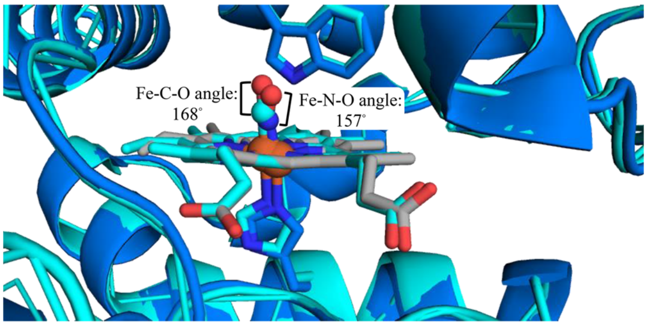

Figure 19. PyMOL overlay of *Ns H-NOX* structures with CO and NO bound. The NO-bound heme is colored grey (PDB: 2O0C) and the CO bound heme is colored cyan (PDB: 2O0G). The presence of Trp74 causes movement of the heme, which can be seen in the overlay of the two structures.

H-NOX proteins from facultative aerobes like *Vibrio cholerae* and *Shewanella oneidensis* (*So*) form a 5C Fe(II)−NO complex upon NO binding.[186,500] For the *H-NOX* protein from *So*, the crystal structure of the NO adduct was also obtained. The *So H-NOX* crystal structure revealed a 5C Fe(II)−NO complex, where the His is displaced by 8.5 Å and the αF helix is rotated by 90°.[189] In this case, the expected 5C Fe(II)−NO complex is observed, but curiously, the NO ligand is bound in the proximal instead of the distal pocket. Especially the *So H-NOX* protein has been used as a model for the *H-NOX* domain of sGC to better understand the structural changes induced by NO binding to the heme. All of these aspects are further discussed below. In addition to studying how gaseous ligands interact with *H-NOX*, the *So H-NOX* protein was also investigated for its role in transduction of chemical signals, by studying how it interacts with signaling partners. Using hydrogen-deuterium exchange mass spectrometry and surface-scanning mutagenesis, it was shown that the NO-bound protein has a higher affinity for HnoK, a signaling histidine kinase partner, than the unligated protein, supporting the importance of NO binding and structural shifts to generate and propagate a signal.[501]

2.2.3. Mechanism of sGC Activation: Basal Activation.

The experiments on the isolated sGC domains and the *H-NOX* protein studies described above reveal the complexity of the putative structural and allosteric effects in sGC activation. The breakthrough cryoEM studies confirmed and further elucidated the domain interactions in the active and inactive states of the protein. The molecular steps of sGC activation have been heavily studied and are still under active investigation.[488,502] sGC was initially thought to undergo a quite simple activation process where NO binding to the heme would lead to full activation. However, kinetic studies on NO binding to sGC quickly unmasked a much more complex activation mechanism. On the basis of comparative activity assays, three activity levels of sGC where identified: resting state activity in the absence of NO, basal activity with ∼1 equiv of NO (∼15% activity), and full activity with excess NO (100% activity), as seen in Scheme 10.[503] Therefore, sGC activation is a two-step process, which is NO concentration dependent (basal vs full activation).

The primary site for NO binding is a 5C ferrous heme *b* ligated by a proximal His (His105 in rat, human, and bovine sGC).[456,504] The His is neutral and not H-bonded to other amino acids or water molecules.[505−509] The heme is thought to be delivered to apo-sGC by GAPDH, which obtains mitochondrial heme and then forms a complex with apo-sGC to insert the heme.[510] sGC has a remarkable selectivity for less than nM levels of NO under aerobic conditions where the O_2 concentration is ~ 260 μM.[511] An explanation of sGC's selectivity is provided by the "sliding scale rule" hypothesis, as described in the following. This hypothesis is based on the analysis of O_2, NO and CO binding data of hundreds of heme proteins (and not just *H-NOX* domains) and model complexes, which led to the discovery of a number of general trends.[512] The name "sliding scale rule" comes from the observed, linear relationship of the $\log(K_D)$ values for NO versus CO versus O_2 binding to most heme proteins, which allows for the prediction

Scheme 10. Model for Basal sGCs Activation by NO, Where NO Binds to the Resting 5C Ferrous Heme, Forming a 6C Ferrous NO Intermediate; Cleavage of the Fe−N_{His} Bond Forming a 5C Ferrous NO Complex Then Leads to Basal Activation of sGC[a]

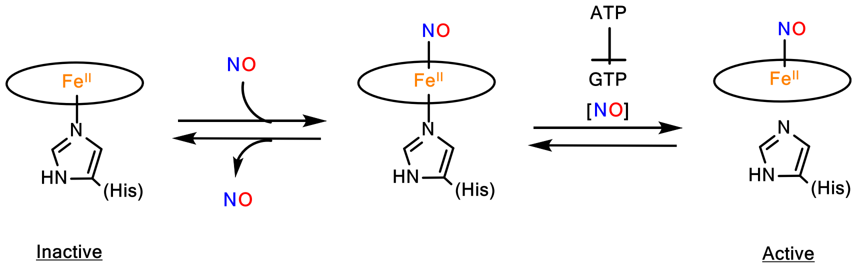

[a] sGC activation is also modulated by ATP and GTP.[503]

Scheme 11. Proposed Mechanism for Full sGC Activation by NO[171]

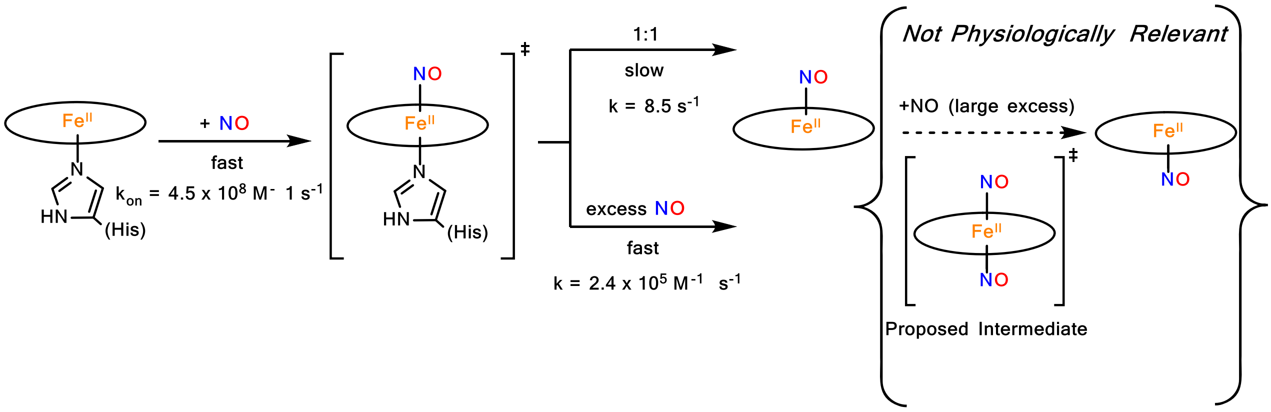

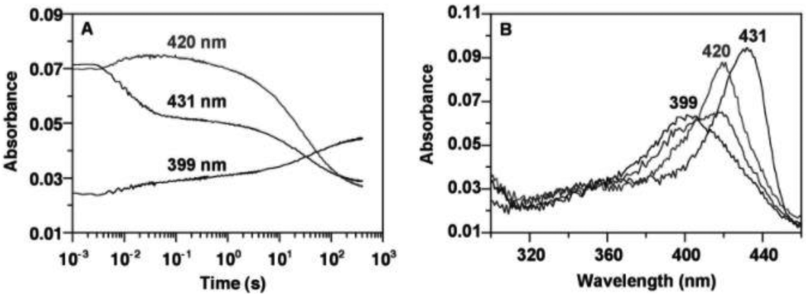

Figure 20. NO binding to heterodimeric sGC using stopped-flow analysis. sGC and NO were mixed anaerobically and absorbance changes at 399, 431, and 420 nm were observed. (A) Signal intensities over time. (B) The 431 nm band corresponds to sGC before NO exposure, the 6C NO-bound intermediate forms immediately after mixing and shows a Soret band at 420 nm, and the 5C NO complex shows the Soret band at 399 nm. Reprinted with permission from ref 516. Copyright 1999 PNAS.

of the affinity of a heme for one ligand if the K_Ds of the two other ligands are known. Five factors were identified that govern gaseous ligand selectivity of heme containing proteins, as follows: 1. the identity of the proximal ligand; 2. the proximal strain of the heme; 3. distal steric hindrance; 4. H-bond donor(s) in the distal pocket; 5. multi-step NO binding. The identity of the proximal ligand in sGC is a neutral His ligand, which is intrinsically able to discern between the three gaseous ligands. This intrinsic selectivity is exemplified by the heme model complex [Fe(PPIX)(MI)] (MI = 1-methylimidazole), which has affinity ratios of $K_D(CO)/K_D(NO) \approx K_D(O_2)/K_D(CO) \approx 10^3-10^4$.[512] This intrinsic affinity ratio contributes but does not fully explain the selectivity between the gaseous ligands. Proximal strain of the heme can tune the Fe−His bond strength, which regulates the kinetic on and off rates of the gaseous ligands. sGC has a lower affinity for all three ligands by approximately two orders of magnitude compared to bacterial *H-NOX* proteins, which is likely due to the increased proximal strain in sGC and the longer Fe−N_{His} bond.[187,463,478,513−515] The relative orientation of the imidazole ring of the proximal histidine can further fine tune the proximal strain. The imidazole ring can either be in the eclipsed or staggered conformation with respect to the Fe−$N_{Pyrrole}$ bonds of the heme. The cryoEM structure of sGC found that the imidazole adopts the eclipsed conformation, which is the more strained conformation.[463] By decreasing the intrinsic affinity for all three gases, sGC discriminates against O_2 binding through proximal strain. This is complemented by the lack of a distal H-bond donor in sGC, which further lowers the affinity of the heme for O_2 (see above). In addition, it has been proposed that "multi-step" NO binding significantly increases the apparent affinity of sGC for NO, due to the formation of a 5C Fe(II)−NO complex, which has a higher affinity for NO than the 6C complex initially formed. This is reflected in the data, where the

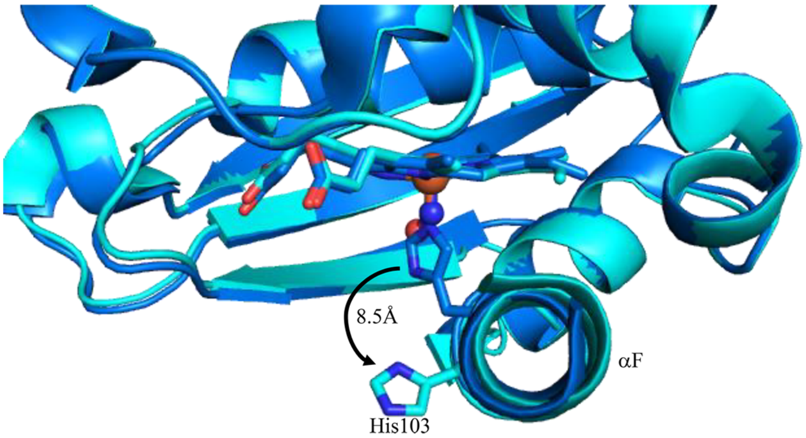

Figure 21. PyMOL generated overlay of the crystal structures of *So H-NOX* protein in the ferrous state (blue, PDB: 4U99) compared to the NO-ligated state (cyan, PDB: 4U9b), demonstrating the conformational changes upon NO binding, with a displacement of His103 by about 8.5 Å. Note that NO is bound in the proximal pocket.

6C complex has a $K_D(NO) = 54$ nM (measured with substoichiometric amounts of NO),[512,516] whereas in the presence of excess NO (which enhances the formation of the 5C complex), the apparent $K_D(NO)_{app} = 1-7.3$ pM, enhancing the apparent affinity of sGC for NO.[513,517,518]

In the resting state of sGC, the heme is 5C and hs ($S_t = 2$) with proximal histidine ligation.[505−509] The 5C ferrous heme is stabilized in sGC with a midpoint reduction potential of +187 mV for full-length bovine sGC and +234 mV (vs NHE) for truncated *M. sexta* sGC.[519,520] To generate a signal after NO binding, the heme needs to be in the ferrous state. In this regard, it is interesting to note that H_2S might play a role in rescuing sGC by reducing the heme back to the ferrous oxidation state, in the case of accidental oxidation, but further studies are needed to confirm these ideas.[521]

NO binding to the ferrous heme follows a diffusion-controlled rate ($k_{6C,on} = (2-5) \times 10^8\ M^{-1}\ s^{-1}$)[522,523] and is the first step in sGC activation, which leads to the formation of a 6C ferrous heme-nitrosyl intermediate, a ls-$\{FeNO\}^7$ complex in the Enemark−Feltham notation, as observed by UV−vis stopped-flow experiments (see Scheme 11) and EPR spectroscopy.[516,524−527] As shown in Figure 20, NO addition to ferrous sGC leads to the disappearance of the Soret band (see refs 528 and 529 for a discussion of heme absorption spectra) of this species at 431 nm and the growth of a new signal at 420 nm, which corresponds to the 6C NO complex.[516] Over the course of 5 min this band disappears and a new Soret feature rises at 399 nm, which corresponds to the 5C ls-$\{FeNO\}^7$ complex.[53] Because of the strong thermodynamic *σ-trans* effect of NO, NO binding induces a cleavage of the Fe−N_{His} bond in the initially formed 6C complex, leading to the formation of the corresponding 5C ferrous heme-nitrosyl complex with NO bound in the distal pocket (see Scheme 11).

Marletta and coworkers further studied these mechanistic steps of basal sGC activation using the *So H-NOX* protein.[189] Using X-ray crystallography in conjecture with different constructs of the protein, they were able to capture snapshots of the process of NO binding and *So H-NOX* activation. They crystallized the ferrous resting state, a mimic with a Mn-substituted heme that forms a 6C Mn(II)−NO complex, to model the 6C intermediate that forms upon initial NO coordination, and the final 5C Fe(II)−NO complex of *So H-NOX*.[189] Figure 21 shows the crystal structures of *So H-NOX* in the ferrous resting state and the NO-bound form (PDB: 4U99 and 4U9B, respectively).[189] In the unliganded state, the heme is coordinated to His103 and highly distorted, due to steric interactions between Pro116 and one of the pyrrole rings of the heme. Importantly, the structure of the 6C Mn(II)−NO form overlays well with the structures of the resting Fe(II) and Mn(II) forms, indicating that no significant structural changes occur before the breaking of the Fe−N_{His} bond. As evident from the overlay of the crystal structures in Figure 21, the breaking of the Fe−N_{His} bond upon NO binding leads to a large displacement of the proximal His103 by 8.5 Å and a relief of the heme distortion (initial RMSD (root-mean square deviation) from planarity: 0.312 Å). The latter provides additional driving force for the breaking of the Fe−N_{His} bond, besides the strong thermodynamic *σ-trans* effect of NO (see below). The His103 dissociation from the heme further causes a 90° shift of the *α*F-helix that carries this His residue. This rotation of the *α*F-helix is thought to be the first step in propagating the NO signal.[189] Other residues on the *α*F-helix were also studied to probe the next steps in the signal transduction pathway, but more work is needed to understand how these events relate to the activation of *So H-NOX*.[530,531] Finally, the perturbation of the heme pocket leads to a ∼2.5 Å rigid body displacement and ∼4° rotation of the distal domain, which is likely also relevant for *So H-NOX* activation.[189] By analogy, similar structural changes are expected for sGC, and ultimately, the relocation of the proximal His along with the relief of the heme distortion are thought to be the key drivers of the conformational changes that ultimately activate the catalytic domain of sGC.[189] Interestingly, the cryoEM studies do not indicate a rotation of the analogous *α*-helix in human sGC, as observed for *So H-NOX*.[462] Finally, it should be noted that the 5C Fe(II)−NO form of *So H-NOX* was crystallized in the presence of excess NO, and curiously, shows the NO ligand on the proximal side of the heme. The implications of this finding are further discussed below.

Analogous to the Mn form of *So H-NOX* described above, the heme cofactor in sGC was also replaced with the analogous Mn(II)- and Co(II)-PPIX and then NO binding was investigated.[532] The Mn(II)/sGC forms a stable 6C NO complex, and accordingly, the Mn complex does not achieve activation of sGC beyond background levels, indicating that the rupture of the Fe−N_{His} bond and the formation of a 5C NO complex is a necessary step for sGC activation (as observed for *So H-NOX*). The Co(II)/sGC, on the other hand, behaves like

Fe and forms a 5C Co(II)−NO complex with scission of the Fe−N_{His} bond, activating the CAT domain of sGC with higher activity compared to the native Fe protein. These results again demonstrate that the breaking of the Fe−N_{His} bond is the key factor for activation of mammalian sGC, which is caused by the thermodynamic *σ-trans* effect of NO. Other structural changes, like heme deformation and pivoting, which are important for O_2-sensing *H-NOX* proteins (see above), may contribute to activation of mammalian sGC, but are not the key factors responsible for stabilizing the catalytically active conformation of the enzyme. In complementary studies, Ni(II) and Cu(II) were also reconstituted into sGC and it was shown that in the absence of the metal-His bond due to the 4C geometries of these complexes, activation was achieved with 63-fold and 32-fold activation over resting state sGC activity (without NO bound), respectively. A decreased conformational freedom of the porphyrin macrocycle, favoring planarity, was also observed.[172]

The basic properties of 5C and 6C ferrous heme-nitrosyl complexes, and the nature of the *σ-trans* effect of NO responsible for the breaking of the Fe−N_{His} bond, have been studied in much detail using model complexes, which is further discussed below. In particular, model complexes are ideally suited to quantify the thermodynamic *σ-trans* effect of NO, using binding constants of N-donor ligands in trans position to NO, Fe−NO and N−O vibrational frequencies, and other spectroscopic properties.

2.2.4. Mechanism of sGC Activation: Full Activation.

Whereas the process of basal activation of sGC is well understood, it is still not clear how exactly full activation (at higher NO concentrations) is accomplished. Three models are currently being considered to explain this two-step activation process: (1) the second binding site model, (2) the NO flip model, or (3) the kinetic model.

The simplest model is the second binding site model, which was initially proposed by Marletta and coworkers,[516] and which is based on the idea that a second binding site for NO exists in the sensor domain of sGC besides the heme, with a lower NO affinity. The first biochemical evidence of a second binding site came from the observation that the Hill coefficient for NO binding to sGC is 2.1, suggesting there is cooperativity.[533] In addition, a UV−vis experiment coupled with an activity measurement of sGC showed that upon addition of excess NO, the UV−vis spectrum remained unchanged, but the activity increased. This indicates that the addition of excess NO is not effecting the 5C ferrous heme−nitrosyl complex.[173] In another UV−vis experiment, butyl isocyanate was added as a strong distal ligand to the ferrous heme, preventing diatomic gases from binding to the heme. Upon addition of excess NO, the Soret band shifted from 429 nm to 432 nm, indicating that the heme environment is being affected, despite NO not being able to bind to the heme. However, the exact nature of the second binding site has not been identified so far.

One possibility would be a Cys residue on the surface of sGC, which could react with NO to form a transient RS−$NO^{\bullet-}$ radical anion.[534] S-Nitrosation is a common reaction in biology (see Section 2.4). However, neutral RS−NO formation requires a one-electron oxidation of NO, so the presence of an oxidant would be necessary (see Section 2.4). In contrast, activation of sGC does not require an oxidant and RS−NO has a long half-life (hours), which is much longer than the timescale for sGC deactivation from the fully activated state back to basal activation. Thus, Marletta and coworkers suggested that the RS−$NO^{\bullet-}$ radical anion instead of RS−NO is formed in sGC, because the formation of RS−$NO^{\bullet-}$ would be freely reversible, and the half-life could be tuned by adjacent residues.[534] However, the specific cysteine residue(s) putatively involved in NO binding could not be identified so far, and it is also not clear how nitrosylation of a surface cysteine could generate a signal, to switch sGC to the fully activated state. Further support for these ideas came from experiments where full length rat sGC was treated with the alkylating agent S-methyl methanethiosulfonate (MMTS), which reacts with thiols to form disulfides. MMTS decreased the activity of sGC, and when the MMTS tag was removed with excess thiol, the activity was restored.[534]

More recently, two cysteine residues potentially involved in signaling were identified, and a new concept was proposed where sGC activity is mediated by thiol/disulfide switches. The dithiol reducing agent tris(2-carboxyethyl)-phosphine was added to sGC and a reduced sGC response to NO was observed, indicating that Cys oxidation is significant in NO activation.[535] Addition of dibromobimane (a probe that fluoresces when it crosslinks two vicinal cysteine thiols) was used to further identify thiol/disulfide pairs of neighboring cysteines.[535] A decrease in fluorescence was observed in NO-stimulated sGC compared to sGC without NO added, suggesting that the NO-stimulated sGC has more Cys masked in disulfide bonds.[535] Mass spectrometry was also used to compare the redox states of the Cys in the tryptic peptides (peptides resulting from the cleavage of proteins downstream to every Lys and Arg residue) when NO is present, and it was found that twelve Cys showed significant differences in NO-bound sGC versus resting sGC. Ten Cys residues were oxidized and two were reduced.[535] Utilizing computational modeling and subsequent mutational analysis, Cys489 and Cys571 located in the β1 subunit were ultimately shown to play a role in sGC activity.[535] This study therefore supports the role of cysteines in the activation mechanism of sGC.[534]

The second mechanistic possibility is the NO flip mechanism, where NO binds to the proximal side of the heme in the fully activated from of sGC (see Scheme 11). This proposal is inspired by studies on *H-NOX* proteins as described above, which, upon addition of excess NO, were crystallized in the 5C Fe(II)−NO form with NO in the proximal pocket (see Figure 21). Similar observations have also been made for Cyt. *c′* (see below). This mechanism was first proposed by Russworm and Koesling, in which a hypothetical dinitrosyl intermediate, NO−Fe(II)−NO or ls-$\{Fe(NO)_2\}^8$ in the Enemark−Feltham notation, is formed on the route to the 5C complex with the proximally coordinated NO, as shown in Scheme 11.[173] Russworm and Koesling found that the presence of reaction products cGMP and pyrophosphate together with NO was necessary for the activation of sGC. On the basis of these experimental findings, it was proposed that in the absence of the products cGMP and pyrophosphate, the NO−Fe(II)−NO intermediate converts to an inactive form of the 5C Fe(II)−NO complex. On the other hand, when products are present, the initial 6C Fe(II)−NO intermediate converts to the fully active 5C Fe(II)−NO complex. This suggests that sGC remains in the low-activity form at low levels of NO, even when products are present, but in the presence of excess NO and products, this low-activity form of sGC can convert to the fully active 5C Fe(II)−NO complex.[173]

The dinitrosyl intermediate has never been spectroscopically observed in the enzyme, but has been captured in model complexes. Ford and coworkers trapped $[Fe(Porph)(NO)_2]$

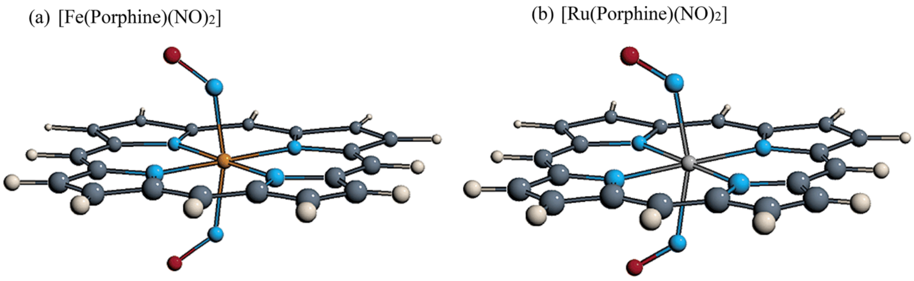

Figure 22. DFT-calculated structures of $[Fe(Porphine)(NO)_2]$ (a) and $[Ru(Porphine)(NO)_2]$ (b) in the trans-*syn* C_{2v}-symmetric conformation, using B3LYP/3-21g.[536]

and $[Ru(Porph)(NO)_2]$ complexes (with $Porph^{2-}$ = TPP^{2-}, OEP^{2-}, and TMP^{2-} (tetramesitylporphyrin dianion)).[536] These species were characterized by IR spectroscopy at 213 K and room temperature, showing N−O stretching frequencies ranging from 1640−1695 cm^{-1}, and DFT calculations. The optimized DFT structures predict that the NO ligands coordinate in the trans-*syn* conformation with C_{2v} symmetry, as shown in Figure 22.[536,537] The Karlin group also obtained a trans dinitrosyl complex, $[Fe(To\text{-}F_2PP)(NO)_2]$ ($To\text{-}F_2PP^{2-}$ = tetra(*ortho*-difluorophenyl)porphyrin dianion), by bubbling NO gas into a solution of $[Fe(To\text{-}F_2PP)(NO)]$ at −80 °C. The dinitrosyl complex was characterized by UV−vis, NMR and EPR spectroscopy, and was found to be EPR silent.[538]

To obtain insight into the speciation of NO complexes in solution, spectroscopic studies are needed. Using rapid freeze quench (RFQ)-EPR spectroscopy with isotopically labeled NO, it was found that NO could indeed coordinate to the proximal side of the heme in full-length sGC.[525] Here, the ferrous form of sGC was first reacted with ^{14}NO to generate the 6C Fe(II)−^{14}NO complex. In the next step, ^{15}NO was added and the sample was frozen after 5 seconds. Two different 5C NO adducts were observed by EPR spectroscopy with either ^{14}NO or ^{15}NO bound. Although this EPR experiment does not directly distinguish between proximally and distally bound NO, the results were interpreted in such a way that the ^{15}NO added in the second addition must initially bind to the proximal side. The ratio of ^{14}NO:^{15}NO was influenced by the concentration of ^{15}NO added. When an equimolar ratio of ^{14}NO:^{15}NO was used, this resulted in sGC populations with 43:57 ^{14}NO:^{15}NO bound. On the other hand, when a ten times excess of ^{15}NO was added, the sGC population changed to 15:85 ^{14}NO:^{15}NO bound. This concentration dependence suggests that on the time scale of this experiment the NO−Fe(II)−NO intermediate forms, but it is not known if and how many times NO is binding and dissociating from the heme, so these results do not truly allow one to distinguish between proximally- and distally-bound NO in the final complex.[525] Nevertheless, this provides evidence that formation of a 5C complex with proximally bound NO is in principle possible in sGC. In opposition to these findings, Yoo et al. used time-resolved absorption spectroscopy on timescales of nanoseconds to milliseconds to study the motion of the proximal His in sGC when NO is present, and in these experiments, the authors did not observe NO binding to the proximal side of the heme.[523]

As mentioned above, the major support for the NO flip mechanism comes from crystallographic studies on *So H-NOX*, which show a 5C Fe(II)−NO complex with the NO ligand on the proximal side of the heme by X-ray crystallography.[189] However, follow-up experiments by Marletta's group later showed that this result is likely an artefact of the experimental conditions used, and that the proximally-bound 5C NO complex is not relevant under physiological conditions.[488] For this purpose, DEER-EPR (double electron-electron resonance) spectroscopy was used to measure the distance between the heme-bound NO in the 5C complex and a spin label attached to the Cys17 residue of *So H-NOX* (Figure 23), which is essentially perpendicular to the heme plane. Here, the spin label is about 23 Å away from a distally-bound NO ligand and about 28 Å away from a proximally-bound NO. These experiments demonstrated that on long time scales (30 min or longer) and under both limiting and excess NO conditions, the predominant species in solution is the 5C Fe(II)−NO complex that has NO bound in the distal pocket, as indicated in Scheme 11, and only minor amounts of *So H-NOX* feature proximally-bound NO. When excess NO was removed, NO was only found on the distal side in the DEER-EPR experiments.[488] On the basis of these findings, it can be concluded that (a) the solid state structures with NO in the proximal pocket might originate from favorable crystallization of these species, maybe due to the fact that crystal contacts on the protein surface needed for crystallization are more accessible in this case, and (b) that the proximal 5C Fe(II)−NO complex might form *in vitro* under high, non-physiological concentrations of NO, but (c) that the distal complex is favored and dominates at physiological NO concentrations.[486,488] Correspondingly, as indicated in Scheme 11, the NO flip mechanism is unlikely and can be ruled out. Therefore, deactivation of sGC would be initiated by simple His rebinding to the heme, followed by NO dissociation.

The last model for full activation of sGC is the kinetic model, where the same distal 5C Fe(II)−NO complex is formed as in

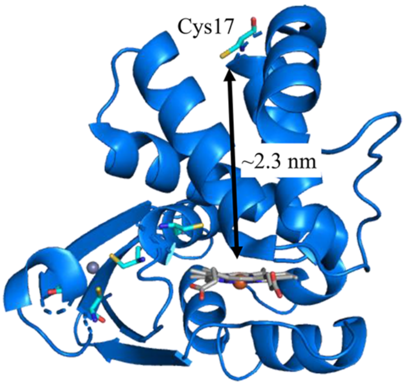

Figure 23. PyMOL generated image of the crystal structure of *So H-NOX* (PDB: 4U99) with Cys17 indicated. A spin label was attached to this Cys to measure the distance to the heme-bound NO in the 5C complex using DEER-EPR.[488]

Scheme 12. Mechanistic Cycle of Cyt. P460, Where the Red Pathway Has Been Observed in HAO (Which Uses a Heme P460-type Cofactor as Active Site), While the Black Pathway Has Been Observed in Cyt. P460[a]

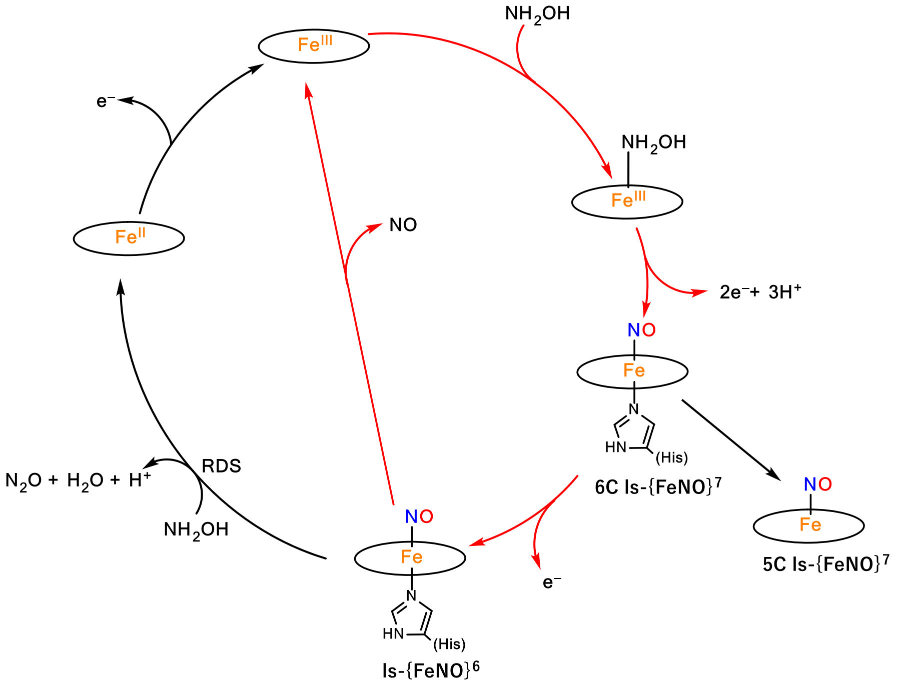

[a] Grey arrow represents the off-pathway formation of a 5C ls-{FeNO}^{7} complex that is not catalytically active.[543]

the case of basal activation, but it forms much faster with excess NO present, which therefore influences the rate of Fe−N$_{His}$ bond cleavage.[516,539] This leads to an overall increase in the amount of cGMP formed in the presence of excess NO. As indicated in Scheme 11, kinetic experiments support this proposal, where the formation of the 5C Fe(II)−NO complex from the corresponding 6C intermediate in the presence of 1 equiv of NO is slow and proceeds with a unimolecular rate constant of $k_{His\text{-}off}$ = 8.5 s^{-1}. Surprisingly, in the presence of excess NO the rate constant increases dramatically and becomes NO-dependent, with a value of $k_{His\text{-}off(NO)}$ = 2.4 × 10^5 M^{-1} s^{-1}.[516] In the latter process, a second NO must somehow act as a "catalyst" to promote the formation of the 5C complex, formally a process that should not depend on the NO concentration (see Scheme 11), but it is currently not clear how this could work mechanistically.[516,540] Additional support for the involvement of two NO molecules in the 6C-to-5C conversion comes from the kinetics of sGC deactivation at low NO concentrations. Ferrous heme has a strong affinity for NO, and therefore, one would expect NO release from the heme of sGC to be slow, but *in vivo* studies show a much faster deactivation, which is not readily explained by this mechanism.[541,542]

Curiously, the Lancaster group observed similar, NO-dependent kinetics for the conversion of a 6C Fe(II)−NO complex to the corresponding 5C species in the enzyme Cyt. P460.[543] Cyt. P460s are found in ammonia oxidizing bacteria (AOBs) and convert hydroxylamine to nitrous oxide in a non-metabolic function, likely to protect the organism from toxic hydroxylamine. Interestingly, in Cyt. P460 a Lys residue is utilized to form one cross-link with the heme, giving rise to its shifted Soret band.[543] In the proposed mechanism (see Scheme 12), hydroxylamine binds to the ferric heme, generating a 6C ls-{FeNO}^{7} intermediate, which was spectroscopically characterized.[543] This 6C complex can either be oxidized to form a ls-{FeNO}^{6} intermediate that then reacts with a second hydroxylamine via nucleophilic attack (see Section 2.3) to generate nitrous oxide, or it can form an off-pathway 5C ls-{FeNO}^{7} species by breaking of the Fe(II)−N$_{His}$ bond, due to the strong thermodynamic *σ-trans* effect of NO. The latter, 5C species is no longer catalytically competent. Whereas wt Cyt. P460 shows a slow, NO-independent conversion of the 6C to the 5C ls-{FeNO}^{7} complex, the Lys70Tyr mutant of Cyt. P460 that eliminates the Lys-heme crosslink undergoes Fe−N$_{His}$ dissociation from the 6C Fe(II)−NO complex through both an NO-independent ($k_{His\text{-}off}$ = 3.8 × 10^{-4} s^{-1}) and an NO-dependent ($k_{His\text{-}off(NO)}$ = 790 M^{-1} s^{-1}) mechanism, and in this way, resembles the properties of sGC.[544] However, as in the case of sGC, the molecular mechanism of the NO-dependent pathway and how a second NO molecule could assist in Fe−N$_{His}$ dissociation are mysterious at this point in time.

2.2.5. NO Binding in Cyt. *c′*.

Cyt. *c′* proteins are found in purple sulfur and non-sulfur bacteria, as well as in several non-photosynthetic and denitrifying bacteria.[545] The function of Cyt. *c′* is not yet fully understood, but it is thought that it could play a role in NO storage, transport or sensing.[546,547] For denitrifying bacteria, Cyt. *c′* may function as an NO scavenger to prevent the buildup of toxic NO in the cell.[127,131] Cyt. *c′* contains a 5C ferric heme *c* cofactor with proximal His coordination. Exposure to NO can lead to the formation of a 6C ferric heme-nitrosyl complex,[548−551] or a 5C Fe(II)−NO species generated by adding reductant to the ferric form along with NO.[127,131,548,550−555] The crystal structure of *Alcaligenes xylosoxidans* Cyt. *c′* revealed NO binding to the proximal side of the heme, when crystallized in the presence of excess NO.[554] Here, it is again proposed that the 5C proximal Fe(II)−NO complex forms from a 6C dinitrosyl intermediate. Despite these mechanistic parallels,[556] it should be noted that the protein structures of Cyt. *c′* and *H-NOX* domains are completely different/unrelated. Similar to *So H-NOX*, it is not always clear for Cyt. *c*′ whether the proximally-bound 5C Fe(II)−NO complex is in fact the major species in solution, or whether this species crystallizes out selectively due to subtle differences in the surface properties or rigidity of the protein in the proximal versus distal 5C Fe(II)−NO state.[554] One possible explanation for the formation of the proximal NO complex relates to the crowded nature of the distal pocket in these proteins. *A. xylosoxidans* Cyt. *c*′ has a bulky distal Leu residue. Mutation of this residue to a less sterically hindered amino acid (Ala, Val, or Ile) leads to the formation of the 6C NO complex, whereas with the Leu present the proximal 5C NO complex forms via a (proposed) transient or non-detectable distal 6C NO intermediate. Kinetic measurements were also performed and revealed that the rate at which the distal NO ligand dissociates plays a key role in determining if the 6C NO or 5C NO product forms. The formation of the 5C NO complex depends on the relatively rapid release of the distal NO from the dinitrosyl intermediate. Here, the distal Leu is the critical bulky group that causes proximal NO coordination to be thermodynamically preferred over the distal NO complex.[557]

Cyt. *c*′ from *Shewanella frigidimarina* has a distal Phe residue instead of a Leu, and a Lys residue in the proximal pocket instead of the more common Arg.[558] The Arg residue could play a role in the rate of His dissociation to form the 5C complex. Only a 5C ls-$\{FeNO\}^7$ complex is detected upon addition of NO to this protein, due to the presence of the bulky Phe as seen in Figure 24. From the crystal structure, the Fe−N−O angle of 123° is the smallest observed for any proximal Fe(II)−NO complex, with only one NO binding mode present. This small angle is potentially due to the presence of the proximal Lys residue. The effect of the structure of the distal and proximal pocket on the properties of this Cyt *c*′, compared to the *A. xylosoxidans* protein, can be related back to the sliding scale rule hypothesis discussed above. The presence of steric bulk in the distal site and the identity of the amino acids around the active site can affect how small molecules bind, which are two of the factors that govern the sliding scale rule.[558]

2.2.6. Basic Properties of Ferrous Heme-Nitrosyls.

2.2.6.1. Five-Coordinate Ferrous Heme-Nitrosyls.

The first crystal structure of a 5C ls-$\{FeNO\}^7$ model complex was reported in 1975 by Scheidt and coworkers.[559] In the original crystal structure of [Fe(TPP)(NO)], this complex shows eightfold disorder of the NO unit, but it was later realized that the disorder is temperature-dependent, and a better defined structure was obtained at 33 K and reported in 2009.[560] Table 3 shows a collection of the structural features of 5C ls-$\{FeNO\}^7$ complexes in iron-porphyrin model complexes and proteins. The geometries of the FeNO units in these complexes do not exhibit much variation despite the variation in porphyrin scaffolds (see Scheme 13).[559−563] These complexes typically show short Fe−NO distances of ∼1.73 Å and Fe−N−O angles of ∼140−145°, with square pyramidal geometries about the iron centers. The iron is displaced toward the axial NO ligand by ∼0.2−0.3 Å and shows a tilting of the Fe−NO bond from the heme normal along with asymmetry in the Fe−$N_{Pyrrole}$ bond distances (see Scheme 13).[24] There are some variations observed in protein crystal structures (see Table 3), which is often due to lower resolutions of these structures and disorder, leading to less well defined metric parameters of their FeNO units. Despite these structural deviations, the spectroscopic properties of the ls-$\{FeNO\}^7$ units in heme proteins are very similar to those of corresponding model complexes. Consistent with the ability of sGC to detect NO at nanomolar concentrations, the binding constants of NO to ferrous hemes are generally very high, with K_{eq} in the range of 10^{10}−10^{12} M^{-1}; representative examples are given in Table 4. For sGC, K_{eq} is ∼4×10^{10} M^{-1}. The binding constants are affected by SCS effects in proteins (see above), which can account for some of the differences seen in the table.

Ferrous heme−nitrosyl complexes generally have $S_t = 1/2$ ground states, which is evident from their EPR spectra.[604] Early work studying ferrous heme−nitrosyls in both model complexes and proteins like Hb and Mb laid the ground work for characterizing these species, as summarized in Table 5.[605,113,115,116,130,604,606] EPR spectra of 5C ls-$\{FeNO\}^7$ complexes generally display g values of ∼2.10, 2.06, and 2.01, as shown in Figure 25, which compares the EPR spectra of the Fe(II)−NO adduct of sGC and the model complex [Fe(T*o*-F_2PP)(NO)].[130] [Fe(OEP)(NO)] was investigated using single crystal EPR spectroscopy and it was found that the principal axis of the minimum g value, g_{min}, is closely aligned with the Fe−NO bond and therefore corresponds to g_z.[607] Figure 26 shows the resulting orientation of the g tensor. With the presence of the ^{14}N nucleus of NO, three strong hyperfine lines are seen for g_{min}, which is a signature for 5C ls-$\{FeNO\}^7$ complexes, and which are therefore easily identified by EPR spectroscopy. The hyperfine pattern comes from the nuclear spin $I = 1$ of ^{14}N, which has been shown by comparison with the EPR spectrum of the corresponding ^{15}NO complex (^{15}N: $I = 1/2$), where only two hyperfine lines are observed.[635] The ^{14}N hyperfine tensor components of the 5C complexes are quite isotropic, with typical hyperfine coupling constants of ∼40, 50, and 45 MHz for the ^{14}N hyperfine tensor components that correspond to g_{max}, g_{mid}, and g_{min}, respectively, as seen in Table 6.[130] Whereas the hyperfine lines for g_{min} are usually well resolved in the spectra, the hyperfine splitting for g_{max} and g_{mid} is usually washed out, likely due to the presence of different conformers of the complexes in solution that differ by the orientation of the NO ligand relative to the porphyrin plane ("rotamers", originating from a rotation of the NO ligand along the Fe−NO bond). Hence, whereas g_{min} is locked in along the Fe−NO bond axis, and therefore, is less affected by the rotamers, g_{max} and g_{mid} and the corresponding hyperfine coupling constants are broadened out. The EPR spectrum of [Fe(T*o*-F_2PP)(NO)] is an exception in this regard, and shows fully resolved hyperfine splittings for all g values, as shown in Figure 25. In comparison, the EPR spectrum of the full length

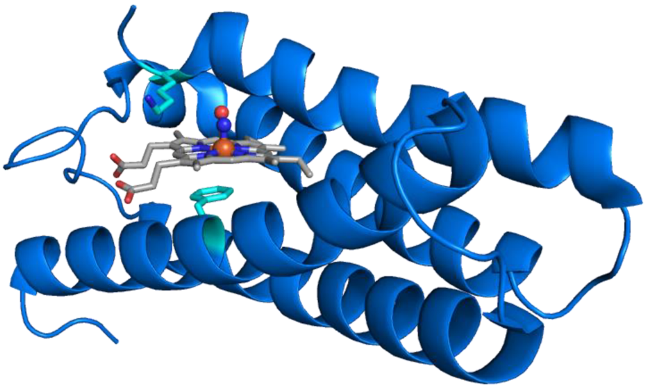

Figure 24. PyMOL generated image of the crystal structure of Cyt. *c*′ from *Shewanella frigidimarina* with NO bound in the proximal pocket (PDB: 4cx9).[558]

Table 3. Examples of 5C and 6C Heme ls-$\{FeNO\}^7$ Complexes

complex/protein	Fe–NO [Å]	N–O [Å]	Fe–Np [Å] (av)	Fe–L [Å]	Fe–N–O [°]	ν(N–O) [cm^{-1}]	ν(Fe–NO) [cm^{-1}]	δ(Fe–N–O) [cm^{-1}]	ref
Five-Coordinate									
[Fe(TPP)(NO)]	1.739	1.163	2.00		144	$1697^a/1676^f$	532^b	371^b	560, 564
[Fe($TPPBr_8$)(NO)]	1.75	1.42	1.986		146	1685^a			565
[Fe(DPDME)(NO)]	1.723	1.187	2.005		143	1651^a			563
[Fe(T*o*-F_2PP)(NO)]	1.738	1.167	2.003		140.4	1683^a			566
[Fe(TpivPP)(NO)] (294 K)	1.72	1.197			143				567
[Fe(TpivPP)(NO)] (158 K)	1.65	1.17	1.991–2.007		137	1675^a			568
[Fe(3,5-Me-BAFP)(NO)]	1.71	1.14	1.99		146	1684^a			569
[Fe(OEP)(NO)]	1.722/ 1.731	1.167/ 1.68	2.004/2.010		144/143	1671^a	522^b	388^b	570
Six-Coordinate									
[Fe(TPP)(MI)(NO)]	1.750	1.182	2.008	2.173	138	1630^a	437^b	563^b	571–573
[Fe(To-F_2PP)(MI)(NO)]	1.752	1.202	2.012	2.188	138	1624^a			564
[Fe(TPP)(Me_2NPy)(NO)]	1.758	1.170	2.006	2.278	140	1653^a			571
[Fe(PPDME)(MI)(NO)]						1618^c			574
[Fe(TPP)(4-MePip)(NO)]	1.751	1.171	2.008	2.285	138	$1640,^a$ 1656^e			571, 575
[Fe(TpivPP)(Py)(NO)]	1.742	1.1941	2.009	2.260	133.4	1635^f			571
tri-[Fe(T*p*-FPP)(MI)(NO)] (100K)[g]	1.752	1.182	2.011	2.169	138.6	1636^a			576
mono-[Fe(T*p*-FPP)(MI)(NO)] (100K)[g]	1.748	1.181	2.002	2.131	137.3	1624^a			576
[Fe(T*p*-OCH_3PP)(MI)(NO)] (100K)[g]	1.749	1.186	2.003	2.166	136.1	1616^a			576
[Fe(T*p*-NO_2PP)(MI)(NO)]	1.755	1.232	2.006	2.164	133.2				577
[Fe(T*p*-CF_3PP)(MI)(NO)] (100K)[g]	1.753	1.192	2.009	2.146	138.1				577
[Fe(OEPO)(Py)(NO)]	1.744	1.190	1.978/1.983/ 2.009/2.012	2.310	138.3	1645^a			578
Heme Proteins									
α-Hb	1.74	1.1			145	1668^d		553^d	574, 579
Hb(II)–NO (α-heme)	1.75	1.13	2.003	2.28	131				580
Hb(II)–NO (β-heme)	1.75	1.15	2.025	2.25	128				581
Mb(II)–NO	2.03	1.14	1.999	2.11	147	1613^d	443^b	547^b	582–584
H64G Mb(II)–NO						1631^d		560^d	585
H64L Mb(II)–NO						1635^d		560^d	585
L29W Mb(II)–NO						1608^d		567^d	585
V68T Mb(II)–NO								551^d	585
V68W Mb(II)–NO						1615^d		551^d	585
H-NOX(II)–NO	1.77	1.15	2.025	2.18	157				478
sGC						1681^d	521^d		586
5C-*Kp*Cld						1680^d	527^d		587
6C-*Kp*Cld						1609^d		548^d	587
cd_1 NIR(II)–NO (*Pp*)	2.0	1.37	2.079	1.98	131				295
cd_1 NIR(II)–NO (*Pa*)	1.8	1.15	2.067	1.98	135				588
rNP1(II)–NO	2.06	1.34	1.980	2.10	120	1611^a			589
	2.02	1.33	1.968	1.99	145				
rNP4(II)–NO	1.73	1.15	141	2.005	2.11				590
Bov. Heart C*c*O(II)–NO						1610^a			591
C*c*O(II)–NO (*Tt*)						1620^d		569^d	592, 593
Cyt c(II)–NO	1.76	1.43	2.01	2.23	113				594
Cyt c′(II)–NO (*Ax*)	1.92	1.16	2.005		132	1624^d		579^d	554, 595
Cyt c′(II)–NO (*Rc*)						1625^d		569^d	596
CCP(II)–NO	1.82			2.04	125,135				597
heme peroxidase(II)–NO	1.79	1.42	2.03	2.14	117				598
HO-1(II)–NO	1.98	1.16	2.01	2.36	150				599
	1.83	1.15	2.01	2.54	151				
HO-2(II)–NO	2.06	1.14	1.99	2.12	125				600
	2.10	1.14	1.99	2.05	119				
P450nor(II)–NO							$544^{d,h}$		305
P450cam(II)–NO						1591^d	$554^{d,h}$		601–603

Table 3. continued

[a]KBr pellet. [b]NRVS. [c]MI (1-methylimidazole) solution. [d]rRaman. [e]Nujol. [f]In solution. [g]Crystal data taken at multiple temperatures. [h]Assignment not clear.

Scheme 13. General Structural Motifs of 5C and 6C Ferrous Heme−Nitrosyl Complexes[a]

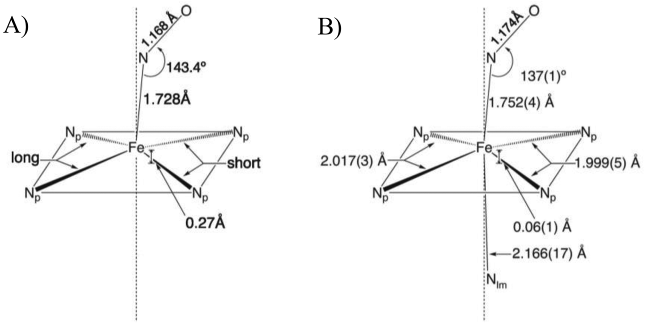

[a]Reprinted with permission from ref 24. Copyright 2013 Springer-Verlag Berlin Heidelberg.

$\alpha 1/\beta 1$ 5C sGC Fe(II)−NO complex has reported g values of 2.083, 2.036, and 2.012, with strong ^{14}N hyperfine splitting again observed for g_{min} (A_z = 45 MHz).[636,637]

Vibrational spectroscopic methods such as rRaman, IR, and nuclear resonance vibrational spectroscopy (NRVS) are well suited to study ferrous heme−nitrosyls because of the sensitivity of their vibrational properties to coordination number, axial ligand identity (or lack thereof in the 5C complexes) and the SCS in proteins. However, heme−nitrosyls tend to be photolabile, so special care has to be taken in rRaman measurements to avoid photodissociation of either NO or the proximal ligand, and subsequent photochemistry.[508] NRVS does not suffer from this problem, since it measures inelastic scattering resulting from the excitation of the ^{57}Fe nucleus at the 14.4125 keV nuclear resonance (Mössbauer) line.[643−645] Typical vibrational energies for 5C ferrous heme−nitrosyls are 1670 − 1700 cm^{-1} for ν(N−O), easily observed by IR spectroscopy as a very intense feature, and 520−540 cm^{-1} for ν(Fe−NO), identified by rRaman and NRVS. On the other hand, the in-plane δ_{ip}(Fe−N−O) bending mode is best identified by NRVS, and typically occurs in the 370−390 cm^{-1} range. For example, [^{57}Fe(OEP)(NO)] exhibits ν(Fe−NO) at 522 cm^{-1} and the in-plane Fe−N−O bending mode at 388 cm^{-1}, which shift to 508 and 381 cm^{-1}, respectively, in the ^{15}N^{18}O isotopically labeled complex.[570] Intense bands at 339 and 301 cm^{-1} correspond to the two components of the in-plane Fe−N$_{Pyrrole}$ stretching mode of E_u symmetry (in ideal D_{4h} symmetry) of the heme, mixed with other porphyrin-based vibrations, as determined by DFT. Using IR spectroscopy, the N−O stretching mode of this complex was determined to be 1671 cm^{-1}. The vibrational data are in agreement with the vibrational properties of the 5C Fe(II)−NO complex in sGC. Here, the Fe−NO and N−O stretching frequencies are observed at 521 and 1681 cm^{-1}, respectively, by rRaman.[647] Table 3 shows an overview of the vibrational properties of 5C ls-{FeNO}^{7} complexes.

The quantum-chemistry centered normal coordinate analysis (QCC-NCA) was used to simulate the vibrational energies, isotope shifts, and NRVS vibrational density of states (VDOS) intensities of ferrous heme−nitrosyls.[564,648] In this method, high level DFT calculations are used to generate a force field for the complex under investigation, and the theoretical force constants derived in this way then serve as a starting point to fit the force constants of the FeNO unit of the complex to reproduce the vibrational data.[648−650] In addition, in the case of NRVS, vibrational intensities can be reproduced as well (not just vibrational frequencies and isotope shifts), which makes a combination of NRVS and QCC-NCA a particularly powerful method for the analysis of the vibrational properties of molecules, including several heme−nitrosyl model complexes.[570,573,651−653] The QCC-NCA analysis produces force constants, which are good descriptors of the Fe−NO and N−O bond strengths in heme−nitrosyls. Comparing force constants is advantageous over comparing vibrational frequencies, since the former do not depend on mode mixing, which can otherwise lead to substantial shifts and splittings of vibrational features.[648] This is a particular problem for Fe−NO stretching and Fe−N−O bending modes, which can be heavily mixed with other metal-ligand stretching and bending modes, and vibrations from larger, organic ligands. Force constants for 5C ferrous heme−nitrosyls can be found in Table 7 and are in the 2.9−3.0 mdyn/Å range for the Fe−NO and 12.0−12.5 mdyn/Å for the N−O bonds, respectively.[564,570,572]

The electronic structure of ferrous heme−nitrosyls, ls-{FeNO}^{7} complexes in the Enemark−Feltham notation,[36] could in principle be of Fe(III)−NO$^-$, Fe(II)−NO$^\bullet$ or Fe(I)−NO$^+$ type. Accordingly, early DFT calculations proposed electronic structures for these species ranging from Fe(III)−NO$^-$ for both the 5C and 6C (imidazole-bound) complexes[656] to Fe(II)−NO$^\bullet$ and even Fe(I)−NO$^+$.[642,657,658] In addition, the electronic properties of ferrous heme−nitrosyls were further investigated using CASSCF and quantum-chemical multireference methods.[659,660] The latter results predict that the ground state of these complexes contains a contribution of the Fe(III)−NO$^-$ electronic state. A general caveat of these methods is their limited ability to predict geometric and spectroscopic properties of coordination compounds, to validate these predictions. The best way to distinguish between these possibilities is to calibrate electronic structure calculations using spectroscopic data, to ensure that the calculations can reproduce key spectroscopic properties of the complexes. Using spectroscopically-calibrated DFT calculations, the electronic structures of ferrous heme−nitrosyls have been re-analyzed as a function of the axial ligand bound in trans position to NO.[24,130,310,564,569,570,572,573,638,651] A simplified (restricted open shell) MO diagram of ferrous heme−nitrosyls is shown in Scheme 14. On the basis of the EPR results, especially the observed, small g shifts, 5C [Fe(Porph)(NO)] complexes contain ls-Fe^{II} centers, with an iron d-electron configuration of $[d_{xz},d_{yz},d_{xy}]^6 \approx [t_2]^6$. The LUMO of the porphyrin ligand corresponds to a pair of degenerate π* orbitals of e_g symmetry, and these can undergo weak π-backbonding interactions with the d_{xz} and d_{yz} orbitals of iron, as indicated in Figure 27. The highest occupied π orbitals of the porphyrin ligand are of a_{2u} and a_{1u} symmetry and play a key role in the optical spectra of metalloporphyrins.[528] The signature Soret and Q bands of porphyrins originate from the corresponding $a_{2u}(\pi) \rightarrow e_g(\pi^*)$ and $a_{1u}(\pi) \rightarrow e_g(\pi^*)$ transitions, mixed via configuration interaction. The highest occupied in-plane orbital of the

Table 4. Binding Constants of NO for Ferrous and Ferric Heme−Nitrosyls in Proteins and Model Complexes

molecule[a]	k_{on} [M^{-1} s^{-1}]	k_{off} [s^{-1}]	K_{eq} [M^{-1}] (k_{on}/k_{off})	T [°C][b]	method	ref
			Ferrous Heme Complexes			
Mb(II)	1.7×10^{7}	1.2×10^{-4}	1.4×10^{11}	20	stopped-flow spectrophotometry	608
Hb(II)	2.4×10^{7}	1×10^{-5}	2.4×10^{12}	20	stopped-flow spectrophotometry	608
Hb(II)	1.8×10^{7}	Tstate: k_1 ~0.004 k_2 ~0.07	4.5×10^{9}	20	stopped-flow spectrophotometry	609
Hb(II)		$25 \pm 1 \times 10^{-4}$		RT	UV−vis spectroscopy	610
cd_1 NIR(II)	$3.9(\pm 0.3) \times 10^{8}$	27.5 ± 1.5	1.4×10^{7}	20	k_{on}: determined by laser photolysis at room temperature k_{off}: determined by stopped-flow spectrophotometry	296
cd_1NIR(II)		3.8 ± 0.4		20	k_{on}: determined by laser photolysis at room temperature k_{off}: determined by stopped-flow spectrophotometry	296
cd_1NIR(II)		31.7 ± 2.0	1.2×10^{7}	20	k_{on}: determined by laser photolysis at room temperature k_{off}: determined by stopped-flow spectrophotometry	296
cd_1NIR(II)		3.5 ± 0.5		20	k_{on}: determined by laser photolysis at room temperature k_{off}: determined by stopped-flow spectrophotometry	296
cd_1NIR(II)		43.5 ± 3.5	8.9×10^{6}	20	k_{on}: determined by laser photolysis at room temperature k_{off}: determined by stopped-flow spectrophotometry	296
cd_1NIR(II)		8 ± 1		20	k_{on}: determined by laser photolysis at room temperature k_{off}: determined by stopped-flow spectrophotometry	296
sGC(II)	1.4×10^{8}			4	stopped-flow spectrophotometry	516
sGC(II)		8.2×10^{-4}		25	stopped-flow spectrophotometry	541
sGC(II)		1.7×10^{-2}		37	UV−visible spectroscopy	542
sGC(II) β_1	$7.1 \pm 2 \times 10^{8}$			4	Stopped-flow spectrophotometry	516
rNP1(II) pH = 5.5			1.3×10^{14}	25	calculated from K^{III}_{eq} in combination with reduction potentials	611
rNP1(II) pH = 7.0			2.0×10^{13}	25	calculated from K^{III}_{eq} in combination with reduction potentials	611
rNP2(II) pH = 5.5			$\sim 4.0 \times 10^{14}$	25	calculated from K^{III}_{eq} in combination with reduction potentials	611
rNP2(II) pH = 7.0			1.1×10^{13}	25	calculated from K^{III}_{eq} in combination with reduction potentials	611
rNP4(II) pH = 5.5			1.7×10^{13}	25	calculated from K^{III}_{eq} in combination with reduction potentials	611
rNP7(II) pH = 5.5			$>1 \times 10^{14}$			612
rNP7(II) pH = 7.0			1.0×10^{13}			612
CcO(II)	8.3	2.87×10^{-5}	2.89×10^{5}		laser photolysis	613
[Fe^{II}(TpivPP-MI)]	8.9×10^{8}			25	laser flash photolysis	614
[Fe^{II}(PPIX)(MI)]	$(1.8 \pm 0.7) \times 10^{8}$	2.9×10^{-4}	5.8×10^{11}	20	laser flash photolysis	615
[Fe^{II}(TPPS)]	1.5×10^{9}	6.4×10^{-4}	2.3×10^{12}	25	laser flash photolysis	616
[Fe^{II}(TMPS)]	1.0×10^{9}			25	laser flash photolysis	616
[Fe^{II}(TPP)]	5.2×10^{9}			RT	laser flash photolysis	617
			Ferric Heme Complexes			
Mb(III)	5.3×10^{4}	14	3.8×10^{3}	20	stopped-flow spectrophotometry	618
Mb(III)	2.2×10^{7}	40	5.5×10^{5}	20	stopped-flow spectrophotometry	618
Hb(III) $\alpha_2\beta_2$	1.71×10^{3}	0.65	2.6×10^{3}	20	stopped-flow spectrophotometry	618
Hb(III) $\alpha_2\beta_2$	6.4×10^{3}	1.5	4.3×10^{3}	20	stopped-flow spectrophotometry	618
Hb(III) β_4	1.3×10^{4}	3	4.3×10^{3}	20	stopped-flow spectrophotometry	618
HRP(III)	1.9×10^{5}	11−13	$(1.55 \pm 0.06) \times 10^{4}$	20	laser flash photolysis	619, 620
rNP1(III) pH = 5.0	$(1.5 \pm 0.1) \times 10^{6}$	0.2 ± 0.01	7.5×10^{6}	25	k_{on} determined by stopped-flow and laser flash photolysis; k_{off} estimated from association reaction data	621
rNP1(III) pH = 8.0	$(1.5 \pm 0.1) \times 10^{6}$	2.2 ± 0.1	6.8×10^{5}	25	k_{on} determined by stopped-flow and laser flash photolysis; k_{off} estimated from association reaction data	621
rNP2(III) pH = 5.0	2.2×10^{7}	0.05 ± 0.01	4.4×10^{8}	25	k_{on} determined by stopped-flow and laser flash photolysis; k_{off} estimated from association reaction data	621
rNP2(III) pH = 8.0	3.3×10^{7}	0.12 ± 0.01	2.8×10^{8}	25	k_{on} determined by stopped-flow and laser flash photolysis; k_{off} estimated from association reaction data	621
rNP3(III) pH = 5.0	7.0×10^{6}	0.05 ± 0.01	1.4×10^{8}	12	k_{on} determined by stopped-flow and laser flash photolysis; k_{off} estimated from association reaction data	621
rNP3(III) pH = 8.0	6.7×10^{6}	0.08 ± 0.01	8.4×10^{7}	12	k_{on} determined by stopped-flow and laser flash photolysis; k_{off} estimated from association reaction data	621
rNP4(III) pH = 5.0	2.1×10^{6}	0.14 ± 0.01	1.5×10^{7}	25	k_{on} determined by stopped-flow and laser flash photolysis; k_{off} estimated from association reaction data	621
rNP4(III) pH = 8.0	2.3×10^{6}	2.6 ± 0.1	8.8×10^{5}	25	k_{on} determined by stopped-flow and laser flash photolysis; k_{off} estimated from association reaction data	621
rNP7(III) pH = 7.5	2.4×10^{6}	0.606 ± 0.13	4.0×10^{6}	25	k_{on} calculated using k_{off} and K_{eq}; k_{off} determined by stopped-flow techniques	612

Table 4. continued

molecule[a]	k_{on} [M^{-1} s^{-1}]	k_{off} [s^{-1}]	K_{eq} [M^{-1}] (k_{on}/k_{off})	T [°C][b]	method	ref
			Ferric Heme Complexes			
nNOS(III)	(5.9−6.2) × 10^6	60−120	4.9 × 10^4−2.1 × 10^6	10−23	laser flash photolysis	622, 623
nNOS(III)		3−5		23	stopped-flow spectrophotometry	622
iNOSoxy(III)	(0.059−1.57) × 10^6	13−118		10	stopped-flow spectrophotometry	624, 625
iNOSoxy(III)		20.7 ± 3.0	5.0 × 10^2−6.8 × 10^5	10	laser flash photolysis	625
iNOSoxy(III)	(0.27 ± 0.03) × 10^6	2.3		10	stopped-flow spectrophotometry	625
eNOS(III)	8.2 × 10^5	70	1.2 × 10^4	10	stopped-flow spectrophotometry	626
nNOS(III)	6.1 × 10^6	60	1.0 × 10^5	23	laser flash photolysis	622
V346I iNOSoxy (III)	0.033 ± 0.003	1.9 ± 0.3	(1.7−4.3) × 10^4	10	laser flash photolysis	625
V346I iNOSoxy (III)		0.77 ± 0.03		10	stopped-flow spectrophotometry	625
Bs-NOS(III)	(0.033 ± 0.003) × 10^6	0.23		10	laser flash photolysis	625
I224V bs-NOS (III)		0.82 ± 0.02		10	laser flash photolysis	625
Cyt c(III)	7.2 × 10^2	4.4 × 10^{-2}	1.6 × 10^4	25	laser photolysis	613
Cyt a_3(III)	2.2 × 10^5			20	stopped-flow spectrophotometry	627, 628
MPO(III)	1.07 × 10^6	10.8	9.9 × 10^4	10	stopped-flow spectrophotometry	629
P450nor(III)	2.6 × 10^7			10	laser flash photolysis	307
P450cam(III) (camphor-free)	3.2 × 10^3	0.35	9.1 × 10^5	25	k_{on} calculated using k_{off} measured using [Ru^{III}(EDTA) H_2O] to scavenge NO	630
P450cam(III) (camphor-free)	5.8 × 10^3			25	k_{on} calculated using k_{off} measured using [Ru^{III}(EDTA) H_2O] to scavenge NO	630
P450cam(III) (camphor-bound)	3.45 × 10^6	1.93	1.79 × 10^7	25	k_{on} calculated using k_{off} measured using [Ru^{III}(EDTA) H_2O] to scavenge NO	630
$P450_{1A2}$(III) (substrate-free)	1.7 × 10^4	0.15	1.1 × 10^5	25	laser flash photolysis	631
$P450_{1A2}$(III) (substrate-present)	1.9 × 10^5	0.51	1.1 × 10^5	25	laser flash photolysis	631
Mtb CYP 125(III)	1.71 × 10^7	11.2 ± 0.1	1.53 × 10^6	10	k_{on} determined through stopped-flow spectroscopy; k_{off} measured using Mb-O_2 as a NO scavenger	632
Mtb CYP 130(III)	2 × 10^3	2.45 ± 0.02	8 × 10^4	23	k_{on} determined through stopped-flow spectroscopy; k_{off} measured using Mb-O_2 as a NO scavenger	632
Mtb CYP 142(III)	9 × 10^5	1.90 ± 0.02	5 × 10^6	23	k_{on} determined through stopped-flow spectroscopy; k_{off} measured using Mb-O_2 as a NO scavenger	632
Catalase(III)	3.0 × 10^7	1.7 × 10^2	1.8 × 10^5	25	laser photolysis	613
PGHS(III)	6.5 × 10^4	60	1.1 × 10^5	21	stopped-flow spectroscopy	633
[Fe^{III}(TPPS)]	0.5 × 10^6	0.5 × 10^3	1.0 × 10^3	25	laser flash photolysis	616
[Fe^{III}(TMPS)]	2.8 × 10^6	0.9 × 10^3	3.1 × 10^3	25	laser flash photolysis	616
[Fe^{III}(SPorph)]	(2.2 ± 0.1) × 10^5	1.8 ± 2.1	1.2 × 10^5	5	stopped-flow spectrophotometry	634

[a] Abbreviations: TpivPP = meso-tetra(*α*,*α*,*α*,*α*-o-pivalamidophenyl)porphyrin^{2-}; TPPS = tetrakis(4-sulfonatophenyl)porphyrin^{2-}; TMPS = tetrakis(3,5-disulfonatomesityl)porphyrin^{2-}; SPorph = *meso-a,a,a,a*-[*o*-[[o-[(acetylthio)methyl]phenoxy]acetamido]phenyl] tris(o-pivalamidophenyl)porphyrin^{2-}. [b] RT = room temperature.

porphyrin possesses b_{1g} symmetry and corresponds to the b_{1g}-symmetric combination of the sp^2 σ-donor orbitals of the four pyrrole nitrogens of the porphyrin. This orbital forms a very strong σ-bond with the unoccupied $d_{x^2-y^2}$ orbital of iron. The MO diagram of nitric oxide has one unpaired electron in the π^* orbitals (see Figure 3). Because ferrous heme−nitrosyls exhibit an S_t = 1/2 ground state, the spin-unrestricted formalism is required, which distinguishes between α (majority) and β (minority) spin orbitals. Here, the single unpaired electron of NO occupies the α-π^*_h (h = horizontal) orbital, which is the NO(π^*) orbital that is located in the plane formed by the bent Fe−N−O unit. Importantly, σ-donation from this α-π^*_h orbital to the metal is only possible via the empty d_{z^2} orbital, because in the ls state of Fe^{II} the t_2 orbitals are fully occupied. In the case of the 5C complexes, there is strong mixing between the π^*_h and d_{z^2} orbitals, which is illustrated by the corresponding bonding combination, α-π^*_{h}_d_{z^2}, which is shown in Figure 26. This orbital constitutes the SOMO (= singly occupied molecular orbital) of the complexes. This orbital interaction leads to a net transfer of about half of an electron from π^*_h of NO to d_{z^2}. In other words, the unpaired electron of NO is fully delocalized over the FeNO unit because of this highly covalent orbital interaction. This is further reflected by the calculated spin populations, which are usually about +0.5 on iron and +0.5 on NO. Other than the strong Fe−NO σ bond that originates from the π^*_h/d_{z^2} interaction, the unoccupied π^* orbital of NO, π^*_v (v = vertical with respect to the FeNO unit), forms a medium-strong π-backbond with one of the fully occupied d_π orbitals of Fe^{II} (d_{yz} in our coordinate system in Scheme 14). The extent of covalency of this orbital interaction is estimated best from the corresponding antibonding combination, π^*_{v}_d_{yz}, which usually shows about 25% Fe^{II}(d) character. In a spin-unrestricted scheme, an additional π-backbond is possible that originates from the interaction of the unoccupied β-π^*_h

Table 5. Comparison of Experimental and Calculated g Values and g Tensor Orientations for Select 5C ls-$\{FeNO\}^7$ [Fe(Porph)(NO)] Complexes

	g values					
complex/protein[a]	g (max)	g (mid)	g (min)	orientation[b]	conditions (solvent, etc.)	ref
[Fe(TPP)(NO)]	2.102	2.064	2.010*		toluene	606
	2.106	2.066	2.013*		toluene	638
	2.098	2.031	2.001*		CH_2Cl_2	571
[Fe(OEP)(NO)]	**2.106**	**2.057**	**2.015***	**g(min)/Fe−NO: 8°**	**single crystal**	607
[Fe(PPIXDME)(NO)]	2.105	2.059	2.010*		toluene	639
[Fe(T*p*-NMe_2PP)(NO)]	2.104		2.010*		toluene	635
[Fe(T*p*-OCH_3PP)(NO)]	2.104		2.010*		toluene	635
[Fe(T*p*-FPP)(NO)]	2.107		2.010*		toluene	635
[Fe(T*per*-F_5PP)(NO)]	2.108	2.028	2.011*		toluene	635
Hb(II)−NO + inositol-P_6	2.070	2.04	2.008*		pH = 7	640
sGC(II)−NO	2.083	2.036	2.012*		pH = 7.4	465
sGC(II) β1-NO isoform	2.083	2.036	2.012*		pH = 7.4	465
sGC(II) β2-NO isoform	2.106	2.025	2.010*		pH = 7.4	465
sGC(II)−NO + YC-1	2.106	2.030	2.011*		pH = 7.4	465
sGC(II)−NO + BAY 41-2272	2.106	2.029	2.010*		pH = 7.4	465
NorBC(II)−NO	∼2.08	∼2.08	2.012*		pH = 7.5	641
PGHS(II)−NO			2.00*		buffer	633
cNP(II)−NO	2.105	2.044	2.013*		pH = 7.5	253
[Fe(P)(NO)][c]	2.049	2.025	2.004(*)	g(min)/Fe−NO: 20°	from DFT calculations	572
[Fe(P)(NO)][d]	2.063	2.005(*)	1.994	g(mid)/Fe−NO: 20°	from DFT calculations	642

[a] PGHS = prostaglandin H synthase; * = shows ^{14}N hyperfine lines of the coordinated NO ligand; (*) = principal axis closest to the Fe−NO bond vector in the calculations. [b] Relative orientation of the principal axis of the given g value with respect to the Fe−N(O) bond or the heme normal (heme⊥). [c] Calculated with B3LYP and the following basis sets: Fe: CP(PPP); N (EPR-II); C, O: TZVP; H: TZV. [d] Calculated with VWN/triple-ζ basis set of Slater-type functions.

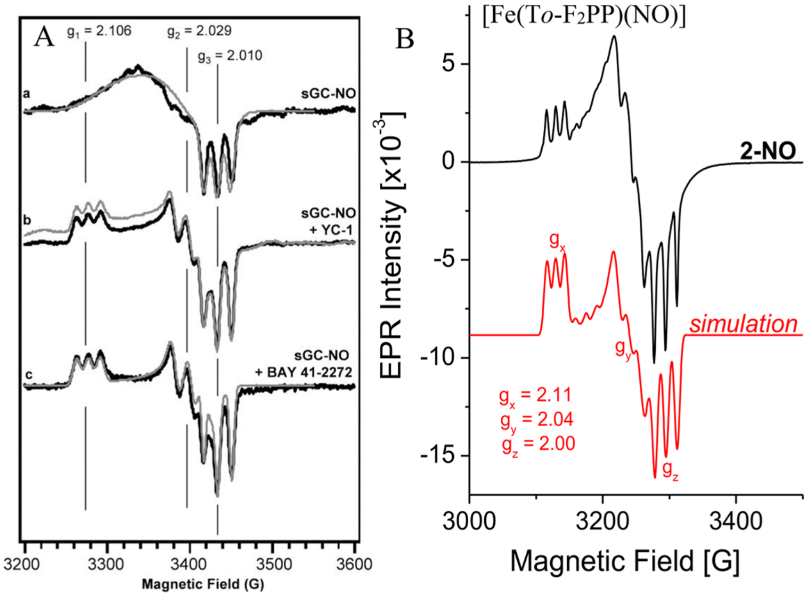

Figure 25. (A) EPR spectra of sGC(II)−NO in the absence (a) and in the presence of activators YC-1 (b) and BAY 41-2272 (c).[465] (B) EPR spectrum of [Fe(T*o*-F_2PP)(NO)] (black) and fit (red).[569] Reprinted with Permission from refs 465 and 569. Copyright 2008 and 2013, American Chemical Society.

orbital of NO with d_{xz}, which can further affect the spin density distribution of the FeNO unit.[570] In short, NO acts as a strong σ-donor and medium-strong π-acceptor ligand in 5C ferrous heme−nitrosyl complexes. Because of the strong σ-donation of NO, these complexes have noticeable Fe(I)−NO^+ character.[21,564,572] Using this electronic structure description, trends in the geometric and electronic structures of 5C ferrous heme−nitrosyls can then be rationalized.

As shown by Spiro and coworkers, the strength of the Fe−NO π-backbond in 5C ferrous heme−nitrosyls can be modulated using [Fe(TPP*)(NO)] (TPP^{*2-} = phenyl-substituted TPP^{2-} derivative) type complexes where the phenyl substituents carry electron withdrawing or donating groups.[661] Here, an inverse correlation of the Fe−NO and N−O stretching frequencies was observed, spanning a range of N−O/Fe−NO stretching frequencies between 1663/530 cm^{-1} for

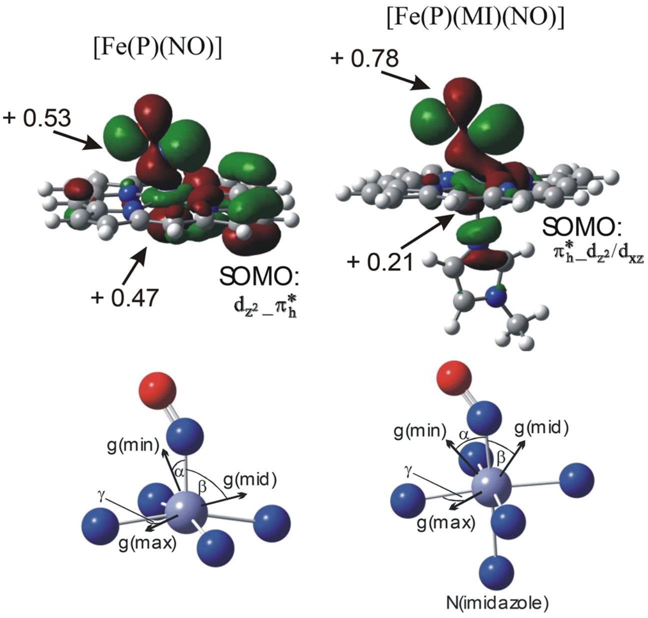

Figure 26. Top: contour plots of the SOMOs of [Fe(Porph)(NO)] and [Fe(Porph)(MI)(NO)] calculated with B3LYP/LanL2DZ*. Bottom: calculated orientation of the principal axes of the *g* tensor relative to the molecular frame. Reprinted with permission from ref 564. Copyright 2006 American Chemical Society.

the most electron donating and 1703/514 cm^{-1} for the most electron withdrawing substituent.[661] In this case, a strengthening of the π-backbond results in a stronger Fe−NO bond and a higher ν(Fe−NO) frequency. This leads to a larger occupation of the π^* orbitals of NO involved in the π-backbond, and in this way (since π^* orbitals are N−O antibonding), leads to a weaker N−O bond and therefore, lower ν(N−O) frequency. In this regard, the complex with the largest ν(Fe−NO) frequency has the strongest Fe−NO and weakest N−O bond. A similar, inverse correlation has been noted before in ferrous heme-carbonyl complexes, and is in general a signature of π-backbonding.[662,663] This variation in π-donating ability of the iron center among electron withdrawing and donating phenyl substituents is attributed to changes in the energy of the occupied porphyrin π orbitals of e_g symmetry (see Figure 27), which can interact with the d_π orbitals of Fe^{II}.[570] In the case of the electron-withdrawing substituents, the porphyrin $e_g(\pi)$ orbitals would decrease in energy, which would in turn lower the d_π orbitals of Fe^{II} in energy, causing their interaction with the π^* acceptor orbitals of NO to become weaker. This would cause a decrease in the Fe−NO bond strength and the Fe−NO vibrational frequency, while simultaneously strengthening the N−O bond and increasing the N−O stretching frequency, giving rise to the inverse correlation observed experimentally. The opposite trend is observed for electron donating substituents.

The Fe−NO σ-bond can also be tuned, but more indirectly (since the 5C complexes lack a trans ligand to NO). By comparing [Fe(OEP)(NO)] and [Fe(TPP)(NO)], the differences in spectroscopic data can be explained by a variation in the Fe−NO σ-bond, that is, the amount of σ-donation from NO(π^*_h) into d_{z^2}.[570] [^{57}Fe(OEP)(NO)] has N−O and Fe−NO vibrational frequencies of 1671/522 cm^{-1} (524 cm^{-1} with n.a.i. Fe) and N−O and Fe−NO force constants of 12.15/2.94 mdyn/Å, while [Fe(TPP)(NO)] shows the corresponding stretching vibrations at 1697/532 cm^{-1}, and the N−O and Fe−NO force constants are 12.53/2.98 mdyn/Å. The slightly lower vibrational frequencies and force constants seen in [Fe(OEP)(NO)] compared to [Fe(TPP)(NO)] can be rationalized by a change in the Fe−NO σ-bond. A change in Fe−NO π-backbonding can be ruled out, since this would give rise to an inverse correlation of the N−O and Fe−NO bond strengths, and hence, vibrational frequencies (see above). The difference in Fe−NO σ-bonding between d_{z^2} of iron and π^*_h of NO likely relates to differences in the energies of the porphyrin π orbitals

Table 6. Experimental and Calculated ^{14}N Hyperfine (A) Tensors of the Nitrosyl Nitrogen in Select 5C ls-{FeNO}^{7} [Fe(Porph)(NO)] Complexes[a]

complex/protein[b]	^{14}N hyperfine A[g] [MHz][c] A [g (max)]	A [g (mid)]	A [g (min)]	orientation[d]	conditions (solvent, etc.)	ref
[Fe(TPP)(NO)]	37.1	49.7	48.7		toluene	606
[Fe(OEP)(NO)]	**40.9**	**49.7**	**42.7**	g/A: 30°	**single crystal**	607
[Fe(PPIXDME)(NO)]	38.3	40.3	46.4		toluene	639
[Fe(T*p*-NMe$_2$PP)(NO)]	44.2		46.7		toluene	635
[Fe(T*p*-OCH$_3$PP)(NO)]	44.2		46.7		toluene	635
[Fe(T*p*-FPP)(NO)]	44.2		47.5		toluene	635
[Fe(T*per*-F$_5$PP)(NO)]	44.3	57.3	48.4		toluene	635
[Fe(T*o*-F$_2$PP)(NO)]	47	46	39		toluene	646
sGC(II)−NO	67	43	45		pH = 7.4	465
sGC(II) β1-NO isoform	67	43	45		pH = 7.4	465
sGC(II) β2-NO isoform	42	54	48		pH = 7.4	465
sGC(II)−NO + YC-1	42	54	48		pH = 7.4	465
sGC(II)−NO + BAY 41-2272	42	54	48		pH = 7.4	465
PGHS(II)−NO			47.6		buffer	633
cNP(II)−NO			47.3		pH = 7.5	253
[Fe(P)(NO)]	28.3	62.0	49.9	g(min)/A[g(min)]: 20°	from DFT calculations	564

[a] Values of the A tensor [MHz] are given relative to the g tensor, that is, a given A value is paired with the g value whose principal axis is closest to the principal axis of this A tensor component. [b] PGHS = prostaglandin H synthase. [c] For the solution data, the A values in MHz have been calculated with the formula: A[MHz] = 1.39916·A_i[G] ·g_i. Strictly speaking, this formula is only valid if the g and A tensors are aligned. Hence, these values have to be treated with some caution. [d] Angle between the principal axes of g and A tensor components as indicated.

Table 7. QCC-NCA Results for 5C and 6C Heme-Nitrosyls

complex/method	vibrational frequency [cm^{-1}][a] ν(N–O)	ν(Fe–NO)	$\delta_{ip/lb}$(Fe–N–O)	force constant [mdyn/Å] f_{N-O}	f_{Fe-NO}	f_{Fe-N-O}[b]	ref
			ls-$\{FeNO\}^7$				
[^{57}Fe(OEP)(NO)]: EXP.	1671 (1595)	522 (508)	388 (381)				570
[Fe(OEP)(NO)]: BP86/LanL2DZ*	1712	620	414	12.798	3.854	0.469	
[^{57}Fe(OEP)(NO)]: QCC-NCA	1671 (1598)	522 (508)	388 (381)	12.148	2.938	0.346	
[Fe(TPP)(NO)]: EXP.	1697 (1625)	532 (515)	371 (365)				572, 564
[Fe(P)(NO)]: BP86/TZVP	1703	595	427	12.709	3.619	0.415	
[Fe(P)(NO)]: QCC-NCA	1698 (1624)	531 (517)	371 (365)	12.530	2.975	0.336	
[^{57}Fe(TPP)(MI)(NO)]: EXP.	1630 (1556)	437 (429)	563 (551)				572, 564
[Fe(TPP)(MI)(NO)]: BP86/TZVP	1668	606	485	12.219	3.241	0.694	651
[^{57}Fe(TPP)(MI)(NO)]: QCC-NCA	1630 (1558)	438 (429)	~562 (547)	11.55	2.574	0.773	
[Fe(P)(MI)(NO)]: BP86/TZVP	1662	609	482	12.224	3.257	0.680	572, 564
[^{57}Fe(P)(MI)(NO)]: QCC-NCA	1628 (1557)	439 (427)	560 (545)	11.55	2.380	0.799	573
			ls-$\{FeNO\}^6$				
[^{57}Fe(TPP)(MI)(NO)](BF_4): EXP.	1896 (1816)	578[c] (~569)	586[c] (~575)				654
[Fe(P)(MI)(NO)]$^+$: BP86/TZVP	1933	639	606/598	15.62	4.82	~0.46	
[^{57}Fe(P)(MI)(NO)]$^+$: QCC-NCA	1897 (1815)	580[c] (566)	587[c] (573)	15.178	3.922	0.368/0.406	

[a] Values in brackets are calculated for the corresponding $^{15}N^{18}O$ labeled complexes. [b] Force constant f_{Fe-N-O} is given in [mdyn Å]. [c] Note that this assignment was later corrected, when it was found that the Fe–NO stretch is at higher energy. In this revised assignment, ν(Fe–NO) is at 586 cm^{-1} and δ_{lb}(Fe–N–O) is at 578 cm^{-1}.[655] However, this switch has a marginal effect on the QCC-NCA force constants.

Scheme 14. Electronic Structure of Ferrous Heme–Nitrosyls[a]

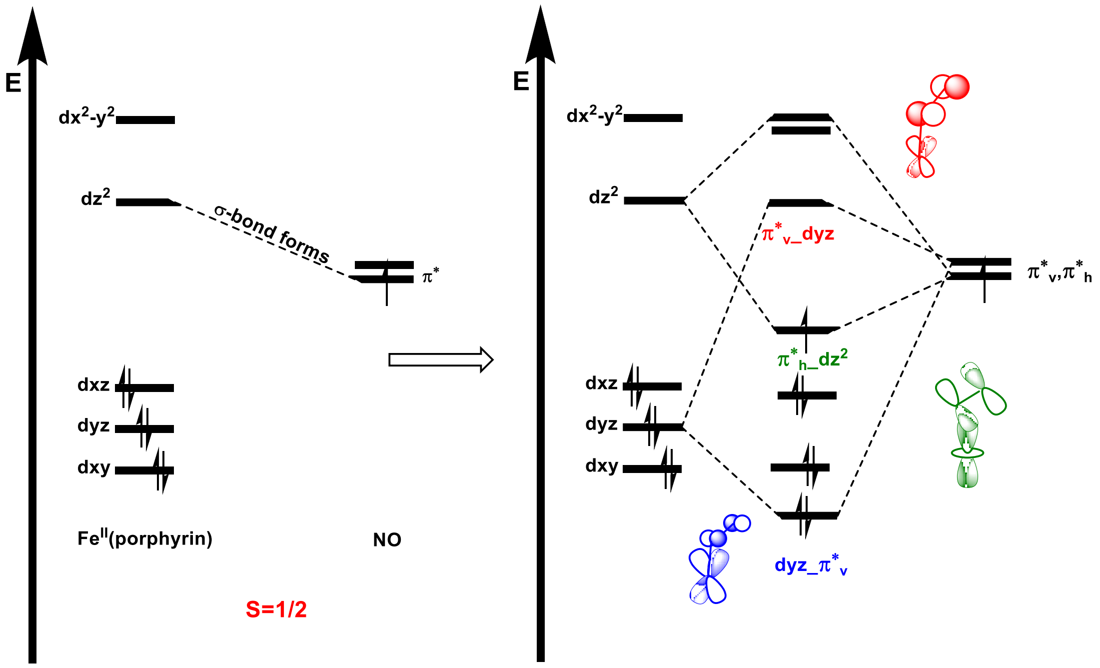

[a] Electron distribution in the ls-Fe^{II} and NO units (left) and general molecular orbital diagram for a ls-$\{FeNO\}^7$ porphyrin complex (right).

between the two macrocycles, OEP^{2-} and TPP^{2-}. In 5C ferrous heme–nitrosyls, the iron center is displaced out of the porphyrin plane, which allows its d_{z^2} orbital to interact with the porphyrin $a_{2u}(\pi)$ orbital (see Figure 27), giving rise to a weak σ interaction. Changes in the porphyrin macrocycle could

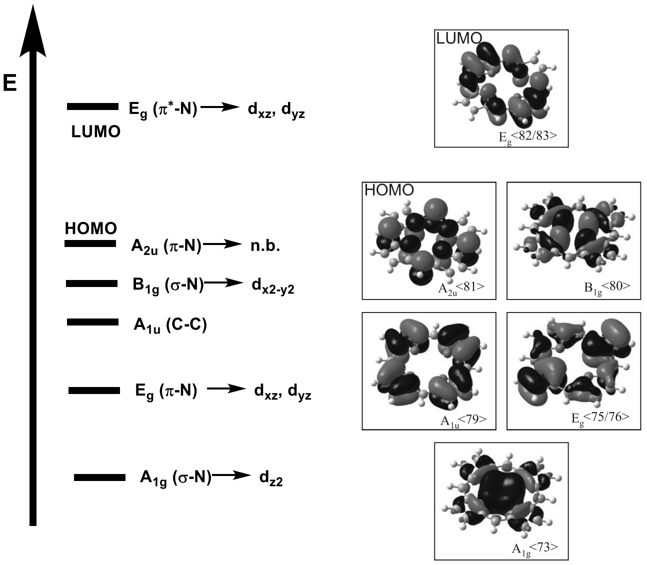

Figure 27. Simplified molecular orbital diagram of the porphine^{2-} ligand with contour plots of important molecular orbitals. Metal d orbitals that could potentially interact with these molecular orbitals are indicated.[570]

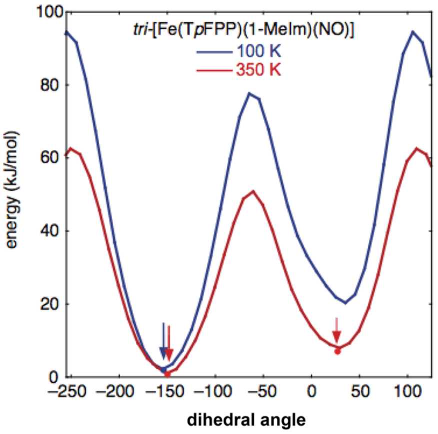

Figure 28. Potential energy diagram calculated for the crystal structure of tri-[Fe(T*p*-FPP)(MI)(NO)], for the rotation of the NO ligand around the Fe−NO bond. Values are plotted for the lowest and highest temperatures for which structural data are available. The crystallographically observed NO positions are shown as points and indicated by arrows. Reprinted with permission from ref 577. Copyright 2009 American Chemical Society.

therefore modulate the energy of the d_{z^2} orbital and, in this way, affect small changes in the Fe−NO σ-bond.[570]

2.2.6.2. Six-Coordinate Ferrous Heme−Nitrosyls. The first crystal structure of a 6C ferrous heme−nitrosyl model complex with axial N-donor coordination (like imidazole, pyridine, and other N heterocycles) in trans position to NO was reported in 1976 by Scheidt and coworkers.[664] This complex, [Fe(TPP)(MI)(NO)] (MI = 1-methylimidazole), shows again disorder of the NO ligand, much like the 5C analogs described above. Here, two major conformations of the bound NO are observed, and even in later work where better crystals were obtained and the structure could be solved to a higher resolution, this disorder could not be overcome.[571] A further improvement was achieved when it was discovered that the disorder was temperature-dependent and fully reversible as a function of temperature.[576] Non-covalent contacts in the crystal were identified as the underlying cause for the formation of the discrete rotamers that are observed in these structures, as determined by mapping out the NO movements in the solids (Figure 28).[577] In addition to MI, other heterocycles including 4-methylpiperidine (4-MePip)[575] and 4-(dimethylamino)-pyridine (Me_2NPy) were used as axial ligands to mimic His coordination in proteins.[571] Table 3 contains a list of structural data for 6C ferrous heme−nitrosyls in model complexes with different N-donor axial ligands and porphyrin scaffolds, as well as structural data obtained for proteins. Despite the broader range of structural parameters seen for proteins (see discussion above), the averaged data are in good agreement with the model complexes. Typical structural parameters for 6C ferrous heme−nitrosyls are 1.72−1.76 and 1.11−1.20 Å for the Fe−NO and N−O bond distances, respectively, and Fe−N−O angles of 135−145° (see Scheme 13). Notably, the crystal structures of the 6C model complexes show very long Fe−N bond distances to the N-donor ligands bound trans to NO, ranging from ~2.18 Å with MI as axial ligand all the way to ~2.45 Å with 4-MePip, indicating that the N-donor ligands are only weakly bound to the iron center, as seen in Figure 29.[571] This is a first illustration of the strong thermodynamic *trans* effect of NO (see below). The most straightforward method for interrogating the *trans* effect of NO is to measure the binding constants of N-donor ligands (MI, pyridine (Py), etc.) to 5C ferrous heme−nitrosyls.[565,665,666] For example, for [Fe(TPP)(NO)] the MI binding constant is only 26 M^{-1}(for Pyr it is 3 M^{-1}),[564] which is four orders of magnitude smaller than that for MI binding to [Fe(TPP)(MI)], where K_{eq} is 7.8×10^4 M^{-1}.[667] N-donor binding constants of 1−100 M^{-1}, corresponding to free binding energies ΔG° of only −1 to −2 kcal/mol, are typical for ferrous heme−nitrosyls and demonstrate that the *trans* effect of NO actually corresponds to a ground state property. Crystal structures further support this conclusion, where the Fe−N_{MI} bond length in [Fe(TPP)(MI)(NO)] is 2.17−2.19 Å,[24] compared to 2.01 Å in [Fe(TPP)$(MI)_2$].[668] Because of this weak binding, it is a challenge to construct a stable 6C Fe(II)−NO complex where the axial N-donor ligand remains bound in solution, without the need for a large excess of the ligand. The rigid benzyl-linker complex [Fe(T*o*-F_2PP-BzIM)(NO)] is able to form a stable 6C complex, as directly shown by EPR and solution IR spectroscopy and further supported by a crystal structure of the Zn^{2+}-bound analog (see Figure 30, left).[646] This same ligand platform was later used by Karlin and coworkers to investigate O_2 activation by ferrous heme model complexes.[669] They also obtained a crystal structure of a corresponding Fe^{II} complex with an isocyanide bound, as shown in Figure 30, right.

As the trans ligand to NO is only weakly bound, causing small structural variations in the FeNO units between the 5C and 6C complexes (see Scheme 13), the electronic structures of these species would be expected to be similar.[564] However, EPR and vibrational spectroscopy show distinct differences between the 5C and 6C complexes, indicating a difference in their electronic structure and possibly reactivity. Table 8 summarizes the EPR parameters of several 6C model complexes and protein species, and provides the necessary references. Typical g values of 6C ferrous heme−nitrosyls are 2.08, 2.00, 1.98 with ^{14}N hyperfine coupling constants of 30−40/60/30 MHz for the three A(^{14}N) tensor components, respectively (see Table 9 for examples and references).[130] Interestingly, in the 6C complexes it is the

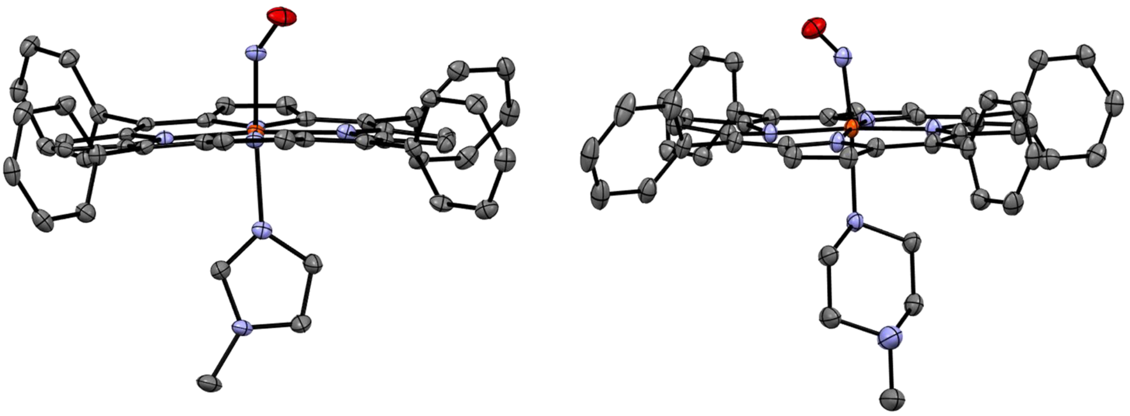

Figure 29. Crystal structures of the ls-{FeNO}^{7} complexes [Fe(TPP)(MI)(NO)] (left; MI = 1-methylimidazole) and [Fe(TPP)(4-MePip)(NO)] (right; 4-MePip = 4-methylpiperazine).[571] All H atoms are omitted for clarity.

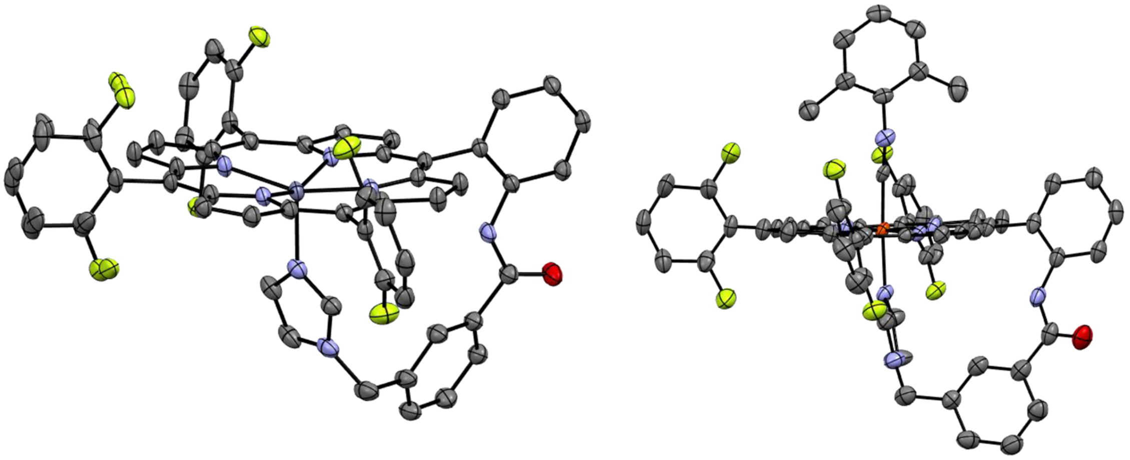

Figure 30. Crystal structures of [Zn(T*o*-F$_2$PP-BzIM)] (left)[646] and [Fe(T*o*-F$_2$PP-BzIM)(DIMPI)] (right; DIMPI = 2,6-dimethylphenylisocyanide).[670] All H atoms are omitted for clarity.

medium g value that shows the well-resolved hyperfine couplings, compared to g_{min} for the 5C compounds.

In the 6C case, a nine-line hyperfine pattern is observed for g_{mid} with typical N-donor ligands bound trans to NO, resulting from strong coupling of the unpaired electron with the ^{14}N nucleus of NO, and weaker coupling with the ^{14}N nucleus of the axially-bound heterocycle (Figure 31).[116,129,130] This difference between the 5C and 6C complexes can be explained by analyzing the single crystal EPR data of 6C Mb(II)−NO and Hb(II)−NO[672,673] in comparison to those of the 5C model complex [Fe(OEP)(NO)],[607] and further correlating these results with DFT calculations.[564] The DFT results show that in the 5C case, the principal axis of g_{min} is closest to the Fe−NO bond vector, while in the 6C case the g tensor is rotated, with the principal axis of the medium g-value, g_{mid}, now closest to the Fe−NO axis (see Figure 26).[564,572,642] As discussed above, it is the g value locked in in the direction of the Fe−NO vector that shows the well-resolved hyperfine couplings, whereas for the other directions, the g and A "strain" (= distribution of values) are increased, washing out the hyperfine couplings.[21] The larger strain for the g values with principal axes in the porphyrin plane (i.e., g_{max}, g_{min} for 6C and g_{max}, g_{mid} for 5C complexes) is believed to originate from the well-known "rotational" disorder of the NO ligand in ferrous heme−nitrosyls (see above). This rotation of the FeNO unit (relative to the heme) changes the directions of the principal axes of the g-values located in the porphyrin plane, which causes slight variations in the magnitudes of these g-values and associated A-values (the g and A "strain"), whereas the orientation of the axial g-value remains almost unchanged. Hyperfine splitting is broadened out, because the g and A strain for the in-plane g values are larger, due to the rotational disorder of NO.[21]

Comparison of the EPR parameters of the 5C and 6C complexes shows smaller g shifts for the latter, indicating a reduction of the spin density (unpaired electron density) on the iron center in the 6C case. At the same time, the ^{14}N hyperfine coupling tensor of NO becomes more anisotropic, with the axial component increasing significantly in the 6C case, which is in agreement with an increase of the spin density in the π^*_h orbital of the NO ligand. These findings are further supported by low-temperature magnetic circular dichroism (MCD)[676] results for 5C [Fe(TPP)(NO)] and 6C [Fe(TPP)(MI)(NO)], revealing a decrease of the spin density on the iron center in the 6C complex, which is marked by the appearance of strong diamagnetic MCD signals in the 6C case.[572] The decrease in spin density on the iron center reduces spin-orbit coupling matrix elements and leads to a decrease in EPR g shifts and paramagnetic MCD **C**-term intensity in the 6C complexes.[642] In summary, the experimental results show that upon binding of an N-donor ligand in trans position to NO, the spin density is pushed back from the iron to the NO ligand.

Table 8. Comparison of Experimental and Calculated g Values and g Tensor Orientations for Select 6C ls-{FeNO}^{7} [Fe(Porph)(L)(NO)]$^{n-}$ (L = Proximal Ligand; n = 0,1) Complexes

complex/protein[a]	g values			orientation[b]	conditions (solvent, etc.)	ref
	g (max)	g (mid)	g (min)			
[Fe(TPP)(MI)(NO)]	2.079	2.004*	1.972		$CHCl_3$	128
	2.074	2.005*	1.978		toluene	638
[Fe(TPP)(Pip)(NO)]	2.08	2.003*	<2.00		toluene	606
[Fe(T*o*-F$_2$PP-BzIM)(NO)]	2.077	2.009*	1.978		DMSO	646
[Fe(PPIXDME)(MI)(NO)]	2.074	2.004*	1.971		$CHCl_3$	122
[Fe(TPP)(Me$_2$NPy)(NO)]	2.069	2.002*	1.973		CH_2Cl_2	571
[Fe(TPP)(4-MePip)(NO)]	2.085	2.003*	1.978		CH_2Cl_2/4-MePip	571
[Fe(T*p*-NMe$_2$PP)(MI)(NO)]	2.073	2.004*	1.968		toluene	635
[Fe(T*p*-OCH$_3$PP)(MI)(NO)]	2.072	2.004*	1.968		toluene	635
[Fe(T*p*-FPP)(MI)(NO)]	2.072	2.004*	1.966		toluene	635
[Fe(T*per*-F$_5$PP)(MI)(NO)]	2.067	2.003*	1.964		toluene	635
[Fe(T*p*-NMe$_2$PP)(Py)(NO)]	2.079	2.005*	1.977		toluene	635
[Fe(T*p*-OCH$_3$PP)(Py)(NO)]	2.078	2.004*	1.978		toluene	635
[Fe(T*p*-FPP)(Py)(NO)]	2.079	2.004*	1.975		toluene	635
[Fe(T*per*-F$_5$PP)(Py)(NO)]	2.075	2.004*	1.971		toluene	635
[Fe(TPP)(SPh)(NO)]$^-$	2.108	2.068	2.013*		$CHCl_3$	638
[Fe(SPorph)(NO)]$^{-}$[c]	2.07	2.00*	<2.00		toluene	671
[Fe(TPP)(H$_4$Tp)(NO)]	2.104	2.054	2.010*		toluene	671
[Fe(TPP)(SPh^{Ome})(NO)]$^-$	2.108	2.067	2.012*		toluene	123
[Fe(TPP)(SPh^F)(NO)]$^-$	2.109	2.067	2.013*		toluene	123
[Fe(PPDME)(H$_4$Tp)(NO)]	2.094	2.049	2.010*		acetone	123
Mb(II)−NO	**2.076**	**2.002***	**1.979**	**g (mid)/heme⊥: 30°**	**single crystal**	672
α-Hb(II)−NO	**2.060**	**2.000***	**1.965**	**g (mid)/heme⊥: 10°**	**single crystal**	673
β-Hb(II)−NO	**2.082**	**2.000***	**1.978**	**g (mid)/heme⊥: 8°**	**single crystal**	673
C*c*O(II)−NO	2.085	2.004*	1.955		buffer	116
Cyt c(II)−NO	2.070	2.003*	2.01		buffer	114, 115
Cyt c peroxidase(II)−NO	2.080	2.004*	1.960		buffer	116
Lactoperoxidase(II)−NO	2.070	2.004*	1.958		buffer	116
HRP(II)−NO	2.080	2.004*	1.955		buffer	116
Catalase(II)−NO	2.050	2.004*	1.97		buffer	116
P450nor(II)−NO	2.082	2.007*	1.970		buffer	674
P450cam(II)−NO	2.073	2.009*	1.976		buffer	119
CPO(II)−NO	2.082	2.004*	1.975		buffer	675
[Fe(P)(MI)(NO)][d]	2.024	1.991(*)	1.955	g (mid)/Fe−NO: 29°	from DFT calculations	572
[Fe(P)(MI)(NO)][e]	2.034	1.995(*)	1.955	g (mid)/Fe−NO: 32°	from DFT calculations	642
[Fe(P)(SMe)(NO)]$^{-}$[f]	2.019	1.994	1.974(*)	g (min)/Fe−NO: 26°	from DFT calculations	638
[Fe(P)(SPh)(NO)]$^{-}$[f]	2.026	1.998	1.972(*)	g (min)/Fe−NO: 36°	from DFT calculations	638

[a] SPorph = *meso-a,a,a,a*-[*o*-[[o-[(acetylthio)methyl]phenoxy]acetamido]phenyl] tris(o-pivalamidophenyl)porphyrin^{2-}; * = shows ^{14}N hyperfine lines of the coordinated NO ligand; (*) = principal axis in the calculations closest to the Fe−NO bond; H$_4$Tp = tetrahydrothiophene. [b] Relative orientation of the principal axis of the given g value with respect to the Fe−N(O) bond or the heme normal (heme⊥). [c] Model complex with axial benzylthiolate coordination. [d] Calculated with B3LYP and the following basis sets: Fe: CP(PPP); N (EPR-II); C, O: TZVP; H: TZV. [e] Calculated with VWN/triple-ζ basis set of Slater-type functions. [f] Calculated with BP86/TZVP.

Mössbauer spectroscopy has also been used to characterize 5C and 6C ferrous heme−nitrosyls. Analysis of the magnetic Mössbauer data of representative complexes supports the proposed rotation of the g tensor in 5C versus 6C ferrous heme−nitrosyls.[571] It was also found that related 5C and 6C complexes have almost identical isomer shifts, δ [mm/s].[571] For example, δ values of ∼0.34 and ∼0.37 mm/s, respectively, have been reported for [Fe(TPP)(MI)(NO)] and [Fe(TPP)(4-MePip)(NO)] (measured at 4.2 K), and for [Fe(TPP)(NO)], δ = 0.33−0.35 mm/s has been determined, again at 4.2 K.[571] DFT calculations are able to reproduce the experimentally observed isomer shifts.[677] The almost identical isomer shifts in the 5C and 6C complexes can be attributed to a reduction in σ-donation from NO to the iron center in the 6C complexes, which is then compensated by increased electron donation from the porphyrin ligand, as the iron center moves into the plane of the porphyrin ring in the 6C complexes. The quadrupole splitting, ΔE_q [mm/s], reflects this change in the balance of in-plane versus out-of-plane electron donation to Fe^{II}. For example, ΔE_q values of 0.73 and ∼0.90 mm/s have been obtained for [Fe(TPP)(MI)(NO)] and [Fe(TPP)(4-MePip)(NO)] at 4.2 K, respectively, which are smaller than ΔE_q = ∼1.25 mm/s reported for the 5C complex [Fe(TPP)(NO)] (also measured at 4.2 K).[571] In this regard, note that DFT methods have been developed to accurately predict quadrupole splitting values for 5C ferrous heme−nitrosyls.[678,657]

Vibrational spectroscopy provides further key insight into the change in Fe−NO bonding between the 5C and 6C ferrous heme−nitrosyls. In the latter complexes, the N−O stretching frequency is typically observed (by IR spectroscopy) in the

Table 9. Comparison of Experimental and Calculated ^{14}N Hyperfine (A) Tensors of the Nitrosyl Nitrogen in Select 6C ls-$\{FeNO\}^7$ $[Fe^{II}(Porph)(L)(NO)]^{n-}$ (L = Proximal Ligand; n = 0,1) Complexes[a]

	^{14}N Hyperfine A [g] [MHz][c]					
complex/protein[b]	A [g(max)]	A [g(mid)]	A [g(min)]	orientation[d]	conditions (solvent, etc.)	ref
$[Fe(To\text{-}F_2PP\text{-}BzIM)(NO)]$	37	62	39	g/A: collinear	DMSO	646
[Fe(TPP)(Pip)(NO)]		60.8			toluene	606
[Fe(PPIXDME)(MI)(NO)]		60.3			$CHCl_3$	122
[Fe(PPIXDME)(Py)(NO)]		60.0			acetone	122
$[Fe(Tp\text{-}NMe_2PP)(MI)(NO)]$		62.0			toluene	635
$[Fe(Tp\text{-}OCH_3PP)(MI)(NO)]$		62.0			toluene	635
[Fe(T*p*-FPP)(MI)(NO)]		63.4			toluene	635
$[Fe(Tper\text{-}F_5PP)(MI)(NO)]$		63.9			toluene	635
$[Fe(Tp\text{-}NMe_2PP)(Py)(NO)]$		61.7			toluene	635
$[Fe(Tp\text{-}OCH_3PP)(Py)(NO)]$		61.4			toluene	635
[Fe(T*p*-FPP)(Py)(NO)]		62.0			toluene	635
$[Fe(Tper\text{-}F_5PP)(Py)(NO)]$		62.0			toluene	635
$[Fe(PPIXDME)(H_4Tp)(NO)]$		43.0	55.1		acetone	123
α-Hb(II)−NO		**29.6/32.9/63.6**[e]		**g (mid)/A (max): 37°**	**single crystal**	673
β-Hb(II)−NO	**44.2**	**62.3**	**26.9**	**g (mid)/A (max): 43°**	**single crystal**	673
CcO(II)−NO		61.7			buffer	116
Cyt c		66.4			buffer	114, 115
Cyt c Peroxidase(II)−NO		58.9			buffer	116
Lactoperoxidase(II)−NO		44.9			buffer	116
HRP(II)−NO		57.5			buffer	116
Catalase(II)−NO		58.9			buffer	116
P450nor(II)−NO		56.2			buffer	674
P450cam(II)−NO		54.0			buffer	119
CPO(II)−NO		56.0			buffer	675
[Fe(P)(MI)(NO)][f]	15.2	84.0	13.2	g (mid)/A (max): 30°	from DFT calculations	564
[Fe(P)(MI)(NO)][g]		29.0/31.5/73.9		not provided	from DFT calculations	657

[a] Values of the A tensor [MHz] are given relative to the *g* tensor, that is, a given A value is paired with the g value whose principal axis is closest to the principal axis of this A tensor component. [b] H_4Tp = tetrahydrothiophene. [c] For the solution data, the A values in MHz have been calculated with the formula: $A[MHz] = 1.39916 \cdot A_i[G] \cdot g_i$. Strictly speaking, this formula is only valid if the g and A tensors are aligned. Hence, these values have to be treated with some caution. [d] Angle between the principal axes of g and A tensor components as indicated. [e] Since the A and g tensors show large differences in their relative orientation, no classification of A with respect to g is useful. [f] Calculated with B3LYP and the following basis sets: Fe: CP(PPP); N (EPR-II); C, O: TZVP; H: TZV. [g] Calculated with BPW91 and the following basis sets: Fe: large Wachter's basis; C, O, N: 6-311G*; H: 6-31G*. In the model system, an Fe−N(NO) bond length of 1.74 Å and an Fe−N−O angle of 145° were used.

1610−1630 cm^{-1} range, distinctively lower compared to the 5C analogs. On the other hand, there has been a long standing debate about the energies of the Fe−NO stretch, ν(Fe−NO), and the in-plane Fe−N−O bend, δ_{ip}(Fe−N−O), in the 6C complexes.[583,585,679−682] This is due to the fact that rRaman spectroscopy, which has historically been used to investigate the vibrational properties of metalloporphyrins, only shows one FeNO-based vibration in the low-energy region (in the 545−570 cm^{-1} range), which was therefore automatically assumed to be the Fe−NO stretch.[679,681,683] Later, detailed single-crystal NRVS investigations showed that this is incorrect (see Figure 32), and that this feature corresponds to the Fe−N−O bending mode,[583] as originally assigned by Benko and Yu.[680] The Fe−NO stretch is located at lower energy, in the ~440 cm^{-1} range, in 6C ferrous heme−nitrosyls.[564,572,573,651] In particular, by utilizing the QCC-NCA method to analyze the IR, rRaman, and single-crystal NRVS data of [Fe(TPP)(MI)(NO)] and of the corresponding $^{15}N^{18}O$ isotope-labeled species, it was shown that the out-of-plane polarized band at 437 cm^{-1} (red spectrum in Figure 32) is the ν(Fe−NO) stretch and that δ_{ip}(Fe−N−O) corresponds to a feature at 563 cm^{-1} with mixed polarization (blue spectrum in Figure 32).[651] It was noted that the δ_{ip}(Fe−N−O) feature at 563 cm^{-1} is strongly mixed with porphyrin-based vibrations and the Fe−NO stretch, causing the observed, mixed polarization of this feature,[573] and that the degree of mixing is further influenced by porphyrin ring substitution.[684,685] In the case of wt Mb(II)−NO, the Fe−NO stretch is located at 443 cm^{-1},[583] whereas the rRaman-active δ_{ip}(Fe−N−O) bending mode is observed in the 545−565 cm^{-1} range for Mb and corresponding, active site mutants.[585,682] Inspection of previously published rRaman data also shows that the ~440 cm^{-1} feature is in fact observed in some cases, confirming that this feature is associated with the Fe(II)−NO unit.[585] Force constants for [Fe(TPP)(MI)(NO)] were further obtained from the QCC-NCA simulations, delivering values of 11.55 mdyn/Å for the N−O and 2.57 mdyn/Å for the Fe−NO bond.[651] This is an important result, as it demonstrates that in the presence of an axial N-donor ligand, the Fe−NO bond is distinctively weaker, illustrated by the drop in the Fe−NO stretch and the associated Fe−NO force constant, compared to the 5C analogs. In addition, these result show that there is a direct correlation of the Fe−NO and N−O bonds strengths, that is, upon coordination of an axial N-donor ligand in trans position to NO, both the Fe−NO and N−O bonds become weaker, as illustrated in Table 7. This direct correlation shows that it is predominantly the Fe−NO σ-bond that is weakened in the 6C complexes, as a change in the strength of the π-backbond would manifest itself in an inverse correlation of the Fe−NO and N−

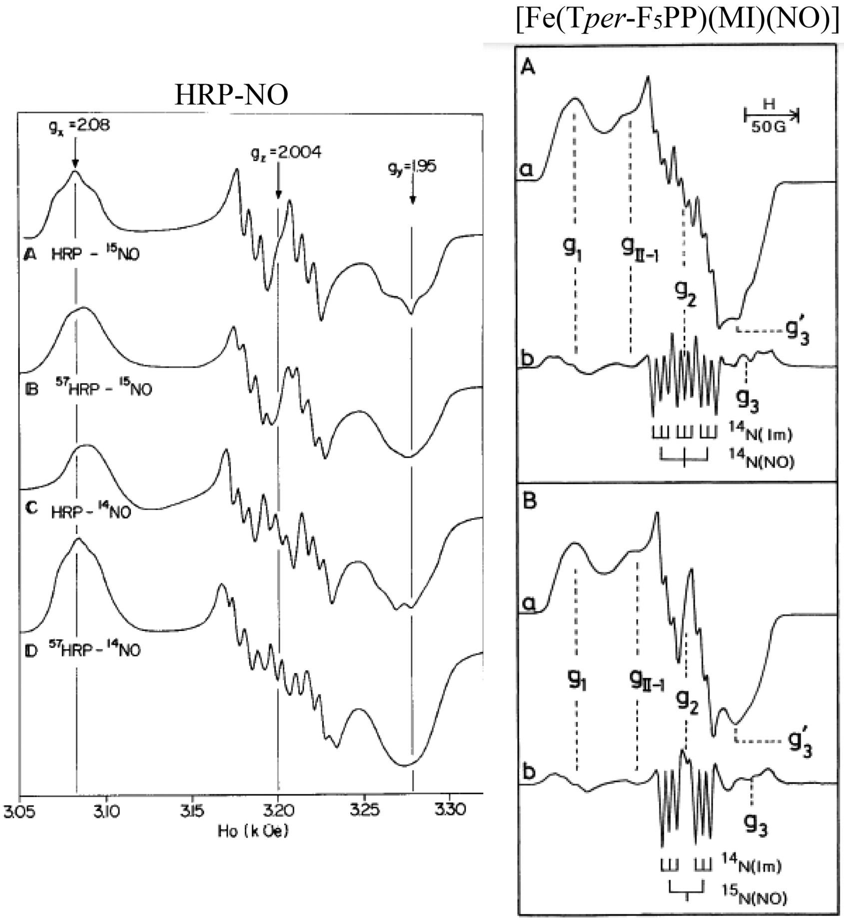

Figure 31. EPR spectra of the 6C ferrous heme−nitrosyl complex of horseradish peroxidase (HRP) with different isotopes (left).[98] EPR spectra of [Fe(T*per*-F$_5$PP)(MI)(NO)] with different isotopes (right; A: ^{14}NO, B: ^{15}NO), displayed as (a) the first derivative and (b) the second derivative.[635] Reprinted with permission from refs 98 and 635. Copyright 1969 and 1991 American Chemical Society and The Chemical Society of Japan, respectively.

O bond strengths (see above). This aspect is further analyzed below.

It should be noted here that there is an apparent disagreement between the NRVS and rRaman data for the complex [Fe(TPP)(MI)(NO)], which is puzzling, considering that for the 5C analog [Fe(TPP)(NO)] and the analogous 6C ferrous heme-carbonyl complex the rRaman and NRVS data are consistent.[573,583,651,662,663,686,687] Spiro and coworkers conducted rRaman studies on a number of [Fe(TPP*)(MI)(NO)] complexes, and in each case, identified one isotope-sensitive band in the 577−587 cm^{-1} range.[688] This feature, observed at 582 cm^{-1} for [Fe(TPP)(MI)(NO)], was then assigned to ν(Fe−NO), and no features around 560 or 440 cm^{-1} were observed. This is surprising, since this is in disagreement with the NRVS data for this complex, but also rRaman data for Mb(II)−NO and corresponding, active site variants, which show isotope-sensitive rRaman features (now assigned to δ_{ip}(Fe−N−O); see above) in the 545−565 cm^{-1} range, consistent with the NRVS data for [Fe(TPP)(MI)(NO)]. One caveat with the rRaman study is that the ls-{FeNO}^{7} complexes were all prepared by reaction of the corresponding ferric precursors with NO gas in EPR tubes,[688] which is problematic in terms of producing pure compounds. As discussed in Section 2.3, the reported rRaman feature for [Fe(TPP)(MI)(NO)] at 582 cm^{-1} is in close agreement with NRVS data for the corresponding ferric heme−nitrosyl, or ls-{FeNO}^{6} complex [Fe(TPP)(MI)(NO)]$^+$, where the Fe−NO stretch is observed in the 580−590 cm^{-1} region (see Table 7).[654,655]

In summary, the distinct differences observed in the spectroscopic properties of 5C and 6C ferrous heme−nitrosyls relate to important differences in the electronic structures of these species. The addition of a N-donor ligand trans to NO causes a decrease in spin density on the Fe center, pushing spin density back onto the NO ligand, as shown by EPR and MCD spectroscopy,[130,572,606] and confirmed by DFT calculations.[564,642] Simultaneously, both the N−O and the Fe−NO bonds are weakened, as seen by shifts in the ν(N−O) and ν(Fe−NO) stretching frequencies from 1670−1700 and 520−540 cm^{-1} in the 5C to 1610−1630 and ∼440 cm^{-1} in the 6C complexes, respectively. The weakening of the Fe−NO bond in the 6C species is also reflected in the NO binding constants (see Table 4).[565] The direct correlation of the N−O and Fe−NO bond strengths indicates a weakening of the Fe−NO σ-bond upon coordination of the N-donor ligand.[564,572,646,651]

2.2.6.3. Thermodynamic σ-trans Effect of NO. The trademark of the basal activation of sGC upon NO binding is the breaking of the Fe(II)−N$_{His}$ bond, as described above, which can be explained by a *trans* effect of NO, as proposed by Traylor and Sharma in 1992.[689] On the basis of the detailed spectroscopic studies on 5C and 6C ferrous heme−nitrosyls described above, the exact electronic origin of this thermody-

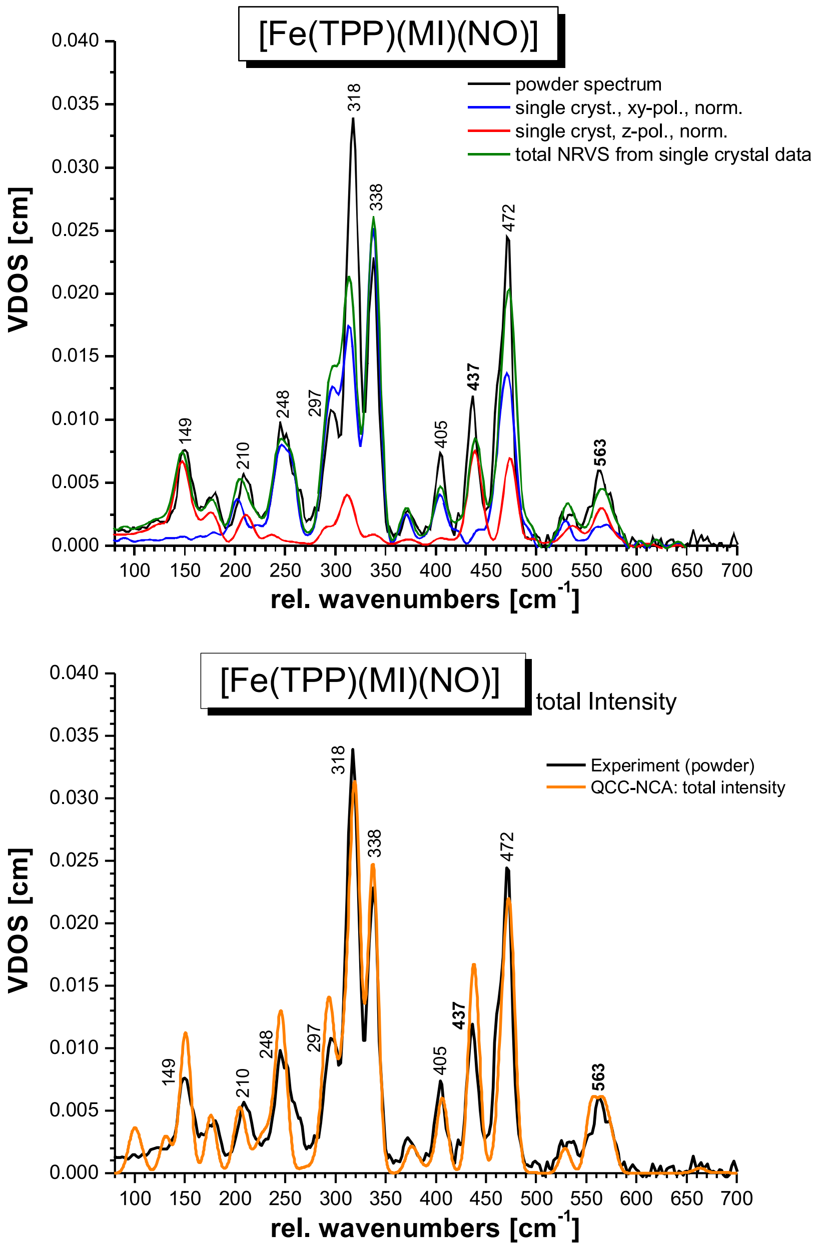

Figure 32. Top: NRVS VDOS spectra of [^{57}Fe(TPP)(MI)(NO)]. Black: powder spectrum; blue and red: normalized single crystal in-plane (blue) and out-of-plane (red) polarized spectra; green: predicted powder spectrum calculated by adding the in-plane and out-of-plane polarized contributions (total NRVS = 1/3 ip + 2/3 oop intensity). Bottom: experimental powder data (black) and total NRVS VDOS intensity from a simulation using the QCC-NCA approach (orange). Reprinted with permission from ref 651. Copyright 2010 American Chemical Society.

namic *trans* effect (more precisely a *trans* interaction, since it is a ground state or thermodynamic effect) can be defined. The analysis of the vibrational data shows that the coordination of an N-donor ligand trans to NO leads to a weakening the Fe−NO σ-bond. This originates from two effects: (a) there is a loss of covalency in the orbital interaction between π^*_h and d_{z^2}, and (b) a mixing of d_{xz} character into d_{z^2} (in the coordinate system used in Scheme 14) causes a rotation of the d_{z^2} orbital off the Fe−N(O) axis, which contributes to (a). The best way to rationalize the *trans* interaction between NO and the axial N-donor ligand is to look at this as a 'competition' between the σ-donor orbitals of NO (π^*_h) and of the N-donor ligand for the d_{z^2} orbital of iron. Since π^*_h is the stronger donor orbital (leading to a stronger bond), it ends up making a bonding combination with d_{z^2}, whereas the interaction between d_{z^2} and the N-donor ligand in the SOMO is actually antibonding (as illustrated in Figure 26). This competition represents the underlying electronic-structural reason for the thermodynamic σ-*trans* effect of NO. The decrease in σ-donation from the π^*_h orbital of NO into d_{z^2} is responsible for the observed weakening of the Fe−NO bond in the 6C complexes, which is evident from their lower Fe−NO stretching frequencies and smaller Fe−NO force constants (2.5−2.6 mdyn/Å).[651] The increased electron density in the π^*_h orbital in the 6C complexes that originates from the reduced σ-donation is ultimately responsible for the simultaneous weakening of the N−O bond, again evident from the vibrational properties (lower N−O stretching frequencies) of these complexes. This change in Fe−NO bonding goes along with a shift in the unpaired electron distribution in the 6C complexes, where spin populations increase to about 80% on

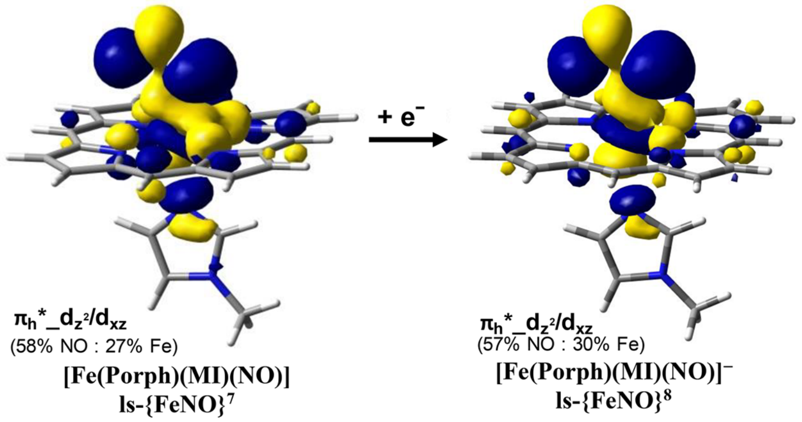

Figure 33. Key π^*_{h}_d_{z^2}/d_{xz} molecular orbitals of [Fe(Porph)(MI)(NO)] and [Fe(Porph)(MI)(NO)]$^-$. Calculated with B3LYP/TZVP on BP86/TZVP optimized structures. Reprinted with permission from ref 569. Copyright 2013 American Chemical Society.

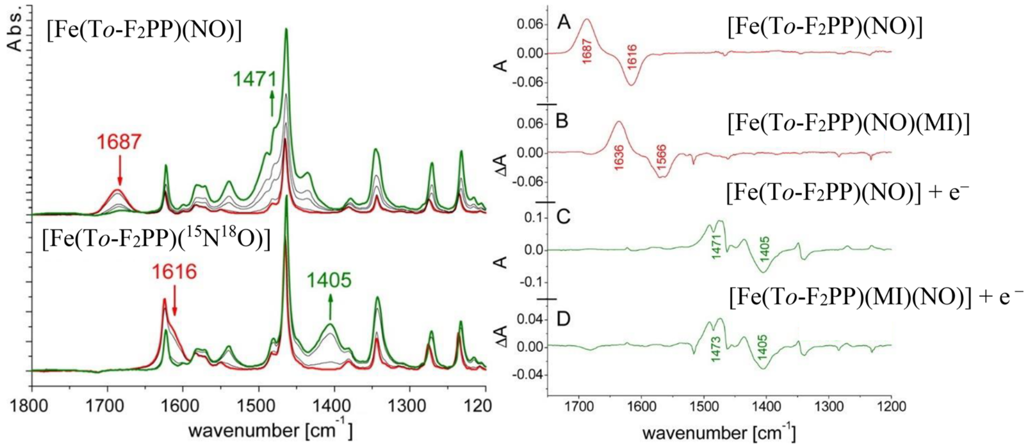

Figure 34. Left: IR spectra for the spectroelectrochemical reduction of [Fe(T*o*-F_2PP)(NO)] and [Fe(T*o*-F_2PP)($^{15}N^{18}O$)]. Right: Difference of NO−$^{15}N^{18}O$ IR spectra for the spectroelectrochemical reduction of [Fe(T*o*-F_2PP)(NO)] (A: ls-$\{FeNO\}^7$; C: ls-$\{FeNO\}^8$) and with MI added (B: ls-$\{FeNO\}^7$, 6C; D: ls-$\{FeNO\}^8$, 5C). Reprinted with permission from ref 569. Copyright 2013 American Chemical Society.

NO and decrease to about 20% on iron (see Figure 26), which directly reflects the reduced covalency of the Fe−NO σ-bond (and hence, the reduced donation of the unpaired electron of NO to Fe^{II}). Results from MCD and EPR spectroscopy directly support this shift in spin density distribution.[572,642] Accordingly, 6C ferrous heme−nitrosyls constitute the paradigm example for the ls-Fe(II)−$NO^{\bullet}$ electronic structure type.

The weakening of the Fe−NO and N−O bonds in the 6C complexes directly relates to the strength of the Fe(II)−(N-donor) bond, so the stronger the N-donor ligand binds, the more pronounced the decrease in Fe−NO and N−O bond strengths.[564,646] The N−O stretch can therefore act as a gauge for the strength of the Fe(II)-(N-donor) bond.[575] For example, in the case of 5C [Fe(TPP)(NO)], the N−O stretching frequency is observed at 1697 cm^{-1}, and upon binding of the weak N-donor ligand 4-dimethylaminopyridine (Me_2NPy), the N−O stretch drops to 1653 cm^{-1}.[571] If a stronger N-donor ligand is used, like in the imidazole-tethered complex [Fe(T*o*-F_2PP-BzIM)(NO)], ν(N−O) is observed at 1644 cm^{-1}.[646] With free MI, like in the complex [Fe(TPP)(MI)(NO)], ν(N−O) decreases all the way to 1630 cm^{-1}. Another indirect way to measure the covalency of the Fe(II)−(N-donor) interaction is the magnitude of the ^{14}N hyperfine coupling constant of the proximal N-donor ligand, available from EPR data.[646] Weak bonding results in a small ^{14}N hyperfine coupling constant, while a stronger, more covalent bond yields a larger ^{14}N hyperfine coupling constant and a cleaner resolution of the hyperfine lines in the EPR spectra.[564,646]

These results again illustrate the nature of a thermodynamic *trans* effect (or *trans* interaction), where the two trans bonds, here Fe−NO and Fe−His/(N-donor ligand), influence each other. As described above, the binding of NO greatly weakens the Fe−His bond in sGC, leading to His dissociation and activation of sGC.

2.2.6.4. Comparison to ls-{FeNO}8 Complexes.

The strongly σ-bonding property of the SOMO of ferrous heme−nitrosyls can further be verified by investigating the corresponding, one-electron reduced ls-$\{FeNO\}^8$ complexes.[569] DFT calculations predict that upon one-electron reduction of ferrous heme−nitrosyls, the SOMO of the complexes simply becomes doubly occupied, without changing the composition of this orbital. This is illustrated in Figure 33, which shows an essentially identical SOMO/HOMO for [Fe(Porph)(NO)] and [Fe(Porph)(NO)]$^-$. This is further confirmed experimentally: as shown in Figure 35, there is a strong correlation between the N−O stretching frequencies of 5C ls-$\{FeNO\}^7$/ls-$\{FeNO\}^8$ pairs of complexes, indicating a conservation of the nature of the SOMO/HOMO in each one of the complexes after reduction.[569] In other words, differences between the SOMOs of 5C ls-$\{FeNO\}^7$ complexes (due to the different porphyrin substituents, etc.) are exactly conserved in the HOMOs of the reduced ls-$\{FeNO\}^8$ complexes. Because of this, double occupation of the SOMO in the reduced complexes should (a) strengthen the Fe−NO bond and (b) further increase the σ-*trans* effect. These predictions can be tested experimentally. In the ls-$\{FeNO\}^8$ complexes, the binding constant of MI trans to NO decreases by several orders of magnitude, directly confirming that the SOMO is responsible for the thermodynamic σ-*trans* effect of NO.[569] This is evident from Figure 34, which shows that the 6C complex [Fe(T*o*-F_2PP)(MI)(NO)] becomes 5C upon one-electron reduction.[569] Hence, the nitroxyl ($^1NO^-$) ligand has in fact a stronger σ-*trans* effect than NO in ferrous heme complexes. Second, rRaman studies by Ryan and coworkers show that the Fe−NO stretching frequency increases from 525 cm^{-1} in [Fe(TPP)(NO)] (in THF) to 549 cm^{-1} in the reduced ls-$\{FeNO\}^8$ complex (despite the fact that reduction increases the Coulomb repulsion between the now doubly occupied π^*_h orbital of NO and d_{xz} of iron, which counteracts this effect),[690] directly demonstrating that the SOMO is Fe−NO bonding in nature. In this way, studies on the reduced iron(II)−nitroxyl model complexes confirm the previous findings about the properties of the SOMOs of ferrous heme−nitrosyls. These results could only be obtained with model complexes, as ls-$\{FeNO\}^8$ complexes are protonated in an aqueous environment (see Section 4.2).[569,691,692] In the presence of acid, ls-$\{FeNO\}^8$ complexes become protonated to the corresponding HNO complexes, which subsequently decompose via release of H_2:[690]

$$2[\mathrm{Fe(Porph)(NHO)}] \rightarrow 2[\mathrm{Fe(Porph)(NO)}] + \mathrm{H_2} \qquad (12)$$

On the basis of these experimental results and DFT calculations, heme ls-$\{FeNO\}^8$ complexes are 5C species with low-spin ground states (S_t = 0), and Fe(II)−NO^- type electronic structures, where a singlet $^1NO^-$ ligand is bound to a ls-Fe^{II}.[569] Here, the electron pair in the π^*_h orbital of the $^1NO^-$ ligand is donated into the empty d_{z^2} orbital of Fe^{II}, as discussed above and shown in Figure 35, leading to a very covalent Fe(II)−NO^- bond. From a charge distribution point of view, the electronic structure can be considered intermediate between Fe(II)−NO^- and Fe(I)−NO (neutral NO, but not $NO^\bullet$, as no spin is generated on the NO ligand; see discussion for ls-$\{FeNO\}^6$ electronic structure in Section 2.3),[70,310] as the σ-bond between π^*_h and d_{z^2} approaches the point of maximum covalency. Part of the negative charge is further stabilized by the porphyrin π system, due to enhanced π-backbonding between the Fe^{II} and the porphyrin $e_g(\pi^*)$ orbitals. Overall similar electronic structures have also been observed for ls-$\{FeNO\}^8$ complexes with non-porphyrin ligands.[68,693,694]

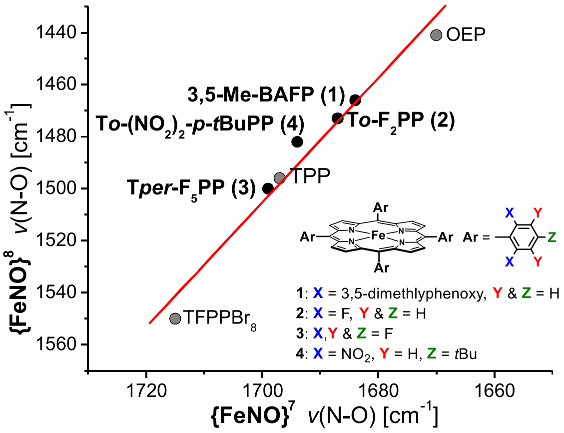

Figure 35. Comparison of N−O stretching frequencies in pairs of 5C ls-$\{FeNO\}^7$ and ls-$\{FeNO\}^8$ complexes with the indicated porphyrin ligands. Reprinted with permission from ref 569. Copyright 2013 American Chemical Society.

So far, only two ls-$\{FeNO\}^8$ porphyrin complexes were structurally characterized. Ryan and coworkers prepared $[Fe(OEP)(NO)]^-$ via reduction of the ls-$\{FeNO\}^7$ precursor, [Fe(OEP)(NO)], with anthracenide.[695] The resulting ls-$\{FeNO\}^8$ complex was crystallized in the form of the potassium (2.2.2) cryptand salt (4,7,13,16,21,24-hexaoxa-1,10-diazabicyclo[8.8.8]-hexacosane) and structurally characterized. Figure 36 shows a representation of the crystal structure. In this complex, the Fe−N−O angle of 127° reflects a severely bent FeNO unit. The Fe−NO and N−O bond distances are 1.731 and 1.168 Å, respectively. Notably, in the ls-$\{FeNO\}^8$ complex, the NO^- ligand strongly interacts with the K^+ cryptand complex, evident from a K-O distance of 3.125 Å. The K−O−N angle is 99°.[695] The second, structurally charcaterized ls-$\{FeNO\}^8$ porphyrin complex was originally reported by Doctorovich and coworkers. This complex, $[Fe(TFPPBr_8)(NO)]^-$, features the extremely electron-poor $TFPPBr_8{}^{2-}$ ligand.[696] Application of this ligand leads to an electron-poor FeNO unit, which is reflected by the unusually high N−O stretching frequency of ~1550 cm^{-1} of this complex. A structural characterization of this complex was successfully conducted later, showing a strongly saddled heme, an Fe−NO bond length of 1.814 Å, and a strongly bent FeNO unit (Fe−N−O angle: 122.4°). The structural features of $[Fe(TFPPBr_8)(NO)]^-$ are therefore consistent with those of $[Fe(OEP)(NO)]^-$.[697] The Doctorovich group also prepared the water-soluble ls-$\{FeNO\}^7$ complex $[Fe(TPPS)(NO)]^{4-}$ ($TPPS^{6-}$ = meso-tetra(4-sulfonatophenyl)porphyrin hexaanion), which was fully characterized using different spectroscopic methods, CV and DFT calculations. This complex shows an N−O stretching frequency of 1668 cm^{-1},[698] which is somewhat on the lower end compared to typical ls-$\{FeNO\}^7$ species. The complex $[Fe(TPPS)(NO)]^{4-}$ was subsequently used to obtain the ls-$\{FeNO\}^8$ adducts $[Fe(TPPS)(HNO)]^{4-}$ and $[Fe(TPPS)(NO)]^{5-}$ in water. Surprisingly, the typically observed, fast disproportionation of the HNO ligand in ferrous heme−NHO complexes is suppressed under these conditions, likely due to the presence of strong hydrogen bonds from

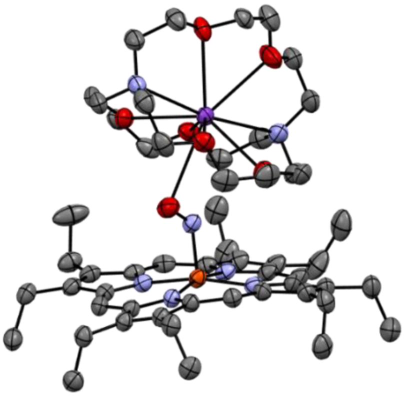

Figure 36. Crystal structure of the ls-$\{FeNO\}^8$ complex [K(2.2.2 crypt)][Fe(OEP)(NO)], where the NO^- ligand is stabilized by interaction with K^+.[695] All H atoms are omitted for clarity.

surrounding water molecules. Correspondingly, the half life of $[Fe(TPPS)(HNO)]^{4-}$ is about 40 s, which allowed the authors to measure the pK_a of the bound HNO ligand, giving a pK_a value of 9.7.[698]

2.2.7. Interaction of sGC with Other Small Molecules. Since mammalian sGC is activated by NO, scientists also explored whether other small molecules could induce sGC activation, and to what extent. As discussed above, O_2 does not bind to sGC. CO does not significantly activate the enzyme,[174,505,506,524] which is in agreement with the fact that CO does not have a thermodynamic *σ-trans* effect like NO. Here, CO binds readily to the ferrous heme in sGC, but does not induce cGMP production due to the stability of the 6C complex,[506] with the proximal His firmly bound to the heme. The same is expected for HNO. This was further elucidated using DFT calculations.[699] For this purpose, the binding constants of MI to the 5C complexes $[Fe(P)(X)]$ (P = porphine^{2-}), where X = NO, CO, HNO, and MI were determined using DFT calculations. First, the known binding constants for X = NO, MI of 26 and 7.8×10^4 M^{-1}, respectively, were used to benchmark different DFT methods, as shown in Figure 37. Weak metal-ligand binding constants are difficult to calculate with DFT methods, but accurate predictions were achieved by including van der Waals interactions. With the best methods identified in this way, calculated MI binding constants of 110 M^{-1} (X = NO) and 5.6×10^5 M^{-1} (X = MI) were obtained, which is reasonably close to the experimentally determined values. When X = HNO and CO, the MI binding constants are consistently predicted to be equal, about 6 orders of magnitude larger than the binding constant for X = NO. This clearly indicates that the thermodynamic *σ-trans* effect induced by HNO is much weaker than that of NO, and that it is in fact comparable to that of CO. This suggests that HNO forms a stable 6C complex with sGC, as observed for CO. This is corroborated by the $Fe-N_{MI}$ bond distances in both model complexes and DFT calculated structures.[699] Related to these predictions, it was found experimentally that NO^- and NO^+ donor salts could not activate sGC.[700,701]

Interestingly, there are some classes of sGC and *H-NOX* proteins (as described above for the case of O_2 sensing) that can be activated by other small molecules beside NO. For example, Cyg11, found in the algae *Chlamydomonas reinhardtii*, is the first sGC with a higher maximum velocity of forming cGMP when CO is bound versus NO.[702] Further investigations on this protein are necessary to elucidate how it is activated by CO.

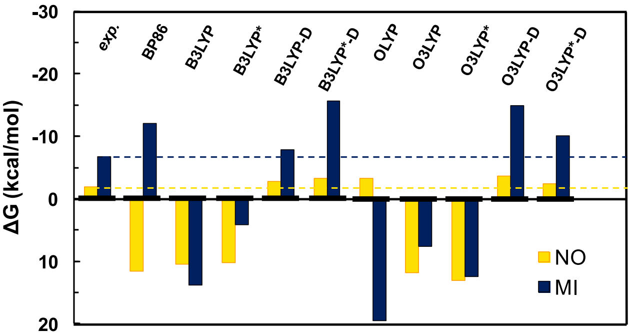

Figure 37. Experimental and DFT-calculated free energies (kcal/mol) for the reaction $[Fe(P)(X)] + MI \rightleftarrows [Fe(P)(MI)(X)]$, where X = NO and MI at 298.15 K. Calculations were performed on BP86/TZVP-optimized structures. Reprinted with permission from ref 73. Copyright 2017 Elsevier Inc.

2.2.8. Outlook. There are many open questions that still remain about sGCs, including the signal transduction mechanism, the number of NO molecules needed for full activation of the enzyme and their binding sites, the conformational states of sGC, and the regulation of sGC activity by ATP and other nucleotides. In addition, post-translational modifications may also play a role in sGC function. Ongoing research is aimed at answering these important questions. Furthermore, sGCs are wide-spread in Nature, and outside of mammalian sGCs, there is still much to be discovered about these interesting proteins.

H-NOX proteins have also been shown to affect bacterial biofilm formation by regulating intracellular cyclic di-GMP concentrations and quorum sensing. A newly discovered family of bacterial NO sensors, called NosP (nitric oxide sensing protein) also regulate biofilm formation.[191] More research in this area is required to fully elucidate the role of NO in bacterial communication, with the potential of finding new therapeutic approaches that target bacterial biofilms.

2.3. Nitric Oxide Transport by Nitrophorins

2.3.1. Nitrophorins from *Rhodnius proxilus* (rNPs). Nitrophorins (NPs) are small heme proteins that function as NO transporters in certain blood sucking insects. In the early 1990's, the first class of NPs was discovered in the salivary glands of the kissing bug (the triatomid bug), *Rhodnius proxilus* (therefore abbreviated rNP).[246,703] The salivary glands of these insects contain NO synthases (see Section 2.1),[704] which produce NO and release it into the saliva. The NO produced in this way subsequently binds to rNPs for transport. When *R. proxilus* bites its prey, the NO-loaded rNPs are released into the wound to ultimately promote vasodilation, using the mammalian, NO-based signaling pathway (see Section 2.2) for the insect's advantage to increase its blood meal. In addition to increased blood flow, the NO that is released prevents platelet aggregation and blood coagulation.[705] The release of NO from NPs is triggered by an increase in pH from 5 to 7.4, inducing conformational changes to the protein (see below), as well as a lower concentration of NO at the site of the wound (compared to the saliva).[246,621,706,707] Additionally, these NO carriers can also bind histamine with very high affinity (dissociation constants $K_D = 1.90 \times 10^{-8}$ and 1.1×10^{-8} M at pH 7.0 and 8.0, respectively), which is released by the mammalian "prey" as an immune response to the insect bite. Here, histamine binds tighter than NO due to the hydrogen-bonding residues in the active site pocket of rNPs, further promoting NO release. In addition, the itching sensation that is normally induced around the bite by histamine release is suppressed due to its competitive binding to the rNPs, thus allowing the bite to go unnoticed.[247,708]

R. proxilus belongs to the *Reduviidae* family within the *Hemiptera* order.[709] Throughout the insect's lifecycle, there are a total of seven different rNP isozymes expressed, with four in the adult stages of *R. prolixus*,[245] designated rNP1−rNP4, and three in the earlier nymph stages of life, rNP5−rNP7.[710−712] The naming system comes from the relative abundance of these proteins in the salivary glands.[711,713] On the basis of the cDNA sequence determined for rNP1−rNP4 and rNP7,[711,714] it was found that rNP1 and rNP4 are 91% identical by sequence, while rNP2 and rNP3 are 78% identical. The rNP7 shows most

Table 10. Crystal Structures of Various Nitrophorins

protein	organism	PDB code	resolution	ref
rNP1(II)−NO	*Rhodnius proxilus*	4NP1	2.3	589
rNP1(III)−NH_3	*Rhodnius proxilus*	2NP1	2.0	247
rNP1(III)−CN	*Rhodnius proxilus*	3NP1	2.3	247
rNP1(III)−histamine	*Rhodnius proxilus*	1NP1	2.0	247
H60C rNP1(III)−histamine	*Rhodnius proxilus*	1U18	1.96	740
H60C rNP1(III)−IM_2	*Rhodnius proxilus*	1U17	1.7	740
rNP2−NO	*Rhodnius proxilus*	1768	1.45	741
rNP2(III)−H_2O[a]	*Rhodnius proxilus*	2A3F	1.4	742
		2AH7	1.7	742
rNP2(II)−H_2O[a]	*Rhodnius proxilus*	2AL0	1.6	742
		2ACP	1.4	742
rNP2(III)−NH_3	*Rhodnius proxilus*	1EUO	2.0	738
D1A rNP2(III)−NH_3	*Rhodnius proxilus*	2EU7	1.2	742
L122/132V rNP2(III)−H_2O[a]	*Rhodnius proxilus*	2AMM	1.9	742
		2ALL	1.47	742
rNP2(III)−CN	*Rhodnius proxilus*	2HYS	1.2	743
rNP2(III)−IM	*Rhodnius proxilus*	1PEE	1.5	741
D1A rNP2(III)−IM		2ASN	1.7	742
L122/132V rNP2(III)−IM	*Rhodnius proxilus*	1PM1	1.1	741
rNP2−pyrimidine	*Rhodnius proxilus*	2GTF	1.4	742
rNP4(III)−NO pH = 5.6	*Rhodnius proxilus*	1ERX	1.4	248
		1KOI	1.08	249
		1X8O	1.01	744
		2ATB[b]	1.0	745
		2AT5[c]	1.22	745
rNP4(III)−NO pH = 7.4	*Rhodnius proxilus*	1X8N	1.08	744
D30A rNP4(III)−NO	*Rhodnius proxilus*	1SXW	1.05	746
D30N rNP4(III)−NO	*Rhodnius proxilus*	1SY3	1.0	746
T121V rNP4(III)−NO	*Rhodnius proxilus*	1SY1	1.0	746
D129A/L130A rNP4(III)−NO	*Rhodnius proxilus*	1SXX	1.01	746
L133V rNP4(III)−NO	*Rhodnius proxilus*	2AT0	1.0	745
V36A/D129A/L130A rNP4(III)−NO pH = 5.6	*Rhodnius proxilus*	2OFR	1.0	747
rNP4(II)−NO	*Rhodnius proxilus*	1YWB	0.97	590
rNP4(III)−H_2O pH = 5.6	*Rhodnius proxilus*	1D3S	1.4	248
		1X8Q	0.85	744
		2AT6[c]	1.22	745
rNP4(II)−H_2O	*Rhodnius proxilus*	1YWD	1.08	590
rNP4(III)−NH_3	*Rhodnius proxilus*	1NP4	1.5	737
		1D2U	1.15	249
		1U0X[d]	1.45	748
		1X8P	0.85	744
rNP4(III)−NH_3[b] pH = 5.6	*Rhodnius proxilus*	3C78	0.98	745
rNP4(III)−NH_3[c] pH = 7.5	*Rhodnius proxilus*	3C77	1.08	745
D30N rNP4(III)−NH_3	*Rhodnius proxilus*	1SXY	1.07	746
E55Q rNP4(III)−NH_3	*Rhodnius proxilus*	3FLL	1.5	708
T121V rNP4(III)−NH_3	*Rhodnius proxilus*	1SY0	1.15	746
D129A/L130A rNP(III)−NH_3	*Rhodnius proxilus*	1SY2	1.0	746
L133V rNP4(III)−NH_3 pH = 7.5	*Rhodnius proxilus*	3C76	1.07	745
rNP4(III)−CN	*Rhodnius proxilus*	1EQD	1.6	248
rNP4(III)−histamine	*Rhodnius proxilus*	1IKE	1.5	249
rNP4(III)−IM	*Rhodnius proxilus*	1IKJ	1.27	249
D30N rNP4(III)−IM pH = 5.6	*Rhodnius proxilus*	1SXU	1.4	746
L122/132V rNP4−IM pH = 5.6	*Rhodnius proxilus*	2AT3	1.0	745
rNP4(III)−4-iodopyrazole pH = 5.6	*Rhodnius proxilus*	1ML7	1.25	611
rNP4(II)−CO pH = 5.6	*Rhodnius proxilus*	1YWCA	0.89	590
rNP4(II)−CO pH = 7.0	*Rhodnius proxilus*	1YWC	1.0	590
Apo−rNP4	*Rhodnius proxilus*	2OFM	1.11	749
cNP(II)−NO, SNO	*Cimex lectularius*	1Y21	1.75	253
cNP(II)−NO	*Cimex lectularius*	1YJH	1.65	750
cNO(III)	*Cimex lectularius*	1NTF	1.8	253
cNP(II)	*Cimex lectularius*	2IMQ	1.3	751

Table 10. continued

protein	organism	PDB code	resolution	ref
cNP(II)−CO	*Cimex lectularius*	1SI6	1.45	752

[a]Two crystalline forms. [b]rNP4 reconstituted with 2,4-dimethyl deutroporphyrin IX. [c]rNP4 reconstituted with deuteroporphyrin IX. [d]Under 200 psi xenon.

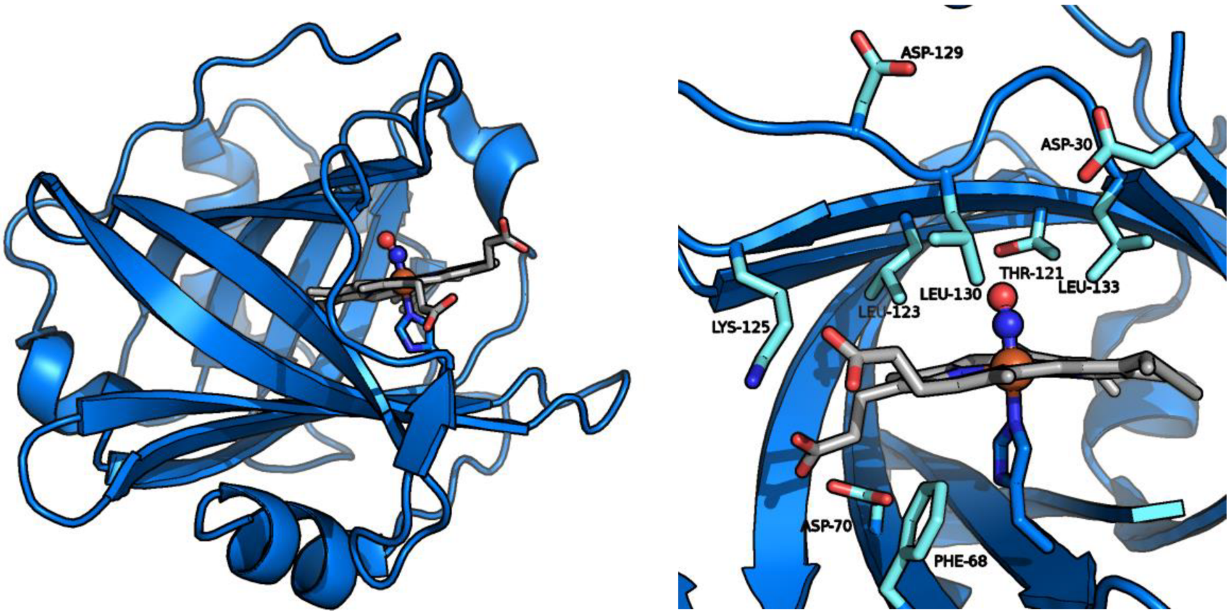

Figure 38. PyMOL generated images of the crystal structure of rNP4(III)−NO (PDB: 1KOI). Left: overall protein structure with lipocalin-like fold. Right: close-up of the active site.

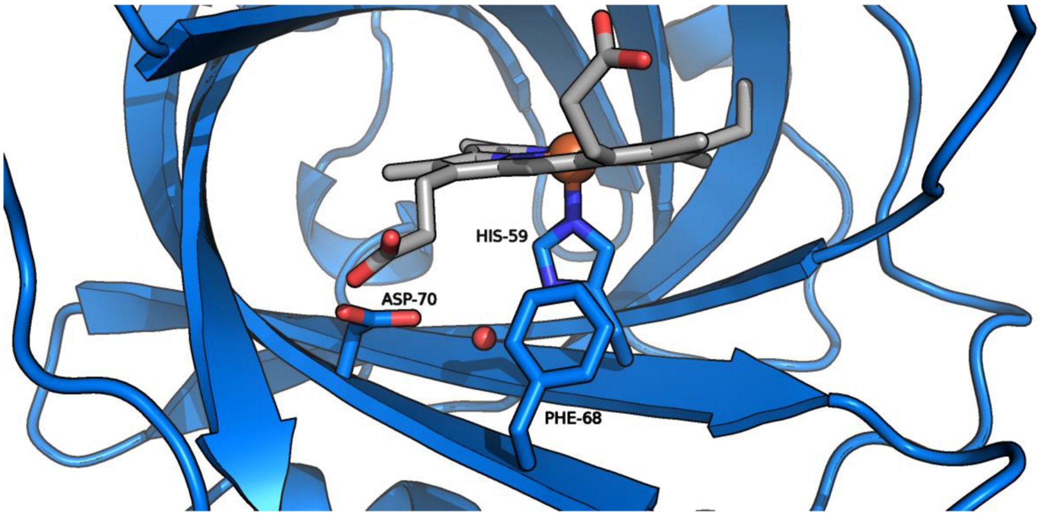

Figure 39. PyMOL generated image of the crystal structure of resting ferric rNP1 with NH_3 bound (PDB: 2NP1). The figure shows the proximal pocket with important residues (see text). The NH_3 molecule bound to the heme is omitted for clarity.

similarity to the rNP2/rNP3 pair.[712] Overall, the rNP1−rNP4 proteins share a 34% sequence identity.[712]

As discussed above, when *R. prolixus* bite their prey, rNPs can bind histamine, successfully blocking the immune response from the victim and allowing the bite to go unnoticed. Since the insects cannot be detected while feeding, it increases the chances of transmitting Chagas disease.[715] If this disease is left untreated, it can lead to weakened heart and gut muscles and eventually death after about ten years.[716] This infection is caused by the protozoan *Trypanosoma cruzi*, which is carried in the feces of *R. prolixus*. After the insect has left, the body continues to release histamine in response to the bite, causing the bite to itch. The victim then scratches the bite, possibly introducing *T. cruzi* into the blood stream, which initiates infection.[716,717] This disease can be found in tropical areas such as Latin America and parts of the U.S., including southern Texas and Arizona.[717] While blood is screened for *T. cruzi* antibodies in Latin America, these tests are not currently being performed in the U.S., making the disease transferrable through blood donations.[717,718] Most of the research on Chagas disease is currently being carried out in Latin America where the disease is most prevalent.[719−733] Two drugs are available to

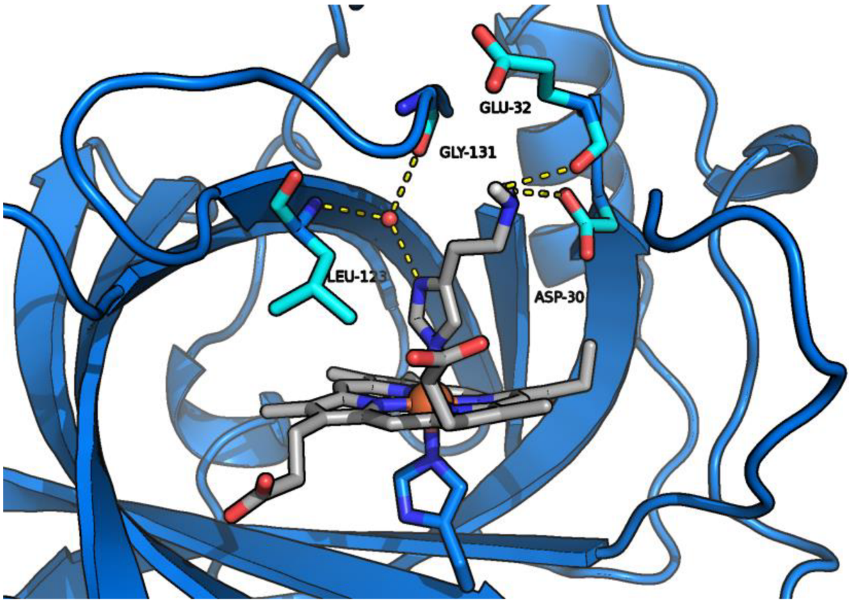

Figure 40. PyMOL generated image of the crystal structure of the rNP1(III)−histamine complex (PDB: 1NP1).

treat this debilitating disease, a nitrofuran called Nifurtimox and a nitroimidazole called Benznidazole. Only the former is approved for use in the U.S. and unfortunately, neither of these medications is very effective in treating the disease.[734] More research is necessary to find improved treatments for Chagas disease.[735,736]

2.3.1.1. Protein Structure. The rNP proteins tend to be small (between 20 and 32 kDa) and based on multiple crystal structures obtained for both wt and mutant ferric and ferrous rNPs (see Table 10),[247−249,589,737,738] they generally show a lipocalin-like structure as shown in Figure 38. Lipocalins are small proteins made almost entirely of β-sheets, which form a barrel-like structure.[739] In the case of rNPs, the barrel is built from eight β-sheets, and the structures further show three α-helices and two stabilizing disulfide bonds (see Figure 38).[247] Here, the open end of the barrel is lined by eight antiparallel β-sheets, which are made up of four loops, AB, CD, EF, and GH. The barrel is closed on the N-terminal side by a single-turn α-helix, followed by three antiparallel β-sheets, which form the BC, DE, and FG loops. The heme *b* cofactor needed for NO binding is located in the center of this barrel (see Figure 38). As shown in Table 10, many crystal structures of rNPs have been reported with bound molecules ranging from diatomics, such as NO, CO, and cyanide, to larger molecules like ammonia, histamine, and water.

The active site of rNPs consists of a ferric heme *b* (protoporphyrin IX) cofactor with axial histidine ligation, which is held in place by electrostatic and hydrophobic interactions (see Figure 38).[247,248,738] This heme cofactor is non-covalently bound to the open end of the rNP barrel structure through hydrogen bonds between the heme propionates and both Lys125 and Asp70, with the latter forming an interesting carboxylate-carboxylate interaction.[247] On the proximal side of this cofactor, the coordinated His is also held in place non-covalently through electrostatic and hydrophobic interactions. This was first analyzed in a crystal structure of ammonia-bound wt ferric rNP1 (PBD: 2NP1), and it was found that the axial His is stabilized by a hydrogen-bonding network in the proximal pocket that includes a water molecule and amino acids Asp70 and Phe68 (see Figure 39).[247] The distal heme cavity, on the other hand, is large and consists of nonpolar amino acid residues (such as leucine), which are conserved throughout most rNPs, and one aspartate (Asp30 in rNP1).[247] These residues keep the distal region free of ordered solvent molecules, and they help stabilize NO when it is bound to the heme cofactor. These are the same residues that encase the histamine imidazole ring upon histamine binding, which is evident from the crystal structure of histamine-bound rNP1 (PDB: 1NP1) in Figure 40.[247] Variations in this pocket have been demonstrated to cause changes in NO binding affinity. NO dissociation constants for rNP1 and rNP4 were determined to be 0.12 and 0.05 μM at pH 5, and 0.85 and 0.54 μM at pH 8, respectively. These values are higher in comparison to wt rNP2 with a K_D of 0.02 μM at pH 8.[621] This difference in NO affinity was further studied experimentally by replacing the large hydrophobic Ile120 residue in rNP2 with a polar Thr to mimic the active sites of rNP1 and rNP4. The resulting K_D was 10 times higher in the mutant rNP2 compared to wt rNP2.[247,248,738] This substitution in the distal pocket indicates that NO binds tighter when it is buried in the hydrophobic active site and protected from solvent molecules, as observed for wt rNP2. Therefore, the SCS of the active site plays a key role in fine-tuning the NO affinity in different rNP isoforms.[621]

2.3.1.2. Function and Mechanism. Ferric heme−nitrosyls tend to be labile towards NO loss (see below) and therefore require a mechanism to stabilize the bound NO and prevent premature NO release.[744,746] In the saliva of *R. proxilus*, the NO concentration is relatively high, which helps to keep the rNPs fully loaded. In the NO-free form, rNPs adopt a conformation where the protein is "open" and the active site is exposed to solvent molecules. Upon NO binding, the structure of rNPs undergoes major conformational changes that help keep NO bound within the active site. Once NO binds to the ferric heme cofactor, the AB and GH loops shift to form the "closed" conformation and the active site is buried in the hydrophobic core of the protein (see Figure 41).[248] In rNP4 in the closed conformation, the NO is surrounded by the hydrophobic residues Leu130, Leu133 and Val136 in the core of the protein, and a hydrogen-bonding network is formed using the Asp30, Glu32 and Asp35 side chains, as seen in the crystal structure of

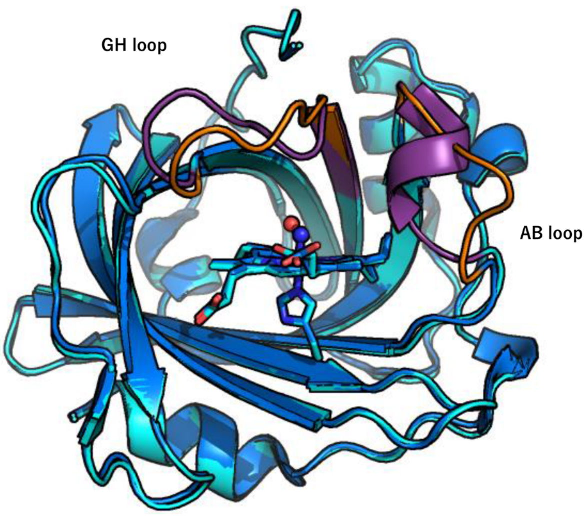

Figure 41. PyMOL generated overlay of the crystal structures of rNP4(III)−NO in the closed conformation (light blue; PDB: 1ERX) and rNP(III)−CN^- in the open conformation (dark blue; PDB: 1EQD, cyanide not shown). In the open conformation, the indicated loops are represented in orange and in the closed conformation, they are represented in purple.

rNP4(III)−NO (here, "rNP4(III)−NO" formally stands for the ls-$\{FeNO\}^6$ complex of ferric rNP4, for redox state tracking; PDB: 1X8N). These same Asp30 and Glu32 residues are also involved in the binding of histamine in the closed conformation, where hydrogen-bonds form between Asp30 and Glu32 and the alkylammonium group of histamine. Glu32 also participates in a hydrogen-bonding network with a well-ordered water molecule. The imidazole ring of histamine is further stabilized by hydrogen-bonding with a well-ordered water molecule that forms three additional hydrogen bonds to the amide groups of Leu123, Gly131, and another water molecule.[247,249] For example, these interactions are observed in the crystal structure of the Fe(III)−histamine complex of rNP1 (PDB: 1NP1; see Figure 40), which may explain the tighter binding of histamine over NO.[247,249] At the N-terminus of the protein in the closed conformation, 13 new hydrogen bonds form while 9 hydrogen bonds that are present in the open conformation are lost.[248] Crystal structures of the rNP4 mutants D30A and D30N (D30 is part of the AB loop) and D129A/D130A (D129 sits in the GH loop) with NO bound demonstrate a complete lack of conformational changes, implying that these residues play a crucial role in stabilizing the closed conformation of the protein.[746] Further experiments using stopped-flow spectroscopy revealed that the pH dependence of NO release was either reduced significantly (for mutations to the AB loop) or lost completely (for mutations to the GH loop) when compared to the native enzyme.[746] These results indicate that the dynamics of the β-barrel are responsible for the pH-dependence of NO release under physiological conditions, and therefore limit NO release from the cavity of the protein in the insect's saliva (at low pH), where the protein adopts the closed conformation in the NO-bound state.[744] Without these pH-responsive loop regions, the protein would not be able to properly function as a NO transporter due to premature NO loss. Upon injection of rNPs into the wound the pH increases from 5.0 in the saliva to 7.4 in human blood, which then triggers the protein to shift to an open conformation where the AB loop swings out and opens the active site (see Figure 41), which allows for smooth NO release into the victim's blood and tissue.

As previously mentioned, the mechanism of NO transport by rNPs begins in the salivary gland, where NO binds to the 5C ferric heme cofactor of rNPs to form a 6C ls-$\{FeNO\}^6$ complex with proximal His ligation.[247−249,589] This is supported by EPR spectroscopy, where the spectrum of the resting state of rNPs shows a signal around $g_{eff} = 6$, indicating the presence of a high-spin ferric heme with an overall spin of $S_t = 5/2$. Upon addition of NO, this signal disappears, as the formed ls-$\{FeNO\}^6$ complex is diamagnetic ($S_t = 0$). This process is completely reversible. The UV−vis spectrum of the 5C ferric resting complex shows the Soret band at 406 nm, which shifts to 422 nm upon NO binding.[246] Using rRaman and IR spectroscopy, the Fe−NO and N−O stretching frequencies of rNP1(III)−NO were reported to be 591 cm^{-1} and 1917/1904 cm^{-1} (two species present in the sample), respectively.[589,753] When the pH of the solution is raised, the $g_{eff} = 6$ signal returns in the EPR spectrum and the Soret band shifts back to 406 nm, indicating the release of NO and the restoration of the resting state.[246]

It is known that ferric heme nitrosyls are intrinsically labile (see below), therefore nitrophorins must stabilize bound NO in the heme pocket to prevent premature NO loss. Structural changes between "open" and "closed" conformations of the protein aid in retaining NO. On the basis of vibrational data as well as hybrid quantum mechanical/molecular mechanics (QM/MM) calculations, the conformational changes in rNPs seem to have little effect on the FeNO unit itself, indicating that NO release is not tuned by the enzyme by altering the NO binding constant to the heme, but simply by influencing NO migration rates from the active site.[754−756] Kinetic studies of rNP1−rNP4 demonstrate biphasic behavior of NO binding and release as shown in Scheme 15.[621] The first phase (k_1 or $k_{on,\,NO}$) represents the formation of the nitrosyl complex. This initial binding phase shows second order rate constants of ~2×10^6 M^{-1} s^{-1} in rNP1 and rNP4, and ~1×10^7 M^{-1} s^{-1} in rNP2 and rNP3, respectively. The second phase (k_2) represents the conformational change from the "open" state to the "closed" state of the protein, which was determined to be ~50 s^{-1} in rNP2.[621] NO release is again biphasic, beginning with a pH-dependent conformational change of the protein from the "closed" state to the "open" state. At pH 5, k_{off} values were determined to be ~0.2 and 0.14 s^{-1} for rNP1 and rNP4, and ~0.05 and 0.05 s^{-1} for rNP2 and rNP3, respectively. Increasing the pH to 8 increases k_{off} values to ~2 and 2.6 s^{-1} for rNP1 and rNP4, and ~0.12 and 0.08 s^{-1} for rNP2 and rNP3, respectively. Once the protein is in the open conformation, the NO dissociates independent of pH (k_{-1} or $k_{off,\,NO}$) with values of ~5 s^{-1} for rNP1 and rNP4, and ~40 s^{-1} for rNP2 and rNP3, respectively.[621] More kinetic details are listed in Table 4.

Additionally, the active sites of rNPs react with the histamines that are produced by the victim as part of the immune response.[246,247,757] With this competitive binding of histamine, the itching sensation at the wound is suppressed,

Scheme 15. NO Binding and Dissociation from rNPs, and Rate Constants

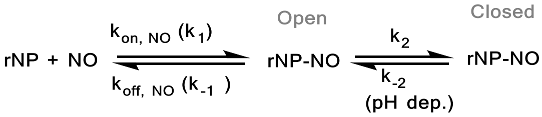

causing the bite to go unnoticed, and at the same time, more NO is released into the blood stream, as histamine competes with NO for binding to the rNPs (see Scheme 16). The strong binding of histamine is further demonstrated by the dissociation constants of histamine and NO. Histamine binds slightly tighter to rNP1 with K_D values of 1.9×10^{-8} and 1.1×10^{-8} M at pH 7 and 8, respectively.[247,621] Under the same conditions, NO displays K_D values of 9.5×10^{-7} and 8.5×10^{-7} M, respectively.[621,706] Similar trends are observed for rNP2 and rNP3.[621] Other antihemostatic functions are demonstrated by rNP2 and rNP7.[612,758] rNP2 interferes with the activation of Factor Xa, which is a key component of the blood coagulation cascade.[758,759] On the other hand, rNP7 also acts as an anticoagulant by binding to L-a-phosphatidyl-L-serine (PS)-containing phospholipid membranes, which are located on the surface of platelets and mast cells that have lost platelet symmetry.[712,760−762] These mechanisms are tightly coupled to other activation events related to coagulation, and therefore prevent blood clotting, which further helps the insect to obtain a sufficient meal before being discovered by the victim.[612,758]

Upon close inspection of the reported crystal structures for *R. prolixus*, the heme cofactor appears extremely distorted from planarity (see Figure 42).[247−249,737,738] Two common distortions of heme cofactors are ruffling and saddling, as shown in Scheme 17. In the case of nitrophorins, the dominant distortion is ruffling, which is defined by rotations of the pyrrole rings around the Fe−N bonds of the heme cofactor. Saddling is observed when one pair of opposite pyrrole rings is tipped up while the other pair is tipped down. The degree of ruffling can be quantified in high resolution crystal structures. Here, the RMSD is calculated relative to the heme mean plane of the 24 heme core atoms.[763] The largest amount of ruffling was reported for the crystal structure of rNP2(III)−NO, where a RMSD value of 0.285 Å is observed.[245] Other highly ruffled structures were reported for rNP2(III)−H_2O, rNP4(III)−NO and rNP4(III)−CN^- with RMSD values of 0.250, 0.189 and 0.214 Å, respectively.[245,249]

The source of this strong ruffling distortion was analyzed using the crystal structure of rNP4. In the distal pocket, there are two leucine residues, Lys213 and Lys133, that are close to the bound NO molecule.[249] Not only do these residues aid in stabilizing the bound substrate, their bulky nature points toward the porphyrin ring which contributes to the ruffling of the heme cofactor.[764,765] This has also been observed in rNP2, where the corresponding residues are L122 and L132. Crystal structures of the NO adduct of the L122V/L132V rNP2(III) double mutant revealed a decreased RMSD value of 0.246 Å, in agreement with these ideas. A similar reduction in the RMSD value (0.208 Å) was also observed in the water-bound crystal structure of the rNP2 double mutant.[245] In the L122V/L132V rNP2 double mutant, the Fe^{II}/Fe^{III} reduction potential of the heme shifts 90 mV more positive compared to wt protein, indicating that heme ruffling plays an important role in tuning the heme reduction potential.[706,766] Note that this relation has previously been established for Cyt. *c*.[764,765]

Scheme 16. Competitive Binding of NO and Histamine to rNPs

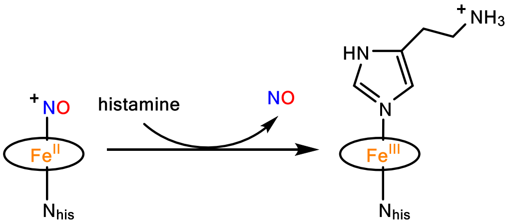

2.3.2. Basic Properties of Ferric Heme−Nitrosyls and Electronic Structure.

As discussed above, upon coordination of NO to the active site heme of rNPs, a 6C ferric heme−nitrosyl, or ls-$\{FeNO\}^6$ complex in the Enemark−Feltham notation, forms that has an axial His ligand bound in trans position to NO. These types of complexes have been studied in much detail using simple model complexes, and much has been learned from these studies that aids in our understanding of the geometric and electronic structures of these species, and how this is affected by the non-innocent nature of NO.

The first crystal structures of ferric heme−nitrosyls were reported by Scheidt and coworkers in 1984 for the 5C complex $[Fe(OEP)(NO)](ClO_4)$ and the 6C complex $[Fe(TPP)(OH_2)(NO)](ClO_4)$, with the latter featuring a water molecule bound trans to NO.[767] These complexes were prepared by the simple reaction of the corresponding ferric porphyrin complexes, utilizing the weakly coordinating counter ion perchlorate, and NO.[767,768] The 5C and 6C complexes show Fe−NO and N−O bond lengths of 1.644 and 1.112 Å, and 1.652 and 1.150 Å, respectively, which are typical for these types of complexes. A selection of representative structural parameters are listed in Table 11. Since ferric heme−nitrosyl complexes are diamagnetic ($S_t = 0$), most spectroscopic characterization of these species has focused on vibrational, electronic, and Mössbauer spectroscopy.[655,767] For the 5C complexes $[Fe(TPP)(NO)]^+$ and $[Fe(OEP)(NO)]^+$, N−O stretching frequencies of 1850 and 1862 cm^{-1} have been obtained by IR spectroscopy.[655,767,769] Interestingly, in the gas phase, "naked" $[Fe(TPP)(NO)]^+$ shows an even lower N−O stretching frequency of 1825 cm^{-1}, indicating an interesting variation in the properties of this complex (and other species as well) when any interference from solvent shells and counterions is excluded.[770] At lower energy, the Fe−NO stretching frequencies for $[Fe(TPP)(NO)]^+$ and $[Fe(OEP)(NO)]^+$ are observed at 585 and 595 cm^{-1}, as determined using NRVS.[655,767,769] Since ferric heme−nitrosyls contain close to linear FeNO units, these complexes feature two essentially isoenergetic Fe−N−O linear bending modes, $\delta_{lb}(Fe−N−O)$, which are observed at 393 and 402 cm^{-1} for $[Fe(TPP)(NO)]^+$ and $[Fe(OEP)(NO)]^+$, respectively.[655,767,769] In proteins, 5C ferric heme−nitrosyl complexes cannot be obtained, as they have a distinct tendency to bind a sixth ligand in trans position to NO (in contrast to ferrous heme−nitrosyls, which show a strong thermodynamic *σ-trans* effect of NO; see Section 2.2). These species are therefore exclusively observed in model systems. The geometric and vibrational properties of other 5C ls-$\{FeNO\}^6$ model complexes can be found in Table 11.

As for the corresponding 6C complexes, it took another 15 years before crystal structures with axial N-donor ligation could be obtained. Here, crystal structures of the 6C complexes $[Fe(OEP)(L)(NO)](ClO_4)$ were reported with various neutral N-donor ligands L bound trans to NO (L = MI, pyrazole (Pz), indazole (Iz), and pyrazine (Prz); see Figure 43).[776] Structurally, the $[Fe(OEP)(MI)(NO)](ClO_4)$ complex features Fe−NO, N−O and Fe−N_{MI} bond distances of 1.647, 1.135, and 1.989 Å, respectively.[776] In 2017, the crystal structure of the analogous TPP^{2-} complex, $[Fe(TPP)(MI)(NO)](PO_2F_2)$, was finally reported. This complex shows Fe−NO, N−O, and Fe−N_{MI} bond lengths of 1.628, 1.148, and

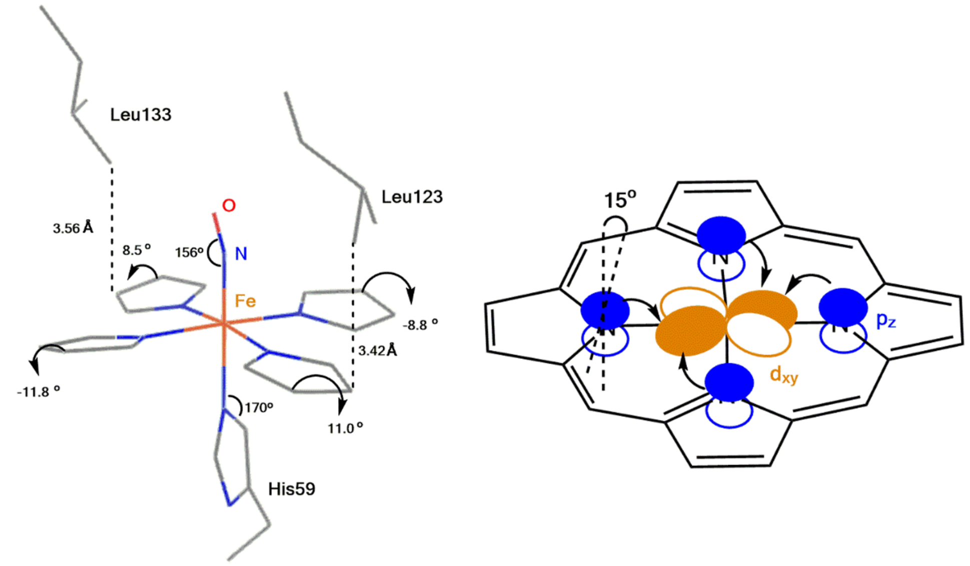

Figure 42. Left: illustration of pyrrole ring rotations in rNP4(III)−NO that define the ruffling distortion. The image was generated using PyMOL (PDB: 1KOI). The meso-carbons of the heme cofactor have been omitted for clarify. Right: interaction of the Fe d_{xy} orbital with the p_z orbitals of the porphyrin nitrogens of the A_{2u} orbital (see Figure 27), enabled by the ruffling distortion. This interaction occurs in the $(d_\pi)^4(d_{xy})^1$ ground state electron configuration.[25,249]

Scheme 17. Schematic Diagram of Heme Distortions Generated Using PyMOL[a]

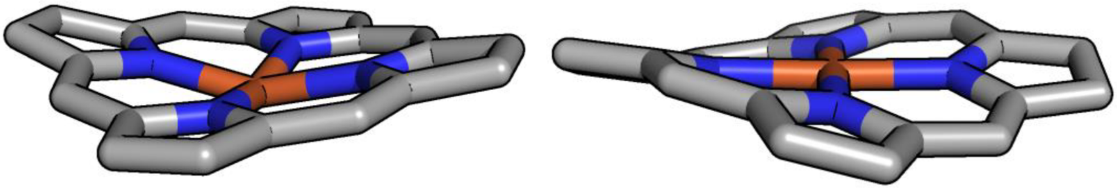

[a]Left: Saddling distortion observed in human myeloperoxidase isoform C (PDB: 1CXP1). Right: Ruffling distortion observed in rNP2(III)−NO (PDB: 1EUO).

1.973 Å, respectively (see Figure 43 and Table 11).[655] More generally, 6C ferric heme−nitrosyls with axial N-donor ligation usually show short Fe−NO bond distances of 1.63−1.65 Å and N−O bond distances in the 1.13−1.15 Å range, as illustrated in Table 11.[771,776,777] The Fe−N−O angles reported for these complexes are typically close to linear, between 170−180°.[768,777] Interestingly, Fe−(N-donor) distances in 6C ls-$\{FeNO\}^6$ complexes are observed between 1.97−2.06 Å,[768] which is similar to analogous $[Fe(Porph)(N\text{-donor})_2]$ complexes. For example, the Fe−N_{MI} bond distances of $[Fe(TPP)(MI)_2](ClO_4)$ and $[Fe(TPP)(MI)(NO)](PO_2F_2)$ are 1.974 and 1.973 Å, respectively.[655,788] Since the Fe−(N-donor) bond lengths in these two different complexes are very similar, it can be concluded that the NO ligand in ferric heme−nitrosyl complexes does not impose a significant thermodynamic *trans* effect on the axial N-donor ligand, opposite to the corresponding heme ls-$\{FeNO\}^7$ complexes discussed in Section 2.2.

Vibrationally, Fe−NO and N−O stretching frequencies of ls-$\{FeNO\}^6$ complexes with axially coordinated N-donor ligands are typically observed in the 580−600 and 1890−1920 cm^{-1} range, respectively, both in proteins and model complexes (see Table 11). For example, $[Fe(TPP)(MI)(NO)](PO_2F_2)$ shows Fe−NO and N−O stretching frequencies of 590 and 1920 cm^{-1},[655] while the corresponding vibrational frequencies in Mb(III)−NO and rNP1(III)−NO are 595 and 1927 cm^{-1}, and 591 and 1917 cm^{-1}, respectively.[589,680,753,782,783] The linear bending modes are observed at quite similar energies as the Fe−NO stretching modes and these features are difficult to discern by NRVS.[654] This problem was recently overcome using single-crystal polarized NRVS for $[Fe(OEP)(2\text{-MeIm})(NO)](ClO_4)$, where these features could be clearly distinguished due to their different polarizations, as shown in Figure 44.[769] The data show ν(Fe−NO) (z-polarized) at 600 cm^{-1} and the two components of the linear bend, δ_{lb}(Fe−N−O) (x, y-polarized), at 574 and 580 cm^{-1}. Table 11 provides a summary of structural and vibrational information available in the literature for 6C ferric heme−nitrosyl complexes in model complexes and proteins.

Ferric hemes show smaller NO binding constants compared to ferrous hemes, which required the rNPs to develop strategies to avoid premature NO loss, whereas ferrous hemes are able to sense and bind NO in the nanomolar range (see Section 2.2). Table 4 provides an overview of NO binding constants obtained for ferric hemes in typical model complexes and proteins. For model complexes, NO binding constants to ferric hemes are typically observed in the 10^3−10^5 M^{-1} range, while in proteins, a larger variation in K_{eq} is observed, typically between 10^3 and 10^8 M^{-1}. In this regard, rNPs display NO binding constants that are at the higher end of this range, as these proteins are specifically designed to hold on to NO; however, their NO binding constants still cannot compete with those of ferrous hemes, which show typical K_{eq} values in the 10^{10}−10^{12} M^{-1} range, up to 10^{14} M^{-1} in select cases. Because of

Table 11. Geometric and Vibrational Properties of Select 5C and 6C ls-$\{FeNO\}^6$ Model Complexes and Proteins

	geometric parameters [Å]/[°]						vibrational frequencies [cm^{-1}]			
complex/protein	ΔFe–NO	ΔN–O	∠Fe–N–O	ΔFe–L	ΔFe–N_P	ref	ν(N–O)	ν(Fe–NO)	δ(Fe–N–O)	ref
Five-Coordinate										
[Fe(OEP)(NO)](ClO_4)·$CHCl_3$	1.644	1.112	177		1.994	771	1868[b,c]	611[d]		772
[Fe(OEP)(NO)](ClO_4)	1.652	1.140	173		1.994	771	1838[b,c]	600[d], 595[e]	402	772,769
[Fe(TPP)(HO-*i*-C_5H_{11})(NO)]$^+$	1.776	0.925	177	2.063	2.013	641	1935[b]			773
[Fe(TPP)(H_2O)(NO)]$^+$	1.652	1.150	174	2.001	1.999	767	1937[b]			767
[Fe(TPP)(NO)](BF_4)	1.640/ 1.665	1.153/ 1.124	178.3/ 177.4		1.986/ 1.990	655	1850[b,g]/1853[b]	585[e,g]	393[e,g]	654, 655
[Fe(SPorph)(NO)]							1828[b]	510[d]		774
[Fe(SPorph-HB)(NO)]							1837[b]	515[d]		774
Six-Coordinate										
[Fe(SP-14)(Py)(NO)]Cl								603[d]		775
[Fe(OEP)(MI)(NO))](ClO_4)	1.647	1.135	177	1.989	2.003	776	1921[c]			776
[Fe(OEP)(2-MI)(NO)](ClO_4)	1.649/ 1.648	1.132/ 1.139	175.6/ 177.4	2.053/ 2.032	2.014/ 2.003	777	1917[c]	600[e]	574, 580[e]	769, 777
[Fe(OEP)(Iz)(NO)]$^+$	1.632	1.136	178	2.010	1.996	776	1914[c]			776
[Fe(OEP)(Pz)(NO)]$^+$	1.627	1.141	177	1.988	2.004	776	1894[c]			776
[Fe(OEP)(Py)(NO)]Cl								602[d]		775
[$\{Fe(OEP)(NO)\}_2$(Prz)]$^{2+}$	1.632	1.131	176.5	2.039	1.995	776	1899[c]			776
[Fe(OEP)(SR-H_2)(NO)]	1.671	1.187	160	2.356	2.01	778		549[d]		21, 778
[Fe(OEP)(*p*-C_6H_4F)(NO)]	1.728	1.153	157.4	2.040	2.016	779	1791[h]			779
[Fe(OETPP)(MI)(NO)]$^+$	1.650	1.1303	177	1.983	2.053	777				
[Fe(TPP)(NO)(NO_2)]	1.671	1.144	169	1.998	1.996	780	1874[b]			654
[Fe(TPP)(MI)(NO)](BF_4)							1896[b]	586[a,e]	578[a,e]	654
[Fe(TPP)(MI)(NO)](PO_2F_2)	1.628	1.148	176.3	1.973	2.001	655	1920[f,g]	590[e,g]		655
[Fe(TPP)(O_2CCF_3)(NO)]	1.618	1.151	175.8	1.899	2.01	781	1907[f]			781
[Fe(TpivPP)(NO_2)(NO)]	1.671/ 1.668	1.144/ 1.132	169.3/180	1.998/ 2.002	1.996/ 2.000	780	1893[h]			780
[Fe(TPP)(Cl)(NO)]	1.668	1.209	180	2.099	2.011	655	1880	563		655
Proteins										
Hb(III)–NO							1925[f]	594[d]		680, 782, 783
Mb(III)–NO							1927[f]	595[d]		584, 680, 784
Mb(III)–NO								596[d]	572[d]	585
Heme *cd*$_1$ NIR(III)–NO							1910[f]			782, 785
NorBC(III)–NO							1904[f]	594[d]		786
rNP1(III)–NO							1917[f]	591[d]	578[d]	589, 753
rNP1(III)–NO							1904[f]			589, 753
rNP2(III)–NO	1.93	1.38	134	2.005		741				
rNP4(III)–NO	1.51	1.20	156	1.960		248				
D30A rNP4(III)–NO	1.69	1.35	139	1.995		746				
D30N rNP4(III)–NO	1.78	1.38	132	2.003		746				
T121V rNP4(III)–NO	1.62	1.29	158	2.003		746				
D129A/L130A rNP4(III)–NO	1.60	1.35	155	2.003		746				
L133V rNP4(III)–NO	1.70	1.13	153	2.005		745				
V36A/D129A/L130A rNP4(III)–NO	1.75	1.31	136	1.975		747				
rNP4(III)–NO	1.72	1.20	137	1.958		745				
rNP4(III)–NO	1.77	1.17	140	1.993		745				
hHO1(III)–NO							1918[f]	596[d]	588[d]	787
HRP(III)–NO[771]							1903[f]	604[d]	574[d]	680, 574, 784
P450nor(III)–NO	1.63	1.16	161	2.31						1453
KpCld(III)–NO							1896	589		587

[a] Corrected assignment; see ref 655. [b] KBr pellet. [c] Nujol. [d] rRaman. [e] NRVS. [f] In solution. [g] SbF_6^- counterion. [h] Solid state.

this, it is important that rNPs remain in the ferric oxidation state, as reduction to the ferrous state and formation of a ls-$\{FeNO\}^7$ complex would severely impede their ability to release NO, rendering them unsuitable as NO transporters.

On the basis of the spectroscopic data discussed above, reactivity studies (see below) and quantum-chemical calculations, ls-$\{FeNO\}^6$ complexes are believed to have Fe(II)–NO^+ ground states, emphasizing the non-innocent nature of the NO ligand. These complexes have very strong and covalent Fe–NO bonds, which is reflected by their short Fe–NO bond distances of ~1.65 Å and high Fe–NO stretching frequencies of ~590 cm^{-1},[24,338] which translates into Fe–NO force constants of about 3.9 mdyn/Å.[654] Here, the Fe–NO bond is dominated by two strong π-backbonds between the d_π orbitals of iron and

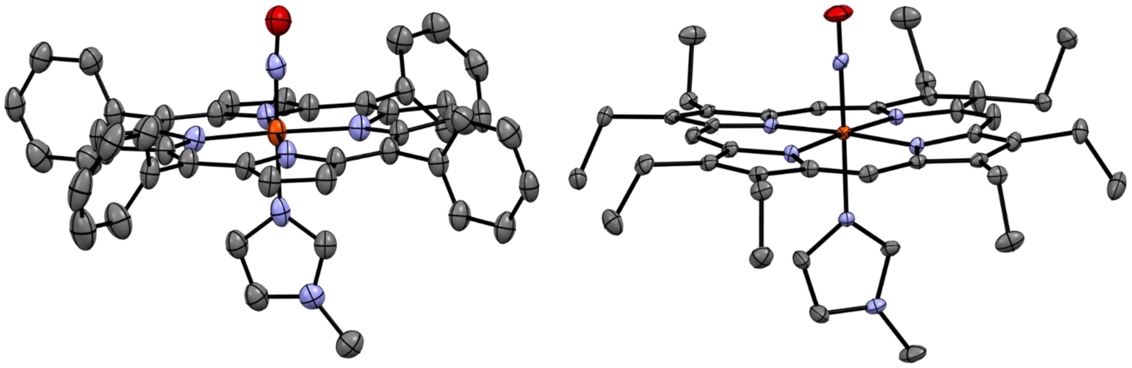

Figure 43. Crystal structures of the 6C ls-$\{FeNO\}^6$ complexes with TPP^{2-} (left) and OEP^{2-} (right) coligands, using MI as the axial ligand bound trans to NO.[655,776] All H atoms and counter ions are omitted for clarity.

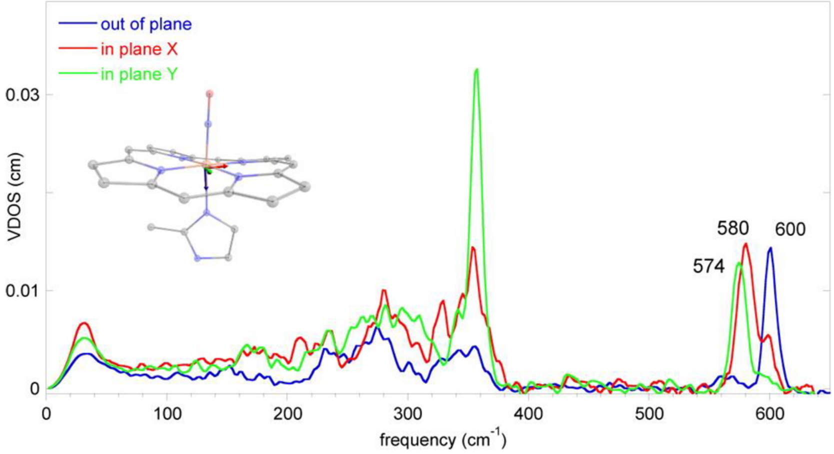

Figure 44. Single-crystal polarized NRVS data for $[Fe(OEP)(2\text{-}MeIm)(NO)](ClO_4)$. Reprinted with Permission from ref 769. Copyright 2014 American Chemical Society.

the two empty π^* orbitals of NO^+, as shown in Figure 45. This interaction is very covalent, with an estimated 25% of NO(π^*) admixture into the corresponding bonding MOs, $d_{xz}\_\pi^*_x$ and $d_{yz}\_\pi^*_y$, in Figure 45 (with the z axis corresponding to the Fe−N−O vector).[654] On the other hand, the Fe−NO σ interaction is weak because of the poor donor abilities of the σ_{ps} orbital of the NO^+ ligand and its very low energy (due to the very short N−O bond distance). The resulting, strong π and weak σ bond in the ground state of ferric heme−nitrosyls leads to a short Fe−NO bond distance and linear FeNO unit, maximizing the Fe−NO π interaction. Interestingly, the bonding in these complexes is analogous to that of the isoelectronic ferrous heme−CO complexes, where π-backbonding is also the dominant interaction between the Fe^{II} center and the diatomic. Here, the NO^+ ligand is a stronger π-acid compared to CO, leading to stronger Fe−NO bonds compared to Fe−CO bonds. This is evident from a comparison of the corresponding metal−ligand stretching frequencies, which are ~590 cm^{-1} for the Fe(II)−NO^+ compared to ~500 cm^{-1} for the Fe(II)−CO bond in the corresponding 6C complexes with axial N-donor coordination.[789,686,687]

The two strong π-backbonds in the Fe(II)−NO^+ ground state of ferric heme−nitrosyls lead to the net transfer of the charge-equivalent of about one electron from the Fe^{II} center back to the NO^+ ligand. This explains the lowering of the N−O stretching frequency from 2390 cm^{-1} observed in "free" NO^+ to ~1900 cm^{-1} in the 6C complexes. This implies that the effective nuclear charge of the Fe center in these complexes should more closely resemble that of Fe^{III}, which is indeed observed by Mössbauer spectroscopy.[771,777] Nevertheless, besides applying the IUPAC rule for orbital analysis ("the winner takes it all"), we also believe that the Fe(II)−NO^+/strong π-backbond description for ferric heme−nitrosyls has merit and is the most accurate representation of the electronic structure of these complexes. The two strong π-backbonds lead to the transfer of roughly the same amount of α- and β-spin density (50% α- and 50% β-spin) back to the NO^+ ligand, leading to charge accumulation on the NO ligand, without generating any spin (hence, atypically, the ligand is NO-(neutral), but not $NO^\bullet$), and no hole in the $[t_{2g}]^6$ shell of the Fe^{II} center results. Therefore, this charge-transfer is an effect of metal-ligand covalency, but does not correspond to a true electron transfer (as would be the case in the open shell Fe(III)−$NO^\bullet$ state; see below), since no net spin on the NO ligand results (note that an electron has a charge but also a spin, so for an electron transfer, a spin has to be generated as well).[654] This difference is not semantic, as the closed-shell Fe(II)−NO^+/strong π-backbond versus open shell ls-Fe(III)−$NO^\bullet$ ground state leads to different electronic properties and Fe−NO/N−O bond strengths of the complexes (see Figure 46 and analysis below). The Fe(II)−NO^+ electronic description of the complexes is also in agreement with their observed reactivity (see below), featuring an electrophilic NO^+ ligand.

Extensive studies by Spiro and coworkers have shown that the strength of the π-backbond in the ferrous heme−CO complexes can be tuned by the protein environment and the

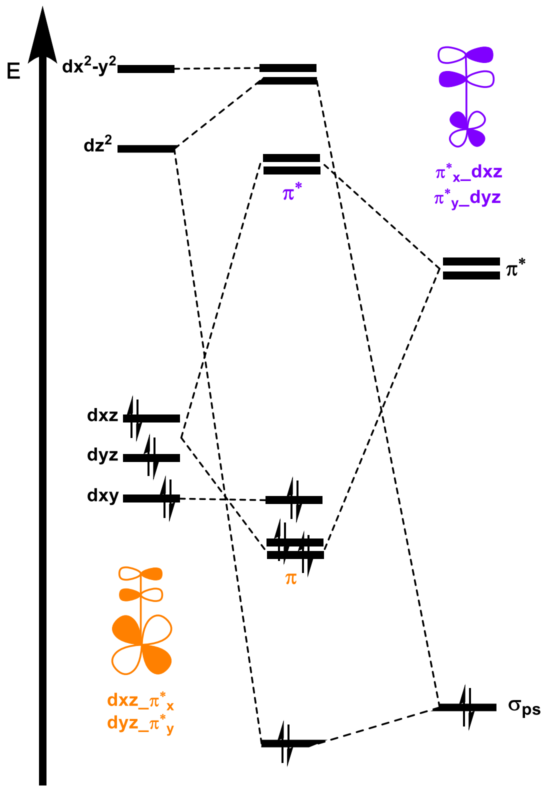

Figure 45. General molecular orbital diagram for ls-$\{FeNO\}^6$ complexes.

proximal ligand trans to CO. These changes result in an inverse correlation between the Fe−CO and C−O bond strengths, and hence, vibrational frequencies.[789] This is due to the fact that an increase in π-backbonding from the Fe^{II} to the CO ligand, for example, increases the strength of the Fe−CO bond, and hence, raises the Fe−CO stretching frequency. Because the electron density is donated into the C−O antibonding π* orbitals of CO, such an increase in π-backbonding then weakens the C−O bond and decreases the C−O stretching frequency at the same time. On the basis of the analogy in the electronic structures of Fe(II)−CO and Fe(II)−NO^+ complexes, a similar inverse correlation of the Fe−NO and N−O stretching frequencies should also exist for ferric heme nitrosyls. This was indeed demonstrated by Soldatova et al. in 2010, using a series of NO adducts of ferric myoglobin and corresponding active-site variants that were studied by UV−vis and rRaman spectroscopy (see Figure 47).[790] Interestingly, DFT calculations further predict that a direct correlation between the Fe−NO and N−O bond strengths can be induced in ferric heme−nitrosyls by introduction of strongly electron-withdrawing substituents at the heme β-positions. This prediction, however, still awaits experimental confirmation.[772,790,791] This effect has been related to a small admixture of a fully Fe−N−O σ antibonding orbital ($d_{z^2}\_\sigma^*$ in our notation) into the occupied porphyrin A_{2u}<81> MO (see Figure 27). In consequence, this orbital interaction causes the partial population of an Fe−N−O antibonding orbital, which explains the trends observed in the DFT results: here, stronger mixing, leading to a larger population of $d_{z^2}\_\sigma^*$, causes a simultaneous decrease of both the Fe−NO and N−O stretching frequencies, and hence, a weakening of both bonds. In addition, this is accompanied by a bending of the FeNO unit. Interestingly, this is fundamentally the same mechanism responsible for the thermodynamic thiolate *σ-trans* effect observed in thiolate-coordinated ls-$\{FeNO\}^6$ complexes,[792] which is further discussed in Section 4.2.

As evident from their structural and vibrational properties discussed above, ferric heme−nitrosyls show strong Fe−NO bonds in their Fe(II)−NO^+ ground states. This is in surprising contrast to the thermodynamic stability of these Fe−NO bonds, as reflected by the corresponding NO binding constants (K_{eq}) to ferric heme, which generally range between 10^3−10^5 M^{-1} (see Table 4). These K_{eq} values correspond to free NO binding energies of only −4 to −7 kcal/mol.[25] Curiously, ferrous heme−nitrosyls, which show lower Fe−NO stretching frequencies, and hence, weaker Fe−NO bond strengths, have larger NO binding constants of 10^{11}−10^{12} M^{-1}, which translates into free NO binding energies of −15 to −16 kcal/mol (see Section 2.2).[25] From this comparison, we can conclude that NO binds relatively weakly to ferric hemes (from the binding constants), yet forms a very strong Fe−NO bond in the ground state of these complexes (from spectroscopy). These seemingly contradictory properties can be explained when considering the different electronic states that are involved in NO-binding to ferric hemes. It should also be noted that the reduction of a ferric to a ferrous heme−nitrosyl complex is generally ligand (NO) centered, going from a linear Fe(II)−NO^+ to a bent Fe(II)−$NO^•$ type complex. This is clearly evident from a large shift in the N−O stretching frequency. For example, the ferric Mb−NO adduct shows ν(N−O) at 1927 cm^{-1}, which shifts to

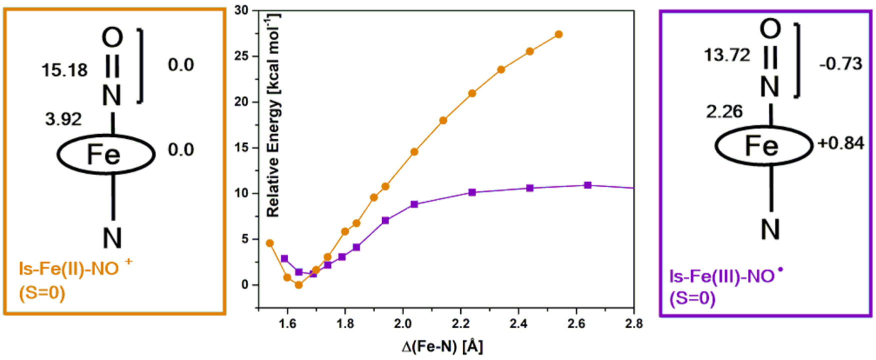

Figure 46. Potential energy surface comparison for ls-$\{FeNO\}^6$ complexes in the Fe(II)−NO^+(orange) and ls-Fe(III)−$NO^•$ (purple) ground state. In each respective box, the force constants (in mdyn/Å) of the Fe−NO and N−O bonds, as well as the spin density on the iron center and the NO ligand, are listed (obtained from single-point B3LYP/TZVP calculations).[654]

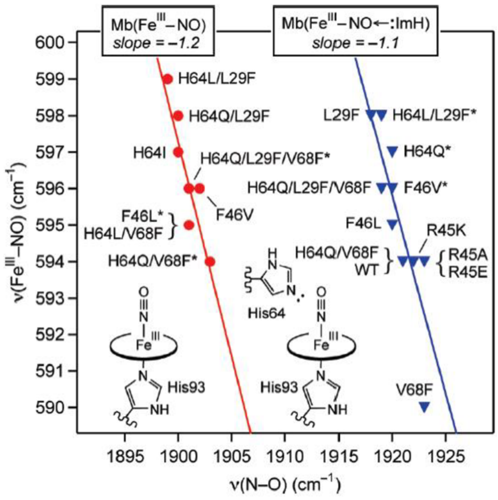

Figure 47. Inverse correlation between the Fe–NO and N–O stretching frequencies of ferric NO adducts of Mb variants with (triangles) and without (circles) proposed lone-pair donation to the bound NO from a distal His64 or Gln64. Reprinted with Permission from ref 790. Copyright 2010 American Chemical Society.

1613 cm^{-1} in the corresponding ls-$\{FeNO\}^7$ complex.[582–584,680,790] Similar shifts are observed in model complexes. For example, [Fe(TPP)(MI)(NO)](SbF_6) and [Fe(TPP)(MI)(NO)] show ν(N–O) at 1920 and 1630 cm^{-1}, respectively.[582–584,655,680,790]

To explain the relatively small binding constants of NO to ferric hemes, the different electronic states involved in NO binding and dissociation need to be considered, as shown in Figure 48. In the Fe(II)–NO$^+$ ground state (orange curve in Figure 48), the potential energy surface (PES) is unusually steep for a metal-ligand bond. This is due to the fact that the underlying dissociation of the complex into Fe^{II} and NO$^+$ is energetically highly unfavorable. The equilibrium Fe–NO distance for the Fe(II)–NO$^+$ ground state is predicted by DFT to be < 1.65 Å, which matches very well with the experimental Fe–NO distances, as shown in Table 11. The FeNO unit is linear in this state. This explains the strong Fe–NO bonds observed experimentally for ferric heme–nitrosyls: this is a property of their Fe(II)–NO$^+$ ground states. When NO undergoes dissociation from the iron center, an electron transfer from Fe^{II} to NO$^+$ occurs at an Fe–NO distance of about 1.7 Å, which allows the complex to cross over to the ls-Fe(III)–NO$^\bullet$ electronic state (purple curve in Figure 48). This is an open shell singlet state where the spins of the ls-Fe^{III} and NO$^\bullet$ are antiferromagnetically (AF) coupled, resulting in a diamagnetic state (S_t = 0). Calculated spin densities for this state are +0.84 on Fe and −0.73 on NO, respectively. Importantly, this electronic state has a distinctively weaker Fe–NO bond compared to the Fe(II)–NO$^+$ ground state, as indicated in Figure 46, resulting in a longer Fe–NO bond distance and lower Fe–NO stretching frequency, due to a weakening of the Fe–NO π-backbond. Hence, although the alternative ls-Fe(III)–NO$^\bullet$ state has been proposed for a number of ls-$\{FeNO\}^6$ complexes (see below), experimental evidence that this state could become the ground state, for example in strongly distorted hemes, is still ambiguous (see Table 11). The Fe–NO dissociation energy in the ls-Fe(III)–NO$^\bullet$ state is greatly reduced, and approximately comparable to ferrous heme–nitrosyls. However, this still cannot explain the small Fe–NO binding constants in ferric heme–nitrosyls. With further elongation of the Fe–NO bond, the iron center undergoes a spin crossover from ls to hs at an Fe–NO distance of about 1.9 Å, and the complex enters the hs-Fe(III)–NO$^\bullet$ (S_t = 2) state (green curve in Figure 48) with a hs-Fe^{III} and again AF coupled spins between Fe and the NO ligand. Importantly, this state is dissociative with respect to the Fe–NO bond, which, as shown in Figure 48 (green curve), causes a substantial decrease in the thermodynamic stability (NO binding constant) of the Fe–NO bond in ferric heme–nitrosyls. Therefore, the fact that ferric heme–nitrosyls have strong Fe–NO bonds in the ground state, yet relatively small NO binding constants is due to the fact that this reflects the intrinsic properties of different electronic states. This is a fundamental property of all ferric heme–nitrosyl complexes and is key to the functioning of nitrophorins. Without this multistate reactivity, in particular the dissociative hs-Fe(III)–NO$^\bullet$ state, the binding constant of NO to ferric heme would be too high, and nitrophorins would not be able to release NO. These electronic properties of ls-$\{FeNO\}^6$ heme complexes are also reflected in the corresponding rate constants. In particular, dissociation rate constants of NO from ferric hemes are larger in comparison to those of ferrous hemes with $k_{\text{off, NO}}$ rates of 10^{-1}–10^2 versus 10^{-5}–10^{-4} s^{-1}, respectively.

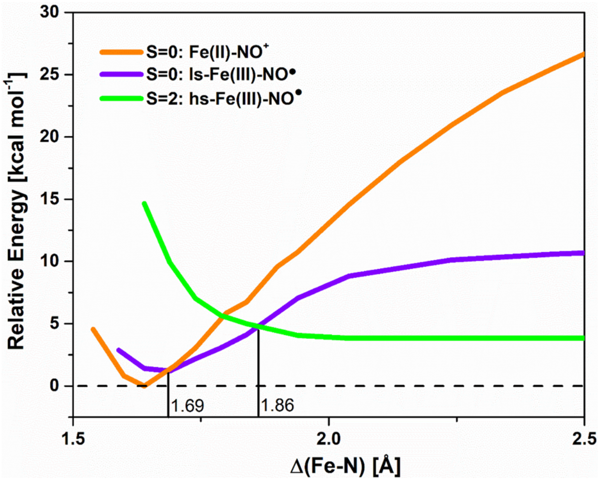

Figure 48. Potential energy surfaces for the closed-shell ls-Fe(II)–NO$^+$ (orange), the open-shell ls-Fe(III)–NO$^\bullet$ (purple, where ls-Fe(III) is AF coupled to NO), and the hs-Fe(III)–NO$^\bullet$ (green, where hs-Fe(III) is AF coupled to NO) state.[654]

In a similar fashion, NOS, which features a ferric heme–nitrosyl enzyme-product complex, would be product-inhibited and unable to release NO efficiently. Note that similar multistate reactivity has also been proposed for ls-$\{MnNO\}^6$ porphyrin complexes, based on quantum-chemical calculations.[793]

In this regard, it is noteworthy that ls-$\{RuNO\}^6$ complexes with Ru(II)–NO$^+$ ground states show strong Ru–NO bonds and much larger NO binding constants.[794–800] This is due to the fact that the Ru center has no propensity to form a hs complex, which means that in Figure 48 the analogous, dissociative hs-Ru(III)–NO$^\bullet$ state is shifted to much higher energy and no longer plays a role for NO binding to Ru(III) centers.[654] Because of this, ls-$\{RuNO\}^6$ complexes are in fact some of the most stable transition metal nitrosyl complexes, and hence, can be used as NO carriers for medical applications, especially in photodynamic therapy.[795–797,801]

https://doi.org/10.1021/acs.chemrev.1c00253
Chem. Rev. XXXX, XXX, XXX–XXX

Table 12. Reduction Potentials for Iron Porphyrins with Imidazole Derivatives as Axial Ligands[a,c]

complex	core type	ligand/$E_{1/2}$ (Fe^{III}/Fe^{II}) (mV)		
		imidazole (Im)	2-methylimidazole (2-MeIm)	$\Delta(E_{1/2})$ = "2-MeIm-Im"
[Fe(OETPP)][d]	saddled	−430	−400	+30
[Fe(OMTPP)][e]	saddled	−396	−290	+106
[Fe(TC_6TPP)][f]	saddled (ruffled)	−387	−300	+87
[Fe(TiPrP)][g]	ruffled or planar	−368	−417	−59
		−343[b]		−74[b]
[Fe(TMP)][h]	ruffled or planar	−169	−212	−43
		−130[b]		−82[b]
[Fe(T*o*-Cl_2PP)][i]	ruffled or planar	−3[b]	−115	−112[b]
[Fe(T*o*-Br_2PP)][j]	ruffled or planar	−40[b]	−131	−91[b]

[a] Measured in DMF. Potentials tabulated versus SCE, mV. [b] MI instead of Im. [c] Reference.[245] [d] $OETPP^{2-}$ = 2,3,7,8,12,13,17,18-octaethyl-5,10,15,20-tetraphenylporphyrin dianion. [e] $OMTPP^{2-}$ = 2,3,7,8,12,13,17,18-octamethyl-5,10,15,20-tetraphenylporphyrin dianion. [f] TC_6TPP^{2-} = 2,3,7,8,12,13,17,18-tetra-*β*,*β*′-tetramethylene-5,10,15,20-tetraphenylporphyrin dianion. [g] $TiPrP^{2-}$ = meso-tetraisopropylporphyrin diaonion. [h] TMP^{2-} = meso-tetramesitylporphyrin dianion. [i] T*o*-Cl_2PP^{2-} = tetra(*ortho*-dichlorophenyl)porphyrin dianion. [j] T*o*-Br_2PP^{2-} = tetra(*ortho*-dibromophenyl)porphyrin dianion.

2.3.3. Influence of Heme Ruffling on Electronic Structure of rNP Hemes.

As discussed above, the rNP ls-$\{FeNO\}^6$ complexes show strongly ruffled hemes. Interestingly, ferrous complexes of rNP4 show less ruffling in comparison to their ferric analogs. This is evident from analyzing crystal structures of the ferrous complexes of rNP4 with H_2O, NO and CO.[249,590] In addition, it was determined that the binding of strong π acceptor ligands, like NO^+, increases the ruffling of the heme compared to the ferrous H_2O complex. On the basis of these results, it was suggested that the degree of distortion is related to the metal oxidation state and the electron deficiency of the heme center.[590] Therefore, the degree of ruffling of the rNP4 complexes increases in the order: Fe(II)−H_2O < Fe(III)−H_2O < Fe(II)−CO < Fe(II)−NO < Fe(II)−NO^+.[590,802]

The important relationship between ruffling and redox potential of ferric hemes has been studied in model complexes, [Fe(*β*-bromo$_{1\text{-}8}$TPP)Cl] (*β*-bromo$_{1\text{-}8}$$TPP^{2-}$ = *β*-pyrrole bromo-substituted tetraphenylporphyrin dianion). By increasing the number of electron withdrawing bromine substituents of the porphyrin macrocycle, the heme distortion increases, and the reduction potential shifts more negative compared to the expected value.[803−805] Unfortunately, when 5−8 bromine substituents were added to the porphyrin macrocycle, the heme adopts a saddling rather than the desired ruffling distortion, so more work needs to be performed to further confirm this trend. Nonetheless, these results demonstrate that highly distorted porphyrins are harder to reduce than their corresponding planar analogs. This trend has also been studied in 6C ferric heme−nitrosyls with axial imidazole ligands. A higher degree of ruffling was observed for hemes with the sterically hindered 2-methylimidazole ligand compared to analogous complexes with the unhindered imidazole and MI ligands. Here, the complexes with the higher distortion demonstrated more negative reduction potentials in comparison to their less ruffled counterparts (see Table 12).[245,806] Similar trends were observed for highly ruffled tetra-isopropylporphyrin complexes.[245,807,808] Taken together, these model complex studies further support the conclusion that heme ruffling stabilizes the Fe^{III} oxidation state, making the ruffled compounds more resistant to reduction.

As discussed below, ferric heme−nitrosyl complexes can undergo reductive nitrosylation in the presence of excess NO gas and base to form the corresponding ferrous heme−nitrosyl complexes.[66,809,810] Since NO is tightly bound to ferrous heme as discussed above, with dissociation constants in the pM range, maintaining a more negative redox potential is important for rNP function to ensure the iron center is not reduced, which would shut down the rNPs' ability to function as NO transporters (by inhibiting NO release). As discussed above, the strong ruffling of the heme in rNPs could be significant by lowering the reduction potential of the heme, thus helping to prevent reduction of the ls-$\{FeNO\}^6$ to the ls-$\{FeNO\}^7$ complex.[245,621,766] Besides the general role of ruffling for decreasing the heme reduction potential, it was further proposed that ruffling also affects the ground state of the ls-$\{FeNO\}^6$ complex. In general, there are two possible electron configurations for ls ferric heme complexes. The d_π electron configuration, $(d_{xy})^2(d_{xz},d_{yz})^3$, is commonly observed for electron transferring ferrichromes *a*, *b*, *c*, *f*, and *o*.[811−815] The second possibility is the so-called d_{xy} electron configuration, $(d_{xz},d_{yz})^4(d_{xy})^1$, which is observed in heme model complexes with very strong π-acceptors as axial ligands (isocyanides, low-basicity pyridines, etc.).[816−822] Here, the single unpaired electron in the d_{xy} orbital does not have the proper symmetry to interact with the porphyrin macrocycle in a planar heme. However, ruffling causes a twisting of the pyrrole nitrogen p_z orbitals of the heme, which can now overlap with the d_{xy} orbital (see Figure 42).[811,816,818] This configuration also allows for spin delocalization via π-donation from the porphyrin ring into the d_{xy} hole. On the basis of these considerations, it was proposed that the ls-$\{FeNO\}^6$ adducts of rNPs actually have the alternative ls-Fe(III)−$NO^\bullet$ (S_t = 0) ground state where the spins of the unpaired electrons of Fe^{III} (located in the d_{xy} orbital) and $NO^\bullet$ are antiferromagnetically coupled, caused by the strong heme ruffling.[245] However, the spectroscopic properties of the ls-$\{FeNO\}^6$ adducts of rNPs do not support this proposal. For example, the Fe−NO and N−O stretching vibrations of rNP1(III)−NO are 591 and 1917 cm^{-1}, respectively,[823] which is in the typical range for ls-$\{FeNO\}^6$ complexes with the Fe(II)−NO^+ ground state.[589,753] On the other hand, recent work by Rogers and coworkers on the NO complexes of ferric chlorite dismutases, wt *Kp* Cld and wt *Da* Cld, shows somewhat low Fe−NO and N−O stretching frequencies of 589 and 591 cm^{-1}, and 1896 and 1898 cm^{-1}, respectively (see Figure 49), for these species, which was taken as evidence of a possible ls-Fe(III)−$NO^\bullet$ ground state in these ls-$\{FeNO\}^6$ adducts.[587] These lower stretching frequencies

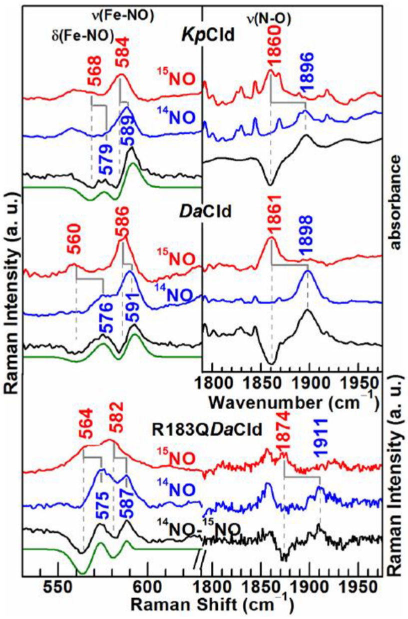

Figure 49. rRaman and FTIR spectra of the ls-$\{FeNO\}^6$ complexes of Clds, showing the δ_{lb}(Fe−NO), ν(Fe−NO), and ν(N−O) stretching bands of these species, together with isotope shifts (see text). Reprinted with permission from ref 587. Copyright 2020 Elsevier Inc.

were observed in the presence of a positively charged distal Arg. Upon replacement of the Arg with a neutral Gln by site directed mutagenesis, the N−O stretching frequency slightly increased in energy, observed at 1911 cm^{-1} (Fe−NO stretch: 587 cm^{-1}).[587] Compared to the DFT predictions (see Figure 46), however, the Fe−NO and N−O stretching frequencies of the ls-$\{FeNO\}^6$ adducts of wt Cld(III) still seem to fall well within the Fe(II)−NO$^+$ electronic structure regime. In addition, a possible ls-Fe(III)−NO$^\bullet$ electronic structure has been invoked for the ls-$\{FeNO\}^6$ adduct of Cyt. P460, caused by the special, crosslinked heme of this enzyme (see Section 2.2).[543] Despite these cases, a definite proof for the existence of a heme-based ls-$\{FeNO\}^6$ complex in the ls-Fe(III)−NO$^\bullet$ ground state is still lacking.

2.3.4. Structure and Function of *Cimex lectularius* Nitrophorins (cNP).

A second class of nitrophorins was later discovered in the bed bug, *Cimex lectularius* (therefore abbreviated cNP), which is structurally and evolutionary unrelated to rNP.[253,824] The 32 kDa cNP protein folds into a β-sandwich core that is surrounded by several α-helices (see Figure 50).[253] The ferric heme *b* active site is located between this β-sandwich and one of the α-helices and is proximally coordinated by Cys60, as shown in Figure 50. In the 5C high spin ferric resting state of cNP, the iron center is shifted 0.36 Å out of the heme plane toward the cysteinate ligand. The cysteinate is further stabilized by a hydrogen bond with Gln56 and van der Waals interactions with Phe64 and Ala21 (see Figure 50),[253] which somewhat resembles the stabilization of the proximal cysteinate ligand by multiple hydrogen bonds in the Cyt. P450 family.[825−828] Interestingly, the distal pocket of cNP contains hydrophobic residues, as observed in rNPs, and three ordered solvent molecules, where one is weakly associated with the ferric heme.[253] On the other hand, the distal pocket of cNP is much smaller compared to rNPs, and therefore, is not able to bind histamine. There also does not seem to exist a mechanism in cNP that would allow it to open or close the active site to improve retention of the bound NO. So overall, cNP is much less sophisticated as an NO transporter compared to rNPs.[247]

Despite the differences in structural make-up and proximal coordination in rNP and cNP proteins, both manage to carry out the same task of NO transport. The role of the proximal Cys ligand for NO transport in cNP has been investigated by studying the H60C mutant of rNP1, which introduces a proximal cysteinate ligand into the rNP scaffold.[740] On the basis of MCD, rRaman and UV-visible spectroscopy, a hs 5C ferric heme complex is present in this case in the absence of NO.[740] Interestingly, upon addition of methylimidazole derivatives to H60C rNP1, the thiolate ligand is replaced, resulting in an imidazole bound complex.[740] The crystal structure of the imidazole-bound rNP1 complex revealed that the rigid β-barrel structure of rNP1 restricts the heme from forming a strong Fe(III)−S_{Cys} bond, allowing for an external methylimidazole derivative to replace it and bind to the ferric heme. Similar to the rNPs, the heme cofactor of cNP is ruffled, presumably to

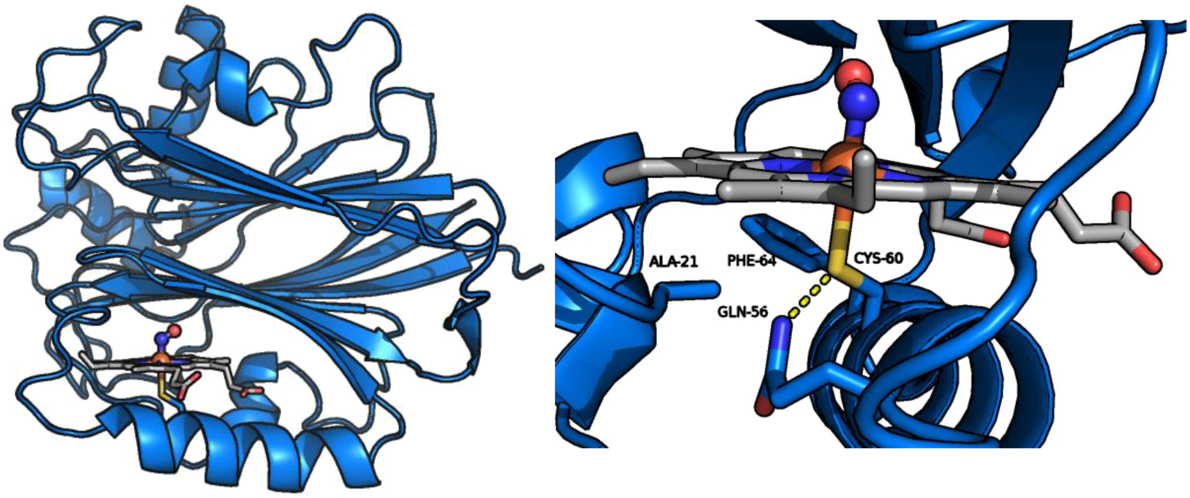

Figure 50. PyMOL generated image of the crystal structure of cNP−NO (PDB: 1YJH). Left: the overall protein structure. Right: the active site and proximal pocket. The strongly bent Fe−N−O unit (120°) indicates that the initially formed ls-$\{FeNO\}^6$ adduct was reduced in the X-ray beam.

stabilize the ferric oxidation state of the heme.[249,253] The presence of the cysteinate ligand in the ls-{FeNO}^{6} adduct of cNP imparts interesting geometric, spectroscopic and electronic properties on this complex, which are different from those of ls-{FeNO}^{6} adducts with axial histidine coordination. The basic properties of thiolate-coordinated ls-{FeNO}^{6} complexes are discussed in more detail in Section 4.2.

The basic mechanism of NO transport in *C. lectularius* nitrophorins is comparable to that of nitrophorins from *R. proxilus*. On the basis of EPR spectroscopy, the resting state of cNP is a 5C hs ferric heme-thiolate complex with rhombic symmetry and effective g values of 7.25, 4.75, and 1.90.[253] Additional signals appear at low temperature with g values of 2.37, 2.25, and 1.94, indicating that a small amount of 6C ls species is present, likely with water bound as the sixth ligand.[829,830] This is supported by the crystal structure of the wt cNP active site, which shows a weakly bound water molecule (Fe−O bond distance: 3.1 Å). Upon addition of NO, the UV−vis spectrum shows a shift of the Soret band from 389 to 437 nm, demonstrating the formation of a 6C ferric heme−nitrosyl complex with proximal cysteinate ligation. When studied by EPR spectroscopy, this species is silent as expected.[253]

Uniquely to cNP, high concentrations of NO (200 μM−2 mM) lead to a further reaction of NO with the the proximal cysteinate ligand of the heme, as shown in Scheme 18.[253] As a consequence, the Fe−S bond undergoes homolytic cleavage resulting in the corresponding 5C ferrous heme−nitrosyl complex, which now shows the Soret band at 402 nm (typical for 5C heme ls-{FeNO}^{7} complexes), and the neutral *S*-nitrosothiol, Cys60−NO. Similar reactions are typically observed for model complexes (see Section 4.2), but not Cyt. P450s, where the proximal cysteinate ligand is protected by a network of hydrogen bonds. This result indicates that in cNP, the cysteinate ligand is therefore more accessible and hence, more reactive compared to Cyt. P450s. Formation of the *S*-nitrosothiol in cNP was further confirmed by X-ray crystallography, as shown in Figure 51. In agreement with this, EPR spectroscopy shows the typical spectrum of a 5C ls-{FeNO}^{7} complex (see Section 2.2) for this species, with g values of 2.105, 2.044, and 2.013 and a strong three-line hyperfine splitting (A = 47.3 MHz) of g_{min}. While the exact mechanism of this process is unknown, there are two current proposals. The first possibility is a concerted mechanism where NO attacks the thiolate concomitant with the homolytic cleavage of the Fe(III)−S_{Cys60} bond. Alternatively, this reaction could occur in two steps, where after NO binding to the ferric heme, homolytic cleavage of the Fe(III)−S_{Cys60} bond occurs, leading to the formation of the corresponding thiyl radical (RS$^\bullet$), followed by reaction with a second molecule of NO to form the RS−NO product. However, the second proposal is less likely since this would require a detectable amount of 5C ls-{FeNO}^{7} complex to form, even in the absence of excess NO, which should be detectable by EPR spectroscopy. On the contrary, when the concentration of NO is lowered, the Cys60−NO product decomposes, as observed by stopped-flow UV−vis absorption spectroscopy. This decomposition likely corresponds to the reaction between the *S*-nitrosothiol and the 5C ferrous heme−nitrosyl complex, to give back the initial ls-{FeNO}^{6} species with axial cysteinate ligation (the reverse process in Scheme 18), accompanied by the release of 1 equiv of NO.[253]

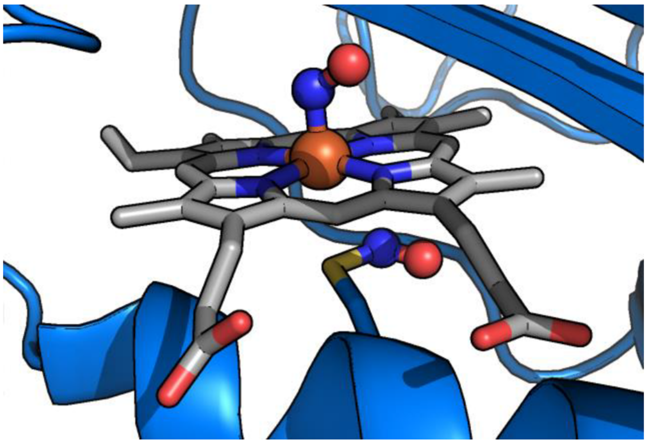

Figure 51. PyMOL generated image of the crystal structure of the 5C ls-{FeNO}^{7} adduct of cNP with *S*-nitrosothiol (Cys−NO) formation, obtained upon the binding two molecules of NO to the active site (PDB: 1Y21).

Scheme 18. Binding of NO in cNP Proteins

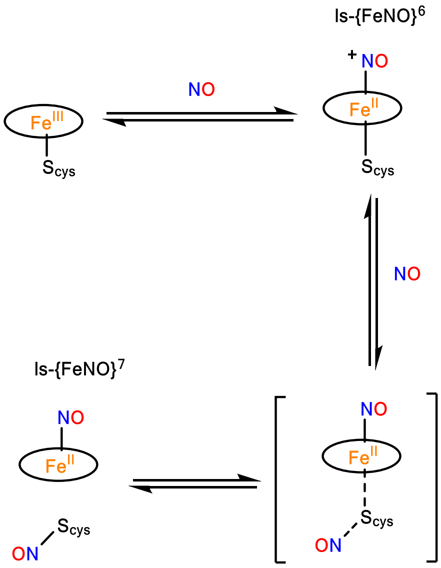

Since the dinitrosylated form of cNP where the proximal Cys60 carries a second equivalent of NO only forms at relatively high NO concentrations, the formation of this species may not be biologically relevant unless these high NO concentrations can be reached in the saliva of *C. lectularius*.[245] Curiously, while high NO concentrations have not been observed in other biological systems, 40% of the *C. lectularius* salivary gland contains nitrophorin protein, suggesting that high concentrations of NO are possible.[824] However, EPR studies of whole-gland homogenates at pH 7 did not indicate the formation of ferrous heme−nitrosyl species.[709] An alternative explanation could be that at neutral pH, the decomposition of the RS−NO group is favored. In any case, more studies need to be carried out to fully elucidate the potential biological relevance of the process of RS−NO formation in cNP.

2.3.5. Reactivity of ls-{FeNO}^{6} Complexes. Because of the Fe(II)−NO$^+$ electronic structure of ferric heme−nitrosyls, the coordinated NO is electrophilic in nature, and reactive towards bases (hydroxide, alcohols, thiols, amines, etc.), as illustrated in Scheme 19. This process is generally referred to as "reductive nitrosylation" or "autoreduction", which, in the presence of excess NO, leads to the formation of the

https://doi.org/10.1021/acs.chemrev.1c00253

Scheme 19. Autoreduction Mechanism of Ferric Hemes in the Presence of Base, ROH, and Excess NO

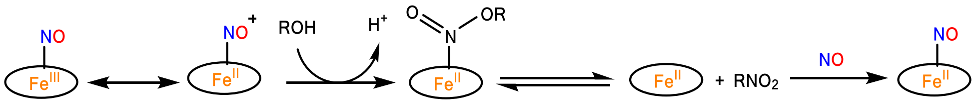

corresponding ferrous heme−nitrosyl complex.[809,810,831] The electrophilic reactivity of the coordinated NO^+ ligand in ls-$\{FeNO\}^6$ complexes has been studied in much detail for nitroprusside, as reviewed in refs 29, 66, 831, and 832. The autoreduction process shows pseudo-first order kinetics with respect to the concentration of the ferric heme−nitrosyl complex, where excess NO formally acts as the reductant.[810] The kinetics and the mechanism of the autoreduction reaction have been investigated in detail by Ford and coworkers.[5,252,833−836] In proteins, rate constants of autoreduction were reported to be 9.67×10^{-4} s^{-1} and 0.64×10^{-4} s^{-1} for met-Hb and met-Mb, respectively.[810] The rate determining step of this process is the attack of the hydroxide ion (or other suitable bases) on the coordinated NO^+, which consequently reduces the ferric heme to the ferrous oxidation state.[836] In the next step, HNO_2 dissociates from the ferrous heme, followed by rapid binding of NO to form a ls-$\{FeNO\}^7$ complex (see Scheme 19).[836,837]

In Mb and Hb, autoreduction occurs at basic and neutral pH, respectively, while in rNPs autoreduction is inhibited.[836] Recent computational work investigated the impact of the SCS in the distal pocket of heme proteins on the pH-dependence of the autoreduction. Although Mb and Hb contain a distal His residue, which acts as a gate for solvent access, the autoreduction reaction occurs under different conditions in these proteins.[838] The computational work shows that the transition state for water acting as a nucleophile and attacking the NO^+ ligand in the Mb(III)−NO adduct has an energy of 15 kcal/mol relative to the reactants, whereas, in contrast, the reaction with hydroxide is barrierless.[837] This evidence supports previous experimental findings that autoreduction occurs at basic pH in Mb. The higher energy barrier at neutral pH is due to a nearby positively charged Arg45 residue. The presence of this residue destabilizes a hydrogen bond between water and the distal His in the transition state, resulting in an energy barrier of 15 kcal/mol.[837] In contrast, the distal pocket of Hb contains a neutral proline, which does not affect the hydrogen bond between water and the distal His (at neutral pH), leading to a much lower energy barrier of only 5 kcal/mol for water attack on the Fe(II)−NO^+ complex.[837] Interestingly, these computational results are also in agreement with the lack of autoreduction activity in rNP at neutral pH. Because the distal cavity is filled with hydrophobic residues in rNPs, the ls-$\{FeNO\}^6$ complex is protected from both hydroxide and water, preventing autoreduction and formation of the corresponding ls-$\{FeNO\}^7$ species. Computationally, this reaction was found to have a transition state energy of 50 kcal/mol, further demonstrating that this reaction is highly unfavorable.[837]

Note that the autoreduction reaction is often used to prepare ferrous heme−nitrosyl model complexes from ferric precursors, although care must be taken to ensure that the reaction actually goes to completion, and does not produce materials that contain ls-$\{FeNO\}^6$ complexes and the ferric precursors as impurities. In the same manner, ferric heme−nitrosyls can serve as a source of NO^+ in biology and nitrosylate thiols, to generate *S*-nitrosothiols, RS−NO. The role of these species in NO storage is further discussed in Section 2.4.[141,839]

Considering the synthesis of model complexes, the reactivity of the coordinated NO can impact the long term stability of ferric heme−nitrosyls in solution. This constitutes a notable challenge for the growth of single crystals of ferric heme−nitrosyls for structural analysis by X-ray diffraction. This is particularly difficult for the biologically relevant, 6C complexes of type [Fe(Porph)(N-donor)(NO)], because in this case, the axial N-donor ligand (imidazole, pyrazole, pyridine, etc.) itself could potentially serve as a base in the autoreduction process. In addition, ferric heme−nitrosyls that are prepared from ferric precursors with weakly coordinating counter ions by direct reaction with NO gas are often prone to NO loss in solution and therefore, have to be handled in the presence of excess NO. This is a notable difference to heme proteins, where the ferric NO adducts are reasonably stable, as discussed above, with NO dissociation rate constants ($k_{off,NO}$) typically observed in the 10^1−10^{-2} s^{-1} range.[25,655] On the other hand, the chemical or electrochemical oxidation of corresponding ls-$\{FeNO\}^7$ precursor complexes constitutes an alternative approach for the bulk synthesis of ferric heme−nitrosyl complexes in high purity. Since the ls-$\{FeNO\}^7$ precursors can be prepared in high purity, this ensures that the resulting ls-$\{FeNO\}^6$ complexes obtained from their oxidation are pure as well. This approach was pioneered by Kadish and coworkers,[840] and has recently been applied to prepare the ls-$\{FeNO\}^6$ complexes $[Fe(TPP)(NO)]^+$ and $[Fe(TPP)(NO)(MI)]^+$ via (electro)chemical one-electron oxidation of [Fe(TPP)(NO)].[655] Here, the oxidation of the ls-$\{FeNO\}^7$ complex [Fe(TPP)(NO)] was followed by solution IR spectroscopy, showing N−O stretching frequencies of 1850 and 1920 cm^{-1} for the 5C and 6C ls-$\{FeNO\}^6$ complexes $[Fe(TPP)(NO)]^+$ and $[Fe(TPP)(NO)(MI)]^+$, respectively, as shown in Figure 52. Using this method, a greatly enhanced stability of the ls-$\{FeNO\}^6$ model complexes was observed, with kinetic NO off rates that are now equal or better than those of corresponding ferric NO adducts in heme proteins.[655] It was further rationalized that the enhanced stability of the ls-$\{FeNO\}^6$ model complexes observed in these experiments is due to the absence of any halide and other impurities in the preparations that start from the ls-$\{FeNO\}^7$ precursors (when used in pure form). The enhanced stability of the ls-$\{FeNO\}^6$ complexes generated in this way, especially the fact that they are stable in the absence of excess NO, is advantageous, as this enables reactivity studies of the complexes with reagents that are otherwise sensitive towards free NO in solution.[655]

Recently, ferric rNPs have been shown to catalyze an unusual reaction, the dismutation of nitrite (with second order rate constants of 0.13 and 0.076 M^{-1} s^{-1} for NP4 and NP7 at pH 7.0, respectively), following the reaction (see Figure 53):[842]

$$3NO_2^- + 2H^+ \rightarrow NO_3^- + 2NO + H_2O \qquad (13)$$

While this reaction is unexpected, related chemistry is not unprecedented since Hb and Mb exhibit nitrite reductase and proposed nitrite anhydrase activity,[140] where NO_2^- can be reduced to NO in mammals, making it a viable source of NO

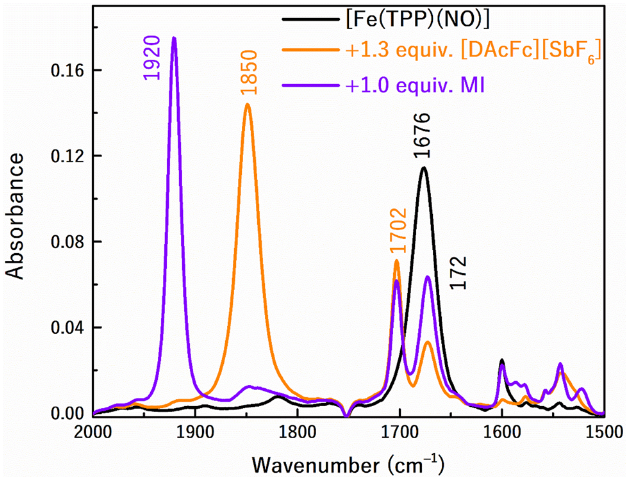

Figure 52. Solution IR spectroscopy of the oxidation of 5C [Fe(TPP)(NO)] (black) to [Fe(TPP)(NO)](SbF_6) (orange). Formation of 6C [Fe(TPP)(MI)(NO)](SbF_6) (purple) is observed upon addition of 1 equiv of MI. Adapted from ref 655. Copyright 2017 American Chemical Society.

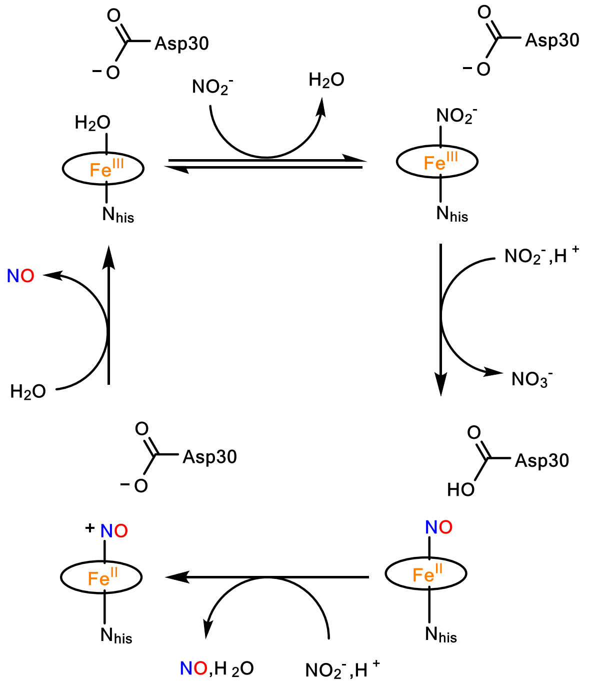

Figure 53. Proposed reaction mechanism of nitrite dismutation by rNP4.[841]

(see Section 4.1). Since nitrite is naturally present in blood (150−600 nM),[843] rNPs could therefore, in principle, use nitrite dismutation to produce additional equivalents of NO after releasing their initial cargo into the victim's wound.[844] The first crystal structures of nitrite-bound rNP4 and rNP7 demonstrated that nitrite binds in the η^1-*N* nitro form to the ferric rNP hemes (see Figure 54), in opposite to the η^1-*O* nitrito binding mode observed in met-Hb and met-Mb (see Section 4.1).[842] This difference in nitrite coordination originates from differences in the hydrogen-bonding residues in the SCS of the heme pocket. Note that the η^1-*N* nitro binding mode is intrinsically preferred by ferric hemes, as observed in model complexes.[845] Since the heme pocket of rNPs contains a number of carboxylate residues, further stabilization of the η^1-*N* nitro ligand likely results. To test the impact of the SCS on the ability of rNPs to dismute nitrite, the L130R rNP4 variant was also investigated.[846] While the crystal structure of the variant indicates that the η^1-N nitro binding mode is preserved, the L130R mutant leads to the complete loss of nitrite dismutation activity. In this case, the mutation causes Asp30 in the AB loop to shift, resulting in a loss of two hydrogen-bonded H_2O molecules in the distal pocket,[846] which were proposed to be crucial for enabling proton transfer to the active site. This conclusion is further supported by the decreased nitrite dismutation activity observed for the D30N rNP4 variant.[846]

In elucidating the reaction mechanism of nitrite dismutation in nitrophorins, the electronic structure of the nitrite-bound ferric heme precursor complex of rNP4 was studied using EPR and electronic absorption spectroscopy.[841] The EPR data taken at 20 K revealed that the complex is ls ferric (S_t = 1/2), exhibiting a highly rhombic EPR signal with g values of 2.74, 2.42, and 1.51.[842] In contrast, room temperature UV−vis spectra of the nitrite adduct exhibit the Soret band at 404 nm, indicative of a hs ferric heme. Further spectroscopic analysis then showed that the nitrite adduct of ferric rNP4 exists in a 7:3 hs/ls equilibrium in solution at room temperature.[841] On the basis of these data, it was proposed that the variation in spin state results from the dynamic coordination mode of NO_2^- in the resting state, where the ls species corresponds to the η^1-*N* nitro complex, whereas the hs species features the η^1-*O* nitrito binding mode. Here, the η^1-*O* nitrite-bound hs ferric heme complex is proposed to be the active form in the nitrite dismutation process; however, more work is needed to confirm these ideas. The reaction itself was determined to correspond to a two-step process (see Figure 53). In the first step, a molecule of nitrite binds and then donates an O atom via oxygen-atom transfer to a second molecule of nitrite to form nitrate and the corresponding ls-$\{FeNO\}^7$ complex. On the basis of reaction kinetics, nitrite binding to the ferric heme is a second order process with respect to nitrite concentration, with a rate constant k of 863 M^{-2} s^{-1}, supporting the consumption of two molecules of NO_2^- in the first step.[841] This step of the reaction also exhibits a pH dependence (first order) with a rate constant of 8.1 M^{-1} s^{-1}.[841] On the basis of further EPR and ^{1}H-ENDOR studies, it was proposed that the crucial Asp30 residue becomes protonated in this first step of the reaction. In the second step, a third molecule of NO_2^- supposedly binds to the iron center in a first order reaction (with respect to nitrite concentration; k = of 0.071 M^{-1} s^{-1}) to release the first molecule of NO and water.[841] Next, it is proposed that proton transfer occurs to the coordinated nitrite (k = 5.87 × 10^3 M^{-1} s^{-1}), forming the second molecule of NO in a corresponding 6C ls-$\{FeNO\}^6$ complex.[841] The last step of the reaction therefore follows the well-known nitrite reduction reaction of ferrous hemes (see Section 4.1). More work is clearly needed to confirm the different steps of the reaction, in particular the unusual O-atom transfer between two nitrite ions.

In addition to the vital Asp30 residue in the distal pocket of nitrophorins, rNP2 and rNP4 were also studied to understand the effect of the proximal histidine donor strength on nitrite dismutation.[847] Here, the Asp70 residue was established as an important hydrogen-bond acceptor to the proximally-bound His ligand in rNP4 (see Figure 54). Because of the electron donating nature of Asp70, the axial His ligand becomes (somewhat) anionic and therefore a stronger donor. This is comparable to the role of the corresponding Asn68 residue in

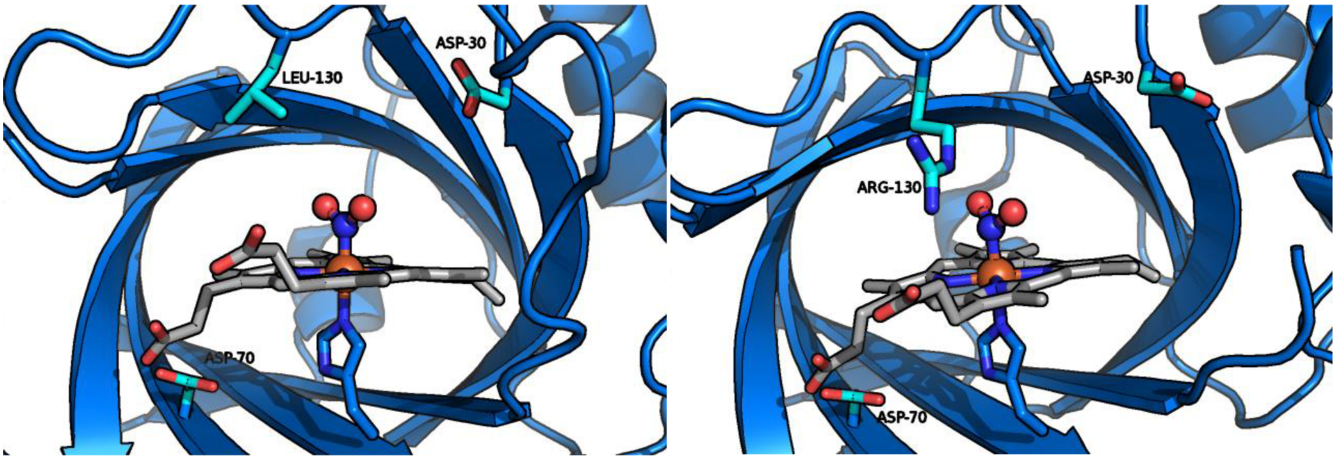

Figure 54. PyMOL generated images of the crystal structures of the active sites of wt ferric rNP4 (PDB: 3MVF, left) and of ferric L130R rNP4 (PDB: 3TGC, right) with bound nitrite.

rNP2. Mutation (removal) of the Asp70 residue in rNP4 then results in a neutral His. The effect of the His donor strength is reflected in the initial rate constant for nitrite dismutation, which increases from 0.023 to 0.07 min^{-1} in wt versus D70A rNP4. In wt rNP2, the initial rate constant is 0.083 min^{-1}.[847]

2.4. Nitric Oxide Storage

Following NO release from nitric oxide synthase, NO must be transported and stored due to its short lifetime within a cell.[848] As NO is highly reactive and short-lived, it may be stored in other forms, including nitrogen oxides, *S*-nitrosothiols, and metal−nitrosyl complexes. Upon release from these storage vessels, NO may be used for its desired functions. Delivery of NO externally has also been studied due to its physiological roles *in vivo* and possible applications in therapeutics. Synthetic NO donating biomaterials have been shown to be a solution for biocompatibility problems of implants, as these devices tend to induce unwanted responses in the body, which can be lessened with NO.[849] Thus, the storage and tunable release of these NO reservoirs, including *S*-nitrosothiols, may constitute a powerful strategy to counteract the body's response to biomedical materials and implants.[850]

Table 13. Proposed Mechanisms for Various Pathways Responsible for the Reduction of Nitrite to Form NO

pathway	proposed mechanism	ref
deoxy-Hb, deoxy-Mb, deoxy-Ngb, and deoxy-Cygb	$NO_2^- + Fe^{2+} + H^+ \rightarrow Fe^{3+} + NO^\bullet + OH^-$	220, 853, 886, 887
proton	$NO_2^- + H^+ \rightarrow HNO_2$	888
	$2HNO_2 \rightarrow H_2O + N_2O_3$	
	$N_2O_3 \rightarrow NO^\bullet + {}^\bullet NO_2$	
carbonic anhydrase	$2NO_2^- + 2H^+ + 2HNO_2 \leftrightarrow H_2O + N_2O_3$	854
	$N_2O_3 \leftrightarrow NO^\bullet + {}^\bullet NO_2$	
Cyt. P450	$RONO + H_2O \rightarrow ROH + HNO_2$	889
	$HNO_2 + H^+ + CP \rightarrow NO^\bullet + H_2O + CP$	
Cyt. *c*	$NO_2^- + 2H^+ + Fe^{2+} \rightarrow Fe^{3+} + NO^\bullet + H_2O$	23
xanthine oxidase and aldehyde oxidase	$NO_2^- + 2H^+ + Mo^{4+} \rightarrow Mo^{5+} + NO^\bullet + H_2O$	855
polyphenol	$PhOH + HNO_2 \rightarrow PhO^\bullet + NO^\bullet + H_2O$	890

2.4.1. Nitrate and Nitrite.

More recently, there has been evidence for NO sources outside of NOS. A study was conducted relating hemolysis and eNOS deficiency in red blood cells (RBCs), because NO derived from a functional eNOS was thought to be important in RBC viability and function.[851] Gladwin and coworkers found that RBC eNOS does not modulate susceptibility to hemolysis, suggesting that the relevant NO production is more likely to occur through reduction of nitrate or nitrite than through an eNOS pathway.[851] Nitrite reduction to NO has been previously discussed in detailed reviews.[23,852] Nitrite was initially viewed as a biologically inert end product to nitric oxide synthase. There is evidence, however, that nitrite is able to be reduced to form NO through several different pathways that include the proteins deoxy-Hb,[220] deoxy-Mb,[853] carbonic anhydrase,[854] xanthine oxidase,[855] aldehyde oxidase,[855] and others (Table 13). In particular, proteins such as deoxy-Hb and deoxy-Mb undergo reduction of nitrite to form NO and H_2O (see Section 4.1). Other enzymes exist that require multiple steps to convert nitrite to NO. Carbonic anhydrase, for example, is dependent on acidic conditions to form the intermediate HNO_2, followed by the formation of H_2O and N_2O_3, and reaction to NO (see Table 13).[854] These pathways have been studied and observed in physiological processes like ischemia and hypoxia.[220,854,856−864] In environments lacking dioxygen, deoxy-Hb and deoxy-Mb have been observed to reduce nitrite to NO.[865] This suggests that the reaction to convert nitrite to NO is dependent upon Hb and Mb deoxygenation. In the case of hypoxic vasodilation, dioxygen is deprived in the body. Many experiments have shown that NO is generated under these conditions from different sources, such as Hb and Mb, and serves as a signaling molecule.[220,853,856,859−862,866−885] The Hb-mediated reduction of nitrite was hypothesized to be a main mechanism for increased NO production during hypoxia to induce vasodilation, and hence, an increase in blood flow to the hypoxic tissue. Alternatively, it has also been suggested that this phenomenon may be mediated by NO metabolites.[891] Separately, both neuroglobin (Ngb)[892−896] and cytoglobin (Cygb)[887,897−900] were found to trigger a response to processes such as oxidative and ischemic stress and support nitrite reduction to NO. Separately, molybdenum-containing enzymes like xanthine oxidase[855,864,901−905] and aldehyde oxidase[855] have been observed to reduce nitrite.

There are two main sources of nitrate that are known, one of which is by way of NO oxidation by oxy-Hb or oxy-Mb (see Section 2.5). The nitrite (produced by NO oxidation) can undergo further oxidation through oxy-Hb or oxy-Mb to form nitrate.[906] The majority of nitrate present in the body is due to dietary intake, with vegetable and water consumption being the most significant carriers of nitrate.[907,908] As the body does not contain any enzymatic nitrate reductases, bacteria are the source responsible for the reduction of nitrate within the human body.[909] Bacteria commonly found in the salivary glands are able to mediate nitrate reduction.[907,910] A study was performed on the levels of nitrate, nitrite, and *S*-nitrosothiol in saliva, plasma and urine, after ingestion of inorganic nitrate.[907] Notably, the nitrite levels in plasma increased 4-fold after consumption of sodium nitrate. However, when the sodium nitrate was not orally digested, the nitrite level did not change significantly. Although nitrate was thought to be biologically inert and possibly carcinogenic,[911] this experiment shows that nitrate can undergo reduction to nitrite (eq 14):

$$NO_3^- + 2e^- + 2H^+ \rightarrow NO_2^- + H_2O \qquad (14)$$

After reduction to nitrite, beneficial effects can be observed by further reduction to the signaling molecule NO. There is a recent, detailed review on the pathways involved in nitric oxide generation from nitrate and nitrite.[912]

2.4.2. *S*-Nitrosothiols. The reaction of NO with free thiols is too slow to have significant biological significance.[913,914] Using anaerobic solutions of NO, Wink and coworkers demonstrated that NO is not capable of nitrosating Cys or glutathione (GSH).[913] However, when aerobic solutions of NO are used, *S*-nitrosothiols ("RS−NO" adducts) from Cys and GSH were observed to form readily ($k_{SNO} \sim (6 \pm 2) \times 10^6$ M^{-2} s^{-1}). This reaction is known as "*S*-nitrosylation" or "*S*-nitrosation". The rapid formation of these RS−NO adducts can be monitored with UV−vis absorption spectroscopy, via their absorption bands at 388 nm.[915,916] The authors propose that the nitrosation reaction of these thiols is caused by nitrogen oxide (NO_x) intermediates, especially the known nitrosating agent N_2O_3, generated in the reaction of free NO and O_2.[913]

Another reaction that NO has been proposed to undergo once it is bound to a ferric heme, generating a ferric heme−nitrosyl complex, is the transfer of NO oxidatively (as NO^+) to cysteines, forming bioactive *S*-nitrosothiols.[917−919] This reaction is enabled by the Fe(II)−NO^+ type electronic structure of heme ls-$\{FeNO\}^6$ complexes, which feature an electrophilic NO^+ ligand that is reactive towards various nucleophiles (such as water, hydroxide, alcohol, amines, thiols, etc.), as described in Section 2.3. The *S*-nitrosation reaction has been shown to be a part of diverse physiological pathways based on NO-bound cysteine (Cys−NO). Utilizing UV−vis absorption spectroscopy and kinetic measurements, Reichenbach and coworkers further demonstrated *S*-nitrosation of GSH with Mb(III)−NO, the ls-$\{FeNO\}^6$ complex of met-Mb, generating GS−NO.[920] The obtained, second-order rate constant for this reaction is 47 ± 1 M^{-1} s^{-1}. Free RS−NO compounds, especially free Cys−NO and *S*-nitrosoglutathione (GS−NO), serve as a common carrier for NO in tissues and allow for distribution through extracellular fluids and into cells.[917−919] However, the main *S*-nitrosoprotein carrying NO within the plasma is believed to be serum albumin. Cys from serum albumin was hypothesized to react with NO due to its abundance in plasma and low pK_a. In plasma, such *S*-nitrosoproteins serve as a long-lived reservoir for NO in comparison to the short lifetime of NO itself.[921] Transferring NO from the *S*-nitrosoproteins to low-molecular-weight thiols like glutathione, leading to the formation of GS−NO, was reported to promote the release of NO.[921]

S-Nitrosothiols are involved in several physiological processes, for example, in the cardiovascular system.[224,922] RS−NO can also play an important role for signal transduction during various cellular processes through transnitrosation, the process of transferring NO from one thiol to another,[839] especially the *S*-nitrosylation of proteins.[923] This allows pathways to induce NO bioactivity far from the location of NO generation.[919,924,925] For example, this process has been proposed to be important for local relaxation of smooth muscle tissue under hypoxic conditions, allowing the muscle to undergo hypoxic vasodilation, and in this way, increase the blood flow in hypoxic tissue.[140,229] Although it is well known that NO signaling can occur through the *S*-nitrosylation of proteins, the mechanism for delivery is disputed. Tannenbaum and White discuss two main mechanisms through which NO signaling occurs.[926] In one model for *S*-nitrosylation of proteins, the formation of the RS−NO bond occurs directly through a protein-protein interaction (i.e., interaction between a NOS and a target protein) with structural motifs and allosteric control driving the NO transfer and specificity.[927] The second model occurs through multiple steps. NO produced by NOS first reacts with the thiyl radical of glutathione to form GS−NO,[928] which then reacts with thioredoxin to form nitrosylated thioredoxin.[929] The subsequent complexation of the nitrosylated thioredoxin with a target protein allows internal NO transfer to yield an *S*-nitrosylated protein and thioredoxin. In this model, protein disulfide isomerase is proposed to be a regularoty partner as it catalyzes denitrosylation.[930−932] More recently, *S*-transnitrosation has also been proposed as a contributing factor in neurodegenerative diseases.[204]

Nitric oxide donating materials have been useful in biomedical devices.[933] Often times, these devices are unreliable due to unwanted responses in the body. Thus, the release of NO can be used to counteract the body's response, for example blood clotting. *S*-nitrosothiols have been shown to be beneficial NO donors for these applications[225] Several *S*-nitrosothiol NO donors are commercially available (Figure 55). Although these NO donating materials are limited by the length of time that NO can be released, a recent report by Hopkins and Frost demonstrates the ability of NO release for longer periods of time through modification of *S*-nitrosothiols with hyperbranched polymers.[934] Implementing biomedical devices with NO donating polymers can increase longevity. Another approach is to equip the biomedical devices, especially catheters, with a small electrochemical cell for electrocatalytic reduction of nitrite to NO, using copper catalysts that are inspired by the active site of CuNIRs.[935−937] This allows for a more controlled production of NO on demand.

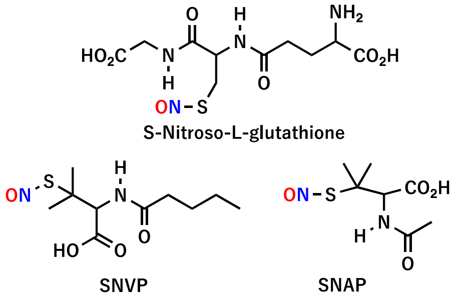

Figure 55. Commercially available NO donors including SNVP,[938] *S*-Nitroso-L-glutathione,[939] and SNAP.[940]

2.4.3. Nitrosamines. Like *S*-nitrosothiols, nitrosamines have also been demonstrated to have therapeutic effects *in vitro*. A number of nitrosamines, known as NONOates, have been synthesized and displayed beneficial results due to having NO-donating properties. These compounds include commercially available *β*-Gal-NONOate,[941] DEA,[942] DETA,[943] MAHMA,[943] PAPA,[943] spermine,[942] PROLI,[944] SULPHO,[942] and DPTA[943] NONOates (Figure 56). Delivering DETA NONOate to adult rats after a stroke, for example, led to increased neurogenesis and cell proliferation, indicating involvement of nitric oxide in these processes and demonstrating the positive effects of using synthetic nitrosamines as therapeutics.[945] Additionally, DETA NONOate was shown to inhibit the growth of tumor cells.[946] NONOates also effect other physiological processes such as glucose transport and metabolism.[947]

2.4.4. Metal−Nitrosyl Complexes. Metal−nitrosyl complexes have been known to be carriers of NO and play an integral part in NO signaling *in vivo*. They also serve as complexes for biomedical applications. Non-heme iron−nitrosyl and dinitrosyl iron complexes (DNICs) are two major classes of metal−nitrosyl complexes that have important roles in NO delivery. These two classes are discussed in further detail in other sections of this review.

The binding of NO to metalloproteins is not limited to iron centers. Copper-containing proteins are involved in the formation, consumption, and regulation of NO as well. For example, CuNIR converts NO_2^- to NO at its type II copper site in bacterial denitrification.[275] CuNIR can also convert NO to N_2O under excess NO,[142] although the reduction of NO to N_2O in the nitrogen cycle is primarily mediated by iron-containing NO reductases (see Section 4). It is long known that NO can bind to type I copper sites of electron transfer proteins.[948] Interestingly, a recent back-to-back publication by two research groups demonstrated that type I copper sites can interconvert NO and S-nitrosothiols (RSNO).[949,950] By employing model complexes based on hydrotris(pyrazolyl)-borate copper thiolate complexes, Warren and coworkers demonstrated that copper mediates the interconversion between NO and RSNO through the reversible insertion of NO into a Cu^{II} thiolate bond, Cu(II)−SR, to form a crystallographically characterized copper(I) *S*-nitrosothiol adduct, Cu(I)−N(O)−SR.[950] Complementary to this model complex study, Lu and coworkers reported spectroscopic evidence for the analogous NO binding at a type I copper site in an engineered azurin, which efficiently captures NO in its cupric form as the analogous Cu(I)−N(O)−Cys adduct.[949] These results imply a potential role of type I copper sites in NO signaling where NO serves as an on/off switch for the electron transfer functions of these proteins.[949−951] It has been suggested that bacteria may prevent high concentrations of NO by utilizing this feedback loop in which NO binding to the type I copper center of azurin could potentially inhibit electron transfer to nitrite reductase, resulting in a downregulation of NO production.[951]

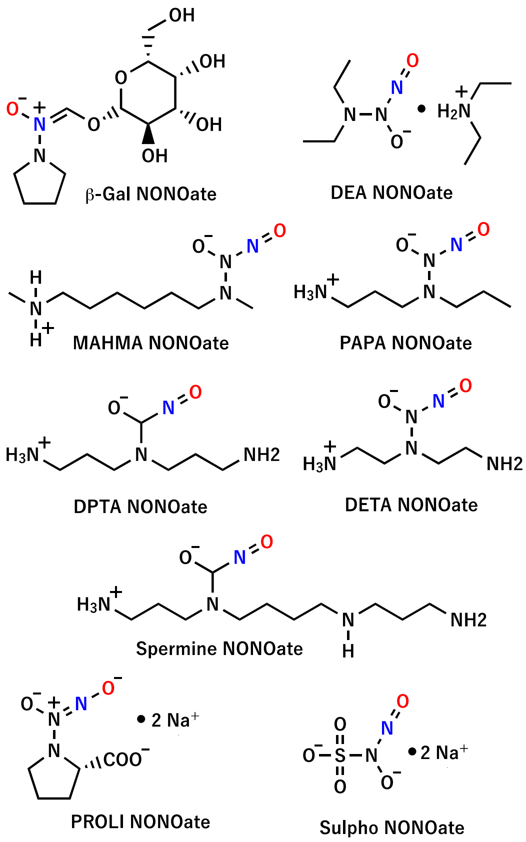

Figure 56. Commercially available nitrosamine NO donors.

Another class of metal−nitrosyl complexes that has been demonstrated as useful NO-releasing complexes are metal organic frameworks (MOF). The open coordination sites of the metals in the porous MOFs allow for binding of NO. These complexes are able to have high adsorption with ∼7 mmol of NO/g of MOF while also being extremely stable.[952] Release is triggered upon exposing these dry MOFs to moisture. Tunability of the structure of MOFs, reviewed by Seabra and Duran, also allows for controlled release of NO for specific biological applications.[953] Finally, many ls-$\{RuNO\}^6$ and ls-$\{MnNO\}^6$ complexes have shown utility as light-triggered NO delivery platforms for photodynamic therapy.[795,797,800,954−962]

2.5. Nitric Oxide Oxidation/Detoxification in Mammals: Peroxynitrite as a Key Intermediate

2.5.1. Nitric Oxide Dioxygenation (NOD). The biosynthesis of excess NO via NOS is deleterious for human health, and correspondingly, NOS activity is closely regulated by a variety of mechanisms (see Section 2.1). Similarly, NO produced in the endothelium would accumulate in the blood and become toxic, once it reaches a μM threshold. Therefore, detoxification mechanisms for NO are required as well, to firmly control its concentration in the body. A vital pathway for scavenging excess NO under aerobic conditions is its reaction with a variety of globins, through a process known as NO dioxygenation (NOD), which is an O_2-dependent metabolic pathway in mammalian cells.[963] In this reaction, NO is converted to nitrate, following eq 3. On the other hand, certain bacteria, for example *E. coli*, use flavohemoglobins (flavoHb) as scavengers to defend against nitrosative stress,[180,184,185,964−968] which was first reported in 1998 by Gardner and coworkers.[969] In mammals, the NOD reaction can be catalyzed by a variety of globins, depending on cell type, including Hb, Mb,[184,970] Cygb, Ngb, and truncated hemoglobins (trHb).[971] In red blood cells, excess NO (from the endothelial cells) reacts with oxy-Hb. The bimolecular reaction of NO with Hb(II)−O_2 or Mb(II)−O_2 displays a large second order rate constant of (6−9) × 10^7 M^{-1} s^{-1},[184,185] which is only limited by the diffusion of NO into the heme pocket of the globin. This NOD process is in fact faster than the reaction of NO with free O_2 in aqueous solution

Scheme 20. Proposed Mechanism for Nitric Oxide Dioxygenation (NOD)[a]

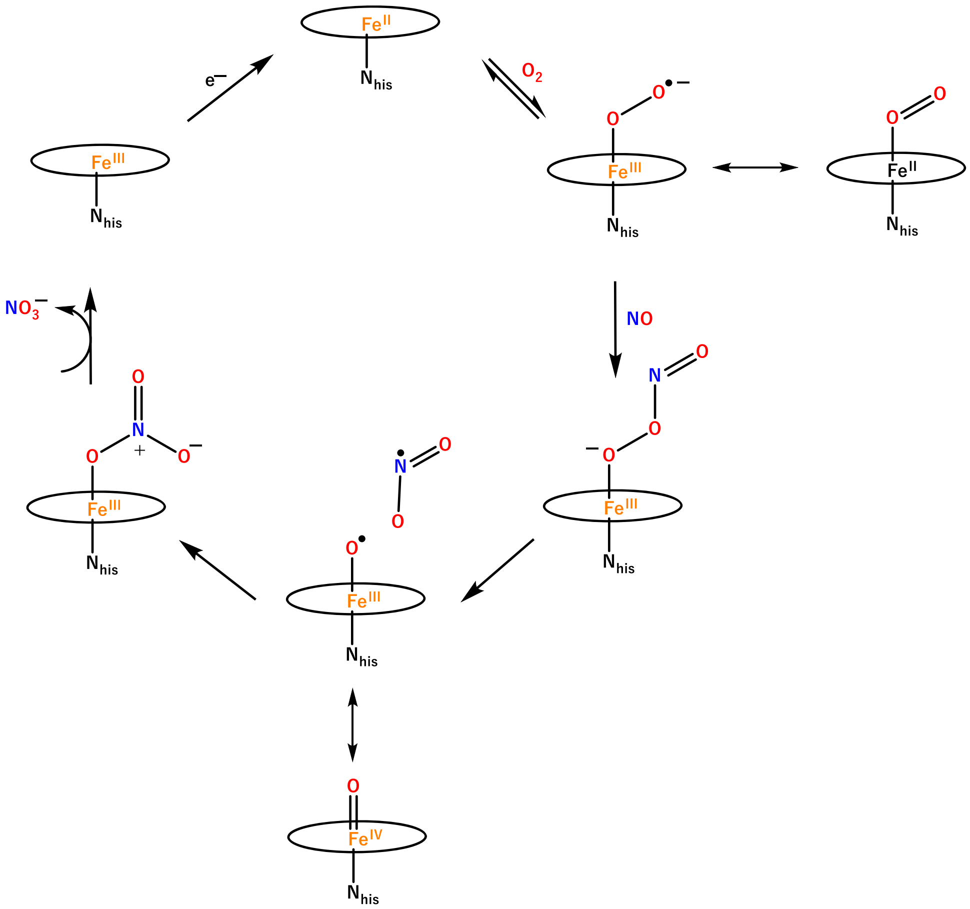

[a] This "high-fidelity" NOD mechanism involves peroxynitrite decomposition via a caged radical intermediate. A concerted rearrangement via a different transition state may also be possible.[973]

(k_{2NO+O2} ~ 6.3 × 10^6 M^{-2} s^{-1}),[972] especially considering the third-order kinetics of this process, but slower than the direct reaction of NO with free superoxide ($k_{NO+O2(-)}$ ~ 6.7 × 10^9 M^{-1} s^{-1}).[197,198]

The reaction of oxy-globins with NO is generally believed to follow the "high fidelity NO dioxygenation" mechanism proposed by Gardner and coworkers, which is shown in Scheme 20.[967,973] Here, the heme-bound O_2, which has partial superoxide character, Fe(III)−$O_2^{\bullet -}$,[974−979] reacts with NO following a radical-radical coupling mechanism (between $NO^{\bullet}$ and Fe(III)−$O_2^{\bullet -}$) to form a peroxynitrite complex, Fe(III)−$OONO^-$, which is a highly reactive intermediate. This is followed by an isomerization event, either (a) concerted or (b) via O−O bond homolysis, forming a caged, short-lived [Fe^{IV}=O $^{\bullet}NO_2$] intermediate. In the latter case, a fast-radical rebound step then yields the Fe−bound nitrate product as shown in Scheme 20. Finally, fast nitrate release generates the met form of the globin. According to this mechanism, the reaction of Hb(II)−O_2 with NO produces NO_3^- stoichiometrically. Isotope labeling experiments further support the overall mechanism shown in Scheme 20, and demonstrate that the two O atoms of bound O_2 are in fact incorporated into the NO_3^- product, via a proposed Fe(III)−peroxynitrite intermediate.[967,980] Since the NO released from the endothelial cells into the blood depletes oxy-Hb, this could, in theory, lead to a dangerous impairment of O_2 transport in RBCs. However, one has to keep in mind that the NO concentration is in the nanomolar range, compared to the millimolar concentration of oxy-Hb.[981] Therefore, under normal physiological conditions, the depletion of oxy-Hb in blood due to endothelial NO is miniscule. However, this can change in certain disease states. In particular, in sepsis, which is an acute infection of the blood, larger amounts of NO are produced as part of the immune response, and this can lead to severe impairment of the blood oxygenation level.[208,982] In animals studies, high NO concentrations from septic shock lead to vasodilation, hypotension, cardiovascular dysfunction, bioenergetic failure, and cellular toxicity, overall contributing to organ failure.[208] It has been shown that patients with septic shock have high plasma nitrite and nitrate concentrations, which is an indication of enhanced NOD activity due to greatly elevated NO levels in the body.[983]

The NOD mechanism has been a controversial topic, both with respect to peroxynitrite formation and the following steps of the reaction. The Fe(III)−peroxynitrite intermediate was first proposed based on stopped-flow UV−vis[185,984,985] and EPR data, obtained for the reaction of Mb(II)−O_2 or Hb(II)−O_2 with NO at various pH (5−9), with an increased stability of the proposed intermediate at higher pH.[967] Here, a transient hs ferric species with a g_{eff} = 6 signal was observed, which was assigned to the Fe(III)−$OONO^-$ intermediate.[967] The putative Fe(III)−$OONO^-$ intermediate from the reaction of Mb(II)−O_2 and NO was further characterized using stopped-flow experiments, coupled to RFQ-rRaman spectroscopy.[986] These studies identified the same species that forms on the millisecond time scale and that was previously assigned to the ferric peroxynitrite intermediate. Importantly, RFQ-rRaman spectroscopy identified a peak at 1282 cm^{-1} for this intermediate, which shifts to 1260 cm^{-1} upon isotope labeling.[986] This mode corresponds to a ν(N−O) stretching vibration of an Fe(III)−nitrato complex, and is not likely associated with a Fe(III)−peroxynitrite species.[987,988] This indicates that peroxynitrite isomerization is either too fast to be observed by stopped-flow measurements, or that such an intermediate does not form in the reaction of oxy-Hb/Mb and NO. In addition, these results show that the ferric nitrate complex formed at the end of the reaction has a surprisingly short life time, with nitrate being quickly released from the ferric heme pocket.

Other studies used a shunt reaction, that is, the reaction of a ferric globin with pre-formed peroxynitrite, to obtain further insight into the second step of the NOD process (according to Scheme 20), which is the peroxynitrite isomerization. Here, the decomposition of peroxynitrite can be monitored by UV−vis spectroscopy, using a characteristic absorption band at 302 nm, at pH 7.6. In these experiments, it is generally observed that the presence of met-Mb accelerates peroxynitrite decomposition ($k \sim 1.03 \times 10^4$ M^{-1} s^{-1}),[989] leading to the formation of 80% nitrate and 20% nitrite, which was taken as initial evidence that a Fe(III)−peroxynitrite complex does form in the process. Using stopped-flow UV−vis absorption spectroscopy to follow the reaction of met-Mb with peroxynitrite, Groves and coworkers were able to show that peroxynitrite isomerization proceeds via a caged radical intermediate.[990] Here, rapid generation of Compound II, the ferryl Mb(IV)=O complex, was demonstrated, with a second order rate constant of $k \sim 1.0 \times 10^4$ M^{-1} s^{-1}.[990] Upon reaction with peroxynitrite, UV−vis spectra show a shift of the Soret band of met-Mb from 409 to 425 nm and a decrease in the intensity of the Q-band at 503 nm, which is accompanied by the simultaneous appearance of new absorption features at 570 and 590 nm. The ferryl Mb(IV)=O intermediate was further confirmed by reacting it with ascorbate (in a double mixing stopped-flow experiment), leading to its reduction back to met-Mb with a rate constant of $k \sim 4.2$ M^{-1} s^{-1}. This rate constant is very similar to that of the known reaction of Compound II of Mb with ascorbate ($k \sim 2.7$ M^{-1} s^{-1}), which was independently determined.[991] Interestingly, in the reaction of met-Mb with peroxynitrite, nitration of Tyr103 is also observed, which can be explained by the escape of some of the NO_2 from the caged radical pair.[990] In short, these results are consistent with the mechanism involving a caged [Fe^{IV}=O $^{\bullet}NO_2$] radical pair intermediate that either dissociates into Fe(IV)=O and NO_2 (cage escape of 10%), or isomerizes to met-Hb and nitrate (the major products).[179] An alternative mechanism, proposed by Herold and coworkers, suggests the direct decay of the Fe(III)−peroxynitrite intermediate to ferric heme and nitrate, following a concerted pathway.[185,992,993] They demonstrated that when reacting peroxynitrite with high concentrations of met-Hb/Mb (200−750 μM), nitrite is not generated. It was proposed that this is due to the fact that under these conditions, peroxynitrite decomposition proceeds entirely via the protein-catalyzed pathway, and that nitrite is only formed from the decomposition of free peroxynitrite in solution. Only nitrate is formed in quantitative yield, which is a finding that is not in agreement with the mechanistic conclusions of Groves and coworkers.[989] This direct decay of the Fe(III)−peroxynitrite intermediate is also supported by a study by Pietraforte et al., who observed quantitative nitrate yields from the decay of 100 μM peroxynitrite in the presence of 500 mM met-Hb at pH 7.4.[994]

In summary, despite much efforts in the field, the exact mechanism of the NOD reaction of oxy-Hb/Mb is still not clear. Studies on the reaction of met-globins with peroxynitrite support formation of an initial peroxynitrite intermediate, followed by peroxynitrite isomerization to nitrate, likely via a caged [Fe^{IV}=O $^{\bullet}NO_2$] radical pair intermediate. Curiously, when oxy-Hb/Mb are reacted with NO, none of these intermediates are observed. For example, Pacheco and coworkers performed time-resolved UV−vis experiments on the reaction of oxy-Mb and NO, and no ferryl Mb(IV)=O intermediate could be detected (in agreement with results from Yukl et al.).[986,995] The different product distribution from the reaction of oxy-Hb/Mb with NO versus that of met-Hb/Mb with peroxynitrite is an indication that NOD may follow isomerization via a concerted mechanism, following formation of the Fe(III)−$OONO^-$ intermediate. One possible explanation for these discrepancies is that the nature of the Fe(III)−$OONO^-$ intermediate differs in these two reactions. Free peroxynitrite exists mostly in the trans form in solution, so in the reaction of free peroxynitrite with met-Hb/Mb, the corresponding trans complex would likely form.[996] In contrast, reaction of oxy-Hb/Mb with NO might generate the *cis* Fe(III)−$OONO^-$ intermediate. This aspect was further elucidated using DFT calculations (see below).

Recently, another globin, Cygb, has been shown to have a high NOD reactivity.[899,998] While Hb and Mb have major roles in NO degradation in RBCs and in skeletal and cardiac muscle, respectively, Cygb has been shown to have an important NOD role in vascular smooth muscle cells (VSMCs), which is critical for vasorelaxation and vascular tone. Unlike met-Hb and met-Mb, which contain 6C heme centers with a distal water ligand, met-Cygb contains a 6C heme with bis-His coordination, with His81 and His113 serving as the proximal and distal ligands, respectively.[998] Similar to Ngb and Hb, Cygb has an allosteric O_2 binding mechanism (Figure 57), where two exposed cysteine residues (Cys38 and Cys83) can generate intra- and intermolecular disulfide bonds, the latter resulting in a homodimer form.[998] The formation of the disulfide has been shown to increase the dissociation rate of the distal His, resulting in a higher apparent extrinsic ligand affinity, similar to Ngb.[999] Cygb therefore has a conformation-dependent O_2 binding affinity, and correspondingly, its NOD reactivity is limited by the rate of the distal His dissociation (after reduction to the ferrous form), which is in the order of 1−2 s^{-1}, and which is then followed by O_2 binding (Scheme 21).[997−999] This is related to the proposed, redox-sensitive O_2 binding mechanism of Cygb. Redox or chemical modification of the exposed Cys residues has been shown to modulate the O_2 binding affinity and accordingly, NOD activity of Cygb.[1000] The reaction of Cygb(II)−O_2 itself with NO is fast, with a rate comparable to that of Mb(II)−O_2.[998,1001]

To find further evidence for the formation of a peroxynitrite complex and study its properties, scientists investigated other [M^{II}(Porph)] complexes (M = Fe, Co, Mn).[181,182,1002,1003] For example, Kurtikyan et al. investigated the NOD reaction using Co-porphyrins, [Co(Porph)(NH_3)(O_2)], as model compounds ($Porph^{2-}$ = TPP^{2-}, TTP^{2-} = tetratolylporphyrin dianion).[181] Utilizing sublimed thin films of the respective O_2-bound Co-porphyrin on KBr at low temperature, they then introduced small amounts of NO into the gas phase at 80−120 K and

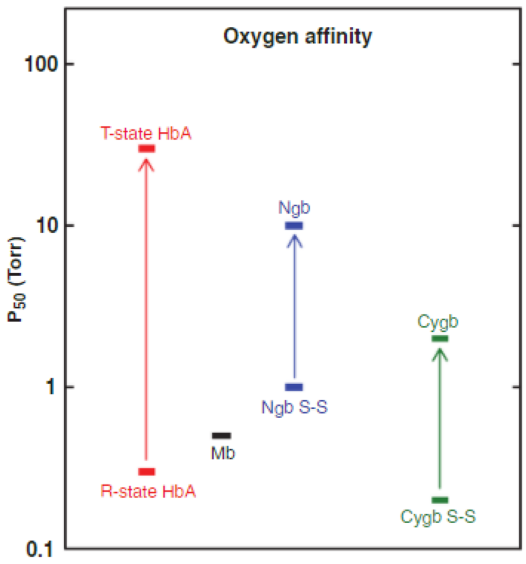

Figure 57. Dioxygen binding affinity for various allosteric states of members of the globin family. For Cygb, the dioxygen affinity is within physiological range, supporting a role in NOD activity. Reprinted with Permission from ref 997. Copyright 2010 American Chemical Society.

Scheme 21. Proposed Mechanism for Cygb-Mediated NO Consumption[a]

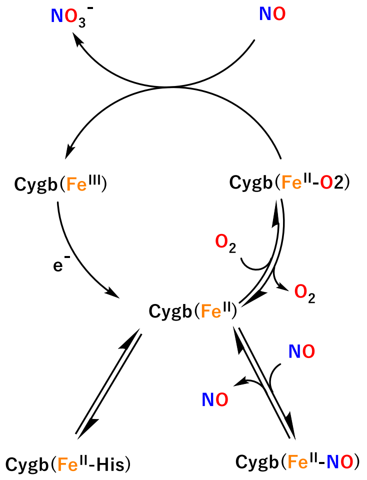

[a] Met-Cygb may be reduced by various reducing systems to produce Cygb(II). Once reduced, Cygb(II) establishes an equilibrium with available ligands such as O_2, NO, or the distal His residue. Cygb(II)−O_2 is the catalytically active species for oxidation of NO to NO_3^-.[998]

followed the reactions by IR spectroscopy.[181] New IR bands at 1596, 954, 740 and 544 cm^{-1} were observed to grow in, and using isotopically labeled $^{18}O_2$, ^{15}NO and $N^{18}O$ and DFT calculations, it was confirmed that these new bands correspond to the 6C Co(III)−peroxynitrite complex, $[Co(Porph)(NH_3)(OONO)]$ (see Table 14).[181] Upon warming (140 to 170 K), $[Co(Porph)(NH_3)(OONO)]$ decomposed to a new species with IR bands at 1480, 1270 and 980 cm^{-1}, which, using again isotope labeling and DFT calculations, were shown to belong to the corresponding 6C Co(III)−nitrato complex. Similar low-temperature (80−120 K) studies were also performed with Mn-porphyrins, and a corresponding 6C peroxynitrite complex was again generated, with IR bands at 1582, 787, and 480 cm^{-1} (see Table 14).[1002] These studies not only demonstrate that Co- and Mn-porphyrins are able to model the NOD reaction, but they also support the proposed mechanism of this process shown in Scheme 20. Recently, Karlin and coworker were able to trap and study an Fe(III)−peroxynitrite complex by adding NO to a stable 6C ferric superoxo complex, $[Fe(To\text{-}F_2PP\text{-}BzIM)(O_2)]$ (note that the ligand is called P^{Im2-} in their report), in THF at low temperatures (−80 °C).[182] The putative Fe(III)−peroxynitrite complex exhibits the Soret and Q bands at 417 and 541 nm, and slowly transforms into the 6C nitrato complex at low temperature. NMR spectra of the intermediate show distinct pyrrolic-proton resonances at −1.0, 8.94 and 18.10 ppm, while EPR revealed a ls rhombic signal with g values of 2.70, 2.25, 1.72. In rRaman experiments, the ferric oxidation state marker band was observed at 1371 cm^{-1}, and a signal at 1570 cm^{-1} indicated a ls complex. Consistent with these findings, X-ray absorption spectroscopy (XAS) data suggest that the peroxynitrite complex is a 6C ls-Fe^{III} species, determined from the distinct edge (7130−7140 eV) and pre-edge (7111.3, 7112.7, and 7113.9 eV) features of the intermediate. Lastly, DFT calculations predict that the *cis*-conformation of the peroxynitrite complex is more stable by 3.7 kcal/mol than the *trans*-isomer.[182] The Karlin group performed similar studies on the reaction of Cu(II)−superoxo complexes with NO, and demonstrated that a bidentate Cu(II)−peroxynitrite complex is generated in solution at low temperature (−80 °C).[1004] The Cu(II)−peroxynitrite complex then undergoes thermal transformation to a Cu(II)−nitrite complex.[1004] Other non-porphyrin peroxynitrito metal complexes have been investigated by Koppenol and coworkers, including pentacyanoperoxynitritocobaltate(III).[1005,1006]

The observation that the peroxynitrite isomerization seems to be too fast for stopped-flow experiments is further supported by theoretical studies by Siegbahn and coworkers.[965] According to their DFT results, the Fe(III)−*cis*-peroxynitrite complex decays via homolytic O−O bond cleavage. This process has a calculated free energy barrier as low as ∼10 kcal/mol. This small barrier would not allow for the accumulation of this species, in agreement with the experimental difficulties of observing this intermediate. The formation of the caged radical species is exergonic by −6.6 to −11.2 kcal/mol, depending on entropic considerations. The net reaction from Fe(II)−O_2 and NO to nitrate and Fe^{III} as the products is highly exergonic at ∼−29 kcal/mol.[965,966] In contrast to these results, the concerted mechanism reportedly failed to yield plausible activation energies.[965] Analogous theoretical studies on truncated Hb provide further support for these conclusions.[1007]

2.5.2. Oxidative Denitrosylation (ODN). While the NOD pathway has been proposed to be the major route of NO detoxification in blood and tissue, starting from oxygenated globins, NO can also be directly scavenged by available Fe^{II} heme sites in deoxy-Hb or -Mb and form corresponding ferrous heme−nitrosyl, or ls-$\{FeNO\}^7$, complexes (see Section 2.2). These Fe(II)−NO complexes can then undergo oxidative denitrosylation (ODN).[1008] In this sense, ODN is the inverse pathway to NOD, where in the NOD case the Fe(II)−O_2 complex reacts with NO, as discussed above, whereas in the ODN case, the Fe(II)−NO complex reacts with O_2. The ODN reaction is therefore particularly important for ferrous heme proteins that are inhibited by NO, due to the fact that ls-$\{FeNO\}^7$ complexes of hemes tend to be very stable and unreactive. In addition, NO has a large rate constant for binding to deoxy-Hb ($k_{Fe(II)+NO} \sim 1.8 \times 10^7\ M^{-1}\ s^{-1}$),[609] three orders of magnitude higher compared to the rate of NO binding to

https://doi.org/10.1021/acs.chemrev.1c00253

Table 14. Experimental IR Frequencies for the Proposed Peroxynitrite Complexes and Corresponding, Isotopically Labeled (^{15}NO, N^{18}O, or ^{18}O$_2$) Species[181,1002]

	peroxynitrite vibrational frequencies [cm^{-1}]				
complex	ν(N=O) [$\Delta\nu$][a]	ν_s(O−N−O), δ(O−N=O) [$\Delta\nu$][a]	ν_{as}(O−O−N) + δ(O−N=O) [$\Delta\nu$][a]	ν_{as}(O−O−N) + δ(O−N=O) [$\Delta\nu$][a]	ν(M−O) [$\Delta\nu$][a]
[Co(TPP)(NH$_3$)(OONO)]	1596	954	740		544
[Co(TPP)(NH$_3$)(^{18}O^{18}ONO)]	1594 [2]	924 [30]	710 [30]		522 [22]
[Co(TPP)(NH$_3$)(OO^{15}NO)]	1564 [32]	946 [8]	737 [3]		542 [2]
[Co(TPP)(NH$_3$)(^{18}O^{18}ON^{18}O)]	1555 [41]	916 [38]	707 [33]		522 [22]
[Mn(TPP)(NO)(OONO)]	1582			787	480
[Mn(TPP)(^{15}NO)(OO^{15}NO)]	1552 [30]			779 [8]	478 [2]
[Mn(TPP)(NO)(^{18}O^{18}ONO)]	1580 [2]			755 [32]	464 [16]

[a] Values of the experimental and calculated isotope shifts, $\Delta\nu = \nu_{normal} - \nu_{isotope}$, are shown in brackets [$\Delta\nu$].

Table 15. Rate Constants for Ferrous Heme−NO Dissociation and Oxidation in Heme Proteins

protein	NO dissociation [s^{-1}]	NO oxidation[a]		ref
Hb	3.2×10^{-4}[b]	$k_1 = 2.0 \times 10^{-4}$ s^{-1}	$k_2 = 1.0 \times 10^{-4}$ s^{-1}	610
Mb	0.9×10^{-5}	$k_1 = 1.3 \times 10^{-4}$ s^{-1}	$k_2 = 2.6 \times 10^{-4}$ s^{-1}	1009, 1010
Ngb	2.0×10^{-4}	$k_1 = 1.6 \times 10^{1}$ M^{-1} s^{-1}	$k_2 = 5.0 \times 10^{-4}$ s^{-1}	1011, 1012
hemopexin	3.2×10^{-4}	$k_1 = 2.4 \times 10^{1}$ M^{-1} s^{-1}	$k_2 = 1.4 \times 10^{-3}$ s^{-1}	1013
iNOSoxy	1.0×10^{-4}	$k_1 = 2.65 \times 10^{4}$ M^{-1} s^{-1}		1014
nNOSoxy	3.9×10^{-4}	$k_1 = 2.30 \times 10^{2}$ M^{-1} s^{-1}	$k_{-1} = 4.7 \times 10^{-2}$ s^{-1}	1015
sGC	7.0×10^{-4}			1009
CcO	1.0×10^{-2}			1016
Pa heme *cd*$_1$ NIR	2.75×10^{1}			296

[a] Second kinetic parameters are referred to as k_{-1} and k_2; in the case of nNOS, it reflects an apparent equilibrium and, in the other proteins, refers to a subsequent reaction. [b] Fast rate; a bi-exponential fit gave values of $k_1 = 3.2 \times 10^{-4}$ s^{-1}; $k_2 = 0.7 \times 10^{-4}$ s^{-1}.

Scheme 22. Proposed Mechanism for Oxidative Denitrosylation of Hb(II)−NO[a]

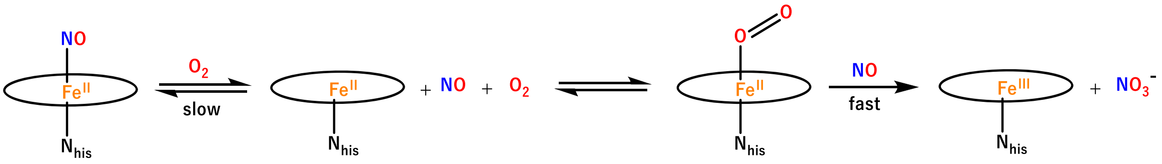

[a] Importantly, NO first dissociates from the heme and is thought to be trapped in a protein cavity, allowing O$_2$ to rapidly bind. This is followed by a fast NOD step (cf. Scheme 20). The NO dissociation is therefore the rate-determining step of the reaction.[610]

residual met-Hb ($k_{Fe(III)+NO} \sim 10^4$ M^{-1} s^{-1}).[618] Once NO is bound to a ferrous heme, the ODN reaction with O$_2$ may occur.[26,833] However, there is one key difference to the NOD reaction: whereas the bimolecular reaction of NO with Hb(II)−O$_2$ (or Mb(II)−O$_2$) displays a large second order rate constant of (6-9) × 10^7 M^{-1} s^{-1}, the rate of oxidation of Hb(II)−NO by O$_2$ is ∼11 orders of magnitude slower, with $k_1 \sim 2.0 \times 10^{-4}$ and $k_2 \sim 1 \times 10^{-4}$ s^{-1} (see Table 15; the time course of the reaction had to be fit with two exponentials).[610] Curiously, these rate constants are comparable to the dissociation rate constants for NO from ferrous heme, for example $k_{off} \sim 3.2 \times 10^{-4}$ s^{-1} for Hb(II)−NO, and, importantly, the rate of the ODN reaction does not depend on the O$_2$ concentration in the range studied (100−850 μM O$_2$). Therefore, the ODN reaction in Hb and other heme proteins is proposed to occur via a three-step process as shown in Scheme 22: first, the rate limiting step occurs, which is the dissociation of NO from the ferrous heme. The released NO is thought to be trapped in a protein cavity in the active site, which does not allow for its reaction with non-coordinated O$_2$.[610,1017] This is followed by rapid binding of O$_2$ to the ferrous heme, and then subsequent reaction of the Fe(II)−O$_2$ complex with NO, following the NOD reaction described above, ultimately yielding ferric heme and nitrate as the products. In the presence of excess NO, the corresponding ferric heme−nitrosyl complex forms. However, this complex easily loses NO (see Section 2.3), so ultimately the ODN process leads to heme denitrosylation and oxidation.

The ODN reaction is also observed for NOS (Scheme 23). In this case, the ferric heme−nitrosyl adduct is formed as the enzyme-product complex (see Section 2.1). If electron transfer to the heme occurs before the NO is released, this leads to the formation of the ferrous heme−nitrosyl complex, which would inhibit the enzyme significantly, as NO release from ferrous heme is slow, as discussed above. However, curiously, the reaction of the ls-{FeNO}^{7} complex of NOS with O$_2$ is much faster compared to Hb and Mb, with rate constants of $k \sim 2.65 \times 10^4$ M^{-1} s^{-1} and 2.30×10^2 M^{-1} s^{-1} for iNOSoxy and nNOSoxy, respectively (see Table 15).[1014] These rates for the ODN reaction in NOS are much faster than NO dissociation

Scheme 23. Proposed Mechanisms for Oxidative Denitrosylation of NOS(II)−NO[a]

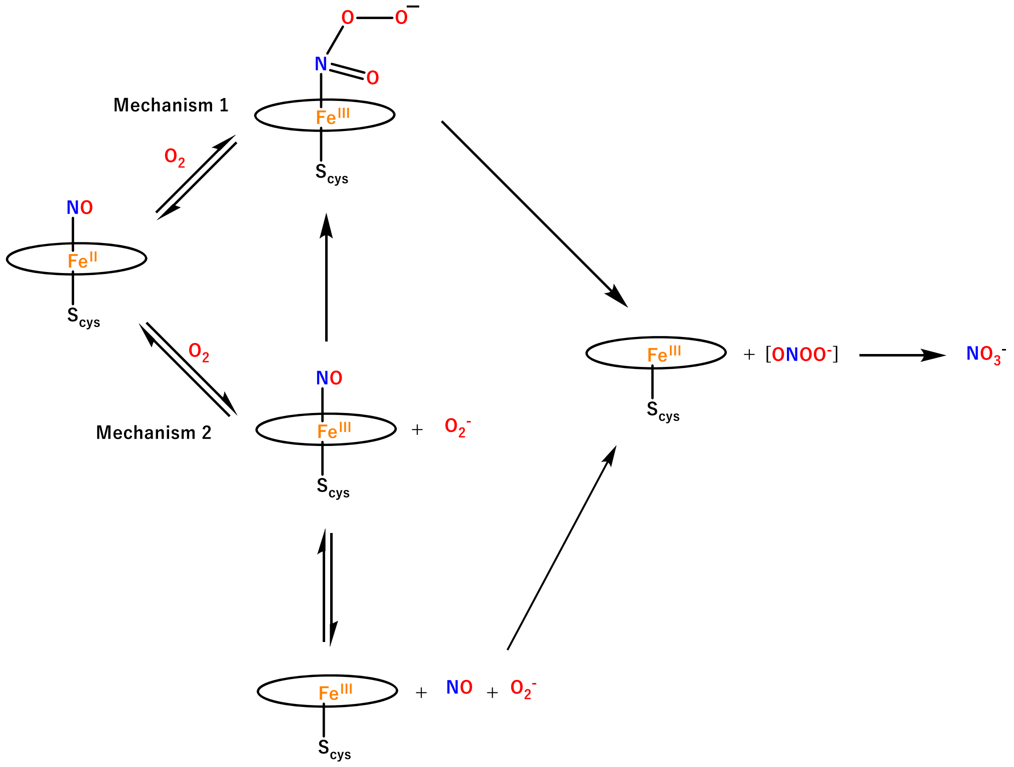

[a] Two possible mechanisms are discussed in the literature: one that involves the formation of an N-bound peroxynitrite complex, and one that is based on the formation of a ferric nitrosyl complex and superoxide in the first step of the reaction. Although the exact mechanism is still under investigation, it has been shown that oxidative denitrosylation in NOS and potentially other P450 enzymes is different from the globins (cf. Scheme 22).[785,1014]

Scheme 24. Proposed Mechanism for Oxidative Denitrosylation (ODN) of the ls-$\{FeNO\}^7$ Complex of NOS Based on DFT Results[a]

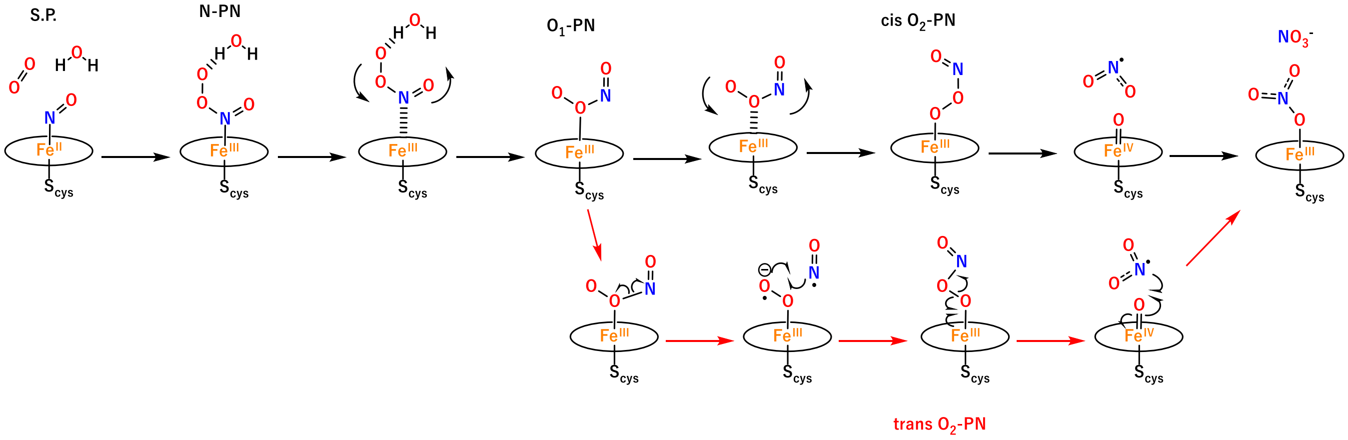

[a] Structures in the proposed reaction pathway follow the black arrows; structures for the alternative pathway follow red arrows. Species are named as follows: S.P., starting point (Fe(II)−NO + $^3O_2$, N—O_2 distance = 3.6 Å); N−PN, N-bound peroxynitrite complex, Fe(III)−N(O)OO⁻; *cis* O_2-PN, terminal O-bound *cis* Fe(III)−OONO⁻; *trans* O_2-PN, terminal O-bound *trans* Fe(III)−OONO⁻; NO_3^-, ferric O-bound nitrato complex, Fe(III)−NO_3^-.[1019]

from the ferrous heme, with the latter again showing rate constants in the 10^{-4} s^{-1} range ($k_{off} \sim 1.0 \times 10^{-4}$ s^{-1} and 3.9×10^{-4} s^{-1} for iNOSoxy and nNOSoxy, respectively).[1014] On the basis of these results, Stuehr and coworkers proposed that in the case of NOS, O_2 is able to directly react with the Fe(II)−NO complex, in contrast to the globins.[1014] In the proposed mechanism, O_2 is trapped in the active site and subsequently attacks the Fe(II)−NO complex, which leads to the formation of an N-bound Fe(III)−peroxynitrite intermediate. This species either quickly dissociates or rearranges to ultimately form ferric NOS and nitrate. Alternatively, O_2 could simply act as an outer-sphere oxidant and generate an Fe(III)−NO complex and superoxide. However, note that this would be an endergonic process, based on the electrochemical potential of the O_2/O_2^- couple (−330 mV)[1015] compared to that of the NOS Fe(III)−NO/Fe(II)−NO couple (−2 mV; both vs SHE).[1018] This equilibrium reaction could then be driven towards product formation if the subsequent reaction between the Fe(III)−NO complex and superoxide would be fast. This reaction, like mechanism 1 in Scheme 23, would similarly produce an Fe(III)−peroxynitrite intermediate. However, more recent work by Stuehr, Lehnert, and coworkers supports an inner-sphere mechanism via the N-bound Fe(III)−N(O)OO^- intermediate as shown in Scheme 24.[1019] Using experimental studies on different NOS enzymes and DFT calculations, it was shown that the heme-thiolate active site of NOS enzymes can stabilize an N-bound Fe(III)−N(O)OO^- intermediate (assisted by hydrogen-bonding from a water molecule; see Figure 58), which then rearranges to the energetically favored O-bound Fe(III)−$OONO^-$ complex,[1019] followed by isomerization to nitrate through a similar mechanism as the NOD reaction proposed for globins. In comparison, hemes with proximal His coordination like the globins have more positive Fe^{II}/Fe^{III} reduction potentials and cannot form the N-bound peroxynitrite complex, because electron transfer from the heme to the N(O)−OO ligand does not occur (Figure 59). Rather, the globins form an Fe(II)−NO—O_2 van-der-Waals adduct, and the reaction cannot proceed from there, in agreement with the experimental results (requiring NO dissociation as the first step of the ODN process in globins).[1019]

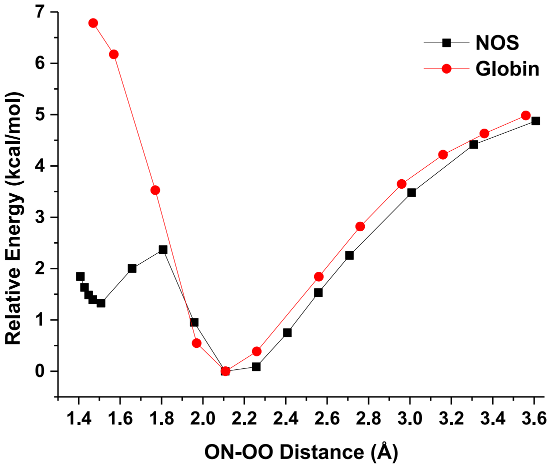

Figure 59. Comparison of the PES scan results for NOS and globin active site models. The relative energies were obtained from PES scans for the reaction of the respective Fe(II)−NO complex with $^3O_2$. Black line: the NOS active site model with a critical H_2O molecule as a hydrogen-bond donor. Red line: the globin active site model with the distal His reside (modelled as 5-ethylimidazole) included. Each point represents a fully optimized structure with only the ON−OO distance fixed. The minimum energy calculated for the Fe(II)−NO/O_2 van-der-Waals complex of each model was set to 0 kcal/mol to allow for a direct comparison of the relative energies for formation of the ferric peroxynitrite intermediate.[1019]

3. DINITROSYL IRON COMPLEXES (DNICS)

In this section, the discovery and major biological and synthetic advances in DNIC chemistry are discussed, including the involvement of [Fe−S] clusters as NO sensors, DNIC synthesis and electronic structure, reactivity of biomimetic DNIC complexes, and therapeutic applications of DNICs. Interested readers are referred to the cited reviews or accounts on the synthetic,[104,1020−1025] biological,[1021,1026−1028] biophysical,[1029−1031] and medicinal[107,1032] aspects of DNICs, as well as a recent 'viewpoint' article by Lu et al.,[106] for additional details.

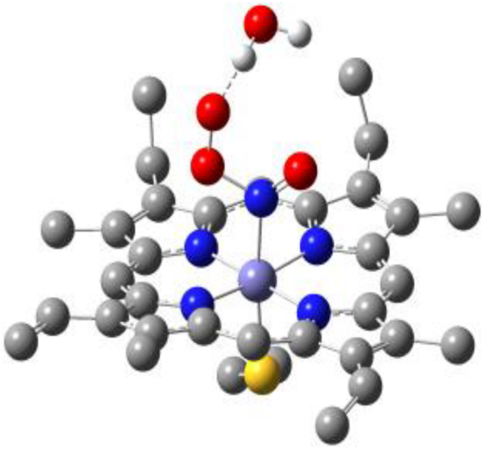

Figure 58. Fully optimized structure of the Fe(III)−**N** (O)OO^-/H_2O heme-thiolate complex (ON−OO distance = 1.508 Å). The two axial hydrogen-bond donors to the thiolate, the heme carboxylic acid side chains and all H atoms (except those of the H_2O molecule) have been removed for clarity.[1019]

3.1. Discovery of DNICs

DNICs in biology were discovered well before the scientific community recognized nitric oxide as an important signaling molecule. In 1964, Anatoly Vanin observed the distinct DNIC electron paramagnetic resonance (EPR) signal at g_{av} = 2.03 while studying free radical chemistry in baker's yeast cells, *Saccharomyces cerevisiae* (Figure 60).[103,1033] Around that time, the Commoner group reported a similar g = 2.03 EPR signal from animal tissues in association with chemical carcinogenesis.[1034] Not until 1967 did Vanin identify the source for this distinct EPR signal to be from complexes best described as $[Fe(NO)_x(SR)_y]$,[1035] which was aided by the independent EPR studies of synthetic iron nitrosyl complexes from the chemistry community.[101,1036] The biological significance of DNICs was not fully understood until NO was recognized as an important signaling molecule in mammals (see Introduction).

Synthetic DNIC chemistry has a much longer history than biological DNICs. As introduced in Section 1.1, the French chemist Roussin reported the first DNIC, the 'red salt', in 1858 along with a bitter-tasting 'black salt' (Figure 60).[89] Subsequent studies by Pavel in Germany reported neutral 'ester' complexes in which the bridging sulfides of the red salt are alkylated (see Figure 8).[90] These early iron nitrosyl complexes are now referred to as Roussin's black salt (RBS) and Roussin's red salt (RRS), and Roussin's red esters (RREs). These complexes began experiencing a renaissance in the 2000s and the DNIC chemistry in this review mostly focuses on the work developed in the last 20 years. The earlier work on non-heme nitrosyls including DNICs has been previously reviewed by Butler and Megson in 2002.[1036] Within the past 60 years there has been incredible research conducted in biological and synthetic DNIC chemistry to better understand DNIC's role in nature, and how we can utilize their vast chemistry for further scientific advancements.

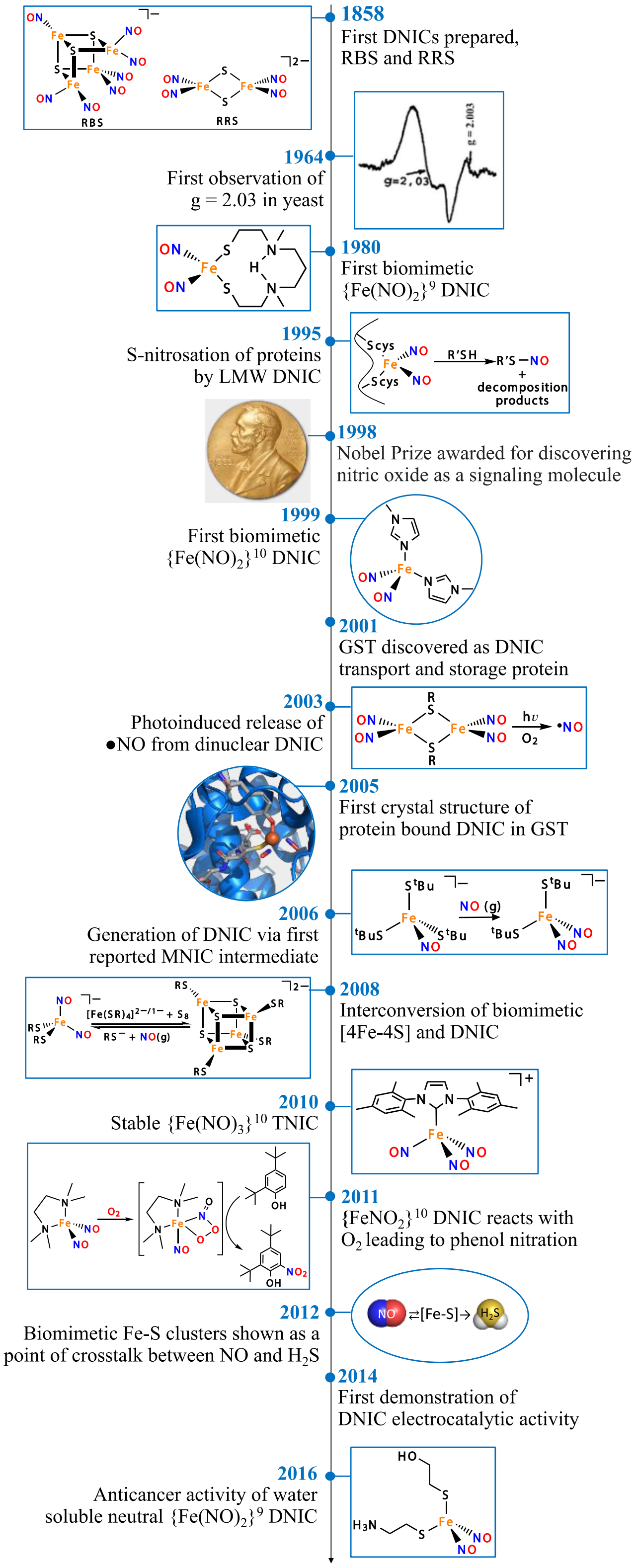

Figure 60. Timeline of major advances in DNIC chemistry.[89,103,1037−1051]

3.2. DNICs in Biology

3.2.1. Generation of DNICs in Cells. As nitric oxide established itself as an endogenously generated signaling molecule, researchers became interested in identifying the source of iron, the nature of the other iron ligands, and the origin of the DNIC formation. Beginning from the early 1990's until recently, two different iron sources have been proposed for the DNIC formation *in vivo*. One source is iron derived from iron−sulfur (Fe−S) proteins (*vide infra*). The other source is free iron from the chelatable iron pool (CIP).[1052−1056] The CIP is a low molecular weight pool of weakly bound non-heme iron and accounts for a minor fraction (less than 5%) of total cellular iron.[1057]

The nature of the ligands for iron can vary depending on the conditions in which DNICs form. Although cysteine is the most common ligand for a DNIC, EPR studies showed that DNICs can be generated with other amino acids or proteins with N- or O-donor ligands.[1058] The formation of a histidine-bound DNIC, $[Fe(NO)_2(His)_2]$, was observed from the thiol-blocked BSA protein.[1039] In 2005, the first and only crystal structure of a biological DNIC was reported, in which the DNIC was supported by a cysteine and a tyrosine side chain of the protein human glutathione transferase (GST).[1043]

It is not entirely clear which thiol ligands in cells form DNICs because low-molecular weight (LMW)-DNICs (e.g., DNICs ligated to free cysteine, glutathione, or other small-molecule thiols) and protein-bound DNICs have very similar EPR features. It is generally believed that both protein-bound and LMW-DNICs coexist in cells, although protein-bound DNICs are more stable and are the dominant form in cells.[1055,1059,1060] LMW-DNICs can be generated from protein-bound DNICs upon thiol addition,[1061,1062] and they can lead to protein post-translational modifications including protein *S*-nitrosylation (see above) and the formation of protein-bound DNICs.[1039,1063] This indicates that an exchange of the DNIC moiety between proteins and LMW-ligands is possible.

Another layer of complexity lies in the fact that LMW-DNICs can reversibly interconvert between the EPR-active monomeric forms and the EPR-silent dimeric forms, known as RREs. The equilibrium between the two forms is dependent on pH and thiol concentration.[1064,1065] RRE is favored at lower pH, while the mononuclear DNIC is predominant at higher pH. Detailed kinetic studies on cysteine-ligated DNICs revealed that at pH 7.4, RRE is formed at relatively low total cysteine concentration, but it rapidly converts to monomeric DNIC upon introduction of additional CysSH.[1065]

3.2.2. Biological Roles of DNICs. DNICs can be viewed as both a decomposition product of Fe−S clusters under nitrosative stress, and as intentionally formed LMW-DNICs that act as NO releasing agents for immune defense and mediate post-translational modifications of proteins, such as *S*-nitrosation of proteins. Endogenous DNICs have been shown to play a role in several processes due to their NO donating ability. One of the best known biological effects of NO is vasodilation via sGC activation.[161−163] As would be expected for an efficient NO donor, LMW-DNICs lead to potent hypotensive effects,[1066−1074] activation of sGC,[1075] inhibition of platelet aggregation,[1076] wound healing,[1077,1078] and penile erectile activity.[1079] Similar to NO that acts as a bifunctional regulator of apoptosis,[1080] DNICs also appear to be involved in anti-apoptotic and apoptotic pathways. An earlier report by Vanin showed that the heat shock protein-70, a well-known cytoprotective protein via its anti-apoptotic function, is induced by a DNIC in rats.[1081] The same group later reported that the application of a DNIC in human Jurkat leukemia cells induced apoptosis even in the presence of a high-level of antiapoptotic protein, Bcl-2.[1082]

LMW-DNICs can covalently modify protein cysteine residues by formation of *S*-nitrosothiols (RS−NOs), an important posttranslational protein modification. The exact mechanism of cellular RS−NO formation remains elusive as there are four other postulated sources of NO besides DNICs, including glutathione−NO, HNO_2 acidification, interactions of NO and O_2, and heme-based Fe−NO complexes.[224,1083] Nevertheless, Lancaster and coworkers provided evidence of Fe-dependent RS−NO formation from DNICs derived from the CIP using RAW 264.7 murine macrophages.[1055,1084] This observation was closely related to an earlier report by Kim and coworkers, in which both DNIC and RS−NO were increased by iron loading and DNIC inactivated capase-3, suggestive of DNIC formation that leads to *S*-nitrosation of their target protein.[1085] A similar protein inhibition by DNIC-derived *S*-nitrosation was observed in enteroviral Protease 2A.[1086]

The biological effects of DNICs are not limited to mimicking free NO or inducing protein *S*-nitrosylation. LMW-DNICs can transfer the dinitrosyl iron unit to a protein to form protein-bound DNICs to exert their unique effects. Such examples include inhibition of glutathione reductase,[1087,1088] inhibition of Na/K ATPase,[1089] and activation of non-selective cation channels.[1090]

DNICs are stored and transported by glutathione transferases (GSTs) and multidrug resistance-associated protein I (MRP1). GSTs are cell defense enzymes that primarily catalyze the reaction of glutathione with toxic compounds, such as NO, for solubilization and excretion.[1091−1093] With readily available access to glutathione, it was postulated and later discovered as a potential DNIC storage and transport protein.[1041,1043,1060,1094] Multidrug resistance-associated protein I (MRP1) is a glutathione transporter that also transports DNICs out of a cell.[1095] There is a close relationship between Fe, NO, glutathione, GST, and MRP1 that is thoroughly discussed by Richardson and coworkers in ref 1095.

3.2.3. DNICs Derived from Iron−Sulfur Sites. Iron−sulfur cluster, [Fe−S], containing proteins are ubiquitous in nature and they range in function from electron transport to DNA repair. Their ability to act as small molecule sensors and regulators not only stems from their Fe centers and inorganic sulfur bridges, but also from their ligation to redox non-innocent ligands such as cysteine, histidine, and tyrosine.[1028,1096,1097] Ever since NO has been recognized as an important signaling molecule, there has been increasing evidence of NO impacting transcription and translation processes in proteins that rely on gaseous signaling pathways for their DNA or RNA binding, such as in [Fe−S] containing aconitase/IRP1,[1098−1100] SoxR,[240,1101−1104] NsrR,[1105−1111] FNR,[1112−1115] and Wbl-type proteins.[1108,1116,1117] Moreover, proteins such as FNR have been found to be more sensitive to NO than its intended signaling partner, O_2,[1118] which raises an interesting question why FNR has evolved to be an O_2 sensor, not an NO sensor. It is postulated that perhaps the protein function is not determined by the cluster chemistry itself but rather through the control of NO accessibility to FNR in the cell.[1028,1118] Not all biological [Fe−S] clusters are intended to sense or store NO, but are nonetheless perfect targets for degradation and decomposition under nitrosative stress.[233,1086,1098,1119−1125] Table 16 and Figure 62 list [Fe−S]-containing proteins associated with NO, for better or for worse, as well as other proteins associated with DNICs.

When NO interacts with [Fe−S] clusters in biological settings it is reported to form dinitrosylated iron complexes as evident by a unique EPR signal at g = 2.03.[101,103,1033−1035,1037] The discovery of EPR-silent dinuclear DNICs upon nitrosylation of FNR in 2002 opened up new questions as to which species, mononuclear or dinuclear, were more prevalent in cells, pointing towards the need for more spectroscopic techniques.[1112] A traditional way of detecting EPR-silent RREs is to convert RREs into EPR-active DNICs by increasing pH or by adding chemical reductants such as sodium diethyldithiocarbamate or sodium dithionite.[1126,1127] However, biomimetic studies have shown that NO/[Fe−S] reactions can generate other products as well, such as mononitrosylated iron complexes (MNICs), RREs, and RBS, some of which are hard/impossible to identify by EPR spectroscopy (Figure 61).[36,1096] The Cramer group used NRVS to identify protein-

Table 16. Proteins Associated with DNICs

protein	function	ref
	[Fe−S] Containing Proteins	
FNR[a]	NO sensing secondary to O_2 sensing in bacteria	1112−1114, 1137
NsrR	regulator of NO stress response	1105−1110
Wbl[b]	controls cell developmental processes; NO sensor	1108, 1109, 1116, 1117, 1138
IRP1[c]	iron regulatory protein; also regulates NO	1139, 1140
SoxR	superoxide and redox sensor; senses and activated by NO	240, 1101−1103, 1141, 1142
aconitase	catalyzes citrate to isocitrate; inhibited by NO	1098, 1139, 1143
nitrogenase	converts nitrogen to ammonia; inhibited by NO	1119
succinate-Q reductase	part of cellular respiration; inhibited by NO	1120
HiPIP[d]	electron transport; inhibited by NO	233, 1130
endonuclease III	DNA repair protein; inhibited by NO, but can be restored	1121, 1144
succinate dehydrogenase	part of ellular respiration; inhibited by NO	1120, 1122
[2Fe−2S] ferredoxin	mediates electron transfer; inhibited by NO but can be repaired by IscA	1123
mammalian ferrochelatase	terminal enzyme of heme biosynthetic pathway in cells; inhibited by NO	1124
NiFe hydrogenase	catalyzes H_2 oxidation; inhibited by NO	1125
Ilvd[e]	amino acid biogenesis in bacteria; inhibited by NO	1145, 1146
	Proteins That Interact with DNICs	
GST[f]	cell defense; DNIC transport and storage protein	1027, 1041, 1043, 1094, 1147−1149
MRP1[g]	glutathione transporter; DNIC transporter	1027, 1095, 1147−1149
mammalian ferritin	iron storage; binding by DNIC	1150
Fur[h]	global iron regulator; inhibited by NO	1151−1153
iron−quinone complex of photosystem II	part of photosynthesis; binding by DNIC	1154
BSA[i]	globular protein; binding and inhibition by DNIC	1039, 1155
NorR	denitrification; global NO response mechanisms	1156−1158

[a] Fumerate and nitrate reductase. [b] WhiB-like protein. [c] Iron regulatory protein. [d] High potential iron−sulfur protein. [e] Dihydroxyacid dehydratase. [f] Gluthione transferases. [g] Multidrug resistance-associated protein I. [h] Ferric uptake regulatory protein. [i] Bovine serum albumin

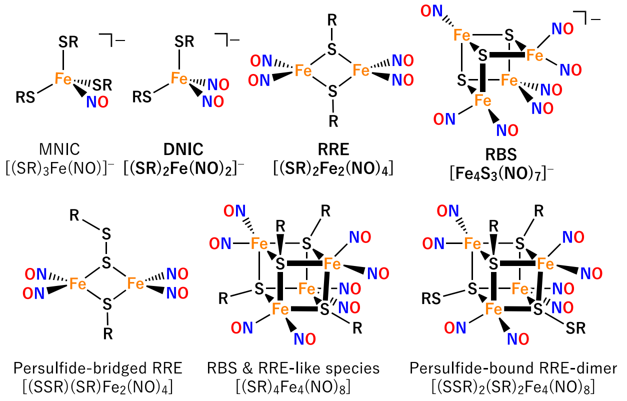

Figure 61. Iron-nitrosylated products of [Fe−S] clusters. Species in bold are the most commonly found products.

bound DNICs as a way to overcome reliance on EPR signals.[1108,1128,1129] More recently, Vincent and coworkers successfully applied attenuated total reflectance IR spectroscopy to characterize these protein-bound nitrosyl species.[1130,1131] Discoveries of other novel [Fe−S]-derived nitrosyl species have been made by mass spectrometry in the research groups of Cowan[233] and Le Brun.[1109,1110,1118] Liaw and coworkers showed that X-ray absorption spectroscopy is another method that can differentiate various iron-nitrosyl species using synthetic complexes.[1132−1136] Since the formation of RREs requires only one thiolate ligand per iron, they can be synthesized from a wider range of [Fe−S] clusters than mononuclear DNICs. The first spectroscopically identified RRE from a Cys$_2$His$_2$-ligated Rieske [2Fe−2S] cluster was reported in 2010, obtained upon nitrosylation of ToMOC, in which the RRE was the high-yielding product with a minor mononuclear DNIC byproduct.[1128] Not only did this study raise questions with respect to the prevalence of RREs in biology, but also regarding the relationship between NO and other non-cysteine bound Fe−S cluster.

Various types of iron−nitrosyl species have been observed from the reaction of NO with [Fe−S] proteins (Figure 62). Nearly all reported NO reactivity of [2Fe−2S] proteins produces either mononuclear- or dinuclear DNICs.[240,1061,1123,1124,1128,1131] One of the best studied [2Fe−2S]/NO-mediated signaling processes is the stress response of *E. coli* against a hostile environment such as the host immune response.[240] The master regulatory protein SoxR bears a [2Fe−2S] cluster that forms protein-bound DNICs upon exposure to NO (see Figure 10), which results in the expression of a group of defense genes that encode antioxidant, metabolic, and repair functions.[240,1102,1103] Although the formation of mononuclear DNICs in SoxR is unquestionable, the EPR quantification for the [2Fe−2S] to DNIC conversion suggested that other EPR-silent product(s) must exist.[240] A study by Yu indicates that different nitrosylated products can be generated from SoxR depending on the oxidation state of the [2Fe−2S] cluster.[1148] NO exposure to oxidized SoxR results in mononuclear DNICs, whereas nitrosylation of reduced SoxR yields product mixtures containing RRE, reduced RRE, and mononuclear DNICs.[1148] Similarly, NO reactivity of other [2Fe−2S] proteins reported the generation of EPR silent products.[240,1061,1120,1128,1131] In 2014, the Vincent group reported that trace O$_2$ plays a critical role in converting mononuclear DNICs to dinuclear DNICs in [2Fe−2S]-containing spinach ferredoxin I,[1131] consistent with the reactivity pattern predicted by synthetic models.[1159] The only exception to the DNIC generation from [2Fe−2S] cofactors is the recently reported Miner 2 protein that contains a Cys$_3$His ligated [2Fe−2S] cluster, which shows reversible binding of NO to the cluster.[1160]

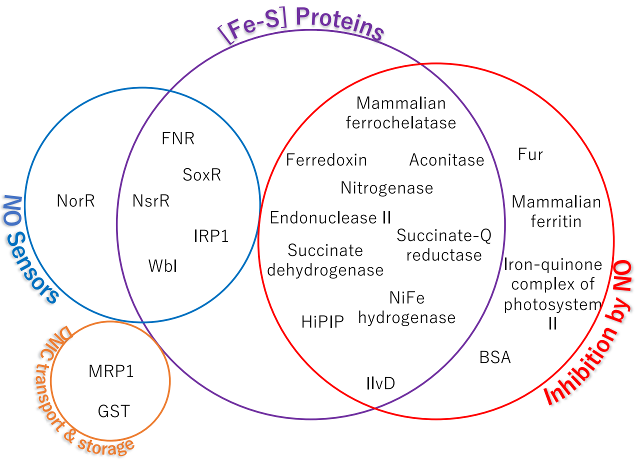

Figure 62. Proteins associated with DNICs and classification into groups.

While there is a general NO reactivity pattern for [2Fe−2S] clusters, the same cannot be said for [4Fe−4S] clusters. There have been several different types of iron−nitrosyl products observed from [4Fe−4S] containing proteins. The NsrR protein is a dedicated NO-sensor found in many microorganisms and it controls the expression of genes involved in NO detoxification and damage repair.[1111] Other known NO sensors in bacteria include the WhiB-like (Wbl) family of regulatory proteins found in actinomycetes.[1116,1117] All of these proteins utilize [4Fe−4S] clusters to sense NO but the nature of the nitrosylated products has remained elusive. Early EPR and UV-vis spectroscopic studies on *B. subtilis* NsrR and *E. coli* FNR showed DNIC formation upon nitrosylation.[1107,1112] However, NRVS studies on [4Fe−4S]-ferredoxin revealed that the EPR silent RBS is the main product from nitrosylation of its [4Fe−4S] cluster.[1129] A couple years later, Mössbauer, NRVS, and DFT studies on WhiD and NsrR (both from *S. coelicolor*) ruled out formation of RBS from these regulatory proteins.[1108] Instead, the authors described the multiple nitrosyl products from WhiD and NsrR as "species related to RBS and RRE" that are different from RBS.[1108] Several structures have been proposed as candidates for the unprecedented "RRE-like" species, which includes an octanitrosyl [Fe$_4$(NO)$_8$(μ_3-SR)$_4$] species,[1116] a persulfide bridged octanitrosyl [Fe$_4$(NO)$_8$(μ_3-SR)$_2$(μ_3-SR)$_2$] species,[1118] and a persulfide bridged dinuclear DNIC,[1110] Figure 61. In the most recent non-denaturing mass spectrometric studies, Le Brun's group reported other new species observed from the NO/NsrR and NO/WhiD reactions. The MS data revealed the presence of protein-bound mono-, di-, and tetra-nitrosyl [4Fe−4S] cluster as intermediates along pathways to formation of product RRE and RBS-like species.[1109] In recent studies with ferroxidans HiPIP, NO reaction with the [4Fe−4S] cluster was reported to produce a mixture of "RBS-like" species and RRE, in which the former was converted to RRE by trace O$_2$.[1130] Another different NO reactivity of [4Fe−4S] cluster was observed in a DNA repair enzyme, endonuclease III (EndoIII).[1121,1144] An early study on this protein reported formation of protein-bound mononuclear DNICs by EPR spectroscopy.[1121,1144] However, more recent studies employing HYSCORE pulse EPR spectroscopy and mass spectrometry revealed that nitrosylation of EndoIII yields a 1:1 mixture of mononuclear DNIC and RRE.[1144]

While unwanted nitrosylation has its consequences, there has been some evidence that iron−nitrosylated clusters could be repaired and restored back into their respective proteins.[1139] In *E. Coli*, YtfE is an Fe-containing protein used to repair iron−sulfur clusters. Cells lacking the *ytfE* gene experience more nitrosative stress and a lack of [Fe−S] cluster proteins, suggesting this particular protein could be involved in repairing [Fe−S] clusters by donating the Fe that it is harboring.[1161−1164] Another repair pathway was found by Ding and coworkers. In the presence of L-cysteine and IscS, they were able to show [Fe−S] cluster restoration after NO damage in both [2Fe−2S] ferredoxin and [4Fe−4S] containing endonuclease III.[1061,1121,1123] The same group also reported that O_2 is required to repair [2Fe−2S] clusters from DNICs.[1123,1165] While the cluster repair mechanism *in vivo* remains unresolved, biomimetic [Fe−S] clusters have become useful tools to study possible routes of [Fe−S] repair. Liaw and coworkers were able to convert a synthetic DNIC, $[S_5Fe(NO)_2]^-$ (**45**), back to its [2Fe−2S] cluster precursor upon photolysis in the presence of S_x and an NO acceptor (Figure 63).[1132] They also demonstrated interconversion of $[(SEt)_2Fe(NO)_2]^-$ (**3**) to [2Fe−2S] in a process that does not require photolysis (*vide infra*).[161]

3.3. Biomimetic and Synthetic DNICs

Chemists were already interested in the structure and bonding of various metal nitrosyl complexes including DNICs before the discovery of biological DNICs in the 1960s. For this reason, complexes prepared in the early 1900s have served as structural models, even though the purpose of preparing those complexes at that time had no relation to biological DNICs (see Figure 64). One such compound is $[Fe(NO)_2(CO)_2]$ (**140**), a neutral tetrahedral $\{Fe(NO)_2\}^{10}$ species that later became a predominant precursor for other DNIC syntheses.[1167] Similarly, the EPR studies on *in situ* generated DNICs from Fe(II), NO, and various anionic ligands by McDonald, Phillips, and Mower in 1965 were not necessarily intended to result in biomimetic models for biological DNICs.[101] Nonetheless, their work made tremendous contributions in the initial analysis of the g = 2.03 EPR signal observed in biology. The first discrete S-ligated biomimetic DNIC was a neutral $\{Fe(NO)_2\}^9$ species designed by Lippard and coworkers and reported in 1980, featuring a bidentate ligand with two thiolate groups bound to the Fe center.[1038] The first biomimetic $\{Fe(NO)_2\}^{10}$ species with histidine-like monodentate N-bound ligands was published in 1999 by the Li group, challenging the scientific community to look at amino acids other than cysteine as potential DNIC binders (Figure 60).[1040] Since then, there are more than 270 synthetic DNICs reported with diverse ligands, oxidation states, and coordination structures (Table 17). DNICs in this review are grouped by the coordination number and nuclearity (Figure 64). The most common form is a tetrahedral $\{Fe(NO)_2\}^{9/10}$ DNIC that is ligated by S-, N-, O-, P-, or NHC-ligands.[104,1022] While these categories are broad, there are a few complexes that stand out such as imidazolate-bound cyclic tetranuclear DNICs (Figure 65),[1168−1171] which are not included in Table 17.

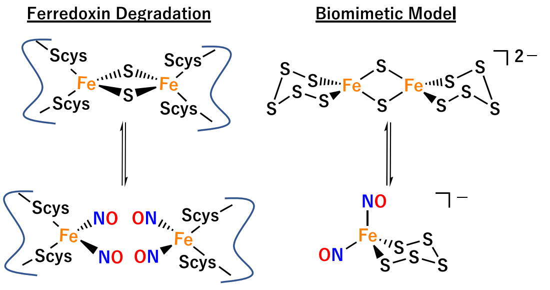

Figure 63. Biological [2Fe−2S] cluster degradation by NO compared to a biomimetic model.[1132,1166]

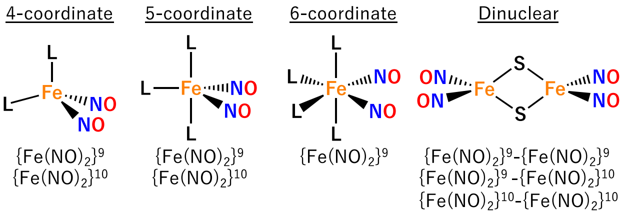

Figure 64. DNIC coordination environments and redox states.

Synthetic DNICs have been characterized by a wide variety of spectroscopic methods to better understand their properties. Along with EPR spectroscopy probing the characteristic g = 2.03 signal, infrared spectroscopy is most commonly used to study DNICs (Table 17). The most common four coordinate DNICs typically have two N−O stretching frequencies that lie between 1670 and 1790 cm^{-1} with a band separation between 40−60 cm^{-1}, depending on the coligands (Table 17). The separation tends to be greater for five- and six-coordinate DNICs or TNICs (80−100 cm^{-1}). On the other hand, dinuclear DNICs have smaller separations (less than 40 cm^{-1}) between the two bands. A number of complexes have been characterized by single crystal X-ray crystallography, which provides evidence of the close to linear Fe−N−O bonds (greater than 160° in most cases) in these complexes. X-ray absorption spectroscopy (XAS) was the first method used for advanced characterization of DNICs and MNICs to gain insights into their electronic structures. Additional characterization techniques include UV−vis, NMR, EPR, NRVS, rRaman, SQUID, and Mössbauer spectroscopy along with theoretical calculations. Table 17 and Figure 66 categorize known mono- and dinuclear DNICs, bimetallic DNICs, and TNICs, with Table 17 listing their available properties including UV−vis absorption, DFT, electrochemistry, EPR, IR, NMR, magnetism, Mössbauer and X-ray absorption (XAS) data, and single crystal X-ray structure information, along with the

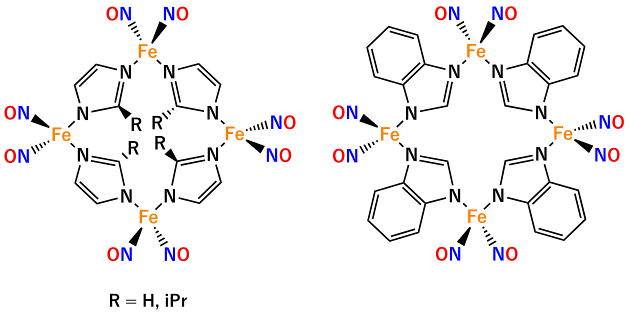

Figure 65. Tetranuclear DNICs with bridging imidazolate groups.

Table 17. Mono- and Dinuclear DNICs, Bimetallic DNICs, and TNICs with Their Available Properties Including UV–vis Absorption (Abs), Density Functional Theory (DFT), Electrochemistry (E), EPR, IR, NMR, Magnetism (Mg), Mössbauer (Mb), X-ray Absorption (XAS), Single Crystal X-ray Structure (XR) Data, and Their Associated Cambridge Crystallographic Data Centre Numbers (CCDC)

Complex	Properties	Ref	IR $\upsilon_{(NO)}$ cm^{-1}	CCDC #
Anionic $\{Fe(NO)_2\}^9$ 4-coordinate monodentate				
S/S-Donors				
$[(SH)_2Fe(NO)_2]^-$ (**1**)	Abs, DFT, EPR, IR, NMR, Mg, XAS, XR	1172	1735, 1686	1424933
$[(S^tBu)_2Fe(NO)_2]^-$ (**2**)	Abs, EPR, IR, XR	1173 1044	1739, 1690	673340
$[(SEt)_2Fe(NO)_2]^-$ (**3**)	Abs, EPR, IR, Mg, XAS, XR	1135,1174	1715, 1674	628677
$[(SCH_2CON(CH_3)_2)_2Fe(NO)_2]^-$ (**4**)	Abs, EPR, IR, XR	1175	1730, 1686	714526
$[(SCH_2CONHCH_3)_2Fe(NO)_2]^-$ (**5**)	Abs, EPR, IR, XR	1175	1743, 1693	714525
$[(SPh)_2Fe(NO)_2]^-$ (**6**)	Abs, EPR, IR, Mb, XAS, XR	1045,1135,1174,1176	1737, 1693	1152264
$[(p\text{-}ClC_6H_4S)_2Fe(NO)_2]^-$ (**7**)	Abs, IR	1177	1748, 1702	
$[(S\text{-}p\text{-}toyl)_2Fe(NO)_2]^-$ (**8**)[a]	Abs, EPR, IR, XR	1045	1738, 1694	717862
$[(2,4,6\text{-}Cl_3C_6H_4S)_2Fe(NO)_2]^-$ (**9**)	Abs, IR	1177	1760, 1713	
$[(SC_6H_4\text{-}o\text{-}NHCOCH_3)_2Fe(NO)_2]^-$ (**10**)	Abs, E, EPR, IR, Mg, XR	1177	1752, 1705	281211
$[(SC_6H_4\text{-}o\text{-}NHCOPh)_2Fe(NO)_2]^-$ (**11**)	Abs, EPR, IR	1178	1752, 1705	
$[(SPh\text{-}NO_2COOH)_2Fe(NO)_2]^-$ (**12**)	Abs, IR, XR	1179	1759, 1732, 1712	856898
$[(2{-}SC_4H_3S)_2Fe(NO)_2]^-$ (**13**)	Abs, E, EPR, IR, XR	1177	1743, 1698	281212
$[(2{-}SC_7H_4SN)_2Fe(NO)_2]^-$ (**14**)	Abs, E, IR, XR	1064,1177,1180	1766, 1716	281210
N/N-Donors				
$[(NO)_2Fe(NO)_2]^-$ (**15**)	Abs, DFT, EPR, IR, Mg, XAS, XR	1181	1776, 1708, 1345	884785
$[(CN)_2Fe(NO)_2]^-$ (**16**)	Abs, EPR, IR,	1182	1810, 1737	
$[(SCN)_2Fe(NO)_2]^-$ (**17**)	Abs, DFT, E, EPR, IR, Mb, XR,	1183	1786, 1718	939384
$[(OCN)_2Fe(NO)_2]^-$ (**18**)	Abs, DFT, EPR, IR, Mb, XR	1183	1766, 1698	939385
$[(N_3)_2Fe(NO)_2]^-$ (**19**)	Abs, EPR, IR, XR	1184	1755, 1698	661959
$[(C_3H_3N_2)_2Fe(NO)_2]^-$ (**20**)	Abs, EPR, IR, XR,	1185	1774, 1712	685886
$[(Imid\text{-}^iPr_2)_2Fe(NO)_2]^-$ (**21**)[b]	EPR, IR	1169	1765, 1699	
$[(SC_3H_4SN)_2Fe(NO)_2]^-$ (**22**)	Abs, E, EPR, IR, XR	1186	1769, 1704	1018892
$[(OC_7H_4SN)_2Fe(NO)_2]^-$ (**23**)	Abs, E, EPR, IR, XR	1180	1791, 1723	810301
$[(Cbz)_2Fe(NO)_2]^-$ (**24**)[c]	Abs, EPR, IR, XR	1187	1748, 1691	759683
$[(N(Ph)_2)_2Fe(NO)_2]^-$ (**25**)	Abs, IR, XR	1188	1727, 1672	876478
$[(N(TMS)_2)_2Fe(NO)_2]^-$ (**26**)[d]	Abs, IR, XR	1188	1711, 1650	876479
$[(N(Mes)(TMS))_2Fe(NO)_2]^-$ (**27**)[d, e]	Abs, DFT, E, EPR, IR, Mg, XAS, XR	1188	1707, 1652	876480
O/O-Donors				
$[(MeO)_2Fe(NO)_2]^-$ (**28**)	Abs, DFT, EPR, XAS, XR	1189	1725, 1662	1866109
$[(OAc)_2Fe(NO)_2]^-$ (**29**)[f]	Abs, EPR, IR, XR,	1190	1771, 1693	785649
$[(OPh)_2Fe(NO)_2]^-$ (**30**)	Abs, DFT, EPR, IR, Mg, XAS, XR	1135	1739, 1674	762501
$[(p\text{-}OPhF)_2Fe(NO)_2]^-$ (**31**)	Abs, EPR, IR, XAS, XR	1135	1751, 1685	762503
$[(ONO)_2Fe(NO)_2]^-$ (**32**)	Abs, EPR, IR, XAS, XR	1135	1775, 1705	762500
$[(\kappa^1\text{-}ONO_2)(ONO)Fe(NO)_2]^-$ (**33**)	EPR, IR, XR	1191	1778, 1707	928499
Halogen-Donors				
$[Cl_2Fe(NO)_2]^-$ (**34**)	DFT, EPR, IR, Mg, XR	1192,1193	1781, 1708	1866200 1867068 1866202 1867069
$[Br_2Fe(NO)_2]^-$ (**35**)	DFT, EPR, IR, Mg, XR	1192,1193	1780, 1710	1866201
$[I_2Fe(NO)_2]^-$ (**36**)	DFT, EPR, IR, Mg, XR	1192,1193	1778, 1719	1867070 1867071 1867073
S/O-Donors				
$[(SPh)(ONO)Fe(NO)_2]^-$ (**37**)	Abs, EPR, IR, XR	1135	1752, 1697	762504
$[(OPh)(SC_4H_3S)Fe(NO)_2]^-$ (**38**)	Abs, EPR, IR, XR	1135	1740, 1681	762502
S/N-Donors				
$[(SEt)(C_3H_3N_2)Fe(NO)_2]^-$ (**39**)	Abs, EPR, IR, XR	1185	1741, 1693	685888
$[(S^tBu)(C_3H_3N_2)Fe(NO)_2]^-$ (**40**)	Abs, EPR, IR, Mg, XR	1185	1741, 1690	685887
$[(SPh)(C_3H_3N_2)Fe(NO)_2]^-$ (**41**)	Abs, EPR, IR, XR	1185	1760, 1708	685889
N/O-Donors				
$[(OPh)(C_3H_3N_2)Fe(NO)_2]^-$ (**42**)	Abs, EPR, IR, XR	1135	1755, 1691	762499
Anionic $\{Fe(NO)_2\}^9$ 4-coordinate bidentate				
S/S-Donors				
$[S(CH_2)_3S)Fe(NO)_2]^-$ (**43**)	Abs, EPR, IR, Mg, XR	1194	1712, 1671	617958
$[S(CH_2)_2S(CH_2)_2S)Fe(NO)_2]^-$ (**44**)		1195	1739, 1694	
$[S_5Fe(NO)_2]^-$ (**45**)	Abs, DFT, EPR, IR, Mg, XAS, XR	1132	1739, 1695	248384
$[\{SCH_2\}_2\text{-}o\text{-}C_6H_4)Fe(NO)_2]^-$ (**46**)	Abs, EPR, IR	1045	1734, 1688	

Table 17. continued

Complex	Properties	Ref	IR $\upsilon_{(NO)}$ cm^{-1}	CCDC #
N/N-Donors				
$[(C_{21}H_8N_2)Fe(NO)_2]^-$ (**47**)	Abs, E, EPR, IR, Mb, XR	1196	1780, 1714	1873229
$[(N_2CHPh)Fe(NO)_2]^-$ (**48**)[g]	Abs, EPR, IR, Mb	232	1761, 1692	
$[(C_{19}H_{32}N_4)_2Fe(NO)_2]^-$ (**49**)	Abs, EPR, IR, XR	232	1831, 1759	1944313
N/S-Donors				
$[(C_{13}H_8N_2S)Fe(NO)_2]^-$ (**50**)	Abs, DFT, E, EPR, IR, Mb, XR	1196	1751, 1700	1873228
$[(SC_6H_4$-*o*-$NCOPh)Fe(NO)_2]^-$ (**51**)	Abs, EPR, IR, XR	1184	1737, 1690	661960
S/O-Donor				
$[(SC_6H_4$-*o*-$COO)Fe(NO)_2]^-$ (**52**)	Abs, EPR, IR, XR	1184	1742, 1688	661957
Anionic $\{Fe(NO)_2\}^9$ - 6-coordinate				
$[(\kappa^1\text{-}ONO_2)_2(\kappa^2\text{-}O_2NO)Fe(NO)_2]^{2-}$ (**53**)	Abs, EPR, IR, Mg, XR	1191	1750, 1656	876538
$[(\kappa^1\text{-}ONO_2)_2Fe(NO)_2]^-$ (**54**)	Abs, EPR, IR, XAS, XR	1191	1790, 1710	876536
Neutral $\{Fe(NO)_2\}^9$ 4-coordinate monodentate				
S/S-Donors				
$[(SCH_2CH_2OH)_2Fe(NO)_2]$ (**55**)		101		
$[(SPh)(S(CH_2)_2NH_3)Fe(NO)_2]$ (**56**)	Abs, EPR, IR, XR	1197	1739, 1693	941001
$[(S(CH_2)_2NH_2)(S(CH_2)_2NH_3)Fe(NO)_2]$ (**57**)	Abs, EPR, IR, XR	1197	1731, 1685	941000
$[(CysS))(S(CH_2)_2NH_3)Fe(NO)_2]$ (**58**)	Abs, EPR, IR	1197	1754, 1710	
$[(S(CH_2)_2OH)(S(CH_2)_2NH_3)Fe(NO)_2]$ (**59**)	Abs, EPR, IR, XR	1051	1733, 1688	1451586
NHC/I-Donor				
$(IMes)Fe(NO)_2I$ (**60**)[h]	DFT, E, EPR, IR, Mg, XR	1198	1782, 1726	1008319
P/P-Donor				
$[(PEt_3)_2Fe(NO)_2]$ (**61**)	E, IR	1199	1694, 1647	
S/N-Donors				
$[(SC_6H_4$-*o*-$NHCOPh)(Im)Fe(NO)_2]$ (**62**)[k]	Abs, EPR, IR, XR	1178	1786, 1722	620972
$[(StBu)(MI)Fe(NO)_2]$ (**63**)[k]	EPR, IR, NMR	1200	1768, 1706	
N/O-Donors				
$[(Im)(ONO)Fe(NO)_2]$ (**64**)[k]	Abs, EPR, IR, XR	39	1800, 1729	733275
$[(MI)(ONO)Fe(NO)_2]$ (**65**)[k]	EPR, IR, Mg	1190,1201	1820, 1749	
O/Cl-Donors				
$[(HMPA)(Cl)Fe(NO)_2]$ (**66**)[l]	EPR, IR	1202	1761, 1699	
P/Cl-Donors				
$[(PN)(Cl)Fe(NO)_2]$ (**67**)[m]	EPR, IR, NMR	1203	1792, 1726	
N/N-Donors				
$[(N(Mes)(TMS))_2Fe(NO)_2]$ (**68**)[d,e]	Abs, DFT, IR, Mg, NMR, XAS, XR	1188	1786, 1733	876481
S/NHC-Donors				
$[(sIMes)(SPh\text{-}4\text{-}NO_2)Fe(NO)_2]$ (**69**)[bh]	E, EPR, IR, XR	1204	1772, 1720	1004081
$[(sIMes)(SPh\text{-}4\text{-}OMe)Fe(NO)_2]$ (**70**)[bh]	E, EPR, IR, XR	1204	1759, 1713	1004078
$[(sIMes)(SPh\text{-}4\text{-}Me)Fe(NO)_2]$ (**71**)[bh]	E, EPR, IR, XR	1204	1761, 1714	1004079
$[(sIMes)(SPh\text{-}4\text{-}Cl)Fe(NO)_2]$ (**72**)[bh]	E, EPR, IR, XR	1204	1767, 1717	1004080
$[(sIMes)(SPh\text{-}4\text{-}CF_3)Fe(NO)_2]$ (**73**)[bh]	E, EPR, IR	1204	1769, 1718	
$[(IMes)(SPh)Fe(NO)_2]$ (**74**)[h]	E, EPR, IR, XR	1047	1763, 1715	829673
$[(NHC\text{-}iPr)(SPh)Fe(NO)_2]$ (**75**)[i]	E, EPR, IR, MS, XR	1169	1757, 1712	851030
$[(SGlu)(IMes)Fe(NO)_2]$ (**76**)[h, j]	EPR, IR, MS, XR	1205	1768, 1718	1511809
Neutral $\{Fe(NO)_2\}^9$ 4-coordinate bidentate				
S/S-Donors				
$[(C_9H_{21}N_2S_2)Fe(NO)_2]$ (**77**)	IR, XR	1038	1740, 1695	1210272
$[H^+bme\text{-}daco)Fe(NO)_2]$ (**78**)[n]	EPR, IR, MS, XR	1195,1206	1739, 1695	250834
N/N-Donors				
$[(Ar\text{-}nacnac)Fe(NO)_2]$ (**79**)[o]	Abs, E, EPR, IR, Mb, XR	232	1761, 1709	744948
Neutral $\{Fe(NO)_2\}^9$ 5-cooridinate				
$[(TMEDA)Fe(NO)_2I]$ (**80**)[p]	Abs, EPR, IR, Mg, XR,	1207,1208	1770, 1715	747897
$[(PyImiS)Fe(NO)_2]$ (**81**)[q]	Abs, EPR, IR, Mg, XAS, XR	1209	1732, 1662	N/A
Neutral $\{Fe(NO)_2\}^9$ 6-cooridinate				
$[(MI)_2(\eta^2\text{-}(ONO)Fe(NO)_2]$ (**82**)[k]	EPR, IR, Mg, XR	1190,1201	1820, 1749	733276
Cationic $\{Fe(NO)_2\}^9$ 4-coordinate monodentate				
S/S-Donors				
$[(S(C(NH_2)_2)_2Fe(NO)_2]^+$ (**83**)	Abs, EPR, IR, Mg, XR	1210,1211	1811, 1747	1538655 1538656
$[(S(C(NHCH_3)_2)_2Fe(NO)_2]^+$ (**84**)	Abs, EPR, IR, Mg, XR	1211,1212	1798, 1727	1538657
NHC-Donors				
$[(NHC\text{-}Me)_2Fe(NO)_2]^+$ (**85**)[t]	EPR, IR, MS	1169	1791, 1723	
$[(NHC\text{-}iPr)_2Fe(NO)_2]^+$ (**86**)[i]	EPR, IR, MS	1169	1789, 1733	
P/P-Donors				
$[(PPh_3)_2Fe(NO)_2]^+$ (**87**)	EPR, IR, XR	1199	1814, 1766	1274517
P/O-Donors				
$[(PPh_3)(OPPh_3)Fe(NO)_2]^+$ (**88**)	EPR, IR, XR	1199	1809, 1746	1274518
O/O-Donors				
$[(OPPh_3)_2Fe(NO)_2]^+$ (**89**)	EPR, IR	1199	1813, 1734	
N/N-Donors				
$[(MI)_2Fe(NO)_2]^+$ (**90**)[k]	EPR	1040		

Table 17. continued

Complex	Properties	Ref	IR $\upsilon_{(NO)}$ cm^{-1}	CCDC #
Cationic $\{Fe(NO)_2\}^9$ 4- coordinate bidentate				
$[(TMEDA)Fe(NO)_2]^+$ (**91**)[p]	IR	1194	1775, 1698	
$[(dmp)Fe(NO)_2]^+$ (**92**)[u]	Abs, EPR IR, Mb, NRVS, XR	652	1840, 1746	1500147
$[(sparteine)Fe(NO)_2]^+$ (**93**)	Abs, EPR, IR	1194	1808, 1739	
$[(^{Me}DDB)Fe(NO)_2][BF_4]^+$ (**94**)[r]	Abs, IR, XR	1213	1834, 1769	1528822
$[(^{Et}DDB)Fe(NO)_2][BF_4]^+$ (**95**)[r]	Abs, IR, XR	1213	1835, 1769	
$[(^{Iso}DDB)Fe(NO)_2][BF_4]^+$ (**96**)[r]	Abs, IR, XAS, XR	1213	1835, 1769	1528823
Cationic $\{Fe(NO)_2\}^9$ 5-coordinate				
$[(DTA)Fe(NO)_2]^+$ (**97**)[v]	Abs, IR, XR	1214	1779, 1702	1410890
$[(PMDTA)Fe(NO)_2]^+$ (**98**)[w]	Abs, E, IR, XR	1214	1768, 1673	1410891
$[(Me_6tren)Fe(NO)_2]^+$ (**99**)[x]	Abs, E, EPR, IR, Mg, XR	1215	1765, 1679	1559817
$[(6\text{-}Me_3\text{-}TMPA)Fe(NO)_2]^+$ (**100**)[ac]	Abs, EPR, IR, XR	1216	1801, 1726	166773
$[(^{iPr}PDI)Fe(NO)_2]^+$ (**101**)[y]	Abs, EPR, IR, Mg, XAS, XR	1209	1794, 1721	
$[(^{DEA}PDI)Fe(NO)_2]^+$ (**102**)[z]	E, EPR, IR, XR	1217	1786, 1682	1494869
$[(^{MeO}PDI)Fe(NO)_2]^+$ (**103**)[aa]	IR, Mg, NMR, XR	1218	1797, 1729	1582614
$[(didpa)Fe(NO)_2]^+$ (**104**)[ab]	E, IR, XR	1219	1786, 1714	1569866
Cationic $\{Fe(NO)_2\}^9$ 6-Coordinate				
$[(TMPA)Fe(NO)_2]^+$ (**105**)[ad]	Abs, EPR, IR, Mg, XAS, XR	1209	1720, 1619	N/A
Dianionic $\{Fe(NO)_2\}^{10}$ 4-coordinate monodentate				
$[(SC_7H_4SN)_2Fe(NO)_2]^{2-}$ (**106**)	Abs, IR, XR	1180	1661, 1613	810300
$[(OC_7H_4SN)_2Fe(NO)_2]^{2-}$ (**107**)	Abs, IR, XR	1180	1662, 1637	810301
Dianionic $\{Fe(NO)_2\}^{10}$ 4-coordinate bidentate				
S/S-Donors				
$[(S(CH_2)_3S)Fe(NO)_2]^{2-}$ (**108**)	DFT, E, IR, XAS, XR	1220	1600, 1556	1402948
$[(S(CH_2)_2S)Fe(NO)_2]^{2-}$ (**109**)	DFT, E, IR, XAS, XR	1220	1600, 1559	1402949
Anionic $\{Fe(NO)_2\}^{10}$ 4-coordinate monodentate				
$[(PPh_3)(NO_2)Fe(NO)_2]^-$ (**110**)	Abs, IR, XR	1190	1693, 1642	785648
Anionic $\{Fe(NO)_2\}^{10}$ 4-coordinate bidentate				
H/H-Donors				
$[(\eta^2\text{-}BH_4)Fe(NO)_2]^-$ (**111**)	Abs, DFT, IR, NMR, XR	1221	1708, 1654	1881645
S/N-Donors				
$[(NC_9H_6\text{-}S))Fe(NO)_2]^-$ (**112**)	Abs, IR, NMR, XAS, XR	1222	1660, 1612	953138
$[(SC_6H_4\text{-}o\text{-}NH_2)Fe(NO)_2]^-$ (**113**)	Abs, IR, NMR, XAS, XR	1222	1657, 1607	953135
$[(SC_6H_4\text{-}o\text{-}N(CH_3)_2Fe(NO)_2]^-$ (**114**)	Abs, IR, XR	1223	1660, 1610	830207
N/N-Donors				
$[(NC_9H_6\text{-}NH)Fe(NO)_2]^-$ (**115**)	Abs, IR, NMR, XAS, XR	1222	1655, 1603	953133
$[(Ar\text{-}nacnac)Fe(NO)_2]^-$ (**116**)[o]	Abs, E, IR, Mb, NMR, XR	232,235	1627, 1567	744949
N/O-Donors				
$[(NC_9H_6\text{-}O)Fe(NO)_2]^-$ (**117**)	Abs, IR, NMR, XAS, XR	1222	1674, 1619	953134
Anionic $\{Fe(NO)_2\}^{10}$ 5-coordinate				
$[(\eta^3\text{-}HCS_2)Fe(NO)_2]^-$ (**118**)	Abs, DFT, IR, NMR, XR	1221	1717, 1648	1881646
Neutral $\{Fe(NO)_2\}^{10}$ 4-coordinate monodentate				
S/S-Donors				
$[K\text{-}18\text{-}crown\text{-}6\ ether]_2[(SEt)_2\ Fe(NO)_2]$ (**119**)	Abs, IR, XR	1136	1614, 1571	882942
N/N-Donors				
$[(MI)_2Fe(NO)_2]$ (**120**)[k]	IR, MS, NMR, XR	1040	1673, 1616	1242097
N/P-Donors				
$[(MI)(PPh_3)Fe(NO)_2]$ (**121**)[k]	Abs, IR, Mg, XR	1190,1201	1698, 1651	733277
NHC-Donors				
$[(NHC\text{-}Me)_2Fe(NO)_2]$ (**122**)[t]	E, IR, MS, XR	1169	1667, 1624	851028
$[(NHC\text{-}iPr)_2Fe(NO)_2]$ (**123**)[i]	E, IR, MS, XR	1169	1664, 1619	851027
NHC/C-Donors				
$[(NHC\text{-}Me)(CO)Fe(NO)_2]$ (**124**)[t]	E, IR, MS, XR	1169	1740, 1697	851026
$[(NHC\text{-}iPr)(CO)Fe(NO)_2]$ (**125**)[i]	E, IR, MS, XR	1169	1738, 1696	851025
$[(IMes)(CO)Fe(NO)_2]$ (**126**)[h]	E, IR, NMR, XR	1047	1744, 1702	829672
P/P-Donors				
$[(P(CH_3)_2Fe(NO)_2]$ **(127)**	IR, NMR, XR	1224	1705, 1660	1840854
$[(PCH_3(C_6H_5)_2Fe(NO)_2]$ (**128**)	Abs, DFT, E, IR, Mb, NMR, XR	1225	1703, 1656	1449122
$[(P(CH_2OH)_3)_2Fe(NO)_2]$ (**129**)	EPR, IR, NMR, XR	1226	1711, 1668	610298
$[(PPh_3)_2Fe(NO)_2]$ (**130**)	E, IR, XR	1227-1229	1724, 1678	1578224
$[(P(C_6H_4\text{-}p\text{-}OCH_3)_3)_2Fe(NO)_2]$ (**131**)	E, IR, NMR, XR	1229	1711, 1667	959031
$[(P(C_6H_4\text{-}p\text{-}CH_3)_3)_2Fe(NO)_2]$ (**132**)	E, IR, NMR, XR	1229,1230	1714, 1670	815453
$[(P(C_6H_4\text{-}p\text{-}F)_3)_2Fe(NO)_2]$ (**133**)	E, IR, NMR, XR	1229,1231	1720, 1682	815454
$[(P(C_6H_4\text{-}p\text{-}Cl)_3)_2Fe(NO)_2]$ (**134**)	E, IR, NMR, XR	1229,1232	1722, 1682	811204
$[(P(C_6H_4\text{-}p\text{-}CF_3)_3)_2Fe(NO)_2]$ (**135**)	E, IR, NMR, XR	1229	1728, 1687	959032
$[(P(C_6H_4\text{-}m\text{-}CH_3)_3)_2Fe(NO)_2]$ (**136**)	E, IR, NMR	1229	1715, 1671	
$[(PPh_2)(Ph\text{-}3\text{-}SO_3Na))_2Fe(NO)_2]$ (**137**)	Abs, IR, MS	1233	1715, 1672	
$[(PTA)_2Fe(NO)_2]$ (**138**)[ae]	IR, NMR, XR	1226	1715, 1668	610299
P/C-Donors				
$[(CO)(PPh_3)Fe(NO)_2]$ (**139**)	IR, XR	1227	1766, 1719,	1142993

Table 17. continued

Complex	Properties	Ref	IR $\upsilon_{(NO)}$ cm^{-1}	CCDC #
C/C -Donors				
[(CO)$_2$Fe(NO)$_2$] (**140**)	IR, XR	1167	1810, 1767	N/A
Neutral {Fe(NO)$_2$}^{10} 4-coordinate bidentate				
N/N-Donors				
[(TMEDA)Fe(NO)$_2$] (**141**)[p]	Abs, IR, NMR, XR	1194	1698, 1644,	617957
[(PMDTA)Fe(NO)$_2$] (**142**)[w]	IR, NMR	1214	1697, 1643	
[(DTA)Fe(NO)$_2$] (**143**)[v]	Abs, IR, NMR, XR	1214	1688, 1634	1410889
[(DIM)Fe(NO)$_2$] (**144**)[af]	IR, NMR, Mb, XR	1234	1697, 1645	1951267
[(bipy)Fe(NO)$_2$] (**145**)[ag]	Abs, E, IR, Mb, MS, NMR, XR	1235,1236	1684, 1619	739760
[(terpy)Fe(NO)$_2$] (**146**)[ah]	Abs, E, IR, MS, NMR, XR	1236	1688, 1621	739759
[(phen)Fe(NO)$_2$] (**147**)[ai]	Abs, E, IR, Mb, MS, NMR	1235,1236	1686, 1614	
[(dmp)Fe(NO)$_2$] (**148**)[u]	E, IR, NMR	1237	1692, 1628	
[(di-2-pyridyl ketone)Fe(NO)$_2$] (**149**)	E, IR, Mb, NMR	1235	1704, 1645	
[(DDB)Fe(NO)$_2$] (**150**)[r]	Abs, E, IR, Mg, XR	1238	1730, 1687	1864718
[(^{Me}DDB)Fe(NO)$_2$] (**151**)[r]	Abs, DFT, E, IR, Mg, XR	1213,1238	1708, 1665	1528819
[(^{Et}DDB)Fe(NO)$_2$] (**152**)[r]	Abs, IR, XR	1213	1708, 1667	1528820
[(^{Iso}DDB)Fe(NO)$_2$] (**153**)[r]	Abs, IR, XR	1213	1713, 1673	1528821
[(BIAN)Fe(NO)$_2$] (**154**)[aj]	Abs, E, IR, Mg, XR	1238	1717, 1683	1864719
[(sparteine)Fe(NO)$_2$] (**155**)	Abs, IR, NMR, XR	1194	1687, 1633	617959
P/P-Donors				
[(HMPE)Fe(NO)$_2$] (**156**)[ak]	EPR, IR, NMR, XR	1226	1711, 1664	610300
[(dppe)$_2$Fe(NO)$_2$] (**157**)[s]	EPR, IR, NMR, XR	1239	1707, 1657	1256805
[(DPPPr)Fe(NO)$_2$] (**158**)[al]	Abs, DFT, E, IR, XR	1240	1708, 1660	965701
[(DPPEt)Fe(NO)$_2$] (**159**)[am]	Abs, DFT, E, IR, XR	1240	1723, 1674	965702
[(DPPBe)Fe(NO)$_2$] (**160**)[an]	Abs, DFT, E, IR, XR	1240	1719, 1675	965700
[(TMBz)Fe(NO)$_2$] (**161**)[ao]	IR, NMR	1226	1715, 1666	
[(triphos)Fe(NO)$_2$] (**162**)[ap]	Abs, DFT, E, IR, Mb, NMR, XR	1225	1707, 1655	1449124
[(triphos^{Si})Fe(NO)$_2$] (**163**)[aq]	Abs, DFT, E, IR, Mb, NMR, XR	1225	1708, 1659	1449125
[(diphos^{Si})Fe(NO)$_2$] (**164**)[ar]	Abs, DFT, E, IR, Mb, NMR, XR	1225	1708,1662	1449123
N/O Donors				
[(^{Me}PyrCO$_2$)Fe(NO)$_2$] (**165**)[as]	DFT, IR, NMR, XAS, XR	1241	1699, 1667 1636	1984680
Neutral {Fe(NO)$_2$}^{10} 5-coordinate				
[(Me$_6$tren)Fe(NO)$_2$] (**166**)[x]	IR, NMR,	1215	1697, 1643	
[(PPh$_3$)(η^2-TCNE)Fe(NO)$_2$] (**167**)[at]	IR, NMR, XR	1242	1836, 1790	N/A
[(κ^3-L^{DPM})Fe(NO)$_2$] (**168**)[bi]	Abs, E, IR, NMR, XR	1243	1840, 1790	1028477
Neutral dinuclear DNICs				
μ-S				
[(μ-SMe)$_2$Fe$_2$(NO)$_4$] (**169**)	IR, NMR	102,1244	1770, 1740	1167460
[(μ-SEt)$_2$Fe$_2$(NO)$_4$] (**170**)	IR, NMR, XAS, XR	96,1135,1166	1809, 1774, 1749	1252104
[(μ-*S*-*n*-Pr)$_2$Fe$_2$(NO)$_4$] (**171**)	Abs, DFT, E, IR, NMR, XR	1245,1246	1673, 1655	691873
[(μ-S(CH$_2$)$_4$CH$_3$)$_2$Fe$_2$(NO)$_4$] (**172**)	XR	1247		1167461
[(μ- SCHMe$_2$)$_2$Fe$_2$(NO)$_4$] (**173**)	Abs, DFT, IR, NMR, XR	1244,1248	1790	991969
[(μ-S^{t}Bu)$_2$Fe$_2$(NO)$_4$] (**174**)	Abs, IR, XR	1044,1173	1778, 1729	605810 1167462
[Fe$_2$(C$_2$H$_5$OS)$_2$(NO)$_4$] (**175**)	IR, XR	1249	1809, 1774, 1748	758697
[(μ-SCH$_2$CH$_2$NH$_2$)$_2$Fe$_2$(NO)$_4$] (**176**)	Abs, IR, NMR, XR	1197	1808, 1774, 1749	940999
[(μ-SC$_2$H$_4$COOH)$_2$Fe$_2$(NO)$_4$] (**177**)	Abs, IR, MS, XR	1233	1811, 1772, 1751	708601
[(μ-SCH$_2$CH$_2$CH$_2$Br)$_2$Fe$_2$(NO)$_4$] (**178**)	IR, NMR	1250	1775, 1750	
[(μ-SCH$_2$CH$_2$NHAc)$_2$Fe$_2$(NO)$_4$] (**179**)	IR, XR	1251	Not specified	990390
[(μ-SCH$_2$CH$_2$NHBoc)$_2$Fe$_2$(NO)$_4$] (**180**)	IR	1251	Not specified	
[(μ-SCH$_2$CONH(CH$_3$)$_2$Fe$_2$(NO)$_4$] (**181**)	Abs, IR,	1175	1810, 1778, 1750	
[(μ-S(CH$_2$)$_2$P(O)(CH$_2$OH)$_2$)$_2$Fe$_2$(NO)$_4$] (**182**)	Abs, IR	1246	1815, 1781, 1756	
[(μ-S(CH$_2$)$_2$P(O)(OEt)$_2$)$_2$Fe$_2$(NO)$_4$] (**183**)	Abs, IR	1246	1811, 1777, 1752	
[(μ-SPh)$_2$Fe$_2$(NO)$_4$] (**184**)	IR, NMR	1250	1780, 1750	812656
[(μ-S-*o*-NH$_2$C$_6$H$_4$) $_2$Fe$_2$(NO)$_4$] (**185**)	Abs, IR, NMR, XR	1252	1779, 1753	668139
[(μ-SC$_6$H$_4$-*o*-N(CH$_3$)$_2$)$_2$Fe$_2$(NO)$_4$] (**186**)	Abs, IR, NMR, XR	1223	1808, 1778, 1752	830208
[(μ-SC$_6$H$_4$-*o*-COOH)$_2$Fe$_2$(NO)$_4$] (**187**)	Abs, IR, NMR	1184	1812, 1782, 1756	
[(μ-SC$_6$H$_4$-*o*-NH-COPh)$_2$Fe$_2$(NO)$_4$] (**188**)	Abs, IR, NMR	1178	1787, 1759	
[(μ-SC$_6$H$_4$-*m*-NH$_2$)$_2$Fe$_2$(NO)$_4$] (**189**)	IR, Mb, XR	1253	1766, 1733	1539665

https://doi.org/10.1021/acs.chemrev.1c00253

Table 17. continued

Complex	Properties	Ref	IR $\upsilon_{(NO)}$ cm^{-1}	CCDC #
[(μ-SC$_6$H$_4$-*m*-OH)$_2$Fe$_2$(NO)$_4$] (**190**)	IR, Mb, XR	1253	1779, 1737	1539666
[(μ-SC$_6$H$_4$-*m*-NO$_2$)$_2$Fe$_2$(NO)$_4$] (**191**)	DFT, E, Mb, XR	1253,1254		939149
[(μ-SCHPh$_2$)$_2$Fe$_2$(NO)$_4$] (**192**)	DFT, IR, XR	1248	1775	992170
[(μ-SCH$_2$Ph)$_2$Fe$_2$(NO)$_4$] (**193**)	Abs, IR, NMR, XR	1250,1252	1779, 1750	668140
[(μ-S(6-Me-2-pyridyl) $_2$Fe$_2$(NO)$_4$] (**194**)	E, IR, NMR, XR	1245	1690, 1670	691874
[(μ-*S(*4,6-dimethyl-2-pyrimidyl)$_2$Fe$_2$(NO)$_4$] (**195**)	E, IR, NMR, XR	1245	1693, 1674	691875
[(PyImiS)$_2$Fe$_2$(NO)$_4$] (**196**)[q]	IR	1209	1806, 1779	
[(μ-PyPepS)$_2$Fe$_2$(NO)$_4$] (**197**)[au]	IR	1209	1807, 1779, 1752	
[(μ-S-NAP)$_2$Fe$_2$(NO)$_4$] (**198**)[av]	Abs, IR, NMR, XR	1200	1808, 1775, 1751	798103
[(μ-(SGlu)$_2$Fe$_2$(NO)$_4$] (**199**)	EPR, IR, MS	1205	1787, 1750	
[(μ-CH$_3$HgS)$_2$Fe$_2$(NO)$_4$] (**200**)	IR, MS, XR	1255	1765, 1742	1120999
[(μ-SC$_5$H$_5$O)$_2$Fe$_2$(NO)$_4$] (**201**)	E, IR, XR	1256	1769, 1720	987520
[(μ-SC$_4$H$_3$SCH$_2$)$_2$Fe$_2$(NO)$_4$] (**202**)	DFT, E, IR, Mb, NMR, XR	1257	1758, 1726	933636
[(μ-SCH$_2$CH$_2$NH$_2$)(μ-SCH$_2$CH$_2$NH$_3$)Fe$_2$(NO)$_4$] (**203**)	Abs, EPR, IR, Mg, XR	1197	1678, 1658	941000
[(μ-SC$_6$H$_5$)(μ-SCH$_2$CH$_2$NH$_3$)Fe$_2$(NO)$_4$] (**204**)	Abs, EPR, IR, XR	1197	1685, 1665	941001
μ-S, μ-CO				
[(μ-CO)(μ-SCH$_2$CH$_2$NH$_3$)Fe$_2$(NO)$_4$] (**205**)	Abs, IR, NMR, XR	1197	1797, 1693	940998
μ-P				
[(μ-P(CF$_3$)$_2$)$_2$Fe$_2$(NO)$_4$] (**206**)	XR	1258		1157943
μ-P, μ-C				
[(μ-CH$_2$)(*η*^{2}-(P,P')-μ-Ph$_2$PPPh$_2$)Fe$_2$(NO)$_4$] (**207**)	IR, NMR, XR	1259-1261	1775, 1745, 1715	1125964 1125965
[(μ-PPh$_2$)(*η*-(C,P)-μ-CH$_2$PPh$_2$)Fe$_2$(NO)$_4$] (**208**)	IR, NMR, XR	1259-1261	1790, 1750, 1732	1125962 1125963
μ-S/N				
[(μ-SC$_7$H$_4$SN)$_2$Fe$_2$(NO)$_4$] (**209**)	Abs, EPR, IR, Mb, Mg, XR	1170,1184,1262	1789, 1736	661958
[(C$_{14}$H$_{12}$N$_3$S)$_2$Fe$_2$(NO)$_4$] (**210**)	Abs, E, IR, XR	1263	1789, 1732	717919
[(μ-SC$_7$H$_5$N$_2$)$_2$Fe$_2$(NO)$_4$] (**211**)	IR, Mb, Mg, MS, XR	1264	1787, 1738	665846
[(μ-C$_3$H$_3$N$_2$S)$_2$Fe$_2$(NO)$_4$] (**212**)	IR, Mb, Mg, XR	1265	1781, 1748, 1716	255995
[(μ-SC$_4$H$_5$N$_2$)$_2$Fe$_2$(NO)$_4$] (**213**)	E, IR, Mb, XR	1266	1782, 1748, 1716	273835
[(μ-C$_2$H$_2$N$_3$S)$_2$Fe$_2$(NO)$_4$] (**214**)	EPR, IR, Mb,	1262	1805, 1796, 1732	
[(μ-C$_2$H$_2$N$_4$S)$_2$Fe$_2$(NO)$_4$] (**215**)	EPR, IR, Mb, XR	1262	1732, 1805	203850
[(μ-SC$_7$H$_5$N$_4$)$_2$Fe$_2$(NO)$_4$] (**216**)	E, EPR, IR, NMR, Mb, Mg, XR	1267	1812, 1741	888010
[(μ-C$_2$H$_3$N$_4$S)$_2$Fe$_2$(NO)$_4$] (**217**)	EPR, IR, Mb	1262	1732, 1794	678842
μ-N/N				
[(N$_2$C$_5$H$_7$)$_2$Fe$_2$(NO)$_4$] (**218**)	IR, XR	1268	1800, 1785, 1735	1142809
[(μ-^{Me}Pyr)$_2$Fe$_2$(NO)$_4$] (**219**)[ax]	Abs, DFT, IR, NMR, XAS, XR	1241	1639, 1593	1984678 1984679
μ-O/O				
[(μ-bdmap)Fe$_2$(NO)$_4$] (**220**)[ay]	Abs, EPR, IR, NMR, XR	1269	1721, 1653	1912354
Anionic dinuclear DNICs				
μ-S				
[(μ-SEt)$_2$Fe$_2$(NO)$_4$]$^-$ (**221**)	Abs, EPR, IR, Mg XR	1270	1670, 1650	698110
[(μ-S^{t}Bu)$_2$Fe$_2$(NO)$_4$]$^-$ (**222**)	Abs, EPR, IR, Mg, XR	1173	1673, 1655	673339
[(μ-SPh-*p*-Cl)Fe$_2$(NO)$_4$]$^-$ (**223**)	Abs, IR, XR	1271	1683, 1667	1430686
[(μ-SC$_6$H$_4$-*o*-N(CH$_3$)$_2$)$_2$Fe$_2$(NO)$_4$]$^-$ (**224**)	Abs, EPR, IR	1223	1684, 1664	
μ-S, μ-CO				
[(μ-CO)(μ-SPh$_2$)Fe$_2$(NO)$_4$]$^-$ (**225**)	Abs, DFT, IR, XAS, XR	1272	1706, 1694	1049177
[(μ-CO)(μ-SC$_6$H$_4$-*o*-N(CH$_3$)$_2$)Fe$_2$(NO)$_4$]$^-$ (**226**)	Abs, IR, XR	1223	1705, 1691	830209
μ-S, μ-elemental S				
[(μ-S)(μ-SMe)Fe$_2$(NO)$_4$]$^-$ (**227**)	Abs, E, EPR, IR, NMR, XR	1166	1719, 1697	735085
[(μ-S)(μ-SEt)Fe$_2$(NO)$_4$]$^-$ (**228**)	Abs, E, EPR, IR, NMR, XR	1166	1709, 1686	735084
[(μ-S)(μ-SPh)Fe$_2$(NO)$_4$]$^-$ (**229**)	Abs, E, EPR, IR, NMR	1166	1721, 1693	
Dicationic dinuclear DNICs				
μ-S				
[(μ-S(CH$_2$)$_2$NH$_3$)$_2$Fe$_2$(NO)$_4$]$^{2+}$ (**230**)	DFT, IR, Mb, XR	1226,1273	1773, 1733	663194 610301
Dianionic dinuclear DNICs				
μ-S				
[(μ-S)$_2$Fe$_2$(NO)$_4$]$^{2-}$ (**231**)	Abs, IR, XR	1166,1274-1277	1666, 1642	1104691
[(μ-S$_2$O$_3$)$_2$Fe$_2$(NO)$_4$]$^{2-}$ (**232**)	IR, NMR, XR	1278	1787, 1758	1193450
[(μ-SC$_3$H$_6$S)Fe$_2$(NO)$_2$]$^{2-}$ (**233**)	IR, XR	1220	1658, 1591	1402953
μ-O/O				

Table 17. continued

Complex	Properties	Ref	IR $\upsilon_{(NO)}$ cm^{-1}	CCDC #
$[(\mu\text{-}MeO)_2Fe_2(NO)_4]^{2-}$ (**234**)	Abs, IR, XR,	1189	1684, 1625, 1578	1866110
$[(\mu\text{-}OPh)_2Fe_2(NO)_4]^{2-}$ (**235**)	Abs, IR, XR	1136	1651, 1602	882944
μ-SCH₂CH₂S				
$[(\mu\text{-}SC_2H_4S)_2Fe_2(NO)_4]^{2-}$ (**236**)	EPR, IR, XR	1220	1725, 1675	1402950
μ-NO, μ-S				
$[(\mu\text{-}NO)\ (\mu\text{-}\varkappa^2\text{-}SC_2H_4S)Fe_2(NO)_3]^{2-}$ (**237**)	IR, NMR, XR	1220	1675, 1624	1402951
$[(\mu\text{-}NO)\ (\mu\text{-}\varkappa^2\text{-}SC_3H_6S)Fe_2(NO)_3]^{2-}$ (**238**)	IR, XR	1220	1670, 1658, 1626, 1591	1402952
$[(\mu\text{-}NO)(\mu\text{-}\varkappa^2\text{-}bdt)Fe_2(NO)_3]^{2-}$ (**239**)	IR, XR	1220	1681, 1633	1402954
Bimetallic DNICs $[M]\cdot[Fe(NO)_2]$				
M = Se				
$[(SePh)_2Fe(NO)_2]^-$ (**240**)	Abs, EPR, IR, XR	1279	1735, 1694	1242246
$[Se_5Fe(NO)_2]^-$ (**241**)	Abs, EPR, IR, Mg, XR	1280	1736, 1697	281348
$[Se(\mu\text{-}CH_2)_3Fe_2(NO)_4]$ (**242**)	IR, NMR, XR	1281	1819, 1784, 1759, 1746	1218992
M = Pt				
$[(Ph_3P)_2Pt(\mu^3\text{-}S)_2Fe_2(NO)_4]$ (**243**)	IR, MS, NMR, XR	1282	1735, 1690	1120835
M = Co				
$[(NO)Co(bme\text{-}dach)(IMes)Fe(NO)_2]^+$ (**244**)[bc, h]	EPR, IR, XR	1283	1794, 1735	893865
M = Fe				
$[\{Fe(NS_3)(CO)\}Fe(NO)_2]$ (**245**)[ba]	IR, Mb, XR	1284	1769, 1722	178002
$[\{Fe(NS_3)(NO)\}Fe(NO)_2]$ (**246**)[ba]	IR, Mb, XR	1284	1789, 1736, 1654	178003
$[\{Fe(NS_3)(CN)\}Fe(NO)_2]^-$ (**247**)[ba]	IR, Mb, XR	1284	1717, 1672	178004
$[(NO)Fe(N_2S_2)Fe(NO)_2]$ (**248**)[bb]	DFT, EPR, IR, XR	1050	1690, 1662, 1640	940518
$[(NO)Fe(N_2S_2)Fe(NO)_2]^+$ (**249**)[bb]	DFT, E, IR, Mb, XR	1050	1796, 1761, 1742	829670
$[(NO)Fe(bme\text{-}dame)Fe(NO)_2]^+$ (**250**)[bj]	DFT, E, IR, XR	1285	1809, 1779, 1743	1815902
$[(NO)Fe(bme\text{-}dame)Fe(NO)_2]$ (**251**)[bj]	DFT, E, EPR, IR, Mg, XR	1285	1696, 1668, 1640	1860846
$[(NO)Fe(bme\text{-}dame)Fe(NO)_2]^-$ (**252**)[bj]	DFT, E, EPR, IR, Mg, XR	1285	1666, 1637, 1607	1815903
$[(ON)Fe(\mu\text{-}S,S\text{-}C_6H_4)_2Fe(NO)_2]^-$ (**253**)	Abs, EPR, IR, Mg, NMR, XR	1286	1766, 1746, 1719	235829
$[(ON)Fe(\mu\text{-}S,S\text{-}C_6H_3Me)_2Fe(NO)_2]^-$ (**254**)	Abs, EPR, IR, Mg, NMR	1286	1764, 1745, 1717	
$[(ON)Fe(S,SO_2\text{-}C_6H_4)(S,S\text{-}C_6H_4)Fe(NO)_2]^-$ (**255**)	Abs, EPR, IR, Mg, NMR, XR	1286	1783, 1762, 1726	235830
$[(dppe)(\eta^5\text{-}C_5Me_5)(CN)Fe]_2\text{–}Fe(NO)_2$ (**256**)[s]	E, IR, MS, XR	1224	1737, 1693	1840824
$[(dppe)(\eta^5\text{-}C_5H_5)Fe\text{-}CN\text{-}Fe(NO)_2(IMes)]^+$ (**257**)[h, s]	E, IR, MS, XR	1224	1795, 1729	1840853
$[(dppe)(\eta^5\text{-}C_5Me_5)Fe\text{–}CN\text{–}Fe(NO)_2(IMes)]^+$ (**258**) [h, s]	E, IR, MS, XR	1224	1790, 1729	1840809
M = Ni				
$[(NO)Ni(\mu\text{-}S(CH_2)_2S(CH_2)_2S)Fe(NO)_2]$ (**259**)	E, EPR, IR, XR	1279	1798, 1763, 1723	1242247
$[Ni(\mu\text{-}S(CH_2)_2N(Et)(CH_2)_3N(Et)(CH_2)_2S)Fe(NO)_2]$ (**260**)	E, IR, XR	1287	1663, 1624	1252248
$[Ni(bme\text{-}dach)]\cdot Fe(NO)_2(CO)]$ (**261**)[bc]	IR, XR	1288	1732, 1689	817759
$[NiN_2S_2\cdot Fe(NO)_2CO]$ (**262**)[bb]	IR	1289	1734, 1690	
$[Ni(bme\text{-}daco)]\cdot[Fe(NO)_2I)_2]$ (**263**)[bb]	DFT, E, EPR, IR, XR	1198	1793, 1731	1008320
$[NiN_2S_2\cdot Fe(NO)_2]$ (**264**)[bb]	DFT, E, IR, XR	1289	1681, 1630	1045461
$[NiN_2S_2\cdot Fe(NO)_2]^+$ (**265**)[bb]	DFT, E, EPR, IR, Mg, NMR	1289	Not specified	
$[(NiN_2S_2)_2\cdot Fe(NO)_2]^+$ (**266**)[bb]	DFT, E, IR, Mg, XR	1289	1790, 1736	1565539
$[NiN_2S_2\cdot Fe(NO)_2]_2^{2+}$ (**267**)[bb]	IR, XR	1289	1895, 1794, 1749, 1732	1045460
M = V				
$[V{\equiv}O(bme\text{-}daco)\cdot Fe(NO)_2I]$ (**268**)[bb]	DFT, E, EPR, IR, Mg, XR	1198	1796, 1733	1008321
M = Rare Earth (Y, Gd)				
$[(Cp^*)_2Y(\mu\text{-}ON)_2Fe(NacNac^{Mes})]$ (**269**)[be]	Abs, IR, NMR, XR	1290	1754, 1684, 1631, 1609, 1548	1909576
$[(Cp^*)_2Y(\mu\text{-}ON)_2Fe(NacNac^{Dipp})]$ (**270**)[bd]	Abs, EPR, IR, NMR, XR	1290	1760, 1721, 1696, 1648, 1623, 1552	1909570
$[(Cp^*)_2Gd(\mu\text{-}ON)_2Fe(NacNac^{Mes})]$ (**271**)[be]	Abs, EPR, IR, NMR, XR	1290	1754, 1679, 1629, 1608,	1909575
			1805, 1761	1909571

Table 17. continued

Complex	Properties	Ref	IR $\upsilon_{(NO)}$ cm^{-1}	CCDC #
$[(Cp^*)_2Gd(\mu\text{-}ON)_2Fe(NacNac^{Dipp})]$ (**272**)[bd]	Abs, IR, NMR, XR	1290	1710, 1648, 1623, 1552	
Neutral $\{Fe(NO)_2\}^{10}$ TNICs				
$[(Cl)Fe(NO)_3]$ (**273**)	DFT. IR, XR	1291,1292	1898, 1789	1722015
$[(Br)Fe(NO)_3]$ (**274**)	DFT, IR, XR	1292	1899, 1794	1729850
$[(I)Fe(NO)_3]$ (**275**)	DFT, IR, XR	1292,1293	1895, 1798	1729088
$[(\eta^1\text{-}BF_4)Fe(NO)_3]$ (**276**)	DFT, IR, NMR, XR	1291	1922, 1814	1722014
$[(\eta^1\text{-}PF_6)Fe(NO)_3]$ (**277**)	E, IR, NMR	1291	1922, 1810	
Cationic $\{Fe(NO)_2\}^{10}$ TNICs				
$[(CO)Fe(NO)_3]^+$ (**278**)	Abs, DFT, IR, NMR, XR	1294	1971, 1876	1962274
$[(EtCN)Fe(NO)_3]^+$ (**279**)	IR, NMR, XR	1291	1939, 1836	224760
$[((CH_2OH)_3P)Fe(NO)_3]^+$ (**280**)	EPR, IR, NMR, XR	1226	1927, 1833	610305
$[(NHC\text{-}Me)Fe(NO)_3]^+$ (**281**)[t]	IR	1169	1915, 1825, 1814	
$[(NHC\text{-}iPr)Fe(NO)_3]^+$ (**282**)[i]	E, IR, XR	1169	1915, 1826, 1810	851029
$[(NHC\text{-}Mes)Fe(NO)_3]^+$ (**283**)[bf]	E, IR, NMR, XR	1047	1932, 1831, 1804	829671
$[(NHC\text{-}MeMes)Fe(NO)_3]^+$ (**284**)[bg]	IR, NMR, XR	1295	1991, 1814	948618
$[(^{Me}DDB)Fe(NO)_3]^+$ (**285**)[r]	Abs, DFT, EPR, IR, XR	1213	1846, 1771, 1753	1528824
$[(^{Et}DDB)Fe(NO)_3]^+$ (**286**)[r]	Abs, IR, XR	1213	1847, 1772, 1753	1528825
$[(^{Iso}DDB)Fe(NO)_3]^+$ (**287**)[r]	Abs, IR	1213	1847, 1773, 1742	

[a] S-*p*-toyl = 4-methylbenzenethiolate. [b] Imid-iPr = 2-isopropylimidazole. [c] Cbz = carbazolate. [d] TMS = trimethylsilane. [e] Mes = mesityl. [f] Ac = acetyl. [g] N_2CHPh = dianion of 2,2′-(phenyl-methylene)bis(3-methylindole)). [h] Imes = 1, 3-bis(2,4,6-trimethylphenyl)imidazole-2-ylidene. [i] NHC-iPr = 1,3-diisopropylimidazol-2-ylidene. [j] SGlu = 1- thio-*β*-D-glucose tetraacetate. [k] Im = imidazole, MI = 1-methylimidazole. [l] HMPA = hexamethylphosphoric triamide. [m] PN = 2-(diphenylphosphino)pyridine. [n] H^+bme-daco = bismercaptoethanediazacyclooctane. [o] Ar-nacnac = anion of $[(2,6\text{-diisopropylphenyl})NC(Me)]_2CH)$. [p] TMEDA = tetramethylethyldiamine. [q] PyImiS = 2-((1-pyridin-2-yl)ethylidene)amino)-benzthiolate. [r] DDB = N,N′-bis(2,6-dialkylphenyl)-1,4-diaza-2,3 dimethyl-1,3-butadiene. [s] dppe = diphenyl phosphinoethane. [t] NHC-Me = 1,3-dimethylimidazol-2-ylidene. [u] dmp = 2,9-dimethyl-1,10-phenanthroline. [v] DTA = diethylenetriamine. [w] PMDTA = N,N,N′,N′′,N′′-pentamethyl-diethylenetriamine. [x] Me_6tren = tris[2-(dimethylamino)ethyl]amine. [y] ^{iPr}PDI = $2,6\text{-}[2,6\text{-}iPr_2\text{-}C_6H_3N{=}CMe]_2C_5H_3N$. [z] ^{DEA}PDI = $[(2,6\text{-}iPrC_6H_3)\text{-}(N{=}CMe)(N(Et)_2C_2H_4)(N{=}CMe)C_5H_3N]$. [aa] ^{MeO}PDI = $[(2,6\text{-}iPrC_6H_3)N{=}CMe)(2\text{-}MeO\text{-}6\text{-}MeC_6H_3)N{=}CMe)-C_5H_3N]$. [ab] didpa = $[(2,6\text{-}iPrC_6H_3)\text{-}(N{=}CMe)(N(iPr)_2C_2H_4)(N{=}CMe)C_5H_3N]$. [ac] 6-$Me_3$-TMPA = tris[(6-methyl-2-pyridyl)methyl)]amine. [ad] TMPA = tris(2-methylpyridyl)amine. [ae] PTA = 1,3,5-triaza-7-phosphatricyclo[3.3.1.1]decane. [af] DIM = N,N′-bis(2,4,6-tri-methylphenyl)-1,4-diaza-2,3-dimethyl-1,3-butadiene. [ag] bipy = 2,2′-bipyridine. [ah] terpy = 2,2′,2′′-terpyridine. [ai] phen = 1,10-phenantroline. [aj] BIAN = N,N′-1,2-acenaphthylenediylidene-bis[2,6-bis(1-methylethyl)]-benzeneamine. [ak] HMPE = 1,2-bis[bis(hydroxymethyl)phosphino]ethane. [al] DPPPr = 1,3-bis(diphenylphosphino)-propane. [am] DPPEt = cis-1,2-bis(diphenylphosphino)ethylene. [an] DPPBe = 1,2-bis(diphenylphosphino)benzene. [ao] TMBz = 1,2-bis[bis-(hydroxymethyl)phosphino]benzene. [ap] triphos = (2-((diphenylphosphanyl)methyl)-2-methyl- propane-1,3-diyl)-bis-(diphenylphosphane)). [aq] triphos^{Si} = ((methylsilanetriyl)tris(methylene))-tris(diphenylphosphane). [ar] diphos^{Si} = bis((diphenylphosphanyl)methyl)diphenylsilane. [as] ^{me}PyrCO$_2$ = 3-methyl-pyrazole-1-carboxylate. [at] TCNE − tetracyanoethylene. [au] PyPepS = $[SC_6H_4\text{-}o\text{-}NHC(O)(C_5H_4N)]$. [av] NAP = *N*-acetyl-D-penicillamine. [ax] ^{Me}Pyr = 3-methylpyrazolate. [ay] bdmap = 1,3-bis(dimethylamino)-2-propanolate. [az] bdt = 4-methyl-1,2-benzenedithiolate. [ba] NS_3 = $[N(CH_2CH_2S)_3]^{3-}$. [bb] N_2S_2 = bme-daco = *N,N*-bis(2-mercaptoethyl)-1,5-diazacyclooctane. [bc] bme-dach = bis-mercaptoethanediazacycloheptane. [bd] NacNac^{Dipp} = anion of $[((2,6\text{-diisopropylphenyl})NCMe))_2CH)]$. [be] NacNac^{Mes} = anion of $[(\text{mesityl})NCMe))_2CH)]$. [bf] NHC-Mes = 1,3-bis(2,4,6-trimethylphenyl)imidazol-2-ylidene. [bg] NHC-MeMes = 1-methyl-3-(2,4,6-trimethylphenyl)imidazol-2-ylidene. [bh] sIMes = 1,3-bis(2,4,6-trimethylphenyl)imidazole. [bi] L^{DPM} = 2,6-bis-(N-2,6-bis(diphenylmethyl)-4-isopropylphenyliminothiolate)pyridine. [bj] bme-dame = bis-mercaptoethyl-diazamethylethane.

associated Cambridge Crystallographic Data Centre (CCDC) registration numbers.

3.3.1. Synthetic Routes. Synthetic routes of DNICs were thoroughly reviewed by Lu and coworkers recently.[1022] There are 4 main strategies to synthesize DNICs: (1) reaction of pre-assembled Fe complexes with NO, (2) reaction of Fe with ligand or *S*-nitrosothiol, and NO, NO^+, NO_2^-, (3) ligand substitution from existing DNICs, and (4) redox interconversion between different electronic states or coordination environments of DNICs (Scheme 25).

3.3.1.1. Method a: Synthesis of Biomimetic DNICs from Iron−Sulfur (Fe−S) Clusters. Taking inspiration from biology, thiolate bound [Fe−S] complexes were reacted with NO, in either its gaseous form or using an NO donor, such as S-trityl thionitrite, resulting in DNIC formation. In Scheme 26a, starting with an all thiolate-bound tetrahedral Fe^{II} complex, addition of one equiv of NO to $[Fe(SR)_4]^{2-}$ leads to the formation of an intermediate mononitrosyliron complex (MNIC) that is subsequentially converted to DNIC with an additional equiv of NO (Scheme 26b).[1044,1173,1174] Similarly, DNIC formation occurs by starting with a diferric [2Fe−2S] thiolate-bound cluster and addition of NO (Scheme 26d).[1045] In the case of thiolate-bound [4Fe−4S] cluster, addition of NO leads to the formation of RBS, but in the presence of thiolate, DNIC formation is achieved as the bridging sulfides are released as elemental sulfur (Scheme 26c).[1045,1296] Complexes such as $[(SR)_2Fe(NO)_2]^-$ where R = ^{t}Bu (**2**), Et (**3**), or Ph (**6**) can be formed using this method. The mononuclear DNICs can be converted to a corresponding dinuclear DNIC, also called RRE, upon removing thiolate ligands by protonation[1178,1200] or oxidation (Scheme 26f).[1159] RRE can also be synthesized directly from the reaction of $[Fe(SR)_4]^{2-}$ with nitrosonium (NO^+) (Scheme 26h).[1044] Addition of thiolate can revert the RRE back to a mononulcear DNIC (Scheme 26e).[1174,1270,1297] If a Cys analog is used in the synthesis, [2Fe−2S] can be directly synthesized from ferric or ferrous tetrathiolate with

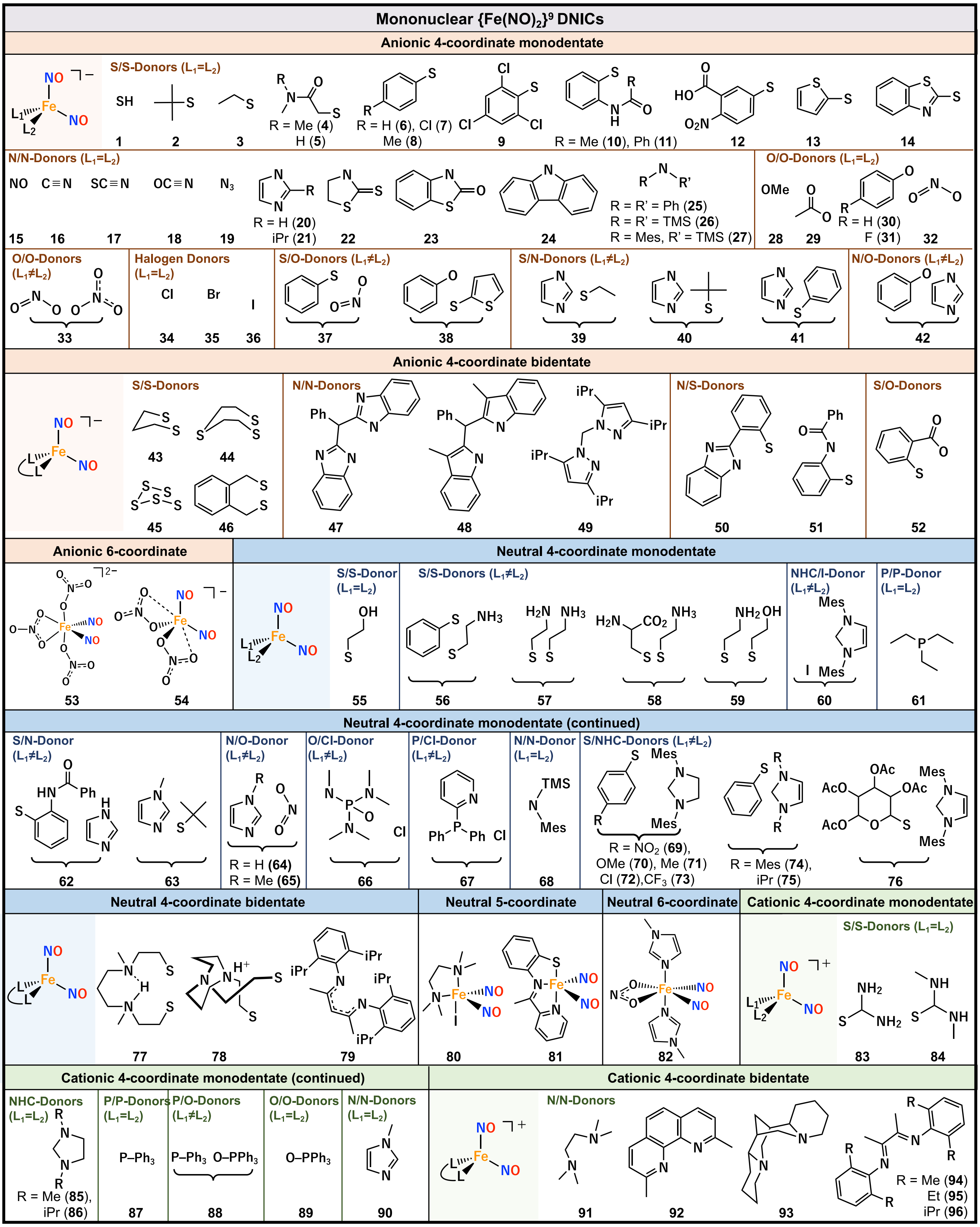

Figure 66. continued

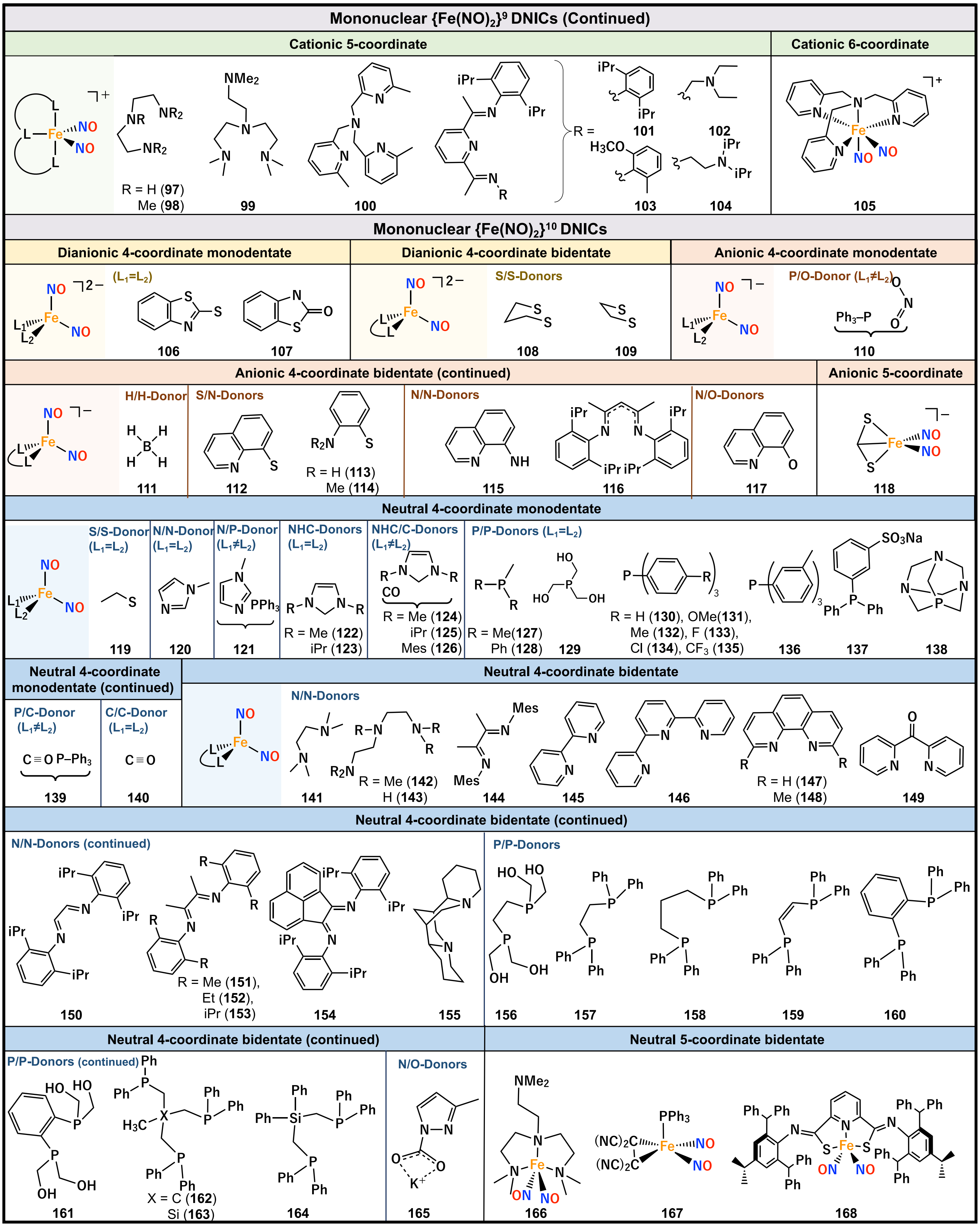

Figure 66. continued

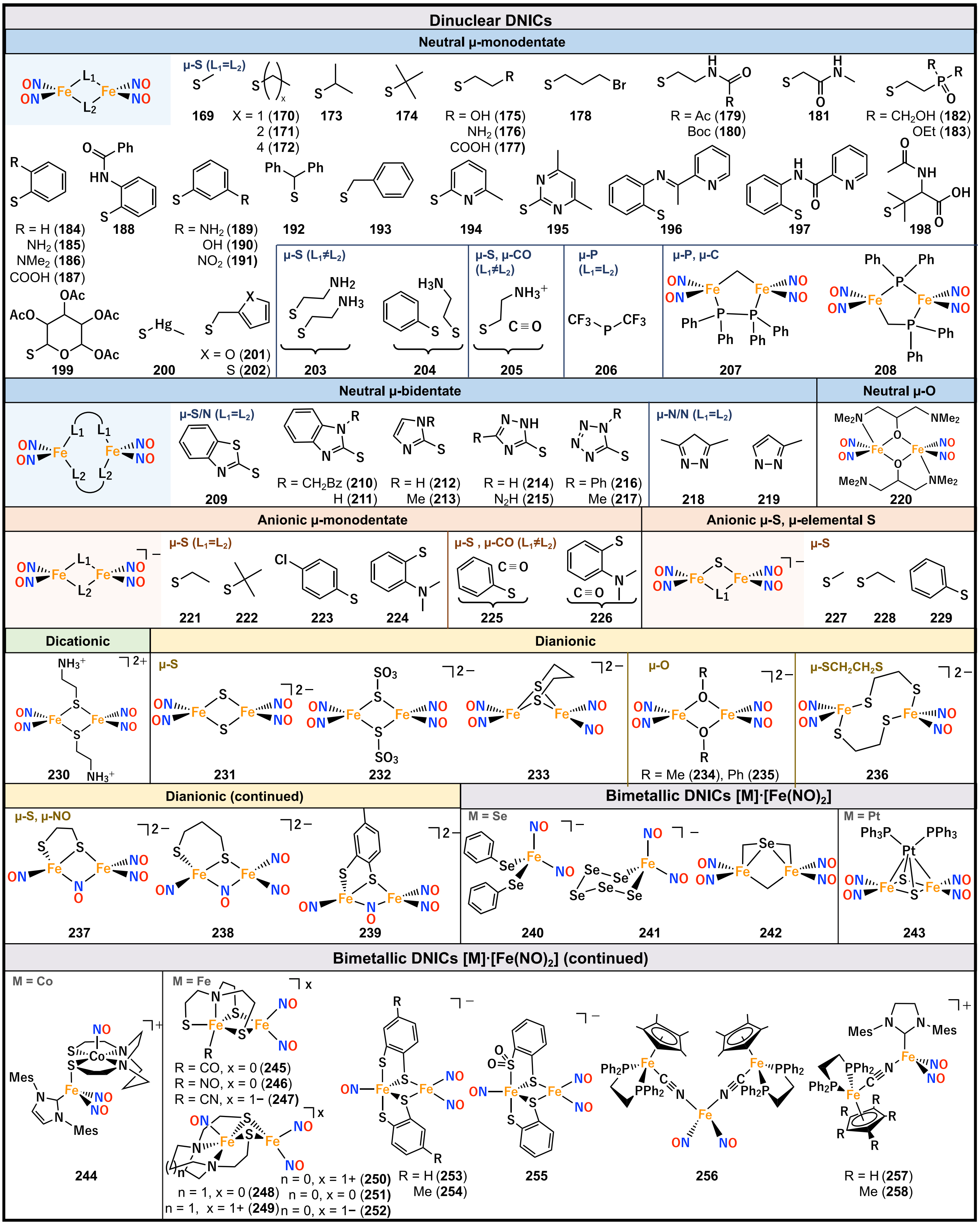

Figure 66. continued

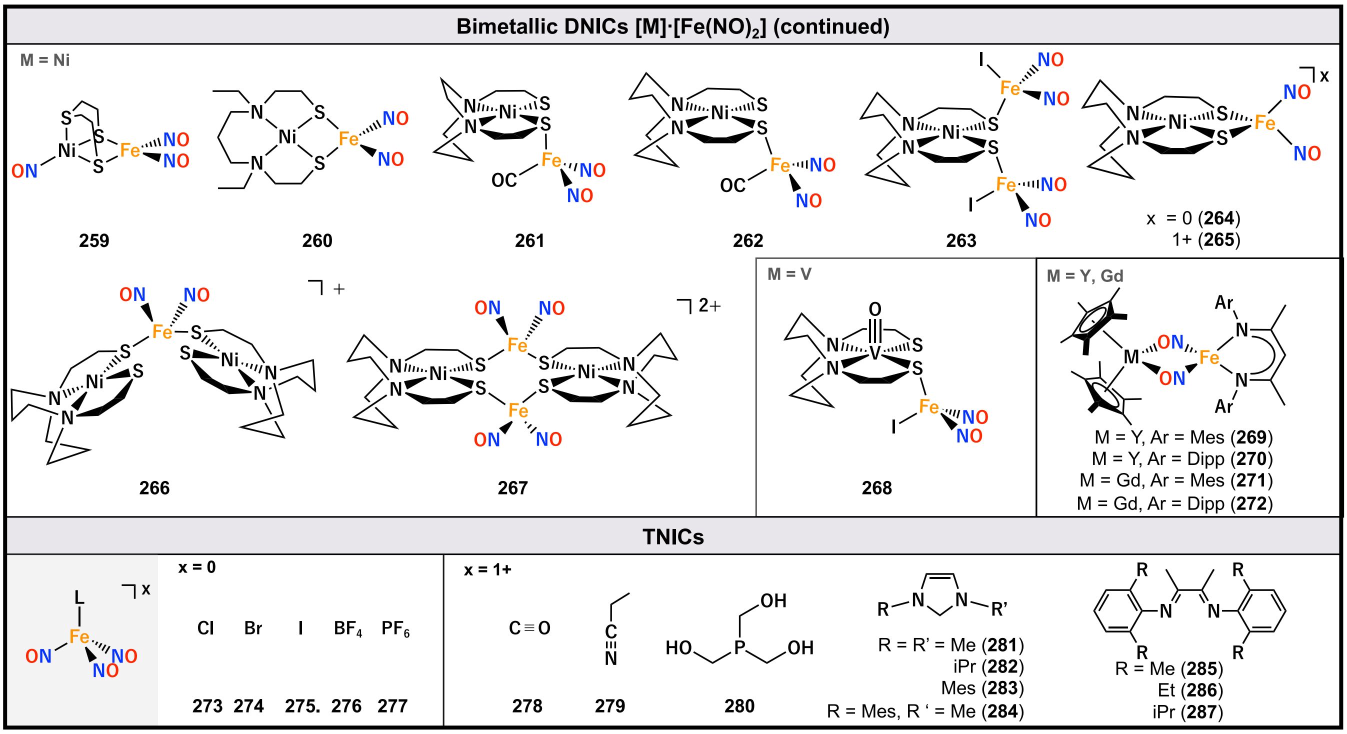

Figure 66. Supporting ligands for mono- and dinuclear DNICs, bimetallic DNICs, and TNICs.

Scheme 25. Main Synthetic Strategies for DNICs

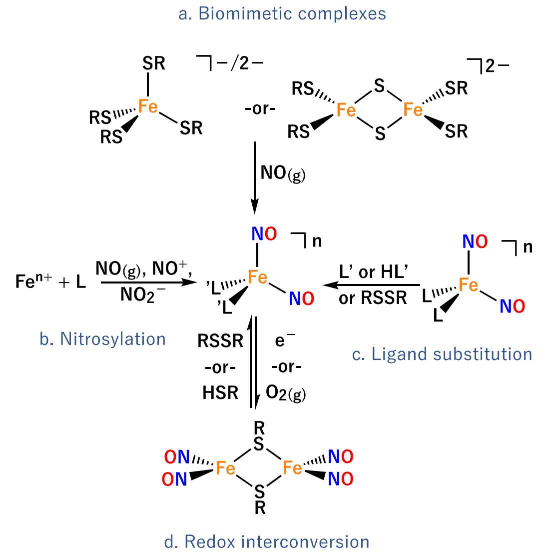

Scheme 26. Routes to DNIC Formation from Biomimetic Thiolate-Bound [Fe–S] Cluster

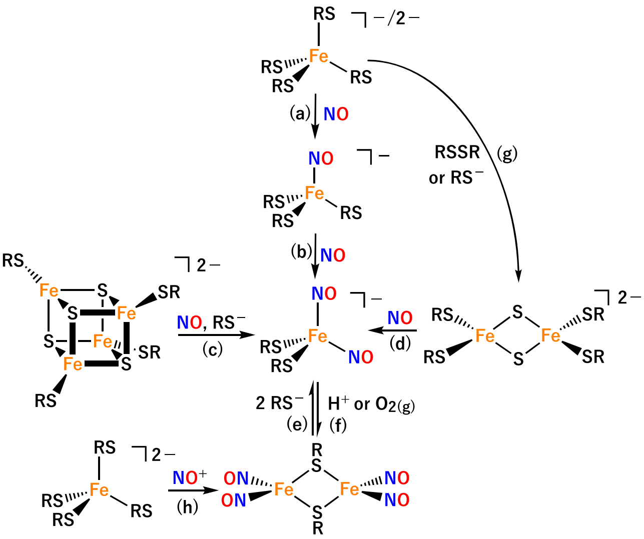

disulfide or thiol to form a [2Fe–2S] cluster (Scheme 26g) which then reacts with NO to yield a DNIC.[242]

3.3.1.2. Method b: Synthesis of DNICs from Free Fe Ions. Synthesizing DNICs from simple Fe salts is the most commonly used technique for biological assays to prepare dinuclear glutathione-, cysteine-, or thiosulfate-bound DNICs.[1298] Specifically, the glutathione-bound dinuclear DNIC is one of the most commonly used DNICs as a therapeutic and is synthetized by combining $FeSO_4$, sodium nitrite, and reduced glutathione.[1068,1299] It is important to note the facile interconversion between mono- and dinuclear DNICs in biological media, and it is generally understood that both exist in an equilibrium. Following the same approach of using Fe salts to form monoculear DNICs, synthetic dinculear DNICs can be formed upon reaction of $FeSO_4$ with thiol and NO_2^-, but the mechanism of this reaction is unclear (Scheme 27).[1249]

3.3.1.3. Method c: Direct Ligand Substitution. Direct ligand substitution using weak binder precursors are popular for synthesizing $\{Fe(NO)_2\}^9$ mononuclear and dinuclear DNICs. The general binding affinity for DNICs follows the trend: thiolates > imidazolates > alkoxides > nitrite/nitrates > halogens. Utilizing binding affinities, one can generate large libraries of DNICs to investigate coligand-based trends such as electronic structure, reactivity with small molecules, and NO releasing capabilities. For example, complexes **10**, **13**, **14**, **19**, **20**, **30–32**, **43**, and **46** have been prepared from halogenated

Scheme 27. Synthesis of a Dinuclear DNIC from Ferrous Sulfate, Thiol, and Nitrite

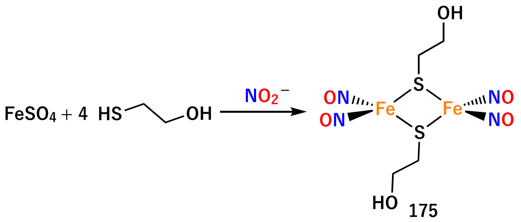

precursors. This method allows one to also control single substitutions using stoichiometric control as seen with complexes **37**, **38**, and **41**. There are also several examples of direct nucleophilic attack on dinclear DNICs to produce mononuclear $\{Fe(NO)_2\}^9$ DNICs, as seen in an alternative preparation of thiolate-bound DNIC complexes 3[1174,1194] and 6,[1270] as well as the synthesis of complexes **4**, **14**, **19**, **51**, **52**, **56−59**, **62**, and **69−75**. Another popular precursor is a bidentate $\{Fe(NO_2\}^{10}$ complex, $[(TMEDA)Fe(NO)_2]$ (**141**), which was used to synthesize rare DNICs via ligand substution, such as complexes **106−109**, **111**, **112**, **117**, **142**, **143**, and the first DNIC that features both linear/bent NO ligands, complex **118**.

The neutral $\{Fe(NO)_2\}^{10}$ complex $[Fe(CO)_2(NO)_2]$ (**140**) is synthesized by reacting $Fe(CO)_5$ and NO_2^- to release $CO_{2(g)}$, forming a MNIC intermediate that can subsequently react with NO^+ to generate a final DNIC product (Scheme 28).[1192,1300] This particular DNIC has been used to cleanly synthesize several four-coordinate $\{Fe(NO)_2\}^{10}$ DNICs, such as complexes **120**, **124−126**, **128**, **131−136**, **141**, **143**, **145−149**, **155**, and **166**, using ligand substitution via nucleophilic attack and release of $CO_{(g)}$. Alternatively, $[Fe(CO)_2(NO)_2]$ can be used to form dinuclear $[\{Fe(NO)_2\}^9]^2$ species, such as complexes **171**, **177**, **188**, **194−199**, **209**, and **219** upon dimerization after oxidative addition of disulfide or thiol (Scheme 29).[1022]

3.3.1.4. Method d: Redox Interconversion. Another synthetic route is to utilize the inherent redox properties of DNICs to alternate between mononuclear $\{Fe(NO)_2\}^9$ and $\{Fe(NO)_2\}^{10}$ complexes. Common reducing agents such as KC_8, $CoCp_2$ and $[HBEt_3]^-$ can directly reduce $\{Fe(NO)_2\}^9$ DNICs to $\{Fe(NO)_2\}^{10}$ as seen in complexes **107**, **108**, and **251**. However, in some cases, reduction of $\{Fe(NO)_2\}^9$ DNICs results in dimerization to form $\{Fe(NO)_2\}^{10}$-$\{Fe(NO)_2\}^{10}$ DNICs, **234** and **235**, to stablizie the electron rich core. Conversely, direct oxidation of $\{Fe(NO)_2\}^{10}$ DNICs results in $\{Fe(NO)_2\}^9$ complexes as seen in complexes **85−87** and **93−98**. Dinuclear DNICs can switch between the three available oxidation states $\{Fe(NO)_2\}^9$-$\{Fe(NO)_2\}^9$, $\{Fe(NO)_2\}^9$-$\{Fe(NO)_2\}^{10}$, and $\{Fe(NO)_2\}^{10}$-$\{Fe(NO)_2\}^{10}$ in $[(\mu\text{-}SR)_2Fe_2(NO)_4]$ where R = Et (**170**), ^{t}Bu (**174**), SPh (**184**) or SPh-*o*-NH_2 (**185**), explaining the g = 2.01 and 1.97 EPR signals found in biological complexes.[1098,1128,1270] Although rare, DNICs can be synthesized from disproportionation of hs-$\{FeNO\}^7$ species as seen for **92**.[652]

Scheme 28. Synthesis of $[Fe(CO)_2(NO)_2]$ (**140**)

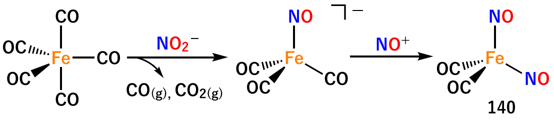

Scheme 29. Synthesis of DNICs from $[Fe(CO)_2(NO)_2]$ (**140**)

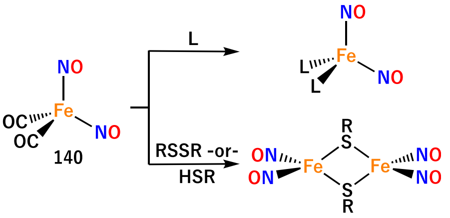

Some of the main hurdles in DNIC synthesis are air sensitivity, water sensitivity, and solubility. However, there are several DNICs, such as complexes **4**, **5**, **12**, **59**, **129**, **137**, **138**, **156**, **161**, **177**, and **230**, that utilize unique ligand designs to break these barriers so they can be used in biologically relevant settings. DNICs are capable of incorporating several elements and handling increasingly large ligand scaffolds to diversify their already vast chemistry.

3.3.2. Electronic Structure of DNICs. As the biological importance of DNICs received recognition, elucidation of their electronic structures became a topic of significant interest. Because of complications arising from the redox non-innocent nature of NO, several different views have been put forward with respect to the electronic structures of DNICs.

In early days when only a limited number of X-ray crystal structures were available for DNICs, researchers heavily relied on IR and EPR spectroscopy to probe the electronic structures of DNICs with the g = 2.03 signal. Two most widely discussed electronic structures were $\{Fe^I(^\bullet NO)_2\}^9$ and $\{Fe^{-I}(NO^+)_2\}^9$, called d^7 and d^9 species at that time, respectively. While many EPR studies preferred Fe^I in a d^7 configuration,[101,233,1098] some researchers viewed the N−O stretching frequencies (1650−1940 cm^{-1}) and the Fe−N−O angles (164−170°) of these species to be more consistent with Fe^{-1}, bonded to two NO^+ ligands, corresponding to a d^9 electron configuration for iron.[1301] Others suggested that the different solid versus solution structures can cause a change of electronic structure, so a d^9 DNIC in the solid state could become a d^7 DNIC in solution.[1302] It should also be noted that a 'd^9 DNIC' description in publications from the 1990s could mean two different species. In one instance, a d^9 DNIC could mean a $\{Fe^{-I}(NO^+)_2\}^9$ species as described above. In other cases, d^9 species refer to a new S = 1/2 paramagnetic species obtained upon reduction of a d^7 DNIC, $\{Fe^I(^\bullet NO)_2\}^9$, with sodium dithionite, implying that iron is reduced by two electrons to have a d^9 configuration.[233,240,1098] However, it was later shown that this presumed 'd^9 DNIC' obtained by reduction is in fact the one-electron reduced form of RRE.[1128,1173,1270]

More than a decade later, Liaw and coworkers provided fresh insights into the electronic structures of DNICs by applying their group's synthetic prowess in combination with a slew of spectroscopic methods, including X-ray absorption and X-ray emission spectroscopy, some of which were not available in the 1990s.[1132−1136] Using the simple $\{Fe(NO)_2\}^9$ DNIC $[S_5Fe(NO)_2]^-$ (**45**), the oxidation state of Fe^I was proposed based on Fe K-/L-edge XAS measurements, and the radical character of NO was deduced from O K-edge XAS. Compound **45** was then described as $\{Fe^I(^\bullet NO)_2\}^9$, in which the spins of Fe^I ($S = 3/2$) and the two NO ligands ($S = 1/2$) are AF coupled, to give $S_t = 1/2$.[1303] The $\{Fe^I(^\bullet NO)_2\}^9$ description for **45** and other anionic DNICs including $[(SPh)_2Fe(NO)_2]^-$ (**6**) was further supported by Dai and Ke from a normal coordinate analysis linking Raman spectroscopy and DFT calculations.[1303] In the following years, however, the Liaw group revised their view on the general electronic structure of $\{Fe(NO)_2\}^9$ DNICs a couple of times, each of which was prompted by extended and deeper studies on DNICs with more advanced spectroscopic methods. They observed that the Fe K-edge XAS pre-edge energies of a large group of $\{Fe(NO)_2\}^9$ DNICs fell in between the values for pure Fe^{II} and Fe^{III} standards, which led them to propose a resonance hybrid of $\{Fe^{I}(^{\bullet}NO)_2\}^9$, $\{Fe^{II}(^{\bullet}NO)(NO^-)\}^9$, and $\{Fe^{III}(NO^-)_2\}^9$ for the general electronic structure of anionic DNICs.[1135] This proposal was further revised after investigating the d manifold energies by S K-edge and Fe K-edge XAS, which, taken together, suggested an $\{Fe^{III}(NO^-)_2\}^9$ electronic structure for $[(SEt)_2Fe(NO)_2]^-$ (**3**).[1133] Finally, a follow-up investigation on the oxidation state of the NO ligands of $[(PhS)_2Fe(NO)_2]^-$ (**6**) and $[(PhO)_2Fe(NO)_2]^-$ (**30**) by valence-to-core X-ray emission spectroscopy revealed the oxidation state of the NO ligands of these DNIC to be -0.77 ± 0.18 and -0.95 ± 0.18, respectively, which led the researchers to settle with the final electronic structure description of $\{Fe^{III}(NO^-)_2\}^9$ for $\{Fe(NO)_2\}^9$ DNICs.[1021,1134]

Further insights into the electronic structures of DNICs came from spectroscopic and theoretical calculations on pairs of $\{Fe(NO)_2\}^{9/10}$ DNICs, probing the consequences of one-electron reduction of $\{Fe(NO)_2\}^9$ species for the electronic structure.[652,1304] An anionic $\{Fe(NO)_2\}^{10}$ DNIC, $[(Ar\text{-}nacnac)Fe(NO)_2]^-$ (**116**) and its oxidized form, $[(Ar\text{-}nacnac)Fe(NO)_2]$ (**79**), are a structurally and spectroscopically well-characterized pair, for which there are only slight differences in their solid-state structures and Mössbauer parameters ($\delta = 0.22$ mm/s and $\Delta E_Q = 1.31$ mm/s for **116**; $\delta = 0.19$ mm/s and $\Delta E_Q = 0.79$ mm/s for **79**).[232,235] Neese and coworkers carried out DFT calculations that were calibrated to experimental Mössbauer parameters to determine the electronic structures of these $\{Fe(NO)_2\}^{9/10}$DNICs. The results suggest that there exist two resonance structures for $\{Fe(NO)_2\}^9$: one where a hs-Fe^{III} ($S = 5/2$) is AF coupled to two triplet NO^- ligands ($S_{(NO)2} = 2$) and one where a hs-Fe^{II} ($S = 2$) is AF coupled to an overall quartet $^4(NO)_2^-$ ligand set ($S_{NO} = 3/2$). The $\{Fe(NO)_2\}^{10}$ state, on the other hand, was assigned to a hs-Fe^{II} AF coupled to two triplet NO^- ligands.[1304] Using another $\{Fe(NO)_2\}^{9/10}$ DNIC pair, $[(dmp)Fe(NO)_2]^+$ (**92**) and $[(dmp)Fe(NO)_2]$ (**148**), Lehnert and coworkers applied nuclear resonance vibrational spectroscopy in conjunction with Mössbauer spectroscopy and DFT calculations to uncover the Fe−NO bonding interactions and electronic structures of these DNICs.[652] The electronic structures observed in the **92**/**148** pair are consistent with the **79**/**110** pair. In both cases, an iron-centered reduction was observed for the $\{Fe(NO)_2\}^9$ to $\{Fe(NO)_2\}^{10}$ conversion, and π-backbonding is significantly enhanced in the $\{Fe(NO)_2\}^{10}$ system as compared to the $\{Fe(NO)_2\}^9$ complex.

3.4. DNIC Reactivity and Small Molecule Activation

The main function of biological DNICs is understood to be storage and transport of NO, but there are several other functions DNICs are capable of inside and outside biological contexts. Synthetic DNICs have been shown to not only release NO, but to stimulate post-translational protein modifications, interact with O_2 and H_2S, and catalyze CO_2 reduction and the hydrogen evolution reaction (HER).

3.4.1. NO Release. NO release from DNICs quickly became a popular topic among synthetic chemists looking to not only understand how it works, but how to take advantage of it by designing ligands that tune their NO-releasing properties. DNICs are stable molecules that can be stored in solution. There are several conditions that can trigger NO release.

3.4.1.1. Photoinduced NO Release. NO release from DNICs by photolysis is the most widely applied method in the laboratory. Investigations by Ford and coworkers reveled photoinduced release of $NO^{\bullet}$ from RREs, $[(\mu\text{-}SR)_2Fe_2(NO)_4]$, where R = CH_3 (**169**), CH_2CH_3 (**170**), CH_2CH_2OH (**175**) and CH_2Ph (**193**). Interestingly, under anaerobic conditions $NO^{\bullet}$ release is reversible, but becomes permanent in the presence of dioxygen.[1042] Using a mononuclear DNIC with a bidentate ligand, $[(H^+bme\text{-}daco)Fe(NO)_2]$ (**78**), Darensbourg and coworkers demonstrated NO^- release using photolysis and heat to a ferric porphyrin, mimicking reductive nitrosylation of heme, while under the same conditions $NO^{\bullet}$ was delivered to Fe^{II} and Co^{II} porphyrins (see Scheme 30).[1195,1206] Similarly, the Lippard group reported NO^- and $NO^{\bullet}$ transfer from $[(Ar\text{-}nacnac)Fe(NO)_2]$ (**79**), in which **79** donated NO^- to $[Fe^{III}(TPP)Cl]$ by photolysis or heat while **79** donated $NO^{\bullet}$ to $[Fe^{II}(TPP)Cl]^-$.[235] Not only showing NO release but also a possible repair mechanism, the DNIC $[S_5Fe(NO)_2]^-$ (**45**) was shown to convert back to its starting [2Fe−2S] form upon photolysis in the presence of an NO-acceptor as described in Section 3.2.3.[1132]

DNICs have been evaluated for their NO releasing ability in therapeutics using photochemical uncaging.[1030] Photochemical release allows for spatial and temporal control of targeted NO release in a cell, but is limited by the penetrating ability of UV to NIR light. To circumvent this disadvantage, Ford and coworkers looked to apply photosensitizers, such as protoporphyrin derivatives and fluorescein, to their dinuclear DNIC model complexes, which improved their NO release properties compared to their earlier models.[1030,1042,1276,1305−1310]

3.4.1.2. Ligand Effects. The nature of the supporting ligands in a DNIC can influence the form of NO that is released: NO^+, $NO^{\bullet}$ or HNO/NO^-.[1187] The compound $[(Cbz)_2Fe(NO)_2]^-$(**24**) was subjected to ligand exchange with $(S_2CNMe_2)_2$, $(PyPepS)_2$, and $P(C_6H_3\text{-}3\text{-}SiMe_3\text{-}2\text{-}SH)_3$, which led to release of NO^+, NO, and NO^-, respectively (see Scheme 31).[1187] The coordination number of iron can also influence the stability of DNICs. The 5C complex $[(TMEDA)Fe(NO)_2I]$ (**80**) is a stable $\{Fe(NO)_2\}^9$ DNIC in solution. However, removing the iodide ligand from **80** generates a meta-stable cationic $\{Fe(NO)_2\}^9$ species that subsequently releases NO.[1208] Lu and coworkers used a series of DNICs, $[(SPh)_2Fe(NO)_2]^-$(**6**), $[(\mu\text{-}SEt)_2Fe_2(NO)_4]$ (**170**) and $[(\mu\text{-}^{Me}Pyr)_2Fe_2(NO)_4]$ (**219**), to test the release of nitroxyl (NO^-) to an awaiting Fe^{III} porphyrin. They found that the

Scheme 30. Transfer of NO^- and $NO^{\bullet}$ from a DNIC

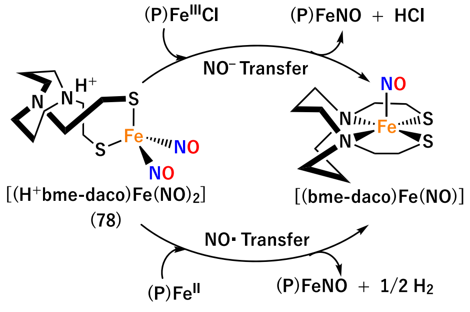

Scheme 31. Ligand Influence on Redox Form of NO That Is Released

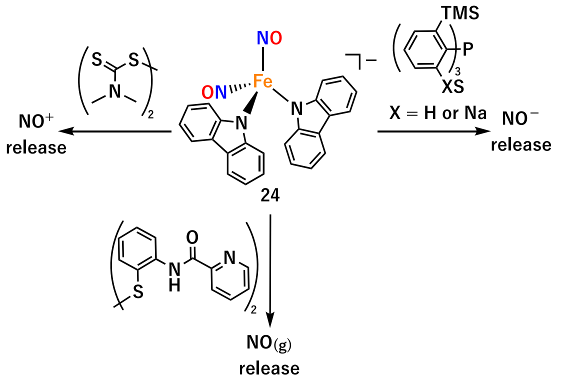

dinculear $\{Fe(NO)_2\}^9$-$\{Fe(NO)_2\}^9$ complex **219** with pyrazolate bridges releases NO^- significantly more efficiently than **6** and **170**. They also observed successful nitroxyl-transfer in aqueous conditions to met-Mb and met-Hb.[1311] XAS studies revealed that the Fe^{III} center in **219** is more electron-deficient compared to other tested DNICs.[1311] All of these examples strongly suggest that the ligand structure and environment largely determine which redox form of NO is released, similar to how one would expect that different biological protein environments could influence the NO release form.

3.4.1.3. Redox Effects. Darensbourg and coworkers discovered that DNICs supported by NHC ligands have superior NO donating ability and they can effectively release NO without photolysis.[1169] From their investigations on the NO-releasing abilities of NHC-bound $\{Fe(NO)_2\}^{9/10}$ DNICs to a NO-trapping agent, an interesting redox-dependent trend was observed. While the $\{Fe(NO)_2\}^9$ DNICs, $[(NHC\text{-}Me)_2Fe(NO)_2]^+$ (**85**) and $[(NHC\text{-}iPr)_2Fe(NO)_2]^+$ (**86**), are able to release NO, their reduced $\{Fe(NO)_2\}^{10}$ analogs, $[(NHC\text{-}Me)_2Fe(NO)_2]$ (**122**) and $[(NHC\text{-}iPr)_2Fe(NO)_2]$ (**123**), are unreactive.[1169] Similarly, Kim and coworkers reported that the otherwise inert, neutral $\{Fe(NO)_2\}^{10}$ DNIC $[(TMEDA)Fe(NO)_2]$ (**141**) spontaneously releases NO upon oxidation, via formation of the meta-stable, cationic $\{Fe(NO)_2\}^9$ DNIC $[(TMEDA)Fe(NO)_2]^+$ (**91**).[1208]

3.4.1.4. NO Release from TNICs. The mysterious trinitrosyl analogs of MNICs and DNICs, trinitrosyliron complexes (TNICs), pose unique challenges as they are hard to characterize due to their diamagnetic $\{Fe(NO)_3\}^{10}$ cores and thermal instability. However, their quick NO releasing capabilities are appealing for pro-drug applications. Darensbourg and coworkers reported an NHC ligand design to stabilize TNICs at room temperature (Scheme 32). Compared to previous models such as **273**−**277** and **280** that feature Lewis base adducts, halogen ligands, and phosphine ligands,[1047,1226,1291−1293] the bulky NHC-bound TNIC complex $[(IMes)Fe(NO)_3]^+$ (**283**) is able to stably transfer one NO moiety and form a $\{Fe(NO)_2\}^9$ DNIC, $[(IMes)(SPh)Fe(NO)_2]$ (**74**; Scheme 32).[1047,1226,1291−1293] Additionally, Liaw and coworkers were able to synthesize TNICs containing a radical NO ligand, $[(^{R}DDB)Fe(NO)_3]^+$ (**285**−**287**), with an unusually long Fe−NO bound, leading to a unique triplet ground state.[1213] The simple addition of $MeCN/H_2O$ into a CH_2Cl_2 solution of **285**−**287** at 25 °C then releases NO as a neutral radical.[1213] The future of TNICs is their use in biomedical applications for NO release.

Scheme 32. NO Transfer from a Stable TNIC

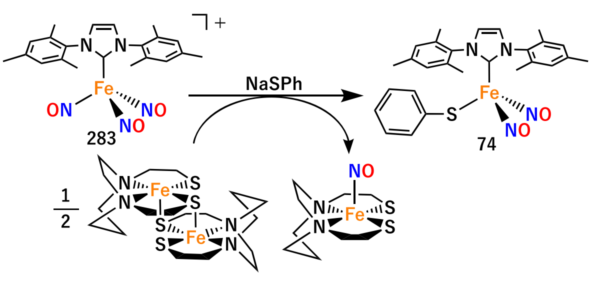

3.4.2. Other Nitrogen Oxides Associated with DNICs.

3.4.2.1. Nitrite and Nitrate. There is a noncanonical pathway for nitric oxide generation beyond nitric oxide synthase (NOS; see Section 2.1), known as the nitrate-nitrite-nitric oxide pathway.[912] The chemical reactivity of DNICs indicates that it might be possible for cellular DNICs to be involved in the nitrate → nitrite → nitric oxide cell signaling pathway. The conversion of DNICs to nitrates is one of the longest known reactivities of synthetic DNICs. In the late 1980s through the 1990s, Postel and coworkers made significant efforts to understand the diverse reactivity of a series of DNICs. One such effort was to study dioxygen reactivity of $\{Fe(NO)_2\}^9$ DNICs including $[Cl_2Fe(NO)_2]^-$ (**34**), which was cocomplexed with $[Fe(NN)_3]^{2+}$, where NN = bpy, 4,4′-dimethyl-2,2′-bipyridine, or phen.[1312] The reaction between $[Fe(NN)_3][Fe(NO)_2Cl_2]_2$ and O_2 results in iron nitrates, $[Fe(NO_3)(NN)Cl_2]$ and $[Fe(NO_3)_2(NN)Cl]$. Interestingly, these iron nitrate complexes and **34** show catalytic activity for the autoxidation of cyclohexene in the presence of O_2 via a radical mechanism. In addition, the nitrato complexes rapidly react with PPh_3 and carry out O atom transfer from nitrate to PPh_3, producing $O{=}PPh_3$ in the absence of O_2.[1312] A similar O_2 reactivity was observed for other neutral $\{Fe(NO)_2\}^9$ DNICs, $[Fe(L)Cl(NO)_2]$ (L= PPh_3 or $OPPh_3$), which quantitatively yielded the pentagonal nitrato compound, $[Fe(NO_3)_2Cl(OPPh_3)_2]$.[1313] The resulting nitrato compound is capable of O atom transfer to PPh_3 or cyclohexene, demonstrating the first example of O atom transfer from a nitrato ligand to an olefin. Postel and coworkers further noticed that the O-atom transfer ability of the iron nitrato complexes is dependent on the number of ligands bound to iron.[1202] When a sterically demanding DNIC, $[(HMPA)(Cl)Fe(NO)_2]$ (**66**), was used, oxygenation resulted in several different types of iron nitrato complexes of which only 5C nitrate complexes, such as $[Fe(NO_3)_2Cl(HMPA)_2]$ or $[Fe(NO_3)Cl_2(HMPA)_2]$, are capable of transferring O atoms to phosphines, while 4C nitrate complexes have no oxidizing capability. The authors suggested that the enhanced electron density on the $Fe(NO_3)_2$ moiety is a key factor for the oxygenation step.[1202]

The O_2 chemistry of DNICs has been revisited in recent years.[1048,1237,1314] Upon exposure to O_2, complexes $[(TMEDA)Fe(NO)_2]$ (**141**) and $[(dmp)Fe(NO)_2]$ (**148**) generate peroxynitrite ($ONOO^-$), which subsequently isomerizes to nitrate (see below). Interestingly, a completely different O_2 reactivity is observed with $[(PMDTA)Fe(NO)_2]$ (**142**), in which the PMDTA ligand has an extra dangling amine moiety compared to the TMEDA ligand in **141**. Unlike **141**, the O_2 reaction with **142** generates nitrite instead. It is proposed that the presumed peroxynitrite intermediate generated from **142** and O_2 undergoes a homolytic O−O bond cleavage aided by the coordination of the dangling amine, suggesting a pathway for NO to nitrite transformation by DNICs (Scheme 33).[1314]

The importance of the coordination number and type of ligands for the NO/nitrite/nitrate transformations by DNICs were investigated. The nitrate-bound DNIC $[(\kappa^1\text{-ONO}_2)_2\text{Fe(NO)}_2]^-$(**54**) forms an N-bound nitro $\{\text{FeNO}\}^6$ complex upon disulfide addition (Scheme 34), presumably via intramolecular association between nitrate and NO genreating $^\bullet\text{NO}_2$.[1191] Upon further treatment with imidazole and the O-atom acceptor dimethyl sulfide, the nitro $\{\text{FeNO}\}^6$ complex releases NO to form a ls-$\{\text{FeNO}\}^7$ species (Scheme 34).[1191] Another example of DNIC-mediated NO_2^- to NO conversion was observed for the nitrite-bound DNIC $[(\text{MI})(\text{ONO})\text{Fe(NO)}_2]$ (**65**). Addition of 1-methylimidazole (MI) to **65** leads to the formation of $[(\text{MI})_2(\eta^2\text{-(ONO)Fe(NO)}_2]$ (**82**). The subsequent addition of PPh_3 to **82** converts its nitrito-ligand into NO, to be released through reductive elimination, generating the $\{\text{Fe(NO)}_2\}^{10}$ DNIC $[(\text{MI})(\text{PPh}_3)\text{Fe(NO)}_2]$ (**121**) (Scheme 35).[1201] The role of imidazole in controlling nitrite activation via a 6C intermediate can potentially be translated to similar processes of NO production in biological systems.[1190,1201] NO release was also seen from an anionic nitro-bound $\{\text{Fe(NO)}_2\}^{10}$ complex, $[(\text{PPh}_3)(\text{NO}_2)\text{Fe(NO)}_2]^-$ (**110**), upon addition of acetic acid, where the $\{\text{Fe(NO)}_2\}^{10}$ center provides the reducing equivalent and converts into a $\{\text{Fe(NO)}_2\}^9$ DNIC, $[(\text{OAc})_2\text{Fe(NO)}_2]^-$ (**29**).[1190]

3.4.2.2. Generation of N_2O. The reductive coupling of two NO ligands in DNICs is rarely observed, although the NO (or NO^-) moieties are in close proximity with sufficient electrons. This is because the strong AF coupling between the individual NO^- ligands and iron forces the spins of the NO^- ligands to be parallel, which hampers the formation of an N−N bond and translates into a large activation barrier.[652] In a rare example, N_2O release was reported by Layfield and coworkers from NacNac-bound $\{\text{Fe(NO)}_2\}^{10}$ DNICs, after coordination of a rare earth metal to the O atoms of the coordinated NO ligands, **269**−**272** (see Table 17, Figure 66 and Scheme 36a).[1290] One mechanistic possibility is that the exophilic rare-earth elements, driving the formation of isonitrosyl bonds, force the DNIC N-atoms into proximity, which is further aided by the bulky coligands. The dinitrosyl unit of $[(\text{Cp}^*)_2\text{Gd}(\mu\text{-ON})_2\text{Fe}(\text{NacNac}^{\text{Dipp}})]$ (**272**), for example, has a substantially smaller N−Fe−N bond angle and a shorter N—N distance compared to the mononuclear DNIC precursor, **116**, by margins of 17.9° and 0.324 Å, respectively. The authors postulate that the sterically enforced positioning of two NO ligands might play a role in overcoming the barrier to N−N coupling and N_2O formation.[1290] However, the observed slow reaction (e.g., 5 days in solution) questions whether the DNIC is actually involved in N_2O formation or whether some other intermediate forms first. Another example of N_2O formation by DNICs was reported by Liaw and coworkers, who prepared an electronically localized dinuclear DNIC bridged by an alkoxide (bdmap^-) coligand (see Scheme 36b).[1269,1315] In this example, the NO ligands of the DNIC serve as redox non-innocent units to facilitate the binding and reductive coupling of exogenous NO. The dinuclear $\{\text{Fe(NO)}_2\}^{10}$-$\{\text{Fe(NO)}_2\}^9$ DNIC reacts with 1 equiv of NO to form a crystallographically characterized *trans*-hyponitrite bound tetranuclear complex, which converts

Scheme 33. O_2 Reactivity Leads to Nitrite Generation

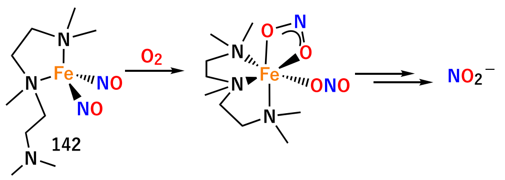

Scheme 34. Nitrate-Bound DNIC $[(\kappa^1\text{-ONO}_2)_2\text{Fe(NO)}_2]^-$ (54) Forms an N-Bound Nitro $\{\text{FeNO}\}^6$ Complex upon Disulfide Addition

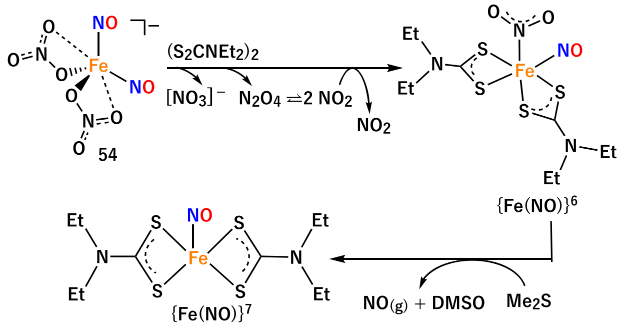

Scheme 35. Conversion of Nitrite to NO Mediated by a DNIC

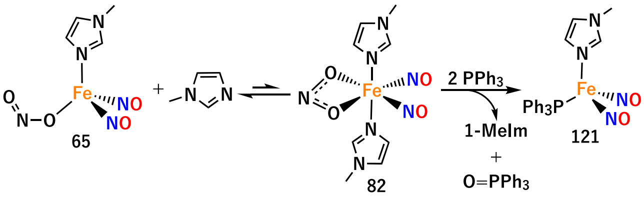

Scheme 36. N_2O Release from DNICs Coupled to Rare Earth Metals and from a Hyponitrite-Coordinated Tetranuclear DNIC

a. N_2O release from DNIC coupled to rare earth metals

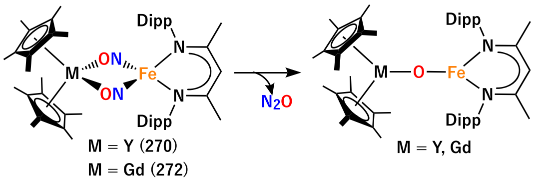

b. N_2O release from hyponitrite-coordianted tetranuclear DNIC

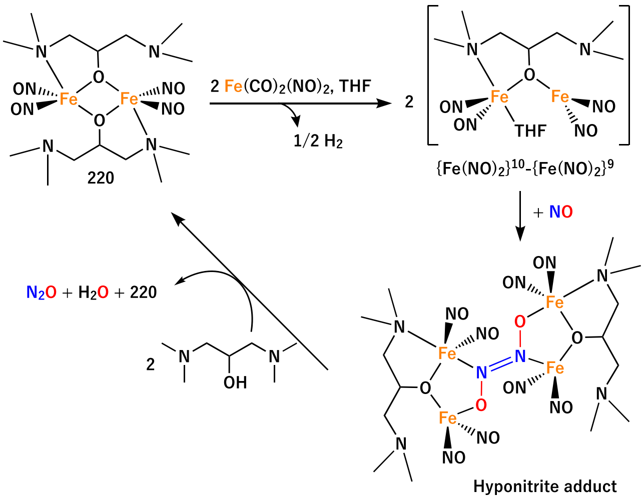

to N_2O upon addition of Hbdmap.[1269,1315] A particularly interesting aspect of this system is the fact that it can switch between NO reduction and NO disproportionation, depending on the conditions.

3.4.2.3. Generation of N_2. A very interesting, although unexpected, generation of N_2 from dinuclear $\{Fe(NO)_2\}^9$ DNICs was reported by Postel and coworkers in 1991.[1316] Dinuclear, neutral $\{Fe(NO)_2\}^9$ complexes using bridging diphosphine ligands, $[Fe(NO)_2Cl]_2(\mu\text{-PP})$, where PP =1,2-bis(diphenylphosphino)ethane or trans-1,2-bis(diphenylphosphino)ethene, were prepared and characterized. The reaction of $[Fe(NO)_2Cl]_2(\mu\text{-PP})$ with excess PP ligand results in a mixture of a $\{Fe(NO)_2\}^{10}$ DNIC, $[Fe-(NO)_2(PP)]$, and an unexpected mononitrosyl iron species, $[Fe(NO)(OPP)]$, where OPP = 1,2-bis(diphenylphosphino)ethane monoxide or trans-1-2-bis(diphenylphosphino)ethene monoxide. During the reaction, evolution of N_2 was detected by gas chromatography (GC), which is likely promoted by an intramolecular redox reaction.[1316]

3.4.3. Biomimetic Post-Translational Modifications.

3.4.3.1. S-Nitrosylation. As described in Section 3.2.2, cellular DNICs induce *S*-nitrosylation of proteins by an unknown mechanism. Ford and coworkers shed light on this reaction by detailed kinetic studies on the DNIC formation mechanism using biological low molecular weight thiols (e.g., cysteine, glutathione) in aqueous media.[1065,1317,1318] Their study suggests a two-step reaction process involving $\{FeNO\}^7$ and $\{FeNO\}^8$ MNIC intermediates that lead to a $\{Fe(NO)_2\}^9$ DNIC in equilibrium with its dinuclear counterpart.[1065,1318] Subsequent EPR studies revealed that the second step generates a thiyl radical as a co-product by the autoreduction of intermediate species $[Fe(NO)(RS)_2]$, suggesting that the trapping of the thiyl radical by NO might be a possible mechanism for cellular *S*-nitrosation in concert with DNIC formation (Scheme 37).[1317]

To elucidate how DNICs can nitrosylate thiols in biology, Liaw and coworkers designed a system where a thiolate-bound dinuclear DNIC, $[(\mu\text{-S}^t\text{Bu})_2Fe_2(NO)_4]$ (**174**), was treated with MI to form an asymmetric, neutral $\{Fe(NO)_2\}^9$ species, $[(\text{StBu})(\text{MI})Fe(NO)_2]$ (**63**), which was then treated with oxidized $(\text{DTC})_2$ to form a proposed MNIC $\{FeNO\}^7$ species, coordinated by the *in situ* formed Brønsted acid, $[\text{LuH}]^+$. Elimination of ^{t}BuSNO occurs after an internal electron transfer event and release of $[\text{LuH}]^+$ (Scheme 38).[1200] The involvement of a Brønsted acid follows similar observations in proteins, where *S*-nitrosylated Cys residues are often surrounded by charged amino acids.[1319] Each example of NO release from synthetic DNICs complements and informs biological studies on how DNICs release NO, what redox forms NO can take, and how DNICs can be used for therapeutics or for protein modifications.

Scheme 37. Proposed Mechanism for Formation of Mono- and Dinuclear DNICs Directly from Fe(II) from the Chelatable Iron Pool (CIP), RSH, and NO in Aqueous Media[1317]

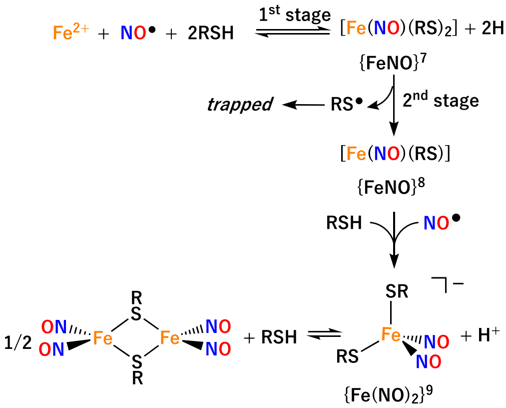

3.4.3.2. Oxidation of Thiols. The glutathione-bound DNIC is an established inhibitor of human glutathione reductase (hGR), a central enzyme in cellular oxidative stress defense.[1087,1088] Crystal structures of inactivated hGR by the DNIC inhibitor revealed that the enzyme lost its function due to oxidation of a critical cysteine residue (Cys63) via an unknown mechanism.[1087] Motivated by this biological finding, the Kim group studied O_2 reactivity of a series of thiolate-bound $\{Fe(NO)_2\}^9$ DNICs, $[(SR)_2Fe(NO)_2]^-$, where R = ^{t}Bu (**2**), Et (**3**), and Ph (**6**).[242,1159] The study shows that O_2 does not oxidize the metal center. Instead, oxidation occurs at the thiolate ligands, resulting in the loss of ligands as disulfide or sulfonic acid, which is accompanied by dimerization of the DNICs to form RREs (Scheme 39).[1159] An analogous monomeric DNIC to RRE transformation by O_2 was reported in [2Fe−2S] ferredoxin by the Vincent group.[1131]

3.4.3.3. Nitration of Phenol via Peroxynitrite. Dioxygen reactivity of N-bound DNICs including $[(\text{TMEDA})Fe(NO)_2]$ (**141**) and $[(\text{dmp})Fe(NO)_2]$ (**148**) was reported by the Kim group.[232,1048,1237] The O_2 reactivity of this group of $\{Fe-(NO)_2\}^{10}$ DNICs presents a sharp contrast to that of thiolate-bound $\{Fe(NO)_2\}^9$ DNICs described above. The reaction of **141** with O_2 generates a low-temperature (e.g., −80 °C) stable, spectroscopically characterized iron-peroxynitrite ($ONOO^-$) intermediate, which isomerizes to nitrate (NO_3^-) upon warming. In the presence of phenolic substrates, the peroxynitrite intermediate induces nitration of the phenol substrates (Scheme 40).[232,1048,1237] Further insight into this reaction came from theoretical studies by the Paul group.[1320] The study suggests that a low-lying triplet state of **141** and an inherent singlet-triplet spin-crossover promoted by a fluxional bite angle of the $Fe-(NO)_2$ unit of **141** makes the peroxynitrite formation possible. The study also suggests that the nitration of phenols is likely facilitated by the release of NO_2.[1320]

3.4.3.4. Other Post-translational Modifications. There are some specific examples of ligand-based reactions of mono- and dinuclear DNICs that can be utilized for post-translational modifications in biology. Belyaev and coworkers demonstrated that the cysteamine-based dinuclear DNIC **230** can be acylated

Scheme 38. RS−NO Formation by DNICs

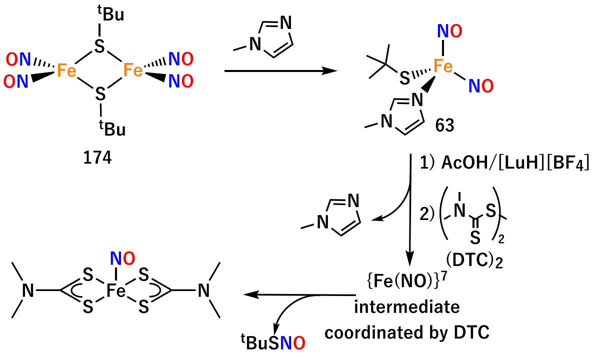

Scheme 39. $\{Fe(NO)_2\}^9$ DNICs React with O_2 to Generate Dinuclear DNICs via S-Based Oxidation

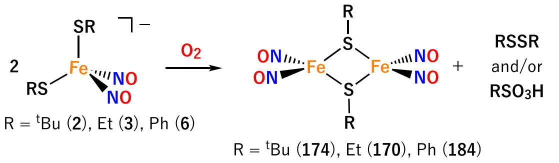

R = ᵗBu (2), Et (3), Ph (6)

R = ᵗBu (174), Et (170), Ph (184)

Scheme 40. $\{Fe(NO)_2\}^{10}$ DNICs React with O_2 to Generate a Peroxynitrite Intermediate That Can Nitrate Phenols

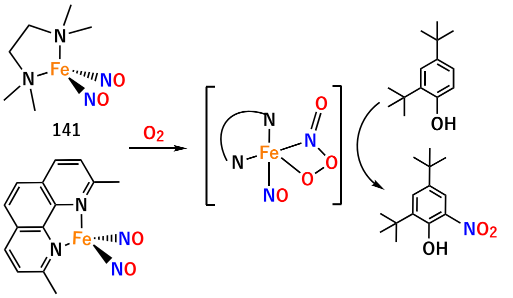

141

148

using acetic anhydride (Scheme 41a).[1251] They suggested that this facile transformation can be used for further bioconjugation in peptides as seen in biological contexts.

Darensbourg and coworkers were able to convert a histidine-based biomimetic DNIC into NHC-bound complexes **124** and **126** while maintaining the DNIC core.[1295] Since the NHC moiety can be derived from an imidazolate group of histidine, it is plausible that NHC-DNICs might exist in cells. This study shows possible conversions of histidine donors once exposed to alkaline conditions (Scheme 41b).[1295]

Another possible post-translational modification by DNICs would be the formation of DNIC adducts with other metallocofactors. Turning to synthetic resources, DNICs bound to metals were synthesized to model such instances. Hughes and coworkers synthesized complexes featuring tetradentate nitrogen-sulfur donor ligands (NS_3; complexes **245**−**247**) where the Fe that is not part of the DNIC is also coordinated to small molecules, CN, CO and NO, in the axial position of the trigonal bipyramidal structure. Notably, the authors did not observe any oxidative changes of the $Fe(NS_3)$ complex once coupled with the $Fe(NO)_2$ moiety.[1284] Additionally, Liaw and coworkers synthesized bimetallic complexes **253** and **254** featuring bidentate thiolate ligands connecting an $\{Fe(NO)_2\}^9$ DNIC via a tether to a hs-$\{FeNO\}^7$ complex, a potential model for DNICs bound to [Fe−S]-containing proteins after nitrosylation.[1286] These examples demonstrate how DNICs could be stored and transported in metalloproteins without consequences to the non-DNIC metal center.

Scheme 41. Biomimetic DNIC Transformations

a. Acylation

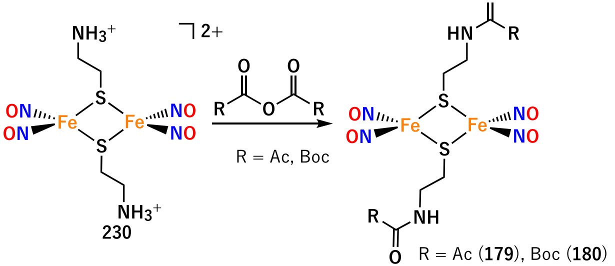

230

R = Ac (179), Boc (180)

b. Histidine mimic to NHC ligation

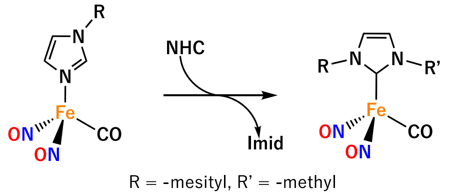

3.4.4. [Fe−S] Cluster Repair. The interconversion between biomimetic DNICs and other nitrosyl iron products or Fe−S cluster is an important topic to help us understand better what the mechanisms of DNIC formation, repair, and reactivity towards other biologically relevant gaseous molecules are in biology. As described in Section 3.3.1 and 3.4.1, MNICs are precursors to DNIC synthesis both in organic[1044] and aqueous media.[1065,1317,1318] The MNIC intermediate was also shown to facilitate cluster repair, starting from a thiolate-bound MNIC being repaired to a [2Fe−2S] cluster by cysteine analogs without the need for any other reagents (Scheme 42a).[242,1321] The repair by cysteine analogs is possible because of their

Scheme 42. Biomimetic Repair of Iron−Nitrosyl Complexes to [Fe−S] Cluster

a. MNIC repair to [2Fe-2S]

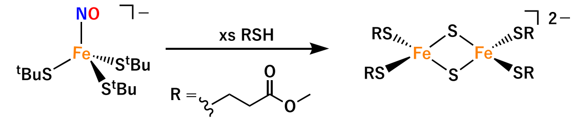

b. DNIC repair to [2Fe-2S]

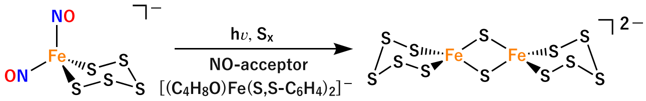

c. DNIC repair to [2Fe-2S] via RRS

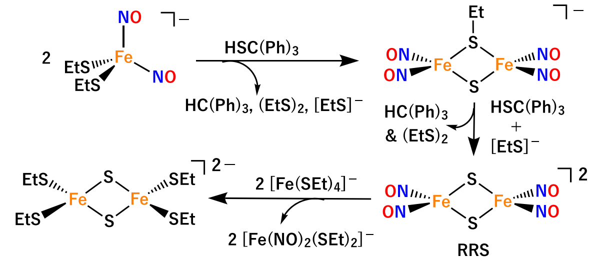

d. DNIC repair to [4Fe-4S]

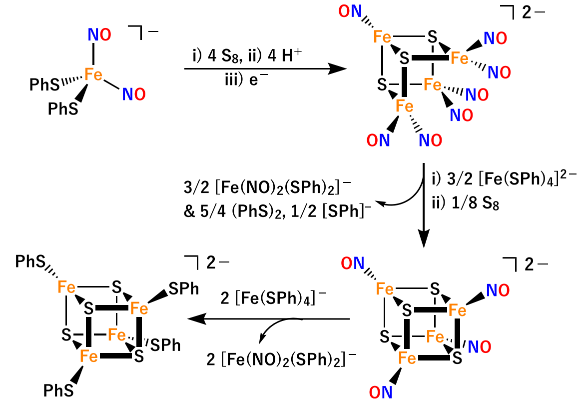

ability to labilize NO from MNICs and their capacity to undergo C−S bond cleavage, providing the necessary sulfide for [2Fe−2S] cluster formation. This mechanism implies that MNICs are likely intermediates in the repair of NO-damaged [2Fe−2S] cluster and that cysteine is a viable molecule responsible for the destabilization of MNICs and the formation of [2Fe−2S] cluster.

The first successful formation of an [2Fe−2S] cluster from a synthetic $\{Fe(NO)_2\}^9$ DNIC was accomplished by photochemistry in the presence of external elemental sulfur (Scheme 42b).[1132] An alternative repair path to [2Fe−2S] cluster (Scheme 42c) involves the formation of Roussin's red salt (RRS) by S atom transfer from $HSCPh_3$ to DNIC with needed electrons provided from thiolate ligands. The subsequent ligand exchange between RRS and $[Fe(SEt)_4]^-$ eventually yields the [2Fe−2S] cluster.[1166] During the DNIC to [2Fe−2S] conversion, a novel anionic mixed thiolate-sulfide bridged RRE, $[(NO)_2Fe(\mu\text{-SEt})(\mu\text{-S})Fe(NO)_2]^-$, was obtained (Scheme 42c). It is conceivable such a mixed thiolate-sulfide bridged RRE may exist as an intermediate in the transformation of biological DNICs to [2Fe−2S] clusters.[1166] Analogous RBS- and RRE-like intermediates were also reported from Co and Ni model complexes, respectively.[1322]

Conversion of DNICs to [4Fe−4S] cluster can be achieved in several steps (Scheme 42d).[1046] DNICs can first be converted to a reduced RBS, $[Fe_4S_3(NO)_7]^{2-}$, by reaction with S_x and HBF_4, followed by reduction with [Na][biphenyl]. The reduced RBS can then be converted to $[Fe_4S_4(NO)_4]^{2-}$ upon further treatment with S_x and $[Fe(SPh)_4]^{2-}$. The final NO radical−thiyl radical ligand exchange between $[Fe_4S_4(NO)_4]^{2-}$ and $[Fe(SPh)_4]^-$ results in the formation of an [4Fe−4S] cluster, $[Fe_4S_4(SPh)_4]^{2-}$. Although this repair path involves rather harsh conditions, the requirement of a pre-assembled $[Fe_4S_4(NO)_4]^{2-}$ cluster is quite intriguing. Indeed, a tetranitrosylated [4Fe−4S] intermediate with an unknown structure has been recently identified during the NsrR/NO reaction by mass spectrometry.[1109] In synthetic modeling chemistry, a tetranitrosyl complex, $[Fe_4S_4(NO)_4]^-$, has been observed as a reaction intermediate during the degradation of $[Fe_4S_4(SPh)_4]^{2-}$ by NO.[1296]

3.4.5. NO-H_2S Crosstalk. While it is understood that biological DNICs can arise from nitrosylation of [Fe−S] cofactors, questions remain as to what happens to the bridging sulfides. Both NO and H_2S are recognized as important signaling molecules and there have been suggestions that NO and H_2S molecules may influence each other in their production and biological effects.[1323−1325] Kim and coworkers hypothesized that H_2S can be generated by the action of NO on [Fe−S] cluster. Hence, the ubiquitous [Fe−S] cofactors may serve as a point of crosstalk between the two gaseous molecules in cells.[1025,1049,1326] Using $[Fe_2S_2(SPh)_4]^{2-}$, they demonstrated that upon nitrosylation of the [2Fe−2S] cluster in the presence of an $H^\bullet$ donor, the bridging sulfides are released as H_2S with concomittent DNIC formation (Scheme 43a).[1326] In recent work,[1327] the authors further demonstrate that the H_2S release from NO/[Fe−S] reactivity can be expanded to include the [4Fe−4S] type and RBS (Scheme 43a). Similar to NO/[2Fe−2S], H_2S was released upon nitrosylation of a model [4Fe−4S] cluster, $[Fe_4S_4(SPh)_4]^{2-}$, in the presence of thiol. This reaction generates an unidentified intermediate which subsequently converts to a DNIC upon thiolate addition. In the absence of thiol, the reaction between [4Fe−4S] and NO generates RBS. Interestingly, RBS converts further to a DNIC with a release of H_2S upon addition of thiol and thiolate. DNICs are not the only product type that forms from a reaction of NO with [Fe−S] clusters. The Kim group reported a MNIC, $[Fe(NO)Cl_3]^-$, as the major product along with the release of a 1:1 mixture of S_x and H_2S when $[Fe_2S_2Cl_4]^{2-}$ was exposed to NO in the presence of acid.[1049]

Scheme 43. H_2S Release by Action of NO at [Fe−S] Clusters and Reversible H_2S Binding at DNICs

a. H_2S release by the action of NO at [Fe-S] clusters

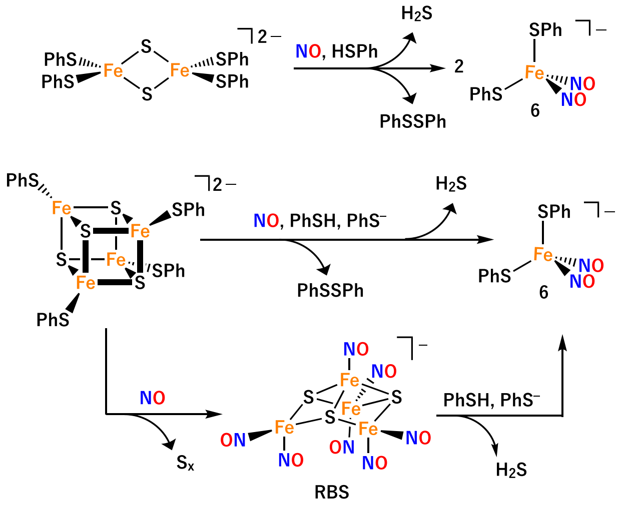

b. Reversible H_2S binding at DNIC

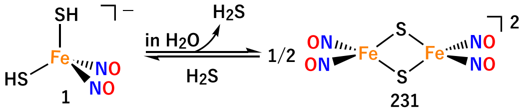

Liaw and coworkers synthesized a novel hydrosulfide-bound DNIC, $[Fe(SH)_2(NO)_2]^-$ (**1**) that rapidly transforms into Roussin's red salt, $[(\mu\text{-S})_2Fe_2(NO)_4]^{2-}$ (**231**), upon dissolution in water, concomitantly releasing H_2S.[1172] These findings suggest that hydrosulfide-bound DNICs can serve as a storage or transport complex for both H_2S and NO (Scheme 43b).[1172] Compound **1** is thermally stable and the reversible transformation of **231** to **1** was observed in the presence of H_2S. In contrast, an anlogous TNIC, $[Fe(SH)(NO)_3]^-$ is thermally unstable and irreversibly forms a dinuclear species.[1172]

3.4.6. Catalytic Activity. In recent years, researchers have also investigated DNICs' electrocatalytic activity for applications such as water splitting, CO_2 reduction and proton reduction. Many of these reactions are based on the idea to recreate reactivity observed in nature using biomimetic complexes.

3.4.6.1. Reduction of Carbon Dioxide. CO_2 reduction is currently a hot topic in chemistry research, one of which DNICs can answer the call by exploiting their one-electron redox capacity via the interconversion between the $\{Fe(NO)_2\}^9$ and $\{Fe(NO)_2\}^{10}$ states. In 2019, Lu and coworkers demonstrated that their novel $\{Fe(NO)_2\}^{10}$ hydride containing DNIC, $[(\eta^2\text{-}BH_4)Fe(NO)_2]^-$ (**111**) is capable of capturing $CO_{2(g)}$ and converting it to formate in the form of $[HB(O_2CH)_3]^-$ (Scheme 44).[1221] In 2020, Liaw and coworkers were able to selectively reduce CO_2 to oxalate by reducing their pyrazolate-bridged $\{Fe(NO)_2\}^9$-$\{Fe(NO)_2\}^9$ dimer to the $\{Fe(NO)_2\}^{10}$-$\{Fe(NO)_2\}^{10}$ state and introducing

Scheme 44. Examples of CO_2 Reduction by DNICs

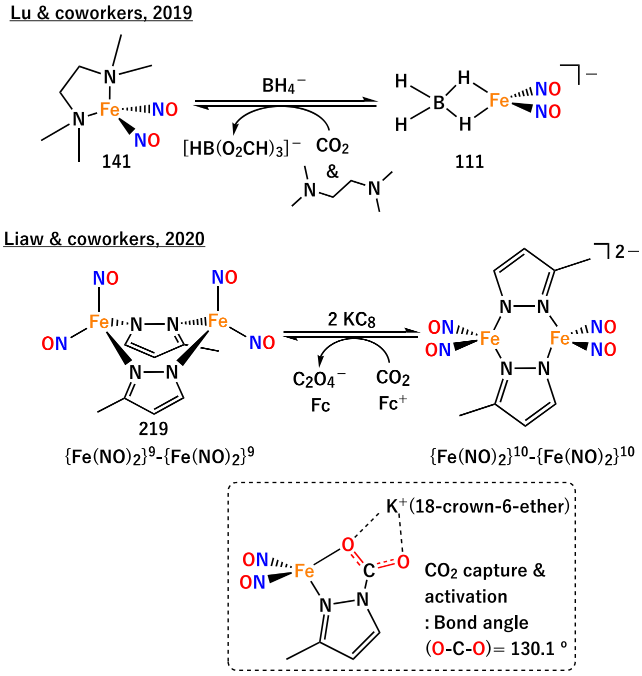

$CO_{2(g)}$, which led to the isolation of oxylic acid in 74.8±1.5% yield (Scheme 44).[1241] More impressively, they were also able to isolate and crystallographically characterize a $\{Fe^{II}(NO^-)_2\}^{10}$ CO_2-bound intermediate species.[1241]

3.4.6.2. Hydrogen Evolution. Inspired by nature, leading researchers in hydrogen evolution reactions (HER) have explored bimetallic enzyme active sites, such as [NiFe]- and [FeFe]-hydrogenases, and corresponding model systems for ways to design the next generation of sustainable catalysts for the electrocatalytic HER.[1328,1329] In 1997, Pohl and coworkers reported a [NiFe]-hydrogenase mimic bearing a dinitrosyl unit, complex **260**, that, despite it being catalytically inactive, served as a starting point and inspiration for following studies (Figure 67).[1287] Darensbourg and coworkers developed the butterfly M(μ-SR)$_2$M' type diiron complex **248** that mimics the [FeFe] hydrogenase active site with an AF coupled $\{FeNO\}^7$-$\{Fe(NO)_2\}^9$ center, which reacts with strong acid leading to H_2 evolution.[1050] The key to success of this catalyst appears to be the coopertivity of the two iron nitrosyl units, both of which can accommodate redox changes, resulting in efficient electron transfer, storage, and proton reduction.[1050,1285] This particular system opened up an avenue for future exploration of different carbon backbones and different metal active sites for HER catalysts including complex **264**.[1024,1289]

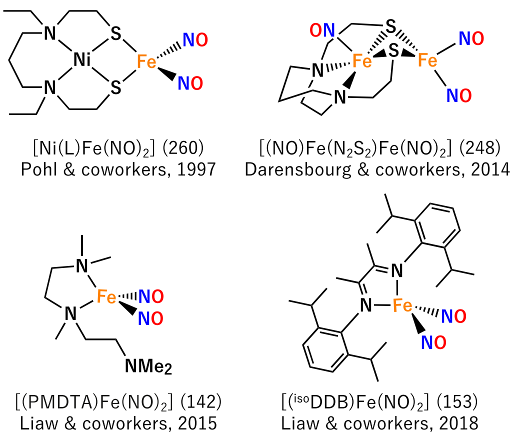
$[Ni(L)Fe(NO)_2]$ (260)
Pohl & coworkers, 1997

$[(NO)Fe(N_2S_2)Fe(NO)_2]$ (248)
Darensbourg & coworkers, 2014

$[(PMDTA)Fe(NO)_2]$ (142)
Liaw & coworkers, 2015

$[(^{iso}DDB)Fe(NO)_2]$ (153)
Liaw & coworkers, 2018

Figure 67. Examples of DNICs that serve as HER catalysts.

Another way to create DNIC-based, efficient HER catalysts is the incorporation of discrete DNIC molecules into heterogeneous electrodes. Complexes **99**, **142** and **153** were incorporated into heterogeneous electrodes to constitute remarkable HER catalysts, capable of reducing protons from water. Liaw and coworkers used the $\{Fe(NO)_2\}^9/\{Fe(NO)_2\}^{10}$ redox couple in DNICs to design complexes for a solid-state hydrogen evolution cathode.[1214,1215,1330] The low-cost PMDTA-bound DNIC **142**, deposited on an electrode, exhibits a low onset potential of -717 mV versus SHE in a neutral 1.0M KCl solution to generate $H_{2(g)}$ from water.[1214] The catalytic activity of DNICs can be further tuned by ligand design. In the case of **153**, the α-diimine ligand allows the catalyst to access three redox states, $\{Fe(NO)_2\}^9$, $\{Fe(NO)_2\}^{10}$ and $[\{Fe(NO)_2\}^{10}\text{-}L^\bullet]$, to more easily accommodate the two electrons necessary for the HER process, and to boost DNIC catalytic acitivity.[1238]

3.5. Therapeutic DNICs

The therapeutic effect of DNICs stems from their ability to release NO in a spatially and temporally restricted manner. The amount of NO released dictates its purpose; at low concentrations in the pico- to nanomolar range NO causes smooth muscle cell relaxation, wound healing, and cell proliferation, while at high concentrations in the micromolar range NO causes cellular apoptosis and DNA damage.[1331] Both natural and synthetic DNICs have been explored for therapeutic effects in areas where endogeneous NO has been known to be employed in the body.[107,1031,1032,1147]

3.5.1. Therapeutic DNICs with Biological Ligands. Biochemists have developed several methods to utilize DNICs containing biological ligands such as cysteine (Cys), glutathione (GSH), cysteamine and thiosulfate ($S_2O_3^{2-}$) (Figure 68). Most commonly used are dinculear DNICs; however, due to the equilibrium that exists between dinuclear and mononuclear DNICs in biological media, one cannot rule out that any of the observed effects may be due to mononuclear DNICs as well (for example, NO release, etc.).

Vanin and coworkers have pioneered numerous biological studies on the effects of NO-releasing DNICs, for example in

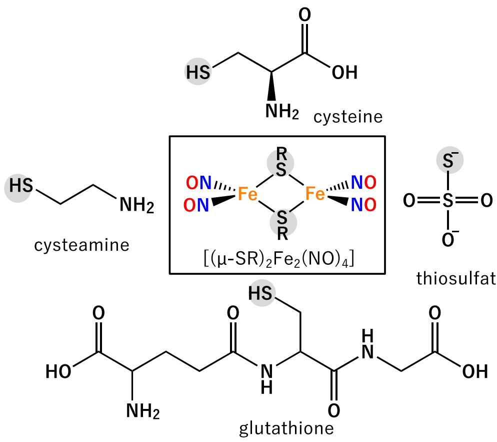

Figure 68. Dinuclear DNICs with biological ligands.

antitumor studies. In one instance they were able to achieve 90% inhibition of tumor growth in mice with Lewis lung carcinoma, using the GSH-bound dinuclear DNIC $[(\mu\text{-GSH})_2Fe_2(NO)_4]$.[1332] Similarly, $[(\mu\text{-GSH})_2Fe_2(NO)_4]$ and the Cys-bound dinuclear DNIC, $[(\mu\text{-Cys})_2Fe_2(NO)_4]$, were used to suppress growth of endometroid tumors in rats.[1333−1336] Further tumor studies by Shumaev and coworkers revealed that $[(\mu\text{-GSH})_2Fe_2(NO)_4]$ is not only able to inhibit platlet aggregation in HeLa tumor cells, but it may also be able to completely prevent platelet aggregation upon early intervention.[1337] Anticancer studies were conducted by Kiselevskii and coworkers using a dinuclear cysteamine-bound DNIC to show antiproliferative activity of this compound in non-small cell lung cancer, breast cancer, ovarian cancer, colonic adenocarcinoma, prostate cancer and erythroblastic leukemia cell lines.[1338]

For many years, Vanin and coworkers studied the vasodilation and hypotensive effects of DNICs, and even developed a $[(\mu\text{-GSH})_2Fe_2(NO)_4]$ containing drug, Oxacom, for hypotention.[1066−1074] These effects are in part due to decreasing red blood cell elasticity, preventing hemolysis. In one study, $[(\mu\text{-GSH})_2Fe_2(NO)_4]$ was shown to decrease elasticity of red blood cells by 40%.[1339] Even under extreme circumstances where HOCl-induced lysis of red blood cells was tested, $[(\mu\text{-GSH})_2Fe_2(NO)_4]$ was shown to inhibit such processes.[1340] Other blood-clotting related activity includes a 21% increase in survival of hemorrhaging rats when treated with $[(\mu\text{-GSH})_2Fe_2(NO)_4]$.[1341] To test external applications of $[(\mu\text{-GSH})_2Fe_2(NO)_4]$, Vanin and coworkers incorportated $[(\mu\text{-GSH})_2Fe_2(NO)_4]$ into a sponge-like collagen matrix for wound healing and tested it on rat skin, assuming the NO released from DNIC decomposition accelerated its therapeutic effects.[1078] Additionally, $[(\mu\text{-GSH})_2Fe_2(NO)_4]$ along with $[(\mu\text{-Cys})_2Fe_2(NO)_4]$ were shown to have positive penile erectile effects.[1079]

DNICs have also been shown to have cyto- and cardioprotective effects, especially in instances where natural NO homeostasis is disrupted and dangerous ROS are introduced.[1342−1345] One such instance is the case of open heart surgery. Veselova and coworkers were able to show enhanced recovery of cardiac function after administering $[(\mu\text{-GSH})_2Fe_2(NO)_4]$. They proposed that the benefit of the DNIC comes from transferring the $[Fe(NO)_2]$ core to awaiting thiols in myocardial proteins, replenishing the oxidatively damaged intracellular DNIC pools.[1343]

Another interesting study was conducted by Timoshin and coworkers, looking at the effects of administering $[(\mu\text{-GSH})_2Fe_2(NO)_4]$ in rats during endotoxin shock. Typically during endotoxin shock, there is an overproduction of NO, but further addition of $[(\mu\text{-GSH})_2Fe_2(NO)_4]$ did not increase NO levels, but rather caused an anti-inflammatory response in rat lungs.[1067,1346]

Contrary to other therapeutic DNICs, Lewandowska and coworkers sought to use DNICs as an iron delivery system to treat anemia. They reported a low-density lipoprotein (LDL)-bound DNIC that was able to increase iron concentration in hepatoma HepG2 cells with low toxicity, showing not only that DNICs are a promising iron-delivery system, but also that LDLs are a new and noteworthy bio-carrier for DNICs.[1347]

3.5.2. Therapeutic Synthetic DNICs.

One consequence of using DNICs with biological ligands is a lack of explicit control over NO release, rather relying on natural homeostatic processes. For example, Vanin and coworkers saw no pro-apoptotic effects in HeLa cells using GSH-, Cys-, or thiosulfate-bound DNICs. They attributed this effect to a lack of spontaneous NO release that would initiate pro-apoptotic effects, and instead suggested that the added DNICs were incorporated into cell surface proteins.[1348] While these results contradict apoptosis seen in Jurkat leukemia cells using a thiosulfate-DNIC complex, it is important to recognize the need for controlled NO release for certain therapeutic applications.[1082]

Liaw, Wang and coworkers answered the call and synthesized a water-soluble neutral DNIC, $[(S(CH_2)_2OH)(S(CH_2)_2NH_3)Fe(NO)_2]$ (**59**), that causes antitumor activity via apoptosis in prostate cancer, breast cancer and non-small cell lung cancer cell lines.[1051] Other synthetic complexes were prepared by Aldoshin and coworkers, including a thiourea based complex, $[(SC(NHCH_3)_2)_2Fe(NO)_2]$ (**84**), that shows cytotoxic effects on human multiple myeloma cells by decreasing intracellular glutathione concentrations and increasing the level of reactive oxygen species, most notably peroxynitrite.[1349]

Another benefit of using synthetic DNICs is the possibility of using photolysis as a method of NO release. Chiou and coworkers synthesized a neutral, dinuclear DNIC, $[(\mu\text{-}SCH_2CH_2P(O)(CH_2OH)_2)_2Fe_2(NO)_4]$ (**182**), as a photochemical prodrug that was found to release NO in mouse melanoma cells, triggering cell death by DNA cleavage.[1246] Timashev and coworkers used a unique approach to combine a photosensitizer, photoditazine, with a glutathione-bound DNIC to reduce inflammation using singlet oxygen generation and to promote skin wound healing via NO release in rats.[1350]

Additional wound healing effects were seen by Yuan, Lu, Liaw and Wang using a mercaptoethanol-bound DNIC to promote angiogenesis and wound healing in diabetic mice by a sustained release of NO, activating the NO-sGC-cGMP pathway (see Section 2.2).[1330] This same complex was also used to regulate the IIS, AMPK and mitochondrial signaling pathways in *C. elegans* by O_2-triggered release of $NO^\bullet$ to extend the lifespan of this organism.[1351]

Anti-inflammatory activity of a 5C DNIC, $[(TMEDA)Fe(NO)_2I]$ (**80**), was reported by Kim and coworkers in murine RAW 264.7 macrophages.[1208] Compound **80** acts as a prodrug and becomes the meta-stable, cationic DNIC $[(TMEDA)Fe(NO)_2]^+$ upon entering the cell. The NO release activity from **80** results in upregulation of the anti-inflammatory protein and cytokine, HO-1 and IL-10, respectively, while at the same time, it leads to downregulation of a pro-inflammatory protein, iNOS, and pro-inflammatory cytokines such as TNF-α and IL-6.[1208]

Further therapeutic DNICs were applied to smooth muscle cells to encourage vascular relaxation and contraction by Darensbourg and Lim. They demonstrated that thiophenolate- and thioglucose-bridged, dinuclear DNICs, $[(\mu\text{-SPh})_2Fe_2(NO)_4]$ (**184**) and $[\mu\text{-(SGlu)}_2Fe_2(NO)_4]$ (**199**), release NO to the cytosol of smooth muscle cells with limited cytotoxity and immunotoxicity over 24 hours, without disrupting the cell's natural processes.[236,1205,1352]

Speaking to the vast library of DNICs, Sanina and coworkers tested sixteen different DNICs that utilize a range of thiophenolate- to thiourea-based ligands against gram positve and negative bacteria, looking for antibacterial effects. They found that these DNICs have comparable effects to other NO donors, with $[(\mu\text{-}SC_6H_4\text{-}m\text{-}OH)_2Fe_2(NO)_4]$ (**190**) having the greatest cytotoxic effects.[1353]

It is clear that DNICs have the ability to provide therapeutic effects in multiple areas of medicine, but there are still several

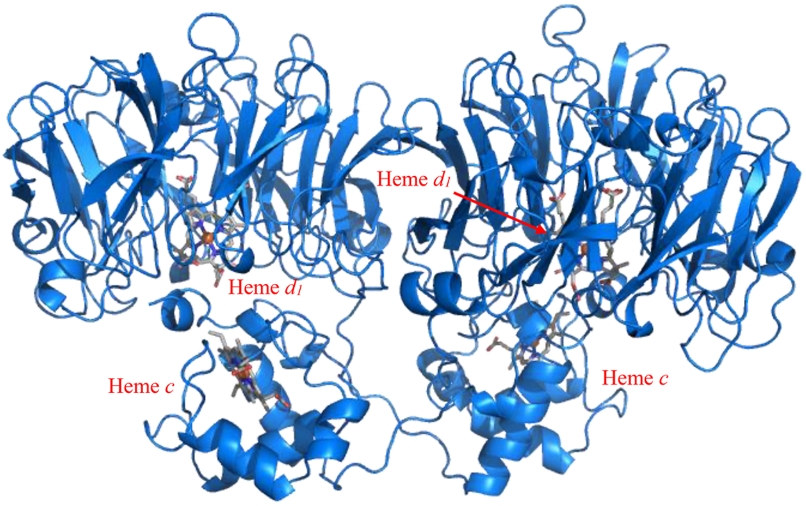

Figure 69. PyMOL generated image of the crystal structure of heme cd_1 NIR from *Pseudomonas aeruginosa* (*Pa* NIR, PDB: 1NIR).

avenues left to be explored. With such diverse structural and electronic properties that can be monitored by several available characterization tools, DNICs have proven to be a formidable platform to use in all areas of chemistry, ranging from modeling biological systems and catalyzing reactions to providing potential therapeutic effects in medical applications.

3.5.3. Synthesis and Applications of Roussin's Black Salt. RBS has its own unique chemistry and applications. The biological effects of RBS were reported back in the 1960s. RBS inhibits the enzyme alcohol dehydrogenase at very low concentration (~1 × 10^{-7} M).[1354,1355] The $[Fe_4S_3(NO)_7]^-$ anion can access four oxidation states, from −1 to −4, with the −1 and −2 states being stable for isolation and characterization.[1356] Under aerobic conditions, RBS will slowly decompose and release NO, but under anaerobic conditions no NO release is observed.[1308,1357,1358] Ford and coworkers explored the quantitative photoreactivity of Roussinate salts. They found that photolysis of RRS produces quantitative yields of RBS, which in turn in the presence of dioxygen slowly photodecomposes to Fe^{III}, NO, sulfur, and unknown Fe^{II} species with a quantum yield of 0.0011. This photodecomposition proved to be toxic to Chinese hamster V79 cells.[1308] Later, flash photolysis experiments on RBS revealed two intermediates that can undergo a reversible, single NO loss, which accounts for the low quantum yields for NO release due to the efficient reverse reaction.[1357] RBS is also thermally stable up to 120 °C, making it an ideal antibacterial agent for thermophilic bacteria.[1275] Interestingly, Adams and coworkers reported that the antimicrobial activity of RBS on the hyperthermophilic archaeon *Pyrococcus furiosus* is due to disrupting the membrane, and less to NO release.[1359] However, with seven equiv of NO per one RBS molecule, researchers have sought to utilize this complex for NO release in therapeutic applications.

Attaching RBS to nanoparticles is an increasingly popular strategy for NO delivery. Ford and coworkers designed a system combining lanthanide-based upconverting nanoparticles (UCNPs) and RBS on a polymer disk (PD) that was able to reproducibly release biorelevant concentrations of pico- to nanomoles of NO upon NIR irradiation.[1360] Tian, Gu, Zhao and coworkers also combined RBS with UCNPs to show cytotoxic effects in Hela and MCF-7 cells after irradiation at 980 nm.[1361] RBS-UNCPs have been continued to be explored for anti-cancer and anti-tumor effects through the NO releasing abilities of RBS.[1362−1365] In a different approach, He, Qian and coworkers used a strategy to create insoluble metal precipitates of RBS with Cu^{2+}, Fe^{2+}, Pb^{2+}, Co^{2+}, and Al^{3+} to prevent the initial cytotoxicity of RBS until the complex is irradiated with NIR light to release NO. Specifically, the Cu-RBS system showed significant *in vivo* antimetastatic effects in a 4T1- LUC primary tumor model.[1366]

4. THE NITROGEN CYCLE

4.1. NO Generation by Nitrite Reduction

Nitrite reductases (NIRs) are important enzymes in the respiratory process of denitrification in bacteria and fungi, catalyzing the reduction of nitrite to NO, according to eq 8, and representing the primary known source of NO in these organisms.[142,1367] As discussed in the Introduction, two different types of NIRs have been characterized, referred to as copper- (class 1) and heme-containing (class 2) NIRs,[142,1367] encoded by the *nir*K and *nir*S genes.[1368,1369] The class 2 enzymes, also known as heme cd_1 NIRs (based on the nature of the hemes that they contain), have been purified from many sources, including *Paracoccus pantotrophus*[1370,1371] (referred to as *Pp* NIR) and *Pseudomonas aeruginosa*[1372] (*Pa* NIR), and are generally located in the periplasmic space.[1369] The heme cd_1 NIRs are the focus of this chapter. These enzymes not only catalyze the one-electron reduction of NO_2^- to NO, but also the four-electron reduction of O_2 to H_2O:

$$O_2 + 4e^- + 4H^+ \rightarrow 2H_2O \tag{15}$$

This heme cd_1 NIR bifunctional activity suggests that oxygen-reducing and denitrifying enzymes could be evolutionarily linked,[315,1373] and implies that CcOs could have evolved from denitrifying enzymes.[314]

4.1.1. Protein Structures of Heme cd_1 Nitrite Reductases. Structural information for these enzymes was obtained from high-resolution crystal structures of both ferric *Pp* NIR (up to 1.55 Å resolution)[1370] and ferric *Pa* NIR (up to 2.15 Å resolution).[1372] In addition, crystal structures of the reduced and nitrite/NO-bound forms of heme cd_1 NIRs are also available.[295,588] Both *Pp* and *Pa* NIR enzymes share overall similar protein structures; both are homodimers (α_2) with two ~60 kDa subunits. As an example, Figure 69 shows the crystal structure of *Pa* NIR. Each monomer is composed of an N-terminal heme *c* domain, and a C-terminal heme d_1 domain. This latter heme is unique to denitrifiers that contain heme cd_1 NIRs.[142] The Fe−Fe distance between heme *c* and heme d_1 is 19.6 Å in *Pa* NIR and 20.6 Å in *Pp* NIR. The N-terminal α-helical domain contains the covalently bound heme *c* that acts as an electron transfer site to the heme d_1 active site. In *Pa* NIR, heme *c* is covalently linked through its exterior vinyl groups to Cys47 and Cys50 (Cys65 and Cys68 in *Pp* NIR). In addition, heme *c* in *Pa* NIR coordinates to His51 and Met88, from the protein backbone, that serve as the two additional (axial) ligands to the 6C iron center. Interestingly, the axial ligands of heme *c* in *Pp* NIR are either two His (His17 and His69) in the ferric state and Met/His (Met 106 and His69) in the ferrous state. Thus, the spectroscopic properties of heme cd_1 NIRs differ between species due to changes in the heme *c* axial coordination in the ferric state. The change in axial coordination of heme *c* in *Pp* NIR upon reduction is due to conformational changes of the enzyme.[295] In contrast, in the *Pa* NIR the axial coordination of heme *c* does not change in the ferrous state. This causes a difference in the reduction potentials of heme *c* in these enzymes. Here, *Pa* NiR heme *c* has a midpoint potential of +288 mV at pH 7. In contrast, *Pp* NIR heme *c* has a potential of +60 mV at 20 °C in the His/His form, whereas the His/Met form of this heme has a potential of +210 mV (all vs SHE).[1374,1375]

The heme d_1 is located in the C-terminal eight-blade β-propeller domain, which binds nitrite and serves as the catalytic site. The heme d_1 structure contains an oxidized porphyrin ring that carries two carbonyl groups (Scheme 4). In the reduced, ferrous state, heme d_1 is 5C with proximal histidine coordination (His182 in *Pa* NIR and His200 in *Pp* NIR), with the sixth coordination site open for substrate binding. In contrast, in the oxidized, ferric state, heme d_1 is 6C in *Pp* NIR with Tyr25 directly ligating to Fe^{III}, with an Fe−O bond distance of 1.85 Å (see Figure 70). Differently, in ferric *Pa* NIR, the corresponding residue Tyr10 is situated in the distal pocket of heme d_1, but a hydroxide serves as the sixth ligand to the heme (see Figure 70). This finding is further supported by EPR data on crystals of this enzyme.[1372] A hydroxide functioning as a ligand for a ferric heme has been observed in several hemoproteins, including Cyt. *c* peroxidases.[597,1376] Additional, important residues in the distal pocket of *Pa* heme d_1 include His327 and His369 aside from Tyr10, which are thought to be involved in substrate binding (via hydrogen bonds) and proton transfer.[1377] In *Pp* NIR, these residues are His345 and His388.[1370] The His residues in the distal pocket participate in a hydrogen-bonding network with nitrite, whereas Tyr25 interacts with a water molecule.

During electron transfer both heme *c* and heme d_1 domains work in concert via an interdomain interaction. In *Pa* NIR, five bonding interactions including hydrogen bonds and one van der Waals contact are present between the heme domains. The interaction between the heme *c* and d_1 domains is further strengthened by the presence of a *c*-d_1 domain linker and the swapping of the N-terminal domain. This occurs because the main chain of the heme *c* domain connects into the heme d_1 domain. In *Pp* NIR, Tyr25 of the heme *c* domain acts as the axial ligand to the ferric heme d_1, and this extension of the N-terminus of the α-helical heme *c* domain into the d_1 domain is stabilized by ∼20 hydrogen bonds and salt bridges between the interface regions of the two domains. In *Pa* NIR, a similar situation is encountered, except that the corresponding Tyr10 does not seem to bind to ferric heme d_1 (see above). Further studies show that the electron transfer between the two cofactors of heme cd_1 NIR occurs via a dynamic redox-controlled conformational rearrangement during reduction and catalysis.[295,1378] Here, crystallographic studies on *Pp* NIR show that the heme *c* domain rotates 60° and shifts approximately 20 Å upon reduction.[1378] This conformational change also gives rise to the change in axial ligation of heme *c* and heme d_1 upon reduction (as described above). In addition, the interaction between heme *c* and heme d_1 is further apparent from the midpoint potential of heme *c* in *Pa* NIR, which changes in the presence of different heme d_1 environments. For example, heme *c* reduction potentials ranging from +294 mV (with no ligand bound to heme d_1), to +290 mV (for NO-bound heme d_1), to +214 mV (for CO-bound heme d_1) and to +380 mV (all vs SHE) for heme d_1-depleted protein have been observed at pH 7.0.[1379]

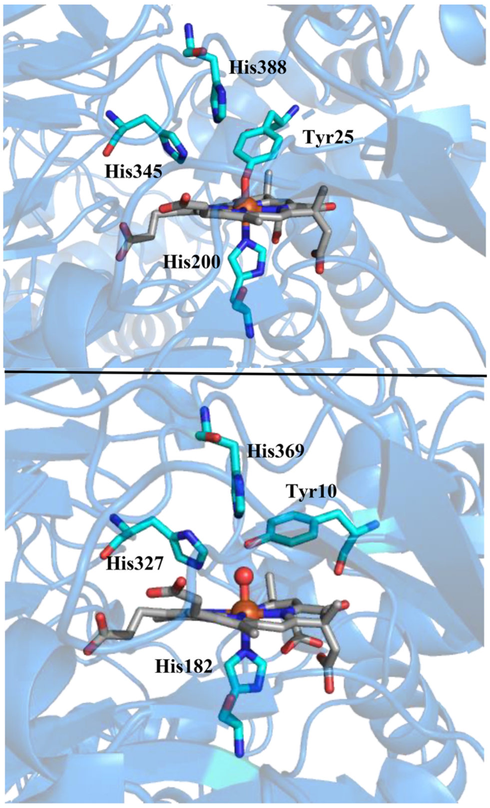

Figure 70. PyMOL generated images of the crystal structures of the ferric heme d_1 active sites of *Paracoccus pantotrophus* heme cd_1 NIR (*Pp* NIR, top; PDB: 1QKS) and *P. aeruginosa* heme cd_1 NIR (bottom; PDB: 1NIR).

The heme cd_1 NIR enzymes can accept electrons from different electron donor proteins. For *Pa* NIR, the identified *in vitro* electron donors are Cyt. c_{551} and azurin.[1372,1380] For *Pp* NIR, the equivalent electron transfer proteins are Cyt. c_{550} and pseudoazurin. Cyt. c_{551} was proposed to be *Pa* NIR's natural redox partner, based on presumed recognition sites identified in the known three-dimensional structures of oxidized and reduced Cyt. c_{551} from *P. aeruginosa*. One potential interaction includes the acidic residues Asp30, Glu35, Glu38, Glu77, and Glu100 in *Pa* NIR and the basic residues Arg47, Lys8, Lys10, Lys21, Lys33, and Lys49 of Cyt. c_{551}. The *Pa* NIR-Cyt. c_{551} interaction was further tested by replacing negatively charged amino acid residues in *Pa* NIR with positively charged amino acids (via mutagenesis), leading to a drastically reduced electron transfer rate with Cyt. c_{551}.[1372] Furthermore, hydrophobic interactions play a role in "pseudo-specific surface" regions where both proteins are considered to interact, leading to a transient but productive complex where electron transfer occurs.[1380] This hydrophobic surface patch has also been observed in the heme *c* domain of *Pp* NIR. Electron transfer from an electron donor to heme *c* is diffusion limited, and shows significant pH dependence.[1381] For example, the intermolecular electron transfer from Cyt. $c_{552(red)}$ to oxidized NIR (in *Pseudomonas nautica* (*Pn*) NIR) shows a second order rate constant of $k \sim (4.1 \pm 0.1) \times 10^5$ M^{-1} s^{-1} at pH 6.3, which decreases to $k \sim (2.2 \pm 1.1) \times 10^4$ M^{-1} s^{-1} at pH 8.0.[1381] The overall rate of electron transfer from heme *c* to d_1 is generally slow ($k \sim 0.1-1.0$ s^{-1}),[1374,1382,1383] but high electron transfer rates have been observed for other heme cd_1 NIRs, as high as 1400 s^{-1} for the *P. pantotrophus* enzyme.[1383−1388]

The crystal structure (at 1.80 Å resolution) of ferrous *Paracoccus denitrificans* GB 17 NIR (referred to as *Pd* NIR) with nitrite-bound heme d_1 was obtained by initially reducing a single crystal of *Pd* NIR with dithionite, followed by soaking the crystal with nitrite, and then freeze-quenching the crystal at 90 K (see Figure 71).[295] Within the active site, nitrite is bound to the heme via the N-atom, generating an η^1-*N* nitro complex. The binding of nitrite in the Fe(II)−NO_2^- complex is further assisted by formation of hydrogen bonds between one of the O atoms of nitrite and the N^{ϵ} atoms of His345 and His388, at distances in the 2.9−3.2 Å range.[295] The two His residues that provide these hydrogen bonds are also utilized for proton transfer during nitrite reduction to NO, to generate water. These conclusions are strongly supported by the nitrite-bound crystal structure of *Pd* NIR, shown in Figure 71. Note that the N-bound nitro isomer is the preferred coordination mode of nitrite to hemes, as observed in model complexes that lack any SCS interactions (see Section 2.3).[142] This binding mode has also been observed for *Cc*NIRs, for example the *Wolinella succinoenes* enzyme,[1389] and sulfite reductase from *E. coli*.[1390]

4.1.2. Mechanism of NO_2^- Reduction in Heme cd_1 NIRs.

The proposed reaction mechanism for nitrite reduction by heme cd_1 NIRs, as shown in Scheme 45, starts with electron transfer from heme *c* (which is reduced by electron transfer proteins such as azurin, pseudoazurin or *c*-type cytochromes, as mentioned above) to heme d_1.[1391] This reduction generates the catalytically active, 5C ferrous state of heme d_1. As discussed above, intramolecular electron transfer between heme *c* and heme d_1 is generally slow, and therefore, in most cases, constitutes the rate-limiting step of NIR catalysis. Similar to the intermolecular electron transfer between external electron donors and heme *c*, a pH dependence of this intramolecular electron transfer step has also been observed.[1381] For example, it has been shown that the electron transfer rate from heme *c* to d_1 is ∼33 s^{-1} at pH 6.3, but decreases to 1.4 ± 0.7 s^{-1} at pH 8.0 in *Pn* NIR.[1381] The slow intramolecular electron transfer rate is due to the extended reorganization of the protein that occurs upon reduction (see above), including the coordination sphere of heme d_1.[1372,1384] With respect to the latter, reduction leads to a displacement of Tyr10 and the dissociation of the OH^- ligand (*Pa* NIR). The Tyr10 displacement also changes the organization of hydrogen bonds at the interface between the two heme domains. This displacement 'opens' the active site and allows nitrite to bind to the reduced heme d_1. Similarly, in *Pp* NIR reduction leads to a displacement of the Tyr25 ligand to heme d_1.

Once heme d_1 becomes reduced, nitrite then binds to the ferrous heme center, via its N atom,[297,1392−1394] as observed in the *Pd* NIR crystal structure (see above), and the bound nitrite is further stabilized by hydrogen-bonding. Crystal structures of ferrous nitrite adducts of *Pa* NIR further support this conclusion.[295,588] The formation of the nitrite complex was observed to occur rapidly, with a large binding constant K_{eq} of 1.2 × 10^6 M^{-1}.[1379] At pH 8.0 (suboptimal conditions), the second order rate constant $k_{on,nitrite}$ was estimatedto be $\geq 10^8$ M^{-1} s^{-1} for *Pa* NIR,[1382] which is orders of magnitude higher than the second-order rate constant for the bimolecular

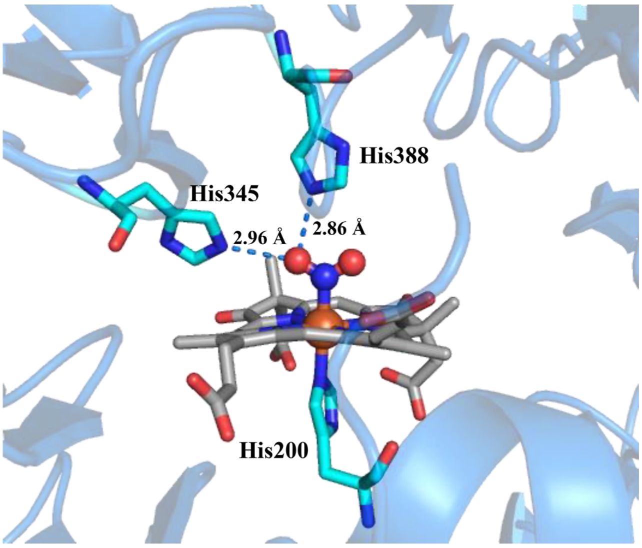

Figure 71. PyMOL generated image of the crystal structure of nitrite-bound ferrous heme d_1 from *Paracoccus denitrificans* GB 17 heme cd_1 NIR (*Pd* NIR, PDB: 1AOM).

Scheme 45. Proposed Mechanism for Reduction of Nitrite to Nitric Oxide by *P. aeruginosa* Heme cd_1 Nitrite Reductase[a]

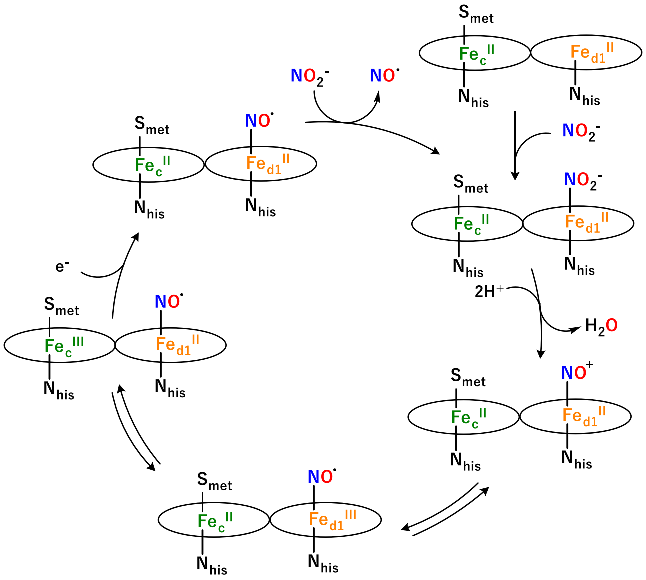

[a]Note that crystal structures of heme cd_1 NIRs show an N-bound nitrite coordinated to heme d_1. The dissociation of NO from the ferrous heme−nitrosyl adduct is surprisingly fast in these enzymes.

reaction of the enzyme with O_2 ($k_{on,O2}$ = 3.3 × 10^4 M^{-1} s^{-1}).[1395,1396] The N-bound coordination mode of nitrite is further supported by spectroscopic results, as described below.[1375,1397] A QM-MM study by Hajdu and coworkers supports the N-bound isomer of nitrite as the catalytically active form, competent for N−O bond cleavage (cf. Scheme 45).[297] The N-bound ferrous heme-nitrite complex then facilitates proton transfer to one of the O atoms of nitrite, which induces heterolytic N−O bond cleavage and formation and release of a water molecule. This process results in a ferric heme−nitrosyl adduct as the enzyme-product complex. This ls-$\{FeNO\}^6$ complex could proceed to release NO, as in the case of NOS (see Section 2.1), but for heme cd_1 NIRs it is actually proposed that reduction occurs first (by an external electron donor), and that NO release is mediated by the fully reduced enzyme that contains the heme d_1 ls-$\{FeNO\}^7$ adduct.[23,296,1398] This result is perplexing, as ls-$\{FeNO\}^6$ complexes generally have much lower binding constants for NO compared to ls-$\{FeNO\}^7$ complexes, at least with regular hemes (see Sections 2.2 and 2.3, and Table 4). Evidence for NO release from ferrous heme d_1 was obtained by Tagawa, Ferguson and coworkers, who observed NO release from the ls-$\{FeNO\}^7$ complex after the enzyme becomes fully reduced via an intermolecular electron transfer.[1386,1399] Experiments by Cutruzzola and coworkers further show that once the ls-$\{FeNO\}^6$ complex is generated, electrons are shuttled to generate a ferrous heme−nitrosyl complex, ls-$\{FeNO\}^7$, prior to NO release.[296,1400] These ideas were ultimately confirmed by Ferguson and coworkers,[1401] in a study on the *Pp* NIR variant M106H, in which heme *c* is fixed in the oxidized state (with a reduction potential of −60 mV vs SHE). Here, it was shown that the reduced heme d_1 is able to reduce nitrite to NO, but the variant would not readily release NO from the resulting heme d_1 ls-$\{FeNO\}^6$ complex.[1401]

The NO dissociation rate from *Pp* NIR is unexpectedly fast, with $k_{off,\ NO}$ = 70 s^{-1}, and similarly, for *Pa* NIR a $k_{off,\ NO}$ = 27.5 s^{-1} was observed at pH 7.[296,1400] These rates of NO release are several orders of magnitude faster than the dissociation of NO from ferrous heme *b* proteins such as Mb and Hb.[608,1402,1403] The EPR spectrum of reduced *Pa* NIR was taken by Greenwood and coworkers, within 4 ms after the addition of excess nitrite, which shows three prominent signals, one at g = 2.01, which is characteristic of a ls-$\{FeNO\}^7$ complex,[1404] and additional signals at *g* = 2.32 and 2.93, corresponding to the His/Met coordinated ferric heme *c*, in agreement with EPR data of oxidized enzyme.[1405,1406] After 110 ms, the intensities of these signals decreased by approximately 50%, which was attributed to electron redistribution within the enzyme, for example by reduction of the ferric heme *c* by the formed heme d_1 ls-$\{FeNO\}^7$ complex. This redistribution has been proposed to generate about an equimolar mixture of the [heme *c* Fe(II)/heme d_1 ls-$\{FeNO\}^6$] and [heme *c* Fe(III)/heme d_1 ls-$\{FeNO\}^7$] forms of the protein. NO dissociation from the ferrous heme−nitrosyl complex to produce ferrous heme d_1 was proposed to finalize the catalytic cycle.

In summary, product release in heme cd_1 NIRs is proposed to occur when both hemes *c* and d_1 are reduced, due to a couple of factors, which is surprising, considering the binding constants of NO with ferric versus ferrous porphyrins (see Sections 2.2 and 2.3). First, the intramolecular heme *c* to d_1 electron transfer triggers conformational changes in the active site that assist in product release,[1399] and, in agreement with this, heme cd_1 NIRs have been observed to work efficiently only in the presence of substrate and electron donors.[1397,1401,1407] In addition, the heme d_1 ls-$\{FeNO\}^6$ complex was observed to be very long-lived in the absence of excess reductant.[1397,1399] Finally, it has been shown that NO does not inhibit heme cd_1 NIR in the presence of excess nitrite, and as NO is accumulated by nitrite reduction, the rate of NO production remains constant.[1408] This interesting property of high nitrite affinity and relatively low NO affinity is the key feature that allows heme cd_1 NIRs to be such efficient catalysts for nitrite reduction.

4.1.3. Spectroscopic Characterization of Heme cd_1 NIRs.

EPR and Mössbauer spectroscopic studies on the ferric form of heme cd_1 NIR from *Thiobacillus denitrificans* showed that both hemes *c* and d_1 are in the ls state (S_t = 1/2), whereas in the ferrous state, heme *c* remains ls whereas heme d_1 becomes 5C and hs.[1409] The ferric heme d_1 shows EPR resonances at g = 2.50, 2.43, and 1.70, similar to those reported for ferric chlorin bis-imidazole complexes.[1409−1411] The heme *c* exhibits a g_{max} EPR resonance at g = 3.60.[1409] In the Mössbauer data, typical parameters for ls ferric hemes were observed, with δ = 0.22 and ΔE_Q = 2.22 mm/s for heme *c* and δ = 0.20 and ΔE_Q = 1.66 mm/s for heme d_1.[1409] In the UV−vis absorption spectrum, ferric *Pp* NIR shows the Soret band at 406 nm, and additional features (including the Q bands) occur at 525, 644 and 792 nm. In the case of ferric *Pa* NIR, the Soret band is located at 411 nm, and the additional features are observed at 520 and 640 nm. Upon reduction, both proteins show similar UV−vis absorption spectra, with the Soret band of heme *c* at 418 nm and the Q bands at 521, 547 and 553 nm. Additionally, ferrous heme d_1 has an absorption feature at 460 nm (Soret band) and a broad Q band at 655 nm. Thomson and coworkers investigated the *T. pantotropha* enzyme using variable-temperature MCD spectroscopy and determined that the ferric heme d_1 exists in a thermal ls/hs mixture with the ls form as the ground state, whereas in *P. stutzeri* heme cd_1 NIR, the ferric d_1 heme is ls at all temperatures.[1412] A weak MCD band was further assigned as the heme d_1 porphyrin-π(a_{1u}, a_{2u}) to ferric Fe(d) charge-transfer transition, observed at 2170 nm.[1412]

In the NIR mechanism, nitrite binds to reduced heme d_1 producing an initial ferrous heme-nitrite, Fe(II)−NO_2^-, complex that has a short lifetime and hence, is hard to capture and study. On the other hand, the ferric analog of this intermediate is stable and can be spectroscopically interrogated. Ferguson and coworkers prepared the ferric nitrite adduct of heme d_1 in *Pp* NIR.[1375] Interestingly, the ferric nitrite complex shows an effective dissociation constant K_d = 1 μM, indicating that ferric heme d_1 has a low affinity for nitrite,[1377] in agreement with the proposed mechanism described above, which indicates that reduction has to occur before nitrite binds to heme d_1. The absorption spectrum of ferric *Pp* NIR in the presence of nitrite shows a prominent peak at 410 nm, due to the ferric heme *c* with His/Met coordination,[1405,1406] and a weaker signal for the nitrite-bound ferric heme d_1 at 643 nm. The nitrite adduct was further characterized by EPR spectroscopy. Here, major rhombic signals were observed at g = 2.94, 2.32, and 1.39, originating from heme *c*, and minor EPR signals were observed at g = 2.51, 2.20, and 1.87, attributed to the His/Tyr-coordinated heme d_1, the ferric resting state.[1412] Interestingly, no signals were observed for the ferric nitrite complex, which the authors attributed to possible relaxation effects in the EPR experiments.

The absorption spectrum of the heme d_1 ls-$\{FeNO\}^6$ (enzyme-product) complex shows a broad Soret band around 460 nm, and Q bands are at 634, 635, and 637 nm for *Pa* NIR, *Pp* NIR and *P. stutzeri* (*Ps*) NIR, respectively.[1413,1414] The IR

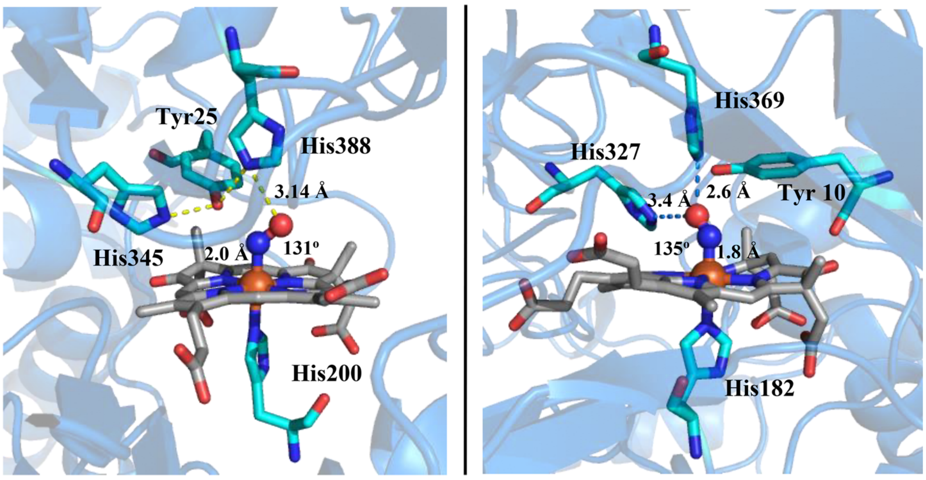

Figure 72. PyMOL generated images of the crystal structures of NO-bound ferrous heme d_1 from *P. denitrificans* GB 17 heme cd_1 NIR (*Pd* NIR, left; PDB: 1AOM) and *P. aeruginosa* heme cd_1 NIR (*Pa* NIR, right; PDB: 1NNO).

spectra of the ls-{FeNO}^{6} complexes of *Ps* NIR and *Pp* NIR show N−O stretching frequencies of 1910 and 1913 cm^{-1}, respectively, that shift to 1874 and 1876 cm^{-1} upon ^{15}NO isotope substitution.[782,1397] These ν(N−O) frequencies are similar to those observed for other ls-{FeNO}^{6} complexes with proximal His coordination (see Section 2.3), for example Hb(III)−NO at 1925 cm^{-1}, indicating that these complexes have the typical Fe(II)−NO$^+$ ground state of these species.[782]

The heme d_1 ls-{FeNO}^{7} adducts of *Pa* NIR[588] and *Pd* NIR[295] have also been studied. Crystal structures of these complexes were determined at 2.65 Å and 1.80 Å resolution, respectively (see Figure 72). In *Pa* NIR, the Fe−NO distance is 1.8 Å and an Fe−N−O angle of 135° was determined (but note that the N−O bond length was fixed at 1.15 Å during structure refinement). These structural parameters are in agreement with the values reported for other ferrous NO adducts of different proteins (see Section 2.2 and Table 3), and are also similar to those in corresponding heme d_1 ls-{FeNO}^{7} model complexes.[1415] Interestingly, in *Pa* NIR, the O atom of the coordinated NO ligand is involved in hydrogen-bonding interactions with the two distal His327 and His369 residues (see Figure 72). These two His residues in the SCS of the active site have been shown to play a critical role in the activation and structural organization of the heme d_1 nitrite complex.[1377]

The influence of the SCS in the distal pocket of wt *Pa* NIR was further interrogated using the variant Y10F, which replaces the critical Tyr10 residue with Phe. Here, NO binding to ferrous heme d_1 was studied using high-frequency W-band EPR, ENDOR (Electron Nuclear Double Resonance) and HYSCORE (Hyperfine Sublevel Correlation) spectroscopy, to determine whether Tyr10 influences the geometry of the FeNO unit and its orientation in the active site.[1416] Interestingly, no significant influence of Tyr10 on the FeNO geometry was observed, which was determined to be similar to that in the crystal structure of wt enzyme.[1370]

The crystal structure of the heme d_1 ls-{FeNO}^{7} adduct of *Pd* NIR features a bent FeNO unit with an Fe−N−O bond angle of 131° and an Fe−NO distance of 2.0 Å (see Figure 72). The SCS in the active site of *Pd* NIR differs from that of *Pa* NIR, containing the distal Tyr25 that participates in a distinct hydrogen-bonding network that connects His345 and His388 with an adjacent water molecule. This Tyr is positioned well to return to ligate the iron center upon NO release from the Fe−nitrosyl adduct, and oxidation to Fe^{III} (resting state).

4.1.4. Role of Heme d_1 in Catalysis.

The heme d_1 with the chemical structure 3,8-dioxo-17-acrylate-porphyrindine (see Scheme 4) belongs to the modified tetrapyrrole group, under the iron-containing dioxo-isobacteriochlorin category. This unusual structure requires a specialized biosynthetic pathway, so far only found in heme cd_1 NIR containing denitrifiers.[1400,1417] Heme d_1 contains two electron-withdrawing carbonyl groups in the periphery, and its iron is less effective at π-backbonding with axial ligands than that of other hemes. This cofactor has an important role in heme cd_1 NIR catalysis; for example, in the ferrous state, this cofactor shows high affinity for anions (including nitrite) and an unexpectedly low affinity for NO compared to other hemes. Hence, one of the proposed key features of heme d_1 is that it allows for facile NO loss at the end of the catalytic cycle, avoiding product inhibition of the enzyme by NO.

The mechanism by which heme cd_1 NIRs accomplish rapid NO release is still not well understood, but heme d_1 contains two features that potentially play an important role in this regard. First, the presence of the two electron-withdrawing carbonyl groups in the structure helps reduce the electron π-backdonation from the occupied d_π orbitals of iron to the NO ligand (see Scheme 14), contributing to a weaker Fe−NO bond in the ls-{FeNO}^{7} state. Second, heme d_1 causes a different d-orbital splitting of the ferric iron center: here, the $(d_{xz}, d_{yz})^4(d_{xy})^1$ electron configuration is observed in the ground state, instead of the common $(d_{xy})^2(d_{xz}, d_{yz})^3$ configuration.[1412,1418] This causes the SOMO of the ferric heme d_1 iron center to be located in the heme plane, instead of being localized out-of-plane. This alternative energy splitting was then proposed to affect the Fe(II)−NO$^\bullet$ π-backbond in the ls-{FeNO}^{7} complex, leading to a weaker Fe−NO bond in the heme d_1 complex compared to *a*, *b* and *c* type hemes.[299,1412]

To investigate the unique functional role of heme d_1 for catalytic nitrite reduction, Hada and coworkers studied the effect of various porphyrin macrocycles on the heme cd_1 NIR mechanism, using synthetic model complexes.[298] Three ferric heme d_1 model complexes were investigated; iron dioxo-octaethylisobacteriochlorin (being the most similar to heme d_1), iron monooxo-octaethylchlorin, and iron OEP (see Scheme 46). Their results indicate that the dioxo-isobacteriochlorin

Scheme 46. Structures of Heme d_1 Analogs Used in Model Complex Studies by Fuji and Coworkers[298]

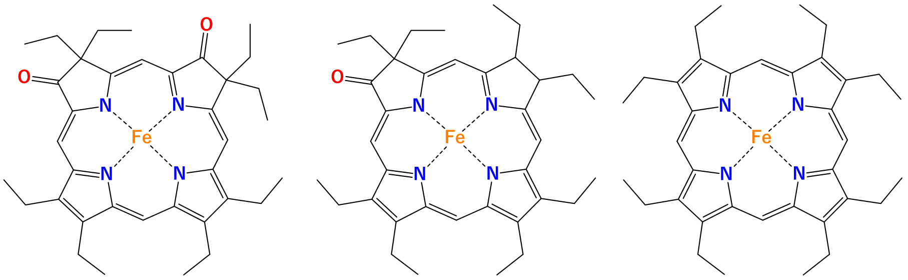

dioxo-octaethylisobacteriochlorin **monooxo-octaethylchlorin** **octaethylporphyrin**

structure has enhanced properties compared to porphyrins and the monooxo-chlorin ligand that are beneficial for NIR activity. First, the dioxo-isobacteriochlorin complex has a more positive Fe^{III}/Fe^{II} reduction potential, −76 and −60 mV (vs SCE) for the *p*-nitrophenolate and bis-MI complexes, respectively, compared to the analogous porphyrin complexes, which have the most negative reduction potentials at −488 and −342 mV (vs SCE).[298] The ferrous dioxo-isobacteriochlorin complex is also better at nitrite binding, with a binding constant K_{eq} of 2.5 × 10^3 M^{-1}, compared to the porphyrin derivative (K_{eq} = 1.4 × 10^2 M^{-1}).[298] On the other hand, the dioxo-isobacteriochlorin complex is the least favored in nitrite reduction, due to the fact that it has the most positive reduction potential out of the three complexes investigated.[298] However, the enzyme can overcome this limitation and enhance the reactivity of this species, for example via SCS effects. In fact, heme cd_1 NIR reconstituted with ferric heme *b* has been reported to have no nitrite reductase activity at all.[1419] Lastly, Hada and coworkers showed that the dioxo-isobacteriochlorin complex has a the highest rate for NO dissociation (this was determined using ligand exchange reactions with *p*-nitrophenolate).[298]

Recent results by Amanullah and Dey further show that a heme d_1 derivative (the iron-chlorin diester complex) has a weak Fe−NO bond in the ls-$\{FeNO\}^7$ complex.[299] They attribute this finding to the electron-withdrawing groups and saturated pyrrole units of the chlorin diester ligand. Here, the higher N−O stretching frequency of 1691 cm^{-1} for this complex (compared to that of [Fe(TPP)(NO)], observed at 1676 cm^{-1} in solution) was taken as evidence for a relatively weak Fe−NO bond in the ls-$\{FeNO\}^7$ complex with the chlorin diester ligand.

Brunori and coworkers used heme cd_1 NIR mutants to show that the heme d_1 active site pocket (cf. Scheme 45) in the enzyme may further assist in promoting fast NO dissociation, a property that has not been observed by heme *b* proteins.[1377,296] Their findings further support the idea that NO dissociates from the ls-$\{FeNO\}^7$ complex. In addition, QM-MM calculations on the heme d_1 active site of *Pd* NIR demonstrate that the release of NO from ferric heme d_1 is influenced by the protonation state of the active site His residues His345 and His388.[297] Not only do the two His help orientate nitrite in the active site, but they also assist with protonation to generate the NO product complex (see above). Their results further suggest that the heme d_1 active site of heme cd_1 NIRs evolved to catalyze the nitrite reduction reaction at the most positive reduction potential possible, while maintaining a suitable catalytic rate.

Brunori and coworkers further investigated the role of the SCS His residues for catalysis by preparing and characterizing two variants of *Pa* NIR, H327A and H369A.[1377,296] Their work demonstrates that both mutants have no nitrite reductase activity, but maintain the enzyme's ability to reduce O_2 to water. This loss of nitrite reduction activity was proposed to originate in part from the loss of product (NO) displacement from the ferric heme d_1 complex. Both mutants show structural variations, including an apparent loss of Tyr10 density, indicating that this residue is no longer present in the active site, as shown by the crystal structures. This causes a significant topological change in the heme *c* domain, including a 20 Å displacement relative to the heme d_1 domain from its original position in wt enzyme. Two suggestions were made to further explain this lack of reactivity of the variants; first, the relocation of heme *c* away from heme d_1 reduces the ability for fast electron transfer, leading to a trapping of NO in the active site as the ls-$\{FeNO\}^6$ complex and slow NO release. Second, the mutants reduce the positive electrostatic potential in the active site pocket, which limits nitrite diffusion into the active site and lowers the rate of NO dissociation. These results further illustrate the importance of the distal His residues His327 and His369 for *Pa* NIR catalysis. Interestingly, although Tyr10 is one of the closest distal residues to the heme d_1 iron center, it does not seem to have a direct involvement in catalysis in *Pa* NIR. As discussed above, Tyr10 does not function as a ligand to heme d_1 in *Pa* NIR either. The lack of participation of Tyr10 in catalysis was further demonstrated by Brunori and coworkers in their study on the Y10F variant of *Pa* NIR. Surprisingly, this variant does not lose nitrite/dioxygen reductase activity.[1388] Here, the nitrite reduction catalytic activity of the mutant and wt *Pa* NIR were measured using reduced cytochrome c_{551} as an electron source. The turnover numbers for Y10F and wt *Pa* NIR are very similar, with 0.58 s^{-1} (K_m = 1.77 μM) and 0.6 s^{-1} (K_m = 0.84 μM), respectively.

4.1.5. NIR Activity of Mb and Hb.

Interestingly, several globins have been shown to also reduce nitrite to NO under hypoxic conditions; these include especially deoxy-Hb and -Mb, which have been characterized as allosterically regulated nitrite reductases.[220,221,228,870,1420,1421] As discussed in Section 2.4, NO produced by NOS is oxidized to nitrite in an aerobic environment, where nitrite then serves as a stable reservoir for NO. Thus, nitrite reduction in eukaryotes is a way to regenerate NO from nitrite.[228,870] This function of deoxy-Hb (and deoxy-Mb) has been proposed to contribute to an important process in mammals, the vasodilation under hypoxic conditions for the re-oxygenation of hypoxic tissue.[220,228,874,1422,1423] Nitrite has also been shown to facilitate other NO-dependent signaling processes such as tissue cGMP accumulation[228] and inhibition of mitochondrial CcO activity.[221,228] Nitrite is found in plasma (50−500 nM) and tissue (0.5−25 μM) and is therefore readily available to generate NO via reaction with deoxy-Hb/Mb.[870,1424,1425] Under low dioxygen saturation conditions, for example in hypoxic tissue, the dominant process is the deoxy-Hb catalyzed nitrite reduction reaction. At high dioxygen saturation, on the other hand, oxy-Hb reacts with nitrite in a complex, autocatalytic process that ultimately oxidizes nitrite to nitrate and oxy-Hb to met-Hb.[1426,1427]

The overall mechanism of nitrite reduction by deoxy-Hb and -Mb is thought to be analogous to that of heme cd_1 NIRs, although some interesting distinctions exist, resulting from the proposed differences in the nitrite binding mode in Hb and Mb, as shown in Scheme 47.[140] Figure 73 shows crystal structures of nitrite-bound horse heart (hh) met-Mb ($\mathrm{Mb(III){-}NO_2^-}$) at 1.20 Å and R-state nitrite-bound human met-Hb ($\mathrm{Hb(III){-}NO_2^-}$) at 1.80 Å.[1428,1429] In both of these cases, the nitrite ligand is observed to bind to $\mathrm{Fe^{III}}$ via one of its O atoms, forming η^1-*O* nitrito complexes. Interestingly, in met-Hb the η^1-*O* nitrito complex is formed in both subunits, where the α subunit contains the *trans* conformation of bound nitrite, and the β subunit contains a distorted *cis* conformation (Scheme 48).[1428,1429] The observation of the η^1-*O* nitrito binding mode was surprising, since the crystal structures of nitrite adducts of heme cd_1 NIRs (Figure 71),[295] the *Cc*NIR from *Wolinella succinogenes*,[1389] the sulfite reductase heme protein from *E. coli*,[1390] as well as ferrous and ferric heme model complexes with bound nitrite[337,1430] all show the η^1-*N* nitro coordination mode. The O-bound form in met-Mb is stabilized by hydrogen-bonding between an O atom of nitrite and the distal His64 residue, as illustrated in Figure 73.[1431] Interestingly, mutation of His64 in Mb to Val (H64V) within the distal pocket "shifts" the nitrite binding mode back to the expected η^1-*N* nitro form (Figure 74). The binding mode of nitrite in Mb is converted back to the η^1-*O* nitrito form upon reestablishing the hydrogen bond via another mutation, H64V/V67R (Figure 75).[1431] Altogether, the mutants help illustrate the importance of hydrogen-bonding within the Mb (and Hb) distal pocket to orient the heme-bound nitrite ligand.

In the case of Hb, nitrite binds to the ferrous form, deoxy-Hb, in the R-state tetrameric form with a second-order rate constant of $k_{\mathrm{on}} \sim 6\ \mathrm{M^{-1}\ s^{-1}}$.[140] For met-Hb, the effective dissociation constant of nitrite from the ferric nitrite complex was obtained using EPR spectroscopy, which led to the determination of a $K_D = 1.8 \pm 0.6$ mM. This value is larger compared to a previously obtained K_D of 0.285 mM.[1432,1433] Nevertheless, this shows that the affinity of met-Hb for nitrite is not very high, and outside of the physiologically relevant range. After binding of nitrite to deoxy-Hb, protonation of the heme-bound nitrite is proposed to occur, leading to electron transfer from the ferrous heme to the coordinated nitrite and release of NO. The main difference to the mechanism of heme cd_1 NIRs originates from the difference in the nitrite binding mode. On the basis of the crystal structures of ferric Hb and Mb where nitrite is O-bound to the heme, as described above, a similar binding mode is also assumed for nitrite bound to deoxy-Hb and -Mb. This means that nitrite reduction would lead to an immediate release of

Scheme 47. Proposed Mechanism of Nitrite Reduction by Deoxy-Hb and -Mb

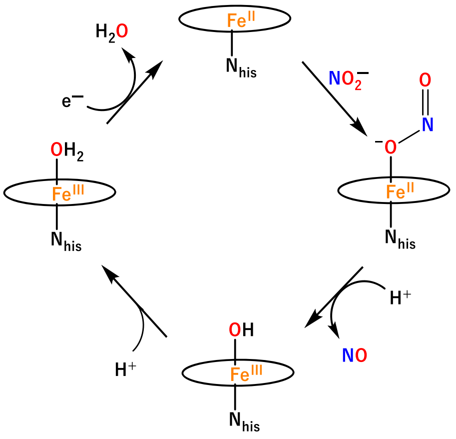

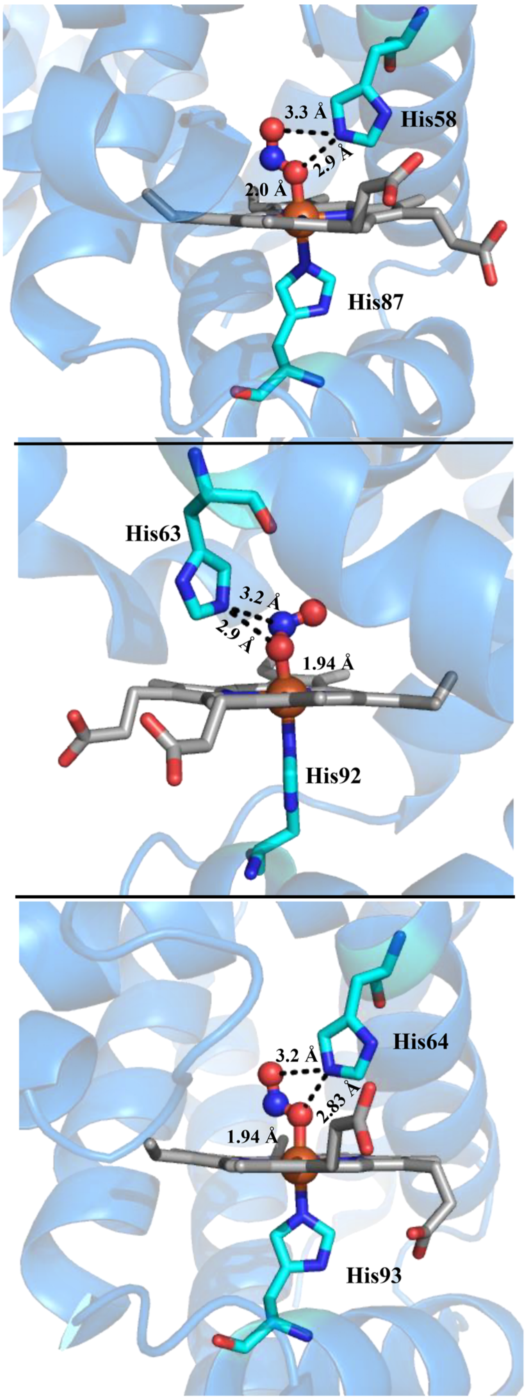

Figure 73. PyMOL generated images of the crystal structures of the ferric nitrite complexes of the α- and β-subunits of Hb (top, middle; PDB: 3D7O) and of Mb (bottom; PDB: 2FRI).

Scheme 48. Two Different Conformations Observed in Nitrite-Bound Ferric Hb[a]

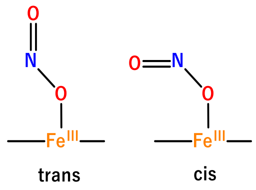

[a] The *trans* conformation is observed in the α subunit, while the *cis* conformation is observed in the β subunit.[1428,1429]

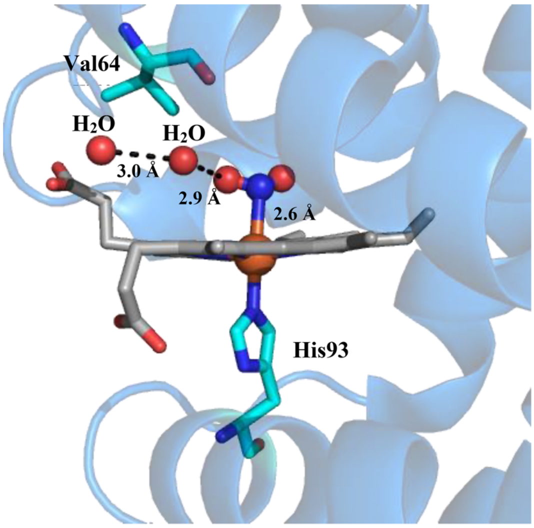

Figure 74. PyMOL generated image of the crystal structure of the ferric nitrite complex of the H64V mutant of Mb (PDB: 3HEP). Nitrite is weakly N-coordinated and further stabilized in the active site by hydrogen-bonding to a network of water molecules.

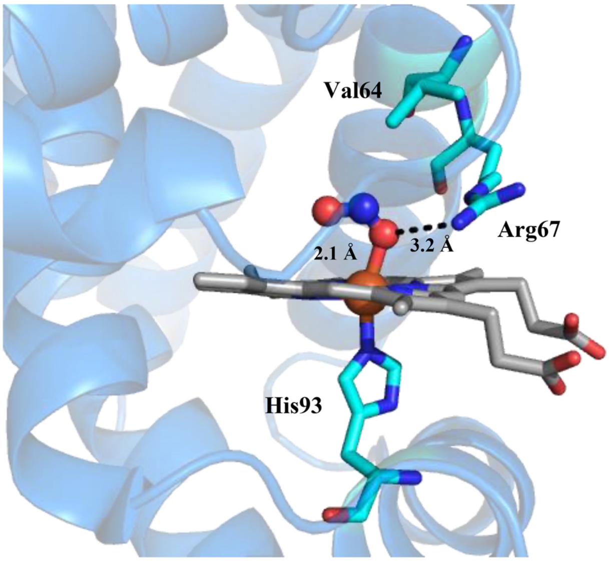

Figure 75. PyMOL generated image of the crystal structure of the ferric nitrite complex of the H64V/V67R mutant of Mb (PDB: 3HEO).

NO, leaving behind the ferric hydroxo complexes, Hb(III)−OH and Mb(III)−OH, at the end of the catalytic cycle. In the case of Hb, some of the released NO would then likely be scavenged by another deoxy-Hb site in the protein and form a stable ls-$\{FeNO\}^7$ complex, Hb(II)−NO. Hence, this process corresponds to an allosteric autocatalytic reaction in which the rate increases due to a conformational change as controlled by newly formed met-Hb and Hb(II)−NO complexes. Once there are no more vacant Fe^{II} heme sites available, the reaction slows down. The reaction is optimally catalyzed at ~50% oxygenation of Hb.[140]

Interestingly, the experimentally observed O-bound form of nitrite in met-Hb and -Mb is not predicted to be the most stable isomer in several DFT studies.[1432,1434,1435] For example, Kim-Shapiro and coworkers reported that the N-bound nitro form is ~7 kcal/mol more stable than the O-bound nitrito isomer. In these calculations, a simple active site model of Mb/Hb was used that includes the distal His.[1432] So the question of how exactly the active sites of Hb and Mb facilitate O-coordination of nitrite is not clear at this point. Full QM/MM studies are likely required to address this point. Similarly, utilizing DFT calculations, Silaghi-Dumitrescu[1434] investigated the possible formation of a ferrous (O-bound) η^1-*O* nitrito complex in Hb and Mb. The N-bound isomer was again found to be thermodynamically favored over the O-bound form by 6 kcal/mol in the ferrous state, and by 4.5 kcal/mol in the ferric form of the heme. The optimized structure indicates a relatively weak Fe(II)O−NO bond (with a predicted bond length of 1.33Å), which would predisposition the complex to cleave off NO (upon protonation) and form an Fe(III)−OH (enzyme-product) complex.[1434] In this way, deoxy-Hb and -Mb could function as efficient NIRs, taking advantage of the *O*-nitrito coordination mode to facilitate NO release.

4.2. NO Breakdown by NO Reductases: Fungal NO Reductase (P450nor)

The fungal enzyme Cyt. P450nor belongs to the Cyt. P450 superfamily, although functionally, it is very different from typical Cyt. P450s.[1436] Instead of performing monooxygenase or other oxidative chemistry by activating O_2, this enzyme conducts the reduction of nitric oxide to nitrous oxide, following eq 5.[300,301,1437] It is interesting to note that Cyt. P450nor is the only enzyme in the Cyt. P450 family to function as a reductase.[1438,1439] Cyt. P450nor is found in soil dwelling fungi and yeasts and operates with a single heme *b* cofactor in the active site that features a proximally bound cysteinate residue, the hallmark of the Cyt. P450 superfamily.[304,1440,1441] This is in contrast to bacterial NORs which perform NO reduction using a dinuclear heme/non-heme iron active site, as discussed in Section 4.3.[312] Additionally, in bacterial denitrification, nitrate is reduced to dinitrogen as the ultimate product, whereas fungal denitrification ends with N_2O, which is subsequently released into the atmosphere.[1367,1442] Because of widespread overfertilization of agricultural soils, which stimulates nitrification and denitrification, fungal N_2O production is thought to make a large contribution to global N_2O emissions, contributing to climate change.[1443] In addition, N_2O is an important ozone-destroying agent.[1444] Since the last step of denitrification in fungi is not fully associated with the respiratory chain, Cyt. P450nor is believed to have a more protective function against NO toxicity in denitrifying fungi.[1441,1442,1445−1448]

Cyt. P450nor isoforms have been isolated from multiple fungi, for example *Fusarium oxyporum* (*Fo* P450nor),[1441,1449] *Cylindrocarpon tonkinense*,[1450,1451] and *Trichosporon cutanuem*.[1452,1453] On the basis of genome analysis, Cyt. P450nor enzymes are present in many other fungi as well.[1454,1455] Most

https://doi.org/10.1021/acs.chemrev.1c00253

of the structural and mechanistic information available to this date is derived from just one representative, *Fo* P450nor, so the diversity of these enzymes remains to be further investigated. The sequence identity of different isozymes of Cyt. P450nor is between 65-83%, and they show an average of 25% (up to 40%) similarity with Cyt. P450 monooxygenases.[1436] Intriguingly, the known genes of fungal Cyt. P450nor tend to show higher sequence homologies with bacterial Cyt. P450s rather than eukaryotic ones, suggesting that lateral gene transfer from bacteria to fungi occurred early in evolution.[1456]

In terms of cell localization, Cyt. P450nors can be found in either the mitochondria, Cyt. P450nor$_A$, or the cytosol, Cyt. P450nor$_B$.[1457] Another difference between these two types of Cyt. P450nor enzymes is that Cyt. P450nor$_A$ contains 26 additional amino acids at the N-terminus which are absent in Cyt. P450nor$_B$. Interestingly, in *F. oxysporum* only one gene, *CYP 55*, encodes both forms of Cyt. P450nor. Here, the amino acid sequence of this gene contains two separate initiation codons for translation.[1452,1457,1458] The sequence of Cyt. P450nor$_A$ contains an extension at the N-terminus which is utilized as a targeting sequence for transportation to the mitochondria, while the sequence of Cyt. P450nor$_B$ contains an acetylated Ala, resulting from post- or co-translational elimination of a methionine residue.[1458] Both mitochondrial and cytosolic forms of Cyt. P450nor were also isolated from *C. tonkinense*; however, in this case two separate genes, *CYP55A2* and *CYP55A3*, were found to code for the two different forms of the enzyme.[1451] It was also determined that Cyt. P450nor$_B$ favors NADPH over NADH, suggesting that Cyt. P450nor$_B$ could act as an electron sink by NADP$^+$ formation as a substrate for the pentose-phosphate cycle.[1459]

The reduction of NO by Cyt. P450nor in *F. oxysporum* is extremely efficient with a turnover frequency of 500 s^{-1} for this reaction,[304] which is much higher compared to those obtained for bacterial NO reductases.[1460] The overall NOR reaction by Cyt. P450nor follows the equation:[304]

$$2NO + NAD(P)H + H^+ \rightarrow N_2O + NAD(P)^+ + H_2O \tag{16}$$

Here, NO reduction proceeds without a separate electron transfer protein (i.e., flavoprotein, iron−sulfur protein, etc.) and instead, a direct two-electron reduction of the ferric heme−nitrosyl intermediate by NAD(P)H is observed.[307,1367] The details of the mechanism are further discussed below.

4.2.1. Cyt. P450nor Structure and Function.

Fungal *Fo* P450nor is made up of 403 amino acids with a molecular weight of 46 kDa.[1440] On the basis of the examination of several crystal structures, the overall fold of Cyt. P450nor is strikingly similar to Cyt. P450 monooxygenases, for example Cyt. P450cam (see Table 18).[774,1440,1461,1464,1466] The main differences between these two proteins are the exact orientations of the F, G, and B′ helices in the tertiary structure (see Figure 76). In Cyt. P450nor, the F and G helices are "flipped up," causing the distal heme pocket to be larger in size. The positioning of these two helices results from steric repulsion between hydrophilic regions on the I and G helices, pushing the G helix farther away from the heme active site, and in this way, opening up the active site in Cyt. P450nor.[1440]

The other main structural difference between Cyt. P450nor and Cyt. P450cam is the position of the B′ helix. In Cyt. P450 monooxygenases, this helix acts as a substrate channel; however, in Cyt. P450nor, this helix is significantly shifted (see Figure 76).[1467−1469] Though Cyt. P450nor does not require binding of an organic substrate during its catalytic cycle, it does interact with an NAD(P)H cofactor that binds in the active site, close to the heme. In this case, it has been proposed that the B′ helix acts as a binding site for NAD(P)H.[1437,1464]

Table 18. Crystal Structures of Cyt. P450nor and Some Key Crystal Structures of Cyt. P450cam

protein	organism	PDB code	resolution (Å)	ref
P450nor(III)	*Fusarium oxysporum*	1ROM	2.0	1440
P450nor(III)	*Fusarium oxysporum*	1EHE	1.7	774
P450nor(III)	*Fusarium oxysporum*	1JFB	1.00	1461
S286V P450nor(III)	*Fusarium oxysporum*	1EHG	1.7	1440
S286T P450nor(III)	*Fusarium oxysporum*	1EHF	1.7	1440
S73/75G P450nor(III)	*Fusarium oxysporum*	1ULW	2.0	1462
P450nor(III)−NO	*Fusarium oxysporum*	1CL6	1.7	1453
S286V P450nor(III)-NO	*Fusarium oxysporum*	1CMN	1.7	1453
S286T P450nor(III)-NO	*Fusarium oxysporum*	1CMJ	1.7	1453
T243N P450nor(III)-NO	*Fusarium oxysporum*	1F24	1.4	305
T243A P450nor(III)-NO	*Fusarium oxysporum*	1F25	1.4	305
T243V P450nor(III)-NO	*Fusarium oxysporum*	1F26	1.4	305
P450nor(III)-CN(*n*-C_4H_9)	*Fusarium oxysporum*	1GEJ	1.5	1463
S73/75G P450nor(III)-NAD*	*Fusarium oxysporum*	1XQD	1.8	1462
P450nor(III)-Br$^-$	*Fusarium oxysporum*	1GED	2.0	1464
P450nor(II)-CO	*Fusarium oxysporum*	2ROM	2.0	1440
P450nor(II)-CO	*Fusarium oxysporum*	1JFC	1.05	1461
P450nor(II)-CN(*n*-C_4H_9)	*Fusarium oxysporum*	1GEI	1.6	1463
P450cam(III)	*Pseudomonas putida*	1PHC	1.6	1465
P450cam(III)-CN(*n*-C_4H_9)	*Pseudomonas putida*	1GEM	2.0	1463
P450cam(II)-CN(*n*-C_4H_9)	*Pseudomonas putida*	1GEK	1.7	1463

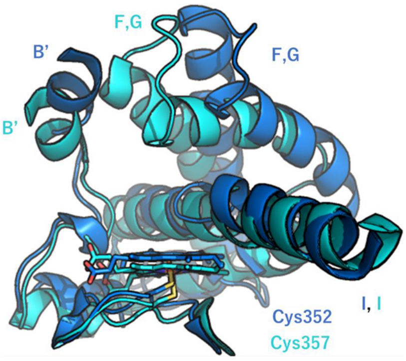

Figure 76. PyMOL generated overlay of the crystal structures of Cyt. P450nor (blue, PDB: 1ROM) and Cyt. P450cam (light blue, PDB: 1PHC), demonstrating the differences in the positioning of the F, G, and B′ helices.

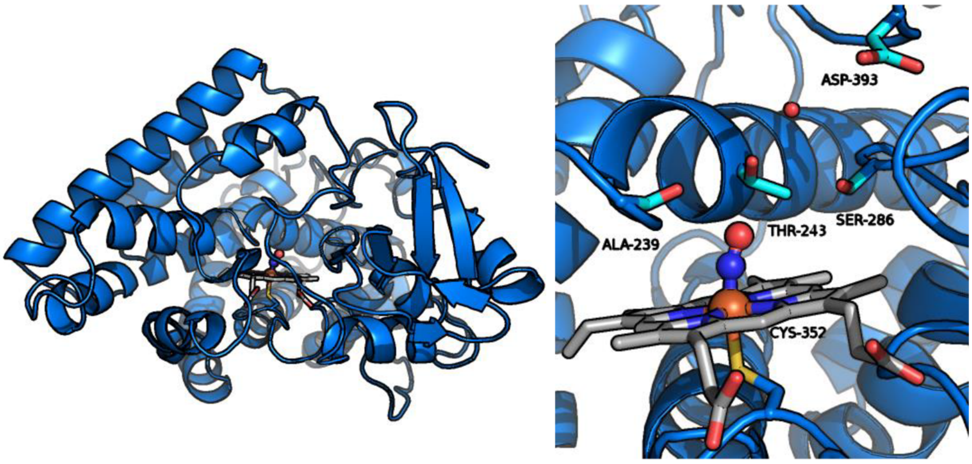

Figure 77. PyMOL generated images of the crystal structure of Cyt. P450nor (left) and a close-up of the ferric active site with bound NO (right; PDB: 1CL6).

Crystal structures of Cyt. P450nor show a cluster of positively charged amino acids (Lys62, Arg64, L291, and Arg392) at the bottom of the B' helix which point toward the distal pocket.[774,1462,1464] Since NAD(P)H is negatively charged, these residues could potentially form ionic interactions with the cofactor, positioning it for electron transfer that is necessary for NO reduction. Previous experiments involving site-directed mutagenesis of this region show that NAD(P)H binding depends on the charge distribution and steric bulk of the B' helix.[1437]

In addition, the B′ helix was determined to influence the selectivity for NADPH versus NADH binding.[1437] For example, *Fo* P450nor uses only NADH, whereas the *T. cutaneum* and *C. tonkinense* enzymes can utilize either NADH or NADPH as electron sources.[1450−1452] Currently, there is no example of a Cyt. P450nor that only employs NADPH in the reduction of NO to N_2O. Upon further inspection of each respective crystal structure, it was found that *Fo* P450nor contains residues with more steric bulk on the distal side of the B′ helix in comparison to the *T. cutaneum* and *C. tonkinense* enzymes.[1437] Other experiments have indicated that NADPH can bind to the B′ helix of *Fo* P450nor; however, electron transfer is blocked by Ser75, preventing NO reduction and N_2O formation.[1437] When this residue is mutated to a smaller Gly residue, the NADPH activity improves in *F. oxysporum* enzyme, as expected. On the basis of these observations, the B′ helix is not only crucial for NAD(P)H binding, but also in determining the binding specificity between NADH and NADPH.

Proton delivery is also crucial for NO reduction by Cyt. P450nor. On the basis of the crystal structures of this enzyme at cryogenic temperatures, the precise position of water molecules has been noted.[774,1466] In one case, a water molecule that is adjacent to the heme iron, Wat99, forms a hydrogen-bonding network with Ser286, Thr243, and Asp393 and is proposed to aid in proton delivery (see Figure 77). If Ser286 is mutated to Val or Thr, the hydrogen-bonding network is interrupted, and NO reduction is no longer observed.[774] While the catalytic activity is disrupted, there is no decrease in the rate constant for NO binding and the formation of the ls-$\{FeNO\}^6$ species (see below). Additionally, if Thr243 is replaced by Asp, Val or Ala, the rates of NADH consumption, Intermediate I formation, and N_2O release are greatly reduced.[1466,1470,1471] For each of these mutants, T243N, T243V, and T243A, the levels of NO reduction are 2%, 0.01%, and 3%, respectively, in comparison to the wt enzyme.[1466] On the basis of these observations, Ser286 and Thr243 are important for proton delivery to the active site. It is interesting to note that this hydrogen-bonding network and the cluster of positively charged residues on the B′ helix are not present in Cyt. P450 monooxygenases, hinting that their presence is required for the unique function of Cyt. P450nor.[1472]

Another important design aspect of Cyt. P450nor is the I helix, which sits next to the heme cofactor in the distal pocket and spans the full length of the enzyme itself (see Figure 76).[1440] In Cyt. P450 monooxygenases, this highly conserved helix is used to stabilize the bound O_2 molecule in the distal pocket;[1473] however, since Cyt. P450nor cannot perform monooxygenase activity, the main role of this helix is to house Thr243, which is needed for proton delivery to the active site as discussed above.[1466] In comparison to Cyt. P450cam, the I helix is also more stretched in Cyt. P450nor, and this structural change is believed to be stabilized by a hydrogen-bonding network including Wat63 and Wat72. It should be noted that these same water molecules also form hydrogen bonds to Thr243 and Ala239; however, the role of this hydrogen-bonding network is believed to be structural, playing no part in proton delivery to the active site heme.[1440]

As previously mentioned, the active site of Cyt. P450nor contains a heme *b* cofactor with a proximally bound cysteinate (a deprotonated Cys) ligand, Cys352 in *Fo* P450nor, which is highly conserved in the gene sequences of fungal NORs.[1436] Crystal structures of *Fo* P450nor confirm that this Cys residue is bound to the heme, as shown in Figure 78. This figure also highlights the main hydrogen-bonding network of the proximal Cys residue (the "Cys pocket") in the active site of Cyt. P450nor. Recent work has shown that the combined strength of the hydrogen bonds to the cysteinate ligand tunes enzyme activity in Cyt. P450 monooxygenases,[1474,1475] and the same is expected here in the context of NO reduction. This aspect is further discussed below. In the 5C hs ferric resting state of Cyt. P450nor, the Fe−S bond distance is 2.17 Å. The heme active site is located between the I and L helices in the distal and proximal pocket, respectively, and is roughly 8 Å away from the surface of the protein (see Figure 77).

4.2.2. Catalytic Cycle of Cyt. P450nor.

The catalytic cycle of Cyt. P450nor is summarized in Scheme 49. In the resting state, the active site contains a mixture of a hs 5C ferric heme-thiolate complex and a ls 6C ferric heme-thiolate with a

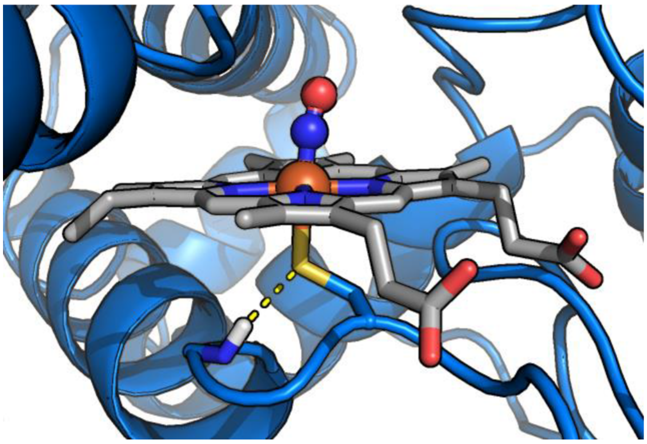

Figure 78. PyMOL generated image of the crystal structure ferric NO-bound Cyt. P450nor, focusing on the proximal pocket and highlighting a key hydrogen bond (from the amide group of Ala354) to the heme-bound cysteinate ligand. The image was generated using PDB: 1CL6.

Scheme 49. Proposed Mechanism of Cyt. P450nor[a]

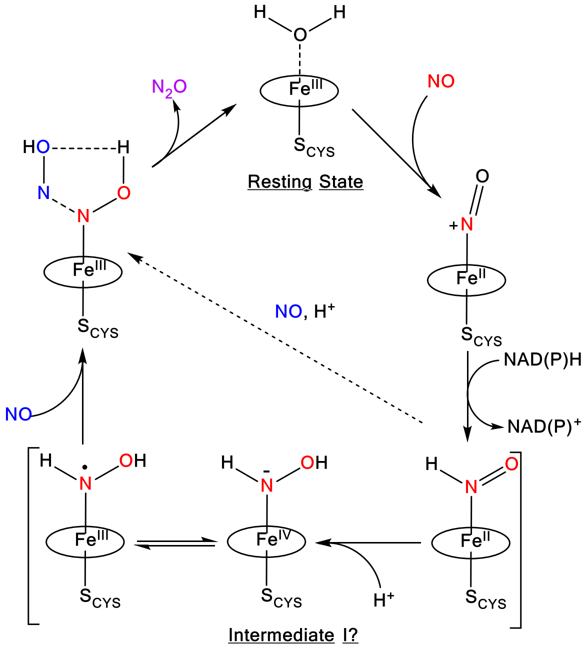

[a] See text for discussion.

bound water molecule.[674] The EPR spectrum shows two signals, one with g_{eff} values of 7.97, 4.12, and 1.75,[1440] corresponding to the hs form, and the other one with g values of 2.44, 2.26, and 1.91, representing the ls complex. This was further confirmed by a single-crystal EPR study at 10 K,[1440] as well as UV–vis spectroscopy.[304,1476] The EPR and UV–vis absorption properties of Cyt. P450nor are generally similar to those obtained for other Cyt. P450s, for example Cyt. P450cam.[1477,1478] It was further proposed that the ratio of hs to ls form in the resting state can have implications for NO reduction. For example, it was shown that the substitution of the native heme *b* of *Fo* Cyt. P450nor with a 2,4-diacetyl-deuteroheme leads to a 6C ls ferric heme center as the only species observed in the ferric resting state, based on UV–vis and rRaman spectroscopy.[1479] As expected, the $k_{on,NO}$ rate constant for the formation of the ferric heme–nitrosyl complex of this form is decreased to 0.24×10^7 M^{-1} s^{-1} and the turnover frequency drops to 84 s^{-1}, in comparison to 1.90×10^7 M^{-1} s^{-1} and 211 s^{-1} for the reconstituted native form, respectively.

Despite the mixture of hs and ls species present in the ferric state, these results show that the hs complex is catalytically active, and that the water molecule must dissociate before NO can bind to the 5C form. This point was further explored by van Eldik and workers, who studied NO association to ferric Cyt. P450cam and ferric model complexes.[630,634,1480,1481] The model complex [Fe(SPorph)], shown in Figure 79, has large positive values of $\Delta H^{\ddagger}$ and $\Delta S^{\ddagger}$ as well as a positive activation volume when reactions with NO are performed in methanol. Here, the rate determining step for NO binding was determined to be the dissociation of the solvent molecule, in this case methanol, from the ferric heme.[1480] Complimentary experiments with Cyt. P450cam revealed that NO binding depends on the presence of camphor in the active site. In the absence of camphor, a 6C water-bound complex forms, whereas the presence of camphor promotes formation of the 5C complex. The $k_{on,NO}$ rate constants for these two forms were determined to be 3.2×10^5 and 3.45×10^6 M^{-1} s^{-1}, respectively, supporting slow NO binding when the sixth coordination site of the heme is occupied.[630,1482,1483]

The Fe^{III}/Fe^{II} reduction potential of Cyt. P450nor is shifted quite negative, −307 mV (vs NHE), in comparison to the Cyt. P450 monooxygenases. For example, Cyt. P450cam shows reduction potentials of −140 and −250 mV (vs NHE) with and without camphor, respectively.[674,1482,1483] Since the ferric form of Cyt. P450nor is catalytically active, this very negative reduction potential might help keep the protein oxidized for efficient turnover. The fact that the ferrous form of Cyt. P450nor does not play a part in the catalytic cycle of the enzyme was proven experimentally via CO inhibition studies, where it was shown that the presence of CO had no effect on turnover.[304]

In pioneering studies, the kinetic scheme of the reaction of Cyt. P450nor with NO was mapped out by Shiro, Shoun and coworkers.[304,307,1485] In the first step of catalysis, NO binds to the ferric heme, forming a 6C ls-$\{FeNO\}^6$ complex, which is the

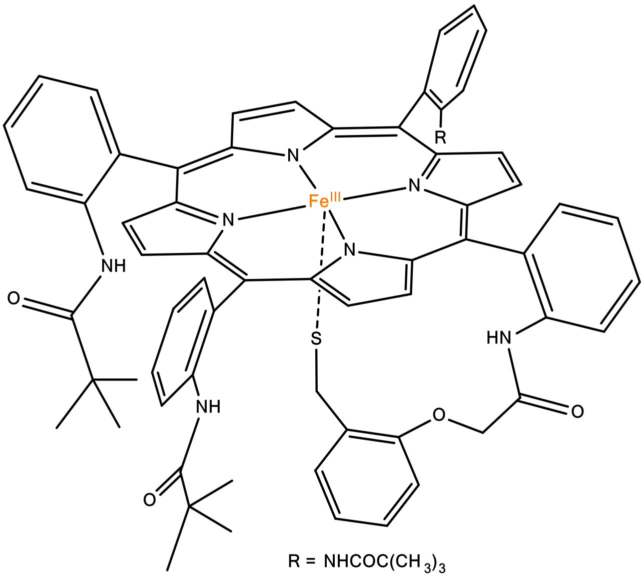

Figure 79. Structure of the [Fe(SPorph)] scaffold, first prepared by Higuchi and coworkers.[1484]

first intermediate of the reaction cycle (see Scheme 49).[304,307,674,1479,1485] The formation of this NO adduct can be monitored by UV−vis, IR and rRaman spectroscopy. In the absorption spectrum, the Soret band shifts from 413 nm to 431 nm upon NO binding to the ferric heme,[307] and the ls-{FeNO}^{6} complex is further characterized by Fe−NO and N−O stretching frequencies of 530 cm^{-1} and 1851 cm^{-1}, respectively.[1485] These vibrational properties are distinctively different from ferric heme−nitrosyls with proximal N-donor ligand coordination (see Section 2.3), indicating that the trans thiolate ligand imparts interesting geometric and electronic properties on this intermediate. This aspect is discussed below. The $k_{on,NO}$ rate constant determined by flash photolysis is 2.6 × 10^7 M^{-1} s^{-1} for the formation of the ls-{FeNO}^{6} complex of Cyt. P450nor at 10 °C (see Table 4).[307] Once NO binds to the ferric heme, the electronic structure of the complex is best described as Fe(II)−NO$^+$. Here, the increased electrophilicity of the bound NO$^+$ ligand (see Section 2.3) is a key feature of the complex that enables its further reaction with NAD(P)H in the next step of catalysis.

Importantly, the ls-{FeNO}^{6} complex of *Fo* P450nor could also be characterized by X-ray crystallography (see Figure 77).[1453,1486] Here, the cysteinate-bound complex shows Fe−NO and N−O bond lengths of 1.6 and 1.2 Å, respectively, with an Fe−N−O bond angle of 160.9°. On the basis of the Fe−NO and N−O vibrational frequencies, these bonds are weaker in comparison to those of ls-{FeNO}^{6} complexes with proximal His coordination, as observed in nitrophorins. The latter complexes also show linear Fe−N−O bonds, as discussed in Section 2.3. The Fe−S_{Cys} bond length in the crystal structure of NO-bound *Fo* P450nor is 2.3 Å. The interesting geometric and spectroscopic properties of ls-{FeNO}^{6} complexes with proximal cysteinate coordination (see Tables 11 and 18) suggest that this axial ligand has a substantial effect on the electronic structures of these species, which may play a role in Cyt. P450nor catalysis. The interesting aspects of the coordination chemistry of NO with Cyt. P450-type active sites are further discussed below.

On the basis of stopped-flow kinetic data, the 6C ls-{FeNO}^{6} intermediate goes on to react with NAD(P)H to form the next species in the catalytic cycle. This result was replicated when using sodium borohydride, suggesting that direct hydride donation from NAD(P)H to the ferric heme−nitrosyl complex is possible.[309] This is a unique reaction in biology that is only observed for Cyt P450nor, although more recently, it has been shown that heme ls-{FeNO}^{6} model complexes can also undergo this reaction (see below).[1462,1487] Further structural evidence that supports this proposal has been obtained by X-ray crystallography. As shown in the crystal structure overlay in Figure 80 (PDB: 1CL6 and 1XQD), the unreactive analogue of NADH, NAAD (nicotinic acid adenine dinucleotide) binds in close proximity to the heme in such a way that it positions the equivalent of the hydride that is to be transferred (from NADH) in this step of the reaction (see Scheme 49) in direct proximity of the electrophilic NO$^+$ ligand. Here, the CH—NO$^+$ distance is estimated to be around 1.9−2.0 Å.[1462,254] A similar binding geometry is anticipated for NAD(P)H, which would allow for facile hydride transfer. It was further determined that hydride transfer from NAD(P)H to the Fe(II)−NO$^+$ unit is the rate determining step of the reaction. Using the synthetic NADH analogue, 4,4-^{2}H,^{2}H-NADH, a kinetic isotope effect of 3.8 ±0.2 was reported for NO reduction by *Fo* P450nor.[309] This hydride transfer generates a new intermediate of the reaction, known as “Intermediate I”, which is catalytically competent for the reaction with the second equiv of NO.[307] Formation of Intermediate I is evident from a shift of the Soret band to 444 nm, determined by stopped-flow experiments. Additionally, NADH was shown to react with the ferric heme−NO complex with a second order rate constant of 0.9 × 10^6 M^{-1} s^{-1} at 10 °C.[307] Further characterization of Intermediate I was obtained by rRaman spectroscopy, which shows an Fe−N stretching frequency of 596 cm^{-1} for this intermediate.[305] Considering that Intermediate I is generated by hydride transfer to a ls-{FeNO}^{6} complex, this species could correspond to an Fe(II)−NHO, or ls-{FeNHO}^{8}, complex. On the basis of computational results, it was further proposed that due to the presence of the proximal thiolate ligand, the Fe(II)−NHO complex should be basic enough to become protonated, potentially generating a Fe−NHOH type species (see Scheme 49).[310] A possible ferrous heme−nitrosyl formulation of Intermediate I was ruled out via control experiments. For example, the ls-{FeNO}^{7} complex of Cyt. P450nor shows the Soret band at 434 nm, while Intermediate I is known to have its Soret band at 444 nm.[307] Also, from rRaman measurements, the Fe−NO stretching frequency of the ls-{FeNO}^{7} adduct is much lower, at 543 cm^{-1}.[305] Though the formation of a Fe(II)−NO intermediate has thus been ruled out, the exact nature of Intermediate I is unknown, partly due to the short lifetime (about 100 ms) of this species. The spontaneous decay of Intermediate I back to the ferric resting state was determined to have a unimolecular rate constant of 0.027 s^{-1} at 10 °C, in the absence of NO.[307] Experiments and computational studies dedicated to elucidating the identity of Intermediate I are discussed below.

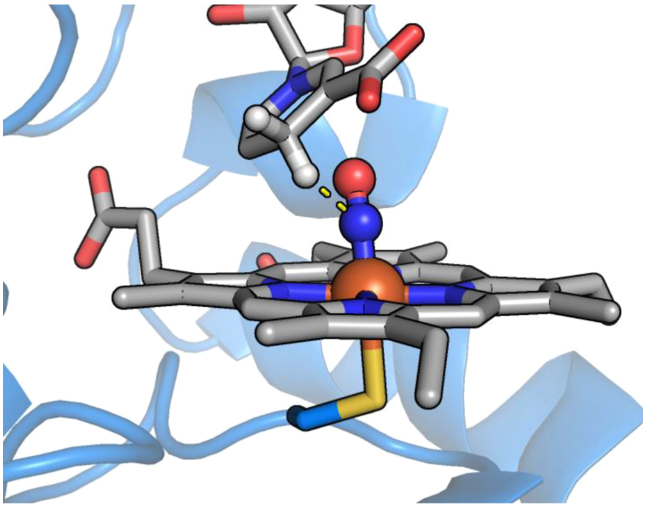

Figure 80. PyMOL generated overlay of the crystal structures of P450nor(III)−NO (PDB: 1CL6) and P450nor(III)−NAAD (PDB: 1XQD), showing how the H atom of NAAD is perfectly positioned for hydride transfer (when the analog NAD(P)H is bound) to the N atom of the coordinated NO$^+$ ligand. The distance between the H atom of NAAD and the N atom of the Fe(II)−NO$^+$ unit is 1.9-2.0 Å.

In the last step of the catalytic cycle, a second molecule of NO enters the reaction to eventually form N_2O and water, as shown in Scheme 49.[307] However, experimentally, no further intermediates of the reaction could be identified, so our knowledge of this second half of the catalytic cycle is very limited, and almost exclusively based on computations. Currently, it is believed that following the formation of

Intermediate I, another molecule of NO enters the catalytic cycle and reacts with Intermediate I under N−N bond formation, to generate a hyponitrite intermediate. After further tautomerization, this intermediate breaks the N−O bond and releases N_2O, generating water in the process to close the catalytic cycle, as shown in Scheme 49. Kinetic parameters that have been determined for *Fo* P450nor include K_M and V_{max}, reported to be 113 nM and ≥1200 s^{-1}, respectively.[304,307]

4.2.3. Interaction of NO with Ferric Hemes with Axial Thiolate-Donor Ligands. As discussed above, the first step in Cyt. P450nor-mediated NO reduction is binding of NO to the ferric heme-thiolate resting state, in order to generate a well characterized ls-$\{FeNO\}^6$ complex. While easily generated and stable in the enzyme environment (also in other Cyt. P450s[1488]), generation and characterization of heme-thiolate ls-$\{FeNO\}^6$ model complexes is much more challenging, mainly due to the reactivity of the thiolate ligand itself with NO. Thus, specialized synthetic hemes and thiolate ligands have been utilized to investigate this reaction. For example, sterically protected 'tailed' heme-thiolate complexes[671] and a doubly hydrogen-bonded thiolate ligand[778] were utilized to obtain the first documented ls-$\{FeNO\}^6$ model complexes with thiolate coordination. In the latter case, the only crystal structure of a thiolate-coordinated ls-$\{FeNO\}^6$ complex was obtained (see Figure 81),[778] which shows similar properties of the FeNO unit (see Table 11) as the ferric NO adduct of Cyt. P450nor (see Figure 77).

The first series of ls-$\{FeNO\}^6$ model complexes with axial thiolate ligation has now been reported by Hunt and Lehnert. These compounds demonstrate the thiolate ligand's effect on the FeNO unit in a systematic way. These complexes were obtained by the reaction of the corresponding 5C ferric heme-thiolate precursors (all with TPP^{2-} as the porphyrin ligand) with NO at −80 °C, and subsequently characterized using low-temperature UV−vis, IR, and rRaman spectroscopy (Figure 82). In these model systems, thiophenolate ligands were used that either contain (a) various electron-withdrawing substituents (i.e., the "electron poor" thiolate series),[792] or (b) one intramolecular hydrogen bond to the thiolate sulfur (ligands $^{-}$SPh-NHPh-*p*R, where R is a functional group allowing for tunability of the hydrogen-bond strength),[1489,1490] as shown in Scheme 50. These model systems allowed for the experimental demonstration that in heme-thiolate ls-$\{FeNO\}^6$ complexes:

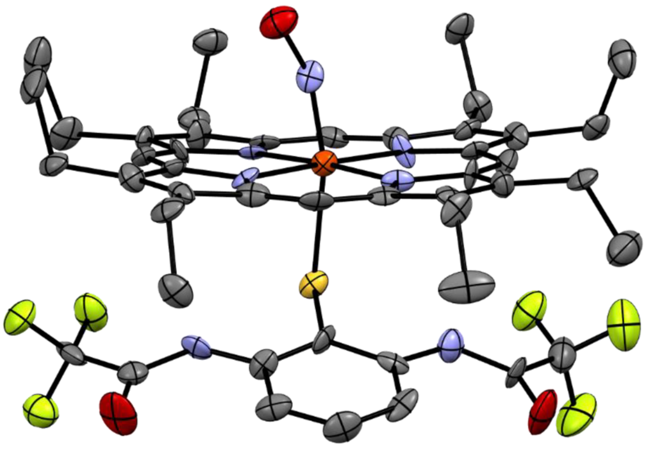

Figure 81. Crystal structure of [Fe(OEP)(S-2,6-$(CF_3CONH)_2C_6H_3$)(NO)]. All H atoms are omitted for clarity.[778]

(i) Both electron-withdrawing groups and hydrogen bonds can modulate the thiolate donor strength in a similar way.[826,1491,1492]

(ii) The thiolate donor strength directly modulates the Fe−NO and N−O bond strengths via a thermodynamic σ-*trans* effect (more precisely, a σ-*trans* interaction, since it is a thermodynamic effect) that can be experimentally quantified by spectroscopic determination of the Fe−NO and N−O stretching frequencies.

(iii) Hydrogen bonds are able to provide additional protection for the thiolate ligand against *S*-nitrosylation and potentially other side reactions as well.[828,1493,1494]

(iv) The cumulative strength of the proximal hydrogen bonds to the thiolate ligand in proteins and model systems can in turn be gauged by determination of the Fe−NO and N−O stretching frequencies of the corresponding ls-$\{FeNO\}^6$ adducts, by comparison of these data to the vibrational correlation plot shown in Figure 83.

The experimental results derived from the data of the 11 new model complexes are in excellent agreement with DFT calculations on Cyt. P450 (heme-thiolate) enzyme mimics,[792,1500] and the collective experimental results available for the NO adducts of different heme-thiolate enzymes.[1485,1495−1497] With findings (i)−(iv) now firmly established, based on experimental data, it is concluded that the differences in Fe−NO and N−O stretching frequencies between different heme-thiolate ls-$\{FeNO\}^6$ protein complexes are largely due to variations in the number and strength of hydrogen bonds to their respective cysteinate sulfurs. Figure 83 compares the data points of the 11 heme-thiolate ls-$\{FeNO\}^6$ model complexes with those reported for ls-$\{FeNO\}^6$ adducts in a number of heme-thiolate proteins (see also Table 19), and shows the two correlation lines established in the model complex studies.[792,1489] The slopes obtained from two different linear fits of the data points in Figure 83 (1.20 and 1.61) establish a direct correlation of the Fe−NO and N−O stretching frequencies, and hence bond strengths, with the donor strength of the axial thiolate ligand. For example, moving from right to left in the correlation plot, the thiolate donor strength increases, leading to a simultaneous weakening of both the Fe−NO and N−O bonds. The slopes of the correlation lines (>1) indicate that the thiolate donor strength has a somewhat larger effect on the N−O stretching frequency. However, note that a comparison of the relative (percent) changes of the vibrational frequencies shows that the total variation in the Fe−NO stretching frequency is actually about three times larger (∼3%) than that observed for the N−O stretching frequency (only ∼1%; see ref 792 for a detailed discussion). This result indicates that the donor strength of the thiolate modulates the Fe−NO bond strength to a far greater extent than the N−O bond strength. This finding therefore supports the idea that a thermodynamic thiolate σ-*trans* effect is the origin of the observed experimental trends in Fe−NO and N−O bond strengths.

DFT calculations further show that the thermodynamic thiolate σ-*trans* effect observed in the ls-$\{FeNO\}^6$ heme-thiolate complexes is in fact equivalent to the underlying orbital interaction responsible for the proposed "push effect" of the thiolate in Cyt. P450 monooxygenase catalysis.[792] This thermodynamic thiolate σ-*trans* effect manifests itself in the population of an Fe−N−O σ-antibonding (σ^*) orbital, which results from the mixing of this orbital into the occupied $S(p_z)$

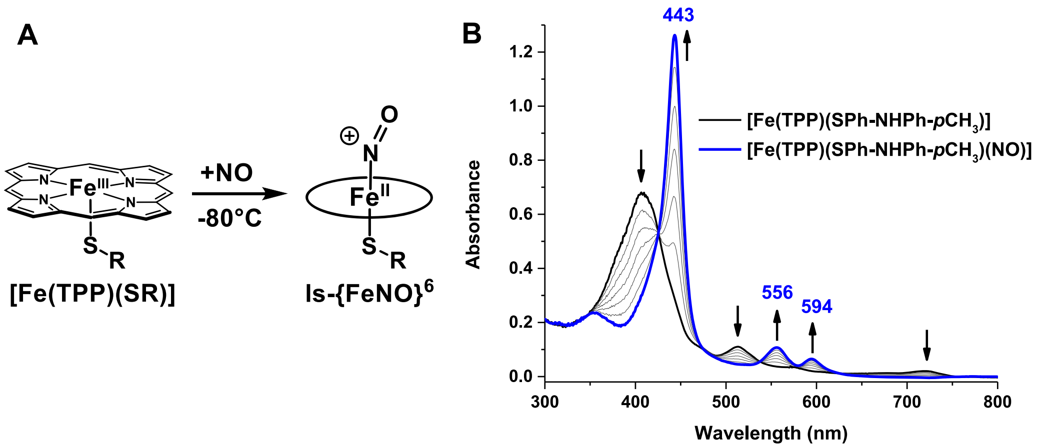

Figure 82. (A) Reaction scheme for the formation of heme-thiolate ls-{FeNO}^{6} model complexes. (B) Low-temperature (−80 °C) UV−vis spectra monitoring the formation of the ls-{FeNO}^{6} heme thiolate complex [Fe(TPP)(SPh-NHPh-pCH$_3$)(NO)] from the reaction of the corresponding 5C ferric heme-thiolate complex with NO gas. Adapted with permission from ref 1489. Copyright 2020 American Chemical Society.

Scheme 50. Two Series of Thiophenolate Ligands Were Used for the Preparation of ls-{FeNO}^{6} Heme-Thiolate Model Complexes[a]

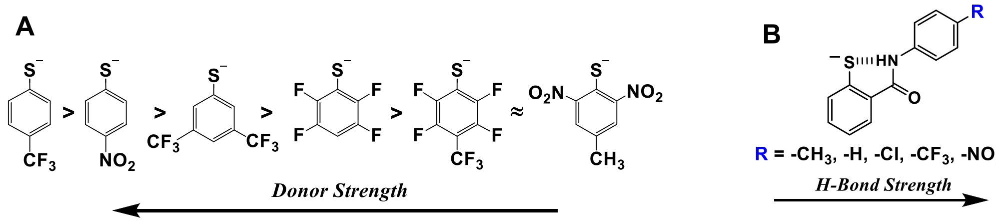

[a](A) The "electron poor" thiolate ligand series arranged in order of thiolate donor strength.[792] (B) The thiophenolate ligand series that contains one intramolecular hydrogen bond (indicated by a dashed line). Here, the R group can be varied to tune the strength of this hydrogen bond.[1489,1490].

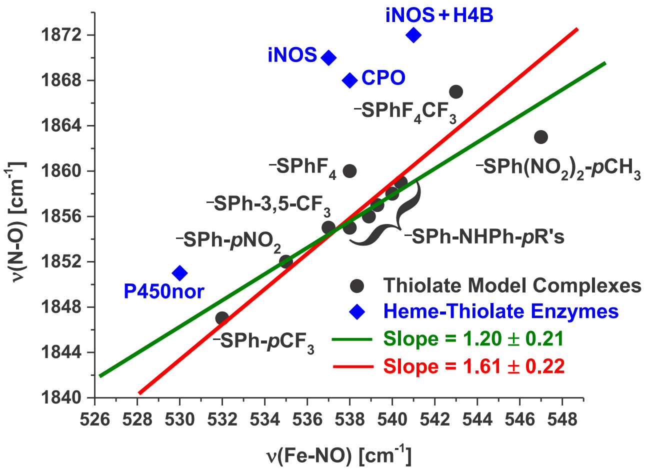

Figure 83. Correlation plot of the experimentally determined ν(Fe−NO) and ν(N−O) stretching frequencies of all 11 heme-thiolate ls-{FeNO}^{6} model complexes (all with TPP^{2-}) in comparison to ls-{FeNO}^{6} adducts of select heme-thiolate enzymes. The green line represents the best linear fit of all 11 data points, slope = 1.20 ± 0.21 (R^2 = 0.76). The red line is the best linear fit of all data points except that of the $^-$SPh(NO$_2$)$_2$-pCH$_3$ complex (see ref 792 for explanation), slope = 1.61 ± 0.22 (R^2 = 0.86). Abbreviations: CPO = chloroperoxidase. Adapted with permission from ref 1489. Copyright 2020 American Chemical Society.

Table 19. Comparison of ν(Fe−NO) and ν(N−O) Stretching Frequencies of Synthetic and Enzymatic Heme-Thiolate ls-{FeNO}^{6} Complexes

thiolate ligand	ν(Fe−NO)	ν(N−O)	ref
$^-$SPhF$_4$CF$_3$	543	1867	792
$^-$SPh-NHPh-pNO$_2$	540.4	1859	1489
$^-$SPhF$_4$	538	1860	792
$^-$SPh-NHPh-pCF$_3$	540	1858	1489
$^-$SPh-NHPh-pCl	539.3	1857	1489
$^-$SPh-NHPh	538.9	1856	1489
$^-$SPh-NHPh-pCH$_3$	538	1855	1489
$^-$SPh-3,5-CF$_3$	537	1855	792
$^-$SPh-pNO$_2$	535	1852	792
$^-$SPh-pCF$_3$	532	1847	792
ls-{FeNO}^{6} Enzyme[a]	ν(Fe−NO)	ν(N−O)	ref
iNOSoxy + H4B	541	1872	1495, 1496
iNOSoxy	537	1870	1495, 1496
CPO	538	1868	1497
P450nor (WT)	530	1851	1485
P450cam	528	1806	1485, 1498
P450$_{BM3}$	526	N/A	1499
P450cam + norcam	524	1818	1485, 1498
P450cam + cam	522	1806	1485, 1498
P450cam + adam	520	1818	1485, 1498

[a]Abbreviations: N/A = not available, cam = camphor, norcam = norcamphor, adam = adamantanone.

donor orbital of the thiolate, mediated by the d$_{z^2}$ orbital (see Figure 84).[792,1500] This effect leads to a simultaneous

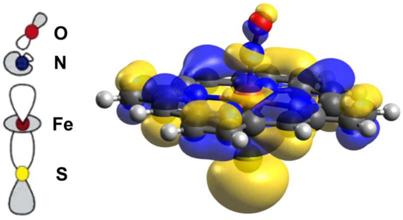

Figure 84. Left: ChemDraw depiction of the axial thiolate donor orbital, d_{z^2} of iron, and the NO σ* orbital. Right: MO contour plot that shows the admixture of the Fe−N−O σ-antibonding (σ*) orbital into the occupied (bonding) $S(p_z)\_d_{z^2}$ MO, mediated by the d_{z^2} orbital. Reprinted with permission from ref 792. Copyright 2019 American Chemical Society.

weakening of the Fe−NO and N−O bond, as observed experimentally, and scales with the donor strength of the thiolate. The "push effect", introduced by Dawson and coworkers,[1474,1501] corresponds to the idea that the strong donicity of the proximal cysteinate ligand helps accelerate heterolytic O−O bond cleavage in the protonated ferric-hydroperoxo intermediate (Compound 0) of Cyt. P450s to form H_2O and Compound I (a ferryl-oxo porphyrin radical cation complex),[1502] compared to the analogous species in histidine-coordinated heme proteins. Here, Compound I is the catalytically-active intermediate responsible for C−H bond cleavage (via H-atom abstraction) in Cyt. P450 monooxygenase catalysis. Thus, as the thermodynamic thiolate σ-*trans* effect is the key orbital interaction responsible for the "push effect", the vibrational data of the ls-$\{FeNO\}^6$ heme-thiolate complexes (which directly quantify the thiolate donor strength) can also be used as a sensitive probe for the magnitude of the "push effect" in different heme-thiolate enzymes and model complexes. By comparison of the vibrational data of the ferric NO adducts of different heme-thiolate enzymes, for example, even subtle differences in their proximal hydrogen-bonding networks, leading to subtle differences in their thiolate donor strengths, can be quantified.[1489]

With these conclusions in mind, the question of how the observed spectroscopic properties of Cyt. P450nor's ls-$\{FeNO\}^6$ complex relate to the enzyme's function can be addressed. In the Cyt. P450nor catalytic cycle, the next step after binding of NO and generation of the heme-thiolate ls-$\{FeNO\}^6$ complex is the direct hydride transfer from NAD(P)H to the N atom of the Fe(II)−NO^+ unit, which in turn leads to the generation of Intermediate I (see Scheme 49). On the basis of model complex studies by Richter-Addo and coworkers[1487,1503] (discussed further below), an axial thiolate should not be necessary to enable the hydride transfer to the Fe(II)−NO^+ unit of ls-$\{FeNO\}^6$ heme complexes. Additionally, based on their spectroscopic characterization, heme-imidazole ls-$\{FeNO\}^6$ complexes have even greater NO^+ character than heme-thiolate ls-$\{FeNO\}^6$ complexes, as indicated by their higher ν(N−O) frequencies (e.g., ∼1900−1920 cm^{-1}).[655] Thus, the role of the proximal hydrogen bonds in this first step of the Cyt. P450nor reaction cycle can be argued to be a weakening of the thiolate's donor strength to a degree that the ls-$\{FeNO\}^6$ complex still has enough Fe(II)−NO^+ character to perform the hydride abstraction efficiently. For example, the ν(N−O) and ν(Fe−NO) stretching frequencies for the ls-$\{FeNO\}^6$ complexes of Cyt. P450cam are reported to range from 1806−1818 cm^{-1} and 520−528 cm^{-1},[1485,1498] respectively, suggesting a very strongly donating thiolate ligand. Additionally, ν(Fe−NO) of the Cyt. $P450_{BM3}$ ls-$\{FeNO\}^6$ complex (another Cyt. P450 monooxygenase) is reported to be 526 cm^{-1},[1499] that is, four wavenumbers lower than that of Cyt. P450nor (530 cm^{-1}). Taken together, these lower Fe−NO and N−O stretching frequencies of the ls-$\{FeNO\}^6$ complexes of Cyt. P450 monooxygenases (i.e., Cyt. P450cam and Cyt. $P450_{BM3}$) directly suggest that they have stronger thiolate donors than Cyt. P450nor. While this strong thiolate donation can be thought of as beneficial for driving O−O bond cleavage and Compound I formation due to a strong thermodynamic thiolate σ-*trans* effect, it is possible that such a strongly donating thiolate could deactivate or at least slow down the hydride abstraction reaction from NAD(P)H in terms of the Cyt. P450nor reaction cycle. That is, a very strongly donating thiolate would greatly weaken the Fe−NO and N−O bond strengths and would decrease the electrophilicity of the NO^+ ligand compared to heme-imidazole ls-$\{FeNO\}^6$ complexes. Thus, the observed ν(N−O) frequency of 1851 cm^{-1} in Cyt. P450nor, which lies right in between of those reported for Cyt. P450cam (1806 cm^{-1}, in the absence of substrate) and typical heme-imidazole ls-$\{FeNO\}^6$ complexes (∼1900 cm^{-1}), suggests that the thiolate donor strength is perfectly tuned to still have enough Fe^{II}−NO^+ character to quickly accept the hydride and move forward in the reaction cycle, while not being too strong of a donor in which hydride acceptance would possibly be impeded. This intermediate thiolate donor strength in Cyt. P450nor can also be seen by comparing its N−O stretching frequency to those of the ls-$\{FeNO\}^6$ complexes of NOS and chloroperoxidase (CPO; observed at 1870 and 1868 cm^{-1}, respectively),[1495−1497] which are known to have weaker thiolate donors than Cyt. P450s due to the presence of stronger proximal hydrogen bonds to their cysteinate ligands.

In summary, the intermediate thiolate donor strength could be an important balancing act by Cyt. P450nor to allow for quick and efficient hydride transfer from NAD(P)H, while still being a strong enough donor to make the Fe(II)−NHO complex (generated from this hydride abstraction) basic enough to be doubly protonated, to give a $Fe^{III/IV}$−$NHOH^{\bullet/-}$ complex, which is believed to be the true nature of Intermediate I (Scheme 49, further discussion below). Additionally, having stronger hydrogen bonds to the thiolate in Cyt. P450nor compared to Cyt. P450 monooxygenases (i.e., Cyt. P450cam and Cyt. $P450_{BM3}$) can be thought of as an important safe guard for the thiolate to increase protection from *S*-nitrosylation in the presences of excess NO, especially if NAD(P)H is not yet bound in the enzyme's active site. For example, the heme-thiolate containing nitrophorin from *C. lectularius* (cNP; see Section 2.3), which only has one significant proximal hydrogen bond to its thiolate ligand, has been shown to form a ls-$\{FeNO\}^6$ complex, followed by *S*-nitrosylation and ls-$\{FeNO\}^7$ complex formation under excess NO.[253] This is also the decomposition pathway observed in our heme-thiolate model complexes that only contain one hydrogen bond.[1489] Hence, having a stronger proximal thiolate hydrogen-bonding network in place than Cyt. P450 monooxygenases would be advantageous for Cyt. P450nor, due to the decreased susceptibility of the thiolate sulfur towards reaction with its substrate, NO. In this context, it should also be noted that NO is more reactive towards thiolates compared to O_2 (the substrate of Cyt. P450 monooxygenases). Therefore, Nature seems to have perfectly tuned the proximal hydrogen bonds in Cyt. P450nor to optimally promote catalytic function while protecting the thiolate ligand against NO.

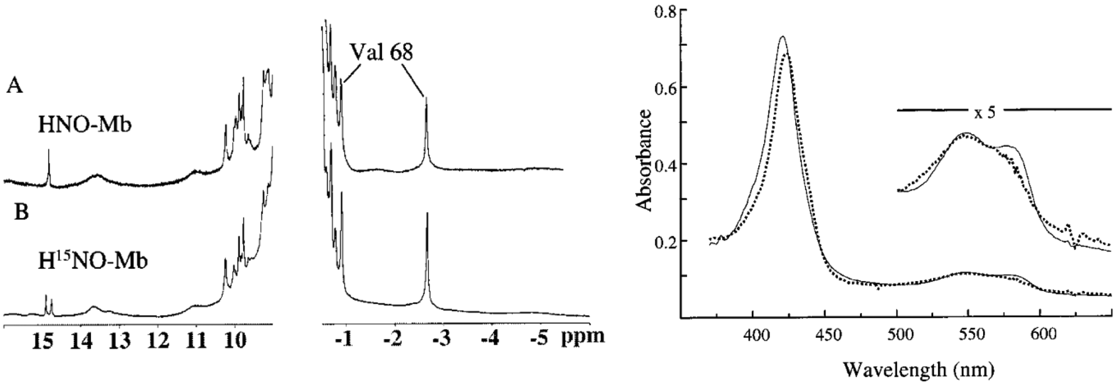

Figure 85. Spectroscopic evidence of Mb−NHO complex formation. Left: ^{1}H-NMR spectra utilizing ^{15}N to show N-protonation. Right: UV−vis spectra demonstrating the formation of Mb−NHO (solid line) from Mb−NO (dotted line). Reprinted with Permission from ref 1504. Copyright 2000 American Chemical Society.

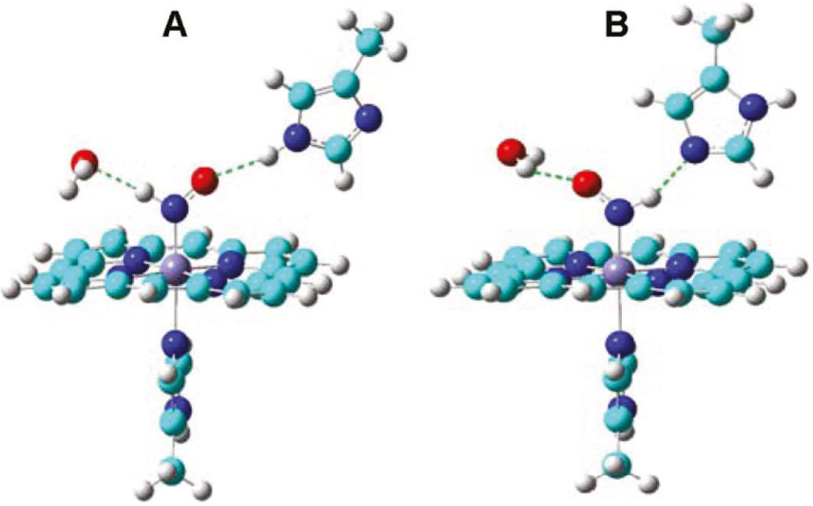

Figure 86. Computational models of Mb(II)−NHO, showing a stabilization of the bound HNO ligand by hydrogen-bonding with His64 and a water molecule. Two possible hydrogen-bonding networks are shown (panel A and B). Reprinted with Permission from ref 1508. Copyright 2011 American Chemical Society.

4.2.4. Ferrous Heme−NHO Complexes.

Ferrous heme−NHO complexes, ls-{FeNHO}^{8} in the Enemark−Feltham notation, have been proposed as intermediates in the catalytic cycles of several enzymes, such as Cyt. P450nor, Cyt. *c* NIR (see Section 4.4),[1389,1505] assimilatory NIR,[1506] and HAO.[271] As shown in the Cyt. P450nor catalytic cycle in Scheme 49, the ferrous HNO intermediate forms right after NAD(P)H performs a direct hydride transfer to the Fe(II)−NO$^+$ adduct. Either this HNO complex, or the corresponding, protonated Fe−NHOH species corresponds to Intermediate I, the catalytically competent intermediate responsible for reaction with the second NO, leading to N−N bond formation. To obtain further insight into this issue, it is therefore useful to consider the basic properties of ferrous heme−NHO complexes. The best characterized HNO complex is the corresponding Mb adduct, prepared by Farmer and coworkers, which shows the Soret band at 423 nm and a characteristic singlet at 14.93 ppm in the ^{1}H-NMR spectrum (see Figure 85).[1506,1507] When the ^{1}H-NMR experiment was repeated with ^{15}N labeling, the singlet became a doublet, further confirming the formation of the Mb(II)−NHO complex where the N atom is protonated. On the basis of extended X-ray absorption fine structure (EXAFS) investigations, the Fe−NHO bond length is 1.82 Å and the Fe−N−O bond is bent in the Mb(II)−NHO complex with an Fe−N−O angle of 131°.[1507] From rRaman spectroscopy, the Fe−NO and N−O stretching frequencies of this species were reported to be 651 and 1385 cm^{-1}, respectively.[1507] Computational work on Mb(II)−NHO further demonstrates that hydrogen bonds formed in the distal pocket between the coordinated HNO, His64 and a H_2O molecule likely aid in stabilizing the complex, as shown in Figure 86. The calculated ^{1}H-NMR shifts and N−O stretching frequences, 15.03 and 15.10 ppm, and 1384 and 1380 cm^{-1}, respectively, obtained in this work for the hydrogen-bond stabilized complexes shown in Figure 86, are in excellent agreement with the experimental values obtained for Mb(II)−NHO, 14.93 ppm and 1385 cm^{-1}.[1508] The electronic structure of this complex was determined to correspond to a ls-Fe^{II} center with a bound singlet HNO ligand (^{1}HNO), with a diamagnetic (S_t = 0) ground state.[308,699] Here, the neutral HNO ligand is believed to be innocent in 5C ferrous heme and corresponding 6C complexes with axial N-donor ligation. In these cases, the ^{1}HNO ligand serves as a weak σ-donor and medium-strong π-acceptor.[73,699] In this sense, ^{1}HNO is somewhat similar to CO when bound to ferrous heme, but not as strong of a π-accepting ligand.[699]

In terms of reactivity, competitive trapping experiments were performed by reaction of Mb−NHO with excess CO gas to monitor the replacement of HNO. Here, the rate constants for HNO binding and dissociation were reported as 4.2×10^9 M^{-1} s^{-1} and 8.9×10^{-5} s^{-1}, respectively.[1509] The unimolecular loss of HNO from Mb was determined to be independent of CO concentration. On the other hand, the bimolecular rate constant for CO binding to Mb was reported to be 5.1×10^5 M^{-1} s^{-1}.[1509] The small rate constant for HNO release from Mb compared to the fast binding constant of CO indicates that HNO dissociation is the rate limiting step. The slow dissociation of HNO is proposed to originate from hydrogen-bond stabilization of the ligand in the distal pocket of Mb, as discussed above (see Figure 86).[1508,1509]

On the other hand, HNO is thought to be highly thiophilic in proteins, favoring "soft" bases such as thiols and phosphines over "hard" bases, for example oxygen containing nucleophiles.[1510−1512] The overall reaction involves nucleophilic attack of the thiol on the electrophilic nitrogen of HNO to give N-hydroxysulfenamide:[1513,1514]

$$\text{RSH} + \text{HNO} \rightarrow \text{RS−NHOH} \qquad (17)$$

However, N-hydroxysulfenamide is unstable and tends to decompose via two possible routes. In one case, this product can rearrange to form a sulfinamide, or it can react with excess thiol to form a disulfide and hydroxylamine. The former case tends to be reversible, while the latter reaction is not as readily reversible. Evidence of this reactivity has been observed in the reaction of HNO with glutathione and with a protein with "activated" thiol (papain). Rate constants for these reactions of $(2\text{-}8) \times 10^6$ and 2×10^7 M^{-1} s^{-1}, respectively, have been determined.[1515−1517] The latter rate constant is surprisingly large, further indicating that HNO can efficiently react with thiols in proteins. A practical application of this reactivity is the anti-alcoholism drug cyanamide, H_2NCN, which decomposes in the body to release HNO, which subsequently reacts with the activated thiol in the enzyme aldehyde dehydrogenase, to inhibit the enzyme.[1518]

Within the last 10 years, several ferrous heme−NHO model complexes have been synthesized and their properties have been characterized in detail. Importantly, Richter-Addo and coworkers were able to model the key hydride transfer step in the Cyt. P450nor mechanism.[1487] This reaction was first demonstrated for Ru complexes, for example $[Ru(TTP)(MI)(NO)](BF_4)$.[80,1519] Later, direct hydride transfer from $[NBu_4](BH_4)$ to the 6C ls-$\{FeNO\}^6$ model complex $[Fe(OEP)(5\text{-}MI)(NO)]^+$ (5-MI = 5-methylimidazole) to form the corresponding 6C HNO complex, [Fe(OEP)(5-MI)(NHO)], was demonstrated.[1487] Formation of this species was monitored by solution IR spectroscopy at −20 °C. The ls-$\{FeNO\}^6$ complex has an N−O stretching frequency of 1912 cm^{-1}. Upon addition of the hydride source, this band decreased in intensity and a new band emerged at 1383 cm^{-1}, which is typical for 6C ferrous heme−NHO complexes (see above). This assignment was further confirmed by ^{1}H-NMR spectroscopy in conjecture with ^{15}NO isotope labeling. Even at low temperature, this Fe(II)−NHO complex disproportionates, forming the corresponding 5C ls-$\{FeNO\}^7$ complex [Fe(OEP)(NO)], evident from the appearance of the N−O stretching band at 1668 cm^{-1}, and H_2.[1487] As discussed in Section 2.2, the fast disproportionation of ferrous heme−NHO complexes in organic solvents, following the reaction in eq 12, has been a major obstacle for the preparation of these types of species.[569,690,691] In contrast, the corresponding, deprotonated heme ls-$\{FeNO\}^8$ complexes are stable (see Section 2.2). The formation of [Fe(OEP)(5-MI)(NHO)] was further confirmed by mass spectrometry and ^{1}H-NMR, which shows a singlet at 13.99 ppm, typical for heme Fe(II)−NHO complexes.[1520] However, the total yield of [Fe(OEP)(5-MI)(NHO)] was only 9%, which precluded further characterization of this species.

Other 6C ls-$\{FeNO\}^6$ complexes, for example $[Fe(PPIXDME)(5\text{-}MI)(NO)]^+$, were later shown to have similar reactivity with $[NBu_4](BH_4)$.[1503] The Richter-Addo group also investigated the hydride transfer reactivity of the corresponding 5C complex, [Fe(OEP)(NO)](OTf) (OTf^- = triflate), with $[NBu_4](BH_4)$. Here, the HNO complex is not formed. Instead, the hydride is transferred to the ferric center to generate a very unstable complex, [Fe(OEP)(H)(NO)], as shown in Scheme 51.

Interestingly, in a follow up study by the Richter-Addo group, it was shown that the addition of NO to [Fe(OEP)(5-MI)(NHO)] leads to the generation of N_2O.[1503] These results indicate that the initially formed HNO complex in the catalytic cycle of Cyt. P450nor (see Scheme 49) could be catalytically competent and react with the second equiv of NO under N−N bond formation. Hence, Intermediate I could actually correspond to the HNO complex. Further studies are needed to solidify these ideas.

Lehnert and coworkers investigated whether steric bulk could be used to stabilize a ferrous heme−NHO complex in a model system. For this purpose, the ferrous precursor [Fe(3,5-Me-BAFP)] (3,5-Me-BAFP^{2-} = 3,5-methyl-bisaryloxyfence porphyrin dianion) was first reduced by bulk electrolysis, followed by the addition of NO to generate the corresponding ls-$\{FeNO\}^8$ complex, $[Fe(3,5\text{-}Me\text{-}BAFP)(NO)]^-$. Addition of acetic acid then led to the reversible formation of [Fe(3,5-Me-BAFP)(NHO)].[569] This complex shows a very similar UV−vis absorption spectrum as Mb(II)−NHO, with the Soret band at 426 nm and the Q band at 545 nm. Over the course of 20 hours, the S = 1/2 signal of the ls-$\{FeNO\}^7$ complex [Fe(3,5-Me-BAFP)(NO)] appeared in the EPR spectra of the HNO complex, signifying disproportionation following eq 12. However, due to the sterically-hindered bis-picket fence porphyrin scaffold used here, this bimolecular decomposition is greatly slowed down, stabilizing the Fe(II)−NHO complex (half-life: ∼5 hours at room temperature).[569] Unfortunately, due to the preparation of [Fe(3,5-Me-BAFP)(NHO)] via bulk electrolysis (with high concentrations of electrolyte), further characterization of this complex could not be accomplished.

One important question related to the biologically-relevant coordination chemistry of HNO is the pK_a of the coordinated HNO ligand, and whether at neutral pH HNO is bound in the

Scheme 51. Hydride Attack on 5C and 6C Ferric Heme−Nitrosyl Model Complexes[a]

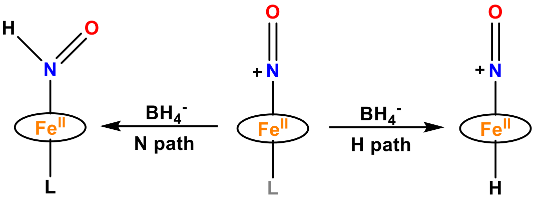

[a]The complex in the middle is either 6C (with ligand L, N path), or 5C (no ligand L, H path). See text for further explanation.

protonated or deprotonated form. To further evaluate the pK_a of metal−NHO complexes, the pK_a of free HNO must be considered. However, there is a challenge in measuring the pK_a of free HNO, since a spin flip occurs after release of a proton from free HNO. This generates a kinetic barrier, thus slowing down proton transfer. At the same time, HNO undergoes fast dimerization and decomposition (to N_2O and H_2O), limiting its life-time in solution. Accordingly, there are two possible pK_a values for the singlet $^1NO^-$ and triplet $^3NO^-$ form, as shown in eq 18:

$$^1HNO \rightarrow {}^{3/1}NO^- + H^+ \qquad (18)$$

In 1970, the pK_a of HNO was reported as 4.7, but this value was recently revised, and pK_a values of ∼11.6 for $^3NO^-$ and ∼23 for $^1NO^-$ were estimated.[14,1521] On the other hand, metal-bound NO^- complexes of ls-$\{FeNO\}^8$ type contain a $^1NO^-$ ligand, so the relevant pK_a value to compare to is ∼23, making this ligand a regular conjugate acid-base pair in these complexes (no change in spin state). Upon coordination to a cationic metal ion, the pk_a of HNO should decrease; however it is not clear how large this effect is. Farmer and coworkers estimated the pK_a of Mb(II)−NHO to be >10, but due to the instability of Mb in alkaline solution, the exact value could not be determined.[1520] This value is comparable to the phenolic acids used for the protonation of $[Fe(OEP)(NO)]^-$ (see Section 2.2).[692,1506] From DFT calculations, the pK_a of Mb(II)−NHO is estimated at ∼14.[73]

On the other hand, using model complexes, the pK_a of coordinated HNO could be determined accurately. For $[Ru(Me_3[9]aneN_3)(bpy)(NO)]^{3+/2+/+}$, Slep and coworkers prepared the whole ls-$\{RuNO\}^{6-8}$ series and the corresponding HNO complex, ls-$\{RuNHO\}^8$, and the pK_A of the bound HNO ligand was determined (9.78) in water.[77,78] For sodium nitroprusside, the ls-$\{FeNHO\}^8$ complex could be obtained as well, with a pK_a of 7.7.[72] However, in this case the nature of the reduced complex is unclear.[29] In the original publication, the HNO complex was proposed to be 6C, $[Fe(CN)_5(NHO)]^{3-}$, but following computational studies indicate that the ls-$\{FeNHO\}^8$ complex is actually 5C.[73] Most recently, Doctorovich and coworkers prepared a water-soluble heme HNO complex, $[Fe(TPPS)(NHO)]^{4-}$, which shows that the disproportion of the HNO adduct can be suppressed in water, likely due to hydrogen bonds formed between the coordinated HNO and the surrounding water molecules (see Section 2.2).[698] The half-life reported for this complex is 40 s and the pK_a of the bound HNO ligand is 9.7.[698] From all of these investigations, it is clear that the coordinated HNO ligand in ls-$\{MNHO\}^8$ type complexes generally has a pK_a ≥ 10, which means that we can safely assume that these types of complexes will be in the protonated (HNO) form at neutral pH.

In contrast, reaction of HNO with ferric heme proteins, for example met-Mb/Hb, leads to HNO deprotonation upon coordination to the ferric heme, followed by electron transfer, ultimately generating stable ls-$\{FeNO\}^7$ complexes.[1509,1522]

One important question in the context of Cyt P450nor is how the axial thiolate (deprotonated Cys) ligand could affect the electronic properties of the ls-$\{FeNHO\}^8$ intermediate. On the basis of DFT studies by the Neese group, it was proposed that the anionic nature of the thiolate could promote the formation of a valence tautomer, with an Fe(III)−$NHO^{\bullet-}$ type electronic structure.[311] Here, electron transfer occurs from the Fe^{II} center to the ^1HNO ligand, generating a $HNO^{\bullet-}$ radical. Recent crystallographic and spectroscopic data support this formulation of Intermediate I. In particular, the N−O stretches of 1330 cm^{-1} and 1290 cm^{-1} obtained for the intermediate with and without NAD^+ present, respectively, suggest that this species is likely singly protonated (potentially with the Fe(III)−$NHO^{\bullet-}$ electronic structure). The formation of such a radical species would be expected to aid in the following reaction with the incoming $NO^\bullet$, corresponding to a radical-radical type coupling reaction, which generally have very low activation barriers (see Scheme 52). In the computational study by the Neese group, this reaction was predicted to be barrierless.[311] Alternatively, DFT calculations predict that the strong electron donation from the axial thiolate ligand increases the basicity of the bound HNO ligand, leading to its further protonation. This possibility is discussed next.

4.2.5. Intermediate I. On the basis of DFT calculations, it was proposed that the presence of the thiolate ligand increases the basicity of the coordinated HNO ligand, allowing the Fe^{II}−NHO complex, generated via the hydride transfer from NAD(P)H, to be protonated at neutral pH, forming an Fe−NHOH type species (see Scheme 49).[310] This is analogous to later work by Green and coworkers, where it was shown that the proximal thiolate ligand in Cyt. P450s increases the basicity of Compound II by 9 log units (compared to Mb), which drives the H-atom abstraction from a substrate C−H bond.[1475,1523] Experimental support for the idea that Intermediate I corresponds to a Fe−NHOH complex comes from pulse radiolysis experiments with H_2NOH, which is known to generate the $^\bullet NHOH$ radical under these conditions, with a rate of 9.5×10^9 M^{-1} s^{-1}.[1524] When H_2NOH is irradiated in the presence of ferric Cyt. P450nor, the Soret band shifts to ∼444 nm, which is identical to the position of the Soret band in Intermediate I, as determined from stopped-flow experiments (see above).[309] Other important information about Intermediate I came from MCD experiments (here, Intermerdiate I was generated by NADH addition to the ls-$\{FeNO\}^6$ adduct), and it was shown that Intermediate I has no MCD **C**-term signal at the Soret band position, observed at 445 nm in these experiments. This further suggests that this species is diamagnetic with $S_t = 0$.[308]

On the basis of DFT calculations, the protonated Fe−NHOH complex can exist in the form of two valence tautomers: either a Fe(IV)−$NHOH^-$ or a Fe(III)−$NHOH^\bullet$ complex.[310,311] Considering that Intermediate I is a diamagnetic species, the Fe(IV)−$NHOH^-$ form would require the Fe^{IV} center to be in the $S_t = 0$ state, which is not observed for

Scheme 52. Proposed Electronic Structures of Intermediate I

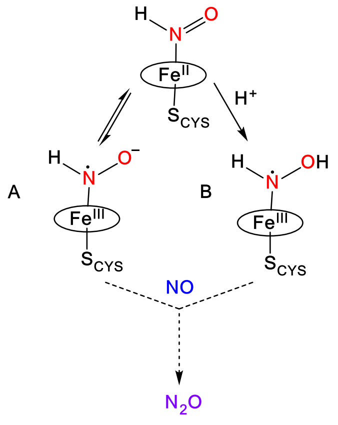

Scheme 53. Overall Reactivity of [Fe(3,5-Me-BAFP)(NHOMe)], Used for the Generation of a Model System for the Fe−NHOH Form of Intermediate I in the Cyt. P450nor Mechanism (See Scheme 49), and the Following Reaction of the Model Complex with NO

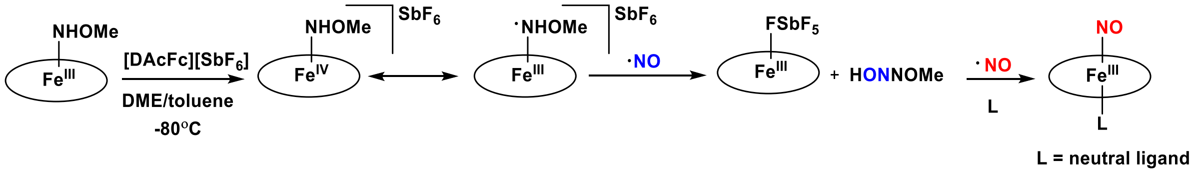

ferryl hemes. Correspondingly, DFT calculations show that the Fe(III)−NHOH• description is the energetically preferred form.[311] Here, the spins of the ls-Fe^{III} center and the •NHOH radical are AF coupled, resulting in the experimentally observed, diamagnetic ground state of Intermediate I. As in the case of the putative Fe(III)−NHO•− form of Intermediate I, this would again enable a radical-radical type coupling reaction between the Fe(III)−NHOH• complex and the incoming NO•, allowing for an essentially barrierless N−N coupling reaction to occur.[306] This conclusion is further supported by Mössbauer-spectroscopic data on Intermediate I. Here, an isomer shift of $\delta = 0.24$ mm/s was obtained for this species, which lies in the range of those reported for ls ferric hemes, $\delta = 0.15 - 0.25$ mm/s.[308] This indicates that Intermediate I likely exists in the ls ferric state, in agreement with the electronic structure of the Fe(III)−NHOH• valence tautomer.

More recently, further insight into the nature of Intermediate I has been obtained using model complex studies. Instead of using the reaction pathway found in the enzyme (hydride transfer to a ls-{FeNO}^{6} complex), this Intermediate I model was prepared following the reaction sequence shown in Scheme 53.[306] For this purpose, the ferric complex [Fe(3,5-Me-BAFP)(NHOMe)] was prepared first, where O-methylhydroxylamide is used as a substitute for hydroxylamide (to increase the stability of the complex) in combination with the sterically shielding 3,5-Me-BAFP^{2-} porphyrin ligand. The crystal structure of this starting material is shown in Figure 87, indicating the desired N-coordination of the NHOMe$^-$ anion to the ferric heme.[306] This complex was further characterized by UV−vis absorption, EPR, rRaman and Mössbauer spectroscopy. One-electron oxidation of this species at −80 °C then generates [Fe(3,5-Me-BAFP)(NHOMe)]$^+$ as a model for Intermediate I. Spectroscopic studies (especially rRaman and Mössbauer) show that in this complex, the iron center is still in the Fe^{III} state, which means that the complex indeed corresponds to the Fe(III)−NHOMe• valence tautomer, and therefore, directly models the electronic structure of Intermediate I. However, with the difference that the model complex is 5C, and hence, hs. This species is very unstable, and decays at −80 °C with a half-life of 68 min, generating the complex [Fe(3,5-Me-BAFP)(SbF$_6$)] (presumably via loss of the •NHOMe radical). Further reactivity studies of this intermediate with NO• were then conducted, to determine whether a Fe(III)−NHOMe• type species is catalytically competent in Cyt. P450nor catalysis. Interestingly, these experiments show that upon addition of 1 equiv of NO•, fast attack on the coordinated •NHOMe radical occurs, likely leading to N−N bond formation. This reaction is very fast, even at −80 °C, as shown in Scheme 53, and completed in ~35 s, generating [Fe(3,5-Me-BAFP)(SbF$_6$)] as the heme product (see Figure 88, left). Here, N−N bond formation would generate a hyponitrous acid analogue, HON−NOMe, the fate of which could not be determined. In the presence of excess NO, the reaction shows a second, slower phase, generating the corresponding ls-{FeNO}^{6} complex from the primary reaction product, [Fe(3,5-Me-BAFP)(SbF$_6$)], by simple NO coordination. The 6C product, [Fe(3,5-Me-BAFP)(L)(NO)]$^+$ (L = solvent, etc.), is easily identified from its characteristic UV−vis absorption features (see Figure 88, right). These results indicate that a Fe(III)−NHOMe• type species is indeed highly reactive towards NO•, even at −80 °C, which is in agreement with a radical-radical type reaction. A Fe(III)−NHOH• species is therefore a good candidate for Intermediate I, based on the observed reactivity.[306]

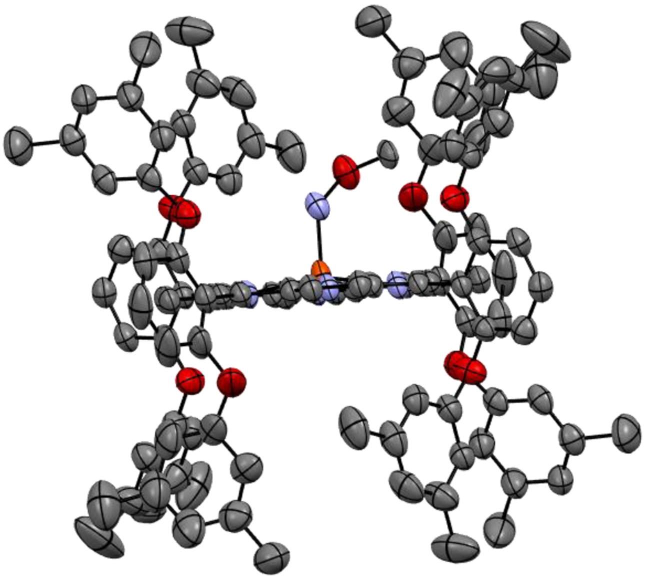

Figure 87. Crystal structure of [Fe(3,5-Me-BAFP)(NHOMe)].[569] All H atoms are omitted for clarity.

In summary, based on spectroscopic studies on Cyt. P450nor, model complex studies, and DFT calculations, there are two possible structures for Intermediate I, the key intermediate in Cyt. P450nor catalysis. This species could either correspond to the ferrous HNO adduct, proposed to have a Fe(III)-NHO•− electronic structure (see Scheme 52), or the corresponding protonated species, which is a Fe(III)−NHOH• complex.[306,308,310,792] Further studies are necessary to fully elucidate the true nature of Intermediate I, and to shed more light on the second half of the catalytic cycle of Cyt. P450nor.

4.3. NO Breakdown by NO Reductases: Bacterial NO Reductase (*c*NOR)

In denitrifying bacteria, *c*NOR (or NorBC) is a periplasmic membrane-bound enzyme that catalyzes the conversion of NO into N_2O via a two-electron reduction, as shown in eq 5.[1525]

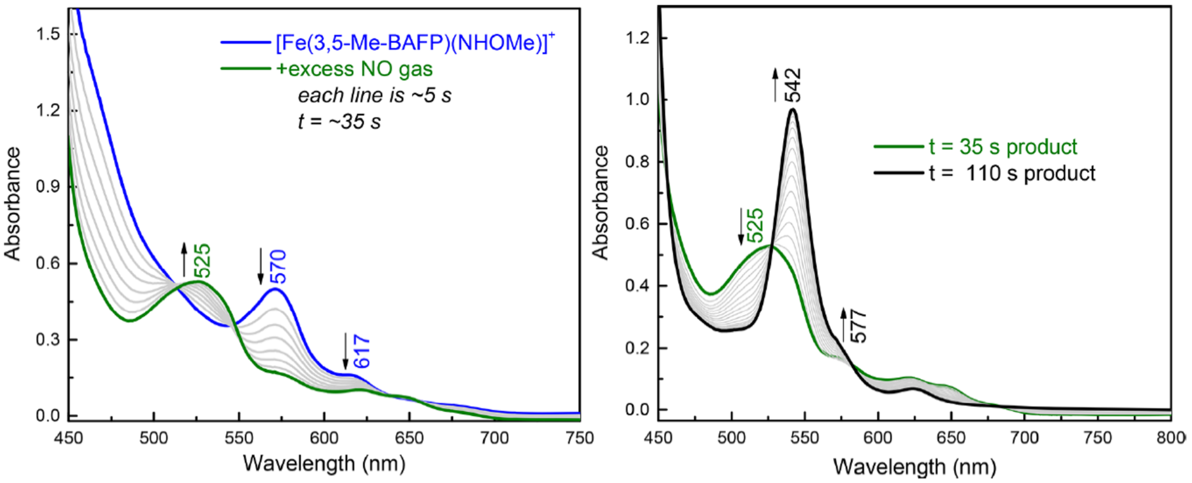

Figure 88. Left: Low-temperature (−80 °C) UV−vis spectra monitoring the reaction of Fe(III)−NHOMe• with excess NO gas. Right: Further reaction of the initial product with NO gas to form a 6C ls-$\{FeNO\}^6$ complex, $[Fe(3,5\text{-}Me\text{-}BAFP)(L)(NO)]^+$, where L is a neutral ligand. Reprinted with Permission from ref 306. Copyright 2019 American Chemical Society.

The breakdown of NO into less toxic N_2O plays a vital role in the denitrification pathway in the nitrogen cycle as discussed in the Introduction, and it also serves as a detoxification mechanism to protect the bacteria from NO toxicity.[302,1525−1527] Bacterial NORs belong to the superfamily of heme-copper oxidases, which are integral membrane oxidoreductases that undergo both anerobic and aerobic respiration in addition to detoxification processes.[1528] The most prominent members of this family are Cyt. *c* oxidases (C*c*Os), the energy generators in aerobic respiration.[1529] Interestingly, *c*NORs are actually considered the ancestors of C*c*Os that existed prior to the development of aerobic respiration.[314,315] There are several types of *c*NORs that are distinguished by their electron sources, including qNOR, Cu_ANOR, eNOR, gNOR and sNOR, as listed in Table 20. All heme-copper oxidases share a conserved catalytic subunit, which includes the active site that is composed of a heme center with a second metal ion, Cu or non-heme iron, in close proximity.

4.3.1. Structural Features of *c*NOR. Most of what is known about bacterial NORs has come from the study of the two-subunit enzyme *c*NOR, which is commonly purified from members of the *Pseudomonas* family, especially *Pseudomonas denitrificans* (*Pd*).[312,1543] These enzymes are heterodimers ($\alpha\beta$), with a smaller NorC subunit (17 kDa), which contains a ls heme *c* with His and Met axial coordination, as first determined by MCD and UV−vis spectroscopic studies.[1544,1545] The heme *c* is responsible for receiving electrons from Cyt. *c* and transferring them to the larger NorB subunit (56 kDa). The midpoint potential of heme *c* in NorC is between +280 to +310 mV in the protein dimer, whereas the potential of this heme drops to +183 mV (all vs NHE) in the isolated NorC subunit, in the absence of interactions with the NorB subunit.[1546] The NorB subunit spans the cytoplasmic membrane with 12 α-helices, in which one α-helix interacts with the single N-terminal transmembrane helix of the NorC subunit. NorB houses the bimetallic active site, as well as a ls heme *b* with bis-His coordination, which is responsible for electron transfer to the active site.[1545] The active site is unique in that it is composed of two different types of iron sites, a heme b_3 center (termed heme b_3 due to its similarity to heme a_3 found in C*c*Os) and a non-heme iron center, labeled Fe_B (in analogy to the Cu_B site in C*c*Os).[303] Heme *b* from isolated NorB has a higher midpoint potential than heme *c* from NorC, located between +322 and +345 mV.[1546,1547] The midpoint potentials of heme b_3 and of the non-heme Fe_B center are +60 and +320 mV (all vs SHE), respectively,[1548] although these values are still under debate with a wide range of redox potentials reported.[1543,1549] Especially the low midpoint potential of heme b_3 is unexpected, and this raises the question of how electrons are transferred and utilized between the iron centers in the active site. The midpoint potentials of *P. nautica c*NOR were determined to be +215 mV for the ls electron transfer heme and -38 mV for heme b_3,[1550] while direct electrochemical measurements showed a lower midpoint potential of -126 mV (all vs SHE) for heme b_3.[1551] Additionally, for the Fe_B center, other reports have indicated a much more negative midpoint potential of approximately -370 mV in *P. nautica c*NOR. This same study found midpoint potentials for heme b_3 to be -160 mV, heme *b* to be +40 mV, and heme *c* to be +200 mV (all vs NHE).[1552]

Bacterial NORs, including *c*NOR, are integral membrane proteins and thus very difficult to express, purify and crystallize. Shiro and coworkers were able to obtain the crystal structure of *c*NOR from *Pseudomonas aeruginosa* (*Pa c*NOR) at a resolution of 2.7 Å (PDB: 3O0R),[313] as shown in Figure 89. Later, the only other available crystal structure for a *c*NOR was reported for the *Roseobacter denitrificans* enzyme, with a resolution of 2.85 Å (PDB: 4XYD).[1553] Both crystal structures show the heme b_3 center bound by an axial His ligand, whereas the non-heme Fe_B is coordinated by three His residues and a glutamate.

Table 20. Various Bacterial NOR Types with Amino Acids Listed That Are Proposed to Be Coordinated to the Fe_B Center[a]

NOR type	Fe_B coordinating ligands	electrogenic (Y/N)	ref
*c*NOR	His, His, His, Glu	N	313, 1530−1532
qNOR	His, His, His, Glu	Y	221, 533
sNOR	His, His, His Asn	Y	1534−1537
gNOR	His, Asp, His, Asp	N	15, 381, 539
NOD	His, His, Asn, Tyr		318, 1540−1542

[a] For each class, it is also indicated whether the enzyme is believed to be electrogenic.

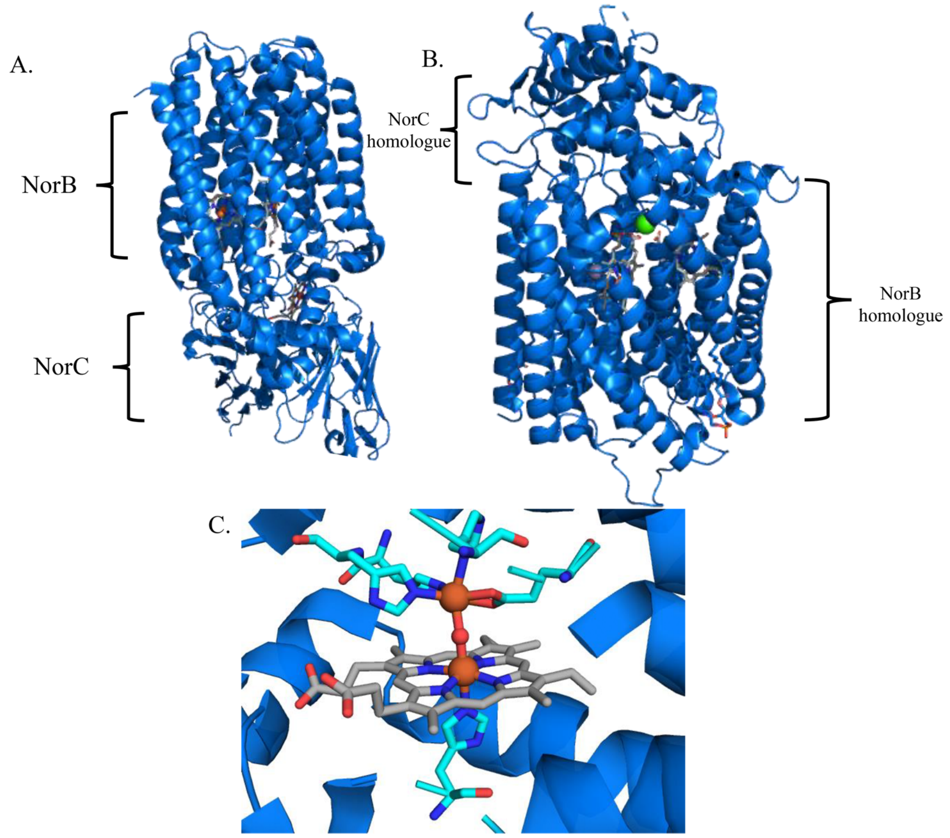

Figure 89. PyMOL generated images of the crystal structures of (A) *c*NOR from *Pseudomonas aeruginosa* (*Pa c*NOR, PDB: 3O0R) with NorC and NorB subunits indicated, (B) qNOR from *Geobacillus stearothermophilus* (PDB: 3AYF) with NorC and NorB homologue units labeled, and (C) the dinuclear active site of *Pa c*NOR.

In addition, in the resting state of *Pa c*NOR, an oxo bridge is present that connects the two Fe centers, putting them in a close proximity of 3.8 Å, as shown in Figure 89.[302] A Ca^{2+} ion is found at the interface of the NorB and NorC subunits that interacts with a water molecule, the propionate groups of the two *b*-type hemes, a Glu residue from NorB, and a Tyr and Gly residue from NorC. The Ca^{2+} ion could thus play a structural role in maintaining the correct protein conformation for efficient electron transfer between the two subunits. An additional metal ion is observed in the crystal structure of the *R. denitrificans* enzyme, in the NorC subunit, facing the periplasm. Initially, based on X-ray anomalous scattering studies, it was proposed that this metal ion is either a Zn^{2+} or Cu^{2+} ion.[1553] Later, ICP-MS and EPR studies identified this metal ion as a Cu^{2+} center.[1554,1555] The role of this Cu^{2+} center has not yet been definitely determined, but it is thought that because of its surface exposed location it might play a role in protein-protein interactions.

More recently, it was proposed that *c*NOR could form a protein complex with heme cd_1 NIR (see Section 4.1),[1556] the enzyme that catalyzes the preceding step in the denitrification pathway (the reduction of nitrite to NO), under physiological conditions.[1557] In this study, a supercomplex made up of one heme cd_1 NiR and two *c*NOR (from *P. aeruginosa*) was identified, but it was noted that a 1:1 ratio of heme cd_1 NiR to *c*NOR is probably more physiologically relevant, due to the limited space around the membrane-embedded *c*NOR. The interface is formed between the heme *c* domain of heme cd_1 NiR and the NorC subunit of *c*NOR, possibly implicating a role of the surface-exposed copper center in this interaction.[1557] In a similar study the interaction of heme cd_1 NiR and *c*NOR (from *P. dentrificans*) was examined using fluorescence spectroscopy. It was found that the electron donation to *c*NOR is inhibited by complexation with heme cd_1 NiR, due to the binding site being in the same location as that of *c*NOR's electron donor. Also, the presence of *c*NOR has an effect on the dimerization of heme cd_1 NiR. There was no evidence of a long-lasting complex formation and the data support a more transient interaction.[1558]

Other roles of the Cu^{2+} center are also possible, for example a structural role and a role in electron transfer. However, with respect to the latter, the 14 Å edge-to-edge distance between the Cu^{2+} center and the heme *c* in the same subunit argue against this possibility.[1559] Also, the residues that coordinate the Cu^{2+} ion are not conserved among *c*NOR sequences, making a role in catalysis for NO reduction to N_2O unlikely, and pointing to the possibility that the presence of the Cu^{2+} ion could also be an artefact from protein workup and crystallization, etc.

Importantly, *c*NORs are non-electrogenic, which means that no energy is stored during substrate reduction because protons and electrons are derived from the same side of the inner mitochondrial membrane, and a charge gradient is not generated across the membrane.[1532] Whereas this is true for most bacterial NORs, it should be mentioned here that there seem to be some exceptions, as indicated in Table 20. In any case, this indicates that *c*NORs may serve a primarily protective function, because NO is highly toxic and NO reduction in denitrification is in most cases not used for energy conservation. Denitrifying organisms operate under steady state nanomolar concentrations of NO.[1560,1561] In this regard, it was shown that an increase in NO concentration to 0.5 mM inhibits transcription of the nirSTB and norCB codons, which inactivates NOR and is lethal to *P. stutzeri* bacteria.[1562] It should also be noted here that anaerobic nitrate/nitrite respiration is significantly less efficient compared to aerobic respiration.[312] For example, in terms of the protons translocated per electron, aerobic respiration with C*c*O as the terminal oxidase pumps 5 H$^+$/e$^-$ during respiration, whereas it is only 3 H$^+$/e$^-$ for denitrification. When protons are not translocated, quinones or hydroxide bind protons and protons are released from hydroquinones. Efficiency can also be compared in terms of the level of quinone produced, where the stoichiometries are 1 H$^+$/e$^-$ for denitrification versus 3 H$^+$/e$^-$ for dioxygen respiration.[312]

Since NO reduction to N$_2$O is a proton-dependent process (see eq 5), a proton channel must exist that connects the active site of the enzyme to the periplasmic protein surface of the NorB subunit. A potential proton channel was revealed in *Pd* *c*NOR by mutagenesis studies. Here, the channel starts from the Glu122 residue on the protein surface. The importance of the Glu122 residue was shown in enzyme variants E122A and E122Q, which show inhibition of proton uptake, demonstrating the need of a protonable side chain at the entry point of the channel for its function.[1563] The variant E122D is able to take up protons, but there is a significant increase in the pKa of the proton donor to the active site, demonstrating the role of Glu122 in defining the optimal proton donor (possibly through a hydrogen-bonding network).[1563] In a separate study, the crystal structure of *Pa* *c*NOR was analyzed for proton channels. Two potential water channels and hydrogen-bonding networks made up of protonable or polar amino acids spanning from the periplasmic side of the membrane to the active site were identified. One proposed channel spans from Gly340 to the heme *c* propionates and another proposed channel starts at Glu57 and ends at the propionates of heme b_3. These channels then lead to a terminal hydrogen-bonding network at the active site. Glu135 in *Pa* *c*NOR, which is the equivalent of Glu122 in *Pd* *c*NOR, sits at the entry point of the proton channel.[313] Three highly conserved amino acids, Glu211, Glu215 and Glu280 are present in the *Pa* *c*NOR at the end of the channels in the active site and are associated with catalytic activity of *c*NOR (Figure 90).[313,1544,1564,1565] In addition to the channels identified in the crystal structures, MD simulations revealed an additional water channel not seen in the static crystal structures, indicating that protein dynamics may play a role in gating proton transfer.[1566] In addition to a proton pathway, an electron pathway is also necessary for NO reduction. On the basis of the crystal structure of *Pa* *c*NOR in concert with biochemical data, a likely pathway for electron transfer was determined as shown in Figure 90. Cyt. bc_1 transfers electrons to Cyt. *c* and pseudoazurin,[1408,1567,1568] both of which can serve as the electron source for *c*NOR, and likely bind to the NorC subunit. The heme *c* located in the NorC subunit is close enough to the interface to serve as a receptor for electrons to enter the protein heterodimer. Electrons then transfer from heme *c* to heme *b* via His and Ala residues oriented toward the heme *b* propionate groups, and then further to heme b_3 by direct contact of the neighboring methyl groups of the hemes *b* and b_3, or by a conserved Phe residue.

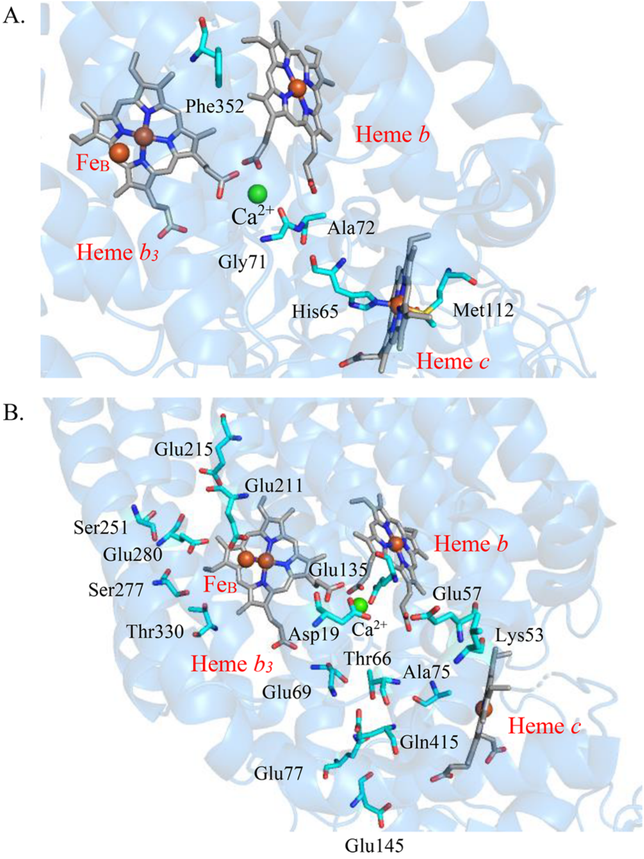

Figure 90. PyMOL generated images of the crystal structure of *Pa* *c*NOR (PDB: 3O0R). (A) Electron transfer pathway and (B) Possible water/proton channels.

4.3.2. Other Members of the Bacterial NOR Family. As evident from Table 20, many bacterial NORs are classified with respect to their electron source. For example, *c*NORs are named after the fact that Cyt. *c* serves as their primary source of electrons. Other important types of bacterial NORs include qNORs, which derive their electrons from quinones such as ubihydroquinone or menahydroquinone, and Cu$_A$NOR.[1569,1570] Interestingly, qNORs are found in non-denitrifying pathogenic bacteria as well as in denitrifying bacteria and archaea.[1571] Their physiological role in pathogens is believed to detoxify NO produced by the immune system of the host,[302,1571−1575] similar to flavodiiron NORs (see Section 5). Compared to *c*NORs, qNORs are single-subunit enzymes that lack the NorC subunit and heme *c* (as shown in Figure 89) and instead, contain a 280 amino acid extension, which is thought to be the binding site of the quinone.[22,1533] Two crystal structures of qNORs have been reported, one from *G. stearothermophilus*, solved at 2.5 Å (PDB: 3AYF; see Figure 89), and the second one from *N. meningitis*, obtained at a resolution of 4.5 Å (PDB: 6FWF).[1576,1577] The active site of *G. stearothermophilus* qNOR is very similar to that of *c*NORs, with a heme b_3 and a non-heme iron center, but in this case with a bridging water ligand and an Fe−Fe distance of 4.6 Å. Zn^{2+} was also found to be coordinated in the non-heme site of *G. stearothermophilus* qNOR, as determined from anomalous difference Fourier maps of the resolved structure, but the Zn$_B$ form was found to be catalytically inactive.[1576] Here, the choice of detergent used in the qNOR purification affects the identity of the metal coordinated in the non-heme site. The low resolution of the *N. meningitis* qNOR structure did not allow for definitive identification of the metal present in the non-heme site.[1577] As mentioned above, potential water channels have been identified in *c*NORs, but inspection of the qNOR crystal structures did not reveal the presence of these channels in the latter enzymes, due to the structural differences between *c*NORs and qNORs. Specifically, an Asp residue in *c*NOR is replaced by a hydrophobic Ala residue in qNOR, which causes the respective channel to collapse. The second channel in *c*NOR is found in the NorC subunit, and this channel is completely absent in qNOR due to the C-terminal region being fused to the catalytic domain in qNOR. On the other hand, the conserved Glu residues (Glu512 and Glu581 in *Pa c*NOR) in the active site of *c*NORs are present in both qNOR structures, allowing for the formation of a water cluster and providing a source of protons for NO reduction. However, this water cluster extends towards the cytoplasm and is lined with polar residues in qNORs, in contrast to *Pa c*NOR. The proton entry site in the cytoplasm of *G. stearothermophilus* qNOR is formed by a salt bridge between a Lys and a Glu residue, both of which are needed for catalytic activity to occur as shown by mutagenesis studies.[1576] MD simulations, focused on the water network formed within this channel, suggest that this could be the catalytic proton transfer pathway.[1576,1578] In *N. meningitis* qNOR the critical Lys residue mentioned above is replaced by a Ser residue, but the overall properties of the water channel seem to be unchanged.[1576] Finally, Cu_ANORs were originally thought to also use quinones as an electron source and were termed qCu_ANOR, but it was later found that these enzymes lack a quinol binding domain and that the quinol binding activity was an artifact due to traces of phenazine ethosulfate present during activity measurements.[1534]

On the basis of genomic surveys and structural predictions, which are based on the conservation of the primary structure of subunit I in all members of the heme-copper oxidase superfamily, and considering diagnostic domains and residues that are specific to bacterial NORs, additional members of the bacterial NOR family have been identified as listed in Table 20. These new members are eNORs,[1579] gNORs[1538,1539] and sNORs.[1534−1537] In these bacterial NORs, there is some variability in the three residues that ligate the Fe_B center (including Glu, Asn, Tyr, Asp, Leu and His residues) according to sequence alignments, in addition to the one conserved His residue in the active site. A SCS Glu residue that might serve as a proton relay site is variably present in the different NOR families as well. In the sNOR family, Cu_ANOR contains a Cu_A site as an electron transfer center, similar to C*c*Os. Specifically, the Cu_A center is a dinuclear $Cu_2(\mu\text{-Cys})_2(\text{His})_2$ site, which takes the place of heme *c* in *c*NORs.[1580,1581] Cu_ANOR is the first NOR purified from a gram-positive bacterium (*B. azotoformans*) and has yet to be successfully crystallized.[1570,1582] A bacterial NOR type enzyme that is supposed to dismutate NO (instead of reducing it) was recently discovered in *M. oxyfera*, as part of a nitrite-driven anaerobic methane oxidation pathway.[318] Here, the NO dismutase (NOD) was proposed to generate O_2, following the reaction:

$$2NO \rightarrow N_2 + O_2 \qquad (19)$$

which is then needed for methane oxidation. This enzyme has a binuclear active site (similar to the heme-copper oxidases) and bears similarity to the qNOR family.[318,1540−1542] Curiously, this enzyme does not seem to contain any electron transfer sites or proton channels (deduced from sequence substitutions that eliminate electron transfer sites and proton channels) toward the active site. However, this protein has not yet been isolated or further characterized, so whether it is in fact able to catalyze the unique NO dismutation reaction is speculative at best at this point in time. More work needs to be conducted on this enzyme to solidify these conclusions.

4.3.3. Proposed Mechanisms of Bacterial NORs: Experimental and Computational Insight. The fully oxidized resting state of *c*NORs is a μ-oxo bridged heme/non-heme diferric complex, as determined by UV−vis, rRaman, MCD spectroscopy, and X-ray crystallography (see Figure 89).[313,1525,1583] The Fe−Fe distance in this state was determined to be 3.8 Å from the crystal structure of *Pa c*NOR.[302,313,1583] In the presence of the μ-oxo bridge, the proximal His is not coordinated to the heme. Karlin and coworkers provided further evidence for the stability of this structure, by showing that μ-oxo bridged diferric heme/non-heme iron model complexes are unreactive towards both pyridine and imidazole bases, evident from crystal structures of the re-isolated, intact μ-oxo bridged complexes (Figure 91).[1584] Upon one-electron reduction of the *Pd c*NOR active site, the μ-oxo bridge is broken and the His rebinds to heme b_3. The pH-dependent properties of this form of the enzyme were also investigated, showing that either water or hydroxide is distally bound to the ferric heme b_3 *trans* to His. The nature of this 6th ligand has a strong influence on the heme b_3 reduction potential.[1545] Richardson and coworkers proposed the 6th ligand to be water, and they showed that NOR activity increases under acidic conditions.[1460,1525,1580,1581,1585−1587] Here, the more positive reduction potential of the water-bound ferric heme b_3 complex should facilitate more rapid electron transfer. In the presence of NO, the ferric heme binds NO to form a ls-$\{FeNO\}^6$ complex with Fe−NO and N−O stretching frequencies of 594 cm^{-1} and 1904 cm^{-1}, respectively.[786,1588] These vibrational properties are typical for 6C ferric heme−nitrosyls with axial His coordination (see Section 2.3).

Cyanide binding studies further identified redox-dependent conformational changes within the active site of *Pd c*NOR, suggesting that a reduction of the Fe_B center opens up the diiron core for the binding and reduction of NO.[1590] Another study proposed that protonation of the diferric μ-oxo core regulates an 'open' or 'closed' form of the active site of

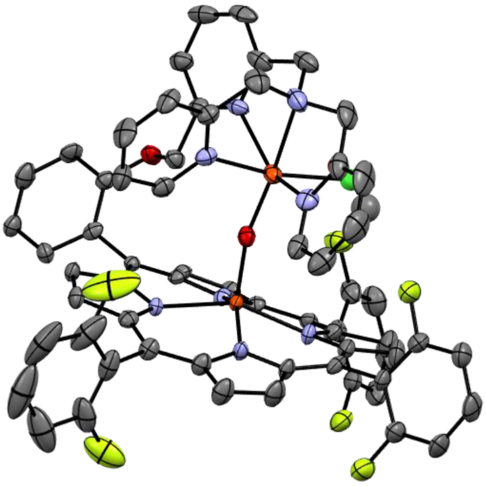

Figure 91. Crystal structure of the μ-oxo bridged complex $[Fe^{III}(^6L)\text{-}Fe^{III}(TMPA)(Cl)]^+$ (^{6}L = 5-(*ortho*-*O*-[(*N*,*N*-bis(2-pyridylmethyl)-2-(6-methoxyl)pyridinemethanamine)phenyl]-10,15,20-tris(2.6-difluorophenyl)porphine).[1589] All H atoms and counter ions are omitted for clarity.

Scheme 54. Mechanistic Scheme for NO Binding to the *c*NOR Active Site, Based on Time-Resolved Spectroscopic Studies[317]

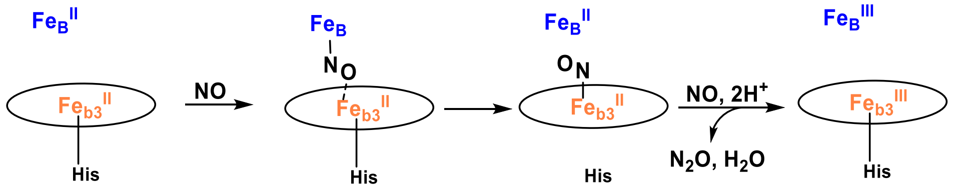

Scheme 55. Proposed Mechanisms for Bacterial NORs, with *trans* Mechanism Shown on Top and *cis*-Heme b_3 Mechanism on Bottom (See Text)

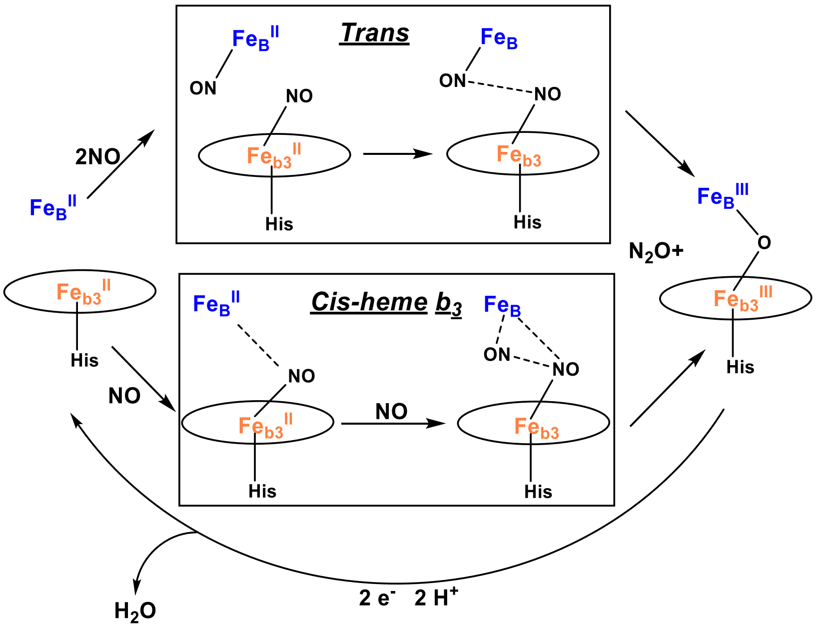

*c*NOR.[786,1588] A rRaman study of the oxidized, resting form of *Pd* cNOR identified two isotope sensitive bands at 815 cm^{-1} and 833 cm^{-1} that were assigned to the Fe−O−Fe stretch. Here, the higher stretching frequency was proposed to originate from hydrogen bonding between the oxo group and adjacent, protonated residues in a more ‘closed’ conformation of the active site. The lower stretching frequency would then correspond to the ‘open’ conformation without additional hydrogen bonding.[786,1588]

In the fully reduced form of the enzyme, the active site is proposed to contain a water molecule, which is formed from the oxo bridge, and the proximal His is coordinated to the Fe center of heme b_3.[1460,1587] EPR spectra of fully reduced *Pa* *c*NOR in single turnover studies in the presence of NO showed a signal with g values of 2.08 and 2.012, with the latter resonance further showing a characteristic three-line hyperfine splitting (A = 45.1 MHz) of ^{14}NO, indicative of the presence of a 5C ferrous heme b_3 nitrosyl complex where the bond to the proximal His has been broken.[641,1591] This result has been taken as evidence that a ferrous heme−nitrosyl complex is involved in *c*NOR catalysis. While it has been suggested that obtaining a fully reduced enzyme is not biologically feasible due to the low reduction potential of heme b_3, these results further indicate that such a state is accessible in the presence of NO. Upon addition of NO to fully reduced *Pa* *c*NOR under turn-over conditions, a non-heme hs-$\{FeNO\}^7$ complex was observed by EPR spectroscopy as well.[1592] This species has an S_t = 3/2 ground state (see Section 5.1) and gives rise to characteristic EPR signals with g_{eff} = 4, 2.[1592] In addition, rRaman[786] and IR[1593] studies of *c*NORs further support binding of NO to the ferrous heme center, which is in agreement with the extremely large binding constants of ferrous hemes for NO (see Section 2.2 and Table 4).[1594]

While the data described above point towards the formation of both heme and non-heme iron-nitrosyl complexes during catalysis, more concrete mechanistic data are missing. Also, NO binding to both the heme and the non-heme iron center in the first step of catalysis would likely lead to a spin-coupled system that would be expected to be EPR silent. This raises the question of whether the iron−nitrosyl complexes observed in the studies described above are in fact on-pathway or off-pathway intermediates.[70] Since *c*NORs are notoriously difficult to work with, progress in our mechanistic understanding of these enzymes has been slow. Recently, utilizing time-resolved UV−vis spectroscopy and IR spectroscopy (for N_2O detection) in combination with a photosensitive, caged NO donor, three stages of NO binding to *Pa* *c*NOR were identified, as shown in Scheme 54.[317] First, on the microsecond timescale, NO enters the active site and binds to the non-heme iron center, forming a hs-$\{FeNO\}^7$ complex. Then, on the tens of microseconds timescale, NO migrates to form a possible 5C heme b_3−NO complex. Finally, on the millisecond timescale, a second NO molecule enters the active site, leading to protonation and electron transfer to promote N−N bond formation, N−O bond cleavage, and N_2O formation.[317]

On the basis of the available data and the general knowledge about iron-nitrosyl chemistry, three main mechanisms have been proposed for *c*NORs over the years, as shown in Scheme

55.[302,303,1595−1597] The mechanistic pathways are speculative because no intermediates of the enzymatic reaction have been spectroscopically characterized, as mentioned above. The *trans* mechanism in Scheme 55, top, goes back to early mechanistic studies by Girsch and de Vries.[1597] Here, it was proposed that one molecule of NO binds to each of the heme b_3 and Fe_B sites. This dinitrosyl intermediate then undergoes a radical-radical type N−N coupling reaction to form a bridging *trans*-hyponitrite intermediate, on path to N_2O generation. After N_2O release, the two ferric iron centers are bridged by an oxo group.[1545,1583,1597,1598] Indirect support for this mechanism comes from the mechanistic studies described above that indicate NO binding to both the heme and the non-heme iron center. The possibility of two diatomics binding simultaneously in the active site of *c*NORs was further investigated using CO as a surrogate for NO. Here, reduced *c*NOR from *B. azotoformans* showed the presence of two C−O stretching bands in the IR spectra, at ∼1970 cm^{-1} corresponding to the heme(II)−CO complex, and at ∼2070 cm^{-1} corresponding to the Fe_B(II)−CO adduct.[1593] It was also found that at low temperatures, the heme(II)−CO complex forms a semi-bridging structure with the Fe_B center, leading to a decreased C−O stretching frequency of ∼1910 cm^{-1} for the heme(II)−CO complex, and a C−O stretch of ∼2050 cm^{-1} for Fe_B(II)−CO.[1593] Similarly, reduced qNOR (*G. stearothermophilus* and *Py. aerophilum*) was reacted with CO and C−O stretching frequencies were detected for both the heme and the non-heme iron−CO complex (by rRaman).[1571,1599] Finally, CO-bound *Pa* cNOR showed a similar result where two CO molecules were found bound in the active site, one per iron center, as demonstrated by X-ray crystallography (see Figure 92; PDB: 3WFC).[1600]

On the other hand, the proposed *trans*-hyponitrite intermediate has never been observed. In addition, both ferrous heme- and non-heme iron−nitrosyl complexes are generally very stable and unreactive, with highly covalent iron−NO bonds (see Sections 2.2 and 5.1), which makes them unlikely species as reactive intermediates in N−N bond formation. Correspondingly, a computational study found that the trans-hyponitrite intermediate would be too high in energy to form (see below).[316] In this regard, it is unexpected that the ferrous heme−nitrosyl species observed by EPR in the reaction of *c*NOR with NO is 5C, as the electronic structures of these species show that the corresponding 6C complexes are expected to be more reactive in radical N−N coupling (see Section 2.2).[564] The inability of ferrous heme−nitrosyls to support radical-radical N−N coupling is best exemplified by the reactivity of corresponding *trans*-hyponitrite bridged iron-porphyrin dimers (see below).[1601] If left in solution, these complexes actually slowly convert to the corresponding ferrous heme−nitrosyl complexes, following the eqn:[1602]

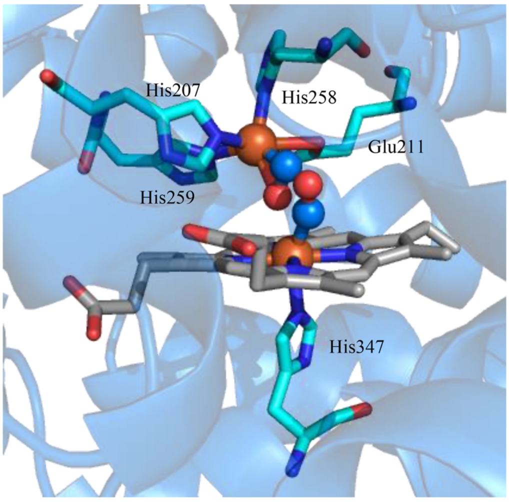

Figure 92. PyMOL generated image of the crystal structure of the active site of *Pa c*NOR (PDB: 3WFC) with two CO molecules bound.

$$\{[Fe(Porph)]_2(\mu\text{-}N_2O_2)\} \rightarrow 2[Fe(Porph)(NO)] \qquad (20)$$

The rate constant observed for the decomposition of $\{[Fe(OEP)]_2(\mu\text{-}N_2O_2)\}$ of 6.4×10^{-5} s^{-1} at room temperature corresponds to a barrier of roughly 20 kcal/mol. Considering that according to DFT calculations, the ferrous-heme nitrosyl product is thermodynamically more stable than the O-bound trans-hyponitrite bridged dimer by roughly 20−25 kcal/mol (in terms of free energy), this results in a very high barrier for the inverse reaction (dimerization of ferrous heme−nitrosyls), which therefore cannot occur. This, in turn, casts further doubt on the feasibility of the *trans* mechanism. The structure and reactivity of heme-based hyponitrite complexes is further discussed below.

The two alternative mechanisms deal with cis coordination, where only one of the two metal sites (heme or non-heme iron) reacts directly with NO, whereas the other metal only serves as an electron reservoir or Lewis acid.[302,1595,1596,1603] In the second mechanistic pathway, termed *cis*-Fe_B, both equivalents of NO bind to the Fe_B site. This pathway was conceptualized based off the observation that non-heme Fe centers can form stable dinitrosyl iron complexes (DNICs), as described in Section 3. This mechanism is no longer considered due to a number of counter arguments. First, it is hard to rationalize how a DNIC could form in the presence of a ferrous heme, which has a very high affinity for NO (see Section 2.2 and Table 4). Second, it has been shown that N−N bond formation between the NO units in a $\{Fe(NO)_2\}^9$ or $\{Fe(NO)_2\}^{10}$ DNIC is highly unfavorable due to the very strong AF coupling between each $^3NO^-$ ligand and the Fe center, causing parallel alignment of the $^3NO^-$ spins.[652] Hence, the reaction is spin forbidden, and in order for an N−N bond to form, the spins of one $^3NO^-$ ligand have to flip, which is energetically highly unfavorable, translating into a large activation barrier. Interestingly, N−N bond formation from a DNIC has recently been observed in the presence of a lanthanide complex, which acts as a strong Lewis acid and binds to the O atoms of the coordinated $^3NO^-$ ligands (see Section 3.4.2 and Figure 93).[1290] However, in this case N_2O formation is slow, and whether N−N bond formation actually occurs in the DNIC, or whether other intermediates are formed first, is unclear.

In the third mechanism, called *cis*-heme b_3, a molecule of NO binds to heme b_3 and then reacts with a second NO molecule in the first step of the reaction (see Scheme 55, bottom). This mechanism was inspired by the findings for Cyt. P450nor (see Section 4.2). A variation of this mechanistic possibility is supported by DFT calculations by Blomberg. Here, the reaction is initiated by two proton-coupled reductions of the diferric resting state of the enzyme, followed by coordination of the first NO ligand to the heme. This leads to the formation of either a strong (initial result)[1604] or weak[316] interaction of the O atom of the coordinated NO with the ferrous Fe_B center, which therefore acts as a Lewis acid. This would lead to an

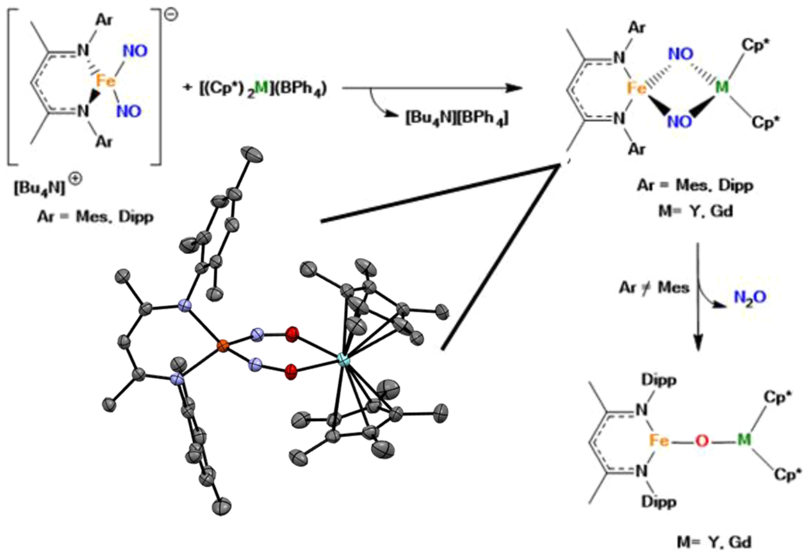

Figure 93. Production of N_2O by activation of the DNIC complex $[Fe(NacNac^{Ar})(NO)_2]^-$ ($NacNac^{Ar-} = [(ArNCMe)_2CH]^-$ with Ar = mesityl, 2,6-diisopropylphenyl) by lanthanide complexes. The crystal structure of the Yttrium compound bound to the DNIC is shown on the bottom, left.[1290] All H atoms are omitted for clarity. Reprinted with permission from ref 17. Copyright 2021 Elsevier Inc.

electrostatic polarization of the NO ligand to give it more $^1NO^-$ character (see Figure 94). This could activate the bound NO ligand for direct reaction with the second NO molecule, again assisted by the Fe_B center, to form a cis-hyponitrite intermediate, as shown in Scheme 56. From there, N_2O release proceeds, leading to the formation of the diferric, oxo-bridged active site.[316] In this study, it is further shown that the *trans* mechanism has a very high energy barrier, due to a very unfavorable N−N bond formation step, as mentioned above.[316] A recent paper from the Blomberg group verifies the validity of the transition states calculated previously by exploring how these results vary when different DFT functionals are considered.[1605] Experimental support for this mechanistic proposal comes from flow flash photolysis experiments, which show coordination of NO to the heme b_3 center, within 2 μs upon photolysis. Here, the disappearance of the Soret band at 433 nm and the appearance of a new Soret band at 410 nm indicates NO coordination to the heme.[1606] Time-resolved visible absorption spectroscopic studies by Shiro's group on *Pa c*NOR, decribed above, further show that after initial coordination of NO to the Fe_B center (within microseconds), the NO migrates to the heme b_3 (in tens of microseconds), before N_2O formation is observed.[317] Finally, studies on a protein model of *c*NOR, a Mb variant, demonstrate that binding of a Fe^{2+} Lewis acid to a heme-coordinated NO does indeed lead to a polarization of the NO ligand, and a shift of the N−O stretch to lower frequency by about 50 cm^{-1}.[1607] However, the polarization of the NO ligand as observed in this study was not sufficient to activate the 6C ls-$\{FeNO\}^7$ complex for N−N bond formation and N_2O generation. These results are further discussed below.

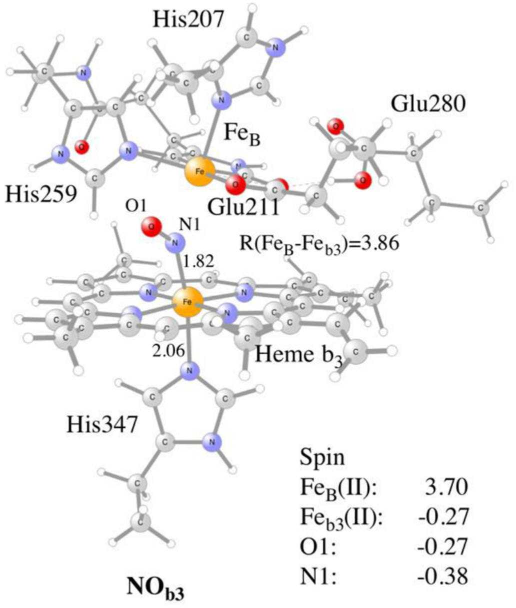

Figure 94. NO binding to heme b_3, bridging to Fe_B, in the *cis*-heme b_3 mechanism, as predicted by DFT calculations. Reprinted with permission from ref 316. Copyright 2017 American Chemical Society.

4.3.4. NO Reduction by Heme−Copper Oxidases.

Analyses of the amino acid sequences of *c*NORs from different organisms[314,315,1608,1609] in concert with spectroscopic investigations[1545,1592,1610] have shown that *c*NORs are closely related to the respiratory heme-copper oxidases like *Cc*Os.[1611] *Cc*O catalyzes the four-electron reduction of O_2 to water as the terminal enzyme in cellular aerobic respiration:[1612]

$$O_2 + 4e^- + 4H^+ + 4H^+_{IN} \rightarrow 2H_2O + 4H^+_{OUT} \qquad (21)$$

*Cc*Os have a similar dinuclear active site as *c*NORs, but instead of the Fe_B center, a Cu ion is present in the active site, termed Cu_B. This Cu_B center is coordinated by three conserved His residues, one of them carrying the direct covalent link to a nearby Tyr.[1612] The difference in the second metal center is due to the differing abundances of Fe and Cu at the time of the common ancestor, with the original active site probably consisting of a diiron core (like *c*NORs) that later mutated to include Cu for O_2 reduction (in *Cc*Os).[302,312,1613,1614] The distances between the two metal centers in the active sites of *c*NOR and *Cc*Os differ, where $\Delta Fe-Fe_B$ = 3.8 Å in *Pa c*NOR (μ-oxo complex)[1578] whereas $\Delta Fe-Cu_B \sim 5$ Å in Cyt. *ba*$_3$ oxidoreductases.[1525,1580,1581,1585,1586] Here, the "*ba*$_3$" label

Scheme 56. *cis*-Heme b_3 Mechanism for *c*NORs, According to Computational Studies[316]

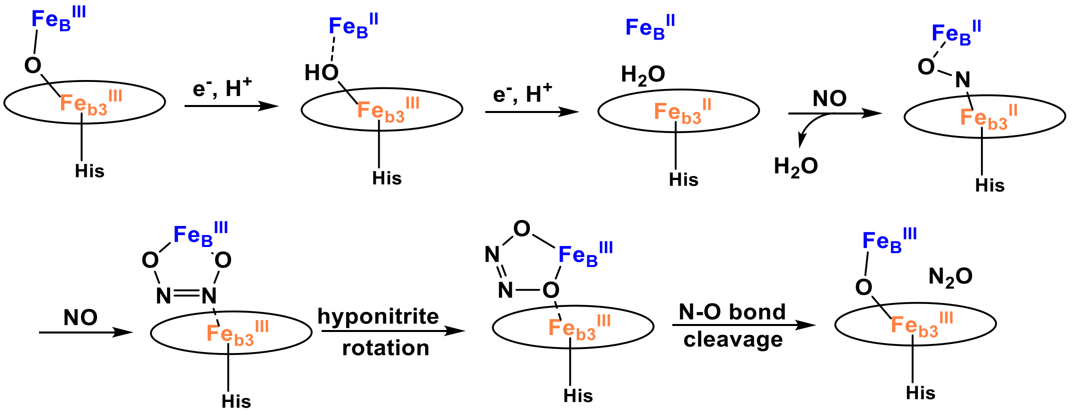

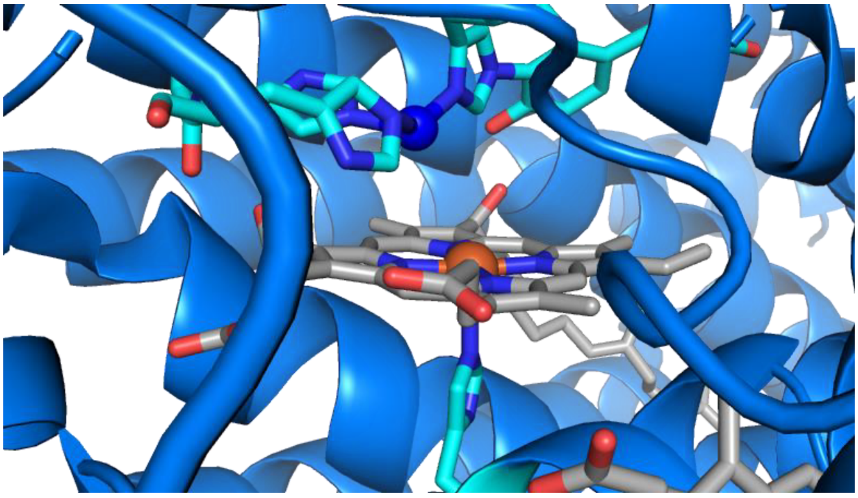

Figure 95. PyMOL generated image of the crystal structure of the active site of Cyt. ba_3 oxidase (PDB: 1XME), with the Cu_B center in blue. Heme a_3 is coordinated by His384.

indicates that there are hemes *b* and a_3 present in the enzyme. In this sense, *c*NOR would be a cbb_3 NOR. C*c*Os and *c*NORs have a conserved membrane topology and conserved amino acids that are necessary for coordination of both the catalytically and redox active metal centers. Specifically, six His are conserved between subunit I of the C*c*Os and the NorB subunit of *c*NORs, and are involved in binding the active site metals.[302,1580,1615,1616] A SCS Tyr residue is covalently linked to one of the His residues that ligate the Cu_B center. This Tyr group is involved in electron and proton transfer/donation during O_2 reduction,[1585,1617−1620] and is located close to the open space between the heme and the Cu_B center, as shown in the crystal structure of Cyt. ba_3 oxidase in Figure 95 (PDB: 1XME).[1621] Table 21 shows that a number of C*c*Os have been crystallized at this point in time.[1580,1581,1586,1622] In contrast to *c*NORs, C*c*Os are able to pump protons across the inner membrane from the negative to the positive side.[1530,1531] The closest structural relationship exists between Cyt. cbb_3-type C*c*Os and *c*NORs. As discussed above, several residues involved in proton transfer to the active site of *Pd* *c*NOR have been identified. This includes in particular Glu122 at the entry point of the proton channel and Glu125 at the end of the channel, which are conserved between *c*NORs and the Cyt. cbb_3-type C*c*Os.[1563] These residues are involved in a proton output pathway in C*c*Os and proton input in *c*NORs. Thus, it appears that the proton input pathway in *c*NORs and the output pathway in the Cyt. cbb_3 C*c*Os are evolutionary related.[1563,1580,1581,1586,1622]

Table 21. Crystal Structures of Various CcOs

molecule	organism	PDB code	resolution (Å)	ref
C*c*O(II)	*Bos taurus* (cattle)	2EIJ	1.90	1623
Cba_3O(II)	*Thermus thermophilus*	3EH3	3.10	1624
C*c*O(II) subunits I and II	*Rhodobacter sphaeroides*	3FYE	2.15	1625
C*c*O(II)-CN subunits I and II	*Rhodobacter sphaeroides*	3FYI	2.20	1625
C*c*O(II)-CO	*Bos taurus* (cattle)	1OCO	2.80	1619
C*c*O(III)	*Bos taurus* (cattle)	2DYR	1.80	1626
C*c*O(III) subunits I and II	*Rhodobacter sphaeroides*	3GSM	2.00	1627
C*c*O(III)-H_2O_2	*Paracoccus denitrificans*	3HB3	2.25	1628
C*c*O(III)-H_2O_2 short X-ray scans	*Bos taurus* (cattle)	2ZXW	2.50	1629
C*c*O(III)-N_3	*Bos taurus* (cattle)	1OCZ	2.90	1619

In addition to the structural similarities described above, C*c*Os and bacterial NORs have cross catalytic reactivity, where each enzyme is able to perform both NO and O_2 reduction, but at diminished efficiencies compared to their preferred substrate. Table 22 provides an overview of the catalytic activities of different enzymes. The ability of C*c*Os to reduce NO varies greatly between different enzymes, with some proteins being inhibited by NO, while others show NO reducing activity.[591,593,1630−1633] Cyt. *ba*$_3$, *caa*$_3$, and *cbb*$_3$ from *T. thermophilus*, *P. stutzeri*, and *R. sphaeroides* show more substantial NO reducing activity; for example, Cyt. *cbb*$_3$ from *P. stutzeri* has an NO reduction rate of 1.0×10^2 mol NO/(mol enzyme) min (see Table 22).[1630−1633] Since Cyt. *caa*$_3$ and *ba*$_3$ are able to reduce NO using an active site that is structurally very similar to that of *c*NORs, the investigation of the reaction mechanism of C*c*Os with NO might provide clues of how *c*NORs operate mechanistically. Upon reaction of reduced Cyt. *ba*$_3$ with NO, a 6C ferrous heme−nitrosyl complex forms with proximal His ligation, as evident from rRaman spectroscopy.[593] Here, rRaman signals at 569 cm^{-1} and 1620 cm^{-1} were observed, corresponding to the Fe−N−O bending and N−O stretching frequencies, respectively, of the ls-$\{FeNO\}^7$ complex (see Section 2.2). The Raman data also suggest that the His ligand bound trans to NO can modulate the Fe−NO bond strength and Fe−N−O angle, as discussed in Section 2.2.[593] X-ray crystal structures of heme-copper oxidases bound by exogenous ligands like CO, CN$^-$, azide and peroxide further show a propensity of the active site heme to form 6C complexes.[593,1619,1625,1628] This is in contrast to what is observed in *c*NORs, where a 5C ferrous heme−nitrosyl complex was identified during enzyme turnover by EPR spectroscopy and by time-resolved UV−vis spectroscopy, where the His is no longer coordinated to the heme (see above and Scheme 54).[317,641,1591] Here, the differences in electronic structures between 5C and 6C ferrous heme−nitrosyls, described in Section 2.2, could have implications for the N−N coupling mechanism in C*c*Os versus *c*NORs.

However, the most significant difference between C*c*Os and bacterial NORs is the nature of the second metal ion in the active site, either Cu or Fe, which could fundamentally change the mechanism of NO reduction. This starts with differences in midpoint potentials: in Cyt. *aa*$_3$ C*c*O, the heme *a*$_3$ and Cu$_B$ sites have reduction potentials of about +340 mV and +250 mV, respectively,[1640] while *Pd c*NOR shows reduction potentials of +60 mV and +320 mV (all vs SHE), respectively, for heme *b*$_3$ and Fe$_B$ (but see also the discussion above for some uncertainties in these numbers).[1548,1611] In early work by Watmough and Cheesman, it was proposed, based on MCD results, that C*c*Os follow a *cis*-Cu$_B$ type mechanism, where the reduction of NO is mediated by Cu and the heme site is responsible for electron transfer and oxygen abstraction.[1595] MCD studies on C*c*Os identified a charge-transfer band at 624 nm, which is indicative of the heme being in the hs ferric state.[1641] Investigations on the oxidized form of Cyt. *bo*$_3$ showed that the binding of two NO molecules to the heme/Cu active site of this enzyme did not cause a significant perturbation of the 624 nm marker band. This was taken as evidence that NO does not interact with the ferric heme, and, in concert with EPR results, suggested that both NO molecules can bind to the Cu$_B$ center.[1595] However, in contrast to these ideas, it is generally believed that NO inhibition of C*c*Os occurs by coordination of NO to the ferrous heme, instead of the Cu$_B$ site,[1534,1642,1643] and correspondingly, ls-$\{FeNO\}^7$ complexes have been identified in C*c*Os as described above.[593,1636,1644−1646] In addition, it has been established in model complexes that Cu(I)−NO complexes are labile and less stable than ferrous heme−nitrosyls, and that ferrous heme has a much larger binding constant for NO than Cu^{I}.[87,546,593,1642,1647,1648] This indicates that a transfer of NO from the heme to the Cu site is unlikely.

Along those lines, Moënne-Loccoz and coworkers have shown that the heme-bound NO in the fully reduced Cyt. *ba*$_3$ from *T. thermophilus* can be photolyzed, leading to NO coordination to the copper center.[1645] Here, the resulting Cu(I)−NO complex shows a very low N−O stretching frequency of 1589 cm^{-1}, which was taken as evidence that the NO is O-bound or side-on bound to the Cu$_B$ center. A crystal structure of NO bound in bovine C*c*O is shown in Figure 96, which indeed exhibits the side-on binding mode of NO to the Cu$_B$ center.[593,1636,1644−1646] It was further proposed that after binding of the first NO to the heme, the N-bound Cu$_B$−NO complex is blocked from forming and the second NO directly produces an O-bound Cu−hyponitrite species, bridging

Table 22. Comparison of Catalytic Activity of Bacterial NORs and Heme−Copper Oxidases for NO Reduction

enzyme	organism	NO reduction rate (mol NO/(mol enzyme) min)	O_2 reduction rate (mol O_2/(mol enzyme) min)	ref
Cyt. *ba*$_3$	*T. thermophilus*	3.0 ± 0.7 (20 °C)		1633
Cyt. *caa*$_3$	*T. thermophilus*	32 ± 8 (20 °C)		1633−1635
	Bovine midochondria		3870 (37 °C)	
Cyt. *cbb*$_3$	*P. stutzeri*	100 ± 9 (20 °C)		1631
Cyt. *bo*	*E. coli*		4545 (35 °C)	1635
Cyt. *bd*	*E. coli*		3660 (35 °C)	1635
Cyt. *bo*$_3$	*E. coli*	0.3 (RT)	~250 (25 °C)[a]	1636−1638
Cyt. *cbb*$_3$	*R. sphaeroides*	~200 (25 °C)[a]	~1000 (25 °C)[a]	1638
*c*NOR	*P. stutzeri*	2200 (30 °C)		1460
*c*NOR	*P. denitrificans*	4020 (20 °C)	600 (20 °C)	1639

[a] TOF in s^{-1}. RT = room temperature.

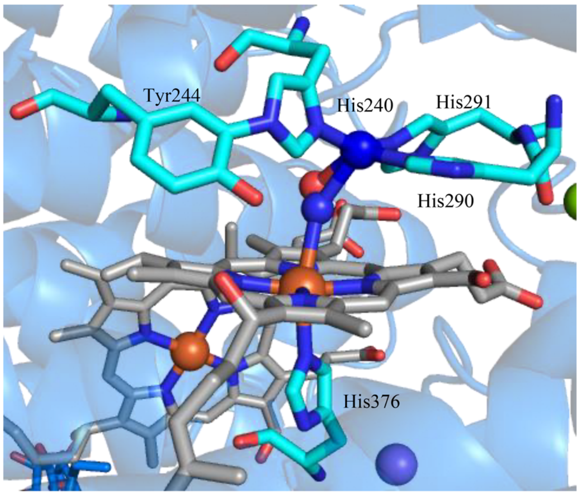

Figure 96. PyMOL generated image of the crystal structure of the bovine C*c*O active site with NO bound to heme *a*$_3$ and the Cu$_B$ site (PDB: 3ABK; Cu is shown in blue).

Scheme 57. Mechanistic Possibilities for NO Reduction by *Cc*Os, According to Computational Studies[a]

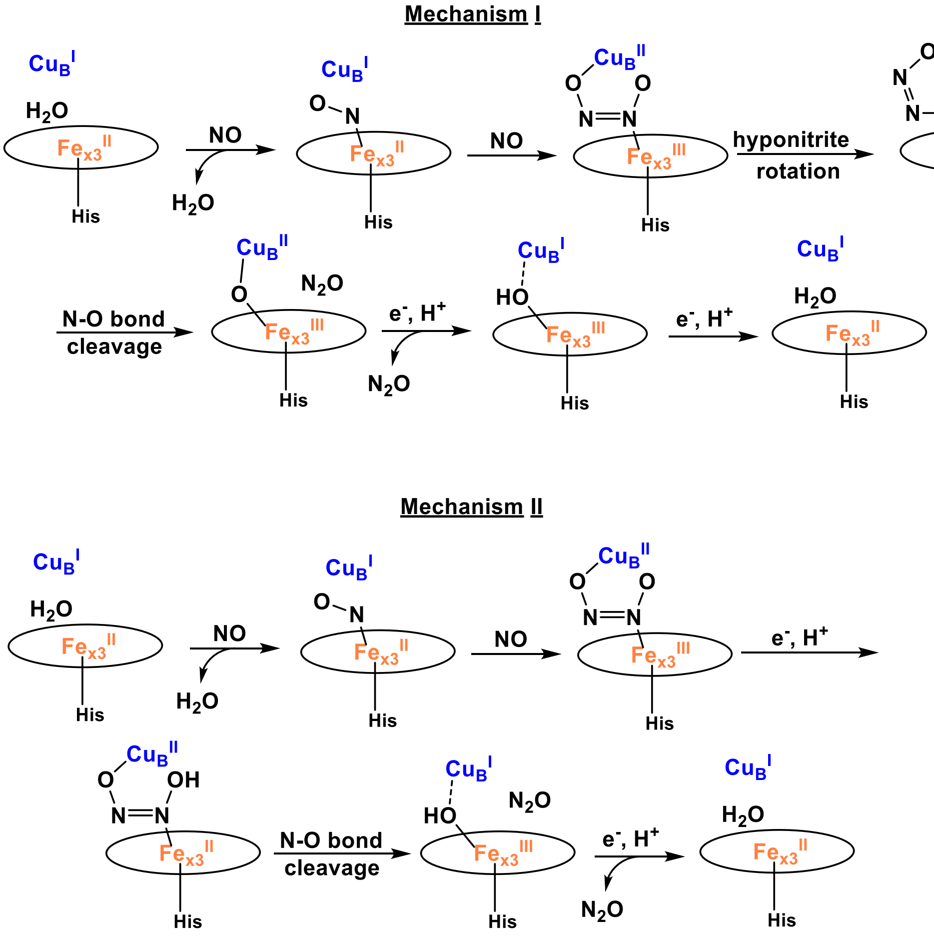

[a]Here, Fe_{x3} represents the different heme cofactors found in *Cc*Os (a, b).[1653].

between the Cu_B and the heme. This mechanism resembles the *cis*-heme b_3 mechanism proposed for *c*NORs. In this sense, the copper center could play an important, direct role in NO activation.[1645]

Additional studies from the Moënne-Loccoz group have shown that two NO molecules can simultaneous be present in the active site of reduced Cyt. bo_3 from *E. coli*.[1649] Unlike in Cyt. ba_3, where upon photolysis the NO that is bound to the heme dissociates and binds to Cu_B, in Cyt. bo_3 upon photolysis of the NO-bound heme, a Cu_B−nitrosyl complex does not form. However, when a gas mixture of CO and NO was used, a heme−nitrosyl and a Cu_B−CO complex were formed, so even though a heme−NO and a Cu_B−NO complex were not simultaneously detected, it is possible that this active site could accommodate two NO molecules. The differences seen between Cyt. bo_3 and Cyt. ba_3 could be attributed to the larger Fe−Cu distance in Cyt. bo_3.[1649] Cyt. bo_3 forms N_2O, but since there is no evidence that a Cu_B−NO complex forms, this could also support the *cis*-heme b_3 mechanism. The role of Cu_B may therefore only be to promote the formation of a heme−hyponitrite complex through electrostatic interactions.[1649]

For Cyt. ba_3, the rRaman-spectroscopic observation of the key hyponitrite intermediate of the *trans* mechanism (see Scheme 55) has been reported,[1650] where an N-coordinated hyponitrite bridges the heme iron and the Cu_B center in the active site.[1588,1651] In this study, NO was added to the oxidized form of the enzyme. Two isotope sensitive bands at 626 cm^{-1} and 1334 cm^{-1}, proposed to correspond to the Fe−N−OH bending and the N−N stretching vibration of the bound hyponitrite, respectively, were subsequently observed, but no signals associated with an Fe−NO complex could be identified.[1650] This is in contrast to the UV−vis spectra of oxidized ba_3 enzyme exposed to NO, where the formation of a ls-$\{FeNO\}^6$ species was observed.[1650] The formation of a reduced hyponitrite intermediate upon addition of NO to oxidized *Cc*O is unexpected. In addition, this intermediate would be expected to be short-lived (as being part of the catalytic mechanism), which was not observed. An alternative explanation for the observed vibrational features is that they could correspond to a Cu(II)−NO_2^- complex, which could form from the reaction of the Cu^I center with excess NO, for example via disproportionation (see heme/copper model complexes below).[87,1648] Nitrite also shows ν(N−O) stretching vibrations in the relevant frequency range of about 1300−1400 cm^{-1}.[1652] In conclusion, while these data do not prove the existence of a hyponitrite intermediate during NO reduction by *Cc*Os, they do provide some support for the *trans* mechanism.

On the basis of all of the data discussed above, it is reasonable to conclude that *Cc*Os and bacterial NORs might operate via different mechanisms, despite the structural similarities. NO reduction in *Cc*Os was further explored computationally for the Cyt. cbb_3 oxidase.[1653] Two closely-related mechanisms for NO reduction by *Cc*Os were evaluated, as shown in Scheme 57. The first mechanism is identical to the *cis*-heme b_3 mechanism in

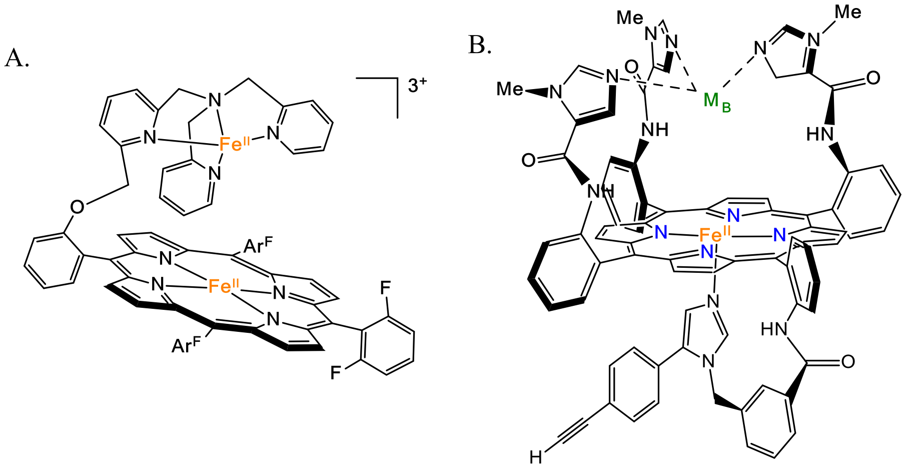

Figure 97. Two *c*NOR model complexes from Karlin and coworkers (A) and Collman and coworkers (B). Model A forms a stable diiron dinitrosyl complex, whereas model B reduces NO to N_2O when M_B = Fe^{II}.[1589,1673]

*c*NORs, and the second mechanism includes a proton-coupled reduction step, which occurs after formation of a hyponitrite intermediate and before N−O bond cleavage. It was found that Cyt. *cbb*$_3$ oxidase has a much higher barrier for the *cis*-heme *b*$_3$ mechanism compared to *c*NORs, which makes this mechanism unlikely. The higher barrier is due to the larger reduction potentials of the active site metal cofactors in C*c*Os compared to *c*NORs, particularly for the non-heme metal. Instead, the second mechanism with the proton-coupled reduction step was found more energetically favorable. Since this study suggests that NO reduction by Cyt. *cbb*$_3$ oxidase follows a somewhat different mechanism compared to *c*NORs, this implies that the type of non-heme metal plays the determining role for the mechanism of NO reduction compared to the exact type of heme cofactor. The difference seen in NOR activity among different C*c*Os may therefore originate from differences outside of the active site, especially related to proton transfer.[1653] Inhibition may then arise when the ferrous heme−nitrosyl complex formed first cannot be activated by the Cu_B center, or when Cu_B may not be able to interact with the second NO molecule, to induce N−N bond formation and NO reduction. This point requires further study.

4.3.5. Synthetic Model Complexes and Protein Models.

Both synthetic and protein-based model systems are useful tools to probe reaction mechanisms and capture key intermediates of NO reduction in dinuclear transition-metal active sites. Several synthetic model complexes have been developed to mimic the *c*NOR active site. Some of the first mimics for *c*NORs were model complexes that were originally designed for heme-copper oxidases, and the Cu was subsequently replaced by a non-heme Fe center.[1584,1598,1654−1668] The first heme/non-heme diiron dinitrosyl complex was synthesized by Karlin and coworkers, using a TPP^{2-} derivative for the heme, with a covalently-linked TMPA (tris(methylpyridyl)amine) ligand to mimic the Fe_B site (see Figure 97, left).[1589] While this complex was able to generate a diferrous dinitrosyl complex, it was not able to catalyze the reduction of NO to N_2O.[1589] The N−O stretching frequencies of this compound were observed at 1798 cm^{-1} for the non-heme FeNO unit and at 1689 cm^{-1} for the 5C ferrous heme−nitrosyl, both in the typical range for these types of species. An EPR signal was seen at g = 2.0, corresponding to a heme ls-$\{FeNO\}^7$ complex, but no signal around g_{eff} = 4, characteristic of a non-heme hs-$\{FeNO\}^7$ species, was observed at 77 K. When the non-heme Fe was replaced by Cu in the TMPA scaffold, N_2O formation was observed. However, in this case it was necessary to start from the iron−dinitrosyl heme complex, formed at low temperature, followed by addition of a Cu^I salt and acid, to allow for N_2O formation to occur.[538,566] Over the years, a number of related complexes with somewhat different heme and non-heme iron components have been developed, and NO coordination to these complexes has been studied.[538,566,1617,1669−1672] These complexes provide benchmarks for the spectroscopic (especially vibrational) properties of heme/non-heme diiron dinitrosyl complexes, with N−O stretching frequencies of the heme component ranging from 1620−1700 cm^{-1} and N−O stretches for the non-heme iron center in the 1720−1810 cm^{-1} range. However, due to the flexible alkyl linkers used in these cases, it is not always clear how much the heme and non-heme iron−nitrosyl complexes interact in these systems, if they do at all.

Collman and coworkers developed the first functional model complex for bacterial NORs, reported in 2008. Here, their original picket-fence porphyrin platform was adopted by equipping three of the pickets with imidazole residues, for coordination to a second transition-metal ion (see Figure 97, right).[1674,1675] Using this scaffold, both heme/non-heme iron and heme/copper complexes were subsequently reported, and their reactivity with NO was studied.[1669,1673] When the diferrous heme/non-heme iron complex was reacted with NO at room temperature, N_2O formation was observed, together with the di-Fe^{III} product.[1670] Further low-temperature studies indicate the potential generation of a ferrous heme(NO)/non-heme(NO) dinitrosyl complex prior to N_2O formation, which would support the *trans* mechanism for *c*NORs (see Scheme 55). Two intermediates were captured and characterized by EPR and rRaman spectroscopy.[1670] The first intermediate was generated upon reaction of the diferrous complex with NO at low temperatures (−80 °C) in CH_2Cl_2, to form a ferrous heme and nitrosylated non-heme iron complex. This species was characterized by an EPR signal at g_{eff} = 3.92. When this intermediate is warmed to room temperature, it forms a heme ls-$\{FeNO\}^6$/non-heme Fe(III)−OH product. The second intermediate was captured by reaction of the diferrous complex in DMF with NO, resulting in a dinitrosyl complex, but the intermediate generated in this way does not go on to form N_2O.

Scheme 58. Proposed N−N Coupling Pathway of Heme ls-$\{FeNO\}^7$ Complexes Assisted by the Lewis Acid BF_3[1676]

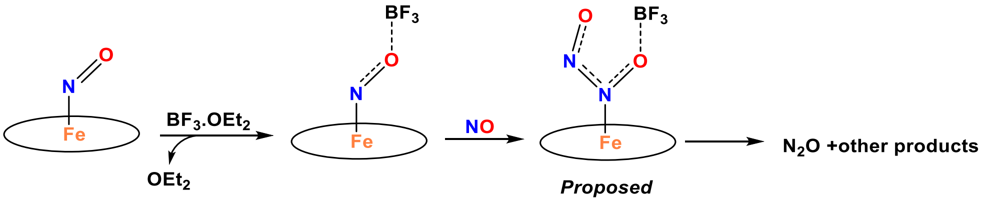

This intermediate was characterized using EPR spectroscopy, showing g values of 2.07, 2.02, 1.96, corresponding to the heme ls-$\{FeNO\}^7$ complex, and g_{eff} = 3.92, originating from the non-heme iron−nitrosyl complex. Further, rRaman spectroscopic studies on this intermediate identify the Fe−N−O bending mode of the ferrous heme−nitrosyl complex at 579 cm^{-1}.[1670] Additional studies show that the diferrous form of the model complex is needed to reduce NO to N_2O.[1673] Reaction of the mixed-valent heme-Fe^{III}/non-heme Fe^{II} form with NO leads to the formation of a mixture of heme ls-$\{FeNO\}^6$/non-heme hs-$\{FeNO\}^7$ and heme ls-$\{FeNO\}^7$/non-heme Fe^{III} complexes, as determined by IR and EPR spectroscopy. Unfortunately, further mechanistic studies could not be conducted, as the preparation of these model complexes is very tedious, and they can only be prepared in small quantities. Catalytic turnover of NO could not be achieved. One key difference between these models and bacterial NORs is the Fe−Fe distance, which is distinctively larger in Collman's model system (estimated to be ≥5 Å).

Recently, the idea that bacterial NORs follow a *cis*-heme b_3 mechanism where the Fe_B center serves as a Lewis acid that activates the heme-bound NO was further tested by Richter-Addo and coworkers. Here, the 5C ls-$\{FeNO\}^7$ complex [Fe(OEP)(NO)] was reacted with the very strong Lewis acid $BF_3{\cdot}OEt_2$, which leads to the formation of the adduct $[Fe(OEP)(NO{\cdot}BF_3)]$.[1676] In this adduct, the N−O stretching frequency drops by ~200 cm^{-1} to lower energy, in agreement with the proposal that this induces distinct $^1NO^-$ character on the bound NO. In fact, this shift in the N−O stretching frequency is about the same as observed upon reduction of the ls-$\{FeNO\}^7$ to the corresponding ls-$\{FeNO\}^8$ complex (see Section 2.2).[1676] Interestingly, addition of NO to the adduct $Fe(OEP)(NO{\cdot}BF_3)]$ leads to N_2O formation, as shown in Scheme 58. The Lewis acids [K(2.2.2-cryptand)]$^+$ and $B(C_6F_5)_3$ can also induce N−N coupling, but with lower N_2O yields.[1676,1677]

The Collman and Karlin groups and other scientists also prepared a large number of heme/copper model complexes.[1617,1674] Interestingly, not only have these compounds been utilized to elucidate the mechanism of O_2 reduction by C*c*Os, but they are also being developed as catalysts for dioxygen reduction in fuel cells.[1678−1683] The Karlin group used a 1:1 mixture of [Fe(T*o*-F_2PP)] and the Cu complex $[Cu(TMPA)(MeCN)]^+$ to produce N_2O. When the reduced heme-Fe^{II}/Cu^I form is reacted with NO in the presence of acid, N_2O formation is observed. In the absence of acid, the ferrous heme−nitrosyl complex forms, whereas the Cu^I center mediates NO disproportionation, leading to the formation of a Cu(II)−nitrito complex.[538] The Karlin group further investigated the interconversion of nitrite and NO by heme/copper centers,[1684,1685] which is a potential mechanism by which C*c*Os could either produce or consume NO, depending on the physiological conditions.[1686−1688] The Collman group also studied the NO reactivity of their heme/copper model system. When the Cu_B is absent, they found that 1 equiv of NO binds to the ferrous heme and forms a ls-$\{FeNO\}^7$ complex that is stable in an aerobic environment. On the other hand, when the reduced Cu^I center is present, O_2 reacts with the Cu^I center of the heme ls-$\{FeNO\}^7$/Cu^I complex and generates O_2^-, which then attacks the ferrous heme−nitrosyl complex, resulting in the heme-Fe^{II}/Cu^{II} form of the complex and nitrate. These results show that NO might play a protective role in C*c*Os, since NO can form a stable ferrous heme−nitrosyl complex with the heme, for example heme a_3, that protects the enzyme against inhibitors such as CN^- and CO.[1669,1673,1689] Reaction with O_2 can then remove NO, and the C*c*O would be re-activated for catalysis (O_2 reduction).

In addition to synthetic model complexes, protein models of heme-copper oxidases were developed in the protein Mb by the Lu group.[1690] For this purpose, a non-heme binding site was engineered into the distal pocket of sperm whale Mb to create functional models for both C*c*Os and bacterial NORs.[1691] Design of a His_3 site as observed in C*c*Os into the Mb distal pocket does not lead to the formation of a stable non-heme iron complex, which was shown by UV−vis spectroscopic studies. However, the further addition of a Glu residue that provides a carboxylate ligand for the non-heme iron center allows for the formation of a stable Fe complex. These results provide support for the necessity of an additional carboxylate ligand in the bacterial NOR active sites for the stable coordination of the Fe_B center. Two generations of the Mb model were developed by the Lu group. The first model, termed Fe_BMb1, has the mutations Leu29His, Phe43His, Val68Glu as mentioned above

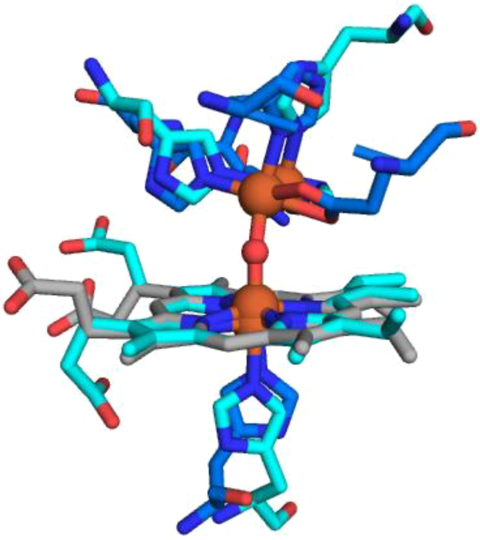

Figure 98. PyMOL generated overlay of the crystal structures of the diiron active site of FeMb1 (PDB: 39KZ, in cyan) and the oxo-bridged active site of *Pa* cNOR (PDB: 3O0R, in grey and blue).

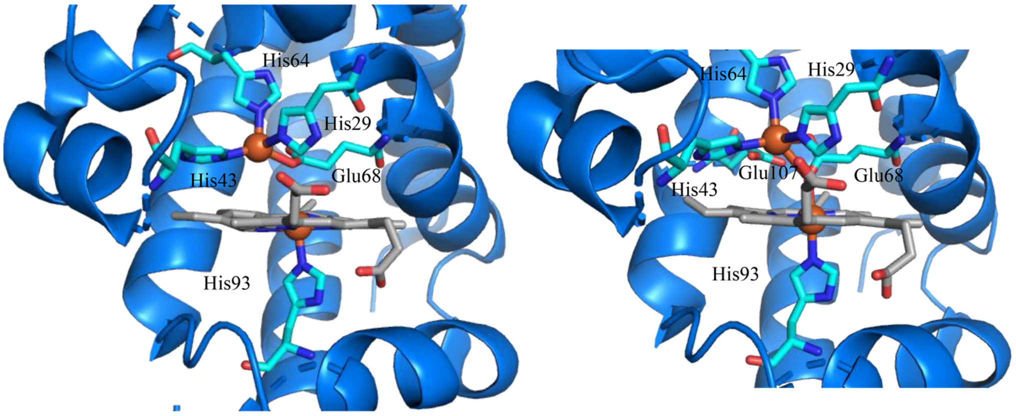

Figure 99. PyMOL generated images of the crystal structures of Mb models of bacterial NORs and heme-copper oxidases from the Lu group. (A) Fe_BMb1 (PDB: 39KZ) and (B) Fe_BMb2 (PDB: 3M39) with an additional Ile107Glu mutation.

to create the Fe_B binding site. The crystal structure of the active site of this Mb variant shows a close agreement of the placement and coordination geometry of the non-heme iron center between the model and the enzyme, as seen in Figure 98.[1691,1692]

One key difference between the two structures is the larger Fe−Fe distance in the model, of about 4.8 Å (see below). The second generation, termed Fe_BMb2, has an additional Ile107Glu mutation, where the newly introduced Glu residue interacts with a water molecule to form a hydrogen-bonding network in the active site. In this way, a proton-transfer pathway was introduced in Fe_BMb2. The addition of this peripheral Glu residue increases the catalytic activity of the model system for NO reduction, allowing for 50% yield of N_2O in a productive single-turnover reaction, yielding twice as much N_2O compared to Fe_BMb1.[1693] This result shows the importance of a proton delivery network via hydrogen-bonding for NOR reactivity.[1693,1694] The active sites of Fe_BMb1 and Fe_BMb2 are shown in Figure 99. Using stopped-flow UV−vis absorption spectroscopy and RFQ-rRaman studies, the reactions of reduced Fe_BMb1 and Fe_BMb2 with excess NO were further analyzed to gain mechanistic insight.[1693] RFQ-rRaman experiments on Fe_BMb1 show that the first NO binds to the reduced Fe_B center, forming a hs-$\{FeNO\}^7$ adduct with an N−O stretching frequency of 1755 cm^{-1} (within 6 ms). The second NO then binds to the ferrous heme to produce a 6C ls-$\{FeNO\}^7$ complex, which shows the Fe−N−O bending mode at 570 cm^{-1}. In Fe_BMb1, the diferrous dinitrosyl intermediate finally converts to a dead-end 5C heme ls-$\{FeNO\}^7$ complex, by dissociation of the Fe−N_{His} bond, and the hs-$\{FeNO\}^7$ complex of the Fe_B center. Here, the 5C heme ls-$\{FeNO\}^7$ complex shows typical Fe−NO and N−O stretching frequencies of 522 cm^{-1} and 1660 cm^{-1}, respectively. In contrast, in Fe_BMb2, in addition to the dead-end 5C heme ls-$\{FeNO\}^7$ complex, the diferrous dinitrosyl intermediate also undergoes N−N bond formation to produce N_2O, albeit with a rate constant of 0.7 s^{-1} at 4 °C.[1693] According to the authors, the formation of this diferrous dinitrosyl intermediate supports the *trans* mechanism proposed for *c*NORs (see Scheme 55, top). Here, the *trans* mechanism could be facilitated by the larger Fe−Fe distance of 4.8 Å in the model compared to *c*NORs.[1693]

A follow-up study then investigated how N−N coupling and N_2O formation are affected by a variation in the heme cofactor. For this purpose, different hemes with varying redox potentials and different non-heme metals (Fe, Zn, Co) were incorporated into Fe_BMb1, and the reactions of the resulting proteins with NO were investigated.[1695,1696] In particular, Fe_BMb1 was equipped with monoformyl and diformyl heme *b* analogs, which tune the reduction potential of the heme from −59 mV (Fe_BMb1) to +53 mV (monoformyl analog) and to +148 mV (diformyl analog, all vs SHE). Interestingly, the maximum number of turnovers was observed for the monoformyl heme complex, using an NO electrode setup to monitor turnovers for NO reduction. In addition, activity was retained when Zn^{II} was loaded into the non-heme site, indicating that the metal ion bound in the Fe_B site might only act as a Lewis acid in the reaction, as proposed for the *cis*-heme b_3 mechanism. Since the reactions were run in the presence of excess reductant, giving multiple turnovers, even in the absence of the redox-active Fe_B center, the authors proposed that the reactions actually follow a semireduced pathway for NO reduction (see Sections V.b and V.c), facilitated by the higher reduction potential of the monoformyl heme.[1695,1696]

The role of the metal ion bound in the Fe_B site was further evaluated in additional studies where the non-heme iron site of Fe_BMb2 was equipped with Fe^{II}, Zn^{II} and Cu^I.[1607] When the non-heme iron binding site is empty, the resulting protein shows the N−O stretching frequency of the 6C ls-$\{FeNO\}^7$ adduct at 1601 cm^{-1}. On the other hand, in the presence of Fe^{II} in the non-heme binding site, the N−O stretching frequency of the heme decreases to 1549 cm^{-1}. A decrease in the N−O stretching frequency was also observed when Zn^{II} was loaded into the non-heme binding site, showing two N−O stretching bands at 1550/1577 cm^{-1}. In the presence of a Cu^I ion, the N−O stretch remains at 1601 cm^{-1}.[1607] Note that in these experiments, turnover was avoided by adding only one equiv of NO. The drop in the N−O stretching frequency in the presence of a divalent metal ion in the non-heme binding site was explained by electrostatic interactions of the metal ion with the O atom of the heme-bound NO. Hence, the divalent metal ion serves as a Lewis acid, activating the heme-bound NO, which supports the *cis*-heme b_3 mechanism as proposed by Blomberg (see above), where the Fe_B center was proposed to serve this role. However, the activation achieved in this way in Fe_BMb2 is not sufficient to induce N−N coupling, evident from the fact that the Zn^{II}-bound form does not produce N_2O upon addition of excess NO.[1607] In the presence of Fe^{II} in the non-heme binding site, N_2O formation is observed, but the reaction is believed to follow a different mechanism (the *trans* mechanism), as described above.

Finally, to study the properties of the ferrous Fe_B−NO complex, studies on Fe_BMb1 with Zn(protoporphyrin IX) substitution for heme *b* were also performed. In the presence of excess NO, an EPR signal with g_{eff} ∼ 4 was observed, corresponding to the formation of a non-heme hs-$\{FeNO\}^7$ complex with an $S_t = 3/2$ ground state (see Section 5.1).[1692] The electronic structure of the non-heme hs-$\{FeNO\}^7$ complex was further investigated using QM/MM calculations and Mössbauer spectroscopic studies, and it was proposed that this complex is best described as a hs-Fe^{II} ($S = 2$) AF coupled to a $NO^{\bullet}$ ligand ($S = 1/2$). However, this hs-$\{FeNO\}^7$ complex has very similar spectroscopic properties as other hs-$\{FeNO\}^7$ complexes, so it is not clear whether this complex really shows different electronic properties (see discussion in Section 5.1).

In addition to their Fe_BMb protein models, the Lu group also studied the NO reactivity of the corresponding systems with copper bound in the non-heme site (besides, of course, extended studies into their O_2 reactivity).[1690] As described above, this myoglobin variant, termed Cu_BMb, contains a His_3 binding site for the copper center.[1697] Cu_BMb is able to reduce NO to N_2O with a rate of 0.033 mol NO/(mol Cu_BMb) s. A 6C heme ls-$\{FeNO\}^7$ species was observed by UV−vis and EPR spectroscopy in these reactions, but further mechanistic studies were not conducted.[1698]

4.3.6. Coordination Chemistry of Hyponitrite.

As indicated in Scheme 55 and discussed above, NO reduction to N_2O according to the *trans* mechanism leads to the formation of an N-bound *trans*-hyponitrite intermediate. On the other hand, the *cis*-heme b_3 mechanism, according to Scheme 56, generates an N,O-bound, bridging *cis*-hyponitrite species after N−N coupling. To gain further insight into the properties of such intermediates, it is therefore insightful to study the coordination chemistry of hyponitrite with hemes. N−N coupling reactions with other transition metals, especially using Co, Ni, Cu, and Ru complexes, are described in Section 5.5.

Richter-Addo and coworkers reported the only known heme−hyponitrite complexes, which were prepared by the reaction of a ferric heme precursor with pre-formed hyponitrite salts. The crystal structure of $[\{Fe(OEP)\}_2(\mu\text{-}N_2O_2)]$ was reported in 2009 and is shown in Figure 100.[1601] The crystal structure shows Fe−O, O−N, and N−N distances of 1.889, 1.375 and 1.250 Å, respectively. The Fe−O−N angle in this structure is 118°, and the N−N−O angle is 108.5°.[1601] The complex was further characterized by IR, NRVS, EPR and MCD spectroscopy and SQUID.[1602] SQUID measurements revealed that the compound is composed of two $S = 3/2$ intermediate-spin ferric iron centers that couple weakly through the hyponitrite bridge, which is further supported by the MCD results. The antisymmetric N−O stretch of the coordinated hyponitrite dianion is located at 982 cm^{-1}, observed by IR spectroscopy, which is typical for hyponitrite complexes, as further confirmed by NRVS and DFT analysis.[1602] Upon reaction of the complex with acid, N_2O formation is observed. Similar reactivity was also reported for the analogue $[\{Fe(PPIXDME)\}_2(\mu\text{-}N_2O_2)]$.[1602]

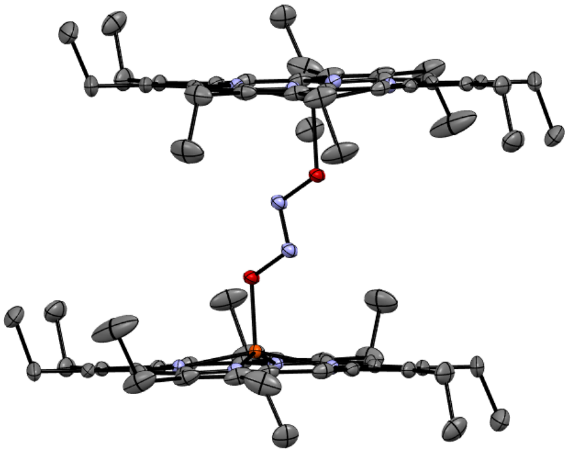

Figure 100. Crystal structure of $[\{Fe(OEP)\}_2(\mu\text{-}N_2O_2)]$.[1601] All H atoms are omitted for clarity.

On the other hand, if $[\{Fe(OEP)\}_2(\mu\text{-}N_2O_2)]$ is left in solution, the complex decomposes over time into two equiv of the ferrous heme−nitrosyl complex, [Fe(OEP)(NO)], following eq 20.[1602] The rate constant of the reaction in the absence of an axial ligand is $k_{obs} = 6.4 \times 10^{-5}\ s^{-1}$.[1602] DFT calculations show that the large barrier for this reaction is due to an unfavourable transition state, either the N-bound hyponitrite dimer, which is disfavoured due to steric interactions, or the O-bound NO complex, as shown in Figure 101. In addition, the calculations show that the ferrous heme−nitrosyl product is thermodynamically more stable than the O-bound hyponitrite-bridged dimer by ∼20 kcal/mol (free energy).[1602] Taken together, these results show that the reverse reaction, the dimerization of ferrous heme−nitrosyl complexes, cannot occur, which indicates that the radical-radical type N−N coupling mechanism, according to the *trans* mechanism, is unfavourable. Interestingly, when MI is added to the solution of $[\{Fe(OEP)\}_2(\mu\text{-}N_2O_2)]$, the rate constant for the formation of [Fe(OEP)(NO)] increases to $k_{obs} = 1.24 \times 10^{-3}\ s^{-1}$. Accordingly, the free-energy barrier for decomposition of $[\{Fe(OEP)\}_2(\mu\text{-}N_2O_2)]$ is reduced by ∼10% when an axial imidazole ligand is present.[1602]

A cofacial bis-porphyrin complex was further synthesized to probe the effect of distance on hyponitrite stability.[1699] To generate $[\{Fe(OEP\text{-}CH_2)\}_2(\mu\text{-}N_2O_2)]$, the corresponding μ-

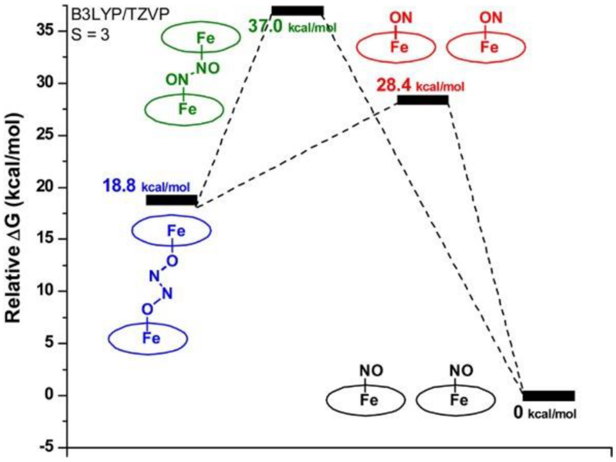

Figure 101. Computational results for the decomposition of $\{[Fe(P)]_2(\mu\text{-}N_2O_2)\}$ into two equivalents of [Fe(P)(NO)] (P^{2-} = porphine dianion, used for the caluclations). Calculated for the $S_t = 3$ state with B3LYP/TZVP. Reprinted with permission from ref 1602. Copyright 2014 American Chemical Society.

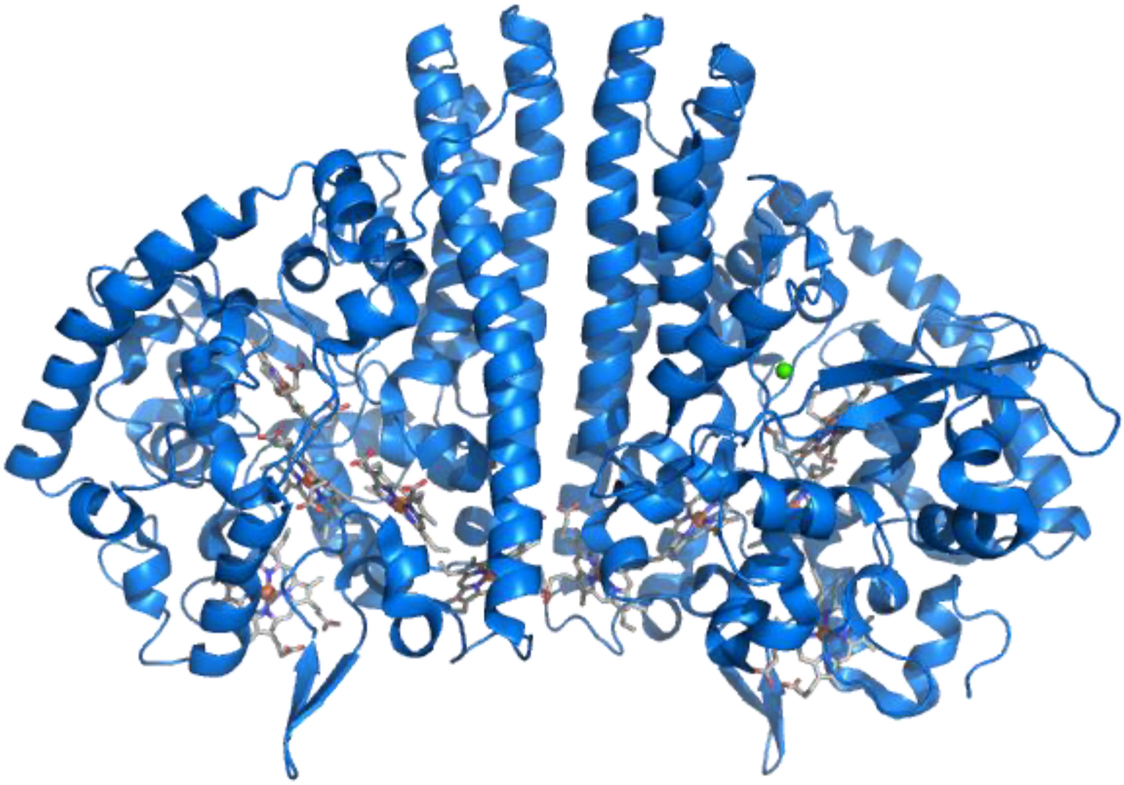

Figure 102. PyMOL generated image of the crystal structure of *Cc*NIR from *S. deleyianum*. (PDB: 1QDB), showing a homodimeric structure for the protein.

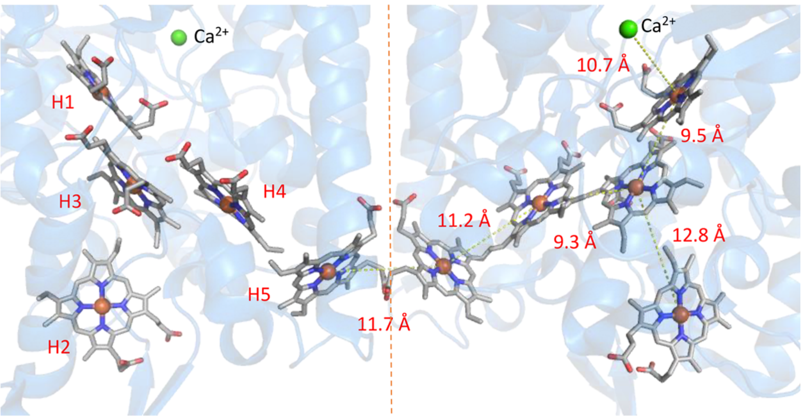

Figure 103. PyMOL generated image of the crystal structure of *Cc*NIR from *S. deleyianum* (PDB: 1QDB). The orientation of the hemes is the same as in Figure 102, with the left monomer showing the numbering scheme of the hemes (with H1 being the active site). The right monomer shows the Fe−Fe distances (Å) between hemes, and the dotted line indicates the dimer interface.

oxo complex was treated with sulfuric acid, followed by addition of $H_2N_2O_2$. [{Fe(OEP-CH_2)}$_2$(μ-N_2O_2)] has an N−O stretching frequency of 992 cm^{-1}. Notably, N_2O formation occurs without the need of acid. Hence, the formed hyponitrite complex is unstable in the absence of $H_2N_2O_2$, and reforms the μ-oxo complex and N_2O. The reduced Fe−Fe distance of 3.4 Å in [{Fe(OEP-CH_2)}$_2$(μ-N_2O_2)] compared to 6.7 Å in [{Fe(OEP)}$_2$(μ-N_2O_2)] is thought to be the reason behind the differences seen in the reactivity of these complexes with respect to N_2O generation.[1699]

4.3.7. Outlook. Despite much research on bacterial NORs, especially *c*NORs, and corresponding model systems, many questions have remained about the mechanism of these enzymes. A major holdup in these efforts has been the difficulty in identifying any intermediates of the NOR reaction in the enzymes. Because of this lack of information, mechanistic proposals for these enzymes have been inspired by model complexes, protein models, and quantum-chemical calculations. Recent studies have elucidated the potential role of the Fe_B center in catalysis, serving as a Lewis acid to activate a heme-bound NO, but more work needs to be conducted to determine whether this proposal holds for NO reduction by *c*NORs. The effect of the Fe_B redox potential has yet to be explored as well. Finally, the role of SCS residues in the active site for catalysis, especially the function of the conserved Glu, remains to be fully elucidated. The relevance of the resting state μ-oxo bridged complex in catalysis has yet to be determined as well. It has been shown that different subclasses of NORs have different

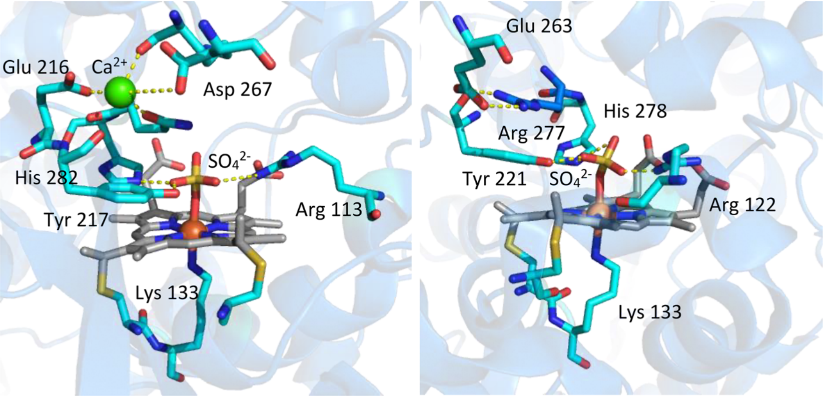

Figure 104. PyMOL generated images of the crystal structures of the active sites of *S. deleyianum* (left; PDB: 1QDB) and *G. lovleyi* NrfA (right; PDB: 6V0A). The critical Ca^{2+} (left) and Arg277 residue (right) in the SCS of the active sites are indicated (see text).

properties and that the catalytic conditions utilized in a study can impact the results. This begs the question if different subclasses of bacterial NORs can follow different mechanisms and if different mechanisms are induced depending on the experimental conditions. There are still a lot of open questions revolving around bacterial NORs that await to be answered.

4.4. Other Processes Involving NO as an Intermediate

4.4.1. Dissimilatory Nitrate Reduction to Ammonia (DNRA). Dissimilatory nitrate reduction to ammonia (DNRA) is an important pathway in the nitrogen cycle that conserves the usable nitrogen in the soil by reversing nitrification.[1700,1701] Dissimilatory nitrate reduction is a two-step process, where nitrate is first reduced to nitrite by nitrate reductases, facilitated by chemoorganic heterotrophic anaerobes.[1702] This step is followed by the reduction of nitrite to ammonium, which is catalyzed by Cyt. *c* nitrite reductases (C*c*NIR or NrfA) in one multi-step reaction, as described by eq 10. NrfA efficiently reduces nitrite without the release of any (potentially toxic) intermediates.

4.4.1.1. Protein Structure of CcNiR. NrfA is an important bacterial enzyme located in the periplasm and encoded by the *nrfA* gene.[1703] NrfA homologs have been isolated and characterized from a number of organisms, including *Wolinella succinogenes*,[325] *E. coli*,[1704] *S. oneidensis*,[1705] *Desulfovibrio desulfuricans*,[1706] *Desulfovibrio vulgaris*,[1707] *Geobacter lovleyi*,[1708] and *Sulfurospirillum deleyianum*.[1709] X-ray crystallography shows a pentaheme homodimeric (α_2) structure for these enzymes (see Figure 102), with a molecular mass ranging from 52 to 65 kDa. One exception includes NrfA from the haloalkaliphilic bacterium *Thioalkalivibrio nitratireducens*, which forms a hexameric structure containing 48 hemes.[1710] NrfA crystal structures further reveal that each monomer contains five *c*-type hemes (Figure 103). These hemes are numbered according to the sequence in which their binding sites occur in the polypeptide chain. The active site Heme 1 is presumed to be five-coordinate (5C) and hs in the ferric resting state of the enzyme. This heme features an unusual proximal lysine ligand. However, the exact role of the Lys residue for catalysis is not known. The remaining four hemes (Heme 2−5; see Figure 103) are bis-His coordinated and are ls in both the ferrous and ferric state, and their role is to shuttle electrons to the active site. The hemes are covalently linked to the peptide backbone by thioether bonds via cysteine residues in a classic heme *c* binding motif for periplasmic proteins such as (Cys-X_1-X_2-Cys-His) or (Cys-X_1-X_2-Cys-Lys). Heme 2 is believed to be the initial entry point for electrons from either NrfH or the NrfBCD complex, and it shuttles electrons to the other hemes and ultimately Heme 1 during catalysis.[325,1707] With respect to external electron sources, it has been shown that the *E. coli* NrfA utilizes a soluble penta-heme cytochrome, NrfB, as the redox partner. In comparison, *W. succinogenes* and *S. deleyianum* NrfA accept electrons from a membrane-anchored tetra-heme cytochrome (NrfH). One of the distinguishing differences between these enzymes are their protein surfaces around Heme 2, which supports the idea that this is the docking site for external redox partners.[1704]

All five hemes within a monomer in the *S. deleyianum* NrfA enzyme are in close contact with one another, as seen in the crystal structure, having Fe−Fe distances between 9−13 Å (see Figures 102 and 103). Hemes 1, 3, and 4 are arranged almost coplanar with edge-to-edge distances below 4 Å, and are close enough to allow for direct π-interactions of the porphyrin rings. Hemes 2 and 5 are farther apart and are perpendicular to their nearby hemes. Heme 5 lies close to the dimer interface (dimerization occurs along the interface of two α-helices via various salt bridges) with a short Fe−Fe distance of 11.7 Å, and it was suggested that electron transfer between the two subunits could occur via these two heme centers.[1711] One of the key questions in this regard is whether Hemes 2−5 act only as a wire to shuttle electrons to the catalytic heme, or whether they could also function as capacitors, storing electrons before, during, or after each catalytic cycle.[1712] The fact that NrfA catalyzes the reduction of nitrite to ammonia without the release of any partially reduced species indicates that electrons can be stored on-site, but the details of how electrons are distributed in the electron storage unit of NrfA and how each heme functions in this regard are not exactly known.

The active site Heme 1, as shown for the *S. deleyianum* NrfA crystal structure in Figure 104, features the Nζ atom of Lys133 as the proximal ligand to the heme, replacing the classic histidine binding motif. Furthermore, in the crystal structure, a sulfate ion binds to the heme via an O atom, with an Fe−O bond length of 2.0 Å (note that sulfate was added externally during the crystallization of the enzyme). Sulfate is further hydrogen-bonded to both His282 and Tyr217 via a single O atom, and the remaining two O atoms interact with a water molecule, which is also hydrogen-bonded to the two propionate side chains of Heme 1. One of the propionate groups further forms a hydrogen bond with Arg113. This sulfate coordination therefore elucidates the extensive hydrogen-bonding network within the active site of NrfA, as indicated in Figure 104. In

Scheme 59. Proposed Reaction Mechanism of Nitrite Reduction by NrfA Mediated by Several Key Proton-Coupled Electron-Transfer (PCET) Steps[326]

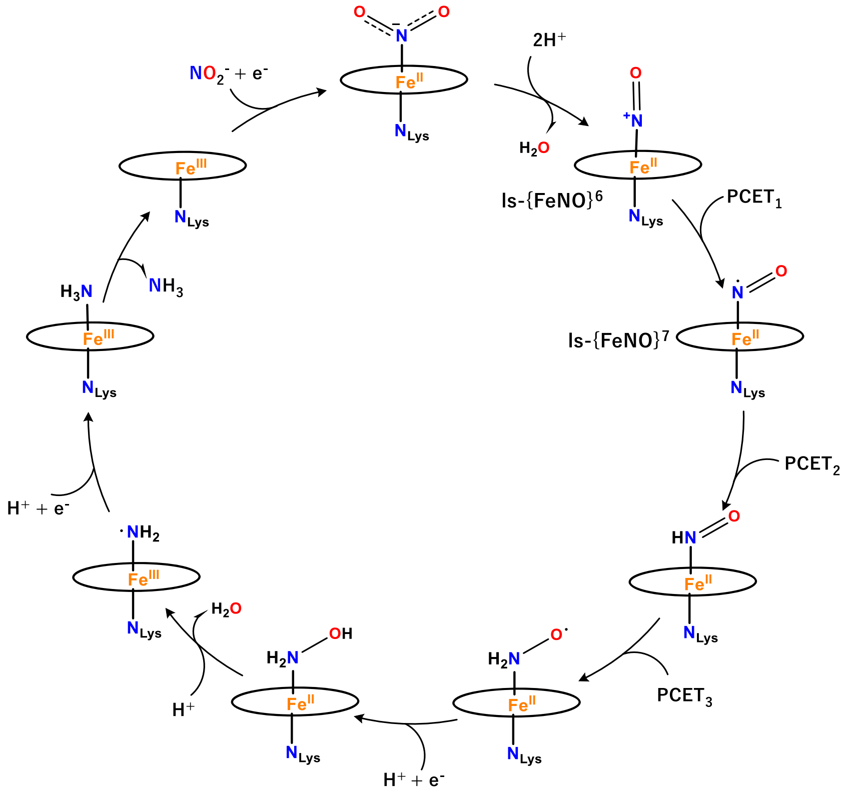

addition, a large electron-density was also detected in the SCS of the active site, which was assigned to a Ca^{2+} cation. Using inductively coupled plasma atomic emission spectroscopy, a stoichiometry of 1.0 ± 0.1 atoms of Ca^{2+} per nitrite reductase monomer was confirmed. The Ca^{2+} ion is coordinated by the carboxylate group of Glu216 in a bidentate manner, Gln281, two peptide carbonyl oxygens and two water molecules. Furthermore, within the active site a positively-charged channel guides nitrite into the active site and a negatively-charged channel guides the positively-charged product (NH_4^+) to the protein surface.[325,1713]

Recently, a new NrfA subclass was identified in *G. lovleyi.*[1708] Structural characterization indicates that unlike the previously characterized NrfA homologs, *G. lovleyi* NrfA has a critical arginine residue in the region otherwise occupied by Ca^{2+}.[1714] Phylogenetic analysis helped confirm that this enzyme represents a new subclass of NrfA.[1715] Like all available NrfA crystal structures,[1389,1716−1720] *G. lovleyi* NrfA crystallizes as a homodimer (Figure 104), but dynamic light scattering characterization suggests that the enzyme actually remains a monomer in solution, even up to a concentration of ~300 μM,[1714] challenging the long held notion that NrfA is a functional dimer.[1716,1721] However, it should be noted that NrfA proteins form a complex with their physiological electron donors, NrfH or NrfBCD, and the exact composition of the resulting complex under physiological conditions is currently unknown.[1707,1708,1717−1719]

4.4.1.2. Catalytic Mechanism of CcNIR. A catalytic mechanism for nitrite reduction by NrfA has been proposed based on crystallographic and computational analysis,[326,1389,1720,1722] but many details, especially concerning the nature of key intermediates, are still under investigation. NrfA reduces nitrite to ammonia with high turnover numbers, for example: *S. deleyianum* (962 s^{-1}), *E. coli* (777 s^{-1}), and *D. desulfuricans* (415 s^{-1}). These enzymes also show a high specific activity, for example up to 1,050 μmol nitrite/(mg enzyme) min at pH 7 for *S. deleyianum* NrfA.[1723] Scheme 59 shows the proposed mechanism for nitrite reduction by CcNIRs, based on detailed computations by Bykov and Neese.[326,1389,1720,1724] The reaction starts off with nitrite binding to the ferrous heme active site of NrfA, forming an η^1-*N* nitro complex. The proposed N-binding mode of nitrite is supported by the observation of the η^1-*N* nitro complex of ferric Heme 1 in the *W. succinogenes* enzyme by X-ray crystallography.[1389] In the ferrous complex, π-backbonding from Fe^{II} to the N-bound nitrite transfers electron density into the nitrite π* orbital (the LUMO of nitrite).[326] This increases the strength of the Fe−N bond and simultaneously weakens the N−O bonds (due to the N−O antibonding nature of the orbital), and thus primes nitrite for N−O bond cleavage.[326] Heterolytic cleavage of the first N−O bond occurs as the initial step of catalysis, assisted by transfer of two protons, generating the ls-$\{FeNO\}^6$ intermediate and a water molecule. A nearby His in the SCS is optimally positioned to mediate the necessary proton transfer to help carry out the N−O bond heterolysis step. In the sulfate-bound crystal structure (see Figure 104), the O atoms of sulfate are in hydrogen-bonding distances to the N atom of this His and to the N atom of an Arg residue in the active site, in both the *S. deleyianum* and the *G. lovleyi* NrfA crystal structures. DFT calculations predict that this proton transfer from the nearby His is moderately endothermic (+4.9 kcal/mol) with a small energy barrier of 5.5 kcal/mol.[326] This reaction resembles the mechanism of nitrite reduction by heme cd_1 NIRs (see Section 4.1).

After the first N−O bond cleavage two rapid reductions occur, generating the complete series of heme−nitrosyl intermediates from ls-$\{FeNO\}^6$ to ls-$\{FeNO\}^8$. DFT calculation predict that the ls-$\{FeNO\}^6$ intermediate has the typical Fe(II)−NO^+ ground state for these types of species (see Section 2.3).[1389,1720] Interestingly, the reduction of the ls-$\{FeNO\}^7$ to the ls-$\{FeNO\}^8$ intermediate is energetically unfeasible, and can only proceed when it is coupled to a proton transfer to directly generate the Fe(II)−NHO intermediate.[1724] This coupled proton transfer provides the driving force for this step, and is in agreement with the observed basicity of ls-$\{FeNO\}^8$ complexes (see Section 4.2). Next, two consecutive electron and proton transfers occur to yield an N-bound Fe(II)−hydroxylamine intermediate. DFT calculations indicate that the Fe(II)−N interaction in this species corresponds to a conventional σ-bond.[1725] A corresponding, ferric hydroxylamine complex was also characterized by X-ray crystallography for *W. succinogenes* NrfA.[1389] The cleavage of the second N−O bond occurs after an initial proton-transfer step that cleaves the N−O bond and releases water.[326] Subsequent electron and proton transfer then yields the product, NH_3, bound to ferric Heme 1.[326] The product can readily dissociate and be directed to the protein surface via a negatively-charged channel within the active site (see above).[325,1713] The catalytic cycle closes with a one-electron reduction of the active site Heme 1 back to the ferrous form that allows for nitrite to bind and begin the next turnover.[326] The complete reaction mechanism is shown in Scheme 59.

Two important factors contribute to efficient nitrite reduction by NrfAs. First, fast electron transfer to the active site heme is necessary for the reaction to proceed, as six electrons total are required for nitrite reduction to ammonia. The required electrons are transferred from a designated membrane-bound reductase, which is either NrfH or the NrfBCD complex (species dependent).[1708,1717−1719] The second critical component required for nitrite reduction are protons, which are supplied through a positively-charged substrate channel.[1706] Importantly, the substrate channel contains a bound calcium ion (for example, in *S. deleyianum* NrfA) or a critical arginine residue (for example, in *G. lovleyi* NrfA) that are in direct proximity to the active site (Figure 104). The role of Ca^{2+} in *S. deleyianum* NrfA within the substrate channel, located only 10.7 Å away from Heme 1, is twofold: first, Ca^{2+} is thought to help increase the structural stability of the active site pocket, and second, it assists in proton-transport to Heme 1 during catalysis. During turnover, water molecules in the channel can provide protons, and the resulting hydroxide ions can be stabilized in the Ca^{2+} coordination sphere, while the protons are shuttled to the active site and take part in catalytic nitrite reduction. It was also demonstrated that Ca^{2+} or arginine are essential for enzyme activity, and when either Ca^{2+} was removed (in *S. deleyianum* NrfA) or Arg277 was substituted by site-directed mutagenesis (in *G. lovleyi* NrfA), the enzymatic activity largely vanished.[1709,1714,1726]

4.4.1.3. Spectroscopic Characterization of NrfA.

UV−vis spectroscopic studies on *E. coli* NrfA by Bamford et al. showed typical absorption spectra for *c*-type cytochromes.[1704] The oxidized form of the enzyme exhibits the Soret band at 409 nm, a Q band at 532 nm, and an additional feature at 630 nm that is assigned to a ligand-to-metal charge-transfer transition originating from the hs Heme 1. Similar features have been observed for other C*c*NIRs.[1711,1727−1729] Reduced *E. coli* NrfA shows the Soret band at 420.5 nm and Q bands at 523.5 and 552 nm. The presence of ls ferric hemes in oxidized NrfA is also supported by MCD spectroscopy, showing Q bands in the 500−600 nm region, which is typical for ls ferric hemes.[1730] Moreover, in the near infrared (NIR) region of the optical spectra, oxidized *E. coli* NrfA has a broad ligand-to-metal charge-transfer band that is observed by MCD spectroscopy at 1470 nm ($\Delta\varepsilon$ = 1.2 mM^{-1} cm^{-1}), with a vibrational sideband to higher energy (1200−1300 nm), which is characteristic for bis-His coordinated ls ferric hemes. Similarly, *W. succinogenes* NrfA has a red-shifted NIR MCD band at 1510 nm ($\Delta\varepsilon$ = 1.2 mM^{-1} cm^{-1}).[1727,1728]

Fully oxidized NrfA has five *c*-type ferric hemes that give rise to unique EPR signals.[1704,1714,1716,1731] Here, it was proposed that Hemes 1 and 3 are weakly exchange-coupled, and thus, give rise to a unique set of EPR signals at g_{eff} = 2.87, >10 (*S. oneidensis* NrfA) and g_{eff} = 3.6, >10 (*E. coli* NrfA).[1704,1716,1721] Studies on metalloproteins and synthetic model complexes have demonstrated that the exact orientation of the imidazole planes in bis-His coordinated hemes greatly influences their EPR properties.[811,815,1732] Hemes with axial imidazole ligands with a close to parallel orientation of the imidazole planes display rhombic EPR spectra with pronounced g anisotropy, and signals for all three g values are usually observed in the spectra, where $g_z > g_y > g_x$. Hemes with a close to perpendicular orientation of the imidazole planes give rise to so-called "g_{max}" (or HALS) spectra with large g anisotropy and $g_{max\ (z)}$ = 3−4, whereas the other resonances are weak and often difficult to observe.[811] The more prominent Hemes 2 and 3 show axial His coordination with parallel imidazole groups. Here, Heme 2 shows EPR signals at g = 2.94, 2.29, 1.52 and 2.92, 2.3, 1.52 for *S. oneidensis* and *E. coli* NrfA, respectively.[1704,1716] Heme 3 signals are not observed in fully oxidized enzyme, due to exchange coupling with Heme 1, but can be identified in samples where Heme 1 has been reduced. Here, the EPR signals of Heme 3 were observed at 3.07, 2.25, ∼1.3 (*S. oneidensis* NrfA).[1716] In contrast, Hemes 4 and 5 show axial His ligation with a perpendicular orientation of the imidazole planes, and give rise to weaker g_{max} signals with g > 3.2 that are often difficult to identify.[1712,1716]

Stein et al. were able to assign the midpoint potentials of the five hemes in *S. oneidensis* NrfA, utilizing spectropotentiometric titrations.[1716] Here, midpoint potentials of −44 mV [Heme 1], −110 mV [Heme 4], −210 mV [Heme 2], −257 mV [Heme 5] and −382 mV [Heme 3] (vs SHE) were reported. Reduction potentials have also been assigned for other NrfA homologs, including *E. coli* NrfA (with midpoint potentials of −37 mV [Heme 2], −107 mV [Heme 1], −323 mV [Heme 3], and −250 to −400 mV [Hemes 4 and 5]; vs SHE)[1704] and *D. desulfuricans* (with midpoint potentials of +7 mV, −20 mV, −55 mV, −120 mV, and −325 mV versus SHE; however, the potentials could not be assigned to individual hemes in this study).[1733] These results provide insight into the sequence of electron transfers to the individual hemes in the pentaheme scaffold of NrfA.

4.4.1.4. Characterization of Intermediates.

Ferrous heme−nitrosyl complexes, ls-$\{FeNO\}^7$ in the Enemark−Feltham notation, have been extensively studied with many spectroscopic and theoretical methods as described in Section 2.2. Most recently, Pacheco and coworker were able to trap a ls-$\{FeNO\}^7$ intermediate in *S. oneidensis* NrfA, using spectropotentiometry.[327] Previously, it had been shown by protein film voltammetry experiments that catalytic turnover in *S. oneidensis*

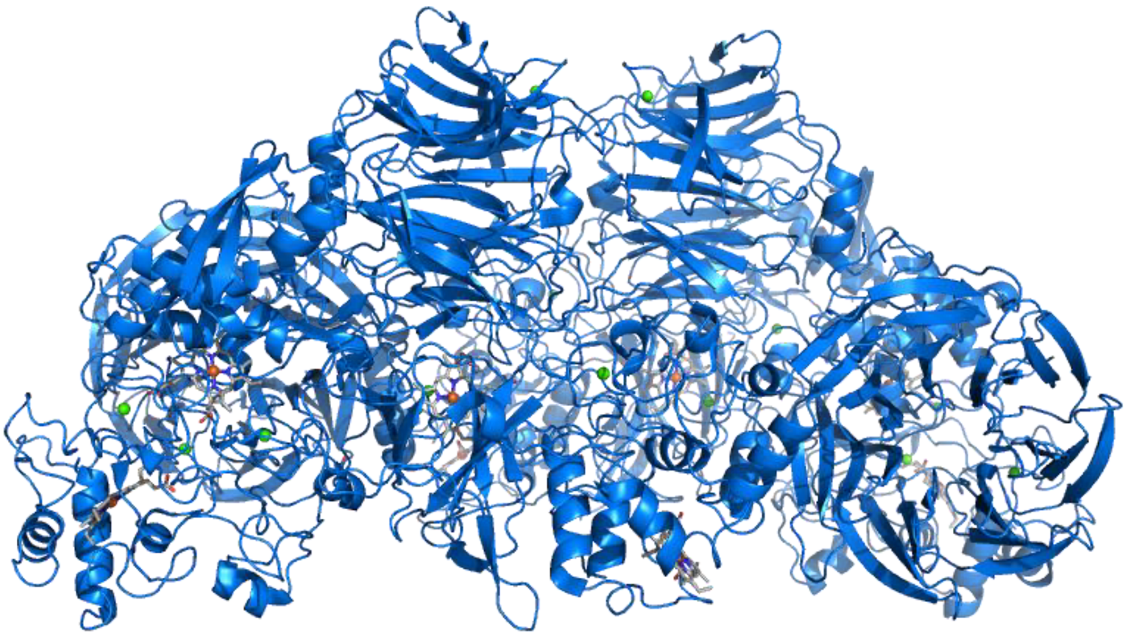

Figure 105. PyMOL generated image of the crystal structure of HZS from *K. stuttgartiensis* (PDB:5C2V).

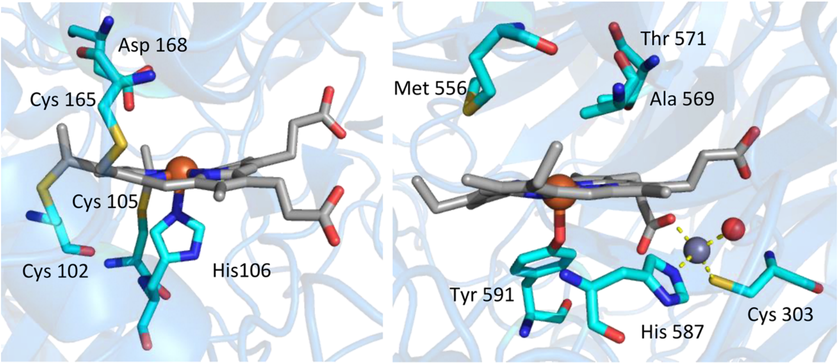

Figure 106. PyMOL generated images of the crystal structures of the active sites of *K. stuttgartiensis* HZS (PDB: 5C2V). Left: Heme γI, where reduction of NO to NH_2OH takes place. Right: Heme αI, where comproportionation of NH_2OH and NH_3 yields hydrazine.

NrfA requires an applied potential of at least −120 mV (vs SHE), which lies below the midpoint potential for the formation of the ls-$\{FeNO\}^7$ complex.[1734,1735] This indicates that it might be possible to trap the ls-$\{FeNO\}^7$ intermediate if a more positive potential is applied that stalls the catalytic cycle, thus preventing ammonia formation. Spectropotentiometric and time-resolved UV−vis absorption experiments indeed show that nitrite-loaded *S. oneidensis* NrfA can be reduced at high applied potential in a concerted two-electron step to generate the ls-$\{FeNO\}^7$ intermediate.[327] This species was then further studied using EPR spectroscopy. The ls-$\{FeNO\}^7$ intermediate shows unexpected EPR-spectral signatures with g = 2.2−2.05 (proposed to arise from exchange interactions between the ls-$\{FeNO\}^7$ Heme 1 and nearby hemes) and g_{eff} = 4.11, 3.9, 2.0 (proposed to correspond to a hs-$\{FeNO\}^7$ system; see Section 5.1).[327] Further work is necessary to fully analyze these unusual EPR-spectroscopic features.

4.4.2. ANAMMOX.

The first obligate intermediate in the ANAMMOX pathway, hydrazine (N_2H_4), is generated from NO and NH_4^+ by the heterotrimeric protein complex hydrazine synthase (HZS).[1736] *In vitro* HZS catalyzes the synthesis of N_2H_4 at a rate of 20 nmol/(mg enzyme) h, which accounts for about 1% of the *in vivo* activity.[329] The slow conversion observed *in vitro* might be due to the use of artificial electron donors, or the possibility that the full metabolic complex is needed for optimal HZS activity, which might have been disrupted during purification.[329] The unique biochemical properties of the ANAMMOX pathway have been studied in *Kuenenia stuttgartiensis*, which is the model organism that most of our knowledge about HZS is derived from.

4.4.2.1. Protein Structure of HZS.

The crystal structure of *K. stuttgartiensis* HZS, solved at 2.7 Å resolution, revealed a multiprotein complex consisting of a crescent-shaped dimer of heterotrimers, $(\alpha\beta\gamma)_2$, with an overall mass of ~330 kDa (see Figure 105).[328] HZS subunits are highly conserved in ANAMMOX bacteria with gene-encoded subunits Kuste2859−Kuste2861 (or KSMBR1_3601−KSMBR1_3603) and upstream gene cluster Kuste2854−Kuste2856 (or KSMBR1_3596−KSMBR1_3598).[1736−1738] The catalytically active unit is composed of one $\alpha\beta\gamma$ heterotrimer,[328] with two of the three subunits (α and γ) containing two *c*-type hemes, one of which (per subunit) has bis-His coordination (hemes αII and γII), while the other two hemes, one per subunit, are thought to be the putative active sites, as they are 5C hemes with unique structural motifs (hemes αI and γI; see Figure 106).[328] The edge-to-edge distance between the two hemes of the γ subunit

Scheme 60. Proposed Catalytic Mechanism for Hydrazine Synthesis by HZS[328]

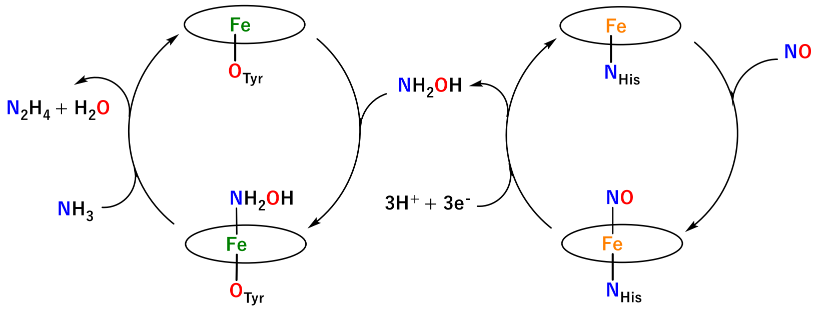

is 15 Å, and a conserved histidine (His144) is positioned between them. On the other hand, the edge-to-edge distance between the two hemes of the α subunit is 31 Å. Within the HZS structure, an intra-protein major tunneling system has been identified that guides substrates into the catalytic heterotrimer, and which also connects the heme sites γI and αI. This tunnel could allow for an intermediate of HZS, proposed to be NH_2OH, to diffuse from the γI site to the second active site, αI. Located inside the tunnel is a 16 amino acid-long loop of the β subunit (β245−260), which contains a conserved glutamate (Glu253) that binds a Mg^{2+} ion. The latter may help guide the intermediate from the γI to the αI site.

The proximal ligand of heme αI is a highly conserved tyrosine (Tyr591), which coordinates to the heme via its phenolate group.[328] In this case, the typical CXXCH heme binding motif is altered and rotated away from the heme, and interestingly, the histidine residue (His587) that is part of the CXXCH loop does not bind to the heme. Instead, His587 is bound to a Zn^{2+} ion that is further coordinated to one of the propionate groups of heme αI and Cys303, generating an atypical coordination sphere for the Zn^{2+} ion.[1739] The heme γI is coordinated to the proximal His106 residue and a distal water molecule that is further hydrogen-bonded to Asp168.[328] Heme γI does not only contain two covalently attached Cys residues within the typical binding motif of *c*-type hemes (Cys102 and Cys105), but it is also covalently attached to a third Cys residue (Cys165), which forms a bond to the C1 porphyrin methyl group. Therefore, both hemes αI and γI are quite unusual with surprising structural features, and it is a puzzling question how these structural features are related to function in HZS.

4.4.2.2. HZS Catalytic Mechanism. The proposed catalytic mechanism of how the HZS heterotrimer mediates hydrazine synthesis is based on preliminary genomic, biochemical, and spectroscopic data, and is summarized in Scheme 60.[328] At this point, this mechanism is highly speculative. The overall reaction proceeds via two half-reactions with the net eqn:

$$NO + NH_4^+ + 3e^- + 2H^+ \rightarrow N_2H_4 + H_2O \tag{22}$$

The catalytic mechanism is facilitated by the two 5C *c*-type hemes of HZS and a major tunneling system containing calcium ions and polar residues that allows intermediates and substrates to move to the respective active sites. First, NO (generated by nitrite reduction mediated by the heme cd_1 NIR e4136 in *K. stuttgartiensis*)[329,1737] is believed to enter the heme γI active site via a specific channel. Once NO binds to the heme, the resulting complex undergoes a three-electron reduction to generate NH_2OH. Electrons from an external electron donor enter the complex at heme γII and are shuttled to heme γI via His144, while protons may come from water molecules near heme γI, assisted by the conserved Asp168. The conserved Kuste2854 gene encodes for a soluble tetraheme *c*-type cytochrome protein, which is the proposed redox partner of HZS based on genomics.[1740] The interaction between the two proteins likely occurs in a surface-exposed region of the $(\alpha\beta\gamma)_2$ complex, where either one of the 6C hemes of HZS (αII and γII) may function as the entry point for the electrons.[1737,1738]

Once NH_2OH is generated at the γI site, it then travels through a designated major tunnel to the heme αI, forming a heme αI-NH_2OH adduct, where hydroxylamine is proposed to coordinate the heme via its N atom. This intermediate sits within a hydrophobic cleft of the enzyme that is proposed to minimize electrostatic shielding of the partial positive charge on the N atom.[328] A minor tunnel system that reaches heme αI from the proximal side of the heme is assumed to be the entry point of the second substrate, NH_4^+.[1741] It was further proposed that the Zn^{2+} site, via an acid/base reaction, would deprotonate the substrate to NH_3. This would allow NH_3 to attack the positively polarized N atom of NH_2OH, ultimately generating N_2H_4 through comproportionation. Nevertheless, this mechanistic proposal remains somewhat dissatisfactory, since an N−N coupling reaction between two nucleophiles, NH_2OH and NH_3, defies chemical intuition. This step would necessitate a harsh electronic perturbation of NH_2OH, and it is hard to imagine how this could occur by simple binding of NH_2OH to heme αI. More work is required to elucidate the mechanism of hydrazine formation by HZS. One possible pathway would be hydroxylamine dehydration, to form a Fe−NH_2^+ type intermediate, which would then be perfectly suited for attack by NH_3, to form an N−N bond and ultimately generate hydrazine.

4.5. NO Generation by Hydroxylamine Oxidation

Hydroxylamine oxidoreductase (HAO) is a multiheme enzyme that catalyzes the three-electron oxidization of NH_2OH to NO in COMAMMOX bacteria, as shown in eqn. 23.[271−273,543]

$$NH_2OH \rightarrow NO + 3e^- + 3H^+ \tag{23}$$

HAO plays an important role in the generation of energy during respiration for these chemoautotrophic bacteria by participating in the second step of aerobic ammonia oxidation.[269,270] The three electrons generated during hydroxylamine turnover are transferred to Cyt. c_{554}.[1742,1743] It should be noted here that for many decades HAO was thought to catalyze the four-electron oxidation of NH_2OH to NO_2^-;[1744] however, recent experimental evidence by Lancaster and coworkers has shown that the generation of nitrite is due to a non-enzymatic reaction of NO with O_2 in the originally conducted assays, and that NO is the actual enzymatic product of HAO-catalyzed hydroxylamine oxidation.[271] The currently proposed mechanism of HAO is further discussed below.

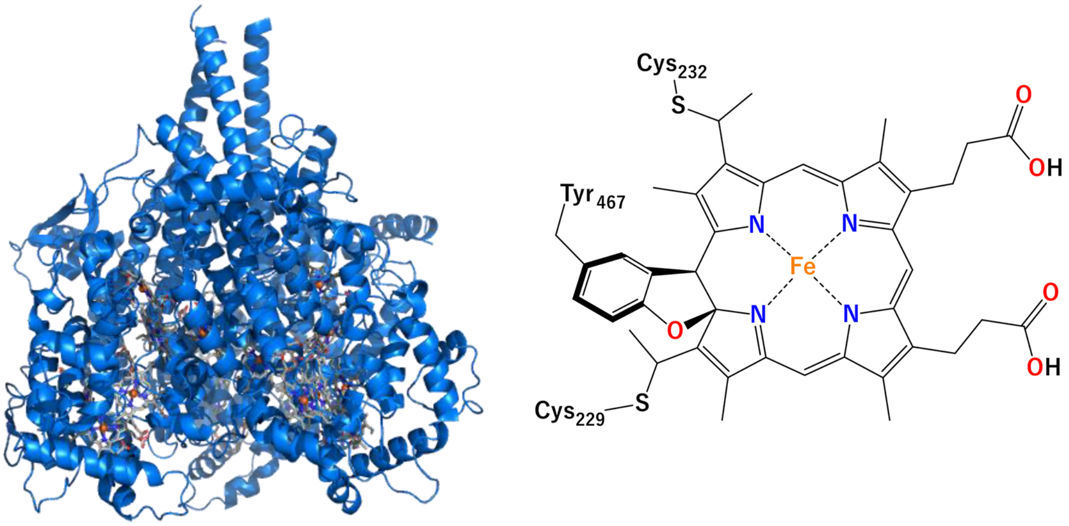

Figure 107. PyMOL generated image of the crystal structure of *N. europaea* HAO at 2.8 Å resolution (left; PDB: 4N4N). Structure of the P460 heme active site of HAO (right).

Note that heme proteins are also able to oxidize NH_2OH to HNO in the presence of H_2O_2.[1745,1746]

4.5.1. Protein Structure of HAO and Spectroscopic Characterization.

The X-ray crystal structures of HAO from *Nitrosomonas europaea* and *Kuenenia stuttgartiensis* show that HAO is a 24-heme homotrimeric protein, containing eight hemes per 67 and 61.5 kDa monomeric subunits, respectively (Figure 107, left).[272,273,1747] Seven of the eight hemes in a monomer subunit are bis-His coordinated *c*-type hemes and are likely involved in transferring electrons from the active site to the electron acceptor, Cyt. c_{554}, as substrate is oxidized.[272] The last heme in the chain is the active site, which, in the resting state, corresponds to a 5C heme with an $S_t = 5/2$ ground state. The active site is termed a "noncanonical" P460 heme. This unique P460 heme, with the typical covalent thioether linkages at Cys229 and Cys232, contains a double crosslink to Tyr491 at the 5′ *meso*-carbon and the pyrrole α-carbon positions of the heme, as shown in Figure 107, right.[272,273] The mechanism of formation of this unique tyrosine-porphyrin crosslink is currently unknown. The seven *c*-type hemes in the monomer of *N. europaea* HAO have midpoint potentials of +288, +11, −10, −162, −192, −265, and −412 mV, along with the P460 heme active site with a midpoint potential of −260 mV (all vs NHE at pH 7).[1748]

The overall trimeric structure of HAO is proposed to have important roles in catalysis. At the N-terminus of the homotrimeric protein is a large central cavity (30 Å wide and 15 Å deep) that has been proposed to be the Cyt. c_{554} binding site, allowing efficient electron transfer during catalysis.[272,273] On the other end, at the C-terminus of the protein, the homotrimeric structure is stabilized by the interaction (via hydrophobic contacts) of six long helices and three pairs of kinked helices.[273] Within the trimeric HAO structure, hemes are arranged in a ring-like motif and it has been proposed that such a ring-like arrangement allows for electron transfer between the subunits, which helps facilitate the extraction of three electrons from the substrate in rapid succession during catalysis.[1749]

HAO's unique P460 heme active site is a part of the large family of proteobacterial *c*-type cytochromes.[1750] The name of the P460 cofactor is derived from its Soret band near 460 nm in the ferrous state, and is typical for *c*-type hemes that feature additional covalent linkages between the heme macrocycle and amino acid side chains, as seen in the double linkage to Tyr 467 in HAOs P460 heme (see Figure 107, right). Furthermore, the unique P460 heme in HAO exhibits a ruffling distortion (see Section 2.3).[272] Ruffled hemes have been shown to have lower midpoint potentials, which might explain the relatively low value of −260 mV (versus NHE at pH 7) observed for the HAO active site,[764] which is lower than typical midpoint potentials for *c*-type hemes (but it is in the range of the other seven HAO *c*-type hemes (+288 to −412 mV); see above).[1748] The novel structure of the P460 heme in HAO may play an important role in catalysis, given its unusual structural and electronic properties.

The UV−vis spectrum of the as-isolated, fully oxidized *K. stuttgartiensis* HAO displays characteristic features of low-spin ferric *c*-type hemes, with a maximum at 408 nm in the Soret band region and a broad feature of lower intensity in the Q-band region between 500 and 600 nm. Upon reduction with dithionite, these features change: the *c*-type hemes now show the Soret band at 418 nm and two Q-bands at 522 and 551 nm, typical for low-spin, bis-His coordinated *c*-type hemes, whereas the Soret band of the P460 heme shifts to 468 nm. Using rRaman spectroscopy, it was further confirmed that the 468 nm feature is in fact the Soret band of the P460 heme, and that this heme is unique with a symmetry lower than that of protoporphyrin IX or chlorin.[1751] Furthermore, Mössbauer spectroscopy of fully reduced *N. europaea* HAO shows that the ferrous P460 heme is high-spin, and exhibits an unusually large quadrupole splitting ($\Delta E_Q = 4.21$ mm/s). Therefore, the iron center experiences the largest electric field gradient of any known naturally occurring ferrous heme center.[1752] The complicated EPR spectrum of as-isolated *N. europaea* HAO (due to the presence of 8 hemes per monomer) shows four distinguishable paramagnetic species, with signals that are influenced by the coupling that occurs within the octaheme unit of a monomer.[1753,1754] In the EPR spectrum of *N. europaea* HAO, species 1 shows signals at $g = 3.03$, 2.26, 1.20, species 2 at $g = 3.11$, 2.19, 1.35, species 3 at $g = 3.06$, 2.28, 1.27 and lastly, species 4 has signals at $g_{eff} = 8$ and corresponds to the P460 heme active site.[1753,1754] The P460 heme does not display a typical high-spin ferric heme EPR signal due to exchange coupling with a nearby heme.[1753,1754]

4.5.2. HAO Catalytic Mechanism. As pointed out above, utilizing NO scavenging assays with *N. europaea* HAO under both aerobic and anaerobic conditions, Caranto et al. showed that in contrast to previous beliefs, HAO catalyzes the three-electron oxidization of NH_2OH to NO, and not the four-electron oxidation to NO_2^-.[271] The currently proposed mechanism of HAO for the oxidation of hydroxylamine is shown in Scheme 12.[271] Kinetic measurements for HAO demonstrate rapid reactivity with substrate with the following parameters: *N. europaea* HAO: $V_{max} = 9.5 \times 10^{-6}$ mol NO/(mg protein) min, $K_m = 3.6 \times 10^{-6}$ M, $k_{cat} = 10.5\ s^{-1}$;[1755] *K. stuttgartiensis* HAO: $V_{max} = 4.8 \times 10^{-6}$ mol NO/(mg protein) min, $K_m = 4.4 \times 10^{-6}$ M, $k_{cat} = 4.9\ s^{-1}$;[1747] and *Methylacidiphilum fumariolicum SolV* (mHAO): $V_{max} = 5.5 \times 10^{-6}$ mol NO/(mg protein) min, $K_m = 1.4 \times 10^{-6}$ M, $k_{cat} = 7.2\ s^{-1}$.[1756]

During catalysis, hydroxylamine first binds to the ferric P460 heme active site, generating a 6C ferric hydroxylamine complex, which subsequently undergoes a two-electron oxidation to generate a proposed ls-$\{FeNO\}^7$ intermediate (see Scheme 12). This ferrous heme−nitrosyl complex then undergoes a one-electron oxidization to produce a ls-$\{FeNO\}^6$ species, which subsequently releases NO to regenerate the ferric P460 heme active site. Interestingly, the inverse reaction of oxidized HAO with NO also leads to the formation of a stable ls-$\{FeNO\}^6$ complex.[1754] Furthermore, DFT calculations suggest that the ruffling of the P460 heme destabilizes the ls-$\{FeNO\}^7$ intermediate and stabilizes the ls-$\{FeNO\}^6$ complex, enabling the oxidation step to occur at catalytic rates.[1757] In addition, it has been suggested that the ruffling increases the affinity of the P460 heme for hydroxylamine. These results illustrate how the chemical modifications of the P460 cofactor contribute in an important way to the ability of the P460 heme to oxidize hydroxylamine. Lastly, the electrons generated by HAO via hydroxylamine oxidation are shuttled to Cyt. c_{554}, which is proposed to serve as the electron acceptor protein under physiological conditions. Stopped-flow kinetic studies on the electron transfer between HAO and Cyt. c_{554} at physiological pH revealed that the first electron is transferred with a rate constant of 250−300 s^{-1}, whereas the second electron transfer is much slower, with a rate constant of only 25−30 s^{-1}.[1758] It was proposed that the protein-protein (HAO-Cyt. c_{554}) complex allows for the rapid transfer of the initial electron to Cyt. c_{554}, while the transfer of the second electron requires a reorganization of the HAO-Cyt. c_{554} complex.[1758]

Maalcke et al. observed a putative ls-$\{FeNO\}^7$ species in the P460 heme active site when *N. europaea* HAO crystals were soaked with hydroxylamine (see Figure 108).[1747] Here, it is proposed that hydroxylamine underwent a two-electron oxidation after binding to the ferric P460 heme in the crystal, generating the ls-$\{FeNO\}^7$ complex. Interestingly, the heme-bound NO shows two hydrogen bonds with the amino acids Asp291 and His292 (both with FeNO—heteroatom distances of 2.6 Å) in the active site. The ls-$\{FeNO\}^7$ complex exhibits an Fe−NO bond length of 1.9 Å and an Fe−N−O angle of 118°, as shown in Figure 108.[1747] The two hydrogen bonds help stabilize the ls-$\{FeNO\}^7$ complex and it is further proposed that both the SCS Asp and His residues assist in hydroxylamine oxidation by abstracting protons from hydroxylamine during catalysis. A similar role of a critical SCS glutamate residue in the Cyt. P460 active site for hydroxylamine oxidation was recently demonstrated by Lancaster and coworkers.[1759]

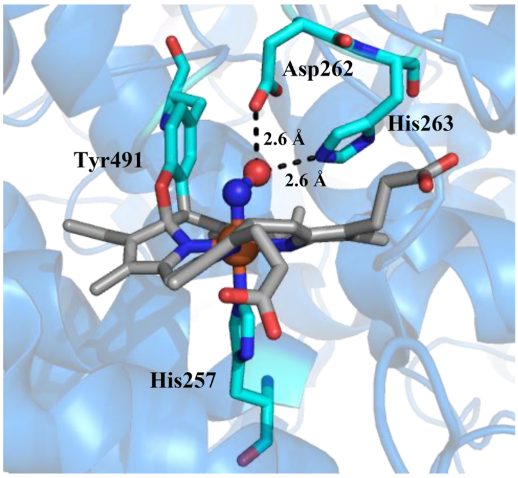

Figure 108. PyMOL generated image of the crystal structure of the active site of *N. europaea* HAO at 2.8 Å resolution, after soaking the crystals with hydroxylamine (PDB: 4N4O).

4.5.3. Comparison to Cyt. P460: Structure and Mechanism. Cyt. P460 is a small heme protein that is found in diverse classes of organisms, including AOBs, methanotrophs, proteobacteria, planctomycetes, acidobacteria, and bacteroidetes.[1750,1760] This enzyme has been shown to oxidize hydroxylamine, similar to HAO,[1761] despite sharing little sequence homology with the latter.[1762] Cyt. P460 has a simple, homodimeric structure, where each subunit only contains one P460 heme cofactor, unlike HAO's trimeric, multiheme structure. Interestingly, the crystal structure of *N. europaea* Cyt. P460 shows a difference in the crosslink of the P460 heme compared to HAO: in Cyt. P460, the *c*-type active site heme contains only a single crosslink between the heme's 13′ meso carbon and the N atom of the Lys70 side chain.[1763] In contrast to HAO, it has been shown that Cyt. P460 catalyzes the oxidation of hydroxylamine to nitrous oxide under aerobic and anaerobic conditions, as shown in eq 24:[1764]

$$2NH_2OH \rightarrow N_2O + H_2O + 4e^- + 4H^+ \qquad (24)$$

As shown in Scheme 12, the mechanism of Cyt. P460 has been proposed to be similar to HAO, where hydroxylamine first binds to the ferric P460 heme active site to generate a ferric hydroxylamine adduct. This adduct then undergoes a two-electron oxidation, generating a 6C ls-$\{FeNO\}^7$ species, which is subsequently oxidized to the analogous ls-$\{FeNO\}^6$ intermediate. At this point the mechanisms split: whereas HAO releases NO to close the catalytic cycle, the ls-$\{FeNO\}^6$ intermediate of Cyt. P460 reacts with a second molecule of hydroxylamine, leading to N−N bond formation and N_2O generation, according to eq 24. Lastly, a one-electron oxidation regenerates the ferric resting state of Cyt. P460. The detailed spectroscopic characterization of these different intermediates of the Cyt. P460 catalytic cycle has helped researchers to better understand the mechanism of HAO, despite the structural differences.[543,1759,1764] This is due to the fact that the many hemes present in HAO make it difficult to characterize intermediates of the reaction with hydroxylamine, in contrast to Cyt. P460. A detailed comparison of HAO and Cyt. P460 is provided in ref 543.

Table 23. Select Examples of hs-$\{FeNO\}^7$ Complexes

complex	ref	total spin S	ν(NO) [cm^{-1}]	CV	crystal structure	DFT	Fe–NO [cm^{-1}]	Fe–NO distance [Å]	Fe–N–O angle	N–O distance [Å]	geometry
				Mononuclear hs-$\{FeNO\}^7$							
$[Fe(TMPA)(BF)(NO)]ClO_4$	1771	3/2	1794		Yes			1.72–1.74	155/162	1.14–1.15	Octahedral
$[Fe(TMPA)(CH_3CN)(NO)](ClO_4)_2$	152	3/2	1810	Yes		Yes	509[a]				Octahedral
$[Fe(TMPA)(OTf)(NO)](OTf)$	1772	3/2 in CH_2Cl_2	1806	Yes	Yes	Yes		1.76	170	1.14	Octahedral
$[Fe(BMPA\text{-}tBu_2PhO)(OTf)(NO)]$	1772	3/2	1742	Yes	Yes			1.78	163	1.10	Octahedral
$[Fe(6\text{-}Me_3TMPA)(BF)(NO)]ClO_4$	1771	3/2	1802								
$[Fe(Me_3TACN)(N_3)_2(NO)]$	145, 1773, 1774	3/2	1690 (IR) 1712 (rR)	Yes	Yes	Yes	436	1.74	156	1.14	Octahedral
$[Fe(TIMEN^{Mes})(NO)]^{2+}$	82	3/2	1806	Yes	Yes	Yes		1.78	178	1.15	Tetrahedral
$[Fe(TMG_3tren)(NO)]^{2+}$	69, 1775	3/2	1739	Yes	Yes	Yes	484[a]	1.75	168	1.15	Trigonal bipyramidal
$[Fe(TMG_2dien)(OTf)(NO)](OTf)$	69	3/2	1770	Yes	Yes			1.75	162	1.16	Trigonal bipyramidal
$[Fe(Ar\text{-}nacnac)(Br)(NO)]$	235	3/2	1777 (C_6D_6)	Yes	Yes			1.64	176	1.22	Tetrahedral
$[Fe(N3PyS)(NO)]^+$	1769, 1776, 1777	3/2 (1/2)	1753	Yes	Yes	Yes		1.73	147	1.15	Octahedral
$[Fe(N3Py^{2Ph}SEtCN)(NO)](BF_4)_2$	1778	3/2	1812			Yes					Octahedral
$[Fe(L^R)(NO)]^-$ R = iPr	1779	3/2	1729	Yes	Yes			1.74	178	1.12	Trigonal bipyramidal
R = cyp		3/2	1739	Yes	Yes			1.74	173	1.14	Trigonal bipyramidal
R = dmp		3/2	1750	Yes	Yes			1.75	160	1.15	Trigonal bipyramidal
$[Fe(pida)(H_2O)(NO)]$	1780	3/2		Yes							
$[Fe(EDTA)(NO)]^{2-}$	145, 1781	3/2	1776				517	1.78[d]	156[d]	1.10[d]	
$[Fe(TMPzA)Cl(NO)]BPh_4$	1771, 1782	3/2	1796		Yes			1.74	157	1.15	Octahedral
$[Fe(salen)(NO)]$	660, 1768	3/2	1710		Yes	Yes		1.78	147	1.09–1.11	Sq. pyrmd
		1/2	1610		Yes	Yes		1.80	127	1.15	
$[Fe(TMC)(NO)](BF_4)_2$	1783	3/2 at r.t.[b]	1840	Yes	Yes			1.74	178	1.14	Sq. pyrmd
$[Fe(TMC)(OH)(NO)]BF_4$	1783		1890	Yes	Yes			1.62	178	1.14	Octahedral
$[NMe_4][Fe(NS_3)(NO)]$	1784	3/2	1639	Yes	Yes	Yes		1.76	146–148	1.11–1.18	Trigonal bipyramidal
$[Fe(BMPA\text{-}Pr)(Cl)(NO)]$	152	3/2	1726	Yes	Yes	Yes	484[a]	1.78	152	1.15	Octahedral
$\{Fe(BMPA\text{-}Pr)(NO)\}_6(OTf)_6$	152	3/2	1784	Yes	Yes	Yes	495[a]	1.76	149[c]	1.17	Octahedral
$\{Fe(BMPA\text{-}Pr)(NO)\}_6(ClO_4)_6$	152	3/2	1777	Yes	Yes			1.72	152[c]	1.18	Octahedral
$[NEt_4][Fe(S^tBu)_3(NO)]$	1044	3/2	1704		Yes	Yes		1.71	174	1.17	Tetrahedral
$[Fe(T1Et4iPrIP)(THF)(OTf)(NO)](OTf)$	1785, 1786	3/2	1831		Yes	Yes		1.77	169–174	1.15	Octahedral
$[Fe(H_2O)_2(ida)(NO)]$	1787	3/2	1772		Yes	Yes		1.78	155	1.11	Octahedral
$[Fe(^{Ph2}TIP)(CysAm)(NO)](BPh_4)$	1788	3/2	1817			Yes					Octahedral
$[Fe(H_2O)_5(NO)]^{2+}$	1789	3/2	1843		Yes	Yes		1.79	161	1.14	Octahedral

[a] Data reported for ^{57}Fe adducts from NRVS meaurements. [b] Exists in spin equilibrium. [c] Average Fe–N–O bond angles reported. [d] EXAFS.

5. NON-HEME IRON CENTERS AND NO

5.1. Mononuclear Non-Heme Iron NO Complexes in Different Oxidation States

Non-heme hs-$\{FeNO\}^7$ complexes are relevant in biology as intermediates in several different classes of enzymes, especially NORs.[641,1576,1592,1765] This includes bacterial rNORs, as discussed in Section 4.3, where the corresponding Fe_B(II)–NO adduct is potentially involved in catalysis, and flavodiiron proteins, which are dinuclear non-heme iron enzymes that are described below. In rNORs and flavodiiron proteins, these intermediates are often short-lived and reactive, so model

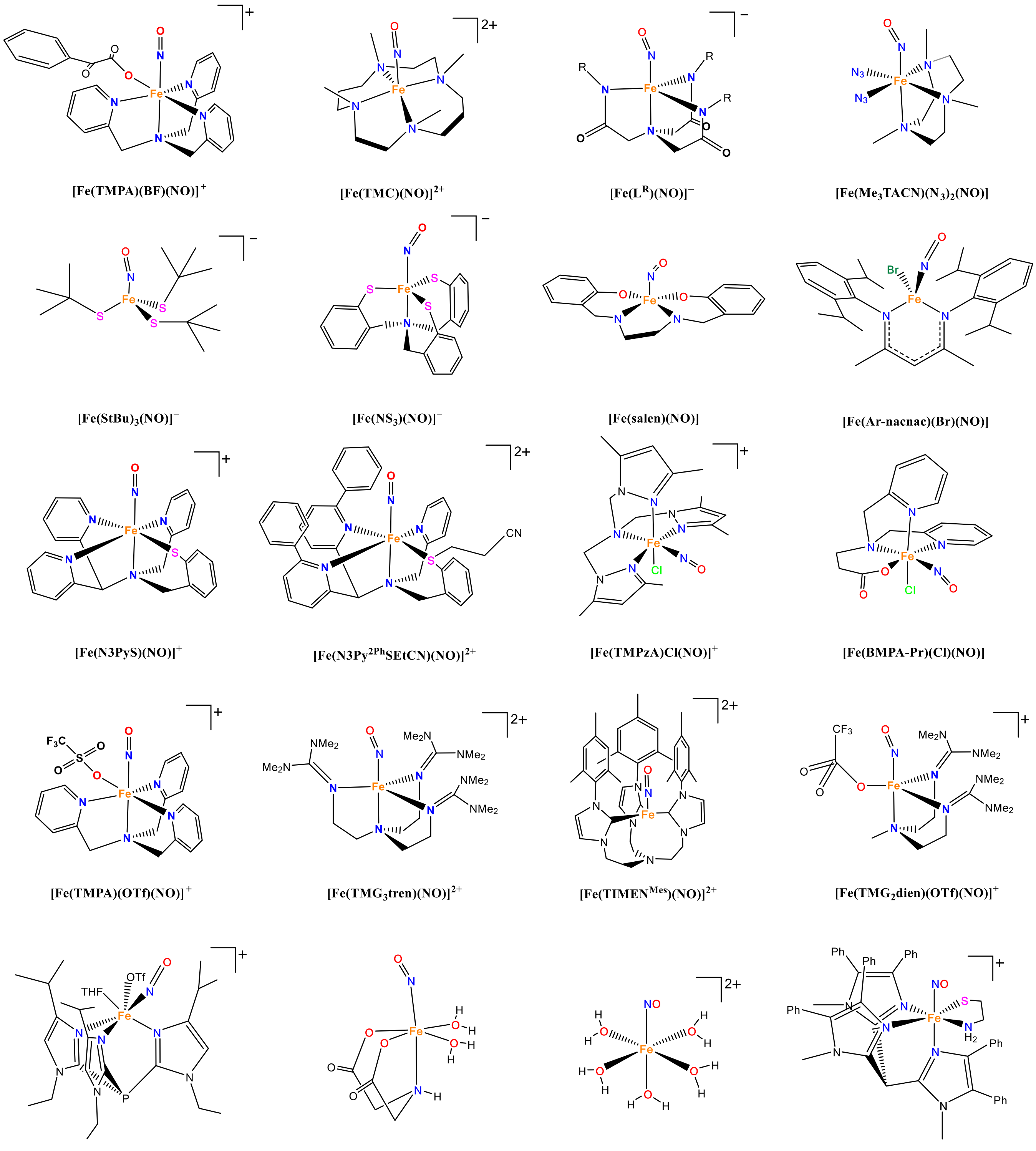

$[Fe(TMPA)(BF)(NO)]^{+}$ $[Fe(TMC)(NO)]^{2+}$ $[Fe(L^{R})(NO)]^{-}$ $[Fe(Me_3TACN)(N_3)_2(NO)]$

$[Fe(StBu)_3(NO)]^{-}$ $[Fe(NS_3)(NO)]^{-}$ [Fe(salen)(NO)] [Fe(Ar-nacnac)(Br)(NO)]

$[Fe(N3PyS)(NO)]^{+}$ $[Fe(N3Py^{2Ph}SEtCN)(NO)]^{2+}$ $[Fe(TMPzA)Cl(NO)]^{+}$ [Fe(BMPA-Pr)(Cl)(NO)]

$[Fe(TMPA)(OTf)(NO)]^{+}$ $[Fe(TMG_3tren)(NO)]^{2+}$ $[Fe(TIMEN^{Mes})(NO)]^{2+}$ $[Fe(TMG_2dien)(OTf)(NO)]^{+}$

$[Fe(T1Et4iPrIP)(THF)(OTf)(NO)]^{+}$ $[Fe(H_2O)_2(ida)(NO)]$ $[Fe(OH_2)_5(NO)]^{2+}$ $[Fe(^{Ph2}TIP)(CysAm)(NO)]^{+}$

Figure 109. Examples of hs-$\{FeNO\}^7$ and related spin-crossover complexes. See Table 23 for structural parameters and references for these compounds.

complexes have been used to investigate their electronic structures and reactivities. In addition, as discussed in the Introduction, NO can be used as a surrogate to study very unstable oxygen intermediates in mononuclear non-heme iron enzymes, especially the Fe(III)−superoxide adducts. Finally, non-heme iron sites are also used as sensors in biology, and they are potentially involved in the biosynthesis of N-nitroso and related natural products (see below as well). Besides the interest in these species originating from their biological relevance, hs-$\{FeNO\}^7$ complexes have also been a rich area of study for coordination chemists due to their interesting electronic properties (see ref 17 for a recent review).

5.1.1. Hs-$\{FeNO\}^7$ Complexes. Over the years, many mononuclear hs-$\{FeNO\}^7$ complexes have been prepared and

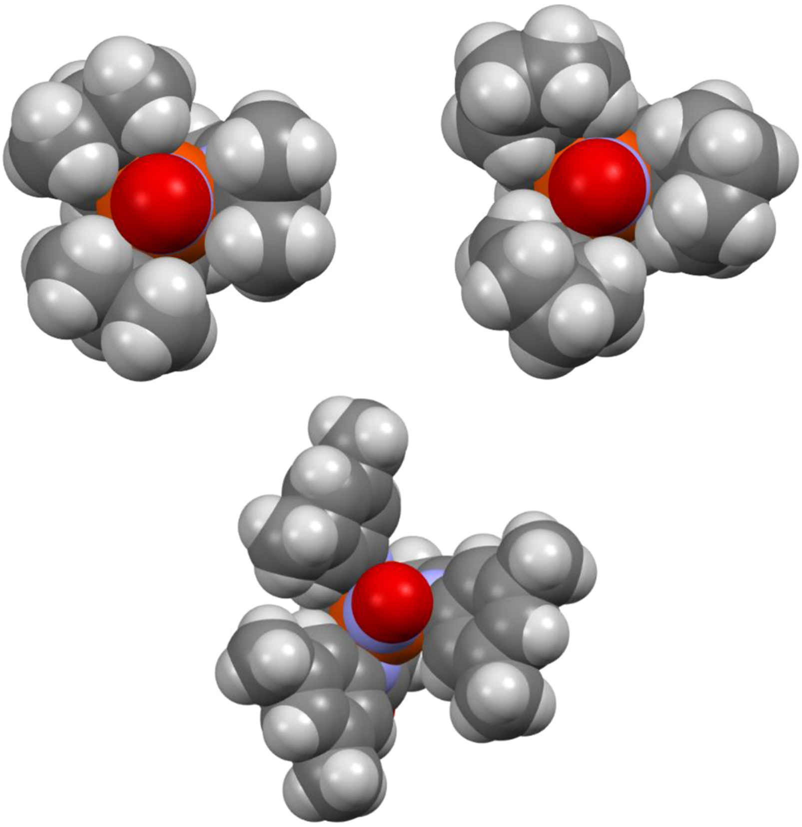

Figure 110. Space filling models of the crystal structures of the K[FeL^R(NO)] series with R = isopropyl/iPr, cyclopentyl/cyp (top, left to right) and 3,5-dimethylphenyl/dmp (bottom), showing a stepwise increase in cavity size.[1779]

studied (see Table 23 for select examples). These species are generally very stable and often unreactive, making them a prime target for detailed spectroscopic investigations to gain a better understanding of their electronic structures.[66,151,1766] Non-heme iron−NO complexes are usually formed by simply reacting an Fe^{II} precursor complex with NO gas. When macrocyclic N_4-type ligands or other strong field ligands are used, ls-{FeNO}^{7} complexes result, which often model the coordination environment and electronic structures of corresponding ferrous heme−nitrosyls (see Section 2.2). One example for such a complex is [Fe(cyclam-ac)(NO)]$^+$, as shown in Figure 4, top middle. With weak field ligands, especially polypyridine and related ligand systems with other N-heterocycles, hs-{FeNO}^{7} complexes usually result. In rare cases, for example by using salen-type ligands, complexes can also be obtained that show a spin-crossover[1767] and exist in the hs and ls state as a function of temperature.[1768−1770] Here, distinct temperature-dependent changes in ν(N−O), magnetic moment and physical properties are observed. Other such examples include complexes that change spin state upon variation of a coligand, for example by different solvent coordination conditions.[1772] The hs-{FeNO}^{7} complexes are usually 5C, either square-pyramidal or trigonal-bipyramidal, or 6C octahedral. Examples for such species, especially those discussed in the following, are shown in Figure 109.

6C hs-{FeNO}^{7} complexes typically show Fe−NO and N−O bond distances around 1.72−1.78 and 1.10−1.18 Å, respectively. Here, strongly anionic ligands lead to an elongation of the Fe−NO and N−O bonds. In the 5C case, for example hs-{FeNO}^{7} complexes with the tri-anionic ligands L$^{R\,3-}$ (see below), Fe−NO and N−O bond distances of 1.73−1.78 Å and 1.11−1.18 Å are observed, respectively. Interestingly, hs-{FeNO}^{7} complexes overall display a wide range of Fe−N−O angles that are affected by both steric and electronic effects, indicating that the FeNO moiety is free to bend in these systems, with little energetic punishment.[151] Without steric constraints, however, the typical bond angle is observed at <160°. Vibrational spectroscopy is a powerful tool to obtain insight into the properties of the Fe−NO bonds in these complexes. Specifically, the N−O and Fe−NO stretching frequencies are prominent features that can be used to probe the electronic structures of these complexes, and these vibrational features are also very sensitive to oxidation state changes of these systems. The N−O stretching mode is both IR and Raman active, and typically falls in the 1700−1820 cm^{-1} range for hs-{FeNO}^{7} complexes. While neutral coligands such as TMPA lead to complexes with higher N−O stretching frequencies, around 1780−1820 cm^{-1}, more electron-donating, anionic coligands shift the N−O stretching frequency to lower energy, in some cases close to 1700 cm^{-1} (see Table 23). The Fe−NO stretch is more difficult to determine, since this mode is often weak and obscured by other features in the low-energy region of the rRaman spectra, and it is often not IR-active. Additionally, many hs-{FeNO}^{7} complexes exhibit photodecomposition upon irradiation with laser light. To avoid these problems, NRVS can be utilized to identify the Fe−NO stretching modes in hs-{FeNO}^{7} complexes and their oxidized and reduced conjuguers.

Borovik and coworkers investigated the relation between steric bulk and the Fe−N−O angle in hs-{FeNO}^{7} complexes. For this purpose, they synthesized hs-{FeNO}^{7} complexes using a series of trianionic ligands H_3L^R with R groups of

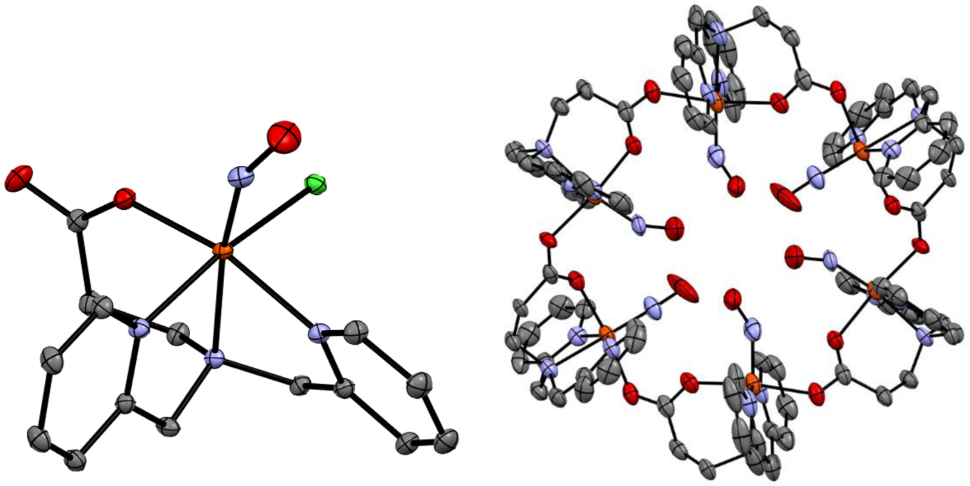

Figure 111. Left: Crystal structure of [Fe(BMPA-Pr)(Cl)(NO)]. Right: Crystal structure of $\{[Fe(BMPA)(NO)]\}_6(OTf)_6$.[152] All H atoms and counter ions (if applicable) are omitted for clarity.

different steric bulk (R = isopropyl/iPr, cyclopentyl/cyp, 3,5-dimethylphenyl/dmp).[1779] X-ray crystallography revealed Fe−NO and N−O bond distances of 1.74/1.74/1.75 Å and 1.12/1.14/1.15 Å for $K[Fe(L^{iPr/cyp/dmp})(NO)]$, respectively. Interestingly, the Fe−N−O angles are observed at 178/173/160° for this series, respectively. These results imply a significant influence of the steric bulk of the SCS on the structure of the FeNO unit. Specifically, $K[Fe(L^{iPr})(NO)]$ has a more restricted cavity with a diameter of ∼3 Å (see Figure 110), which results in a nearly linear Fe−N−O angle of 178°. A larger cavity, ∼8 Å in diameter, is formed by planar phenyl rings in $K[Fe(L^{dmp})(NO)]$. This leads to a much smaller Fe−N−O angle of 160°, which is in accordance with those reported for other hs-$\{FeNO\}^7$ complexes that lack steric hindrance around the NO binding site. IR spectroscopy revealed N−O stretching frequencies of 1729/1739/1750 cm^{-1} for the $K[Fe(L^{iPr/cyp/dmp})(NO)]$ series, respectively, which is in the typical range for hs-$\{FeNO\}^7$ complexes.

In another study, Berto et al. investigated hs-$\{FeNO\}^7$ complexes with the general formula [Fe(BMPA-Pr)(NO)]X (BMPA-Pr^- = N-propanoate-N,N-bis(2-pyridylmethyl)amine anion; X = Cl^-, OTf^-, ClO_4^-).[152] Whereas the complex with X = Cl^- produces a typical mononuclear hs-$\{FeNO\}^7$ species, as revealed by X-ray crystallography (see Figure 111, left), the application of a non-coordinating counter ion (X = OTf^-, ClO_4^-) led to the formation of "metallacrown" structures,[1790,1791] $\{[Fe(BMPA)(NO)]\}_6(X)_6$, where six complexes come together and form a ring. Here, the individual building blocks are connected by the carboxylate groups of the coligands (see Figure 111, right), and all six NO moieties point towards the center of the ring. Regardless, the geometries of all of these hs-$\{FeNO\}^7$ units are pseudo-octahedral. Structural parameters of these complexes are typical, and listed in Table 23. IR spectroscopic data of [Fe(BMPA-Pr)(Cl)(NO)] revealed ν(N−O) at 1726 cm^{-1}, while the metallacrowns have larger N−O stretching frequencies of 1777 and 1784 cm^{-1} for $\{[Fe(BMPA)(NO)]\}_6(ClO_4)_6$ and $\{[Fe(BMPA)(NO)]\}_6(OTf)_6$, respectively.

The properties of hs-$\{FeNO\}^7$ complexes have been studied in much detail using a variety of spectroscopic techniques including UV−vis absorption, IR, rRaman, MCD, EPR, XAS and NRVS, besides other methods. Since NO is a non-innocent ligand, the electronic structure of hs-$\{FeNO\}^7$ complexes is not a priori clear (see Scheme 3). Solomon and coworkers used XAS, rRaman, UV−vis absorption, MCD and EPR spectroscopy in combination with scattered-wave (SW) SCF-Xα calculations to investigate the electronic structures of the hs-$\{FeNO\}^7$ complexes $[Fe(Me_3TACN)(N_3)_2(NO)]$ and $[Fe(EDTA)(NO)]^{2-}$ as well as that of the ferrous NO adduct of the enzyme soybean lipoxygenase.[144,145] These studies showed that hs-$\{FeNO\}^7$ complexes are best described as hs-Fe(III)−$^3NO^-$ systems, where the spins of hs-Fe^{III} (S = 5/2) and the triplet $^3NO^-$ ligand (S = 1) are AF coupled, resulting in the experimentally observed S_t = 3/2 spin state of these complexes.[145] This electronic structure is illustrated in the MO diagram in Figure 112. Further studies by Lehnert and coworkers have shown that the $^3NO^-$ ligand acts predominantly

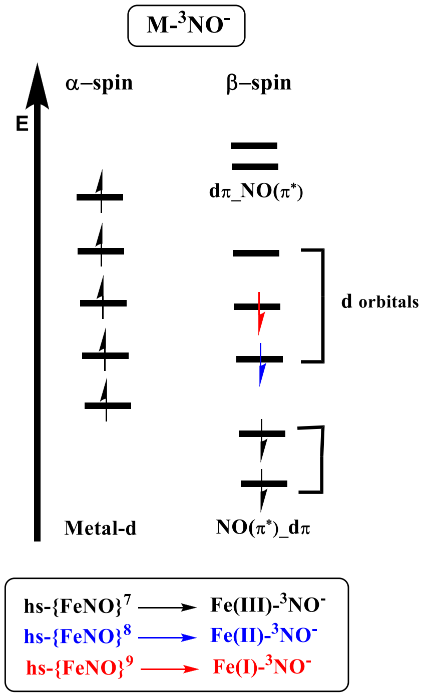

Figure 112. MO diagram showing the typical electronic structure of different hs-$\{MNO\}^{7-9}$ complexes, as indicated.

as a strong π-donor ligand in these complexes, leading to a very covalent Fe−NO bond.[74,152] This is reflected by the strong admixture of d-orbital character into the singly-occupied (β-spin, in a spin-unrestricted scheme) $^3NO^-(\pi^*)$ orbitals. The corresponding bonding combinations, $\pi^*_x\_d_{xz}$ and $\pi^*_y\_d_{yz}$ (with the Fe−N(O) vector corresponding to the z axis), usually have around 20-35% d_{xz}/d_{yz} contributions, as shown in Figure 113, middle. Unlike the original SW SCF-Xα calculations by Solomon and coworkers, DFT calculations with typical functionals (BP86, B3LYP, etc.) do not show significant σ donation from the 2σ^* orbital of $^3NO^-$ to the hs-Fe^{III} center.[151,152] Instead, a weak π-backbonding interaction between the occupied (mixed) α-d_{z^2}/d_{xz} orbital of Fe and the empty in-plane α-π^* orbital of $^3NO^-$ is sometimes observed, which is related to the bending of the FeNO unit. Overall, $^3NO^-$ is a weak π-acceptor (α-spin manifold) and a strong π-donor (β-spin manifold) ligand in hs-$\{FeNO\}^7$ complexes.

The covalency of the Fe−NO bond is further modulated by the properties of the coligand. This was first investigated in a series of [Fe(BMPA-Pr)(NO)](X) (X = Cl^-, ClO_4^-, OTf^-; see above) and related complexes, using vibrational spectroscopy coupled to DFT calculations.[152] Complexes with strongly donating, anionic ligands decrease the effective nuclear charge of iron which, in turn, lowers π-donation from the singly occupied π^* orbitals of $^3NO^-$ to the iron center. This leads to weaker Fe−NO bonds, and because this increases the electron density in the N−O antibonding π^* orbitals, this simultaneously weakens the N−O bond as well. Consequently, the weaker Fe−NO and N−O bonds lead to lower Fe−NO and N−O stretching frequencies in the presence of more electron-rich iron centers. In contrast, neutral ligands increase the effective nuclear charge of the iron center which then leads to an increase in π-donation from the $^3NO^-$ ligand, thus strengthening the Fe−NO and N−O bonds simultaneously, and increasing the corresponding stretching frequencies. The experimental trend in the Fe−NO and N−O vibrational frequencies of [Fe(BMPA-Pr)(NO)](X) and related complexes directly supports these conclusions, as shown in Figure 114.[152] Importantly, the data show a direct correlation of the Fe−NO and N−O vibrational frequencies, in agreement with these ideas. An inverse correlation, which would be indicative of a primary change in π-backbonding along the series, is not observed. In the case of very electron-deficient iron centers, as in the case of the brown ring compound, $[Fe(OH_2)_5(NO)]^{2+}$ (N−O stretch: ∼1843 cm^{-1}), it has recently been proposed that these complexes could also adopt a hs-Fe(II)−NO$^\bullet$ electronic structure, but further experimental work is necessary to support this claim.[1789]

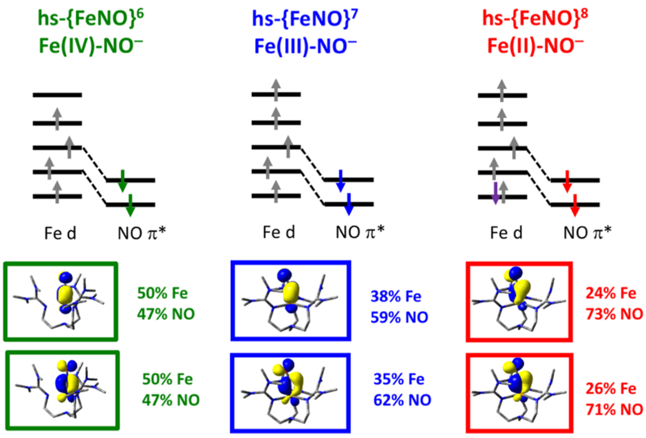

Figure 113. Electronic structure of the hs-$\{FeNO\}^{6-8}$ series with the TMG$_3$tren coligand.[74] Reprinted with permission from ref 88. Copyright 2019 American Chemical Society.

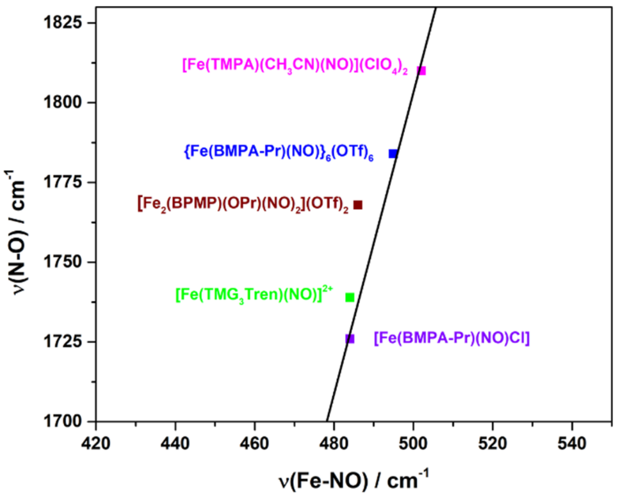

Figure 114. Correlation plot showing the experimental trend in the Fe−NO and N−O vibrational frequencies of [Fe(BMPA-Pr)(NO)]-(X) and related complexes, as indicated.[152]

The hs-Fe(III)−$^3NO^-$ electronic structure description of hs-$\{FeNO\}^7$ complexes is further reflected in a direct correlation between the Fe−N−O angles and the N−O stretching frequencies in these complexes, as first noted by Ferman and coworkers.[1786] This correlation is again explained by the modulation of the π-donation from the bound $^3NO^-$ (S = 1) ligand to the hs-Fe^{III} center. Here, stronger π-donation from the $^3NO^-$ ligand leads to stronger Fe−NO π-bonds and a more linear FeNO unit, to optimize the overlap between the Fe(d_π) and $NO^-(\pi^*)$ orbitals (which maximizes in a linear Fe−N−O geometry). At the same time, the increased π-donation from the $^3NO^-$ ligand also leads to a strengthening of the N−O bond and an increase in the N−O stretching frequency, as described above. The observed, direct correlation between the Fe−N−O angle and ν(N−O) therefore further supports the bonding description of hs-$\{FeNO\}^7$ complexes outlined above. At the same time, this correlation shows that besides steric effects, as determined by Borovik and coworkers (see above), electronic effects also influence the Fe−N−O angle, via the magnitude of π-donation from the $^3NO^-$ ligand to the iron center.

Another illustrative example in this regard are hs-$\{FeNO\}^7$ complexes with the sterically unhindered TMPA coligand (see Figure 109). The crystal structure of [Fe(TMPA)(OTf)-(NO)](OTf) revealed Fe−NO and N−O bond lengths of 1.76 and 1.15 Å, respectively, and an Fe−N−O bond angle of 170° for this compound.[1772] This is surprising, considering the similarities between this complex and [Fe(TMPA)(BF)(NO)]-(ClO_4) (BF^- = benzoylformate; Fe−N−O angle: 155/162° for two conformational isomers) reported earlier by Que and coworkers.[1771] These findings again support the idea that the Fe−N−O angle is also related to electronic factors; specifically, a very covalent Fe−NO bond due to an electron-poor iron center. Correspondingly, IR spectroscopy revealed a ν(N−O) of 1806 cm^{-1} for [Fe(TMPA)(OTf)(NO)](OTf), compared to 1794 cm^{-1} for [Fe(TMPA)(BF)(NO)](ClO_4).

The electronic structure of hs-{FeNO}^{7} complexes is further reflected by their physical and spectroscopic properties. EPR spectra of hs-{FeNO}^{7} complexes usually show axial symmetry ($E/D < 0.05$),[151] with $g_{eff} = 4$ and 2, indicative of their $S_t = 3/2$ spin states, but some cases with more rhombic EPR signals have also been reported. For example, $[Fe(EDTA)(NO)]^{2-}$ and $[Fe(Me_3TACN)(N_3)_2(NO)]$ show E/D values of 0.015 and ~0, respectively, with D values of +12−20 cm^{-1} and +12 cm^{-1} for these complexes, respectively.[145] In the case of the ferrous NO adduct of FeSOD, a split $S_t = 3/2$ signal is observed, corresponding to two distinct, rhombic hs-{FeNO}^{7} species with E/D values of 0.154 (major) and 0.128 (minor) and D values of +6 and +12 cm^{-1}, respectively.[146] [Fe(TMPA)(OTf)(NO)](OTf) is an example for a complex that shows a solvent-dependent spin state change.[1772] In a non-coordinating solvent such as CH_2Cl_2, the typical $S_t = 3/2$ EPR spectrum is observed with signals at $g_{eff} = 3.91$ and 2.00. However, EPR data recorded in a coordinating solvent such as CH_3CN revealed a new signal at $g = 2$, indicating the partial formation of a ls-{FeNO}^{7} complex with $S_t = 1/2$. This is in accordance with the observation of a new peak at 1701 cm^{-1} in the solution IR spectrum of [Fe(TMPA)(OTf)(NO)](OTf) in CH_3CN, corresponding to the N−O stretch of the ls species. This spin state change is likely due to coordination of CH_3CN to the complex in solution, displacing triflate as the 6th ligand. In this regard, it is worth noting that ferrous TMPA complexes are close to the spin crossover point.[1792]

Magnetic susceptibility measurements further support these findings and reveal magnetic moments (μ_{eff}) in the range of 4.0−4.5 μ_{BM} at room temperature for hs-{FeNO}^{7} complexes, in agreement with their $S_t = 3/2$ ground states. In comparison, for an ideal $S_t = 3/2$ system, the spin-only magnetic moment is 3.87 μ_{BM} (calculated from the equation $\mu_S = g\sqrt{S(S+1)}\ \mu_{BM}$). The often-observed larger magnetic moments in hs-{FeNO}^{7} complexes have been explained by either the population of low-lying excited electronic states at room temperature, or the presence of residual angular momentum in the ground state (by spin-orbit coupling with low-lying excited electronic states).[82,145,1773]

The oxidation state of iron in hs-{FeNO}^{7} complexes has been assessed both by Fe K-edge XAS and Mössbauer spectroscopy.[69,82,145,1769,1793] First, in XAS, the edge position is correlated with the iron oxidation state, where a shift in the edge position of >1.5 eV is usually associated with a change in oxidation state of the metal (in closely related complexes with the same overall coordination environment). In one example, a shift in the Fe K-edge to higher energy by ~2 eV was observed upon NO coordination to the ferrous precursor, $[Fe(TMC)(N_3)](BF_4)$, yielding $[Fe(TMC)(NO)](BF_4)_2$.[145,1773] This shift in the Fe K-edge is consistent with an oxidation of the iron center from Fe^{II} to Fe^{III} upon NO binding. In addition, Fe K-edge XAS also shows a pre-edge feature, which corresponds to the 1s → 3d transition, revealing additional information about the oxidation state of the metal center. A single band is observed between 7111 and 7113 eV for hs-{FeNO}^{7} complexes. This single feature is indicative of the ferric oxidation state, while ferrous complexes usually show additional transitions leading to a splitting of the 1s → 3d transition.[145] A very good example for this utility of XAS was given in a study on a series of analogous Fe^{II}, Fe^{III}, and hs-{FeNO}^{7} complexes with the EDTA^{4-} ligand scaffold (see Figure 115).[144,145] In this study, the pre-edge energies of the Fe^{II} and Fe^{III} complexes were identified at 7111.5 and 7112.9 eV, respectively. In comparison, the pre-edge feature of the NO complex was observed at 7112.8 eV. Not only does the pre-edge energy of $[Fe(EDTA)(NO)]^{2-}$ lie close to that of the oxidized iron-EDTA complex, the intensity and shape of the feature is also more similar to the ferric complex, supporting a hs-Fe(III)−^{3}NO$^-$ electronic structure of the complex. In a different study, sulfur K-edge XAS was used to determine the oxidation state of iron in a hs-{FeNO}^{7} complex with a thiolate coligand.[1769]

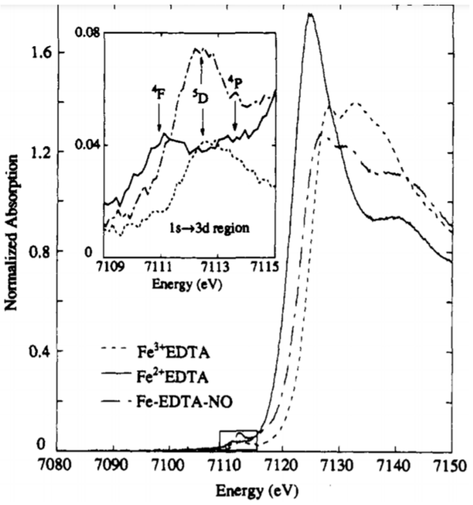

Figure 115. Fe K-edge XAS data collected for ferrous, ferric, and ferrous nitrosyl complexes using EDTA^{4-}. Samples were collected at 85 K using 50 mM concentrations, and data were normalized using standard pre-edge background subtraction and spline fitting techniques. Reprinted with permission from ref 144. Copyright 1992 American Chemical Society.

Using Mössbauer spectroscopy, the isomer shift can be used as a sensitive probe of iron oxidation state, in a series of closely related complexes. For example, the hs-Fe^{II} complex $[Fe(TMG_3tren)(CH_3CN)](OTf)_2$ (TMG_3tren = 1,1,1-tris{2-[N^2-(1,1,3,3-tetramethylguanidinio)]ethyl}amine) shows an isomer shift δ = 0.98 mm/s, which shifts to 0.48 mm/s upon NO binding and formation of $[Fe(TMG_3tren)(NO)](OTf)_2$.[69,74] The isomer shift is sensitive to the effective nuclear charge of the ^{57}Fe center, where δ decreases as the oxidation state of the ^{57}Fe center increases. In this case, since the electronic structure of the nitrosylated complex is again of hs-Fe(III)−^{3}NO$^-$ type, the isomer shift decreases, indicating a change in the oxidation state of the metal center from Fe^{II} to Fe^{III} upon NO binding.

Optical spectra of non-heme hs-{FeNO}^{7} complexes have been obtained using both UV−vis and MCD spectroscopy for a variety of systems. Because of the different selection rule of MCD spectroscopy, this technique is particularly sensitive for electronic transitions that involve the metal center in a given complex (i.e., ligand field and metal-to-ligand and ligand-to-metal charge-transfer transitions).[529,676,1794,1795] In addition, by performing variable-temperature variable-field (VTVH) experiments, one can determine the polarizations of the optical transitions in a complex, which further assists in spectral assignments.[1796,1797] Typically, broad, medium-intense features are observed in the 300−700 nm range for hs-{FeNO}^{7} complexes that are generally assigned to ^{3}NO$^-$(π^*) → Fe(III) charge-transfer transitions and ligand field transitions.[145−147] For example, $[Fe(EDTA)(NO)]^{2-}$ and $[Fe(Me_3TACN)(N_3)_2(NO)]$ show at least five distinct transitions in the visible region of the absorption spectrum. These signals were assigned

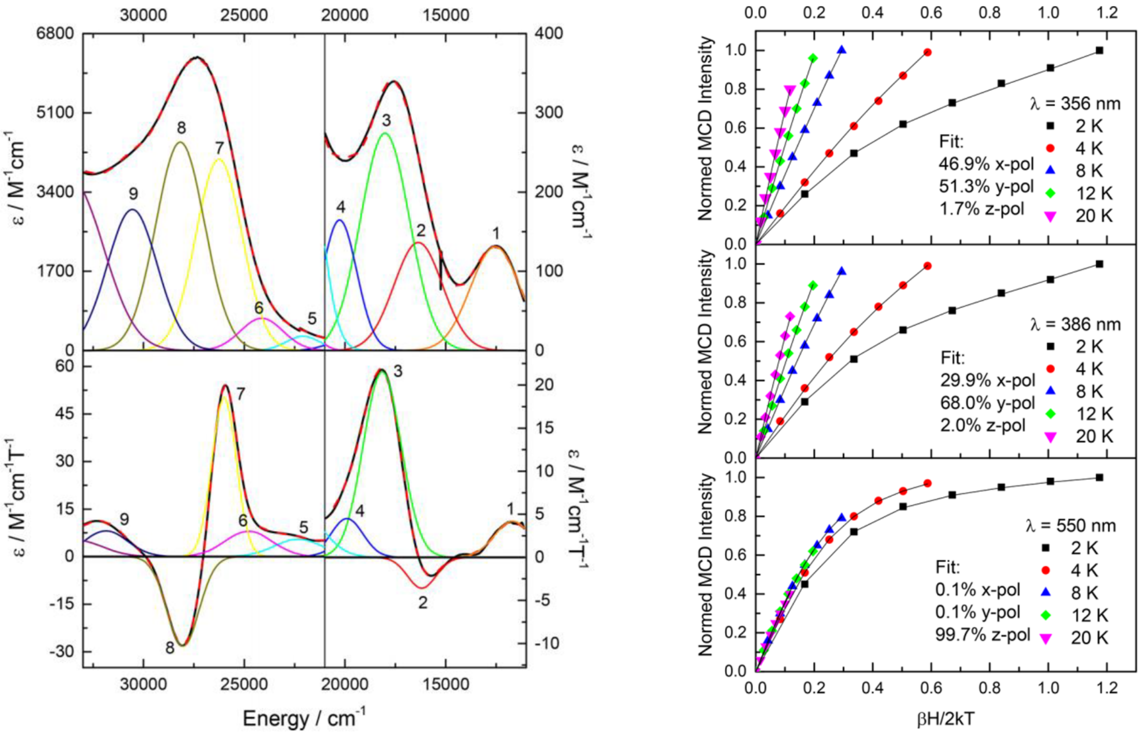

Figure 116. Left: Gaussian fit of the UV−vis (top) and low-temperature MCD (bottom) spectra of the hs-$\{FeNO\}^7$ complex $[Fe(TMG_3tren)(NO)]^{2+}$. Right: MCD saturation isotherms of bands 3, 7 and 8 at 550, 386 and 356 nm, respectively. Reprinted with permission from ref 69. Copyright 2018 American Chemical Society.

to two d-d transitions ($\leq$15 000 cm^{-1}) and three $^3NO^-(\pi^*) \rightarrow$ Fe(III) charge-transfer transitions (18 000−25 000 cm^{-1}).[145] Similarly, MCD spectroscopy revealed seven unique electronic transitions in the visible region for the ferrous NO adduct of FeSOD, which were again assigned to a combination of $^3NO^-(\pi^*) \rightarrow$ Fe(III) charge-transfer and d-d transitions.[146]

The hs-$\{FeNO\}^7$ complex $[Fe(TMG_3tren)(NO)]^{2+}$ mentioned above is another species whose optical properties were analyzed in detail.[69,1775] This complex is a 5C trigonal-bipyramidal species with typical Fe−NO and N−O bond distances of 1.75 and 1.15 Å, and an Fe−N−O bond angle of 168°. The vibrational properties of this complex are typical as well, with ν(N−O) = 1739 cm^{-1} and ν(Fe−NO) = 484 cm^{-1}. $[Fe(TMG_3tren)(NO)]^{2+}$ shows an intense absorption band at 368 nm and two lower-intensity features at 569 nm and 800 nm in the UV−vis spectrum. To gain further insight into the nature of these electronic transitions, VTVH MCD measurements were performed.[69] As shown in Figure 116, the intense absorption band at 368 nm is resolved into two features that form a so-called pseudo **A**-term signal (bands 7 and 8, Figure 116) by MCD spectroscopy. The two absorption features at lower energy are further resolved into four bands, as shown in Figure 116. Interestingly, bands 1−4 at low energy and the pseudo-**A** term signal at higher energy show completely different saturation behavior, as shown in Figure 116, right. While a strong nesting behavior of the saturation isotherms is observed for the high energy bands 7 and 8, an overlaid behavior is observed for the low-energy bands 1-4. By fitting these VTVH isotherms, it was shown that the higher energy features 7 and 8 are in-plane (xy) polarized (with the z direction corresponding to the Fe−N(O) vector), and hence, belong to guanidine-to-iron charge-transfer transitions. In contrast, the lower energy band at 550 nm (band 3) is completely z-polarized, and thus, was assigned to an $^3NO^-(\pi^*) \rightarrow Fe^{III}$ charge-transfer transition.[69]

In a few cases, hs-$\{FeNO\}^7$ complexes have been shown to undergo a disproportionation reaction to form $\{Fe(NO)_2\}^9$ DNICs, following the eqn:

$$2\,\text{hs-}\{FeNO\}^7 \rightarrow \{Fe(NO)_2\}^9 + \text{“}Fe^{III}\text{”} \tag{25}$$

The first observation of this reaction was reported by Que and coworkers, discovered by exposing the ferrous complex $[Fe(6\text{-}Me_3TMPA)(CatH)(NO)]X$ (6-Me_3TMPA = tris[(6-methylpyridyl)methyl]amine; CatH$^-$ = monoprotonated catecholate) to NO gas.[1798] Here, a brown, metastable hs-$\{FeNO\}^7$ complex was initially formed in solution, before a slow change in color of the solution to purple-blue was observed. Characterization of this brown solution with EPR spectroscopy revealed a typical axial $S_t = 3/2$ signal with g_{eff} = 4.0, 3.9, 2.0 (E/D = 0.006), identifying this species as a hs-$\{FeNO\}^7$ complex. The final NO-containing product was structurally and spectroscopically characterized as the $\{Fe(NO)_2\}^9$ complex $[Fe(6\text{-}Me_3TMPA)(NO)_2](ClO_4)$. A similar reaction was also observed by Speelman et al.[652] Here, reaction of a solution of $Fe(CH_3CN)_2(OTf)_2$ and dmp (dimethylphenanthroline) with NO gas led to the formation and isolation of the $\{Fe(NO)_2\}^9$ complex $[Fe(dmp)(NO)_2](OTf)$, which was subsequently characterized. When the reaction was carried out at −80 °C, formation of a hs-$\{FeNO\}^7$ complex as an intermediate of the reaction was demonstrated. This complex was found to be stable at low temperature, but upon warming up of the solution to room temperature, disproportionation and formation of the DNIC product was observed.[652] Interestingly, the hs ferric product obtained after formation of the DNIC, according to eq 25, is capable of oxidizing excess NO gas to regenerate the ferrous precursor complex, which subsequently binds NO and

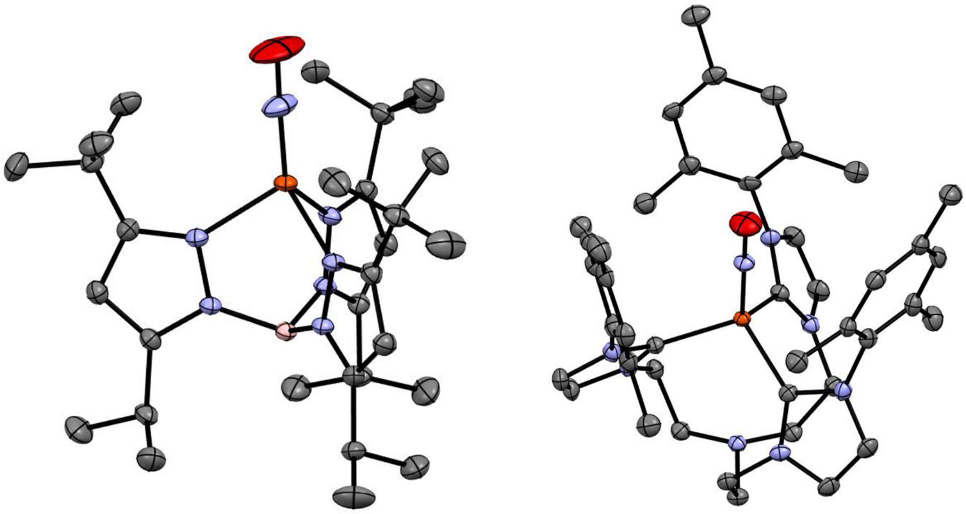

Figure 117. Left: Crystal structure of the stable hs-$\{FeNO\}^8$ complex [Fe(L3)(NO)].[84] Right: Crystal structure of the hs-$\{FeNO\}^8$ complex [Fe(TIMEN^{Mes})(NO)](BF_4).[82] All H atoms and counter ions (if applicable) are omitted for clarity.

produces more $\{Fe(NO)_2\}^9$ DNIC. This is different from the observations by Que and coworkers, where the ferric product of the reaction does not react further with NO.

5.1.2. Hs-$\{FeNO\}^8$ Complexes. Using electrochemical means or chemical one-electron reduction, the hs-$\{FeNO\}^7$ complexes can be reduced by one electron to their hs-$\{FeNO\}^8$ counterparts. Curiously, whereas hs-$\{FeNO\}^7$ complexes are very stable, as discussed above, the hs-$\{FeNO\}^8$ complexes are unstable and reactive. In diiron complexes of [hs-$\{FeNO\}^7]_2$ type, reduction induces N−N coupling and N_2O formation, as discussed below. In the case of mononuclear hs-$\{FeNO\}^8$ complexes, the major reaction seems to be disproportionation, to form DNICs. However, the mechanism of this reaction is currently not well understood. Speelman et al. characterized the 5C hs-$\{FeNO\}^8$ complex [Fe(TMG_3tren)(NO)]$^+$, as part of a study on the only available series of stable hs-$\{FeNO\}^{6-8}$ complexes with a single coligand scaffold (see Figure 4, bottom).[69,1775] The hs-$\{FeNO\}^8$ species was structurally characterized by EXAFS and shows an Fe−NO bond distance of 1.76 Å and an Fe−N−O angle of 150°. Upon one-electron reduction of the hs-$\{FeNO\}^7$ precursor, the N−O stretch shifts from 1748 cm^{-1} to 1618 cm^{-1}. Similarly, the hs-$\{FeNO\}^8$ complex also has a weaker Fe−NO bond, with an Fe−NO stretch of 435 cm^{-1} compared to 484 cm^{-1} in the hs-$\{FeNO\}^7$ analog. [Fe(TMG_3tren)(NO)]$^+$ is paramagnetic with a magnetic moment of 3.1 μ_B, determined by the Evans method, which is relatively close to the spin-only value for an $S_t = 1$ system ($\mu_{eff} = 2.87\ \mu_B$). Mössbauer and XANES data both show that reduction of the hs-$\{FeNO\}^7$ to the hs-$\{FeNO\}^8$ complex is iron based.[69] These findings are further supported by DFT calculations and show that the hs-$\{FeNO\}^8$ complex has an hs-Fe(II)−$^3NO^-$ type electronic structure, where the spins of the hs-Fe^{II} ($S = 2$) and the $^3NO^-$ ligand ($S = 1$) are AF coupled, to give a total spin of $S_t = 1$ (see Figure 113, right).[69] Here, reduction leads to the double occupation of the d_{xy} orbital, which is non-bonding with respect to the FeNO unit, allowing for reduction of the complex at relatively mild potentials (compared to ls-$\{FeNO\}^7$ systems in hemes, where the $\pi^*_{h}\_d_{z^2}$ orbital is occupied upon reduction; see Section 2.2).[74,1775] [Fe(TMG_3tren)(NO)]$^+$ is therefore the first fully characterized hs-$\{FeNO\}^8$ complex in the literature.

Structural characterization of hs-$\{FeNO\}^8$ complexes is challenging, as they are often unstable. The first report of a crystal structure of such a compound was published by Fujisawa and coworkers.[84] The 4C hs-$\{FeNO\}^8$ complex [Fe(L3)(NO)] (L3$^-$ = hydrotris(3-tertiary butyl-5-isopropyl-1-pyrazolyl)-borate anion; see Figure 117) is surprisingly stable at room temperature, and does not show any propensity for decomposition, in contrast to the 5C complex [Fe(TMG_3tren)-(NO)]$^+$. Here, the bulky hydrotris(pyrazolyl)borate coligand, L3$^-$, was thought to contribute to the stability of the complex by preventing bimolecular decomposition and DNIC formation (see below). Indeed, Speelman et al. showed that removing the steric protection around the FeNO unit in [Fe(TMG_3tren)-(NO)]$^{2+}$ by using the less bulky ligand TMG_2dien greatly reduces the stability of the resulting hs-$\{FeNO\}^8$ complex.[69] [Fe(L3)(NO)] shows Fe−NO and N−O bond distances of 1.68 and 1.19 Å, respectively, with an Fe−N−O angle of 177°. Vibrational spectroscopy revealed ν(N−O) = 1696 cm^{-1} and ν(Fe−NO) = 554 cm^{-1} for this compound. It is notable that the Fe−NO stretch of [Fe(L3)(NO)] has a much higher frequency compared to that of [Fe(TMG_3tren)(NO)]$^+$ (554 vs 435 cm^{-1}), indicating a much stronger Fe−NO bond in the 4C complex. This strong Fe−NO bond further contributes to the stability of [Fe(L3)(NO)].[84] NMR data show that this complex is paramagnetic with an $S_t = 1$ ground state. [Fe(L3)(NO)] is thought to have the same hs-Fe(II)−$^3NO^-$ type ground state as [Fe(TMG_3tren)(NO)]$^+$, but with much stronger π-donation from the $^3NO^-$ ligand to the hs-Fe^{II} center, evident from the higher Fe−NO and N−O stretching frequencies of [Fe(L3)-(NO)] compared to [Fe(TMG_3tren)(NO)]$^+$.

Recently, additional hs-$\{FeNO\}^8$ complexes were reported by the Goldberg and Meyer groups. Goldberg and coworkers synthesized the 6C hs-$\{FeNO\}^8$ complex [Fe(N3PyS)(NO)] (N3PyS$^-$ = N-[2-phenylthiomethyl-N-(2-pyridinylmethyl-N,N-bis(2-pyridinylmethyl)methylamine]), featuring a Fe−NO bond distance of 1.68 Å as determined by EXAFS.[1769,1799] IR spectroscopy revealed ν(N−O) = 1588 cm^{-1} for this complex, which is close to the value of 1618 cm^{-1} determined for [Fe(TMG_3tren)(NO)]$^+$. DFT calculations support an $S_t = 1$ ground state for [Fe(N3PyS)(NO)]. This complex slowly self-decayed over 20 hours in solution to form N_2O (~54% yield, based on an intermolecular N−N bond

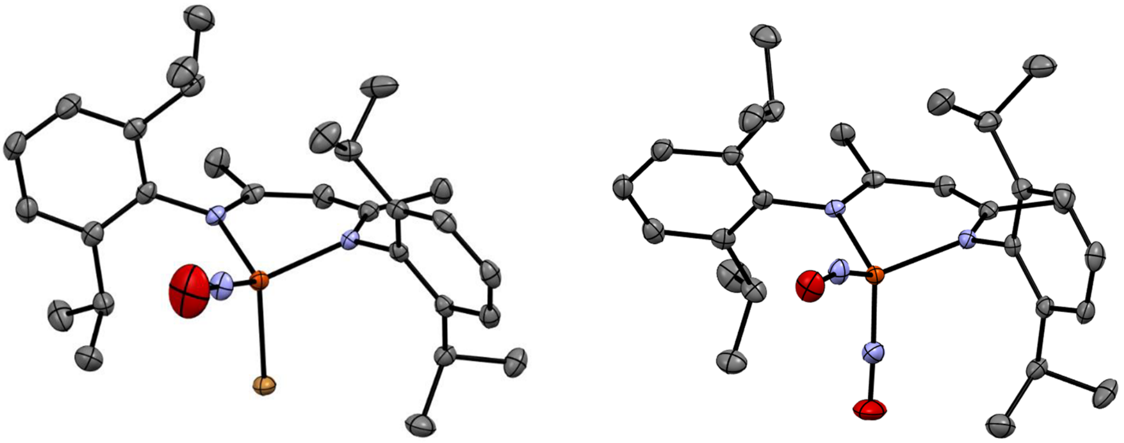

Figure 118. Left: Crystal structure of the hs-$\{FeNO\}^7$ complex [Fe(Ar-nacnac)(Br)(NO)]. Right: Crystal structure of the $\{Fe(NO)_2\}^{10}$ complex $[Bu_4N][Fe(Ar\text{-}nacnac)(NO)_2]$.[232,235] All H atoms and counter ions (if applicable) are omitted for clarity.

formation mechanism; see below).[1799] In a subsequent study, Goldberg and coworkers increased the stability of their 6C hs-$\{FeNO\}^8$ complex by replacing the thiolate donor of $N3PyS^-$ with a sterically encumbered thioether ligand, using the $N3Py^{2Ph}SEtCN$ ligand scaffold (see Figure 109).[1778] The hs-$\{FeNO\}^8$ complex $[Fe(N3Py^{2Ph}SEtCN)(NO)](BF_4)$ was synthesized via chemical reduction of the corresponding hs-$\{FeNO\}^7$ precursor. The metastable complex $[Fe(N3Py^{2Ph}SEtCN)(NO)](BF_4)$ was characterized by Mössbauer spectroscopy, which shows an isomer shift $\delta = 0.89$ mm/s and a quadrupole splitting $\Delta E_Q = 1.42$ mm/s for this compound. The data were best fitted with an $S_t = 1$ ground state, which is also supported by DFT calculations. The rRaman spectra revealed $\nu(N-O) = 1656\ cm^{-1}$ for this compound, which is higher in energy compared to the N−O stretching frequency of [Fe(N3PyS)(NO)] (observed at 1588 cm^{-1}). The increased stability of $[Fe(N3Py^{2Ph}SEtCN)(NO)](BF_4)$ over [Fe(N3PyS)(NO)] is again credited to the increased steric bulk in the former complex.[1778]

Meyer and coworkers reported the 4C hs-$\{FeNO\}^8$ complex $[Fe(TIMEN^{Mes})(NO)]^+$ ($TIMEN^{Mes}$ = tris[2-(3-mesitylimidazol-2-ylidene)ethyl]amine; see Figure 117), which features steric protection for the FeNO moiety by a bulky tris-NHC ligand (NHC = N-heterocyclic carbene).[82] X-ray crystallography revealed Fe−NO and N−O bond distances of 1.68 and 1.18 Å for this complex, and an Fe−N−O angle of 180°. This is in good agreement with the structural parameters of the 4C complex [Fe(L3)(NO)] described above (1.68 and 1.19 Å, respectively, and 177°). Provided that both complexes possess a distorted tetrahedral geometry with steric protection in the SCS, it is reasonable to expect these similarities in bonding parameters. IR spectroscopy revealed $\nu(N-O)$ at 1686 cm^{-1} for $[Fe(TIMEN^{Mes})(NO)]^+$, which is also very similar to the N−O stretching frequency of [Fe(L3)(NO)] (1696 cm^{-1}). Magnetic susceptibility measurements of $[Fe(TIMEN^{Mes})(NO)]^+$ revealed a magnetic moment $\mu_{eff} = 3.28\ \mu_B$, which indicates an overall spin state $S_t = 1$. This complex is again described as a hs-Fe(II)−$^3NO^-$ type species, in agreement with the other hs-$\{FeNO\}^8$ complexes described above.

All of the hs-$\{FeNO\}^8$ complexes described above were prepared in dry solvents, so it is not clear how such complexes would behave in an aqueous environment. The only clue in this regard comes from a cryo-reduction study on the ferrous NO adduct of the enzyme TauD.[153] In this case, initial formation of a hs-$\{FeNO\}^8$ complex was observed, with an $S_t = 1$ ground state. Annealing of the sample presumably led to the formation of the corresponding HNO complex, hs-$\{FeNHO\}^8$ ($S_t = 2$). These results indicate that non-heme hs-$\{FeNO\}^8$ complexes could potentially be protonated, if generated in an aqueous environment, like their heme ls-$\{FeNO\}^8$ analogs (see Section 4.2). More work is necessary to elucidate the behavior of these species under biological conditions.

Many hs-$\{FeNO\}^8$ complexes are unstable and reactive, as mentioned above. The most common reaction of mononuclear hs-$\{FeNO\}^8$ complexes is disproportionation, following the reaction:

$$\begin{aligned} &2\,\text{hs-}\{FeNO\}^7 + 2e^- \\ &\quad\rightarrow 2\,\text{hs-}\{FeNO\}^8 \\ &\quad\rightarrow \{Fe(NO)_2\}^{10} + \text{“}Fe^{II}\text{”} \end{aligned} \qquad (26)$$

This reaction was first reported by Lippard and coworkers in 2011.[235] Here, reduction of the 4C hs-$\{FeNO\}^7$ complex [Fe(Ar-nacnac)(Br)(NO)] (Ar-nacnac$^-$ = anion of [(2,6-diisopropylphenyl)NC(Me)]$_2$CH) by one-electron (using $CoCp^*_2$; Cp^{*-} = pentamethylcyclopentadienyl anion) was studied, and the resulting reaction products, a DNIC compound and an Fe^{II} complex, were characterized. In addition, the DNIC product $[Fe(Ar\text{-}nacnac)(NO)_2]^-$ was also independently synthesized. However, the presumed hs-$\{FeNO\}^8$ intermediate that would form immediately after reduction (see eq 26) could not be observed, so the detailed mechanism of the reaction remained mysterious. The hs-$\{FeNO\}^7$ complex, [Fe(Ar-nacnac)(Br)(NO)], was structurally characterized, showing Fe−NO and N−O bond distances of 1.64 and 1.22 Å, respectively, and an almost linear Fe−N−O unit (176°; see Figure 118). IR spectroscopy revealed $\nu(N-O) = 1777\ cm^{-1}$ for this complex. The resulting $\{Fe(NO)_2\}^{10}$ DNIC shows two characteristic N−O stretching bands in the IR spectrum, at 1627 and 1567 cm^{-1}. This complex was also structurally characterized, as shown in Figure 118.

Following the initial report by Lippard's group, additional examples for this disproportionation reaction, according to eq 26, were reported.[69] Another example is the hs-$\{FeNO\}^7$ complex $[Fe(BMPA\text{-}tBu_2PhO)(OTf)(NO)]$ ($BMPA\text{-}tBu_2PhOH$ = N-(3,5-di-tert-butyl-2-hydroxybenzyl)-*N*,*N*-di-(2-pyridylmethyl)]amine).[1772] This is a typical hs-$\{FeNO\}^7$ complex with Fe−NO and N−O bond distances of 1.78 and

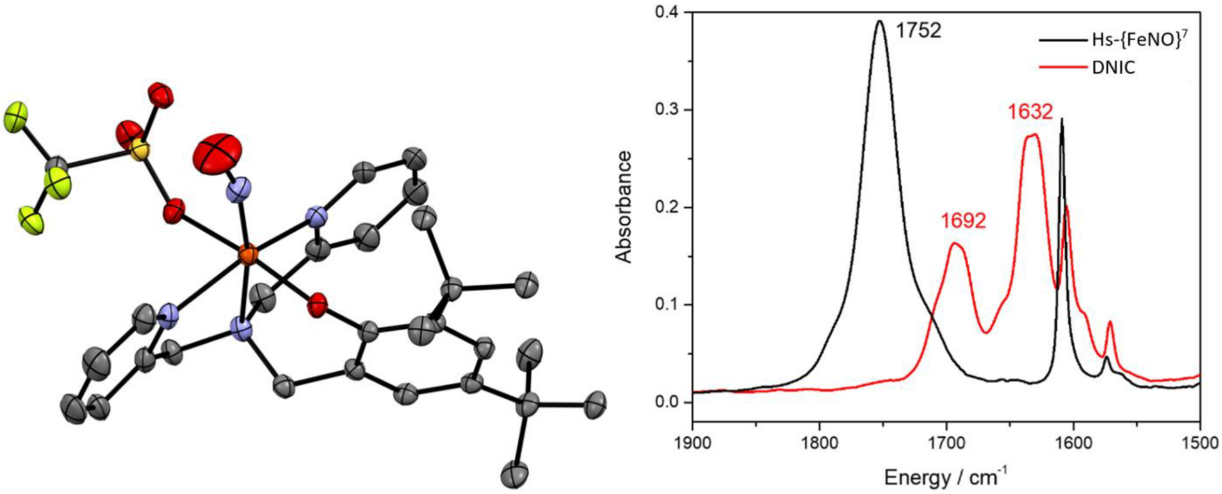

Figure 119. Left: Crystal structure of the hs-$\{FeNO\}^7$ precursor complex [Fe(BMPA-tBu$_2$PhO)(OTf)(NO)]. All H atoms are omitted for clarity. Right: Solution IR spectra showing the characteristic N−O stretching bands of the starting material and the DNIC product after one-electron reduction. Adapted with permission from ref 1772. Copyright 2019 Wiley-VCH Verlag GmbH & Co. KGaA.

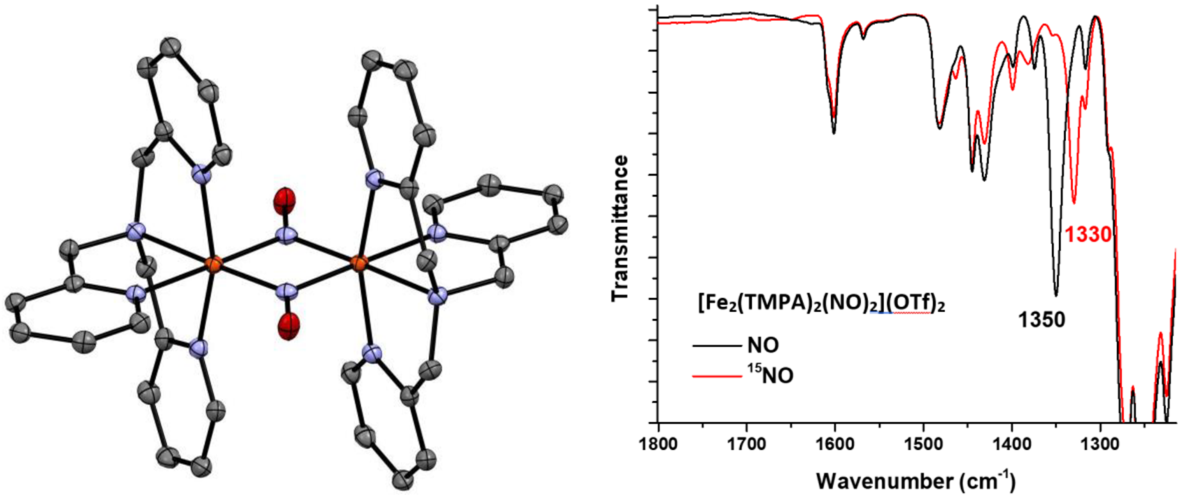

Figure 120. Left: Crystal structure of the complex [Fe$_2$(TMPA)$_2$(NO)$_2$](OTf)$_2$ with a Fe$_2$(NO)$_2$ diamond core structure. All H atoms and counter ions are omitted for clarity. Right: The solid state IR spectrum of [Fe$_2$(TMPA)$_2$(NO)$_2$](OTf)$_2$ showing the shift of the N−O stretch at 1350 cm^{-1} to 1330 cm^{-1} upon ^{15}NO labeling. Adapted with permission from ref 1772. Copyright 2019 Wiley-VCH Verlag GmbH & Co. KGaA.

1.10 Å, respectively, and an Fe−N−O angle of 163°. As shown in Figure 119, upon one-electron reduction, the N−O stretch of this complex at 1752 cm^{-1} vanished, and new N−O stretching bands appeared at 1692 and 1632 cm^{-1}, indicative of the formation of a $\{Fe(NO)_2\}^{10}$ DNIC. Curiously, however, when the analogous hs-$\{FeNO\}^7$ complex [Fe(TMPA)(OTf)(NO)]$^+$ was reduced by one-electron, the N−O stretch of this complex disappeared, but no new N−O stretching band(s) belonging to a DNIC or a hs-$\{FeNO\}^8$ product appeared in the 1500-1800 cm^{-1} range. N$_2$O formation was also not observed. Careful characterization of the reaction product revealed the formation of an unusual complex, [Fe$_2$(TMPA)$_2$(NO)$_2$](OTf)$_2$, which contains an Fe$_2$(NO)$_2$ diamond core structure as shown in Figure 120.[1772] Here, two ls-Fe^{II} centers are bridged by two $^1NO^-$ ligands, resulting in a strictly diamagnetic species, even at room temperature. This complex provides insight into the mechanism of DNIC formation, according to eq 26, as shown in Figure 121.[88] Here, it is proposed that after formation of the hs-$\{FeNO\}^8$ complex, dimerization and formation of a complex with an Fe$_2$(NO)$_2$ diamond core structure occurs. If the Fe^{II} centers remain hs, as in the case of one-electron reduced [Fe(BMPA-tBu$_2$PhO)(OTf)(NO)], one Fe^{II} center is expelled from the dimer, leading to DNIC formation (Figure 121, bottom left). However, as described above, [Fe(TMPA)(OTf)(NO)]$^+$ is unique in that this complex is close to the spin crossover point. Here, one-electron reduction and formation of the Fe$_2$(NO)$_2$ dimer induces a spin crossover of the Fe^{II} centers, which stabilizes the structure and allows for [Fe$_2$(TMPA)$_2$(NO)$_2$](OTf)$_2$ to be isolated (Figure 121, bottom right). In this sense, [Fe$_2$(TMPA)$_2$(NO)$_2$](OTf)$_2$ represents the "spin-trapped" version of the critical Fe$_2$(NO)$_2$ intermediate, responsible for DNIC formation according to eq 26.[88] This mechanism also explains why sterically bulky ligands are able to suppress this disproportionation of hs-$\{FeNO\}^8$ complexes, as in this case the critical Fe$_2$(NO)$_2$ intermediate cannot form.

5.1.3. Hs-$\{FeNO\}^9$ Complexes.

The only hs-$\{FeNO\}^9$ complex reported so far is [Fe(TIMEN^{Mes})(NO)], which was obtained by Meyer and coworkers by one-electron reduction of the hs-$\{FeNO\}^8$ complex [Fe(TIMEN^{Mes})(NO)]$^+$ described

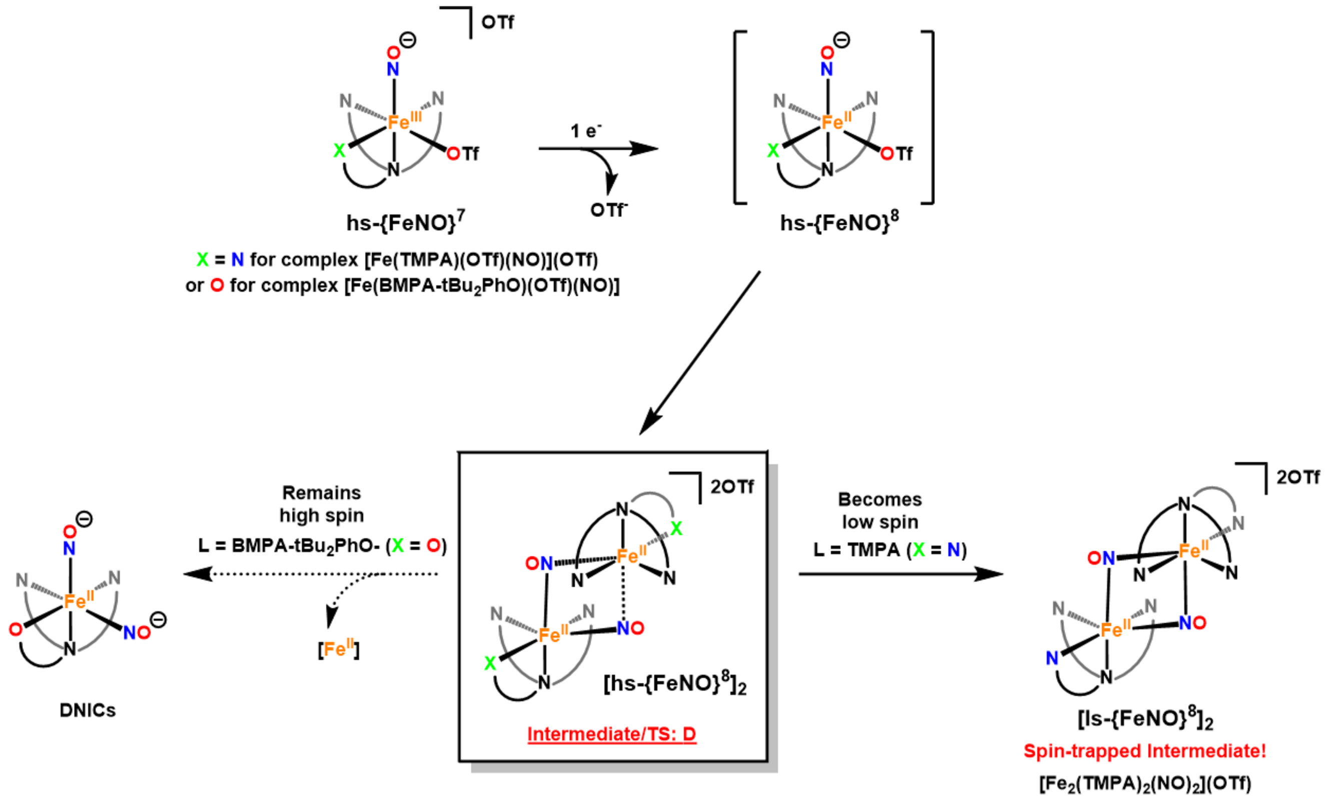

Figure 121. Proposed mechanism for DNIC formation from hs-$\{FeNO\}^8$ complexes based on the recent discovery of $[Fe_2(TMPA)_2(NO)_2]$-$(OTf)_2$.[1772] Reprinted with permission from ref 88. Copyright 2019 American Chemical Society.

above (see Figure 6).[82] The structure of this complex was determined using X-ray crystallography, which shows Fe−NO and N−O bond distances of 1.67 and 1.22 Å, respectively, and an Fe−N−O angle of 179°. The N−O stretching frequency of this species is observed at 1550 cm^{-1}. Magnetic susceptibility measurements of solid $[Fe(TIMEN^{Mes})(NO)]$ revealed an effective magnetic moment μ_{eff} = 1.88 μ_B, indicating that this complex has an S_t = 1/2 ground state. EPR spectroscopy confirmed the S_t = 1/2 spin state, showing an axial EPR spectrum with g = 2. DFT calculations and experimental data support the assignment of a hs-Fe(I)−$^3NO^-$ electronic structure to this complex (see Figure 112), where the hs-Fe^I (S = 3/2) center is AF coupled to the $^3NO^-$ ligand (S = 1).[82] Compared to the hs-$\{FeNO\}^8$ analog, $[Fe(TIMEN^{Mes})$-$(NO)]^+$, the hs-$\{FeNO\}^9$ complex shows quite similar π-donation from the $^3NO^-$ ligand to the iron center, but clearly enhanced π-backbonding, in agreement with the lower N−O stretching frequency in the hs-$\{FeNO\}^9$ system.

5.1.4. Hs-$\{FeNO\}^6$ Complexes. Even though a lot of progress has been made in understanding the reductive chemistry of hs-$\{FeNO\}^7$ complexes, and the reactivity of the resulting hs-$\{FeNO\}^8$ species, investigations into the properties of corresponding one-electron oxidized hs-$\{FeNO\}^6$ complexes are rare. To this date, only one example of a stable hs-$\{FeNO\}^6$ complex, $[Fe(TMG_3tren)(NO)]^{3+}$, has been reported (see Figure 4).[74] This complex was structurally characterized and shows Fe−NO and N−O bond distances of 1.68 and 1.14 Å, respectively, and the Fe−N−O angle is 180°. Vibrational characterization further revealed N−O and Fe−NO stretching frequencies of 1879 and 594 cm^{-1} for this complex, respectively, the latter being indicative of a very strong Fe−NO bond. The complex has an S_t = 1 ground state. Mössbauer spectroscopy revealed an isomer shift of δ = 0.06 mm/s^{-1} and a quadrupole splitting of ΔE_Q = 0.48 mm/s for this complex. Here, the isomer shift shows a distinctive decrease compared to that of the hs-$\{FeNO\}^7$ precursor (δ = 0.48 mm/s, ΔE_Q = −1.42 mm/s). This significant change of the isomer shift implies a metal centered oxidation. Importantly, the isomer shift and quadrupole splitting of $[Fe(TMG_3tren)(NO)]^{3+}$ are also very similar to that of the reported Fe(IV)−oxo complex $[Fe(TMG_3tren)(O)]^{2+}$ (δ = 0.09, ΔE_Q = 0.29 mm/s).[1800,1801] The Mössbauer isomer shift is sensitive to the oxidation state of the iron center (in a series of closely related complexes with overall similar coordination spheres), and these data clearly suggest that iron is in the Fe^{IV} state in the hs-$\{FeNO\}^6$ complex.[74] This finding is further supported by Fe K-edge XAS data.[69] Finally, UV−vis absorption data revealed an intense absorption band at 515 nm for the hs-$\{FeNO\}^6$ complex. With the help of VTVH MCD measurements, this feature was assigned to the guanidine-to-iron charge-transfer transition that occurs at 368 nm in the hs-$\{FeNO\}^7$ complex. The distinct shift to lower energy of this "spectator" charge-transfer transition upon oxidation of the hs-$\{FeNO\}^7$ to the hs-$\{FeNO\}^6$ complex is a further indication of an iron-based oxidation in this process.[69] The complex $[Fe(TMG_3tren)$-$(NO)]^{3+}$ has an unexpectedly large *D* value of about +30 cm^{-1}, evident from the unusual temperature- and field dependence of both the Mössbauer and MCD data of this species.[69] All of these data support the assignment of a Fe(IV)−$^3NO^-$ type electronic structure to this complex, where the electron spins of the hs-Fe^{IV} center (S = 2) and the $^3NO^-$ ligand (S = 1) are AF coupled, resulting in the observed S_t = 1 ground state (see Figure 113, left). Hence, along the whole hs-$\{FeNO\}^{6-8}$ series with the TMG_3tren coligand (see Figure 4), the same type of electronic structure is observed, where a $^3NO^-$ ligand is bound to a hs-Fe center, serving as a strong π-donor ligand.[69] As the oxidation state of the metal increases from Fe^{II} in hs-$\{FeNO\}^8$ to Fe^{IV} in hs-$FeNO\}^6$, the amount of π-donation from the $^3NO^-$ ligand to the iron center increases, giving rise to a more covalent Fe−NO bond, as shown in Figure 113. On the basis of these considerations, both the Fe−NO and N−O stretching frequencies would be expected to increase along the hs-$\{FeNO\}^{6-8}$ series, as observed experimentally.

Besides the work on the complexes with the TMG_3tren ligand system, other researchers attempted to prepare hs-$\{FeNO\}^6$ complexes as well, but so far, without success. Lippard and coworker reported the 5C complex $[Fe(TAML)(NO)]^-$ (TAML = tetraamidomacrocyclic ligand tetraanion), which bears a close to linear Fe−N−O bond (with an angle of 172°) and an N−O stretching frequency of 1797 cm^{-1}.[1802] Initially, this complex was proposed to have an $S_t = 1$ ground state, but it was later shown by Nam and coworkers that this complex is in fact diamagnetic, and hence, of ls-$\{FeNO\}^6$ type.[1803] Surprisingly, $[Fe(TAML)(NO)]^-$ can reversibly bind NO when purged with N_2, which is a rare property for non-heme FeNO complexes. Goldberg and coworkers also recently prepared an $\{FeNO\}^6$ complex using the $N3PyS^-$ ligand scaffold, via chemical oxidation of the $\{FeNO\}^7$ precursor $[Fe(N_3PyS)(NO)](BF_4)$.[1769] However, the resulting complex $[Fe(N_3PyS)(NO)]^{2+}$ was shown to be diamagnetic, and hence, is of ls-$\{FeNO\}^6$ type. This species has an Fe−NO bond distance of 1.69 Å (from EXAFS) and an N−O stretch of 1909 cm^{-1}, in agreement with the Fe(II)−NO^+ type electronic structure proposed for this complex. Solvent-dependent NO photolability was further observed for this compound, indicating that it can release NO cleanly without decomposition in the presence of a coordinating solvent. Photolability of ls-$\{FeNO\}^6$ complexes with non-heme ligand systems has been observed before, for example by Mascharak and coworkers.[1804,1805] Similar complexes with sulfur ligation also serve as models for the active site of the enzyme nitrile hydratase.[1806−1809]

5.1.5. A ls-$\{FeNO\}^{8-10}$ Series. Recently, a detailed structural and electronic investigation of a series of ls-$\{FeNO\}^{8-10}$ complexes has been reported (see Figure 6, top). This series pushes our understanding of the redox chemistry in FeNO complexes to a new boundary by stabilizing a ls-$\{FeNO\}^{10}$ complex, which is extremely rare in the literature.[81] This ls-$\{FeNO\}^{8-10}$ series employs the strongly donating tris[2-(di-iso-propylphosphino)-phenyl]borane ligand (TPB) to stabilize the low-valent oxidation state of iron in these complexes. Importantly, the borane group in the ligand backbone can serve as a Lewis acid to accept electron density from the iron center to stabilize the ls-$\{FeNO\}^{10}$ state. X-ray crystallography revealed Fe−NO and N−O bond distances and Fe−N−O angles of 1.66/1.67/1.65 Å, 1.16/1.19/1.22 Å, and 176/176/179° for the ls-$\{FeNO\}^{8-10}$ complexes, respectively. While the ls-$\{FeNO\}^8$ and ls-$\{FeNO\}^{10}$ complexes are diamagnetic, the ls-$\{FeNO\}^9$ complex is paramagnetic with a total spin of $S_t = 1/2$. Vibrational spectroscopy (IR and NRVS) further showed that these complexes have strong Fe−NO bonds, with Fe−NO and N−O stretching frequencies of 610/583/602 cm^{-1} and 1745/1667/1568 cm^{-1}, respectively, along the ls-$\{FeNO\}^{8-10}$ series.[83] Interestingly, a QCC-NCA analysis of the NRVS data revealed force constants for the Fe−B bond of 0.51/0.42/1.56 mdyn/Å for the ls-$\{FeNO\}^{8-10}$ series. This result suggests that a Fe−B single bond is formed in the ls-$\{FeNO\}^{10}$ complex, where iron now takes on the role of the Lewis base and donates an electron pair in the d_{z^2} orbital to the boron Lewis acid. In this sense, the [Fe(TPB)] platform can store two electrons in the Fe−B bond upon reduction of the iron center to the formally Fe(-II) oxidation state, and these electrons can then be utilized for small molecule activation, for example in N_2 activation.[81,83,653,1810] Even though boron is not used in this regard in biology, other Lewis acids can potentially act in such a way to stabilize reactive intermediates of NO chemistry and of other small-molecule activation processes.

5.2. Flavodiiron Proteins and NO Reduction by Non-Heme Diiron Centers

Outside the context of denitrification, NO eliminating enzymes are also found in pathogens that are capable of combatting nitrosative stress. Besides nitric oxide dioxygenases (see Section 2.5), pathogens can also express bacterial NORs (see Section 4.3) and non-heme flavodiiron nitric oxide reductases (FNORs) in low oxygen environments.[210] FNORs are scavenging flavodiiron proteins whose gene sequences are found in numerous pathogens,[1811−1814] including *Escherichia coli*, *Salmonella enterica*, *Treponema denticola*, and *Desulfovibrio vulgaris*.[215,1815−1819] Moreover, the regulator sequences for these FNORs have also been identified in the bacterial pathogens *Klebsiella pneumoniae*, *Vibrio vulnificus*, and *Salmonella typhimurium*.[211] Considering the ability of these pathogens to counteract NO-based immune defense mechanisms[194,196] and prolong disease, studying these enzymes is of particular interest. Unsolved questions surrounding these enzymes include (but are not limited to) what determines specificity of NO reduction activity in these enzymes, what is the mechanism of this reaction, how does the SCS contribute to catalysis and what is the nature of the key, N−N-coupled intermediates. These questions, along with structural and reactivity properties, are addressed in the following.

5.2.1. Protein Structure of Flavodiiron Proteins and Reactivity. In enzymes, NO reduction by catalytic non-heme diiron sites has been shown in flavodiiron proteins (FDPs). Generally, FDPs contain a conserved minimal structural core that consists of N-terminal metallo-β-lactamase-like and C-terminal flavodoxin-like domains.[216] The metallo-β-lactamase-like domain houses the diiron catalytic site, whereas the flavodoxin-like domain contains a flavin mononucleotide (FMN) cofactor capable of transferring electrons to the diiron site.[216] Within a single monomer of the minimal structural core, the diiron site and the FMN cofactor are ∼35 Å away, which renders electron transfer between them essentially impossible without additional cofactors.[216,217] However, in the "head-to-tail homodimer" quaternary structure of FDPs (see Figure 122), the two monomers are arranged such that the diiron site of one monomer is only ∼5 Å away from the FMN cofactor of the other monomer, enabling fast and efficient electron transfer between them.[217]

As shown in Table 24, nine classes of FDPs have been identified thus far, based on the presence of different domains for the binding of external electron donating partners.[1820] The simplest class of FDPs, Class A, only contains the minimal structural core described above and these enzymes are dependent on exogenous redox partners to directly reduce the FMN cofactor for turnover.[217] Examples include Rubredoxin Oxygen:Oxidoreductase (ROO) from *Desulfovibrio gigas* (*Dg* ROO) and FDPs from *Thermotoga maritima* (*Tm* FDP), *Moorella thermoacetica* (*Mt* FDP), among others.[217,1821]

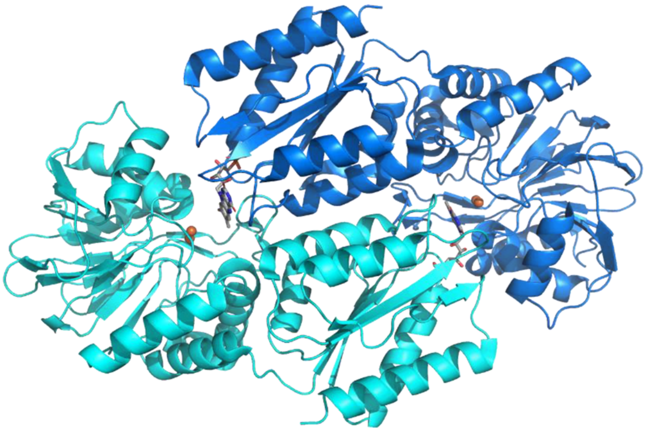

Figure 122. PyMOL generated image of the crystal structure of *M. thermoacetica* FDP (*Mt* FDP; PDB: 1YCH), showing the homodimer with the two monomers in blue and cyan in a "head-to-tail" arrangement. Iron atoms and FMN are shown as orange spheres and gray ball-and-stick models, respectively.

Table 24. Different Classes of FDPs.

class	domains (from N-terminal to C-terminal)[a]	example organisms[b]
A	MβL—Fd	*M. Thermoacetica, D. gigas, D. vulgaris, T. maritima, E. histolytica, G. intestinalis, T. denticola, M. marburgensis, C. acetobutylicum*
B	MβL—Fd—Rd_c	*E. coli*
C	MβL—Fd—FlvR	*Synechocystis* sp. PCC6803
D	MβL—Fd—Rd_s	N/I
E	MβL—Fd—FeS	N/I
F	MβL—Fd—Rd_s—NROR	*Clostridium difficile*
G	MβL—Fd—FlvR—Rd_s	N/I
H	MβL—Fd—Rd_s—FlvR—Rd_s	N/I
I	MβL—Fd—Dx—Nir	N/I

[a] MβL: diiron-containing metallo-β-lactamase-like domain; Fd: FMN-containing flavodoxin-like domain; Rd_c: canonical rubredoxin-like domain; FlvR: NAD(P)H:flavin oxidoreductase-like domain; Rd_s: short rubredoxin-like domain; FeS: iron−sulfur cluster; NROR: NADH:rubredoxin oxidoreductase-like domain; Dx: desulforedoxin-like domain; Nir: neelaredoxin-like domain. [b] N/I: not yet isolated.

Other classes of FDPs rely on one or more additional domains to the minimal structural core that serve to transfer electrons to the FMN cofactor, though they may serve additional functions as well. Class B FDPs utilize a canonical rubredoxin domain that interacts with exogenous redox partners, which is well documented with flavorubredoxin in *E. coli* (*Ec* FlRd) and its redox partner NADH:flavorubredoxin oxidoreductase.[1822] On the other hand, Class C FDPs incorporate an NAD(P)H:flavin oxidoreductase-like domain, as observed for FDPs from *Synechocystis* sp. PCC6803 cyanobacteria.[1823] To date, Class F are the most complex FDPs that have been isolated, observed in *Clostridium difficile*. These proteins contain a short rubredoxin domain as well as an NADH:rubredoxin oxidoreductase domain.[1824] Other classes of FDPs (classes D, E, G, H, and I) are theorized to exist based on amino acid sequencing and domain predictions but have yet to be isolated and studied.[1820]

FDPs can be grouped together based on how well these enzymes mediate dioxygen reductase (O_2R) or nitric oxide reductase (NOR) activity, which is given in eqn.s 15 and 5, respectively. FDPs were first recognized as O_2Rs for their ability to protect microanaerobic bacteria from residual O_2, by reducing it in a non-metabolic (scavenging) function to water.[216] In addition, because of how FDPs act as scavenging enzymes in the presence of O_2 and NO to counteract oxidative and nitrosative stress, respectively, it is hypothesized that NOR function evolved from O_2R function in these enzymes.[210] However, it is worth noting that not all FDPs have NOR or O_2R functionality (see Table 25). While *Dg* ROO and *Mt* FDP exhibit NOR and O_2R reactivity at similar rates, *Tm* FDP and FDP from *E. histolytica* exhibit better O_2R than NOR reactivity.[215,1821,1825,1826] On the other hand, *Ec* FlRd exhibits better NOR than O_2R activity, making this enzyme a bona fide flavodiiron nitric oxide reductase (FNOR).[1822] However, there are no obvious differences in the iron coordination spheres and active site structures between O_2Rs and NORs, so the structural or electronic differences responsible for this dichotomy have yet to be definitively determined (see discussion below).

Considering the primary coordination sphere, the diiron core binding motif is generally conserved across all FDPs. In the diiron core, each iron is 5C with a sixth site left open for substrate binding, as shown in Figure 123.[217] Here, each iron coordinates to two histidine residues and one carboxylate residue (either aspartate or glutamate). Bridging hydroxo and carboxylate (usually aspartate) ligands position the iron centers between 3.3−3.6 Å apart. A notable exception includes *Dg* ROO, which has one of the histidine ligands unbound from one of the irons and replaced with water.[216] Kurtz and coworkers expressed deflavinated *Tm* FDP with mutated plasmids that replace His90 (one of the Fe-coordinating histidine ligands) to

Table 25. NOR and O_2R Activities of FDPs

organism	class/lifestyle	k_{cat} of NOR Activity [s^{-1}]	k_{cat} of O_2R activity [s^{-1}]	ref
C. acetobutylicum[a]	A/Anaerobic	**34**	5	1828
D. gigas	A/Anaerobic	14.9 ± 3.2[b]	50.5 ± 10[b]	215
D. vulgaris	A/Anaerobic	12	17	1817
E. histolytica	A/Anaerobic	∼0.1[b]	∼21[b]	1825
G. intestinalis	A/Anaerobic	0.2	37.7 ± 8.3	1829
M. thermoacetica	A/Anaerobic	**48**	50	1826
T. denticola	A/Anaerobic	1.3	28	1815
T. maritima	A/Anaerobic	0.03 ± 0.01	2.6 ± 0.2	1821
E. coli	B/Anaerobic	**14.9 ± 6.7**[b]	N/A[c]	213
Synechocystis sp. PCC6803	C/Aerobic	N/A[c]	0.4	1830
C. difficile	F/Anaerobic	0.20 ± 0.01	16.0 ± 1.3	1824

[a] Refers to *Ca* FprA2. [b] Mol NO or O_2 (mol enzyme)$^{-1}$s^{-1}. [c] Not available due to kinetics not being measured.

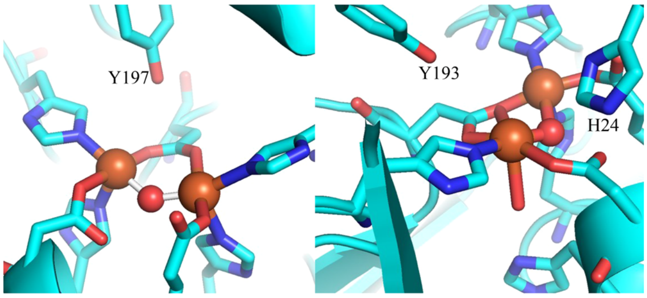

Figure 123. Left: PyMOL generated image of the crystal structure of the active site of deflavinated *T. maritima* FDP, including the proposed SCS hydrogen-bond donor Y197 (PDB: 1VME). Right: PyMOL generated image of the crystal structure of the active site of *D. gigas* ROO, including the proposed SCS hydrogen-bond donors H24 and Y193 (PDB: 1E5D).

assess whether altering the primary coordination sphere of one of the iron centers would modulate NOR or O_2R activity.[1821] Among the variants, there exists little change to the substrate binding pocket, other Fe-coordinating residues, and Fe−ligand distances. For the H90N and H90A variants, the respective Fe−O_{Asn} and Fe−OH_2 bond distances are 2.3 and 2.4 Å, respectively, versus 2.4 Å for the Fe−N_{His} bond in wt enzyme.[1821] Not surprising, this variation in the primary coordination sphere does not drastically alter steady-state NOR activity (0.05 and 0.09 equiv NO consumed/s for H90A and H90N, respectively, versus 0.03 equiv NO consumed/s for wt enzyme), as is the case for steady-state O_2R activity.[1821] In addition, total conservation of the primary coordination sphere is observed for both *Mt* FDP and *Tm* FDP, although lower NOR reactivity (relative to O_2R reactivity) was found in the latter compared to the former enzyme (see Table 25).[1821,1826] Hence, the primary coordination sphere of FDPs does not seem to dictate NOR versus O_2R reactivity.

Differences between primary NORs and similarly NOR- and O_2R-active enzymes start to come to light when considering the SCS and beyond. Comparison of two class A FDPs, *Dg* ROO and *Mt* FDP, shows that both enzymes contain histidine and tyrosine residues within hydrogen-bonding distances of iron-bound substrates, and both enzymes act as decent NORs.[215,1826] Moreover, mutation studies using *Mt* FDP revealed a ~7-fold and ~34-fold reduction in NOR reactivity when the tyrosine and histidine residues (Y195 and H25, represented for the analgous *Dg* ROO as Y193 and H24 in Figure 123), respectively, were substituted for non-hydrogen bonding residues.[217] While it is clear that the SCS residues Tyr and His are important for NOR activity, whether these residues truly distinguish NORs from O_2Rs is not clear, since it was not reported how their removal by mutagenesis affected the O_2R activity of the enzyme. In *M. marburgensis* FDP, the SCS Tyr is oriented away from the active site, towards one of the carboxylate residues, but this enzyme still shows O_2R activity, which indirectly supports these ideas (assuming that the Tyr stays in this position during catalysis).[1827] In addition, *Tm* FDP, which is primarily a O_2R (see Table 25), lacks the histidine that is available for hydrogen-bonding in the SCS of the *Mt* FDP active site.[1821] The *Tm* FDP active site does contain the SCS tyrosine (see Figure 123), and site-directed mutagenesis studies show that this residue is crucial for NOR activity of this enzyme.[1831] Beyond the catalytic site, clusters of aromatic residues have been found in conserved positions near the active site and the FMN cofactor of most FDPs, which include tryptophan and tyrosine residues.[1832] These amino acids are hypothesized to protect the enzymes from oxidative damage when dioxygen reduction occurs, by reducing radical species or highly reactive intermediates.[1816]

5.2.2. Basic Spectroscopic Characterization of Flavodiiron Proteins.

The diferric resting state, the diferrous catalytically active state, and mono- and dinitrosyl intermediates of FDPs have been investigated using a variety of spectroscopic methods. In particular, the Kurtz group used the *Tm* FDP to obtain a detailed characterization of these species, which provides further insight into the intricate layout of the FDP active site and establishes design principles for the preparation of corresponding diiron model complexes (see below).

The catalytically active state of FDPs corresponds to the diferrous form, which is EPR silent. Mössbauer spectroscopy on diferrous *Tm* FDP shows one quadrupole doublet, with an isomer shift of 1.15 mm/s and a quadrupole splitting of 2.39 mm/s, indicating that the active site contains two electronically identical iron centers. The Mössbauer parameters are comparable to those of other non-heme diferrous proteins and show that the iron centers are hs-Fe^{II}.[1833] Moreover, from variable-temperature Mössbauer spectroscopy at high field (7

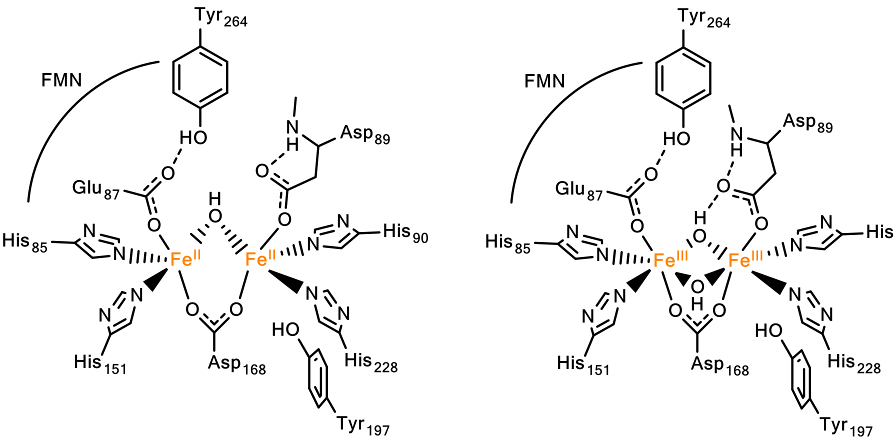

Figure 124. Left: Schematic structure of the diferrous (catalytically active) state of the active site of *T. maritima* FDP (PDB: 1VME). Right: Schematic structure of the diferric state (after turnover) of *T. maritima* FDP. Derived from DFT calculations coupled to Mössbauer and EPR spectroscopy.[1834]

T), the *Tm* FDP diferrous state has relatively strongly AF exchange-coupled Fe^{II} centers, with an exchange-coupling constant $J = -16$ cm^{-1} (for $H = -2J(S_A \cdot S_B)$).[1834] Considering the *Tm* FDP resting (oxidized) state, Mössbauer spectroscopy revealed again just one quadrupole doublet, with an isomer shift of 0.47 mm/s and a quadrupole splitting of 0.99 mm/s, which is typical for hs-Fe^{III} centers.[1833] Interestingly, using parallel-mode EPR spectroscopy, temperature-dependent signals were identified near $g_{eff} = 8$ and $g_{eff} = 12$ for the diferric resting state of *Tm* FDP (corresponding to transitions within the $S = 2$ and $S = 3$ manifolds), from which the exchange-coupling constant was calculated to be $J = -10$ cm^{-1}, indicative of AF coupling between the hs-Fe^{III} centers.[1834] Aside from the iron oxidation states, the difference in exchange-coupling constants of *Tm* FDP in the reduced and oxidized state is best explained by structural differences. Using DFT calculations, different structural models with different types (oxo, hydroxo, or water) and number of bridging ligands were tested (by comparison of DFT-predicted versus experimental exchange coupling constants and Mössbauer isomer shifts and quadrupole splittings) for both the reduced and oxidized *Tm* FDP active site. For the *Tm* FDP oxidized state, the best model features an additional hydroxo bridge between the two hs-Fe^{III} centers (missing in the crystal structure), where one of the hydroxo bridges is hydrogen-bonded to the D89 side chain (an iron-coordinating residue), as shown in Figure 124.[1834] In contrast, the reduced state is best modeled by just one hydroxo bridge, as expected from crystallography. In the case of the oxidized state, the difference between the spectroscopically-validated structure and the one observed by X-ray crystallography was attributed to the absence of the Flavin cofactor in the crystal structure. However, it is also possible that the simple confinement of the enzyme in the crystal and the associated restriction in conformational freedom may be responsible for the observed differences. Nevertheless, the retention of at least one hydroxo bridge in the reduced and oxidized states of FDPs could be responsible for maintaining syn (or cis)-oriented open coordination sites in the diiron core and appropriate Fe−Fe distances for optimal N−N coupling reactivity.

Binding of one NO to FDPs in the fully reduced state results in the formation of a diferrous mononitrosyl species, which is designated as hs-Fe^{II}/hs-$\{FeNO\}^7$ in the following. When titrated with 1 equiv of NO per diiron site, this species forms at relatively high yield. It exhibits an $S_t = 1/2$ EPR signal at $g = 2.04$ (for *Tm* FDP), which can be attributed to a hs-$\{FeNO\}^7$ ($S = 3/2$) center AF coupled to a hs-Fe^{II} ($S = 2$).[1835] Using temperature-dependent EPR data for the *Tm* FDP, the exchange coupling constant between the two iron sites was calculated to be $J = -8.5$ cm^{-1}. Additional characterization of this species is available from rRaman spectroscopy.[1765] Using deflavinated *Tm* FDP (deflavo-*Tm* FDP), an isotope sensitive band at 451 cm^{-1} was identified (442 cm^{-1} with ^{15}NO and 436 cm^{-1} with $^{15}N^{18}O$), assigned as the Fe−NO stretch.[1765] The Fe−N−O bending mode could not be identified. Using IR difference spectroscopy, the ν(N−O) stretch was identified at 1681 cm^{-1} (1652 cm^{-1} with ^{15}NO).[1836] The surprisingly low ν(N−O) mode was suggested to originate from a semibridging binding mode of NO, where the O atom of the coordinated NO and the adjacent hs-Fe^{II} center interact weakly electrostatically. This interaction leads to an increase in electron density in the NO(π*) orbitals, resulting in the shift of the N−O stretch to lower energy. These ideas are further supported by DFT calculations.[1835] It is worth noting that DFT calculations further predict that in the absence of the semibridging binding mode for the hs-Fe^{II}/hs-$\{FeNO\}^7$ intermediate, the exchange coupling constant J would increase by nearly a factor of 1.4, relative to that of the diferrous state.[1835] In contrast, the semibridging binding mode of the hs-Fe^{II}/hs-$\{FeNO\}^7$ state leads to a smaller exchange coupling constant relative to that of the diferrous state by nearly a factor of 2. Interestingly, this smaller than expected value of J results from additional contributions to the exchange coupling constant via the Fe−N−O···Fe(II) path that cancel against the contributions that arise from the coupling of the iron centers via the hydroxo path.[1835]

When excess NO is added to reduced FDP, the diferrous dinitrosyl, [hs-$\{FeNO\}^7$]$_2$, intermediate forms. Unlike the diferrous mononitrosyl complex, this species is EPR silent, which is attributed to the AF coupling of the two hs-$\{FeNO\}^7$ ($S = 3/2$) units, resulting in $S_t = 0$. This species was characterized by Mössbauer spectroscopy (see below), which led to the determination of an exchange-coupling constant of $J = -30$ cm^{-1} for this complex.[1835] This unusually strong AF coupling is attributed to weak $^{-}$ON···NO^{-} interactions that contribute to the total exchange coupling of the system.[1835] Using again deflavo-*Tm* FDP, rRaman spectroscopy shows one isotope-sensitive band at 459 cm^{-1} (452 cm^{-1} with ^{15}NO and 447 cm^{-1} with $^{15}N^{18}O$) for the [hs-$\{FeNO\}^7$]$_2$ complex that is assigned to the Fe−NO stretch.[1765] The N−O stretch is observed at higher energy and is assigned to a band at 1749 cm^{-1} (1719 cm^{-1} with ^{15}NO and 1679 cm^{-1} with $^{15}N^{18}O$). Additionally, the ν(N−O) mode was identified using IR difference spectroscopy, at 1751 cm^{-1} (1721 cm^{-1} with ^{15}NO), in agreement with the rRaman result.[1765]

5.2.3. Rapid Freeze-Quench Experiments with Flavodiiron Proteins.

Stopped-flow and RFQ techniques have been utilized over the years to study transient intermediates of FDP-catalyzed NOR activity, and to determine rate constants for different parts of the reaction. Specifically, RFQ experiments coupled to EPR and Mössbauer spectroscopy have provided key insight into the reaction of *Tm* FDP and variants with NO, though the FDP from *Desulfovibrio vulgaris* (*Dv* FDP) has also been studied. For rapid kinetics and trapping of intermediates of NO reduction, *Tm* FDP has the advantage that the wt enzyme and variants have relatively slow NOR kinetics, relative to their O_2R activity (see Table 25).[1765,1821] While more work using RFQ-coupled spectroscopy is needed, especially on enzymes that are primary FNORs, the work conducted to date has yielded considerable insight into how FDPs catalyze NO reduction.

Stopped-flow experiments on wt *Tm* FDP by Caranto et al. show that coordination of the first NO ligand to the reduced diiron core of the enzyme is exceedingly fast and proceeds within the mixing time of the solutions (about 1.3 ms).[1833] This is followed by a slower phase, which proceeds in 130 ms and which corresponds to the binding of the second NO and the formation of a diiron dinitrosyl intermediate, [hs-$\{FeNO\}^7$]$_2$. These assignments are based on the characteristic UV−vis absorption features of non-heme hs-$\{FeNO\}^7$ complexes, and were further confirmed by Mössbauer spectroscopy (see below). The [hs-$\{FeNO\}^7$]$_2$ intermediate then decays over the course of 120 seconds, along with the appearance of oxidized FMN cofactor. Importantly, only after forming the [hs-$\{FeNO\}^7$]$_2$ intermediate does cofactor oxidation occur. Using RFQ-EPR, sub-stoichiometric amounts of NO (∼0.5 equiv NO per diiron site) were added to *Tm* FDP to yield an intense $S_t =$

Table 26. RFQ Experiments on Fully Reduced *Tm* FDP Using ~3 equiv NO per Diiron Site[1833]

quench time [s]	% Fe^{II}_2	% Fe^{II}/hs-{FeNO}^{7}	% [hs-{FeNO}^{7}]$_2$	% Fe^{III}_2	% hs-{FeNO}^{7} or inactive [hs-{FeNO}^{7}]$_2$[b]
0[a]	80	0	0	20	0
0.02	16	76	0	0	8
0.2	0	54	41	0	5
2	0	69	28	0	3
20	0	90	0	0	10
120	0	80	0	13	7

[a]Measured with NO-free solution. [b]Reported as sum of both species.

1/2 signal after 200 ms.[1833] With a g-value of 2.10, the rapidly forming species was identified as the diferrous mononitrosyl intermediate (see above), where the hs-Fe^{II} (S = 2) is AF coupled to the hs-{FeNO}^{7} (S = 3/2) center, in agreement with the stopped-flow results. Using RFQ-Mössbauer spectroscopy, reactions with excess NO (~3 equiv NO per diiron site) were conducted and then quenched at multiple time points, as shown in Table 26. After 20 ms, the spectrum reveals a mixture of species that, based on simulated Mössbauer spectra, match up to the hs-Fe^{II}/hs-{FeNO}^{7} species (76%) and the starting diferrous complex (16%), among others.

Samples quenched at 200 ms and 2 s after NO addition also reveal a mixture of species, including the hs-Fe^{II}/hs-{FeNO}^{7} intermediate (54%) and a new species, identified as the [hs-{FeNO}^{7}]$_2$ complex (41%; isomer shift δ = 0.71 mm/s and ΔE_Q = 1.85 mm/s). The data further show that the latter species is diamagnetic (S_t = 0), indicative of AF coupling between two S = 3/2 hs-{FeNO}^{7} centers. After 120 s, the [hs-{FeNO}^{7}]$_2$ intermediate has completely disappeared and a new Fe^{III}_2 complex appears (13%; isomer shift δ = 0.47 mm/s and ΔE_Q = 0.99 mm/s), which is the product after N_2O release. Hence, even under RFQ conditions, no intermediate can be observed between the initial dinitrosyl intermediate and the diferric product. Accompanying UV−vis measurements further show that a single turnover completes with the formation of the diferric product, before any Flavin oxidation occurs. In summary, these stopped-flow and RFQ experiments on *Tm* FDP have two important mechanistic implications: first, the diiron dinitrosyl intermediate, [hs-{FeNO}^{7}]$_2$, is the catalytically competent intermediate that is formed prior to any N_2O generation, ruling out other pathways where N−N coupling starts from the diiron mononitrosyl complex,[1837] and second, the reaction follows the direct coupling pathway, where the Flavin is not directly involved in catalysis (see below).

The latter result was further solidified in a follow up study by Kurtz and coworkers on deflavo-*Tm* FDP, which still undergoes NO reduction, albeit at a slower rate and lower yield than the wt enzyme.[1833,1838] Using RFQ-EPR, sub-stoichiometric amounts of NO (0.6 equiv NO per diiron site) were added to deflavo-*Tm* FDP and quenched after 200 ms to yield an intense S_t = 1/2 signal with a g value of ~2, which corresponds to the hs-Fe^{II}/hs-{FeNO}^{7} intermediate.[1838] Using RFQ-Mössbauer, excess NO (~3 equiv NO per diiron site) was added and first quenched after 100 ms to yield a prominent [hs-{FeNO}^{7}]$_2$ species, comprising 55% of total iron in the sample. This species shows isomer shift and quadrupole splitting parameters of 0.74 and 1.85 mm/s, respectively. Additionally, a Fe^{III}_2 species appears in the Mössbauer spectra with isomer shift and quadrupole splitting parameters of 0.44 and 0.92 mm/s, respectively, which are distinct from the as-isolated, oxidized state of deflavo-*Tm* FDP. After 60 s, the Fe^{III}_2 product is the predominant species in the Mössbauer spectra, and no signal of the starting Fe^{II}_2 species remains. With the absence of the FMN cofactor, these RFQ experiments demonstrate the ability of *Tm* FDP to reduce NO to N_2O via an [hs-{FeNO}^{7}]$_2$ intermediate, without the assistance of the Flavin cofactor.

What remains to be seen is how these results translate to other enzymes which are more dedicated NORs than *Tm* FDP, although the role of the [hs-{FeNO}^{7}]$_2$ complex as the central intermediate is now generally accepted in the field. The latter conclusion is supported by the available structural data (see above) that show two 5C iron centers in the FDP active sites, predispositioned for the binding of two NO molecules in the first steps of catalysis.

Hendrich and coworkers also performed RFQ experiments on the *Tm* FDP variant mentioned above where the SCS tyrosine residue has been replaced with a phenylalanine by mutagenesis.[1831] Using RFQ-Mössbauer experiments, substoichiometric NO (0.5 equiv NO per diiron site) was added and the reaction was quenched after 200 ms, leading to the identification of a number of species. The main component is the [hs-{FeNO}^{7}]$_2$ intermediate (30%), which gives rise to a well resolved quadrupole doublet with isomer shift and quadrupole splitting parameters of 0.76 and 1.89 mm/s, respectively. Other species present in the sample are a hs-Fe^{II}/hs-{FeNO}^{7} adduct and a diferric contaminent. After 90 s, the spectrum shows a broad hs-Fe^{II}/hs-{FeNO}^{7} signal (similar to that observed at 200 ms), but no diferric product. Even when more NO was added to this quenched sample, the reaction did not proceed. Correspondingly, steady state NOR assays with NADH showed no NADH oxidation. These results demonstrate that the Y197F *Tm* FDP variant is still able to bind NO at the active site, but is unable to induce N−N bond formation and N_2O generation, pointing towards the importance of the SCS Tyr for catalysis, especially for the N−N bond forming step. These aspects were further investigated using DFT calculations, which is discussed below.

More recently, Hendrich and co-workers reported RFQ experiments for *Dv* FDP, which has been shown to exhibit better NOR activity than *Tm* FDP (see Table 25).[1817,1835] Using RFQ-Mössbauer experiments, stoichiometric NO (2 equiv NO per diiron site) was added and reactions were quenched after 100 ms to yield a prominent quadrupole doublet, comprising 85% of total iron in the sample, with isomer shift and quadrupole splitting parameters of 0.71 and 1.85 mm/s, respectively.[1835] This doublet corresponds to a [hs-{FeNO}^{7}]$_2$ complex, with similar spectroscopic properties compared to the analogous intermediate in *Tm* FDP, and it was further confirmed (from high-field studies) that this species has a diamagnetic ground state, as expected for a diferrous dinitrosyl complex. The rapid and prominent formation of the diferrous dinitrosyl intermediate is not surprising, considering *Dv* FDP is a better FNOR than *Tm* FDP. This could imply that FDPs with better NOR activity might have a

Scheme 61. Mechanistic Possibilities for N−N Coupling from the [hs-$\{FeNO\}^7]_2$ Intermediate in FNORs

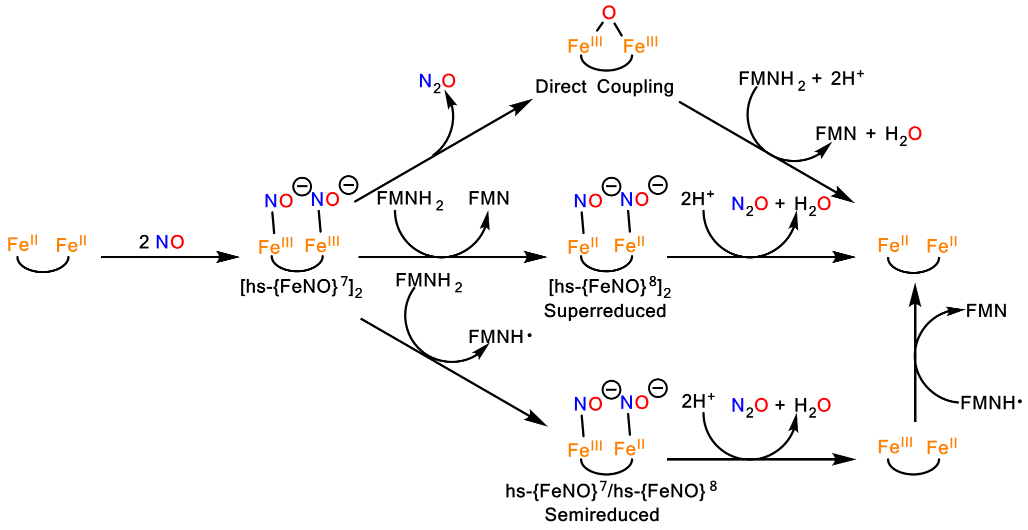

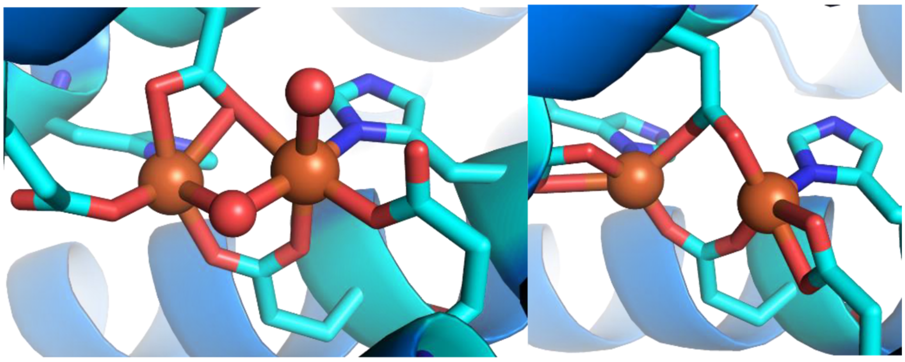

Figure 125. Left: PyMOL generated image of the crystal structure of the active site of soluble methane monooxygenase (sMMO; PDB: 1FYZ), showing an Fe−Fe distance of 3.28 Å.[1844] Right: PyMOL generated image of the crystal structure of the active site of ribonucleotide reductase (RNR; PDB: 1XIK), with an Fe−Fe distance of 3.90 Å.[1845]

larger binding constant for the second NO. These RFQ results constitute the first such data reported for FDPs other than *Tm* FDP and further support the finding that the transient [hs-$\{FeNO\}^7]_2$ complex is the catalytically competent intermediate for NOR activity in these enzymes.

5.2.4. Catalytic Cycle: Mechanistic Possibilities. On the basis of the RFQ studies described above,[1833,1835,1838] it is clear that NO reduction in FNORs is mediated by a diferrous dinitrosyl intermediate, [hs-$\{FeNO\}^7]_2$, that forms in the initial steps of catalysis. From here, several pathways exist as shown in Scheme 61 that vary based on the potential involvement of the FMN cofactor in the reaction, whether it is only used to reduce the diiron site after turnover or whether it is involved in generating additional reactive intermediates from the [hs-$\{FeNO\}^7]_2$ complex. The RFQ single turnover experiments described above indicate that the FMN cofactor is not directly involved in NO reduction in *Tm* FDP, and hence, this enzyme follows the direct coupling pathway in Scheme 61, top. Here, the [hs-$\{FeNO\}^7]_2$ intermediate is capable of promoting N−N coupling and subsequent N_2O release. The immediate product of the reaction would be a diferric μ-oxo (or μ-hydroxo) species, which the FMN cofactor then reduces back to the active diferrous state, accompanied by water release. Questions related to how N−N coupling is accomplished from the [hs-$\{FeNO\}^7]_2$ intermediate still need to be addressed, and whether this is the preferred pathway under turnover. In addition, the question remains whether more dedicated FNORs also follow the direct coupling pathway, as NO reduction in *Tm* FDP is relatively slow (a single turnover completes in ∼20 s). In this regard, it should be noted that the diferrous dinitrosyl adducts of soluble methane monooxygenase (sMMO) and ribonucleotide reductase (RNR) can be prepared (see Figure 125 for possible coordination sites), but these species are incapable of promoting the NOR reaction.[1839,1840] In addition, a number of diferrous dinitrosyl model complexes have been prepared, and these species tend to be stable as well, due to their very covalent Fe−NO bonds in the hs-$\{FeNO\}^7$ state (see above).[152] In the light of these observations, it is therefore not clear how FNORs promote the direct NO coupling pathway. In addition, no intermediate of the N−N coupling reaction in FDPs has been observed so far, so additional questions remain with respect to the nature of the N−N coupled intermediates that are formed prior to N_2O release.

Alternatively, the FMN cofactor could reduce the [hs-$\{FeNO\}^7]_2$ intermediate by either one or two electrons (and potentially transfer protons) under turnover, creating highly reactive hs-$\{FeNO\}^7$/hs-$\{FeNO\}^8$ or [hs-$\{FeNO\}^8]_2$ intermediates prior to N−N bond formation. These pathways are shown in Scheme 61, middle and bottom, and are referred to as the semireduced and superreduced mechanisms, respectively. In particular, the semireduced mechanism has been demonstrated in model complexes as a highly efficient pathway for NO

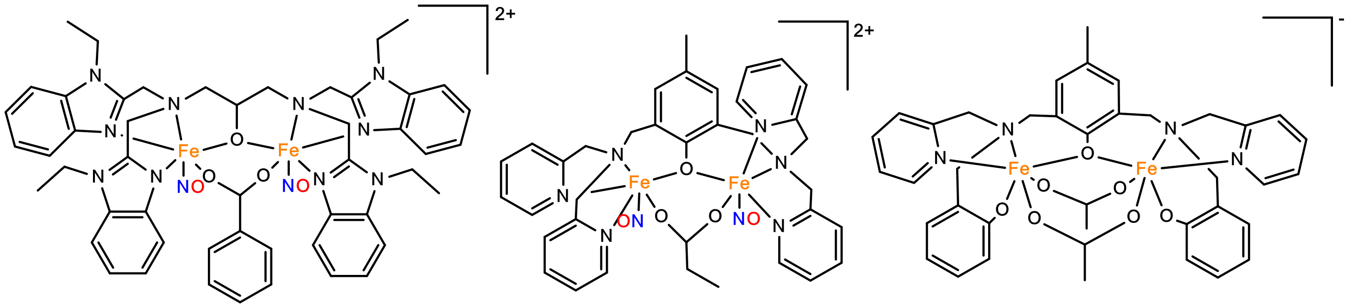

Feig et al, 1996 Zheng et al, 2013 Dong et al, 2018

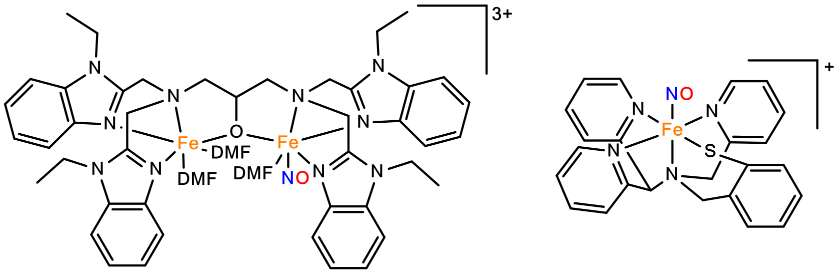

Jana et al, 2017 Confer et al, 2017

Figure 126. Functional model complexes for FNORs that show N_2O generation via photochemistry, direct reduction, semireduction, and superreduction.

reduction (see below).[1841−1843] In this case, N−N bond formation from the hs-$\{FeNO\}^7$/hs-$\{FeNO\}^8$ intermediate yields N_2O and a mixed-valent Fe^{II}/Fe^{III} μ-oxo (or μ-hydroxo) product. This step would be followed by another electron and proton transfer to the diiron center to release water and regenerate the diferrous active site. A variation of the semireduced pathway is the superreduced mechanism, where the FMN cofactor transfers two electrons (and possibly protons) to the diferrous dinitrosyl complex, generating a [hs-$\{FeNO\}^8]_2$ intermediate, which subsequently releases N_2O and water and regenerates the diferrous form of the active site. Intramolecular superreduction has not been observed yet in model complexes, possibly because the semireduced mechanism is so efficient that the complex proceeds to generate N_2O after the first reductive equivalent has been transferred to the [hs-$\{FeNO\}^7]_2$ complex.[88] Just like in the case of the RFQ studies on *Tm* FDP, intermediates of NO reduction have not been observed in model complexes either, leaving us with a large knowledge gap about the nature of the N−N coupled intermediates in these systems (and which are therefore omitted in Scheme 61). Further studies are necessary to elucidate the mechanistic details of NO reduction by non-heme diiron complexes. Mechanistic insight from DFT calculations is discussed in Section 5.4.

Alternative explanations for the lack of NOR reactivity of sMMO and RNR have recently been proposed, based on spectroscopic and theoretical studies on *Tm* FDP.[1835] One possible explanation involves the differences in bridging ligands between the iron centers in the active sites of NOR-active FDPs and the NOR-unreactive enzymes sMMO and RNR. For the diferrous forms of sMMO and RNR, the exchange coupling constants between the iron centers are only $J = 0.5$ cm^{-1} and $J = -0.5$ cm^{-1}, respectively.[1846,1847] Compared to diferrous *Tm* FDP, this weaker exchange coupling can be attributed to the lack of hydroxo bridges between the iron centers.[1844,1845] However, the presence of bridging carboxylates only may not be enough to (a) force the open binding sites on the iron centers to be in the proper syn conformation, and (b) keep the iron centers at a close distance. Accordingly, the lack of NOR activity in sMMO and RNR could be linked to less rigid diiron centers in these enzymes that impede N−N coupling. Another possible explanation is based on the fact that both sMMO and RNR lack proper SCS residues near the diiron site, unlike many FDPs (see Figure 123).[1844,1845] Here, the lack of a tyrosine or histidine SCS residue could preclude NOR activity in these enzymes, as demonstrated in mutagenesis experiments with FDPs that highlight the crucial roles of these amino acid side chains for catalysis (see above).[217,1831] Theoretical insight into the mechanistic roles of these SCS residues for FNOR catalysis is further discussed in Section 5.4.

5.3. Diiron Model Complexes for FDPs

5.3.1. The First Synthetic Diiron Dinitrosyl Complex.

Besides the enzymatic studies on FDPs, scientists have investigated the fundamental reactivity of NO with diiron sites using model complexes. As outlined in Section 1, synthetic models can complement studies on the corresponding enzymes as they provide a better handle on geometric and electronic effects on reactivity, and potentially allow for the trapping of intermediates at low temperatures. As evident from this chapter, model complexes have in fact successfully been used to map out all of the NO reduction pathways for FNORs shown in Scheme 61. The first diiron dinitrosyl model complex was reported in 1996 by Lippard and coworkers.[1848] This complex, $[Fe_2(N\text{-}Et\text{-}HPTB)(O_2CPh)(NO)_2](BF_4)_2$ (H[N-Et-HPTB] = N,N,N′,N′-tetrakis(2-(1-ethylbenzimidazolyl))-2-hydroxy-1,3-diaminopropane; see Figure 126) first demonstrated that diiron sites are capable of stabilizing the [hs-$\{FeNO\}^7]_2$ motif. The corresponding diferrous precursor complex was first generated and characterized both structurally and spectroscopically by Dong et al. and reported in 1993.[1849] This light yellow complex exhibits an intense UV−vis absorption band at 330 nm in acetonitrile (ε = 2400 M^{-1} cm^{-1}). Mössbauer spectroscopy shows parameters typical for hs-Fe^{II} for this compound with an isomer shift δ = 1.07 mm/s and a quadrupole splitting ΔE_Q = 3.13 mm/s. In this case, the two hs-Fe^{II} centers are AF coupled with an exchange coupling constant $J = -10.5$ cm^{-1} (and D =

Table 27. Spectroscopic Parameters for Select Diiron Model Complexes of FNORs

complex	ν(N−O) [cm^{-1}]	Δ [mm/s]	ΔE_Q [mm/s]	J [cm^{-1}][a]	ref
$[Fe_2(N\text{-}Et\text{-}HPTB)(O_2CPh)]^{2+}$		1.07	3.13	−10.5	1849
$[Fe_2(N\text{-}Et\text{-}HPTB)(O_2CPh)(NO)_2](BF_4)_2$	1785	0.67	1.44	−23	1848
$[Fe_2(N\text{-}Et\text{-}HPTB)(DMF)_3(NO)](BF_4)_3$	1768	1.21/0.63	3.05/1.35	−11.7	1851
$[L\{Fe(NO)\}_2(\mu\text{-}OR)](BPh_4)_2$	1745	0.65	1.43	~0	1852
$[Fe_2(BPMP)(OPr)](X)_2$		1.19	2.89	−3.6	1842
$[Fe_2(BPMP)(OPr)(NO)_2](X)_2$	1760	0.70	1.72	−7	1842
$[CoCp_2][Fe_2((Py_2PhO_2)MP)(OAc)_2]$		1.25	2.97		1853
Tm FDP$_{\text{di-NO}}$	1749[b]	0.71	1.85	−30	1765, 1835
Tm FDP$_{\text{mono-NO}}$	1681[b]	1.15/0.68	2.05/−1.56	−8.5	1835, 1836

[a] Using the Hamiltonian: $H = -2J(S_1 \cdot S_2)$. [b] From deflavo-*Tm* FDP.

8.9 cm^{-1}, E/D = 0.11 and g = 2.06). Upon reacting this precursor complex with NO gas in acetonitrile (or dichloromethane, propionitrile), an immediate color change from yellow to dark brown-green was observed. Recrystallization yielded dark green needles of the dinitrosyl complex, which is further characterized by an N−O stretching frequency of 1785 cm^{-1}. X-ray crystallography revealed two equivalent hs-$\{FeNO\}^7$ units that display short Fe−NO bonds of 1.75 Å and N−O distances of 1.15 Å, and Fe−N−O angles of about 167°. Importantly, these two hs-$\{FeNO\}^7$ moieties are coplanar with the NO ligands slightly pointing away from each another. The major linkage between the hs-$\{FeNO\}^7$ centers is an alkoxide bridge, with an Fe−O-Fe angle of 118°. UV−vis absorption spectra of the dinitrosyl complex show a weak band at 620 nm (ε = 579 M^{-1} cm^{-1}) and a shoulder at 520 nm (ε = 395 M^{-1} cm^{-1}). Room temperature magnetic susceptibility measurements indicate a magnetic moment approaching 5.48 μ_B, which is consistent with two uncoupled hs-$\{FeNO\}^7$ (S_t = 3/2) centers.[151] Temperature-dependent magnetic susceptibility measurements further indicate AF coupling between the hs-$\{FeNO\}^7$ units, with J = −23 cm^{-1}. Finally, Mössbauer data exhibit a single quadrupole doublet with an isomer shift of 0.67 mm/s and a quadrupole splitting of 1.44 mm/s, which are typical for non-heme hs-$\{FeNO\}^7$ complexes (see Table 27).

Interestingly, it was found later that upon irradiation with white light at 15 K, this complex proceeds to form N_2O at high yield (90%), as evident from the observation of a new signal at 2223 cm^{-1} in the IR spectra, which is the N−N stretching band of N_2O.[1850] During the first two minutes of irradiation, IR spectroscopy revealed a new signal at 1695 cm^{-1} (1665 cm^{-1} with ^{15}NO), which decreases over time, concomitant with the increase in the N_2O signal at 2223 cm^{-1}. This unusually low N−O stretching band (for a hs-$\{FeNO\}^7$ complex) is similar to that of the mononitrosyl adduct of *Tm* FDP, which is observed at 1681 cm^{-1} (see Section 5.2).[1836] Both species have been assigned to semi-bridged hs-Fe^{II}/hs-$\{FeNO\}^7$ complexes as shown in Scheme 62, where the coordinated NO ligand forms a weak electrostatic interaction with the second iron center (Fe2 in Scheme 62). The interaction of the NO ligand with Fe2, which acts as a Lewis acid, reduces charge donation of the bound $^3NO^-$ ligand to Fe1, which manifests itself in the relatively low N−O stretch, but also a reduced magnetic exchange coupling between the two iron centers (see Section 5.2).[1835] It was further proposed by Lippard and coworkers that this special binding mode activates the NO ligand for electrophilic attack by the second NO (that is initially photolized).[1850] A transient hyponitrite intermediate was then proposed to form in this reaction, which ultimately decays to produce N_2O. Although these seminal studies paved the way for further model complex studies on FNORs, the observed reactivity is unlikely to be biologically relevant, due to the requirement for light activation. In addition, as discussed in Section 5.2, NO reduction by FDPs is thought to proceed through a key $[\text{hs-}\{FeNO\}^7]_2$ dinitrosyl intermediate, which differs from the findings for $[Fe_2(N\text{-}Et\text{-}HPTB)(O_2CPh)(NO)_2]^{2+}$. Another interesting question is whether other types of photochemical reactions could also contribute to N_2O generation in this model complex.

Scheme 62. Diferrous Mononitrosyl Complex Showing a Weak Electrostatic Interaction between NO and Fe$_2$ (Dashed Line)[a]

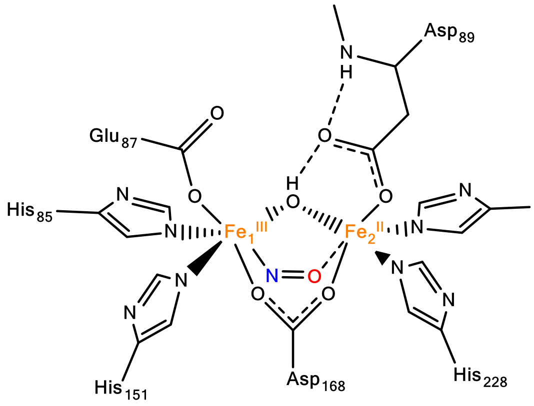

[a] Adapted from DFT results for *Tm* FDP.[1835].

5.3.2. First Functional Model for FNORs: Semireduced Mechanism for NO Reduction.

Lehnert and coworkers showed that a similar stabilization of a $[\text{hs-}\{FeNO\}^7]_2$ complex can be achieved in the model complex $[Fe_2(BPMP)(OPr)(NO)_2](X)_2$ (X = BPh_4^-, OTf$^-$, BF_4^-; BPMP$^-$ = 2,6-bis[(bis(2-pyridylmethyl)amino)-methyl]-4-methylphenolate anion; see Figure 126).[1842,1843] This complex closely captures the coordination environment of the active site of FNORs, using a central phenolate group to model the bridging hydroxide, appended pyridyl donors instead of imidazole groups (from His), and a bridging carboxylate ligand to complete the coordination spheres of the iron centers. While the BPMP$^-$ ligand is symmetric, X-ray crystallography of this complex revealed that the coordination environment around each iron site is different, with one NO bound trans to a tertiary amine while the other NO is bound trans to a pyridine. This asymmetry is reflected in slight differences in the Fe−NO bond distances of 1.77 and 1.80 Å and Fe−N−O bond angles of 156° and 145° for the FeNO units with the NO ligand trans to the tertiary amine and the pyridine, respectively. The crystal structure of this complex, shown in Figure 127, further reveals that the two NO ligands are bound in a coplanar or syn/cis geometry with an (O)N−Fe−Fe−N(O) dihedral angle of only 6°, leading to an (O)N−N(O) distance of only 2.80 Å. This binding mode reflects the assumed geometry of the dinitrosyl adduct in FNORs (see above). Further work showed that this is due to the presence of the bridging carboxylate ligand, which forces the two FeNO units into the cis geometry.[1854] This coplanar geometry is important in allowing for fast and efficient N−N coupling and N_2O formation (see below). From vibrational spectroscopy, the Fe−NO and N−O stretching frequencies of $[Fe_2(BPMP)(OPr)(NO)_2]^{2+}$ are 487 and 1760 cm^{-1}, respectively, which compares well with other hs-$\{FeNO\}^7$ complexes (see Section 5.1) and the corresponding vibrational frequencies (459 and 1749 cm^{-1}) reported for deflavo-*Tm* FDP. This complex is further characterized by a broad charge-transfer band at 410 nm. Mössbauer spectroscopy of the diferrous precursor, $[Fe_2(BPMP)(OPr)](OTf)_2$, shows one quadrupole doublet with an isomer shift of 1.19 mm/s and a quadrupole splitting of 2.89 mm/s, similar to Lippard's complex. In the dinitrosyl complex, the isomer shift is 0.70 mm/s, indicative of partial iron oxidation, in agreement with the Fe(III)−NO^- type electronic structure of non-heme hs-$\{FeNO\}^7$ centers (see Section 5.1), and the quadrupole splitting is $\Delta E_Q = 1.72$ mm/s. SQUID magnetic susceptibility data on the diferrous precursor indicate AF coupling between the hs-Fe^{II} centers, with a coupling constant $J = -3.6$ cm^{-1}. Binding of NO increases the AF coupling ($J = -7$ cm^{-1}; see Table 27), again indicative of partial oxidation of the iron centers in the NO-bound form, which increases the covalent interaction of the iron centers with the phenolate bridge, and in this way, enhances the AF coupling across the bridge. Because of this, the [hs-$\{FeNO\}^7]_2$ complex has a total spin $S_t = 0$ in the ground state. It is notable here that the AF coupling of the iron centers is enhanced in FNORs and $[Fe_2(N\text{-}Et\text{-}HPTB)(O_2CPh)(NO)_2]^{2+}$ compared to $[Fe_2(BPMP)(OPr)(NO)_2]^{2+}$. This is due to hydroxide/alkoxide bridges in the former, which mediate stronger covalent interactions with the iron centers, leading to enhanced AF exchange coupling and increased *J* coupling constants compared to phenolate-bridged systems.

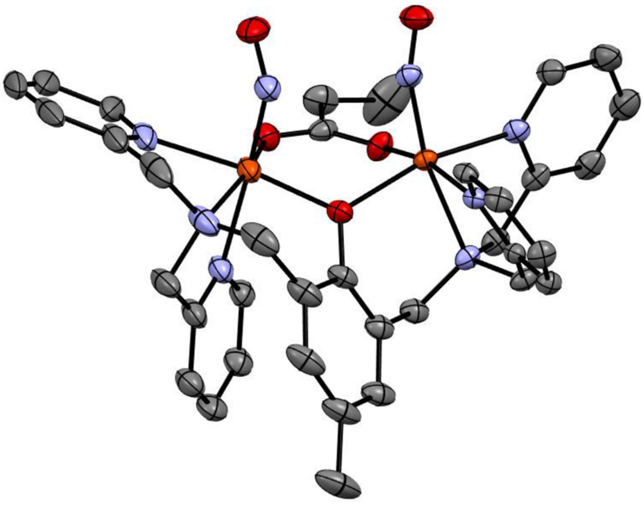

Figure 127. Crystal structure of the complex $[Fe_2(BPMP)(OPr)(NO)_2](BPh_4)_2$.[1843] All H atoms and counter ions are omitted for clarity.

Cyclic voltammetry of $[Fe_2(BPMP)(OPr)(NO)_2]^{2+}$ shows an irreversible reduction at −1.15 V versus Fc^+/Fc. Further IR-spectroelectrochemical studies then demonstrate that this reduction leads to the generation of N_2O (Figure 128, left), where the decrease in the intensity of the N−O stretching band at 1765 cm^{-1} (in CH_2Cl_2 solution) and the rise of the N−N stretch of N_2O at 2223 cm^{-1} exactly track with each other (Figure 128, right), and no intermediates of the reaction can be identified. These data show that $[Fe_2(BPMP)(OPr)(NO)_2]^{2+}$ is in fact a functional model complex for FNORs.[1842] Chemical reduction with $CoCp_2$ and isotope scrambling experiments further demonstrate that one equiv of reductant is sufficient for intramolecular N−N coupling and quantitative N_2O formation. Hence, $[Fe_2(BPMP)(OPr)(NO)_2]^{2+}$ constitutes the paradigm example for the semireduced pathway, according to Scheme 61. Further stopped-flow IR experiments were conducted to establish rate constants for N_2O formation by this complex, but it turned out that the reaction is in fact complete within the dead time (156 ms) of the instrument, as shown in Figure 129.[1842] This result translates into a lower limit for $k_{obs} > 10^2$ s^{-1} at room temperature. These data therefore indicate that intramolecular semireduction is a highly efficient and fast process, and therefore constitutes a mechanistic possibility for FNORs and a paradigm for a synthetic (electrocatalytic) process aimed at cleanly reducing NO to N_2O. Low-temperature chemical reduction experiments further show that N−N coupling and N_2O release can proceed even at −80 °C, indicating that the process has a small activation barrier, in agreement with the fast kinetics observed in the stopped-flow IR measurements. These low-temperature experiments further allowed for the identification of the mixed-valent Fe^{II}/Fe^{III} product after N_2O release by EPR spectroscopy. Here, the two iron centers are AF coupled and give rise to a characteristic $S_t = 1/2$ EPR signal, typically observed for exchange-coupled, mixed-valent Fe^{II}/Fe^{III} dimers.[1855] Curiously, when the reaction mixture is warmed to room temperature or the reaction is directly performed at room temperature, the mixed-valent product is EPR silent, which is a result that could not be fully rationalized in the initial studies.[1842]

Subsequent studies by Majumdar's group identified the diiron dinitrosyl complex $[Fe_2(N\text{-}Et\text{-}HPTB)(DMF)_2(NO)_2](BF_4)_3$ as a second example of a [hs-$\{FeNO\}^7]_2$ system that can undergo semireduction.[1841] This complex uses the same coligand as Lippard's compound, $[Fe_2(N\text{-}Et\text{-}HPTB)(O_2CPh)(NO)_2](BF_4)_2$, but has two dimethylformamide (DMF) solvent molecules bound to the iron centers to complete their 6C coordination spheres. The Fe−NO and N−O bond distances of this complex are 1.729 and 1.748 Å and 1.123 and 1.147 Å, respectively. The Fe−N−O bond angles, 175° and 165°, of the two FeNO units are also different, showing that the structure is asymmetric. The N−O stretch of this complex is observed at 1782 cm^{-1}, very similar to that of Lippard's original complex with the bridging benzoate group. Mössbauer spectroscopy of $[Fe_2(N\text{-}Et\text{-}HPTB)(DMF)_2(NO)_2](BF_4)_3$ shows a quadrupole doublet with an isomer shift of 0.64 mm/s and a quadrupole splitting of 1.33 mm/s. The two hs-$\{FeNO\}^7$ units are again AF coupled, with $J = -28$ cm^{-1}. Upon one-electron reduction with $CoCp_2$, $[Fe_2(N\text{-}Et\text{-}HPTB)(DMF)_2(NO)_2](BF_4)_3$ shows quantitative N_2O formation, and thus, this complex is the second reported example of a [hs-$\{FeNO\}^7]_2$ complex that is able to undergo semireduction.[1841] In the product mixture obtained after N_2O

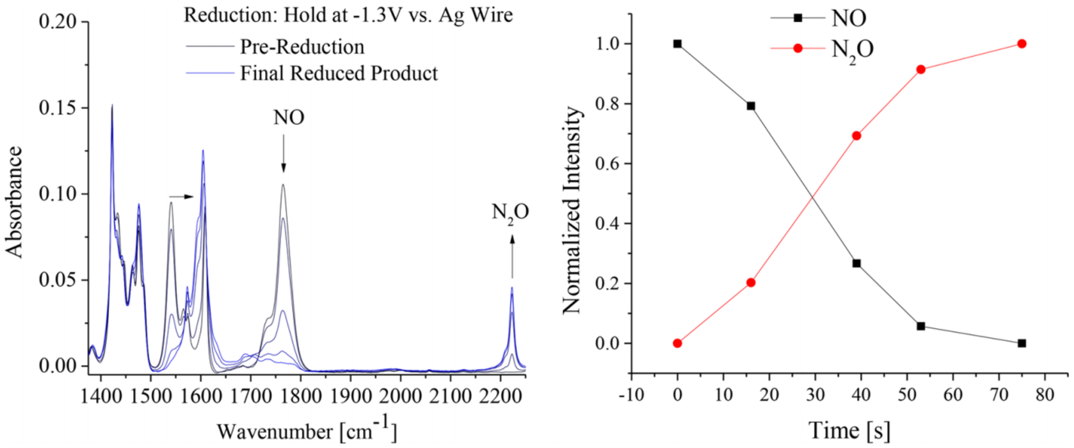

Figure 128. Left: IR-spectroelectrochemical (IR-SEC) monitoring of the reduction of ~5 mM $[Fe_2(BPMP)(OPr)(NO)_2]^{2+}$ upon applying a potential of −1.3 V (vs Ag wire), showing the loss of the N−O stretching band at 1765 cm^{-1} along with an increase of the N−N stretching band of N_2O at 2223 cm^{-1} and a shift of the carboxylate band over time (indicated by the arrow). Right: The plot of normalized intensities of the NO and N_2O bands over time illustrates the direct conversion of NO to N_2O without the formation of any observable intermediates on the IR-SEC time scale. Reprinted with permission from ref 1842. Copyright 2018 American Chemical Society.

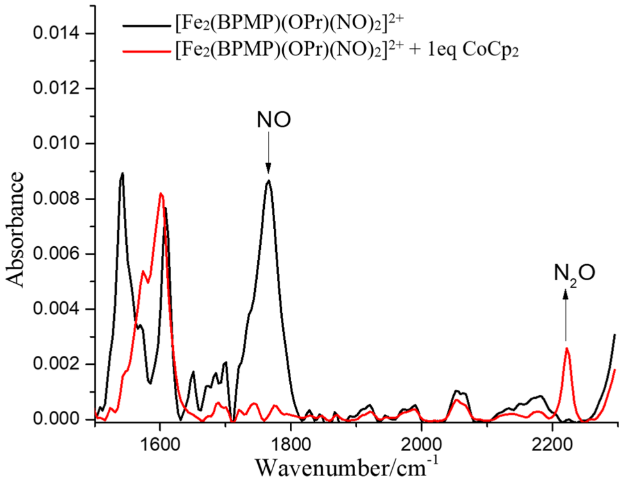

Figure 129. Stopped-flow IR experiment monitoring the reduction of 8.1 mM $[Fe_2(BPMP)(OPr)(NO)_2]^{2+}$ in CH_2Cl_2 with one equiv of $CoCp_2$. The data show that completion of the N−N coupling process and N_2O release occur within the 156 ms dead time of the instrument. Reprinted with permission from ref 1842. Copyright 2018 American Chemical Society.

release, a mixed-valent Fe^{II}/Fe^{III} complex was identified, evident from EPR spectroscopy, showing an S_t = 1/2 signal with g = 1.55, 1.79, 2.03. Mass spectrometry identified several products, including the Fe^{II}/Fe^{III} dimer $[Fe_2(N\text{-}Et\text{-}HPTB)(\mu\text{-}O)]^{2+}$, likely responsible for the observed EPR signals, and the tetranuclear complexes $[Fe_4(N\text{-}Et\text{-}HPTB)_2(\mu\text{-}OH)_3(\mu\text{-}O)]^{3+}$ and $[Fe_4(N\text{-}Et\text{-}HPTB)_2(\mu\text{-}OH)_2(\mu\text{-}O)]^{4+}$, which are EPR silent. These species are likely in equilibrium in solution. The tetranuclear complex $[Fe_4(N\text{-}Et\text{-}HPTB)_2(\mu OH)_2(\mu\text{-}O)]^{4+}$ was further characterized by X-ray crystallography as shown in Figure 130a.[1841] When $[Fe_2(N\text{-}Et\text{-}HPTB)(NO)_2(DMF)_2]^{3+}$ was treated with two equiv of $CoCp_2$, a different tetranuclear complex was isolated and also characterized by X-ray crystallography as shown in Figure 130b. The isolation of these tetranuclear complexes is a significant accomplishment, as this indicates that dinuclear model complexes of FNORs have a tendency to dimerize via the oxo groups that are formed when N_2O is released from the corresponding dinitrosyl complexes. This finding would explain why the room temperature one-electron reduction product of $[Fe_2(BPMP)(OPr)(NO)_2]^{2+}$ is EPR silent (see above), likely due to the formation of similar tetrameric or oligomeric species in solution.[1842] Most recently, semireduction has also been demonstrated by Majumdar's group for a hydrosulfide-coordinated diiron dinitrosyl complex, $[Fe_2(N\text{-}Et\text{-}HPTB)(SH)(DMF)(NO)_2](BF_4)_2$.[1856]

5.3.3. The Superreduced Mechanism. Majumdar's group was also able to prepare a mononitrosyl analog, $[Fe_2(N\text{-}Et\text{-}HPTB)(DMF)_3(NO)](BF_4)_3$ (see Figure 126), of their dinitrosyl complex discussed above.[1841,1851] To synthesize this complex, a redox synthetic strategy was employed. First $[Fe_2(N\text{-}Et\text{-}HPTB)(CH_3COS)](BF_4)_2$ was prepared by addition of CH_3COSH into the reaction mixture during the metalation of the H[N-Et-HPTB] ligand. By treatment of this complex with $[NO](BF_4)$, the bridging thioacetate ligand may form CH_3COSNO, which can then undergo homolytic cleavage to generate NO and the $CH_3COS^\bullet$ radical. It was further proposed that this radical remains bound to one of the iron centers, creating an asymmetry in the coordination environment of this complex. This asymmetry subsequently induces selective formation of the mononitrosyl complex, hs-Fe^{II}/hs-$\{FeNO\}^7$. X-ray crystallography revealed Fe−NO and N−O bond distances of 1.78 Å and 1.07 Å, respectively, and an Fe−N−O angle of 160.5° for this complex, which are all similar to the dinitrosyl analog. The N−O stretch of this species is located at 1768 cm^{-1} in the solid state, which is lower in energy compared to that of the dinitrosyl complex. Mössbauer spectroscopy shows distinct signals for both iron sites, with an isomer shift of 1.21 mm/s and a quadrupole splitting of 3.05 mm/s for the hs-Fe^{II} center (S = 2) and δ = 0.63 mm/s and ΔE_Q = 1.35 mm/s for the hs-$\{FeNO\}^7$ unit (S = 3/2). The magnetic exchange coupling between the hs-Fe^{II} and the hs-$\{FeNO\}^7$ center is reduced in the mononitrosyl complex, with J = −11.7 cm^{-1},[1841] compared to the dinitrosyl analog (see above and Table 27). Interestingly, addition of 0.5 equiv of $CoCp_2$ to a solution of $[Fe_2(N\text{-}Et\text{-}HPTB)(DMF)_3(NO)](BF_4)_3$ at room temperature only generates ~50% N_2O, indicating that the mononitrosyl complex is not able to undergo semireduction, in contrast to its dinitrosyl analog. This again emphasizes the importance of the $[\text{hs-}\{FeNO\}^7]_2$ intermediate in promoting

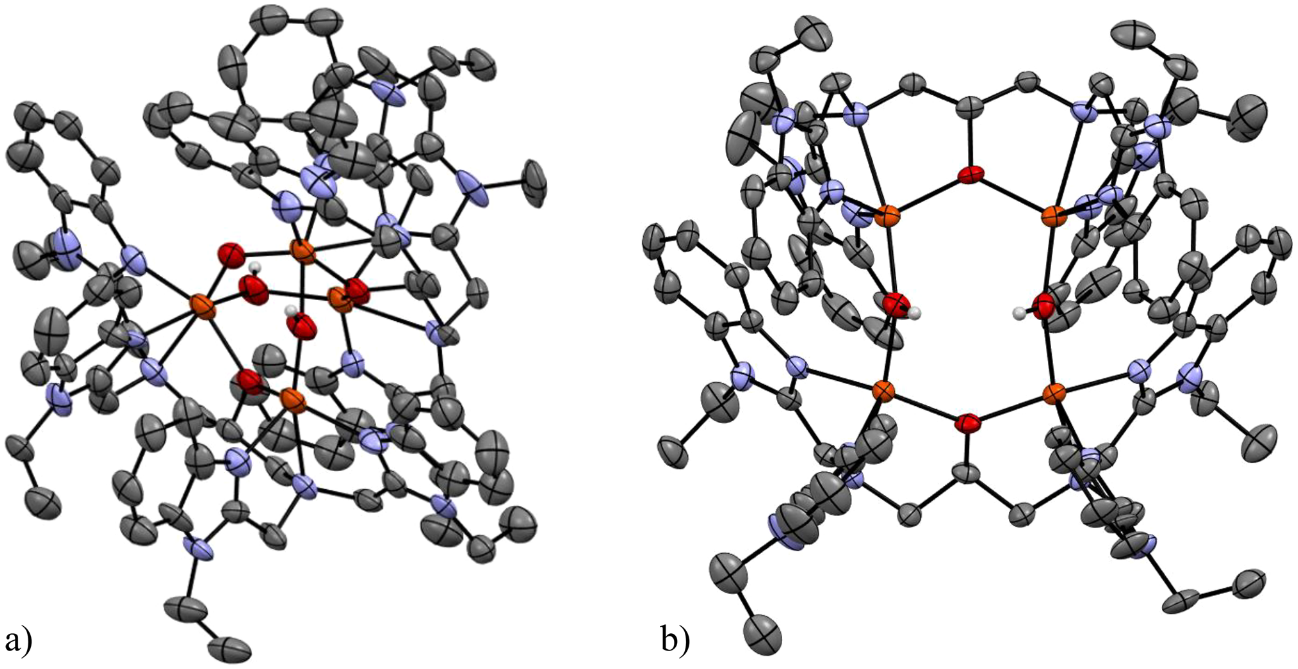

Figure 130. X-ray crystal structures of the tetranuclear complexes that form after the reduction of $[Fe_2(N\text{-}Et\text{-}HPTB)(DMF)_2(NO)_2](BF_4)_3$with one equivalent (a) or two equivalents (b) of $CoCp_2$.[1841] All H atoms (except for bridging OH^-) and counter ions are omitted for clarity.

efficient N−N coupling and N_2O formation. For the mononitrosyl complex, addition of one equiv of reductant is required for quantitative N_2O production, which shows that this complex follows the superreduced pathway (see Scheme 61); however, in an intermolecular fashion where two reduced hs-Fe^{II}/hs-$\{FeNO\}^8$ intermediates have to come together to induce N−N coupling, giving 89% N_2O yield within 5 minutes. Hence, additional activation energy is required to induce N−N bond formation in mononitrosyl complexes, where the two hs-$\{FeNO\}^7$ units are not held in close proximity by the ligand scaffold, requiring superreduction to achieve N_2O generation.

Similar intermolecular superreduction has also been observed for the mononuclear ls-$\{FeNO\}^7$ complex $[Fe(N_3PyS)(NO)](BF_4)$ (see above and Figure 126).[1776,1799] X-ray crystallography revealed Fe−NO and N−O distances of 1.73 Å and 1.15 Å, respectively, and an Fe−N−O angle of 147° for this complex. Unlike other non-heme $\{FeNO\}^7$ model complexes, this compound shows a ls-$\{FeNO\}^7$ ground state, as evident from EPR spectroscopy, which shows a rhombic EPR signal at g = 2.071, 2.022, 1.976 and strong hyperfine coupling with the coordinated NO ligand, with $A(^{14}N)$ = 27, 60, 28 MHz. These properties are in fact very similar to those of ls-$\{FeNO\}^7$ complexes in hemes (see Section 2.2). $[Fe(NO)(N_3PyS)]^+$ exhibits two N−O stretching bands at 1660 and 1753 cm^{-1} in ATR-IR, with the latter presumably belonging to a small amount of a hs component. The complex was further characterized by Mössbauer and X-ray absorption spectroscopy. Upon treatment with 1 equiv of reductant, the N−O stretch shifts to 1588 cm^{-1}, as observed by rRaman spectroscopy, indicating the formation of a hs-$\{FeNO\}^8$ complex. This conclusion is confirmed by the Evans method, which revealed an S_t = 1 ground state for this complex. From rRaman spectroscopy, the Fe−NO stretching mode of the hs-$\{FeNO\}^8$ complex is observed at 498 cm^{-1}, which is in between the Fe−NO stretching frequencies of the hs-$\{FeNO\}^8$ complexes $[Fe(TMG_3tren)(NO)]^+$ (435 cm^{-1}, unstable) and [Fe(L3)(NO)] (553 cm^{-1}, stable). Accordingly, the hs-$\{FeNO\}^8$ complex $[Fe(NO)(N_3PyS)]$ is metastable and slowly decays at 23 °C ($t_{1/2}$ = 0.5 h), accompanied by a color change of the solution from purple to red-orange.[1799] This decay process is accompanied by the generation of substoichiometric amounts of N_2O (54%) over 20 hours. This observation supports the idea that N_2O formation by this complex follows an intermolecular superreduced mechanism.

In summary, these results demonstrate that reduction is a potent means of activating otherwise stable non-heme hs-$\{FeNO\}^7$ complexes for N−N coupling and N_2O formation.[88] In diiron dinitrosyl model complexes, intramolecular semireduction is identified as a very efficient and fast means to induce N_2O formation, in a process with a very small activation energy. Superreduction is only observed for mononitrosyl complexes so far, and proceeds in an intermolecular fashion. We believe that this is due to the fact that semireduction is such an efficient pathway that once a $[hs\text{-}\{FeNO\}^7]_2$ complex is reduced by one electron, the resulting hs-$\{FeNO\}^7$/hs-$\{FeNO\}^8$ intermediate quickly proceeds by N−N bond formation without the need to "wait" for the second reductive equivalent to be delivered. These results are further supported by DFT calculations, as discussed below. In contrast, in mononitrosyl complexes where the two FeNO units are not locked into a syn/cis position, in close proximity, the N−N coupling reaction is less efficient and has a higher energy barrier, and the reaction can only proceed via the superreduced pathway.

5.3.4. Reactivity of a Trans Diiron Dinitrosyl Dimer.

So far, both examples of $[hs\text{-}\{FeNO\}^7]_2$ complexes discussed above that produce N_2O via semireduction have the two NO ligands bound in a syn/cis position. One interesting question in this regard is how the N−N bond formation step depends on the relative orientation of the two FeNO units. Meyer and coworkers prepared the complex $[L\{Fe(NO)\}_2(\mu\text{-}OR)](BPh_4)_2$ (L = 7,7′-((1H-pyrazole-3,5-diyl)bis(methylene))bis-

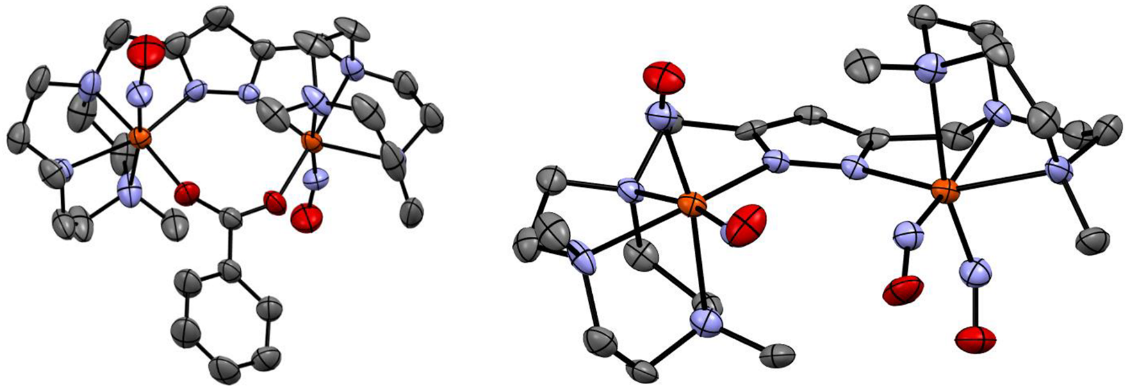

Figure 131. Left: Crystal structure of the complex $[L\{Fe(NO)\}_2(\mu\text{-}OR)](BPh_4)_2$, which features two NO ligands coordinated in a trans orientation. Right: Crystal structure of the dinuclear DNIC that forms after the one-electron reduction of the dinitrosyl complex on the left.[1852] All H atoms and counter ions are omitted for clarity.

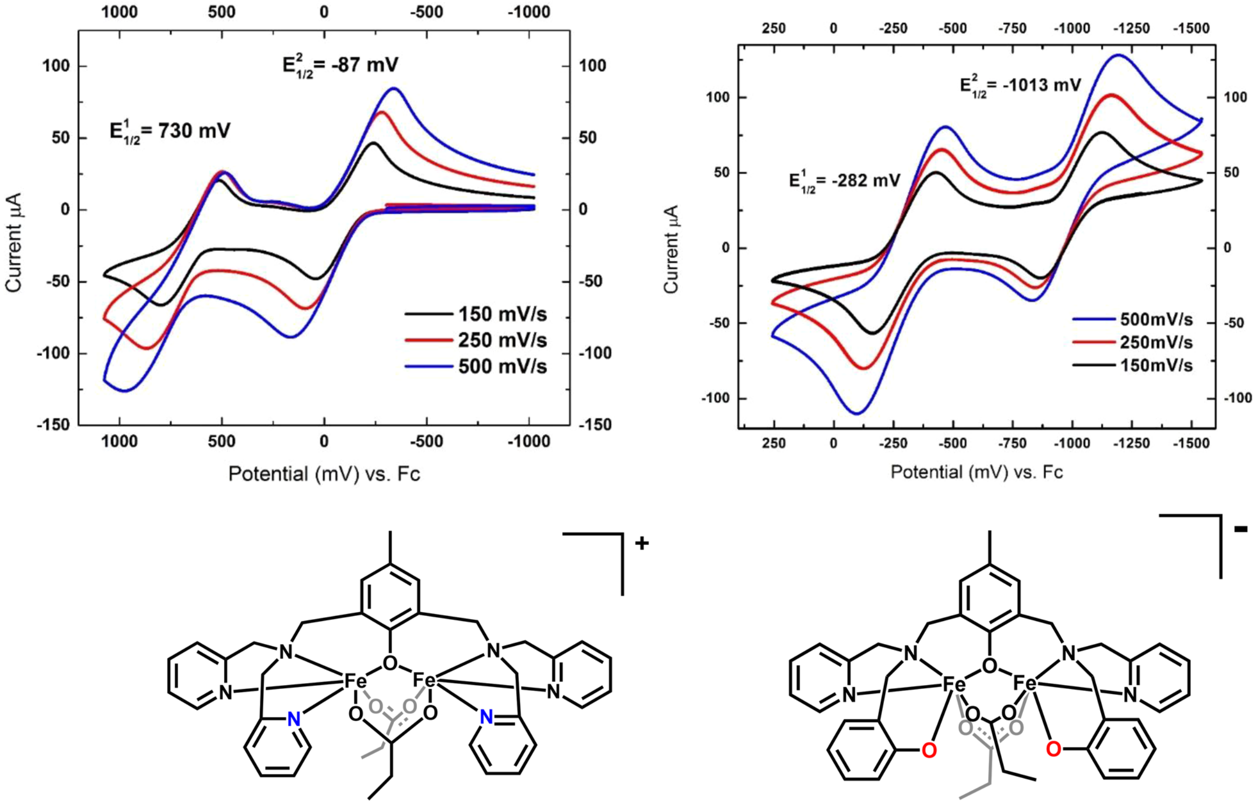

Figure 132. Left: $[Fe_2(BPMP)(OPr)_2](X)$ and its redox potentials measured by cyclic voltammetry. Right: $[CoCp_2][Fe_2((Py_2PhO_2)MP)(OAc)_2]$ with the redox potentials shifted by about −1 V, due to the use of a more electron-donating coligand. Adapted with permission from ref 88. Copyright 2019 American Chemical Society.

(1,4-dimethyl-1,4,7-triazonane anion; OR^- = benzoate, acetate), which, based on X-ray crystallography (for the benzoate complex), features a trans conformation of the two NO ligands (see Figure 131, left).[1852] The average Fe−NO and N−O bond distances in this complex are 1.77 Å and 1.15 Å, respectively. The Fe−N−O angles are in the typical range of 149−154°. The complex was further characterized by UV−vis spectroscopy, showing absorption bands at 445 nm (ε = 1540 M^{-1} cm^{-1}), 560 nm (ε = 325 M^{-1} cm^{-1}) and 675 nm (ε = 240 M^{-1} cm^{-1}). The N−O stretch of this complex is located at 1745 cm^{-1}, which is close to the value observed for deflavo-*Tm* FDP (1749 cm^{-1}). Mössbauer spectroscopy shows an isomer shift of 0.65 mm/s and a quadrupole splitting of 1.43 mm/s for this complex, which is in the typical range of other $[hs\text{-}\{FeNO\}^7]_2$ adducts (see Table 27). Even though the complex is bridged by a pyrazolate and a carboxylate group (see Figure 131, left), the two hs-$\{FeNO\}^7$ units are expected to be essentially magnetically uncoupled (as observed for the diferrous precursor complex). Upon reducing this complex with one equiv of $CoCp_2$, no N_2O gas formation was observed. Instead, IR spectroscopy revealed the formation of a DNIC, evident from the appearance of two IR bands sensitive to NO isotope substitution: one intense feature at 1670 cm^{-1} was easily identified, whereas the second feature was obscured by the carboxylate stretch of the coligand (but subsequently identified at 1549 cm^{-1} in the $^{15}N^{18}O$ complex). Mössbauer spectroscopy

Scheme 63. $Fe^{II}_2/Fe^{II}Fe^{III}$ Reduction Potentials of Diiron Model Complexes Relative to That of *E. coli.* Flavorubredoxin[a]

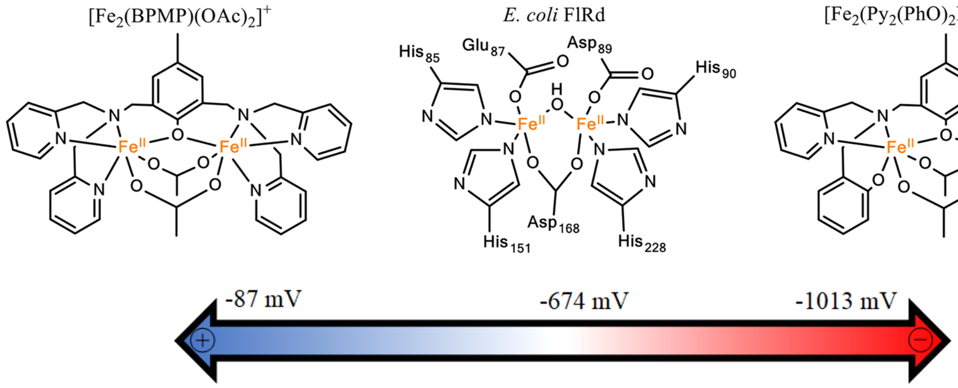

[a]Potentials are referenced against the Fc^+/Fc standard.

Scheme 64. Catalytic Cycle of NO Reduction by $[CoCp_2][Fe_2((Py_2PhO_2)MP)(OAc)_2]$[1853]

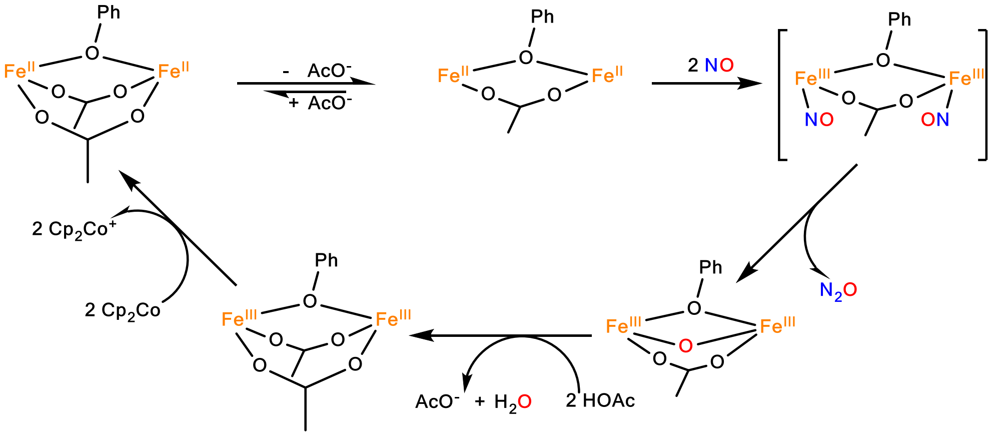

revealed the presence of two products: one species (57% yield) with δ = 1.16 mm/s and ΔE_Q = 2.66 mm/s, assigned to hs-Fe(II), and one species (43% yield) with δ = 0.48 mm/s and ΔE_Q = 0.50 mm/s, in agreement with the formation of a DNIC. The products were subsequently characterized by X-ray crystallography, which shows the surprising formation of a dimer of $\{Fe(NO)_2\}^9$ DNICs and a diferrous complex, the former is shown in Figure 131, right.[1852] Despite this unexpected product, these results confirm that upon one-electron reduction, $[L\{Fe(NO)\}_2(\mu\text{-OR})]^+$ simply undergoes disproportionation (instead of N_2O formation), a reaction that is commonly observed for mononuclear hs-$\{FeNO\}^8$ complexes (eq 26; see Section 5.1.2). The IR spectrum of the isolated $[\{Fe(NO)_2\}^9]_2$ dimer shows N−O stretching frequencies of 1690 and 1575 cm^{-1}, where the band separation of $\Delta\nu$(N−O) = 115 cm^{-1} is typical for 6C $\{Fe(NO)_2\}^9$ moieties. This study once again emphasizes the importance of the syn/cis orientation of the NO ligands in the diiron core to enable fast and efficient N−N bond formation and N_2O production in these types of complexes.

5.3.5. Tuning the Reduction Potentials of the Diiron Model Complexes. As discussed above, RFQ-spectroscopic experiments by Kurtz and coworkers on *Tm* FDP have provided strong evidence that this enzyme follows the direct NO reduction pathway (Scheme 61, top).[88] In contrast, all model complexes described above form stable NO complexes that need reductive activation to induce N−N coupling and N_2O formation. One important aspect to consider in rationalizing this difference is redox potential. As shown in Figure 132, left, the complex $[Fe_2(BPMP)(OPr)_2](X)$ shows $Fe^{II}_2/Fe^{II}Fe^{III}$ and $Fe^{II}Fe^{III}/Fe^{III}_2$ reduction potentials of −87 and +730 mV (all potentials discussed in this section are given vs the Fc^+/Fc standard),[88] which is significantly more positive than the corresponding reduction potentials in FDPs. For example, for *Ec* FlRd the $Fe^{II}_2/Fe^{II}Fe^{III}$ and $Fe^{II}Fe^{III}/Fe^{III}_2$ potentials were determined to be around −674 and −604 mV (vs Fc^+/Fc), respectively.[1822] Hence, in this sense, the $Fe_2(BPMP)^{3+}$ core can only serve as a one-electron reductant during NO reduction, as the $Fe^{II}Fe^{III}/Fe^{III}_2$ potential is too positive to be accessible for this process. Therefore, Lehnert and coworkers hypothesized that one of the reasons why the model complexes cannot undergo the direct reduction pathway is that their reduction potentials are too positive. To test this hypothesis, a modification to the $BPMP^-$ ligand scaffold was made where one of the pyridine groups per iron center was replaced by a stronger donating, anionic phenolate group. Please note that this ligand and other, related $BPMP^-$ derivatives are well known in the literature and have been used in the past to model purple acid phosphatase enzymes.[1857−1861] Cyclic voltammetry measurements of the corresponding complex $[CoCp_2]$-$[Fe_2((Py_2PhO_2)MP)(OAc)_2]$ (see Figure 126) indeed revealed reduction potentials that are shifted negative by about 1 V, observed at −282 and −1013 mV (see Figure 132, right), compared to the original complex.[1853] The range of reduction potentials for the $Fe^{II}_2/Fe^{II}Fe^{III}$ couples in these model complexes and the *Ec* FIRd is further illustrated in Scheme 63.

Importantly, even though the solid state structure of $[CoCp_2][Fe_2((Py_2PhO_2)MP)(OAc)_2]$ shows that both iron centers are 6C, and hence, coordinatively saturated, UV−vis experiments revealed that there is a change in coordination number in solution.[1853] At room temperature, this complex shows a broad absorption band at 530 nm (e = 2620 M^{-1} cm^{-1}, in CH_2Cl_2). When the solution is cooled to −80 °C, this signal gradually and reversibly disappears, leaving a weak feature at around 500 nm in the absorption spectrum. These results indicate that in solution, the bridging carboxylate ligands of $[CoCp_2][Fe_2((Py_2PhO_2)MP)(OAc)_2]$ are fluxional and can dissociate (partly or completely) to form 5C iron centers. At lower temperature, the carboxylate ligand(s) rebind, driven by entropy, leading to the 6C structure observed by X-ray crystallography. Reaction of $[CoCp_2][Fe_2((Py_2PhO_2)MP)(OAc)_2]$ with NO at room temperature leads to an immediate color change of the solution and formation of quantitative amounts of N_2O and the diferric complex, likely bridged by an oxo group (see Scheme 64).[1853] The latter is evident from Mössbauer spectroscopy: whereas the diferrous starting complex shows an isomer shift and quadrupole splitting of 1.25 and 2.97 mm/s, typical for hs-Fe^{II}, the product after NO addition shows a shift in the isomer shift and quadrupole splitting to 0.53 and 0.80 mm/s, respectively. The latter values are typical for hs-Fe^{III}. These results constitute the first observation of direct NO reduction by a diiron model complex, in support of the mechanistic findings for *Tm* FDP, and they further imply that reduction potential is one important parameter that determines which path in Scheme 61 a diiron center can take for NO reduction.

In addition, by treating the diferric reaction product with acetic acid (to remove the oxo bridge as water), and then re-reducing the complex, multiple turnovers of NO reduction, generating quantitative amounts of N_2O, can be catalyzed, as indicated in Scheme 64.[1853] When the reaction of $[CoCp_2][Fe_2((Py_2PhO_2)MP)(OAc)_2]$ with NO was conducted at −80 °C, the appearance of a new absorption band at 430 nm with a shoulder at 525 nm was observed, which was formed with a k_{obs} = 0.1 s^{-1}. Under these conditions, the direct reduction of NO to N_2O still happens, albeit with a slower rate, and the yield of N_2O (10−30%) is highly dependent on the amount of NO added. These findings support the idea that the carboxylate bridges are bound at low temperature, reducing the affinity of the diferrous complex for NO. Solution IR spectra taken at −80 °C reveal two bands at 1726 and 1707 cm^{-1}, which are assigned to hs-$\{FeNO\}^7$ complexes based on their $^{15}N^{18}O$ isotope sensitivity, constituting intermediates of the reaction. Mössbauer spectroscopy indicates the presence of multiple species in solution, including the diferrous starting material, a diamagnetic $[\text{hs-}\{FeNO\}^7]_2$ complex, in agreement with the results from IR spectroscopy, and a mixed-valent Fe^{II}/Fe^{III} dimer where the iron centers are ferromagnetically coupled. These species are kinetically trapped as off-pathway intermediates at low temperature, and proceed to generate more N_2O when the reaction mixture is warming up.[1853]

In summary, these results show that reduction potential is an important factor in tuning a diiron core for direct NO reduction to N_2O, but the question remains what happens at the intermittent reduction potentials observed for FDPs. In addition, as mentioned above, SCS residues in the enzymes assist in NOR catalysis, which is another factor that remains to be explored. Importantly, $[CoCp_2][Fe_2((Py_2PhO_2)MP)(OAc)_2]$ can perform multiple cycles of (quantitative) NO reduction to N_2O in the presence of acetic acid, which mimics the reactivity of FNORs.

5.4. Computational Studies on the Mechanism of NO Reduction by Diiron Complexes

Because of the lack of experimental insight, computational studies have been used to investigate the complete mechanism of NO reduction by FNORs, including the role of the critical active site Tyr residue (see Figure 123). In addition, computational studies were conducted to investigate why the model complex $[Fe_2(BPMP)(OPr)(NO)_2]^{2+}$ requires semi-reduction to produce N_2O, and what the N−N coupled intermediates of this process look like. Importantly, these studies determined that besides the N−N coupling step, another critical step of the reaction is N−O bond cleavage, to release N_2O. This latter step critically depends on the binding mode of the hyponitrite intermediate, which was unexpected. These results are discussed in the following.

5.4.1. Computational Studies on the Mechanism of NO Reduction by the Model Complex $[Fe_2(BPMP)(OPr)(NO)_2]^{2+}$.

DFT calculations reproduce the diamagnetic ground state (S_t = 0) of $[Fe_2(BPMP)(OPr)(NO)_2]^{2+}$, with two AF coupled hs-$\{FeNO\}^7$ units.[1862] Here, each hs-$\{FeNO\}^7$ group has the typical hs-Fe(III)−$^3NO^-$ ground state, where the spins of the hs-Fe^{III} (S = 5/2) center and the $^3NO^-$ (S = 1) ligand are strongly AF coupled, resulting in a total spin of S_t = 3/2 (see Section 5.1). Each hs-$\{FeNO\}^7$ unit has a rather covalent Fe−NO bond, in agreement with the stability of this complex. As illustrated in Figure 133, N−N bond formation is not energetically favored as the diferrous dinitrosyl is too stable: as the N−N bond distance between the two NO units decreases, the energy increases, but no minimum for an N−N coupled product is observed. The dissociative nature of this potential energy surface (PES) is consistent with the stability of $[\text{hs-}\{FeNO\}^7]_2$ complexes in general (see above).

Two-electron reduction of $[Fe_2(BPMP)(OPr)(NO)_2]^{2+}$ leads to the $[\text{hs-}\{FeNO\}^8]_2$ state, $[Fe_2(BPMP)(OPr)(NO)_2]^0$. As discussed in Section 5.1, this is expected to lead to the double occupation of the d_{xy} orbital of iron (with the Fe−N(O) vector corresponding to the z axis), leading to a hs-Fe(II)−$^3NO^-$ electronic structure.[1862] In $[Fe_2(BPMP)(OPr)(NO)_2]^0$, this is indeed observed for the FeNO unit that is trans to the *tert*-amine group. However, interestingly, in the other FeNO unit (trans to a pyridine), it is the Fe−NO antibonding d_{xz}_NO(π*) orbital that becomes occupied upon reduction. This leads to a distinctively more activated hs-$\{FeNO\}^8$ unit in the latter case. This difference in activation between the two hs-$\{FeNO\}^8$ units is reflected in their calculated properties; for example, the predicted N−O stretching frequencies (1564 vs

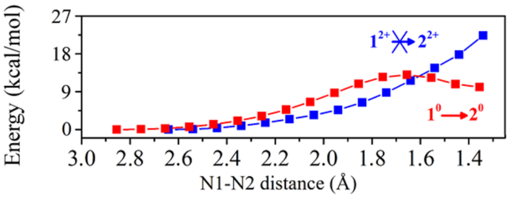

Figure 133. Differences in the energy profile between $[Fe_2BPMP(OPr)(NO)_2]^{2+}$ (labeled **1^{2+}**) and its two-electron reduced form (labeled **1^0**) along the N−N coupling reaction coordinate. Changes in total energies of **1^{2+}** and **1^0** are marked in blue and red, respectively. Calculated using the BP86 method. Adapted with permission from ref 1862. Copyright 2018 American Chemical Society.

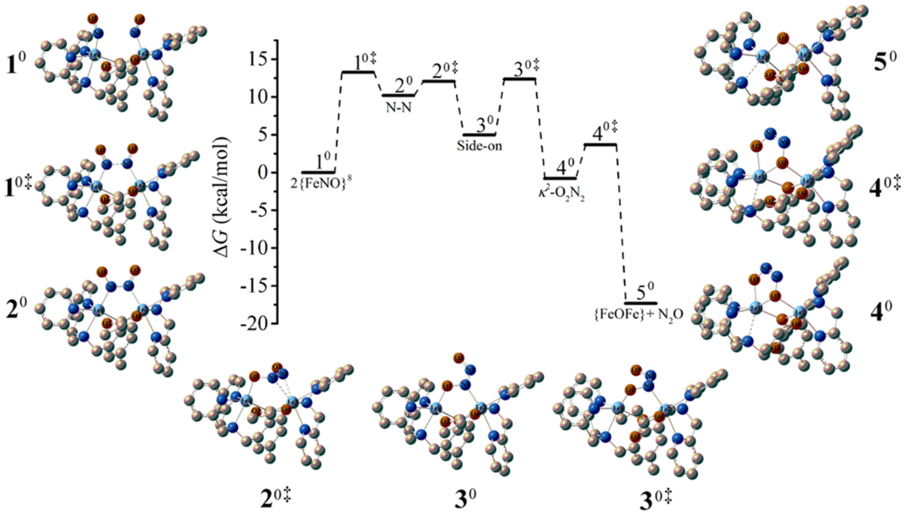

Figure 134. Proposed reaction pathway for N_2O generation from the two-electron reduced form of $[Fe_2BPMP(OPr)(NO)_2]^{2+}$, labeled $\mathbf{1^0}$ in the scheme, corresponding to a [hs-$\{FeNO\}^8]_2$ system. Calculated using the BP86 method. All intermediates and transition states are fully optimized. Reprinted with permission from ref 1862. Copyright 2018 American Chemical Society.

1487 cm^{-1}; note that the two N−O stretches in the reduced complex are essentially uncoupled). The [hs-$\{FeNO\}^8]_2$ state is activated for N−N coupling and N_2O formation, as shown in Figure 133, and the complete PES for this process is shown in Figure 134 (calculated with BP86).[1862] Here, N−N bond formation proceeds via a radical-radical N−N coupling mechanism, with a free energy barrier of 13.7 kcal/mol, leading to the formation of an N-bound *cis*-hyponitrite complex. This step of the reaction is energonic, with a calculated ΔG = +12.6 kcal/mol. Formation of the N−N bond of hyponitrite requires a significant weakening of the Fe−NO π-interactions, which is the origin of the observed free energy barrier for this reaction. This reduction in covalency of the Fe−NO bonds leads to a localization of the two π*-electrons of each $^3NO^-$ ligand on the newly formed hyponitrite ($N_2O_2^{2-}$) unit that is now bound to the diiron core. Upon complete formation of $N_2O_2^{2-}$ (intermediate $\mathbf{2^0}$ in Figure 134), it is clear that the N atoms have converted to approximate sp^2 hybridization, resulting in a completely conjugated $O{-}N{-}N{-}O^{2-}$ unit. The calculated N−N bond distance in the resulting intermediate is 1.371 Å. Since hyponitrite prefers to bind to transition metal centers via its O atoms (see Section 4.3), as evident from recent crystallographic data for Ni(II) and Fe(III) hyponitrite complexes,[1601,1602,1864,1865] the next step of the reaction corresponds to a rotation of the hyponitrite ligand into a "side-on" binding mode, in which hyponitrite coordinates in an Fe−O−N−Fe fashion (see intermediate $\mathbf{3^0}$ in Figure 134). Unlike N−N coupling, formation of this hyponitrite intermediate has a small free energy activation barrier of ∼5 kcal/mol and is overall exergonic (ΔG = −4.7 kcal/mol). Experimental evidence for the viability of such a species comes from a recent report by Meyer and coworkers, which shows this side-on binding mode of hyponitrite experimentally in a dinickel complex (see Figure 135).[1863] Interestingly, the direct cleavage of the N−O bond from this side-on bound hyponitrite complex has a high-energy transition state with a free energy barrier of 25.8 kcal/mol, making this pathway an unrealistic option. A similar N−O bond cleavage step has recently been proposed in a computational study on the superreduced mechanism using an FNOR active-site model.[1866] In this study, a side-on binding motif of $N_2O_2^{2-}$, similar to the one described above, was also predicted, and a large energy barrier of 21.5 kcal/mol was calculated for N−O bond cleavage from this intermediate. Using further PES scans, an additional binding mode of hyponitrite was discovered for the model complex, where one of the hyponitrite O atoms bridges the two iron centers in a μ-oxo fashion, while the other O atom binds to only one iron. This κ^2-$O_2N_2^{2-}$ complex is shown as intermediate $\mathbf{4^0}$ in Figure 134. This binding mode is enabled by the ability of the bridging carboxylate ligand to switch to monodentate coordination, as shown in Scheme 65. The κ^2-$O_2N_2^{2-}$ intermediate is perfectly primed for N_2O release, and this reaction proceeds with a small free energy activation barrier of only 5.6 kcal/mol in a very exergonic step (ΔG = −19.0 kcal/mol), generating the diferrous-μ-oxo product (labeled $\mathbf{5^0}$ in Figure 134) and N_2O.[1862] Given the spontaneity of this reaction in the absence of a proton source, this calculated pathway supports the notion that N_2O release is a sufficient driving force for NO reduction in these diiron systems. A second, and somewhat surprising result from this study is that the hyponitrite binding mode actually has a large impact on the energy barrier for N_2O release.[1862] The largest energy barrier for NO reduction in the model complex is the

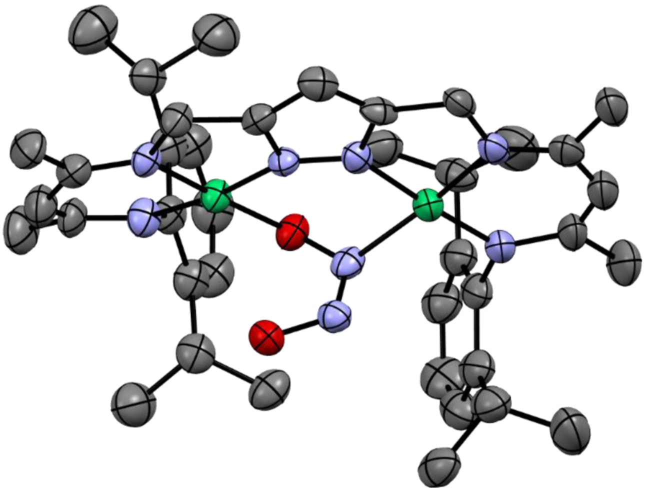

Figure 135. Crystal structure of K[$Ni_2L(\mu$-$N_2O_2)$]. H atoms and counterion have been omitted for clarity.[1863]

Scheme 65. Formation of N_2O from Hyponitrite and the Importance of the Carboxylate Shift[a]

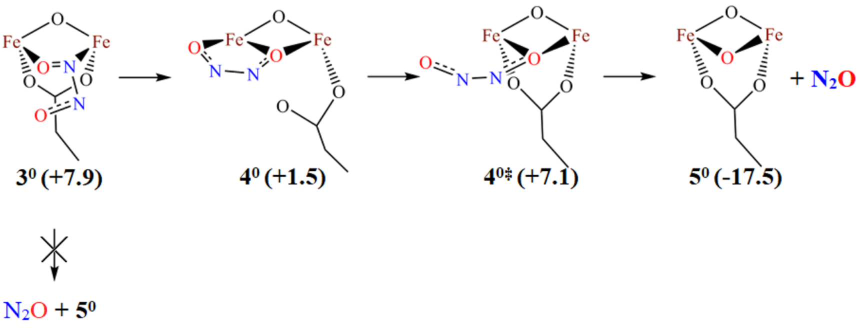

[a] For simplicity, only the μ-O group of the bridging phenolate of the $BPMP^-$ ligand is shown. Relative free energies shown in parentheses are in kcal/mol (see Figure 134). Adapted with permission from ref 1862. Copyright 2018 American Chemical Society.

N−N bond formation step, with a calculated barrier of 13.7 kcal/mol. Considering that experimentally, this reaction proceeds in less than 150 ms at room temperature (see above), this barrier is likely an overestimate. Indeed, when hybrid functionals are used, the energy barrier for this step decreases significantly, to 7−8 kcal/mol, which is in good agreement with experiment.[1862]

Finally, it is interesting to consider how this energy landscape for NO reduction changes when the semireduced pathway is considered, that is, when the reaction starts from the one-electron reduced, mixed-valent hs-$\{FeNO\}^7$/hs-$\{FeNO\}^8$ species. In this case, N−N coupling proceeds with a barrier of 14 kcal/mol in an overall endergonic process (ΔG = +13.0 kcal/mol).[1862] Surprisingly, this result is identical (within error) with the free energy profile observed for the N−N coupling reaction that starts from the two-electron reduced intermediate, [hs-$\{FeNO\}^8]_2$ (see Figure 136). Further steps along the PES were also calculated to be similar, albeit each intermediate is now a mixed-valent complex. Hence, both the semi- and superreduced pathway were found to be capable of NO reduction, with very similar potential free energy landscapes. This strongly supports the experimental finding that one-electron reduction of $[Fe_2(BPMP)(OPr)(NO)_2]^{2+}$ is indeed sufficient to induce fast and efficient N_2O formation, following the semireduced pathway.[1842,1862]

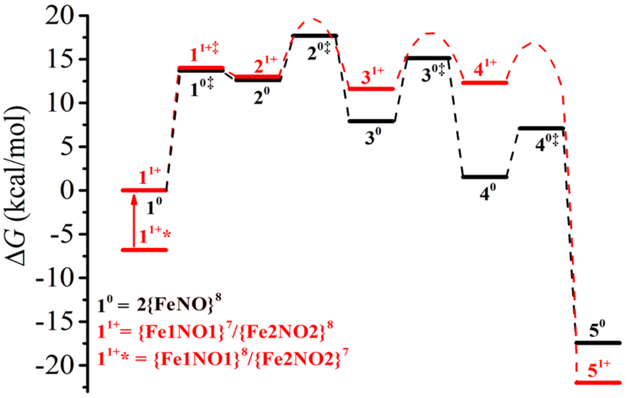

Figure 136. Comparison of the proposed reaction pathways for N_2O generation from the one- and two-electron reduced forms of $[Fe_2BPMP(OPr)(NO)_2]^{2+}$, labeled $\mathbf{1^{1+}}/\mathbf{1^{1+*}}$ and $\mathbf{1^0}$ in the scheme, respectively. Note that the one-electron reduced form exists in two possible valence tautomers, as indicated. For $\mathbf{1^{1+}}$, the free energies of the transition states were not calculated, except for $\mathbf{1^{1+‡}}$. Lastly, the free energy difference between the two valence tautomers, $\mathbf{1^{1+}}/\mathbf{1^{1+*}}$, is likely overestimated (with B3LYP, these lie within 1.3 kcal/mol of one another). The reaction will therefore proceed from the tautomer with the lower activation energy, as the tautomers are in thermal equilibrium. Calculated using the BP86/TZVP method. Reprinted with permission from ref 1862. Copyright 2018 American Chemical Society.

5.4.2. Role of the Second Coordination Sphere.

The in-depth computational study on the model complex $[Fe_2(BPMP)(OPr)(NO)_2]^{2+}$ (see above) lays out the fundamental reaction coordinate for NO reduction in diiron systems. However, important questions remained, especially with respect to the factors that allow FDPs to catalyze NO reduction following the direct coupling pathway. Two recent computational studies have sought to address this issue, and to explore the role that the active site Tyr could play in NO reduction in FDPs. Both studies consider formation of a hyponitrite intermediate through N−N coupling, isomerization of the hyponitrite intermediate, and N−O cleavage to yield N_2O, as in the case of the reaction mechanism for the model complex. While these two studies find it necessary to include the active site Tyr residue in NO reduction, there are important distinctions found, which are discussed below.

Chen and coworkers used quantum mechanical/molecular mechanical (QM/MM) calculations to compare reaction pathways for FNORs with and without the critical Tyr residue.[1867] As a starting point for structure optimizations, the crystal structure of deflavinated *Tm* FDP was used. Following the direct coupling mechanism (see Scheme 61, top) and starting from the diferrous dinitrosyl intermediate, the calculations predict that NO reduction and N_2O release are thermodynamically feasible, with a total energy change of −28.3 and −14.9 kcal/mol with and without the Tyr residue, respectively (see Figure 137). Importantly, the calculations predict that the Tyr residue lowers the activation energies for the N−N bond formation and the N−O bond cleavage step by about a factor of two.[1867] For N−N bond formation, the calculated activation energy drops from +9.6 to +4.3 kcal/mol with the Tyr, and similarly, for N−O bond cleavage, the activation energy decreases from +9.5 to +4.3 kcal/mol. Finally, the Tyr also assists in the isomerization of hyponitrite from N,N-binding to N,O-binding to the diiron center, bearing resemblance to the isomerization discussed in the previous section for the model complex (calculations for this transition state were not included here). In terms of the products predicted after N_2O release, there are also differences: when the Tyr residue is involved, the diferric product has a bis-μ-hydroxo μ-carboxylate core structure, where transfer of a proton from

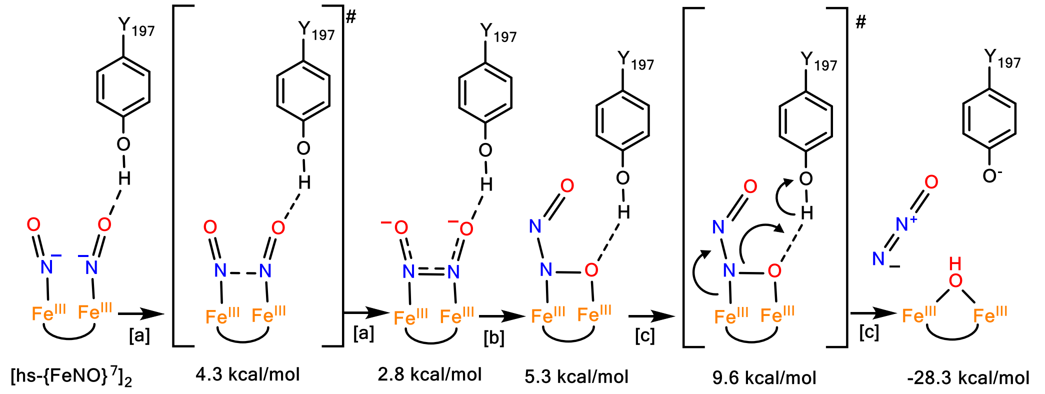

Figure 137. Direct coupling mechanism involving Y197, as proposed by Chen and coworkers.[1867] Energies indicated in the figure are relative to the starting [hs-{FeNO}^{7}]$_2$ complex. Boxed letters correspond to reaction steps ([a]: N−N bond formation; [b]: hyponitrite isomerization; [c]: N−O bond cleavage). Transition states are indicated in brackets.

Tyr forms the second bridging μ-hydroxo group after N−O bond cleavage. In the absence of the Tyr, the diiron site is in the unusual Fe^{II}/Fe^{IV}-oxo state with a μ-hydroxo μ-carboxylate core structure after N−O bond cleavage. However, in the latter case proton transfer could also be mediated by water molecules, so this is likely an artefact from the model used for the calculations. Nevertheless, these calculations show that the presence of the Tyr residue leads to favorable energy barriers for the direct coupling pathway.

Additionally, Chen and coworkers also explored the role of the Tyr residue in the semireduced mechanism.[1867] Starting from the hs-{FeNO}^{7}/hs-{FeNO}^{8} intermediate (see Scheme 61, bottom), calculations predict that the N−N bond formation, hyponitrite isomerization, and N−O bond cleavage steps are all energetically favorable, no matter the presence or absence of the Tyr residue. Similar to the direct coupling mechanism, the activation energy for N−N coupling is lower when the Tyr residue is present (+0.4 kcal/mol versus +1.3 kcal/mol without Tyr). Interestingly, in the semireduced pathway, hyponitrite isomerization in the presence of the Tyr residue results in an Fe^{II}Fe^{III} mixed-valent intermediate where the hyponitrite binds to one Fe^{III} in a bidentate, O,O′-chelating form. In the absence of the Tyr, this binding mode is strongly disfavored, as it raises the activation energy for N−O bond cleavage by 9 kcal/mol. Hence, without the Tyr, the isomerized hyponitrite intermediate would be the same as predicted for the direct coupling pathway. Lastly, N−O bond cleavage results in slightly different diiron products in the presence and absence of the Tyr residue (a mixed-valent diiron bis-μ-hydroxo μ-carboxylate species for the former and a mixed-valent diiron μ-hydroxo μ-carboxylate for the latter, which also contains a terminal Fe−O unit).

In summary, the results of Chen and coworkers lead to a number of important conclusions, some of which should be further tested in future experimental studies.[1867] First, comparing the semireduced and direct reduction pathways, the former has more driving force and a lower barrier for N−N bond formation, as observed for the model complex. In both cases, the Tyr residue lowers the barrier for N−N bond formation by means of hydrogen-bonding to one of the bound NO ligands. On the other hand, semireduction is counterproductive for N−O bond cleavage, as the energy barrier for this step increases from +4.3 to +7.0 kcal/mol in the direct coupling versus the semireduced mechanism. The Tyr further assists in N−O bond cleavage by transferring its proton to the hyponitrite intermediate, to form a bridging hydroxide group as N_2O is released. This prediction is quite peculiar, considering the pK_a for Tyr residues is usually between 9−10, and there are, according to the crystal structures of several FDPs, nearby amino acids (one of the iron-chelating carboxylates) that can also form hydrogen bonds with water molecules to possibly provide protons (see Figure 124).[1821] Unfortunately, as mentioned above, the barriers for hyponitrite isomerization were not calculated in this study. The main conclusion from the study by Lu et al. is that the Tyr residue critically assists in N−N bond formation, and that the reaction can proceed via the direct coupling mechanism.

In an alternative study, Bominaar and coworkers performed straight DFT calculations on a truncated *Tm* FDP active site model that does not include the protein matrix.[1831] Starting from the diferrous dinitrosyl intermediate and proceeding along the direct coupling pathway, it was proposed in this study that N−N coupling to form the hyponitrite intermediate is followed by protonation of the coordinated hyponitrite, subsequent hyponitrite isomerization, and finally N−O bond cleavage to release N_2O and form the diferric bis-μ-hydroxo μ-carboxylate product. In their results, formation of the hyponitrite intermediate is endergonic by +3.8 kcal/mol and has a free energy activation barrier of +7.9 kcal/mol. In terms of activation energy, the barrier is calculated to be +4.9 kcal/mol, which is comparable to the results by Lu et al. The role of the Tyr residue in N−N bond formation was not further investigated in this work. The following protonation of the hyponitrite ligand is necessary to facilitate the isomerization of the hyponitrite intermediate and subsequent N−O bond cleavage. However, because the protonation process was not modeled in the calculations, this step represents a discontinuity of the PES, and accordingly, this study does not provide a complete energy profile for the NOR reaction. Upon protontation of the hyponitrite intermediate, isomerization occurs, albeit the free energy activation barrier was calculated to be +12.7 kcal/mol for this step. The authors note that if the diferric hyponitrite intermediate would not be protonated, this activation barrier would be 5 kcal/mol higher. In addition, calculations using phenylalanine substitution for the active site Tyr residue resulted in activation energies of about +20 kcal/mol for the hyponitrite rotation, which indicates that the Tyr residue critically assists in this process. Although this energy barrier for isomerization is rather high, subsequent N−O cleavage was found to be energetically favorable, with a change

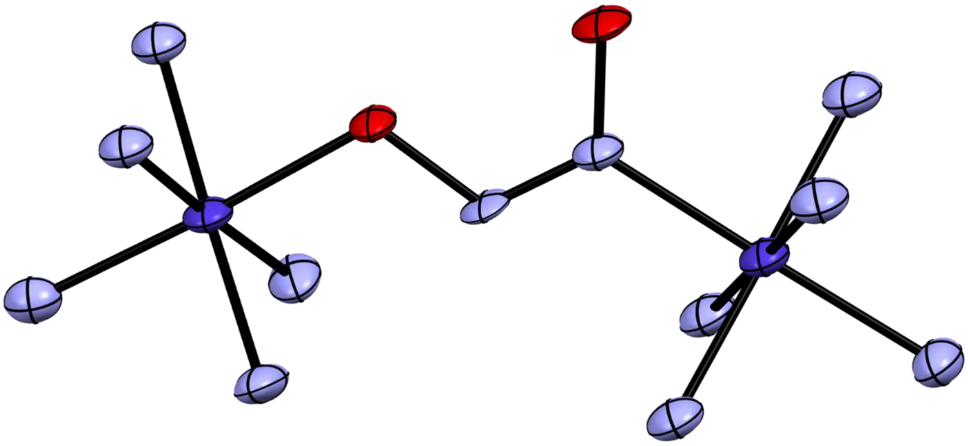

Figure 138. Crystal structure of $[\{Co(NH_3)_5\}_2(\mu\text{-}N_2O_2)](NO_3)_2Br_2$. H atoms and counter ions are omitted for clarity.[1871]

in total energy of −30.4 kcal/mol and a low activation barrier ($\Delta E^\ddagger$ = +1.3 kcal/mol). Additionally, an unprotonated diferric hyponitrite intermediate would make this activation barrier about twenty-fold higher.

The key difference between the two theoretical studies on the mechanism of NO reduction by FNORs lies in the exact role of the Tyr for catalysis. Both studies conclude that the direct reduction pathway is feasible, and in the study by the Chen group, the proposed, main role of the Tyr is to lower the barrier for N−N bond formation to form the hyponitrite intermediate, which is in agreement with the findings for the model complex described above. In contrast, the study by Bominaar and coworkers proposes hyponitrite rotation to be the rate limiting step that is critically influenced by the presence of the Tyr group. These results provide testable hypotheses that should be further tested in future experimental studies both on FNORs and on diiron model complexes.

5.5. Mechanistic Insight into N−N Bond Formation from Other Model Complexes

Further key insight into the mechanistic details of N−N bond formation from two coordinated NO ligands has been obtained by studies on other transition metal complexes that are able to mediate this reaction. These studies provide a broad perspective on "what is possible" in this reaction space, and give inspiration for mechanistic possibilities for the biologically relevant mono- and diiron active sites found in NORs, as described in this review. A number of relevant studies in this area are outlined in the following. More information is available from a recent review.[17]

5.5.1. N−N Coupling in Co Complexes. Early studies on cobalt-nitrosyl compounds include the target complex $[Co(NH_3)_5(NO)]^{2+}$, where, depending on the reaction conditions, 'red' and 'black' products were isolated.[1868] Here, 'black' salts were obtained by reacting various Co^{II} salts at low temperatures with ammonia and NO; however, these products were found to be unstable at ambient temperatures. Interestingly, at low temperatures, the 'black' salt reacts with excess NO gas to form N_2O, nitrite, and $[Co(NH_3)_5(OH)]^{2+}$. It was hypothesized that in this process, two equiv of NO and one equiv of $[Co(NH_3)_5(NO)]^{2+}$ form N_2O in aqueous solution via a cobalt-mediated disproportionation mechanism. Furthermore, it was suggested that the above reaction goes through a transient $Co(III)-N_2O_2^-$ intermediate. On the other hand, 'red' salts were obtained by the same reaction conditions as for the 'black' salts but at ambient temperatures, and by running reactions for longer periods of time. Early conductivity and vibrational spectroscopy studies on the 'red' products suggested that these are dimeric species.[1869] Moreover, based on the observation of an IR band at 1050 cm^{-1}, this dimer was predicted to be a bridged hyponitrite complex.[1869] Later, the crystal structure of this 'red' salt was obtained and it was confirmed to be a dicobalt complex with a bridging *cis*-hyponitrite ligand, as shown in Figure 138. Here, two $[Co(NH_3)_5]^{3+}$ centers are bridged by an N,O-coordinated *cis*-hyponitrite.[1870] Assuming that a mononuclear $[Co(NH_3)_5(NO)]^{2+}$ species forms first, this likely represents the first example of N−N coupling of two coordinated NO ligands, leading to the formation of a hyponitrite complex.

Since the report of the dicobalt−hyponitrite complex, subsequent studies have been undertaken to explore cobalt−nitrosyl compounds as a way to model NO reduction reactions in biological systems, and as potential HNO donors. Harrop's group used the diamine-dipyrrolidine ligand scaffold to study reduced metal−nitrosyl centers and their ability to undergo NO reduction.[1872] Here, the $\{CoNO\}^9$ complex $[K(18\text{-crown-6})][Co(LN_4^{Ph})(NO)]$ ($LN_4^{Ph\,2-}$ = (N^1E,N^2E)-N^1,N^2-bis((1H-pyrrol-2-yl)methylene)-benzene-1,2-diamine dianion) was synthesized by reduction of the corresponding ls-$\{CoNO\}^8$ precursor with KC_8. EPR studies and DFT calculations establish the anionic complex to be a hs-$\{CoNO\}^9$ system, with the majority of the spin-density located on the Co center, and a hs-Co(II)−$^3NO^-$ ground state. Here, the spins of the hs-Co(II) center ($S = 3/2$) are AF coupled to the $^3NO^-$ ligand ($S = 1$), yielding an overall spin of $S_t = 1/2$ (see Figure 112).[1872] Upon reacting this complex with $HBF_4 \cdot Et_2O$ in water, N_2O gas was detected in the reaction headspace, indicative of NO reduction; however, this was hypothesized to occur via the intermediate formation of a Co(II)−NHO complex.[1872] Supporting DFT calculations suggest an increase in the Co−NO bond length upon protonation of the nitroxyl ligand in the hs-$\{CoNO\}^9$ complex, indicating that the Co−N bond is considerably weaker in the protonated species. In the Co(II)−NHO complex, DFT calculations further predict that the Co center changes to ls, resulting in a ls-Co(II)−^{1}NHO type species.[1872] On the basis of these findings, it was further hypothesized that HNO simply dissociated from the ls-$\{CoHNO\}^9$ species, and that the free HNO then dimerizes in solution to produce N_2O and water. These findings are potentially relevant in the context of the superreduced mechanism for FNORs, in which an alternative possibility

Scheme 66. Reaction Scheme for N_2O Formation from the Complex $[Ni(bipy)_2(NO)](PF_6)$[1864a]

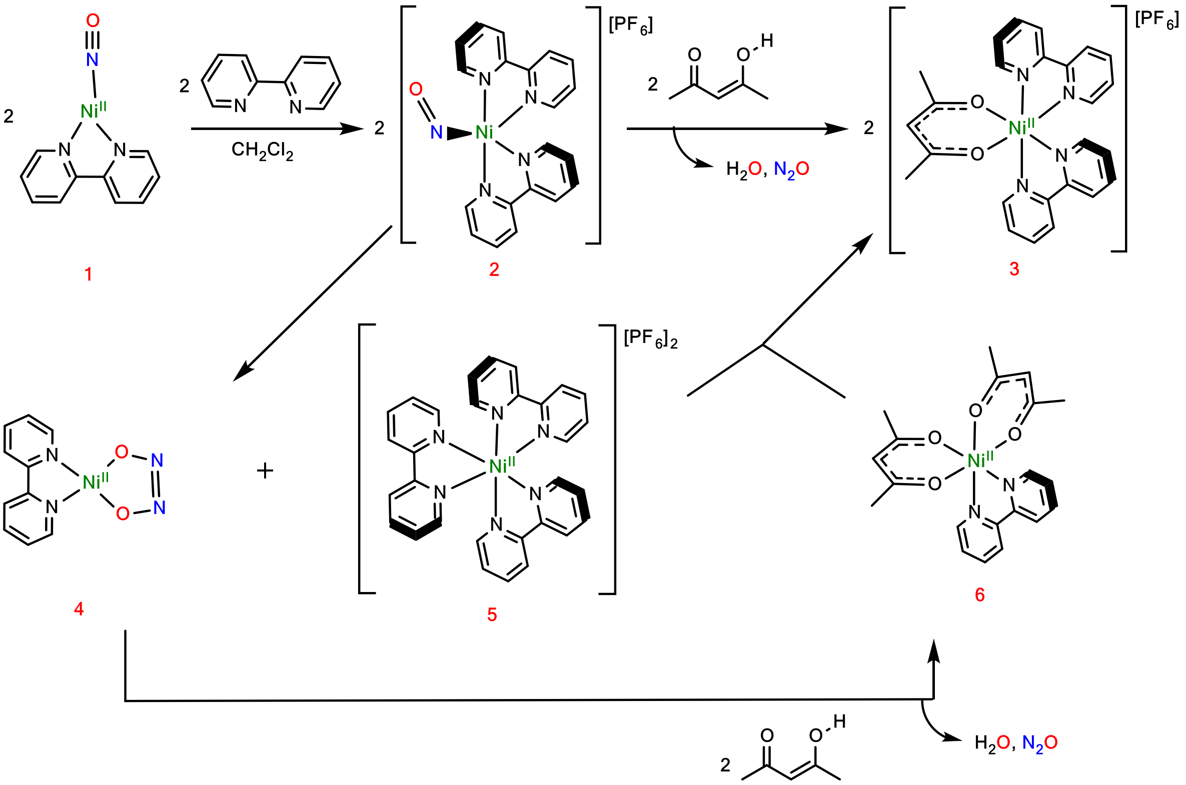

[a]Adapted with permission from ref 17. Copyright 2021 Elsevier Inc.

would entail formation of a protonated $[\{FeNHO\}^8]_2$ dimer, instead of [hs-$\{FeNO\}^8]_2$, preceding N_2O release and water formation. Here, N_2O formation could also result from the release of HNO into the active site of the enzyme, followed by HNO dimerization.[1837]

5.5.2. N−N Coupling in Ni Complexes. Hayton and coworkers observed N−N coupling in 5C $\{NiNO\}^{10}$ complexes, as shown in Scheme 66. Addition of 1 equiv of 2,2-bipyridine (bipy) to the three-coordinate $\{NiNO\}^{10}$ complex $[Ni(NO)(CH_3NO_2)_3]^+$ resulted in the formation of the stable 5C complex $[Ni(bipy)_2(NO)]^+$.[1864] $[Ni(bipy)_2(NO)](PF_6)$ has an interesting geometry that is in between trigonal-bipyramidal and square-pyramidal. The crystal structure of this complex shows Ni−NO and N−O bond distances of 1.762 and 1.207 Å, respectively. The Ni−N−O unit is strongly bent in this complex (Ni−N−O angle = 129.5°). The N−O stretch is observed at a very low frequency, 1567 cm^{-1}, which indicates that the complex has a Ni(II)−NO^- type electronic structure with a strongly reduced NO^- ligand. Over time in dichloromethane solution, $[Ni(bipy)_2(NO)]^+$ decomposes forming $[Ni(bipy)_3]^{2+}$ and N_2O. Interestingly, when $[Ni(bipy)_2(NO)]^+$ was dissolved in acetonitrile, the *cis*-hyponitrite complex $[Ni(bipy)(k^2\text{-}O_2N_2)]$ could be isolated. As determined from the crystal structure (see Figure 139), this *cis*-hyponitrite complex has Ni-O bond lengths of 1.800 Å, O−N bond lengths of 1.384 and 1.391 Å, and an N−N bond length of 1.240 Å. Treatment of this complex with H(acac) in dichloromethane generates N_2O, alongside with the formation of $[Ni(bipy)(acac)_2]$, as shown in Scheme 66, bottom. This reaction can also be conducted in one step, by the direct treatment of $[Ni(bipy)_2(NO)]^+$ with H(acac), which also leads to the liberation of N_2O. Here, it was suspected that N_2O was generated via a bimetallic intermediate; nonetheless, this does not preclude the possibility of the hyponitrite intermediate forming in this reaction as well. In a follow-up study using the 5C $\{NiNO\}^{10}$ complex $[Ni(bipy)(Me_2phen)(NO)]^+$, it was shown that reaction of this species with exogenous NO yields N_2O and a bridging nitrite product, suggesting that in this case, N_2O is formed via NO disproportionation, and not NO reduction.[1873] Interestingly, reaction of $[Ni(bipy)(NO)]^+$ with $[Ni(bipy)_2(NO)]^+$ results in the formation of a trimetallic nickel complex, held together by ligation through a *cis*-hyponitrite ligand. In summary, 5C $\{NiNO\}^{10}$ complexes seem to be able to form hyponitrite via N−N coupling of two coordinated NO^- ligands. Since the exact electronic structure of the critical reactive intermediate, $[Ni(bipy)_2(NO)]^+$, is not known, it is not clear whether this reaction proceeds via a similar radical-radical coupling of two

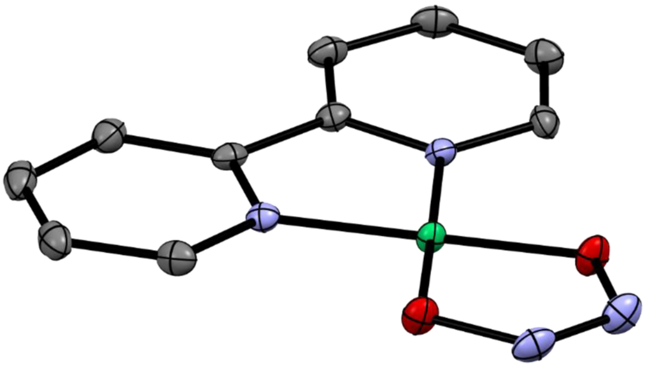

Figure 139. Crystal structure of $[Ni(bipy)(k^2\text{-}O_2N_2)]$.[1864] H atoms are omitted for clarity.

coordinated $^3NO^-$ ligands, as in the case of the diiron complexes (see above), but in an intermolecular fashion, or whether the mechanism is different. It is also possible that loss of NO occurs in acetonitrile solution, followed by attack of free NO on another $[Ni(bipy)_2(NO)]^+$ complex, potentially forming a $Ni(NO)_2$ motif prior to N−N bond formation. Further work is necessary to elucidate the exact mechanism of the reaction that leads to the formation of the hyponitrite intermediate and N_2O.

Warren and coworkers explored N−N bond formation in $\{NiNO\}^{11}$ complexes. The reduction of their hs-$\{NiNO\}^{10}$ complex $[Ni(^iPr_2NN_{F6})(NO)]$ (described as a hs-Ni(II)−$^3NO^-$ species; $^iPr_2NN_{F6}$ is a diketiminato-type ligand) with KC_8 in THF and 1 equiv of 18-crown-6 led to the isolation of $[K(18\text{-crown-}6)(THF)][Ni(^iPr_2NN_{F6})(NO)]$.[1874] This complex is square-planar with a side-on bound NO ligand that is stabilized by interaction with the $[K(18\text{-crown-}6)(THF)]^+$ cation (see Figure 140). As determined from the crystal structure, this $\{NiNO\}^{11}$ species has rather short Ni−nitrosyl distances, with Ni−N and Ni-O bond lenghts of 1.853 and 1.839 Å, respectively. Additionally, the N−O bond length of the nitrosyl ligand is uniquely long (1.270 Å), suggesting this nitrosyl is rather activated. On the basis of EPR data, DFT calculations, and Ni K-edge XAS data, it is proposed that this $\{NiNO\}^{11}$ species is best described as a ls-Ni^{II} ($S = 0$) center bound to a $^2NO^{2-}$ ligand ($S = 1/2$), to give rise to a total spin $S_t = 1/2$. Considering the presence of an unpaired electron in this square planar species, proposed to be located on the $^2NO^{2-}$ ligand, it is not surprising that further reaction of this species with $NO^\bullet$ leads to the formation of the corresponding *cis*-hyponitrite complex, where the hyponitrite is O,O-coordinated to the nickel center. Upon treatment with acid ($HBF_4{\cdot}Et_2O$), N_2O is released quantitatively (in ∼76% yield) to yield a dinickel bis-μ-hydroxo product. These results show that, given the appropriate electronic requirements, hyponitrite formation and subsequent N_2O release can be mediated by a mononuclear transition metal center, if the coordinated NO-based ligand or derivative has sufficient radical character. So in this sense, this reaction roughly models the mechanism of Cyt. P450nor (see Section 4.2), where protonation is proposed to be used to create a radical-type, NO-derived ligand ($^\bullet NHOH$) that is activated for N−N coupling.

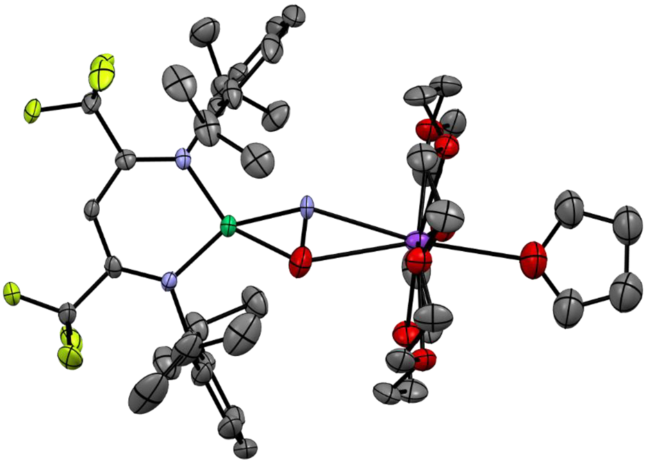

Figure 140. Crystal structure of $[K(18\text{-crown-}6)(THF)][Ni(^iPr_2NN_{F6})(NO)]$.[1874] H atoms are omitted for clarity.

5.5.3. N−N Coupling in Ru Complexes. Apart from diiron dinitrosyl complexes (see above), significant progress in modeling dimetallic dinitrosyl systems has been made by Arikawa, Onishi, and coworkers, with their diruthenium complexes. First reported in 2007, the mononuclear ls-$\{RuNO\}^6$ complex $[Ru(Tp)(Cl)_2(NO)]$ (Tp^- = hydrotris(pyrazolyl)borate) has a distorted octahedral geometry and shows a typical N−O stretching frequency of 1893 cm^{-1}. When this complex was refluxed with pyrazole and triethylamine, a dimer of two ls-$\{RuNO\}^7$ complexes could be isolated.[1875] The crystal structure of the product indicates the presence of a weak N−N bond between the coordinated NO ligands, with an N−N bond distance of 1.861 Å. On the other hand, the N−O distances are short at 1.197 and 1.193 Å. These structural parameters indicate the formation of a di-Ru complex with a bound, neutral *cis*-ONNO dimer. The formation of this product is proposed to follow a two-step mechanism, where a [ls-$\{RuNO\}^7]_2$ dimer of two ls-Ru(II)−$NO^\bullet$ units is formed first, followed by a radical N−N bond formation step that leads to the generation of the final product with the bridging, neutral *cis*-ONNO ligand (see Scheme 67). Hence, this reaction represents the paradigm of a radical-radical N−N coupling mechanism, equivalent to the *trans*-mechanism proposed for bacterial NORs (see Section 4.3), which features a radical-radical N−N bond formation step between two coordinated NO ligands as the key step towards N_2O generation.[70,254,1876] The product, $[\{Ru(Tp)\}_2(\mu\text{-}Cl)(\mu\text{-Me-pz})\{\mu\text{-}\kappa^2\text{−}N(=O)\text{−}N(=O)\}]$, shows an N−O stretching frequency of ∼1605 cm^{-1}, again indicating the presence of a neutral *cis*-ONNO ligand, compared to the hyponitrite ($N_2O_2^{2-}$) intermediate typically expected in NO reduction. Oxidation of the N−N coupled product using 2 equiv of $AgBF_4$ yielded the corresponding [ls-$\{RuNO\}^6]_2$ dimer (see Scheme 67), as confirmed by the high-energy N−O stretching frequency of 1930 cm^{-1} of the product, which is very different from that of the starting material, $[Ru(Tp)(Cl)_2(NO)]$. Reduction of this product then regenerates $[\{Ru(Tp)\}_2(\mu\text{-}Cl)(\mu\text{-Me-pz})\{\mu\text{-}\kappa^2\text{−}N(=O)\text{−}N(=O)\}]$. Upon exposure of the latter species to acid ($HBF_4{\cdot}Et_2O$), N_2O is liberated and a diruthenium μ-oxo product is formed, albeit both in low yields (∼25% and 21%, respectively), as well as the [ls-$\{RuNO\}^6]_2$ dimer. Unlike for ls-$\{FeNO\}^7$ complexes (see Section 4.3), the reaction described above is able to occur in this [ls-$\{RuNO\}^7]_2$ dimer due to the different electronic properties of each respective metal-nitrosyl species. In ls-$\{FeNO\}^7$ complexes, a strong σ-bond is present between the d_{z^2} orbital of ls-Fe^{II} and the π^*_h orbital of NO (see Scheme 14), which constitutes the SOMO of the complex (see Section 2.2). This is contrasted by ls-$\{RuNO\}^7$ complexes where the SOMO is best described as the antibonding combination between the NO(π^*_h) and a Ru(d_π) orbital.[17,24] Here, the relatively weaker Ru−NO bond gives rise to the observed radical reactivity.

In a follow-up study, it was reported that upon addition of HBF_4 in diethyl ether to the aforementioned di-Ru^{III} μ-oxo complex, the corresponding di-Ru^{III} μ-hydroxo species forms in decent yields.[1877] This μ-hydroxo complex was then shown to react with excess NO to give back the corresponding $[\{RuNO\}^6]_2$ dimer. The inclusion of acid in this diruthenium system therefore establishes a complete cycle for studying NO reduction.

A more recent study sought to modify this diruthenium system by substituting the bridging chloride for an additional bridging pyrazolate group.[1878] Here, a diruthenium bis(μ-pyrazolato) complex was synthesized with an additional μ-oxo

Scheme 67. N–N Bond Formation in a Dinuclear Ru Complex, Leading to the Generation of a Neutral *cis*-ONNO Ligand[1875a]

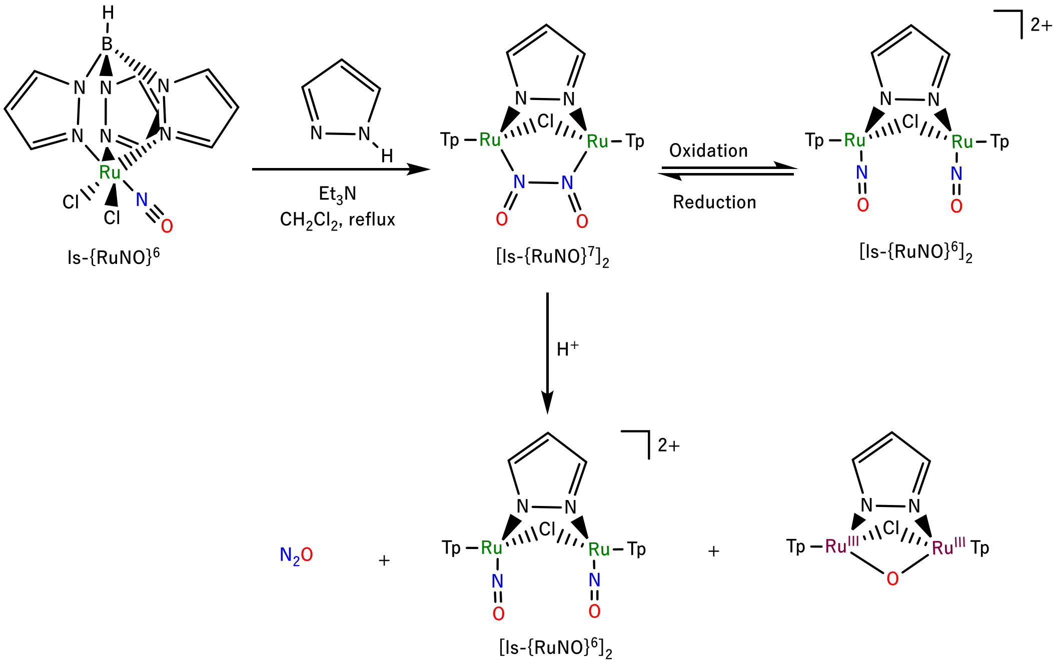

[a]Adapted with permission from ref 17. Copyright 2021 Elsevier Inc.

Scheme 68. Synthesis of a bis-Pyrazolato ls-{RuNO}^{7} Dimer and Following N–N Bond Formation[a]

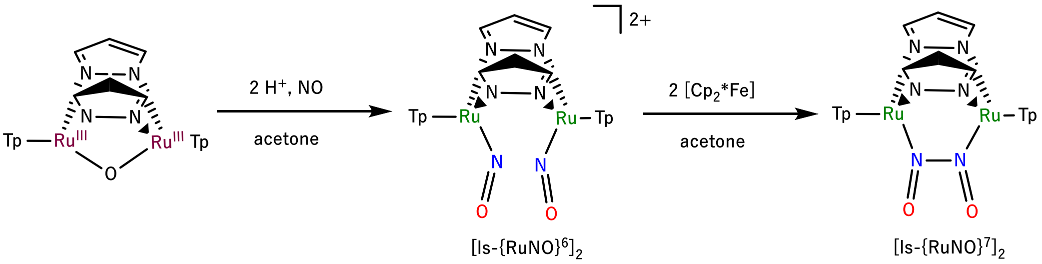

[a]N$_2$O is released from the coordinated *cis*-ONNO ligand upon irradiation with light.[1878]

Scheme 69. N–N Bond Formation by Reaction of [Cu(TMPA)(MeCN)]$^+$ and NO in Methanol, Resulting in a Hyponitrite-Bridged Cu^{II} Dimer[1880a]

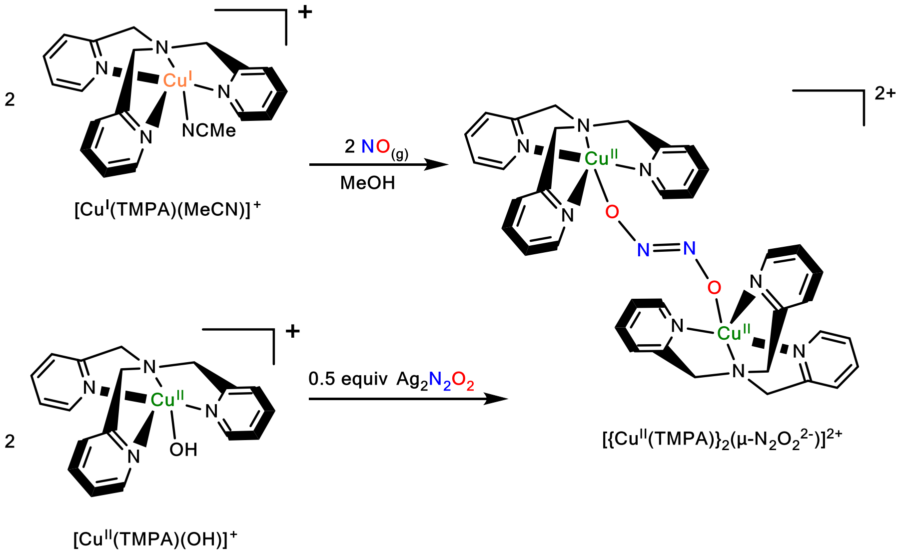

[a]Adapted with permission from ref 17. Copyright 2021 Elsevier Inc.

group. Reacting this species with 2 equiv of HBF_4 and excess NO then gives the corresponding [ls-$\{RuNO\}^6]_2$ dimer. Subsequent reduction with 2 equiv $FeCp*_2$ yields the diruthenium *cis*-ONNO complex, as shown in Scheme 68. This species, similar to the μ-Cl analog described above, has short N−O bond distances of 1.234 and 1.202 Å. This species exhibits an N−O stretching frequency of 1589 cm^{-1}. Given these structural and spectroscopic data, this complex is again best described as a Ru^{II} dimer with a coordinated *cis*-ONNO ligand (as opposed to a bound hyponitrite). Addition of acid to this complex was found to oxidize this species back to the [ls-$\{RuNO\}^6]_2$ dimer. Furthermore, it was found that irradiation of the *cis*-ONNO complex in diethyl ether is sufficient to liberate N_2O. While variation exists between the non-heme diiron and diruthenium systems, the latter result is in agreement with the findings for the diiron model complexes of FNORs (see above), showing that the production of water is not a requirement (and not the main driving force) for N_2O generation in the NO reduction reaction.[1862]

5.5.4. N−N Coupling in Cu Complexes. Significant new developments in copper-nitrosyl chemistry include the reports by Karlin and co-workers about the first Cu-only system able to mediate N−N coupling of two coordinated NO ligands. It is known for a long time that Cu^I complexes can mediate the disproportion of NO, leading to the generation of N_2O and the corresponding Cu(II)−nitrite complexes:[87,1648,1652,1879]

$$3NO \rightarrow N_2O + NO_2 \qquad (27a)$$

$$Cu(I) + NO_2 \rightarrow Cu(II){-}NO_2^- \qquad (27b)$$

In 2017, Karlin and coworkers reported that reaction of $[Cu(TMPA)(MeCN)]^+$ with NO in methanol generates the *trans*-hyponitrite bridged di-Cu^{II} complex $[\{Cu(TMPA)\}_2(\mu\text{-}N_2O_2)]^{2+}$, likely via a mononuclear $\{CuNO\}^{11}$ intermediate (see Scheme 69).[1880] Since $\{CuNO\}^{11}$ complexes have Cu(I)−$NO^\bullet$ electronic structures,[87,1881] this reaction corresponds to the second, clear example of a radical-radical type N−N coupling reaction by coordinated $NO^\bullet$ ligands, besides the Ru system described above. The crystal structure of this complex (see Figure 141) shows an O-bound *trans*-hyponitrite bridge with Cu-O and N−N distances of 1.911 and 1.257 Å, respectively. Notably, the formation of the hyponitrite complex is critically dependent on the presence of the polar protic solvent methanol, as the stability of the complex is hypothesized to be dependent on solvent-based hydrogen-bonding interactions with the hyponitrite bridge. Upon addition of HCl, the di-Cu^{II} hyponitrite complex was observed to decay to release N_2O via an NO-disproportionation mechanism. Here, N_2O formed quantitatively in ∼85% yield (based on the stoichiometry of the disproportionation reaction), along with $[Cu^{II}(TMPA)(NO_2)]^+$ and $[Cu^I(TMPA)]^+$, demonstrating NO disproportionation instead of NO reduction. This result implies that the hyponitrite intermediate could be the key intermediate not only for NO reduction, but also for the NO-disproportionation process.[1879,1882] Another example of Cu-mediated NO reductive coupling leading to hyponitrite formation was reported by Agapie and coworkers, for a tricopper cluster.[1883]

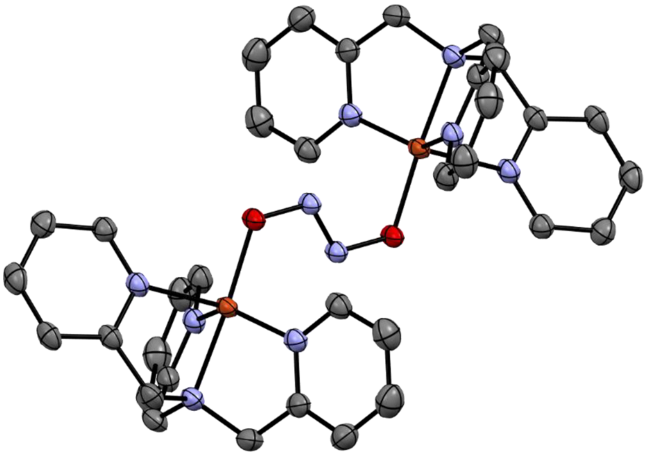

Figure 141. Crystal structure of $[\{Cu(TMPA)\}_2(\mu\text{-}N_2O_2)](ClO_4)_2$.[1880] H atoms and counter ions are omitted for clarity.

In a follow-up study, Karlin and coworkers later reported a variation of this chemistry, where a TMPA derivative was used that carries hydrogen-bond donating amide groups in the SCS.[1884] Reaction of the corresponding Cu^I complex $[Cu(PV\text{-}TMPA)]^+$ (PV = pivolato) with NO was hypothesized to form a short-lived hyponitrite-bridged di-Cu^{II} intermediate at low temperature, as determined by UV−vis spectroscopy. This intermediate was further studied with DFT calculations, and it was predicted that this species has a similar structure as $[\{Cu(TMPA)\}_2(\mu\text{-}N_2O_2)]^{2+}$. Over the course of two hours, this intermediate decayed, giving rise to quantitative N_2O formation (∼86% yield) and an isolable iminoxide-coordinated Cu^{II} species, $[Cu(PV'\text{-}TMPA)]^+$. Here, the amide groups of the modified TMPA ligand serve as an internal proton source, promoting N_2O formation, along with the generation of a water molecule. In this way, the presence of the internal acids stirs the reaction away from NO disproportionation towards NO reduction.

5.6. Non-Heme Iron Proteins in NO Signaling

While decomposition of Fe−S cluster ([2Fe−2S] and [4Fe−4S] cluster in particular) into DNICs upon exposure to NO serves as a common mechanism to sense NO in transcription factors (see Section 3.2), there are also examples of non-heme iron centers in NO signaling. To date, the most prominent example of a non-heme iron center used in NO signaling is the enhancer binding protein NorR. Observed in *E. coli* with orthologs contained in other bacterial species, NorR is responsible for controlling the cellular response to NO-related stress in low dioxygen environments.[211,214,1885] Upon exposure to NO, NorR induces transcription of the *norVW* operon in a σ^{54}-dependent mechanism to express flavorubredoxin and its associated redox partner, which reduce NO to N_2O using a non-heme diiron center (see above).[210,211] The activity of NorR requires reversible binding of NO at its N-terminal mononuclear iron-containing GAF domain to form a hs-$\{FeNO\}^7$ species.[243,1886] Once NO is bound, activated NorR has its AAA+ domain catalyze ATP hydrolysis to couple to promoter DNA for transcribing the *norVW* operon.[243] Interestingly, it was recently demonstrated that transcription of the *norVW* operon is blocked in the presence of hydrogen peroxide, with the mononuclear iron center oxidized and unable to bind to NO.[1887] Here, the GAF domain acts as a negative regulator, inhibiting DNA binding, and it is sensitive to an oxidizing environment. Considering the mononuclear iron center in NorR is a crucial regulator for defense against NO and nitrosative stress, studying this NO binding domain and its relation to other NorR domains is of particular interest to better understand this defense system, and NO signaling in bacteria in general.

Characterized by site-directed mutagenesis and structural modeling studies, the iron site in the GAF domain of NorR is predicted to contain three aspartates, one cysteine, and one arginine (see Figure 142, left); moreover, this site has the potential to be either 5C or 6C, depending on whether one aspartate binds to the iron in a bidentate fashion or not.[1886] Upon forming the hs-$\{FeNO\}^7$ species, it is proposed that the arginine ligand is displaced by NO, which induces a conformational change in the GAF domain (as suggested in Figure 142, right).[1888] This, in turn, relieves AAA+ restrictions and allows ATP hydrolysis and subsequent σ^{54}-AAA+ interaction for activating transcription. Additionally, it was also proposed that the GAF domain regulates the binding affinity by interacting with the C-terminal DNA-binding domain and, potentially, the DNA substrate.[1889] While there is a limited understanding of the exact structure of the GAF domain, studies thus far have implicated a non-heme iron site in having significant influence over the NO stress defense mechanism in NorR-containing bacteria.

In addition, the metalloregulators from the ferric uptake regulator (Fur) family form Fe−S cluster-free DNICs upon exposure to NO. The most studied example for these kinds of NO signaling systems is Fur from *E. coli*. As a global transcription regulator, Fur is well known for controlling siderophore synthesis and uptake, oxidative and acidic-stress response, and other iron acquisition mechanisms.[244,1153,1890] A native Zn enzyme, Fur contains two metal binding sites: a tight Zn^{II} binding site reminiscent of a zinc finger, and a regulatory binding site.[1890] Here, the regulatory binding site forms a 6C complex with Fe^{II}, with two histidines, one monodentate glutamate, one bidentate aspartate, and one water molecule (see Figure 143).[1890,1891] It is worth noting that Fur acts as a transcriptional repressor when the regulatory binding site contains Fe^{II}; moreover, Fur is inactive at low cellular Fe concentrations, when these repressed genes can be transcribed.[244,1153] Additionally, in its Fe^{II}-bound state (denoted hereafter as the active state, Fe^{II}-Fur), Fur maintains its coordination environment and the bound iron is a hs-Fe^{II}, according to EXAFS and Mössbauer studies.[1892] Upon exposure to NO at micromolar concentrations, Fe^{II}-Fur is inhibited; moreover, it is proposed that NO binding replaces either the bound water molecule or induces a carboxylate shift in the aspartate ligand (predicted to be a similar case as illustrated in Scheme 65).[244,1153] Further investigations into Fe^{II}-Fur and its NO reactivity by Michaud-Soret and coworkers demonstrate that the NO-bound species has an EPR signal of $S_t = 1/2$; moreover, this species was also characterized by Mössbauer spectroscopy to be the major species (85%; isomer shift $\delta = 0.20$ mm/s and $\Delta E_Q = -0.92$ mm/s) that forms in the reaction with NO.[1153] Considering the low isomer shift, and the hyperfine tensors for ^{57}Fe and ^{14}N, this suggests that the $S_t = 1/2$ species is a $\{Fe(NO)_2\}^9$ DNIC. This species was also characterized by IR spectroscopy, leading to the identification of two isotope-sensitive bands at 1762 and 1715 cm^{-1}, in agreement with typical ν(N−O) vibrational frequencies found in $\{Fe(NO)_2\}^9$ DNICs.[1153] Interestingly, Mössbauer spectroscopy revealed a minor product species as well (15%; isomer shift $\delta = 0.19$ mm/s and $\Delta E_Q = 1.04$ mm/s), which is diamagnetic. This minor species was also characterized by IR spectroscopy and was assigned a ν(N−O) vibrational frequency of 1787 cm^{-1} (1750 cm^{-1} with ^{15}NO). Interestingly, this species is EPR silent and diamagnetic, which was taken as evidence that the minor species could be an unprecedented $\{Fe(NO)_2\}^8$ DNIC.[1153] While the presence of these species is indicative of Fur deactivation by NO, further investigations are required to probe the biological relevance of these DNIC species, and how Fur would return to the Fe^{II}-Fur (active) state at low NO concentrations.

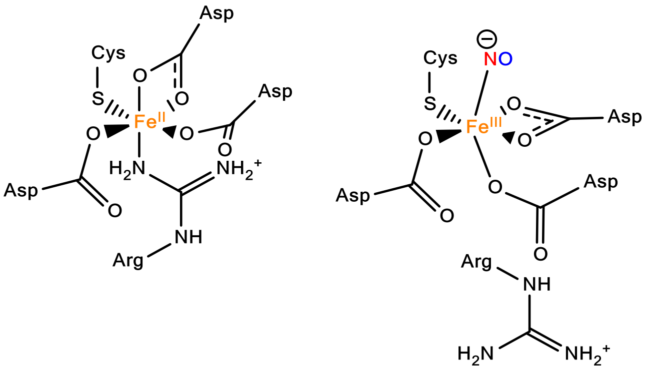

Figure 142. Predicted ferrous site of the N-terminal GAF domain in NorR (left) and proposed hs-$\{FeNO\}^7$ adduct formed after NO binding (right). See text for details.

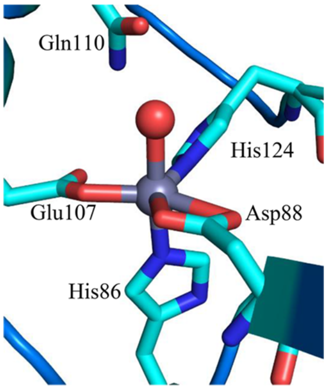

Figure 143. PyMOL generated image of the crystal structure of the zinc-bound metal regulatory site of Fur from *P. aeruginosa* (PDB: 1MZB). A bound water molecule is held in place through hydrogen-bonding interactions with Q110.[1891]

The peroxide stress regulator PerR is another non-heme iron-based transcription factor that is inhibited by NO.[1893] As a member of the Fur protein family, PerR acts as a transcription repressor for genes associated with alkyl hydroperoxide reductase and other enzymes. Here, H_2O_2 deactivates PerR by oxidizing two metal-binding histidine residues, allowing the associated genes to be transcribed.[1894] PerR, like Fur, is a native Zn protein with a tight Zn^{2+} binding site and a regulatory binding site, where replacing Zn^{2+} in the latter activates the regulator.[1893,1895] Moreover, this regulatory binding site has a resemblance to that of Fur, containing three histidines and two glutamates as ligands.[1895] So far, no studies have been reported that investigate any iron−nitrosyl products of PerR; however, considering PerR is structurally similar to Fur, one could imagine that such products could be DNICs. Further investigations are necessary to identify such species.

Scheme 70. Biosynthetic Generation of the N-Nitrosourea Group of Streptozotocin (SZN) by the Non-Heme Iron Enzyme SznF/StzF[a]

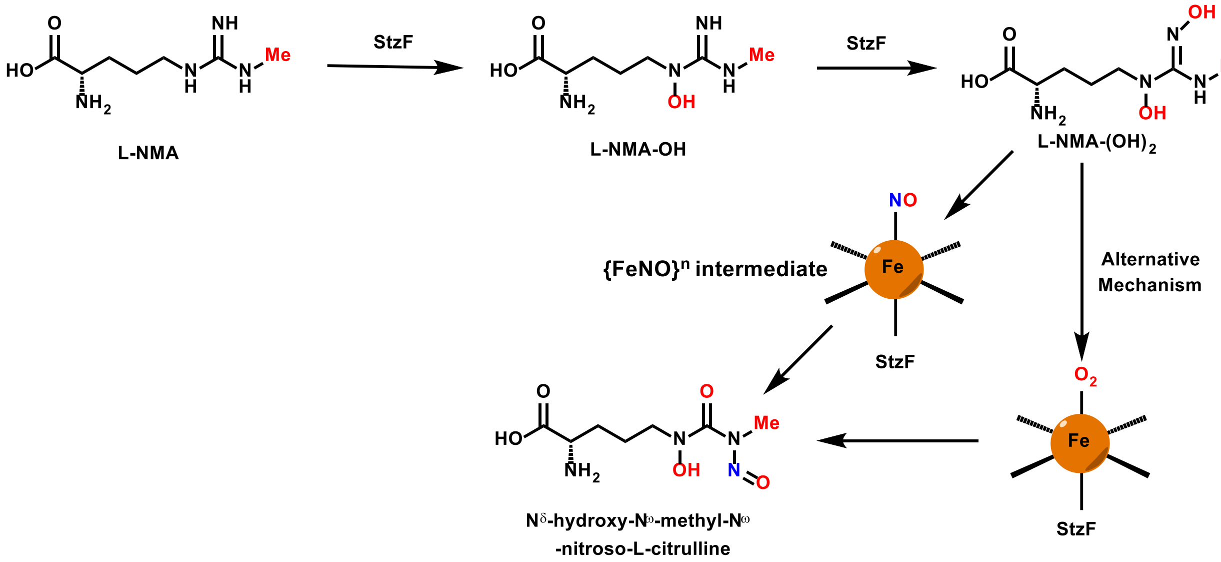

[a]Reprinted with permission from ref 88. Copyright 2019 American Chemical Society.

5.7. Biosynthesis of N−N Bond Containing Natural Products

Natural products containing N−N bonds offer a glimpse into novel biosynthetic pathways that yield a variety of bioactive molecules. Found in microorganisms, plants and marine life, this class of natural products possesses structural diversity, including the presence of N−N bonds in functional groups or in larger heterocyclic motifs.[88,1896] Within this class of natural products, the N-nitroso functional group has gathered particular interest. Molecules containing this functional group (i.e., streptozotocin (SZN), N-nitroglycine) have been shown to exhibit anti-cancer properties.[1896] However, the biosynthetic pathways for these natural products have yet to be fully understood and have thus attracted considerable attention. A commonly observed biosynthetic strategy is N-oxygenation of amines to more reactive functional groups that are susceptible to nucleophilic attack from other amines; furthermore, this strategy depends on Flavin-dependent hydroxylases and metalloproteins (either heme proteins or cupin domain-containing non-heme iron proteins) for N−N bond formation.[1897,1898] Other strategies include radical initiation for N−N linked heterocycles and the use of ATP for diazo species.[1897] The biosynthesis of N-nitroso groups often relies on N-nitrosation of amines by reactive nitrogen species sourced from nitrites; however, recent feeding experiments involving ^{15}N-labeled nitrite and other nitrogen-based salts failed to yield isotopically labeled SZN.[1899] Here, the lack of ^{15}N-labeled SZN suggests that this, and possibly other natural products, are assembled from more novel biosynthesis pathways. For example, nitrosamines and nitramines have been proposed to be synthesized using NO-dependent pathways, where NO is generated specifically for this purpose by dedicated enzymes (such as bacterial NOS or other L-arginine oxidizing enzymes).[1897] As elaborated on below, the use of NO for N−N bond formation in these natural products provides not only another curious use for NO in biological systems, but also stimulates additional interest in N-nitroso metabolites.

Recently, investigations have implicated non-heme iron proteins and NO in the biosynthesis of N-nitroso based natural products. One such series of investigations focused on the biosynthetic pathway of SZN, with a non-heme iron protein being expressed as part of a larger SZN biosynthetic gene cluster.[1899] Once the *N*-methyl-L-arginine (L-MNA) intermediate has been generated from L-arginine by a methyltransferase, the non-heme iron enzyme StzF (also called SznF) is responsible for the N-nitrosation of L-MNA to generate an N-methyl-N-nitroso-carbamoyl intermediate in a manner resembling NOS (Scheme 70). Here, L-MNA undergoes two hydroxylation steps before addition of NO to form the N-nitroso-carbamoyl group. It is worth noting that the hydroxylation steps occur at a dioxygen-activating non-heme diiron site (HDO-domain), and it is hypothesized that each hydroxylation step is mediated by a diferric peroxo intermediate or a species derived from it.[1900] In the following step, N-nitrosation is believed to occur at the cupin domain (a monoiron site bound to three histidines) of StzF in the presence of dioxygen; however, it is not clear whether the reaction proceeds via an Fe−NO intermediate or an Fe−O_2 intermediate.[1899] Another investigation observed that reacting L-MNA with StzF exclusively forms NO and an N-methyl-carbamoyl intermediate, which suggests that a downstream enzymatic process may be responsible for N-nitrosation instead.[1901] Regardless, it is also worth noting that StzF homologs are widely distributed across bacteria.[1899] While much work is necessary to ascertain the role of StzF in N-nitrosation, these recent findings highlight the importance of these N-nitroso and related natural products, and promise exciting future investigations into their biosynthetic pathways.

Aside from the SZN biosynthesis pathway, two additional pathways also predict the use of non-heme iron enzymes for N-nitrosation chemistry. One biosynthetic pathway for N-nitroglycine has been suggested to involve non-heme iron enzymes in the organism *Streptomyces noursei*. This conclusion is based on identifying gene sequences similar to non-heme iron enzymes involved in other biosynthetic pathways; however, further work is needed to determine if the *S. noursei* enzymes indeed have the proposed function.[1902] Another biosynthetic pathway worth mentioning is that for L-alanosine, as reported by Ryan and co-workers.[1898] For the L-alanosine biosynthesis pathway, the associated gene cluster was found to include an N-terminal cupin domain-containing protein (AlnA), analogous to StzF in the SZN biosynthetic pathway. While work on the L-alanosine biosynthetic pathway suggests NO is used for N-nitrosation, the exact role of AlnA in this pathway has yet to be determined. These findings suggest, in tandem with the findings for the SZN biosynthetic pathway discussed above, that there exist similarities in synthetic strategies for N-nitroso and similar for N−N group containing natural products across many bacterial genera. Moreover, enzymes including AlnA could have a regulatory role besides their synthetic role. This is an exciting new area in bioinorganic chemistry with many new discoveries to be expected in the near future.

6. CONCLUSIONS

Nitric oxide is an amazing biological signaling agent that has been the subject of intense research for the past 40+ years. This is showcased by this large review, which just deals with the biologically-relevant coordination chemistry of iron and NO. As described in this review, our current understanding of the biological roles of NO came from contributions across many disciplines. A deeper understanding of the interactions between transition-metal ions and NO, in particular, has provided valuable insights because metal ions are the ultimate targets of NO in cells. Because of the complications originating from the redox non-innocent nature of NO, elucidation of electronic structures and prediction of chemical reactivity of metal−NO species has been one of the major challenges. Recent advances in this area have now given us clearer pictures of many biological processes involving NO as a signaling molecule or as a metabolic intermediate. Besides the many important roles of hemes and iron−sulfur sites in the biological chemistry of NO, new and exciting research areas have evolved more recently, which include non-heme iron-based NO detoxification and signaling pathways as seen in flavodiiron proteins and NO sensors (like NorR and Fur), NO-sensing [Fe−S] regulatory proteins, noncanonical NO/nitrite/nitrate signaling pathways, nitroxyl (HNO) signaling, protein post-translational modifications catalyzed by metal−nitrosyls, and evolving biomedical applications including new therapeutics and imaging tools. New roles for nitric oxide in neurodegenerative diseases are emerging as well.[204] New proteins and pathways involved in NO metabolism are still being discovered in the nitrogen cycle, which features some of the most exotic heme proteins known.[258] The field is actively growing and expanding, and we are excited about the prospects of the many new developments in the years to come.

AUTHOR INFORMATION

Corresponding Authors

Nicolai Lehnert − *Department of Chemistry and Department of Biophysics, University of Michigan, Ann Arbor, Michigan 48109-1055, United States*; orcid.org/0000-0002-5221-5498; Email: lehnertn@umich.edu

Eunsuk Kim − *Department of Chemistry, Brown University, Providence, Rhode Island 02912, United States*; orcid.org/0000-0001-8803-0666; Email: eunsuk_kim@brown.edu

Authors

Hai T. Dong − *Department of Chemistry and Department of Biophysics, University of Michigan, Ann Arbor, Michigan 48109-1055, United States*; orcid.org/0000-0002-8914-3045

Jill B. Harland − *Department of Chemistry and Department of Biophysics, University of Michigan, Ann Arbor, Michigan 48109-1055, United States*

Andrew P. Hunt − *Department of Chemistry and Department of Biophysics, University of Michigan, Ann Arbor, Michigan 48109-1055, United States*; orcid.org/0000-0003-0565-9050

Elizabeth C. Manickas − *Department of Chemistry and Department of Biophysics, University of Michigan, Ann Arbor, Michigan 48109-1055, United States*

Kady M. Oakley − *Department of Chemistry, Brown University, Providence, Rhode Island 02912, United States*

John Pham − *Department of Chemistry, Brown University, Providence, Rhode Island 02912, United States*

Garrett C. Reed − *Department of Chemistry and Department of Biophysics, University of Michigan, Ann Arbor, Michigan 48109-1055, United States*

Victor Sosa Alfaro − *Department of Chemistry and Department of Biophysics, University of Michigan, Ann Arbor, Michigan 48109-1055, United States*; orcid.org/0000-0001-8149-5137

Complete contact information is available at:
https://pubs.acs.org/10.1021/acs.chemrev.1c00253

Notes

The authors declare no competing financial interest.

Biographies

Nicolai Lehnert obtained a Diploma in Chemistry in 1995 from the Heinrich-Heine-University Düsseldorf, Germany. He then moved to the Johannes Gutenberg-University Mainz, Germany, where he received his Ph.D. in 1999 under supervision of Priv.-Doz. Dr. F. Tuczek and Prof. P. Gütlich. From 1999 to 2001, he conducted postdoctoral research with Prof. E. I. Solomon at Stanford University. He then moved back to Germany for his Habilitation, which he received in 2006 from the Christian-Albrechts-University Kiel, Germany, working with Prof. F. Tuczek. In 2006, he accepted a faculty position at the University of Michigan. His work is focused on the coordination chemistry of nitric oxide as it pertains to biological systems, in particular NO reductases but also heme proteins and biocatalysis.

Eunsuk Kim was born and raised in South Korea. She received her B.S. degree from Sangmyung University and M.S. degree from Korea University under the guidance of Professor Ho. G. Jang. She moved to the United States in 1998 and obtained her Ph.D. in 2004 at Johns Hopkins University while working with Professor Kenneth D. Karlin. After two postdoctoral stints in the laboratories of Professor Bruce Demple at Harvard University, and Professor John M. Essigmann at MIT as an LSRF (Life Sciences Research Foundation) postdoctoral fellow, she joined the faculty at Brown University in 2008. Her research interests include bioinorganic chemistry of redox signaling, bio-inspired catalysts for chalcogen atom transfer, and molecular informatics and computing.

Hai T. Dong was born and raised in Vietnam. He received his B.S. degree in Chemistry from the University of Cincinnati, Ohio. While there, his research focused on the synthesis and characterization of Janus POCOP pincer complexes of nickel. He then moved to the University of Michigan, Ann Arbor, where he received his Ph.D. in 2021 working with Prof. Nicolai Lehnert. His thesis focused on the synthesis and characterization of model complexes of FNORs. While there, he was also part of multiple collaborative efforts including an international collaboration focused on investigating the unique electronic structure of high-valent metal oxo complexes. He is starting his next chapter as a Postdoctoral Scholar Research Associate at Caltech working with Prof. Theodor Agapie and Prof. Jonas Peters in the effort to generate liquid fuels from sunlight, water, CO_2, and nitrogen as part of the Liquid Sunlight Alliance (LiSA).

Jill B. Harland began her research career at the University of Nevada Las Vegas in Dr. Paul Forster's laboratory, designing materials for carbon dioxide capture utilizing computational methods. She then went on to receive her B.S. degree in Chemistry from the University of Delaware. During her time there, she synthesized and characterized nickel scorpionate ligand systems in the bioinorganic group of Dr. Charles Riordan. In addition, she studied carbon dioxide capture employing ionic liquids under the supervision of Dr. John Newberg. Currently, she is pursuing her Ph.D. at the University of Michigan under the supervision of Prof. Nicolai Lehnert, developing synthetic model complexes to mimic the heme/non-heme iron active site of bacterial nitric oxide reductase.

Andrew P. Hunt graduated from Kent State University in 2013, receiving his B.S. degree with a concentration in Biological Chemistry and departmental honors in Chemistry, where he worked under Prof. Nicola Brasch studying the reactions of cobalamins with reactive oxygen species. He then studied under Prof. Nicolai Lehnert at the University of Michigan receiving his Ph.D. in Inorganic Chemistry in 2019, where his research focused on the reactions of heme-thiolate enzymes and model complexes with nitric oxide (NO) as well as electrochemical mediated NO generation via use of copper-ligand catalysts. From 2019−2020, he studied with Prof. Mark Meyerhoff at the University of Michigan as a Postdoctoral Researcher Fellow, and he currently works for NOTA Laboratories LLC as a Senior Research Scientist, where his work has focused on the research and development of NO generation-based technologies for uses in therapeutic biomedical applications.

Elizabeth C. Manickas earned her B.S. degree in Chemistry with a concentration in biochemistry in 2018 from Shippensburg University of Pennsylvania. While there, she was mentored by Dr. Curtis Zaleski and Dr. Allison Predecki, synthesizing and characterizing metallacrowns and investigating their use in biomedical applications. She is currently pursuing her Ph.D. at the University of Michigan with guidance from Prof. Nicolai Lehnert.

Kady M. Oakley (Ferguson) was born in October of 1993. Raised in her hometown of Norton, MA, she graduated as salutatorian from Norton High School in 2012. She then attended Worcester Polytechnic Institute (WPI) where she received her B.S. in Chemistry with a minor in Biology in 2016. Her interest in bioinorganic chemistry began in the laboratory of Prof. Shawn Burdette at WPI by developing zinc photocages to probe zinc homeostasis in cells. She is currently a Ph.D. candidate at Brown University in the group of Prof. Eunsuk Kim where she synthesizes biomimetic iron−sulfur complexes and studies their reactivity with biologically relevant signaling molecules such as NO and O_2. She is also part of a collaborative team that uses small molecules to compute and store information. Outside of the laboratory, she enjoys shopping, decorating, and spending time with her husband, Dalton, and her new baby boy, Grayson.

John Pham, Jr. (born 1998) was raised in Windsor, Connecticut. After graduating from Northwest Catholic High School, he attended Colgate University and received his B.A. in Chemistry and Applied Mathematics. While there, his research was centered around ruthenium catalysts used for ester hydrogenation reactions with Prof. Anthony Chianese. He is currently pursuing his Ph.D. at Brown University with the guidance of Prof. Eunsuk Kim. His research focuses on the reactivity between synthetic iron−sulfur clusters and nitric oxide, which are important to various biological functions.

Garrett C. Reed received their B.S. degree with honors in Biochemistry from Miami University in 2019. While there, they did their undergraduate research with Prof. David Tierney and worked with cobalt-substituted metalloproteins and model complexes. In addition, in summer 2018, they focused on the synthesis of potential pharmaceutical candidates under the supervision of Prof. Richard Taylor, in collaboration with the Drugs for Neglected Diseases Institute. They are currently a Ph.D. candidate at the University of Michigan, under the supervision of Prof. Nicolai Lehnert. Their project is focused on redox tuning of non-heme diiron model complexes of flavodiiron nitric oxide reductases.

Victor Sosa Alfaro received his B.S. in Chemistry with a concentration in Biochemistry from Sonoma State University. During his undergraduate study, he primarily worked with Prof. Jon Fukuto on the chemical biology of hydropersulfides. He worked at San Jose State University with Prof. Leonel Cheruzel on engineering light-driven Cytochrome P450s. Currently, he is working towards his Ph.D. in Prof. Nicolai Lehnert's laboratory at the University of Michigan where his research focuses on developing biocatalysts (carbene transferases) and studying the mechanism of Cytochrome *c* nitrite reductase.

ACKNOWLEDGMENTS

First and foremost, we want to give a special acknowledgment to Prof. Wolfgang Kaim on the occasion of his 70th birthday. Over the years, this work was supported by several grants from the National Science Foundation (CHE-0846235, CHE-1305777, CHE-1464696, CHE-1608331, and CHE-2002885 to NL, and CHE-1254733 and CHE-1807845 to EK), the National Institutes of Health (HL132037-01A1 to NL), the U.S. Department of Energy, Office of Science, Basic Energy Sciences (DE-SC0018173 to NL), the Dow Corning Corporation, and IBM. HTD acknowledges support from the Eastman Summer Research Fellowship and the Robert W. Parry Scholarship (University of Michigan). VSA acknowledges support from a Rackham Merit Fellowship and a Robert W. Parry Scholarship (both University of Michigan).

ABBREVIATIONS

4C = four-coordinate
5C = five-coordinate
6C = six-coordinate
AF coupling = antiferromagnetic coupling
AMO = ammonia monooxygenase
ANAMMOX = anaerobic ammonium-oxidizing bacteria
AOA = ammonia oxidizing archaea
AOB = ammonia oxidizing bacteria
BMPA = bis(methylpyridyl)amine
bpy = bipyridine
CC domain = coiled-coil domain
C*c*O = cytochrome *c* oxidase
cGMP = cyclic guanosine-3′,5′-monophosphate
cNP = *Cimex lectularius* nitrophorin
COMAMMOX = complete ammonia-oxidizing bacteria
CPO = chloroperoxidase
Cs H-NOX = *Caldanaerobacter subterraneus H-NOX* protein
Cygb = cytoglobin
Cyt. = cytochrome
DEER-EPR = double electron-electron resonance EPR spectroscopy

deoxy-Hb or deoxy-Mb = ferrous Hb or Mb = Hb(II) or Mb(II)
DFT = density functional theory
Dg ROO = *Desulfovibrio gigas* rubredoxin oxygen:oxidoreductase
DMF = dimethylformamide
DNIC = dinitrosyl iron complex
DNRA = dissimilatory nitrate reduction to ammonia
Ec FlRd = *Escherichia coli* flavorubredoxin
ENDOR = electron-nuclear double resonance spectroscopy
eNOS = endothelial NOS
EPR = electron paramagnetic resonance spectroscopy
EXAFS = extended X-ray absorption fine structure
FAD = flavin adenine dinucleotide
Fc = ferrocene, $FeCp_2$ (Cp^- = cyclopentadienyl anion)
FDP = flavodiiron protein
FMN = flavin mononucleotide
FNOR = flavodiiron NO reductase
Fo P450nor = *Fusarium oxyporum* Cyt. P450nor
GSH = glutathione
GS-NO = nitrosoglutathione
H_4B = tetrahydrobiopterin
HAO = hydroxylamine oxidoreductase
Hb = hemoglobin
HDH = hydrazine dehydrogenase
HRP = horseradish peroxidase
hs = high-spin
H-NOX = heme nitric oxide/oxygen sensor domains
HYSCORE = hyperfine sublevel correlation spectroscopy
HZS = hydrazine synthase
iNOS = inducible NOS
Iz = indazole
LMW = low molecular weight
ls = low-spin
Mb = myoglobin
MCD = magnetic circular dichroism spectroscopy
met-Hb or met-Mb = ferric Hb or Mb = Hb(III) or Mb(III)
MI = 1-methylimidazole
MNIC = mononitrosyl iron complex
MPO = myeloperoxidase
Mt FDP = *Moorella thermoacetica* FDP
N2OR = nitrous oxide reductase
NADH = nicotinamide adenine dinucleotide (reduced form)
NADPH = nicotinamide adenine dinucleotide phosphate (reduced form)
NCA = normal coordinate analysis
Ngb = neuroglobin
NHC = N-heterocyclic carbene
NHE = normal hydrogen electrode (E ≈ 0.000 V vs SHE)
NIR = nitrite reductase
NMR = nuclear magnetic resonance spectroscopy
nNOS = neuronal NOS
NO = nitric oxide
NOB = nitrite-oxidizing bacteria
NOD = nitric oxide dioxygenation
NOHA = N^G-hydroxy-L-arginine
NOR = nitric oxide reductase
NOS = nitric oxide synthase
NosP = nitric oxide sensing protein
NP = nitrophorin
NRVS = nuclear resonance vibrational spectroscopy
Ns H-NOX = *Nostoc sp H-NOX* protein
NXR = nitrite oxidoreductase
O_2 = dioxygen
ODN = oxidative denitrosylation
OEP = octaethylporphyrin dianion
OTf^- = triflate anion
oxy-Hb or oxy-Mb = ferrous Hb or Mb with O_2 bound = Hb(II)−O_2 or Mb(II)−O_2
P = porphine dianion
*Pa c*NOR = *Pseudomonas aeruginosa c*NOR
Pa NIR = *Pseudomonas aeruginosa* NIR
PAS domain = Per/Arnt/Sim-like domain
PCET = proton-coupled electron-transfer
*Pd c*NOR = *Pseudomonas denitrificans c*NOR
Pd NIR = *Paracoccus denitrificans* GB 17 NIR
PES = potential energy surface
PGHS = prostaglandin H synthase
Phen = phenanthroline
pMMO = particulate methane monooxygenase
Pn NIR = *Pseudomonas nautica* NIR
Porph = general porphyrin dianion ligand
PPIX = protoporphyrin IX dianion (porphyrin ligand in heme *b*)
PPIXDME = protoporphyrin IX dimethylester dianion
Pp NIR = *Paracoccus pantotrophus* NIR
Prz = pyrazine
Pyr = pyridine
Pz = pyrazole
QCC-NCA = quantum-chemistry centered normal coordinate analysis
RBC = red blood cell
RBS = Roussin's black salt
*Rd c*NOR = *Roseobacter denitrificans c*NOR
RFQ = rapid freeze quench
RMSD = root−mean−square deviation
rNP = *Rhodnius prolixus* nitrophorin
RNR = ribonucleotide reductase
rRaman = resonance Raman spectroscopy
RRE = Roussin's red ester
RRS = Roussin's red salt
RS-NO = nitrosothiol
SCE = saturated calomel electrode (E = +241 mV vs SHE)
SCS = second coordination sphere
sGC = soluble guanylate cyclase
SHE = standard hydrogen electrode (E = 0.000 V by definition)
sMMO = soluble methane monooxygenase
SNP = sodium nitroprusside
So H-NOX = *Shewanella oneidensis H-NOX* protein
SQUID = superconducting quantum interference device
Tm FDP = *Thermotoga maritima* FDP
TMPA = tris(methylpyridyl)amine, also called TPA
TNIC = trinitrosyl iron complex
Tp = hydrotris(pyrazolyl)borate anion
TPP = tetraphenylporphyrin dianion
TPP* = general TPP dianion derivative with phenyl substituents
VDOS = vibrational density of states
XAS = X-ray absorption spectroscopy

REFERENCES

(1) Forte, E.; Van Den Bergh, H. The heat of formation of the nitric oxide dimer and its UV spectrum. *Chem. Phys.* **1978**, *30*, 325−331.
(2) Dkhissi, A.; Soulard, P.; Perrin, A.; Lacome, N. The NO dimer. *J. Mol. Spectrosc.* **1997**, *183*, 12−17.

(3) Dinerman, C. E.; Ewing, G. E. Infrared spectrum, structure, and heat of formation of gaseous (NO)$_2$. *J. Chem. Phys.* **1970**, *53*, 626−631.

(4) Greenwood, N. N.; Earnshaw, A. *Chemistry of the elements*; 2nd ed.; Elsevier, 2012; Vol. *412*, pp 445−447.

(5) Ford, P. C.; Lorkovic, I. M. Mechanistic aspects of the reactions of nitric oxide with transition-metal complexes. *Chem. Rev.* **2002**, *102*, 993−1017.

(6) McKellar, A. R. W.; Watson, J. K. G.; Howard, B. J. The NO dimer: ^{15}N isotopic infrared spectra, line-widths, and force field. *Mol. Phys.* **1995**, *86*, 273−286.

(7) Laane, J.; Ohlsen, J. R. Characterization of nitrogen oxides by vibrational spectroscopy. *Prog. Inorg. Chem.* **2007**, *27*, 465−513.

(8) Milligan, D. E.; Jacox, M. E. Matrix-isolation study of the interaction of electrons and alkali metal atoms with various nitrogen oxides. Infrared spectra of the species NO$^-$, NO$_2^-$, and N$_2$O$_2^-$. *J. Chem. Phys.* **1971**, *55*, 3404−3418.

(9) Malinski, T.; Taha, Z.; Grunfeld, S.; Patton, S.; Kapturczak, M.; Tomboulian, P. Diffusion of nitric oxide in the aorta wall monitored in situ by porphyrinic microsensors. *Biochem. Biophys. Res. Commun.* **1993**, *193*, 1076−1082.

(10) Möller, M.; Botti, H.; Batthyany, C.; Rubbo, H.; Radi, R.; Denicola, A. Direct measurement of nitric oxide and oxygen partitioning into liposomes and low density lipoprotein. *J. Biol. Chem.* **2005**, *280*, 8850−8854.

(11) Zacharia, I. G.; Deen, W. M. Diffusivity and solubility of nitric oxide in water and saline. *Ann. Biomed. Eng.* **2005**, *33*, 214−222.

(12) Battino, R. 2 - Nitric Oxide. *IUPAC Solubility Series: Oxides of Nitrogen*; Young, C. L., Ed.; Pergamon: Amsterdam, 1981; pp 260−351.

(13) Lehnert, N.; Scheidt, W. R. Inorganic Chemistry FORUM: The coordination chemistry of nitric oxide and its significance for metabolism, signaling and toxicity in biology. *Inorg. Chem.* **2010**, *49* (14), 6223.

(14) Bartberger, M. D.; Liu, W.; Ford, E.; Miranda, K. M.; Switzer, C.; Fukuto, J. M.; Farmer, P. J.; Wink, D. A.; Houk, K. N. The reduction potential of nitric oxide (NO) and its importance to NO biochemistry. *Proc. Natl. Acad. Sci. U. S. A.* **2002**, *99*, 10958−10963.

(15) Stanbury, D. M. Reduction potentials involving inorganic free radicals in aqueous solution. *Advances in Inorganic Chemistry*; Sykes, A. G., Ed.; Academic Press, 1989; Vol. *33*; pp 69−138.

(16) Mingos, D. M. P. Historical introduction to nitrosyl complexes. *Struct. Bonding* **2014**, *153*, 1−44.

(17) Harland, J. B.; Manickas, E. C.; Hunt, A. P.; Lehnert, N. Reactivity and structure of complexes of small molecules: nitric oxide. *Comprehensive Coordination Chemistry III*; Constable, E., Parkin, G., Que, L., Jr., Eds.; Elsevier, 2021; pp 806−874.

(18) Richter-Addo, G. B.; Legzdins, P. *Metal Nitrosyls*; Oxford University Press: Oxford, UK, 1992.

(19) Jørgensen, C. K. Differences between the four halide ligands, and discussion remarks on trigonal-bipyramidal complexes, on oxidation states, and on diagonal elements of one-electron energy. *Coord. Chem. Rev.* **1966**, *1*, 164−178.

(20) Mingos, D. M. P. A review of complexes of ambivalent and ambiphilic Lewis acid/bases with symmetry signatures and an alternative notation for these noninnocent ligands. *J. Organomet. Chem.* **2014**, *751*, 153−173.

(21) Goodrich, L. E.; Paulat, F.; Praneeth, V. K. K.; Lehnert, N. Electronic structure and reactivity of heme-nitrosyls and its significance for nitric oxide sensing, transport, and catalysis in biological systems. *Inorg. Chem.* **2010**, *49*, 6293−6316.

(22) Ferousi, C.; Majer, S. H.; DiMucci, I. M.; Lancaster, K. M. Biological and bioinspired inorganic N-N bond-forming reactions. *Chem. Rev.* **2020**, *120*, 5252−5307.

(23) Maia, L. B.; Moura, J. J. G. How biology handles nitrite. *Chem. Rev.* **2014**, *114*, 5273−5357.

(24) Lehnert, N.; Scheidt, W. R.; Wolf, M. W. Structure and bonding in heme-nitrosyl complexes and implications for biology. *Struct. Bonding* **2013**, *154*, 155−224.

(25) Lehnert, N.; Berto, T. C.; Galinato, M. G. I.; Goodrich, L. E. The role of heme-nitrosyls in the biosynthesis, transport, sensing, and detoxification of nitric oxide (NO) in biological systems: Enzymes and model complexes. *The Handbook of Porphyrin Science*; Kadish, K. M., Smith, K. M., Guilard, R., Eds.; World Scientific: New Jersey, 2011; Vol. *14*; pp 1−247.

(26) Cheng, L.; Richter-Addo, G. B. Binding and activation of nitric oxide by metalloporphyrins and heme. *The Porphyrin Handbook*; Kadish, K. M., Smith, K. M., Guilard, R., Eds.; Academic Press: New York, 2000; Vol. *4*; pp 219−291.

(27) *Metalloenzymes in denitrification*; Moura, I., Moura, J. J. G., Pauleta, S. R., Maia, L. B., Eds.; The Royal Society of Chemistry: Cambridge, UK, 2017.

(28) Manoharan, P. T.; Hamilton, W. C. The crystal structure of sodium nitroprusside. *Inorg. Chem.* **1963**, *2*, 1043−1047.

(29) Olabe, J. A. Coordination chemistry of nitric oxide and biological signaling. *Science Reviews from the End of the World* **2020**, *2*, 64−99.

(30) Playfair, L. XXIV. On the nitroprussides, a new class of salts. *Philos. Trans. R. Soc. Lond.* **1849**, *139*, 477−518.

(31) Que, L., Jr. The Road to non-heme oxoferryls and beyond. *Acc. Chem. Res.* **2007**, *40*, 493−500.

(32) Larson, V. A.; Battistella, B.; Ray, K.; Lehnert, N.; Nam, W. Iron and manganese oxo complexes, oxo wall and beyond. *Nat. Rev. Chem.* **2020**, *4*, 404−419.

(33) Paliani, G.; Poletti, A.; Santucci, A. Vibrational spectrum of sodium nitroprusside. Normal coordinate analysis for the Fe-(CN)$_5$NO^{2-} ion. *J. Mol. Struct.* **1971**, *8*, 63−74.

(34) Johnson, B. F. G.; McCleverty, J. A. Nitric oxide compounds of transition metals. *Prog. Inorg. Chem.* **2007**, *7*, 277−359.

(35) Connelly, N. G. Recent developments in transition metal nitrosyl chemistry. *Inorg. Chim. Acta, Rev.* **1972**, *6*, 47−89.

(36) Enemark, J. H.; Feltham, R. D. Principles of structure, bonding, and reactivity for metal nitrosyl complexes. *Coord. Chem. Rev.* **1974**, *13*, 339−406.

(37) Hieber, W.; Beutner, H. Über Nitrosyltricarbonylferrat(-I), [Fe(CO)$_3$NO]$^-$. *Z. Naturforsch., B: J. Chem. Sci.* **1960**, *15*, 323−324.

(38) Klein, J. E. M. N.; Miehlich, B.; Holzwarth, M. S.; Bauer, M.; Milek, M.; Khusniyarov, M. M.; Knizia, G.; Werner, H.-J.; Plietker, B. The electronic ground state of [Fe(CO)$_3$(NO)]-: a spectroscopic and theoretical study. *Angew. Chem., Int. Ed.* **2014**, *53*, 1790−1794.

(39) Burkhardt, L.; Vukadinovic, Y.; Nowakowski, M.; Kalinko, A.; Rudolph, J.; Carlsson, P.-A.; Jacob, C. R.; Bauer, M. Electronic structure of the Hieber anion [Fe(CO)$_3$(NO)]$^-$ revisited by x-ray emission and absorption spectroscopy. *Inorg. Chem.* **2020**, *59*, 3551−3561.

(40) Bohnenberger, J.; Krossing, I. Stable salts of heteroleptic iron carbonyl/nitrosyl cations. *Angew. Chem., Int. Ed.* **2020**, *59*, 5581−5585.

(41) Beck, W. IR-Absorptionsmessungen an Nitrosyltricarbonylferraten(-I). *Chem. Ber.* **1961**, *94*, 1214−1217.

(42) Johnson, C. C. Mechanisms of actions and toxicity of nitroprusside. *Exp. Biol. Med.* **1928**, *26*, 102−103.

(43) Page, I. H.; Corcoran, A. C.; Dustan, H. P.; Koppanyi, T. Cardiovascular actions of sodium nitroprusside in animals and hypertensive patients. *Circulation* **1955**, *11*, 188−198.

(44) Taylor, T. H.; Styles, M.; Lamming, A. J. Sodium nitroprusside as a hypotensive agent in general anaesthesia. *Br. J. Anaesth.* **1970**, *42*, 859−864.

(45) Hottinger, D. G.; Beebe, D. S.; Kozhimannil, T.; Prielipp, R. C.; Belani, K. G. Sodium nitroprusside in 2014: a clinical concepts review. *J. Anaesthesiol. Clin. Pharmacol.* **2014**, *30*, 462−471.

(46) Culotta, E.; Koshland, D. E., Jr. NO news is good news. *Science* **1992**, *258*, 1862−1865.

(47) Moncada, S.; Palmer, R. M.; Higgs, E. A. Nitric oxide: physiology, pathophysiology, and pharmacology. *Pharmacol. Rev.* **1991**, *43*, 109−142.

(48) Khodashova, T. S. X-ray study of nitrosopentammineruthenium trichloride crystals. *J. Struct. Chem.* **1966**, *6*, 678−684.

(49) Joly, A. Sur les combinaisons nitrosees du ruthenium. *Compt. rendus Acad. Sci.* **1889**, *108*, 854−857.

(50) Joly, A. Sur les combinaisons du ruthenium. *Compt. rendus Acad. Sci.* **1889**, *108*, 1300−1303.

(51) Werner, A. Zur Kenntnis der Ruthenium-Ammoniakverbindungen. Beitrag III zur Theorie der Hydrolyse. *Ber. Dtsch. Chem. Ges.* **1907**, *40*, 2614−2628.

(52) Gleu, K.; Büddecker, I. Nitroso-Pentammine des Rutheniums. *Z. Anorg. Allg. Chem.* **1952**, *268*, 202−220.

(53) Armor, J. N.; Scheidegger, H. A.; Taube, H. A bimolecular mechanism for substitution. *J. Am. Chem. Soc.* **1968**, *90*, 5928−5929.

(54) Bottomley, F.; Crawford, J. R. Reactions of nitrosylpentaammineruthenium(II) with hydroxylamine, hydrazine, and ammonia. *J. Chem. Soc. D* **1971**, 200−201.

(55) Bottomley, F. Nitrosyl complexes of ruthenium. *Coord. Chem. Rev.* **1978**, *26*, 7−32.

(56) Bottomley, F. Reinvestigation of the crystal and molecular structures of pentamminenitrosylruthenium trichloride hydrate and *trans*-tetra-ammine-hydroxonitrosylruthenium dichloride. *J. Chem. Soc., Dalton Trans.* **1974**, *15*, 1600−1605.

(57) Cleare, M. J.; Griffith, W. P. Halogeno-carbonyl and -nitrosyl complexes of the platinum metals, and their vibrational spectra. *J. Chem. Soc. A* **1969**, 372−380.

(58) Paulat, F.; Kuschel, T.; Näther, C.; Praneeth, V. K. K.; Sander, O.; Lehnert, N. Spectroscopic properties and electronic structure of pentammineruthenium(II) dinitrogen oxide and corresponding nitrosyl complexes: binding mode of N_2O and reactivity. *Inorg. Chem.* **2004**, *43*, 6979−6994.

(59) Mercer, E. E.; McAllister, W. A.; Durig, J. R. An infrared study of the directive influences by ligands in nitrosylruthenium complexes. *Inorg. Chem.* **1966**, *5*, 1881−1886.

(60) Manoharan, P. T.; Gray, H. B. Electronic structure of nitroprusside ion. *J. Am. Chem. Soc.* **1965**, *87*, 3340−3348.

(61) Raynor, J. B. On the formalism of treating the linear nitric oxide ligand as NO^+. *Inorg. Chim. Acta* **1972**, *6*, 347−348.

(62) Sidgwick, N. V.; Bailey, R. W. Structures of the metallic carbonyl and nitrosyl compounds. *Proc. Roy. Soc. A* **1934**, *144*, 521−537.

(63) Fletcher, J. M.; Jenkins, I. L.; Lever, F. M.; Martin, F. S.; Powell, A. R.; Todd, R. Nitrato and nitro complexes of nitrosylruthenium. *J. Inorg. Nucl. Chem.* **1955**, *1*, 378−401.

(64) Bottomley, F.; Brooks, W. V. F.; Clarkson, S. G.; Tong, S.-B. Electrophilic behaviour of the co-ordinated nitrosyl cation. *J. Chem. Soc., Chem. Commun.* **1973**, *23*, 919−920.

(65) Bottomley, F. Electrophilic behavior of coordinated nitric oxide. *Acc. Chem. Res.* **1978**, *11*, 158−163.

(66) Roncaroli, F.; Videla, M.; Slep, L. D.; Olabe, J. A. New features in the redox coordination chemistry of metal nitrosyls {$M-NO^+$; $M-NO^\bullet$; $M-NO^-$ (HNO)}. *Coord. Chem. Rev.* **2007**, *251*, 1903−1930.

(67) Gao, Y.; Toubaei, A.; Kong, X.; Wu, G. Solving the 170-year-old mystery about red-violet and blue transient intermediates in the Gmelin reaction. *Chem. - Eur. J.* **2015**, *21*, 17172−17177.

(68) Serres, R. G.; Grapperhaus, C. A.; Bothe, E.; Bill, E.; Weyhermüller, T.; Neese, F.; Wieghardt, K. Structural, spectroscopic, and computational study of an octahedral, non-heme {Fe-NO}$^{6-8}$ series: [Fe(NO)(cyclam-ac)]$^{2+/+/0}$. *J. Am. Chem. Soc.* **2004**, *126*, 5138−5153.

(69) Speelman, A. L.; White, C. J.; Zhang, B.; Alp, E. E.; Zhao, J.; Hu, M.; Krebs, C.; Penner-Hahn, J.; Lehnert, N. Non-heme high-spin {FeNO}$^{6-8}$ complexes: one ligand platform can do it all. *J. Am. Chem. Soc.* **2018**, *140*, 11341−11359.

(70) Speelman, A.; Lehnert, N. Heme versus non-heme iron-nitroxyl {FeN(H)O}^{8} complexes: electronic structure and biologically relevant reactivity. *Acc. Chem. Res.* **2014**, *47*, 1106−1116.

(71) Kupper, C.; Rees, J. A.; Dechert, S.; DeBeer, S.; Meyer, F. Complete series of {FeNO}^{8}, {FeNO}^{7}, and {FeNO}^{6} complexes stabilized by a tetracarbene macrocycle. *J. Am. Chem. Soc.* **2016**, *138*, 7888−7898.

(72) Montenegro, A. C.; Amorebieta, V. T.; Slep, L. D.; Martin, D. F.; Roncaroli, F.; Murgida, D. H.; Bari, S. E.; Olabe, J. A. Three redox states of nitrosyl: NO^+, $NO^\bullet$, and NO, -HNO interconvert reversibly on the same pentacyanoferrate(II) platform. *Angew. Chem., Int. Ed.* **2009**, *48*, 4213−4216.

(73) Van Stappen, C.; Goodrich, L. E.; Lehnert, N. The interaction of HNO with transition metal centers and its biological significance. Insight into electronic structure from theoretical calculations. *The Chemistry and Biology of Nitroxyl (HNO)*; Doctorovich, F., Farmer, P. J., Marti, M. A., Eds.; Elsevier: Amsterdam, Netherlands, 2017; pp 155−192.

(74) Speelman, A.; Zhang, B.; Krebs, C.; Lehnert, N. Structural and spectroscopic characterization of a high-spin {FeNO}^{6} complex with an iron(IV)-NO c - electronic structure. *Angew. Chem., Int. Ed.* **2016**, *55*, 6685−6688.

(75) Wilson, R. D.; Ibers, J. A. Coordinated nitrosyl hydride: structural and spectroscopic study of dichlorocarbonyl(nitrosyl hydride)bis(triphenylphosphine)osmium(II). *Inorg. Chem.* **1979**, *18*, 336−343.

(76) Singh, P.; Fiedler, J.; Záliš, S.; Duboc, C.; Niemeyer, M.; Lissner, F.; Schleid, T.; Kaim, W. Spectroelectrochemistry and DFT analysis of a new {RuNO}^{n} redox system with multifrequency EPR suggesting conformational isomerism in the {RuNO}^{7} state. *Inorg. Chem.* **2007**, *46*, 9254−9261.

(77) Codesido, N. O.; Weyhermüller, T.; Olabe, J. A.; Slep, L. D. Nitrosyl-centered redox and acid-base interconversions in [Ru(Me$_3$[9]aneN$_3$)(bpy)(NO)]$^{3,2,1+}$. The pKa of HNO for its nitroxyl derivative in aqueous solution. *Inorg. Chem.* **2014**, *53*, 981−997.

(78) Levin, N.; Codesido, N. O.; Marcolongo, J. P.; Albores, P.; Weyhermueller, T.; Olabe, J. A.; Slep, L. D. Remarkable changes of the acidity of bound nitroxyl (HNO) in the [Ru(Me$_3$[9]aneN$_3$)(L^2)(NO)]n + family (n = 1-3). Systematic structural and chemical exploration and bioinorganic chemistry implications. *Inorg. Chem.* **2018**, *57*, 12270−12281.

(79) Melenkivitz, R.; Hillhouse, G. L. Synthesis, structure, and reactions of a nitroxyl complex of iridium(III), *cistrans*-IrHCl$_2$(NH=O)(PPh$_3$)$_2$. *Chem. Commun.* **2002**, 660−661.

(80) Sellmann, D.; Gottschalk-Gaudig, T.; Häußinger, D.; Heinemann, F. W.; Hess, B. A. [Ru(HNO)('py^{bu}S$_4$')], the first HNO complex resulting from hydride addition to a NO complex ('py^{bu}S$_4$'$^{2-}$=2,6-Bis(2-mercapto- 3,5-di-*tert*-butylphenylthio)-dimethylpyridine(2-)). *Chem. - Eur. J.* **2001**, *7*, 2099−2103.

(81) Chalkley, M. J.; Peters, J. C. A triad of highly reduced, linear iron nitrosyl complexes: {FeNO}$^{8-10}$. *Angew. Chem., Int. Ed.* **2016**, *55*, 11995−11998.

(82) Keilwerth, M.; Hohenberger, J.; Heinemann, F. W.; Sutter, J.; Scheurer, A.; Fang, H.; Bill, E.; Neese, F.; Ye, S.; Meyer, K. A series of iron nitrosyl complexes {Fe-NO}$^{6-9}$ and a fleeting {Fe-NO}^{10} intermediate en route to a metalacyclic Iron nitrosoalkane. *J. Am. Chem. Soc.* **2019**, *141*, 17217−17235.

(83) Dong, H. T.; Chalkley, M. J.; Oyala, P. H.; Zhao, J.; Alp, E. E.; Hu, M. Y.; Peters, J. C.; Lehnert, N. Exploring the limits of dative boratrane bonding: iron as a strong Lewis base in low-valent non-heme iron-nitrosyl complexes. *Inorg. Chem.* **2020**, *59*, 14967−14982.

(84) Fujisawa, K.; Soma, S.; Kurihara, H.; Ohta, A.; Dong, H. T.; Minakawa, Y.; Zhao, J.; Alp, E. E.; Hu, M. Y.; Lehnert, N. Stable ferrous mononitroxyl {FeNO}^{8} complex with a hindered hydrotris(pyrazolyl)borate coligand: structure, spectroscopic characterization, and reactivity toward NO and O_2. *Inorg. Chem.* **2019**, *58*, 4059−4062.

(85) Fujisawa, K.; Soma, S.; Kurihara, H.; Dong, H. T.; Bilodeau, M.; Lehnert, N. A cobalt-nitrosyl complex with a hindered hydrotris(pyrazolyl)borate coligand: detailed electronic structure, and reactivity towards dioxygen. *Dalton Trans.* **2017**, *46*, 13273−13289.

(86) Soma, S.; Van Stappen, C.; Kiss, M.; Szilagyi, R. K.; Lehnert, N.; Fujisawa, K. Distorted tetrahedral nickel-nitrosyl complexes: spectroscopic characterization and electronic structure. *JBIC, J. Biol. Inorg. Chem.* **2016**, *21*, 757−775.

(87) Fujisawa, K.; Tateda, A.; Miyashita, Y.; Okamoto, K.; Paulat, F.; Praneeth, V. K. K.; Merkle, A.; Lehnert, N. Structural and

spectroscopic characterization of mononuclear copper(I) nitrosyl complexes: end-on versus side-on coordination of NO to copper(I). *J. Am. Chem. Soc.* **2008**, *130*, 1205−1213.

(88) Lehnert, N.; Fujisawa, K.; Camarena, S.; Dong, H. T.; White, C. J. Activation of non-heme iron-nitrosyl complexes: turning up the heat. *ACS Catal.* **2019**, *9*, 10499−10518.

(89) Roussin, F. Z. Recherches sur les nitrosulfures doubles de fer (nouvelle classe de sels). *Ann. Chim. Phys.* **1858**, *52*, 285−303.

(90) Pavel, O. Über Nitrososulfide und Nitrosocyanide. *Ber. Dtsch. Chem. Ges.* **1882**, *15*, 2600−2615.

(91) Marchlewski, L.; Sachs, J. Studien über Roussins Salz. *Z. Anorg. Allg. Chem.* **1892**, *2*, 175−181.

(92) Hofmann, K. A.; Wiede, O. F. Weitere Mitteilungen über Nitrosoverbindungen des Eisens. *Z. Anorg. Allg. Chem.* **1895**, *9*, 295−303.

(93) Reihlen, H.; von Friedolsheim, A. Über komplexe Stickoxydverbindungen und das sogenannte einwertige Eisen. *Liebigs Ann. Chem.* **1927**, *457*, 71−82.

(94) Cambi, L.; Szegö, L. Suscettibilità magnetica, spettri d'assorbimento e costituzione dei nitrososolfuri del ferro(1). *Atti Accad. Lincei* **1931**, *13*, 168−172.

(95) Johansson, G.; Lipscomb, W. N. The structure of Roussin's black salt $CsFe_4S_3(NO)_7 \cdot H_2O$. *Acta Crystallogr.* **1958**, *11*, 594−598.

(96) Thomas, J. T.; Robertson, J. H.; Cox, E. G. The crystal structure of Roussin's red ethyl ester. *Acta Crystallogr.* **1958**, *11*, 599−604.

(97) Holm, R. H.; Kennepohl, P.; Solomon, E. I. Structural and functional aspects of metal sites in biology. *Chem. Rev.* **1996**, *96*, 2239−2314.

(98) Butler, A. R.; Glidewell, C.; Li, M.-H. Nitrosyl complexes of iron−sulfur clusters. *Adv. Inorg. Chem.* **1988**, *32*, 335−393.

(99) Gall, R. S.; Chu, C. T.-W.; Dahl, L. F. Preparation, structure, and bonding of two cubane-like iron-nitrosyl complexes, $Fe_4(NO)_4((_3\text{-}S)_4$ and $Fe_4(NO)_4((_3\text{-}S)_2((_3\text{-}NC(CH_3)_3)_2$. Stereochemical consequences of bridging ligand substitution on a completely bonding tetrametal cluster unit and of different terminal ligands on cubane-like Fe_4S_4 core. *J. Am. Chem. Soc.* **1974**, *96*, 4019−4023.

(100) Chu, C. T.-W.; Lo, F. Y.-K.; Dahl, L. F. Synthesis and stereochemical analysis of the $[Fe_4(NO)_4((_3\text{-}S)_4]^n$ series (n = 0, -1) which possesses a cubanelike Fe_4S_4 core: direct evidence for the antibonding tetrametal character of the unpaired electron upon a one-electron reduction of a completely bonding tetrahedral metal cluster. *J. Am. Chem. Soc.* **1982**, *104*, 3409−3422.

(101) McDonald, C. C.; Phillips, W. D.; Mower, H. F. An electron spin resonance study of some complexes of iron, nitric oxide, and anionic ligands. *J. Am. Chem. Soc.* **1965**, *87*, 3319−3326.

(102) Butler, A. R.; Glidewell, C.; Hyde, A. R.; Walton, J. C. Formation of paramagnetic mononuclear iron nitrosyl complexes from diamagnetic di- and tetranuclear iron-sulphur nitrosyls: characterisation by EPR spectroscopy and study of thiolate and nitrosyl ligand exchange reactions. *Polyhedron* **1985**, *4*, 797−809.

(103) Vanin, A. F.; Nalbandyan, R. M. Free radicals of a new type in yeast cells. *Biofizika* **1965**, *10*, 167−168.

(104) Tran, C. T.; Skodje, K. M.; Kim, E. Monomeric dinitrosyl iron complexes: synthesis and reactivity. *Prog. Inorg. Chem.* **2014**, *59*, 339−380.

(105) Lewandowska, H.; Kalinowska, M.; Brzoska, K.; Wojciuk, K.; Wojciuk, G.; Kruszewski, M. Nitrosyl iron complexes—synthesis, structure and biology. *Dalton Trans.* **2011**, *40*, 8273−8289.

(106) Lu, T.-T.; Wang, Y.-M.; Hung, C.-H.; Chiou, S.-J.; Liaw, W.-F. Bioinorganic chemistry of the natural $[Fe(NO)_2]$ motif: evolution of a functional model for NO-related biomedical application and revolutionary development of a translational model. *Inorg. Chem.* **2018**, *57*, 12425−12443.

(107) Hsiao, H.-Y.; Chung, C.-W.; Santos, J. H.; Villaflores, O. B.; Lu, T.-T. Fe in biosynthesis, translocation, and signal transduction of NO: toward bioinorganic engineering of dinitrosyl iron complexes into NO-delivery scaffolds for tissue engineering. *Dalton Trans.* **2019**, *48*, 9431−9453.

(108) Chu, C. T.-W.; Dahl, L. F. Structural characterization of $[AsPh_4]^+[Fe_4(NO)_7((_3\text{-}S)_3]]s]]$-. Stereochemical and bonding relationship of the Roussin black monoanion with the red ethyl ester, $Fe_2(NO)_4((_2\text{-}SC_2H_5)_2$, and $Fe_4(NO)_4((_3\text{-}S)_4$. *Inorg. Chem.* **1977**, *16*, 3245−3251.

(109) Lin, X.; Zheng, A.; Lin, S.; Huang, J.; Lu, J. Crystal and molecular structure of a typical red Roussin salt $(Me_4N)_2[Fe_2S_2(NO)_4]$. *J. Struct. Chem. (Wuhan)* **1982**, *1*, 79−88.

(110) Sanina, N. A.; Filipenko, O. S.; Aldoshin, S. M.; Ovanesyana, N. S. Influence of the cation on the properties of binuclear iron nitrosyl complexes. Synthesis and crystal structure of $[Pr_4{}^nN]_2[Fe_2S_2(NO)_4]$. *Russ. Chem. Bull.* **2000**, *49*, 1109−1112.

(111) Gardner, P. R.; Martin, L. A.; Hall, D.; Gardner, A. M. Dioxygen-dependent metabolism of nitric oxide in mammalian cells. *Free Radical Biol. Med.* **2001**, *31*, 191−204.

(112) Weinberger, B.; Laskin, D. L.; Heck, D. E.; Laskin, J. D. The toxicology of inhaled nitric oxide. *Toxicol. Sci.* **2001**, *59*, 5−16.

(113) Kon, H. Paramagnetic resonance study of nitric oxide hemoglobin. *J. Biol. Chem.* **1968**, *243*, 4350−4357.

(114) Kon, H. Electron paramagnetic resonance of nitric oxide cytochrome *c*. *Biochem. Biophys. Res. Commun.* **1969**, *36*, 423−427.

(115) Kon, H.; Kataoba, N. Electron paramagnetic resonance of nitric oxide-protoheme complexes with some nitrogenous base. Model systems of nitric oxide hemoproteins. *Biochemistry* **1969**, *8*, 4757−4762.

(116) Yonetani, T.; Yamamoto, H.; Erman, J. E.; Leigh, J. S., Jr.; Reed, G. H. Electromagenetic properties of hemoproteins. V. Optical and electron paramagnetic resonance characteristics of nitric oxide derivatives of metalloporphyrin-apohemoprotein complexes. *J. Biol. Chem.* **1972**, *247*, 2447−2455.

(117) Brunori, M.; Falcioni, G.; Rotilio, G. Kinetic properties and electron paramagnetic resonance spectra of the nitric oxide derivative of hemoglobin components of trout (*Salmo irideus*). *Proc. Natl. Acad. Sci. U. S. A.* **1974**, *71*, 2470−2472.

(118) Perutz, M. F.; Kilmartin, J. V.; Nagai, K.; Szabo, A.; Simon, S. R. Influence of globin structures on the state of the heme. IV. Ferrous low spin derivatives. *Biochemistry* **1976**, *15*, 378−387.

(119) O'Keeffe, D. H.; Ebel, R. E.; Peterson, J. A. Studies of the oxygen binding site of cytochrome P-450. Nitric oxide as a spin-label probe. *J. Biol. Chem.* **1978**, *253*, 3509−3516.

(120) Yoshimura, T. The nitrogen oxide complex of the iron(II) protoporphyrin IX dimethyl ester. *Bull. Chem. Soc. Jpn.* **1978**, *51*, 1237−1238.

(121) Doetschman, D. C.; Schwartz, S. A.; Utterback, S. G. The electron spin distribution in nitrosylhemoglobin. *Chem. Phys.* **1980**, *49*, 1−8.

(122) Yoshimura, T. Electron paramagnetic resonance study of the interaction of nitrosylprotoheme dimethylester with nitrogenous bases. *Inorg. Chim. Acta* **1980**, *46*, 69−76.

(123) Yoshimura, T. Electron paramagnetic resonance study of the interaction of nitrosyl(protoporphyrin IX dimethyl ester)iron(II) with sulfur- and oxygen-donor ligands. *Inorg. Chim. Acta* **1982**, *57*, 99−105.

(124) Yoshimura, T.; Ozaki, T. Electronic spectra of nitrosyi-(protoporphyrin IX dimethyl ester)iron(II) and its complexes with nitrogenous bases as model systems for nitrosylhemoproteins. *Arch. Biochem. Biophys.* **1984**, *229*, 126−135.

(125) Yoshimura, T.; Suzuki, S.; Nakahara, A.; Iwasaki, H.; Masuko, M.; Matsubara, T. Spectral properties of nitric oxide complexes of cytochrome *c*' from *Alcaligenes sp.* NCD3 11015. *Biochemistry* **1986**, *25*, 2436−2442.

(126) Yoshimura, T.; Suzuki, S. The pH dependence of the stereochemistry around the heme group in NO-cytochrome *c* (horse heart). *Inorg. Chim. Acta* **1988**, *152*, 241−249.

(127) Yoshimura, T.; Shidara, S.; Ozaki, T.; Kamada, H. Five coordinated nitrosylhemoprotein in the whole cells of denitrifying bacterium, *Achromobacter xylosoxidans* NCIB 11015. *Arch. Microbiol.* **1993**, *160*, 498−500.

(128) Hüttermann, J.; Burgard, C.; Kappl, R. Proton ENDOR from randomly oriented NO-ligated haemoglobin: approaching the

structural basis for the R-T transition. *J. Chem. Soc., Faraday Trans.* **1994**, *90*, 3077−3087.

(129) Henry, Y. A. Utilization of nitric oxide as a paramagnetic probe of the molecular oxygen binding site of metalloenzymes. *Nitric Oxide Research from Chemistry to Biology: EPR Spectroscopy of Nitrosylated Compounds*; Henry, Y. A., Guissani, A., Ducastel, B., Eds.; Landes Company: Austin, 1997; pp 98−144.

(130) Lehnert, N. Electron paramagnetic resonance and low-temperature magnetic circular dichroism spectroscopy of ferrous heme nitrosyls. *The Smallest Biomolecules: Diatomics and their Interactions with Heme Proteins*; Ghosh, A., Ed.; Elseviere: Amsterdam, Netherlands, 2008; pp 147−171.

(131) Yoshimura, T.; Iwasaki, H.; Shidara, S.; Suzuki, S.; Nakahara, A.; Matsubara, T. Nitric oxide complex of cytochrome *c*′ in cells of denitrifying bacteria. *J. Biochem.* **1988**, *103*, 1016−1019.

(132) Pegg, R. B.; Shahidi, F. *Nitrite Curing of Meat. The N-Nitrosamine Problem and Nitrite Alternatives*; Food & Nutrition Press: Trumbull, CT, 2000.

(133) Møller, J. K. S.; Skibsted, L. H. Nitric oxide and myoglobins. *Chem. Rev.* **2002**, *102*, 1167−1178.

(134) Haldane, J. The red colour of salted meat. *J. Hyg.* **1901**, *1*, 115−122.

(135) Hermann, L. Über die Wirkungen des Stickstoffoxydgases auf das Blut. *Archiv für Anat. und Physiol.* **1865**, 469−481.

(136) Gamgee, A. Researches on the blood. On the action of nitrites on blood. *Phil. Trans. R. Soc. London* **1868**, *158*, 589−625.

(137) Fox, J. B.; Thomson, J. S. The formation of green heme pigments from metmyoglobin and methemoglobin by the action of nitrite. *Biochemistry* **1964**, *3*, 1323−1328.

(138) Yi, J.; Thomas, L. M.; Musayev, F. N.; Safo, M. K.; Richter-Addo, G. B. Crystallographic trapping of heme loss intermediates during the nitrite-induced degradation of human hemoglobin. *Biochemistry* **2011**, *50*, 8323−8332.

(139) Yi, J.; Richter-Addo, G. B. Unveiling the three-dimensional structure of the green pigment of nitrite-cured meat. *Chem. Commun.* **2012**, *48*, 4172−4174.

(140) Gladwin, M. T.; Grubina, R.; Doyle, M. P. The new chemical biology of nitrite reactions with hemoglobin: R-state catalysis, oxidative denitrosylation, and nitrite reductase/anhydrase. *Acc. Chem. Res.* **2009**, *42*, 157−167.

(141) Angelo, M.; Singel, D. J.; Stamler, J. S. An S-nitrosothiol (SNO) synthase function of hemoglobin that utilizes nitrite as a substrate. *Proc. Natl. Acad. Sci. U. S. A.* **2006**, *103*, 8366−8371.

(142) Averill, B. A. Dissimilatory nitrite and nitric oxide reductases. *Chem. Rev.* **1996**, *96*, 2951−2964.

(143) Brooks, J. The action of nitrite on haemoglobin in the absence of oxygen. *Proc. R. Soc. Med.* **1937**, *123*, 368−382.

(144) Zhang, Y.; Pavlosky, M. A.; Brown, C. A.; Westre, T. E.; Hedman, B.; Hodgson, K. O.; Solomon, E. I. Spectroscopic and theoretical description of the electronic structure of the S = 3/2 nitrosyl complex of non-heme iron enzymes. *J. Am. Chem. Soc.* **1992**, *114*, 9189−9191.

(145) Brown, C. A.; Pavlosky, M. A.; Westre, T. E.; Zhang, Y.; Hedman, B.; Hodgson, K. O.; Solomon, E. I. Spectroscopic and theoretical description of the electronic structure of S = 3/2 iron-nitrosyl complexes and their relation to O_2 activation by non-heme iron enzyme active sites. *J. Am. Chem. Soc.* **1995**, *117*, 715−732.

(146) Jackson, T. A.; Yikilmaz, E.; Miller, A.-F.; Brunold, T. C. Spectroscopic and computational study of a non-heme iron $\{Fe\text{-}NO\}^7$ system: exploring the geometric and electronic structures of the nitrosyl adduct of iron superoxide dismutase. *J. Am. Chem. Soc.* **2003**, *125*, 8348−8363.

(147) Diebold, A. R.; Brown-Marshall, C. D.; Neidig, M. L.; Brownlee, J. M.; Moran, G. R.; Solomon, E. I. Activation of α-keto acid-dependent dioxygenases: application of an $\{FeNO\}^7/\{FeO_2\}^8$ methodology for characterizing the initial steps of O_2 activation. *J. Am. Chem. Soc.* **2011**, *133*, 18148−18160.

(148) Blaesi, E. J.; Gardner, J. D.; Fox, B. G.; Brunold, T. C. Spectroscopic and computational characterization of the NO adduct of substrate-bound Fe(II) cysteine dioxygenase: insights into the mechanism of O_2 activation. *Biochemistry* **2013**, *52*, 6040−6051.

(149) Martinie, R. J.; Livada, J.; Chang, W.-c.; Green, M. T.; Krebs, C.; Bollinger, J. M., Jr.; Silakov, A. Experimental correlation of substrate position with reaction outcome in the aliphatic halogenase, SyrB2. *J. Am. Chem. Soc.* **2015**, *137*, 6912−6919.

(150) Solomon, E. I.; Brunold, T. C.; Davis, M. I.; Kemsley, J. N.; Lee, S.-K.; Lehnert, N.; Neese, F.; Skulan, A. J.; Yang, Y.-S.; Zhou, J. Geometric and electronic structure/function correlations in non-heme iron enzymes. *Chem. Rev.* **2000**, *100*, 235−350.

(151) Berto, T. C.; Speelman, A.; Zheng, S.; Lehnert, N. Mono- and dinuclear non-heme iron-nitrosyl complexes: models for key intermediates in bacterial nitric oxide reductases. *Coord. Chem. Rev.* **2013**, *257*, 244−259.

(152) Berto, T. C.; Hoffman, M. B.; Murata, Y.; Landenberger, K. B.; Alp, E. E.; Zhao, J.; Lehnert, N. Structural and electronic characterization of non-heme Fe(II)-nitrosyls as biomimetic models of the Fe_B center of bacterial nitric oxide reductase (NorBC). *J. Am. Chem. Soc.* **2011**, *133*, 16714−16717.

(153) Ye, S.; Price, J. C.; Barr, E. W.; Green, M. T.; Bollinger, J. M.; Krebs, C.; Neese, F. Cryoreduction of the NO-adduct of taurine:α-ketoglutarate dioxygenase (TauD) yields an elusive $\{FeNO\}^8$ species. *J. Am. Chem. Soc.* **2010**, *132*, 4739−4751.

(154) Snyder, S. H. Nitric oxide: first in a new class of neurotransmitters. *Science* **1992**, *257*, 494−496.

(155) Butler, A. R.; Williams, D. L. H. The physiological role of nitric oxide. *Chem. Soc. Rev.* **1993**, *22*, 233−241.

(156) Bredt, D. S.; Snyder, S. H. Nitric oxide: a physiologic messenger molecule. *Annu. Rev. Biochem.* **1994**, *63*, 175−195.

(157) Feelisch, M.; Stamler, J. S. *Methods in nitric oxide research*; Wiley: Chichester, 1996.

(158) Ignarro, L. *Nitric oxide: Biology and pathobiology*; Academic Press: San Diego, 2000.

(159) Wink, D. A.; Mitchell, J. B. Chemical biology of nitric oxide: insights into regulatory, cytotoxic, and cytoprotective mechanisms of nitric oxide. *Free Radical Biol. Med.* **1998**, *25*, 434−456.

(160) Thomas, D. D.; Ridnour, L. A.; Isenberg, J. S.; Flores-Santana, W.; Switzer, C. H.; Donzelli, S.; Hussain, P.; Vecoli, C.; Paolocci, N.; Ambs, S.; Colton, C. A.; Harris, C. C.; Roberts, D. D.; Wink, D. A. The chemical biology of nitric oxide: Implications in cellular signaling. *Free Radical Biol. Med.* **2008**, *45*, 18−31.

(161) Furchgott, R. F. Endothelium-derived relaxing factor: discovery, early studies, and identification as nitric oxide (Noble Lecture). *Angew. Chem., Int. Ed.* **1999**, *38*, 1870−1880.

(162) Ignarro, L. Nitric oxide: a unique endogenous signaling molecule in vascular biology (Nobel Lecture). *Angew. Chem., Int. Ed.* **1999**, *38*, 1882−1892.

(163) Murad, F. Discovery of some of the biological effects of nitric oxide and its role in cell signaling (Nobel Lecture). *Angew. Chem., Int. Ed.* **1999**, *38*, 1856−1868.

(164) Stuehr, D. J. Structure-function aspects in the nitric oxide synthases. *Annu. Rev. Pharmacol. Toxicol.* **1997**, *37*, 339−359.

(165) Gorren, A. C. F.; Mayer, B. Nitric-oxide synthase: a cytochrome P450 family foster child. *Biochim. Biophys. Acta, Gen. Subj.* **2007**, *1770*, 432−445.

(166) Santolini, J. The molecular mechanism of mammalian NO-synthase: a story of electrons and protons. *J. Inorg. Biochem.* **2011**, *105*, 127−141.

(167) Childers, K. C.; Garcin, E. D. Nitric Oxide: Synthesis and Action. *eLS*; John Wiley & Sons, Ltd.: Chichester, 2017; pp 1−10.

(168) Gantner, B. N.; LaFond, K. M.; Bonini, M. G. Nitric oxide in cellular adaptation and disease. *Redox Biol.* **2020**, *34*, 101550.

(169) Ford, P. C.; Miranda, K. M. The solution chemistry of nitric oxide and other reactive nitrogen species. *Nitric Oxide* **2020**, *103*, 31−46.

(170) Stanbury, D. M. Reactivity of inorganic radicals in aqueous solution. *Physical Inorganic Chemistry, Reactions, Processes, and Applications*; Bakac, A., Ed.; Wiley, 2010; pp 395−427.

(171) Hunt, A. P.; Lehnert, N. Heme-nitrosyls: electronic structure implications for function in biology. *Acc. Chem. Res.* **2015**, *48*, 2117−2125.

(172) Carr, H. S.; Tran, D.; Reynolds, M. F.; Burstyn, J. N.; Spiro, S. Activation of soluble guanylyl cyclase by four-coordinate metalloporphyrins: evidence for a role for porphyrin confirmation. *Biochemistry* **2002**, *41*, 10149−10157.

(173) Russwurm, M.; Koesling, D. NO activation of guanylyl cyclase. *EMBO J.* **2004**, *23*, 4443−4450.

(174) Cary, S. P. L.; Winger, J. A.; Derbyshire, E. R.; Marletta, M. A. Nitric oxide signaling: no longer simply on or off. *Trends Biochem. Sci.* **2006**, *31*, 231−239.

(175) Derbyshire, E. R.; Marletta, M. A. Structure and regulation of soluble guanylate cyclase. *Annu. Rev. Biochem.* **2012**, *81*, 533−559.

(176) Farah, C.; Michel, L. Y. M.; Balligand, J.-L. Nitric oxide signalling in cardiovascular health and disease. *Nat. Rev. Cardiol.* **2018**, *15*, 292.

(177) Vaughn, M. W.; Kuo, L.; Liao, J. C. Estimation of nitric oxide production and reaction rates in tissue by use of a mathematical model. *Am. J. Physiol.: Heart Circ. Physiol.* **1998**, *274*, H2163−H2176.

(178) Loscalzo, J. Nitric oxide insufficiency, platelet activation, and arterial thrombosis. *Circ. Res.* **2001**, *88*, 756−762.

(179) Su, J.; Groves, J. T. Mechanisms of peroxynitrite interactions with heme proteins. *Inorg. Chem.* **2010**, *49*, 6317−6329.

(180) Gardner, P. R. Nitric oxide dioxygenase function and mechanism of flavohemoglobin, hemoglobin, myoglobin and their associated reductases. *J. Inorg. Biochem.* **2005**, *99*, 247−266.

(181) Kurtikyan, T. S.; Eksuzyan, S. R.; Hayrapetyan, V. A.; Martirosyan, G. G.; Hovhannisyan, G. S.; Goodwin, J. A. Nitric oxide dioxygenation reaction by oxy-coboglobin models: in-situ low-temperature FTIR characterization of coordinated peroxynitrite. *J. Am. Chem. Soc.* **2012**, *134*, 13861−13870.

(182) Sharma, S. K.; Schaefer, A. W.; Lim, H.; Matsumura, H.; Moënne-Loccoz, P.; Hedman, B.; Hodgson, K. O.; Solomon, E. I.; Karlin, K. D. A six-coordinate peroxynitrite low-spin iron(III) porphyrinate complex—the product of the reaction of nitrogen monoxide (·NO(g)) with a ferric-superoxide species. *J. Am. Chem. Soc.* **2017**, *139*, 17421−17430.

(183) Herold, S.; Koppenol, W. H. Peroxynitritometal complexes. *Coord. Chem. Rev.* **2005**, *249*, 499−506.

(184) Eich, R. F.; Li, T.; Lemon, D. D.; Doherty, D. H.; Curry, S. R.; Aitken, J. F.; Mathews, A. J.; Johnson, K. A.; Smith, R. D.; Phillips, G. N., Jr.; Olson, J. S. Mechanism of NO-induced oxidation of myoglobin and hemoglobin. *Biochemistry* **1996**, *35*, 6976−6983.

(185) Herold, S.; Exner, M.; Nauser, T. Kinetic and mechanism studies of the NO-mediated oxidation of oxymyoglobin and oxyhemoglobin. *Biochemistry* **2001**, *40*, 3385−3395.

(186) Karow, D. S.; Pan, D.; Tran, R.; Pellicena, P.; Presley, A.; Mathies, R. A.; Marletta, M. A. Spectroscopic characterization of the soluble guanylate cyclase-like heme domains from *Vibrio cholerae* and *Thermoanaerobacter tengcongensis*. *Biochemistry* **2004**, *43*, 10203−10211.

(187) Pellicena, P.; Karow, D. S.; Boon, E. M.; Marletta, M. A.; Kuriyan, J. Crystal structure of an oxygen-binding heme domain related to soluble guanylate cyclases. *Proc. Natl. Acad. Sci. U. S. A.* **2004**, *101*, 12854−12859.

(188) Boon, E. M.; Marletta, M. A. Ligand specificity of H-NOX domains: from sGC to bacterial NO sensors. *J. Inorg. Biochem.* **2005**, *99*, 892−902.

(189) Herzik, M. A., Jr.; Jonnalagadda, R.; Kuriyan, J.; Marletta, M. A. Structural insights into the role of iron-histidine bond cleavage in nitric oxide-induced activation of H-NOX gas sensor proteins. *Proc. Natl. Acad. Sci. U. S. A.* **2014**, *111*, E4156−E4164.

(190) Shimizu, T.; Huang, D.; Yan, F.; Stranava, M.; Bartosova, M.; Fojtíková, V.; Martínková, M. Gaseous O_2, NO, and CO in signal transduction: structure and function relationships of heme-based gas sensors and heme-redox sensors. *Chem. Rev.* **2015**, *115*, 6491−6533.

(191) Hossain, S.; Nisbett, L.-M.; Boon, E. M. Discovery of two bacterial nitric oxide-responsive proteins and their roles in bacterial biofilm regulation. *Acc. Chem. Res.* **2017**, *50*, 1633−1639.

(192) Fang, F. C. Mechanisms of nitric oxide-related antimicrobial activity. *J. Clin. Invest.* **1997**, *99*, 2818−2825.

(193) Bogdan, C. Nitric oxide and the immune response. *Nat. Immunol.* **2001**, *2*, 907−916.

(194) Wink, D. A.; Hines, H. B.; Cheng, R. Y. S.; Switzer, C. H.; Flores-Santana, W.; Vitek, M. P.; Ridnour, L. A.; Colton, C. A. Nitric oxide and redox mechanisms in the immune response. *J. Leukocyte Biol.* **2011**, *89*, 873−891.

(195) Stuehr, D. J.; Gross, S. S.; Sakuma, I.; Levi, R.; Nathan, C. F. Activated murine macrophages secrete a metabolite of arginine with the bioactivity of endothelium-derived relaxing factor and the chemical reactivity of nitric oxide. *J. Exp. Med.* **1989**, *169*, 1011−1020.

(196) MacMicking, J.; Xie, Q.-W.; Nathan, C. Nitric oxide and macrophage function. *Annu. Rev. Immunol.* **1997**, *15*, 323−350.

(197) Huie, R. S.; Padmaja, S. The reaction of NO with superoxide. *Free Radical Res. Commun.* **1993**, *18*, 195−199.

(198) Nauser, T.; Koppenol, W. The rate constant of the reaction of superoxide with nitrogen monoxide: approaching the diffusion limit. *J. Phys. Chem. A* **2002**, *106*, 4084−4086.

(199) Nathan, C. Is iNOS beginning to smoke? *Cell* **2011**, *147*, 257−258.

(200) Russell, J. A.; Singer, J.; Bernard, G. R.; Wheeler, A.; Fulkerson, W.; Hudson, L.; Schein, R.; Summer, W.; Wright, P.; Walley, K. R. Changing pattern of organ dysfunction in early human sepsis is related to mortality. *Crit. Care Med.* **2000**, *28*, 3405−3411.

(201) Smith, K. J.; Lassmann, H. The role of nitric oxide in multiple sclerosis. *Lancet Neurol.* **2002**, *1*, 232−241.

(202) Cameron, N. E.; Cotter, M. A. Nitric oxide, peripheral neuropathy, and diabetes. *Nitric Oxide and Free Radicals in Peripheral Neurotransmission. Nitric Oxide in Biology and Medicine*; Kalsner, S., Ed.; Birkhäuser: Boston, Massachusetts, 2000; Vol. *2*; pp 307−326.

(203) Brown, G. C.; Bal-Price, A. Inflammatory neurodegeneration mediated by nitric oxide, glutamate, and mitochondria. *Mol. Neurobiol.* **2003**, *27*, 325−355.

(204) Nakamura, T.; Oh, C. K.; Liao, L.; Zhang, X.; Lopez, K. M.; Gibbs, D.; Deal, A. K.; Scott, H. R.; Spencer, B.; Masliah, E.; Rissman, R. A.; Yates, J. R., 3rd; Lipton, S. A. Noncanonical transnitrosylation network contributes to synapse loss in Alzheimer's disease. *Science* **2021**, *371*, 371.

(205) Kuhl, S. J.; Rosen, H. Nitric oxide and septic shock. From bench to bedside. *West. J. Med.* **1998**, *163*, 176−181.

(206) Murray, P. T.; Wylam, M. E.; Umans, J. G. Nitric oxide and septic vascular dysfunction. *Anesth. Analg.* **2000**, *90*, 89−101.

(207) Vincent, J.-L.; Zhang, H.; Szabo, C.; Preiser, J.-C. Effects of nitric oxide in septic shock. *Am. J. Respir. Crit. Care Med.* **2000**, *161*, 1781−1785.

(208) Titheradge, M. A. Nitric oxide in septic shock. *Biochim. Biophys. Acta, Bioenerg.* **1999**, *1411*, 437−455.

(209) Khatua, S.; Majumdar, A. Flavodiiron nitric oxide reductases: recent developments in the mechanistic study and model chemistry for the catalytic reduction of NO. *J. Inorg. Biochem.* **2015**, *142*, 145−153.

(210) Gardner, A. M.; Helmick, R. A.; Gardner, P. R. Flavorubredoxin, an inducible catalyst for nitric oxide reduction and detoxification in *Escherichia coli*. *J. Biol. Chem.* **2002**, *277*, 8172−8177.

(211) Gardner, A. M.; Gessner, C. R.; Gardner, P. R. Regulation of the nitric oxide reduction operon (*norRVW*) in *Escherichia coli*. Role of NorR and in the nitric oxide stress response. *J. Biol. Chem.* **2003**, *278*, 10081−10086.

(212) Hutchings, M. I.; Mandhana, N.; Spiro, S. The NorR protein of *Escherichia coli* activates expression of the flavorubredoxin gene norV in response to reactive nitrogen species. *J. Bacteriol.* **2002**, *184*, 4640−4643.

(213) Gomes, C. M.; Giuffrè, A.; Forte, E.; Vicente, J. B.; Saraiva, L. M.; Brunori, M.; Teixeira, M. A novel type of nitric-oxide reductase. *Escherichia Coli* flavorubredoxin. *J. Biol. Chem.* **2002**, *277*, 25273−25276.

(214) Tucker, N. P.; D'Autréaux, B.; Studholme, D. J.; Spiro, S.; Dixon, R. DNA binding activity of the *Escherichia coli* nitric oxide sensor NorR suggests a conserved target sequence in diverse proteobacteria. *J. Bacteriol.* **2004**, *186*, 6656−6660.

(215) Rodrigues, R.; Vicente, J. B.; Félix, R.; Oliveira, S.; Teixeira, M.; Rodrigues-Pousada, C. *Desulfovibrio gigas* flavodiiron protein affords protection against nitrosative stress in vivo. *J. Bacteriol.* **2006**, *188*, 2745−2751.

(216) Frazão, C.; Silva, G.; Gomes, C. M.; Matias, P.; Coelho, R.; Sieker, L.; Macedo, S.; Liu, M. Y.; Oliveira, S.; Teixeira, M.; Xavier, A. V.; Rodrigues-Pousada, C.; Carrondo, M. A.; Le Gall, J. Structure of a dioxygen reduction enzyme from *Desulfovibrio gigas*. *Nat. Struct. Biol.* **2000**, *7*, 1041−1045.

(217) Silaghi-Dumitrescu, R.; Kurtz, D. M., Jr.; Ljungdahl, L. G.; Lanzilotta, W. N. X-ray crystal structures of *Moorella thermoacetica* FprA. Novel diiron site structure and mechanistic insights into a scavenging nitric oxide reductase. *Biochemistry* **2005**, *44*, 6492−6501.

(218) Vicente, J. B.; Carrondo, M. A.; Teixeira, M.; Frazão, C. Structural studies on flavodiiron proteins. *Methods Enzymol.* **2008**, *437*, 3−19.

(219) Gardner, A. M.; Gardner, P. R. Flavohemoglobin detoxifies nitric oxide in aerobic, but not anaerobic *Escherichia coli*: Evidence for a novel inducible anaerobic nitric oxide scavenging activity. *J. Biol. Chem.* **2000**, *277*, 8166−8171.

(220) Cosby, K.; Partovi, K. S.; Crawford, J. H.; Patel, R. P.; Reiter, C. D.; Martyr, S.; Yang, B. K.; Waclawiw, M. A.; Zalos, G.; Xu, X.; Huang, K. T.; Shields, H.; Kim-Shapiro, D. B.; Schechter, A. N.; Cannon, R. O.; Gladwin, M. T. Nitrite reduction to nitric oxide by deoxyhemoglobin vasodilates the human circulation. *Nat. Med.* **2003**, *9*, 1498−1505.

(221) Shiva, S.; Huang, Z.; Grubina, R.; Sun, J.; Ringwood, L. A.; MacArthur, P.; Xu, X.; Murphy, E.; Darley-Usmar, V.; Gladwin, M. T. Deoxymyoglobin is a nitrite reductase that generates nitric oxide and regulates mitochondrial respiration. *Circ. Res.* **2007**, *100*, 654−661.

(222) Broniowska, K. A.; Hogg, N. The chemical biology of S-nitrosothiols. *Antioxid. Redox Signaling* **2012**, *17*, 969−980.

(223) Keszler, A.; Zhang, Y.; Hogg, N. Reaction between nitric oxide, glutathione, and oxygen in the presence and absence of protein: How are S-nitrosothiols formed? *Free Radical Biol. Med.* **2010**, *48*, 55−64.

(224) Foster, M. W.; Hess, D. T.; Stamler, J. S. Protein *S*-nitrosylation in health and disease: a current perspective. *Trends Mol. Med.* **2009**, *15*, 391−404.

(225) Williams, D. L. H. The chemistry of S-nitrosothiols. *Acc. Chem. Res.* **1999**, *32*, 869−876.

(226) Hwang, S.; Cha, W.; Meyerhoff, M. E. Polymethacrylates with a covalently linked Cu^{II}-cyclen complex for the in-situ generation of nitric oxide from nitrosothiols in blood. *Angew. Chem., Int. Ed.* **2006**, *45*, 2745−2748.

(227) Zhang, S.; Çelebi-Ölçüm, N.; Melzer, M. M.; Houk, K. N.; Warren, T. H. Copper(I) nitrosyls from reaction of copper(II) thiolates with *S*-nitrosothiols: mechanism of NO release from RSNOs at Cu. *J. Am. Chem. Soc.* **2013**, *135*, 16746−16749.

(228) Crawford, J. T.; Scott Isbel, T.; Huang, Z.; Shiva, S.; Chacko, B.; Schechter, A. N.; Darley-Usmar, V.; Kerby, J.; Lang, J.; Kraus, D.; Ho, C.; Gladwin, M. T.; Patel, R. Hypoxia, red blood cells, and nitrite regulate NO-dependent hypoxic vasodilation. *Blood* **2006**, *1007*, 566−574.

(229) Singel, D. J.; Stamler, J. S. Chemical physiology of blood flow regulation by red blood cells: the role of nitric oxide and S-nitrosohemoglobin. *Annu. Rev. Physiol.* **2005**, *67*, 99−145.

(230) Venkateswara, P.; Holm, R. H. Synthetic analogs of the active sites of iron−sulfur proteins. *Chem. Rev.* **2004**, *104*, 527−559.

(231) Tsai, M. L.; Tsou, C. C.; Liaw, W. F. Dinitrosyl iron complexes (DNICs): from biomimetic synthesis and spectroscopic characterization towards unveiling the biological and catalytic roles of DNICs. *Acc. Chem. Res.* **2015**, *48*, 1184−1193.

(232) Tonzetich, Z. J.; Do, L. H.; Lippard, S. J. Dinitrosyl iron complexes relevant to Rieske cluster nitrosylation. *J. Am. Chem. Soc.* **2009**, *131*, 7964−7965.

(233) Foster, M. W.; Cowan, J. A. Chemistry of nitric oxide with protein-bound iron sulfur centers. Insights on physiological reactivity. *J. Am. Chem. Soc.* **1999**, *121*, 4093−4100.

(234) Pereira, J. C. M.; Iretskii, A. V.; Han, R.-M.; Ford, P. C. Dinitrosyl iron complexes with cysteine. Kinetics studies of the formation and reactions of DNICs in aqueous solution. *J. Am. Chem. Soc.* **2015**, *137*, 328−336.

(235) Tonzetich, Z. J.; Héroguel, F.; Do, L. H.; Lippard, S. J. Chemistry of nitrosyliron complexes supported by a *β*-diketiminate ligand. *Inorg. Chem.* **2011**, *50*, 1570−1579.

(236) Pectol, D. C.; Khan, S.; Chupik, R. B.; Elsabahy, M.; Wooley, K. L.; Darensbourg, M. Y.; Lim, S.-M. Toward the optimization of dinitrosyl iron complexes as therapeutics for smooth muscle cells. *Mol. Pharmaceutics* **2019**, *16*, 3178−3187.

(237) Vanin, A. F. *Dinitrosyl iron complexes as a "working form" of nitric oxide in living organisms*; Cambridge Scholars Publishing: Cambridge, UK, 2019.

(238) Wu, C.-R.; Huang, Y.-D.; Hong, Y.-H.; Liu, Y.-H.; Narwane, M.; Chang, Y.-H.; Dinh, T. K.; Hsieh, H.-T.; Hseuh, Y.-J.; Wu, P.-C.; Pao, C.-W.; Chan, T.-S.; Hsu, I.-J.; Chen, Y.; Chen, H.-C.; Chin, T.-Y.; Lu, T.-T. Endogenous conjugation of biomimetic dinitrosyl iron complex with protein vehicles for oral delivery of nitric oxide to brain and activation of hippocampal neurogenesis. *JACS Au* **2021**, *1*, 998−1013.

(239) Vanin, A. F.; Tronov, V. A.; Borodulin, R. R. Nitrosonium cation as a cytotoxic component of dinitrosyl iron complexes with thiol-containing ligands (based on the experimental work on MCF7 human breast cancer cell culture). *Cell Biochem. Biophys.* **2021**, *79*, 93−102.

(240) Ding, H.; Demple, B. Direct nitric oxide signal transduction via nitrosylation of iron−sulfur centers in the SoxR transcription activator. *Proc. Natl. Acad. Sci. U. S. A.* **2000**, *97*, 5146−5150.

(241) Cruz-Ramos, H.; Crack, J.; Wu, G.; Hughes, M. N.; Scott, C.; Thompson, A. J.; Green, J.; Poole, R. K. NO sensing by FNR: regulation of the *Escherichia coli* NO-detoxifying flavohaemoglobin, *Hmp. EMBO J.* **2002**, *21*, 3235−3244.

(242) Fitzpatrick, J.; Kim, E. New synthetic routes to iron−sulfur clusters: deciphering the repair chemistry of [2Fe-2S] clusters from mononitrosyl iron complexes. *Inorg. Chem.* **2015**, *54*, 10559−10567.

(243) D'Autréaux, B.; Tucker, N. P.; Dixon, R.; Spiro, S. A non-haem iron centre in the transcription factor NorR senses nitric oxide. *Nature* **2005**, *437*, 769−772.

(244) D'Autréaux, B.; Touati, D.; Bersch, B.; Latour, J.-M.; Michaud-Soret, I. Direct inhibition by nitric oxide of the transcriptional ferric uptake regulation protein via nitrosylation of the iron. *Proc. Natl. Acad. Sci. U. S. A.* **2002**, *99*, 16619−16624.

(245) Walker, F. A. Nitric oxide interaction with insect nitrophorins and thoughts on the electron configuration of the $\{FeNO\}^6$ complex. *J. Inorg. Biochem.* **2005**, *99*, 216−236.

(246) Ribeiro, J. M. C.; Hazzard, J. M. H.; Nussenzveig, R. H.; Champagne, D. E.; Walker, F. A. Reversible binding of nitric oxide by a salivary heme protein from a bloodsucking insect. *Science* **1993**, *260*, 539−541.

(247) Weichsel, A.; Andersen, J. F.; Champagne, D. E.; Walker, F. A.; Montfort, W. R. Crystal structures of a nitric oxide transport protein from a blood-sucking insect. *Nat. Struct. Biol.* **1998**, *5*, 304−309.

(248) Weichsel, A.; Andersen, J. F.; Roberts, S. A.; Montfort, W. R. Nitric oxide binding to nitrophorin 4 induces complete distal pocket burial. *Nat. Struct. Biol.* **2000**, *7*, 551−554.

(249) Roberts, S. A.; Weichsel, A.; Qiu, Y.; Shelnutt, J. A.; Walker, F. A.; Montfort, W. R. Ligand-induced heme ruffling and bent NO geometry in ultra-high-resolution structures of nitrophorin 4. *Biochemistry* **2001**, *40*, 11327−11337.

(250) Sun, Y.; Benabbas, A.; Zeng, W.; Kleingardner, J. G.; Bren, K. L.; Champion, P. M. Investigations of heme distortion, low-frequency vibrational excitations, and electron transfer in cytochrome *c*. *Proc. Natl. Acad. Sci. U. S. A.* **2014**, *111*, 6570−6575.

(251) Coleman, R. E.; Vilbert, A. C.; Lancaster, K. M. The heme-Lys cross-link in cytochrome P460 promotes catalysis by enforcing

secondary coordination sphere architecture. *Biochemistry* **2020**, *59*, 2289−2298.

(252) Ford, P. C.; Fernandez, B. O.; Lim, M. D. Mechanisms of reductive nitrosylation in iron and copper models relevant to biological systems. *Chem. Rev.* **2005**, *105*, 2439−2455.

(253) Weichsel, A.; Maes, E. M.; Andersen, J. F.; Valenzuela, J. G.; Shokhireva, T. K.; Walker, F. A.; Montfort, W. R. Heme-assisted S-nitrosation of a proximal thiolate in a nitric oxide transport protein. *Proc. Natl. Acad. Sci. U. S. A.* **2005**, *102*, 594−599.

(254) Lehnert, N.; Dong, H. T.; Harland, J. B.; Hunt, A. P.; White, C. J. Reversing nitrogen fixation. *Nat. Rev. Chem.* **2018**, *2*, 278−289.

(255) Lancaster, K. M.; Caranto, J. D.; Majer, S. H.; Smith, M. A. Alternative bioenergy: updates to and challenges in nitrification metalloenzymology. *Joule* **2018**, *2*, 421−441.

(256) Richardson, D. J.; Watmough, N. J. Inorganic nitrogen metabolism in bacteria. *Curr. Opin. Chem. Biol.* **1999**, *3*, 207−219.

(257) Ferguson, S. J. Nitrogen cycle enzymology. *Curr. Opin. Chem. Biol.* **1998**, *2*, 182−193.

(258) Lehnert, N.; Musselman, B. W.; Seefeldt, L. C. Viewpoint: grand challenges in the nitrogen cycle. *Chem. Soc. Rev.* **2021**, *50*, 3640−3646.

(259) Winogradsky, S. On the nitrifying organisms. *Sciences* **1890**, *110*, 1013−1016.

(260) Hooper, A. B.; Vannelli, T.; Bergmann, D. J.; Arciero, D. M. Enzymology of the oxidation of ammonia to nitrite by bacteria. *Antonie van Leeuwenhoek* **1997**, *71*, 59−67.

(261) Kozlowski, J. A.; Kits, K. D.; Stein, L. Y. Comparison of nitrogen oxide metabolism among diverse ammonia-oxidizing bacteria. *Front. Microbiol.* **2016**, *7*, 1090.

(262) Kozlowski, J. A.; Stieglmeier, M.; Schleper, C.; Klotz, M. G.; Stein, L. Y. Pathways and key intermediates required for obligate aerobic ammonia-dependent chemolithotrophy in bacteria and Thaumarchaeota. *ISME J.* **2016**, *10*, 1836−1845.

(263) Könneke, M.; Bernhard, A. E.; José, R.; Walker, C. B.; Waterbury, J. B.; Stahl, D. A. Isolation of an autotrophic ammonia-oxidizing marine archaeon. *Nature* **2005**, *437*, 543−546.

(264) Francis, C. A.; Beman, J. M.; Kuypers, M. M. M. New processes and players in the nitrogen cycle: the microbial ecology of anaerobic and archaeal ammonia oxidation. *ISME J.* **2007**, *1*, 19−27.

(265) Hooper, A. B.; Arciero, D.; Bergmann, D.; Hendrich, M. P. The oxidation of ammonia as an energy source in bacteria. *Respiration in Archaea and Bacteria*; Zannoni, D., Ed.; Springer: Dordrecht, Netherlands, 2005; Vol. *16*; pp 121−147.

(266) Kuypers, M. M.; Marchant, H. K.; Kartal, B. The microbial nitrogen-cycling network. *Nat. Rev. Microbiol.* **2018**, *16*, 263−276.

(267) Winogradsky, S. Contributions a la morphologie des organisms de la nitrification. *Arch. Sci. Biol. (St. Petersbourg)* **1892**, *1*, 87−137.

(268) Daims, H.; Lücker, S.; Wagner, M. A new perspective on microbes formerly known as nitrite-oxidizing bacteria. *Trends Microbiol.* **2016**, *24*, 699−712.

(269) Daims, H.; Lebedeva, E. V.; Pjevac, P.; Han, P.; Herbold, C.; Albertsen, M.; Jehmlich, N.; Palatinszky, M.; Vierheilig, J.; Bulaev, A.; et al. Complete nitrification by *Nitrospira* bacteria. *Nature* **2015**, *528*, 504−509.

(270) Van Kessel, M. A. H. J.; Speth, D. R.; Albertsen, M.; Nielsen, P. H.; Op den Camp, H. J. M.; Kartal, B.; Jetten, M. S. M.; Lücker, S. Complete nitrification by a single microorganism. *Nature* **2015**, *528*, 555−559.

(271) Caranto, J. D.; Lancaster, K. M. Nitric oxide is an obligate bacterial nitrification intermediate produced by hydroxylamine oxidoreductase. *Proc. Natl. Acad. Sci. U. S. A.* **2017**, *114*, 8217−8222.

(272) Cedervall, P.; Hooper, A. B.; Wilmot, C. M. Structural studies of hydroxylamine oxidoreductase reveal a unique heme cofactor and a previously unidentified interaction partner. *Biochemistry* **2013**, *52*, 6211−6218.

(273) Igarashi, N.; Moriyama, H.; Fujiwara, T.; Fukumori, Y.; Tanaka, N. The 2.8 structure of hydroxylamine oxidoreductase from a nitrifying chemoautotrophic bacterium, *Nitrosomonas europaea*. *Nat. Struct. Biol.* **1997**, *4*, 276−284.

(274) Hille, R. The molybdenum oxotransferases and related enzymes. *Dalton Trans.* **2013**, *42*, 3029−3042.

(275) Merkle, A. C.; Lehnert, N. Binding and activation of nitrite and nitric oxide by copper nitrite reductase and corresponding model complexes. *Dalton Trans.* **2012**, *41*, 3355−3368.

(276) Horrell, S.; Kekilli, D.; Strange, R. W.; Hough, M. A. Recent structural insights into the function of copper nitrite reductases. *Metallomics* **2017**, *9*, 1470−1482.

(277) Godden, J. W.; Turley, S.; Teller, D. C.; Adman, E. T.; Liu, M. Y.; Payne, W. J.; LeGall, J. The 2.3 Angstrom x-ray structure of nitrite reductase from *Achromobacter cycloclastes*. *Science* **1991**, *253*, 438−442.

(278) Ghosh, S.; Dey, A.; Sun, Y.; Scholes, C. P.; Solomon, E. I. Spectroscopic and computational studies of nitrite reductase: proton induced electron transfer and backbonding contributions to reactivity. *J. Am. Chem. Soc.* **2009**, *131*, 277−288.

(279) Krzemiński, Ł.; Ndamba, L.; Canters, G. W.; Aartsma, T. J.; Evans, S. D.; Jeuken, L. J. C. Spectroelectrochemical investigation of intramolecular and interfacial electron-transfer rates reveals differences between nitrite reductase at rest and during turnover. *J. Am. Chem. Soc.* **2011**, *133*, 15085−15093.

(280) Horrell, S.; Antonyuk, S. V.; Eady, R. R.; Hasnain, S.; Hough, M. A.; Strange, R. W. Serial crystallography captures enzyme catalysis in copper nitrite reductase at atomic resolution from one crystal. *IUCrJ* **2016**, *3*, 271−281.

(281) Lintuluoto, M.; Lintuluoto, J. M. DFT study on enzyme turnover including proton and electron transfers of copper-containing nitrite reductase. *Biochemistry* **2016**, *55*, 4697−4707.

(282) Qin, X.; Deng, L.; Hu, C.; Li, L.; Chen, X. Copper-containing nitrite reductase employing proton-coupled spin-exchanged electron-transfer and multiproton synchronized transfer to reduce nitrite. *Chem. - Eur. J.* **2017**, *23*, 14900−14910.

(283) Lintuluoto, M.; Lintuluoto, J. M. Intra-electron transfer induced by protonation in copper-containing nitrite reductase. *Metallomics* **2018**, *10*, 565−578.

(284) Tocheva, E. I.; Rosell, F. I.; Mauk, A. G.; Murphy, M. E. P. Side-on copper-nitrosyl coordination by nitrite reductase. *Science* **2004**, *304*, 867−870.

(285) Usov, O. M.; Sun, Y.; Grigoryants, V. M.; Shapleigh, J. P.; Scholes, C. P. EPR-ENDOR of the Cu(I)NO complex of nitrite reductase. *J. Am. Chem. Soc.* **2006**, *128*, 13102−13111.

(286) Merkle, A. C.; Lehnert, N. The side-on copper(I) nitrosyl geometry in copper nitrite reductase is due to steric interactions with isoleucine-257. *Inorg. Chem.* **2009**, *48*, 11504−11506.

(287) Fukuda, Y.; Tse, K. M.; Nakane, T.; Nakatsu, T.; Suzuki, M.; Sugahara, M.; Inoue, S.; Masuda, T.; Yumoto, F.; Matsugaki, N.; Nango, E.; Tono, K.; Joti, Y.; Kameshima, T.; Song, C.; Hatsui, T.; Yabashi, M.; Nureki, O.; Murphy, M. E. P.; Inoue, T.; Iwata, S.; Mizohata, E. Redox-coupled proton transfer mechanism in nitrite reductase revealed by femtosecond crystallography. *Proc. Natl. Acad. Sci. U. S. A.* **2016**, *113*, 2928−2933.

(288) Hedison, T. M.; Shanmugam, M.; Heyes, D. J.; Edge, R.; Scrutton, N. S. Active intermediates in copper nitrite reductase reactions probed by a cryotrapping-electron paramagnetic resonance approach. *Angew. Chem., Int. Ed.* **2020**, *59*, 13936−13940.

(289) Fukuda, Y.; Hirano, Y.; Kusaka, K.; Inoue, T.; Tamada, T. High-resolution neutron crystallography visualizes an OH-bound resting state of a copper-containing nitrite reductase. *Proc. Natl. Acad. Sci. U. S. A.* **2020**, *117*, 4071−4077.

(290) Halsted, T. P.; Yamashita, K.; Gopalasingam, C. C.; Shenoy, R. T.; Hirata, K.; Ago, H.; Ueno, G.; Blakeley, M. P.; Eady, R. R.; Antonyuk, S. V.; Yamamoto, M.; Hasnain, S. S. Catalytically important damage-free structures of a copper nitrite reductase obtained by femtosecond X-ray laser and room-temperature neutron crystallography. *IUCrJ* **2019**, *6*, 761−772.

(291) Ellis, M. J.; Grossmann, J. G.; Eady, R. R.; Hasnain, S. S. Genomic analysis reveals widespread occurrence of new classes of copper nitrite reductases. *JBIC, J. Biol. Inorg. Chem.* **2007**, *12*, 1119−1127.

(292) Tsuda, A.; Ishikawa, R.; Koteishi, H.; Tange, K.; Fukuda, Y.; Kobayashi, K.; Inoue, T.; Nojiri, M. Structural and mechanistic insights into the electron flow through protein for cytochrome *c*-tethering copper nitrite reductase. *J. Biochem.* **2013**, *154*, 51−60.

(293) Dong, J.; Sasaki, D.; Eady, R. R.; Antonyuk, S. V.; Hasnain, S. S. Identification of a tyrosine switch in copper-haem nitrite reductases. *IUCrJ* **2018**, *5*, 510−518.

(294) Sasaki, D.; Watanabe, T. F.; Eady, R. R.; Garratt, R. C.; Antonyuk, S. V.; Hasnain, S. S. Structures of substrate- and product-bound forms of a multi-domain copper nitrite reductase shed light on the role of domain tethering in protein complexes. *IUCrJ* **2020**, *7*, 557−565.

(295) Williams, P. A.; Fülöp, V.; Garman, E. F.; Saunders, N. F. W.; Ferguson, S. J.; Hajdu, J. Haem-ligand switching during catalysis in crystals of a nitrogen-cycle enzyme. *Nature* **1997**, *389*, 406−412.

(296) Rinaldo, S.; Arcovito, A.; Brunori, M.; Cutruzzola, F. Fast dissociation of nitric oxide from ferrous *Pseudomonas aeruginosa* cd_1 nitrite reductase. *J. Biol. Chem.* **2007**, *282*, 14761−14767.

(297) Ranghino, G.; Scorza, E.; Sjögren, T.; Williams, P. A.; Ricci, M.; Hajdu, J. Quantum mechanical interpretation of nitrite reduction by cytochrome cd_1 nitrite reductase from *Paracoccus pantotrophus*. *Biochemistry* **2000**, *39*, 10958−10966.

(298) Fujii, H.; Yamaki, D.; Ogura, T.; Hada, M. The functional role of the structure of the dioxo-isobacteriochlorin in the catalytic site of cytochrome cd_1 for the reduction of nitrite. *Chem. Sci.* **2016**, *7*, 2896−2906.

(299) Amanullah, S.; Dey, A. The role of porphyrin peripheral substituents in determining the reactivities of ferrous nitrosyl species. *Chem. Sci.* **2020**, *11*, 5909−5921.

(300) Daiber, A.; Shoun, H.; Ullrich, V. Nitric oxide reductase ($P450_{nor}$) from *Fusarium oxysporum*. *J. Inorg. Biochem.* **2005**, *99*, 185−193.

(301) McQuarters, A. B.; Wirgau, N. E.; Lehnert, N. Model complexes of key intermediates in fungal cytochrome P450 nitric oxide reductase (P450nor). *Curr. Opin. Chem. Biol.* **2014**, *19*, 82−89.

(302) Zumft, W. G. Nitric oxide reductases of prokaryotes with emphasis on the respiratory, heme-copper oxidase type. *J. Inorg. Biochem.* **2005**, *99*, 194−215.

(303) Shiro, Y. Structure and function of bacterial nitric oxide reductases. *Biochim. Biophys. Acta, Bioenerg.* **2012**, *1817*, 1907−1913.

(304) Nakahara, K.; Tanimoto, T.; Hatano, K.; Usuda, K.; Shoun, H. Cytochrome P-450 55A1 (P-450dNIR) acts as nitric oxide reductase employing NADH as the direct electron donor. *J. Biol. Chem.* **1993**, *268*, 8350−8355.

(305) Obayashi, E.; Takahashi, S.; Shiro, Y. Electronic structure of reaction intermediate of cytochrome P450nor in its nitric oxide reduction. *J. Am. Chem. Soc.* **1998**, *120*, 12964−12965.

(306) McQuarters, A. B.; Blaesi, E. J.; Kampf, J.; Alp, E. E.; Zhao, J.; Hu, M.; Krebs, C.; Lehnert, N. Synthetic model complex of the key intermediate in cytochrome P450 nitric oxide reductase. *Inorg. Chem.* **2019**, *58*, 1398−1413.

(307) Shiro, Y.; Fujii, M.; Iizuka, T.; Adachi, S.; Tsukamoto, K.; Nakahara, K.; Shoun, H. Spectroscopic and kinetic studies on reaction of cytochrome P450nor with nitric oxide. *J. Biol. Chem.* **1995**, *270*, 1617−1623.

(308) Riplinger, C.; Bill, E.; Daiber, A.; Ullrich, V.; Shoun, H.; Neese, F. New insights into the nature of observable reaction intermediates in cytochrome P450 NO reductase by using a combination of spectroscopy and quantum mechanics/molecular mechanics calculations. *Chem. - Eur. J.* **2014**, *20*, 1602−1614.

(309) Daiber, A.; Nauser, T.; Takaya, N.; Kudo, T.; Weber, P.; Hultschig, C.; Shoun, H.; Ullrich, V. Isotope effects and intermediates in the reduction of NO by $P450_{nor}$. *J. Inorg. Biochem.* **2002**, *88*, 343−352.

(310) Lehnert, N.; Praneeth, V. K. K.; Paulat, F. Electronic structure of iron(II)-porphyrin nitroxyl complexes: molecular mechanism of fungal nitric oxide reductase (P450nor). *J. Comput. Chem.* **2006**, *27*, 1338−1351.

(311) Riplinger, C.; Neese, F. The reaction mechanism of cytochrome P450 NO reductase: a detailed quantum mechanics/molecular mechanics study. *ChemPhysChem* **2011**, *12*, 3192−3203.

(312) Wasser, I. M.; de Vries, S.; Moënne-Loccoz, P.; Schröder, I.; Karlin, K. D. Nitric oxide in biological denitrification: Fe/Cu metalloenzymes and metal complex NO_x redox chemistry. *Chem. Rev.* **2002**, *102*, 1201−1234.

(313) Hino, T.; Matsumoto, Y.; Nagano, S.; Sugimoto, H.; Fukumori, Y.; Murata, T.; Iwata, S.; Shiro, Y. Structural basis of biological N_2O generation by bacterial nitric oxide reductase. *Science* **2010**, *330*, 1666−1670.

(314) Saraste, M.; Castresana, J. Cytochrome oxidase evolved by tinkering with denitrification enzymes. *FEBS Lett.* **1994**, *341*, 1−4.

(315) van der Oost, J.; de Boer, A. P. N.; de Gier, J.-W. L.; Zumft, W. G.; Stouthamer, A. H.; van Spanning, R. J. M. The heme-copper oxidase family consists of three distinct types of terminal oxidases and is related to nitric oxide reductase. *FEMS Microbiol. Lett.* **1994**, *121*, 1−10.

(316) Blomberg, M. R. A. Can reduction of NO to N_2O in cytochrome *c* dependent nitric oxide reductase proceed through a trans-mechanism? *Biochemistry* **2017**, *56*, 120−131.

(317) Takeda, H.; Kimura, T.; Nomura, T.; Horitani, M.; Yokota, A.; Matsubayashi, A.; Ishii, S.; Shiro, Y.; Kubo, M.; Tosha, T. Timing of NO binding and protonation in the catalytic reaction of bacterial nitric oxide reductase as established by time-resolved spectroscopy. *Bull. Chem. Soc. Jpn.* **2020**, *93*, 825−833.

(318) Ettwig, K. F.; Butler, M. K.; Le Paslier, D.; Pelletier, E.; Mangenot, S.; Kuypers, M. M. M.; Schreiber, F.; Dutilh, B. E.; Zedelius, J.; de Beer, D.; Gloerich, J.; Wessels, H. J. C. T.; van Alen, T.; Luesken, F.; Wu, M. L.; van de Pas-Schoonen, K. T.; Op den Camp, H. J. M.; Janssen-Megens, E. M.; Francoijs, K.-J.; Stunnenberg, H.; Weissenbach, J.; Jetten, M. S. M.; Strous, M. Nitrite-driven anaerobic methane oxidation by oxygenic bacteria. *Nature* **2010**, *464*, 543−548.

(319) Dell'Acqua, S.; Pauleta, S. R.; Moura, I.; Moura, J. J. G. The tetranuclear copper active site of nitrous oxide reductase: the Cu_Z center. *JBIC, J. Biol. Inorg. Chem.* **2011**, *16*, 183−194.

(320) Brown, K.; Tegoni, M.; Prudêncio, M.; Pereira, A. S.; Besson, S.; Moura, J. J.; Moura, I.; Cambillau, C. A novel type of catalytic copper cluster in nitrous oxide reductase. *Nat. Struct. Biol.* **2000**, *7*, 191−195.

(321) Chen, P.; Cabrito, I.; Moura, J. J. G.; Moura, I.; Solomon, E. I. Spectroscopic and electronic structure studies of the μ_4-sulfide bridged tetranuclear Cu_Z cluster in N_2O reductase: molecular insight into the catalytic mechanism. *J. Am. Chem. Soc.* **2002**, *124*, 10497−10507.

(322) Johnston, E. M.; Dell'Acqua, S.; Ramos, S.; Pauleta, S. R.; Moura, I.; Solomon, E. I. Determination of the active form of the tetranuclear copper sulfur cluster in nitrous oxide reductase. *J. Am. Chem. Soc.* **2014**, *136*, 614−617.

(323) Pomowski, A.; Zumft, W. G.; Kroneck, P. M. H.; Einsle, O. N_2O binding at a [4Cu:2S] copper-sulphur cluster in nitrous oxide reductase. *Nature* **2011**, *477*, 234−237.

(324) Simon, J.; Kroneck, P. M. H. The production of ammonia by multiheme cytochromes *c*. The Metal-Driven Biogeochemistry of Gaseous Compounds in the Environment. *Metal Ions in Life Science*; Kroneck, P. M. H., Sosa Torres, M. E., Eds.; Springer: Dordrecht, 2014; Vol. *14*; pp 211−236.

(325) Einsle, O.; Stach, P.; Messerschmidt, A.; Simon, J.; Kröger, A.; Huber, R.; Kroneck, P. M. H. Cytochrome *c* nitrite reductase from *Wolinella succinogenes.* Structure at 1.6 resolution, inhibitor binding, and heme-packing motifs. *J. Biol. Chem.* **2000**, *275*, 39608−39616.

(326) Bykov, D.; Neese, F. Six-electron reduction of nitrite to ammonia by cytochrome *c* nitrite reductase: insights from density functional theory studies. *Inorg. Chem.* **2015**, *54*, 9303−9316.

(327) Ali, M.; Stein, N.; Mao, Y.; Shahid, S.; Schmidt, M.; Bennett, B.; Pacheco, A. A. Trapping of a putative intermediate in the cytochrome *c* nitrite reductase (*cc*NiR)-catalyzed reduction of nitrite: implications for the *cc*NiR reaction mechanism. *J. Am. Chem. Soc.* **2019**, *141*, 13358−13371.

(328) Dietl, A.; Ferousi, C.; Maalcke, W. J.; Menzel, A.; de Vries, S.; Keltjens, J. T.; Jetten, M. S. M.; Kartal, B.; Barends, T. R. M. The inner workings of the hydrazine synthase multiprotein complex. *Nature* **2015**, *527*, 394−397.

(329) Kartal, B.; Maalcke, W. J.; de Almeida, N. M.; Cirpus, I.; Gloerich, J.; Geerts, W.; Op den Camp, H. J. M.; Harhangi, H. R.; Janssen-Megens, E. M.; Francoijs, K.-J.; et al. Molecular mechanism of anaerobic ammonium oxidation. *Nature* **2011**, *479*, 127−130.

(330) Akram, M.; Dietl, A.; Mersdorf, U.; Prinz, S.; Maalcke, W.; Keltjens, J.; Ferousi, C.; de Almeida, N. M.; Reimann, J.; Kartal, B.; et al. A 192-heme electron transfer network in the hydrazine dehydrogenase complex. *Sci. Adv.* **2019**, *5*, No. eaav4310.

(331) Maalcke, W. J.; Reimann, J.; de Vries, S.; Butt, J. N.; Dietl, A.; Kip, N.; Mersdorf, U.; Barends, T. R. M.; Jetten, M. S. M.; Keltjens, J. T.; et al. Characterization of anammox hydrazine dehydrogenase, a key N_2-producing enzyme in the global nitrogen cycle. *J. Biol. Chem.* **2016**, *291*, 17077−17092.

(332) Yu, F.; Cangelosi, V. M.; Zastrow, M. L.; Tegoni, M.; Plegaria, J. S.; Tebo, A. G.; Mocny, C. S.; Ruckthong, L.; Qayyum, H.; Pecoraro, V. L. Protein design: toward functional metalloenzymes. *Chem. Rev.* **2014**, *114*, 3495−3578.

(333) Lu, Y.; Berry, S. M.; Pfister, T. D. Engineering novel metalloproteins: design of metal-binding sites into native protein scaffolds. *Chem. Rev.* **2001**, *101*, 3047−3080.

(334) Korendovych, I. V.; DeGrado, W. F. De novo protein design, a retrospective. *Q. Rev. Biophys.* **2020**, *53*, No. e3.

(335) Lin, Y. W.; Wang, J. Y.; Lu, Y. Functional tuning and expanding of myoglobin by rational protein design. *Sci. China: Chem.* **2014**, *57*, 346−355.

(336) Savelieff, M. G.; Lu, Y. Cu_A centers and their biosynthetic models in azurin. *JBIC, J. Biol. Inorg. Chem.* **2010**, *15*, 461−483.

(337) Wyllie, G. R. A.; Scheidt, W. R. Solid-state structures of metalloporphyrin NO_x compounds. *Chem. Rev.* **2002**, *102*, 1067−1090.

(338) Walker, F. A.; Simonis, U. Iron porphyrin chemistry. *Encyclopedia of Inorganic Chemistry*, 2nd ed.; King, R. B., Ed.; John Wiley & Sons, Ltd.: Chichester, 2005; Vol. *4*; pp 2390−2521.

(339) Bignon, E.; Rizza, S.; Filomeni, G.; Papaleo, E. Use of computational biochemistry for elucidating molecular mechanisms of nitric oxide synthase. *Comput. Struct. Biotechnol. J.* **2019**, *17*, 415−429.

(340) Sato, M.; Hida, N.; Umezawa, Y. Imaging the nanomolar range of nitric oxide with an amplifier-coupled fluorescent indicator in living cells. *Proc. Natl. Acad. Sci. U. S. A.* **2005**, *102*, 14515.

(341) Palmer, R. M. J.; Ashton, D. S.; Moncada, S. Vascular endothelial cells synthesize nitric oxide from L-arginine. *Nature* **1988**, *333*, 664−666.

(342) Balligand, J.-L.; Kobzik, L.; Han, X.; Kaye, D. M.; Belhassen, L.; O'Hara, D. S.; Kelly, R. A.; Smith, T. W.; Michel, T. Nitric oxide-dependent parasympathetic signaling is due to activation of constitutive endothelial (type III) nitric oxide synthase in cardiac myocytes. *J. Biol. Chem.* **1995**, *270*, 14582−14586.

(343) Wallerath, T.; Gath, I.; Aulitzky, W.; Pollock, J. S.; Kleinert, H.; Förstermann, U. Identification of the NO synthase isoforms expressed in human neutrophil granulocytes, megakaryocytes and platelets. *Thromb. Haemostasis* **1997**, *77*, 163−167.

(344) Straub, A. C.; Lohman, A. W.; Billaud, M.; Johnstone, S. R.; Dwyer, S. T.; Lee, M. Y.; Bortz, P. S.; Best, A. K.; Columbus, L.; Gaston, B.; Isakson, B. E. Endothelial cell expression of haemoglobin α regulates nitric oxide signalling. *Nature* **2012**, *491*, 473−477.

(345) Gladwin, M. T.; Kim-Shapiro, D. B. Vascular biology: Nitric oxide caught in traffic. *Nature* **2012**, *491*, 344−345.

(346) Kondo, K.; Bhushan, S.; King, A. L.; Prabhu, S. D.; Hamid, T.; Koenig, S.; Murohara, T.; Predmore, B. L.; Gojon, G., Sr.; Gojon, G., Jr.; Wang, R.; Karusula, N.; Nicholson, C. K.; Calvert, J. W.; Lefer, D. J. H_2S protects against pressure overload-induced heart failure via upregulation of endothelial nitric oxide synthase. *Circulation* **2013**, *127*, 1116−1127.

(347) Schwarz, P. M.; Kleinert, H.; Forstermann, U. Potential functional significance of brain-type and muscle-type nitric oxide synthase I expressed in adventitia and media of rat aorta. *Arterioscler., Thromb., Vasc. Biol.* **1999**, *19*, 2584−2590.

(348) Choate, J. K.; Danson, E. J. F.; Morris, J. F.; Paterson, D. J. Peripheral vagal control of heart rate is impaired in neuronal NOS knockout mice. *Am. J. Physiol. Heart Circ. Physiol.* **2001**, *281*, H2310−H2317.

(349) Chachlaki, K.; Prevot, V. Nitric oxide signalling in the brain and its control of bodily functions. *Br. J. Pharmacol.* **2020**, *177*, 5437−5458.

(350) Forstermann, U.; Sessa, W. C. Nitric oxide synthases: regulation and function. *Eur. Heart J.* **2012**, *33*, 829−837.

(351) Ito, N.; Ruegg, U. T.; Kudo, A.; Miyagoe-Suzuki, Y.; Takeda, S.-i. Activation of calcium signaling through Trpv1 by nNOS and peroxynitrite as a key trigger of skeletal muscle hypertrophy. *Nat. Med. (N. Y., NY, U. S.)* **2013**, *19*, 101−106.

(352) Wilcox, J. N.; Subramanian, R. R.; Sundell, C. L.; Tracey, W. R.; Pollock, J. S.; Harrison, D. G.; Marsden, P. A. Expression of multiple isoforms of nitric oxide synthase in normal and atherosclerotic vessels. *Arterioscler., Thromb., Vasc. Biol.* **1997**, *17*, 2479−2488.

(353) Balligand, J. L.; Ungureanu-Longrois, D.; Simmons, W. W.; Pimental, D.; Malinski, T. A.; Kapturczak, M.; Taha, Z.; Lowenstein, C. J.; Davidoff, A. J.; Kelly, R. A.; et al. Cytokine-inducible nitric oxide synthase (iNOS) expression in cardiac myocytes. Characterization and regulation of iNOS expression and detection of iNOS activity in single cardiac myocytes in vitro. *J. Biol. Chem.* **1994**, *269*, 27580−27588.

(354) Cho, H. J.; Xie, Q. W.; Calaycay, J.; Mumford, R. A.; Swiderek, K. M.; Lee, T. D.; Nathan, C. Calmodulin is a subunit of nitric oxide synthase from macrophages. *J. Exp. Med.* **1992**, *176*, 599−604.

(355) Long, R.; Light, B.; Talbot, J. A. Mycobacteriocidal action of exogenous nitric oxide. *Antimicrob. Agents Chemother.* **1999**, *43*, 403−405.

(356) Mashimo, H.; Goyal, R. K. Lessons from genetically engineered animal models. IV. Nitric oxide synthase gene knockout mice. *Am. J. Physiol.* **1999**, *277*, G745−750.

(357) Liu, R. H.; Baldwin, B.; Tennant, B. C.; Hotchkiss, J. H. Elevated formation of nitrate and N-nitrosodimethylamine in woodchucks (Marmota monax) associated with chronic woodchuck hepatitis virus infection. *Cancer Res.* **1991**, *51*, 3925−3929.

(358) Liu, R. H.; Jacob, J. R.; Tennant, B. C.; Hotchkiss, J. H. Nitrite and nitrosamine synthesis by hepatocytes isolated from normal woodchucks (Marmota monax) and woodchucks chronically infected with woodchuck hepatitis virus. *Cancer Res.* **1992**, *52*, 4139−4143.

(359) Corbett, J. A.; Tilton, R. G.; Chang, K.; Hasan, K. S.; Ido, Y.; Wang, J. L.; Sweetland, M. A.; Lancaster, J. R.; Williamson, J. R.; McDaniel, M. L. Aminoguanidine, a novel inhibitor of nitric oxide formation, prevents diabetic vascular dysfunction. *Diabetes* **1992**, *41*, 552.

(360) Corbett, J. A.; Lancaster, J. R., Jr.; Sweetland, M. A.; McDaniel, M. L. Interleukin-1 beta-induced formation of EPR-detectable iron-nitrosyl complexes in islets of Langerhans. Role of nitric oxide in interleukin-1 beta-induced inhibition of insulin secretion. *J. Biol. Chem.* **1991**, *266*, 21351−21354.

(361) Corbett, J. A.; Wang, J. L.; Sweetland, M. A.; Lancaster, J. R., Jr.; McDaniel, M. L. Interleukin 1 beta induces the formation of nitric oxide by beta-cells purified from rodent islets of Langerhans. Evidence for the beta-cell as a source and site of action of nitric oxide. *J. Clin. Invest.* **1992**, *90*, 2384−2391.

(362) Forrester, M. T.; Benhar, M.; Stamler, J. S. Nitrosative stress in the ER: A new role for S-nitrosylation in neurodegenerative diseases. *ACS Chem. Biol.* **2006**, *1*, 355−358.

(363) Yao, D.; Gu, Z.; Nakamura, T.; Shi, Z.-Q.; Ma, Y.; Gaston, B.; Palmer, L. A.; Rockenstein, E. M.; Zhang, Z.; Masliah, E.; Uehara, T.; Lipton, S. A. Nitrosative stress linked to sporadic Parkinson's disease: S-nitrosylation of parkin regulates its E3 ubiquitin ligase activity. *Proc. Natl. Acad. Sci. U. S. A.* **2004**, *101*, 10810−10814.

(364) Pant, K.; Bilwes, A. M.; Adak, S.; Stuehr, D. J.; Crane, B. R. Structure of a nitric oxide synthase heme protein from Bacillus subtilis. *Biochemistry* **2002**, *41*, 11071−11079.

(365) Mogen, A. B.; Carroll, R. K.; James, K. L.; Lima, G.; Silva, D.; Culver, J. A.; Petucci, C.; Shaw, L. N.; Rice, K. C. Staphylococcus aureus nitric oxide synthase (saNOS) modulates aerobic respiratory metabolism and cell physiology. *Mol. Microbiol.* **2017**, *105*, 139−157.

(366) Chaudhari, S. S.; Kim, M.; Lei, S.; Razvi, F.; Alqarzaee, A. A.; Hutfless, E. H.; Powers, R.; Zimmerman, M. C.; Fey, P. D.; Thomas, V. C. Nitrite derived from endogenous bacterial nitric oxide synthase activity promotes aerobic respiration. *mBio* **2017**, *8*, No. e00887-00817.

(367) Kinkel, T. L.; Ramos-Montañez, S.; Pando, J. M.; Tadeo, D. V.; Strom, E. N.; Libby, S. J.; Fang, F. C. An essential role for bacterial nitric oxide synthase in Staphylococcus aureus electron transfer and colonization. *Nat. Microbiol.* **2017**, *2*, 16224.

(368) Hansler, A.; Chen, Q.; Ma, Y.; Gross, S. S. Untargeted metabolite profiling reveals that nitric oxide bioynthesis is an endogenous modulator of carotenoid biosynthesis in Deinococcus radiodurans and is required for extreme ionizing radiation resistance. *Arch. Biochem. Biophys.* **2016**, *589*, 38−52.

(369) Patel, B. A.; Moreau, M.; Widom, J.; Chen, H.; Yin, L.; Hua, Y.; Crane, B. R. Endogenous nitric oxide regulates the recovery of the radiation-resistant bacterium Deinococcus radiodurans from exposure to UV light. *Proc. Natl. Acad. Sci. U. S. A.* **2009**, *106*, 18183−18188.

(370) James, K. L.; Mogen, A. B.; Brandwein, J. N.; Orsini, S. S.; Ridder, M. J.; Markiewicz, M. A.; Bose, J. L.; Rice, K. C. Interplay of nitric oxide synthase (NOS) and SrrAB in modulation of Staphylococcus aureus metabolism and virulence. *Infect. Immun.* **2019**, *87*, No. e00570.

(371) Popova, T. G.; Teunis, A.; Vaseghi, H.; Zhou, W.; Espina, V.; Liotta, L. A.; Popov, S. G. Nitric oxide as a regulator of B. anthracis pathogenicity. *Front. Microbiol.* **2015**, *6*, 6.

(372) Sapp, A. M.; Mogen, A. B.; Almand, E. A.; Rivera, F. E.; Shaw, L. N.; Richardson, A. R.; Rice, K. C. Contribution of the nos-pdt operon to virulence phenotypes in methicillin-sensitive Staphylococcus aureus. *PLoS One* **2014**, *9*, No. e108868.

(373) van Sorge, N. M.; Beasley, F. C.; Gusarov, I.; Gonzalez, D. J.; von Köckritz-Blickwede, M.; Anik, S.; Borkowski, A. W.; Dorrestein, P. C.; Nudler, E.; Nizet, V. Methicillin-resistant Staphylococcus aureus bacterial nitric-oxide synthase affects antibiotic sensitivity and skin abscess development. *J. Biol. Chem.* **2013**, *288*, 6417−6426.

(374) Tejero, J.; Stuehr, D. Tetrahydrobiopterin in nitric oxide synthase. *IUBMB Life* **2013**, *65*, 358−365.

(375) Lowe, P. N.; Smith, D.; Stammers, D. K.; Riveros-Moreno, V.; Moncada, S.; Charles, I.; Boyhan, A. Identification of the domains of neuronal nitric oxide synthase by limited proteolysis. *Biochem. J.* **1996**, *314* (1), 55−62.

(376) Sheta, E. A.; McMillan, K.; Masters, B. S. Evidence for a bidomain structure of constitutive cerebellar nitric oxide synthase. *J. Biol. Chem.* **1994**, *269*, 15147−15153.

(377) Siddhanta, U.; Wu, C.; Abu-Soud, H. M.; Zhang, J.; Ghosh, D. K.; Stuehr, D. J. Heme iron reduction and catalysis by a nitric oxide synthase heterodimer containing one reductase and two oxygenase domains. *J. Biol. Chem.* **1996**, *271*, 7309−7312.

(378) Fischmann, T. O.; Hruza, A.; Niu, X. D.; Fossetta, J. D.; Lunn, C. A.; Dolphin, E.; Prongay, A. J.; Reichert, P.; Lundell, D. J.; Narula, S. K.; Weber, P. C. Structural characterization of nitric oxide synthase isoforms reveals striking active-site conservation. *Nat. Struct. Biol.* **1999**, *6*, 233−242.

(379) Adak, S.; Ghosh, S.; Abu-Soud, H. M.; Stuehr, D. J. Role of reductase domain cluster 1 acidic residues in neuronal nitric-oxide synthase. Characterization of the FMN-FREE enzyme. *J. Biol. Chem.* **1999**, *274*, 22313−22320.

(380) Brunner, K.; Tortschanoff, A.; Hemmens, B.; Andrew, P. J.; Mayer, B.; Kungl, A. J. Sensitivity of flavin fluorescence dynamics in neuronal nitric oxide synthase to cofactor-induced conformational changes and dimerization. *Biochemistry* **1998**, *37*, 17545−17553.

(381) Bredt, D. S.; Snyder, S. H. Isolation of nitric oxide synthetase, a calmodulin-requiring enzyme. *Proc. Natl. Acad. Sci. U. S. A.* **1990**, *87*, 682−685.

(382) Abu-Soud, H. M.; Stuehr, D. J. Nitric oxide synthases reveal a role for calmodulin in controlling electron transfer. *Proc. Natl. Acad. Sci. U. S. A.* **1993**, *90*, 10769.

(383) Crane, B. R.; Arvai, A. S.; Ghosh, D. K.; Wu, C.; Getzoff, E. D.; Stuehr, D. J.; Tainer, J. A. Structure of nitric oxide synthase oxygenase dimer with pterin and substrate. *Science* **1998**, *279*, 2121−2126.

(384) Alderton, W. K.; Cooper, C. E.; Knowles, R. G. Nitric oxide synthases: structure, function and inhibition. *Biochem. J.* **2001**, *357*, 593−615.

(385) Crane, B. R.; Arvai, A. S.; Ghosh, D. K.; Wu, C.; Getzoff, E. D.; Stuehr, D. J.; Tainer, J. A. Structure of nitric oxide synthase oxygenase dimer with pterin and substrate. *Science* **1998**, *279*, 2121−2126.

(386) Presta, A.; Weber-Main, A. M.; Stankovich, M. T.; Stuehr, D. J. Comparative effects of substrates and pterin cofactor on the heme midpoint potential in inducible and neuronal nitric oxide synthases. *J. Am. Chem. Soc.* **1998**, *120*, 9460−9465.

(387) Zweier, J. L.; Chen, C.-A.; Druhan, L. J. S-glutathionylation reshapes our understanding of endothelial nitric oxide synthase uncoupling and nitric oxide/reactive oxygen species-mediated signaling. *Antioxid. Redox Signaling* **2011**, *14*, 1769−1775.

(388) Ramachandran, J.; Peluffo, R. D. Threshold levels of extracellular L-arginine that trigger NOS-mediated ROS/RNS production in cardiac ventricular myocytes. *Am. J. Physiol. Cell Physiol.* **2017**, *312*, C144−C154.

(389) Cortese-Krott, M. M.; Rodriguez-Mateos, A.; Sansone, R.; Kuhnle, G. G. C.; Thasian-Sivarajah, S.; Krenz, T.; Horn, P.; Krisp, C.; Wolters, D.; Heiß, C.; Kröncke, K.-D.; Hogg, N.; Feelisch, M.; Kelm, M. Human red blood cells at work: identification and visualization of erythrocytic eNOS activity in health and disease. *Blood* **2012**, *120*, 4229−4237.

(390) Li, H.; Igarashi, J.; Jamal, J.; Yang, W.; Poulos, T. L. Structural studies of constitutive nitric oxide synthases with diatomic ligands bound. *JBIC, J. Biol. Inorg. Chem.* **2006**, *11*, 753−768.

(391) Doukov, T.; Li, H.; Soltis, M.; Poulos, T. L. Single crystal structural and absorption spectral characterizations of nitric oxide synthase complexed with Nω-hydroxy-l-arginine and diatomic ligands. *Biochemistry* **2009**, *48*, 10246−10254.

(392) Jansen Labby, K.; Li, H.; Roman, L. J.; Martásek, P.; Poulos, T. L.; Silverman, R. B. Methylated Nω-hydroxy-l-arginine analogues as mechanistic probes for the second step of the nitric oxide synthase-catalyzed reaction. *Biochemistry* **2013**, *52*, 3062−3073.

(393) Li, H.; Raman, C. S.; Martásek, P.; Masters, B. S. S.; Poulos, T. L. Crystallographic studies on endothelial nitric oxide synthase complexed with nitric oxide and mechanism-aased inhibitors. *Biochemistry* **2001**, *40*, 5399−5406.

(394) Chreifi, G.; Li, H.; McInnes, C. R.; Gibson, C. L.; Suckling, C. J.; Poulos, T. L. Communication between the zinc and tetrahydrobiopterin binding sites in nitric oxide synthase. *Biochemistry* **2014**, *53*, 4216−4223.

(395) Raman, C. S.; Li, H.; Martásek, P.; Král, V.; Masters, B. S. S.; Poulos, T. L. Crystal structure of constitutive endothelial nitric oxide synthase: A paradigm for pterin function involving a novel metal center. *Cell* **1998**, *95*, 939−950.

(396) Garcin, E. D.; Arvai, A. S.; Rosenfeld, R. J.; Kroeger, M. D.; Crane, B. R.; Andersson, G.; Andrews, G.; Hamley, P. J.; Mallinder, P. R.; Nicholls, D. J.; St-Gallay, S. A.; Tinker, A. C.; Gensmantel, N. P.; Mete, A.; Cheshire, D. R.; Connolly, S.; Stuehr, D. J.; Berg, A.; Wallace, A. V.; Tainer, J. A.; Getzoff, E. D. Anchored plasticity opens doors for selective inhibitor design in nitric oxide synthase. *Nat. Chem. Biol.* **2008**, *4*, 700−707.

(397) Do, H. T.; Li, H.; Chreifi, G.; Poulos, T. L.; Silverman, R. B. Optimization of blood-brain barrier permeability with potent and selective human neuronal nitric oxide synthase inhibitors having a 2-aminopyridine scaffold. *J. Med. Chem.* **2019**, *62*, 2690−2707.

(398) Fedorov, R.; Ghosh, D. K.; Schlichting, I. Crystal structures of cyanide complexes of P450cam and the oxygenase domain of inducible nitric oxide synthase—structural models of the short-lived oxygen complexes. *Arch. Biochem. Biophys.* **2003**, *409*, 25−31.

(399) Pant, K.; Crane, B. R. Nitrosyl-heme structures of Bacillus subtilis nitric oxide synthase have implications for understanding substrate oxidation. *Biochemistry* **2006**, *45*, 2537−2544.

(400) Pant, K.; Bilwes, A. M.; Adak, S.; Stuehr, D. J.; Crane, B. R. Structure of a nitric oxide synthase heme protein from Bacillus subtilis. *Biochemistry* **2002**, *41*, 11071−11079.

(401) Stuehr, D. J.; Cho, H. J.; Kwon, N. S.; Weise, M. F.; Nathan, C. F. Purification and characterization of the cytokine-induced macrophage nitric oxide synthase: an FAD- and FMN-containing flavoprotein. *Proc. Natl. Acad. Sci. U. S. A.* **1991**, *88*, 7773−7777.

(402) Yui, Y.; Hattori, R.; Kosuga, K.; Eizawa, H.; Hiki, K.; Kawai, C. Purification of nitric oxide synthase from rat macrophages. *J. Biol. Chem.* **1991**, *266*, 12544−12547.

(403) Bhat, N. R.; Zhang, P.; Bhat, A. N. Cytokine induction of inducible nitric oxide synthase in an oligodendrocyte cell line. *J. Neurochem.* **1999**, *72*, 472−478.

(404) Kim, S.-J.; Ha, M.-S.; Choi, E.-Y.; Choi, J.-I.; Choi, I.-S. Nitric oxide production and inducible nitric oxide synthase expression induced by Prevotella nigrescens lipopolysaccharide. *FEMS Immunol. Med. Microbiol.* **2005**, *43*, 51−58.

(405) Flinspach, M. L.; Li, H.; Jamal, J.; Yang, W.; Huang, H.; Hah, J.-M.; Gómez-Vidal, J. A.; Litzinger, E. A.; Silverman, R. B.; Poulos, T. L. Structural basis for dipeptide amide isoform-selective inhibition of neuronal nitric oxide synthase. *Nat. Struct. Mol. Biol.* **2004**, *11*, 54−59.

(406) Xue, F.; Fang, J.; Lewis, W. W.; Martásek, P.; Roman, L. J.; Silverman, R. B. Potent and selective neuronal nitric oxide synthase inhibitors with improved cellular permeability. *Bioorg. Med. Chem. Lett.* **2010**, *20*, 554−557.

(407) White, K. A.; Marletta, M. A. Nitric oxide synthase is a cytochrome P-450 type hemoprotein. *Biochemistry* **1992**, *31*, 6627−6631.

(408) Stuehr, D. J.; Kwon, N. S.; Nathan, C. F.; Griffith, O. W.; Feldman, P. L.; Wiseman, J. Nω-Hydroxy-L-arginine is an intermediate in the biosynthesis of nitric oxide from L-arginine. *J. Biol. Chem.* **1991**, *266*, 6259−6263.

(409) Stuehr, D. J.; Kwon, N. S.; Nathan, C.; Griffith, O. W.; Feldman, P. L.; WiseMan, J. Nω-hydroxy-L-arginine is an intermediate in the biosynthesis of nitric oxide from L-arginine. *J. Biol. Chem.* **1991**, *266*, 6259−6263.

(410) White, K. A.; Marletta, M. A. Nitric oxide synthase is a cytochrome P-450 type hemoprotein. *Biochemistry* **1992**, *31*, 6627−6631.

(411) Hurshman, A. R.; Krebs, C.; Edmondson, D. E.; Huynh, B. H.; Marletta, M. A. Formation of a pterin radical in the reaction of the heme domain of inducible nitric oxide synthase with oxygen. *Biochemistry* **1999**, *38*, 15689−15696.

(412) Wei, C.-C.; Wang, Z.-Q.; Wang, Q.; Meade, A. L.; Hemann, C.; Hille, R.; Stuehr, D. J. Rapid kinetic studies link tetrahydrobiopterin radical formation to heme-dioxy reduction and arginine hydroxylation in inducible nitric-oxide synthase. *J. Biol. Chem.* **2001**, *276*, 315−319.

(413) Mayer, B.; John, M.; Heinzel, B.; Werner, E. R.; Wachter, H.; Schultz, G.; Böhme, E. Brain nitric oxide synthase is a biopterin- and flavin-containing multi-functional oxido-reductase. *FEBS Lett.* **1991**, *288*, 187−191.

(414) Tejero, J.; Biswas, A.; Wang, Z.-Q.; Page, R. C.; Haque, M. M.; Hemann, C.; Zweier, J. L.; Misra, S.; Stuehr, D. J. Stabilization and characterization of a heme-oxy reaction intermediate in inducible nitric-oxide synthase. *J. Biol. Chem.* **2008**, *283*, 33498−33507.

(415) Brunel, A.; Lang, J.; Couture, M.; Boucher, J.-L.; Dorlet, P.; Santolini, J. Oxygen activation in NO synthases: evidence for a direct role of the substrate. *FEBS Open Bio* **2016**, *6*, 386−397.

(416) de Visser, S. P.; Tan, L. S. Is the bound substrate in nitric oxide synthase protonated or neutral and what is the active oxidant that performs substrate hydroxylation? *J. Am. Chem. Soc.* **2008**, *130*, 12961−12974.

(417) Visser, S. P. d. Density functional theory (DFT) and combined quantum mechanical/molecular mechanics (QM/MM) studies on the oxygen activation step in nitric oxide synthase enzymes. *Biochem. Soc. Trans.* **2009**, *37*, 373−377.

(418) Cho, K.-B.; Carvajal, M. A.; Shaik, S. First half-reaction mechanism of nitric oxide synthase: The role of proton and oxygen coupled electron transfer in the reaction by quantum mechanics/molecular mechanics. *J. Phys. Chem. B* **2009**, *113*, 336−346.

(419) Bredt, D. S.; Snyder, S. H. Nitric oxide mediates glutamate-linked enhancement of cGMP levels in the cerebellum. *Proc. Natl. Acad. Sci. U. S. A.* **1989**, *86*, 9030−9033.

(420) Davydov, R.; Sudhamsu, J.; Lees, N. S.; Crane, B. R.; Hoffman, B. M. EPR and ENDOR characterization of the reactive intermediates in the generation of NO by cryoreduced oxy-nitric oxide synthase from Geobacillus stearothermophilus. *J. Am. Chem. Soc.* **2009**, *131*, 14493−14507.

(421) Poulos, T. L. Heme enzyme structure and function. *Chem. Rev.* **2014**, *114*, 3919−3962.

(422) Shamovsky, I.; Belfield, G.; Lewis, R.; Narjes, F.; Ripa, L.; Tyrchan, C.; Öberg, L.; Sjö, P. Theoretical studies of the second step of the nitric oxide synthase reaction: Electron tunneling prevents uncoupling. *J. Inorg. Biochem.* **2018**, *181*, 28−40.

(423) Tierney, D. L.; Huang, H.; Martasek, P.; Masters, B. S.; Silverman, R. B.; Hoffman, B. M. ENDOR spectroscopic evidence for the position and structure of NG-hydroxy-L-arginine bound to holo-neuronal nitric oxide synthase. *Biochemistry* **1999**, *38*, 3704−3710.

(424) Mak, P. J.; Duggal, R.; Denisov, I. G.; Gregory, M. C.; Sligar, S. G.; Kincaid, J. R. Human cytochrome CYP17A1: The structural basis for compromised lyase activity with 17-hydroxyprogesterone. *J. Am. Chem. Soc.* **2018**, *140*, 7324−7331.

(425) Mak, P. J.; Gregory, M. C.; Denisov, I. G.; Sligar, S. G.; Kincaid, J. R. Unveiling the crucial intermediates in androgen production. *Proc. Natl. Acad. Sci. U. S. A.* **2015**, *112*, 15856−15861.

(426) Akhtar, M.; Wright, J. N.; Lee-Robichaud, P. A review of mechanistic studies on aromatase (CYP19) and 17alpha-hydroxylase-17,20-lyase (CYP17). *J. Steroid Biochem. Mol. Biol.* **2011**, *125*, 2−12.

(427) Huang, H.; Hah, J.-M.; Silverman, R. B. Mechanism of nitric oxide synthase. Evidence that direct hydrogen atom abstraction from the O-H bond of N^G-hydroxyarginine is not relevant to the mechanism. *J. Am. Chem. Soc.* **2001**, *123*, 2674−2676.

(428) Wei, C.-C.; Wang, Z.-Q.; Hemann, C.; Hille, R.; Stuehr, D. J. A tetrahydrobiopterin radical forms and then becomes reduced during Nω-hydroxyarginine oxidation by nitric-oxide synthase. *J. Biol. Chem.* **2003**, *278*, 46668−46673.

(429) Cho, K.-B.; Gauld, J. W. Second half-reaction of nitric oxide synthase: Computational insights into the initial step and key proposed intermediate. *J. Phys. Chem. B* **2005**, *109*, 23706−23714.

(430) Robinet, J. J.; Cho, K.-B.; Gauld, J. W. A density functional theory investigation on the mechanism of the second half-reaction of nitric oxide synthase. *J. Am. Chem. Soc.* **2008**, *130*, 3328−3334.

(431) Papale, D.; Bruckmann, C.; Gazur, B.; Miles, C. S.; Mowat, C. G.; Daff, S. Oxygen activation in neuronal NO synthase: resolving the consecutive mono-oxygenation steps. *Biochem. J.* **2012**, *443*, 505−514.

(432) Adak, S.; Aulak, K. S.; Stuehr, D. J. Direct evidence for nitric oxide production by a nitric-oxide synthase-like protein from Bacillus subtilis. *J. Biol. Chem.* **2002**, *277*, 16167−16171.

(433) Wang, Z.-Q.; Lawson, R. J.; Buddha, M. R.; Wei, C.-C.; Crane, B. R.; Munro, A. W.; Stuehr, D. J. Bacterial flavodoxins support nitric oxide production by Bacillus subtilis nitric-oxide synthase. *J. Biol. Chem.* **2007**, *282*, 2196−2202.

(434) Gusarov, I.; Starodubtseva, M.; Wang, Z.-Q.; McQuade, L.; Lippard, S. J.; Stuehr, D. J.; Nudler, E. Bacterial nitric-oxide synthases operate without a dedicated redox partner. *J. Biol. Chem.* **2008**, *283*, 13140−13147.

(435) Schneiker, S.; Perlova, O.; Kaiser, O.; Gerth, K.; Alici, A.; Altmeyer, M. O.; Bartels, D.; Bekel, T.; Beyer, S.; Bode, E.; Bode, H. B.; Bolten, C. J.; Choudhuri, J. V.; Doss, S.; Elnakady, Y. A.; Frank, B.; Gaigalat, L.; Goesmann, A.; Groeger, C.; Gross, F.; Jelsbak, L.; Jelsbak, L.; Kalinowski, J.; Kegler, C.; Knauber, T.; Konietzny, S.; Kopp, M.; Krause, L.; Krug, D.; Linke, B.; Mahmud, T.; Martinez-Arias, R.; McHardy, A. C.; Merai, M.; Meyer, F.; Mormann, S.; Muñoz-Dorado, J.; Perez, J.; Pradella, S.; Rachid, S.; Raddatz, G.; Rosenau, F.; Rückert, C.; Sasse, F.; Scharfe, M.; Schuster, S. C.; Suen, G.; Treuner-Lange, A.;

Velicer, G. J.; Vorhölter, F.-J.; Weissman, K. J.; Welch, R. D.; Wenzel, S. C.; Whitworth, D. E.; Wilhelm, S.; Wittmann, C.; Blöcker, H.; Pühler, A.; Müller, R. Complete genome sequence of the myxobacterium *Sorangium cellulosum*. *Nat. Biotechnol.* **2007**, *25*, 1281−1289.

(436) Agapie, T.; Suseno, S.; Woodward, J. J.; Stoll, S.; Britt, R. D.; Marletta, M. A. NO formation by a catalytically self-sufficient bacterial nitric oxide synthase from Sorangium cellulosum. *Proc. Natl. Acad. Sci. U. S. A.* **2009**, *106*, 16221.

(437) Healy, F. G.; Wach, M.; Krasnoff, S. B.; Gibson, D. M.; Loria, R. The txtAB genes of the plant pathogen Streptomyces acidiscabies encode a peptide synthetase required for phytotoxin thaxtomin A production and pathogenicity. *Mol. Microbiol.* **2000**, *38*, 794−804.

(438) Bignell, D. R.; Fyans, J. K.; Cheng, Z. Phytotoxins produced by plant pathogenic Streptomyces species. *J. Appl. Microbiol.* **2014**, *116*, 223−235.

(439) Kers, J. A.; Wach, M. J.; Krasnoff, S. B.; Widom, J.; Cameron, K. D.; Bukhalid, R. A.; Gibson, D. M.; Crane, B. R.; Loria, R. Nitration of a peptide phytotoxin by bacterial nitric oxide synthase. *Nature* **2004**, *429*, 79−82.

(440) Gusarov, I.; Nudler, E. NO-mediated cytoprotection: Instant adaptation to oxidative stress in bacteria. *Proc. Natl. Acad. Sci. U. S. A.* **2005**, *102*, 13855−13860.

(441) Martin, E.; Sharina, I.; Seminara, A. R.; Krumenacker, J.; Murad, F. *Nitric oxide, cell signaling and gene expression*; Taylor and Francis Group: Boca Raton, FL, 2005; pp 167−216.

(442) Buechler, W. A.; Ivanova, K.; Wolfram, G.; Drummer, C.; Heim, J. M.; Gerzer, R. Soluble guanylyl cyclase and platelet function. *Ann. N. Y. Acad. Sci.* **1994**, *714*, 151−157.

(443) Denninger, J. W; Marletta, M. A Guanylate cyclase and the NO/cGMP signaling pathway. *Biochim. Biophys. Acta, Bioenerg.* **1999**, *1411*, 334−350.

(444) Munzel, T.; Feil, R.; Mulsch, A.; Lohmann, S. M.; Hofmann, F.; Walter, U. Physiology and pathophysiology of vascular signaling controlled by guanosine 3′,5′-cyclic monophosphate-dependent protein kinase. *Circulation* **2003**, *108*, 2172−2183.

(445) Warner, T. D.; Mitchell, J. A.; Sheng, H.; Murad, F. Effects of cyclic GMP on smooth muscle relaxation. *Adv. Pharmacol.* **1994**, *26*, 171−194.

(446) Li, H.; Poulos, T. Structure-function studies on nitric oxide synthases. *J. Inorg. Biochem.* **2005**, *99*, 293−305.

(447) Stuehr, D. J.; Tejero, J.; Haque, M. M. Structural and mechanistic aspects of flavoproteins: electron transfer through the nitric oxide synthase flavoprotein domain. *FEBS J.* **2009**, *276*, 3959−3974.

(448) Pan, J.; Xu, Q.; Lin, Y.-W.; Zhong, F.; Tan, X. Human soluble guanylate cyclase as a nitric oxide sensor for NO-signalling reveals a novel function of nitrite reductase. *Chem. Commun.* **2013**, *49*, 7454−7456.

(449) Bian, K.; Doursout, M. F.; Murad, F. Vascular system: role of nitric oxide in cardiovascular diseases. *J. Clin. Hypertens.* **2008**, *10*, 304−310.

(450) Coggins, M. P.; Bloch, K. D. Nitric oxide in the pulmonary vasculature. *Arterioscler., Thromb., Vasc. Biol.* **2007**, *27*, 1877−1885.

(451) Evgenov, O. V.; Pacher, P.; Schmidt, P. M.; Haskó, G.; Schmidt, H. H. H. W.; Stasch, J.-P. NO-independent stimulators and activators of soluble guanylate cyclase: discovery and therapeutic potential. *Nat. Rev. Drug Discovery* **2006**, *5*, 755−768.

(452) Fitzpatrick, D. A.; O'Halloran, D. M.; Burnell, A. M. Multiple lineage specific expansions within the guanylyl cyclase gene family. *BMC Evol. Biol.* **2006**, *6*, 26.

(453) Schaap, P. Guanylyl cyclases across the tree of life. *Front. Biosci., Landmark Ed.* **2005**, *10*, 1485−1498.

(454) Boon, E. M.; Marletta, M. A. Ligand discrimination in soluble guanylate cyclase and the H-NOX family of heme sensor proteins. *Curr. Opin. Chem. Biol.* **2005**, *9*, 441−446.

(455) Boon, E. M.; Davis, J. H.; Tran, R.; Karow, D. S.; Huang, S. H.; Pan, D.; Miazgowicz, M. M.; Mathies, R. A.; Marletta, M. A. Nitric oxide binding to prokaryotic homologs of the soluble guanylate cyclase *β*1 *H-NOX* domain. *J. Biol. Chem.* **2006**, *281*, 21892−21902.

(456) Zhao, Y.; Marletta, M. A. Localization of the heme binding region of soluble guanylyl cyclase. *Biochemistry* **1997**, *36*, 15959−15964.

(457) Wedel, B.; Harteneck, C.; Foerster, J.; Friebe, A.; Schultz, G.; Koesling, D. Functional domains of soluble guanylyl cyclase. *J. Biol. Chem.* **1995**, *270*, 24871−24875.

(458) Koesling, D. Studying the structure and regulation of soluble guanylyl cyclase. *Methods* **1999**, *19*, 485−493.

(459) Wilson, E. M.; Chinkers, M. Identification of sequences mediating guanylyl cyclase dimerization. *Biochemistry* **1995**, *34*, 4696−4701.

(460) Campbell, M. G.; Underbakke, E. S.; Potter, C. S.; Carragher, B.; Marletta, M. A. Single-particle EM reveals the higher-order domain architecture of soluble guanylate cyclase. *Proc. Natl. Acad. Sci. U. S. A.* **2014**, *111*, 2960−2965.

(461) Fritz, B. G.; Roberts, S. A.; Ahmed, A.; Breci, L.; Li, W.; Weichsel, A.; Brailey, J. L.; Wysocki, V. H.; Tama, F.; Montfort, W. R. Molecular model of a soluble guanylyl cyclase fragment determined by small-angle X-ray scattering and chemical cross-linking. *Biochemistry* **2013**, *52*, 1568−1582.

(462) Horst, B. G.; Yokom, A. L.; Rosenberg, D. J.; Morris, K. L.; Hammel, M.; Hurley, J. H.; Marletta, M. A. Allosteric activation of the nitric oxide receptor soluble guanylate cyclase mapped by cryo-electron microscopy. *eLife* **2019**, *8*, No. e50634.

(463) Kang, Y.; Liu, R.; Wu, J.-X.; Chen, L. Structural insights into the mechanism of human soluble guanylate cyclase. *Nature* **2019**, *574*, 206−210.

(464) Ko, F.-N.; Wu, C.-C.; Kuo, S.-C.; Lee, F.-Y.; Teng, C.-M. YC-1, a novel activator of platelet guanylate cyclase. *Blood* **1994**, *84*, 4226−4233.

(465) Derbyshire, E. R.; Gunn, A.; Ibrahim, M.; Spiro, S.; Britt, R. D.; Marletta, M. A. Characterization of two different five-coordinate soluble guanylate cyclase ferrous-nitrosyl complexes. *Biochemistry* **2008**, *47*, 3892−3899.

(466) Friebe, A.; Schultz, G.; Koesling, D. Sensitizing soluble guanylyl cyclase to become a highly CO-sensitive enzyme. *EMBO J.* **1996**, *15*, 6863−6868.

(467) Stones, J. R.; Marletta, M. A. Synergistic activation of soluble guanylate cyclase by YC-1 and carbon monoxide: implications for the role of cleavage of the iron-histidine bond during activation by nitric oxide. *Chem. Biol.* **1998**, *5*, 255−261.

(468) Pal, B.; Li, Z.; Ohta, T.; Takenaka, S.; Tsuyama, S.; Kitagawa, T. Resonance Raman study on synergistic activation of soluble guanylate cyclase by imidazole, YC-1 and GTP. *J. Inorg. Biochem.* **2004**, *98*, 824−832.

(469) Li, Z. Q.; Pal, B.; Takenaka, S.; Tsuyama, S.; Kitagawa, T. Resonance Raman evidence for the presence of two heme pocket conformations with varied activities in CO-bound bovine soluble guanylate cyclase and their conversion. *Biochemistry* **2005**, *44*, 939−946.

(470) Makino, R.; Obayashi, E.; Homma, N.; Shiro, Y.; Hori, H. YC-1 facilitates release of the proximal His residue in the NO and CO complexes of solubly guanylate cyclase. *J. Biol. Chem.* **2003**, *278*, 11130−11137.

(471) Martin, E.; Czarnecki, K. J. V.; Murad, F.; Kincaid, J. R.; et al. Resonance Raman and infrared spectroscopic studies of high-output forms of human soluble guanylyl cyclase. *J. Am. Chem. Soc.* **2005**, *127*, 4625−4631.

(472) Weichsel, A.; Kievenaar, J. A.; Curry, R.; Croft, J. T.; Montfort, W. R. Instability in a coiled-coil signaling helix is conserved for signal transduction in soluble guanylyl cyclase. *Protein Sci.* **2019**, *28*, 1830−1839.

(473) Khalid, R. R.; Maryam, A.; Fadouloglou, V. E.; Siddiqi, A. R.; Zhang, Y. Cryo-EM density map fitting driven in-silico structure of human soluble guanylate cyclase (hsGC) reveals functional aspects of inter-domain cross talk upon NO binding. *J. Mol. Graphics Modell.* **2019**, *90*, 109−119.

(474) Childers, K. C.; Yao, X.-Q.; Giannakoulias, S.; Amason, J.; Hamelberg, D.; Garcin, E. D. Synergistic mutations in soluble guanylyl cyclase (sGC) reveal a key role for interfacial regions in the sGC activation mechanism. *J. Biol. Chem.* **2019**, *294*, 18451−18464.

(475) Khalid, R. R.; Maryam, A.; Sezerman, O. U.; Mylonas, E.; Siddiqi, A. R.; Kokkinidis, M. Probing the structural dynamics of the catalytic domain of human soluble guanylate cyclase. *Sci. Rep.* **2020**, *10*, 1−15.

(476) Purohit, R.; Weichsel, A.; Montfort, W. R. Crystal structure of the alpha subunit PAS domain from soluble guanylyl cyclase. *Protein Sci.* **2013**, *22*, 1439−1444.

(477) Hespen, C. W.; Bruegger, J. J.; Phillips-Piro, C. M.; Marletta, M. A. Structural and functional evidence indicates selective oxygen signaling in *Caldanaerobacter subterraneus H-NOX*. *ACS Chem. Biol.* **2016**, *11*, 2337−2346.

(478) Ma, X.; Sayed, N.; Beuve, A.; van den Akker, F. NO and CO differentially activate soluble guanylate cyclase via a heme pivot-bend mechanism. *EMBO J.* **2007**, *26*, 578−588.

(479) Ma, X.; Beuve, A.; Van den Akker, F. Crystal structure of the signaling helix coiled-coil domain of the β1 subunit of the soluble guanylyl cyclase. *BMC Struct. Biol.* **2010**, *10*, 2.

(480) Allerston, C. K.; von Delft, F.; Gileadi, O. Crystal structures of the catalytic domain of human soluble guanylate cyclase. *PLoS One* **2013**, *8*, No. e57644.

(481) Seeger, F.; Quintyn, R.; Tanimoto, A.; Williams, G. J.; Tainer, J. A.; Wysocki, V. H.; Garcin, E. D. Interfacial residues promote an optimal alignment of the catalytic center in human soluble guanylate cyclase: heterodimerization is required but not sufficient for activity. *Biochemistry* **2014**, *53*, 2153−2165.

(482) Underbakke, E. S.; Iavarone, A. T.; Chalmers, M. J.; Pascal, B. D.; Novick, S.; Griffin, P. R.; Marletta, M. A. Nitric oxide-induced conformational changes in soluble guanylate cyclase. *Structure* **2014**, *22*, 602−611.

(483) Kosarikov, D. N.; Young, P.; Uversky, V. N.; Gerber, N. C. Human soluble guanylate cyclase: functional expression, purification and structural characterization. *Arch. Biochem. Biophys.* **2001**, *388*, 185−197.

(484) Musci, G.; Metz, G. D.; Tsunematsu, H.; Berliner, L. J. 4,4′-Bis[8-(phenylamino)naphthalene-1-sulfonate] binding to human thrombins: a sensitive exo site fluorescent affinity probe. *Biochemistry* **1985**, *24*, 2034−2039.

(485) Choi, J.-K.; Kim, I.-S.; Kwon, T.-I.; Parker, W.; Song, P. S. Spectral perturbations and oligomer/monomer formation in 124-kilodalton *Avena* phytochrome. *Biochemistry* **1990**, *29*, 6883−6891.

(486) Guo, Y.; Marletta, M. A. Structural insight into *H-NOX* gas sensing and cognate signaling protein regulation. *ChemBioChem* **2019**, *20*, 7−19.

(487) Nioche, P.; Berka, V.; Vipond, J.; Minton, N.; Tsai, A.-L.; Raman, C. S. Femtomolar sensitivity of a NO sensor from *Clostridium botulinum*. *Science* **2004**, *306*, 1550−1553.

(488) Guo, Y.; Suess, D. L. M.; Herzik, M. A.; Lavarone, A. T.; Britt, R. D.; Marletta, M. A. Regulation of nitric oxide signaling by formation of a distal receptor-ligand complex. *Nat. Chem. Biol.* **2017**, *13*, 1216−1221.

(489) Winter, M. B.; Herzik, M. A.; Kuriyan, J.; Marletta, M. A. Tunnels modulate ligand flux in a heme nitric oxide/oxygen binding (H-NOX) domain. *Proc. Natl. Acad. Sci. U. S. A.* **2011**, *108*, E881−E889.

(490) Tsai, A.-L.; Berka, V.; Martin, F.; Ma, X.; van den Akker, F.; Fabian, M.; Olson, J. S. Is *Nostoc H-NOX* a NO sensor or redox switch? *Biochemistry* **2010**, *49*, 6587−6599.

(491) Spiro, T. G. Pulling NO out of thin air. *Nat. Chem. Biol.* **2005**, *1*, 6−7.

(492) Gong, W.; Hao, B.; Chan, M. K. New mechanistic insights from structural studies of the oxygen-sensing domain of *Bradyrhizobium japonicum* FixL. *Biochemistry* **2000**, *39*, 3955−3962.

(493) Higuchi, Y.; Kusunoki, M.; Matsuura, Y.; Yasuoka, N.; Kakudo, M. Refined structure of cytochrome c_3 at 1.8 resolution. *J. Mol. Biol.* **1984**, *172*, 109−139.

(494) Vojtechovsky, J.; Chu, K.; Berendzen, J.; Sweet, R. M.; Schlichting, I. Crystal structures of myoglobin-ligand complexes at near-atomic resolution. *Biophys. J.* **1999**, *77*, 2153−2174.

(495) Hao, B.; Isaza, C.; Soltis, M.; Chan, M. K.; et al. Structure-based mechanism of O_2 sensing and ligand discrimination by the FixL heme domain of *Bradyrhizobium japonicum*. *Biochemistry* **2002**, *41*, 12952−12958.

(496) Olea, C., Jr.; Boon, E. M.; Pellicena, P.; Kuriyan, J.; Marletta, M. A. Probing the function of heme distortion in the H-NOX family. *ACS Chem. Biol.* **2008**, *3*, 703−710.

(497) Olea, C., Jr.; Herzik, M. A., Jr.; Kuriyan, J.; Marletta, M. A. Structural insights into the molecular mechanism of H-NOX activation. *Protein Sci.* **2010**, *19*, 881−887.

(498) Boon, E. M.; Huang, S. H.; Marletta, M. A. A molecular basis for NO selectivity in soluble guanylate cyclase. *Nat. Chem. Biol.* **2005**, *1*, 53−59.

(499) Rothkegel, C.; Schmidt, P. M.; Stoll, F.; Schroder, H.; Schmidt, H. H.; Stasch, J. P. Identification of residues crucially involved in soluble guanylate cyclase activation. *FEBS Lett.* **2006**, *580*, 4205−4213.

(500) Price, M. S.; Chao, L. Y.; Marletta, M. A. *Shewanella oneidensis* MR-1 H-NOX regulation of a histidine kinase by nitric oxide. *Biochemistry* **2007**, *46*, 13677−13683.

(501) Rao, M.; Herzik, M. A., Jr.; Iavarone, A. T.; Marletta, M. A. Nitric oxide-induced conformational changes govern *H-NOX* and histidine kinase interaction and regulation in *Shewanella oneidensis*. *Biochemistry* **2017**, *56*, 1274−1284.

(502) Horst, B. G.; Marletta, M. A. Physiological activation and deactivation of soluble guanylate cyclase. *Nitric Oxide* **2018**, *77*, 65−74.

(503) Cary, S. P. L.; Winger, J. A.; Marletta, M. A. Tonic and acute nitric oxide signaling through soluble guanylate cyclase is mediated by nonheme nitric oxide, ATP, and GTP. *Proc. Natl. Acad. Sci. U. S. A.* **2005**, *102*, 13064−13069.

(504) Zhao, Y.; Schelvis, J. P.; Babcock, G. T.; Marletta, M. A. Identification of histidine 105 in the 1 subunit of soluble guanylate cyclase as the heme proximal ligand. *Biochemistry* **1998**, *37*, 4502−4509.

(505) Stone, J. R.; Marletta, M. A. Soluble guanylate cyclase from bovine lung: activation with nitric oxide and carbon monoxide and spectral characterization of the ferrous and ferric states. *Biochemistry* **1994**, *33*, 5636−5640.

(506) Burstyn, J. N.; Yu, A. E.; Dierks, E. A.; Hawkins, B. H.; Dawson, J. H. Studies of the heme coordination and ligand binding properties of soluble guanylyl cyclase (sGC): Characterization of Fe(II)sGC and Fe(II)sGC(CO) by electronic absorption and magnetic circular dichroism spectroscopies and failure of CO to activate enzyme. *Biochemistry* **1995**, *34*, 5896−5903.

(507) Deinum, G.; Stone, R. J.; Babcock, G. T.; Marletta, M. A. Binding of nitric oxide and carbon monoxide to soluble guanylate cyclase as observed with resonance Raman spectroscopy. *Biochemistry* **1996**, *35*, 1540−1547.

(508) Yu, A. E.; Hu, S.; Spiro, T. G.; Burstyn, J. N. Resonance Raman spectroscopy of soluble guanylyl cyclase reveals displacement of distal and proximal heme ligands by NO. *J. Am. Chem. Soc.* **1994**, *116*, 4117−4118.

(509) Fan, B.; Gupta, G.; Danziger, R. S.; Friedman, J. M.; Rousseau, D. L. Resonance Raman characterization of soluble guanylate cyclase expressed from baculovirus. *Biochemistry* **1998**, *37*, 1178−1184.

(510) Dai, Y.; Sweeny, E. A.; Schlanger, S.; Ghosh, A.; Stuehr, D. J. GAPDH delivers heme to soluble guanylyl cyclase. *J. Biol. Chem.* **2020**, *295*, 8145−8154.

(511) Wu, G.; Martin, E.; Berka, V.; Liu, W.; Garcin, E. D.; Tsai, A.-L. A new paradigm for gaseous ligand selectivity of hemoproteins highlighted by soluble guanylate cyclase. *J. Inorg. Biochem.* **2021**, *214*, 111267.

(512) Tsai, A.-L.; Berka, V.; Martin, E.; Olson, J. S. A “sliding scale rule” for selectivity among NO, CO, and O_2 by heme protein sensors. *Biochemistry* **2012**, *51*, 172−186.

(513) Wu, G.; Liu, W.; Berka, V.; Tsai, A.-L. Gaseous ligand selectivity of the *H-NOX* sensor protein from *Shewanella oneidensis* and comparison to those of other bacterial *H-NOX*s and soluble guanylyl cyclase. *Biochimie* **2017**, *140*, 82−92.

(514) Erbil, W. K.; Price, M. S.; Wemmer, D. E.; Marletta, M. A. A structural basis for H-NOX signaling in *Shewanella oneidensis* by trapping a histidine kinase inhibitory conformation. *Proc. Natl. Acad. Sci. U. S. A.* **2009**, *106*, 19753−19760.

(515) Zhao, Y.; Hoganson, C.; Babcock, G. T.; Marletta, M. A. Structural changes in the heme proximal pocket induced by nitric oxide binding to soluble guanylate cyclase. *Biochemistry* **1998**, *37*, 12458−12464.

(516) Zhao, Y.; Brandish, P. E.; Ballou, D. P.; Marletta, M. A. A molecular basis for nitric oxide sensing by soluble guanylate cyclase. *Proc. Natl. Acad. Sci. U. S. A.* **1999**, *96*, 14753−14758.

(517) Wu, G.; Liu, W.; Berka, V.; Tsai, A.-L. The selectivity of *Vibrio cholerae H-NOX* for gaseous ligands follows the "sliding scale rule" hypothesis. Ligand interactions with both ferrous and ferric *Vc H-NOX*. *Biochemistry* **2013**, *52*, 9432−9446.

(518) Wu, G.; Liu, W.; Berka, V.; Tsai, A.-L. H-NOX from *Clostridium botulinum* like H-NOX from *Thermoanaerobacter tengcongensis* binds oxygen but with a less stable oxyferrous heme intermediate. *Biochemistry* **2015**, *54*, 7098−7109.

(519) Fritz, B. G.; Hu, X.; Brailey, J. L.; Berry, R. E.; Walker, F. A.; Montfort, W. R. Oxidation and loss of heme in soluble guanylyl cyclase from *Manduca sexta*. *Biochemistry* **2011**, *50*, 5813−5815.

(520) Makino, R.; Park, S.-y.; Obayashi, E.; Iizuka, T.; Hori, H.; Shiro, Y. Oxygen binding and redox properties of the heme in soluble guanylate cyclase implications for the mechanism of ligand discrimination. *J. Biol. Chem.* **2011**, *286*, 15678−15687.

(521) Zhou, Z.; Martin, E.; Sharina, I.; Esposito, I.; Szabo, C.; Bucci, M.; Cirino, G.; Papapetropoulos, A. Regulation of soluble guanylyl cyclase redox state by hydrogen sulfide. *Pharmacol. Res.* **2016**, *111*, 556−562.

(522) Tsai, A.-L.; Berka, V.; Sharina, I.; Martin, E. Dynamic ligand exchange in soluble guanylyl cyclase (sGC) implications for sGC regulation and desensitization. *J. Biol. Chem.* **2011**, *286*, 43182−43192.

(523) Yoo, B.-K.; Lamarre, I.; Martin, J.-L.; Rappaport, F.; Negrerie, M. Motion of proximal histidine and structural allosteric transition in soluble guanylate cyclase. *Proc. Natl. Acad. Sci. U. S. A.* **2015**, *112*, E1697−E1704.

(524) Stone, J. R.; Sands, R. H.; Dunham, W. R.; Marletta, M. A. Spectral and ligand-binding properties of an unusual hemoprotein, the ferric form of soluble guanylate cyclase. *Biochemistry* **1996**, *35*, 3258−3262.

(525) Martin, E.; Berka, V.; Sharina, I.; Tsai, A.-L. Mechanism of binding of NO to soluble guanylyl cyclase: implication for the second NO binding to the heme proximal site. *Biochemistry* **2012**, *51*, 2737−2746.

(526) Martin, E.; Berka, V.; Tsai, A. L.; Murad, F. Soluble guanylyl cyclase: the nitric oxide receptor. *Methods Enzymol.* **2005**, *396*, 478−492.

(527) Makino, R.; Matsuda, H.; Obayashi, E.; Shiro, Y.; Iizuka, T.; Hori, H. EPR characterization of axial bond in metal center of native and cobalt-substituted guanylate cyclase. *J. Biol. Chem.* **1999**, *274*, 7714−7723.

(528) Gouterman, M. Optical spectra and electronic structure of porphyrins and related rings. *The Porphyrins*; Dolphin, D. H., Ed.; Academic Press: New York, 1979; Vol. *III*, Part A; pp 1−156.

(529) Lehnert, N. Elucidating second coordination sphere effects in heme proteins using low-temperature magnetic circular dichroism spectroscopy. *J. Inorg. Biochem.* **2012**, *110*, 83−93.

(530) Baskaran, P.; Heckler, E. J.; van den Akker, F.; Beuve, A. Identification of residues in the heme domain of soluble guanylyl cyclase that are important for basal and stimulated catalytic activity. *PLoS One* **2011**, *6*, No. e26976.

(531) Baskaran, P.; Heckler, E. J.; Van Den Akker, F.; Beuve, A. Aspartate 102 in the heme domain of soluble guanylyl cyclase has a key role in NO activation. *Biochemistry* **2011**, *50*, 4291−4297.

(532) Dierks, E. A.; Hu, S.; Vogel, K. M.; Yu, A. E.; Spiro, T. G.; Burstyn, J. N. Demonstration of the role of scission of the proximal histidine- iron bond in the activation of soluble guanylyl cyclase through metalloporphyrin substitution studies. *J. Am. Chem. Soc.* **1997**, *119*, 7316−7323.

(533) Bellamy, T. C.; Griffiths, C.; Garthwaite, J. Differential sensitivity of guanylyl cyclase and mitochondrial respiration to nitric oxide measured using clamped concentrations. *J. Biol. Chem.* **2002**, *277*, 31801−31807.

(534) Fernhoff, N. B.; Derbyshire, E. R.; Marletta, M. A. A nitric oxide/cysteine interaction mediates the activation of soluble guanylate cyclase. *Proc. Natl. Acad. Sci. U. S. A.* **2009**, *106*, 21602−21607.

(535) Alapa, M.; Cui, C.; Shu, P.; Li, H.; Kholodovych, V.; Beuve, A. Selective cysteines oxidation in soluble guanylyl cyclase catalytic domain is involved in NO activation. *Free Radical Biol. Med.* **2021**, *162*, 450−460.

(536) Patterson, J. C.; Lorkovic, I. M.; Ford, P. C. Spectroscopic and density functional studies of the dinitrosyl metalloporphyrin complexes $Fe(P)(NO)_2$ and $Ru(P)(NO)_2$. *Inorg. Chem.* **2003**, *42*, 4902−4908.

(537) Conradie, J.; Wondimagegn, T.; Ghosh, A. Molecular structure and conformation of dinitrosylheme. *J. Am. Chem. Soc.* **2003**, *125*, 4968−4969.

(538) Wang, J.; Schopfer, M. P.; Puiu, S. C.; Sarjeant, A. A. N.; Karlin, K. D. Reductive coupling of nitrogen monoxide (NO) facilitated by heme/copper complexes. *Inorg. Chem.* **2010**, *49*, 1404−1419.

(539) Stone, J. R.; Marletta, M. A. Spectral and kinetic studies on the activation of soluble guanylate cyclase by nitric oxide. *Biochemistry* **1996**, *35*, 1093−1099.

(540) Ballou, D. P.; Zhao, Y.; Brandish, P. E.; Marletta, M. A. Revisiting the kinetics of nitric oxide (NO) binding to soluble guanylate cyclase: The simple NO-binding model is incorrect. *Proc. Natl. Acad. Sci. U. S. A.* **2002**, *99*, 12097−12101.

(541) Kharitonov, V. G.; Russwurm, M.; Magde, D.; Sharma, V. S.; Koesling, D. Dissociation of nitric oxide from soluble guanylate cyclase. *Biochem. Biophys. Res. Commun.* **1997**, *239*, 284−286.

(542) Brandish, P. E.; Buechler, W. A.; Marletta, M. A. Regeneration of the ferrous heme of soluble guanylate cyclase from the nitric oxide complex" acceleration by thiols and oxyhemoglobin. *Biochemistry* **1998**, *37*, 16898−16907.

(543) Coleman, R. E.; Lancaster, K. M. Heme P460: a (cross) link to nitric oxide. *Acc. Chem. Res.* **2020**, *53*, 2925−2935.

(544) Vilbert, A. C.; Caranto, J. D.; Lancaster, K. M. Influences of the heme-lysine crosslink in cytochrome P460 over redox catalysis and nitric oxide sensitivity. *Chem. Sci.* **2018**, *9*, 368−379.

(545) Yamanaka, T. *The biochemistry of bacterial cytochromes*; Springer-Verlag, K. G.: Berlin, 1992.

(546) Mayburd, A. L.; Kassner, R. J. Mechanism and biological role of nitric oxide binding to cytochrome *c*ʿ. *Biochemistry* **2002**, *41*, 11582−11591.

(547) Choi, P. S.; Grigoryants, V. M.; Abruna, H. D.; Scholes, C. P.; Shapleigh, J. P. Regulation and function of cytochrome *c*′ in *Rhodobacter sphaeroides* 2.4.3. *J. Bacteriol.* **2005**, *187*, 4077−4085.

(548) Meyer, T. E.; Kamen, M. D. New perspectives on *c*-type cytochromes. *Adv. Protein Chem.* **1982**, *35*, 105−212.

(549) Ren, Z.; Meyer, T.; McRee, D. E. Atomic structure of a cytochrome *c*′ with an unusual ligand-controlled dimer dissociation at 1.8 resolution. *J. Mol. Biol.* **1993**, *243*, 433−445.

(550) Suzuki, S.; Yoshimura, T.; Nakahara, A.; Iwasaki, H.; Shidara, S.; Matsubara, T. Electronic and magnetic circular dichroism spectra of pentacoordinate nitrosylhemes in cytochromes *c*′ from nonphotosynthetic bacteria and their model complexes. *Inorg. Chem.* **1987**, *26*, 1006−1008.

(551) Yasui, M.; Harada, S.; Kai, Y.; Kasai, N.; Kusunoki, M.; Matsuura, Y. Three-dimensional structure of ferricytochrome *c*′ from *Rhodospirillum rubrum* at 2.8 resolution. *J. Biochem.* **1992**, *111*, 317−324.

(552) Finzel, B. C.; Weber, P. C.; Hardman, K. D.; Salemme, F. R. Structure of ferricytochrome *c*′ from *Rhodospirillum molischianum* at 1.67 resolution. *J. Mol. Biol.* **1985**, *186*, 627−643.

(553) Iwasaki, H.; Yoshimura, T.; Suzuki, S.; Shidara, S. Spectral properties of *Achromobacter xylosoxidans* cytochromes *c*′ and their NO complexes. *Biochim. Biophys. Acta, Bioenerg.* **1991**, *1058*, 79−82.

(554) Lawson, D. M.; Stevenson, C. E.; Andrew, C. R.; Eady, R. R. Unprecedented proximal binding of nitric oxide to heme: implications for guanylate cyclase. *EMBO J.* **2000**, *19*, 5661−5671.

(555) Lawson, D. M.; Stevenson, C. E.; Andrew, C. R.; George, S. J.; Eady, R. R. A two-faced molecule offers NO explanation: the proximal binding of nitric oxide to haem. *Biochem. Soc. Trans.* **2003**, *31*, 553−557.

(556) Martí, M. A.; Capece, L.; Crespo, A.; Doctorovich, F.; Estrin, D. A. Nitric oxide interaction with cytochrome c′ and its relevance to guanylate cyclase. Why does the iron histidine bond break? *J. Am. Chem. Soc.* **2005**, *127*, 7721−7728.

(557) Kekilli, D.; Petersen, C. A.; Pixton, D. A.; Ghafoor, D. D.; Abdullah, G. H.; Dworkowski, F. S. N.; Wilson, M. T.; Heyes, D. J.; Hardman, S. J. O.; Murphy, L. M.; et al. Engineering proximal vs. distal heme-NO coordination via dinitrosyl dynamics: implications for NO sensor design. *Chem. Sci.* **2017**, *8*, 1986−1994.

(558) Manole, A.; Kekilli, D.; Svistunenko, D. A.; Wilson, M. T.; Dobbin, P. S.; Hough, M. A. Conformational control of the binding of diatomic gases to cytochrome *c*′. *JBIC, J. Biol. Inorg. Chem.* **2015**, *20*, 675−686.

(559) Scheidt, W. R.; Frisse, M. E. Nitrosylmetalloporphyrins. II. Synthesis and molecular stereochemistry of nitrosyl-*α*,*β*,*γ*,*δ*-tetraphenylporphinatoiron(II). *J. Am. Chem. Soc.* **1975**, *97*, 17−21.

(560) Silvernail, N. J.; Olmstead, M. M.; Noll, B. C.; Scheidt, W. R. Tetragonal to triclinic - a phase change for [Fe(TPP)(NO)]. *Inorg. Chem.* **2009**, *48*, 971−977.

(561) Ellison, M. K.; Scheidt, W. R. Structural distortion in five-coordinate nitrosyl iron porphyrins. Axial ligand tilting and its effect on equatorial geometry. *J. Am. Chem. Soc.* **1997**, *119*, 7404−7405.

(562) Scheidt, W. R.; Duval, H. F.; Neal, T. J.; Ellison, M. K. Intrinsic structural distortions in five-coordinate (nitrosyl)iron(II) porphyrinate derivatives. *J. Am. Chem. Soc.* **2000**, *122*, 4651−4659.

(563) Wyllie, G. R. A.; Scheidt, W. R. NO orientation and tilting in (nitrosyl)iron(II) deuteroporphyrin IX. *Inorg. Chem.* **2003**, *42*, 4259−4261.

(564) Praneeth, V. K. K.; Näther, C.; Peters, G.; Lehnert, N. Spectroscopic properties and electronic structure of five- and six-coordinate iron(II) porphyrin NO complexes: effect of the axial N-donor ligand. *Inorg. Chem.* **2006**, *45*, 2795−2811.

(565) Bohle, D. S.; Hung, C.-H. Ligand-promoted rapid nitric oxide dissociation from ferrous porphyrin nitrosyls. *J. Am. Chem. Soc.* **1995**, *117*, 9584−9585.

(566) Wang, J.; Schopfer, M. P.; Sarjeant, A. A. N.; Karlin, K. D. Heme-copper assembly mediated reductive coupling of nitrogen monoxide. *J. Am. Chem. Soc.* **2009**, *131*, 450−451.

(567) Nasri, H.; Haller, K. J.; Wang, Y.; Hyunh, B. H.; Scheidt, W. R. Reaction of bis(nitro)[a,a,a,a,-meso-tetrakis(o-pivalamidophenyl)-porhinato]iron(III) with 2,3,5,6-tetrafluorthiophenol and 2,3,5,6-tetrafluorothiophenolate. EPR and Moessbauer spectra and molecular structures. *Inorg. Chem.* **1992**, *31*, 3459−3467.

(568) Cheng, L.; Powell, D. R.; Khan, M. A.; Richter-Addo, G. B. The first unambiguous determination of a nitrosyl-to-nitrite conversion in an iron nitrosyl porphyrin. *Chem. Commun.* **2000**, 2301−2302.

(569) Goodrich, L. E.; Saikat, R.; Alp, E. E.; Zhao, J.; Hu, M. Y.; Lehnert, N. Electronic structure and biologically relevant reactivity of low-spin $\{FeNO\}^8$ porphyrin model complexes: new insight from a bis-picket fence porphyrin. *Inorg. Chem.* **2013**, *52*, 7766−7780.

(570) Lehnert, N.; Galinato, M. G. I.; Paulat, F.; Richter-Addo, G. B.; Sturhahn, W.; Xu, N.; Zhao, J. Nuclear resonance vibrational spectroscopy applied to [Fe(OEP)(NO)]: the vibrational assignments of five-coordinate ferrous heme nitrosyls and implications for electronic structure. *Inorg. Chem.* **2010**, *49*, 4133−4148.

(571) Wyllie, G. R. A.; Schulz, C. E.; Scheidt, W. R. Five- to six-coordination in (nitrosyl)iron(II) porphyrinates: effects of binding the sixth ligand. *Inorg. Chem.* **2003**, *42*, 5722−5734.

(572) Praneeth, V. K. K.; Neese, F.; Lehnert, N. Spin density distribution in five- and six-coordinate iron(II)-porphyrin NO complexes evidenced by magnetic circular dichroism spectroscopy. *Inorg. Chem.* **2005**, *44*, 2570−2572.

(573) Paulat, F.; Berto, T. C.; DeBeer George, S.; Goodrich, L. E.; Praneeth, V. K. K.; Sulok, C. D.; Lehnert, N. Vibrational assignments of six-coordinate ferrous heme nitrosyls: new insight from nuclear resonance vibrational spectroscopy. *Inorg. Chem.* **2008**, *47*, 11449−11451.

(574) Maxwell, J. C.; Caughey, W. S. An infrared study of nitric oxide bonding to heme B and hemoglobin A. Evidence for inositol hexaphosphate induced cleavage of proximal histidine to iron bonds. *Biochemistry* **1976**, *15*, 388−396.

(575) Scheidt, W. R.; Brinegar, A. C.; Ferro, E. B.; Kirner, J. F. Nitrosometalloporphyrins, 4. Molecular sterochemistry of the two crystalline forms of nitrosyl- *α*-tetraphenylporphinato(4-methylpiperidine)iron(II). A structural correlation with v(NO). *J. Am. Chem. Soc.* **1977**, *99*, 7315−7322.

(576) Silvernail, N. J.; Pavlik, J. W.; Noll, B. C.; Schulz, C. E.; Scheidt, W. R. Reversible NO motion in crystalline [Fe(Porph)(1-MeIm)-(NO)] derivatives. *Inorg. Chem.* **2008**, *47*, 912−920.

(577) Silvernail, N. J.; Barabanschikov, A.; Sage, J. T.; Noll, B. C.; Scheidt, W. R. Mapping NO movements in crystalline [Fe(Porph)-(NO)(1-MeIm)]. *J. Am. Chem. Soc.* **2009**, *131*, 2131−2140.

(578) Rath, S. P.; Koerner, R.; Olmstead, M. M.; Balch, A. L. Reversible binding of nitric oxide and carbon-carbon bond formation in a meso-hydroxylated heme. *J. Am. Chem. Soc.* **2003**, *125*, 11798−11799.

(579) Deatherage, J. F.; Moffat, K. Structure of nitric oxide hemoglobin. *J. Mol. Biol.* **1979**, *134*, 401−417.

(580) Chan, N. L.; Rogers, P. H.; Arnone, A. Crystal structure of the S-nitroso form of liganded human hemoglobin. *Biochemistry* **1998**, *37*, 16459−16464.

(581) Chan, N. L.; Kavanaugh, J. S.; Rogers, P. H.; Arnone, A. Crystallographic analysis of the interaction of nitric oxide with quaternary-T human hemoglobin. *Biochemistry* **2004**, *43*, 118−132.

(582) Copeland, D. M.; West, A. H.; Richter-Addo, G. B. Crystal structure of ferrous horse heart myoglobin complexed with nitric oxide and nitrosoethane. *Proteins: Struct., Funct., Genet.* **2003**, *53*, 182−192.

(583) Zeng, W.; Silvernail, N. J.; Wharton, D. C.; Georgiev, G. Y.; Leu, B. M.; Scheidt, W. R.; Zhao, J.; Sturhahn, W.; Alp, E. E.; Sage, J. T. Direct probe of iron vibrations elucidates NO activation of heme proteins. *J. Am. Chem. Soc.* **2005**, *125*, 11200−11201.

(584) Miller, L. M.; Pedraza, A. J.; Chance, M. R. Identification of conformational substrates involved in nitric oxide binding to ferric and ferrous myoglobin through difference Fourier transform infrared spectroscopy (FTIR). *Biochemistry* **1997**, *36*, 12199−12207.

(585) Tomita, T.; Hirota, S.; Ogura, T.; Olson, J. S.; Kitagawa, T. Resonance Raman investigation of Fe-N-O of nitrosylheme in myoglobin and mutants. *J. Phys. Chem. B* **1999**, *103*, 7044−7054.

(586) Pal, B.; Kitagawa, T. Interactions of soluble guanylate cyclase with diatomics as probed by resonance Raman spectroscopy. *J. Inorg. Biochem.* **2005**, *99*, 267−279.

(587) Geeraerts, Z.; Heskin, A. K.; DuBois, J.; Rodgers, K. R.; Lukat-Rodgers, G. S. Structure and reactivity of chlorite dismutase nitrosyls. *J. Inorg. Biochem.* **2020**, *211*, 111203.

(588) Nurizzo, D.; Cutruzzola, F.; Arese, M.; Bourgeois, D.; Brunori, M.; Cambillau, C.; Tegoni, M. Conformational changes occuring upon reduction and NO binding in nitrite reductase from *Pseudomonas aeruginosa*. *Biochemistry* **1998**, *37*, 13987−13996.

(589) Ding, X. D.; Weichsel, A.; Andersen, J. F.; Shokhireva, T. K.; Balfour, C.; Pierik, A. J.; Averill, B. A.; Montfort, W. R.; Walker, F. A. Nitric oxide binding to the ferri- and ferroheme states of nitrophorin 1, a reversible NO-binding heme protein from the saliva of the blood-sucking insect, *Rhodnius prolixus*. *J. Am. Chem. Soc.* **1999**, *121*, 128−138.

(590) Maes, E. M.; Roberts, S. A.; Weichsel, A.; Montfort, W. R. Ultrahigh resolution structures of nitrophorin 4: heme distortion in ferrous CO and NO complexes. *Biochemistry* **2005**, *44*, 12690−12699.

(591) Zhao, X.-J.; Sampath, V.; Caughey, W. S. Infrared characterization of nitric oxide bonding to bovine heart cytochrome *c* oxidase and myoglobin. *Biochem. Biophys. Res. Commun.* **1994**, *204*, 537−543.

(592) Pinakoulaki, E.; Ohta, T.; Soulimane, T.; Kitagawa, T.; Varotsis, C. Simultaneous resonance Raman detection of the heme a_3-Fe-CO and Cu_B-CO species in CO-bound ba_3-cytochrome *c* oxidase from *Thermus thermophilus*. Evidence for a charge transfer Cu_B-CO transition. *J. Biol. Chem.* **2004**, *279*, 22791−22794.

(593) Pinakoulaki, E.; Ohta, T.; Soulimane, T.; Kitagawa, T.; Varotsis, C. Detection of the His-heme Fe^{2+}-NO species in the reduction of NO to N_2O by ba_3-oxidase from *Thermus thermophilus*. *J. Am. Chem. Soc.* **2005**, *127*, 15161−15167.

(594) Leys, D.; Backers, K.; Meyer, T. E.; Hagen, W. R.; Cusanovich, M. A.; Van Beeumen, J. J. Crystal structures of oxygen-binding cytochrome c from *Rhodobacter sphaeroides*. *J. Biol. Chem.* **2000**, *275*, 16050−16056.

(595) Andrew, C. R.; George, S. J.; Lawson, D. M.; Eady, R. R. Six- to five-coordinate heme-nitrosyl conversion in cytochrome *c*′ and its relevance to guanylate cyclase. *Biochemistry* **2002**, *41*, 2353−2360.

(596) Andrew, C. R.; Kemper, L. J.; Busche, T. L.; Tiwari, A. M.; Kecskes, M. C.; Stafford, J. M.; Croft, L. C.; Lu, S.; Moenne-Loccoz, P.; Huston, W.; Moir, J. W. B.; Eady, R. R. Accessibility of the distal heme face, rather than Fe-His bond strength, determines the heme-nitrosyl coordination number of cytochromes c′: evidence from spectroscopic studies. *Biochemistry* **2005**, *44*, 8664−8672.

(597) Edwards, S. L.; Poulos, T. L. Ligand binding and structural perturbations in cytochrome *c* peroxidase. *J. Biol. Chem.* **1990**, *265*, 2588−2595.

(598) Badyal, S. K.; Joyce, M. G.; Sharp, K. H.; Seward, H. E.; Mewies, M.; Basran, J.; MacDonald, I. K.; Moody, P. C.; Raven, E. L. Conformational mobility in the active site of heme peroxidase. *J. Biol. Chem.* **2006**, *281*, 24512−24520.

(599) Lad, L.; Ortiz de Montellano, P. R.; Poulos, T. L. Crystal structures of ferrous and ferrous-NO forms of verdoheme in a complex with human heme oxygenase-1: catalytic implications for heme cleavage. *J. Inorg. Biochem.* **2004**, *98*, 1686−1695.

(600) Sugishima, M.; Hagiwara, Y.; Zhang, X.; Yoshida, T.; Migita, C. T.; Fukuyama, K. Crystal structure of dimeric heme oxygenase-2 from *Synechocystis* sp. PCC 6803 in complex with heme. *Biochemistry* **2005**, *44*, 4257−4266.

(601) Hu, S.; Kincaid, J. R. Resonance Raman spectra of the nitric oxide adducts of ferrous cytochrome P450cam in the presence of various substrates. *J. Am. Chem. Soc.* **1991**, *113*, 9760−9766.

(602) Nagano, S.; Shimada, H.; Tarumi, A.; Hishiki, T.; Kimata-Ariga, Y.; Egawa, T.; Suematsu, M.; Park, S. Y.; Adachi, S.; Shiro, Y.; Ishimura, Y. Infrared spectroscopic and mutational studies on putidaredoxin-induced conformational changes in ferrous CO-P450cam. *Biochemistry* **2003**, *42*, 14507−14514.

(603) Unno, M.; Christian, J. F.; Sjodin, T.; Benson, D. E.; MacDonald, I. D.; Sligar, S. G.; Champion, P. M. Complex formation of cytochrome $P450_{cam}$ with putidaredoxin. *J. Biol. Chem.* **2002**, *277*, 2547−2553.

(604) Henry, Y. A.; Guissani, A.; Ducastel, B. *Nitric oxide research from chemistry to biology: EPR spectroscopy of nitrosylated compounds*; Landes Company: Austin, 1997.

(605) Sancier, K. M.; Freeman, G.; Mills, J. S. Electron spin resonance of nitric oxide-hemoglobin complexes in solution. *Science* **1962**, *137*, 752−754.

(606) Wayland, B. B.; Olson, L. W. Spectroscopic studies and bonding model for NO complexes of iron porphyrins. *J. Am. Chem. Soc.* **1974**, *96*, 6037−6041.

(607) Hayes, R. G.; Ellison, M. K.; Scheidt, W. R. Definitive assignment of the g tensor of [Fe(OEP)(NO)] by single-crystal EPR. *Inorg. Chem.* **2000**, *39*, 3665−3668.

(608) Moore, E. G.; Gibson, Q. H. Cooperativity in the dissociation of nitric oxide from hemoglobin. *J. Biol. Chem.* **1976**, *251*, 2788−2794.

(609) Morris, R. J.; Gibson, Q. H. The role of diffusion in limiting the rate of ligand binding to hemoglobin. *J. Biol. Chem.* **1980**, *255*, 8050−8053.

(610) Herold, S.; Röck, G. Mechanistic studies of the oxygen-mediated oxidation of nitrosylhemoglobins. *Biochemistry* **2005**, *44*, 6223−6231.

(611) Berry, R. E.; Ding, X. D.; Shokhireva, T. K.; Weichsel, A.; Montfort, W. R.; Walker, F. A. Axial ligand complexes of the *Rhodnius* nitrophorins: reduction potentials, binding constants, EPR spectra, and structures of the 4-iodopyrazole and imidazole complexes of NP4. *JBIC, J. Biol. Inorg. Chem.* **2004**, *9*, 135−144.

(612) Knipp, M.; Yang, F.; Berry, R. E.; Zhang, H.; Shokhirev, M. N.; Walker, F. A. Spectroscopic and functional characterization of nitrophorin 7 from the blood-feeding insect *Rhodnius prolixus* reveals an important role of its isoform-specific N-terminus for proper protein function. *Biochemistry* **2007**, *46*, 13254−13268.

(613) Hoshino, M.; Ozawa, K.; Seki, H.; Ford, P. C. Photochemistry of nitric oxide adducts of water-soluble iron(III) porphyrin and ferrihemoproteins studied by nanosecond laser photolysis. *J. Am. Chem. Soc.* **1993**, *115*, 9568−9575.

(614) Komatsu, T.; Matsukawa, Y.; Tsuchida, E. Nitrosyl iron(II) complex of meso-tetrakis(*α*-*o*-pivalamidophenyl)porphyrin with a covalently linked 2-methylimidazolylalkyl group. *Chem. Lett.* **2000**, *29*, 1060−1061.

(615) Rose, E. J.; Hoffman, B. M. Nitric oxide ferrohemes: kinetics of formation and photodissociation quantum yields. *J. Am. Chem. Soc.* **1983**, *105*, 2866−2873.

(616) Laverman, L. E.; Ford, P. C. Mechanistic studies of nitric oxide reactions with water soluble iron(II), cobalt(II), and iron(III) porphyrin complexes in aqueous solutions: Implications for biological activity. *J. Am. Chem. Soc.* **2001**, *123*, 11614−11622.

(617) Hoshino, M.; Kogure, M. Photochemistry of nitrosyl porphyrins in the temperature range 180-300 K and the effects of pyridine on photodenitrosylation of nitrosyliron tetraphenylporphyrin. *J. Phys. Chem.* **1989**, *93*, 5478−5484.

(618) Sharma, V. S.; Traylor, T. G.; Gardiner, R.; Mizukami, H. Reaction of nitric oxide with heme proteins and model compounds of hemoglobin. *Biochemistry* **1987**, *26*, 3837−3843.

(619) Kobayashi, K.; Tamura, M.; Hayashi, K. Kinetic analysis of the recombination of NO with ferrihemoproteins by the flash photolysis method. *Biochemistry* **1982**, *21*, 729−732.

(620) Qiang, L.; Zhu, S.; Ma, H.; Zhou, J. Investigation on binding of nitric oxide to horseradish peroxidase by absorption spectrometry. *Spectrochim. Acta, Part A* **2010**, *75*, 417−421.

(621) Andersen, J. F.; Ding, X. D.; Balfour, C.; Shokhireva, T. K.; Champagne, D. E.; Walker, F. A.; Montfort, W. R. Kinetics and equilibria in ligand binding by nitrophorins 1-4: evidence for stabilization of a nitric oxide-ferriheme complex through a ligand-induced conformational trap. *Biochemistry* **2000**, *39*, 10118−10131.

(622) Scheele, J. S.; Bruner, E.; Kharitonov, V. G.; Martasek, P.; Roman, L. J.; Masters, B. S. S.; Sharma, V. S.; Magde, D. Kinetics of NO ligation with nitric-oxide synthase by flash photolysis and stopped-flow spectrophotometry. *J. Biol. Chem.* **1999**, *274*, 13105−13110.

(623) Boggs, S.; Huang, L.; Stuehr, D. J. Formation and reactions of the heme-dioxygen intermediate in the first and second steps of nitric oxide synthesis as studied by stopped-flow spectroscopy under single-turnover conditions. *Biochemistry* **2000**, *39*, 2332−2339.

(624) Abu-Soud, H. M.; Wu, C.; Ghosh, D. K.; Stuehr, D. J. Stopped-flow analysis of CO and NO binding to inducible nitric oxide synthase. *Biochemistry* **1998**, *37*, 3777−3786.

(625) Wang, Z. Q.; Wei, C. C.; Sharma, M.; Pant, K.; Crane, B. R.; Stuehr, D. J. A conserved Val to Ile switch near the heme pocket of animal and bacterial nitric-oxide synthases helps determine their distinct catalytic profiles. *J. Biol. Chem.* **2004**, *279*, 19018−19025.

(626) Abu-Soud, H. M.; Gachhui, R.; Raushel, F. M.; Stuehr, D. J. The ferrous-dioxy complex of neuronal nitric oxide synthase. Divergent effects of L-arginine and tetrahydrobiopterin on its stability. *J. Biol. Chem.* **1997**, *272*, 17349−17353.

(627) Cooper, C. E.; Torres, J.; Sharpe, M. A.; Wilson, M. T. Nitric oxide ejects electrons from the binuclear centre of cytochrome *c* oxidase by reacting with oxidised copper: A general mechanism for the interaction of copper proteins with nitric oxide? *FEBS Lett.* **1997**, *414*, 281−284.

(628) Giuffrè, A.; Stubauer, G.; Brunori, M.; Sarti, P.; Torres, J.; Wilson, M. T. Chloride bound to oxidized cytochrome *c* oxidase controls the reaction with nitric oxide. *J. Biol. Chem.* **1998**, *273*, 32475−32478.

(629) Abu-Soud, H. M.; Hazen, S. L. Nitric oxide Is a physiological substrate for mammalian peroxidases. *J. Biol. Chem.* **2000**, *275*, 37524−37532.

(630) Franke, A.; Stochel, G.; Jung, C.; Van Eldik, R. Substrate binding favors enhanced NO binding to P450cam. *J. Am. Chem. Soc.* **2004**, *126*, 4181−4191.

(631) Nakano, T.; Sato, H.; Watanabe, A.; Ito, O.; Shimizu, T. Conserved Glu318 at the cytochrome P450 1A2 distal site is crucial in the nitric oxide complex stability. *J. Biol. Chem.* **1996**, *271*, 8570−8574.

(632) Ouellet, H.; Lang, J.; Couture, M.; Ortiz de Montellano, P. R. Reaction of *Mycobacterium tuberculosis* cytochrome P450 enzymes with nitric oxide. *Biochemistry* **2009**, *48*, 863−872.

(633) Tsai, A.-L.; Wei, C.; Kulmacz, R. J. Interaction between nitric oxide and prostaglandin H synthase. *Arch. Biochem. Biophys.* **1994**, *313*, 367−372.

(634) Franke, A.; Hessenauer-Ilicheva, N.; Meyer, D.; Stochel, G.; Woggon, W.-D.; van Eldik, R. Thermodynamic and kinetic studies on the binding of nitric oxide to a new enzyme mimic of cytochrome P450. *J. Am. Chem. Soc.* **2006**, *128*, 13611−13624.

(635) Yoshimura, T. Five- and six-coordinated nitrosyl iron(II) complexes of tetrakis (p-substituted phenyl)porphyrins. Substituent effects on the EPR parameters and the NO stretching frequencies. *Bull. Chem. Soc. Jpn.* **1991**, *64*, 2819−2828.

(636) Stone, J. R.; Sands, R. H.; Dunham, W. R.; Marletta, M. A. Electron paramagnetic resonance spectral evidence for the formation of a pentacoordinate nitrosyl-heme complex on soluble guanylate cyclase. *Biochem. Biophys. Res. Commun.* **1995**, *207*, 572−577.

(637) Yazawa, S.; Tsuchiya, H.; Hori, H.; Makino, R. Functional characterization of two nucleotide-binding sites in solubly guanylate cyclase. *J. Biol. Chem.* **2006**, *281*, 21763−21770.

(638) Praneeth, V. K. K.; Haupt, E.; Lehnert, N. Thiolate coordination to Fe(II)-porphyrin NO centers. *J. Inorg. Biochem.* **2005**, *99*, 940−948 (Erratum: p 1744)..

(639) Yoshimura, T. EPR spectra of five-coordinate nitrosyl-(protoporphyrin IX dimethyl ester)iron(II) in toluene under various conditions. *Inorg. Chim. Acta* **1986**, *125*, L27−L29.

(640) Hille, R.; Olson, J. S.; Palmer, G. Spectral transitions of nitrosyl hemes during ligand binding to hemoglobin. *J. Biol. Chem.* **1979**, *254*, 12110−12120.

(641) Kumita, H.; Matsuura, K.; Hino, T.; Takahashi, S.; Hori, H.; Fukumori, Y.; Morishima, I.; Shiro, Y. NO reduction by nitric-oxide reductase from denitrifying bacterium *Pseudomonas aeruginosa*: characterization of reaction intermediates that appear in the single turnover cycle. *J. Biol. Chem.* **2004**, *279*, 55247−55254.

(642) Patchkovskii, S.; Ziegler, T. Structural origin of two paramagnetic species in six-coordinated nitrosoiron(II) porphyrins revealed by density functional theory analysis of the g tensors. *Inorg. Chem.* **2000**, *39*, 5354−5364.

(643) Sage, J. T.; Paxson, C.; Wyllie, G. R. A.; Sturhahn, W.; Durbin, S. M.; Champion, P. M.; Alp, E. E.; Scheidt, W. R. Nuclear resonance vibrational spectroscopy of a protein active-site mimic. *J. Phys.: Condens. Matter* **2001**, *13*, 7707−7722.

(644) Sturhahn, W. Nuclear resonant spectroscopy. *J. Phys.: Condens. Matter* **2004**, *16*, S497−S530.

(645) Scheidt, W. R.; Li, J.; Sage, J. T. What can be learned from nuclear resonance vibrational spectroscopy: vibrational dynamics and hemes. *Chem. Rev.* **2017**, *117*, 12532−12563.

(646) Berto, T. C.; Praneeth, V. K. K.; Goodrich, L. E.; Lehnert, N. Iron-porphyrin NO complexes with covalently attached N-donor ligands: the formation of a stable six-coordinate species in solution. *J. Am. Chem. Soc.* **2009**, *131*, 17116−17126.

(647) Tomita, T.; Ogura, T.; Tsuyama, S.; Imai, Y.; Kitagawa, T. Effects of GTP on bound nitric oxide of soluble guanylate cyclase probed by resonance Raman spectroscopy. *Biochemistry* **1997**, *36*, 10155−10160.

(648) Lehnert, N. Quantum chemistry centered normal coordinate analysis (QCC-NCA): Routine application of normal coordinate analysis for the simulation of the vibrational spectra of large molecules. *The Encyclopedia of Inorganic Chemistry*; Solomon, E. I., King, R. B., Scott, R. A., Eds.; John Wiley & Sons: Chichester, United Kingdom, 2009; pp 123−140.

(649) Rush III, T. S.; Kozlowski, P. M.; Piffat, C. A.; Kumble, R.; Zgierski, M. Z.; Spiro, T. G. Computational modeling of metalloporphyrin structure and vibrational spectra: porphyrin ruffling in NiTPP. *J. Phys. Chem. B* **2000**, *104*, 5020−5034.

(650) Paulat, F.; Praneeth, V. K. K.; Näther, C.; Lehnert, N. Quantum chemistry-based analysis of the vibrational spectra of five-coordinate metalloporphyrins [M(TPP)Cl]. *Inorg. Chem.* **2006**, *45*, 2835−2856.

(651) Lehnert, N.; Sage, J. T.; Silvernail, N. J.; Scheidt, W. R.; Alp, E. E.; Sturhahn, W.; Zhao, J. Oriented single-crystal nuclear resonance vibrational spectroscopy of [Fe(TPP)(MI)(NO)]: quantitative assessment of the trans effect of NO. *Inorg. Chem.* **2010**, *49*, 7197−7215.

(652) Speelman, A. L.; Zhang, B.; Silakov, A.; Skodje, K. M.; Alp, E. E.; Zhao, J.; Hu, M. Y.; Kim, E.; Krebs, C.; Lehnert, N. Unusual synthetic pathway for an $\{Fe(NO)_2\}^9$ dinitrosyl iron complex (DNIC) and insight into DNIC electronic structure via nuclear resonance vibrational spectroscopy. *Inorg. Chem.* **2016**, *55*, 5485−5501.

(653) Thompson, N. B.; Oyala, P. H.; Dong, H. T.; Chalkley, M. J.; Zhao, J.; Alp, E. E.; Hu, M.; Lehnert, N.; Peters, J. C. Electronic structures of an $[Fe(NNR_2)]^{+/0/-}$ redox series: ligand noninnocence and implications for catalytic nitrogen fixation. *Inorg. Chem.* **2019**, *58*, 3535−3549.

(654) Praneeth, V. K. K.; Paulat, F.; Berto, T. C.; DeBeer George, S.; Näther, C.; Sulok, C. D.; Lehnert, N. Electronic structure of six-coordinate iron(III)-porphyrin NO adducts: the elusive iron(III)-NO(radical) state and its influence on the properties of these complexes. *J. Am. Chem. Soc.* **2008**, *130*, 15288−15303.

(655) McQuarters, A. B.; Kampf, J.; Alp, E. E.; Hu, M. Y.; Zhao, J.; Lehnert, N. Ferric heme-nitrosyl complexes: kinetically robust or unstable intermediates? *Inorg. Chem.* **2017**, *56*, 10513−10528.

(656) Rovira, C.; Kunc, K.; Hutter, J.; Ballone, P.; Parrinello, M. Equilibrium geometries and electronic structure of iron-porphyrin complexes: a density functional study. *J. Phys. Chem. A* **1997**, *101*, 8914−8925.

(657) Zhang, Y.; Gossman, W.; Oldfield, E. A density functional theory investigation of Fe-N-O bonding in heme proteins and model systems. *J. Am. Chem. Soc.* **2003**, *125*, 16387−16396.

(658) Ghosh, A.; Wondimagegn, T. J. A theoretical study of axial tilting and equatorial asymmetry in metalloporphyrin-nitrosyl complexes. *J. Am. Chem. Soc.* **2000**, *122*, 8101−8102.

(659) Boguslawski, K.; Jacob, C. R.; Reiher, M. Can DFT accurately predict spin densities? Analysis of discrepancies in iron nitrosyl complexes. *J. Chem. Theory Comput.* **2011**, *7*, 2740−2752.

(660) Radoń, M.; Broclawik, E.; Pierloot, K. Electronic structure of selected $\{FeNO\}^7$ complexes in heme and non-heme architectures: a density functional and multireference ab initio study. *J. Phys. Chem. B* **2010**, *114*, 1518−1528.

(661) Vogel, K. M.; Kozlowski, P. M.; Zgierski, M. Z.; Spiro, T. G. Determinants of the FeXO (X = C, N, O) vibrational frequencies in heme adducts from experiment and density functional theory. *J. Am. Chem. Soc.* **1999**, *121*, 9915−9921.

(662) Ray, G. B.; Li, X.-Y.; Ibers, J. A.; Sessler, J. L.; Spiro, T. G. How far can proteins bend the FeCO unit? Distal polar and steric effects in heme proteins and models. *J. Am. Chem. Soc.* **1994**, *116*, 162−176.

(663) Spiro, T. G.; Wasbotten, I. H. CO as a vibrational probe of heme protein active sites. *J. Inorg. Biochem.* **2005**, *99*, 34−44.

(664) Scheidt, W. R.; Piciulo, P. L. Synthesis and molecular stereochemistry of nitrosyl- a, b, c, d-tetraphenylporphinato(1-methylimidazole)iron(II). *J. Am. Chem. Soc.* **1976**, *98*, 1913−1919.

(665) Choi, I.-K.; Ryan, M. D. The electrochemistry of iron porphyrin nitrosyls in the presence of pyridines and amines. *Inorg. Chim. Acta* **1988**, *153*, 25−30.

(666) Liu, Y.; DeSilva, C.; Ryan, M. D. Electrochemistry of nitrite reductase model compounds 6. Voltammetric and spectroelectrochemical studies of iron(II) nitrosyl complexes with porphyrins, hydroprophyrins and porphinones. *Inorg. Chim. Acta* **1997**, *258*, 247−255.

(667) Portela, C. F.; Magde, D.; Traylor, T. G. The ortho effect in ligation of iron tetraphenylporphyrins. *Inorg. Chem.* **1993**, *32*, 1313−1320.

(668) Li, J.; Nair, S. M.; Noll, B. C.; Schulz, C. E.; Scheidt, W. R. Relative axial ligand orientation in bis(imidazole)iron(II) porphyrinates: are "picket fence" derivatives different? *Inorg. Chem.* **2008**, *47*, 3841−3850.

(669) Li, Y.; Sharma, S. K.; Karlin, K. D. New heme-dioxygen and carbon monoxide adducts using pyridyl or imidazolyl tailed porphyrins. *Polyhedron* **2013**, *58*, 190−196.

(670) Sharma, S. K.; Kim, H.; Rogler, P. J.; Siegler, M. A.; Karlin, K. D. Isocyanide or nitrosyl complexation to hemes with varying tethered axial base ligand donors: synthesis and characterization. *JBIC, J. Biol. Inorg. Chem.* **2016**, *21*, 729−743.

(671) Suzuki, N.; Higuchi, T.; Urano, Y.; Kikuchi, K.; Uchida, T.; Mukai, M.; Kitagawa, T.; Nagano, T. First synthetic NO-heme-thiolate complex relevant to nitric oxide synthase and cytochrome P450nor. *J. Am. Chem. Soc.* **2000**, *122*, 12059−12060.

(672) Hori, H.; Ikeda-Saito, M.; Yonetani, T. Electromagnetic properties of hemoproteins. VI. Single crystal EPR of myoglobin nitroxide. Freezing-induced reversible changes in the molecular orientation of the ligand. *J. Biol. Chem.* **1981**, *256*, 7849−7855.

(673) Utterback, S. G.; Doetschman, D. C.; Szumowski, J.; Rizos, A. K. EPR study of the structure and spin distribution at the binding site in human nitrosylhemoglobin single crystals. *J. Chem. Phys.* **1983**, *78*, 5874−5880.

(674) Shiro, Y.; Fujii, M.; Isogai, Y.; Adachi, S.; Iizuka, T.; Obayashi, E.; Makino, R.; Nakahara, K.; Shoun, H. Iron-ligand structure and iron redox property of nitric oxide reductase cytochrome P450nor from *Fusarium oxysporum*: relevance to its NO reduction activity. *Biochemistry* **1995**, *34*, 9052−9058.

(675) Chiang, R.; Makino, R.; Spomer, W. E.; Hager, L. P. Chloroperoxidase: P-450 type absorption in the absence of sulfhydryl groups? *Biochemistry* **1975**, *14*, 4166−4171.

(676) Lehnert, N.; DeBeer George, S.; Solomon, E. I. Recent advances in bioinorganic spectroscopy. *Curr. Opin. Chem. Biol.* **2001**, *5*, 176−187.

(677) Zhang, Y.; Mao, J.; Oldfield, E. ^{57}Fe Mössbauer isomer shifts of heme protein model systems: electronic structure calculations. *J. Am. Chem. Soc.* **2002**, *124*, 7829−7839.

(678) Zhang, Y.; Mao, J.; Godbout, N.; Oldfield, E. Mössbauer quadrupole splittings and electronic structure in heme proteins and model systems: a density functional theory investigation. *J. Am. Chem. Soc.* **2002**, *124*, 13921−13930.

(679) Tsubaki, M.; Yu, N. T. Resonance Raman investigation of nitric oxide bonding in nitrosylhemoglobin A and -myoglobin: detection of bound nitrogen-oxygen stretching and iron-nitric oxide stretching vibrations from the hexacoordinated nitric oxide-heme complex. *Biochemistry* **1982**, *21*, 1140−1144.

(680) Benko, B.; Yu, N. T. Resonance Raman studies of nitric oxide binding to ferric and ferrous hemoproteins: Detection of Fe(III)-NO stretching, Fe(III)-N-O bending, and Fe(II)-N-O bending vibrations. *Proc. Natl. Acad. Sci. U. S. A.* **1983**, *80*, 7042−7046.

(681) Chottard, G.; Mansuy, D. Resonance Raman studies of hemoglobin complexes with nitric oxide, nitrosobenzene and nitrosomethane: Observation of the metal-ligand vibrations. *Biochem. Biophys. Res. Commun.* **1977**, *77*, 1333−1338.

(682) Coyle, C. M.; Vogel, K. M.; Rush, T. S., III; Kozlowski, P. M.; Williams, R.; Spiro, T. G.; Dou, Y.; Ikeda-Saito, M.; Olson, J. S.; Zgierski, M. Z. FeNO structure in distal pocket mutants of myoglobin based on resonance Raman spectroscopy. *Biochemistry* **2003**, *42*, 4896−4903.

(683) Stong, J. D.; Burke, J. M.; Daly, P.; Wright, P.; Spiro, T. G. Resonance Raman spectra of nitrosyl heme proteins and of porphyrin analogues. *J. Am. Chem. Soc.* **1980**, *102*, 5815−5819.

(684) Peng, Q.; Pavlik, J. W.; Silvernail, N. J.; Alp, E. E.; Hu, M. Y.; Zhao, J.; Sage, J. T.; Scheidt, W. R. 3D motions of iron in six-coordinate $\{FeNO\}^7$ hemes by nuclear resonance vibration spectroscopy. *Chem. - Eur. J.* **2016**, *22*, 6323−6332.

(685) Silvernail, N. J.; Barabanschikov, A.; Pavlik, J. W.; Noll, B. C.; Zhao, J.; Alp, E. E.; Sturhahn, W.; Sage, J. T.; Scheidt, W. R. Interplay of structure and vibrational dynamics in six-coordinate heme nitrosyls. *J. Am. Chem. Soc.* **2007**, *129*, 2200−2201.

(686) Rai, B. K.; Durbin, S. M.; Prohofsky, E. W.; Sage, J. T.; Ellison, M. K.; Roth, A.; Scheidt, W. R.; Sturhahn, W.; Alp, E. E. Direct determination of the complete set of iron normal modes in a porphyrin-imidazole model for carbonmonoxy-heme proteins: [Fe(TPP)(CO)(1-MeIm)]. *J. Am. Chem. Soc.* **2003**, *125*, 6927−6936.

(687) Leu, B. M.; Silvernail, N. J.; Zgierski, M. Z.; Wyllie, G. R. A.; Ellison, M. K.; Scheidt, W. R.; Zhao, J.; Sturhahn, W.; Alp, E. E.; Sage, J. T. Quantitative vibrational dynamics of iron in carbonyl porphyrins. *Biophys. J.* **2007**, *92*, 3764−3783.

(688) Ibrahim, M.; Xu, C.; Spiro, T. G. Differential sensing of protein influences by NO and CO vibrations in heme adducts. *J. Am. Chem. Soc.* **2006**, *128*, 16834−16845.

(689) Traylor, T. G.; Sharma, V. S. Why NO? *Biochemistry* **1992**, *31*, 2847−2849.

(690) Choi, I.-K.; Liu, Y.; Feng, D.; Paeng, K.-J.; Ryan, M. D. Electrochemical and spectroscopic studies of iron porphyrin nitrosyls and their reduction products. *Inorg. Chem.* **1991**, *30*, 1832−1839.

(691) Rahman, M. H.; Liu, Y.; Ryan, M. D. Proton transfer versus hydrogen bonding in a reduced iron porphyrin nitrosyl complex. *Inorg. Chem.* **2019**, *58*, 13788−13795.

(692) Rahman, M. H.; Ryan, M. D. Redox and spectroscopic properties of iron porphyrin nitroxyl in the presence of weak acids. *Inorg. Chem.* **2017**, *56*, 3302−3309.

(693) Patra, A. K.; Dube, K. S.; Sanders, B. C.; Papaefthymiou, G. C.; Conradie, J.; Ghosh, A.; Harrop, T. C. A thermally stable $\{FeNO\}^8$ complex: properties and biological reactivity of reduced MNO systems. *Chem. Sci.* **2012**, *3*, 364−369.

(694) Sanders, B. C.; Patra, A. K.; Harrop, T. C. Synthesis, properties, and reactivity of a series of non-heme $\{FeNO\}^{7/8}$ complexes: implications for Fe-nitroxyl coordination. *J. Inorg. Biochem.* **2013**, *118*, 115−127.

(695) Kundakarla, N.; Lindeman, S.; Rahman, M. H.; Ryan, M. D. X-ray structure and properties of the ferrous octaethylporphyrin nitroxyl complex. *Inorg. Chem.* **2016**, *55*, 2070−2075.

(696) Pellegrino, J.; Bari, S. E.; Bikiel, D. E.; Doctorovich, F. Successful stabilization of the elusive species $\{FeNO\}^8$ in a heme model. *J. Am. Chem. Soc.* **2010**, *132*, 989−995.

(697) Hu, B.; Li, J. One electron makes differences: from heme $\{FeNO\}^7$ to $\{FeNO\}^8$. *Angew. Chem., Int. Ed.* **2015**, *54*, 10579−10582.

(698) Mazzeo, A. M.; Pellegrino, J.; Doctorovich, F. Water-soluble nitroxyl porphyrin complexes Fe^{II}TPPSHNO and Fe^{II}TPPSNO$^-$ obtained from isolated Fe^{II}TPPSNO$^\bullet$. *J. Am. Chem. Soc.* **2019**, *141*, 18521−18530.

(699) Goodrich, L. E.; Lehnert, N. The *trans* effect of nitroxyl (HNO) in ferrous heme systems: Implications for soluble guanylate cyclase activation by HNO. *J. Inorg. Biochem.* **2013**, *118*, 179−186.

(700) Kimura, H.; Mittal, C. K.; Murad, F. Activation of guanylate cyclase from rat liver and other tissues by sodium azide. *J. Biol. Chem.* **1975**, *250*, 8016−8022.

(701) Dierks, E. A.; Burstyn, J. N. Nitric oxide (NO·), the only nitrogen monoxide redox form capable of activating soluble guanylyl cyclase. *Biochem. Pharmacol.* **1996**, *51*, 1593−1600.

(702) Horst, B. G.; Stewart, E. M.; Nazarian, A. A.; Marletta, M. A. Characterization of a carbon monoxide-activated soluble guanylate cyclase from *Chlamydomonas reinhardtii*. *Biochemistry* **2019**, *58*, 2250−2259.

(703) Moncada, S.; Martin, J. F.; et al. VASODILATION: evolution of nitric oxide. *Lancet* **1993**, *341*, 1511.

(704) Ribeiro, J. M. C.; Nussenzveig, R. H. Nitric oxide synthase activity from a hematophagous insect salivary gland. *FEBS Lett.* **1993**, *330*, 165−168.

(705) Mollace, V.; Salvemini, D.; Anggard, E.; Vane, J. Nitric oxide from vascular smooth muscle cells: regulation of platelet reactivity and smooth muscle cell guanylate cyclase. *Br. J. Pharmacol.* **1991**, *104*, 633−638.

(706) Andersen, J. F.; Champagne, D. E.; Weichsel, A.; Ribeiro, J. M. C.; Balfour, C. A.; Dress, V.; Montfort, W. R. Nitric oxide binding and crystallization of recombinant nitrophorin I, a nitric oxide transport protein from the blook-sucking bug *Rhodnius Proxilus*. *Biochemistry* **1997**, *36*, 4423−4428.

(707) Martí, M. A.; Lebrero, M. C. G.; Roitberg, A. E.; Estrin, D. A. Bond or cage effect: how nitrophorins transport and release nitric oxide. *J. Am. Chem. Soc.* **2008**, *130*, 1611−1618.

(708) Berry, R. E.; Shokhirev, M. N.; Ho, A. Y. W.; Yang, F.; Shokhireva, T. K.; Zhang, H.; Weichsel, A.; Montfort, W. R.; Walker, F. A. Effect of mutation of carboxyl side-chain amino acids near the heme on the midpoint potentials and ligand binding constants of nitrophorin 2 and its NO, histamine, and imidazole complexes. *J. Am. Chem. Soc.* **2009**, *131*, 2313−2327.

(709) Valenzuela, J. G.; Walker, F. A.; Ribeiro, J. M. C. A salivary nitrophorin (nitric-oxide-carrying hemoprotein) in the bedbug *Cimex lectularius*. *J. Exp. Biol.* **1995**, *198*, 1519−1526.

(710) Moreira, M. F.; Coelho, H. S. L.; Zingali, R. B.; Oliveira, P. L.; Masuda, H. Changes in salivary nitrophorin profile during the life cycle of the blood-sucking bug *Rhodnius prolixus*. *Insect Biochem. Mol. Biol.* **2003**, *33*, 23−28.

(711) Ribeiro, J. M. C.; Andersen, J.; Silva-Neto, M. A. C.; Pham, V. M.; Garfield, M. K.; Valenzuela, J. G. Exploring the sialome of the blood-sucking bug *Rhodnius prolixus*. *Insect Biochem. Mol. Biol.* **2004**, *34*, 61−79.

(712) Andersen, J. F.; Gudderra, N. P.; Francischetti, I. M. B.; Valenzuela, J. G.; Ribeiro, J. M. C. Recognition of anionic phospholipid membranes by an antihemostatic protein from a blood-feeding insect. *Biochemistry* **2004**, *43*, 6987−6994.

(713) Sweet, M. H. On the original feeding habits of the *Hemiptera* (Insecta). *Ann. Entomol. Soc. Am.* **1979**, *72*, 575−579.

(714) Champagne, D. E.; Nussenzveig, R. H.; Ribeiro, J. M. C. Purification, partial characterization, and cloning of nitric oxide-carrying heme proteins (nitrophorins) from salivary glands of the blood-sucking insect *Rhodnius prolixus*. *J. Biol. Chem.* **1995**, *270*, 8691−8695.

(715) Walker, F. A.; Montfort, W. R. The nitric oxide-releasing heme proteins from the saliva of the blood-sucking insect *Rhodnius prolixus*. *Adv. Inorg. Chem.* **2000**, *51*, 295−358.

(716) *Parasites - American Trypanosomiasis (also known as Chagas Disease)*; Centers for Disease Control and Prevention, 2019. https://www.cdc.gov/parasites/chagas/index.html (accessed 07-09-2021).

(717) Desforges, J. F.; Kirchhoff, L. V. American trypanosomiasis (Chagas' disease)–a tropical disease now in the United States. *N. Engl. J. Med.* **1993**, *329*, 639−644.

(718) McNeil, D. G., Jr. Rare infection threatens to spread in blood supply. *New York Times* **2003**, 18.

(719) Almeida, I. C.; Camargo, M. M.; Procópio, D. O.; Silva, L. S.; Mehlert, A.; Travassos, L. R.; Gazzinelli, R. T.; Ferguson, M. A. J. Highly purified glycosylphosphatidylinositols from *Trypanosoma cruzi* are potent proinflammatory agents. *The EMBO Journal* **2000**, *19*, 1476−1485.

(720) Moreno, B.; Urbina, J. A.; Oldfield, E.; Bailey, B. N.; Rodrigues, C. O.; Docampo, R. ^{31}P NMR spectroscopy of *Trypanosoma brucei*, *Trypanosoma cruzi*, and *Leishmania major*: Evidence for high levels of condensed inorganic phosphates. *J. Biol. Chem.* **2000**, *275*, 28356−28362.

(721) De Avalos, S. V.; Blader, I. J.; Fisher, M.; Boothroyd, J. C.; Burleigh, B. A. Immediate/early response to *Trypanosoma cruzi* infection involves minimal modulation of host cell transcription. *J. Biol. Chem.* **2002**, *277*, 639−644.

(722) Nozaki, T.; Shigeta, Y.; Saito-Nakano, Y.; Imada, M.; Kruger, W. D. Characterization of transsulfuration and cysteine biosynthetic pathways in the protozoan hemoflagellate, *Trypanosoma cruzi*: isolation and molecular characterization of cystathionine β-synthase and serine acetyltransferase from *Trypanosoma*. *J. Biol. Chem.* **2001**, *276*, 6516−6523.

(723) Wilkinson, S. R.; Meyer, D. J.; Taylor, M. C.; Bromley, E. V.; Miles, M. A.; Kelly, J. M. The *Trypanosoma cruzi* enzyme TcGPXI is a glycosomal peroxidase and can be linked to trypanothione reduction by glutathione or tryparedoxin. *J. Biol. Chem.* **2002**, *277*, 17062−17071.

(724) Wilkinson, S. R.; Temperton, N. J.; Mondragon, A.; Kelly, J. M. Distinct mitochondrial and cytosolic enzymes mediate trypanothione-dependent peroxide metabolism in *Trypanosoma cruzi*. *J. Biol. Chem.* **2000**, *275*, 8220−8225.

(725) Pavão, F.; Castilho, M. S.; Pupo, M. T.; Dias, R. L. A.; Correa, A. G.; Fernandes, J. B.; da Silva, M. F. G. F.; Mafezoli, J.; Vieira, P. C.; Oliva, G. Structure of *Trypanosoma cruzi* glycosomal glyceraldehyde-3-phosphate dehydrogenase complexed with chalepin, a natural product inhibitor, at 1.95 resolution. *FEBS Lett.* **2002**, *520*, 13−17.

(726) Rigden, D. J.; Monteiro, A. C. S.; de Sá, M. F. G. The protease inhibitor chagasin of *Trypanosoma cruzi* adopts an immunoglobulin-type fold and may have arisen by horizontal gene transfer. *FEBS Lett.* **2001**, *504*, 41−44.

(727) Villalta, F.; Smith, C. M.; Ruiz-Ruano, A.; Lima, M. F. A ligand that *Trypanosoma cruzi* uses to bind to mammalian cells to initiate infection. *FEBS Lett.* **2001**, *505*, 383−388.

(728) Reyes-Vivas, H.; Hernández-Alcantara, G.; López-Velazquez, G.; Cabrera, N.; Pérez-Montfort, R.; Tuena de Gómez-Puyou, M.; Gómez-Puyou, A. Factors that control the reactivity of the interface cysteine of triosephosphate isomerase from *Trypanosoma brucei* and *Trypanosoma cruzi*. *Biochemistry* **2001**, *40*, 3134−3140.

(729) Oza, S. L.; Tetaud, E.; Ariyanayagam, M. R.; Warnon, S. S.; Fairlamb, A. H. A single enzyme catalyses formation of trypanothione from glutathione and spermidine in *Trypanosoma cruzi*. *J. Biol. Chem.* **2002**, *277*, 35853−35861.

(730) Navarro, M.; Cisneros-Fajardo, E. J.; Lehmann, T.; Sánchez-Delgado, R. A.; Atencio, R.; Silva, P.; Lira, R.; Urbina, J. A. Toward a novel metal-based chemotherapy against tropical diseases. 6. Synthesis and characterization of new copper(II) and gold(I) clotrimazole and ketoconazole complexes and evaluation of their activity against *Trypanosoma cruzi*. *Inorg. Chem.* **2001**, *40*, 6879−6884.

(731) Pereira, C. A.; Alonso, G. D.; Ivaldi, S.; Silber, A.; Alves, M. J. M.; Bouvier, L. A.; Flawiá, M. M.; Torres, H. N. Arginine metabolism in *Trypanosoma cruzi* is coupled to parasite stage and replication. *FEBS Lett.* **2002**, *526*, 111−114.

(732) Judice, W. A. S.; Cezari, M. H. S.; Lima, A. P. C. A.; Scharfstein, J.; Chagas, J. R.; Tersariol, I. L. S.; Juliano, M. A.; Juliano, L. Comparison of the specificity, stability and individual rate constants with respective activation parameters for the peptidase activity of cruzipain and its recombinant form, cruzain, from *Trypanosoma cruzi*. *Eur. J. Biochem.* **2001**, *268*, 6578−6586.

(733) Pereira, C. A.; Alonso, G. D.; Paveto, M. C.; Iribarren, A.; Cabanas, M. L.; Torres, H. N.; Flawiá, M. M. *Trypanosoma cruzi* arginine kinase characterization and cloning: a novel energetic pathway in protozoan parasites. *J. Biol. Chem.* **2000**, *275*, 1495−1501.

(734) Kirchhoff, L. V.; Bacchi, C. J.; Wittner, M.; Tanowitz, H. B. American Trypanosomiasis (Chagas disease). *Curr. Treat Options Infect. Dis.* **2000**, *2*, 59−65.

(735) Silva, A. C. C.; Brelaz-de-Castro, M. C. A.; Leite, A. C. L.; Pereira, V. R. A.; Hernandes, M. Z. Chagas disease treatment and rational drug discovery: a challenge that remains. *Front. Pharmacol.* **2019**, *10*, 873.

(736) Müller Kratz, J. Drug discovery for chagas disease: A viewpoint. *Acta Trop.* **2019**, *198*, 105107.

(737) Andersen, J. F.; Weichsel, A.; Balfour, C. A.; Champagne, D. E.; Montfort, W. R. The crystal structure of nitrophorin 4 at 1.5 å resolution: transport of nitric oxide by a lipocalin-based heme protein. *Structure* **1998**, *6*, 1315−1327.

(738) Andersen, J. F.; Montfort, W. R. The crystal structure of nitrophorin 2: a trifunctional antihemostatic protein from the saliva of *Rhodnius prolixus*. *J. Biol. Chem.* **2000**, *275*, 30496−30503.

(739) Flower, D. R. The lipocalin protein family: structure and function. *Biochem. J.* **1996**, *318*, 1−14.

(740) Vetter, S. W.; Terentis, A. C.; Osborne, R. L.; Dawson, J. H.; Goodin, D. B. Replacement of the axial histidine heme ligand with cysteine in nitrophorin 1: spectroscopic and crystallographic characterization. *JBIC, J. Biol. Inorg. Chem.* **2009**, *14*, 179−191.

(741) Weichsel, A.; Montfort, W. R. Conformational change and heme ruffling in nitrophorin 2, a nitric oxide carrier from kissing bug. *RCSB Protein Data Bank*, in press.

(742) Weichsel, A.; Berry, R. E.; Walker, F. A.; Montfort, W. R. Crystal structures, ligand induced conformational change and heme deformation in complexes of nitrophorin 2, a nitric oxide transport protein from *Rhodnius prolixus*. *RCSB Protein Data Bank*, in press.

(743) Shokhireva, T. K.; Weichsel, A.; Smith, K. M.; Berry, R. E.; Shokhirev, N. V.; Balfour, C. A.; Zhang, H.; Montfort, W. R.; Walker, F. A. Assignment of the ferriheme resonances of the low-spin complexes of nitrophorins 1 and 4 by ^{1}H and ^{13}C NMR spectroscopy: comparison to structural data obtained from X-ray crystallography. *Inorg. Chem.* **2007**, *46*, 2041−2056.

(744) Kondrashov, D. A.; Roberts, S. A.; Weichsel, A.; Montfort, W. R. Protein functional cycle viewed at atomic resolution: conformational change and mobility in nitrophorin 4 as a function of pH and NO binding. *Biochemistry* **2004**, *43*, 13637−13647.

(745) Amoia, A. M.; Montfort, W. R. Heme distortion in nitrophorin 4: high resolution structures of mutated positions L123V and L133V and heme altered proteins. *RCSB Protein Data Bank*, in press.

(746) Maes, E. M.; Weichsel, A.; Andersen, J. F.; Shepley, D.; Montfort, W. R. Role of binding site loops in controlling nitric oxide release: structure and kinetics of mutant forms of nitrophorin 4. *Biochemistry* **2004**, *43*, 6679−6690.

(747) Amoia, A. M.; Montfort, W. R. Ligand protection and nitric oxide intermediates with heme in nitrophorin 4: kinetic and structural analyses of a loop mutant. *RCSB Protein Data Bank*, in press.

(748) Nienhaus, K.; Maes, E. M.; Weichsel, A.; Montfort, W. R.; Nienhaus, G. U. Structural dynamics controls nitric oxide affinity in nitrophorin 4. *J. Biol. Chem.* **2004**, *279*, 39401−39407.

(749) Amoia, A. M.; Montfort, W. R. Apo-nitrophorin 4 at atomic resolution. *Protein Sci.* **2007**, *16*, 2076−2081.

(750) Weichsel, A.; Badgandi, H.; Montfort, W. R. Crystal structure of *Cimex* nitrophorin NO complex. *RCSB Protein Data Bank*, in press.

(751) Weichsel, A.; Badgandi, H.; Montfort, W. R. Crystallographic and spectroscopic characterization of ferrous complexes of *Cimex* nitrophorin, a heme-thiolate protein from the bedbug. *RCSB Protein Data Bank*, in press.

(752) Weichsel, A.; Montfort, W. R. Structure of *Cimex* nitrophorin complex with carbon monoxide. *RCSB Protein Data Bank*, in press.

(753) Maes, E. M.; Walker, F. A.; Montfort, W. R.; Czernuszewicz, R. S. Resonance Raman spectroscopic study of nitrophorin 1, a nitric oxide-binding heme protein form *Rhodnius prolixus* and its nitrosyl and cyano adducts. *J. Am. Chem. Soc.* **2001**, *123*, 11664−11672.

(754) Menyhárd, D. K.; Keserü, G. M. Protonation state of Asp30 exerts crucial influence over surface loop rearrangements responsible for NO release in nitrophorin 4. *FEBS Lett.* **2005**, *579*, 5392−5398.

(755) Kondrashov, D. A.; Montfort, W. R. Nonequilibrium dynamics simulations of nitric oxide release: Comparative study of nitrophorin and myoglobin. *J. Phys. Chem. B* **2007**, *111*, 9244−9252.

(756) Swails, J. M.; Meng, Y.; Walker, F. A.; Marti, M. A.; Estrin, D. A.; Roitberg, A. E. pH-dependant mechanism of nitric oxide release in nitrophorins 2 and 4. *J. Phys. Chem. B* **2009**, *113*, 1192−1201.

(757) Ribeiro, J. M. C.; Walker, F. A. High affinity histamine-binding and antihistaminic activity of the salivary nitric oxide-carrying heme protein (nitrophorin) of *Rhodnius prolixus*. *J. Exp. Med.* **1994**, *180*, 2251−2257.

(758) Ribeiro, J. M. C.; Schneider, M.; Guimaraes, J. A. Purification and characterization of prolixin S (nitrophorin 2), the salivary anticoagulant of the blood-sucking bug *Rhodnius prolixus*. *Biochem. J.* **1995**, *308*, 243−249.

(759) Sun, J.; Yamaguchi, M.; Yuda, M.; Miura, K.; Takeya, H.; Hirai, M.; Matsuoka, H. P.; Ando, K.; Watanabe, T.; Suzuki, K.; Chinzei, Y. Purification, characterization and cDNA cloning of a novel anticoagulant of the intrinsic pathway, (prolixin-S) from salivary gland of the blood sucking bug, *Rhodnius proxilus*. *Thromb. Haemostasis* **1996**, *75*, 573−577.

(760) Andersen, J. F.; Gudderra, N. P.; Francischetti, I. M. B.; Ribeiro, J. M. C. The role of salivary lipocalins in blood feeding by *Rhodnius prolixus*. *Arch. Insect Biochem. Physiol.* **2005**, *58*, 97−105.

(761) Callahan, M. K.; Williamson, P.; Schlegel, R. A. Surface expression of phosphatidylserine on macrophages is required for phagocytosis of apoptotic thymocytes. *Cell Death Differ.* **2000**, *7*, 645−653.

(762) Hirt, U. A.; Leist, M. Rapid, noninflammatory and PS-dependent phagocytic clearance of necrotic cells. *Cell Death Differ.* **2003**, *10*, 1156−1164.

(763) Scheidt, W. R. Systematics of the stereochemistry of porphyrins and metalloporphyrins. *The Porphyrin Handbook*; Kadish, K. M., Smith, K. M., Guilard, R., Eds.; Academic Press: New York, 2000; Vol. *3*, Chapter 16; pp 49−112.

(764) Liptak, M. D.; Wen, X.; Bren, K. L. NMR and DFT investigation of heme ruffling: Functional implications for cytochrome c. *J. Am. Chem. Soc.* **2010**, *132*, 9753−9763.

(765) Can, M.; Krucinska, J.; Zoppellaro, G.; Andersen, N. H.; Wedekind, J. E.; Hersleth, H.-P.; Andersson, K. K.; Bren, K. L. Structural characterization of *Nitrosomonas europaea* cytochrome c_{552} variants with marked differences in electronic structure. *ChemBioChem* **2013**, *14*, 1828.

(766) Shokhireva, T. K.; Berry, R. E.; Uno, E.; Balfour, C. A.; Zhang, H.; Walker, F. A. Electrochemical and NMR spectroscopic studies of distal pocket mutants of nitrophorin 2: Stability, structure, and dynamics of axial ligand complexes. *Proc. Natl. Acad. Sci. U. S. A.* **2003**, *100*, 3778−3783.

(767) Scheidt, W. R.; Lee, Y. J.; Hatano, K. Preparation and structural characterization of nitrosyl complexes of ferric porphyrinates. Molecular structure of aquonitrosyl(meso-tetraphenylporphinato)-iron(III) perchlorate and nitrosyl(octaethylporphinato)iron(III) perchlorate. *J. Am. Chem. Soc.* **1984**, *106*, 3191−3198.

(768) Scheidt, W. R.; Ellison, M. K. The synthetic and structural chemistry of heme derivatives with nitric oxide ligands. *Acc. Chem. Res.* **1999**, *32*, 350−359.

(769) Li, J.; Peng, Q.; Oliver, A. G.; Alp, E. E.; Hu, M. Y.; Zhao, J.; Sage, J. T.; Scheidt, W. R. Comprehensive Fe-ligand vibration identification in $\{FeNO\}^{6}$ hemes. *J. Am. Chem. Soc.* **2014**, *136*, 18100−18110.

(770) Lanucara, F.; Chiavarino, B.; Crestoni, M. E.; Scuderi, D.; Sinha, R. K.; MaÑtre, P.; Fornarini, S. Naked five-coordinate $Fe^{III}(NO)$ porphyrin complexes: vibrational and reactivity features. *Inorg. Chem.* **2011**, *50*, 4445−4452.

(771) Ellison, M. K.; Schulz, C. E.; Scheidt, W. R. Structural and electronic characterization of nitrosyl(octaethylporphinato)iron(III) perchlorate derivatives. *Inorg. Chem.* **2000**, *39*, 5102−5110.

(772) Linder, D. P.; Rodgers, K. R.; Banister, J.; Wyllie, G. R. A.; Ellison, M. K.; Scheidt, W. R. Five-coordinate $Fe^{III}NO$ and $Fe^{II}CO$ porphyrinates: where are the electrons and why does it matter? *J. Am. Chem. Soc.* **2004**, *126*, 14136−14148.

(773) Yi, G.-B.; Chen, L.; Khan, M. A.; Richter-Addo, G. B. Activation of thionitrites and isoamyl nitrite by group 8 metalloporphyrins and the subsequent generation of nitrosyl thiolates and alkoxides of ruthenium and osmium porphyrins. *Inorg. Chem.* **1997**, *36*, 3876−3885.

(774) Shimizu, H.; Park, S. Y.; Lee, D. S.; Shoun, H.; Shiro, Y. Crystal structures of cytochrome P450nor and its mutants (Ser286 Val, Thr) in the ferric resting state at cryogenic temperature: a comparative analysis with monooxygenase cytochrome P450s. *J. Inorg. Biochem.* **2000**, *81*, 191−205.

(775) Lipscomb, L. A.; Lee, B.-S.; Yu, N.-T. Resonance Raman investigation of nitric oxide bonding in iron porphyrins: detection of the Fe-NO stretching vibration. *Inorg. Chem.* **1993**, *32*, 281−286.

(776) Ellison, M. K.; Scheidt, W. R. Synthesis, molecular structures, and properties of six-coordinate $[Fe(OEP)(L)(NO)]^+$ derivatives: elusive nitrosyl ferric porphyrins. *J. Am. Chem. Soc.* **1999**, *121*, 5210−5219.

(777) Ellison, M. K.; Schulz, C. E.; Scheidt, W. R. Nitrosyliron(III) porphyrinates: porphyrin core conformation and FeNO geometry. Any correlation? *J. Am. Chem. Soc.* **2002**, *124*, 13833−13841.

(778) Xu, N.; Powell, D. R.; Cheng, L.; Richter-Addo, G. B. The first structurally characterized nitrosyl heme thiolate model complex. *Chem. Commun.* **2006**, 2030−2032.

(779) Richter-Addo, G. B.; Wheeler, R. A.; Hixson, C. A.; Chen, L.; Khan, M. A.; Ellison, M. K.; Schulz, C. E.; Scheidt, W. R. Unexpected nitrosyl-group bending in six-coordinate $\{M(NO)\}^6$ -bonded aryl-(iron) and -(ruthenium) porphyrins. *J. Am. Chem. Soc.* **2001**, *123*, 6314−6326.

(780) Ellison, M. K.; Schulz, C. E.; Scheidt, W. R. Syntheses, characterization, and structural studies of several (nitro)(nitrosyl)-iron(III) porphyrinates: $[Fe(Porph)(NO_2)(NO)]$. *Inorg. Chem.* **1999**, *38*, 100−108.

(781) Xu, N.; Goodrich, L. E.; Lehnert, N.; Powell, D. R.; Richter-Addo, G. B. Preparation of the elusive (por)Fe(NO)(O-ligand) complex by diffusion of nitric oxide into a crystal of the precursor. *Angew. Chem., Int. Ed.* **2013**, *52*, 3896−3900.

(782) Wang, Y.; Averill, B. A. Direct observation by FTIR spectroscopy of the ferrous heme-NO^+ intermediate in reduction of nitrite by a dissimilatory heme cd_1 nitrite reductase. *J. Am. Chem. Soc.* **1996**, *118*, 3972−3973.

(783) Sampath, V.; Zhao, J.; Caughey, W. S. Characterization of interactions of nitric oxide with human hemoglobin A by infrared spectroscopy. *Biochem. Biophys. Res. Commun.* **1994**, *198*, 281−287.

(784) Tomita, T.; Haruta, N.; Aki, M.; Kitagawa, T.; Ikeda-Saito, M. UV resonance Raman detection of a ligand vibration on ferric nitrosyl heme proteins. *J. Am. Chem. Soc.* **2001**, *123*, 2666−2667.

(785) Arnold, E. V.; Bohle, D. S. Isolation and oxygenation reactions of nitrosylmyoglobins. *Methods Enzymol.* **1996**, *2269*, 41−55.

(786) Pinakoulaki, E.; Gemeinhardt, S.; Saraste, M.; Varotsis, C. Nitric-oxide reductase. Structure and properties of the catalytic site from resonance Raman scattering. *J. Biol. Chem.* **2002**, *277*, 23407−23413.

(787) Wang, J.; Lu, S.; Moënne-Loccoz, P.; Ortiz de Montellano, P. R. Interaction of nitric oxide with human heme oxygenase-1. *J. Biol. Chem.* **2003**, *278*, 2341−2347.

(788) Higgins, T. B.; Safo, M. K.; Scheidt, W. R. Molecular structure of bis (1-methylimidazole)(meso-tetraphenylporphinato) iron (III) perchlorate. *Inorg. Chim. Acta* **1990**, *178*, 261−267.

(789) Spiro, T. G.; Ibrahim, M.; Wasbotten, I. H. CO, NO, and O_2 as vibrational probes of heme protein active sites. *The Smallest Biomolecules: Diatomics and their Interactions with Heme Proteins*; Ghosh, A., Ed.; Elseviere: Amsterdam, Netherlands, 2008; pp 95−123.

(790) Soldatova, A. V.; Ibrahim, M.; Olson, J. S.; Czernuszewicz, R. S.; Spiro, T. G. New light on NO bonding in Fe(III) heme proteins from resonance Raman spectroscopy and DFT modeling. *J. Am. Chem. Soc.* **2010**, *132*, 4614−4625.

(791) Linder, D. P.; Rodgers, K. R. Fe-N-O structure and bonding in six-coordinate $\{FeNO\}^6$ porphyrinates containing imidazole: implications for reactivity of coordinated NO. *Inorg. Chem.* **2005**, *44*, 1367−1380.

(792) Hunt, A. P.; Lehnert, N. The thiolate trans effect in heme $\{FeNO\}^6$ complexes and beyond: insight into the nature of the push effect. *Inorg. Chem.* **2019**, *58*, 11317−11332.

(793) Scheidt, W. R.; Hatano, K.; Rupprecht, G. A.; Piciulo, P. L. Nitrosylmetallopophyrins. 5. Molecular stereochemistry of nitrosyl (5,10,15,20-tetratolylporphinato)manganese(II) and nitrosyl(4-methylpiperidine)(5,10,15,20-tetraphenylporphinato)manganese(II). *Inorg. Chem.* **1979**, *18*, 292−299.

(794) Merkle, A. C.; McQuarters, A. B.; Lehnert, N. Synthesis, spectroscopic analysis and photolabilization of water soluble ruthenium(III)-nitrosyl complexes. *Dalton Trans.* **2012**, *41*, 8047−8059.

(795) Heilman, B. J.; Gonzales, M. A.; Mascharak, P. K. Photoactive metal nitrosyl and carbonyl complexes derived from designed auxiliary ligands: an emerging class of photochemotherapeutics. *Prog. Inorg. Chem.* **2014**, *58*, 185−224.

(796) Rodrigues, F. P.; Pestana, C. R.; Polizello, A. C. M.; Pardo-Andreu, G. L.; Uyemura, S. A.; Santos, A. C.; Alberici, L. C.; da Silva, R. S.; Curti, C. Release of NO from a nitrosyl ruthenium complex through oxidation of mitochondrial NADH and effects on mitochondria. *Nitric Oxide* **2012**, *26*, 174−181.

(797) Rodrigues, F. P.; Carneiro, Z. A.; Mascharak, P.; Curti, C.; da Silva, R. S. Incorporation of a ruthenium nitrosyl complex into liposomes, the nitric oxide released from these liposomes and HepG2 cell death mechanism. *Coord. Chem. Rev.* **2016**, *306*, 701−707.

(798) Caramori, G. F.; Kunitz, A. G.; Andriani, K. F.; Doro, F. G.; Frenking, G.; Tfouni, E. The nature of Ru-NO bonds in ruthenium tetraazamacrocycle nitrosyl complexes — a computational study. *Dalton Trans.* **2012**, *41*, 7327−7339.

(799) Lahiri, G. K.; Kaim, W. Electronic structure alternatives in nitrosylruthenium complexes. *Dalton Trans.* **2010**, *39*, 4471−4478.

(800) Tfouni, E.; Krieger, M.; McGarvey, B. R.; Franco, D. W. Structure, chemical and photochemical reactivity and biological activity of some ruthenium amine nitrosyl complexes. *Coord. Chem. Rev.* **2003**, *236*, 57−69.

(801) Rose, M. J.; Mascharak, P. K. Photoactive ruthenium nitrosyls: Effects of light and potential application as NO donors. *Coord. Chem. Rev.* **2008**, *252*, 2093−2114.

(802) Shelnutt, J. A.; Song, X.-Z.; Ma, J.-G.; Jia, S.-L.; Jentzen, W.; Medforth, C. J. Nonplanar porphyrins and their significance in proteins. *Chem. Soc. Rev.* **1998**, *27*, 31−41.

(803) Kadish, K. M.; D'Souza, F.; Villard, A.; Autret, M.; Van Caemelbecke, E.; Bianco, P.; Antonini, A.; Tagliatesta, P. Effect of porphyrin ring distortion on redox potentials of beta-brominated-pyrrole iron(III) tetraphenylporphyrins. *Inorg. Chem.* **1994**, *33*, 5169−5170.

(804) Tagliatesta, P.; Li, J.; Autret, M.; Van Caemelbecke, E.; Villard, A.; D'Souza, F.; Kadish, K. M. Electrochemistry and spectral characterization of oxidized and reduced $(TPPBr_x)FeCl$ where $TPPBr_x$ is the dianion of beta-brominated-pyrrole tetraphenylporphyrin and x varies from 0 to 8. *Inorg. Chem.* **1996**, *35*, 5570−5576.

(805) Duval, H.; Bulach, V.; Fischer, J.; Renner, M. W.; Fajer, J.; Weiss, R. Correlation of macrocycle distortion with oxidation potentials of iron(III) porphyrins: molecule structure of teh sterically crowded chloro-iron(III) 7,8,17,18-tetrabromo-5,10,15,20-tetraphenylporphyrin. *JBIC, J. Biol. Inorg. Chem.* **1997**, *2*, 662−666.

(806) Nesset, M. J. M.; Shokhirev, N. V.; Enemark, P. D.; Jacobson, S. E.; Walker, F. A. Models of the cytochromes. redox properties and thermodynamic stabilities of complexes of "hindered" iron(III) and iron(II) tetraphenylporphyrinates with substituted pyridines and imidazoles. *Inorg. Chem.* **1996**, *35*, 5188−5200.

(807) Ema, T.; Senge, M. O.; Nelson, N. Y.; Ogoshi, H.; Smith, K. M. 5, 10, 15, 20-tetra-tert-butylporphyrin and its remarkable reactivity in the 5- and 15-positions. *Angew. Chem., Int. Ed. Engl.* **1994**, *33*, 1879−1881.

(808) Jentzen, W.; Simpson, M. C.; Hobbs, J. D.; Song, X.; Ema, T.; Nelson, N. Y.; Medforth, C. J.; Smith, K. M.; Veyrat, M.; Mazzanti, M.; et al. Ruffling in a series of nickel(II) meso-tetrasubstituted porphyrins as a model for the conserved ruffling of the heme of cytochromes *c*. *J. Am. Chem. Soc.* **1995**, *117*, 11085−11097.

(809) Ehrenberg, A.; Szczepkowski, T. W.; et al. Properties and structure of the compounds formed between cytochrome *c* and nitric oxide. *Acta Chem. Scand.* **1960**, *14*, 1684−1692.

(810) Addison, A. W.; Stephanos, J. J. Nitrosyliron(III) hemoglobin: autoreduction and spectroscopy. *Biochemistry* **1986**, *25*, 4104−4113.

(811) Walker, F. A. Magnetic spectroscopic (EPR, ESEEM, Mössbauer, MCD and NMR) studies of low-spin ferriheme centers and their corresponding heme proteins. *Coord. Chem. Rev.* **1999**, *185*, 471−534.

(812) Yatsunyk, L. A.; Carducci, M. D.; Walker, F. A. Low-spin ferriheme models of the cytochromes: correlation of molecular structure with EPR spectral type. *J. Am. Chem. Soc.* **2003**, *125*, 15986−16005.

(813) Safo, M. K.; Gupta, G. P.; Watson, C. T.; Simonis, U.; Walker, F. A.; Scheidt, W. R. Models of the cytochromes *b*. Low-spin bis-ligated (porphinato)iron(III) complexes with unusual molecular structures and NMR, EPR, and Moessbauer spectra. *J. Am. Chem. Soc.* **1992**, *114*, 7066−7075.

(814) Ogura, H.; Yatsunyk, L.; Medforth, C. J.; Smith, K. M.; Barkigia, K. M.; Renner, M. W.; Melamed, D.; Walker, F. A. Molecular structures and magnetic resonance spectroscopic investigations of highly distorted six-coordinate low-spin iron(III) porphyrinate complexes. *J. Am. Chem. Soc.* **2001**, *123*, 6564−6578.

(815) Walker, F. A. Models of the bis-histidine-ligated electron-transferring cytochromes. Comparative geometric and electronic structure of low-spin ferro-and ferrihemes. *Chem. Rev.* **2004**, *104*, 589−616.

(816) Safo, M. K.; Walker, F. A.; Raitsimring, A. M.; Walters, W. P.; Dolata, D. P.; Debrunner, P. G.; Scheidt, W. R. Axial ligand orientation in iron(III) porphyrinates: effect of axial d-acceptors. Characterization of the low-spin complex $[Fe(TPP(4\text{-}CNPy)_2]ClO_4$. *J. Am. Chem. Soc.* **1994**, *116*, 7760−7770.

(817) Yatsunyk, L. A.; Walker, F. A. NMR and EPR spectroscopic and structural studies of low-spin, $(d_{xz}, d_{yz})^4 (d_{xy})^1$ ground state Fe(III) bis-tert-butylisocyanide complexes of dodecasubstituted porphyrins. *Inorg. Chem.* **2004**, *43*, 4341−4352.

(818) Walker, F. A.; Nasri, H.; Turowska-Tyrk, I.; Mohanrao, K.; Watson, C. T.; Shokhirev, N. V.; Debrunner, P. G.; Scheidt, W. R. Acid ligands in iron(III) porphyrinates. Characterization of low-spin bis(tert-butylisocyanide)(porphyrinato) iron(III) complexes having $(d_{xz}, d_{yz})^4 (d_{xy})^1$ ground states. *J. Am. Chem. Soc.* **1996**, *118*, 12109−12118.

(819) Simonneaux, G.; Schunemann, V.; Morice, C.; Carel, L.; Toupet, L.; Winkler, H.; Trautwein, A. X.; Walker, F. A. Structural, magnetic, and dynamic characterization of the $(d_{xz}, d_{yz})^4 (d_{xy})^1$ ground-state low-spin iron(III) tetraphenylporphyrinate complex $[(p\text{-TTP})Fe(2,6\text{-XylylNC})_2]CF_3SO_3$. *J. Am. Chem. Soc.* **2000**, *122*, 4366−4377.

(820) Ikeue, T.; Ohgo, Y.; Saitoh, T.; Nakamura, M.; Fujii, H.; Yokoyama, M. Spin distribution in low-spin (meso-tetraalkylporphyrinato) iron(III) complexes with $(d_{xz}, d_{yz})^4 (d_{xy})^1$ configuration. Studies by ^{1}H NMR, ^{13}C NMR, and EPR spectroscopies. *J. Am. Chem. Soc.* **2000**, *122*, 4068−4076.

(821) Ikezaki, A.; Tukada, H.; Nakamura, M. Control of electronic structure of a six-coordinate iron(III) porphyrin radical by means of axial ligands. *Chem. Commun.* **2008**, 2257−2259.

(822) Ohgo, Y.; Neya, S.; Hashizume, D.; Ozeki, T.; Nakamura, M. Unusual electronic structure of bis-isocyanide complexes of iron(III) porphyrinoids. *Dalton Trans.* **2012**, *41*, 3126−3129.

(823) Moeser, B.; Janoschka, A.; Wolny, J. A.; Paulsen, H.; Filippov, I.; Berry, R. E.; Zhang, H.; Chumakov, A. I.; Walker, F. A.; Schünemann, V. Nuclear inelastic scattering and Mössbauer spectroscopy as local probes for ligand binding modes and electronic properties in proteins: vibrational behavior of a ferriheme center inside a β-barrel protein. *J. Am. Chem. Soc.* **2012**, *134*, 4216−4228.

(824) Valenzuela, J. G.; Ribeiro, J. M. C. Purification and cloning of the salivary nitrophorin from the hemipteran *Cimex lectularius*. *J. Exp. Biol.* **1998**, *201*, 2659−2664.

(825) Poulos, T. L. The role of the proximal ligand in heme enzymes. *JBIC, J. Biol. Inorg. Chem.* **1996**, *1*, 356−359.

(826) Couture, M.; Adak, S.; Stuehr, D. J.; Rousseau, D. L. Regulation of the properties of the heme-NO complexes in nitric-oxide synthase by hydrogen bonding to the proximal cysteine. *J. Biol. Chem.* **2001**, *276*, 38280−38288.

(827) Yoshioka, S.; Tosha, T.; Takahashi, S.; Ishimori, K.; Hori, H.; Morishima, I. Roles of the proximal hydrogen bonding network in cytochrome P450cam-catalyzed oxygenation. *J. Am. Chem. Soc.* **2002**, *124*, 14571−14579.

(828) Galinato, M. G. I.; Spolitak, T.; Ballou, D. P.; Lehnert, N. Elucidating the role of the hydrogen bonding network in ferric cytochrome P450cam and corresponding mutants using magnetic circular dichroism spectroscopy. *Biochemistry* **2011**, *50*, 1053−1069.

(829) Peisach, J.; Blumberg, W. E.; Ogawa, S.; Rachmilewitz, E. A.; Oltzik, R. The effects of protein conformation on the heme symmetry in high spin ferric heme proteins as studied by electron paramagnetic resonance. *J. Biol. Chem.* **1971**, *246*, 3342−3355.

(830) Chevion, M.; Peisach, J.; Blumberg, W. E. Imidazole, the ligand trans to mercaptide in ferric cytochrome P-450. An EPR study of proteins and model compounds. *J. Biol. Chem.* **1977**, *252*, 3637−3645.

(831) Franke, A.; Roncaroli, F.; van Eldik, R. Mechanistic studies on the activation of NO by iron and cobalt complexes. *Eur. J. Inorg. Chem.* **2007**, *2007*, 773−798.

(832) Chacón Villalba, M. E.; Güida, J. A.; Varetti, E. L.; Aymonino, P. J. The structure of the FeNO group in two metastable states (MS1 and MS2) of the nitroprusside anion in $Na_2[Fe(CN)_5NO]\bullet 2H_2O$. Infrared spectra and quantum chemistry calculations for the normal and the ^{15}NO and N^{18}O isotopic substituted substance. *Inorg. Chem.* **2003**, *42*, 2622−2627.

(833) Lim, M. D.; Lorkovic, I. M.; Ford, P. C. NO and NO_x interactions with group 8 metalloporphyrins. *J. Inorg. Biochem.* **2005**, *99*, 151−165.

(834) Fernandez, B. O.; Lorkovic, I. M.; Ford, P. C. Nitrite catalyzes reductive nitrosylation of the water-soluble ferri-heme model Fe^{III}(TPPS) to Fe^{II}(TPPS)(NO). *Inorg. Chem.* **2003**, *42*, 2−4.

(835) Fernandez, B. O.; Lorkovic, I. M.; Ford, P. C. Mechanisms of ferriheme reduction by nitric oxide: nitrite and general base catalysis. *Inorg. Chem.* **2004**, *43*, 5393−5402.

(836) Hoshino, M.; Maeda, M.; Konishi, R.; Seki, H.; Ford, P. C. Studies on the reaction mechanisms for reductive nitrosylation of ferrihemoproteins in buffer solutions. *J. Am. Chem. Soc.* **1996**, *118*, 5702−5707.

(837) Foglia, N. O.; Bari, S. E.; Estrin, D. A. In silico insight into the reductive nitrosylation of ferric hemeproteins. *Inorg. Chem.* **2020**, *59*, 3631−3641.

(838) Olson, J. S.; Mathews, A. J.; Rohlfs, R. J.; Springer, B. A.; Egeberg, K. D.; Sligar, S. G.; Tame, J.; Renaud, J. P.; Nagai, K. The role of the distal histidine in myoglobin and haemoglobin. *Nature* **1988**, *336*, 265−266.

(839) Smith, B. C.; Marletta, M. A. Mechanisms of S-nitrosothiol formation and selectivity in nitric oxide signaling. *Curr. Opin. Chem. Biol.* **2012**, *16*, 498−506.

(840) Mu, X. H.; Kadish, K. M. In situ FTIR and UV-visible spectroelectrochemical studies of iron nitrosyl porphyrins in non-aqueous media. *Inorg. Chem.* **1988**, *27*, 4720−4725.

(841) He, C.; Howes, B. D.; Smulevich, G.; Rumpel, S.; Reijerse, E. J.; Lubitz, W.; Cox, N.; Knipp, M. Nitrite dismutase reaction mechanism: kinetic and spectroscopic investigation of the interaction between nitrophorin and nitrite. *J. Am. Chem. Soc.* **2015**, *137*, 4141−4150.

(842) He, C.; Ogata, H.; Knipp, M. Formation of the complex of nitrite with the ferriheme b β-barrel proteins nitrophorin 4 and nitrophorin 7. *Biochemistry* **2010**, *49*, 5841−5851.

(843) Kleinbongard, P.; Dejam, A.; Lauer, T.; Rassaf, T.; Schindler, A.; Picker, O.; Scheeren, T.; Gödecke, A.; Schrader, J.; Schulz, R.; et al. Plasma nitrite reflects constitutive nitric oxide synthase activity in mammals. *Free Radical Biol. Med.* **2003**, *35*, 790−796.

(844) He, C.; Knipp, M. Formation of nitric oxide from nitrite by the ferriheme *b* protein nitrophorin 7. *J. Am. Chem. Soc.* **2009**, *131*, 12042−12043.

(845) Nasri, H.; Wang, Y.; Hanh, H. B.; Walker, F. A.; Scheidt, W. R. Reactions of bis(nitro)(α-tetrakis(*o*-pivalamidophenyl)porphinato)-ferrate(III) with pyridine and imidazole. EPR and Moessbauer spectra and molecular structures of the mixed-ligand species. *Inorg. Chem.* **1991**, *30*, 1483−1489.

(846) He, C.; Ogata, H.; Knipp, M. Insertion of an H-bonding residue into the distal pocket of the ferriheme protein nitrophorin 4: effect on nitrite iron coordination and nitrite disproportionation. *Chem. Biodiversity* **2012**, *9*, 1761−1775.

(847) He, C.; Ogata, H.; Lubitz, W. Elucidation of the heme active site electronic structure affecting the unprecedented nitrite dismutase activity of the ferriheme *b* proteins, the nitrophorins. *Chem. Sci.* **2016**, *7*, 5332−5340.

(848) Thomas, D. D.; Liu, X.; Kantrow, S. P.; Lancaster, J. R., Jr. The biological lifetime of nitric oxide: implications for the perivascular dynamics of NO and O2. *Proc. Natl. Acad. Sci. U. S. A.* **2001**, *98*, 355−360.

(849) Hetrick, E. M.; Prichard, H. L.; Klitzman, B.; Schoenfisch, M. H. Reduced foreign body response at nitric oxide-releasing subcutaneous implants. *Biomaterials* **2007**, *28*, 4571−4580.

(850) Pant, J.; Goudie, M. J.; Hopkins, S. P.; Brisbois, E. J.; Handa, H. Tunable nitric oxide release from S-nitroso-N-acetylpenicillamine via catalytic copper nanoparticles for biomedical applications. *ACS Appl. Mater. Interfaces* **2017**, *9*, 15254−15264.

(851) Kanias, T.; Wang, L.; Lippert, A.; Kim-Shapiro, D. B.; Gladwin, M. T. Red blood cell endothelial nitric oxide synthase does not modulate red blood cell storage hemolysis. *Transfusion (Malden, MA, U. S.)* **2013**, *53*, 981−989.

(852) Lundberg, J. O.; Weitzberg, E.; Gladwin, M. T. The nitrate-nitrite-nitric oxide pathway in physiology and therapeutics. *Nat. Rev. Drug Discovery* **2008**, *7*, 156−167.

(853) Shiva, S.; Huang, Z.; Grubina, R.; Sun, J.; Ringwood, L. A.; MacArthur, P. H.; Xu, X.; Murphy, E.; Darley-Usmar, V. M.; Gladwin, M. T. Deoxymyoglobin is a nitrite reductase that generates nitric oxide and regulates mitochondrial respiration. *Circ. Res.* **2007**, *100*, 654−661.

(854) Aamand, R.; Dalsgaard, T.; Jensen, F. B.; Simonsen, U.; Roepstorff, A.; Fago, A. Generation of nitric oxide from nitrite by carbonic anhydrase: a possible link between metabolic activity and vasodilation. *Am. J. Physiol.* **2009**, *297*, H2068−H2074.

(855) Maia, L. B.; Moura, J. J. G. Nitrite reduction by xanthine oxidase family enzymes: a new class of nitrite reductases. *JBIC, J. Biol. Inorg. Chem.* **2011**, *16*, 443−460.

(856) Webb, A.; Bond, R.; McLean, P.; Uppal, R.; Benjamin, N.; Ahluwalia, A. Reduction of nitrite to nitric oxide during ischemia protects against myocardial ischemia-reperfusion damage. *Proc. Natl. Acad. Sci. U. S. A.* **2004**, *101*, 13683.

(857) Webb, A. J.; Milsom, A. B.; Rathod, K. S.; Chu, W. L.; Qureshi, S.; Lovell, M. J.; Lecomte, F. MJ.; Perrett, D.; Raimondo, C.; Khoshbin, E.; Ahmed, Z.; Uppal, R.; Benjamin, N.; Hobbs, A. J.; Ahluwalia, A. Mechanisms underlying erythrocyte and endothelial nitrite reduction to nitric oxide in hypoxia. *Circ. Res.* **2008**, *103*, 957−964.

(858) Baker, J. E.; Su, J.; Fu, X.; Hsu, A.; Gross, G. J.; Tweddell, J. S.; Hogg, N. Nitrite confers protection against myocardial infarction: role of xanthine oxidoreductase, NADPH oxidase and K(ATP) channels. *J. Mol. Cell. Cardiol.* **2007**, *43*, 437−444.

(859) Crawford, J. H.; Isbell, T. S.; Huang, Z.; Shiva, S.; Chacko, B. K.; Schechter, A. N.; Darley-Usmar, V. M.; Kerby, J. D.; Lang, J. D., Jr.; Kraus, D.; Ho, C.; Gladwin, M. T.; Patel, R. P. Hypoxia, red blood cells, and nitrite regulate NO-dependent hypoxic vasodilation. *Blood* **2006**, *107*, 566−574.

(860) Duranski, M. R.; Greer, J. J. M.; Dejam, A.; Jaganmohan, S.; Hogg, N.; Langston, W.; Patel, R. P.; Yet, S.-F.; Wang, X.; Kevil, C. G.; Gladwin, M. T.; Lefer, D. J. Cytoprotective effects of nitrite during in vivo ischemia-reperfusion of the heart and liver. *J. Clin. Invest.* **2005**, *115*, 1232−1240.

(861) Hunter, C. J.; Dejam, A.; Blood, A. B.; Shields, H.; Kim-Shapiro, D. B.; Machado, R. F.; Tarekegn, S.; Mulla, N.; Hopper, A. O.; Schechter, A. N.; Power, G. G.; Gladwin, M. T. Inhaled nebulized nitrite is a hypoxia-sensitive NO-dependent selective pulmonary vasodilator. *Nat. Med.* **2004**, *10*, 1122−1127.

(862) Nagababu, E.; Ramasamy, S.; Abernethy, D. R.; Rifkind, J. M. Active nitric oxide produced in the red cell under hypoxic conditions by deoxyhemoglobin-mediated nitrite reduction. *J. Biol. Chem.* **2003**, *278*, 46349−46356.

(863) Totzeck, M.; Hendgen-Cotta, U. B.; Luedike, P.; Berenbrink, M.; Klare, J. P.; Steinhoff, H.-J.; Semmler, D.; Shiva, S.; Williams, D.; Kipar, A.; Gladwin, M. T.; Schrader, J.; Kelm, M.; Cossins, A. R.; Rassaf, T. Nitrite regulates hypoxic vasodilation via myoglobin-dependent nitric oxide generation. *Circulation* **2012**, *126*, 325−334.

(864) Zhang, Z.; Naughton, D.; Winyard, P. G.; Benjamin, N.; Blake, D. R.; Symons, M. C. R. Generation of Nitric Oxide by a Nitrite Reductase Activity of Xanthine Oxidase: A Potential Pathway for Nitric Oxide Formation in the Absence of Nitric Oxide Synthase Activity. *Biochem. Biophys. Res. Commun.* **1998**, *249*, 767−772.

(865) Salhany, J. M. Kinetics of reaction of nitrite with deoxy hemoglobin after rapid deoxygenation or predeoxygenation by dithionite measured in solution and bound to the cytoplasmic domain of band 3 (SLC4A1). *Biochemistry* **2008**, *47*, 6059−6072.

(866) Bryan, N. S.; Calvert, J. W.; Elrod, J. W.; Gundewar, S.; Ji, S. Y.; Lefer, D. J. Dietary nitrite supplementation protects against myocardial ischemia-reperfusion injury. *Proc. Natl. Acad. Sci. U. S. A.* **2007**, *104*, 19144.

(867) Dezfulian, C.; Raat, N.; Shiva, S.; Gladwin, M. T. Role of the anion nitrite in ischemia-reperfusion cytoprotection and therapeutics. *Cardiovasc. Res.* **2007**, *75*, 327−338.

(868) Dejam, A.; Hunter, C. J.; Tremonti, C.; Pluta, R. M.; Hon, Y. Y.; Grimes, G.; Partovi, K.; Pelletier, M. M.; Oldfield, E. H.; Cannon, R. O., 3rd; Schechter, A. N.; Gladwin, M. T. Nitrite infusion in humans and nonhuman primates: endocrine effects, pharmacokinetics, and tolerance formation. *Circulation* **2007**, *116*, 1821−1831.

(869) Bryan, N. S.; Calvert, J. W.; Gundewar, S.; Lefer, D. J. Dietary nitrite restores NO homeostasis and is cardioprotective in endothelial nitric oxide synthase-deficient mice. *Free Radical Biol. Med.* **2008**, *45*, 468−474.

(870) Huang, Z.; Shiva, S.; Kim-Shapiro, D. B.; Patel, R. P.; Ringwood, L. A.; Irby, C. E.; Huang, K. T.; Ho, C.; Hogg, N.; Schechter, A. N.; Gladwin, M. T. Enzymatic function of hemoglobin as a nitrite reductase that produces NO under allosteric control. *J. Clin. Invest.* **2005**, *115*, 2099−2107.

(871) Gladwin, M. T.; Raat, N. J. H.; Shiva, S.; Dezfulian, C.; Hogg, N.; Kim-Shapiro, D. B.; Patel, R. P. Nitrite as a vascular endocrine nitric oxide reservoir that contributes to hypoxic signaling, cytoprotection, and vasodilation. *Am. J. Physiol. Heart Circ. Physiol.* **2006**, *291*, H2026−H2035.

(872) Raat, N. J. H.; Noguchi, A. C.; Liu, V. B.; Raghavachari, N.; Liu, D.; Xu, X.; Shiva, S.; Munson, P. J.; Gladwin, M. T. Dietary nitrate and nitrite modulate blood and organ nitrite and the cellular ischemic stress response. *Free Radical Biol. Med.* **2009**, *47*, 510−517.

(873) Kozlov, A. V.; Costantino, G.; Sobhian, B.; Szalay, L.; Umar, F.; Nohl, H.; Bahrami, S.; Redl, H. Mechanisms of vasodilatation induced by nitrite instillation in intestinal lumen: possible role of hemoglobin. *Antioxid. Redox Signaling* **2005**, *7*, 515−521.

(874) Tsuchiya, K.; Kanematsu, Y.; Yoshizumi, M.; Ohnishi, H.; Kirima, K.; Izawa, Y.; Shikishima, M.; Ishida, T.; Kondo, S.; Kagami, S.; Takiguchi, Y.; Tamaki, T. Nitrite is an alternative source of NO in vivo. *Am. J. Physiol. Heart Circ. Physiol.* **2005**, *288*, H2163−H2170.

(875) Hataishi, R.; Rodrigues, A. C.; Neilan, T. G.; Morgan, J. G.; Buys, E.; Shiva, S.; Tambouret, R.; Jassal, D. S.; Raher, M. J.; Furutani, E.; Ichinose, F.; Gladwin, M. T.; Rosenzweig, A.; Zapol, W. M.; Picard, M. H.; Bloch, K. D.; Scherrer-Crosbie, M. Inhaled nitric oxide decreases infarction size and improves left ventricular function in a

murine model of myocardial ischemia-reperfusion injury. *Am. J. Physiol. Heart Circ. Physiol.* **2006**, *291*, H379−H384.

(876) Dalsgaard, T.; Simonsen, U.; Fago, A. Nitrite-dependent vasodilation is facilitated by hypoxia and is independent of known NO-generating nitrite reductase activities. *Am. J. Physiol. Heart Circ. Physiol.* **2007**, *292*, H3072−H3078.

(877) Isbell, T. S.; Gladwin, M. T.; Patel, R. P. Hemoglobin oxygen fractional saturation regulates nitrite-dependent vasodilation of aortic ring bioassays. *Am. J. Physiol. Heart Circ. Physiol.* **2007**, *293*, H2565−H2572.

(878) Rassaf, T.; Flögel, U.; Drexhage, C.; Hendgen-Cotta, U.; Kelm, M.; Schrader, J. Nitrite reductase function of deoxymyoglobin. *Circ. Res.* **2007**, *100*, 1749−1754.

(879) Alzawahra, W. F.; Talukder, M. A. H.; Liu, X.; Samouilov, A.; Zweier, J. L. Heme proteins mediate the conversion of nitrite to nitric oxide in the vascular wall. *Am. J. Physiol. Heart Circ. Physiol.* **2008**, *295*, H499−H508.

(880) Hendgen-Cotta, U. B.; Merx, M. W.; Shiva, S.; Schmitz, J.; Becher, S.; Klare, J. P.; Steinhoff, H.-J.; Goedecke, A.; Schrader, J.; Gladwin, M. T.; Kelm, M.; Rassaf, T. Nitrite reductase activity of myoglobin regulates respiration and cellular viability in myocardial ischemia-reperfusion injury. *Proc. Natl. Acad. Sci. U. S. A.* **2008**, *105*, 10256.

(881) Minneci, P. C.; Deans, K. J.; Shiva, S.; Zhi, H.; Banks, S. M.; Kern, S.; Natanson, C.; Solomon, S. B.; Gladwin, M. T. Nitrite reductase activity of hemoglobin as a systemic nitric oxide generator mechanism to detoxify plasma hemoglobin produced during hemolysis. *Am. J. Physiol. Heart Circ. Physiol.* **2008**, *295*, H743−H754.

(882) Dufour, S. P.; Patel, R. P.; Brandon, A.; Teng, X.; Pearson, J.; Barker, H.; Ali, L.; Yuen, A. H. Y.; Smolenski, R. T.; González-Alonso, J. Erythrocyte-dependent regulation of human skeletal muscle blood flow: role of varied oxyhemoglobin and exercise on nitrite, S-nitrosohemoglobin, and ATP. *Am. J. Physiol. Heart Circ. Physiol.* **2010**, *299*, H1936−H1946.

(883) Cantu-Medellin, N.; Vitturi, D. A.; Rodriguez, C.; Murphy, S.; Dorman, S.; Shiva, S.; Zhou, Y.; Jia, Y.; Palmer, A. F.; Patel, R. P. Effects of T- and R-state stabilization on deoxyhemoglobin-nitrite reactions and stimulation of nitric oxide signaling. *Nitric Oxide* **2011**, *25*, 59−69.

(884) Ormerod, J. O. M.; Ashrafian, H.; Maher, A. R.; Arif, S.; Steeples, V.; Born, G. V. R.; Egginton, S.; Feelisch, M.; Watkins, H.; Frenneaux, M. P. The role of vascular myoglobin in nitrite-mediated blood vessel relaxation. *Cardiovasc. Res.* **2011**, *89*, 560−565.

(885) Patel, R. P.; Hogg, N.; Kim-Shapiro, D. B. The potential role of the red blood cell in nitrite-dependent regulation of blood flow. *Cardiovasc. Res.* **2011**, *89*, 507−515.

(886) Tiso, M.; Tejero, J.; Basu, S.; Azarov, I.; Wang, X.; Simplaceanu, V.; Frizzell, S.; Jayaraman, T.; Geary, L.; Shapiro, C.; Ho, C.; Shiva, S.; Kim-Shapiro, D. B.; Gladwin, M. T. Human neuroglobin functions as a redox-regulated nitrite reductase. *J. Biol. Chem.* **2011**, *286*, 18277−18289.

(887) Li, H.; Hemann, C.; Abdelghany, T. M.; El-Mahdy, M. A.; Zweier, J. L. Characterization of the mechanism and magnitude of cytoglobin-mediated nitrite reduction and nitric oxide generation under anaerobic conditions. *J. Biol. Chem.* **2012**, *287*, 36623−36633.

(888) Benjamin, N.; O'Driscoll, F.; Dougall, H.; Duncan, C.; Smith, L.; Golden, M.; McKenzie, H. Stomach NO synthesis. *Nature* **1994**, *368*, 502−502.

(889) Li, H.; Liu, X.; Cui, H.; Chen, Y.-R.; Cardounel, A. J.; Zweier, J. L. Characterization of the mechanism of cytochrome P450 reductase-cytochrome P450-mediated nitric oxide and nitrosothiol generation from organic nitrates. *J. Biol. Chem.* **2006**, *281*, 12546−12554.

(890) Gago, B.; Lundberg, J. O.; Barbosa, R. M.; Laranjinha, J. Red wine-dependent reduction of nitrite to nitric oxide in the stomach. *Free Radical Biol. Med.* **2007**, *43*, 1233−1242.

(891) Umbrello, M.; Dyson, A.; Pinto, B. B.; Fernandez, B. O.; Simon, V.; Feelisch, M.; Singer, M. Short-term hypoxic vasodilation in vivo is mediated by bioactive nitric oxide metabolites, rather than free nitric oxide derived from haemoglobin-mediated nitrite reduction. *J. Physiol. (Oxford, U. K.)* **2014**, *592*, 1061−1075.

(892) Jung, K.-H.; Chu, K.; Ko, S.-Y.; Lee, S.-T.; Sinn, D.-I.; Park, D.-K.; Kim, J.-M.; Song, E.-C.; Kim, M.; Roh, J.-K. Early intravenous infusion of sodium nitrite protects brain against in vivo ischemia-reperfusion injury. *Stroke* **2006**, *37*, 2744−2750.

(893) Sun, Y.; Jin, K.; Mao, X. O.; Zhu, Y.; Greenberg, D. A. Neuroglobin is up-regulated by and protects neurons from hypoxic-ischemic injury. *Proc. Natl. Acad. Sci. U. S. A.* **2001**, *98*, 15306.

(894) Sun, Y.; Jin, K.; Peel, A.; Mao, X. O.; Xie, L.; Greenberg, D. A. Neuroglobin protects the brain from experimental stroke in vivo. *Proc. Natl. Acad. Sci. U. S. A.* **2003**, *100*, 3497.

(895) Herold, S.; Fago, A.; Weber, R. E.; Dewilde, S.; Moens, L. Reactivity studies of the Fe(III) and Fe(II)NO forms of human neuroglobin reveal a potential role against oxidative stress. *J. Biol. Chem.* **2004**, *279*, 22841−22847.

(896) Khan, A. A.; Wang, Y.; Sun, Y.; Mao, X. O.; Xie, L.; Miles, E.; Graboski, J.; Chen, S.; Ellerby, L. M.; Jin, K.; Greenberg, D. A. Neuroglobin-overexpressing transgenic mice are resistant to cerebral and myocardial ischemia. *Proc. Natl. Acad. Sci. U. S. A.* **2006**, *103*, 17944.

(897) Singh, S.; Manda, S. M.; Sikder, D.; Birrer, M. J.; Rothermel, B. A.; Garry, D. J.; Mammen, P. P. A. Calcineurin activates cytoglobin transcription in hypoxic myocytes. *J. Biol. Chem.* **2009**, *284*, 10409−10421.

(898) Halligan, K. E.; Jourd'heuil, F. L.; Jourd'heuil, D. Cytoglobin is expressed in the vasculature and regulates cell respiration and proliferation via nitric oxide dioxygenation. *J. Biol. Chem.* **2009**, *284*, 8539−8547.

(899) Liu, X.; Follmer, D.; Zweier, J. R.; Huang, X.; Hemann, C.; Liu, K.; Druhan, L. J.; Zweier, J. L. Characterization of the function of cytoglobin as an oxygen-dependent regulator of nitric oxide concentration. *Biochemistry* **2012**, *51*, 5072−5082.

(900) Gardner, A. M.; Cook, M. R.; Gardner, P. R. Nitric-oxide dioxygenase function of human cytoglobin with cellular reductants and in rat hepatocytes. *J. Biol. Chem.* **2010**, *285*, 23850−23857.

(901) Millar, T. M.; Stevens, C. R.; Benjamin, N.; Eisenthal, R.; Harrison, R.; Blake, D. R. Xanthine oxidoreductase catalyses the reduction of nitrates and nitrite to nitric oxide under hypoxic conditions. *FEBS Lett.* **1998**, *427*, 225−228.

(902) Godber, B. L. J.; Doel, J. J.; Sapkota, G. P.; Blake, D. R.; Stevens, C. R.; Eisenthal, R.; Harrison, R. Reduction of nitrite to nitric oxide catalyzed by xanthine oxidoreductase. *J. Biol. Chem.* **2000**, *275*, 7757−7763.

(903) Li, H.; Samouilov, A.; Liu, X.; Zweier, J. L. Characterization of the magnitude and kinetics of xanthine oxidase-catalyzed nitrite reduction: Evaluation of its role in nitric oxide generation in anoxic tissues. *J. Biol. Chem.* **2001**, *276*, 24482−24489.

(904) Li, H.; Samouilov, A.; Liu, X.; Zweier, J. L. Characterization of the magnitude and kinetics of xanthine oxidase-catalyzed nitrate reduction: Evaluation of its role in nitrite and nitric oxide generation in anoxic tissues. *Biochemistry* **2003**, *42*, 1150−1159.

(905) Li, H.; Samouilov, A.; Liu, X.; Zweier, J. L. Characterization of the effects of oxygen on xanthine oxidase-mediated nitric oxide formation. *J. Biol. Chem.* **2004**, *279*, 16939−16946.

(906) Doyle, M. P.; Hoekstra, J. W. Oxidation of nitrogen oxides by bound dioxygen in hemoproteins. *J. Inorg. Biochem.* **1981**, *14*, 351−358.

(907) Lundberg, J. O.; Govoni, M. Inorganic nitrate is a possible source for systemic generation of nitric oxide. *Free Radical Biol. Med.* **2004**, *37*, 395−400.

(908) Chilvers, C.; Inskip, H.; Caygill, C.; Bartholomew, B.; Fraser, P.; Hill, M. A survey of dietary nitrate in well-water users. *Int. J. Epidemiol.* **1984**, *13*, 324−331.

(909) Weitzberg, E.; Lundberg, J. O. N. Nonenzymatic nitric oxide production in humans. *Nitric Oxide* **1998**, *2*, 1−7.

(910) Duncan, C.; Dougall, H.; Johnston, P.; Green, S.; Brogan, R.; Leifert, C.; Smith, L.; Golden, M.; Benjamin, N. Chemical generation

of nitric oxide in the mouth from the enterosalivary circulation of dietary nitrate. *Nat. Med.* **1995**, *1*, 546−551.

(911) Tannenbaum, S. R.; Correa, P. Nitrate and gastric cancer risks. *Nature* **1985**, *317*, 675−676.

(912) Kapil, V.; Khambata, R. S.; Jones, D. A.; Rathod, K.; Primus, C.; Massimo, G.; Fukuto, J. M.; Ahluwalia, A. The noncanonical pathway for *in vivo* nitric oxide generation: the nitrate-nitrite-nitric oxide pathway. *Pharmacol. Rev.* **2020**, *72*, 692.

(913) Wink, D. A.; Nims, R. W.; Darbyshire, J. F.; Christodoulou, D.; Hanbauer, I.; Cox, G. W.; Laval, F. L. J.; Cook, J. A.; Krishna, M. C.; DeGraff, W.; Mitchell, J. B. Reaction kinetics for nitrosation of cysteine and glutathione in aerobic nitric oxide solutions at neutral pH. Insights into the fate and physiological effects of intermediates generated in the NO/O_2 reaction. *Chem. Res. Toxicol.* **1994**, *7*, 519−525.

(914) Pryor, W. A.; Church, D. F.; Govindan, C. K.; Crank, G. Oxidation of thiols by nitric oxide and nitrogen dioxide: synthetic utility and toxicological implications. *J. Org. Chem.* **1982**, *47*, 156−159.

(915) Stamler, J. S.; Jaraki, O.; Osborne, J.; Simon, D. I.; Keaney, J.; Vita, J.; Singel, D.; Valeri, C. R.; Loscalzo, J. Nitric oxide circulates in mammalian plasma primarily as an S nitroso adduct of serum albumin. *Proc. Natl. Acad. Sci. U. S. A.* **1992**, *89*, 7674−7677.

(916) Williams, D. L. H.: *Nitrosation*; Cambridge University Press: New York, 1988; pp 173−194.

(917) Stamler, J. S.; Simon, D.; Osborne, J.; Mullins, M.; Jaraki, O.; Michel, T.; Singel, D. J.; Loscalzo, J. S-nitrosylation of proteins with nitric oxide: synthesis and characterization of biologically active compounds. *Proc. Natl. Acad. Sci. U. S. A.* **1992**, *89*, 444−448.

(918) Stamler, J. S.; Osborne, J. A.; Jaraki, O.; Rabbani, L. E.; Mullins, M.; Singel, D. J.; Loscalzo, J. Adverse vascular effects of homocysteine are modulated by endothelium-derived relaxing factor and related oxides of nitrogen. *J. Clin. Invest.* **1993**, *91*, 308−318.

(919) Luchsinger, B. P.; Rich, E. N.; Gow, A. J.; Williams, E. M.; Stamler, J. S.; Singel, D. J. Routes to S-nitroso-hemoglobin formation with heme redox and preferential reactivity in the beta subunits. *Proc. Natl. Acad. Sci. U. S. A.* **2003**, *100*, 461−466.

(920) Reichenbach, G.; Sabatini, S.; Palombari, R.; Palmerini, C. A. Reaction mechanism between nitric oxide and glutathione mediated by Fe(III) myoglobin. *Nitric Oxide* **2001**, *5*, 395−401.

(921) Stamler, J. S.; Jaraki, O.; Osborne, J.; Simon, D. I.; Keaney, J.; Vita, J.; Singel, D.; Valeri, C. R.; Loscalzo, J. Nitric oxide circulates in mammalian plasma primarily as an S-nitroso adduct of serum albumin. *Proc. Natl. Acad. Sci. U. S. A.* **1992**, *89*, 7674−7677.

(922) Muller, B.; Kleschyov, A. L.; Alencar, J. L.; Vanin, A.; Stoclet, J.-C. Nitric oxide transport and storage in the cardiovascular system. *Ann. N. Y. Acad. Sci.* **2002**, *962*, 131−139.

(923) Jaffrey, S. R.; Erdjument-Bromage, H.; Ferris, C. D.; Tempst, P.; Snyder, S. H. Protein S-nitrosylation: a physiological signal for neuronal nitric oxide. *Nat. Cell Biol.* **2001**, *3*, 193−197.

(924) Gonzalez-Alonso, J.; Olsen, D. B.; Saltin, B. Erythrocyte and the regulation of human skeletal muscle blood flow and oxygen delivery: role of circulating ATP. *Circ. Res.* **2002**, *91*, 1046−1055.

(925) Dejam, A.; Hunter, C. J.; Pelletier, M. M.; Hsu, L. L.; Machado, R. F.; Shiva, S.; Power, G. G.; Kelm, M.; Gladwin, M. T.; Schechter, A. N. Erythrocytes are the major intravascular storage sites of nitrite in human blood. *Blood* **2005**, *106*, 734−739.

(926) Tannenbaum, S. R.; White, F. M. Regulation and specificity of S-nitrosylation and denitrosylation. *ACS Chem. Biol.* **2006**, *1*, 615−618.

(927) Hess, D. T.; Matsumoto, A.; Kim, S.-O.; Marshall, H. E.; Stamler, J. S. Protein S-nitrosylation: purview and parameters. *Nat. Rev. Mol. Cell Biol.* **2005**, *6*, 150−166.

(928) Lancaster, J. R. Nitroxidative, nitrosative, and nitrative stress: Kinetic predictions of reactive nitrogen species chemistry under biological conditions. *Chem. Res. Toxicol.* **2006**, *19*, 1160−1174.

(929) Nikitovic, D.; Holmgren, A. S-nitrosoglutathione is cleaved by the thioredoxin system with liberation of glutathione and redox regulating nitric oxide. *J. Biol. Chem.* **1996**, *271*, 19180−19185.

(930) Sliskovic, I.; Raturi, A.; Mutus, B. Characterization of the S-denitrosation activity of protein disulfide isomerase. *J. Biol. Chem.* **2005**, *280*, 8733−8741.

(931) Uehara, T.; Nakamura, T.; Yao, D.; Shi, Z.-Q.; Gu, Z.; Ma, Y.; Masliah, E.; Nomura, Y.; Lipton, S. A. S-Nitrosylated protein-disulphide isomerase links protein misfolding to neurodegeneration. *Nature* **2006**, *441*, 513−517.

(932) Zai, A.; Rudd, M. A.; Scribner, A. W.; Loscalzo, J. Cell-surface protein disulfide isomerase catalyzes transnitrosation and regulates intracellular transfer of nitric oxide. *J. Clin. Invest.* **1999**, *103*, 393−399.

(933) Wo, Y.; Brisbois, E. J.; Bartlett, R. H.; Meyerhoff, M. E. Recent advances in thromboresistant and antimicrobial polymers for biomedical applications: just say yes to nitric oxide (NO). *Biomater. Sci.* **2016**, *4*, 1161−1183.

(934) Hopkins, S. P.; Frost, M. C. S-nitroso-N-acetyl-D-penicillamine modified hyperbranched polyamidoamine for high-capacity nitric oxide storage and release. *Bioengineering* **2020**, *7*, 7.

(935) Qin, Y.; Zajda, J.; Brisbois, E. J.; Ren, H.; Toomasian, J. M.; Major, T. C.; Rojas-Pena, A.; Carr, B.; Johnson, T.; Haft, J. W.; Bartlett, R. H.; Hunt, A. P.; Lehnert, N.; Meyerhoff, M. E. Portable nitric oxide (NO) generator based on electrochemical reduction of nitrite for potential applications in inhaled NO therapy and cardiopulmonary bypass surgery. *Mol. Pharmaceutics* **2017**, *14*, 3762−3771.

(936) Konopińska, K. K.; Schmidt, N. J.; Hunt, A. P.; Lehnert, N.; Wu, J.; Xi, C.; Meyerhoff, M. E. Comparison of copper(II)-ligand complexes as mediators for preparing electrochemically modulated nitric oxide-releasing catheters. *ACS Appl. Mater. Interfaces* **2018**, *10*, 25047−25055.

(937) Hunt, A. P.; Batka, A. E.; Hosseinzadeh, M.; Gregory, J. D.; Haque, H. K.; Ren, H.; Meyerhoff, M. E.; Lehnert, N. Nitric oxide generation on demand for biomedical applications via electrocatalytic nitrite reduction by copper BMPA- and BEPA-carboxylate complexes. *ACS Catal.* **2019**, *9*, 7746−7758.

(938) Megson, I. L.; Morton, S.; Greig, I. R.; Mazzei, F. A.; Field, R. A.; Butler, A. R.; Caron, G.; Gasco, A.; Fruttero, R.; Webb, D. J. N-Substituted analogues of S-nitroso-N-acetyl-D,L-penicillamine: chemical stability and prolonged nitric oxide mediated vasodilatation in isolated rat femoral arteries. *Br. J. Pharmacol.* **1999**, *126*, 639−648.

(939) Radomski, M. W.; Rees, D. D.; Dutra, A.; Moncada, S. S-nitroso-glutathione inhibits platelet activation in vitro and in vivo. *Br. J. Pharmacol.* **1992**, *107*, 745−749.

(940) Roy, B.; du Moulinet d'Hardemare, A.; Fontecave, M. New thionitrites: Synthesis, stability, and nitric oxide generation. *J. Org. Chem.* **1994**, *59*, 7019−7026.

(941) Wu, X.; Tang, X.; Xian, M.; Wang, P. G. Glycosylated diazeniumdiolates: a novel class of enzyme-activated nitric oxide donors. *Tetrahedron Lett.* **2001**, *42*, 3779−3782.

(942) Maragos, C. M.; Morley, D.; Wink, D. A.; Dunams, T. M.; Saavedra, J. E.; Hoffman, A.; Bove, A. A.; Isaac, L.; Hrabie, J. A.; Keefer, L. K. Complexes of.NO with nucleophiles as agents for the controlled biological release of nitric oxide. Vasorelaxant effects. *J. Med. Chem.* **1991**, *34*, 3242−3247.

(943) Hrabie, J. A.; Klose, J. R.; Wink, D. A.; Keefer, L. K. New nitric oxide-releasing zwitterions derived from polyamines. *J. Org. Chem.* **1993**, *58*, 1472−1476.

(944) Saavedra, J. E.; Southan, G. J.; Davies, K. M.; Lundell, A.; Markou, C.; Hanson, S. R.; Adrie, C.; Hurford, W. E.; Zapol, W. M.; Keefer, L. K. Localizing antithrombotic and vasodilatory activity with a novel, ultrafast nitric oxide donor. *J. Med. Chem.* **1996**, *39*, 4361−4365.

(945) Zhang, R.; Zhang, L.; Zhang, Z.; Wang, Y.; Lu, M.; LaPointe, M.; Chopp, M. A nitric oxide donor induces neurogenesis and reduces functional deficits after stroke in rats. *Ann. Neurol.* **2001**, *50*, 602−611.

(946) Pervin, S.; Singh, R.; Chaudhuri, G. Nitric oxide-induced cytostasis and cell cycle arrest of a human breast cancer cell line (MDA-MB-231): potential role of cyclin D1. *Proc. Natl. Acad. Sci. U. S. A.* **2001**, *98*, 3583−3588.

(947) Young, M. E.; Radda, G. K.; Leighton, B. Nitric oxide stimulates glucose transport and metabolism in rat skeletal muscle in vitro. *Biochem. J.* **1997**, *322*, 223−228.

(948) Gorren, A. C. F.; de Boer, E.; Wever, R. The reaction of nitric oxide with copper proteins and the photodissociation of copper-NO complexes. *Biochim. Biophys. Acta, Protein Struct. Mol. Enzymol.* **1987**, *916*, 38−47.

(949) Tian, S.; Liu, J.; Cowley, R. E.; Hosseinzadeh, P.; Marshall, N. M.; Yu, Y.; Robinson, H.; Nilges, M. J.; Blackburn, N. J.; Solomon, E. I.; Lu, Y. Reversible S-nitrosylation in an engineered azurin. *Nat. Chem.* **2016**, *8*, 670−677.

(950) Zhang, S.; Melzer, M. M.; Sen, S. N.; Çelebi-Ölçüm, N.; Warren, T. H. A motif for reversible nitric oxide interactions in metalloenzymes. *Nat. Chem.* **2016**, *8*, 663−669.

(951) Samanta, S.; Lehnert, N. A switch for blue copper proteins? *Nat. Chem.* **2016**, *8*, 639−641.

(952) McKinlay, A. C.; Xiao, B.; Wragg, D. S.; Wheatley, P. S.; Megson, I. L.; Morris, R. E. Exceptional behavior over the whole adsorption-storage-delivery cycle for NO in porous metal organic frameworks. *J. Am. Chem. Soc.* **2008**, *130*, 10440−10444.

(953) Seabra, A. B.; Duran, N. Nitric oxide-releasing vehicles for biomedical applications. *J. Mater. Chem.* **2010**, *20*, 1624−1637.

(954) Eroy-Reveles, A. A.; Leung, Y.; Beavers, C. M.; Olmstead, M. M.; Mascharak, P. K. Near-infrared light activated release of nitric oxide from designed photoactive manganese nitrosyls: strategy, design, and potential as NO donors. *J. Am. Chem. Soc.* **2008**, *130*, 4447−4458.

(955) Rose, M. J.; Mascharak, P. K. *Fiat Lux*: selective delivery of high flux of nitric oxide (NO) to biological targets using photoactive metal nitrosyls. *Curr. Opin. Chem. Biol.* **2008**, *12*, 238−244.

(956) Merkle, A. C.; Fry, N. L.; Mascharak, P. K.; Lehnert, N. Mechanism of NO photodissociation in photolabile manganese-NO complexes with pentadentate N5 ligands. *Inorg. Chem.* **2011**, *50*, 12192−12203.

(957) Heinrich, T. A.; Tedesco, A. C.; Fukuto, J. M.; da Silva, R. S. Production of reactive oxygen and nitrogen species by light irradiation of a nitrosyl phthalocyanine ruthenium complex as a strategy for cancer treatment. *Dalton Trans.* **2014**, *43*, 4021−4025.

(958) Xiang, H.-J.; Deng, Q.; An, L.; Guo, M.; Yang, S.-P.; Liu, J.-G. Tumor cell specific and lysosome-targeted delivery of nitric oxide for enhanced photodynamic therapy triggered by 808 nm near-infrared light. *Chem. Commun.* **2016**, *52*, 148−151.

(959) Ramos, L. C. B.; Rodrigues, F. P.; Biazzotto, J. C.; de Paula Machado, S.; Slep, L. D.; Hamblin, M. R.; da Silva, R. S. Targeting the mitochondrial VDAC in hepatocellular carcinoma using a polyclonal antibody-conjugated to a nitrosyl ruthenium complex. *JBIC, J. Biol. Inorg. Chem.* **2018**, *23*, 903−916.

(960) Giri, B.; Saini, T.; Kumbhakar, S.; Muley, A.; Misra, A.; Maji, S. Near-IR light-induced photorelease of nitric oxide (NO) on ruthenium nitrosyl complexes: formation, reactivity, and biological effects. *Dalton Trans.* **2020**, *49*, 10772−10785.

(961) Crisalli, M. A.; Franco, L. P.; Silva, B. R.; Holanda, A. K. M.; Bendhack, L. M.; Da Silva, R. S.; Ford, P. C. Nitric oxide release from a photoactive water-soluble ruthenium nitrosyl. Biological effects. *J. Coord. Chem.* **2018**, *71*, 1690−1703.

(962) Xie, L.; Bai, H.; Song, L.; Liu, C.; Gong, W.; Wang, W.; Zhao, X.; Takemoto, C.; Wang, H. Structural and photodynamic studies on nitrosylruthenium-complexed serum albumin as a delivery system for controlled nitric oxide release. *Inorg. Chem.* **2021**, *60*, 8826−8837.

(963) Vinogradov, S. N.; Moens, L. Diversity of globin function: enzymatic, transport, storage, and sensing. *J. Biol. Chem.* **2008**, *283*, 8773−8777.

(964) Dou, Y.; Maillet, D. H.; Eich, R. F.; Olson, J. S. Myoglobin as a model system for designing heme protein based blood substitutes. *Biophys. Chem.* **2002**, *98*, 127−148.

(965) Blomberg, L. M.; Blomberg, M. R. A.; Siegbahn, P. E. M. A theoretical study of myoglobin working as a nitric oxide scavenger. *JBIC, J. Biol. Inorg. Chem.* **2004**, *9*, 923−935.

(966) Goldstein, S.; Merenyi, G.; Samuni, A. Kinetics and mechanism of $\bullet NO_2$ reacting with various oxidation states of myoglobin. *J. Am. Chem. Soc.* **2004**, *126*, 15694−15701.

(967) Olson, J. S.; Foley, E. W.; Rogge, C.; Tsai, A.-L.; Doyle, M. P.; Lemon, D. D. NO scavenging and the hypertensive effect of hemoglobin-based blood substitutes. *Free Radical Biol. Med.* **2004**, *36*, 685−697.

(968) Wade, R. S.; Castro, C. E. Reactions of oxymyoglobin with NO, NO_2, and NO_2- under argon and in air. *Chem. Res. Toxicol.* **1996**, *9*, 1382−1390.

(969) Gardner, P. R.; Gardner, A. M.; Martin, L. A.; Salzman, A. L. Nitric oxide dioxygenase: An enzymatic function for flavohemoglobin. *Proc. Natl. Acad. Sci. U. S. A.* **1998**, *95*, 10378−10383.

(970) Eich, R. F. *Reactions of nitric oxide with myoglobin*; Rice University: Houston, 1997; pp 27−55, 99−110.

(971) Ascenzi, P.; Pesce, A. Peroxynitrite scavenging by *Campylobacter jejuni* truncated hemoglobin P. *JBIC, J. Biol. Inorg. Chem.* **2017**, *22*, 1141−1150.

(972) Kharitonov, V. G.; Sundquist, A. R.; Sharma, V. S. Kinetics of nitric oxide autoxidation in aqueous solution. *J. Biol. Chem.* **1994**, *269*, 5881−5883.

(973) Gardner, P. R.; Gardner, A. M.; Brashear, W. T.; Suzuki, T.; Hvitved, A. N.; Setchell, K. D. R.; Olson, J. S. Hemoglobins dioxygenate nitric oxide with high fidelity. *J. Inorg. Biochem.* **2006**, *100*, 542−550.

(974) Weiss, J. J. Nature of the iron-oxygen bond in oxyhaemoglobin. *Nature* **1964**, *202*, 83−84.

(975) Wittenberg, J. B.; Wittenberg, B. A.; Peisach, J.; Blumberg, W. E. On the state of the iron and the nature of the ligand in oxyhemoglobin. *Proc. Natl. Acad. Sci. U. S. A.* **1970**, *67*, 1846−1853.

(976) Balagopalakrishna, C.; Abugo, O. O.; Horsky, J.; Manoharan, P. T.; Nagababu, E.; Rifkind, J. M. Superoxide produced in the heme pocket of the β-chain of hemoglobin reacts with the β-93 cysteine to produce a thiyl radical. *Biochemistry* **1998**, *37*, 13194−13202.

(977) Singha, A.; Das, P. K.; Dey, A. Resonance Raman spectroscopy and density functional theory calculations on ferrous porphyrin dioxygen adducts with different axial ligands: correlation of ground state wave function and geometric parameters with experimental vibrational frequencies. *Inorg. Chem.* **2019**, *58*, 10704−10715.

(978) Yan, J. J.; Kroll, T.; Baker, M. L.; Wilson, S. A.; Decréau, R.; Lundberg, M.; Sokaras, D.; Glatzel, P.; Hedman, B.; Hodgson, K. O.; Solomon, E. I. Resonant inelastic X-ray scattering determination of the electronic structure of oxyhemoglobin and its model complex. *Proc. Natl. Acad. Sci. U. S. A.* **2019**, *116*, 2854−2859.

(979) Shaik, S.; Chen, H. Lessons on O_2 and NO bonding to heme from ab initio multireference/multiconfiguration and DFT calculations. *JBIC, J. Biol. Inorg. Chem.* **2011**, *16*, 841−855.

(980) Gardner, A. M.; Gardner, P. R.; Brashear, W.; Setchell, K. D. R.; Olson, J. S. Fidelity of O-atom transfer in the mechanism of nitric oxide dioxygenation by oxy-hemoglobins. *Free Rad. Biol. Med.* **2001**, *31*, S78.

(981) de Villota, E. D.; Carmona, M. T. G.; Rubio, J. J.; de Andres, S. R. Equality of the in vivo and *in vitro* oxygen-binding capacity of haemoglobin in patients with severe respiratory disease. *Br. J. Anaesth.* **1981**, *53*, 1325−1328.

(982) Cinelli, M. A.; Do, H. T.; Miley, G. P.; Silverman, R. B. Inducible nitric oxide synthase: Regulation, structure, and inhibition. *Med. Res. Rev.* **2020**, *40*, 158−189.

(983) Annane, D.; Sanquer, S.; Sébille, V.; Faye, A.; Djuranovic, D.; Raphaël, J. C.; Gajdos, P.; Bellissant, E. Compartmentalised inducible nitric-oxide synthase activity in septic shock. *Lancet* **2000**, *355*, 1143−1148.

(984) Herold, S. Kinetic and spectroscopic characterization of an intermediate peroxynitrite complex in the nitrogen monoxide induced oxidation of oxyhemoglobin. *FEBS Lett.* **1999**, *443*, 81−84.

(985) Herold, S. Mechanistic studies of the oxidation of pyridoxalated hemoglobin polyoxyethylene conjugate by nitrogen monoxide. *Arch. Biochem. Biophys.* **1999**, *372*, 393−398.

(986) Yukl, E. T.; de Vries, S.; Moënne-Loccoz, P. The millisecond intermediate in the reaction of nitric oxide with oxymyoglobin is an iron(III)-nitrato complex, not a peroxynitrite. *J. Am. Chem. Soc.* **2009**, *131*, 7234−7235.

(987) Tsai, J. H.; Harrison, J. G.; Martin, J. C.; Hamilton, T. P.; van der Woerd, M.; Jablonsky, M. J.; Beckman, J. S. Role of Conformation of Peroxynitrite Anion ($ONOO^-$) with Its Stability and Toxicity. *J. Am. Chem. Soc.* **1994**, *116*, 4115−4116.

(988) Lo, W.-J.; Lee, Y.-P.; Tsai, J.-H.; Tsai, H.-H.; Hamilton, T. P.; Harrison, J. G.; Beckman, J. S. Infrared absorption of cis-and trans-alkali-metal peroxynitrites (MOONO, M= Li, Na, and K) in solid argon. *J. Chem. Phys.* **1995**, *103*, 4026−4034.

(989) Bourassa, J. L.; Ives, E. P.; Marqueling, A. L.; Shimanovich, R.; Groves, J. T. Myoglobin catalyzes its own nitration. *J. Am. Chem. Soc.* **2001**, *123*, 5142−5143.

(990) Su, J.; Groves, J. T. Direct detection of the oxygen rebound intermediates, ferryl Mb and NO_2, in the reaction of metMyoglobin with peroxynitrite. *J. Am. Chem. Soc.* **2009**, *131*, 12979−12988.

(991) KrogerOhlsen, M.; Skibsted, L. H. Kinetics and mechanism of reduction of ferrylmyoglobin by ascorbate and D-isoascorbate. *J. Agric. Food Chem.* **1997**, *45*, 668−676.

(992) Herold, S.; Shivashankar, K. Metmyoglobin and methemoglobin catalyze the isomerization of peroxynitrite to nitrate. *Biochemistry* **2003**, *42*, 14036−14046.

(993) Herold, S.; Shivashankar, K.; Mehl, M. Myoglobin scavenges peroxynitrite without being significantly nitrated. *Biochemistry* **2002**, *41*, 13460−13472.

(994) Pietraforte, D.; Salzano, A. M.; Scorza, G.; Marino, G.; Minetti, M. Mechanism of peroxynitrite interaction with ferric hemoglobin and identification of nitrated tyrosine residues. CO_2 inhibits heme-catalyzed scavenging and isomerization. *Biochemistry* **2001**, *40*, 15300−15309.

(995) Koebke, K. J.; Pauly, D. J.; Lerner, L.; Liu, X.; Pacheco, A. A. Does the oxidation of nitric oxide by oxyMyoglobin share an intermediate with the metMyoglobin-catalyzed isomerization of peroxynitrite? *Inorg. Chem.* **2013**, *52*, 7623−7632.

(996) Schopfer, M. P.; Mondal, B.; Lee, D.-H.; Sarjeant, A. A. N.; Karlin, K. D. Heme/O_2/•NO nitric oxide dioxygenase (NOD) reactivity: phenolic nitration via a putative heme-peroxynitrite intermediate. *J. Am. Chem. Soc.* **2009**, *131*, 11304−11305.

(997) Lechauve, C.; Chauvierre, C.; Dewilde, S.; Moens, L.; Green, B. N.; Marden, M. C.; Célier, C.; Kiger, L. Cytoglobin conformations and disulfide bond formation. *FEBS J.* **2010**, *277*, 2696−2704.

(998) Zweier, J. L.; Ilangovan, G. Regulation of nitric oxide metabolism and vascular tone by cytoglobin. *Antioxid. Redox Signaling* **2020**, *32*, 1172−1187.

(999) Hamdane, D.; Kiger, L.; Dewilde, S.; Green, B. N.; Pesce, A.; Uzan, J.; Burmester, T.; Hankeln, T.; Bolognesi, M.; Moens, L.; et al. The redox state of the cell regulates the ligand binding affinity of human neuroglobin and cytoglobin. *J. Biol. Chem.* **2003**, *278*, 51713−51721.

(1000) Zhou, D.; Hemann, C.; Boslett, J.; Luo, A.; Zweier, J. L.; Liu, X. Oxygen binding and nitric oxide dioxygenase activity of cytoglobin are altered to different extents by cysteine modification. *FEBS Open Bio* **2017**, *7*, 845−853.

(1001) Liu, X.; Tong, J.; Zweier, J. R.; Follmer, D.; Hemann, C.; Ismail, R. S.; Zweier, J. L. Differences in oxygen-dependent nitric oxide metabolism by cytoglobin and myoglobin account for their differing functional roles. *FEBS J.* **2013**, *280*, 3621−3631.

(1002) Kurtikyan, T. S.; Hayrapetyan, V. A.; Hovhannisyan, A. A.; Martirosyan, G. G.; Hovhannisyan, G. S.; Iretskii, A. V.; Ford, P. C. Nitric oxide dioxygenation by O_2 adducts of manganese porphyrins. *Inorg. Chem.* **2020**, *59*, 17224−17233.

(1003) Kurtikyan, T. S.; Eksuzyan, S. R.; Goodwin, J. A.; Hovhannisyan, G. S. Nitric oxide interaction with oxy-coboglobin models containing trans-pyridine ligand: two reaction pathways. *Inorg. Chem.* **2013**, *52*, 12046−12056.

(1004) Maiti, D.; Lee, D.-H.; Narducci Sarjeant, A. A.; Pau, M. Y. M.; Solomon, E. I.; Gaoutchenova, K.; Sundermeyer, J.; Karlin, K. D. Reaction of a copper-dioxygen complex with nitrogen monoxide (•NO) leads to a copper (II)-peroxynitrite species. *J. Am. Chem. Soc.* **2008**, *130*, 6700−6701.

(1005) Wick, P. K.; Kissner, R.; Koppenol, W. H. Synthesis and characterization of tris (tetraethylammonium) pentacyanoperoxynitritocobaltate(III). *Helv. Chim. Acta* **2000**, *83*, 748−754.

(1006) Wick, P. K.; Kissner, R.; Koppenol, W. H. Hydrolysis and photolysis of tris (tetraethylammonium) pentacyanoperoxynitritocobaltate(III): evidence for a novel complex, pentacyanonitratocobaltate(III). *Helv. Chim. Acta* **2001**, *84*, 3057−3062.

(1007) Crespo, A.; Marti, M. A.; Kalko, S. G.; Morreale, A.; Orozco, M.; Gelpi, J. L.; Luque, F. J.; Estrin, D. A. Theoretical study of the truncated hemoglobin HbN: exploring the molecular basis of the NO detoxification mechanism. *J. Am. Chem. Soc.* **2005**, *127*, 4433−4444.

(1008) Gow, A.; Luchsinger, B. P.; Pawloski, J. R.; Singel, D. J.; Stamler, J. S. The oxyhemoglobin reaction of nitric oxide. *Proc. Natl. Acad. Sci. U. S. A.* **1999**, *96*, 9027−9032.

(1009) Kharitonov, V. G.; Sharma, V. S.; Magde, D.; Koesling, D. Kinetics of nitric oxide dissociation from five-and six-coordinate nitrosyl hemes and heme proteins, including soluble guanylate cyclase. *Biochemistry* **1997**, *36*, 6814−6818.

(1010) Møller, J. K. S.; Skibsted, L. H. Mechanism of nitrosylmyoglobin autoxidation: temperature and oxygen pressure effects on the two consecutive reactions. *Chem. - Eur. J.* **2004**, *10*, 2291−2300.

(1011) Herold, S.; Fago, A.; Weber, R. E.; Dewilde, S.; Moens, L. Reactivity studies of the Fe(III) and Fe(II) NO forms of human neuroglobin reveal a potential role against oxidative stress. *J. Biol. Chem.* **2004**, *279*, 22841−22847.

(1012) Van Doorslaer, S.; Dewilde, S.; Kiger, L.; Nistor, S. V.; Goovaerts, E.; Marden, M. C.; Moens, L. Nitric oxide binding properties of neuroglobin: a characterization by EPR and flash photolysis. *J. Biol. Chem.* **2003**, *278*, 4919−4925.

(1013) Fasano, M.; Antonini, G.; Ascenzi, P. O_2-mediated oxidation of hemopexin-heme(II)-NO. *Biochem. Biophys. Res. Commun.* **2006**, *345*, 704−712.

(1014) Tejero, J.; Santolini, J.; Stuehr, D. J. Fast ferrous heme-NO oxidation in nitric oxide synthases. *FEBS J.* **2009**, *276*, 4505−4514.

(1015) Ilan, Y. A.; Czapski, G.; Meisel, D. The one-electron transfer redox potentials of free radicals I. The oxygen/superoxide system. *Biochim. Biophys. Acta, Bioenerg.* **1976**, *430*, 209−224.

(1016) Sarti, P.; Giuffre, A.; Forte, E.; Mastronicola, D.; Barone, M. C.; Brunori, M. Nitric oxide and cytochrome *c* oxidase: mechanisms of inhibition and NO degradation. *Biochem. Biophys. Res. Commun.* **2000**, *274*, 183−187.

(1017) Møller, J. K. S.; Skibsted, L. H. Mechanism of nitrosylmyoglobin autoxidation: temperature and oxygen pressure effects on the two consecutive reactions. *Chem. - Eur. J.* **2004**, *10*, 2291−2300.

(1018) Ost, T. W.; Daff, S. Thermodynamic and kinetic analysis of the nitrosyl, carbonyl and dioxy heme complexes of neuronal nitric-oxide synthase. The roles of substrate and tetrahydrobiopterin in oxygen activation. *J. Biol. Chem.* **2005**, *280*, 965−973.

(1019) Tejero, J.; Hunt, A. P.; Santolini, J.; Lehnert, N.; Stuehr, D. J. Mechanism and regulation of ferrous heme-nitric oxide (NO) oxidation in NO synthases. *J. Biol. Chem.* **2019**, *294*, 7904−7916.

(1020) Li, L.; Li, L. Recent advances in multinuclear metal nitrosyl complexes. *Coord. Chem. Rev.* **2016**, *306*, 678−700.

(1021) Tsai, M.-L.; Tsou, C.-C.; Liaw, W.-F. Dinitrosyl iron complexes (DNICs): from biomimetic synthesis and spectroscopic characterization toward unveiling the biological and catalytic roles of DNICs. *Acc. Chem. Res.* **2015**, *48*, 1184−1193.

(1022) Cho, S.-L.; Liao, C.-J.; Lu, T.-T. Synthetic methodology for preparation of dinitrosyl iron complexes. *JBIC, J. Biol. Inorg. Chem.* **2019**, *24*, 495−515.

(1023) Denny, J. A.; Darensbourg, M. Y. Approaches to quantifying the electronic and steric properties of metallodithiolates as ligands in coordination chemistry. *Coord. Chem. Rev.* **2016**, *324*, 82−89.

(1024) Pulukkody, R.; Darensbourg, M. Y. Synthetic advances inspired by the bioactive dinitrosyl iron unit. *Acc. Chem. Res.* **2015**, *48*, 2049−2058.

(1025) Fitzpatrick, J.; Kim, E. Synthetic modeling chemistry of iron−sulfur clusters in nitric oxide signaling. *Acc. Chem. Res.* **2015**, *48*, 2453−2461.

(1026) Vanin, A. F. What is the mechanism of nitric oxide conversion into nitrosonium ions ensuring S-nitrosating processes in living organisms. *Cell Biochem. Biophys.* **2019**, *77*, 279−292.

(1027) Lok, H. C.; Sahni, S.; Richardson, V.; Kalinowski, D. S.; Kovacevic, Z.; Lane, D. J.; Richardson, D. R. Glutathione S-transferase and MRP1 form an integrated system involved in the storage and transport of dinitrosyl-dithiolato iron complexes in cells. *Free Radical Biol. Med.* **2014**, *75*, 14−29.

(1028) Crack, J. C.; Green, J.; Thomson, A. J.; Le Brun, N. E. Iron−sulfur cluster sensor-regulators. *Curr. Opin. Chem. Biol.* **2012**, *16*, 35−44.

(1029) Vanin, A. F. EPR characterization of dinitrosyl iron complexes with thiol-containing ligands as an approach to their identification in biological objects: an overview. *Cell Biochem. Biophys.* **2018**, *76*, 3−17.

(1030) Ford, P. C. Photochemical delivery of nitric oxide. *Nitric Oxide* **2013**, *34*, 56−64.

(1031) Vanin, A. F.; Burbaev, D. S. Electronic and spatial structures of water-soluble dinitrosyl iron complexes with thiol-containing ligands underlying their ability to act as nitric oxide and nitrosonium ion donors. *J. Biophys.* **2011**, *2011*, 878236.

(1032) Vanin, A. F. Dinitrosyl iron complexes with thiol-containing ligands as a "working form" of endogenous nitric oxide. *Nitric Oxide* **2016**, *54*, 15−29.

(1033) Vanin, A. F.; Nalbandyan, R. M. Free radical species with unpaired electron localization on sulfur atom in yeast cells. *Biofizika (Rus.)* **1966**, 178−179.

(1034) Vithayathil, A. J.; Ternberg, J. L.; Commoner, B. Changes in electron spin resonance signals of rat liver during chemical carcinogenesis. *Nature* **1965**, *207*, 1246−1249.

(1035) Vanin, A. F. Identification of divalent iron complexes with cysteine in biological objects by the ear method. *Biokhimiya (Rus.)* **1967**, *1967*, 228−232.

(1036) Butler, A. R.; Megson, I. L. Non-heme iron nitrosyls in biology. *Chem. Rev.* **2002**, *102*, 1155−1165.

(1037) Nalbandyan, R. M.; Vanin, A. F. Free radicals in yeast cells. *Abstracts of the Meeting "Free Radicals Processes in Biological Systems"*; Moscow, 1964; Vol. *18*.

(1038) Baltusis, L. M.; Karlin, K. D.; Rabinowitz, H. N.; Dewan, J. C.; Lippard, S. J. Synthesis and structure of Fe(L'H)$(NO)_2$, a tetracoordinate complex having a twelve-membered chelate ring, and Its conversion to pentacoordinate FeL (NO) through formal loss of "HNO" (L' = $SCH_2CH_2NMeCH_2CH_2CH_2NMeCH_2CH_2S$). *Inorg. Chem.* **1980**, *19*, 2627−2632.

(1039) Boese, M.; Mordvintcev, P. I.; Vanin, A. F.; Busse, R.; Mülsch, A. S-nitrosation of serum albumin by dinitrosyl-iron complex. *J. Biol. Chem.* **1995**, *270*, 29244−29249.

(1040) Reginato, N.; McCrory, C. T. C.; Pervitsky, D.; Li, L. Synthesis, X-ray crystal structure, and solution behavior of Fe$(NO)_2$(1-MeIm)$_2$: implications for nitrosyl non-heme-iron complexes with g = 2.03. *J. Am. Chem. Soc.* **1999**, *121*, 10217−10218.

(1041) Bello, M. L.; Nuccetelli, M.; Caccuri, A. M.; Stella, L.; Parker, M. W.; Rossjohn, J.; McKinstry, W. J.; Mozzi, A. F.; Federici, G.; Polizio, F.; Pedersen, J. Z.; Ricci, G. Human glutathione transferase P1-1 and nitric oxide carriers; a new role for an old enzyme. *J. Biol. Chem.* **2001**, *276*, 42138−42145.

(1042) Conrado, C. L.; Bourassa, J. L.; Egler, C.; Wecksler, S.; Ford, P. C. Photochemical investigation of Roussin's red salt esters: $Fe_2(\mu\text{-}SR)_2(NO)_4$. *Inorg. Chem.* **2003**, *42*, 2288−2293.

(1043) Cesareo, E.; Parker, L. J.; Pedersen, J. Z.; Nuccetelli, M.; Mazzetti, A. P.; Pastore, A.; Federici, G.; Caccuri, A. M.; Ricci, G.; Adams, J. J.; Parker, M. W.; Lo Bello, M. Nitrosylation of human glutathione transferase P1-1 with dinitrosyl diglutathionyl iron complex *in vitro* and *in vivo*. *J. Biol. Chem.* **2005**, *280*, 42172−42180.

(1044) Harrop, T. C.; Song, D.; Lippard, S. J. Interaction of nitric oxide with tetrathiolato iron (II) complexes: relevance to the reaction pathways of iron nitrosyls in sulfur-rich biological coordination environments. *J. Am. Chem. Soc.* **2006**, *128*, 3528−3529.

(1045) Harrop, T. C.; Tonzetich, Z. J.; Reisner, E.; Lippard, S. J. Reactions of synthetic [2Fe-2S] and [4Fe-4S] clusters with nitric oxide and nitrosothiols. *J. Am. Chem. Soc.* **2008**, *130*, 15602−15610.

(1046) Tsou, C.-C.; Lin, Z. S.; Lu, T.-T.; Liaw, W.-F. Transformation of dinitrosyl iron complexes $[(NO)_2Fe(SR)_2]^-$ (R = Et, Ph) into [4Fe-4S] clusters $[Fe_4S_4(SPh)_4]^{2-}$: relevance to the repair of the nitric oxide-modified ferredoxin [4Fe-4S] clusters. *J. Am. Chem. Soc.* **2008**, *130*, 17154−17160.

(1047) Hsieh, C.-H.; Darensbourg, M. Y. A $\{Fe(NO)_3\}^{10}$ trinitrosyliron complex stabilized by an n-heterocyclic carbene and the cationic and neutral $\{Fe(NO)_2\}^{9/10}$ products of its NO release. *J. Am. Chem. Soc.* **2010**, *132*, 14118−14125.

(1048) Tran, N. G.; Kalyvas, H.; Skodje, K. M.; Hayashi, T.; Möenne-Loccoz, P.; Callan, P. E.; Shearer, J.; Kirschenbaum, L. J.; Kim, E. Phenol nitration induced by an $\{Fe(NO)_2\}^{10}$ dinitrosyl iron complex. *J. Am. Chem. Soc.* **2011**, *133*, 1184−1187.

(1049) Tran, C. T.; Kim, E. Acid-dependent degradation of a [2Fe-2S] cluster by nitric oxide. *Inorg. Chem.* **2012**, *51*, 10086−10088.

(1050) Hsieh, C.-H.; Ding, S.; Erdem, Ö. F.; Crouthers, D. J.; Liu, T.; McCrory, C. C. L.; Lubitz, W.; Popescu, C. V.; Reibenspies, J. H.; Hall, M. B.; Darensbourg, M. Y. Redox active iron nitrosyl units in proton reduction electrocatalysis. *Nat. Commun.* **2014**, *5*, 3684.

(1051) Wu, S.-C.; Lu, C.-Y.; Chen, Y.-L.; Lo, F.-C.; Wang, T.-Y.; Chen, Y.-J.; Yuan, S.-S.; Liaw, W.-F.; Wang, Y.-M. Water-soluble dinitrosyl iron complex (DNIC): a nitric oxide vehicle triggering cancer cell death via apoptosis. *Inorg. Chem.* **2016**, *55*, 9383−9392.

(1052) Vanin, A. F.; Men'shikov, G. B.; Moroz, I. A.; Mordvintcev, P. I.; Serezhenkov, V. A.; Burbaev, D. S. The source of non-heme iron that binds nitric oxide in cultivated macrophages. *Biochim. Biophys. Acta, Mol. Cell Res.* **1992**, *1135*, 275−279.

(1053) Kozlov, A. V.; Yegorov, D. Y.; Vladimirov, Y. A.; Azizova, O. A. Intracellular free iron in liver tissue and liver homogenate: studies with electron paramagnetic resonance on the formation of paramagnetic complexes with desferal and nitric oxide. *Free Radical Biol. Med.* **1992**, *13*, 9−16.

(1054) Hickok, J. R.; Sahni, S.; Shen, H.; Arvind, A.; Antoniou, C.; Fung, L. W.; Thomas, D. D. Dinitrosyliron complexes are the most abundant nitric oxide-derived cellular adduct: biological parameters of assembly and disappearance. *Free Radical Biol. Med.* **2011**, *51*, 1558−1566.

(1055) Toledo, J. C., Jr.; Bosworth, C. A.; Hennon, S. W.; Mahtani, H. A.; Bergonia, H. A.; Lancaster, J. R., Jr. Nitric oxide-induced conversion of cellular chelatable iron into macromolecule-bound paramagnetic dinitrosyliron complexes. *J. Biol. Chem.* **2008**, *283*, 28926−28933.

(1056) Lewandowska, H.; Meczyńska, S.; Sochanowicz, B.; Sadlo, J.; Kruszewski, M. Crucial role of lysosomal iron in the formation of dinitrosyl iron complexes in vivo. *JBIC, J. Biol. Inorg. Chem.* **2007**, *12*, 345−352.

(1057) Kakhlon, O.; Cabantchik, Z. I. The labile iron pool: characterization, measurement, and participipation in cellular processes. *Free Radical Biol. Med.* **2002**, *33*, 1037−1046.

(1058) Woolum, J. C.; Tiezzi, E.; Commoner, B. Electron spin resonance of iron-nitric oxide complexes with amino acids, peptides and proteins. *Biochim. Biophys. Acta, Protein Struct.* **1968**, *160*, 311−320.

(1059) Ueno, T.; Yoshimura, T. The physiological activity and in vivo distribution of dinitrosyl dithiolato iron complex. *Jpn. J. Pharmacol.* **2000**, *82*, 95−101.

(1060) Turella, P.; Pedersen, J. Z.; Caccuri, A. M.; De Maria, F.; Mastroberardino, P.; Lo Bello, M.; Federici, G.; Ricci, G. Glutathione transferase superfamily behaves like storage proteins for dinitrosyl-diglutathionyl-iron complex in heterogeneous systems. *J. Biol. Chem.* **2003**, *278*, 42294−42299.

(1061) Rogers, P. A.; Ding, H. L-cysteine-mediated destabilization of dinitrosyl iron complexes in proteins. *J. Biol. Chem.* **2001**, *276*, 30980−30986.

(1062) Mülsch, A.; Mordvintcev, P.; Vanin, A. F.; Busse, R. The potent vasodilating and guanylyl cyclase activating dinitrosyl-iron(II) complex is stored in a protein-bound form in vascular tissue and is released by thiols. *FEBS Lett.* **1991**, *294*, 252−256.

(1063) Voevodskaya, N. V.; Serezhenkov, V. A.; Cooper, C. E.; Kubrina, L. N.; Vanin, A. F. Exogenous ferrous iron is required for the nitric oxide-catalysed destruction of the iron-sulphur centre in adrenodoxin. *Biochem. J.* **2002**, *368*, 633−639.

(1064) Vanin, A. F.; Poltorakov, A. P.; Mikoyan, V. D.; Kubrina, L. N.; Burbaev, D. S. Polynuclear water-soluble dinitrosyl iron complexes with cysteine or glutathione ligands: electron paramagnetic resonance and optical studies. *Nitric Oxide* **2010**, *23*, 136−149.

(1065) Pereira, J. C.; Iretskii, A. V.; Han, R. M.; Ford, P. C. Dinitrosyl iron complexes with cysteine. Kinetics studies of the formation and reactions of DNICs in aqueous solution. *J. Am. Chem. Soc.* **2015**, *137*, 328−336.

(1066) Timoshin, A. A.; Lakomkin, V. L.; Abramov, A. A.; Ruuge, E. K.; Vanin, A. F. Hypotensive effect and accumulation of dinitrosyl iron complexes in blood and tissues after intravenous and subcutaneous injection. *Bull. Exp. Biol. Med.* **2016**, *162*, 207−210.

(1067) Timoshin, A. A.; Lakomkin, V. L.; Abramov, A. A.; Ruuge, E. K.; Kapel'ko, V. I.; Chazov, E. I.; Vanin, A. F. The hypotensive effect of the nitric monoxide donor Oxacom at different routs of its administration to experimental animals. *Eur. J. Pharmacol.* **2015**, *765*, 525−532.

(1068) Chazov, E. I.; Rodnenkov, O. V.; Zorin, A. V.; Lakomkin, V. L.; Gramovich, V. V.; Vyborov, O. N.; Dragnev, A. G.; Timoshin, A. A.; Buryachkovskaya, L. I.; Abramov, A. A.; Massenko, V. P.; Arzamastsev, E. V.; Kapelko, V. I.; Vanin, A. F. Hypotensive effect of Oxacom® containing a dinitrosyl iron complex with glutathione: Animal studies and clinical trials on healthy volunteers. *Nitric Oxide* **2012**, *26*, 148−156.

(1069) Lakomkin, V. L.; Vanin, A. F.; Timoshin, A. A.; Kapelko, V. I.; Chazov, E. I. Long-lasting hypotensive action of stable preparations of dinitrosyl-iron complexes with thiol-containing ligands in conscious normotensive and hypertensive rats. *Nitric Oxide* **2007**, *16*, 413−418.

(1070) Vedernikov, Y. P.; Mordvintcev, P. I.; Malenkova, I. V.; Vanin, A. F. Effect of dieyhyldithiocarbamate on the activity of nitric oxide-releasing vasodilators. *Eur. J. Pharmacol.* **1992**, *212*, 125−128.

(1071) Vanin, A. F.; Mokh, V. P.; Serezhenkov, V. A.; Chazov, E. I. Vasorelaxing activity of stable powder preparations of dinitrosyl iron complexes with cysteine or glutathione ligands. *Nitric Oxide* **2007**, *16*, 322−330.

(1072) Mokh, V. P.; Poltorakov, A. P.; Serezhenkov, V. A.; Vanin, A. F. On the nature of a compound formed from dinitrosyl-iron complexes with cysteine and responsible for a long-lasting vasorelaxation. *Nitric Oxide* **2010**, *22*, 266−274.

(1073) Flitney, F. W.; Megson, I. L.; Thomson, J. L. M.; Kennovin, G.D.; Butler, A.R. Vasodilator responses of rat isolated tail artery enhanced by oxygen-dependent, photochemical release of nitric oxide from iron-sulphur-nitrosyls. *Brit. J. Pharmacol.* **1996**, *117*, 1549−1557.

(1074) Vedernikov, Y. P.; Mordvintcev, P. I.; Malenkova, I. V.; Vanin, A. F. Similarity between the vasorelaxing activity of dinitrosyl iron cysteine complexes and endothelium-derived relaxing factor. *Eur. J. Pharmacol.* **1992**, *211*, 313−317.

(1075) Severina, I. S.; Bussygina, O. G.; Pyatakova, N. V.; Malenkova, I. V.; Vanin, A. F. Activation of soluble guanylate cyclase by NO donors—S-nitrosothiols, and dinitrosyl-iron complexes with thiol-containing ligands. *Nitric Oxide* **2003**, *8*, 155−163.

(1076) Mordvintsev, P. I.; Rudneva, V. G.; Vanin, A. F.; Shimkevich, L. L.; Khodorov, B. I. Inhibition of platelet aggregation by dinitrosyl iron complexes with low molecular weight ligands. *Biokhimiia* **1986**, *51*, 1851−1857.

(1077) Shekhter, A. B.; Rudenko, T. G.; Serezhenkov, V. A.; Vanin, A. F. Dinitrosyl-iron complexes with cysteine or glutathione accelerate skin wound healing in animals. *Biophysics* **2007**, *52*, 539−547.

(1078) Shekhter, A. B.; Rudenko, T. G.; Istranov, L. P.; Guller, A. E.; Borodulin, R. R.; Vanin, A. F. Dinitrosyl iron complexes with glutathione incorporated into a collagen matrix as a base for the design of drugs accelerating skin wound healing. *Eur. J. Pharm. Sci.* **2015**, *78*, 8−18.

(1079) Andreyev-Andriyevsky, A. A.; Mikoyan, V. D.; Serezhenkov, V. A.; Vanin, A. F. Penile erectile activity of dinitrosyl iron complexes with thiol-containing ligands. *Nitric Oxide* **2011**, *24*, 217−223.

(1080) Kim, Y.-M.; Bombeck, C. A.; Billiar, T. R. Nitric oxide as a bifunctional regulator of apoptosis. *Circ. Res.* **1999**, *84*, 253−256.

(1081) Malyshev, I. Y.; Malugin, A. V.; Golubeva, L. Y.; Zenina, T. A.; Manukhina, E. B.; Mikoyan, V. D.; Vanin, A. F. Nitric oxide donor induces HSP70 accumulation in the heart and in cultured cells. *FEBS Lett.* **1996**, *391*, 21−23.

(1082) Kleschyov, A. L.; Strand, S.; Schmitt, S.; Gottfried, D.; Skatchkov, M.; Sjakste, N.; Daiber, A.; Umansky, V.; Munzel, T. Dinitrosyl-iron triggers apoptosis in Jurkat cells despite overexpression of Bcl-2. *Free Radical Biol. Med.* **2006**, *40*, 1340−1348.

(1083) Hess, D. T.; Matsumoto, A.; Kim, S. O.; Marshall, H. E.; Stamler, J. S. Protein S-nitrosylation: purview and parameters. *Nat. Rev. Mol. Cell Biol.* **2005**, *6*, 150−166.

(1084) Bosworth, C. A.; Toledo, J. C., Jr.; Zmijewski, J. W.; Li, Q.; Lancaster, J. R., Jr. Dinitrosyliron complexes and the mechanism(s) of cellular protein nitrosothiol formation from nitric oxide. *Proc. Natl. Acad. Sci. U. S. A.* **2009**, *106*, 4671−4676.

(1085) Kim, Y.-M.; Chung, H.-T.; Simmons, R. L.; Billiar, T. R. Cellular non-heme iron content Is a determinant of nitric oxide-mediated apoptosis, necrosis, and caspase inhibition. *J. Biol. Chem.* **2000**, *275*, 10954−10961.

(1086) Badorff, C.; Fichtlscherer, B.; Muelsch, A.; Zeiher, A. M.; Dimmeler, S. Selective delivery of nitric oxide to a cellular target: a pseudosubstrate-coupled dinitrosyl-iron complex inhibits the enteroviral protease 2A. *Nitric Oxide* **2002**, *6*, 305−312.

(1087) Becker, K.; Savvides, S. N.; Keese, M.; Schirmer, R. H.; Karplus, P. A. Enzyme inactivation through sulfhydryl oxidation by physiologic NO-carriers. *Nat. Struct. Biol.* **1998**, *5*, 267−271.

(1088) Keese, M. A.; Böse, M.; Mülsch, A.; Schirmer, R. H.; Becker, K. Dinitrosyl-dithiol-iron complexes, nitric oxide (NO) carriers *in vivo* as potent inhibitors of human glutathione reductase and glutathione-S-transferase. *Biochem. Pharmacol.* **1997**, *54*, 1307−1313.

(1089) Boldyrev, A. A.; Bulygina, E. R.; Kramarenko, G. G.; Vanin, A. F. Effect of nitroso compounds on Na/K-ATPase. *Biochim. Biophys. Acta, Bioenerg.* **1997**, *1321*, 243−251.

(1090) Giannone, G.; Takeda, K.; Kleschyov, A. L. Novel activation of non-selective cationic channels by dinitrosyl iron-thiosulfate in PC12 cells. *J. Physiol.* **2000**, *529*, 735−745.

(1091) Armstrong, R. Structure, catalytic mechansim, and evolution of the glutathione transferases. *Chem. Res. Toxicol.* **1997**, *10*, 2−18.

(1092) Bocedi, A.; Fabrini, R.; Farrotti, A.; Stella, L.; Ketterman, A. J.; Pedersen, J. Z.; Allocati, N.; Lau, P. C.; Grosse, S.; Eltis, L. D.; Ruzzini, A.; Edwards, T. E.; Morici, L.; Del Grosso, E.; Guidoni, L.; Bovi, D.; Lo Bello, M.; Federici, G.; Parker, M. W.; Board, P. G.; Ricci, G. The impact of nitric oxide toxicity on the evolution of the glutathione transferase superfamily: a proposal for an evolutionary driving force. *J. Biol. Chem.* **2013**, *288*, 24936−24947.

(1093) Pedersen, J. Z.; De Maria, F.; Turella, P.; Federici, G.; Mattei, M.; Fabrini, R.; Dawood, K. F.; Massimi, M.; Caccuri, A. M.; Ricci, G. Glutathione transferases sequester toxic dinitrosyl-iron complexes in cells. A protection mechanism against excess nitric oxide. *J. Biol. Chem.* **2007**, *282*, 6364−6371.

(1094) De Maria, F.; Pedersen, J. Z.; Caccuri, A. M.; Antonini, G.; Turella, P.; Stella, L.; Lo Bello, M.; Federici, G.; Ricci, G. The specific interaction of dinitrosyl-diglutathionyl-iron complex, a natural NO carrier, with the glutathione transferase superfamily: suggestion for an evolutionary pressure in the direction of the storage of nitric oxide. *J. Biol. Chem.* **2003**, *278*, 42283−42293.

(1095) Watts, R. N.; Hawkins, C.; Ponka, P.; Richardson, D. R. Nitrogen monoxide (NO)-mediated iron release from cells is linked to

NO-induced glutathione efflux via multidrug resistance-associated protein 1. *Proc. Natl. Acad. Sci. U. S. A.* **2006**, *103*, 7670−7675.

(1096) Beinert, H.; Holm, R. H.; Münck, E. Iron−sulfur clusters: nature's modular, multipurpose structures. *Science* **1997**, *277*, 653−659.

(1097) Rouault, T. A. Biogenesis of iron−sulfur clusters in mammalian cells: new insights and relevance to human disease. *Dis. Models & Mech.* **2012**, *5*, 155−164.

(1098) Kennedy, M. C.; Antholine, W. E.; Beinert, H. An EPR investigation of the products of the reaction of cytosolic and mitochondrial aconitases with nitric oxide. *J. Biol. Chem.* **1997**, *272*, 20340−20347.

(1099) Bouton, C.; Drapier, J.-C. Iron regulatory proteins as NO signal transducers. *Sci. Signaling* **2003**, *182*, No. pe17.

(1100) Ramirez, L.; Simontacchi, M.; Murgia, I.; Zabaleta, E.; Lamattina, L. Nitric oxide, nitrosyl iron complexes, ferritin and frataxin: a well equipped team to preserve plant iron homeostasis. *Plant Sci.* **2011**, *181*, 582−592.

(1101) Lo, F.-C.; Chen, C.-L.; Lee, C.-M.; Tsai, M.-C.; Lu, T.-T.; Liaw, W.-F.; Yu, S. S.-F. A study of NO trafficking from dinitrosyl-iron complexes to the recombinant *E. coli* transcriptional factor SoxR. *JBIC, J. Biol. Inorg. Chem.* **2008**, *13*, 961−972.

(1102) Fujikawa, M.; Kobayashi, K.; Kozawa, T. Mechanistic studies on formation of the dinitrosyl iron complex of the [2Fe-2S] cluster of SoxR protein. *J. Biochem.* **2014**, *156*, 163−172.

(1103) Kobayashi, K. Sensing mechanisms in the redox-regulated, [2Fe-2S] cluster-containing, bacterial transcriptional factor SoxR. *Acc. Chem. Res.* **2017**, *50*, 1672−1678.

(1104) Lo, F.-C.; Lee, J.-F.; Liaw, W.-F.; Hsu, I.-J.; Tsai, Y.-F.; Chan, S. I.; Yu, S. S.-F. The metal core structures in the recombinant *Escherichia coli* transcriptional factor SoxR. *Chem. - Eur. J.* **2012**, *18*, 2565−2577.

(1105) Tucker, N. P.; Hicks, M. G.; Clarke, T. A.; Crack, J. C.; Chandra, G.; Le Brun, N. E.; Dixon, R.; Hutchings, M. I. The transcriptional repressor protein NsrR senses nitric oxide directly via a [2Fe-2S] cluster. *PLoS One* **2008**, *3*, No. e3623.

(1106) Kommineni, S.; Yukl, E.; Hayashi, T.; Delepine, J.; Geng, H.; Moënne-Loccoz, P.; Nakano, M. M. Nitric oxide-sensitive and -insensitive interaction of *Bacillus subtilis* NsrR with a ResDE-controlled promoter. *Mol. Microbiol.* **2010**, *78*, 1280−1293.

(1107) Yukl, E. T.; Elbaz, M. A.; Nakano, M. M.; Moënne-Loccoz, P. Transcription factor NsrR from *Bacillus subtilis* senses nitric oxide with a 4Fe-4S cluster. *Biochemistry* **2008**, *47*, 13084−13092.

(1108) Serrano, P. N.; Wang, H.; Crack, J. C.; Prior, C.; Hutchings, M. I.; Thomson, A. J.; Kamali, S.; Yoda, Y.; Zhao, J.; Hu, M. Y.; Alp, E. E.; Oganesyan, V. S.; Le Brun, N. E.; Cramer, S. P. Nitrosylation of nitric-oxide-sensing regulatory proteins containing [4Fe-4S] clusters gives rise to multiple iron-nitrosyl complexes. *Angew. Chem., Int. Ed.* **2016**, *55*, 14575−14579.

(1109) Crack, J. C.; Le Brun, N. E. Mass spectrometric identification of [4Fe-4S]$(NO)_x$ intermediates of nitric oxide sensing by regulatory iron−sulfur cluster proteins. *Chem. - Eur. J.* **2019**, *25*, 3675−3684.

(1110) Crack, J. C.; Hamilton, C. J.; Le Brun, N. E. Mass spectrometric detection of iron nitrosyls, sulfide oxidation and mycothiolation during nitrosylation of the NO sensor [4Fe-4S] NsrR. *Chem. Commun.* **2018**, *54*, 5992−5995.

(1111) Volbeda, A.; Dodd, E. L.; Darnault, C.; Crack, J. C.; Renoux, O.; Hutchings, M. I.; Le Brun, N. E.; Fontecilla-Camps, J. C. Crystal structures of the NO sensor NsrR reveal how its iron−sulfur cluster modulates DNA binding. *Nat. Commun.* **2017**, *8*, 15052.

(1112) Cruz-Ramos, H.; Crack, J.; Wu, G.; Hughes, M. N.; Scott, C.; Thomson, A. J.; Green, J.; Poole, R. K. NO sensing by FNR: regulation of the *Escherichia coli* NO-detoxyfying flavohaemmoglobin, Hmp. *EMBO J.* **2002**, *21*, 3235−3244.

(1113) Kiley, P. J.; Beinert, H. Oxygen sensing by the global regulator FNR: the role of the iron−sulfur cluster. *FEMS Microbiol. Rev.* **1998**, *22*, 341−352.

(1114) Crack, J. C.; Jervis, A. J.; Gaskell, A. A.; White, G. F.; Green, J.; Thomson, A. J.; Le Brun, N. E. Signal perception by FNR: the role of the iron−sulfur cluster. *Biochem. Soc. Trans.* **2008**, *36*, 1144−1148.

(1115) Crack, J. C.; Green, J.; Thomson, A. J.; Le Brun, N. E. Iron−sulfur clusters as biological sensors: the chemistry of reactions with molecular oxygen and nitric oxide. *Acc. Chem. Res.* **2014**, *47*, 3196−3205.

(1116) Crack, J. C.; Smith, L. J.; Stapleton, M. R.; Peck, J.; Watmough, N. J.; Buttner, M. J.; Buxton, R. S.; Green, J.; Oganesyan, V. S.; Thomson, A. J.; Le Brun, N. E. Mechanistic insight into the nitrosylation of the [4Fe-4S] cluster of WhiB-like proteins. *J. Am. Chem. Soc.* **2011**, *133*, 1112−1121.

(1117) Smith, L. J.; Stapleton, M. R.; Fullstone, G. J.; Crack, J. C.; Thomson, A. J.; Le Brun, N. E.; Hunt, D. M.; Harvey, E.; Adinolfi, S.; Buxton, R. S.; Green, J. *Mycobacterium tuberculosis* WhiB1 is an essential DNA-binding protein with a nitric oxide-sensitive iron−sulfur cluster. *Biochem. J.* **2010**, *432*, 417−427.

(1118) Crack, J. C.; Stapleton, M. R.; Green, J.; Thomson, A. J.; Le Brun, N. E. Mechanism of [4Fe-4S]$(Cys)_4$ cluster nitrosylation is conserved among NO-responsive regulators. *J. Biol. Chem.* **2013**, *288*, 11492−11502.

(1119) Meyer, J. Comparison of carbon monoxide, nitric oxide, and nitrite as inhibitors of the nitrogenase from *Clostridium pasteurianum*. *Arch. Biochem. Biophys.* **1981**, *210*, 246−256.

(1120) Welter, R.; Yu, L.; Yu, C.-A. The effects of nitric oxide on electron transport complexes. *Arch. Biochem. Biophys.* **1996**, *331*, 9−14.

(1121) Rogers, P. A.; Eide, L.; Klungland, A.; Ding, H. Reversible inactivation of *E. coli* endonuclease III via modification of its [4Fe-4S] cluster by nitric oxide. *DNA Repair* **2003**, *2*, 809−817.

(1122) Salerno, J. C.; Ohnishi, T.; et al. Tetranuclear and binuclear iron−sulfur clusters in succinate dehydrogenase: a method of iron quantification by formation of paramagnetic complexes. *Biochem. Biophys. Res. Commun.* **1976**, *73*, 833−840.

(1123) Yang, W.; Rogers, P. A.; Ding, H. Repair of nitric oxide-modified ferredoxin [2Fe-2S] cluster by cysteine desulfurase (IscS). *J. Biol. Chem.* **2002**, *277*, 12868−12873.

(1124) Sellers, V. M.; Johnson, M. K.; Dailey, H. A. Function of the [2Fe-2S] cluster in mammalian ferrochelatase: a possible role as a nitric oxide sensor. *Biochemistry* **1996**, *35*, 2699−2704.

(1125) Ceccaldi, P.; Etienne, E.; Dementin, S.; Guigliarelli, B.; Léger, C.; Burlat, B. Mechanism of inhibition of NiFe hydrogenase by nitric oxide. *Biochim. Biophys. Acta, Bioenerg.* **2016**, *1857*, 454−461.

(1126) Vanin, A. F.; Mikoyan, V. D.; Kubrina, L. N.; Borodulin, R. R.; Burgova, E. N. Mono- and binuclear dinitrosyl iron complexes with thiol-containing ligands in various biosystems. *Biophysics* **2015**, *60*, 603−612.

(1127) Borodulin, R. R.; Kubrina, L. N.; Serezhenkov, V. A.; Burbaev, D. S.; Mikoyan, V. D.; Vanin, A. F. Redox conversions of dinitrosyl iron complexes with natural thiol-containing ligands. *Nitric Oxide* **2013**, *35*, 35−41.

(1128) Tinberg, C. E.; Tonzetich, Z. J.; Wang, H.; Do, L. H.; Yoda, Y.; Cramer, S. P.; Lippard, S. J. Characterization of iron dinitrosyl species formed in the reaction of nitric oxide with a biological Rieske center. *J. Am. Chem. Soc.* **2010**, *132*, 18168−18176.

(1129) Tonzetich, Z. J.; Wang, H.; Mitra, D.; Tinberg, C. E.; Do, L. H.; Jenney, F. E.; Adams, M. W. W.; Cramer, S. P.; Lippard, S. J. Identification of protein-bound dinitrosyl iron complexes by nuclear resonance vibrational spectroscopy. *J. Am. Chem. Soc.* **2010**, *132*, 6914−6916.

(1130) Grabarczyk, D. B.; Ash, P. A.; Myers, W. K.; Dodd, E. L.; Vincent, K. A. Dioxygen controls the nitrosylation reactions of a protein-bound [4Fe4S] cluster. *Dalton Trans.* **2019**, *48*, 13960−13970.

(1131) Grabarczyk, D. B.; Ash, P. A.; Vincent, K. A. Infrared spectroscopy provides insight into the role of dioxygen in the nitrosylation pathway of a [2Fe2S] cluster iron−sulfur protein. *J. Am. Chem. Soc.* **2014**, *136*, 11236−11239.

(1132) Tsai, M.-L.; Chen, C.-C.; Hsu, I.-J.; Ke, S.-C.; Hsieh, C.-H.; Chiang, K.-A.; Lee, G.-H.; Wang, Y.; Chen, J.-M.; Lee, J.-F.; Liaw, W.-F. Photochemistry of the dinitrosyl iron complex $[S_5Fe(NO)_2]^-$

leading to reversible formation of $[S_5Fe(\mu\text{-}S)_2FeS_5]^{2-}$: spectroscopic characterization of species relevant to the nitric oxide modification and repair of [2Fe-2S] ferredoxins. *Inorg. Chem.* **2004**, *43*, 5159−5167.

(1133) Lu, T.-T.; Lai, S.-H.; Li, Y.-W.; Hsu, I. J.; Jang, L.-Y.; Lee, J.-F.; Chen, I.-C.; Liaw, W.-F. Discrimination of mononuclear and dinuclear dinitrosyl iron complexes (DNICs) by S K-edge X-ray absorption spectroscopy: insight into the electronic structure and reactivity of DNICs. *Inorg. Chem.* **2011**, *50*, 5396−5406.

(1134) Lu, T.-T.; Weng, T.-C.; Liaw, W.-F. X-ray emission spectroscopy: a spectroscopic measure for the determination of NO oxidation states in Fe-NO complexes. *Angew. Chem., Int. Ed.* **2014**, *53*, 11562−11566.

(1135) Tsai, M.-C.; Tsai, F.-T.; Lu, T.-T.; Tsai, M.-L.; Wei, Y.-C.; Hsu, I.-J.; Lee, J.-F.; Liaw, W.-F. Relative binding affinity of thiolate, imidazolate, phenoxide, and nitrite toward the $\{Fe(NO)_2\}$ motif of dinitrosyl iron complexes (DNICs): the characteristic pre-edge energy of $\{Fe(NO)_2\}^9$ DNICs. *Inorg. Chem.* **2009**, *48*, 9579−9591.

(1136) Yeh, S.-W.; Lin, C.-W.; Li, Y.-W.; Hsu, I.-J.; Chen, C.-H.; Jang, L.-Y.; Lee, J.-F.; Liaw, W.-F. Insight into the dinuclear $\{Fe(NO)_2\}^{10}\{Fe(NO)_2\}^{10}$ and mononuclear $\{Fe(NO)_2\}^{10}$ dinitrosyliron complexes. *Inorg. Chem.* **2012**, *51*, 4076−4087.

(1137) Zhang, B.; Crack, J. C.; Subramanian, S.; Green, J.; Thomson, A. J.; Le Brun, N. E.; Johnson, M. K. Reversible cycling between cysteine persulfide-ligated [2Fe-2S] and cysteine-ligated [4Fe-4S] clusters in the FNR regulatory protein. *Proc. Natl. Acad. Sci. U. S. A.* **2012**, *109*, 15734−15739.

(1138) Singh, A.; Guidry, L.; Narasimhulu, K. V.; Mai, D.; Trombley, J.; Redding, K. E.; Giles, G. I.; Lancaster, J. R., Jr.; Steyn, A. J. *Mycobacterium tuberculosis* WhiB3 responds to O_2 and nitric oxide via its [4Fe-4S] cluster and is essential for nutrient starvation survival. *Proc. Natl. Acad. Sci. U. S. A.* **2007**, *104*, 11562−11567.

(1139) Bouton, C.; Chauveau, M. J.; Lazereg, S.; Drapier, J. C. Recycling of RNA binding iron regulatory protein 1 into an aconitase after nitric oxide removal depends on mitochondrial ATP. *J. Biol. Chem.* **2002**, *277*, 31220−31227.

(1140) Drapier, J.-C. Interplay between NO and [Fe-S] clusters: relevance to biological systems. *Methods* **1997**, *11*, 319−319.

(1141) Gu, M.; Imlay, J. A. The SoxRS response of *Escherichia coli* is directly activated by redox-cycling drugs rather than by superoxide. *Mol. Microbiol.* **2011**, *79*, 1136−1150.

(1142) Vasil'eva, S. V.; Stupakova, M. V.; Lobysheva, I. I.; Mikoyan, V. D.; Vanin, A. F. Activation of the *Escherichia coli Sox*RS-regulon by nitric oxide and its physiological donors. *Biochemistry* **2001**, *66*, 984−988.

(1143) Pieper, G. M.; Halligan, N. L.; Hilton, G.; Konorev, E. A.; Felix, C. C.; Roza, A. M.; Adams, M. B.; Griffith, O. W. Non-heme iron protein: a potential target of nitric oxide in acute cardiac allograft rejection. *Proc. Natl. Acad. Sci. U. S. A.* **2003**, *100*, 3125−3130.

(1144) Ekanger, L. A.; Oyala, P. H.; Moradian, A.; Sweredoski, M. J.; Barton, J. K. Nitric oxide modulates endonuclease III redox activity by a 800 mV negative shift upon $[Fe_4S_4]$ cluster nitrosylation. *J. Am. Chem. Soc.* **2018**, *140*, 11800−11810.

(1145) Duan, X.; Yang, J.; Ren, B.; Tan, G.; Ding, H. Reactivity of nitric oxide with the [4Fe-4S] cluster of dihydroxyacid dehydratase from *Escherichia coli*. *Biochem. J.* **2009**, *417*, 783−789.

(1146) Ren, B.; Zhang, N.; Yang, J.; Ding, H. Nitric oxide-induced bacteriostasis and modification of iron-sulphur proteins in *Escherichia coli*. *Mol. Microbiol.* **2008**, *70*, 953−964.

(1147) Kovacevic, Z.; Sahni, S.; Lok, H.; Davies, M. J.; Wink, D. A.; Richardson, D. R. Regulation and control of nitric oxide (NO) in macrophages: Protecting the "professional killer cell" from its own cytotoxic arsenal via MRP1 and GSTP1. *Biochim. Biophys. Acta, Gen. Subj.* **2017**, *1861*, 995−999.

(1148) Suryo Rahmanto, Y.; Kalinowski, D. S.; Lane, D. J.; Lok, H. C.; Richardson, V.; Richardson, D. R. Nitrogen monoxide (NO) storage and transport by dinitrosyl-dithiol-iron complexes: long-lived NO that is trafficked by interacting proteins. *J. Biol. Chem.* **2012**, *287*, 6960−6968.

(1149) Richardson, D. R.; Lok, H. C. The nitric oxide-iron interplay in mammalian cells: transport and storage of dinitrosyl iron complexes. *Biochim. Biophys. Acta, Gen. Subj.* **2008**, *1780*, 638−651.

(1150) Lee, M.; Arosio, P.; Cozzi, A.; Chasteen, N. D. Identification of the EPR-active iron-nitrosyl complexes in mammalian ferritins. *Biochemistry* **1994**, *33*, 3679−3687.

(1151) D'Autréaux, B.; Touati, D.; Bersch, B.; Latour, J. M.; Michaud-Soret, I. Direct inhibition by nitric oxide of the transcriptional ferric uptake regulation protein via nitrosylation of the iron. *Proc. Natl. Acad. Sci. U. S. A.* **2002**, *99*, 16619−16624.

(1152) Mukhopadhyay, P.; Zheng, M.; Bedzyk, L. A.; LaRossa, R. A.; Storz, G. Prominent roles of the NorR and Fur regulators in the *Escherichia coli* transcriptional response to reactive nitrogen species. *Proc. Natl. Acad. Sci. U. S. A.* **2004**, *101*, 745−750.

(1153) D'Autréaux, B.; Horner, O.; Oddou, J.-L.; Jeandey, C.; Gambarelli, S.; Berthomieu, C.; Latour, J.-M.; Michaud-Soret, I. Spectroscopic description of the two nitrosyl-iron complexes responsible for Fur inhibition by nitric oxide. *J. Am. Chem. Soc.* **2004**, *126*, 6005−6016.

(1154) Goussias, C.; Deligiannakis, Y.; Sanakis, Y.; Ioannidis, N.; Petrouleas, V. Probing subtle coordination changes in the iron-quinone complex of photosystem II during charge separation, by the use of NO. *Biochemistry* **2002**, *41*, 15212−15223.

(1155) Shumaev, K. B.; Gubkin, A. A.; Serezhenkov, V. A.; Lobysheva, II; Kosmachevskaya, O. V.; Ruuge, E. K.; Lankin, V. Z.; Topunov, A. F.; Vanin, A. F. Interaction of reactive oxygen and nitrogen species with albumin- and methemoglobin-bound dinitrosyl-iron complexes. *Nitric Oxide* **2008**, *18*, 37−46.

(1156) D'Autréaux, B.; Tucker, N. P.; Dixon, R.; Spiro, S. A non-haem iron centre in the transcription factor NorR senses nitric oxide. *Nature* **2005**, *437*, 769−772.

(1157) Pohlmann, A.; Cramm, R.; Schmelz, K.; Friedrich, B. A novel NO-responding regulator controls the reduction of nitric oxide in *Ralstonia eutropha*. *Mol. Microbiol.* **2000**, *38*, 626−638.

(1158) Gardner, A. M.; Gessner, C. R.; Gardner, P. R. Regulation of the nitric oxide reduction operon (*norRVW*) in *Escherichia coli*. Role of NorR and σ^{54} in the nitric oxide stress response. *J. Biol. Chem.* **2003**, *278*, 10081−10086.

(1159) Fitzpatrick, J.; Kalyvas, H.; Shearer, J.; Kim, E. Dioxygen mediated conversion of $\{Fe(NO)_2\}^9$ dinitrosyl iron complexes to Roussin's red esters. *Chem. Commun.* **2013**, *49*, 5550−5552.

(1160) Cheng, Z.; Landry, A. P.; Wang, Y.; Ding, H. Binding of nitric oxide in CDGSH-type [2Fe-2S] clusters of the human mitochondrial protein Miner2. *J. Biol. Chem.* **2017**, *292*, 3146−3153.

(1161) Lo, F.-C.; Hsieh, C.-C.; Maestre-Reyna, M.; Chen, C.-Y.; Ko, T.-P.; Horng, Y.-C.; Lai, Y.-C.; Chiang, Y.-W.; Chou, C.-M.; Chiang, C.-H.; Huang, W.-N.; Lin, Y.-H.; Bohle, D. S.; Liaw, W.-F. Crystal structure analysis of the repair of iron centers protein YtfE and its interaction with NO. *Chem. - Eur. J.* **2016**, *22*, 9768−9776.

(1162) Nobre, L. S.; Garcia-Serres, R.; Todorovic, S.; Hildebrandt, P.; Teixeira, M.; Latour, J. M.; Saraiva, L. M. *Escherichia coli* RIC is able to donate iron to iron−sulfur clusters. *PLoS One* **2014**, *9*, No. e95222.

(1163) Justino, M. C.; Vicente, J. B.; Teixeira, M.; Saraiva, L. M. New genes implicated in the protection of anaerobically grown *Escherichia coli* against nitric oxide. *J. Biol. Chem.* **2005**, *280*, 2636−2643.

(1164) Justino, M. C.; Almeida, C. C.; Teixeira, M.; Saraiva, L. M. *Escherichia coli* di-iron YtfE protein is necessary for the repair of stress-damaged iron−sulfur clusters. *J. Biol. Chem.* **2007**, *282*, 10352−10359.

(1165) Yang, J.; Duan, X.; Landry, A. P.; Ding, H. Oxygen is required for the L-cysteine-mediated decomposition of protein-bound dinitrosyl-iron complexes. *Free Radical Biol. Med.* **2010**, *49*, 268−274.

(1166) Lu, T.-T.; Huang, H.-W.; Liaw, W.-F. Anionic mixed thiolate-sulfide-bridged Roussin's red esters $[(NO)_2Fe(\mu\text{-}SR)(\mu\text{-}S)Fe(NO)_2]^-$ (R = Et, Me, Ph): a key intermediate for transformation of dinitrosyl iron complexes (DNICs) to [2Fe-2S] clusters. *Inorg. Chem.* **2009**, *48*, 9027−9035.

(1167) Brockway, L. O.; Anderson, J. S. The molecular structures of iron nitrosocarbonyl $Fe(NO)_2(CO)_2$ and cobalt nitroscocarbonyl $Co(NO)(CO)_3$. *Trans. Faraday Soc.* **1937**, *33*, 1233−1239.

(1168) Wang, X.; Sundberg, E. B.; Li, L.; Kantardjieff, K. A.; Herron, S. R.; Lim, M.; Ford, P. C. A cyclic tetra-nuclear dinitrosyl iron complex $[Fe(NO)_2(imidazolate)]_4$: synthesis, structure and stability. *Chem. Commun.* **2005**, 477−479.

(1169) Hess, J. L.; Hsieh, C.-H.; Reibenspies, J. H.; Darensbourg, M. Y. N-heterocyclic carbene ligands as mimics of imidazoles/histidine for the stabilization of di- and trinitrosyl iron complexes. *Inorg. Chem.* **2011**, *50*, 8541−8552.

(1170) Hess, J. L.; Hsieh, C.-H.; Brothers, S. M.; Hall, M. B.; Darensbourg, M. Y. Self-assembly of dinitrosyl iron units into imidazolate-edge-bridged molecular squares: characterization including Mössbauer spectroscopy. *J. Am. Chem. Soc.* **2011**, *133*, 20426−20434.

(1171) Li, L. Some coordination chemistry of non-heme iron nitrosyl complexes. *Comments Inorg. Chem.* **2002**, *23*, 335−353.

(1172) Tsou, C.-C.; Chiu, W.-C.; Ke, C.-H.; Tsai, J.-C.; Wang, Y.-M.; Chiang, M.-H.; Liaw, W.-F. Iron(III) bound by hydrosulfide anion ligands: NO-promoted stabilization of the $[Fe^{III}\text{-}SH]$ motif. *J. Am. Chem. Soc.* **2014**, *136*, 9424−9433.

(1173) Tsou, C.-C.; Lu, T.-T.; Liaw, W.-F. EPR, UV−vis, IR, and X-ray demonstration of the anionic dimeric dinitrosyl iron complex $[(NO)_2Fe(\mu\text{-}S^tBu)_2Fe(NO)_2]^-$: relevance to the products of nitrosylation of cytosolic and mitochondrial aconitases, and high-potential iron proteins. *J. Am. Chem. Soc.* **2007**, *129*, 12626−12627.

(1174) Lu, T.-T.; Chiou, S.-J.; Chen, C.-Y.; Liaw, W.-F. Mononitrosyl tris(thiolate) iron complex $[Fe(NO)(SPh)_3]]s]]$-. *Inorg. Chem.* **2006**, *45*, 8799−8806.

(1175) Chiou, S.-J.; Wang, C.-C.; Chang, C.-M. Synthesis of dinitrosyl iron complexes (DNICs) with intramolecular hydrogen bonding. *J. Organomet. Chem.* **2008**, *693*, 3582−3586.

(1176) Strasdeit, H.; Krebs, B.; Henkel, G. Synthesis and structure of $[Fe(SPh)_2(NO)_2]^-$, the "monomer" of Roussin's phenyl ester. *Z. Naturforsch., B: J. Chem. Sci.* **1986**, *41*, 1357−1362.

(1177) Tsai, F.-T.; Chiou, S.-J.; Tsai, M.-C.; Tsai, M.-L.; Huang, H.-W.; Chiang, M.-H.; Liaw, W.-F. Dinitrosyl iron complexes (DNICs) $[L_2Fe(NO)_2]]s]]$-. *Inorg. Chem.* **2005**, *44*, 5872−5881.

(1178) Tsai, M.-L.; Liaw, W.-F. Neutral $\{Fe(NO)_2\}^9$ dinitrosyliron complex (DNIC) $[(SC_6H_4\text{-}o\text{-}NHCOPh)(Im)Fe(NO)_2]$ (Im = imidazole): interconversion among the anionic/neutral $\{Fe(NO)_2\}^9$ DNICs and Roussin's red ester. *Inorg. Chem.* **2006**, *45*, 6583−6585.

(1179) Lin, Z.-S.; Lo, F.-C.; Li, C.-H.; Chen, C.-H.; Huang, W.-N.; Hsu, I.-J.; Lee, J.-F.; Horng, J.-C.; Liaw, W.-F. Peptide-bound dinitrosyliron complexes (DNICs) and neutral/reduced-form Roussin's red esters (RREs/rRREs): understanding nitrosylation of [Fe-S] clusters leading to the formation of DNICs and RREs using a de novo design strategy. *Inorg. Chem.* **2011**, *50*, 10417−10431.

(1180) Wang, J.-H.; Chen, C.-H. New members of the $\{Fe(NO)_2\}^{10}$ dinitrosyliron complexes bound with [thiolate, thiolate] and [amide, amide] ligations. *Inorg. Chem.* **2010**, *49*, 7644−7646.

(1181) Lin, Z.-S.; Chiou, T.-W.; Liu, K.-Y.; Hsieh, C.-C.; Yu, J.-S.; Liaw, W.-F. A dinitrosyliron complex within the homoleptic $Fe(NO)_4$ anion: NO as nitroxyl and nitrosyl ligands within a single structure. *Inorg. Chem.* **2012**, *51*, 10092−10094.

(1182) Roncaroli, F.; van Eldik, R.; Olabe, J. A. Release of NO from reduced nitroprusside ion. Iron-dinitrosyl formation and NO-disproportionation reactions. *Inorg. Chem.* **2005**, *44*, 2781−2790.

(1183) Hsieh, C.-H.; Brothers, S. M.; Reibenspies, J. H.; Hall, M. B.; Popescu, C. V.; Darensbourg, M. Y. Ambidentate thiocyanate and cyanate ligands in dinitrosyl iron complexes. *Inorg. Chem.* **2013**, *52*, 2119−2124.

(1184) Tsai, M.-L.; Hsieh, C.-H.; Liaw, W.-F. Dinitrosyl iron complexes (DNICs) containing S/N/O ligation: transformation of Roussin's red ester into the neutral $\{Fe(NO)_2\}^{10}$ DNICs. *Inorg. Chem.* **2007**, *46*, 5110−5117.

(1185) Huang, H.-W.; Tsou, C.-C.; Kuo, T.-S.; Liaw, W.-F. New members of a class of dinitrosyliron complexes (DNICs): interconversion and spectroscopic discrimination of the anionic $\{Fe(NO)_2\}^9$ $[(NO)_2Fe(C_3H_3N_2)_2]^-$ and $[(NO)_2Fe(C_3H_3N_2)(SR)]^-$ ($C_3H_3N_2$ = deprotonated imidazole; R = ^{t}Bu, Et, Ph). *Inorg. Chem.* **2008**, *47*, 2196−2204.

(1186) Chen, C.-H.; Wang, J.-H.; Huang, J.-Y.; Hsieh, C.-H. A new member of tetranuclear dinitrosyl iron complexes (DNICs) with 2-mercaptothiazoline ligand: synthesis, structure and properties. *Res. Chem. Intermed.* **2014**, *40*, 2217−2227.

(1187) Lu, T.-T.; Chen, C.-H.; Liaw, W.-F. Formation of the distinct redox-interrelated forms of nitric oxide from reaction of dinitrosyl iron complexes (DNICs) and substitution ligands. *Chem. - Eur. J.* **2010**, *16*, 8088−8095.

(1188) Tsou, C.-C.; Tsai, F.-T.; Chen, H.-Y.; Hsu, I.-J.; Liaw, W.-F. Insight into one-electron oxidation of the $\{Fe(NO)_2\}^9$ dinitrosyl iron complex (DNIC): aminyl radical stabilized by $[Fe(NO)_2]$ motif. *Inorg. Chem.* **2013**, *52*, 1631−1639.

(1189) Liu, P.-H.; Tsai, F.-T.; Chen, B.-H.; Hsu, I.-J.; Hsieh, H.-H.; Liaw, W.-F. Insight into chalcogenolate-bound $\{Fe(NO)_2\}^9$ dinitrosyl iron complexes (DNICs): covalent character *versus* ionic character. *Dalton Trans.* **2019**, *48*, 6040−6050.

(1190) Tsai, F.-T.; Chen, P.-L.; Liaw, W.-F. Roles of the distinct electronic structures of the $\{Fe(NO)_2\}^9$ and $\{Fe(NO)_2\}^{10}$ dinitrosyliron complexes in modulating nitrite binding modes and nitrite activation pathways. *J. Am. Chem. Soc.* **2010**, *132*, 5290−5299.

(1191) Tsai, F.-T.; Lee, Y.-C.; Chiang, M.-H.; Liaw, W.-F. Nitrate-to-nitrite-to-nitric oxide conversion modulated by nitrate-containing $\{Fe(NO)_2\}^9$ dinitrosyl iron complex (DNIC). *Inorg. Chem.* **2013**, *52*, 464−473.

(1192) Connelly, N. G.; Gardner, C. Simple halogenonitrosyl anions of iron. *J. Chem. Soc., Dalton Trans.* **1976**, 1525−1527.

(1193) In-Iam, A.; Wolf, M.; Wilfer, C.; Schaniel, D.; Woike, T.; Klüfers, P. $\{FeNO\}^7$ -type halogenido nitrosyl ferrates: syntheses, bonding, and photoinduced linkage isomerism. *Chem. - Eur. J.* **2019**, *25*, 1304−1325.

(1194) Hung, M.-C.; Tsai, M.-C.; Lee, G.-H.; Liaw, W.-F. Transformation and structural discrimination between the neutral $\{Fe(NO)_2\}^{10}$ dinitrosyliron complexes (DNICs) and the anionic cationic $\{Fe(NO)_2\}^9$ DNICs. *Inorg. Chem.* **2006**, *45*, 6041−6047.

(1195) Chiang, C.-Y.; Miller, M. L.; Reibenspies, J. H.; Darensbourg, M. Y. Bismercaptoethanediazacyclooctane as a N_2S_2 chelating agent and Cys-X-Cys mimic for Fe(NO) and $Fe(NO)_2$. *J. Am. Chem. Soc.* **2004**, *126*, 10867−10874.

(1196) Schiewer, C. E.; Müller, C. S.; Dechert, S.; Bergner, M.; Wolny, J. A.; Schünemann, V.; Meyer, F. Effect of oxidation and protonation states on [2Fe-2S] cluster nitrosylation giving $\{Fe(NO)_2\}^9$ dinitrosyl iron complexes (DNICs). *Inorg. Chem.* **2019**, *58*, 769−784.

(1197) Lu, C.-Y.; Liaw, W.-F. Formation pathway of Roussin's red ester (RRE) via the reaction of a $\{Fe(NO)_2\}^{10}$ dinitrosyliron complex (DNIC) and thiol: facile synthetic route for synthesizing cysteine-containing DNIC. *Inorg. Chem.* **2013**, *52*, 13918−13926.

(1198) Pinder, T. A.; Montalvo, S. K.; Hsieh, C.-H.; Lunsford, A. M.; Bethel, R. D.; Pierce, B. S.; Darensbourg, M. Y. Metallodithiolates as ligands to dinitrosyl iron complexes: toward the understanding of structures, equilibria, and spin coupling. *Inorg. Chem.* **2014**, *53*, 9095−9105.

(1199) Atkinson, F. L.; Blackwell, H. E.; Brown, N. C.; Connelly, N. G.; Crossley, J. G.; Orpen, A. G.; Rieger, A. L.; Rieger, P. H. Synthesis of the 17-electron cations $[FeL(L')(NO)_2]^+$ (L, L' = PPh_3, $OPPh_3$): structure and bonding in four-coordiniate metal dinitrosyl complex catalysts. *J. Chem. Soc., Dalton Trans.* **1996**, 3491−3502.

(1200) Tsou, C.-C.; Liaw, W.-F. Transformation of the $\{Fe(NO)_2\}^9$ dinitrosyl iron complexes (DNICs) into S-nitrosothiols (RSNOs) triggered by acid-base pairs. *Chem. - Eur. J.* **2011**, *17*, 13358−13366.

(1201) Tsai, F.-T.; Kuo, T.-S.; Liaw, W.-F. Dinitrosyl iron complexes (DNICs) bearing O-bound nitrito ligand: reversible transformation between the six-coordinate $\{Fe(NO)\}^9$ $[(1\text{-}MeIm)_2(\eta^2\text{-}ONO)Fe(NO)_2]$ (g = 2.013) and four-coordinate $\{Fe(NO)_2\}^9$ $[(1\text{-}MeIm)(ONO)Fe(NO)_2]$ (g = 2.03). *J. Am. Chem. Soc.* **2009**, *131*, 3426−3427.

(1202) Wah, H. L. K.; Postel, M.; Tomi, F. The iron-nitrato/iron-nitrosyl couple in the presence of hexamethylphosphoric triamide and its relevance to oxygen activation and transfer. X-ray structure of $Fe(NO_3)(Cl)_2(HMPA)_2$. *Inorg. Chem.* **1989**, *28*, 233−238.

(1203) Guillaume, P.; Postel, M. Reactivity of 2-(diphenylphosphino)pyridine and 2-(diphenylphosphine otide)-pyridine towards iron nitrosyl complexes and its relevance to oxygen activation. *Inorg. Chim. Acta* **1995**, *233*, 109−112.

(1204) Pulukkody, R.; Kyran, S. J.; Drummond, M. J.; Hsieh, C.-H.; Darensbourg, D. J.; Darensbourg, M. Y. Hammett correlations as test of mechanism of CO-induced disulfide elimination from dinitrosyl iron complexes. *Chem. Sci.* **2014**, *5*, 3795−3802.

(1205) Pulukkody, R.; Chupik, R. B.; Montalvo, S. K.; Khan, S.; Bhuvanesh, N.; Lim, S.-M.; Darensbourg, M. Y. Toward biocompatible dinitrosyl iron complexes: sugar-appended thiolates. *Chem. Commun.* **2017**, *53*, 1180−1183.

(1206) Chiang, C.-Y.; Darensbourg, M. Y. Iron nitrosyl complexes as models for biological nitric oxide transfer reagents. *JBIC, J. Biol. Inorg. Chem.* **2006**, *11*, 359−370.

(1207) Chen, C.-H.; Ho, Y.-C.; Lee, G.-H. Synthesis and reactivity of the five-coordinate $\{Fe(NO)_2\}^9$ $[(TMEDA)Fe(NO)_2I]$. *J. Organomet. Chem.* **2009**, *694*, 3395−3400.

(1208) Skodje, K. M.; Kwon, M.-Y.; Chung, S. W.; Kim, E. Coordination-triggered NO release from a dinitrosyl iron complex leads to anti-inflammatory activity. *Chem. Sci.* **2014**, *5*, 2374−2378.

(1209) Shih, W.-C.; Lu, T.-T.; Yang, L.-B.; Tsai, F.-T.; Chiang, M.-H.; Lee, J.-F.; Chiang, Y.-W.; Liaw, W.-F. New members of a class of dinitrosyliron complexes (DNICs): the characteristic EPR signal of the six-coordinate and five-coordinate $\{Fe(NO)_2\}^9$ DNICs. *J. Inorg. Biochem.* **2012**, *113*, 83−93.

(1210) Sanina, N. A.; Aldoshin, S. M.; Shmatko, N. y. Y.; Korchagin, D. V.; Shilov, G. V.; Knyazkina, E. V.; Ovanesyan, N. S.; Kulikov, A. V. Nitrosyl iron complexes with enhanced NO donating ability: synthesis, structure and properties of a new type of salt with the DNIC cations $[Fe(SC(NH_2)_2)_2(NO)_2]^+$. *New J. Chem.* **2015**, *39*, 1022−1030.

(1211) Shmatko, N. Y.; Korchagin, D. V.; Shilov, G. V.; Ovanesyan, N. S.; Kulikov, A. V.; Sanina, N. A.; Aldoshin, S. M. The cationic dinitrosyl iron complexes family with thiocarbamide derivatives: Synthesis, structure and properties in the solid state. *Polyhedron* **2017**, *137*, 72−80.

(1212) Shmatko, N. Y.; Korchagin, D. V.; Shilov, G. V.; Sanina, N. A.; Aldoshin, S. M. Molecular and crystal structure of a cationic dinitrosyl iron complex with 1,3-dimethylthiourea. *J. Struct. Chem.* **2017**, *58*, 353−355.

(1213) Ke, C.-H.; Chen, C.-H.; Tsai, M.-L.; Wang, H.-C.; Tsai, F.-T.; Chiang, Y.-W.; Shih, W.-C.; Bohle, D. S.; Liaw, W.-F. $\{Fe(NO)_2\}^9$ dinitrosyl iron complex acting as a vehicle for the NO radical. *J. Am. Chem. Soc.* **2017**, *139*, 67−70.

(1214) Chiou, T.-W.; Lu, T.-T.; Wu, Y.-H.; Yu, Y.-J.; Chu, L.-K.; Liaw, W.-F. Development of a dinitrosyl iron complex molecular catalyst into a hydrogen evolution cathode. *Angew. Chem., Int. Ed.* **2015**, *54*, 14824−14829.

(1215) Li, W.-L.; Chiou, T.-W.; Chen, C.-H.; Yu, Y.-J.; Chu, L.-K.; Liaw, W.-F. Electrodeposited-film electrodes derived from a precursor dinitrosyl iron complex for electrocatalytic water splitting. *Dalton Trans.* **2018**, *47*, 7128−7134.

(1216) Jo, D.-H.; Chiou, Y.-M.; Que, L. Models for extradiol cleaving catechol dioxygenases: syntheses, structures, and reactivities of iron(II)-monoanionic catecholate complexes. *Inorg. Chem.* **2001**, *40*, 3181−3190.

(1217) Kwon, Y. M.; Delgado, M.; Zakharov, L. N.; Seda, T.; Gilbertson, J. D. Nitrite reduction by a pyridinediimine complex with a proton-responsive secondary coordination sphere. *Chem. Commun.* **2016**, *52*, 11016−11019.

(1218) Burns, K. T.; Marks, W. R.; Cheung, P. M.; Seda, T.; Zakharov, L. N.; Gilbertson, J. D. Uncoupled redox-inactive Lewis acids in the secondary coordination sphere entice ligand-based nitrite reduction. *Inorg. Chem.* **2018**, *57*, 9601−9610.

(1219) Delgado, M.; Gilbertson, J. D. Ligand-based reduction of nitrate to nitric oxide utilizing a proton-responsive secondary coordination sphere. *Chem. Commun.* **2017**, *53*, 11249−11252.

(1220) Yeh, S.-W.; Lin, C.-W.; Liu, B.-H.; Tsou, C.-C.; Tsai, M.-L.; Liaw, W.-F. Chelate-thiolate-coordinate ligands modulating the configuration and electrochemical property of dinitrosyliron complexes (DNICs). *Chem. - Eur. J.* **2015**, *21*, 16035−16046.

(1221) Huang, H.-C.; Ching, W.-M.; Tseng, Y.-T.; Chen, C.-H.; Lu, T.-T. Transformation of the hydride-containing dinitrosyl iron complex $[(NO)_2Fe(\eta^2\text{-}BH_4)]^-$ into $[(NO)_2Fe(\eta^3\text{-}HCS_2)]^-$ *via* reaction with CS_2. *Dalton Trans.* **2019**, *48*, 5897−5902.

(1222) Lo, F.-C.; Ho, Y.-C.; Chang, P.-Y.; Lee, G.-H.; Kuo, T.-S.; Chen, J.-L.; Chen, C.-H. New members of a class of monomeric $\{Fe(NO)_2\}^{10}$ dinitrosyliron complexes and a dimeric $\{Fe(NO)_2\}^{10}$-$\{Fe(NO)_2\}^{10}$ dinitrosyliron complex. *Eur. J. Inorg. Chem.* **2014**, *2014*, 3499−3509.

(1223) Chen, C.-H.; Chiou, S.-J.; Chen, H.-Y. Dinuclear $[\{Fe(NO)_2\}^{10}\text{-}\{Fe(NO)_2\}^{10}]$ dinitrosyl iron complex with thiolate-CO-bridged ligands. *Inorg. Chem.* **2010**, *49*, 2023−2025.

(1224) Ghosh, P.; Quiroz, M.; Pulukkody, R.; Bhuvanesh, N.; Darensbourg, M. Y. Bridging cyanides from cyanoiron metalloligands to redox-active dinitrosyl iron units. *Dalton Trans.* **2018**, *47*, 11812−11819.

(1225) Wittkamp, F.; Nagel, C.; Lauterjung, P.; Mallick, B.; Schatzschneider, U.; Apfel, U.-P. Phosphine-ligated dinitrosyl iron complexes for redox-controlled NO release. *Dalton Trans.* **2016**, *45*, 10271−10279.

(1226) Dillinger, S. A.; Schmalle, H. W.; Fox, T.; Berke, H. Developing iron nitrosyl complexes as NO donor prodrugs. *Dalton Trans.* **2007**, 3562−3571.

(1227) Albano, V. G.; Araneo, A.; Bellon, P. L.; Ciani, G.; Manassero, M. Stereochemistry of tetrahedral complexes of group VIII metals. Crystal and molecular structures of dinitrosylcarbonyltriphenylphosphineiron, $Fe(NO)_2(CO)(PPh_3)$, and of ditrosylbis(triphenylphosphine)iron, $Fe(NO)_2(PPh_3)_2$. *J. Organomet. Chem.* **1974**, *67*, 413−422.

(1228) Malatesta, L.; Aràneo, A. The interaction of iron and cobalt nitrosyl carbonyls with triaryl phosphites and triaryl-phosphones, -arsines, and -stibines. *J. Chem. Soc.* **1957**, 3803−3805.

(1229) Jones, M. W.; Powell, D. R.; Richter-Addo, G. B. Synthesis, characterization, and fiber-optic infrared reflectance spectroelectrochemical studies of some dinitrosyl iron diphosphine complexes $Fe(NO)_2L_2$ ($L = P(C_6H_4X)_3$). *J. Organomet. Chem.* **2014**, *754*, 63−74.

(1230) Jones, M. W.; Powell, D. R.; Richter-Addo, G. B. Dinitrosylbis[tris(4-methylphen-yl)phosphane]iron. *Acta Crystallogr., Sect. E: Struct. Rep. Online* **2011**, *67*, No. m331.

(1231) Jones, M. W.; Powell, D. R.; Richter-Addo, G. B. Dinitrosylbis[tris-(4-fluorophenyl)phosphane]iron chloroform monosolvate. *Acta Crystallogr., Sect. E: Struct. Rep. Online* **2011**, *67*, No. m332.

(1232) Jones, M. W.; Powell, D. R.; Richter-Addo, G. B. Dinitrosylbis[tris(4-chlorophenyl)phosphane]iron. *Acta Crystallogr., Sect. E: Struct. Rep. Online* **2011**, *67*, No. m247.

(1233) Chen, Y.-J.; Ku, W.-C.; Feng, L.-T.; Tsai, M.-L.; Hsieh, C.-H.; Hsu, W.-H.; Liaw, W.-F.; Hung, C.-H.; Chen, Y.-J. Nitric oxide physiological responses and delivery mechanisms probed by water-soluble Roussin's red ester and $\{Fe(NO)_2\}^{10}$ DNIC. *J. Am. Chem. Soc.* **2008**, *130*, 10929−10938.

(1234) Beagan, D. M.; Carta, V.; Caulton, K. G. A reagent for heteroatom borylation, including iron mediated reductive deoxygenation of nitrate yielding a dinitrosyl complex. *Dalton Trans.* **2020**, *49*, 1681−1687.

(1235) Dessy, R. E.; Charkoudian, J. C.; Rheingold, A. L. Organometallic electrochemistry. XVII. Electric charge distribution organometallic compounds, tetrahedral derivatives of $Co(CO)_3(NO)$ and $Fe(CO)_2(NO)_2$. *J. Am. Chem. Soc.* **1972**, *94*, 738−745.

(1236) Wang, R.; Wang, X.; Sundberg, E. B.; Nguyen, P.; Grant, G. P.; Sheth, C.; Zhao, Q.; Herron, S.; Kantardjieff, K. A.; Li, L. Synthesis, structures, spectroscopic and electrochemical properties of dinitrosyl iron complexes with bipyridine, terpyridine, and 1,10-phenathroline. *Inorg. Chem.* **2009**, *48*, 9779−9785.

(1237) Skodje, K. M.; Williard, P. G.; Kim, E. Conversion of $\{Fe(NO)_2\}^{10}$ dinitrosyl iron to nitrato iron(III) species by molecular oxygen. *Dalton Trans.* **2012**, *41*, 7849−7851.

(1238) Ke, C.-H.; Shih, W.-C.; Tsai, F.-T.; Tsai, M.-L.; Ching, W.-M.; Hsieh, H.-H.; Liaw, W.-F. Electrocatalytic water reduction beginning with a $\{Fe(NO)_2\}^{10}$-reduced dinitrosyliron complex: identification of nitrogen-doped $FeO_x(OH)_y$ as a real heterogeneous catalyst. *Inorg. Chem.* **2018**, *57*, 14715−14726.

(1239) Li Kam Wah, H.; Postel, M.; Pierrot, M. Structure-activity correlation in iron nitrosyl complexes: crystal structures of $[Fe(NO)_2(Cl)]_2(\mu\text{-dppe})$ and $Fe(NO)_2(dppe)$. *Inorg. Chim. Acta* **1989**, *165*, 215−220.

(1240) Holloway, L. R.; Clough, A. J.; Li, J. Y.; Tao, E. L.; Tao, F. M.; Li, L. A combined experimental and theoretical study of dinitrosyl iron complexes containing chelating bis(diphenyl)phosphinoX (X = benzene, propane and ethylene): X-ray crystal structures and properties influenced by the presence or absence of pi-bonds in chelating ligands. *Polyhedron* **2014**, *70*, 29−38.

(1241) Tseng, Y.-T.; Ching, W.-M.; Liaw, W.-F.; Lu, T.-T. Dinitrosyl iron complex $[K\text{-}18\text{-crown-}6\text{-ether}][(NO)_2Fe(^{Me}PyrCO_2)]$: intermediate for capture and reduction of carbon dioxide. *Angew. Chem., Int. Ed.* **2020**, *59*, 11819−11823.

(1242) Li, L.; Enright, G. D.; Preston, K. F. Synthesis and X-ray crystal structure of a novel iron nitrosyl complex, $Fe(NO)_2PPh_3(\eta^2\text{-TCNE})$. *Organometallics* **1994**, *13*, 4686−4688.

(1243) Suzuki, T.; Matsumoto, J.; Kajita, Y.; Inomata, T.; Ozawa, T.; Masuda, H. Nitrosyl and carbene iron complexes bearing a k^3-SNS thioamide pincer type ligand. *Dalton Trans.* **2015**, *44*, 1017−1022.

(1244) Butler, A. R.; Glidewell, C.; Hyde, A. R.; McGinnis, J. Nitrogen-15 and carbon-13 NMR study of Roussin salts and esters and of pentacyanoferrate complexes. *Inorg. Chem.* **1985**, *24*, 2931−2934.

(1245) Wang, R.; Camacho-Fernandez, M. A.; Xu, W.; Zhang, J.; Li, L. Neutral and reduced Roussin's red salt ester $[Fe_2(\mu\text{-RS})_2(NO)_4]$ (R = *n*-Pr, *t*-Bu, 6-methyl-2-pyridyl and 4,6-dimethyl-2-pyrimidyl): synthesis, X-ray crystal structures, spectroscopic, electrochemical and density functional theoretical investigations. *Dalton Trans.* **2009**, 777−786.

(1246) Chang, H.-H.; Huang, H.-J.; Ho, Y.-L.; Wen, Y.-D.; Huang, W.-N.; Chiou, S.-J. The water-soluble Roussin's red ester acting as a potential photochemical NO-delivery agent: photolysis reactions, DNA cleavage and anticancer activity. *Dalton Trans.* **2009**, 6396−6402.

(1247) Glidewell, C.; Harman, M. E.; Hursthouse, M. B.; Johnson, I. L.; Motevalli, M. The conformation of Roussin esters - crystal and molecular-structures of bis(methanethiolato)bis(dinitrosyliron), bis(pentanethiolato)bis(dinitrosyliron), and bis(2-methylpropane-2-thiolato)bis(dinitrosyliron). *J. Chem. Res.-S.* **1988**, 212−213.

(1248) Davidovich, P. B.; Gurzhiy, V. V.; Sanina, N. A.; Shchukarev, A. V.; Garabadzhiu, A. V.; Belyaev, A. N. Synthesis and structure of dinitrosyl iron complexes with secondary thiolate bridging ligands $[Fe_2(\mu\text{-SCHR}_2)_2(NO)_4]$, R = Me, Ph. *Polyhedron* **2015**, *90*, 197−201.

(1249) Lee, H. M.; Chiou, S.-J. *trans*-Bis(μ-2-hydroxy-ethanethiolato-k^2S:S)bis[dinitrosyliron(II)](Fe-Fe). *Acta Crystallogr., Sect. E: Struct. Rep. Online* **2009**, *65*, No. m1600.

(1250) Rauchfuss, T. B.; Weatherill, T. D. Roussin's red salt revisited: reactivity of $Fe_2(\mu\text{-E})_2(NO)_4{}^{2-}$ (E = S, Se, Te) and related compounds. *Inorg. Chem.* **1982**, *21*, 827−830.

(1251) Davidovich, P. B.; Gurzhy, V. V.; Belyaev, A. N. Synthesis and structure of novel dinitrosyl iron complexes $[Fe_2(\mu\text{-SCH}_2CH_2NHR)_2(NO)_4]$. *Russ. J. Gen. Chem.* **2014**, *84*, 719−721.

(1252) Harrop, T. C.; Song, D.; Lippard, S. J. Reactivity pathways for nitric oxide and nitrosonium with iron complexes in biologically relevant sulfur coordination spheres. *J. Inorg. Biochem.* **2007**, *101*, 1730−1738.

(1253) Kozub, G. I.; Sanina, N. A.; Emel'yanova, N. S.; Utenishev, A. N.; Kondrat'eva, T. y. A.; Khrustalev, V. N.; Ovanesyan, N. S.; Kupchinskaya, N. E.; Aldoshin, S. M. $[Fe_2(\mu\text{-SR})_2(NO)_4]^0$ complexes with R being phenolyl with different substituents in the meta-position: Synthesis, structure, and NO release. *Inorg. Chim. Acta* **2018**, *480*, 132−139.

(1254) Sanina, N. A.; Krivenko, A. G.; Manzhos, R. A.; Emel'yanova, N. S.; Kozub, G. I.; Korchagin, D. V.; Shilov, G. V.; Kondrat'eva, T. A.; Ovanesyan, N. S.; Aldoshin, S. M. Influence of aromatic ligand on the redox activity of neutral binuclear tetranitrosyl iron complexes $[Fe_2(\mu\text{-SR})_2(NO)_4]$: experiments and quantum-chemical modeling. *New J. Chem.* **2014**, *38*, 292−301.

(1255) Mak, T. C. W.; Book, L.; Chieh, C.; Gallagher, M. K.; Song, L.-C.; Seyferth, D. The structures of di-p-methyhnercurithio-bis-(dinitrosyliron) and di-p-methyl- mercurithio-bis(tricarbonyliron): a comparison of $(\mu\text{-CH}_3HgS)_2Fe_2(NO)_4$ and $(\mu\text{-CH}_3HgS)_2Fe_2(CO)_6$. *Inorg. Chim. Acta* **1983**, *73*, 159−164.

(1256) Sanina, N. A.; Kozub, G. I.; Kondratéva, T. A.; Korchagin, D. V.; Shilov, G. V.; Emelýanova, N. S.; Manzhos, R. A.; Krivenko, A. G.; Aldoshin, S. M. Synthesis, structure, NO-donor and redox activity of bis-(2-methylfuranethiolate)tetranitrosyl diiron. *J. Mol. Struct.* **2014**, *1075*, 159−165.

(1257) Davidovich, P. B.; Fischer, A. I.; Korchagin, D. V.; Panchuk, V. V.; Shchukarev, A. V.; Garabadzhiu, A. V.; Belyaev, A. N. Synthesis, structure, biochemical, and docking studies of a new dinitrosyl iron complex $[Fe_2(\mu\text{-SC}_4H_3SCH_2)_2(NO)_4]$. *J. Mol. Struct.* **2015**, *1092*, 137−142.

(1258) Clegg, W. Crystal structure of Bis[μ-bis(trifluoromethyl)-phosphido]-tetranitrosyldiiron, $Fe_2(NO)_4[\mu\text{-P}(CF_3)_2]_2$. *Inorg. Chem.* **1976**, 15.

(1259) Yu, Y.-F.; Chau, C.-N.; Wojcicki, A.; Calligaris, M.; Nardin, G.; Balducci, G. Reduction chemistry of $Fe_2(NO)_4(\mu\text{-PPh}_2)_2$ and selective synthesis of isomeric doubly bridged methylenetetraphenylbiphosphine and (diphenylphosphido)methylenediphenylphosphine complexes. *J. Am. Chem. Soc.* **1984**, *106*, 3704−3705.

(1260) Chau, C.-N.; Yu, Y.-F.; Wojcicki, A.; Calligaris, M.; Nardin, G.; Balducci, G. Synthesis and characterization of isomeric binuclear double-bridged alkylidene-tetraphenyldiphosphine and diphenylphosphido-methylenediphenylphosphine iron nitrosyl complexes. *Organometallics* **1987**, *6*, 308−316.

(1261) Chau, C.-N.; Wojcicki, A.; Calligaris, M.; Nardin, G. Synthesis and structure of new phosphido-bridged iron-cobalt and iron-nickel nitrosyl complexes. *Inorg. Chim. Acta* **1990**, *168*, 105−113.

(1262) Rakova, O. A.; Sanina, N. A.; Aldoshin, S. M.; Goncharova, N. V.; Shilov, G. V.; Shulga, Y. M.; Ovanesyan, N. S. Synthesis and characterization of potential NO donors: novel iron−sulfur nitrosyls containing the μ-N-C-S skeleton. *Inorg. Chem. Commun.* **2003**, *6*, 145−148.

(1263) Wang, R.; Xu, W.; Zhang, J.; Li, L. Synthesis, characterization and crystal structure of a dinuclear iron nitrosyl complex with 2-mercapto-1-[2-(4-pyridyl)-ethyl]-benzimidazolyl. *J. Mol. Struct.* **2009**, *923*, 110−113.

(1264) Sanina, N.; Roudneva, T.; Shilov, G.; Morgunov, R.; Ovanesyan, N.; Aldoshin, S. Structure and properties of binuclear nitrosyl iron complex with benzimidazole-2-thiolyl. *Dalton Trans.* **2009**, 1703−1706.

(1265) Sanina, N. A.; Aldoshin, S. M.; Rudneva, T. N.; Golovina, N. I.; Shilov, G. V.; Shulga, Y. M.; Ovanesyan, N. S.; Ikorskiy, V. N.; Ovcharenko, V. I. Bi-nuclear nitrosyl iron complex with 2-mercaptoimidazolyl: synthesis, structure and magnetic properties. *J. Mol. Struct.* **2005**, *752*, 110−114.

(1266) Sanina, N. A.; Rudneva, T. N.; Aldoshin, S. M.; Shilov, G. V.; Kortchagin, D. V.; Shul'ga, Y. M.; Martynenko, V. M.; Ovanesyan, N. S. Influence of CH_3 group of μ-N-C-S ligand on the properties of $[Fe_2(C_4H_5N_2S)_2(NO)_4]$ complex. *Inorg. Chim. Acta* **2006**, *359*, 570−576.

(1267) Sanina, N. A.; Kozub, G. I.; Kondrat'eva, T. A.; Shilov, G. V.; Korchagin, D. V.; Emel'yanova, N. S.; Poleshchuk, O. K.; Chernyak, A. V.; Kulikov, A. V.; Mushenok, F. B.; Ovanesyan, N. S.; Aldoshin, S. M. Structure and properties of bis(1-phenyl-1h-tetrazole-5-thiolate)diiron tetranitrosyl. *J. Mol. Struct.* **2013**, *1041*, 183−189.

(1268) Chong, K.S.; Rettig, S.J.; Storr, A.; Trotter, J. Synthesis and structure of 3,5-dimethylpyrazolyl iron and cobalt dinitrosyl dimers. *Can. J. Chem.* **1979**, *57*, 3119−3125.

(1269) Wu, W.-Y.; Hsu, C.-N.; Hsieh, C.-H.; Chiou, T.-W.; Tsai, M.-L.; Chiang, M.-H.; Liaw, W.-F. NO-to-$[N_2O_2]^{2-}$ -to-N_2O conversion triggered by $\{Fe(NO)_2\}^{10}$-$\{Fe(NO)_2\}^9$ dinuclear dinitrosyl iron complex. *Inorg. Chem.* **2019**, *58*, 9586−9591.

(1270) Lu, T.-T.; Tsou, C.-C.; Huang, H.-W.; Hsu, I.-J.; Chen, J.-M.; Kuo, T.-S.; Wang, Y.; Liaw, W.-F. Anionic Roussin's red esters (RREs) syn-/anti-$[Fe(\mu\text{-SEt})(NO)_2]^{2-}$: the critical role of thiolate ligands in regulating the transformation of RREs into dinitrosyl iron complexes and the anionic RREs. *Inorg. Chem.* **2008**, *47*, 6040−6050.

(1271) Rhine, M. A.; Sanders, B. C.; Patra, A. K.; Harrop, T. C. Overview and new insights into the thiol reactivity of coordinated NO in $\{MNO\}^{6/7/8}$ (M = Fe, Co) complexes. *Inorg. Chem.* **2015**, *54*, 9351−9366.

(1272) Lo, F.-C.; Li, Y.-W.; Hsu, I.-J.; Chen, C.-H.; Liaw, W.-F. Insight into the reactivity and electronic structure of dinuclear dinitrosyl iron complexes. *Inorg. Chem.* **2014**, *53*, 10881−10892.

(1273) Rudneva, T. N.; Sanina, N. A.; Lyssenko, K. A.; Aldoshin, S. M.; Antipin, M. Y.; Ovanesyan, N. S. Synthesis and structure of a water-soluble nitrosyl iron complex with cysteamine ligand. *Mendeleev Commun.* **2009**, *19*, 253−255.

(1274) Butler, A. R.; Glidewell, C.; Li, M.-H. Nitrosyl complexes of iron−sulfur clusters. *Advances in Inorganic Chemistry*; Academic Press, 1988; Vol. *32*; pp 335−393.

(1275) Roussin, M. L. Recherches sur les nitrosulfures doubles de fer (nouvelle classe de sels). *Ann. Chim. Phys.* **1858**, *52*, 285−303.

(1276) Bourassa, J. L.; Ford, P. C. Flash and continuous photolysis studies of Roussin's red salt dianion $Fe_2S_2(NO)_4^{2-}$ in solution. *Coord. Chem. Rev.* **2000**, *200-202*, 887−900.

(1277) Lin, X.; Huang, J.; Lu, J. The crystal and molecular structure of a typical red roussin salt $(Me_4N)_2[Fe_2S_2(NO)_4]$. *Acta Crystallogr., Sect. A: Found. Crystallogr.* **1981**, *37*, C232.

(1278) Glidewell, C.; Lambert, R. J.; Hursthouse, M. B.; Motevalli, M. Synthesis and properties of the bis(μ-thiosuIphato-S)-bis-(dinitrosylferrate)(2-) anion. Crystal and molecular structure of bis[bis(triphenylphosphoranylidene)-ammonium] bis(μ-thiosulphato-S)-bis(dinitrosylferrate). *J. Chem. Soc., Dalton Trans.* **1989**, 2061−2064.

(1279) Liaw, W.-F.; Chiang, C.-Y.; Lee, G.-H.; Peng, S.-M.; Lai, C.-H.; Darensbourg, M. Y. Heterobimetallics of nickel-iron dinitrosyl: electronic control by chelate and diatomic ligands. *Inorg. Chem.* **2000**, *39*, 480−484.

(1280) Chen, T.-N.; Lo, F.-C.; Tsai, M.-L.; Shih, K.-N.; Chiang, M.-H.; Lee, G.-H.; Liaw, W.-F. Dinitrosyl iron complexes $[E_5Fe(NO)_2]^-$ (E=S, Se): a precursor of Roussin's black salt $[Fe_4E_3(NO)_7]^-$. *Inorg. Chim. Acta* **2006**, *359*, 2525−2533.

(1281) Mathur, P.; Manimaran, B.; Hossain, M.; Rheingold, A. L.; Liable-Sands, L. M.; Yap, G. P. A. Synthesis and structural characterisation of a novel tris-methylene bridged compound $(NO)_4Fe_2Se(\mu\text{-}CH_2)_3$. *J. Organomet. Chem.* **1997**, *540*, 165−168.

(1282) Mazany, A. M.; Fackler, J. P.; Gallagher, M. K.; Seyferth, D. Synthesis and the crystal and molecular structure of a platinum-bridged derivative of Roussin's red salt, $(Ph_3P)_2Pt(\mu_3\text{-}S)_2Fe_2(NO)_4$. *Inorg. Chem.* **1983**, *22*, 2593−2596.

(1283) Hsieh, C.-H.; Chupik, R. B.; Pinder, T. A.; Darensbourg, M. Y. Dinitrosyl iron adducts of $(N_2S_2)M(NO)$ complexes (M=Fe, Co) as metallodithiolate ligands. *Polyhedron* **2013**, *58*, 151−155.

(1284) Davies, S. C.; Evans, D. J.; Hughes, D. L.; Konkol, M.; Richards, R. L.; Sanders, J. R.; Sobota, P. Mononuclear, binuclear, trinuclear and tetranuclear iron complexes of the $N(CH_2CH_2S)_3^{3-}$ (NS_3) ligand with nitrosyl co-ligands. *J. Chem. Soc. Dalton Trans.* **2002**, 2473−2482.

(1285) Ghosh, P.; Ding, S.; Quiroz, M.; Bhuvanesh, N.; Hsieh, C.-H.; Palacios, P. M.; Pierce, B. S.; Darensbourg, M. Y.; Hall, M. B. Structural and electronic responses to the three redox levels of $Fe(NO)N_2S_2$-$Fe(NO)_2$. *Chem. - Eur. J.* **2018**, *24*, 16003−16008.

(1286) Chen, H.-W.; Lin, C.-W.; Chen, C.-C.; Yang, L.-B.; Chiang, M.-H.; Liaw, W.-F. Homodinuclear iron thiolate nitrosyl compounds $[(ON)Fe(S,S\text{-}C_6H_4)_2Fe(NO)_2]^-$ and $[(ON)Fe(SO_2,S\text{-}C_6H_4)(S,S\text{-}C_6H_4)Fe(NO)_2]^-$ with $\{Fe(NO)\}^7$-$\{Fe(NO)_2\}^9$ electronic coupling: new members of a class of dinitrosyl iron complexes. *Inorg. Chem.* **2005**, *44*, 3226−3232.

(1287) Osterloh, F.; Saak, W.; Haase, D.; Pohl, S. Synthesis, X-ray structure and electrochemical characterisation of a binuclear thiolate bridged Ni-Fe-nitrosyl complex, related to the active site of NiFe hydrogenase. *Chem. Commun.* **1997**, 979−980.

(1288) Hsieh, C.-H.; Chupik, R. B.; Brothers, S. M.; Hall, M. B.; Darensbourg, M. Y. *cis*-Dithiolatonickel as metalloligand to dinitrosyl iron units: the di-metallic structure of $Ni(\mu\text{-SR})[Fe(NO)_2]$ and an unexpected, abbreviated metalloadamantyl cluster, $Ni_2(\mu\text{-SR})_4[Fe(NO)_2]_3$. *Dalton Trans.* **2011**, *40*, 6047−6053.

(1289) Ghosh, P.; Ding, S.; Chupik, R. B.; Quiroz, M.; Hsieh, C.-H.; Bhuvanesh, N.; Hall, M. B.; Darensbourg, M. Y. A matrix of heterobimetallic complexes for interrogation of hydrogen evolution reaction electrocatalysts. *Chem. Sci.* **2017**, *8*, 8291−8300.

(1290) Bar, A. K.; Heras Ojea, M. J.; Tang, J.; Layfield, R. A. Coupling of Nitric Oxide and Release of Nitrous Oxide from Rare-Earth-Dinitrosyliron Complexes. *J. Am. Chem. Soc.* **2020**, *142*, 4104−4107.

(1291) Hayton, T. W.; McNeil, W. S.; Patrick, B. O.; Legzdins, P. Toward binary nitrosyls: distinctly bent Fe-N-O linkages in base-stabilized $Fe(NO)_3^+$ complexes. *J. Am. Chem. Soc.* **2003**, *125*, 12935−12944.

(1292) Beck, W.; Klapötke, T. M.; Mayer, P. Structure of bromotrinitrosyl iron, $[Fe(NO)_3Br]$, and DFT calculations of the structures of $[Fe(NO)_3X]$ (X = Cl, Br, I). *Z. Anorg. Allg. Chem.* **2006**, *632*, 417−420.

(1293) Beck, W.; Enzmann, A.; Mayer, P. Formation and structure of iodotrinitrosyliron, $[Fe(NO)_3I]$. *Z. Anorg. Allg. Chem.* **2005**, *631*, 105−109.

(1294) Bohnenberger, J.; Krossing, I. Stable salts of heteroleptic iron carbonyl/nitrosyl cations. *Angew. Chem., Int. Ed.* **2020**, *59*, 5581−5585.

(1295) Hsieh, C.-H.; Pulukkody, R.; Darensbourg, M. Y. A dinitrosyl iron complex as a platform for metal-bound imidazole to N-heterocyclic carbene conversion. *Chem. Commun.* **2013**, *49*, 9326−9328.

(1296) Victor, E.; Lippard, S. J. A tetranitrosyl [4Fe-4S] cluster forms en route to Roussin's black anion: nitric oxide reactivity of $[Fe_4S_4(LS_3)L']^{22}$. *Inorg. Chem.* **2014**, *53*, 5311−5320.

(1297) Hung, M.-C.; Tsai, M.-C.; Lee, G.-H.; Liaw, W.-F. Transformation and structural discrimination between the neutral $\{Fe(NO)_2\}^{10}$ dinitrosyliron complexes (DNICs) and the anionic/cationic $\{Fe(NO)_2\}^9$ DNICs. *Inorg. Chem.* **2006**, *45*, 6041−6047.

(1298) Vanin, A. F.; Borodulin, R. R.; Mikoyan, V. D. Dinitrosyl iron complexes with natural thiol-containing ligands in aqueous solutions: synthesis and some physico-chemical characteristics (A methodological review). *Nitric Oxide* **2017**, *66*, 1−9.

(1299) Borodulin, R. R.; Kubrina, L. N.; Shvydkiy, V. O.; Lakomkin, V. L.; Vanin, A. F. A simple protocol for the synthesis of dinitrosyl iron complexes with glutathione: EPR, optical, chromatographic and biological characterization of reaction products. *Nitric Oxide* **2013**, *35*, 110−115.

(1300) Stevens, R. E.; Gladfelter, W. L. Nucleophilic nitrosylations of metal carbonyls using bis(triphenylphosphine)nitrogen(1+) nitrite. *Inorg. Chem.* **1983**, *22*, 2034−2042.

(1301) Bryar, T. R.; Eaton, D. R. Electronic configuration and structure of paramagnetic iron dinitrosyl complexes. *Can. J. Chem.* **1992**, *70*, 1917−1926.

(1302) Vanin, A. F.; Sanina, N. A.; Serezhenkov, V. A.; Burbaev, D.; Lozinsky, V. I.; Aldoshin, S. M. Dinitrosyl-iron complexes with thiol-containing ligands: spatial and electronic structures. *Nitric Oxide* **2007**, *16*, 82−93.

(1303) Dai, R. J.; Ke, S. C. Detection and determination of the $\{Fe(NO)_2\}$ core vibrational features in dinitrosyl-iron complexes from experiment, normal coordinate analysis, and density functional theory:

an avenue for probing the nitric oxide oxidation state. *J. Phys. Chem. B* **2007**, *111*, 2335−2346.

(1304) Ye, S.; Neese, F. The unusual electronic structure of dinitrosyl iron complexes. *J. Am. Chem. Soc.* **2010**, *132*, 3646−3647.

(1305) Wecksler, S. R.; Hutchinson, J.; Ford, P. C. Toward development of water soluble dye derivatized nitrosyl compounds for photochemical delivery of NO. *Inorg. Chem.* **2006**, *45*, 1192−1200.

(1306) Wecksler, S. R.; Mikhailovsky, A.; Korystov, D.; Ford, P. C. A two-photon antenna for photochemical delivery of nitric oxide from a water-soluble, dye-derivatized iron nitrosyl complex using NIR light. *J. Am. Chem. Soc.* **2006**, *128*, 3831−3837.

(1307) Conrado, C. L.; Wecksler, S.; Egler, C.; Magde, D.; Ford, P. C. Synthesis and photochemical properties of a novel iron−sulfur-nitrosyl cluster derivatized with the pendant chromophore protoporphyrin IX. *Inorg. Chem.* **2004**, *43*, 5543−5549.

(1308) Bourassa, J.; DeGraff, W.; Kudo, S.; Wink, D. A.; Mitchell, J. B.; Ford, P. C. Photochemistry of Roussin's red salt, $Na_2[Fe_2S_2(NO)_4]$, and of Roussin's black salt, $NH_4[Fe_4S_3(NO)_7]$. *in situ* nitric oxide generation to sensitize γ-radiation induced cell death. *J. Am. Chem. Soc.* **1997**, *119*, 2853−2860.

(1309) Wecksler, S.; Mikhailovsky, A.; Ford, P. C. Photochemical production of nitric oxide via two-photon excitation with NIR light. *J. Am. Chem. Soc.* **2004**, *126*, 13566−13567.

(1310) Wecksler, S. R.; Mikhailovsky, A.; Korystov, D.; Buller, F.; Kannan, R.; Tan, L.-S.; Ford, P. C. Single- and two-photon properties of a dye-derivatized Roussin's red salt ester ($Fe_2(\mu\text{-}RS)_2(NO)_4$) with a large TPA cross section. *Inorg. Chem.* **2007**, *46*, 395−402.

(1311) Tseng, Y.-T.; Chen, C.-H.; Lin, J.-Y.; Li, B.-H.; Lu, Y.-H.; Lin, C.-H.; Chen, H.-T.; Weng, T.-C.; Sokaras, D.; Chen, H.-Y.; Soo, Y.-L.; Lu, T.-T. To transfer or not to transfer? Development of a dinitrosyl iron complex as a nitroxyl donor for the nitroxylation of an Fe^{III}-porphyrin center. *Chem. - Eur. J.* **2015**, *21*, 17570−17573.

(1312) Wah, H. L. K.; Postel, M.; Tomi, F.; Agbossou, F.; Ballivettkatchenko, D.; Urso, F. Activation of molecular-oxygen by iron nitrosyls in the presence of bidentate nitrogen ligands (2,2'-bipyridine, 4,4'-dimethyl-2,2'-bipyridine and 1,10-phenanthroline). *Inorg. Chim. Acta* **1993**, *205*, 113−118.

(1313) Tomi, F.; Wah, H. L. K.; Postel, M. Iron-nitrato iron-nitrosyl: a new redox couple for the activation and transfer of dioxygen. X-ray structure of $Fe(NO_3)_2(OPPh_3)_2Cl$. *New J. Chem.* **1988**, *12*, 289−292.

(1314) Lu, S.; Chiou, T.-W.; Li, W.-L.; Wang, C.-C.; Wang, Y.-M.; Lee, W.-Z.; Lu, T.-T.; Liaw, W.-F. Dinitrosyliron complex [(PMDTA)-$Fe(NO)_2$]: intermediate for nitric oxide monooxygenation activity in nonheme iron complex. *Inorg. Chem.* **2020**, *59*, 8308−8319.

(1315) Wu, W.-Y.; Tsai, M.-L.; Lai, Y.-A.; Hsieh, C.-H.; Liaw, W.-F. NO reduction to N_2O triggered by a dinuclear dinitrosyl iron complex via the associated pathways of hyponitrite formation and NO disproportionation. *Inorg. Chem.* **2021**, *60*, 15874−15889.

(1316) Guillaume, P.; Wah, H. L. K.; Postel, M. Coordinated NO as a source of oxygen - reactivity of the $Fe(NO)_2$ moiety in the presence of the bidentate phosphane 1,2-bis(diphenylphosphino)ethane (dppe) and 1,2-bis(diphenylphosphino)ethene (dppen). *Inorg. Chem.* **1991**, *30*, 1828−1831.

(1317) Truzzi, D. R.; Augusto, O.; Ford, P. C. Thiyl radicals are co-products of dinitrosyl iron complex (DNIC) formation. *Chem. Commun.* **2019**, *55*, 9156−9159.

(1318) Truzzi, D. R.; Augusto, O.; Iretskii, A. V.; Ford, P. C. Dynamics of dinitrosyl iron complex (DNIC) formation with low molecular weight thiols. *Inorg. Chem.* **2019**, *58*, 13446−13456.

(1319) Doulias, P. T.; Greene, J. L.; Greco, T. M.; Tenopoulou, M.; Seeholzer, S. H.; Dunbrack, R. L.; Ischiropoulos, H. Structural profiling of endogenous S-nitrosocysteine residues reveals unique features that accommodate diverse mechanisms for protein S-nitrosylation. *Proc. Natl. Acad. Sci. U. S. A.* **2010**, *107*, 16958−16963.

(1320) Banerjee, A.; Sen, S.; Paul, A. Theoretical investigations on the mechanistic aspects of O_2 activation by a biomimetic dinitrosyl iron complex. *Chem. - Eur. J.* **2018**, *24*, 3330−3339.

(1321) Fitzpatrick, J.; Kalyvas, H.; Filipovic, M. R.; Ivanović-Burmazović, I.; MacDonald, J. C.; Shearer, J.; Kim, E. Transformation of a mononitrosyl iron complex to a [2Fe-2S] cluster by a cysteine analogue. *J. Am. Chem. Soc.* **2014**, *136*, 7229−7232.

(1322) Tennyson, A. G.; Dhar, S.; Lippard, S. J. Synthesis and characterization of $\{Ni(NO)\}^{10}$ and $\{Co(NO)_2\}^{10}$ complexes supported by thiolate ligands. *J. Am. Chem. Soc.* **2008**, *130*, 15087−15098.

(1323) Kolluru, G. K.; Shen, X.; Kevil, C. G. A tale of two gases: NO and H_2S, foes or friends for life? *Redox Biol.* **2013**, *1*, 313−318.

(1324) Fukuto, J. M.; Carrington, S. J.; Tantillo, D. J.; Harrison, J. G.; Ignarro, L. J.; Freeman, B. A.; Chen, A.; Wink, D. A. Small molecule signaling agents: the integrated chemistry and biochemistry of nitrogen oxides, oxides of carbon, dioxygen, hydrogen sulfide, and their derived species. *Chem. Res. Toxicol.* **2012**, *25*, 769−793.

(1325) Kajimura, M.; Fukuda, R.; Bateman, R. M.; Yamamoto, T.; Suematsu, M. Interactions of multiple gas-transducing systems: hallmarks and uncertainties of CO, NO, and H_2S gas biology. *Antioxid. Redox Signaling* **2010**, *13*, 157−192.

(1326) Tran, C. T.; Williard, P. G.; Kim, E. Nitric oxide reactivity of [2Fe-2S] clusters leading to H_2S generation. *J. Am. Chem. Soc.* **2014**, *136*, 11874−11877.

(1327) Oakley, K. M.; Zhao, Z.; Lehane, R. L.; Ma, J.; Kim, E. Generation of H_2S from thiol-dependent NO reactivity of model [4Fe-4S] cluster and Roussin's black anion. *Inorg. Chem.* **2021**, *60*, 15910−15917.

(1328) Prasad, P.; Selvan, D.; Chakraborty, S. Biosynthetic approaches towards the design of artificial hydrogen-evolution catalysts. *Chem. - Eur. J.* **2020**, *26*, 12494−12509.

(1329) Schilter, D.; Camara, J. M.; Huynh, M. T.; Hammes-Schiffer, S.; Rauchfuss, T. B. Hydrogenase enzymes and their synthetic models: the role of metal hydrides. *Chem. Rev.* **2016**, *116*, 8693−8749.

(1330) Lu, S.; Chiang, J. C.; Chiou, T. W.; Liaw, W. F. Dinitrosyl iron complexes: From molecular electrocatalysts to electrodeposited-film electrodes for hydrogen evolution reaction. *J. Chin. Chem. Soc.* **2019**, *66*, 1186−1194.

(1331) Mocellin, S.; Bronte, V.; Nitti, D. Nitric oxide, a double edged sword in cancer biology: searching for therapeutic opportunities. *Med. Res. Rev.* **2007**, *27*, 317−352.

(1332) Vanin, A. F.; Ostrovskaya, L. A.; Korman, D. B.; Rykova, V. A.; Bluchterova, N. V.; Fomina, M. M. The antitumor properties of dinitrosyl iron complexes with thiol-containing ligands and S-nitrosoglutathione in experiments. *Biophysics* **2020**, *65*, 39−50.

(1333) Burgova, E. N.; Khristidis, Y. I.; Kurkov, A. V.; Mikoyan, V. D.; Shekhter, A. B.; Adamyan, L. V.; Timashev, P. S.; Vanin, A. F. The inhibiting effect of dinitrosyl iron complexes with thiol-containing ligands on the growth of endometrioid tumours in rats with experimental endometriosis. *Cell Biochem. Biophys.* **2019**, *77*, 69−77.

(1334) Burgova, E. N.; Tkachev Ncapital A, C.; Adamyan, L. V.; Mikoyan, V. D.; Paklina, O. V.; Stepanyan, A. A.; Vanin, A. F. Dinitrosyl iron complexes with glutathione suppress experimental endometriosis in rats. *Eur. J. Pharmacol.* **2014**, *727*, 140−147.

(1335) Burgova, E. N.; Tkachev, N. A.; Paklina, O. V.; Mikoyan, V. D.; Adamyan, L. V.; Vanin, A. F. The effect of dinitrosyl iron complexes with glutathione and S-nitrosoglutathione on the development of experimental endometriosis in rats: a comparative studies. *Eur. J. Pharmacol.* **2014**, *741*, 37−44.

(1336) Vanin, A. F.; Burgova, E. N.; Adamyan, L. V. Dinitrosyl iron complexes with glutathione suppress surgically induced experimental endometriosis in rats. *Austin J. Reprod. Med. Infertil.* **2015**, *2*, 1019−1031.

(1337) Shamova, E. V.; Shishlo, L. M.; Gorudko, I. V.; Aleksandrova, E. N.; Cherenkevich, S. N.; Shumaev, K. B. Effect of ditorsoyl iron complexes on platelet aggregation induced by HeLa cervical carcinoma cells. *Bull. Exp. Biol. Med.* **2011**, *150*, 372−374.

(1338) Zhukova, O. S.; Smirnova, Z. S.; Chikileva, I. O.; Kiselevskii, M. V. Antiproliferative activity of a new nitrosyl iron complex with cysteamine in human tumor cells *in vitro*. *Bull. Exp. Biol. Med.* **2017**, *162*, 583−588.

(1339) Shamova, E. V.; Bichan, O. D.; Drozd, E. S.; Gorudko, I. V.; Chizhik, S. A.; Shumaev, K. B.; Cherenkevich, S. N.; Vanin, A. F.

Regulation of the functional and mechanical properties of platelet and red blood cells by nitric oxide donors. *Biophysics* **2011**, *56*, 237−242.

(1340) Shumaev, K. B.; Gorudko, I. V.; Kosmachevskaya, O. V.; Grigorieva, D. V.; Panasenko capital O, C.; Vanin, A. F.; Topunov, A. F.; Terekhova, M. S.; Sokolov, A. V.; Cherenkevich, S. N.; Ruuge, E. K. Protective effect of dinitrosyl iron complexes with glutathione in red blood cell lysis induced by hypochlorous acid. *Oxid. Med. Cell. Longevity* **2019**, *2019*, 2798154.

(1341) Remizova, M. I.; Kochetygov, N. I.; Gerbout, K. A.; Lakomkin, V. L.; Timoshin, A. A.; Burgova, E. N.; Vanin, A. F. Effect of dinitrosyl iron complexes with glutathione on hemorrhagic shock followed by saline treatment. *Eur. J. Pharmacol.* **2011**, *662*, 40−46.

(1342) Shumaev, K. B.; Dudylina, A. L.; Ivanova, M. V.; Pugachenko, I. S.; Ruuge, E. K. Dinitrosyl iron complexes: Formation and antiradical action in heart mitochondria. *BioFactors* **2018**, *44*, 237−244.

(1343) Pisarenko, O.; Studneva, I.; Timoshin, A.; Veselova, O. Protective efficacy of dinitrosyl iron complexes with reduced glutathione in cardioplegia and reperfusion. *Pfluegers Arch.* **2019**, *471*, 583−593.

(1344) Gizatullin, A. R.; Akentieva, N. P.; Sanina, N. A.; Shmatko, N. Y.; Goryachev, N. S.; Shkondina, N. I.; Prichodchenko, T. R.; Zhelev, N.; Aldoshin, S. M. Effect of dinitrosyl iron complexes (NO donors) on the metabolic processes in human fibroblasts. *Dokl. Biochem. Biophys.* **2018**, *483*, 337−340.

(1345) Timoshin, A. A.; Drobotov, D. Y.; Tskitishvili, O. V.; Serebryakova, L. I.; Pisarenko, O. I.; Ruuge, E. K.; Vanin, A. F. Protective effect of dinitrosyl-iron complexes with glutathione in rat myocardial regional ischemia: a microdialysis assay study. *Dokl. Biochem. Biophys.* **2010**, *432*, 106−109.

(1346) Timoshin, A. A.; Lakomkin, V. L.; Abramov, A. A.; Vanin, A. F.; Ruuge, E. K. The biological effect of dinitrosyl iron complexes with glutathione upon nitric oxide hyperproduction induced by endotoxin shock. *Biophysics* **2019**, *64*, 89−94.

(1347) Lewandowska, H.; M̆̈czyńska-Wielgosz, S.; Sikorska, K.; Sadlo, J.; Dudek, J.; Kruszewski, M. LDL dinitrosyl iron complex: A new transferrin-independent route for iron delivery in hepatocytes. *BioFactors* **2018**, *44*, 192−201.

(1348) Giliano, N. Y.; Konevega, L. V.; Noskin, L. A.; Serezhenkov, V. A.; Poltorakov, A. P.; Vanin, A. F. Dinitrosyl iron complexes with thiol-containing ligands and apoptosis: studies with HeLa cell cultures. *Nitric Oxide* **2011**, *24*, 151−159.

(1349) Akentieva, N. P.; Sanina, N. A.; Prichodchenko, T. R.; Gizatullin, A. R.; Shkondina, N. I.; Shushanov, S. S.; Stupina, T. S.; Aldoshin, S. M. Anticancer activity of dinitrosyl iron complex (NO donor) on the multiple myeloma cells. *Dokl. Biochem. Biophys.* **2019**, *486*, 238−242.

(1350) Solovieva, A. B.; Vanin, A. F.; Shekhter, A. B.; Glagolev, N. N.; Aksenova, N. A.; Mikoyan, V. D.; Kotova, S. L.; Rudenko, T. G.; Fayzullin, A. L.; Timashev, P. S. Is it possible to combine photodynamic therapy and application of dinitrosyl iron complexes in the wound treatment? *Nitric Oxide* **2019**, *83*, 24−32.

(1351) Huang, H.-W.; Lin, Y.-H.; Lin, M.-H.; Huang, Y.-R.; Chou, C.-H.; Hong, H.-C.; Wang, M.-R.; Tseng, Y.-T.; Liao, P.-C.; Chung, M.-C.; Ma, Y.-J.; Wu, S.-C.; Chuang, Y.-J.; Wang, H.-D.; Wang, Y.-M.; Huang, H.-D.; Lu, T.-T.; Liaw, W.-F. Extension of *C. elegans* lifespan using the.NO-delivery dinitrosyl iron complexes. *JBIC, J. Biol. Inorg. Chem.* **2018**, *23*, 775−784.

(1352) Pectol, D. C.; Khan, S.; Elsabahy, M.; Wooley, K. L.; Lim, S.-M.; Darensbourg, M. Y. Effects of glutathione and histidine on NO release from a dimeric dinitrosyl iron complex (DNIC). *Inorg. Chem.* **2020**, *59*, 16998−17008.

(1353) Mumyatova, V. A.; Kozub, G. I.; Kondrat'eva, T. A.; Terent'ev, A. A.; Sanina, N. A. Antibacterial activity of [1Fe-2S]- and [2Fe-2S]-nitrosyl complexes as nitric oxide donors. *Russ. Chem. Bull.* **2019**, *68*, 1025−1030.

(1354) Dobry-Duclaux, A. Sur la détermination des sites actifs de certaines enzymes au moyen d'un nouveau réactif spécifique, le sel de Roussin. II. *Biochim. Biophys. Acta* **1960**, *39*, 44−52.

(1355) Dobry-Duclaux, A. Sur la détermination des sites actifs de certaines enzymes au moyen d'un nouveau réactif spécifique, le sel de Roussin. I. *Biochim. Biophys. Acta* **1960**, *39*, 33−44.

(1356) D'Addario, S.; Demartin, F.; Grossi, L.; Iapalucci, M. C.; Laschi, F.; Longoni, G.; Zanello, P. Redox behavior of the black Roussinate $[Fe_4S_3(NO)_7]^-$ monoanion. Synthesis and spectroscopic characterization of the $[Fe_4S_3(NO)_7]^{n-}$ (n = 2, 3) anions and crystal structures of the mono- and dianions in their $[NEt_4]^+$ salts. *Inorg. Chem.* **1993**, *32*, 1153−1160.

(1357) Bourassa, J.; Lee, B.; Bernard, S.; Schoonover, J.; Ford, P. C. Flash photolysis studies of Roussin's black salt anion $Fe_4S_3(NO)^{7-}$. *Inorg. Chem.* **1999**, *38*, 2947−2952.

(1358) Chmura, A.; Szacilowski, K.; Stasicka, Z. The role of photoinduced electron transfer processes in photodegradation of the $[Fe_4(\mu_3\text{-}S)_3(NO)_7]^-$ cluster. *Nitric Oxide* **2006**, *15*, 370−379.

(1359) Hamilton-Brehm, S. D.; Schut, G. J.; Adams, M. W. Antimicrobial activity of the iron−sulfur nitroso compound Roussin's black salt $[Fe_4S_3(NO)_7]$ on the hyperthermophilic archaeon *Pyrococcus furiosus*. *Appl. Environ. Microbiol.* **2009**, *75*, 1820−1825.

(1360) Burks, P. T.; Garcia, J. V.; GonzalezIrias, R.; Tillman, J. T.; Niu, M.; Mikhailovsky, A. A.; Zhang, J.; Zhang, F.; Ford, P. C. Nitric oxide releasing materials triggered by near-infrared excitation through tissue filters. *J. Am. Chem. Soc.* **2013**, *135*, 18145−18152.

(1361) Zhang, X.; Tian, G.; Yin, W.; Wang, L.; Zheng, X.; Yan, L.; Li, J.; Su, H.; Chen, C.; Gu, Z.; Zhao, Y. Controllable generation of nitric oxide by near-infrared-sensitized upconversion nanoparticles for tumor therapy. *Adv. Funct. Mater.* **2015**, *25*, 3049−3056.

(1362) Dong, K.; Ju, E.; Gao, N.; Wang, Z.; Ren, J.; Qu, X. Synergistic eradication of antibiotic-resistant bacteria based biofilms in vivo using a NIR-sensitive nanoplatform. *Chem. Commun.* **2016**, *52*, 5312−5315.

(1363) Tan, L.; Huang, R.; Li, X.; Liu, S.; Shen, Y.-M. Controllable release of nitric oxide and doxorubicin from engineered nanospheres for synergistic tumor therapy. *Acta Biomater.* **2017**, *57*, 498−510.

(1364) Zhang, X.; Guo, Z.; Liu, J.; Tian, G.; Chen, K.; Yu, S.; Gu, Z. Near infrared light triggered nitric oxide releasing platform based on upconversion nanoparticles for synergistic therapy of cancer stem-like cells. *Sci. Bull.* **2017**, *62*, 985−996.

(1365) Lan, Y.; Zhu, X.; Tang, M.; Wu, Y.; Zhang, J.; Liu, J.; Zhang, Y. Construction of a near-infrared responsive upconversion nanoplatform against hypoxic tumors via NO-enhanced photodynamic therapy. *Nanoscale* **2020**, *12*, 7875−7887.

(1366) Chen, L.; He, Q.; Lei, M.; Xiong, L.; Shi, K.; Tan, L.; Jin, Z.; Wang, T.; Qian, Z. Facile coordination-precipitation route to insoluble metal Roussin's black salts for NIR-responsive release of NO for anti-metastasis. *ACS Appl. Mater. Interfaces* **2017**, *9*, 36473−36477.

(1367) Zumft, W. Cell biology and molecular basis of denitrification. *Microbiol. Mol. Biol. Rev.* **1997**, *61*, 533−616.

(1368) Glockner, A. B.; Zumft, W. G. Sequence analysis of an internal 9.72-kb segment from the 30-kb denitrification gene cluster of *Pseudomonas stutzeri*. *Biochim. Biophys. Acta, Bioenerg.* **1996**, *1277*, 6−12.

(1369) Rinaldo, S.; Cutruzzolà, F. Nitrite reductases in denitrification. *Biology of the nitrogen cycle*; Elsevier, 2007; pp 37−55.

(1370) Fülöp, V.; Moir, J. W. B.; Ferguson, S. J.; Hajdu, J. The anatomy of a bifunctional enzyme: structural basis for reduction of oxygen to water and synthesis of nitric oxide by cytochrome cd_1. *Cell* **1995**, *81*, 369−377.

(1371) Rainey, F. A.; Kelly, D. P.; Stackebrandt, E.; Burghart, J.; Hiraishi, A.; Katayama, Y.; Wood, A. P. A re-evaluation of the taxonomy of *Paracoccus* denitrificans and a proposal for the combination *Paracoccus pantotrophus* comb. nov. *Int. J. Syst. Evol. Microbiol.* **1999**, *49*, 645−651.

(1372) Nurizzo, D.; Silvestrini, M.-C.; Mathieu, M.; Cutruzzola, F.; Bourgeouis, D.; Fülöp, V.; Hajdu, J.; Brunori, M.; Tegoni, M.; Cambillau, C. N-terminal arm exchange is observed in the 2.15A crystal structure of oxidized nitrite reductase from *Pseudomonas aeruginosa*. *Structure* **1997**, *5*, 1157−1171.

(1373) Castresana, J.; Lubben, M.; Saraste, M.; Higgins, D. Evolution of cytochrome oxidase, an enzyme older than atmospheric oxygen. *EMBO J.* **1994**, *13*, 2516−2525.

(1374) Silvestrini, M.-C.; Tordi, M. G.; Musci, G.; Brunori, M. The kinetics of electron transfer between *Pseudomonas aeruginosa* cytochrome c_{551} and its oxidase. *Biochem. J.* **1982**, *203*, 445−451.

(1375) Allen, J. W. A.; Higham, C. W.; Zajicek, R. S.; Watmough, N. J.; Ferguson, S. J. A novel, kinetically stable, catalytically active, all-ferric, nitrite-bound complex of *Paracoccus pantotrophus* cytochrome cd_1. *Biochem. J.* **2002**, *366*, 883−888.

(1376) Wolf, M. W.; Rizzolo, K.; Elliott, S. J.; Lehnert, N. Resonance Raman, electron paramagnetic resonance, and magnetic circular dichroism spectroscopic investigation of diheme cytochrome *c* peroxidases from *Nitrosomonas europaea* and *Shewanella oneidensis*. *Biochemistry* **2018**, *57*, 6416−6433.

(1377) Cutruzzola, F.; Brown, K.; Wilson, E. K.; Bellelli, A.; Arese, M.; Tegoni, M.; Cambillau, C.; Brunori, M. The nitric reductase from *Pseudomonas aeruginosa*: Essential role of two active-site histidines in the catalytic and structural properties. *Proc. Natl. Acad. Sci. U. S. A.* **2001**, *98*, 2232−2237.

(1378) Sjögren, T.; Hajdu, J. The structure of an alternative form of *Paracoccus pantotrophus* cytochrome cd_1 nitrite reductase. *J. Biol. Chem.* **2001**, *276*, 29450−29455.

(1379) Silvestrini, M. C.; Falcinelli, S.; Ciabatti, I.; Cutruzzola, F.; Brunori, M. *Pseudomonas aeruginosa* nitrite reductase (or cytochrome oxidase): an overview. *Biochimie* **1994**, *76*, 641−654.

(1380) Silvestrini, M.-C.; Tordi, M. G.; Citro, G.; Vecchini, P.; Brunori, M. Monomeric *Pseudomonas aeruginosa* nitrite reductase: preparation, characterization and kinetic properties. *J. Inorg. Biochem.* **1995**, *57*, 169−180.

(1381) Lopes, H.; Besson, S.; Moura, I.; Moura, J. J. G. Kinetics and inter- and intramolecular electron transfer of *Pseudomonas nautica* cytochrome cd_1 nitrite reductase: regulation of the NO-bound end product. *JBIC, J. Biol. Inorg. Chem.* **2001**, *6*, 55−62.

(1382) Silvestrini, M.-C.; Tordi, M. G.; Musci, G.; Brunori, M. The reaction of *Pseudomonas* nitrite reductase and nitrite. *J. Biol. Chem.* **1990**, *265*, 11785−11787.

(1383) Parr, S. R.; Barber, D.; Greenwood, C.; Brunori, M. The electron transfer reaction between azurin and cytochrome oxidase from *Pseudomonas aeruginosa*. *Biochem. J.* **1977**, *167*, 447−455.

(1384) Farver, O.; Brunori, M.; Cutruzzola, F.; Rinaldo, S.; Wherland, S.; Pecht, I. Intramolecular electron transfer in *Pseudomonas aeruginosa* cd_1 nitrite reductase. *Biophys. J.* **2009**, *96*, 2849−2856.

(1385) Farver, O.; Kroneck, P. M. H.; Zumft, W.; Pecht, I. Intramolecular electron transfer in cytochrome cd_1 nitrite reductase from *Pseudomonas stutzeri*; kinetics and thermodynamics. *Biophys. Chem.* **2002**, *98*, 27−34.

(1386) Kobayashi, K.; Koppenhoefer, S. J.; Ferguson, S. J.; Watmough, N. J.; Tagawa, S. Intramolecular electron transfer from *c* heme to d_1 heme in bacterial cytochrome cd_1 nitrite reductase occurs over the same distances at very different rates depending on the source of the enzyme. *Biochemistry* **2001**, *40*, 8542−8547.

(1387) Schichman, S. A.; Gray, H. B. Kinetics of the anerobic reduction of ferricytochrome cd_1 by Fe(EDTA)^{22}. Evidence for biomolecular and intramolecular electron tranfers to the d_1 hemes. *J. Am. Chem. Soc.* **1981**, *103*, 7794−7795.

(1388) Cutruzzola, F.; Arese, M.; Grasso, S.; Bellelli, A.; Brunori, M. Tyrosine 10 in the *c*-heme domain is not involved in the catalytic mechanism of nitrite reductase from *Pseudomonas aeruginosa*. *FEBS Lett.* **1997**, *412*, 365−369.

(1389) Einsle, O.; Messerschmidt, A.; Huber, R.; Kroneck, P. M. H.; Neese, F. Mechanism of the six-electron reduction of nitrite to ammonia by cytochrome *c* nitrite reductase. *J. Am. Chem. Soc.* **2002**, *124*, 11737−11745.

(1390) Crane, B. R.; Siegel, L. M.; Getzoff, E. D. Probing the catalyic mechanism of sulfite reductase by x-ray crystallography: structures of the *Escherichia coli* hemoprotein complex with substrates, inhibitors, intermediates and products. *Biochemistry* **1997**, *36*, 12120−12137.

(1391) Berks, B. C.; Ferguson, S. J.; Moir, J. W. B.; Richardson, D. J. Enzymes and associated electron transport systems that catalyse the respiratory reduction of nitrogen oxides and oxyanions. *Biochim. Biophys. Acta, Bioenerg.* **1995**, *1232*, 97−173.

(1392) Nasri, H.; Wang, Y.; Hanh, H. B.; Scheidt, W. R. Nitrite-bound five-coordinate low-spin iron(II) model complex for the prosthetic group of nitrite reductase with an unusually large quadrupole splitting. Synthesis, Moessbauer properties, and molecular structure of the complex (nitro)(α-tetrakis(*o*-pivalamidophenyl)-porphinato)iron(II). *J. Am. Chem. Soc.* **1991**, *113*, 717−719.

(1393) Martí, M. A.; Crespo, A.; Bari, S. E.; Doctorovich, F. A.; Estrin, D. A. QM-MM study of nitrite reduction by nitrite reductase of *Pseudomonas aeruginosa*. *J. Phys. Chem. B* **2004**, *108*, 18073−18080.

(1394) Nasri, H.; Ellison, M. K.; Krebs, C.; Huynh, B. H.; Scheidt, W. R. Highly variable -bonding in the interaction of iron(II) porphyrinates with nitrite. *J. Am. Chem. Soc.* **2000**, *122*, 10795−10804.

(1395) Greenwood, C.; Barber, D.; Parr, S. R.; Antonini, E.; Brunori, M.; Colosimo, A. The reaction of *Pseudomonas aeruginosa* cytochrome *c*-551 oxidase with oxygen. *Biochem. J.* **1978**, *173*, 11−17.

(1396) Centola, F.; Rinaldo, S.; Brunori, M.; Cutruzzolà, F. Critical role of His369 in the reactivity of *Pseudomonas aeruginosa* cytochrome cd_1 nitrite reductase with oxygen. *FEBS J.* **2006**, *273*, 4495−4503.

(1397) George, S. J.; Allen, J. W.; Ferguson, S. J.; Thorneley, R. N. Time-resolved infrared spectroscopy reveals a stable ferric heme-NO intermediate in the reaction of *Paracoccus pantotrophus* cytochrome cd_1 nitrite reductase with nitrite. *J. Biol. Chem.* **2000**, *275*, 33231−33237.

(1398) Radoul, M.; Bykov, D.; Rinaldo, S.; Cutruzzola, F.; Neese, F.; Goldfarb, D. Dynamic hydrogen-bonding network in the distal pocket of the nitrosyl complex of *Pseudomonas aeruginosa* cd_1 nitrite reductase. *J. Am. Chem. Soc.* **2011**, *133*, 3043−3055.

(1399) Sam, K. A.; Strampraad, M. J. F.; de Vries, S.; Ferguson, S. J. Very early reaction intermediates detected by microsecond time scale kinetics of cytochrome cd_1-catalyzed reduction of nitrite. *J. Biol. Chem.* **2008**, *283*, 27403−27409.

(1400) Rinaldo, S.; Sam, K. A.; Castiglione, N.; Stelitano, V.; Arcovito, A.; Brunori, M.; Allen, J. W. A.; Ferguson, S. J.; Cutruzzolà, F. Observation of fast release of NO from ferrous d_1 haem allows formulation of a unified reaction mechanism for cytochrome cd_1 nitrite reductases. *Biochem. J.* **2011**, *435*, 217−225.

(1401) Zajicek, R. S.; Cartron, M. L.; Ferguson, S. J. Probing the unusual oxidation/reduction behavior of *Paracoccus pantotrophus* cytochrome cd_1 nitrite reductase by replacing a switchable methionine heme iron ligand with histidine. *Biochemistry* **2006**, *45*, 11208−11216.

(1402) Azizi, F.; Kielbasa, J. E.; Adeyiga, A. M.; Maree, R. D.; Frazier, M.; Yakubu, M.; Shields, H.; King, S. B.; Kim-Shapiro, D. B. Rates of nitric oxide dissociation from hemoglobin. *Free Radical Biol. Med.* **2005**, *39*, 145−151.

(1403) Cassoly, R.; Gibson, Q. H. Conformation, co-operativity and ligand binding in human hemoglobin. *J. Mol. Biol.* **1975**, *91*, 301−313.

(1404) Johnson, M. K.; Thomson, A. J.; Walsh, T. A.; Barber, D.; Greenwood, C. Electron paramagnetic resonance studies on *Pseudomonas* nitrosyl nitrite reductase. Evidence for multiple species in the electron paramagnetic resonance spectra of nitrosyl haemoproteins. *Biochem. J.* **1980**, *189*, 285−294.

(1405) Koppenhoefer, S. J.; Little, R. H.; Lowe, D. G.; Ferguson, S. J.; Watmough, N. J. Oxidase reaction of cytochrome cd_1 from *Paracoccus pantotrophus*. *Biochemistry* **2000**, *39*, 4028−4036.

(1406) Allen, J. W. A.; Watmough, N. J.; Ferguson, S. J. A switch in heme axial ligation prepares *Paracoccus pantotrophus* cytochrome cd_1 for catalysis. *Nat. Struct. Biol.* **2000**, *7*, 885−888.

(1407) Richter, C. D.; Allen, J. W. A.; Higham, C. W.; Koppenhöfer, A.; Zajicek, R. S.; Watmough, N. J.; Ferguson, S. J. Cytochrome cd_1, reductive activation and kinetic analysis of a multifunctional respiratory enzyme. *J. Biol. Chem.* **2002**, *277*, 3093−3100.

(1408) Carr, G. J.; Page, M. D.; Ferguson, S. J. The energy-conserving nitric-oxide-reductase system in *Paracoccus denitrificans*: distinction from the nitrite reductase that catalyses synthesis of nitric oxide and evidence from trapping experiments for nitric oxide as a free intermediate during denitrification. *Eur. J. Biochem.* **1989**, *179*, 683−692.

(1409) Hyunh, B. H.; Lui, M. C.; Moura, I.; Ljungdahl, P. O.; Munck, E.; Payne, W. J.; Peck, H. D., Jr.; DerVartanian, D. V.; LeGall, J. Mössbauer and EPR studies on nitrite reductase from *Thiobacillus denitrificans*. *J. Biol. Chem.* **1982**, *257*, 9576−9581.

(1410) Peisach, J.; Blumberg, W. E.; Adler, A. Electron paramagnetic resonance studies of iron porphin and chlorin systems. *Ann. N. Y. Acad. Sci.* **1973**, *206*, 310−327.

(1411) Stolzenberg, A. M.; Strauss, S. H.; Holm, R. H. Iron(II, III)-chlorin and-isobacteriochlorin complexes. Models of the heme prosthetic groups in nitrite and sulfite reductases: Means of formation and spectroscopic and redox properties. *J. Am. Chem. Soc.* **1981**, *103*, 4763−4778.

(1412) Cheesman, M. R.; Ferguson, S. J.; Moir, J. W. B.; Zumft, W. G.; Thomson, A. J.; et al. Two enzymes with a common function but different heme ligands in the forms as isolated. Optical and magnetic properties of the heme groups in the oxidized forms of nitrite reductase, cytochrome cd_1, from *Pseudomonas stutzeri* and *Thiophaeria pantotropha*. *Biochemistry* **1997**, *36*, 16267−16276.

(1413) Shimada, H.; Orii, Y. The nitric oxide compounds of *Pseudomonas aeruginosa* nitrite reductase and their propbable participation in the nitrite reduction. *FEBS Lett.* **1975**, *54*, 237−240.

(1414) Silverstrini, M. C.; Colosimo, A.; Brunori, M.; Walsh, T. A.; Barber, D.; Greenwood, C. A re-evaluation of some basic structural and functional properties of *Pseudomonas* cytochrome oxidase. *Biochem. J.* **1979**, *183*, 701−709.

(1415) Ozawa, K.; Sakamoto, E.; Ichikawa, T.; Watanabe, T.; Morishima, I. Model studies of nitrosyl intermediates in the catalytic cycle of dissimilatory nitrite reductases. *Inorg. Chem.* **1995**, *34*, 6362−6370.

(1416) Radoul, M.; Centola, F.; Rinaldo, S.; Cutruzzola, F.; Pecht, I.; Goldfarb, D. Heme d_1 nitrosyl complex of cd_1 nitrite reductase studied by high-field-pulse electron paramagnetic resonance spectoscopy. *Inorg. Chem.* **2009**, *48*, 3913−3915.

(1417) Brindley, A. A.; Zajicek, R.; Warren, M. J.; Ferguson, S. J.; Rigby, S. E. J. NirJ, a radical SAM family member of the d_1 heme biogenesis cluster. *FEBS Lett.* **2010**, *584*, 2461−2466.

(1418) Das, T. K.; Wilson, E. K.; Cutruzzolà, F.; Brunori, M.; Rousseau, D. L. Binding of NO and CO to the d_1 heme of cd_1 nitrite reductase from *Pseudomonas aeruginosa*. *Biochemistry* **2001**, *40*, 10774−10781.

(1419) Hill, K. E.; Wharton, D. C. Reconstitution of the apoenzyme of cytochrome oxidase from *Pseudomonas aeruginosa* with heme d_1 and other heme groups. *J. Biol. Chem.* **1978**, *253*, 489−495.

(1420) Rassaf, T.; Flogel, U.; Drexhage, C.; Hendgen-Cotta, U.; Kelm, M.; Schrader, J. Nitrite reductase function of deoxyhemoglobin: oxygen sensor and regulator of cardiac energetics and function. *Circ. Res.* **2007**, *100*, 1749−1754.

(1421) Nagababu, E.; Ramasamy, S.; Abernethy, D.; Rifkind, J. M. Active nitric oxide produced in the red cell under hypoxic conditions by deoxyhemoglobin-mediated nitrite reduction. *J. Biol. Chem.* **2003**, *278*, 46349−46356.

(1422) Hunter, C. J.; Dejam, A.; Blood, A.; Shields, H.; Kim-Shapiro, D. B.; Machade, R.; Tarekegn, S.; Mulla, N.; Hopper, A.; Schechter, A. N.; Power, G. G.; Gladwin, M. T. Inhaled nebulized nitrite is a hypoxia selective sensitive NO-dependent pulmonary vasodilator. *Nat. Med.* **2004**, *10*, 1122−1127.

(1423) Kozlov, A. V.; Costantino, G.; Sobhian, B.; Szalay, L.; Umar, F.; Nohl, H.; Bahrami, S.; Redl, H. Mechanisms of vasodilation induced by nitrite instillation in intestinal lumen: Possible role of haemoglobin. *Antioxid. Redox Signaling* **2005**, *7*, 515−521.

(1424) Huang, K. T.; Keszler, A.; Patel, N.; Patel, R. P.; Gladwin, M. T.; Kim-Shapiro, D. B.; Hogg, N. The reaction between nitrite and deoxyhemoglobin: reassessment of reaction kinetic and stoichiometry. *J. Biol. Chem.* **2005**, *280*, 31126−31131.

(1425) Feelisch, M.; Fernandez, B. O.; Bryan, N. S.; Garcia-Saura, M. F.; Bauer, S.; Whitlock, D. R.; Ford, P. C.; Janero, D. R.; Rodriguez, J.; Ashrafian, H. Tissue processing of nitrite in hypoxia: an intricate interplay of nitric oxide-generating and -scavenging systems. *J. Biol. Chem.* **2008**, *283*, 33927−33934.

(1426) Kim-Shapiro, D. B.; Gladwin, M. T.; Patel, R. P.; Hogg, N. The reaction between nitrite and hemoglobin: the role of nitrite in hemoglobin-mediated hypoxic vasodilation. *J. Inorg. Biochem.* **2005**, *99*, 237−246.

(1427) Kosaka, H.; Imaizumi, K.; Tyuma, I. Mechanism of autocatalytic oxidation of oxyhemoglobin by nitrite. An intermediate detected by electron spin resonance. *Biochim. Biophys. Acta, Protein Struct. Mol. Enzymol.* **1982**, *702*, 237−241.

(1428) Copeland, D. M.; Soares, A. S.; West, A. H.; Richter-Addo, G. B. Crystal structures of the nitrite and nitric oxide complexes of horse heart myoglobin. *J. Inorg. Biochem.* **2006**, *100*, 1413−1425.

(1429) Yi, J.; Safo, M. K.; Richter-Addo, G. B. The nitrite anion binds to human hemoglobin via the uncommon O-nitrito mode. *Biochemistry* **2008**, *47*, 8247−8249.

(1430) Nasri, H.; Ellison, M. K.; Shang, M.; Schulz, C. E.; Scheidt, W. R. Variable π-bonding in iron(II) porphyrinates with nitrite, CO, and tert-butyl isocyanide: characterization of $[Fe(TpivPP)(NO_2)(CO)]^-$. *Inorg. Chem.* **2004**, *43*, 2932−2942.

(1431) Yi, J.; Heinecke, J.; Tan, H.; Ford, P. C.; Richter-Addo, G. B. The distal pocket histidine residue in horse heart myoglobin directs the O-binding mode of nitrite to the heme iron. *J. Am. Chem. Soc.* **2009**, *131*, 18119−18128.

(1432) Basu, S.; Grubina, R.; Huang, J.; Conradie, J.; Huang, Z.; Jeffers, A.; Jiang, A.; He, X.; Azarov, I.; Seibert, R.; Mehta, A.; Patel, R.; King, S. B.; Hogg, N.; Ghosh, A.; Gladwin, M. T.; Kim-Shapiro, D. B. Catalytic generation of N_2O_3 by the concerted nitrite reductase and anhydrase activity of hemoglobin. *Nat. Chem. Biol.* **2007**, *3*, 785−794.

(1433) Schwab, D. E.; Stamler, J. S.; Singel, D. J. Nitrite-methemoglobin inadequate for hypoxic vasodilation. *Nat. Chem. Biol.* **2009**, *5*, 366.

(1434) Silaghi-Dumitrescu, R. Linkage isomerism in nitrite reduction by cytochrome cd_1 nitrite reductase. *Inorg. Chem.* **2004**, *43*, 3715−3718.

(1435) Berto, T. C.; Lehnert, N. Density functional theory modeling of the proposed nitrite anhydrase function of hemoglobin in hypoxia sensing. *Inorg. Chem.* **2011**, *50*, 7361−7363.

(1436) Kizawa, H.; Tomura, D.; Oda, M.; Fukamizu, A.; Hoshino, T.; Gotoh, O.; Yasui, T.; Shoun, H. Nucleotide sequence of the unique nitrate/nitrite-inducible cytochrome P-450 cDNA from *Fusarium oxysporum*. *J. Biol. Chem.* **1991**, *266*, 10632−10637.

(1437) Zhang, L.; Kudo, T.; Takaya, N.; Shoun, H. The B' helix determines cytochrome P450nor specificity for the electron donors NADH and NADPH. *J. Biol. Chem.* **2002**, *277*, 33842−33847.

(1438) Denisov, I. G.; Makris, T. M.; Sligar, S. G.; Schlichting, I. Structure and chemistry of cytochrome P450. *Chem. Rev.* **2005**, *105*, 2253−2277.

(1439) Peterson, J. A.; Graham, S. E. A close family resemblance: the importance of structure in understanding cytochromes P450. *Structure* **1998**, *6*, 1079−1085.

(1440) Park, S.-Y.; Shimizu, H.; Adachi, S.; Nagagawa, A.; Tanaka, I.; Nakahara, K.; Shoun, H.; Obayashi, E.; Nakamura, H.; Iizuka, T.; Shiro, Y. Crystal structure of nitric oxide reductase from denitrifying fungus *Fusarium oxysporum*. *Nat. Struct. Biol.* **1997**, *4*, 827−832.

(1441) Shoun, H.; Tanimoto, T. Denitrification by the fungus *Fusarium oxysporum* and involvement of cytochrome P-450 in the respiratory nitrite reduction. *J. Biol. Chem.* **1991**, *266*, 11078−11082.

(1442) Takaya, N.; Shoun, H. Nitric oxide reduction, the last step in denitrification by *Fusarium oxysporum* is obligatorily mediated by cytochrome P450nor. *Mol. Gen. Genet.* **2000**, *263*, 342−348.

(1443) U.S. Environmental Protection Agency. *Overview of greenhouse gases*; U.S. EPA, 2021. https://www.epa.gov/ghgemissions/overview-greenhouse-gases (accessed 03-29-2021).

(1444) Ravishankara, A. R.; Daniel, J. S.; Portmann, R. W. Nitrous oxide (N_2O): the dominant ozone-depleting substance emitted in the 21st century. *Science* **2009**, *326*, 123−125.

(1445) Kobayashi, M.; Matsuo, Y.; Takimoto, A.; Suzuki, S.; Maruo, F.; Shoun, H. Denitrification, a novel type of respiratory metabolism in fungal mitochondrion. *J. Biol. Chem.* **1996**, *271*, 16263−16267.

(1446) Zhou, Z.; Takaya, N.; Sakairi, M. A. C.; Shoun, H. Oxygen requirement for the denitrification by the filamentous fungus *Fusarium oxysporum*. *Arch. Microbiol.* **2001**, *175*, 19−25.

(1447) Takaya, N.; Kuwazaki, S.; Adachi, Y.; Suzuki, S.; Kikuchi, T.; Nakamura, H.; Shiro, Y.; Shoun, H. Hybrid respiration in the denitrifying mitochondria of *Fusarium oxysporum*. *J. Biochem.* **2003**, *133*, 461−465.

(1448) Tanimoto, T.; Nakahara, K.; Shoun, H. Diauxic growth of *Fusarium oxysporum* during aerobic culture in the presence of nitrate/nitrite. *Biosci., Biotechnol., Biochem.* **1992**, *56*, 2058−2059.

(1449) Shoun, H.; Suyama, W.; Yasui, T. Soluble, nitrate/nitrite-inducible cytochrome P-450 of the fungus, *Fusarium oxysporum*. *FEBS Lett.* **1989**, *244*, 11−14.

(1450) Usuda, K.; Toritsuka, N.; Matsuo, Y.; Kim, D. H.; Shoun, H. Denitrification by the fungus *Cylindrocarpon tonkinense*: anaerobic cell growth and two isozyme forms of cytochrome P-450nor. *Appl. Environ. Microbiol.* **1995**, *61*, 883−889.

(1451) Kudo, T.; Tomura, D.; Liu, D. L.; Dai, X. Q.; Shoun, H. Two isozymes of P450nor of *Cylindrocarpon tonkinense*: molecular cloning of the cDNAs and genes, expressions in the yeast, and the putative NAD(P)H-binding site. *Biochimie* **1996**, *78*, 792−799.

(1452) Zhang, L.; Takaya, N.; Kitazume, T.; Kondo, T.; Shoun, H. Purification and cDNA cloning of nitric oxide reductase cytochrome P450nor (CYP55A4) from *Trichosporon cutaneum*. *Eur. J. Biochem.* **2001**, *268*, 3198−3204.

(1453) Shimizu, H.; Park, S.-Y.; Gomi, Y.; Arakawa, H.; Nakamura, H.; Adachi, S.-I.; Obayashi, E.; Iizuka, T.; Shoun, H.; Shiro, Y. Proton delivery in NO reduction by fungal nitric-oxide reductase. Cryogenic crystallography, spectroscopy, and kinetics of ferric-NO complexes of wild-type and mutant enzymes. *J. Biol. Chem.* **2000**, *275*, 4816−4826.

(1454) Shoun, H.; Kano, M.; Baba, I.; Takaya, N.; Matsuo, M. Denitrification by actinomycetes and purification of dissimilatory nitrite reductase and azurin from *Streptomyces thioluteus*. *J. Bacteriol.* **1998**, *180*, 4413−4415.

(1455) Shoun, H.; Kim, D. H.; Uchiyama, H.; Sugiyama, J. Denitrification by fungi. *FEMS Microbiol. Lett.* **1992**, *94*, 277−282.

(1456) Tomura, D.; Obika, K.; Fukamizu, A.; Shoun, H. Nitric oxide reductase cytochrome P-450 gene, CYP55, of the fungus *Fusarium oxysporum* containing a potential binding-site for FNR, the transcription factor involved in the regulation of anaerobic growth of *Escherichia coli*. *J. Biochem.* **1994**, *116*, 88−94.

(1457) Takaya, N.; Suzuki, S.; Kuwazaki, S.; Shoun, H.; Maruo, F.; Yamaguchi, M.; Takeo, K. Cytochrome P450nor, a novel class of mitochondrial cytochrome P450 involved in nitrate respiration in the fungus *Fusarium oxysporum*. *Arch. Biochem. Biophys.* **1999**, *372*, 340−346.

(1458) Nakahara, K.; Shoun, H. N-terminal processing and amino acid sequence of two isoforms of nitric oxide reductase cytochrome P450nor from *Fusarium oxysporum*. *J. Biochem.* **1996**, *120*, 1082−1087.

(1459) Watsuji, T. O.; Takaya, N.; Nakamura, A.; Shoun, H. A possible role of NADPH-dependent cytochrome P450nor isozyme in glycolysis under denitrifying conditions. *Biosci., Biotechnol., Biochem.* **2003**, *67*, 1109−1114.

(1460) Heiss, B.; Frunzke, K.; Zumft, W. G. Formation of the NN bond from nitric oxide by a membrane-bound cytochrome *bc* complex of nitrate-respiring (denitrifying) *Pseudomonas stutzeri*. *J. Bacteriol.* **1989**, *171*, 3288−3297.

(1461) Shimizu, H.; Park, S.-Y.; Shiro, Y.; Adachi, S.-I. Crystal structure of nitric oxide reductase (cytochrome P450nor) at atomic resolution. *Acta Crystallogr., Sect. D: Biol. Crystallogr.* **2002**, *58*, 81.

(1462) Oshima, R.; Fushinobu, S.; Su, F.; Zhang, L.; Takaya, N.; Shoun, H. Structural evidence for direct hydride transfer from NADH to cytochrome P450nor. *J. Mol. Biol.* **2004**, *342*, 207−217.

(1463) Lee, D. S.; Park, S. Y.; Yamane, K.; Obayashi, E.; Hori, H.; Shiro, Y. Structural characterization of n-butyl-isocyanide complexes of cytochromes P450nor and P450cam. *Biochemistry* **2001**, *40*, 2669−2677.

(1464) Kudo, T.; Takaya, N.; Park, S. Y.; Shiro, Y.; Shoun, H. A positively charged cluster formed in the heme-distal pocket of cytochrome P450nor is essential for interaction with NADH. *J. Biol. Chem.* **2001**, *276*, 5020−5026.

(1465) Poulos, T. L.; Finzel, B. C.; Howard, A. J. Crystal structure of substrate-free *Pseudomonas putida* cytochrome P-450. *Biochemistry* **1986**, *25*, 5314−5322.

(1466) Obayashi, E.; Shimizu, H.; Park, S. Y.; Shoun, H.; Shiro, Y. Mutation effects of a conserved threonine (Thr243) of cytochrome P450nor on its structure and function. *J. Inorg. Biochem.* **2000**, *82*, 103−111.

(1467) Cupp-Vickery, J. R.; Poulos, T. L. Structure of cytochrome P450eryF involved in erythromycin biosynthesis. *Nat. Struct. Mol. Biol.* **1995**, *2*, 144−153.

(1468) Gotoh, O. Substrate recognition sites in cytochrome P450 family 2 (CYP2) proteins inferred from comparative analyses of amino acid and coding nucleotide sequences. *J. Biol. Chem.* **1992**, *267*, 83−90.

(1469) Hasemann, C. A.; Ravichandran, K. G.; Peterson, J. A.; Deisenhofer, J. Crystal structure and refinement of cytochrome P450terp at 2.3 resolution. *J. Mol. Biol.* **1994**, *236*, 1169−1185.

(1470) Okamoto, N.; Tsuruta, K.; Imai, Y.; Tomura, D.; Shoun, H. Fungal P450nor: expression in *Escherichia coli* and site-directed mutageneses at the putative distal region. *Arch. Biochem. Biophys.* **1997**, *337*, 338−344.

(1471) Okamoto, N.; Imai, Y.; Shoun, H.; Shiro, Y. Site-directed mutagenesis of the conserved threonine (Thr243) of the distal helix of fungal cytochrome P450nor. *Biochemistry* **1998**, *37*, 8839−8847.

(1472) Zhang, L.; Kudo, T.; Takaya, N.; Shoun, H. Distribution, structure and function of fungal nitric oxide reductase P450nor—recent advances. *Int. Congr. Ser.* **2002**, *1233*, 197−202.

(1473) Poulos, T. L.; Finzel, B. C.; Howard, A. J. High-resolution crystal structure of cytochrome P450cam. *J. Mol. Biol.* **1987**, *195*, 687−700.

(1474) Sono, M.; Roach, M. P.; Coulter, E. D.; Dawson, J. H. Heme-containing oxygenases. *Chem. Rev.* **1996**, *96*, 2841−2887.

(1475) Yosca, T. H.; Rittle, J.; Krest, C. M.; Onderko, E. L.; Silakov, A.; Calixto, J. C.; Behan, R. K.; Green, M. T. Understanding C-H bond activation in cytochrome P450: the ferryl pKa and the role of thiolate ligation. *Science* **2013**, *342*, 825−829.

(1476) Shoun, H.; Sudo, Y.; Seto, Y.; Beppu, T. Purification and properties of a cyotchrome P-450 of a fungus, *Fusarium oxysporum*. *J. Biochem.* **1983**, *94*, 1219−1229.

(1477) Lipscomb, J. D. Electron paramagnetic resonance detectable states of cytochrome P-450cam. *Biochemistry* **1980**, *19*, 3590−3599.

(1478) Dawson, J. H.; Sono, M. Cytochrome P-450 and chloroperoxidase: thiolate-ligated heme enzymes. Spectroscopic determination of their active-site structures and mechanistic implications of thiolate ligation. *Chem. Rev.* **1987**, *87*, 1255−1276.

(1479) Singh, U. P.; Obayashi, E.; Takahashi, S.; Iizuka, T.; Shoun, H.; Shiro, Y. The effects of heme modification on reactivity, ligand binding properties and iron-coordination structures of cytochrome P450nor. *Biochim. Biophys. Acta, Protein Struct. Mol. Enzymol.* **1998**, *1384*, 103−111.

(1480) Franke, A.; Stochel, G.; Suzuki, N.; Higuchi, T.; Okuzono, K.; van Eldik, R. Mechanistic studies on the binding of nitric oxide to a synthetic heme-thiolate complex relevant to cytochrome P450. *J. Am. Chem. Soc.* **2005**, *127*, 5360−5375.

(1481) Ivanovic-Burmazovic, I.; van Eldik, R. Metal complex-assisted activation of small molecules. From NO to superoxide and peroxides. *J. Chem. Soc. Dalton Trans.* **2008**, 5259−5275.

(1482) *Molecular mechanisms of oxygen activation*; Gunsalus, I. C., Meeks, J. R., Lipscomb, J. D., Debrunner, P., Munck, E., Eds.; Academic Press: New York, 1974, pp 599−613.

(1483) *Oxygenase and oxygen metabolism*; Makino, T., Iizuka, T., Sakaguchi, K., Ishimura, Y., Eds.; Academic Press: New York, 1982, pp 466−477.

(1484) Higuchi, T.; Uzu, S.; Hirobe, M. Synthesis of a highly stable iron porphyrin coordinated by alkylthiolate anion as a model for cytochrome P-450 and its catalytic activity in O-O bond cleavage. *J. Am. Chem. Soc.* **1990**, *112*, 7051−7053.

(1485) Obayashi, E.; Tsukamoto, K.; Adachi, S.; Takahashi, S.; Nomura, M.; Iizuka, T.; Shoun, H.; Shiro, Y. Unique binding of nitric oxide to ferric nitric oxide reductase from *Fusarium oxysporum* elucidated with infrared, resonance Raman, and x-ray absorption spectroscopies. *J. Am. Chem. Soc.* **1997**, *119*, 7807−7816.

(1486) Tosha, T.; Nomura, T.; Nishida, T.; Saeki, N.; Okubayashi, K.; Yamagiwa, R.; Sugahara, M.; Nakane, T.; Yamashita, K.; Hirata, K.; Ueno, G.; Kimura, T.; Hisano, T.; Muramoto, K.; Sawai, H.; Takeda, H.; Mizohata, E.; Yamashita, A.; Kanematsu, Y.; Takano, Y.; Nango, E.; Tanaka, R.; Nureki, O.; Shoji, O.; Ikemoto, Y.; Murakami, H.; Owada, S.; Tono, K.; Yabashi, M.; Yamamoto, M.; Ago, H.; Iwata, S.; Sugimoto, H.; Shiro, Y.; Kubo, M. Capturing an initial intermediate during the P450nor enzymatic reaction using time-resolved XFEL crystallography and caged-substrate. *Nat. Commun.* **2017**, *8*, 1585.

(1487) Abucayon, E. G.; Khade, R. L.; Powell, D. R.; Zhang, Y.; Richter-Addo, G. B. Hydride attack on a coordinated ferric nitrosyl: experimental and DFT evidence for the formation of a heme model-HNO derivative. *J. Am. Chem. Soc.* **2016**, *138*, 104−107.

(1488) Quaroni, L. G.; Seward, H. E.; McLean, K. J.; Girvan, H. M.; Ost, T. W. B.; Noble, M. A.; Kelly, S. M.; Price, N. C.; Cheesman, M. R.; Smith, W. E.; Munro, A. W. Interaction of nitric oxide with cytochrome P450 BM3. *Biochemistry* **2004**, *43*, 16416−16431.

(1489) Hunt, A. P.; Subhra, S.; Dent, M. R.; Milbauer, M. W.; Burstyn, J. N.; Lehnert, N. Model complexes elucidate the role of the hydrogen-bonding network in cytochrome P450s. *Inorg. Chem.* **2020**, *59*, 8034−8043.

(1490) Dent, M. R.; Milbauer, M. W.; Hunt, A. P.; Aristov, M. M.; Guzei, I. A.; Lehnert, N.; Burstyn, J. N. Electron paramagnetic resonance spectroscopy as a probe of hydrogen bonding in heme-thiolate proteins. *Inorg. Chem.* **2019**, *58*, 16011−16027.

(1491) Davydov, R.; Im, S.; Shanmugam, M.; Gunderson, W. A.; Pearl, N. M.; Hoffman, B. M.; Waskell, L. Role of the proximal cysteine hydrogen bonding interaction in cytochrome P450 2B4 studied by cryoreduction, electron paramagnetic resonance, and electron-nuclear double resonance spectroscopy. *Biochemistry* **2016**, *55*, 869−883.

(1492) Solomon, E. I.; Gorelsky, S. I.; Dey, A. Metal-thiolate bonds in bioinorganic chemistry. *J. Comput. Chem.* **2006**, *27*, 1415−1428.

(1493) Das, P. D.; Samanta, S.; McQuarters, A. B.; Lehnert, N.; Dey, A. Valence tautomerism in synthetic models of cytochrome P450. *Proc. Natl. Acad. Sci. U. S. A.* **2016**, *113*, 6611−6616.

(1494) Rana, A.; Amanullah, S.; Das, P. K.; McQuarters, A. B.; Lehnert, N.; Dey, A. Formally ferric heme carbon monoxide adduct. *J. Am. Chem. Soc.* **2019**, *141*, 5073−5077.

(1495) Li, D.; Stuehr, D. J.; Yeh, S.-R.; Rousseau, D. L. Heme distortion modulated by ligand-protein interactions in inducible nitric-oxide synthase. *J. Biol. Chem.* **2004**, *279*, 26489−26499.

(1496) Horn, M.; Nienhaus, K.; Nienhaus, G. U. Fourier transform infrared spectroscopy study of ligand photodissociation and migration in inducible nitric oxide synthase. *F1000Research* **2014**, *3*, 290.

(1497) Hu, S.; Kincaid, J. R. Heme active-site structural characterization of chloroperoxidase by resonance Raman spectroscopy. *J. Biol. Chem.* **1993**, *268*, 6189−6193.

(1498) Hu, S.; Kincaid, J. R. Resonance Raman characterization of nitric oxide adducts of cytochrome P450cam: the effect of substrate structure on the iron-ligand vibrations. *J. Am. Chem. Soc.* **1991**, *113*, 2843−2850.

(1499) Deng, T.-J.; Proniewicz, L. M.; Kincaid, J. R.; Yeom, H.; Macdonald, I. D. G.; Sligar, S. G. Resonance Raman studies of cytochrome P450BM3 and its complexes with exogenous ligands. *Biochemistry* **1999**, *38*, 13699−13706.

(1500) Paulat, F.; Lehnert, N. Electronic structure of ferric heme nitrosyl complexes with thiolate coordination. *Inorg. Chem.* **2007**, *46*, 1547−1549.

(1501) Dawson, J. H.; Holm, R. H.; Trudell, J. R.; Barth, G.; Linder, R. E.; Bunnenberg, E.; Djerassi, C.; Tang, S. C. Oxidized cytochrome P-450. Magnetic circular dichroism evidence for thiolate ligation in the substrate-bound form. Implications for the catalytic mechanism. *J. Am. Chem. Soc.* **1976**, *98*, 3707−3709.

(1502) McQuarters, A. B.; Wolf, M. W.; Hunt, A. P.; Lehnert, N. 1958-2014: after 56 years of research, cytochrome P450 reactivity finally explained. *Angew. Chem., Int. Ed.* **2014**, *53*, 4750−4752.

(1503) Abucayon, E. G.; Khade, R. L.; Powell, D. R.; Shaw, M. J.; Zhang, Y.; Richter-Addo, G. B. Over or under: hydride attack at the metal versus the coordinated nitrosyl ligand in ferric nitrosyl porphyrins. *Dalton Trans.* **2016**, *45*, 18259−18266.

(1504) Lin, R.; Farmer, P. J. The HNO adduct of myoglobin: synthesis and charcterization. *J. Am. Chem. Soc.* **2000**, *122*, 2393−2394.

(1505) Mowat, C. G.; Chapman, S. K. Multi-heme cytochromes - new structures, new chemistry. *J. Chem. Soc. Dalton Trans.* **2005**, 3381−3389.

(1506) Farmer, P. J.; Sulc, F. Coordination chemistry of the HNO ligand with hemes and synthetic coordination complexes. *J. Inorg. Biochem.* **2005**, *99*, 166−184.

(1507) Immoos, C. E.; Sulc, F.; Farmer, P. J.; Czarnecki, K.; Bocian, D. F.; Levina, A.; Aitken, J. B.; Armstrong, R. S.; Lay, P. A. Bonding in HNO-myoglobin as characterized by x-ray absorption and resonance Raman spectroscopies. *J. Am. Chem. Soc.* **2005**, *127*, 814−815.

(1508) Yang, L.; Ling, Y.; Zhang, Y. HNO binding in a heme protein: structures, spectroscopic properties, and stabilities. *J. Am. Chem. Soc.* **2011**, *133*, 13814−13817.

(1509) Zapata, A. L.; Kumar, M. R.; Pervitsky, D.; Farmer, P. J. A singular value decomposition approach for kinetic analysis of reactions of HNO with myoglobin. *J. Inorg. Biochem.* **2013**, *118*, 171−178.

(1510) Paolocci, N.; Jackson, M. I.; Lopez, B. E.; Miranda, K.; Tocchetti, C. G.; Wink, D. A.; Hobbs, A. J.; Fukuto, J. M. The pharmacology of nitroxyl (HNO) and its therapeutic potential: Not just the janus face of NO. *Pharmacol. Ther.* **2007**, *113*, 442−458.

(1511) Fukuto, J. M.; Carrington, S. J. HNO signaling mechanisms. *Antioxid. Redox Signaling* **2011**, *14*, 1649−1657.

(1512) Bartberger, M. D.; Fukuto, J. M.; Houk, K. N. On the acidity and reactivity of HNO in aqueous solution and biological systems. *Proc. Natl. Acad. Sci. U. S. A.* **2001**, *98*, 2194−2198.

(1513) Doyle, M. P.; Mahapatro, S. N.; Broene, R. D.; Guy, J. K. Oxidation and reduction of hemoproteins by trioxodinitrate(II). The role of nitrosyl hydride and nitrite. *J. Am. Chem. Soc.* **1988**, *110*, 593−599.

(1514) Wong, P. S.-Y.; Hyun, J.; Fukuto, J. M.; Shirota, F. N.; DeMaster, E. G.; Shoeman, D. W.; Nagasawa, H. T. Reaction between S-nitrosothiols and thiols: generation of nitroxyl (HNO) and subsequent chemistry. *Biochemistry* **1998**, *37*, 5362−5371.

(1515) Jackson, M. I.; Han, T. H.; Serbulea, L.; Dutton, A.; Ford, E.; Miranda, K. M.; Houk, K. N.; Wink, D. A.; Fukuto, J. M. Kinetic feasibility of nitroxyl reduction by physiological reductants and biological implications. *Free Radical Biol. Med.* **2009**, *47*, 1130−1139.

(1516) Väänänen, A. J.; Salmenperä, P.; Hukkanen, M.; Miranda, K. M.; Harjula, A.; Rauhala, P.; Kankuri, E. Persistent susceptibility of cathepsin B to irreversible inhibition by nitroxyl (HNO) in the presence of endogenous nitric oxide. *Free Radical Biol. Med.* **2008**, *45*, 749−755.

(1517) Miranda, K. M. The chemistry of nitroxyl (HNO) and implications in biology. *Coord. Chem. Rev.* **2005**, *249*, 433−455.

(1518) DeMaster, E. G.; Redfern, B.; Nagasawa, H. T. Mechanisms of inhibition of aldehyde dehydrogenase by nitroxyl, the active metabolite of the alcohol deterrent agent cyanamide. *Biochem. Pharmacol.* **1998**, *55*, 2007−2015.

(1519) Lee, J.; Richter-Addo, G. B. A nitrosyl hydride complex of a heme model [Ru(ttp)(HNO)(1-MeIm)] (ttp=tetratolylporphyrinato dianion). *J. Inorg. Biochem.* **2004**, *98*, 1247−1250.

(1520) Kumar, M. R.; Fukuto, J. M.; Miranda, K. M.; Farmer, P. J. Reactions of HNO with heme proteins: new routes to HNO-heme complexes and insight into physiological effects. *Inorg. Chem.* **2010**, *49*, 6283−6292.

(1521) Shafirovich, V.; Lymar, S. V. Nitroxyl and its anion in aqueous solutions: Spin states, protic equilibria, and reactivities toward oxygen and nitric oxide. *Proc. Natl. Acad. Sci. U. S. A.* **2002**, *99*, 7340−7345.

(1522) Shi, Y.; Zhang, Y. Mechanisms of HNO reactions with ferric heme proteins. *Angew. Chem., Int. Ed.* **2018**, *57*, 16654−16658.

(1523) Yosca, T. H.; Ledray, A. P.; Ngo, J.; Green, M. T. A new look at the role of thiolate ligation in cytochrome P450. *JBIC, J. Biol. Inorg. Chem.* **2017**, *22*, 209−220.

(1524) Buxton, G. V.; Greenstock, C. L.; Helman, W. P.; Ross, A. B. Critical review of rate constants for reactions of hydrated electrons, hydrogen atoms and hydroxyl radicals. *J. Phys. Chem. Ref. Data* **1988**, *17*, 513−886.

(1525) Field, S. J.; Prior, L.; Roldán, M. D.; Cheesman, M. R.; Thomson, A. J.; Spiro, S.; Butt, J. N.; Watmough, N. J.; Richardson, D. J. Spectral properties of bacterial nitric-oxide reductase: resolution of pH-dependent forms of the active site heme b 3. *J. Biol. Chem.* **2002**, *277*, 20146−20150.

(1526) Bell, L. C.; Ferguson, S. J. Nitric and nitrous oxide reductases are active under aerobic conditions in cells of *Thiosphaera pantotropha*. *Biochem. J.* **1991**, *273*, 423−427.

(1527) Philippot, L.; Hallin, S.; Schloter, M. Ecology of denitrifying prokaryotes in agricultural soil. *Adv. Agron.* **2007**, *96*, 249−305.

(1528) Sousa, F. L.; Alves, R. J.; Ribeiro, M. A.; Pereira-Leal, J. B.; Teixeira, M.; Pereira, M. M. The superfamily of heme-copper oxygen reductases: types and evolutionary considerations. *Biochim. Biophys. Acta, Bioenerg.* **2012**, *1817*, 629−637.

(1529) Yoshikawa, S.; Shimada, A. Reaction mechanism of cytochrome *c* oxidase. *Chem. Rev.* **2015**, *115*, 1936−1989.

(1530) Bell, L. C.; Richardson, D. J.; Ferguson, S. J. Identification of nitric oxide reductase activity in *Rhodobacter capsulatus*: the electron transport pathway can either use or bypass both cytochrome c_2 and the cytochrome bc_1 complex. *Microbiology* **1992**, *138*, 437−443.

(1531) Shapleigh, J. P.; Payne, W. J. Nitric oxide-dependent proton translocation in various denitrifiers. *J. Bacteriol.* **1985**, *163*, 837−840.

(1532) Blomberg, M. R. A. How quantum chemistry can solve fundamental problems in bioenergetics. *Int. J. Quantum Chem.* **2015**, *115*, 1197−1201.

(1533) Cramm, R.; Siddiqui, R. A.; Friedrich, B. Two isofunctional nitric oxide reductases in *Alcaligenes eutrophus* H16. *J. Bacteriol.* **1997**, *179*, 6769−6777.

(1534) Al-Attar, S.; de Vries, S. An electrogenic nitric oxide reductase. *FEBS Lett.* **2015**, *589*, 2050−2057.

(1535) Stein, L. Y.; Arp, D. J.; Berube, P. M.; Chain, P. S. G.; Hauser, L.; Jetten, M. S. M.; Klotz, M. G.; Larimer, F. W.; Norton, J. M.; Op den Camp, H. J. M.; et al. Whole-genome analysis of the ammonia-oxidizing bacterium, *Nitrosomonas eutropha* C91: implications for niche adaptation. *Environ. Microbiol.* **2007**, *9*, 2993−3007.

(1536) Heylen, K.; Keltjens, J. Redundancy and modularity in membrane-associated dissimilatory nitrate reduction in *Bacillus*. *Front. Microbiol.* **2012**, *3*, 371.

(1537) Cho, C. M.-H.; Yan, T.; Liu, X.; Wu, L.; Zhou, J.; Stein, L. Y. Transcriptome of a *Nitrosomonas europaea* mutant with a disrupted nitrite reductase gene (*NirK*). *Appl. Environ. Microbiol.* **2006**, *72*, 4450−4454.

(1538) Sievert, S. M.; Scott, K. M.; Klotz, M. G.; Chain, P. S. G.; Hauser, L. J.; Hemp, J.; Hügler, M.; Land, M.; Lapidus, A.; Larimer, F. W.; et al. Genome of the epsilonproteobacterial chemolithoautotroph *Sulfurimonas denitrificans*. *Appl. Environ. Microbiol.* **2008**, *74*, 1145−1156.

(1539) Welte, C. U.; Rasigraf, O.; Vaksmaa, A.; Versantvoort, W.; Arshad, A.; Op den Camp, H. J. M.; Jetten, M. S. M.; Lüke, C.; Reimann, J. Nitrate-and nitrite-dependent anaerobic oxidation of methane. *Environ. Microbiol. Rep.* **2016**, *8*, 941−955.

(1540) Reimann, J.; Jetten, M. S. M.; Keltjens, J. T. Metal enzymes in "impossible" microorganisms catalyzing the anaerobic oxidation of ammonium and methane. *Sustaining life on planet Earth: metalloenzymes mastering dioxygen and other chewy gases*; Kroneck, P. M. H., Sosa Torres, M. E., Eds.; Springer, 2015; pp 257−313.

(1541) Ettwig, K. F.; Speth, D. R.; Reimann, J.; Wu, M. L.; Jetten, M. S. M.; Keltjens, J. T. Bacterial oxygen production in the dark. *Front. Microbiol.* **2012**, *3*, 273.

(1542) Zhang, Y.; Ma, A.; Liu, W.; Bai, Z.; Zhuang, X.; Zhuang, G. The occurrence of putative nitric oxide dismutase (NOD) in an alpine wetland with a new dominant subcluster and the potential ability for a methane sink. *Archaea* **2018**, *2018*, 2018.

(1543) Watmough, N. J.; Field, S. J.; Hughes, R. J. L.; Richardson, D. J. The bacterial respiratory nitric oxide reductase. *Biochem. Soc. Trans.* **2009**, *37*, 392−399.

(1544) Butland, G.; Spiro, S.; Watmough, N. J.; Richardson, D. J. Two conserved glutamates in the bacterial nitric oxide reductase are essential for activity but not assembly of the enzyme. *J. Bacteriol.* **2001**, *183*, 189−199.

(1545) Cheesman, M. R.; Zumft, W. G.; Thomson, A. J. The MCD and EPR of the heme centers of nitric oxide reductase from *Pseudomonas stutzeri:* evidence that the enzyme is structurally related to the heme-copper oxidases. *Biochemistry* **1998**, *37*, 3994−4000.

(1546) Oubrie, A.; Gemeinhardt, S.; Field, S. J.; Marritt, S.; Thomson, A. J.; Saraste, M.; Richardson, D. J. Properties of a soluble domain of subunit C of a bacterial nitric oxide reductase. *Biochemistry* **2002**, *41*, 10858−10865.

(1547) Kastrau, D. H. W.; Heiss, B.; Kroneck, P. M. H.; Zumft, W. G. Nitric oxide reductase from *Pseudomonas stutzeri* a novel cytochrome *bc* complex. *Eur. J. Biochem.* **1994**, *222*, 293−303.

(1548) Flock, U.; Reimann, J.; et al. Proton transfer in bacterial nitric oxide reductase. *Biochem. Soc. Trans.* **2006**, *34*, 188−190.

(1549) Field, S. J.; Thorndycroft, F. H.; Matorin, A. D.; Richardson, D. J.; Watmough, N. J. The respiratory nitric oxide reductase (NorBC) from *Paracoccus denitrificans*. *Methods Enzymol.* **2008**, *437*, 79−99.

(1550) Timóteo, C. G.; Pereira, A. S.; Martins, C. E.; Naik, S. G.; Duarte, A. G.; Moura, J. J. G.; Tavares, P.; Huynh, B. H.; Moura, I. Low-spin heme b_3 in the catalytic center of nitric oxide reductase from *Pseudomonas nautica*. *Biochemistry* **2011**, *50*, 4251−4262.

(1551) Cordas, C. M.; Pereira, A. S.; Martins, C. E.; Timóteo, C. G.; Moura, I.; Moura, J. J. G.; Tavares, P. Nitric oxide reductase: direct electrochemistry and electrocatalytic activity. *ChemBioChem* **2006**, *7*, 1878−1881.

(1552) Cordas, C. M.; Duarte, A. G.; Moura, J. J. G.; Moura, I. Electrochemical behaviour of bacterial nitric oxide reductase—evidence of low redox potential non-heme Fe_B gives new perspectives on the catalytic mechanism. *Biochim. Biophys. Acta, Bioenerg.* **2013**, *1827*, 233−238.

(1553) Crow, A.; Matsuda, Y.; Arata, H.; Oubrie, A. Structure of the membrane-intrinsic nitric oxide reductase from *Roseobacter denitrificans*. *Biochemistry* **2016**, *55*, 3198−3203.

(1554) Matsuda, Y.; Inamori, K.-i.; Osaki, T.; Eguchi, A.; Watanabe, A.; Kawabata, S.-i.; Iba, K.; Arata, H. Nitric oxide-reductase homologue that contains a copper atom and has cytochrome *c*-oxidase activity from an aerobic phototrophic bacterium *Roseobacter denitrificans*. *J. Biochem.* **2002**, *131*, 791−800.

(1555) Matsuda, Y.; Uchida, T.; Hori, H.; Kitagawa, T.; Arata, H. Structural characterization of a binuclear center of a Cu-containing NO reductase homologue from *Roseobacter denitrificans*: EPR and resonance Raman studies. *Biochim. Biophys. Acta, Bioenerg.* **2004**, *1656*, 37−45.

(1556) Tosha, T.; Yamagiwa, R.; Sawai, H.; Shiro, Y. NO dynamics in microbial denitrification system. *Chem. Lett.* **2021**, *50*, 280−288.

(1557) Terasaka, E.; Yamada, K.; Wang, P.-H.; Hosokawa, K.; Yamagiwa, R.; Matsumoto, K.; Ishii, S.; Mori, T.; Yagi, K.; Sawai, H.; et al. Dynamics of nitric oxide controlled by protein complex in bacterial system. *Proc. Natl. Acad. Sci. U. S. A.* **2017**, *114*, 9888−9893.

(1558) Albertsson, I.; Sjöholm, J.; Ter Beek, J.; Watmough, N. J.; Widengren, J.; Ädelroth, P. Functional interactions between nitrite reductase and nitric oxide reductase from *Paracoccus denitrificans*. *Sci. Rep.* **2019**, *9*, 1−12.

(1559) Gray, H. B.; Winkler, J. R. Long-range electron transfer. *Proc. Natl. Acad. Sci. U. S. A.* **2005**, *102*, 3534−3539.

(1560) Goretski, J.; Zafiriou, O. C.; Hollocher, T. C. Steady-state nitric oxide concentrations during denitrification. *J. Biol. Chem.* **1990**, *265*, 11535−11538.

(1561) Kalkowski, I.; Conrad, R. Metabolism of nitric oxide in denitrifying *Pseudomonas aeruginosa* and nitrate-respiring *Bacillus cereus*. *FEMS Microbiol. Lett.* **1991**, *82*, 107−112.

(1562) Vollack, K. U.; Zumft, W. G. Nitric oxide signaling and transcriptional control of denitrification genes in *Pseudomonas stutzeri*. *J. Bacteriol.* **2001**, *183*, 2516−2526.

(1563) Flock, U.; Thorndycroft, F. H.; Matorin, A. D.; Richardson, D. J.; Watmough, N. J.; Adelroth, P. Defining the proton entry point in the bacterial respiratory nitric-oxide reductase. *J. Biol. Chem.* **2008**, *283*, 3839−3845.

(1564) Reimann, J.; Flock, U.; Lepp, H.; Honigmann, A.; Ädelroth, P. A pathway for protons in nitric oxide reductase from *Paracoccus denitrificans*. *Biochim. Biophys. Acta, Bioenerg.* **2007**, *1767*, 362−373.

(1565) Flock, U.; Lachmann, P.; Reimann, J.; Watmough, N. J.; Adelroth, P. Exploring the terminal region of the proton pathway in the bacterial nitric oxide reductase. *J. Inorg. Biochem.* **2009**, *103*, 845−850.

(1566) Pisliakov, A. V.; Hino, T.; Shiro, Y.; Sugita, Y. Molecular dynamics simulations reveal proton transfer pathways in cytochrome *c*-dependent nitric oxide reductase. *PLoS Comput. Biol.* **2012**, *8*, No. e1002674.

(1567) Koutny, M.; Kucera, I.; Tesarık, R.; Turanek, J.; Van Spanning, R. J.M. Pseudoazurin mediates periplasmic electron flow in a mutant strain of *Paracoccus denitrificans* lacking cytochrome c_{550}. *FEBS Lett.* **1999**, *448*, 157−159.

(1568) Moir, J. W. B.; Ferguson, S. J. Properties of a *Paracoccus denitrificans* mutant deleted in cytochrome c_{550} indicate that a copper protein can substitute for this cytochrome in electron transport to nitrite, nitric oxide and nitrous oxide. *Microbiology* **1994**, *140*, 389−397.

(1569) Cramm, R.; Pohlmann, A.; Friedrich, B. Purification and characterization of the single-component nitric oxide reductase from *Ralstonia eutropha* H16. *FEBS Lett.* **1999**, *460*, 6−10.

(1570) Suharti Strampraad, M. J. F.; Schroder, I.; de Vries, S. A novel copper A containing menaquinol NO reductase from *Bacillus azotoformans*. *Biochemistry* **2001**, *40*, 2622−2639.

(1571) Terasaka, E.; Okada, N.; Sato, N.; Sako, Y.; Shiro, Y.; Tosha, T. Characterization of quinol-dependent nitric oxide reductase from *Geobacillus stearothermophilus*: enzymatic activity and active site structure. *Biochim. Biophys. Acta, Bioenerg.* **2014**, *1837*, 1019−1026.

(1572) Hendriks, J.; Oubrie, A.; Castresana, J.; Urbani, A.; Gemeinhardt, S.; Saraste, M. Nitric oxide reductases in bacteria. *Biochim. Biophys. Acta, Bioenerg.* **2000**, *1459*, 266−273.

(1573) Stevanin, T. M.; Moir, J. W. B.; Read, R. C. Nitric oxide detoxification systems enhance survival of *Neisseria meningitidis* in human macrophages and in nasopharyngeal mucosa. *Infect. Immun.* **2005**, *73*, 3322−3329.

(1574) Kakishima, K.; Shiratsuchi, A.; Taoka, A.; Nakanishi, Y.; Fukumori, Y. Participation of nitric oxide reductase in survival of *Pseudomonas aeruginosa* in LPS-activated macrophages. *Biochem. Biophys. Res. Commun.* **2007**, *355*, 587−591.

(1575) De Vries, S.; Schröder, I. Comparison between the nitric oxide reductase family and its aerobic relatives, the cytochrome oxidases. *Biochem. Soc. Trans.* **2002**, *30*, 662−667.

(1576) Matsumoto, Y.; Tosha, T.; Pisliakov, A. V.; Hino, T.; Sugimoto, H.; Nagano, S.; Sugita, Y.; Shiro, Y. Crystal structure of quinol-dependent nitric oxide reductase from *Geobacillus stearothermophilus*. *Nat. Struct. Mol. Biol.* **2012**, *19*, 238.

(1577) Gonska, N.; Young, D.; Yuki, R.; Okamoto, T.; Hisano, T.; Antonyuk, S.; Hasnain, S. S.; Muramoto, K.; Shiro, Y.; Tosha, T.; et al. Characterization of the quinol-dependent nitric oxide reductase from the pathogen *Neisseria meningitidis* an electrogenic enzyme. *Sci. Rep.* **2018**, *8*, 1−13.

(1578) Tosha, T.; Shiro, Y. Crystal structures of nitric oxide reductases provide key insights into functional conversion of respiratory enzymes. *IUBMB Life* **2013**, *65*, 217−226.

(1579) Murali, R. *Studies on the cytochrome bd-type oxygen reductase superfamily and the discovery of a novel nitric oxide reductase*; University of Illinois at Urbana-Champaign, 2016.

(1580) Iwata, S.; Ostermeier, C.; Ludwig, B.; Michel, H. Structure at 2.8 resolution of cytochrome *c* oxidase from *Paracoccus denitrificans*. *Nature* **1995**, *376*, 660−669.

(1581) Tsukihara, T.; Aoyama, H.; Yamashita, E.; Tomizaki, T.; Yamaguchi, H.; Shinzawa-Itoh, K.; Nakashima, R.; Yaono, R.; Yoshikawa, S. Structures of metal sites of oxidized bovine heart cytochrome *c* oxidase at 2.8. *Science* **1995**, *269*, 1069−1074.

(1582) Pichinoty, F.; Mandel, M.; Garcia, J.-L. The properties of novel denitrifying *Bacillus* cultures found in tropical soils. *J. Gen. Microbiol.* **1979**, *115*, 419−430.

(1583) Moënne-Loccoz, P.; Richter, O.-M. H.; Huang, H.; Wasser, I. M.; Ghiladi, R. A.; Karlin, K. D.; de Vries, S. Nitric oxide reductase from *Paracoccus denitrificans* contains an oxo-bridged heme/non-heme diiron center. *J. Am. Chem. Soc.* **2000**, *122*, 9344−9345.

(1584) Wasser, I. M.; Martens, C. F.; Verani, C. N.; Rentschler, E.; Huang, H.-W.; Moënne-Loccoz, P.; Zakharov, L. N.; Rheingold, A. L.; Karlin, K. D. Synthesis and spectroscopy of n-oxo (O^{22})-bridged heme/non-heme diiron complexes: models for the active site of nitric oxide reductase. *Inorg. Chem.* **2004**, *43*, 651−662.

(1585) Ostermeier, C.; Harrenga, A.; Ermler, U.; Michel, H. Structure at 2.7 resolution of the *Paracoccus denitrificans* two-subunit cytochrome *c* oxidase complexed with an antibody FV fragment. *Proc. Natl. Acad. Sci. U. S. A.* **1997**, *94*, 10547−10553.

(1586) Tsukihara, T.; Aoyama, H.; Yamashita, E.; Tomizaki, T.; Yamaguchi, H.; Shinzawa-Itoh, K.; Nakashima, R.; Yaono, R.; Yoshikawa, S. The whole structure of the 13-subunit oxidized cytochrome *c* oxidase at 2.8. *Science* **1996**, *272*, 1136−1144.

(1587) Dermastia, M.; Turk, T.; Hollocher, T. C. Nitric oxide reductase. Purification from *Paracoccus denitrificans* with use of a single column and some characteristics. *J. Biol. Chem.* **1991**, *266*, 10899−10905.

(1588) Pinakoulaki, E.; Varotsis, C. Nitric oxide activation and reduction by heme-copper oxidoreductases and nitric oxide reductase. *J. Inorg. Biochem.* **2008**, *102*, 1277−1287.

(1589) Wasser, I. M.; Huang, H.; Moënne-Loccoz, P.; Karlin, K. D. Heme/non-heme diiron(II) complexes and O$_2$, CO, and NO adducts as reduced and substrate-bound models for the active site of bacterial nitric oxide reductase. *J. Am. Chem. Soc.* **2005**, *127*, 3310−3320.

(1590) Grönberg, K. L. C.; Watmough, N. J.; Thomson, A. J.; Richardson, D. J.; Field, S. J. Redox-dependent open and closed forms of the active site of the bacterial respiratory nitric-oxide reductase revealed by cyanide binding studies. *J. Biol. Chem.* **2004**, *279*, 17120−17125.

(1591) Sakurai, T.; Sakurai, N.; Matsumoto, H.; Hirota, S.; Yamauchi, O. Roles of four iron centers in *Paracoccus halodenitrificans* nitric oxide reductase. *Biochem. Biophys. Res. Commun.* **1998**, *251*, 248−251.

(1592) Hendriks, J.; Warne, A.; Gohlke, U.; Haltia, T.; Ludovici, C.; Lübben, M.; Saraste, M. The active site of the bacterial nitric oxide reductase is a dinuclear iron center. *Biochemistry* **1998**, *37*, 13102−13109.

(1593) Lu, S.; Suharti de Vries, S.; Moënne-Loccoz, P. Two CO molecules can bind concomitantly at the diiron site of NO reductase from *Bacillus azotoformans*. *J. Am. Chem. Soc.* **2004**, *126*, 15332−15333.

(1594) Cooper, C. E. Nitric oxide and iron proteins. *Biochim. Biophys. Acta, Bioenerg.* **1999**, *1411*, 290−309.

(1595) Watmough, N. J.; Cheesman, M. R.; Butler, C. S.; Little, R. H.; Greenwood, C.; Thomson, A. J. The dinuclear center of cytochrome *bo*$_3$ from *Escherichia coli*. *J. Bioenerg. Biomembr.* **1998**, *30*, 55−62.

(1596) Butler, C. S.; Seward, H. E.; Greenwood, C.; Thomson, A. J. *Fast* cytochrome *b*$_o$ from *Escherichia coli* binds two molecules of nitric oxide at Cu$_B$. *Biochemistry* **1997**, *36*, 16259−16266.

(1597) Girsch, P.; de Vries, S. Purification and initial kinetic and spectroscopic characterization of NO reductase from *Paracoccus denitrificans*. *Biochim. Biophys. Acta, Bioenerg.* **1997**, *1318*, 202−216.

(1598) Martens, C. F.; Murthy, N. N.; Obias, H. V.; Karlin, K. D. Oxo-bridged haem/non-haem iron complexes. *Chem. Commun.* **1996**, 629−630.

(1599) De Vries, S.; Strampraad, M. J. F.; Lu, S.; Moënne-Loccoz, P.; Schröder, I. Purification and characterization of the MQH$_2$: NO oxidoreductase from the hyperthermophilic archaeon *Pyrobaculum aerophilum*. *J. Biol. Chem.* **2003**, *278*, 35861−35868.

(1600) Sato, N.; Ishii, S.; Sugimoto, H.; Hino, T.; Fukumori, Y.; Sako, Y.; Shiro, Y.; Tosha, T. Structures of reduced and ligand-bound nitric oxide reductase provide insights into functional differences in respiratory enzymes. *Proteins: Struct., Funct., Genet.* **2014**, *82*, 1258−1271.

(1601) Xu, N.; Campbell, A. L. O.; Powell, D. R.; Khandogin, J.; Richter-Addo, G. B. A stable hyponitrite-bridged iron porphyrin complex. *J. Am. Chem. Soc.* **2009**, *131*, 2460−2461.

(1602) Berto, T. C.; Xu, N.; Lee, S. R.; McNeil, A. J.; Alp, E. E.; Zhao, J.; Richter-Addo, G. B.; Lehnert, N. Characterization of the bridged hyponitrite complex $\{[\mathrm{Fe(OEP)}]_2((\text{-}\mathrm{N_2O_2}))\}$: reactivity of hyponitrite complexes and biological relevance. *Inorg. Chem.* **2014**, *53*, 6398−6414.

(1603) Lin, R.; Farmer, P. J. O atom transfer from nitric oxide catalyzed by Fe(TPP). *J. Am. Chem. Soc.* **2001**, *123*, 1143−1150.

(1604) Blomberg, M. R. A.; Siegbahn, P. E. M. Improved free energy profile for reduction of NO in cytochrome *c* dependent nitric oxide reductase (*c*NOR). *J. Comput. Chem.* **2016**, *37*, 1810−1818.

(1605) Blomberg, M. R. A. The importance of exact exchange—a methodological investigation of NO reduction in heme-copper oxidases. *J. Chem. Phys.* **2021**, *154*, 055103.

(1606) Hendriks, J.; Jasaitis, A.; Saraste, M.; Verkhovsky, M. I. Proton and electron pathways in the bacterial nitric oxide reductase. *Biochemistry* **2002**, *41*, 2331−2340.

(1607) Hayashi, T.; Miner, K. D.; Yeung, N.; Lin, Y.-W.; Lu, Y.; Moënne-Loccoz, P. Spectroscopic characterization of mononitrosyl complexes in heme-nonheme diiron centers within the myoglobin scaffold (Fe$_B$Mbs): relevance to denitrifying NO reductase. *Biochemistry* **2011**, *50*, 5939−5947.

(1608) Arai, H.; Igarashi, Y.; Kodama, T. The structural genes for nitric oxide reductase from *Pseudomonas aeruginosa*. *Biochim. Biophys. Acta, Gene Struct. Expression* **1995**, *1261*, 279−284.

(1609) de Boer, A. P. N.; van der Oost, J.; Reijnders, W. N. M.; Westerhoff, H. V.; Stouthamer, A. H.; van Spanning, R. J. M. Mutational analysis of the nor gene cluster which encodes nitric-oxide reductase from *Paracoccus denitrificans*. *Eur. J. Biochem.* **1996**, *242*, 592−600.

(1610) Moënne-Loccoz, P.; de Vries, S. Structural characterization of the catalytic high-spin heme *b* of nitric oxide reductase: a resonance Raman study. *J. Am. Chem. Soc.* **1998**, *120*, 5147−5152.

(1611) Grönberg, K. L. C.; Roldán, M. D.; Prior, L.; Butland, G.; Cheesman, M. R.; Richardson, D. J.; Spiro, S.; Thomson, A. J.; Watmough, N. J. A low-redox potential heme in the dinuclear center of bacterial nitric oxide reductase: implications for the evolution of energy-conserving heme-copper oxidases. *Biochemistry* **1999**, *38*, 13780−13786.

(1612) Lyons, J. A.; Hilbers, F.; Caffrey, M. Structure and function of bacterial cytochrome *c* oxidases. *Cytochrome Complexes: Evolution, Structures, Energy Transduction, and Signaling*; Springer, 2016; Vol. *41*; pp 307−329.

(1613) Papa, S.; Capitanio, N.; Villani, G. A cooperative model for protonmotive heme-copper oxidases. The role of heme a in the proton pump of cytochrome c oxidase. *FEBS Lett.* **1998**, *439*, 1−8.

(1614) Bhagi-Damodaran, A.; Michael, M. A.; Zhu, Q.; Reed, J.; Sandoval, B. A.; Mirts, E. N.; Chakraborty, S.; Moënne-Loccoz, P.; Zhang, Y.; Lu, Y. Why copper is preferred over iron for oxygen activation and reduction in haem-copper oxidases. *Nat. Chem.* **2017**, *9*, 257−263.

(1615) Zumft, W. G. The biological role of nitric oxide in bacteria. *Arch. Microbiol.* **1993**, *160*, 253−264.

(1616) Zumft, W. G.; Braun, C.; Cuypers, H. Nitric oxide reductase from *Pseudomonas stutzeri*. *Eur. J. Biochem.* **1994**, *219*, 481−490.

(1617) Adam, S. M.; Wijeratne, G. B.; Rogler, P. J.; Diaz, D. E.; Quist, D. A.; Liu, J. J.; Karlin, K. D. Synthetic Fe/Cu complexes: toward understanding heme-copper oxidase structure and function. *Chem. Rev.* **2018**, *118*, 10840−11022.

(1618) Pereira, M. M.; Santana, M.; Teixeira, M. A novel scenario for the evolution of haem-copper oxygen reductases. *Biochim. Biophys. Acta, Bioenerg.* **2001**, *1505*, 185−208.

(1619) Yoshikawa, S.; Shinzawa-Itoh, K.; Nakashima, R.; Yaono, R.; Yamashita, E.; Inoue, N.; Yao, M.; Fei, M. J.; Libeu, C. P.; Mizushima, T. Redox-coupled crystal structural changes in bovine heart cytochrome *c* oxidase. *Science* **1998**, *280*, 1723−1729.

(1620) Hemp, J.; Robinson, D. E.; Ganesan, K. B.; Martinez, T. J.; Kelleher, N. L.; Gennis, R. B. Evolutionary migration of a post-translationally modified active-site residue in the proton-pumping heme-copper oxygen reductases. *Biochemistry* **2006**, *45*, 15405−15410.

(1621) Hunsicker-Wang, L. M.; Pacoma, R. L.; Chen, Y.; Fee, J. A.; Stout, C. D. A novel cryoprotection scheme for enhancing the diffraction of crystals of recombinant cytochrome *ba*$_3$ oxidase from *Thermus thermophilus*. *Acta Crystallogr., Sect. D: Biol. Crystallogr.* **2005**, *61*, 340−343.

(1622) Yoshikawa, S.; Shinzawa-Itoh, K.; Yamashita, E.; Tsukihara, T. Mitochondrial cytochrome *c* oxidase. *Handbook of Metalloproteins*; Messerschmidt, A., Huber, R., Poulos, T., Wieghardt, K., Eds.; Wiley: Chichester, England, 2001; Vol. *1*.

(1623) Muramoto, K.; Hirata, K.; Shinzawa-Itoh, K.; Yoko-O, S.; Yamashita, E.; Aoyama, H.; Tsukihara, T.; Yoshikawa, S. A histidine residue acting as a controlling site for dioxygen reduction and proton pumping by cytochrome *c* oxidase. *Proc. Natl. Acad. Sci. U. S. A.* **2007**, *104*, 7881−7886.

(1624) Liu, B.; Chen, Y.; Doukov, T.; Soltis, S. M.; Stout, C. D.; Fee, J. A. Combined microspectrophotometric and crystallographic examination of chemically reduced and x-ray radiation-reduced forms of cytochrome *ba*$_3$ oxidase from *Thermus thermophilus*: structure of the reduced form of the enzyme. *Biochemistry* **2009**, *48*, 820−826.

(1625) Qin, L.; Liu, J.; Mills, D.; Proshlyakov, D. A.; Hiser, C.; Ferguson-Miller, S. Redox dependent conformational changes in cytochrome *c* oxidase suggest a gating mechanism for proton uptake. *Biochemistry* **2009**, *48*, 5121−5130.

(1626) Shinzawa-Itoh, K.; Aoyama, H.; Muramoto, K.; Terada, H.; Kurauchi, T.; Tadehara, Y.; Yamasaki, A.; Sugimura, T.; Kurono, S.; Tsujimoto, K.; et al. Structures and physiological roles of 13 integral lipids of bovine heart cytochrome *c* oxidase. *EMBO J.* **2007**, *26*, 1713−1725.

(1627) Qin, L.; Hiser, C.; Mulichak, A.; Garavito, R. M.; Ferguson-Miller, S. Identification of conserved lipid/detergent-binding sites in a high-resolution structure of the membrane protein cytochrome *c* oxidase. *Proc. Natl. Acad. Sci. U. S. A.* **2006**, *103*, 16117−16122.

(1628) Koepke, J.; Olkhova, E.; Angerer, H.; Müller, H.; Peng, G.; Michel, H. High resolution crystal structure of *Paracoccus denitrificans* cytochrome *c* oxidase: New insights into the active site and the proton transfer pathways. *Biochim. Biophys. Acta, Bioenerg.* **2009**, *1787*, 635−645.

(1629) Aoyama, H.; Muramoto, K.; Shinzawa-Itoh, K.; Hirata, K.; Yamashita, E.; Tsukihara, T.; Ogura, T.; Yoshikawa, S. A peroxide bridge between Fe and Cu ions in the O$_2$ reduction site of fully oxidized cytochrome *c* oxidase could suppress the proton pump. *Proc. Natl. Acad. Sci. U. S. A.* **2009**, *106*, 2165−2169.

(1630) Brudvig, G. W.; Stevens, T. H.; Chan, S. I. Reactions of nitric oxide with cytochrome *c* oxidase. *Biochemistry* **1980**, *19*, 5275−5285.

(1631) Forte, E.; Urbani, A.; Saraste, M.; Sarti, P.; Brunori, M.; Giuffrè, A. The cytochrome *cbb*$_3$ from *Pseudomonas stutzeri* displays nitric oxide reductase activity. *Eur. J. Biochem.* **2001**, *268*, 6486−6490.

(1632) Giuffre, A.; Barone, M. C.; Brunori, M.; D'Itri, E.; Ludwig, B.; Malatesta, F.; Müller, H. W.; Sarti, P. Nitric oxide reacts with the single-electron reduced active site of cytochrome *c* oxidase. *J. Biol. Chem.* **2002**, *277*, 22402−22406.

(1633) Giuffrè, A.; Stubauer, G.; Sarti, P.; Brunori, M.; Zumft, W. G.; Buse, G.; Soulimane, T. The heme copper oxidases of *thermos theromophilus* catalyze the reduction of nitric oxide: Evolutionary implications. *Proc. Natl. Acad. Sci. U. S. A.* **1999**, *96*, 14718−14723.

(1634) Cooper, C. E.; Davies, N. A.; Psychoulis, M.; Canevari, L.; Bates, T. E.; Dobbie, M. S.; Casley, C. S.; Sharpe, M. A. Nitric oxide and peroxynitrite cause irreversible increases in the K_m for oxygen of mitochondrial cytochrome oxidase: in vitro and in vivo studies. *Biochim. Biophys. Acta, Bioenerg.* **2003**, *1607*, 27−34.

(1635) Mason, M. G.; Shepherd, M.; Nicholls, P.; Dobbin, P. S.; Dodsworth, K. S.; Poole, R. K.; Cooper, C. E. Cytochrome *bd* confers nitric oxide resistance to *Escherichia coli*. *Nat. Chem. Biol.* **2009**, *5*, 94−96.

(1636) Butler, C. S.; Forte, E.; Maria Scandurra, F.; Arese, M.; Giuffré, A.; Greenwood, C.; Sarti, P. Cytochrome *bo3* from Escherichia coli: the binding and turnover of nitric oxide. *Biochem. Biophys. Res. Commun.* **2002**, *296*, 1272−1278.

(1637) Kita, K. K. K. A. Y.; Konishi, K.; Anraku, Y. Terminal oxidases of *Escherichia coli* aerobic respiratory chain. I. Purification and properties of cytochrome b_{562}-*o* complex from cells in the early exponential phase of aerobic growth. *J. Biol. Chem.* **1984**, *259*, 3368−3374.

(1638) Huang, Y.; Reimann, J.; Lepp, H.; Drici, N.; Ädelroth, P. Vectorial proton transfer coupled to reduction of O_2 and NO by a heme-copper oxidase. *Proc. Natl. Acad. Sci. U. S. A.* **2008**, *105*, 20257−20262.

(1639) Fujiwara, T.; Fukumori, Y. Cytochrome *cb*-type nitric oxide reductase with cytochrome *c* oxidase activity from *Paracoccus denitrificans* ATCC 35512. *J. Bacteriol.* **1996**, *178*, 1866−1871.

(1640) Malatesta, F.; Antonini, G.; Sarti, P.; Brunori, M. Structure and function of a molecular machine: cytochrome *c* oxidase. *Biophys. Chem.* **1995**, *54*, 1−33.

(1641) Cheesman, M. R.; Watmough, N. J.; Gennis, R. B.; Greenwood, C.; Thomson, A. J. Magnetic-circular-dichroism studies of *Escherichia coli* cytochrome *bo*. *Eur. J. Biochem.* **1994**, *219*, 595−602.

(1642) Torres, J.; Darley-Usmar, V.; Wilson, M. T. Inhibition of cytochrome *c* oxidase in turnover by nitric oxide: mechanism and implications for control of respiration. *Biochem. J.* **1995**, *312*, 169−173.

(1643) Brown, G. C. Nitric oxide inhibition of cytochrome oxidase and mitochondrial respiration: implications for inflammatory, neurodegenerative and ischaemic pathologies. *Mol. Cell. Biochem.* **1997**, *174*, 189−192.

(1644) Loullis, A.; Pinakoulaki, E. Probing the nitrite and nitric oxide reductase activity of cbb_3 oxidase: resonance Raman detection of a six-coordinate ferrous heme-nitrosyl species in the binuclear b_3/Cu_B center. *Chem. Commun.* **2015**, *51*, 17398−17401.

(1645) Hayashi, T.; Lin, I.-J.; Chen, Y.; Fee, J. A.; Moënne-Loccoz, P. Fourier transform infrared characterization of a Cu_B-nitrosyl complex in cytochrome ba_3 from *Thermus thermophilus*: relevance to NO reductase activity in heme-copper terminal oxidases. *J. Am. Chem. Soc.* **2007**, *129*, 14952−14958.

(1646) Ohta, K.; Muramoto, K.; Shinzawa-Itoh, K.; Yamashita, E.; Yoshikawa, S.; Tsukihara, T. X-ray structure of the NO-bound Cu_B in bovine cytochrome *c* oxidase. *Acta Crystallogr., Sect. F: Struct. Biol. Cryst. Commun.* **2010**, *66*, 251−253.

(1647) Stevens, T. H.; Brudvig, G. W.; Bocian, D. F.; Chan, S. I. Structure of cytochrome a_3-Cu_{a3} couple in cytochrome *c* oxidase as revealed by nitric oxide binding studies. *Proc. Natl. Acad. Sci. U. S. A.* **1979**, *76*, 3320−3324.

(1648) Schneider, J. L.; Carrier, S. M.; Ruggiero, C. E.; Young, J. V. G.; Tolman, W. B. Influences of ligand environments on the spectroscopic properties and disproportionation reactivity of copper-nitrosyl complexes. *J. Am. Chem. Soc.* **1998**, *120*, 11408−11418.

(1649) Hayashi, T.; Lin, M. T.; Ganesan, K.; Chen, Y.; Fee, J. A.; Gennis, R. B.; Moënne-Loccoz, P. Accommodation of two diatomic molecules in cytochrome *bo*3: insights into NO reductase activity in terminal oxidases. *Biochemistry* **2009**, *48*, 883−890.

(1650) Varotsis, C.; Ohta, T.; Kitagawa, T.; Soulimane, T.; Pinakoulaki, E. The structure of the hyponitrite species in a heme Fe-Cu binuclear center. *Angew. Chem., Int. Ed.* **2007**, *46*, 2210−2214.

(1651) Ohta, T.; Kitagawa, T.; Varotsis, C. Characterization of a bimetallic-bridging intermediate in the reduction of NO to N_2O: a density functional theory study. *Inorg. Chem.* **2006**, *45*, 3187−3190.

(1652) Lehnert, N.; Cornelissen, U.; Neese, F.; Ono, T.; Noguchi, Y.; Okamoto, K.; Fujisawa, K. Synthesis and spectroscopic characterization of copper(II)-nitrito complexes with hydrotris(pyrazolyl)-borate and related coligands. *Inorg. Chem.* **2007**, *46*, 3916−3933.

(1653) Blomberg, M. R. A. Role of the two metals in the active sites of heme copper oxidases-a study of NO reduction in cbb_3 cytochrome *c* oxidase. *Inorg. Chem.* **2020**, *59*, 11542−11553.

(1654) Obias, H. V.; van Strijdonck, G. P. F.; Lee, D.-H.; Ralle, M.; Blackburn, N. J.; Karlin, K. D. Heterobinucleating ligand-induced structural and chemical variations in $[(L)Fe^{III}\text{-}O\text{-}Cu^{II}]^+$ -oxo complexes. *J. Am. Chem. Soc.* **1998**, *120*, 9696−9697.

(1655) Ghiladi, R. A.; Ju, T. D.; Lee, D.-H.; Moënne-Loccoz, P.; Kaderli, S.; Neuhold, Y.-M.; Zuberbühler, A. D.; Woods, A. S.; Cotter, R. J.; Karlin, K. D. Formation and characterization of a high-spin heme-copper dioxygen (peroxo) complex. *J. Am. Chem. Soc.* **1999**, *121*, 9885−9886.

(1656) Kopf, M.-A.; Karlin, K. D. Dioxygen reactivity of reduced heme and heme-copper complexes utilizing tetraarylporphyrinates tethered with both a pyridyl axial ligand and N,N-bis[2-(2-pyridyl)-ethyl]amine chelate. *Inorg. Chem.* **1999**, *38*, 4922−4923.

(1657) Kim, E.; Shearer, J.; Lu, S.; Moënne-Loccoz, P.; Helton, M. E.; Kaderli, S.; Zuberbuhler, A. D.; Karlin, K. D. Heme/Cu/O_2 reactivity: change in $Fe^{III}\text{-}(O_2^{22})\text{-}Cu^{II}$ unit peroxo binding geometry effected by tridentate copper chelation. *J. Am. Chem. Soc.* **2004**, *126*, 12716−12717.

(1658) Kim, E.; Helton, M. E.; Lu, S.; Moënne-Loccoz, P.; Incarvito, C. D.; Rheingold, A. L.; Kaderli, S.; Zuberbuhler, A. D.; Karlin, K. D. Tridentate copper ligand influences on heme-peroxo-copper formation and properties: reduced, superoxo, and n-peroxo iron/copper complexes. *Inorg. Chem.* **2005**, *44*, 7014−7029.

(1659) Ju, T. D.; Woods, A. S.; Cotter, R. J.; Moënne-Loccoz, P.; Karlin, K. D. Dioxygen and nitric oxide reactivity of a reduced heme/non-heme diiron(II) complex $[(^5L)Fe^{II}\text{—}Fe^{II}\text{-}Cl]^+$. Using a tethered tetraarylporphyrin for the development of an active site reactivity model for bacterial nitric oxide reductase. *Inorg. Chim. Acta* **2000**, *297*, 362−372.

(1660) Collman, J. P.; Fu, L.; Herrmann, P. C.; Wang, Z.; Rapta, M.; Bröring, M.; Schwenninger, R.; Boitrel, B. A functional model of cytochrome *c* oxidase: thermodynamic implications. *Angew. Chem., Int. Ed.* **1998**, *37*, 3397−3400.

(1661) Collman, J. P.; Rapta, M.; Bröring, M.; Raptova, L.; Schwenninger, R.; Boitrel, B.; Fu, L.; L'Her, M. Close structural analogues of the cytochrome *c* oxidase Fe_{a3}/Cu_B center show clean 4e c. *J. Am. Chem. Soc.* **1999**, *121*, 1387−1388.

(1662) Collman, J. P.; Boulatov, R.; Shiryaeva, I. M.; Sunderland, C. J. Distal Cu ion protects synthetic heme/Cu analogues of cytochrome oxidase against inhibition by CO and cyanide. *Angew. Chem., Int. Ed.* **2002**, *41*, 4139−4142.

(1663) Collman, J. P.; Sunderland, C. J.; Boulatov, R. Biomimetic studies of terminal oxidases: trisimidazole picket metalloporphyrins. *Inorg. Chem.* **2002**, *41*, 2282−2291.

(1664) Sasaki, T.; Nakamura, N.; Naruta, Y. Formation and spectroscopic characterization of the peroxo $Fe^{III}\text{-}Cu^{II}$ complex. A modeling reaction of the heme-Cu site in cytochrome *c* oxidase. *Chem. Lett.* **1998**, *27*, 351−352.

(1665) Chishiro, T.; Shimazaki, Y.; Tani, F.; Tachi, Y.; Naruta, Y.; Karasawa, S.; Hayami, S.; Maeda, Y. Isolation and crystal structure of a peroxo-bridged heme-copper complex. *Angew. Chem., Int. Ed.* **2003**, *42*, 2788−2791.

(1666) Liu, J.-G.; Naruta, Y.; Tani, F. A functional model of the cytochrome *c* oxidase active site: unique conversion of a heme--peroxo-Cu^{II} intermediate into heme-superoxo/Cu^I. *Angew. Chem., Int. Ed.* **2005**, *44*, 1836−1840.

(1667) Didier, A.; L'Her, M.; Boitrel, B. Substituted tren-capped porphyrins: probing the influence of copper in synthetic models of cytochrome *c* oxidase. *Org. Biomol. Chem.* **2003**, *1*, 1274−1276.

(1668) Amanullah, S.; Singha, A.; Dey, A. Tailor made iron porphyrins for investigating axial ligand and distal environment contributions to electronic structure and reactivity. *Coord. Chem. Rev.* **2019**, *386*, 183−208.

(1669) Collman, J. P.; Dey, A.; Decreau, R. A.; Yang, Y.; Hosseini, A.; Solomon, E. I.; Eberspacher, T. A. Interaction of nitric oxide with a functional model of cytochrome *c* oxidase. *Proc. Natl. Acad. Sci. U. S. A.* **2008**, *105*, 9892−9896.

(1670) Collman, J. P.; Dey, A.; Yang, Y.; Decreau, R. A.; Ohta, T.; Solomon, E. I. Intermediates involved in the two electron reduction of NO to N_2O by a functional synthetic model of heme containing bacterial NO reductase. *J. Am. Chem. Soc.* **2008**, *130*, 16498−16499.

(1671) Schopfer, M. P.; Wang, J.; Karlin, K. D. Bioinspired heme, heme/nonheme diiron, heme/copper, and inorganic NO_x chemistry: $\bullet NO_{(g)}$ oxidation, peroxynitrite-metal chemistry, and $\bullet NO_{(g)}$ reductive coupling. *Inorg. Chem.* **2010**, *49*, 6267−6282.

(1672) Dey, A.; Ghosh Dey, S. Model compounds for nitric oxide reductase. *Metalloenzymes in Denitrification*; Moura, I., Moura, J. J. G., Pauleta, S. R., Maia, L. B., Eds.; Royal Society of Chemistry, 2017; pp 185−224.

(1673) Collman, J. P.; Yang, Y.; Dey, A.; Decreau, R. A.; Ghosh, S.; Ohta, T.; Solomon, E. I. A functional nitric oxide reductase model. *Proc. Natl. Acad. Sci. U. S. A.* **2008**, *105*, 15660−15665.

(1674) Collman, J. P.; Boulatov, R.; Sunderland, C. J.; Fu, L. Functional analogues of cytochrome *c* oxidase, myoglobin, and hemoglobin. *Chem. Rev.* **2004**, *104*, 561−588.

(1675) Ghosh Dey, S.; Dey, A. NO and O_2 reactivities of synthetic functional models of nitric oxide reductase and cytochrome *c* oxidase. *Dalton Trans.* **2011**, *40*, 12633−12647.

(1676) Abucayon, E. G.; Khade, R. L.; Powell, D. R.; Zhang, Y.; Richter-Addo, G. B. Lewis acid activation of the ferrous heme-NO fragment toward the N-N coupling reaction with NO to generate N_2O. *J. Am. Chem. Soc.* **2018**, *140*, 4204−4207.

(1677) Abucayon, E. G.; Khade, R. L.; Powell, D. R.; Zhang, Y.; Richter-Addo, G. B. Not limited to iron: A cobalt heme-NO model facilitates N-N coupling with external NO in the presence of a Lewis acid to generate N_2O. *Angew. Chem., Int. Ed.* **2019**, *58*, 18598−18603.

(1678) Zhang, H.; Huang, L.; Chen, J.; Liu, L.; Zhu, X.; Wu, W.; Dong, S. Bionic design of cytochrome c oxidase-like single-atom nanozymes for oxygen reduction reaction in enzymatic biofuel cells. *Nano Energy* **2021**, *83*, 105798.

(1679) Le, J. M.; Bren, K. L. Engineered enzymes and bioinspired catalysts for energy conversion. *ACS Energy Lett.* **2019**, *4*, 2168−2180.

(1680) Zhang, W.; Lai, W.; Cao, R. Energy-related small molecule activation reactions: oxygen reduction and hydrogen and oxygen evolution reactions catalyzed by porphyrin- and corrole-based systems. *Chem. Rev.* **2017**, *117*, 3717−3797.

(1681) Yu, Y.; Cui, C.; Liu, X.; Petrik, I. D.; Wang, J.; Lu, Y. A designed metalloenzyme achieving the catalytic rate of a native enzyme. *J. Am. Chem. Soc.* **2015**, *137*, 11570−11573.

(1682) Mukherjee, S.; Bhagi, A.; Mukherjee, A.; Mukherjee, M.; Lu, Y.; Dey, A. A biosynthetic model of cytochrome *c* oxidase as an electrocatalyst for oxygen reduction. *Nat. Commun.* **2015**, *6*, 8467.

(1683) Collman, J. P.; Devaraj, N. K.; Decréau, R. A.; Yang, Y.; Yan, Y.-L.; Ebina, W.; Eberspacher, T. A.; Chidsey, C. E. D. A cytochrome *c* oxidase model catalyzes oxygen to water reduction under rate-limiting electron flux. *Science* **2007**, *315*, 1565−1568.

(1684) Hematian, S.; Siegler, M. A.; Karlin, K. D. Heme/copper assembly mediated nitrite and nitric oxide interconversion. *J. Am. Chem. Soc.* **2012**, *134*, 18912−18915.

(1685) Hematian, S.; Kenkel, I.; Shubina, T. E.; Dürr, M.; Liu, J. J.; Siegler, M. A.; Ivanovic-Burmazovic, I.; Karlin, K. D. Nitrogen oxide atom-transfer redox chemistry; mechanism of NO(g) to nitrite conversion utilizing μ-oxo heme-Fe^{III}-O-Cu^{II} constructs. *J. Am. Chem. Soc.* **2015**, *137*, 6602−6615.

(1686) Mason, M. G.; Nicholls, P.; Wilson, M. T.; Cooper, C. E. Nitric oxide inhibition of respiration involves both competitive (heme) and noncompetitive (copper) binding to cytochrome *c* oxidase. *Proc. Natl. Acad. Sci. U. S. A.* **2006**, *103*, 708−713.

(1687) Antunes, F.; Boveris, A.; Cadenas, E. On the biologic role of the reaction of NO withoxidized cytochrome *c* oxidase. *Antioxid. Redox Signaling* **2007**, *9*, 1569−1579.

(1688) Cooper, C. E.; Mason, M. G.; Nicholls, P. A dynamic model of nitric oxide inhibition of mitochondrial cytochrome *c* oxidase. *Biochim. Biophys. Acta, Bioenerg.* **2008**, *1777*, 867−876.

(1689) Collman, J. P.; Ghosh, S. Recent applications of a synthetic model of cytochrome *c* oxidase: beyond functional modeling. *Inorg. Chem.* **2010**, *49*, 5798−5810.

(1690) Reed, C. J.; Lam, Q. N.; Mirts, E. N.; Lu, Y. Molecular understanding of heteronuclear active sites in heme-copper oxidases, nitric oxide reductases, and sulfite reductases through biomimetic modelling. *Chem. Soc. Rev.* **2021**, *50*, 2486−2539.

(1691) Yeung, N.; Lin, Y. W.; Gao, Y. G.; Zhao, X.; Russell, B. S.; Lei, L.; Miner, K. D.; Robinson, H.; Lu, Y. Rational design of a structural and functional nitric oxide reductase. *Nature* **2009**, *462*, 1079−1082.

(1692) Chakraborty, S.; Reed, J.; Ross, M.; Nilges, M. J.; Petrik, I. D.; Ghosh, S.; Hammes-Schiffer, S.; Sage, J. T.; Zhang, Y.; Schulz, C. E.; et al. Spectroscopic and computational study of a nonheme iron nitrosyl center in a biosynthetic model of nitric oxide reductase. *Angew. Chem.* **2014**, *126*, 2449−2453.

(1693) Matsumura, H.; Hayashi, T.; Chakraborty, S.; Lu, Y.; Moënne-Loccoz, P. The production of nitrous oxide by the heme/nonheme diiron center of engineered myoglobins (Fe_BMbs) proceeds through a *trans*-iron-nitrosyl dimer. *J. Am. Chem. Soc.* **2014**, *136*, 2420−2431.

(1694) Lin, Y.-W.; Yeung, N.; Gao, Y.-G.; Miner, K. D.; Tian, S.; Robinson, H.; Lu, Y. Roles of glutamates and metal ions in a rationally designed nitric oxide reductase based on myoglobin. *Proc. Natl. Acad. Sci. U. S. A.* **2010**, *107*, 8581−8586.

(1695) Bhagi-Damodaran, A.; Reed, J. H.; Zhu, Q.; Shi, Y.; Hosseinzadeh, P.; Sandoval, B. A.; Harnden, K. A.; Wang, S.; Sponholtz, M. R.; Mirts, E. N.; et al. Heme redox potentials hold the key to reactivity differences between nitric oxide reductase and heme-copper oxidase. *Proc. Natl. Acad. Sci. U. S. A.* **2018**, *115*, 6195−6200.

(1696) Sabuncu, S.; Reed, J. H.; Lu, Y.; Moënne-Loccoz, P. Nitric oxide reductase activity in heme-nonheme binuclear engineered myoglobins through a one-electron reduction cycle. *J. Am. Chem. Soc.* **2018**, *140*, 17389−17393.

(1697) Bhagi-Damodaran, A.; Kahle, M.; Shi, Y.; Zhang, Y.; Ädelroth, P.; Lu, Y. Insights into how heme reduction potentials modulate enzymatic activities of a myoglobin-based functional oxidase. *Angew. Chem., Int. Ed.* **2017**, *56*, 6622−6626.

(1698) Zhao, X.; Yeung, N.; Russell, B. S.; Garner, D. K.; Lu, Y. Catalytic reduction of NO to N_2O by a designed heme copper center in myoglobin: implications for the role of metal ions. *J. Am. Chem. Soc.* **2006**, *128*, 6766−6767.

(1699) Xu, N.; Abucayon, E. G.; Powell, D. R.; Richter-Addo, G. B. A bridged di-iron porphyrin hyponitrite complex as a model for biological N_2O production from hyponitrite. *Nitric Oxide* **2016**, *52*, 16−20.

(1700) Cole, J. A. The rapid accumulation of large quantities of ammonia during nitrite reduction by *Escherichia coli*. *FEMS Microbiol. Lett.* **1978**, *4*, 327−329.

(1701) Cole, J. A.; Brown, C. M. Nitrite reduction to ammonia by fermentative bacteria: a short circuit in the biological nitrogen cycle. *FEMS Microbiol. Lett.* **1980**, *7*, 65−72.

(1702) Sørensen, J. Capacity for denitrification and reduction of nitrate to ammonia in a coastal marine sediment. *Appl. Environ. Microbiol.* **1978**, *35*, 301−305.

(1703) Darwin, A.; Hussain, H.; Griffiths, L.; Grove, J.; Sambongi, Y.; Busby, S.; Cole, J. Regulation and sequence of the structural gene for cytochrome c_{552} from *Escherichia coli*: not a hexahaem but a 50kDa tetrahaem nitrite reductase. *Mol. Microbiol.* **1993**, *9*, 1255−1265.

(1704) Bamford, V. A.; Angove, H. C.; Seward, H. E.; Thomson, A. J.; Cole, J. A.; Butt, J. N.; Hemmings, A. M.; Richardson, D. J. Structure and spectroscopy of the periplasmic cytochrome *c* nitrite reductase from *Escherichia coli*. *Biochemistry* **2002**, *41*, 2921−2931.

(1705) Youngblut, M.; Judd, E. T.; Srajer, V.; Sayyed, B.; Goelzer, T.; Elliott, S. J.; Schmidt, M.; Pacheco, A. A. Laue crystal structure of *Shewanella oneidensis* cytochrome *c* nitrite reductase from a high-yield expression system. *JBIC, J. Biol. Inorg. Chem.* **2012**, *17*, 647−662.

(1706) Cunha, C. A.; Macieira, S.; Dias, J. M.; Almeida, G.; Gonçalves, L. L.; Costa, C.; Lampreia, J.; Huber, R.; Moura, J. J. G.; Moura, I.; et al. Cytochrome *c* nitrite reductase from *Desulfovibrio desulfuricans* ATCC 27774: The relevance of the two calcium sites in the structure of the catalytic subunit (NrfA). *J. Biol. Chem.* **2003**, *278*, 17455−17465.

(1707) Rodrigues, M. L.; Oliveira, T. F.; Pereira, I. A. C.; Archer, M. X-ray structure of the membrane-bound cytochrome *c* quinol dehydrogenase NrfH reveals novel haem coordination. *EMBO J.* **2006**, *25*, 5951−5960.

(1708) Reguera, G.; Kashefi, K. The electrifying physiology of *Geobacter* bacteria, 30 years on. *Adv. Microb. Physiol.* **2019**, *74*, 1−96.

(1709) Einsle, O.; Messerschmidt, A.; Stach, P.; Bourenkov, G. P.; Bartunik, H. D.; Huber, R.; Kroneck, P. M. H. Structure of cytochrome *c* nitrite reductase. *Nature* **1999**, *400*, 476−480.

(1710) Polyakov, K. M.; Boyko, K. M.; Tikhonova, T. V.; Slutsky, A.; Antipov, A. N.; Zvyagilskaya, R. A.; Popov, A. N.; Bourenkov, G. P.; Lamzin, V. S.; Popov, V. O. High-resolution structural analysis of a novel octaheme cytochrome *c* nitrite reductase from the haloalkaliphilic bacterium *Thioalkalivibrio nitratireducens*. *J. Mol. Biol.* **2009**, *389*, 846−862.

(1711) Schumacher, W.; Hole, U.; Kroneck, M. H. Ammonia-forming cytochrome *c* nitrite reductase from *Sulfurospirillum deleyianum* is a tetraheme protein: new aspects of the molecular composition and spectroscopic properties. *Biochem. Biophys. Res. Commun.* **1994**, *205*, 911−916.

(1712) Sosa Alfaro, V.; Campeciño, J.; Tracy, M.; Elliott, S. J.; Hegg, E. L.; Lehnert, N. Elucidating electron storage and distribution within the pentaheme scaffold of cytochrome *c* nitrite reductase (NrfA). *Biochemistry* **2021**, *60*, 1853−1867.

(1713) Einsle, O.; Stach, P.; Messerschmidt, A.; Klimmek, O.; Simon, J.; Kröger, A.; Kroneck, P. M. H. Crystallization and preliminary x-ray analysis of the membrane-bound cytochrome *c* nitrite reductase complex (NrfHA) from *Wolinella succinogenes*. *Acta Crystallogr., Sect. D: Biol. Crystallogr.* **2002**, *58*, 341−342.

(1714) Campeciño, J.; Lagishetty, S.; Wawrzak, Z.; Sosa Alfaro, V.; Lehnert, N.; Reguera, G.; Hu, J.; Hegg, E. Cytochrome *c* nitrite reductase from *Geobacter lovleyi* represents a new NrfA subclass. *J. Biol. Chem.* **2020**, *295*, 11455−11465.

(1715) Welsh, A.; Chee-Sanford, J. C.; Connor, L. M.; Löffler, F. E.; Sanford, R. A. Refined NrfA phylogeny improves PCR-based nrfA gene detection. *Appl. Environ. Microbiol.* **2014**, *80*, 2110−2119.

(1716) Stein, N.; Love, D.; Judd, E. T.; Elliott, S. J.; Bennett, B.; Pacheco, A. A. Correlations between the electronic properties of *Shewanella oneidensis* cytochrome *c* nitrite reductase (ccNiR) and its structure: effects of heme oxidation state and active site ligation. *Biochemistry* **2015**, *54*, 3749−3758.

(1717) Simon, J.; Gross, R.; Einsle, O.; Kroneck, P. M. H.; Kröger, A.; Klimmek, O. A NapC/NirT-type cytochrome *c* (NrfH) is the mediator between the quinone pool and the cytochrome *c* nitrite reductase of *Wolinella succinogenes*. *Mol. Microbiol.* **2000**, *35*, 686−696.

(1718) Simon, J.; Pisa, R.; Stein, T.; Eichler, R.; Klimmek, O.; Gross, R. The tetraheme cytochrome *c* NrfH is required to anchor the cytochrome *c* nitrite reductase (NrfA) in the membrane of *Wolinella succinogenes*. *Eur. J. Biochem.* **2001**, *268*, 5776−5782.

(1719) Simon, J. Enzymology and bioenergetics of respiratory nitrite ammonification. *FEMS Microbiol. Rev.* **2002**, *26*, 285−309.

(1720) Bykov, D.; Neese, F. Substrate binding and activation in the active site of cytochrome *c* nitrite reductase: a density functional study. *JBIC, J. Biol. Inorg. Chem.* **2011**, *16*, 417−430.

(1721) Youngblut, M.; Pauly, D. J.; Stein, N.; Walters, D.; Conrad, J. A.; Moran, G. R.; Bennett, B.; Pacheco, A. A. *Shewanella oneidensis* cytochrome *c* nitrite reductase (*cc*NiR) does not disproportionate hydroxylamine to ammonia and nitrite, despite a strongly favorable driving force. *Biochemistry* **2014**, *53*, 2136−2144.

(1722) Clarke, T. A.; Hemmings, A. M.; Burlat, B.; Butt, J. N.; Cole, J. A.; Richardson, D. J. Comparison of the structural and kinetic properties of the cytochrome *c* nitrite reductases from *Escherichia coli Wolinella succinogenes Sulfurospirillum deleyianum* and *Desulfovibrio desulfuricans*. *Biochem. Soc. Trans.* **2006**, *34*, 143−145.

(1723) Moreno, C.; Costa, C.; Moura, I.; Le Gall, J.; Liu, M. Y.; Payne, W. J.; van Dijk, C.; Moura, J. J. G. Electrochemical studies of the hexaheme nitrite reductase from *Desulfovibrio desulfuricans* ATCC 27774. *Eur. J. Biochem.* **1993**, *212*, 79−86.

(1724) Bykov, D.; Neese, F. Reductive activation of the heme iron-nitrosyl intermediate in the reaction mechanism of cytochrome *c* nitrite reductase: a theoretical study. *JBIC, J. Biol. Inorg. Chem.* **2012**, *17*, 741−760.

(1725) Rudolf, M.; Einsle, O.; Neese, F.; Kroneck, P. M. H. Pentahaem cytochrome *c* nitrite reductase: reaction with hydroxylamine, a potential reaction intermediate and substrate. *Biochem. Soc. Trans.* **2002**, *30*, 649−652.

(1726) Bewley, K. D.; Ellis, K. E.; Firer-Sherwood, M. A.; Elliott, S. J. Multi-heme proteins: Nature's electronic multi-purpose tool. *Biochim. Biophys. Acta, Bioenerg.* **2013**, *1827*, 938−948.

(1727) Blackmore, R. S.; Brittain, T.; Gadsby, P. M. A.; Greenwood, C.; Thomson, A. J. Electron paramagnetic resonance and magnetic circular dichroism studies of a hexa-heme nitrite reductase from *Wolinella succinogenes*. *FEBS Lett.* **1987**, *219*, 244−248.

(1728) Blackmore, R. S.; Gadsby, P. M. A.; Greenwood, C.; Thomson, A. J. Spectroscopic studies of partially reduced forms of *Wolinella succinogenes* nitrite reductase. *FEBS Lett.* **1990**, *264*, 257−262.

(1729) Pereira, I. A. C.; LeGall, J.; Xavier, A. V.; Teixeira, M. Characterization of a heme *c* nitrite reductase from a non-ammonifying microorganism, *Desulfovibrio vulgaris* Hildenborough. *Biochim. Biophys. Acta, Protein Struct. Mol. Enzymol.* **2000**, *1481*, 119−130.

(1730) Thomson, A. J.; Cheesman, M. R.; George, S. J. Variable-temperature magnetic circular dichroism. *Methods Enzymol.* **1993**, *226*, 199−232.

(1731) Burlat, B.; Gwyer, J. D.; Poock, S.; Clarke, T.; Cole, J. A.; Hemmings, A. M.; Cheesman, M. R.; Butt, J. N.; Richardson, D. J. Cytochrome *c* nitrite reductase: from structural to physicochemical analysis. *Biochem. Soc. Trans.* **2005**, *33*, 137−140.

(1732) Zoppellaro, G.; Bren, K. L.; Ensign, A. A.; Harbitz, E.; Kaur, R.; Hersleth, H. P.; Ryde, U.; Hederstedt, L.; Andersson, K. K. Studies of ferric heme proteins with highly anisotropic/highly axial low spin ($S= 1/2$) electron paramagnetic resonance signals with bis-Histidine and histidine-methionine axial iron coordination. *Biopolymers* **2009**, *91*, 1064−1082.

(1733) Costa, C.; Moura, J. J.; Moura, I.; Liu, M. Y.; Peck, H. D., Jr.; LeGall, J.; Wang, Y. N.; Huynh, B. H. Hexaheme nitrite reductase from *Desulfovibrio desulfuricans*. Mössbauer and EPR characterization of the heme groups. *J. Biol. Chem.* **1990**, *265*, 14382−14388.

(1734) Judd, E. T.; Youngblut, M.; Pacheco, A. A.; Elliott, S. J. Direct electrochemistry of *Shewanella oneidensis* cytochrome *c* nitrite reductase: evidence of interactions across the dimeric interface. *Biochemistry* **2012**, *51*, 10175−10185.

(1735) Judd, E. T.; Stein, N.; Pacheco, A. A.; Elliott, S. J. Hydrogen bonding networks tune proton-coupled redox steps during the enzymatic six-electron conversion of nitrite to ammonia. *Biochemistry* **2014**, *53*, 5638−5646.

(1736) Van De Graaf, A. A.; De Bruijn, P.; Robertson, L. A.; Jetten, M. S. M.; Kuenen, J. G. Metabolic pathway of anaerobic ammonium oxidation on the basis of ^{15}N studies in a fluidized bed reactor. *Microbiology* **1997**, *143*, 2415−2421.

(1737) Strous, M.; Pelletier, E.; Mangenot, S.; Rattei, T.; Lehner, A.; Taylor, M. W.; Horn, M.; Daims, H.; Bartol-Mavel, D.; Wincker, P.;

et al. Deciphering the evolution and metabolism of an anammox bacterium from a community genome. *Nature* **2006**, *440*, 790−794.

(1738) Frank, J.; Lücker, S.; Vossen, R. H. A. M.; Jetten, M. S. M.; Hall, R. J.; Op den Camp, H. J. M.; Anvar, S. Y. Resolving the complete genome of *Kuenenia stuttgartiensis* from a membrane bioreactor enrichment using single-molecule real-time sequencing. *Sci. Rep.* **2018**, *8*, 1−10.

(1739) Auld, D. S. Zinc coordination sphere in biochemical zinc sites. *BioMetals* **2001**, *14*, 271−313.

(1740) Kartal, B.; de Almeida, N. M.; Maalcke, W. J.; Op den Camp, H. J. M.; Jetten, M. S. M.; Keltjens, J. T. How to make a living from anaerobic ammonium oxidation. *FEMS Microbiol. Rev.* **2013**, *37*, 428−461.

(1741) Van Der Star, W. R. L.; Dijkema, C.; de Waard, P.; Picioreanu, C.; Strous, M.; van Loosdrecht, M. C. M. An intracellular pH gradient in the anammox bacterium *Kuenenia stuttgartiensis* as evaluated by ^{31}P NMR. *Appl. Microbiol. Biotechnol.* **2010**, *86*, 311−317.

(1742) Andersson, K. K.; Lipscomb, J. D.; Valentine, M.; Münck, E.; Hooper, A. B. Tetraheme cytochrome c-554 from *Nitrosomonas europaea*. Heme-heme interactions and ligand binding. *J. Biol. Chem.* **1986**, *261*, 1126−1138.

(1743) Yamanaka, T.; Shinra, M. Cytochrome c-552 and cytochrome c-554 derived from *Nitrosomonas europaea*. Purification, properties, and their function in hydroxylamine oxidation. *J. Biochem.* **1974**, *75*, 1265−1273.

(1744) Hendrich, M. P.; Logan, M.; Andersson, K. K.; Arciero, D. M.; Lipscomb, J. D.; Hooper, A. B. The active site of hydroxylamine oxidoreductase from *Nitrosomonas*: evidence for a new metal cluster in enzymes. *J. Am. Chem. Soc.* **1994**, *116*, 11961−11968.

(1745) Donzelli, S.; Espey, M. G.; Flores-Santana, W.; Switzer, C. H.; Yeh, G. C.; Huang, J.; Stuehr, D. J.; King, S. B.; Miranda, K. M.; Wink, D. A. Generation of nitroxyl by heme protein-mediated peroxidation of hydroxylamine but not N-hydroxy-L-arginine. *Free Radical Biol. Med.* **2008**, *45*, 578−584.

(1746) Álvarez, L.; Suárez, S. A.; González, P. J.; Brondino, C. D.; Doctorovich, F.; Martí, M. A. The underlying mechanism of HNO production by the myoglobin-mediated oxidation of hydroxylamine. *Inorg. Chem.* **2020**, *59*, 7939−7952.

(1747) Maalcke, W. J.; Dietl, A.; Marritt, S. J.; Butt, J. N.; Jetten, M. S. M.; Keltjens, J. T.; Barends, T. R. M.; Kartal, B. Structural basis of biological NO generation by octaheme oxidoreductases. *J. Biol. Chem.* **2014**, *289*, 1228−1242.

(1748) Collins, M. J.; Arciero, D. M.; Hooper, A. B. Optical spectropotentiometric resolution of the hemes of hydroxylamine oxidoreductase. Heme quantitation and pH dependence of E$_{\text{m}}$. *J. Biol. Chem.* **1993**, *268*, 14655−14662.

(1749) Kurnikov, I. V.; Ratner, M. A.; Pacheco, A. A. Redox equilibria in hydroxylamine oxidoreductase. Electrostatic control of electron redistribution in multielectron oxidative processes. *Biochemistry* **2005**, *44*, 1856−1863.

(1750) Elmore, B. O.; Bergmann, D. J.; Klotz, M. G.; Hooper, A. B. Cytochromes P460 and c′-beta; a new family of high-spin cytochromes *c*. *FEBS Lett.* **2007**, *581*, 911−916.

(1751) Andersson, K. K.; Babcock, G. T.; Hooper, A. B. P460 of hydroxylamine oxidoreductase of *Nitrosomonas europaea*: Soret resonance Raman evidence for a novel heme-like structure. *Biochem. Biophys. Res. Commun.* **1991**, *174*, 358−363.

(1752) Andersson, K. K.; Kent, T. A.; Lipscomb, J. D.; Hooper, A. B.; Münck, E. Mössbauer, EPR, and optical studies of the P-460 center of hydroxylamine oxidoreductase from *Nitrosomonas*. A ferrous heme with an unusually large quadrupole splitting. *J. Biol. Chem.* **1984**, *259*, 6833−6840.

(1753) Hendrich, M. P.; Petasis, D.; Arciero, D. M.; Hooper, A. B. Correlations of structure and electronic properties from EPR spectroscopy of hydroxylamine oxidoreductase. *J. Am. Chem. Soc.* **2001**, *123*, 2997−3005.

(1754) Hendrich, M. P.; Upadhyay, A. K.; Riga, J.; Arciero, D. M.; Hooper, A. B. Spectroscopic characterization of the NO adduct of hydroxylamine oxidoreductase. *Biochemistry* **2002**, *41*, 4603−4611.

(1755) Hooper, A. B.; Nason, A. Characterization of hydroxylamine-cytochrome *c* reductase from the chemoautotrophs *Nitrosomonas europaea* and *Nitrosocystis oceanus*. *J. Biol. Chem.* **1965**, *240*, 4044−4057.

(1756) Versantvoort, W.; Pol, A.; Jetten, M. S. M.; van Niftrik, L.; Reimann, J.; Kartal, B.; Op den Camp, H. J. M. Multiheme hydroxylamine oxidoreductases produce NO during ammonia oxidation in methanotrophs. *Proc. Natl. Acad. Sci. U. S. A.* **2020**, *117*, 24459−24463.

(1757) Fernández, M. L.; Estrin, D. A.; Bari, S. E. Theoretical insight into the hydroxylamine oxidoreductase mechanism. *J. Inorg. Biochem.* **2008**, *102*, 1523−1530.

(1758) Arciero, D. M.; Balny, C.; Hooper, A. B. Spectroscopic and rapid kinetic studies of reduction of cytochrome c_{554} by hydroxylamine oxidoreductase from *Nitrosomonas europaea*. *Biochemistry* **1991**, *30*, 11466−11472.

(1759) Smith, M. A.; Majer, S. H.; Vilbert, A. C.; Lancaster, K. M. Controlling a burn: outer-sphere gating of hydroxylamine oxidation by a distal base in cytochrome P460. *Chem. Sci.* **2019**, *10*, 3756−3764.

(1760) Bergmann, D. J.; Zahn, J. A.; Hooper, A. B.; DiSpirito, A. A. Cytochrome P460 genes from the methanotroph *Methylococcus capsulatus* Bath. *J. Bacteriol.* **1998**, *180*, 6440−6445.

(1761) Numata, M.; Saito, T.; Yamazaki, T.; Fukumori, Y.; Yamanaka, T. Cytochrome P-460 of *Nitrosomonas europaea*: further purification and further characterization. *J. Biochem.* **1990**, *108*, 1016−1021.

(1762) Zahn, J. A.; Duncan, C.; DiSpirito, A. A. Oxidation of hydroxylamine by cytochrome P-460 of the obligate methylotroph *Methylococcus capsulatus* Bath. *J. Bacteriol.* **1994**, *176*, 5879−5887.

(1763) Pearson, A. R.; Elmore, B. O.; Yang, C.; Ferrara, J. D.; Hooper, A. B.; Wilmot, C. M. The crystal structure of cytochrome P460 of *Nitrosomonas europaea* reveals a novel cytochrome fold and heme-protein cross-link. *Biochemistry* **2007**, *46*, 8340−8349.

(1764) Caranto, J. D.; Vilbert, A. C.; Lancaster, K. M. *Nitrosomonas europaea* cytochrome P460 is a direct link between nitrification and nitrous oxide emission. *Proc. Natl. Acad. Sci. U. S. A.* **2016**, *113*, 14704−14709.

(1765) Hayashi, T.; Caranto, J. D.; Wampler, D. A.; Kurtz, D. M., Jr.; Moënne-Loccoz, P. Insights into the nitric oxide reductase mechanism of flavodiiron proteins from a flavin-free enzyme. *Biochemistry* **2010**, *49*, 7040−7049.

(1766) Lewandowska, H. Coordination chemistry of nitrosyls and its biochemical implications. *Nitrosyl Complexes in Inorganic Chemistry, Biochemistry and Medicine I*; Mingos, D. M. P., Ed.; Springer: Berlin Heidelberg, 2014; pp 45−114.

(1767) Hauser, A. Ligand field theoretical considerations. *Top. Curr. Chem.* **2004**, *233*, 49−58.

(1768) Haller, K. J.; Johnson, P. L.; Feltham, R. D.; Enemark, J. H.; Ferraro, J. R.; Basile, L. J. Effects of temperature and pressure on the molecular and electronic structure of N,N′-ethylenebis-(salicylideneiminato)nitrosyliron, Fe(NO)(salen). *Inorg. Chim. Acta* **1979**, *33*, 119−130.

(1769) Dey, A.; Confer, A. M.; Vilbert, A. C.; Moënne-Loccoz, P.; Lancaster, K. M.; Goldberg, D. P. A nonheme sulfur-ligated {FeNO}^{6} complex and comparison with redox-interconvertible {FeNO}^{7} and {FeNO}^{8} analogues. *Angew. Chem., Int. Ed.* **2018**, *57*, 13465−13469.

(1770) Piñeiro-López, L.; Ortega-Villar, N.; Muñoz, M. C.; Molnár, G.; Cirera, J.; Moreno-Esparza, R.; Ugalde-Saldívar, V. M.; Bousseksou, A.; Ruiz, E.; Real, J. A. Electronic structure modulation in an exceptionally stable non-heme nitrosyl iron(II) spin-crossover complex. *Chem. - Eur. J.* **2016**, *22*, 12741−12751.

(1771) Chiou, Y.-M.; Que, J. L. Model studies of -keto acid-dependent nonheme iron enzymes: nitric oxide adducts of [Fe$^{\text{II}}$(L)-(O$_2$CCOPh)](ClO$_4$) complexes. *Inorg. Chem.* **1995**, *34*, 3270−3278.

(1772) Dong, H. T.; Speelman, A. L.; Kozemchak, C. E.; Sil, D.; Krebs, C.; Lehnert, N. The Fe$_2$(NO)$_2$ diamond core: a unique structural motif in non-heme iron−NO chemistry. *Angew. Chem. Int. Ed.* **2019**, *58*, 17695−17699.

(1773) Pohl, K.; Wieghardt, K.; Nuber, B.; Weiss, J. Preparation and magnetism of the binuclear iron(II) complexes $[\{Fe(C_9H_{21}N_3)X_2\}_2]$ (X = NCS, NCO, or N_3) and their reaction with NO. Crystal structures of $[\{Fe(C_9H_{21}N_3)(NCS)_2\}_2]$ and $[Fe(C_9H_{21}N_3)(NO)(N_3)_2]$. *J. Chem. Soc., Dalton Trans.* **1987**, 187−192.

(1774) Schenk, G.; Pau, M. Y. M.; Solomon, E. I. Comparison between the geometric and electronic structures and reactivities of $\{FeNO\}^7$ and $\{FeO_2\}^8$ complexes: A density functional theory study. *J. Am. Chem. Soc.* **2004**, *126*, 505−515.

(1775) Speelman, A. L.; Lehnert, N. Characterization of a high-spin non-heme $\{FeNO\}^8$ complex: implications for the reactivity of iron nitroxyl species in biology. *Angew. Chem., Int. Ed.* **2013**, *52*, 12283−12287.

(1776) McQuilken, A. C.; Ha, Y.; Sutherlin, K. D.; Siegler, M. A.; Hodgson, K. O.; Hedman, B.; Solomon, E. I.; Jameson, G. N. L.; Goldberg, D. P. Preparation of non-heme $\{FeNO\}^7$ models of cysteine dioxygenase: sulfur versus nitrogen ligation and photorelease of nitric oxide. *J. Am. Chem. Soc.* **2013**, *135*, 14024−14027.

(1777) McQuilken, A. C.; Matsumura, H.; Dürr, M.; Confer, A. M.; Sheckelton, J. P.; Siegler, M. A.; McQueen, T. M.; Ivanović-Burmazović, I.; Moënne-Loccoz, P.; Goldberg, D. P. Photoinitiated reactivity of a thiolate-ligated, spin-crossover nonheme $\{FeNO\}^7$ complex with dioxygen. *J. Am. Chem. Soc.* **2016**, *138*, 3107−3117.

(1778) Confer, A. M.; Sabuncu, S.; Siegler, M. A.; Moënne-Loccoz, P.; Goldberg, D. P. Mononuclear, nonheme, high-spin $\{FeNO\}^{7/8}$ complexes supported by a sterically encumbered N_4S-thioether ligand. *Inorg. Chem.* **2019**, *58*, 9576−9580.

(1779) Ray, M.; Golombek, A. P.; Hendrich, M. P.; Yap, G. P. A.; Liable-Sands, L. M.; Rheingold, A. L.; Borovik, A. S. Structure and magnetic properties of trigonal bipyramidal iron nitrosyl complexes. *Inorg. Chem.* **1999**, *38*, 3110−3115.

(1780) Shepherd, R. E.; Sweetland, M. A.; Junker, D. E. Ligand field factors in promoting S = 3/2 $\{FeNO\}^7$ nitrosyls. *J. Inorg. Biochem.* **1997**, *65*, 1−14.

(1781) Westre, T. E.; Di Cicco, A.; Filipponi, A.; Natoli, C. R.; Hedman, B.; Solomon, E. I.; Hodgson, K. O. Determination of the Fe-NO angle in $\{FeNO\}^7$ complexes using multiple-scattering EXAFS analysis by GNXAS. *J. Am. Chem. Soc.* **1994**, *116*, 6757−6768.

(1782) Randall, C. R.; Zang, Y.; True, A. E.; Que, L., Jr.; Charnock, J. M.; Garner, C. D.; Fujishima, Y.; Schofield, C. J.; Baldwin, J. E. X-ray absorption studies of the ferrous active site of isopenicillin N synthase and related model complexes. *Biochemistry* **1993**, *32*, 6664−6673.

(1783) Hodges, K. D.; Wollmann, R. G.; Kessel, S. L.; Hendrickson, D. N.; Van Derveer, D. G.; Barefield, E. K. Preparations and properties of nitrosyl complexes of iron tetramethylcyclam. X-ray structures of $[Fe(C_{14}H_{32}N_4)NO](BF_4)_2$, a S = 3/2-1/2 spin-equilibrium complex, and $[Fe(C_{14}H_{32}N_4)(NO)(OH)](ClO_4)_2 \bullet CH_3CN$. *J. Am. Chem. Soc.* **1979**, *101*, 906−917.

(1784) Conradie, J.; Quarless, D. A.; Hsu, H.-F.; Harrop, T. C.; Lippard, S. J.; Koch, S. A.; Ghosh, A. Electronic structure and FeNO conformation of nonheme iron-thiolate-NO complexes: an experimental and DFT study. *J. Am. Chem. Soc.* **2007**, *129*, 10446−10456.

(1785) Banerjee, A.; Li, J.; Speelman, A. L.; White, C. J.; Pawlak, P. L.; Brennessel, W. W.; Lehnert, N.; Chavez, F. A. A structural model for the iron-nitrosyl adduct of gentisate dioxygenase. *Eur. J. Inorg. Chem.* **2018**, *2018*, 4797−4804.

(1786) Li, J.; Banerjee, A.; Pawlak, P. L.; Brennessel, W. W.; Chavez, F. A. Highest recorded N-O stretching frequency for 6-coordinate $\{Fe\text{-}NO\}^7$ complexes: an iron nitrosyl model for His_3 active sites. *Inorg. Chem.* **2014**, *53*, 5414−5416.

(1787) Wolf, M.; Klüfers, P. Structure and bonding of high-spin nitrosyl-iron(II) compounds with mixed N,O-chelators and aqua ligands. *Eur. J. Inorg. Chem.* **2017**, *2017*, 2303−2312.

(1788) Fischer, A. A.; Stracey, N.; Lindeman, S. V.; Brunold, T. C.; Fiedler, A. T. Synthesis, x-ray structures, electronic properties, and O_2/NO reactivities of thiol dioxygenase active-site models. *Inorg. Chem.* **2016**, *55*, 11839−11853.

(1789) Monsch, G.; Klüfers, P. $[Fe(H_2O)_5(NO)]^{2+}$, the "brown-ring" chromophore. *Angew. Chem., Int. Ed.* **2019**, *58*, 8566−8571.

(1790) Lutter, J. C.; Zaleski, C. M.; Pecoraro, V. L. Metallacrowns: Spramolecular constructs with potential in extended solids, solution-state dynamics, molecular magnetism, and imaging. *Advances in Inorganic Chemistry*; van Eldik, R., Puchta, R., Eds.; Academic Press, 2018; Vol. *71*, pp 177−246.

(1791) Lah, M. S.; Pecoraro, V. L. Isolation and characterization of $\{Mn^{II}[Mn^{III}(\text{salicylhydroximate})]_4(\text{acetate})_2(DMF)_6\} \bullet 2DMF$: an inorganic analog of M^{2+}(12-crown-4). *J. Am. Chem. Soc.* **1989**, *111*, 7258−7259.

(1792) Zang, Y.; Kim, J.; Dong, Y.; Wilkinson, E. C.; Appelman, E. H.; Que, L., Jr. Models for nonheme iron intermediates: structural basis for tuning the spin states of Fe(TPA) complexes. *J. Am. Chem. Soc.* **1997**, *119*, 4197−4205.

(1793) Sun, N.; Liu, L. V.; Dey, A.; Villar-Acevedo, G.; Kovacs, J. A.; Darensbourg, M. Y.; Hodgson, K. O.; Hedman, B.; Solomon, E. I. S K-edge x-ray absorption spectroscopy and density functional theory studies of high and low spin $\{FeNO\}^7$ thiolate complexes: exchange stabilization of electron delocalization in $\{FeNO\}^7$ and $\{FeO_2\}^8$. *Inorg. Chem.* **2011**, *50*, 427−436.

(1794) Stephens, P. J. Magnetic circular dichroism. *Adv. Chem. Phys.* **2007**, *35*, 197−264.

(1795) Solomon, E. I.; Pavel, E. G.; Loeb, K. E.; Campochiaro, C. Magnetic circular dichroism spectroscopy as a probe of the geometric and electronic structure of non-heme ferrous enzymes. *Coord. Chem. Rev.* **1995**, *144*, 369−460.

(1796) Neese, F.; Solomon, E. I. MCD C-term signs, saturation behavior, and determination of band polarizations in randomly oriented systems with spin S > 1/2. Applications to S = 1/2 and S = 5/2. *Inorg. Chem.* **1999**, *38*, 1847−1865.

(1797) Oganesyan, V. S.; George, S. J.; Cheesman, M. R.; Thomson, A. J. A novel, general method of analyzing magnetic circular dichroism spectra and magnetization curves of high-spin metal ions: Application to the protein oxidized rubredoxin, *Desulfovibrio gigas*. *J. Chem. Phys.* **1999**, *110*, 762−777.

(1798) Jo, D.-H.; Chiou, Y.-M.; Que, L., Jr. Models for extradiol cleaving catechol dioxygenases: syntheses, structures, and reactivities of iron(II)-monoanionic catecholate complexes. *Inorg. Chem.* **2001**, *40*, 3181−3190.

(1799) Confer, A. M.; McQuilken, A. C.; Matsumura, H.; Moënne-Loccoz, P.; Goldberg, D. P. A nonheme, high-spin $\{FeNO\}^8$ complex that spontaneously generates N_2O. *J. Am. Chem. Soc.* **2017**, *139*, 10621−10624.

(1800) England, J.; Guo, Y.; Farquhar, E. R.; Young, V. G., Jr.; Münck, E.; Que, L., Jr. The crystal structure of a high-spin oxoiron(IV) complex and characterization of its self-decay pathway. *J. Am. Chem. Soc.* **2010**, *132*, 8635−8644.

(1801) England, J.; Martinho, M.; Farquhar, E. R.; Frisch, J. R.; Bominaar, E. L.; Münck, E.; Que, L., Jr. A synthetic high-spin oxoiron(IV) complex: generation, spectroscopic characterization, and reactivity. *Angew. Chem., Int. Ed.* **2009**, *48*, 3622−3626.

(1802) Pluth, M. D.; Lippard, S. J. Reversible binding of nitric oxide to an Fe(III) complex of a tetra-amido macrocycle. *Chem. Commun.* **2012**, *48*, 11981−11983.

(1803) Hong, S.; Yan, J. J.; Karmalkar, D. G.; Sutherlin, K. D.; Kim, J.; Lee, Y.-M.; Goo, Y.; Mascharak, P. K.; Hedman, B.; Hodgson, K. O.; Karlin, K. D.; Solomon, E. I.; Nam, W. A mononuclear nonheme $\{FeNO\}^6$ complex: synthesis and structural and spectroscopic characterization. *Chem. Sci.* **2018**, *9*, 6952−6960.

(1804) Patra, A. K.; Rose, M. J.; Olmstead, M. M.; Mascharak, P. K. Reactions of nitric oxide with a low-spin Fe(III) center ligated to a tetradentate dicarboxamide N4 ligand: parallels between heme and non-heme systems. *J. Am. Chem. Soc.* **2004**, *126*, 4780−4781.

(1805) Eroy-Reveles, A. A.; Hoffman-Luca, C. G.; Mascharak, P. K. Formation of a triply bridged μ-oxo diiron(III) core stabilized by two deprotonated carboxamide groups upon photorelease of NO from a $\{Fe\text{-}NO\}^6$ iron nitrosyl. *Dalton Trans.* **2007**, 5268−5274.

(1806) Rose, M. J.; Betterley, N. M.; Mascharak, P. K. Thiolate S-oxygenation controls nitric oxide (NO) photolability of a synthetic iron nitrile hydratase (Fe-NHase) model derived from mixed carboxamide/thiolate ligand. *J. Am. Chem. Soc.* **2009**, *131*, 8340−8341.

(1807) Lugo-Mas, P.; Taylor, W.; Schweitzer, D.; Theisen, R. M.; Xu, L.; Shearer, J.; Swartz, R. D.; Gleaves, M. C.; DiPasquale, A.; Kaminsky, W.; Kovacs, J. A. Properties of square-pyramidal alkyl-thiolate Fe^{III} complexes, including an analogue of the unmodified form of nitrile hydratase. *Inorg. Chem.* **2008**, *47*, 11228−11236.

(1808) Lugo-Mas, P.; Dey, A.; Xu, L.; Davin, S. D.; Benedict, J.; Kaminsky, W.; Hodgson, K. O.; Hedman, B.; Solomon, E. I.; Kovacs, J. A. How does single oxygen atom addition affect the properties of an Fe-nitrile hydratase analogue? The compensatory role of the unmodified thiolate. *J. Am. Chem. Soc.* **2006**, *128*, 11211−11221.

(1809) Shearer, J.; Jackson, H. L.; Schweitzer, D.; Rittenberg, D. K.; Leavy, T. M.; Kaminsky, W.; Scarrow, R. C.; Kovacs, J. A. The first example of a nitrile hydratase model complex that reversibly binds nitriles. *J. Am. Chem. Soc.* **2002**, *124*, 11417−11428.

(1810) Anderson, J. S.; Rittle, J.; Peters, J. C. Catalytic conversion of nitrogen to ammonia by an iron model complex. *Nature* **2013**, *501*, 84−87.

(1811) Wasserfallen, A.; Ragettli, S.; Jouanneau, Y.; Leisinger, T. A family of flavoproteins in the domains archaea and bacteria. *Eur. J. Biochem.* **1998**, *254*, 325−332.

(1812) Arkenberg, A.; Runkel, S.; Richardson, D. J.; Rowley, G. The production and detoxification of a potent cytotoxin, nitric oxide, by pathogenic enteric bacteria. *Biochem. Soc. Trans.* **2011**, *39*, 1876−1879.

(1813) Sarti, P.; Fiori, P. L.; Forte, E.; Rappelli, P.; Teixeira, M.; Mastronicola, D.; Sanciu, G.; Giuffré, A.; Brunori, M. *Trichomonas vaginalis* degrades nitric oxide and expresses a flavorubredoxin-like protein: a new pathogenic mechanism? *Cell. Mol. Life Sci.* **2004**, *61*, 618−623.

(1814) Vine, C. E.; Cole, J. A. Unresolved sources, sinks, and pathways for the recovery of enteric bacteria from nitrosative stress. *FEMS Microbiol. Lett.* **2011**, *325*, 325.

(1815) Frederick, R. E.; Caranto, J. D.; Masitas, C. A.; Gebhardt, L. L.; MacGowan, C. E.; Limberger, R. J.; Kurtz, D. M., Jr. Dioxygen and nitric oxide scavenging by *Treponema denticola* flavodiiron protein: a mechanistic paradigm for catalysis. *JBIC, J. Biol. Inorg. Chem.* **2015**, *20*, 603−613.

(1816) Romão, C. V.; Vicente, J. B.; Borges, P. T.; Victor, B. L.; Lamosa, P.; Silva, E.; Pereira, L.; Bandeiras, T. M.; Soares, C. M.; Carrondo, M. A.; Turner, D.; Teixeira, M.; Frazão, C. Structure of *Escherichia coli* flavodiiron nitric oxide reductase. *J. Mol. Biol.* **2016**, *428*, 4686−4707.

(1817) Silaghi-Dumitrescu, R.; Ng, K. Y.; Viswanathan, R.; Kurtz, D. M. A flavo-diiron protein from *Desulfovibrio vulgaris* with oxidase and nitric oxide reductase activities. Evidence for an in vivo nitric oxide scavenging function. *Biochemistry* **2005**, *44*, 3572−3579.

(1818) Eriksson, S.; Lucchini, S.; Thompson, A.; Rhen, M.; Hinton, J. C. D. Unravelling the biology of macrophage infection by gene expression profiling of intracellular *Salmonella enterica*. *Mol. Microbiol.* **2003**, *47*, 103−118.

(1819) Mills, P. C.; Rowley, G.; Spiro, S.; Hinton, J. C. D.; Richardson, D. J. A combination of cytochrome *c* nitrite reductase (NrfA) and flavorubredoxin (NorV) protects *Salmonella enterica* serovar Typhimurium against killing by NO in anoxic environments. *Microbiology* **2008**, *154*, 1218−1228.

(1820) Folgosa, F.; Martins, M.; Teixeira, M. Diversity and complexity of flavodiiron NO/O_2 reductases. *FEMS Microbiol. Lett.* **2018**, *365*, No. fnx267.

(1821) Fang, H.; Caranto, J. D.; Mendoza, R.; Taylor, A. B.; Hart, P. J.; Kurtz, D. M. Histidine ligand variants of a flavo-diiron protein: effects on structure and activities. *JBIC, J. Biol. Inorg. Chem.* **2012**, *17*, 1231−1239.

(1822) Vicente, J. B.; Teixeira, M. Redox and spectroscopic properties of the *Escherichia coli* nitric oxide-detoxifying system involving flavorubredoxin and its NADH-oxidizing redox partner. *J. Biol. Chem.* **2005**, *280*, 34599−34608.

(1823) Borges, P.; Romao, C.; Saraiva, L.; Gonçalves, V.; Carrondo, M.; Teixeira, M.; Frazão, C. Analysis of a new flavodiiron core structural arrangement in Flv1-ΔFlR protein from *Synechocystis* sp. PCC6803. *J. Struct. Biol.* **2019**, *205*, 91−102.

(1824) Folgosa, F.; Martins, M. C.; Teixeira, M. The multidomain flavodiiron protein from *Clostridium difficile* 630 is an NADH:oxygen oxidoreductase. *Sci. Rep.* **2018**, *8*, 10164.

(1825) Vicente, J.; Tran, V.; Pinto, L.; Teixeira, M.; Singh, U. A detoxifying oxygen reductase in the anaerobic protozoan *Entamoeba histolytica*. *Eukaryotic Cell* **2012**, *11*, 1112−1118.

(1826) Silaghi-Dumitrescu, R.; Coulter, E. D.; Das, A.; Ljungdahl, L. G.; Jameson, G. N. L.; Huynh, B. H.; Kurtz, D. M., Jr. A flavodiiron protein and high molecular weight rubredoxin from *Moorella thermoacetica* with nitric oxide reductase activity. *Biochemistry* **2003**, *42*, 2806−2815.

(1827) Seedorf, H.; Hagemeier, C.; Shima, S.; Thauer, R.; Warkentin, E.; Ermler, U. Structure of coenzyme $F_{420}H_2$ oxidase (FprA), a di-iron flavoprotein from methanogenic Archaea catalyzing the reduction of O_2 to H_2O. *FEBS J.* **2007**, *274*, 1588−1599.

(1828) Hillmann, F.; Riebe, O.; Fischer, R.; Mot, A.; Caranto, J.; Kurtz, D.; Bahl, H. Reductive dioxygen scavenging by flavo-diiron proteins of *Clostridium acetobutylicum*. *FEBS Lett.* **2009**, *583*, 241−245.

(1829) Di Matteo, A.; Scandurra, F. M.; Testa, F.; Forte, E.; Sarti, P.; Brunori, M.; Giuffre, A. The O_2-scavenging flavodiiron protein in the human parasite *Giardia intestinalis*. *J. Biol. Chem.* **2008**, *283*, 4061−4068.

(1830) Vicente, J. B.; Gomes, C. M.; Wasserfallen, A.; Teixeira, M. Module fusion in an A-type flavoprotein from the cyanobacterium *Synechocystis* condenses a multiple-component pathway in a single polypeptide chain. *Biochem. Biophys. Res. Commun.* **2002**, *294*, 82−87.

(1831) Biswas, S.; Kurtz, D. M.; Montoya, S. R.; Hendrich, M. P.; Bominaar, E. L. The catalytic role of a conserved tyrosine in nitric oxide-reducing non-heme diiron enzymes. *ACS Catal.* **2020**, *10*, 8177−8186.

(1832) Martins, M. C.; Romão, C. V.; Folgosa, F.; Borges, P. T.; Frazão, C.; Teixeira, M. How superoxide reductases and flavodiiron proteins combat oxidative stress in anaerobes. *Free Radical Biol. Med.* **2019**, *140*, 36−60.

(1833) Caranto, J. D.; Weitz, A.; Hendrich, M. P.; Kurtz, D. M., Jr. The nitric oxide reductase mechanism of a flavo-diiron protein: identification of active-site intermediates and products. *J. Am. Chem. Soc.* **2014**, *136*, 7981−7992.

(1834) Weitz, A. C.; Giri, N.; Caranto, J. D.; Kurtz, D. M.; Bominaar, E. L.; Hendrich, M. P. Spectroscopy and DFT calculations of a flavo-diiron enzyme implicate new diiron site structures. *J. Am. Chem. Soc.* **2017**, *139*, 12009−12019.

(1835) Weitz, A. C.; Giri, N.; Frederick, R. E.; Kurtz, D. M.; Bominaar, E. L.; Hendrich, M. P. Spectroscopy and DFT calculations of flavo-diiron nitric oxide reductase identify bridging structures of NO-coordinated diiron intermediates. *ACS Catal.* **2018**, *8*, 11704−11715.

(1836) Hayashi, T.; Caranto, J. D.; Matsumura, H.; Kurtz, D. M., Jr.; Moënne-Loccoz, P. Vibrational analysis of mononitrosyl complexes in hemerythrin and flavodiiron proteins: relevance to detoxifying NO reductase. *J. Am. Chem. Soc.* **2012**, *134*, 6878−6884.

(1837) Kurtz, D. M., Jr. Flavo-diiron enzymes: nitric oxide or dioxygen reductases? *Dalton Trans.* **2007**, 4115−4121.

(1838) Caranto, J. D.; Weitz, A.; Giri, N.; Hendrich, M. P.; Kurtz, D. M., Jr. A diferrous-dinitrosyl intermediate in the N_2O-generating pathway of a deflavinated flavo-diiron protein. *Biochemistry* **2014**, *53*, 5631−5637.

(1839) Coufal, D. E.; Tavares, P.; Pereira, A. S.; Hyunh, B. H.; Lippard, S. J. Reactions of nitric oxide with the reduced non-heme diiron center of the soluble methane monooxygenase hydroxylase. *Biochemistry* **1999**, *38*, 4504−4513.

(1840) Haskin, C. J.; Ravi, N.; Lynch, J. B.; Muenck, E.; Que, L., Jr. Reaction of NO with the reduced R2 protein of ribonucleotide reductase from *Escherichia coli*. *Biochemistry* **1995**, *34*, 11090−11098.

(1841) Jana, M.; White, C. J.; Pal, N.; Demeshko, S.; Meyer, F.; Lehnert, N.; Majumdar, A.; et al. Functional models for the mono- and dinitrosyl intermediates of FNORs: semireduction versus superreduction of NO. *J. Am. Chem. Soc.* **2020**, *142*, 6600−6616.

(1842) White, C. J.; Speelman, A. L.; Kupper, C.; Demeshko, S.; Meyer, F.; Shanahan, J. P.; Alp, E. E.; Hu, M.; Zhao, J.; Lehnert, N. The semireduced mechanism for nitric oxide reduction by non-heme diiron complexes: modeling flavodiiron nitric oxide reductases. *J. Am. Chem. Soc.* **2018**, *140*, 2562−2574.

(1843) Zheng, S.; Berto, T. C.; Dahl, E. W.; Hoffman, M. B.; Speelman, A. L.; Lehnert, N. The functional model complex $[Fe_2(BPMP)(OPr)(NO)_2](BPh_4)_2$ provides insight into the mechanism of flavodiiron NO reductases. *J. Am. Chem. Soc.* **2013**, *135*, 4902−4905.

(1844) Rosenzweig, A. C.; Nordlund, P.; Takahara, P. M.; Frederick, C. A.; Lippard, S. J. Geometry of the soluble methane monooxygenase catalytic diiron center in two oxidation states. *Chem. Biol.* **1995**, *2*, 409−418.

(1845) Logan, D. T.; Su, X.-D.; Berg, A.; Regnström, K.; Hajdu, J.; Eklund, H.; Nordlund, P. Crystal structure of reduced protein R2 of ribonucleotide reductase: the structural basis for oxygen activation at a dinuclear iron site. *Structure* **1996**, *4*, 1053−1064.

(1846) Hendrich, M. P.; Munck, E.; Fox, B. G.; Lipscomb, J. D. Integer-spin EPR studies of the fully reduced methane monooxygenase hydroxylase component. *J. Am. Chem. Soc.* **1990**, *112*, 5861−5865.

(1847) Pulver, S. C.; Tong, W. H.; Bollinger, J. M.; Stubbe, J.; Solomon, E. I. Circular dichroism and magnetic circular dichroism studies of the fully reduced binuclear non-heme iron active site in the *Escherichia coli* R2 subunit of ribonucleoside diphosphate reductase. *J. Am. Chem. Soc.* **1995**, *117*, 12664−12678.

(1848) Feig, A. L.; Bautista, M. T.; Lippard, S. J. A carboxylate-bridged non-heme diiron dinitrosyl complex. *Inorg. Chem.* **1996**, *35*, 6892−6898.

(1849) Dong, Y.; Menage, S.; Brennan, B. A.; Elgren, T. E.; Jang, H. G.; Pearce, L. L.; Que, L., Jr. Dioxygen binding to diferrous centers. Models for diiron-oxo proteins. *J. Am. Chem. Soc.* **1993**, *115*, 1851−1859.

(1850) Jiang, Y.; Hayashi, T.; Matsumura, H.; Do, L. H.; Majumdar, A.; Lippard, S. J.; Moënne-Loccoz, P. Light-induced N_2O production from a non-heme iron-nitrosyl dimer. *J. Am. Chem. Soc.* **2014**, *136*, 12524−12527.

(1851) Jana, M.; Pal, N.; White, C. J.; Kupper, C.; Meyer, F.; Lehnert, N.; Majumdar, A. Functional mononitrosyl diiron(II) complex mediates the reduction of NO to N_2O with relevance for flavodiiron NO reductases. *J. Am. Chem. Soc.* **2017**, *140*, 14380−14383.

(1852) Kindermann, N.; Schober, A.; Demeshko, S.; Lehnert, N.; Meyer, F. Reductive transformations of a pyrazolate-based bioinspired diiron-dinitrosyl complex. *Inorg. Chem.* **2016**, *55*, 11538−11550.

(1853) Dong, H. T.; White, C. J.; Zhang, B.; Krebs, C.; Lehnert, N. Non-heme diiron model complexes can mediate direct NO reduction: mechanistic insight into flavodiiron NO reductases. *J. Am. Chem. Soc.* **2018**, *140*, 13429−13440.

(1854) White, C. J. *Modelling flavodiiron nitric oxide reductases: geometric and electronic structure of key intermediates and mechanistic insights*; University of Michigan, 2020.

(1855) Kurtz, D. M. Oxo- and hydroxo-bridged diiron complexes: a chemical perspective on a biological unit. *Chem. Rev.* **1990**, *90*, 585−606.

(1856) Pal, N.; White, C. J.; Demeshko, S.; Meyer, F.; Lehnert, N.; Majumdar, A. A monohydrosulfidodinitrosyldiiron complex that generates $N_{-2}O$ as a model for flavodiiron nitric oxide reductases: reaction mechanism and electronic structure. *Inorg. Chem.* **2021**, *60*, No. asap.

(1857) Lanznaster, M.; Neves, A.; Bortoluzzi, A. J.; Aires, V. V. E.; Szpoganicz, B.; Terenzi, H.; Severino, P. C.; Fuller, J. M.; Drew, S. C.; Gahan, L. R.; Hanson, G. R.; Riley, M. J.; Schenk, G. A new heterobinuclear Fe^{III}Cu^{II} complex with a single terminal Fe^{III}-O(phenolate) bond. Relevance to purple acid phosphatases and nucleases. *JBIC, J. Biol. Inorg. Chem.* **2005**, *10*, 319−332.

(1858) Lanznaster, M.; Neves, A.; Bortoluzzi, A. J.; Szpoganicz, B.; Schwingel, E. New Fe^{III}Zn^{II} complex containing a single terminal Fe-O$_{\text{phenolate}}$ bond as a structural and functional model for the active site of red kidney bean purple acid phosphatase. *Inorg. Chem.* **2002**, *41*, 5641−5643.

(1859) Neves, A.; de Brito, M. A.; Vencato, I.; Drago, V.; Griesar, K.; Haase, W. Fe^{III}Fe^{III} and Fe^{II}Fe^{III} complexes as synthetic analogues for the oxidized and reduced forms of purple acid phosphatases. *Inorg. Chem.* **1996**, *35*, 2360−2368.

(1860) Neves, A.; Lanznaster, M.; Bortoluzzi, A. J.; Peralta, R. A.; Casellato, A.; Castellano, E. E.; Herrald, P.; Riley, M. J.; Schenk, G. An unprecedented Fe^{III}((-OH)Zn^{II} complex that mimics the structural and functional properties of purple acid phosphatases. *J. Am. Chem. Soc.* **2007**, *129*, 7486−7487.

(1861) Peralta, R. A.; Bortoluzzi, A. J.; de Souza, B.; Jovito, R.; Xavier, F. R.; Couto, R. A. A.; Casellato, A.; Nome, F.; Dick, A.; Gahan, L. R.; Schenk, G.; Hanson, G. R.; de Paula, F. C. S.; Pereira-Maia, E. C.; de, P.; Machado, S.; Severino, P. C.; Pich, C.; Bortolotto, T.; Terenzi, H.; Castellano, E. E.; Neves, A.; Riley, M. J. Electronic structure and spectro-structural correlations of Fe^{III}Zn^{II} biomimetics for purple acid phosphatases: relevance to DNA cleavage and cytotoxic activity. *Inorg. Chem.* **2010**, *49*, 11421−11438.

(1862) Van Stappen, C.; Lehnert, N. Mechanism of N-N bond formation by transition metal-nitrosyl complexes: modeling flavodiiron nitric oxide reductases. *Inorg. Chem.* **2018**, *57*, 4252−4269.

(1863) Ferretti, E.; Dechert, S.; Demeshko, S.; Holthausen, M. C.; Meyer, F. Reductive nitric oxide coupling at a dinickel core: isolation of a key *cis*-hyponitrite intermediate en route to N_2O formation. *Angew. Chem., Int. Ed.* **2019**, *58*, 1705−1709.

(1864) Wright, A. M.; Wu, G.; Hayton, T. W. Formation of N_2O from a nickel nitrosyl: isolation of the cis-$[N_2O_2]^{2-}$ intermediate. *J. Am. Chem. Soc.* **2012**, *134*, 9930−9933.

(1865) Wright, A. M.; Hayton, T. W. Recent developments in late metal nitrosyl chemistry. *Comments Inorg. Chem.* **2012**, *33*, 207−248.

(1866) Attia, A. A. A.; Silaghi-Dumitrescu, R. Super-reduced mechanism of nitric oxide reduction in flavo-diiron NO reductases. *Eur. J. Inorg. Chem.* **2014**, *2014*, 6061−6065.

(1867) Lu, J.; Bi, B.; Lai, W.; Chen, H. Origin of nitric oxide reduction activity in flavo-diiron NO reductase: key roles of the second coordination sphere. *Angew. Chem., Int. Ed.* **2019**, *58*, 3795−3799.

(1868) Gans, P. Reactions of nitric oxide with cobalt(II) ammine complexes and other reducing agents. *J. Chem. Soc. A* **1967**, 943−946.

(1869) Feltham, R. D. Metal nitrosyls. IV. On the red and black isomers of cobalt nitrosopentaammines. *Inorg. Chem.* **1964**, *3*, 1038−1039.

(1870) Hoskins, B. F.; Whillans, F. D. Crystal and molecular structure of a μ-hyponitrito-bis[penta-amminecobalt(III)] salt: the nature of the red nitrosylpenta-amminecobalt(III) cation. *J. Chem. Soc., Dalton Trans.* **1973**, 607−611.

(1871) Villalba, M. E. C.; Navaza, A.; Güida, J. A.; Varetti, E. L.; Aymonino, P. J. New structural study and reinterpretation of the vibrational spectra of the a-*N,O*-hyponitrite bis[pentamminecobalt-(III)]$^{4+}$ cation. *Inorg. Chim. Acta* **2006**, *359*, 707−712.

(1872) Walter, M. R.; Dzul, S. P.; Rodrigues, A. V.; Stemmler, T. L.; Telser, J.; Conradie, J.; Ghosh, A.; Harrop, T. C. Synthesis of Co^{II}-NO^{-} complexes and their reactivity as a source of nitroxyl. *J. Am. Chem. Soc.* **2016**, *138*, 12459−12471.

(1873) Wright, A. M.; Zaman, H. T.; Wu, G.; Hayton, T. W. Mechanistic insights into the formation of N_2O by a nickel nitrosyl complex. *Inorg. Chem.* **2014**, *53*, 3108−3116.

(1874) Kundu, S.; Phu, P. N.; Ghosh, P.; Kozimor, S. A.; Bertke, J. A.; Stieber, S. C. E.; Warren, T. H. Nitrosyl linkage isomers: NO coupling to N_2O at a mononuclear site. *J. Am. Chem. Soc.* **2019**, *141*, 1415−1419.

(1875) Arikawa, Y.; Asayama, T.; Moriguchi, Y.; Agari, S.; Onishi, M. Reversible N-N coupling of NO ligands on dinuclear ruthenium complexes and subsequent N_2O evolution: relevance to nitric oxide reductase. *J. Am. Chem. Soc.* **2007**, *129*, 14160−14161.

(1876) Arikawa, Y.; Onishi, M. Reductive N-N coupling of NO molecules on transition metal complexes leading to N_2O. *Coord. Chem. Rev.* **2012**, *256*, 468−478.

(1877) Arikawa, Y.; Matsumoto, N.; Asayama, T.; Umakoshi, K.; Onishi, M. Conversion of oxido-bridged dinuclear ruthenium complex to dicationic dinitrosyl ruthenium complex using proton and nitric oxide: Completion of NO reduction cycle. *Dalton Trans.* **2011**, *40*, 2148−2150.

(1878) Arikawa, Y.; Hiura, J.; Tsuchii, C.; Kodama, M.; Matsumoto, N.; Umakoshi, K. A synthetic NO reduction cycle on a bis(pyrazolato)-bridged dinuclear ruthenium complex including photo-induced transformation. *Dalton Trans.* **2018**, *47*, 7399−7401.

(1879) Ruggiero, C. E.; Carrier, S. M.; Tolman, W. B. Reductive disproportionation of NO mediated by copper complexes: modeling N_2O generation by copper proteins and heterogeneous catalysts. *Angew. Chem., Int. Ed. Engl.* **1994**, *33*, 895−897.

(1880) Wijeratne, G. B.; Hematian, S.; Siegler, M. A.; Karlin, K. D. Copper(I)/NO(g) reductive coupling producing a trans-hyponitrite bridged dicopper(II) complex: redox reversal giving copper(I)/NO(g) disproportionation. *J. Am. Chem. Soc.* **2017**, *139*, 13276−13279.

(1881) Ruggiero, C. E.; Carrier, S. M.; Antholine, W. E.; Whittaker, J. W.; Cramer, C. J.; Tolman, W. B. Synthesis and structural and spectroscopic characterization of mononuclear copper nitrosyl complexes: models for nitric oxide adducts of copper proteins and copper-exchanged zeolites. *J. Am. Chem. Soc.* **1993**, *115*, 11285−11298.

(1882) Metz, S. N_2O formation via reductive disproportionation of NO by mononuclear copper complexes: a mechanistic DFT study. *Inorg. Chem.* **2017**, *56*, 3820−3833.

(1883) Lionetti, D.; De Ruiter, G.; Agapie, T. A trans-hyponitrite intermediate in the reductive coupling and deoxygenation of nitric oxide by a tricopper-Lewis acid complex. *J. Am. Chem. Soc.* **2016**, *138*, 5008−5011.

(1884) Wijeratne, G. B.; Bhadra, M.; Siegler, M. A.; Karlin, K. D. Copper(I) complex mediated nitric oxide reductive coupling: ligand hydrogen bonding derived proton transfer promotes N_2O(g) release. *J. Am. Chem. Soc.* **2019**, *141*, 17962−17967.

(1885) Büsch, A.; Pohlmann, A.; Friedrich, B.; Cramm, R. A DNA region recognized by the nitric oxide-responsive transcriptional activator NorR Is conserved in β- and γ-proteobacteria. *J. Bacteriol.* **2004**, *186*, 7980.

(1886) Tucker, N. P.; D'Autréaux, B.; Yousafzai, F. K.; Fairhurst, S. A.; Spiro, S.; Dixon, R. Analysis of the nitric oxide-sensing non-heme iron center in the NorR regulatory protein. *J. Biol. Chem.* **2008**, *283*, 908−918.

(1887) Baptista, J.; Justino, M.; Melo, A.; Teixeira, M.; Saraiva, L. Oxidative stress modulates the nitric oxide defense promoted by *Escherichia coli* flavorubredoxin. *J. Bacteriol.* **2012**, *194*, 3611−3617.

(1888) Bush, M.; Ghosh, T.; Tucker, N.; Zhang, X.; Dixon, R. Nitric oxide-responsive interdomain regulation targets the R^{54}-interaction surface in the enhancer binding protein NorR. *Mol. Microbiol.* **2010**, *77*, 1278−1288.

(1889) Bush, M.; Ghosh, T.; Sawicka, M.; Moal, I. H.; Bates, P. A.; Dixon, R.; Zhang, X. The structural basis for enhancer-dependent assembly and activation of the AAA transcriptional activator NorR. *Mol. Microbiol.* **2015**, *95*, 17−30.

(1890) Adrait, A.; Jacquamet, L.; Le Pape, L.; Gonzalez de Peredo, A.; Aberdam, D.; Hazemann, J.-L.; Latour, J.-M.; Michaud-Soret, I. Spectroscopic and saturation magnetization properties of the manganese- and cobalt-substituted Fur (ferric uptake regulation) protein from *Escherichia coli*. *Biochemistry* **1999**, *38*, 6248−6260.

(1891) Pohl, E.; Haller, J. C.; Mijovilovich, A.; Meyer-Klaucke, W.; Garman, E.; Vasil, M. L. Architecture of a protein central to iron homeostasis: crystal structure and spectroscopic analysis of the ferric uptake regulator. *Mol. Microbiol.* **2003**, *47*, 903−915.

(1892) Jacquamet, L.; Dole, F.; Jeandey, C.; Oddou, J.-L.; Perret, E.; Le Pape, L.; Aberdam, D.; Hazemann, J.-L.; Michaud-Soret, I.; Latour, J.-M. First spectroscopic characterization of Fe^{II}-Fur, the physiological active form of the Fur protein. *J. Am. Chem. Soc.* **2000**, *122*, 394−395.

(1893) Moore, C.; Nakano, M.; Wang, T.; Ye, R.; Helmann, J. Response of *Bacillus subtilis* to nitric oxide and the nitrosating agent sodium nitroprusside. *J. Bacteriol.* **2004**, *186*, 4655−4664.

(1894) Lee, J.-W.; Helmann, J. D. The PerR transcription factor senses H_2O_2 by metal-catalysed histidine oxidation. *Nature* **2006**, *440*, 363−367.

(1895) Kebouchi, M.; Saul, F.; Taher, R.; Landier, A.; Beaudeau, B.; Dubrac, S.; Weber, P.; Haouz, A.; Picardeau, M.; Benaroudj, N. Structure and function of the *Leptospira interrogans* peroxide stress regulator (PerR), an atypical PerR devoid of a structural metal-binding site. *J. Biol. Chem.* **2018**, *293*, 497−509.

(1896) Blair, L. M.; Sperry, J. Natural products containing a nitrogen-nitrogen bond. *J. Nat. Prod.* **2013**, *76*, 794−812.

(1897) Caranto, J. D. The emergence of nitric oxide in the biosynthesis of bacterial natural products. *Curr. Opin. Chem. Biol.* **2019**, *49*, 130−138.

(1898) Wang, M.; Niikura, H.; He, H.-Y.; Daniel-Ivad, P.; Ryan, K. S. Biosynthesis of the N-N-Bond-containing compound l-alanosine. *Angew. Chem., Int. Ed.* **2020**, *59*, 3881−3885.

(1899) Ng, T. L.; Rohac, R.; Mitchell, A. J.; Boal, A. K.; Balskus, E. P. An N-nitrosating metalloenzyme constructs the pharmacophore of streptozotocin. *Nature* **2019**, *566*, 94−99.

(1900) McBride, M. J.; Sil, D.; Ng, T. L.; Crooke, A. M.; Kenney, G. E.; Tysoe, C. R.; Zhang, B.; Balskus, E. P.; Boal, A. K.; Krebs, C.; Bollinger, J. M. A peroxodiiron(III/III) intermediate mediating both N-hydroxylation steps in biosynthesis of the N-nitrosourea pharmacophore of streptozotocin by the multi-domain metalloenzyme SznF. *J. Am. Chem. Soc.* **2020**, *142*, 11818−11828.

(1901) He, H.-Y.; Henderson, A. C.; Du, Y.-L.; Ryan, K. S. Two-enzyme pathway links L-arginine to nitric oxide in N-Nitroso biosynthesis. *J. Am. Chem. Soc.* **2019**, *141*, 4026−4033.

(1902) Graham, D. E.; Spain, J. C.; Parry, R. J.; Hettich, R. L.; Mahan, K. M.; Klingeman, D. M.; Giannone, R. J.; Gulvick, C. A.; Fida, T. T. *Nitration enzyme toolkit for the biosynthesis of energetic materials*; Oak Ridge National Laboratory: Oak Ridge, TN, 2018.